

Beniamino Murgante Osvaldo Gervasi
Sanjay Misra Nadia Nedjah
Ana Maria A.C. Rocha David Taniar
Bernady O. Apduhan (Eds.)

LNCS 7333

Computational Science and Its Applications – ICCSA 2012

12th International Conference
Salvador de Bahia, Brazil, June 2012
Proceedings, Part I

1
Part I

 Springer

Commenced Publication in 1973

Founding and Former Series Editors:

Gerhard Goos, Juris Hartmanis, and Jan van Leeuwen

Editorial Board

David Hutchison

Lancaster University, UK

Takeo Kanade

Carnegie Mellon University, Pittsburgh, PA, USA

Josef Kittler

University of Surrey, Guildford, UK

Jon M. Kleinberg

Cornell University, Ithaca, NY, USA

Alfred Kobsa

University of California, Irvine, CA, USA

Friedemann Mattern

ETH Zurich, Switzerland

John C. Mitchell

Stanford University, CA, USA

Moni Naor

Weizmann Institute of Science, Rehovot, Israel

Oscar Nierstrasz

University of Bern, Switzerland

C. Pandu Rangan

Indian Institute of Technology, Madras, India

Bernhard Steffen

TU Dortmund University, Germany

Madhu Sudan

Microsoft Research, Cambridge, MA, USA

Demetri Terzopoulos

University of California, Los Angeles, CA, USA

Doug Tygar

University of California, Berkeley, CA, USA

Gerhard Weikum

Max Planck Institute for Informatics, Saarbruecken, Germany

Beniamino Murgante Osvaldo Gervasi
Sanjay Misra Nadia Nedjah
Ana Maria A.C. Rocha David Taniar
Bernady O. Apduhan (Eds.)

Computational Science and Its Applications – ICCSA 2012

12th International Conference
Salvador de Bahia, Brazil, June 18-21, 2012
Proceedings, Part I

Volume Editors

Beniamino Murgante

University of Basilicata, Potenza, Italy, E-mail: beniamino.murgante@unibas.it

Oswaldo Gervasi

University of Perugia, Italy, E-mail: osvaldo@unipg.it

Sanjay Misra

Federal University of Technology, Minna, Nigeria, E-mail: smisra@futminna.edu.ng

Nadia Nedjah

State University of Rio de Janeiro, Brazil, E-mail: nadia@eng.uerj.br

Ana Maria A. C. Rocha

University of Minho, Braga, Portugal, E-mail: arocha@dps.uminho.pt

David Taniar

Monash University, Clayton, VIC, Australia, E-mail: david.taniar@infotech.monash.edu.au

Bernady O. Apduhan

Kyushu Sangyo University, Fukuoka, Japan, E-mail: bob@is.kyusan-u.ac.jp

ISSN 0302-9743

e-ISSN 1611-3349

ISBN 978-3-642-31124-6

e-ISBN 978-3-642-31125-3

DOI 10.1007/978-3-642-31125-3

Springer Heidelberg Dordrecht London New York

Library of Congress Control Number: 2012939389

CR Subject Classification (1998): C.2.4, C.2, H.4, F.2, H.3, D.2, F.1, H.5, H.2.8, K.6.5, I.3

LNCS Sublibrary: SL 1 – Theoretical Computer Science and General Issues

© Springer-Verlag Berlin Heidelberg 2012

This work is subject to copyright. All rights are reserved, whether the whole or part of the material is concerned, specifically the rights of translation, reprinting, re-use of illustrations, recitation, broadcasting, reproduction on microfilms or in any other way, and storage in data banks. Duplication of this publication or parts thereof is permitted only under the provisions of the German Copyright Law of September 9, 1965, in its current version, and permission for use must always be obtained from Springer. Violations are liable to prosecution under the German Copyright Law.

The use of general descriptive names, registered names, trademarks, etc. in this publication does not imply, even in the absence of a specific statement, that such names are exempt from the relevant protective laws and regulations and therefore free for general use.

Typesetting: Camera-ready by author, data conversion by Scientific Publishing Services, Chennai, India

Printed on acid-free paper

Springer is part of Springer Science+Business Media (www.springer.com)

Preface

This four-part volume (LNCS 7333-7336) contains a collection of research papers from the 12th International Conference on Computational Science and Its Applications (ICCSA 2012) held in Salvador de Bahia, Brazil, during June 18–21, 2012. ICCSA is one of the successful international conferences in the field of computational sciences, and this year for the first time in the history of the ICCSA conference series it was held in South America. Previously the ICCSA conference series have been held in Santander, Spain (2011), Fukuoka, Japan (2010), Suwon, Korea (2009), Perugia, Italy (2008), Kuala Lumpur, Malaysia (2007), Glasgow, UK (2006), Singapore (2005), Assisi, Italy (2004), Montreal, Canada (2003), (as ICCS) Amsterdam, The Netherlands (2002), and San Francisco, USA (2001).

The computational science community has enthusiastically embraced the successive editions of ICCSA, thus contributing to making ICCSA a focal meeting point for those interested in innovative, cutting-edge research about the latest and most exciting developments in the field. We are grateful to all those who have contributed to the ICCSA conference series.

ICCSA 2012 would not have been made possible without the valuable contribution of many people. We would like to thank all session organizers for their diligent work, which further enhanced the conference level, and all reviewers for their expertise and generous effort, which led to a very high quality event with excellent papers and presentations. We specially recognize the contribution of the Program Committee and local Organizing Committee members for their tremendous support and for making this congress a very successful event. We would like to sincerely thank our keynote speakers, who willingly accepted our invitation and shared their expertise.

We also thank our publisher, Springer, for accepting to publish the proceedings and for their kind assistance and cooperation during the editing process.

Finally, we thank all authors for their submissions and all conference attendees for making ICCSA 2012 truly an excellent forum on computational science, facilitating the exchange of ideas, fostering new collaborations and shaping the future of this exciting field. Last, but certainly not least, we wish to thank our readers for their interest in this volume. We really hope you find in these pages interesting material and fruitful ideas for your future work.

We cordially invite you to visit the ICCSA website—<http://www.iccsa.org>—where you can find relevant information about this interesting and exciting event.

June 2012

Oswaldo Gervasi
David Taniar

Organization

ICCSA 2012 was organized by Universidade Federal da Bahia (Brazil), Universidade Federal do Recôncavo da Bahia (Brazil), Universidade Estadual de Feira de Santana (Brazil), University of Perugia (Italy), University of Basilicata (Italy), Monash University (Australia), and Kyushu Sangyo University (Japan).

Honorary General Chairs

Antonio Laganà	University of Perugia, Italy
Norio Shiratori	Tohoku University, Japan
Kenneth C.J. Tan	Qontix, UK

General Chairs

Oswaldo Gervasi	University of Perugia, Italy
David Taniar	Monash University, Australia

Program Committee Chairs

Bernady O. Apduhan	Kyushu Sangyo University, Japan
Beniamino Murgante	University of Basilicata, Italy

Workshop and Session Organizing Chairs

Beniamino Murgante	University of Basilicata, Italy
--------------------	---------------------------------

Local Organizing Committee

Frederico V. Prudente	Universidade Federal da Bahia, Brazil (Chair)
Mirco Ragni	Universidade Estadual de Feira de Santana, Brazil
Ana Carla P. Bitencourt	Universidade Federal do Recôncavo da Bahia, Brazil
Cassio Pigozzo	Universidade Federal da Bahia, Brazil
Angelo Duarde	Universidade Estadual de Feira de Santana, Brazil
Marcos E. Barreto	Universidade Federal da Bahia, Brazil
José Garcia V. Miranda	Universidade Federal da Bahia, Brazil

International Liaison Chairs

Jemal Abawajy	Deakin University, Australia
Marina L. Gavrilova	University of Calgary, Canada
Robert C.H. Hsu	Chung Hua University, Taiwan
Tai-Hoon Kim	Hannam University, Korea
Andrés Iglesias	University of Cantabria, Spain
Takashi Naka	Kyushu Sangyo University, Japan
Rafael D.C. Santos	National Institute for Space Research, Brazil

Workshop Organizers

Advances in High-Performance Algorithms and Applications (AHPAA 2012)

Massimo Cafaro	University of Salento, Italy
Giovanni Aloisio	University of Salento, Italy

Advances in Web-Based Learning (AWBL 2012)

Mustafa Murat Inceoglu	Ege University, Turkey
------------------------	------------------------

Bio-inspired Computing and Applications (BIOCA 2012)

Nadia Nedjah	State University of Rio de Janeiro, Brazil
Luiza de Macedo Mourell	State University of Rio de Janeiro, Brazil

Computer-Aided Modeling, Simulation, and Analysis (CAMSA 2012)

Jie Shen	University of Michigan, USA
Yuqing Song	Tianjing University of Technology and Education, China

Cloud Computing and Its Applications (CCA 2012)

Jemal Abawajy	University of Deakin, Australia
Oswaldo Gervasi	University of Perugia, Italy

Computational Geometry and Applications (CGA 2012)

Marina L. Gavrilova	University of Calgary, Canada
---------------------	-------------------------------

Chemistry and Materials Sciences and Technologies (CMST 2012)

Antonio Laganà

University of Perugia, Italy

Cities, Technologies and Planning (CTP 2012)

Giuseppe Borruso

University of Trieste, Italy

Beniamino Murgante

University of Basilicata, Italy

Computational Tools and Techniques for Citizen Science and Scientific Outreach (CTTCS 2012)

Rafael Santos

National Institute for Space Research, Brazil

Jordan Raddick

Johns Hopkins University, USA

Ani Thakar

Johns Hopkins University, USA

Econometrics and Multidimensional Evaluation in the Urban Environment (EMEUE 2012)

Carmelo M. Torre

Polytechnic of Bari, Italy

Maria Cerreta

Università Federico II of Naples, Italy

Paola Perchinunno

University of Bari, Italy

Future Information System Technologies and Applications (FISTA 2012)

Bernady O. Apduhan

Kyushu Sangyo University, Japan

Geographical Analysis, Urban Modeling, Spatial Statistics (GEOG-AN-MOD 2012)

Stefania Bertazzon

University of Calgary, Canada

Giuseppe Borruso

University of Trieste, Italy

Beniamino Murgante

University of Basilicata, Italy

International Workshop on Biomathematics, Bioinformatics and Biostatistics (IBBB 2012)

Unal Ufuktepe

Izmir University of Economics, Turkey

Andrés Iglesias

University of Cantabria, Spain

International Workshop on Collective Evolutionary Systems (IWCES 2012)

Alfredo Milani
Clement Leung

University of Perugia, Italy
Hong Kong Baptist University, Hong Kong

Mobile Communications (MC 2012)

Hyunseung Choo

Sungkyunkwan University, Korea

Mobile Computing, Sensing, and Actuation for Cyber Physical Systems (MSA4CPS 2012)

Moonseong Kim
Saad Qaisar

Korean intellectual Property Office, Korea
NUST School of Electrical Engineering and
Computer Science, Pakistan

Optimization Techniques and Applications (OTA 2012)

Ana Maria Rocha

University of Minho, Portugal

Parallel and Mobile Computing in Future Networks (PMCFUN 2012)

Al-Sakib Khan Pathan

International Islamic University Malaysia,
Malaysia

PULSES - Transitions and Nonlinear Phenomena (PULSES 2012)

Carlo Cattani
Ming Li
Shengyong Chen

University of Salerno, Italy
East China Normal University, China
Zhejiang University of Technology, China

Quantum Mechanics: Computational Strategies and Applications (QMCSA 2012)

Mirco Ragni
Frederico Vasconcellos

Universidade Federal de Bahia, Brazil

Prudente
Angelo Marconi Maniero

Universidade Federal de Bahia, Brazil
Universidade Federal de Bahia, Brazil

Ana Carla Peixoto Bitencourt

Universidade Federal do Recôncavo da Bahia,
Brazil

Remote Sensing Data Analysis, Modeling, Interpretation and Applications: From a Global View to a Local Analysis (RS 2012)

Rosa Lasaponara Institute of Methodologies for Environmental
Analysis, National Research Council, Italy
Nicola Masini Archaeological and Monumental Heritage
Institute, National Research Council, Italy

Soft Computing and Data Engineering (SCDE 2012)

Mustafa Matt Deris Universiti Tun Hussein Onn Malaysia, Malaysia
Tutut Herawan Universitas Ahmad Dahlan, Indonesia

Software Engineering Processes and Applications (SEPA 2012)

Sanjay Misra Federal University of Technology Minna,
Nigeria

Software Quality (SQ 2012)

Sanjay Misra Federal University of Technology Minna,
Nigeria

Security and Privacy in Computational Sciences (SPCS 2012)

Arijit Ukil Tata Consultancy Services, India

Tools and Techniques in Software Development Processes (TTSDP 2012)

Sanjay Misra Federal University of Technology Minna,
Nigeria

Virtual Reality and Its Applications (VRA 2012)

Oswaldo Gervasi University of Perugia, Italy
Andr es Iglesias University of Cantabria, Spain

Wireless and Ad-Hoc Networking (WADNet 2012)

Jongchan Lee
Sangjoon Park

Kunsan National University, Korea
Kunsan National University, Korea

Program Committee

Jemal Abawajy	Daekin University, Australia
Kenny Adamson	University of Ulster, UK
Filipe Alvelos	University of Minho, Portugal
Paula Amaral	Universidade Nova de Lisboa, Portugal
Hartmut Asche	University of Potsdam, Germany
Md. Abul Kalam Azad	University of Minho, Portugal
Michela Bertolotto	University College Dublin, Ireland
Sandro Bimonte	CEMAGREF, TSCF, France
Rod Blais	University of Calgary, Canada
Ivan Bleic	University of Sassari, Italy
Giuseppe Borruso	University of Trieste, Italy
Alfredo Buttari	CNRS-IRIT, France
Yves Caniou	Lyon University, France
José A. Cardoso e Cunha	Universidade Nova de Lisboa, Portugal
Leocadio G. Casado	University of Almeria, Spain
Carlo Cattani	University of Salerno, Italy
Mete Celik	Erciyes University, Turkey
Alexander Chemeris	National Technical University of Ukraine “KPI”, Ukraine
Min Young Chung	Sungkyunkwan University, Korea
Gilberto Corso Pereira	Federal University of Bahia, Brazil
M. Fernanda Costa	University of Minho, Portugal
Gaspar Cunha	University of Minho, Portugal
Carla Dal Sasso Freitas	Universidade Federal do Rio Grande do Sul, Brazil
Pradesh Debba	The Council for Scientific and Industrial Research (CSIR), South Africa
Frank Devai	London South Bank University, UK
Rodolphe Devillers	Memorial University of Newfoundland, Canada
Prabu Dorairaj	NetApp, India/USA
M. Irene Falcao	University of Minho, Portugal
Cherry Liu Fang	U.S. DOE Ames Laboratory, USA
Edite M.G.P. Fernandes	University of Minho, Portugal
Jose-Jesus Fernandez	National Centre for Biotechnology, CSIS, Spain
Maria Antonia Forjaz	University of Minho, Portugal
Maria Celia Furtado Rocha	PRODEB–PósCultura/UFBA, Brazil
Akemi Galvez	University of Cantabria, Spain
Paulino Jose Garcia Nieto	University of Oviedo, Spain
Marina Gavrilova	University of Calgary, Canada

Jerome Gensel	LSR-IMAG, France
Maria Giaoutzi	National Technical University, Athens, Greece
Andrzej M. Goscinski	Deakin University, Australia
Alex Hagen-Zanker	University of Cambridge, UK
Malgorzata Hanzl	Technical University of Lodz, Poland
Shanmugasundaram Hariharan	B.S. Abdur Rahman University, India
Eligius M.T. Hendrix	University of Malaga/Wageningen University, Spain/The Netherlands
Hisamoto Hiyoshi	Gunma University, Japan
Fermin Huarte	University of Barcelona, Spain
Andres Iglesias	University of Cantabria, Spain
Mustafa Inceoglu	EGE University, Turkey
Peter Jimack	University of Leeds, UK
Qun Jin	Waseda University, Japan
Farid Karimipour	Vienna University of Technology, Austria
Baris Kazar	Oracle Corp., USA
DongSeong Kim	University of Canterbury, New Zealand
Taihoon Kim	Hannam University, Korea
Ivana Kolingerova	University of West Bohemia, Czech Republic
Dieter Kranzlmüller	LMU and LRZ Munich, Germany
Antonio Laganà	University of Perugia, Italy
Rosa Lasaponara	National Research Council, Italy
Maurizio Lazzari	National Research Council, Italy
Cheng Siong Lee	Monash University, Australia
Sangyoun Lee	Yonsei University, Korea
Jongchan Lee	Kunsan National University, Korea
Clement Leung	Hong Kong Baptist University, Hong Kong
Chendong Li	University of Connecticut, USA
Gang Li	Deakin University, Australia
Ming Li	East China Normal University, China
Fang Liu	AMES Laboratories, USA
Xin Liu	University of Calgary, Canada
Savino Longo	University of Bari, Italy
Tinghuai Ma	NanJing University of Information Science and Technology, China
Sergio Maffioletti	University of Zurich, Switzerland
Ernesto Marcheggiani	Katholieke Universiteit Leuven, Belgium
Antonino Marvuglia	Research Centre Henri Tudor, Luxembourg
Nicola Masini	National Research Council, Italy
Nirvana Meratnia	University of Twente, The Netherlands
Alfredo Milani	University of Perugia, Italy
Sanjay Misra	Federal University of Technology Minna, Nigeria
Giuseppe Modica	University of Reggio Calabria, Italy

José Luis Montaña	University of Cantabria, Spain
Beniamino Murgante	University of Basilicata, Italy
Jiri Nedoma	Academy of Sciences of the Czech Republic, Czech Republic
Laszlo Neumann	University of Girona, Spain
Kok-Leong Ong	Deakin University, Australia
Belen Palop	Universidad de Valladolid, Spain
Marcin Paprzycki	Polish Academy of Sciences, Poland
Eric Pardede	La Trobe University, Australia
Kwangjin Park	Wonkwang University, Korea
Ana Isabel Pereira	Polytechnic Institute of Braganca, Portugal
Maurizio Pollino	Italian National Agency for New Technologies, Energy and Sustainable Economic Development, Italy
Alenka Poplin	University of Hamburg, Germany
Vidyasagar Potdar	Curtin University of Technology, Australia
David C. Prospero	Florida Atlantic University, USA
Wenny Rahayu	La Trobe University, Australia
Jerzy Respondek	Silesian University of Technology Poland
Ana Maria A.C. Rocha	University of Minho, Portugal
Humberto Rocha	INESC-Coimbra, Portugal
Alexey Rodionov	Institute of Computational Mathematics and Mathematical Geophysics, Russia
Cristina S. Rodrigues	University of Minho, Portugal
Octavio Roncero	CSIC, Spain
Maytham Safar	Kuwait University, Kuwait
Haiduke Sarafian	The Pennsylvania State University, USA
Qi Shi	Liverpool John Moores University, UK
Dale Shires	U.S. Army Research Laboratory, USA
Takuo Suganuma	Tohoku University, Japan
Ana Paula Teixeira	University of Tras-os-Montes and Alto Douro, Portugal
Senhorinha Teixeira	University of Minho, Portugal
Parimala Thulasiraman	University of Manitoba, Canada
Carmelo Torre	Polytechnic of Bari, Italy
Javier Martinez Torres	Centro Universitario de la Defensa Zaragoza, Spain
Giuseppe A. Trunfio	University of Sassari, Italy
Unal Ufuktepe	Izmir University of Economics, Turkey
Mario Valle	Swiss National Supercomputing Centre, Switzerland
Pablo Vanegas	University of Cuenca, Ecuador
Piero Giorgio Verdini	INFN Pisa and CERN, Italy
Marco Vizzari	University of Perugia, Italy
Koichi Wada	University of Tsukuba, Japan

Krzysztof Walkowiak
 Robert Weibel
 Roland Wismüller
 Mudasser Wyne
 Chung-Huang Yang
 Xin-She Yang
 Salim Zabir
 Albert Y. Zomaya

Wroclaw University of Technology, Poland
 University of Zurich, Switzerland
 Universität Siegen, Germany
 SOET National University, USA
 National Kaohsiung Normal University, Taiwan
 National Physical Laboratory, UK
 France Telecom Japan Co., Japan
 University of Sydney, Australia

Sponsoring Organizations

ICCSA 2012 would not have been possible without tremendous support of many organizations and institutions, for which all organizers and participants of ICCSA 2012 express their sincere gratitude:



Universidade Federal da Bahia, Brazil
 (<http://www.ufba.br>)



Universidade Federal do Recôncavo da Bahia,
 Brazil
 (<http://www.ufrb.edu.br>)



Universidade Estadual de Feira de Santana,
 Brazil
 (<http://www.uefs.br>)



University of Perugia, Italy
 (<http://www.unipg.it>)



University of Basilicata, Italy
 (<http://www.unibas.it>)



MONASH University

Monash University, Australia
(<http://monash.edu>)



九州産業大学
KYUSHU SANGYO UNIVERSITY

Kyushu Sangyo University, Japan
(www.kyusan-u.ac.jp)



Brazilian Computer Society
(www.sbc.org.br)



Coordenação de Aperfeiçoamento de Pessoal de
Nível Superior (CAPES), Brazil
(<http://www.capes.gov.br>)



National Council for Scientific and
Technological Development (CNPq), Brazil
(<http://www.cnpq.br>)



SECRETARIA DE CIÊNCIA,
TECNOLOGIA E INOVAÇÃO



Fundação de Amparo à Pesquisa do Estado
da Bahia (FAPESB), Brazil
(<http://www.fapesb.ba.gov.br>)

Table of Contents – Part I

Workshop on Advances in High Performance Algorithms and Applications (AHPAA 2012)

Processor Allocation for Optimistic Parallelization of Irregular Programs	1
<i>Francesco Versaci and Keshav Pingali</i>	
Feedback-Based Global Instruction Scheduling for GPGPU Applications	15
<i>Constantin Timm, Markus Görlich, Frank Weichert, Peter Marwedel, and Heinrich Müller</i>	
Parallel Algorithm for Landform Attributes Representation on Multicore and Multi-GPU Systems	29
<i>Murilo Boratto, Pedro Alonso, Carla Ramiro, Marcos Barreto, and Leandro Coelho</i>	
The Performance Model of an Enhanced Parallel Algorithm for the SOR Method	44
<i>Italo Epicoco and Silvia Mocavero</i>	
Performance Driven Cooperation between Kernel and Auto-tuning Multi-threaded Interval B&B Applications	57
<i>Juan Francisco Sanjuan-Estrada, Leocadio Gonzalez Casado, Immaculada García, and Eligius M.T. Hendrix</i>	
k NN-Borůvka-GPU: A Fast and Scalable MST Construction from k NN Graphs on GPU	71
<i>Ahmed Shamsul Arefin, Carlos Riveros, Regina Berretta, and Pablo Moscato</i>	

Workshop on Bio-inspired Computing and Applications (BIOCA 2012)

Global Hybrid Ant Bee Colony Algorithm for Training Artificial Neural Networks	87
<i>Habib Shah, Rozaida Ghazali, Nazri Mohd Nawi, and Mustafa Mat Deris</i>	
The Effect of Intelligent Escape on Distributed SER-Based Search	101
<i>Daniel S.F. Alves, Felipe M.G. França, Luiza de Macedo Mourelle, Nadia Nedjah, and Priscila M.V. Lima</i>	

ACO-Based Static Routing for Network-on-Chips	113
<i>Luneque Silva Jr., Nadia Nedjah, Luiza de Macedo Mourelle, and Fábio Gonçalves Pessanha</i>	
A Genetic Algorithm Assisted by a Locally Weighted Regression Surrogate Model	125
<i>Leonardo G. Fonseca, Heder S. Bernardino, and Helio J.C. Barbosa</i>	
Swarm Robots with Queue Organization Using Infrared Communication	136
<i>Rafael Mathias de Mendonça, Nadia Nedjah, and Luiza de Macedo Mourelle</i>	
Swarm Grid: A Proposal for High Performance of Parallel Particle Swarm Optimization Using GPGPU	148
<i>Rogério M. Calazan, Nadia Nedjah, and Luiza de Macedo Mourelle</i>	
An Artificial Immune System Approach to Associative Classification	161
<i>Samir A. Mohamed Elsayed, Sanguthevar Rajasekaran, and Reda A. Ammar</i>	

Workshop on Computational Geometry and Applications (CGA 2012)

A Review on Delaunay Refinement Techniques	172
<i>Sanderson L. Gonzaga de Oliveira</i>	
Axis-Parallel Dimension Reduction for Biometric Research	188
<i>Kushan Ahmadian and Marina Gavrilova</i>	
An Overview of Procedures for Refining Triangulations	198
<i>Sanderson L. Gonzaga de Oliveira</i>	
DEM Interpolation from Contours Using Medial Axis Transformation	214
<i>Joonsoo Choi, Jaewee Heo, Kwang-Soo Hahn, and Junho Kim</i>	
Analysis of a High Definition Camera-Projector Video System for Geometry Reconstruction	228
<i>José Luiz de Souza Filho, Roger Correia Silva, Dhiego Oliveira Sad, Renan Dembogurski, Marcelo Bernardes Vieira, Sócrates de Oliveira Dantas, and Rodrigo Silva</i>	
Video-Based Face Verification with Local Binary Patterns and SVM Using GMM Supervectors	240
<i>Tiago F. Pereira, Marcus A. Angeloni, Flávio O. Simões, and José Eduardo C. Silva</i>	

GPU-Based Influence Regions Optimization	253
<i>Marta Fort and J. Antoni Sellarès</i>	
Fast and Simple Approach for Polygon Schematization	267
<i>Serafino Cicerone and Matteo Cermignani</i>	
On Counting and Analyzing Empty Pseudo-triangles in a Point Set	280
<i>Sergey Kopeliovich and Kira Vyatkina</i>	
Workshop on Chemistry and Materials Sciences and Technologies (CMST 2012)	
Quantum Reactive Scattering Calculations on GPU	292
<i>Leonardo Pacifici, Danilo Nalli, and Antonio Laganà</i>	
Tuning Heme Functionality: The Cases of Cytochrome <i>c</i> Oxidase and Myoglobin Oxidation	304
<i>Vangelis Daskalakis, Stavros C. Farantos, and Constantinos Varotsis</i>	
Theoretical and Experimental Study of the Energy and Structure of Fragment Ions Produced by Double Photoionization of Benzene Molecules	316
<i>Marzio Rosi, Pietro Candori, Stefano Falcinelli, Maria Suelly Pedrosa Mundim, Fernando Pirani, and Franco Vecchiocattivi</i>	
Theoretical Study of Reactions Relevant for Atmospheric Models of Titan: Interaction of Excited Nitrogen Atoms with Small Hydrocarbons	331
<i>Marzio Rosi, Stefano Falcinelli, Nadia Balucani, Piergiorgio Casavecchia, Francesca Leonori, and Dimitris Skouteris</i>	
Efficient Workload Distribution Bridging HTC and HPC in Scientific Computing	345
<i>Carlo Manuali, Alessandro Costantini, Antonio Laganà, Marco Cecchi, Antonia Ghiselli, Michele Carpené, and Elda Rossi</i>	
Taxonomy Management in a Federation of Distributed Repositories: A Chemistry Use Case	358
<i>Sergio Tasso, Simonetta Pallottelli, Michele Ferroni, Riccardo Bastianini, and Antonio Laganà</i>	
Grid Enabled High Level <i>ab initio</i> Electronic Structure Calculations for the N_2+N_2 Exchange Reaction	371
<i>Marco Verdicchio, Leonardo Pacifici, and Antonio Laganà</i>	

A Bond-Bond Portable Approach to Intermolecular Interactions: Simulations for N-methylacetamide and Carbon Dioxide Dimers	387
<i>Andrea Lombardi, Noelia Faginas Lago, Antonio Laganà, Fernando Pirani, and Stefano Falcinelli</i>	
A Grid Execution Model for Computational Chemistry Applications Using the GC3Pie Framework and the AppPot VM Environment	401
<i>Alessandro Costantini, Riccardo Murri, Sergio Maffioletti, and Antonio Laganà</i>	
The MPI Structure of Chimere	417
<i>Antonio Laganà, Stefano Crocchianti, Giorgio Tentella, and Alessandro Costantini</i>	
A New Statistical Method for the Determination of Dynamical Features of Molecular Dication Dissociation Processes	432
<i>Maria Suely Pedrosa Mundim, Pietro Candori, Stefano Falcinelli, Kleber Carlos Mundim, Fernando Pirani, and Franco Vecchiocattivi</i>	
Workshop on Cities, Technologies and Planning (CTP 2012)	
SWOT Analysis of Information Technology Industry in Beijing, China Using Patent Data	447
<i>Lucheng Huang, Kangkang Wang, Feifei Wu, Yan Lou, Hong Miao, and Yanmei Xu</i>	
Using 3D GeoDesign for Planning of New Electricity Networks in Spain	462
<i>Francisco-Javier Moreno Marimbaldo, Federico-Vladimir Gutiérrez Corea, and Miguel-Ángel Manso Callejo</i>	
Assessment of Online PPGIS Study Cases in Urban Planning	477
<i>Geisa Bugs</i>	
e-Participation: Social Media and the Public Space	491
<i>Gilberto Corso Pereira, Maria Célia Furtado Rocha, and Alenka Poplin</i>	
Ubicomp and Environmental Designers: Assembling a Collective Work towards the Development of Sustainable Technologies	502
<i>Renato Cesar Ferreira de Souza</i>	
Sustainable Micro-business in Environmental Unsustainability and Economic Inefficiency	518
<i>José G. Vargas-Hernández</i>	

Efficient Visualization of the Geometric Information of CityGML: Application for the Documentation of Built Heritage	529
<i>Iñaki Prieto, Jose Luis Izkara, and Francisco Javier Delgado del Hoyo</i>	
ICT to Evaluate Participation in Urban Planning: Remarks from a Case Study	545
<i>Francesco Rotondo and Francesco Selicato</i>	
A Spatial Data Infrastructure Situation-Aware to the 2014 World Cup	561
<i>Wellington Moreira de Oliveira, Jugurta Lisboa Filho, and Alcione de Paiva Oliveira</i>	
Towards a Two-Way Participatory Process	571
<i>António Silva and Jorge Gustavo Rocha</i>	
An Automatic Procedure to Select Areas for Transfer Development Rights in the Urban Market	583
<i>Carmelo Maria Torre, Pasquale Balena, and Romina Zito</i>	
General Track on Computational Methods, Algorithms and Scientific Application	
Magnetic Net and a Bouncing Magnetic Ball	599
<i>Haiduke Sarafian</i>	
Autonomous Leaves Graph Applied to the Simulation of the Boundary Layer around a Non-symmetric NACA Airfoil	610
<i>Sanderson Lincoln Gonzaga de Oliveira and Mauricio Kischinhevsky</i>	
Sinimbu – Multimodal Queries to Support Biodiversity Studies	620
<i>Gabriel de S. Fedel, Claudia Bauzer Medeiros, and Jefersson Alex dos Santos</i>	
Comparison between Genetic Algorithms and Differential Evolution for Solving the History Matching Problem	635
<i>Elisa P. dos Santos Amorim, Carolina R. Xavier, Ricardo Silva Campos, and Rodrigo W. dos Santos</i>	
An Adaptive Mesh Algorithm for the Numerical Solution of Electrical Models of the Heart	649
<i>Rafael S. Oliveira, Bernardo M. Rocha, Denise Burgarelli, Wagner Meira Jr., and Rodrigo W. dos Santos</i>	
Decision Model to Predict the Implant Success	665
<i>Ana Cristina Braga, Paula Vaz, João C. Sampaio-Fernandes, António Felino, and Maria Purificação Tavares</i>	

Multiscale Modeling of Heterogeneous Media Applying AEH to 3D Bodies	675
<i>Bárbara de Melo Quintela, Daniel Mendes Caldas, Michèle Cristina Resende Farage, and Marcelo Lobosco</i>	
A Three-Dimensional Computational Model of the Innate Immune System	691
<i>Pedro Augusto F. Rocha, Micael P. Xavier, Alexandre B. Pigozzo, Barbara de M. Quintela, Gilson C. Macedo, Rodrigo Weber dos Santos, and Marcelo Lobosco</i>	
System Dynamics Metamodels Supporting the Development of Computational Models of the Human Innate Immune System	707
<i>Igor Knop, Alexandre Pigozzo, Barbara Quintela, Gilson C. Macedo, Ciro Barbosa, Rodrigo Weber dos Santos, and Marcelo Lobosco</i>	
Exact and Asymptotic Computations of Elementary Spin Networks: Classification of the Quantum–Classical Boundaries	723
<i>Ana Carla P. Bitencourt, Annalisa Marzuoli, Mirco Ragni, Roger W. Anderson, and Vincenzo Aquilanti</i>	
Performance of DFT and MP2 Approaches for Geometry of Rhenium Allenylidenes Complexes and the Thermodynamics of Phosphines Addition	738
<i>Cecilia Coletti and Nazzareno Re</i>	
Author Index	753

Table of Contents – Part II

Workshop on Econometrics and Multidimensional Evaluation in the Urban Environment (EMEUE 2012)

Knowledge and Innovation in Manufacturing Sector: The Case of Wedding Dresses in Southern Italy	1
<i>Annunziata de Felice, Isabella Martucci, and Dario A. Schirone</i>	
Marketing Strategies: Support and Enhancement of Core Business	17
<i>Dario Antonio Schirone and Germano Torkan</i>	
The Rational Quantification of Social Housing: An Operative Research Model	27
<i>Gianluigi De Mare, Antonio Nesticò, and Francesco Tajani</i>	
Simulation of Users Decision in Transport Mode Choice Using Neuro-Fuzzy Approach	44
<i>Mauro Dell’Orco and Michele Ottomanelli</i>	
Multidimensional Spatial Decision-Making Process: Local Shared Values in Action	54
<i>Maria Cerreta, Simona Panaro, and Daniele Cannatella</i>	
A Proposal for a Stepwise Fuzzy Regression: An Application to the Italian University System	71
<i>Francesco Campobasso and Annarita Fanizzi</i>	
Cluster Analysis for Strategic Management: A Case Study of IKEA	88
<i>Paola Perchinunno and Dario Antonio Schirone</i>	
Clustering for the Localization of Degraded Urban Areas	102
<i>Silvestro Montrone and Paola Perchinunno</i>	
A BEP Analysis of Energy Supply for Sustainable Urban Microgrids	116
<i>Pasquale Balena, Giovanna Mangialardi, and Carmelo Maria Torre</i>	
The Effect of Infrastructural Works on Urban Property Values: The <i>asse attrezzato</i> in Pescara, Italy	128
<i>Sebastiano Carbonara</i>	
Prospect of Integrate Monitoring: A Multidimensional Approach	144
<i>Marco Selicato, Carmelo Maria Torre, and Giovanni La Trofa</i>	

The Use of Ahp in a Multiactor Evaluation for Urban Development Programs: A Case Study 157
Luigi Fusco Girard and Carmelo Maria Torre

Assessing Urban Transformations: A SDSS for the Master Plan of Castel Capuano, Naples 168
Maria Cerreta and Pasquale De Toro

Workshop on Geographical Analysis, Urban Modeling, Spatial Statistics (Geo-An-Mod 2012)

Computational Context to Promote Geographic Information Systems toward Human-Centric Perspectives 181
Luis Paulo da Silva Carvalho and Paulo Caetano da Silva

Voronoi-Based Curve Reconstruction: Issues and Solutions 194
Mehran Ghandehari and Farid Karimipour

Geovisualization and Geostatistics: A Concept for the Numerical and Visual Analysis of Geographic Mass Data 208
Julia Gonschorek and Lucia Tyrallová

Spatio-Explorative Analysis and Its Benefits for a GIS-integrated Automated Feature Identification 220
Lucia Tyrallová and Julia Gonschorek

Peer Selection in P2P Service Overlays Using Geographical Location Criteria 234
Adriano Fiorese, Paulo Simões, and Fernando Boavida

Models for Spatial Interaction Data: Computation and Interpretation of Accessibility 249
Morton E. O’Kelly

Am I Safe in My Home? Fear of Crime Analyzed with Spatial Statistics Methods in a Central European City 263
Daniel Lederer

Developing a GIS Based Decision Support System for Resource Allocation in Earthquake Search and Rescue Operation 275
Abolfazl Rasekh and Ali Reza Vafaeinezhad

Concepts, Compass and Computation: Models for Directional Part-Whole Relationships 286
Gaurav Singh, Rolf A. de By, and Ivana Ivánová

SIGHabitar – Business Intelligence Based Approach for the Development of Land Information Systems: The Multipurpose Technical Cadastre of Ouro Preto, Brazil	302
<i>João Tácio C. Silva, José Francisco V. Rezende, Érika Fidêncio, Tarick Melo, Brayan Neves, and Joubert C. Lima e Tiago G.S. Carneiro</i>	
Rehabilitation and Reconstruction of Asphalts Pavement Decision Making Based on Rough Set Theory	316
<i>Shaaban M. Shaaban and Hossam A. Nabwey</i>	
Cartographic Circuits Inside GIS Environment for the Construction of the Landscape Sensitivity Map in the Case of Cremona	331
<i>Pier Luigi Paolillo, Umberto Baresi, and Roberto Bisceglie</i>	
Cloud Classification in JPEG-compressed Remote Sensing Data (LANDSAT 7/ETM+)	347
<i>Erik Borg, Bernd Fichtelmann, and Hartmut Asche</i>	
A Probabilistic Rough Set Approach for Water Reservoirs Site Location Decision Making	358
<i>Shaaban M. Shaaban and Hossam A. Nabwey</i>	
Definition and Analysis of New Agricultural Farm Energetic Indicators Using Spatial OLAP	373
<i>Sandro Bimonte, Kamal Boulil, Jean-Pierre Chanut, and Marilys Pradel</i>	
Validating a Smartphone-Based Pedestrian Navigation System Prototype: An Informal Eye-Tracking Pilot Test	386
<i>Mario Kluge and Hartmut Asche</i>	
Open Access to Historical Atlas: Sources of Information and Services for Landscape Analysis in an SDI Framework	397
<i>Raffaella Brumana, Daniela Oreni, Branka Cuca, Anna Rampini, and Monica Pepe</i>	
From Concept to Implementation: Web-Based Cartographic Visualisation with CartoService	414
<i>Hartmut Asche and Rita Engemaier</i>	
Multiagent Systems for the Governance of Spatial Environments: Some Modelling Approaches	425
<i>Domenico Camarda</i>	
A Data Fusion System for Spatial Data Mining, Analysis and Improvement	439
<i>Silvija Stankute and Hartmut Asche</i>	

Dealing with Multiple Source Spatio-temporal Data in Urban Dynamics Analysis	450
<i>João Peixoto and Adriano Moreira</i>	
Public Decision Processes: The Interaction Space Supporting Planner's Activity	466
<i>Giuseppe B. Las Casas, Lucia Tilio, and Alexis Tsoukiàs</i>	
Selection and Scheduling Problem in Continuous Time with Pairwise-Interdependencies	481
<i>Ivan Blečić, Arnaldo Cecchini, and Giuseppe A. Trunfio</i>	
Parallel Simulation of Urban Dynamics on the GPU	492
<i>Ivan Blečić, Arnaldo Cecchini, and Giuseppe A. Trunfio</i>	
Geolocalization as Wayfinding and User Experience Support in Cultural Heritage Locations	508
<i>Letizia Bollini and Roberto Falcone</i>	
Climate Alteration in the Metropolitan Area of Bari: Temperatures and Relationship with Characters of Urban Context	517
<i>Pierangela Loconte, Claudia Ceppi, Giorgia Lubisco, Francesco Mancini, Claudia Piscitelli, and Francesco Selicato</i>	
Study of Sustainability of Renewable Energy Sources through GIS Analysis Techniques	532
<i>Emanuela Caiaffa, Alessandro Marucci, and Maurizio Pollino</i>	
The Comparative Analysis of Urban Development in Two Geographic Regions: The State of Rio De Janeiro and the Campania Region	548
<i>Massimiliano Bencardino, Iaria Greco, and Pitter Reis Ladeira</i>	
Land-Use Dynamics at the Micro Level: Constructing and Analyzing Historical Datasets for the Portuguese Census Tracts	565
<i>António M. Rodrigues, Teresa Santos, Raquel Faria de Deus, and Dulce Pimentel</i>	
Using Hydrodynamic Modeling for Estimating Flooding and Water Depths in Grand Bay, Alabama	578
<i>Vladimir J. Alarcon and William H. McAnally</i>	
Comparison of Two Hydrodynamic Models of Weeks Bay, Alabama	589
<i>Vladimir J. Alarcon, William H. McAnally, and Surendra Pathak</i>	
Connections between Urban Structure and Urban Heat Island Generation: An Analysis through Remote Sensing and GIS	599
<i>MariaLUCE Stanganelli and Marco Soravia</i>	

Taking the Leap: From Disparate Data to a Fully Interactive SEIS for the Maltese Islands	609
<i>Saviour Formosa, Elaine Sciberras, and Janice Formosa Pace</i>	
Analyzing the Central Business District: The Case of Sassari in the Sardinia Island	624
<i>Silvia Battino, Giuseppe Borruso, and Carlo Donato</i>	
That's ReDO: Ontologies and Regional Development Planning	640
<i>Francesco Scorza, Giuseppe B. Las Casas, and Beniamino Murgante</i>	
A Landscape Complex Values Map: Integration among <i>Soft</i> Values and <i>Hard</i> Values in a Spatial Decision Support System	653
<i>Maria Cerreta and Roberta Mele</i>	
Analyzing Migration Phenomena with Spatial Autocorrelation Techniques	670
<i>Beniamino Murgante and Giuseppe Borruso</i>	
From Urban Labs in the City to Urban Labs on the Web	686
<i>Viviana Lanza, Lucia Tilio, Antonello Azzato, Giuseppe B. Las Casas, and Piergiuseppe Pontrandolfi</i>	
General Track on Geometric Modelling, Graphics and Visualization	
Bilayer Segmentation Augmented with Future Evidence	699
<i>Silvio Ricardo Rodrigues Sanches, Valdinei Freire da Silva, and Romero Tori</i>	
A Viewer-dependent Tensor Field Visualization Using Multiresolution and Particle Tracing	712
<i>José Luiz Ribeiro de Souza Filho, Marcelo Caniato Renhe, Marcelo Bernardes Vieira, and Gildo de Almeida Leonel</i>	
Abnormal Gastric Cell Segmentation Based on Shape Using Morphological Operations	728
<i>Noor Elaiza Abdul Khalid, Nurnabilah Samsudin, and Rathiah Hashim</i>	
A Bio-inspired System for Boundary Detection in Color Natural Scenes	739
<i>Karin S. Komati, Evandro O.T. Salles, and Mario Sarcinelli-Filho</i>	
Author Index	753

Table of Contents – Part III

Workshop on Optimization Techniques and Applications (OTA 2012)

Incorporating Radial Basis Functions in Pattern Search Methods: Application to Beam Angle Optimization in Radiotherapy Treatment Planning	1
<i>Humberto Rocha, Joana M. Dias, Brigida C. Ferreira, and Maria do Carmo Lopes</i>	
On the Complexity of a Mehrotra-Type Predictor-Corrector Algorithm	17
<i>Ana Paula Teixeira and Regina Almeida</i>	
Design of Wood Biomass Supply Chains	30
<i>Tiago Costa Gomes, Filipe Pereira e Alvelos, and Maria Sameiro Carvalho</i>	
On Solving a Stochastic Programming Model for Perishable Inventory Control	45
<i>Eliugius M.T. Hendrix, Rene Haijema, Roberto Rossi, and Karin G.J. Pauls-Worm</i>	
An Artificial Fish Swarm Filter-Based Method for Constrained Global Optimization	57
<i>Ana Maria A.C. Rocha, M. Fernanda P. Costa, and Edite M.G.P. Fernandes</i>	
Solving Multidimensional 0–1 Knapsack Problem with an Artificial Fish Swarm Algorithm	72
<i>Md. Abul Kalam Azad, Ana Maria A.C. Rocha, and Edite M.G.P. Fernandes</i>	
Optimization Model of COTS Selection Based on Cohesion and Coupling for Modular Software Systems under Multiple Applications Environment	87
<i>Pankaj Gupta, Shilpi Verma, and Mukesh Kumar Mehlawat</i>	
A Derivative-Free Filter Driven Multistart Technique for Global Optimization	103
<i>Florabela P. Fernandes, M. Fernanda P. Costa, and Edite M.G.P. Fernandes</i>	

On Lower Bounds Using Additively Separable Terms in Interval B&B	119
<i>José L. Berenguel, Leocadio G. Casado, I. García, Eligius M.T. Hendrix, and F. Messine</i>	
A Genetic Algorithm for the Job Shop on an ASRS Warehouse	133
<i>José Figueiredo, José A. Oliveira, Luis Dias, and Guilherme A.B. Pereira</i>	
On Solving the Profit Maximization of Small Cogeneration Systems	147
<i>Ana C.M. Ferreira, Ana Maria A.C. Rocha, Senhorinha F.C.F. Teixeira, Manuel L. Nunes, and Luís B. Martins</i>	
Global Optimization Simplex Bisection Revisited Based on Considerations by Reiner Horst	159
<i>Eligius M.T. Hendrix, Leocadio G. Casado, and Paula Amaral</i>	
Application of Variance Analysis to the Combustion of Residual Oils . . .	174
<i>Manuel Ferreira and José Carlos Teixeira</i>	
Warehouse Design and Planning: A Mathematical Programming Approach	187
<i>Carla A.S. Geraldés, Maria Sameiro Carvalho, and Guilherme A.B. Pereira</i>	
Application of CFD Tools to Optimize Natural Building Ventilation Design	202
<i>José Carlos Teixeira, Ricardo Lomba, Senhorinha F.C.F. Teixeira, and Pedro Lobarinhas</i>	
 Workshop on Mobile Communications (MC 2012)	
Middleware Integration for Ubiquitous Sensor Networks in Agriculture	217
<i>Junghoon Lee, Gyung-Leen Park, Min-Jae Kang, Ho-Young Kwak, Sang Joon Lee, and Jikwang Han</i>	
Usage Pattern-Based Prefetching: Quick Application Launch on Mobile Devices	227
<i>Hokwon Song, Changwoo Min, Jeehong Kim, and Young Ik Eom</i>	
EIMOS: Enhancing Interactivity in Mobile Operating Systems	238
<i>Sunwook Bae, Hokwon Song, Changwoo Min, Jeehong Kim, and Young Ik Eom</i>	

Development of Mobile Hybrid MedIntegraWeb App for Interoperation between u-RPMS and HIS	248
<i>Young-Hyuk Kim, Il-Kown Lim, Jae-Pil Lee, Jae-Gwang Lee, and Jae-Kwang Lee</i>	
A Distributed Lifetime-Maximizing Scheme for Connected Target Coverage in WSNs	259
<i>Duc Tai Le, Thang Le Duc, and Hyunseung Choo</i>	
Reducing Last Level Cache Pollution in NUMA Multicore Systems for Improving Cache Performance	272
<i>Deukhyeon An, Jeehong Kim, JungHyun Han, and Young Ik Eom</i>	
The Fast Handover Scheme for Mobile Nodes in NEMO-Enabled PMIPv6	283
<i>Changyong Park, Junbeom Park, Hao Wang, and Hyunseung Choo</i>	
A Reference Model for Virtual Resource Description and Discovery in Virtual Networks	297
<i>Yuemei Xu, Yanni Han, Wenjia Niu, Yang Li, Tao Lin, and Song Ci</i>	
TV Remote Control Using Human Hand Motion Based on Optical Flow System	311
<i>Soonmook Jeong, Taehoun Song, Keyho Kwon, and Jae Wook Jeon</i>	
Fast and Reliable Data Forwarding in Low-Duty-Cycle Wireless Sensor Networks	324
<i>Junseong Choe, Nguyen Phan Khanh Ha, Junguye Hong, and Hyunseung Choo</i>	
Workshop on Mobile-Computing, Sensing, and Actuation for Cyber Physical Systems (MSA4CPS 2012)	
Neural Network and Physiological Parameters Based Control of Artificial Pancreas for Improved Patient Safety	339
<i>Saad Bin Qaisar, Salman H. Khan, and Sahar Imtiaz</i>	
A Genetic Algorithm Assisted Resource Management Scheme for Reliable Multimedia Delivery over Cognitive Networks	352
<i>Salman Ali, Ali Munir, Saad Bin Qaisar, and Junaid Qadir</i>	
Performance Analysis of WiMAX Best Effort and ertPS Service Classes for Video Transmission	368
<i>Hassan Abid, Haroon Raja, Ali Munir, Jaweria Amjad, Aliya Mazhar, and Dong-Young Lee</i>	

Jump Oriented Programming on Windows Platform (on the x86)	376
<i>Jae-Won Min, Sung-Min Jung, Dong-Young Lee, and Tai-Myoung Chung</i>	
Cryptanalysis and Improvement of a Biometrics-Based Multi-server Authentication with Key Agreement Scheme	391
<i>Hakhyun Kim, Woongryul Jeon, Kwangwoo Lee, Yunho Lee, and Dongho Won</i>	
Rate-Distortion Optimized Transcoder Selection for Multimedia Transmission in Heterogeneous Networks	407
<i>Haroon Raja and Saad Bin Qaisar</i>	
Formal Probabilistic Analysis of Cyber-Physical Transportation Systems	419
<i>Atif Mashkooor and Osman Hasan</i>	
 Workshop on Remote Sensing (RS 2012)	
DEM Reconstruction of Coastal Geomorphology from DINSAR	435
<i>Maged Marghany</i>	
Three-Dimensional Coastal Front Visualization from RADARSAT-1 SAR Satellite Data	447
<i>Maged Marghany</i>	
A New Self-Learning Algorithm for Dynamic Classification of Water Bodies	457
<i>Bernd Fichtelmann and Erik Borg</i>	
DEM Accuracy of High Resolution Satellite Images	471
<i>Mustafa Yanalak, Nebiye Musaoglu, Cengizhan Ipbuker, Elif Sertel, and Sinasi Kaya</i>	
Low Cost Pre-operative Fire Monitoring from Fire Danger to Severity Estimation Based on Satellite MODIS, Landsat and ASTER Data: The Experience of FIRE-SAT Project in the Basilicata Region (Italy)	481
<i>Antonio Lanorte, Fortunato De Santis, Angelo Aromando, and Rosa Lasaponara</i>	
Investigating Satellite Landsat TM and ASTER Multitemporal Data Set to Discover Ancient Canals and Acqueduct Systems	497
<i>Rosa Lasaponara and Nicola Masini</i>	
Using Spatial Autocorrelation Techniques and Multi-temporal Satellite Data for Analyzing Urban Sprawl	512
<i>Gabriele Nolè, Maria Danese, Beniamino Murgante, Rosa Lasaponara, and Antonio Lanorte</i>	

General Track on Information Systems and Technologies

A Framework for QoS Based Dynamic Web Services Composition	528
<i>Jigyasu Nema, Rajdeep Niyogi, and Alfredo Milani</i>	
Data Summarization Model for User Action Log Files	539
<i>Eleonora Gentili, Alfredo Milani, and Valentina Poggioni</i>	
User Modeling for Adaptive E-Learning Systems	550
<i>Birol Ciloglugil and Mustafa Murat Inceoglu</i>	
An Experimental Study of the Combination of Meta-Learning with Particle Swarm Algorithms for SVM Parameter Selection	562
<i>Péricles B.C. de Miranda, Ricardo B.C. Prudêncio, Andre Carlos P.L.F. de Carvalho, and Carlos Soares</i>	
An Investigation into Agile Methods in Embedded Systems Development	576
<i>Caroline Oliveira Albuquerque, Pablo Oliveira Antonino, and Elisa Yumi Nakagawa</i>	
Heap Slicing Using Type Systems	592
<i>Mohamed A. El-Zawawy</i>	
Using Autonomous Search for Generating Good Enumeration Strategy Blends in Constraint Programming	607
<i>Ricardo Soto, Broderick Crawford, Eric Monfroy, and Víctor Bustos</i>	
Evaluation of Normalization Techniques in Text Classification for Portuguese	618
<i>Merley da Silva Conrado, Víctor Antonio Laguna Gutiérrez, and Solange Oliveira Rezende</i>	
Extracting Definitions from Brazilian Legal Texts	631
<i>Edilson Ferneda, Hércules Antonio do Prado, Augusto Herrmann Batista, and Marcello Sandi Pinheiro</i>	
A Heuristic Diversity Production Approach	647
<i>Hamid Parvin, Hosein Alizadeh, Sajad Parvin, and Behzad Maleki</i>	
Structuring Taxonomies from Texts: A Case-Study on Defining Soil Classes	657
<i>Hércules Antonio do Prado, Edilson Ferneda, Francisco Carlos da Luz Rodrigues, Éder Martins de Souza, Osmar Abílio de Carvalho Jr., and Alfredo José Barreto Luiz</i>	
Exploring Fuzzy Ontologies in Mining Generalized Association Rules . . .	667
<i>Rodrigo Moura Juvenil Ayres, Marcela Xavier Ribeiro, and Marilde Terezinha Prado Santos</i>	

BTA: Architecture for Reusable Business Tier Components with Access Control	682
<i>Óscar Mortágua Pereira, Rui L. Aguiar, and Maribel Yasmina Santos</i>	
Analysing the PDDL Language for Argumentation-Based Negotiation Planning	698
<i>Ariel Monteserin, Luis Berdún, and Analía A. Amandi</i>	
Predicting Potential Responders in Twitter: A Query Routing Algorithm	714
<i>Cleyton Caetano de Souza, Jonathas José de Magalhães, Evandro Barros de Costa, and Joseana Macêdo Fechine</i>	
Towards a Goal Recognition Model for the Organizational Memory	730
<i>Marcelo G. Armentano and Analía A. Amandi</i>	
SART: A New Association Rule Method for Mining Sequential Patterns in Time Series of Climate Data	743
<i>Marcos Daniel Cano, Marilde Terezinha Prado Santos, Ana Maria H. de Avila, Luciana A.S. Romani, Agma J.M. Traina, and Marcela Xavier Ribeiro</i>	
Author Index	759

Table of Contents – Part IV

Workshop on Software Engineering Processes and Applications (SEPA 2012)

Modeling Road Traffic Signals Control Using UML and the MARTE Profile	1
<i>Eduardo Augusto Silvestre and Michel dos Santos Soares</i>	
Analysis of Techniques for Documenting User Requirements	16
<i>Michel dos Santos Soares and Daniel Souza Cioquetta</i>	
Predicting Web Service Maintainability via Object-Oriented Metrics: A Statistics-Based Approach	29
<i>José Luis Ordiales Coscia, Marco Crasso, Cristian Mateos, Alejandro Zunino, and Sanjay Misra</i>	
Early Automated Verification of Tool Chain Design	40
<i>Matthias Biehl</i>	
Using UML Stereotypes to Support the Requirement Engineering: A Case Study	51
<i>Vitor A. Batista, Daniela C.C. Peixoto, Wilson Pádua, and Clarindo Isaías P.S. Pádua</i>	
Identifying Business Rules to Legacy Systems Reengineering Based on BPM and SOA	67
<i>Gleison S. do Nascimento, Cirano Iochpe, Lucinéia Thom, André C. Kalsing, and Álvaro Moreira</i>	
Abstraction Analysis and Certified Flow and Context Sensitive Points-to Relation for Distributed Programs	83
<i>Mohamed A. El-Zawawy</i>	
An Approach to Measure Understandability of Extended UML Based on Metamodel	100
<i>Yan Zhang, Yi Liu, Zhiyi Ma, Xuying Zhao, Xiaokun Zhang, and Tian Zhang</i>	
Dealing with Dependencies among Functional and Non-functional Requirements for Impact Analysis in Web Engineering	116
<i>José Alfonso Aguilar, Irene Garrigós, Jose-Norberto Mazón, and Anibal Zaldívar</i>	

Assessing Maintainability Metrics in Software Architectures Using COSMIC and UML	132
<i>Eudisley Gomes dos Anjos, Ruan Delgado Gomes, and Mário Zenha-Rela</i>	
Plagiarism Detection in Software Using Efficient String Matching	147
<i>Kusum Lata Pandey, Suneeta Agarwal, Sanjay Misra, and Rajesh Prasad</i>	
Dynamic Software Maintenance Effort Estimation Modeling Using Neural Network, Rule Engine and Multi-regression Approach	157
<i>Ruchi Shukla, Mukul Shukla, A.K. Misra, T. Marwala, and W.A. Clarke</i>	

Workshop on Software Quality (SQ 2012)

New Measures for Maintaining the Quality of Databases	170
<i>Hendrik Decker</i>	
A New Way to Determine External Quality of ERP Software	186
<i>Ali Orhan Aydin</i>	
Towards a Catalog of Spreadsheet Smells	202
<i>Jácome Cunha, João P. Fernandes, Hugo Ribeiro, and João Saraiva</i>	
Program and Aspect Metrics for MATLAB	217
<i>Pedro Martins, Paulo Lopes, João P. Fernandes, João Saraiva, and João M.P. Cardoso</i>	
A Suite of Cognitive Complexity Metrics	234
<i>Sanjay Misra, Murat Koyuncu, Marco Crasso, Cristian Mateos, and Alejandro Zunino</i>	
Complexity Metrics for Cascading Style Sheets	248
<i>Adewole Adewumi, Sanjay Misra, and Nicholas Ikhu-Omoregbe</i>	
A Systematic Review on the Impact of CK Metrics on the Functional Correctness of Object-Oriented Classes	258
<i>Yasser A. Khan, Mahmoud O. Elish, and Mohamed El-Attar</i>	

Workshop on Security and Privacy in Computational Sciences (SPCS 2012)

Pinpointing Malicious Activities through Network and System-Level Malware Execution Behavior	274
<i>André Ricardo Abed Grégio, Vitor Monte Afonso, Dario Simões Fernandes Filho, Paulo Lício de Geus, Mario Jino, and Rafael Duarte Coelho dos Santos</i>	

A Malware Detection System Inspired on the Human Immune System	286
<i>Isabela Liane de Oliveira, André Ricardo Abed Grégio, and Adriano Mauro Cansian</i>	
Interactive, Visual-Aided Tools to Analyze Malware Behavior	302
<i>André Ricardo Abed Grégio, Alexandre Or Cansian Baruque, Vitor Monte Afonso, Dario Simões Fernandes Filho, Paulo Lício de Geus, Mario Jino, and Rafael Duarte Coelho dos Santos</i>	
Interactive Analysis of Computer Scenarios through Parallel Coordinates Graphics	314
<i>Gabriel D. Cavalcante, Sebastien Tricaud, Cleber P. Souza, and Paulo Lício de Geus</i>	
Methodology for Detection and Restraint of P2P Applications in the Network	326
<i>Rodrigo M.P. Silva and Ronaldo M. Salles</i>	
Workshop on Soft Computing and Data Engineering (SCDE 2012)	
Text Categorization Based on Fuzzy Soft Set Theory	340
<i>Bana Handaga and Mustafa Mat Deris</i>	
Cluster Size Determination Using JPEG Files	353
<i>Nurul Azma Abdullah, Rosziati Ibrahim, and Kamaruddin Malik Mohamad</i>	
Semantic Web Search Engine Using Ontology, Clustering and Personalization Techniques	364
<i>Noryusliza Abdullah and Rosziati Ibrahim</i>	
Granules of Words to Represent Text: An Approach Based on Fuzzy Relations and Spectral Clustering	379
<i>Patrícia F. Castro and Geraldo B. Xexéo</i>	
Multivariate Time Series Classification by Combining Trend-Based and Value-Based Approximations	392
<i>Bilal Esmael, Arghad Arnaout, Rudolf K. Fruhwirth, and Gerhard Thonhauser</i>	

General Track on High Performance Computing and Networks

Impact of <i>pay-as-you-go</i> Cloud Platforms on Software Pricing and Development: A Review and Case Study	404
<i>Fernando Pires Barbosa and Andrea Schwertner Charão</i>	
Resilience for Collaborative Applications on Clouds: Fault-Tolerance for Distributed HPC Applications	418
<i>Toàn Nguyễn and Jean-Antoine Désidéri</i>	
T-DMB Receiver Model for Emergency Alert Service	434
<i>Seong-Geun Kwon, Suk-Hwan Lee, Eung-Joo Lee, and Ki-Ryong Kwon</i>	
A Framework for Context-Aware Systems in Mobile Devices	444
<i>Eduardo Jorge, Matheus Farias, Rafael Carmo, and Wesley Vieira</i>	
A Simulation Framework for Scheduling Performance Evaluation on CPU-GPU Heterogeneous System	457
<i>Flavio Vella, Igor Neri, Osvaldo Gervasi, and Sergio Tasso</i>	
Influence of Topology on Mobility and Transmission Capacity of Human-Based DTNs	470
<i>Danilo A. Moschetto, Douglas O. Freitas, Lourdes P.P. Poma, Ricardo Aparecido Perez de Almeida, and Cesar A.C. Marcondes</i>	
Towards a Computer Assisted Approach for Migrating Legacy Systems to SOA	484
<i>Gonzalo Salvatierra, Cristian Mateos, Marco Crasso, and Alejandro Zunino</i>	
1+1 Protection of Overlay Distributed Computing Systems: Modeling and Optimization	498
<i>Krzysztof Walkowiak and Jacek Rak</i>	
Scheduling and Capacity Design in Overlay Computing Systems	514
<i>Krzysztof Walkowiak, Andrzej Kasprzak, Michał Kosowski, and Marek Miziołek</i>	
GPU Acceleration of the <i>caffa3d.MB</i> Model	530
<i>Pablo Igounet, Pablo Alfaro, Gabriel Usera, and Pablo Ezzatti</i>	
Security-Effective Fast Authentication Mechanism for Network Mobility in Proxy Mobile IPv6 Networks	543
<i>Illkyun Im, Young-Hwa Cho, Jae-Young Choi, and Jongpil Jeong</i>	
An Architecture for Service Integration and Unified Communication in Mobile Computing	560
<i>Ricardo Aparecido Perez de Almeida and Hélio C. Guardia</i>	

Task Allocation in Mesh Structure: 2Side LeapFrog Algorithm and Q-Learning Based Algorithm	576
<i>Iwona Pozniak-Koszalka, Wojciech Proma, Leszek Koszalka, Maciej Pol, and Andrzej Kasprzak</i>	
Follow-Ups: A Distributed Ubiquitous Healthcare System Simulated by MannaSim	588
<i>Maria Luísa Amarante Ghizoni, Aduino Santos, and Linyer Beatrys Ruiz</i>	
Adaptive Dynamic Frequency Scaling for Thermal-Aware 3D Multi-core Processors	602
<i>Hong Jun Choi, Young Jin Park, Hsien-Hsin Lee, and Cheol Hong Kim</i>	
A Context-Aware Service Model Based on the OSGi Framework for u-Agricultural Environments	613
<i>Jongsun Choi, Sangjoon Park, Jongchan Lee, and Yongyun Cho</i>	
A Security Framework for Blocking New Types of Internet Worms in Ubiquitous Computing Environments	622
<i>Iksu Kim and Yongyun Cho</i>	
Quality Factors in Development Best Practices for Mobile Applications	632
<i>Euler Horta Marinho and Rodolfo Ferreira Resende</i>	
ShadowNet: An Active Defense Infrastructure for Insider Cyber Attack Prevention	646
<i>Xiaohui Cui, Wade Gasior, Justin Beaver, and Jim Treadwell</i>	
Author Index	655

Processor Allocation for Optimistic Parallelization of Irregular Programs*

Francesco Versaci^{1,**} and Keshav Pingali²

¹ University of Padova & Technische Universität Wien
versacif@dei.unipd.it

² University of Texas at Austin
pingali@cs.utexas.edu

Abstract. Optimistic parallelization is a promising approach for the parallelization of irregular algorithms: potentially interfering tasks are launched dynamically, and the runtime system detects conflicts between concurrent activities, aborting and rolling back conflicting tasks. However, parallelism in irregular algorithms is very complex. In a regular algorithm like dense matrix multiplication, the amount of parallelism can usually be expressed as a function of the problem size, so it is reasonably straightforward to determine how many processors should be allocated to execute a regular algorithm of a certain size (this is called the processor allocation problem). In contrast, parallelism in irregular algorithms can be a function of input parameters, and the amount of parallelism can vary dramatically during the execution of the irregular algorithm. Therefore, the processor allocation problem for irregular algorithms is very difficult.

In this paper, we describe the first systematic strategy for addressing this problem. Our approach is based on a construct called the *conflict graph*, which (i) provides insight into the amount of parallelism that can be extracted from an irregular algorithm, and (ii) can be used to address the processor allocation problem for irregular algorithms. We show that this problem is related to a generalization of the *unfriendly seating problem* and, by extending Turán's theorem, we obtain a worst-case class of problems for optimistic parallelization, which we use to derive a lower bound on the exploitable parallelism. Finally, using some theoretically derived properties and some experimental facts, we design a quick and stable control strategy for solving the processor allocation problem heuristically.

Keywords: Irregular algorithms, Optimistic parallelization, Automatic parallelization, Amorphous data-parallelism, Processor allocation, Unfriendly seating, Turán's theorem.

* Supported by PAT-INFN Project *AuroraScience*, by MIUR-PRIN Project *Algo-DEEP*, and by the University of Padova Projects *STPD08JA32* and *CPDA099949*.

** Corresponding author.

1 Introduction

The advent of on-chip multiprocessors has made parallel programming a mainstream concern. Unfortunately writing correct and efficient parallel programs is a challenging task for the average programmer. Hence, in recent years, many projects [14,10,3,20] have tried to automate parallel programming for some classes of algorithms. Most of them focus on *regular* algorithms such as Fourier transforms [9,19] and dense linear algebra routines [4]. Automation is more difficult when the algorithms are *irregular* and use pointer-based data structures such as graphs and sets. One promising approach is based on the concept of *amorphous data parallelism* [17]. Algorithms are formulated as iterative computations on *work-sets*, and each iteration is identified as a quantum of work (task) that can potentially be executed in parallel with other iterations. The Galois project [18] has shown that algorithms formulated in this way can be parallelized automatically using *optimistic parallelization*: iterations are executed speculatively in parallel and, when an iteration conflicts with concurrently executing iterations, it is rolled-back. Algorithms that have been successfully parallelized in this manner include Survey propagation [5], Boruvka’s algorithm [6], Delauney triangulation and refinement [12], and Agglomerative clustering [21].

In a regular algorithm like dense matrix multiplication, the amount of parallelism can usually be expressed as a function of the problem size, so it is reasonably straightforward to determine how many processors should be allocated to execute a regular algorithm of a certain size (this is called the *processor allocation* problem). In contrast, parallelism in irregular algorithms can be a function of input parameters, and the amount of parallelism can vary dramatically during the execution of the irregular algorithm [16]. Therefore, the processor allocation problem for irregular algorithms is very difficult. Optimistic parallelization complicates this problem even more: if there are too many processors and too little parallel work, not only might some processors be idle but speculative conflicts may actually retard the progress of even those processors that have useful work to do, increasing both program execution time and power consumption. *This paper*¹ presents the first systematic approach to addressing the processor allocation problem for irregular algorithms under optimistic parallelization, and it makes the following contributions.

- We develop a simple graph-theoretic model for optimistic parallelization and use it to formulate processor allocation as an optimization problem that balances parallelism exploitation with minimizing speculative conflicts (Section 2).
- We identify a worst-case class of problems for optimistic parallelization; to this purpose, we develop an extension of Turán’s theorem [2] (Section 3).
- Using these ideas, we develop an adaptive controller that dynamically solves the processor allocation problem for amorphous data-parallel programs, providing rapid response to changes in the amount of amorphous data-parallelism (Section 4).

¹ A brief announcement of this work has been presented at SPAA’11 [23].

2 Modeling Optimistic Parallelization

A typical example of an algorithm that exhibits amorphous data-parallelism is Dalauney mesh refinement, summarized as follows. A triangulation of some planar region is given, containing some “bad” triangles (according to some quality criterion). To remove them, each bad triangle is selected (in any arbitrary order), and this triangle, together with triangles that lie in its *cavity*, are replaced with new triangles. The retriangulation can produce new bad triangles, but this process can be proved to halt after a finite number of steps. Two bad triangles can be processed in parallel, given that their cavities do not overlap.

There are also algorithms, which exhibit amorphous data-parallelism, for which the order of execution of the parallel tasks cannot be arbitrary, but must satisfy some constraints (e.g., in discrete event simulations the events must commit chronologically). We will not treat this class of problems in this work, but we will focus only on *unordered* algorithms [16]. A different context in which there is no roll-back and tasks do not conflict, but obey some precedence relations, is treated in [1].

Optimistic parallelization deals with amorphous data-parallelism by maintaining a work-set of the tasks to be executed. At each temporal step some tasks are selected and speculatively launched in parallel. If, at runtime, two processes modify the same data a conflict is detected and one of the two has to abort and roll-back its execution. Neglecting the details of the various amorphous data-parallel algorithms, we can model their common behavior at a higher level with a simple graph-theoretic model: we can think a scheduler as working on a dynamic graph $G_t = (V_t, E_t)$, where the nodes represent computations we want to do, but we have no initial knowledge of the edges, which represent conflicts between computations (see Fig. 1). At time step t the system picks uniformly at random m_t nodes (the *active* nodes) and tries to process them concurrently. When it processes a node it figures out if it has some connections with other executed nodes and, if a neighbor node happens to have been processed before it, aborts, otherwise the node is considered processed, is removed from the graph and some operations may be performed in the neighborhood, such as adding new nodes with edges or altering the neighbors. The time taken to process conflicting and non-conflicting nodes is assumed to be the same, as it happens, e.g., for Dalauney mesh refinement.

2.1 Control Optimization Goal

When we run an optimistic parallelization we have two contrasting goals: we both want to maximize the work done, achieving high parallelism, but at the same time we want to minimize the conflicts, hence obtaining a good use of the processors time. (Furthermore, for some algorithms the roll-back work can be quite resource-consuming.) These two goals are not compatible, in fact if we naïvely try to minimize the total execution time the system is forced to use always all the available processors, whereas if we try to minimize the time wasted from aborted processes the system uses only one processor. Therefore in the following we choose a trade-off goal and cast it in our graph-theoretic model.

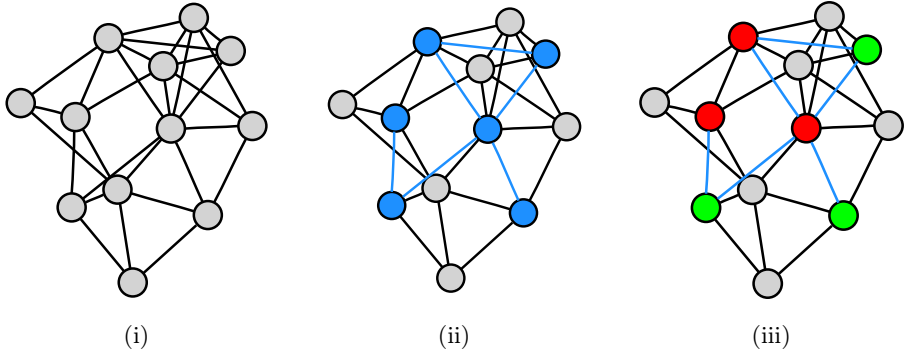


Fig. 1. Optimistic parallelization. (i) Nodes represent possible computations, edges conflicts between them. (ii) m nodes are chosen at random and run concurrently. (iii) At runtime the conflicts are detected, some nodes abort and their execution is rolled back, leaving a maximal independent set in the subgraph induced by the initial nodes choice.

Let $G = (V, E)$ be a computations/conflicts (CC) graph with $n = |V|$ nodes. When a scheduler chooses, uniformly at random, m nodes to be run, the ordered set $\pi_m(\cdot)$ by which they commit can be modeled as a random permutation: if $i < j$ then $\pi_m(i)$ commits before $\pi_m(j)$ (if there is a conflict between $\pi_m(i)$ and $\pi_m(j)$ then $\pi_m(i)$ commits and $\pi_m(j)$ aborts, if $\pi_m(i)$ aborted due to conflicts with previous processes $\pi_m(j)$ can commit, if not conflicting with other committed processes). Let $k_t(\pi_m)$ be the number of aborted processes due to conflicts and $r_t(\pi_m) \in [0, 1]$ the ratio of conflicting processors observed at time t (i.e. $r_t(\pi_m) \triangleq k_t(\pi_m)/m$). We define the *conflict ratio* $\bar{r}_t(m)$ to be the expected r that we obtain when the system is run with m processors:

$$\bar{r}_t(m) \triangleq \mathbb{E}_{\pi_m} [r_t(\pi_m)] \quad , \quad (1)$$

where the expectation is computed uniformly over the possible prefixes of length m of the n nodes permutations. The control problem we want to solve is the following: *given $r(\tau)$ and m_τ for $\tau < t$, choose $m_t = \mu_t$ such that $\bar{r}_t(\mu_t) \simeq \rho$, where ρ is a suitable parameter.*

Remark 1. If we want to dynamically control the number of processors, ρ must be chosen different from zero, otherwise the system converges to use only one processor, thus not being able to identify available parallelism. A value of $\rho \in [20\%, 30\%]$ is often reasonable, together with the constraint $m_t \geq 2$.

3 Exploiting Parallelism

In this section we study how much parallelism can be extracted from a given CC graph and how its sparsity can affect the conflict ratio. To this purpose we obtain a worst case class of graphs and use it to analytically derive a lower bound for

the exploitable parallelism (i.e., an upper bound for the conflict ratio). We make extensive use of finite differences (i.e., discrete derivatives), which are defined recursively as follows. Let $f : \mathbb{Z} \rightarrow \mathbb{R}$ be a real function defined on the integers, then the i -th (forward) finite difference of f is

$$\Delta_f^i(k) = \Delta_f^{i-1}(k+1) - \Delta_f^{i-1}(k) \quad , \quad \text{with } \Delta_f^0(k) = f(k) \quad . \quad (2)$$

(In the following we will omit Δ 's superscript when equal to one, i.e., $\Delta \triangleq \Delta^1$.)

First, we obtain two basic properties of \bar{r} , which are given by the following propositions.

Proposition 1. *The conflict ratio function $\bar{r}(m)$ is non-decreasing in m .*

To prove Prop. [1](#) we first need a lemma:

Lemma 1. *Let $\bar{k}(m) \triangleq \mathbb{E}_{\pi_m} [k(\pi_m)]$. Then \bar{k} is a non-decreasing convex function, i.e. $\Delta_{\bar{k}}(m) \geq 0$ and $\Delta_{\bar{k}}^2(m) \geq 0$.*

Proof. Let $\tilde{k}(\pi_m, i)$ be the expected number of conflicting nodes running $r = m + i$ nodes concurrently, the first m of which are π_m and the last i are chosen uniformly at random among the remaining ones. By definition, we have

$$\mathbb{E}_{\pi_m} [\tilde{k}(\pi_m, i)] = \bar{k}(m+i) \quad . \quad (3)$$

In particular,

$$\tilde{k}(\pi_m, 1) = k(\pi_m) + \Pr[(m+1)\text{-th conflicts}] \quad , \quad (4)$$

which brings

$$\bar{k}(m+1) = \mathbb{E}_{\pi_m} [\tilde{k}(\pi_m, 1)] = \bar{k}(m) + \eta \quad , \quad (5)$$

with $\eta = \bar{k}(m+1) - \bar{k}(m) = \Delta_{\bar{k}}(m) \geq 0$, hence proving the monotonicity of \bar{k} . Consider now

$$\tilde{k}(\pi_m, 2) = k(\pi_m) + \Pr[(m+1)\text{-th conflicts}] + \Pr[(m+2)\text{-th conflicts}] \quad . \quad (6)$$

If the $(m+1)$ -th node does not add any edge, then we have

$$\Pr[(m+1)\text{-th conflicts}] = \Pr[(m+2)\text{-th conflicts}] \quad , \quad (7)$$

but since it may add some edges the probability of conflicting the second time is in general larger and thus $\Delta_{\bar{k}}^2(m) \geq 0$. \square

Proof (Prop. [1](#)). Since $\bar{r}(m) = \bar{k}(m)/m$, its finite difference can be written as

$$\Delta_{\bar{r}}(m) = \frac{m\Delta_{\bar{k}}(m) - \bar{k}(m)}{m(m+1)} \quad . \quad (8)$$

Because of Lemma [1](#) and being $\bar{k}(1) = 0$ we have

$$\bar{k}(m+1) \leq m\Delta_{\bar{k}}(m) \quad , \quad (9)$$

which finally brings

$$\Delta_{\bar{r}}(m) = \frac{m\Delta_{\bar{k}}(m) - \bar{k}(m)}{m(m+1)} \geq \frac{\bar{k}(m+1) - \bar{k}(m)}{m(m+1)} = \frac{\Delta_{\bar{k}}(m)}{m(m+1)} \geq 0 \quad . \quad (10)$$

□

Proposition 2. *Let G be a CC graph, with n nodes and average degree d , then the initial derivative of \bar{r} depends only on n and d as*

$$\Delta_{\bar{r}}(1) = \frac{d}{2(n-1)} \quad . \quad (11)$$

Proof. Since

$$\Delta_{\bar{r}}(1) = \frac{\Delta_{\bar{k}}(1) - \bar{k}(1)}{2} = \frac{\bar{k}(2)}{2} \quad , \quad (12)$$

we just need to obtain $\bar{k}(2)$. Let \tilde{k} be defined as in the proof on Lemma [11](#) and $\pi_1 = v$ a node chosen uniformly at random. Then

$$\bar{k}(2) = \mathbb{E}_v \left[\tilde{k}(v, 1) \right] = \mathbb{E}_v \left[\frac{d_v}{n-1} \right] = \frac{\mathbb{E}_v [d_v]}{n-1} = \frac{d}{n-1} \quad . \quad (13)$$

□

A measure of the available parallelism for a given CC graph has been identified in [15](#) considering, at each temporal step, a maximal independent set of the CC graph. The expected size of a maximal independent set gives a reasonable and computable estimate of the available parallelism. However, this is not enough to predict the actual amount of parallelism that a scheduler can exploit while keeping a low conflict ratio, as shown in the following example.

Example 1. Let $G = K_{n^2} \cup D_n$ where K_{n^2} is the complete graph of size n^2 and D_n a disconnected graph of size n (i.e. G is made up of a clique of size n^2 and n disconnected nodes). For this graph every maximal independent set is maximum too and has size $n+1$, but if we choose $n+1$ nodes uniformly at random and then compute the conflicts we obtain that, on average, there are only 2 independent nodes.

A more realistic estimate of the performance of a scheduler can be obtained by analyzing the CC graph sparsity. The average degree of the CC graph is linked to the expected size of a maximal independent set of the graph by the following well known theorem (in the variant shown in [2](#) or [22](#)):

Theorem 1. (*Turán, strong formulation*). *Let $G = (V, E)$ be a graph, $n = |V|$ and let d be the average degree of G . Then the expected size of a maximal independent set, obtained choosing greedily the nodes from a random permutation, is at least $s = n/(d+1)$.*

Remark 2. The previous bound is existentially tight: let K_d^n be the graph made up of $s = n/(d + 1)$ cliques of size $d + 1$, then the average degree is d and the size of every maximal (and maximum) independent set is exactly s . Furthermore, every other graph with the same number of nodes and edges has a bigger average maximal independent set.

The study of the expected size of a maximal independent set in a given graph is also known as the *unfriendly seating problem* [7,8] and is particularly relevant in statistical physics, where it is usually studied on mesh-like graphs [11]. The properties of the graph K_d^n has suggested us the formulation of an extension of the Turán's theorem. We prove that the graphs K_d^n provide a worst case (for a given degree d) for the generalization of this problem obtained by focusing on maximal independent set of induced subgraphs. This allows, when given a target conflict ratio ρ , the computation of a lower bound for the parallelism a scheduler can exploit.

Theorem 2. *Let G be a graph with same nodes number and degree of K_d^n and let $EM_m(G)$ be the expected size of a maximal independent set of the subgraph induced by a uniformly random choice of m nodes in G , then*

$$EM_m(G) \geq EM_m(K_d^n) . \quad (14)$$

To prove it we first need the following lemma.

Lemma 2. *The function $\eta_j(x) \triangleq \prod_{i=1}^j (n - i - x)$ is convex for $x \in [0, n - j]$.*

Proof. We prove by induction on j that, for $x \in [0, n - j]$,

$$\eta_j(x) \geq 0 \quad , \quad \eta'_j(x) \leq 0 \quad , \quad \eta''_j(x) \geq 0 \quad . \quad (15)$$

Base case Let $\eta_0(x) = 1$. The properties above are easily verified.

Induction Since $\eta_j(x) = \eta_{j-1}(x)(n - j - x)$, we obtain

$$\eta'_j(x) = -\eta_{j-1}(x) + (n - j - x)\eta'_{j-1}(x) \quad , \quad (16)$$

which is non-positive by inductive hypotheses. Similarly,

$$\eta''_j(x) = -2\eta'_{j-1}(x) + (n - j - x)\eta''_{j-1}(x) \quad (17)$$

is non-negative. □

Proof (Thm. 2). Consider a random permutation π of the nodes of a generic graph G that has the same number of nodes and edges of K_d^n . We assume the prefix of length m of π (i.e. $\pi(1), \dots, \pi(m)$) forms the active nodes and focus on the following independent set IS_m in the subgraph induced: a node v is in $IS_m(G, \pi)$ if and only if it is in the first m positions of π and it has no neighbors preceding it. Let $b_m(G)$ be the expected size of $IS_m(G, \pi)$ averaged over all possible π 's (chosen uniformly):

$$b_m(G) \triangleq \mathbb{E}_\pi [\# IS_m(G, \pi)] \quad . \quad (18)$$

Since for construction $b_m(G) \leq \text{EM}_m(G)$ whereas $b_m(K_d^n) = \text{EM}_m(K_d^n)$, we just need to prove that $b_m(K_d^n) \leq b_m(G)$. Given a generic node v of degree d_v and a random permutation π , its probability to be in $\text{IS}_m(G, \pi)$ is

$$\Pr[v \in \text{IS}_m(G, \pi)] = \frac{1}{n} \sum_{j=1}^m \prod_{i=1}^{j-1} \frac{n-i-d_v}{n-i} . \quad (19)$$

By the linearity of the expectation we can write b as

$$b_m(G) = \frac{1}{n} \sum_{v=v_1}^{v_n} \sum_{j=1}^m \prod_{i=1}^{j-1} \frac{n-i-d_v}{n-i} = \mathbb{E}_v \left[\sum_{j=1}^m \prod_{i=1}^{j-1} \frac{n-i-d_v}{n-i} \right] , \quad (20)$$

$$b_m(K_d^n) = \sum_{j=1}^m \prod_{i=1}^{j-1} \frac{n-i-d}{n-i} = \sum_{j=1}^m \prod_{i=1}^{j-1} \frac{n-i-\mathbb{E}_v[d_v]}{n-i} . \quad (21)$$

To prove that $\text{EM}_m(G) \geq \text{EM}_m(K_d^n)$ is thus enough showing that

$$\forall j \quad \mathbb{E}_v \left[\prod_{i=1}^j (n-i-d_v) \right] \geq \prod_{i=1}^j (n-i-\mathbb{E}_v[d_v]) , \quad (22)$$

which can be done applying Jensen's inequality [13], since in Lemma 2 we have proved the convexity of $\eta_j(x) \triangleq \prod_{i=1}^j (n-i-x)$. \square

Corollary 1. *The worst case for a scheduler among the graphs with the same number of nodes and edges is obtained for the graph K_d^n (for which we can analytically approximate the performance, as shown in §3.1).*

Proof. Since

$$\bar{r}(m) = \frac{m - \text{EM}_m(G)}{m} = 1 - \frac{1}{m} \text{EM}_m(G) , \quad (23)$$

the thesis follows. \square

3.1 Analysis of the Worst-Case Performance

Theorem 3. *Let d be the average degree of $G = (V, E)$ with $n = |V|$ (for simplicity we assume $n/(d+1) \in \mathbb{N}$). The conflict ratio is bounded from above as*

$$\bar{r}(m) \leq 1 - \frac{n}{m(d+1)} \left(1 - \prod_{i=1}^m \frac{n-d-i}{n+1-i} \right) . \quad (24)$$

Proof. Let $s = n/(d+1)$ be the number of connected components in K_d^n . Because of Thm. 2 and Cor. 1 it suffices to show that

$$\text{EM}_m(K_d^n) = s \left(1 - \prod_{i=1}^m \frac{n-d-i}{n+1-i} \right) . \quad (25)$$

The probability for a connected component k of K_d^n not to be accessed when m nodes are chosen is given by the following hypergeometric

$$\Pr[k \text{ not hit}] = \frac{\binom{n-d-1}{m} \binom{d+1}{0}}{\binom{n}{m}} = \prod_{i=1}^m \frac{n-d-i}{n+1-i} . \quad (26)$$

Let X_k be a random variable that is 1 when component k is hit and 0 otherwise. We have that $\mathbb{E}[X_k] = 1 - \prod_{i=1}^m \frac{n-d-i}{n+1-i}$ and, by the linearity of the expectation, the average number of components accessed is

$$\mathbb{E} \left[\sum_{k=1}^s X_k \right] = \sum_{k=1}^s \mathbb{E}[X_k] = s \left(1 - \prod_{i=1}^m \frac{n-d-i}{n+1-i} \right) . \quad (27)$$

□

Corollary 2. *When n and m increase the bound is well approximated by*

$$\bar{r}(m) \leq 1 - \frac{n}{m(d+1)} \left[1 - \left(1 - \frac{m}{n} \right)^{d+1} \right] . \quad (28)$$

Proof. Stirling approximation for the binomial, followed by low order terms deletion in the resulting formula. □

Corollary 3. *If we set $m = \alpha s = \frac{\alpha n}{d+1}$ we obtain*

$$\bar{r}(m) \leq 1 - \frac{1}{\alpha} \left[1 - \left(1 - \frac{\alpha}{d+1} \right)^{d+1} \right] \leq 1 - \frac{1}{\alpha} [1 - e^{-\alpha}] . \quad (29)$$

4 Controlling Processors Allocation

In this section we will design an efficient control heuristic that dynamically chooses the number of processes to be run by a scheduler, in order to obtain high parallelism while keeping the conflict ratio low. In the following we suppose that the properties of G_t are varying slowly compared to the convergence of m_t toward μ_t under the algorithm we will develop (see [§4.1](#)), so we can consider $G_t = G$ and $\mu_t = \mu$ and thus our goal is making m_t converge to μ .

Since the conflict ratio is a non-decreasing function of the number of launched tasks m (Prop. [1](#)) we could find $m \simeq \mu$ by bisection simply noticing that

$$\bar{r}(m') \leq \rho \leq \bar{r}(m'') \quad \Rightarrow \quad m' \leq \mu \leq m'' . \quad (30)$$

The control we propose is slightly more complex and is based on recurrence relations, i.e., we compute m_{t+1} as a function F of the target conflict ratio ρ and of the parameters which characterize the system at the previous timestep:

$$m_{t+1}^F = F(\rho, r_t, m_t) . \quad (31)$$

The initial value m_0 for a recurrence can be chosen to be 2 but, if we have an estimate of the CC graph average degree d , we can choose a smarter value: in fact applying Cor. 3 we are sure that using, e.g., $m = \frac{n}{2(d+1)}$ processors we will have at most a conflict ratio of 21.3%.

Algorithm 1. Pseudo-code of the proposed hybrid control algorithm

```

// Tunable parameters
1  $m_0 = 2;$        $m_{\max} = 1024;$        $m_{\min} = 2;$ 
2  $T = 4;$        $r_{\min} = 3\%;$        $\alpha_0 = 25\%;$        $\alpha_1 = 6\%;$ 
// Variables
3  $m \leftarrow m_0;$        $r \leftarrow 0;$        $t \leftarrow 0;$ 
// Main loop
4 while nodes to elaborate  $\neq 0$  do
5    $t \leftarrow t + 1;$ 
6   if  $m > m_{\max}$  then  $m \leftarrow m_{\max};$ 
7   else if  $m < m_{\min}$  then  $m \leftarrow m_{\min};$ 
8   Launch the scheduler with  $m$  nodes;
9    $r \leftarrow r + \text{new conflict ratio};$ 
10  if  $(t \bmod T) = T - 1$  then
11     $r \leftarrow r/T;$ 
12     $\alpha \leftarrow \left| 1 - \frac{r}{\rho} \right|;$ 
13    if  $\alpha > \alpha_0$  then
14      if  $r < r_{\min}$  then  $r \leftarrow r_{\min};$ 
15       $m \leftarrow \left\lceil \frac{\rho}{r} m \right\rceil;$ 
16    else if  $\alpha > \alpha_1$  then
17       $m \leftarrow \lceil (1 - r + \rho) m \rceil;$ 
18     $r \leftarrow 0;$ 

```

Our control heuristic (Algorithm 1) is a hybridization of two simple recurrences. The first recurrence is quite natural and increases m based on the distance between r and ρ :

$$\text{Recurrence A: } m_{t+1}^A = (1 - r_t + \rho)m_t . \quad (32)$$

The second recurrence exploits some experimental facts. In Fig. 2 we have plotted the conflict ratio functions for three CC graphs with the same size and average degree (note that initial derivative is the same for all the graphs, in accordance with Prop. 2). We see that conflict ratios which reach a high value ($\bar{r}(n) > \frac{1}{2}$) are initially well approximated by a straight line (for m such that $\bar{r}(m) \leq \rho = 20 \div 30\%$), whereas functions that deviates from this behavior do not raise too much. This suggests us to assume an initial linearity in controlling m_t , as done by the following recurrence:

$$\text{Recurrence B: } m_{t+1}^B = \frac{\rho}{r_t} m_t . \quad (33)$$

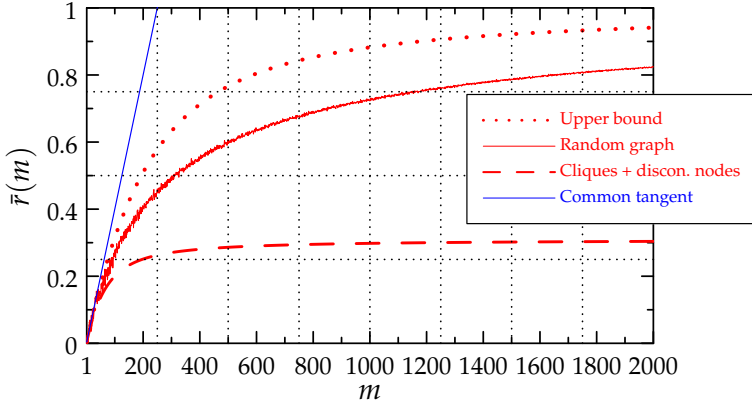


Fig. 2. A plot of $\bar{r}(m)$ for some graphs with $n = 2000$ and $d = 16$: (i) the worst case upper bound of Cor. 2 (ii) a random graph (edges chosen uniformly at random until desired degree is reached; data obtained by computer simulation) (iii) a graph unions of cliques and disconnected nodes.

The two recurrences can be roughly compared as follows (see Fig. 3): Recurrence A has a slower convergence than Recurrence B, but it is less susceptible to noise (the variance that makes r_t realizations different from \bar{r}_t). This is the reason for which we chose to merge them in an hybrid algorithm: initially, when the difference between r and ρ is big, we use Recurrence B to exploit its quick convergence and then Recurrence A is adopted, for a finer tuning of the control.

4.1 Experimental Evaluation

In the practical implementation of the control algorithm we have made the following optimizations:

- Since r_t can have a big variance, especially when m is small, we decided to apply the changes to m every T steps, using the averaged values obtained in these intervals, to smooth the oscillations.
- To further reduce the oscillations we apply a change only if the observed r_t is sufficiently different from ρ (e.g. more than 6%), thus avoiding small variations in the steady state, which interfere with locality exploitation because of the data moving from one processor to another.
- Another problem that must be considered is that for small values of m the variance is much bigger, so it is better to tune separately this case using different parameters (this optimization is not shown in the pseudo-code).

To validate our controller we have run the following simulation: a random CC graph of fixed average degree d is taken and the controller runs on it, starting with $m_0 = 2$. We are interested in seeing how many temporal steps it takes to converge to $m_t \simeq \mu$. As can be seen in [15] the parallelism profile of many practical applications can vary quite abruptly, e.g., Delauney mesh refinement

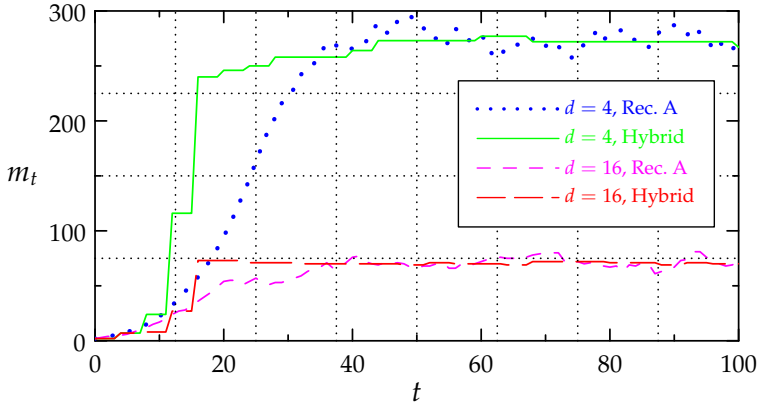


Fig. 3. Comparison between two realizations of the hybrid algorithm and one that only uses Recurrence A, for two different random graphs ($n = 2000$ in both cases). The hybrid version has different parameters for m greater or smaller than 20. ρ was chosen to be 20%. The proposed algorithm proves to be both quick in convergence and stable.

can go from no parallelism to one thousand possible parallel tasks in just 30 temporal steps. Therefore, an algorithm that wants to efficiently control the processors allocations for these problems must adapt very quickly to changes in the available parallelism. Our controller, that uses the very fast Recurrence B in the initial phase, proves to do a fast enough job: as shown in Fig. 3 in about 15 steps the controller converges close to the desired μ value.

5 Conclusions and Future Work

Automatic parallelization of irregular algorithms is a rich and complex subject and will offer many difficult challenges to researchers in the next future. In this paper we have focused on the processor allocation problem for unordered data-morphous algorithms; it would be extremely valuable to obtain similar results for the more general and difficult case of *ordered* algorithms (e.g., discrete event simulation), in particular it is very hard to obtain good estimates of the available parallelism for such algorithms, given the complex dependencies arising between the concurrent tasks. Another aspect which needs investigation, especially in the ordered context, is whether some statical properties of the behavior of irregular algorithms can be modeled, extracted and exploited to build better controllers, able to dynamically adapt to the different execution phases.

As for a real-world implementation, the proposed control heuristic is now being integrated in the Galois system and it will be evaluated on more realistic workloads.

Acknowledgments. We express our gratitude to Gianfranco Bilardi for the valuable feedback on recurrence-based controllers and to all the Galois project members for the useful discussions on optimistic parallelization modeling.

References

1. Agrawal, K., Leiserson, C.E., He, Y., Hsu, W.J.: Adaptive work-stealing with parallelism feedback. *ACM Trans. Comput. Syst.* 26(3), 7:1–7:32 (2008), <http://doi.acm.org/10.1145/1394441.1394443>
2. Alon, N., Spencer, J.: *The probabilistic method*. Wiley-Interscience (2000)
3. An, P., Jula, A., Rus, S., Saunders, S., Smith, T.G., Tanase, G., Thomas, N., Amato, N.M., Rauchwerger, L.: *Stapl: An Adaptive, Generic Parallel C++ Library*. In: Dietz, H.G. (ed.) *LCPC 2001*. LNCS, vol. 2624, pp. 193–208. Springer, Heidelberg (2003)
4. Blackford, L.S., Choi, J., Cleary, A., D’Azevedo, E., Demmel, J., Dhillon, I., Dongarra, J., Hammarling, S., Henry, G., Petitet, A., Stanley, K., Walker, D., Whaley, R.C.: *ScaLAPACK Users’ Guide*. Society for Industrial and Applied Mathematics, Philadelphia (1997)
5. Braunstein, A., Mézard, M., Zecchina, R.: Survey propagation: An algorithm for satisfiability. *Random Struct. Algorithms* 27(2), 201–226 (2005)
6. Eppstein, D.: Spanning trees and spanners. In: Sack, J., Urrutia, J. (eds.) *Handbook of Computational Geometry*, pp. 425–461. Elsevier (2000)
7. Freedman, D., Shepp, L.: Problem 62-3, an unfriendly seating arrangement. *SIAM Review* 4(2), 150 (1962), <http://www.jstor.org/stable/2028372>
8. Friedman, H.D., Rothman, D., MacKenzie, J.K.: Problem 62-3. *SIAM Review* 6(2), 180–182 (1964), <http://www.jstor.org/stable/2028090>
9. Frigo, M., Johnson, S.G.: The design and implementation of FFTW3. *Proceedings of the IEEE* 93(2), 216–231 (2005); special issue on Program Generation, Optimization, and Platform Adaptation
10. Frigo, M., Leiserson, C.E., Randall, K.H.: The implementation of the Cilk-5 multithreaded language. In: *PLDI*, pp. 212–223 (1998)
11. Georgiou, K., Kranakis, E., Krizanc, D.: Random maximal independent sets and the unfriendly theater seating arrangement problem. *Discrete Mathematics* 309(16), 5120–5129 (2009), <http://www.sciencedirect.com/science/article/B6V00-4W55T4X-2/2/72d38a668c737e68edf497512e606e12>
12. Guibas, L.J., Knuth, D.E., Sharir, M.: Randomized incremental construction of delaunay and voronoi diagrams. *Algorithmica* 7(4), 381–413 (1992)
13. Jensen, J.: Sur les fonctions convexes et les inégalités entre les valeurs moyennes. *Acta Mathematica* 30(1), 175–193 (1906)
14. Kalé, L.V., Krishnan, S.: Charm++: A portable concurrent object oriented system based on C++. In: *OOPSLA*, pp. 91–108 (1993)
15. Kulkarni, M., Burtscher, M., Cascaval, C., Pingali, K.: Lonestar: A suite of parallel irregular programs. In: *ISPASS*, pp. 65–76. IEEE (2009)
16. Kulkarni, M., Burtscher, M., Inkulu, R., Pingali, K., Cascaval, C.: How much parallelism is there in irregular applications? In: Reed, D.A., Sarkar, V. (eds.) *PPOPP*, pp. 3–14. ACM (2009)

17. Méndez-Lojo, M., Nguyen, D., Proutzos, D., Sui, X., Hassaan, M.A., Kulkarni, M., Burtscher, M., Pingali, K.: Structure-driven optimizations for amorphous data-parallel programs. In: Govindarajan, R., Padua, D.A., Hall, M.W. (eds.) PPOPP, pp. 3–14. ACM (2010)
18. Pingali, K., Nguyen, D., Kulkarni, M., Burtscher, M., Hassaan, M.A., Kaleem, R., Lee, T.H., Lenharth, A., Manevich, R., Méndez-Lojo, M., Proutzos, D., Sui, X.: The tao of parallelism in algorithms. In: Proceedings of the 32nd ACM SIGPLAN Conference on Programming Language Design and Implementation, PLDI 2011, pp. 12–25. ACM, New York (2011), <http://doi.acm.org/10.1145/1993498.1993501>
19. Püschel, M., Moura, J., Johnson, J., Padua, D., Veloso, M., Singer, B., Xiong, J., Franchetti, F., Gacic, A., Voronenko, Y., Chen, K., Johnson, R., Rizzolo, N.: Spiral: Code generation for dsp transforms. Proceedings of the IEEE 93(2), 232–275 (2005)
20. Reinders, J.: Intel threading building blocks. O’Reilly & Associates, Inc., Sebastopol (2007)
21. Tan, P.N., Steinbach, M., Kumar, V.: Introduction to Data Mining. Addison-Wesley (2005)
22. Tao, T.: Additive combinatorics. Cambridge University Press (2006)
23. Versaci, F., Pingali, K.: Brief announcement: processor allocation for optimistic parallelization of irregular programs. In: Proceedings of the 23rd ACM Symposium on Parallelism in Algorithms and Architectures, SPAA 2011, pp. 261–262. ACM, New York (2011), <http://doi.acm.org/10.1145/1989493.1989533>

Feedback-Based Global Instruction Scheduling for GPGPU Applications

Constantin Timm¹, Markus Görlich¹, Frank Weichert²,
Peter Marwedel¹, and Heinrich Müller²

¹ Computer Science 12, TU Dortmund, Germany
`constantin.timm@postamt.cs.uni-dortmund.de`

² Computer Science 7, TU Dortmund, Germany
`frank.weichert@tu-dortmund.de`

Abstract. In the face of the memory wall even in high bandwidth systems such as GPUs, an efficient handling of memory accesses and memory-related instructions is mandatory. Up to now, memory performance considerations were only made for GPGPU applications at source code level. This is not enough when optimizing an application towards high performance: The code has to be optimized at assembly level as well. Due to the spreading of GPGPU-capable hardware in smaller and smaller devices, the energy consumption of a program is – besides the performance – an important optimization goal.

In this paper, a novel compiler optimization technique, called FALIS (Feedback-based and memory-Aware global Instruction Scheduling), is presented based on global instruction scheduling and multi-objective genetic algorithms. The approach uses a profiling-based feedback in order to take the measured performance and energy consumption values inside a compiler into account. Profiling on the real hardware platform is important in order to consider the characteristics of the underlying hardware. FALIS increases runtime performance of a GPGPU application by up to 13.02% and decreases energy consumption by up to 10.23%.

Keywords: Energy-Aware Systems, Compilers, GPGPU, Multi-Objective Genetic Algorithm, Profiling.

1 Introduction

The development of faster single core processors and the availability of higher performance due to higher clock frequency is at an impasse [2]. The shift towards multi-core and many-core systems is tedious because of the increasing complexity on programming and the efficient utilization of parallelism. Furthermore, the memory wall [13] still exists, i.e. the processing speed is much higher than the memory speed. In the face of this memory wall, an efficient utilization of memory accesses and memory-related operations is mandatory. This also applies to multi- and many-core systems such as GPUs which can be utilized – enabled by GPGPU (General Purpose Computing on Graphics Processing Units) – for

HPC (High Performance Computing) applications in scientific and industrial contexts [17]. Due to green computing, considering energy consumption in the GPGPU software design process is important. Therefore, energy consumption and runtime performance are the two optimization targets in this paper. One of the most powerful and most interesting compiler optimization techniques for improving the execution order of instructions and therefore for memory and memory-related instructions, is instruction scheduling (IS). IS is used in this work to optimize the memory utilization of GPGPU applications. A novel partitioning method for scheduling on linear code sections will be presented. This method enables the scheduler to place the memory and memory-related instructions in the code of GPGPU applications in a more efficient manner, meaning that the available memory bandwidth is better utilized.

Most of the average case optimization techniques at compiler level have the drawback that they lack the capability to optimize the code in an elaborated way since they have no knowledge of the actual hardware platform. Therefore, this paper presents a profiling-based approach which feeds profiled performance indicators back into the compiler backend in order to achieve better solutions.

The major contributions of this paper are summarized as follows:

1. A global instruction scheduling method was integrated in the Nvidia CUDA compiler [15].
2. A multi-objective genetic algorithm was employed around the compilation process to optimize GPGPU applications with an adaptive IS towards the characteristic of the underlying hardware platform.

The remainder of the paper is organized as follows: After this introduction, Section 2 discusses related work. The main concepts of this paper is presented in Section 3 where a genetic global instruction scheduling is introduced. Section 4 evaluates the performance of the techniques presented in the preceding section. The paper ends with a conclusion of the work and an overview of possible future work.

2 Related Work

In [23], the authors showed that in traditional single core environments, instruction scheduling can have a negative effect on energy consumption. The authors of [9] developed an algorithm called balanced scheduling which performs scheduling of the instructions based on an assumption on instruction level parallelism. However, energy consumption was not part of that work and the runtime environment was not taken into account, as it has to be done for a GPU with its hardware thread scheduler. For special purpose system such as DSPs, several approaches with instruction scheduling methods [12,25] exist to produce optimized applications with respect to performance [12] and energy consumption [25]. Both works only targeted single core and single thread code. The first work which used local instruction scheduling for optimizing GPGPU applications was presented in [5]. In that work, a performance degradation was possible, because

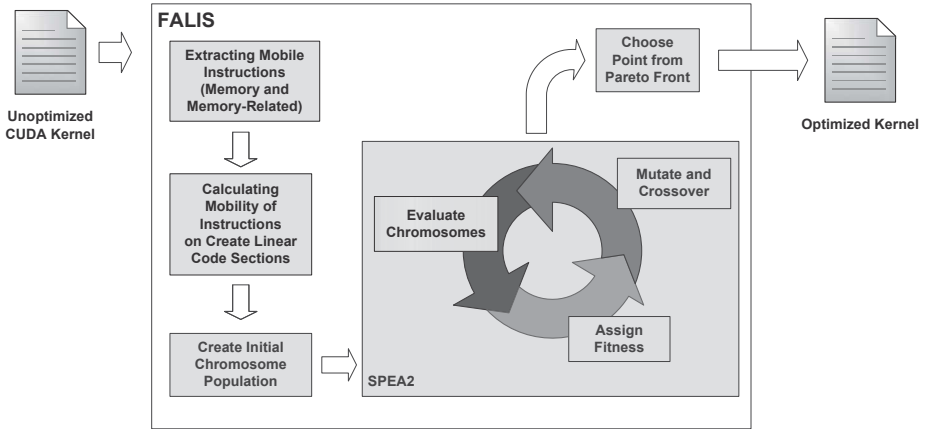


Fig. 1. FALIS Framework Structure

the optimizations had no information about the later stages of the compilation process and the runtime performance. A work optimizing GPGPU application towards better energy consumption and performance by applying local instruction scheduling was presented in [21]. The proposed method can be employed as a pre-optimization step for this work as it did not focus on memory instructions. Overall, it can be summarized that not all aspects of instruction scheduling for GPGPU applications have taken into account. In addition to that there were several papers published which have taken the energy consumption of GPGPU applications from a software perspective into account [4,19,20,26]. In these papers it was shown that software can be written in an energy efficient manner, but it was also shown that this is time-consuming, if there is no efficient tool (e.g. compiler) support. The latter is done within the novel FALIS framework.

3 FALIS

The FALIS (Feedback-based and memory-Aware global Instruction Scheduling) framework (as depicted in Figure 1) is presented in this section. FALIS applies instruction scheduling in order to optimize the CUDA kernels of a GPGPU application. Therefore, a genetic algorithm interfaces with the code generation module of the NVOpenCC compiler. In this module which works on a low level intermediate representation called Whirl [16], all memory and memory-related instructions are extracted as described in section 3.1. Afterwards, for all these instructions the basic block sequences are created where an instruction can be scheduled to (Section 3.2) and a mobility interval is calculated. The mobility interval comprises the positions in the Whirl intermediate representation of a kernel, where memory and memory-related instructions can be positioned. Finally, the sequences of instructions are optimized towards the objectives energy

<code>/*01c0*/</code>	<code>SYNC 01d0;</code>	<code>/*01c0*/</code>	<code>SYNC 01d0;</code>
<code>/*01c8*/</code>	<code>ST g[0x411], R8;</code>	<code>/*01c8*/</code>	<code>ST g[0x411], R8;</code>
<code>/*01d0*/</code>	<code>NOP;</code>	<code>/*01d0*/</code>	<code>MOV R10, R124;</code>
<code>/*01d8*/</code>	<code>BAR.SYNC;</code>	<code>/*01d8*/</code>	<code>BAR.SYNC;</code>
<code>/*01e0*/</code>	<code>MOV R10, R124;</code>	<code>/*01e0*/</code>	<code>...</code>

Unoptimized Sequence
Optimized Sequence

Fig. 2. Exemplary Unfavourable Instruction Sequences

consumption and runtime performance by employing a Genetic Algorithm (GA) named SPEA2 [27] (Section 3.3).

3.1 Extracting Mobile Instructions

The list of instructions relevant for optimization, called mobile instructions (*Mob_Ins*), can comprise all load and store operations for the different memories (const, global/local, shared) and memory-related instructions such as (barrier) synchronisation statements. The reason, why the latter are also considered is described in the following. The atomic runtime entity of a Nvidia GPGPU application is a thread. A thread runs on a single streaming processor (SP) of a graphics card. A set of threads, called a block, is allocated on one streaming multiprocessor which is a group of several SPs. At block level, there is no memory consistency – except in the thread itself. Nevertheless, threads of a block can force a consistent view on the shared memory by using synchronisation statements. They have to be added to the thread at source code level by the programmer. In [21], it was revealed that the performance can be decreased by such statements due to the requirement of adding additional instructions at machine code level, ensuring a proper timing. The evaluation results showed that it is not always mandatory to add these instructions if other existing instructions can substitute them (as depicted in Figure 2 – on the left-hand side). The substitution possibly can save cycles, resulting in performance increase and energy consumption decrease. Thus, the approach presented in this paper can also treat synchronisation statements, in addition to memory instructions. For them, a position in the code should be revealed which lead to a better performance or/and lower energy consumption. In the scope of FALIS, the position of each extracted mobile instruction is variable. The variability is explained in the following section.

3.2 Calculating Mobility of Instructions on Linear Code Sections

The purpose of instruction scheduling is to schedule mobile instructions in way that they access the GPU’s memory system in an efficient way. In the following, mobile instruction positioning paradigms (MIPP), which can be beneficial and therefore are supported by FALIS, are presented. For the first MIPP, the

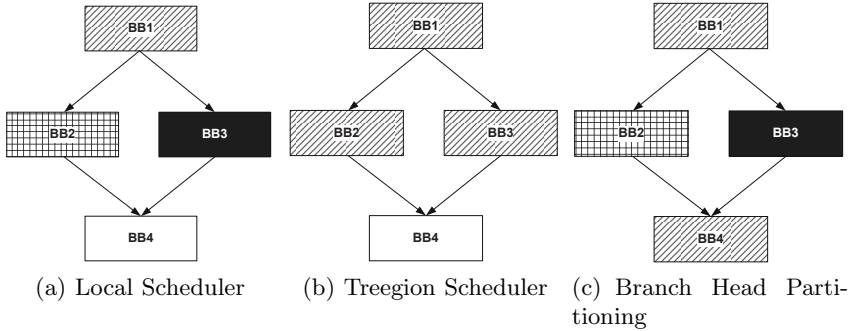


Fig. 3. Reachability of Different Instruction Scheduling Methods

memory instructions are close so that their sequence (depending on instruction dependencies) can possibly be changed. Within the second MIPP, they are far away from each other so that they cannot interfere with each other. The latter is, in particular, important when the limited bandwidth of the graphics cards' main memory should be utilized in an efficient way. This method is based on the observation of the authors of [8]. In that work the authors revealed that many concurrent memory accesses can decrease performance. Figure 3 shows different methods for scheduling instructions. In Figure 3(a) one can see that within local instruction scheduling, the first MIPP is applicable due to the capability to schedule instructions near to each other. Local instruction scheduling can only schedule an instruction inside one basic block as denoted by the different layouts of the basic blocks. In Figures 3(a), 3(b) and 3(c), different layouts mean that instructions cannot be moved from one basic block to another. While basic blocks with the same layout mean that instructions can possibly be exchanged between them. But for the second MIPP local instruction scheduling is not enough. Therefore, methods considering several basic blocks for scheduling of instructions are required. An example for a state-of-the-art technique is TREEGION scheduling [1]. It only schedules to neighbouring basic blocks and therefore, this method is not able to handle the second MIPP in an efficient manner. In addition to that, TREEGION scheduling uses compensation code which may adversely affect the performance objective because code which is executed predicated is slower than normally executed code on the GPU [7]. Therefore, a technique called *branch-head-partitioning* was introduced in [6] which enables a global scheduler to schedule on linear code portions (e.g. linear code sections inside loops) without the use of compensation code but with the possibility to schedule an instruction far away from the original basic block as depicted in Figure 3(c).

The Nvidia compiler works on a combined control flow and data dependency graph $G = (V, E)$. $V = \{i_1, \dots, i_n\}$ is the set of all instructions in intermediate representation of one kernel and $E \subseteq V \times V$ are the data dependencies or control

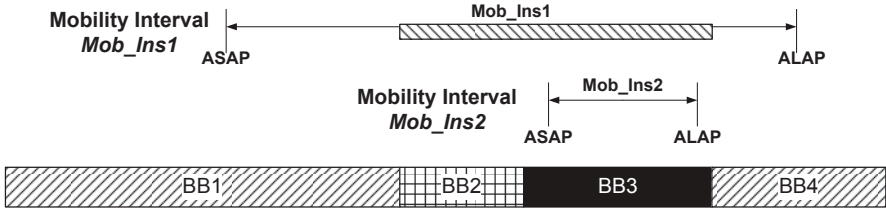


Fig. 4. Mobility of Mobile Instructions (*Mob_Ins*)

flow dependencies between two instructions. *Branch-head-partitioning* [6] creates new dependency edges in the combined control flow and data dependency graph G . The combined control flow and data dependency graph comprises also the barrier synchronisation statements. In order to take the barrier synchronisation instruction for global instruction scheduling into account, the original combined control flow and data dependency graph G is used as a basis. In order to maintain the semantics of a kernel, for each load/store instruction $i_x \in V$ preceding a barrier synchronisation instruction $i_y \in V$ ($x < y$), a dependency edge is inserted between i_x and i_y . The same is done for a barrier synchronisation instruction and all succeeding load/store instructions. All control flow edges of the original combined control flow and data dependency graph G were replaced by edges between non-branch instructions. This enables single instructions to be moved over branches, if there are no data dependencies in the branch..

For calculating the mobility of a mobile instruction, firstly, ASAP scheduling (As Soon As Possible) [22] is conducted with the help of the control flow and data dependency graph G . This reveals the lower bound to where the memory instruction can be relocated. In a second step a scheduling with scheduling policy ALAP (As Late As Possible) [11] is performed to determine the upper bound for positions. Both, ASAP and ALAP were originally used at the synthesis of hardware but also work on other graphs like combined control flow and data dependency graph utilized in the paper. The mobility interval for a mobile instruction is, as depicted in Figure 4, the interval between the ASAP and the ALAP position. The shaded area for mobile instructions in Figure 4 marks positions where *Mob_Ins1* can not be scheduled to, because the instruction can not be placed inside a branch if it is not placed there before. The mobility values are then employed by FALIS in order to optimize a program. As it was revealed in [21], a GA is an appropriate optimization technique in the field of instruction scheduling for GPGPU applications since it can cope with effects of the warp scheduler of Nvidia graphics cards.

3.3 Multi-Objective Genetic Algorithm Specification

FALIS utilizes a multi-objective genetic algorithm, which uses real profiling data to evaluate the optimization potential of a solution. In the following, terms in the scope of FALIS are presented in more detail:

- **Gene** g : Basic feature which represents the position of a certain instruction inside the linear basic block sequences for one CUDA kernel. The minimal and maximal value for each gene is the interval limited by the positions evaluated by the ASAP and the ALAP schedule.
- **Chromosome** c : Gene sequence g_1, \dots, g_n . $g_i (i \in [1, n])$ is the assignment of position to a mobile instruction. There are n mobile instructions in the code.
- **Individual** I : An element of the solution space ($I \in \mathcal{I}$). It comprises a chromosome. The set of all individuals is denoted as \mathcal{I} in the following.
- **Population** \mathcal{I}_x : Set of considered individuals $\mathcal{I}_x \subseteq \mathcal{I}$.

Energy and Runtime Measurement: The two major goals of the optimization process are energy consumption decrease and performance increase. Both are measured with a performance and energy benchmarking system as depicted in Figure 5. Due to the major focus of benchmarking the GPGPU application executed by the graphics card, the power consumption of the system hosting the graphics card is not measured. The power consumption is measured with power clamps at the power supply lines of the PCI Express bus for 12V and 3.3V. Therefore the power supply lines of the PCI express bus have been extended to measure the current with the power clamps. If a graphics card needs even more power from the main system power supply it is also possible to measure the current through this interface.

The power consumption of a graphics card is described as:

$$P(t) = P^{3.3V}(t) + P^{12V}(t) \quad (1)$$

where P^{12V} is the power consumption (W) at the 12V power supply lines, $P^{3.3V}$ is a power consumption (W) at the 3.3V power supply lines and t is a time value in the runtime interval of kernel. The energy consumption and the runtime of a GPGPU application kernel are evaluated as follows: The runtime interval $[T_0, T_{run}]$ is delimited by trigger signals (TS) in the source code which are initiated by the host and can be measured at the output of the RS232 serial port. The end signal is triggered after a `cudaThreadSynchronize()` command (also in the host code) which forces CUDA to finish the kernel execution until this position in the source code. A certain energy $E(I)$ is consumed for the runtime $runtime(I)$ ($[T_0, T_{run}]$) for individual I (representing a particular scheduling for one kernel):

$$E(I) = \sum_{t \in [T_0, T_{run}]} \frac{P(t)}{f_s} \quad (2)$$

in which f_s is the sampling frequency (s^{-1} or *Hertz*) of the oscilloscope measurements, $P(t)$ the power consumption in Watt (W), E is the energy in Joule (J) and t is the time in the runtime interval.

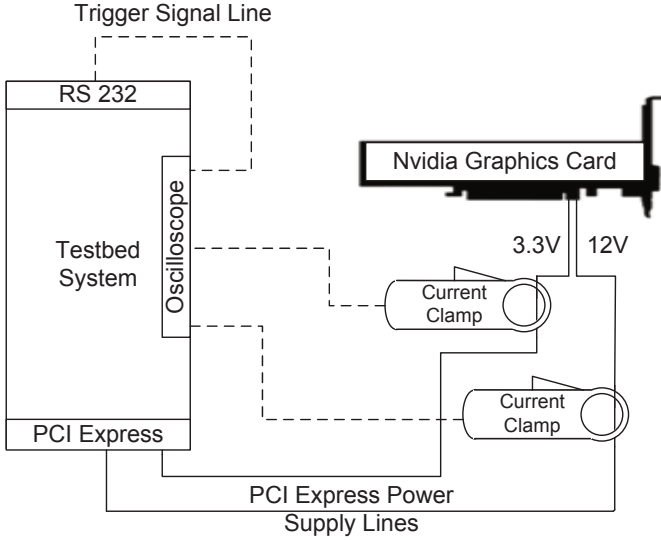


Fig. 5. Energy and Runtime Evaluation Framework

FALIS Workflow: The work flow of the genetic algorithm – in a more abstract form as opposed to the detailed description of SPEA2 in [27] – comprises several steps and starts with the generation of an initial population \mathcal{I}_x with $x = 0$. For the individuals in that population $I \in \mathcal{I}_x$, the fitness values are evaluated. Based on these fitness values, a selection of the most appropriate candidates for the creation of the next generation \mathcal{I}_{x+1} is done. The schematic of the workflow of SPEA2 is depicted in Figure 1. A subset of the elements of the \mathcal{I}_{x+1} -th population take part in evolutionary processes:

- *Crossover*: Exchange of a part of the genes between two individuals $I, I' \in \mathcal{I}_x$.
- *Mutation*: Randomized mutation of genes of an individual $I \in \mathcal{I}_x$.

In FALIS, *Crossover* and *Mutation* change the position of the memory and memory-related instruction which can lead to the situation that invalid individuals can be created, which represent a GPGPU application which can have another semantics with respect to the original version. Therefore, an individual validator was implemented which checks, with the help of a control flow graph and a data dependency graph if the created program is correct. In FALIS, when population size μ is reached in the selection process for population \mathcal{I}_{x+1} , the complete process restarts with this population. The complete process is repeated until the population converges or a fixed number of evolutions is accomplished.

The fitness function enables the assessment of the quality of an individual $I \in \mathcal{I}$ with regard to a certain objective. In order to determine better solutions for each kernel, each individual of a population is evaluated with regard to the

fitness function by FALIS. In contrast to single objective genetic algorithms, in multi-objective algorithms several competing objectives must be handled. This can be done, e.g. with a fitness function and selection process tailored towards multi-objectives. The most important method of SPEA2 is the multi-objective fitness function. SPEA2 assigns the fitness $f(I) = R(I) + D(I)$ to an individual I , according to the following equations.

$$R(I) = \sum_{J \in \mathcal{I}_x, J \succ I} S(J) \quad (3)$$

is the raw fitness of an individual I which takes into account the strength

$$S(J) = \{Z | Z \in \mathcal{I}_x, J \succ Z\} \quad (4)$$

of the individuals J which dominate I . $I \succ J$ is the Pareto dominance function defined in [24] and means I dominates J , if the condition

$$\begin{aligned} runtime_{ratio}(I) &\leq runtime_{ratio}(J) \wedge \\ E_{ratio}(I) &\leq E_{ratio}(J) \wedge \\ (runtime_{ratio}(I) < runtime_{ratio}(J) \vee \\ E_{ratio}(I) < E_{ratio}(J)) \end{aligned} \quad (5)$$

is true. The reference individual without scheduling for calculating the performance increase and energy consumption decrease is defined as I_{un} with mobile instructions at their original position. The *runtime* improvement for an individual I is specified as the runtime of the scheduled version $runtime(I)$ with respect to the completely unchanged version of the benchmark $runtime_{ratio}(I) = \frac{runtime(I)}{runtime(I_{un})}$. The *energy consumption* reduction $E_{ratio}(I) = \frac{E(I)}{E(I_{un})}$ is, analogously to the *runtime* improvement, defined as the energy consumption of the scheduled version $E(I)$ in comparison to the energy consumption of unchanged benchmark code $E(I_{un})$. In addition to that SPEA2 also provides a *correction function* $D(I)$ to take density information into account. With this approach, it is possible to optimize CUDA kernels towards several objectives. FALIS is designed to optimize the objectives energy consumption and performance. The runtime and energy consumption values are stored for each individual, but only the individuals on the pareto-front are interesting for the application designer, as they minimize at least one objective.

4 Evaluation

In this section, the optimization capability of FALIS is evaluated. This is accomplished towards the following to objectives: runtime and energy consumption. First of all, an overview of the benchmarks and the test system is given and then results are presented.

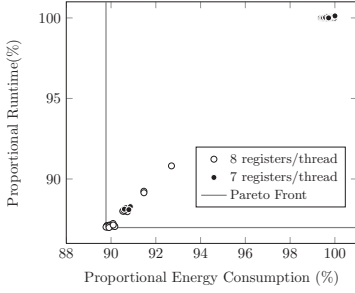
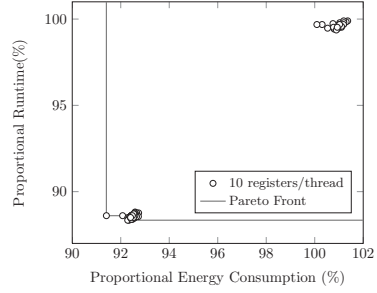
(a) Kernel *convolutionRowsKernel* [14](b) Kernel *srad_cuda_1* [3]

Fig. 6. Proportional Energy Consumption (E_{ratio}) and Proportional Runtime ($runtime_{ratio}$) Reduction for all Evaluated Individuals

4.1 Experimental Environment and Theoretical Evaluation

The benchmark suite for this evaluation contains benchmarks from the following sources:

- Nvidia CUDA examples [14]
- VSIPL-GPU-Library [10]
- Rodinia benchmark suite [3].

The benchmark suite comprises a large variety of application domains such as: medical imaging, data mining, image processing, pattern recognition, simulation etc. The benchmark characteristics cover benchmarks with and without extensive main memory utilization and benchmarks which are more computationally expensive. The system used in this study consists of the following components: AMD Phenom X4 9650 (Processor), 4GB DDR3 PC1066 (Main Memory). The power clamp was a *Hameg - HZO50* and the oscilloscope was a Digilent Electronics Explorer Board. For the SPEA2 implementation in FALIS the JECO library [18] was utilized. The graphics card used in these tests was a Nvidia 9500 GT (shader clock speed : 1107 MHz and memory clock speed: 400 MHz). The probability values for SPEA2 were 40% for *mutation* and 20% for *crossover*. The start population size depends on the number of genes in a chromosome of a certain benchmark to ensure that the solution space is sufficiently explored. Due to the specialisation to memory and memory-related instructions, not all benchmarks of the three benchmarks suites show a performance increase or energy consumption decrease. Only the following benchmarks show significant optimization gain and will be taken into account in the results section:

- Kernel *convolutionRowsKernel*, benchmark *convolutionSeparable* [14]
- Kernel *convolutionColumnsKernel*, benchmark *convolutionSeparable* [14]
- Kernel *srad_cuda_1*, benchmark *SRAD* [3]
- Kernel *CUDAkernelQuantizationShort*, benchmark *dct8x8* [14]
- Kernel *d_recursiveGaussian_rgba*, benchmark *recursiveGaussian* [14]
- Kernel *cuda_compute_flux*, benchmark *cfid* [3]

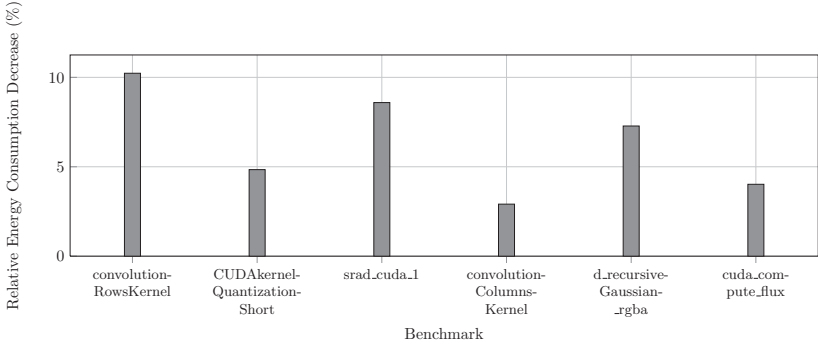


Fig. 7. Energy Consumption Analysis of Optimized Benchmarks

4.2 Results

Figures 7 and 8 depict the improvements achieved with FALIS for benchmarks leading to a performance increase (shown in Figure 8) or an energy consumption decrease (shown in Figure 7) as listed in the former section. The maximal value for reducing the energy consumption is 10.23% and the maximal value for runtime decrease is 13.02%. They were measured for kernel *convolutionRowsKernel* of the benchmark *convolutionSeparable* [14]. Another kernel which was accelerated significantly was the kernel *srad_cuda_1* of benchmark *SRAD* [3]. Detailed evaluations of explored solutions are depicted in Figure 6(a) respectively Figure 6(b). Single points inside the figures show the runtime and energy consumption decrease for one individual. The Pareto-optimal points are connected with a line called Pareto front. A runtime decrease of 11.66% and an energy consumption decrease of 8.59% was achieved for kernel *srad_cuda_1* (chromosome length: 64). As one can see from Figure 6(b), there are two clusters. One cluster comprises solutions which have an impact on the runtime and the energy consumption. The other exemplary kernel is depicted in Figure 6(a) (chromosome length: 304). The energy consumption decreases up to 10.23% and the runtime decreases up to 13.02%. Within the optimization of kernel *convolution-RowsKernel*, the change in register utilization – 7 registers per thread changed to 8 registers per thread – has a positive effect on the runtime and the energy consumption. The performance of kernel *CUDAkernelQuantizationShort* of benchmark *dct8x8* can be increased by 4.84% and energy consumption is decreased by 3.7%. The performance of kernel *CUDAkernelQuantizationShort* of benchmark *dct8x8* can be increased by 4.84% and energy consumption is decreased by 3.7%. In addition to that performance of kernel *d_recursiveGaussian_rgba* of benchmark *recursiveGaussian* is increased by 8.13% and energy consumption is decreased by 7.28%.

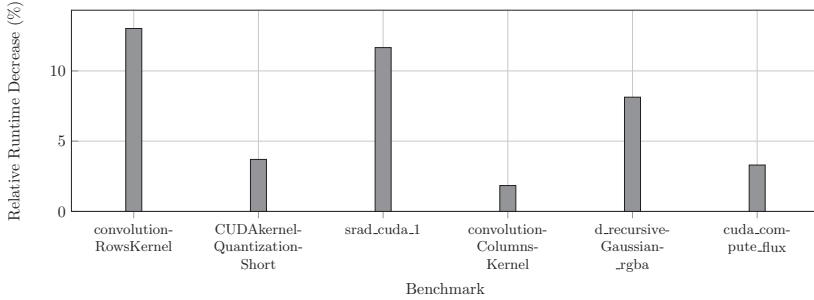


Fig. 8. Runtime Analysis of Optimized Benchmarks

5 Conclusion

GPGPU application optimizations are usually performed manually in a time-consuming trial-and-error process without efficient compiler support. Additionally, the lack of energy consumption aware optimizations is unfavorable for green computing and the utilization of GPGPU-capable chips in mobile systems. Therefore, this paper presents a novel multi-objective optimization process based on global instruction scheduling methods, called FALIS, which optimizes the energy consumption and the runtime simultaneously. For solving this optimization problem, a genetic algorithm was used which feeds profiling data back to the optimization process. Due to the utilization of a state-of-the-art multi-objective genetic algorithm it was possible to optimize an GPGPU application towards two objectives: runtime and energy consumption. FALIS was focus on memory and memory-related instructions which can have a great impact on GPGPU application performance in the face of the memory wall problem. With FALIS reductions of up to 10.23% in energy consumption and 13.02% in runtime could be achieved for real-world benchmarks.

In the study presented in this paper, memory and memory-related instructions have been taken as relevant instructions to be scheduled. However, it could possibly advantageous to schedule also other instructions such as the instructions used to calculated the addresses for the memory accesses. Therefore, in future works it will be evaluated if optimized scheduling of more types of instructions is even more beneficial for the energy consumption and the performance.

Acknowledgement. Part of the work on this paper has been supported by Deutsche Forschungsgemeinschaft (DFG) within the Collaborative Research Center SFB 876 "Providing Information by Resource-Constrained Analysis", project B2.

References

1. Banerjia, S., Havanki, W.A., Conte, T.M.: Treeregion Scheduling for Highly Parallel Processors. In: Lengauer, C., Griebel, M., Gorlatch, S. (eds.) Euro-Par 1997. LNCS, vol. 1300, pp. 1074–1078. Springer, Heidelberg (1997)
2. De Bosschere, K., Luk, W., Martorell, X., Navarro, N., O’Boyle, M., Pnevmatikatos, D., Ramírez, A., Sainrat, P., Sez nec, A., Stenström, P., Temam, O.: High-Performance Embedded Architecture and Compilation Roadmap. In: Stenström, P. (ed.) Transactions on High-Performance Embedded Architectures and Compilers I. LNCS, vol. 4050, pp. 5–29. Springer, Heidelberg (2007)
3. Che, S., Boyer, M., Meng, J., Tarjan, D., Sheaffer, J.W., Lee, S.H., Skadron, K.: Rodinia: A Benchmark Suite for Heterogeneous Computing. In: Proceedings of the IEEE International Symposium on Workload Characterization (IISWC), pp. 44–54 (2009)
4. Cho, S., Melhem, R.: Corollaries to Amdahl’s Law for Energy. IEEE Computer Architecture Letters, 25–28 (2008)
5. Dominguez, R., Kaeli, D.R.: Improving the open64 backend for GPUs. Poster at Google Summer School (2009)
6. Görlich, M.: Untersuchung und Verbesserung der Speicherzugriffsverteilung in GPGPU-Programmen unter Nutzung von lokalen Schedulingmethoden. Master’s thesis, Embedded System Group, Faculty of Computer Science, TU Dortmund (2011)
7. Han, T.D., Abdelrahman, T.S.: Reducing branch Divergence in GPU Programs. In: Proceedings of the Fourth Workshop on General Purpose Processing on Graphics Processing Units, pp. 1–8 (2011)
8. Hong, S., Kim, H.: An Analytical Model for a GPU Architecture with Memory-level and Thread-level Parallelism Awareness. In: Proceedings of the 36th Annual International Symposium on Computer Architecture (ISCA), pp. 152–163 (2009)
9. Kerns, D.R., Eggers, S.J.: Balanced Scheduling: Instruction Scheduling When Memory Latency is Uncertain. In: Proceedings of the ACM SIGPLAN Conference on Programming Language Design and Implementation (PLDI), pp. 278–289 (1993)
10. Kerr, A., Campbell, D., Richards, M.: GPU VSIPL: High-Performance VSIPL Implementation for GPUs. In: Proceedings of the 12th High Performance Embedded Computing Workshop (HPEC), Lexington, Massachusetts, USA (2008)
11. Kung, S.Y., Kailath, T., Whitehouse, H.J.: VLSI and Modern Signal Processing. Prentice Hall Professional Technical Reference (1984)
12. Leupers, R.: Instruction Scheduling for Clustered VLIW DSPs. In: Proceedings of the International Conference on Parallel Architecture and Compilation Techniques (PACT), pp. 291–300 (2000)
13. Machanick, P.: Approaches to Addressing the Memory Wall. Technical report, School of IT and Electrical Engineering, University of Queensland (2002)
14. NVIDIA Corporation: CUDA Architecture (2009)
15. NVIDIA Corporation: The CUDA Compiler Driver NVCC (2009)
16. Open64 Project at Rice University: Open64 Compiler: Whirl Intermediate Representation (2007), www.mcs.anl.gov/OpenAD/open64A.pdf
17. Owens, J., Luebke, D., Govindaraju, N., Harris, M., Krüger, J., Lefohn, A., Purcell, T.: A Survey of General-Purpose Computation on Graphics Hardware. Computer Graphics Forum, 80–113 (2007)

18. Risco-Martin, J.: Java Evolutionary COmputation library (JECO) (2012), <https://sourceforge.net/projects/jeco>
19. Rofouei, M., Stathopoulos, T., Ryffel, S., Kaiser, W., Sarrafzadeh, M.: Energy-Aware High Performance Computing with Graphic Processing Units. In: Proceedings of the Workshop on Power Aware Computing and Systems, HotPower (2008)
20. Timm, C., Gelenberg, A., Marwedel, P., Weichert, F.: Energy Considerations within the Integration of General Purpose GPUs in Embedded Systems. In: Proceedings of the Annual International Conference on Advances in Distributed and Parallel Computing, ADPC (2010)
21. Timm, C., Weichert, F., Marwedel, P., Müller, H.: Multi-Objective Local Instruction Scheduling for GPGPU Applications. In: Proceedings of the International Conference on Parallel and Distributed Computing Systems, PDCS (2011)
22. Tseng, C.J., Siewiorek, D.: Automated Synthesis of Data Paths in Digital Systems. *IEEE Transactions on Computer-Aided Design of Integrated Circuits and Systems*, 379–395 (1986)
23. Valluri, M., John, L.: Is Compiling for Performance == Compiling for Power? In: Proceedings of the Workshop on Interaction between Compilers and Computer Architectures, INTERACT (2001)
24. Voorneveld, M.: Characterization of Pareto Dominance. *Operations Research Letters*, 7–11 (2003)
25. Wang, Z., Hu, X.S.: Energy-Aware Variable Partitioning and Instruction Scheduling for Multibank Memory Architectures. *ACM Transactions on Design Automation of Electronic Systems (TODAES)*, 369–388 (2005)
26. Woo, D.H., Lee, H.H.: Extending Amdahl’s Law for Energy-Efficient Computing in the Many-Core Era. *IEEE Computer*, 24–31 (2008)
27. Zitzler, E., Giannakoglou, K., Tsahalis, D., Periaux, J., Papailiou, K., Fogarty, T., Ler, E.Z., Laumanns, M., Thiele, L.: SPEA2: Improving the Strength Pareto Evolutionary Algorithm For Multiobjective Optimization. In: Proceedings of the International Conference on Evolutionary and Deterministic Methods for Design, Optimization and Control with Applications to Industrial and Societal Problems, EUROGEN (2001)

Parallel Algorithm for Landform Attributes Representation on Multicore and Multi-GPU Systems

Murilo Boratto¹, Pedro Alonso², Carla Ramiro²,
Marcos Barreto³, and Leandro Coelho¹

¹ Núcleo de Arquitetura de Computadores e Sistemas Operacionais (ACSO),
Universidade do Estado da Bahia (UNEB),
Salvador, Bahia, Brazil

{muriloboratto, leandrocoelho}@uneb.br

² Departamento de Sistemas Informáticos y Computación (DSIC),
Universidad Politécnica de Valencia (UPV),
Valencia, España

{palonso, cramiro}@dsic.upv.es

³ Laboratório de Sistemas Distribuídos (LaSiD),
Universidade Federal da Bahia (UFBA),
Salvador, Bahia, Brazil

marcoseb@dcc.ufba.br

Abstract. Mathematical models are often used to simplify landform representation. Its importance is due to the possibility of describing phenomena by means of mathematical models from a data sample. High processing power is needed to represent large areas with a satisfactory level of details. In order to accelerate the solution of complex problems, it is necessary to combine two basic components in heterogeneous systems formed by a multicore with one or more GPUs. In this paper, we present a methodology to represent landform attributes on multicore and multi-GPU systems using high performance computing techniques for efficient solution of two-dimensional polynomial regression model that allow to address large problem instances.

Keywords: Mathematical Modeling, Landform Representation, Parallel Computing, Performance Estimation, Multicore, Multi-GPU.

1 Introduction

Some recent events have encouraged the development of applications that represent geophysical resources efficiently. Among these representations, mathematical models for representing landform attributes stand out, based on two-dimensional polynomial equations [8]. Landform attributes representation problem using polynomial equations had already been studied in [1]. However, distributed processing was not used in that work, which implied the usage of a high degree polynomial, thus limiting the area representation. It occurred because the greater the represented information, the greater computational power is needed. Furthermore, a high degree polynomial is required to represent a large area correctly, which also demands a great computational power.

Among the reasons for fulfilling landform representation, we focus on measuring agricultural areas, having as preponderant factors: plantation design, water resource optimization, logistics and minimization of erosive effects. Consequently, landform representation process becomes a fundamental and needful tool in efficient agriculture operation, especially in the agricultural region located in São Francisco river valley, which stands out as one of the largest viniculture and fruit export areas in Brazil. In addition, one of the main problems that make efficiency use difficult in agricultural productivity factors in this areas occurred due to soil erosion associated with inappropriate land use. In this context, the work proposed here contributes to the characterization of soil degradation processes.

Today it is usual to have computational systems formed by a multicore with one or more Graphics Processing Units (GPUs) [13]. These systems are heterogeneous, due to different types of memory and different speeds of computation between CPU and GPU cores. In order to accelerate the solution of complex problems it is necessary to use the aggregated computational power of the two subsystems. Heterogeneity introduces new challenges to algorithm design and system software. Our main goal is to fully exploit all the CPU cores and all GPU devices on these systems to support matrix computation [14]. Our approach achieves the objective of maximum efficiency by an appropriate balancing of the workload among all these computational resources.

The purpose of this paper is to present a methodology for landform attributes representation of São Francisco river valley region based on two-dimensional polynomial regression method on multicore and multi-GPU systems. Section 2 briefly describes the mathematical model. Section 3 explains the parallel model on multicore and multi-GPU systems and the parallel implementation. Section 4 presents the experimental results. Conclusions and future work section closes the paper.

2 Mathematical Model

A mathematical landform model is a computational mathematical representation of a phenomenon that occurs within a region of the earth surface [7]. This model can represent plenty of geographic information from a site such as: geological, geophysical, humidity, altitude, terrain, etc. One available technique to accomplish this representation is the Regular Grid Model [11]. This work makes the surface mapping with a global fitting using the polynomial regression technique. This technique fits a two-dimensional polynomial that best describes the data variation from a sample. The problem is that high computational power demanded to perform the regression in a large data set made the process very limited. Polynomial regression is a mathematical modeling that attempts to describe the relation among observed phenomena.

Figure 1 shows an example of a Regular Grid representation generated from a regular sparse sample that represents information of an area altitude. According to Rawlings [10], modeling can be understood as the development of a mathematical analytical model that describes the behavior of a random variable of interest. This model is used to describe the behavior of independent variables whose relationship with the dependent variable is best represented in a non-linear equation. The relationship among variables is described by two-dimensional polynomial functions, where the fluctuation of the

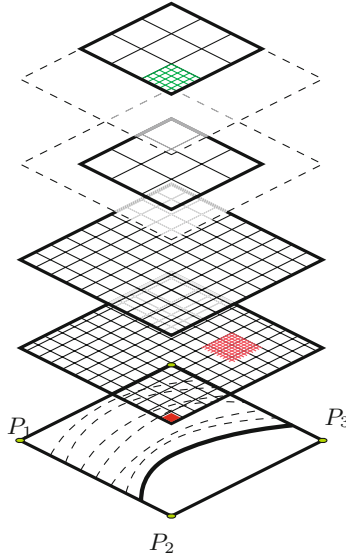


Fig. 1. Model for landform attributes representation: Regular Grid

dependent variable y is related to the fluctuation of the independent variable. Particularly, in the case study developed in this project, the non-linear regression has been used to describe the relationship between two independent variables (latitude and longitude) and a dependent variable (height). The mathematical model we use provides the estimation of the coefficients of two-dimensional polynomial functions, of different degrees in x and y , which represent terrain altitude variation from any area.

When using mathematical regression models, the most widely used estimation method of parameters is the Ordinary Least Squares [5] that consists of the estimation of a function to represent a set of points minimizing the deviations squared. Given a set of geographic coordinates (x, y, z) , taking the estimated altitude as estimation function of these points, a polynomial of degree r and s in x and y can be given as Equation 1, with ε_{ij} as the error estimated by Equation 2, where $0 \leq i \leq m$ and $0 \leq j \leq n$,

$$\widehat{z} = f(x_i, y_j) = \sum_{k=0}^r \sum_{l=0}^s a_{kl} x_i^k y_j^l, \quad (1)$$

$$\varepsilon_{ij} = z_{ij} - \widehat{z}_{ij}. \quad (2)$$

The coefficients a_{kl} ($k = 0, 1, \dots, r; l = 0, 1, \dots, s$) that minimize the function error of the estimation function $f(x, y)$, can be obtained by solving Equation 3 for $c = 0, 1, \dots, r$ and $d = 0, 1, \dots, s$,

$$\frac{\partial \xi}{\partial a_{cd}} = 0, \quad (3)$$

where,

$$\xi = \sum_{i=0}^m \sum_{j=0}^n \varepsilon_{ij}^2 = \sum_{i=0}^m \sum_{j=0}^n (z_{ij} - \widehat{z}_{ij})^2.$$

From Equations 4 to 10 we get the development of Equation 3

$$\varepsilon_{ij}^2 = (z_{ij} - \sum_{k=0}^r \sum_{l=0}^s a_{kl} x_i^k y_j^l)^2, \quad (4)$$

$$z_{ij} = \sum_{k=0}^r \sum_{l=0}^s a_{kl} x_i^k y_j^l + \varepsilon_{ij}, \quad (5)$$

$$\xi = \sum_{i=0}^m \sum_{j=0}^n (z_{ij} - \sum_{k=0}^r \sum_{l=0}^s a_{kl} x_i^k y_j^l)^2, \quad (6)$$

$$\frac{\partial \xi}{\partial a_{cd}} = 2 \sum_{i=0}^m \sum_{j=0}^n [(z_{ij} - \sum_{k=0}^r \sum_{l=0}^s a_{kl} x_i^k y_j^l)^2] x_i^c y_j^d, \quad (7)$$

$$2 \sum_{i=0}^m \sum_{j=0}^n [(z_{ij} - \sum_{k=0}^r \sum_{l=0}^s a_{kl} x_i^k y_j^l)^2] x_i^c y_j^d = 0, \quad (8)$$

$$\sum_{i=0}^m \sum_{j=0}^n \sum_{k=0}^r \sum_{l=0}^s a_{kl} x_i^{k+c} y_j^{l+d} = \sum_{i=0}^m \sum_{j=0}^n z_{ij} x_i^c y_j^d, \quad (9)$$

$$\sum_{i=0}^m \sum_{j=0}^n [z_{ij} x_i^c y_j^d - (\sum_{k=0}^r \sum_{l=0}^s a_{kl} x_i^{k+c} y_j^{l+d})] = 0. \quad (10)$$

The particularized form of the polynomial can be exemplified for $r = s = n$ case, from Equation 11, where:

$$\widehat{Z}_{ij}(x_i, y_i) = a_{00} x^0 y^0 + a_{01} x^0 y^1 + \dots + a_{nn} x^n y^n. \quad (11)$$

Developing Equation 10 for the same particular case, we obtain Equations 12 and 13 9. The final solution is summarized in the matrix representation form $Ax = b$, where A is the matrix formed by x_{lc} terms, vector x is formed by the a_{kl} terms and vector b is formed by b_l terms.

$$x_{lc} = \sum_{i=0}^m \sum_{j=0}^n x_i^\alpha y_j^\beta, \quad (12)$$

$$b_l = \sum_{i=0}^m \sum_{j=0}^n Z_{ij} x_i^\gamma y_j^\delta. \quad (13)$$

This information is valid for any matrix format that is intended to represent and to any degree of two-dimensional polynomial, which is to be fitted.

3 Parallel Computational Model

One of the most decisive concepts to successfully program modern GPU and multicore computers uses GPU and multicore processors is the underlying model of the parallel computer. A GPU card connected to a sequential computer can be considered as an isolated parallel computer fitting a SIMD model, i.e. a set of up to 512 (depending on model) processors running the same instruction simultaneously, each on its own set of data. On the other hand, CPU can be seen as a set of independent computational resources (core) that can cooperate in the solution of a given problem.

Thus, a realistic programming model should consider the host system comprising CPU cores and graphic cards as a whole thus leading to a heterogeneous parallel computer model. We follow a model similar to the one described in [2], where the machine is considered as a set of computing resources with different characteristics connected via independent links to a shared global memory. Such model would be characterized by the number and type of concurrent computational resources with different access time to reach each resource and the different types and levels of memory (Figure 2). Programming such a heterogeneous environment poses challenges at two different levels. At the first one, the programming models for CPUs and GPUs are very different. The performance of each single host subsystem depends on the availability of exploiting the algorithm’s intrinsic parallelism and how it can be tailored to be fitted in the GPU or CPU cores. At a second level, the challenge consists of how the whole problem can be partitioned into pieces (tasks) and how they can be delivered to CPU cores or GPU cards so that the workload is evenly distributed between these subsystems.

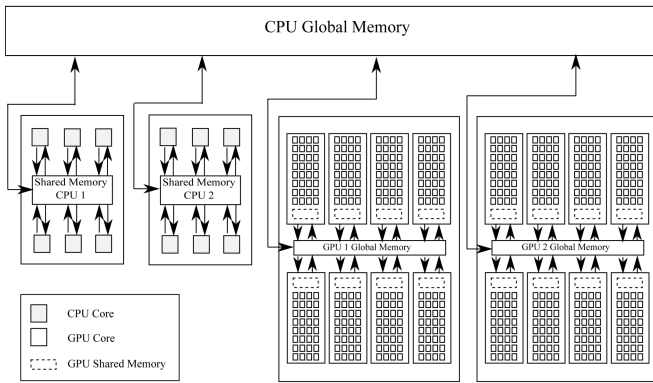


Fig. 2. Heterogeneous parallel computer model

The partition of the problem into tasks and the scheduling of these tasks can be based on performance models obtained from previous executions or on a more sophisticated strategy. This strategy is based on small and fast benchmarks representative of the application that allows to predict, at runtime, the amount of workload that should be dispatched to each resource so that it would minimize the total execution time. Currently, we focus our work on how to leverage the heterogeneous concurrent underlying hardware to minimize the time-to-solution of our application leaving the study of more sophisticated strategies of workload distribution to further research.

3.1 The Parallel Algorithm

In particular, the algorithm for the construction of matrix A of order $N = (s + 1)^2$ with a polynomial degree s can be seen in Algorithm 1. Arrays x and y have been previously loaded from a file and stored in such a way that allows to simplify two sums in only one

of length $n = m^2$. Routine `matrixComputation` receives as arguments the arrays x and y , the length of the sum (n) and the order of the polynomial (s), and returns a pointer to the output matrix A .

Algorithm 1. Routine `matrixComputation` for the construction of matrix A .

```

1: int N = (s+1)*(s+1);
2: for( int k = 0; k < N; k++ ) {
3:   for( int l = 0; l < N; l++ ) {
4:     int exp1 = k/s+l/s;
5:     int exp2 = k*s+l*s;
6:     int ind = k+l*N;
7:     for ( int i=0; i<n; i++ ) {
8:       A[ind] += pow( x[i], exp1 ) * pow( y[i], exp2 );
9:     }
10:  }
11: }
```

The construction of matrices A and b (Equations [12](#) and [13](#)) is by far the most expensive part of the overall process. However, there exists a great opportunity for parallelism in this computation. It is not hard to see that all the elements of the matrix can be calculated simultaneously. Furthermore, each term of the sum can be calculated independently. This can be performed to partition the sum into chunks of different sizes. Our parallel program is based on this approach since the usual value for the order of the polynomial s ranges from 2 to 20, yielding matrices of order from 9 to 441 (variable N), whereas the length of the sum ranges from 1,3 to 25,4 million terms (variable n), depending on how fine the grid is desired. We partition the sum into chunks, each one with a given size so they do not be necessarily equal. The application firstly spawns a number of `nthreads` where each one (`thread_id`) will work on a different sum-chunk yielding a matrix `A_[thread_id]`. We consider here `A_[thread_id]` as a pointer to a linear array of length $N \times N$. The result, i.e. matrix A , is the sum of all these matrices so $A = A_[0] + A_[1] + \dots + A_[nthreads-1]$.

Function `matrixComputation` can be easily modified to work on these particular matrices that present the computation over chunks of arrays x and y . Everything discussed for the computation of matrix A can be extrapolated to the computation of vector b including its computation in the same routine.

Now, we consider our heterogeneous system consisting of two CPU processors with six cores each and two identical GPUs. The workload consisting of the computation of matrix A and array b has been separated into two main parts in order to deliver its computation to both the multicore CPU system and two-GPUs system. Algorithm [2](#) shows the scheme used to partition the workload into these two pieces by means of the `if` branching which starts in line 4. Because it is necessary to have one CPU thread linked to each GPU, we initialize the runtime with a total of `nthreads`, i.e., as many CPU threads as CUDA devices [3](#) plus a number of CPU threads that will be linked to a CPU core each. This is carried out through an OpenMP [4](#) pragma directive (lines 1 and 2).

The first two CPU threads is binded to two GPUs devices and the rest is binded to CPU virtual processors. The right number of CPU threads can be fewer than the available number of CPU in some cases. Someteimes, we got better results with a number of threads larger than number of cores since we have the Intel Hyper-Threading [6] capability activated. We have employed a static strategy to dispatch data and tasks to the CPU cores and to the GPUs, i.e., the percentage of workload delivered to each system is an input to the algorithm provided by the user. Once given the desired percentage of computation, the size of data is calculated before calling Algorithm 2 so that variable `sizeGPU` stores the number of terms of the sum (lines 7–9 of Algorithm 1) that each one of two GPUs will compute, and variable `sizeCPU` stores the total amount of terms that all the cores of the CPU system will compute. Each system will perform computation if the piece of data assigned is larger than zero.

Algorithm 2. Using multiple GPU devices and cores.

```

1:  omp_set_num_threads(nthreads);
2:  #pragma omp parallel {
3:  int thread_id = omp_get_thread_num();
4:  if( sizeGPU ) {                               /* GPU Computing */
5:    int gpu_id = 2*thread_id;
6:    int first = thread_id * sizeGPU;
7:    cudaSetDevice(gpu_id);
8: matrixGPU(A,b,&(x[first]),&(y[first]),&(z[first]),sizeGPU,s);
9:  } else {
10:   if( sizeCPU ) {                               /* CPU Computing */
11:     int cpu_thread_id = thread_id-2;
12:     int first = 2*sizeGPU+cpu_thread_id*sizeThr;
13:     int size = thread_id==(nthreads-1)?sizeLth:sizeThr;
14: matrixCPU(A,b,&(x[first]),&(y[first]),&(z[first]),size,s);
15:   }
16: }
17: }
```

Matrix A and vector b are the output data of Algorithm 2. They are the sum of the partial sums computed by each system. We use arrays of matrices A_{-} and b_{-} described earlier to store these partial results independently whether they were computed by a CPU core or a GPU device. Once the threads are joined (after line 17) a total sum of these partial results is performed by the main thread to form A and b . Each thread works on a different piece of arrays x , y , and z . Routines `matrixCPU` and `matrixGPU` are adaptations of Algorithm 1 that receive pointers to the suitable location in arrays x , y and z (set in variable `first` in lines 6 and 12, respectively) and the length of the sum, i.e., `sizeGPU` for the each GPU or `size` for each CPU core. These routines also include the computation of vector b that was omitted in Algorithm 1. The total amount of work performed by the CPU system (line 13) is divided into equal chunks of size `sizeThr` (`sizeThr=sizeCPU/(nthreads-2)`) except for the last core which is

`sizeLth`, i.e., `sizeThr` plus the remaining terms. The GPU devices in our system are identified with integers 0 and 2 (`gpu_id`), which explains line 5.

3.2 The CUDA Kernel

The computation performed by each GPU is implemented in the `matrixGPU` function, called in line 8 of Algorithm 2. This function firstly performs the usual operations of allocating memory in GPU and uploading data from the CPU to the GPU kernel. Thus, it is supposed that arrays A , x and y have been previously uploaded into the card's global memory. For the sake of simplicity we restrict the explanation to the computation of matrix A since the computation of vector b can be easily deduced.

The construction of matrix A through a CUDA kernel has a great opportunity of parallelism. In this case, we exploit both, the fact that all the elements of matrix A can be computed concurrently and that each term of the sum is independent of any other one. In order to exploit all this concurrency we used a grid of three-dimensional thread blocks. The thread blocks have dimension `BLKSZ_X`×`BLKSZ_Y`×`BLKSZ_Z` whose values are macro definitions in the first three lines of Algorithm 3. Each thread is located in the block through 3 coordinates which are represented by variables X , Y and Z (lines 9–11). The thread blocks are arranged in a three-dimensional grid. The first dimension is 1, and the other two are $\lceil N/BLKSZ_Y \rceil$ and $\lceil N/BLKSZ_Z \rceil$, respectively, being N the dimension of matrix A and `idiv` an integer function which returns the length of the last two dimensions. The following code is within `matrixGPU` function and shows this arrangement and the call to the kernel:

```
1: dim3 dimGrid( 1, idiv( N, BLKSZ_Y ), idiv( N, BLKSZ_Z ) );
2: dim3 dimBlock( BLKSZ_X, BLKSZ_Y, BLKSZ_Z );
3: kernel<<< dimGrid, dimBlock >>>( A, x, y, s, n, N );
```

The aim is that all the threads within a block calculate concurrently the core computation of line 27. The thread with coordinates (X,Y,Z) is assigned to calculate the terms of the sum $x+i$, with $i = 0 :BLKSZ_X: n$. This operation is specified by the loop which starts in line 19. The exponents `exp1` and `exp2` depend on the row (k) and column (l) indexes of the sought-after matrix A . These indexes are calculated in lines 7 and 8, respectively, based on coordinates Y and Z of the thread. All the threads in the block use data in arrays x and y so, before calculation in line 27, a piece of these arrays must be loaded into the shared memory from the global memory. Shared memory is a rapid access memory space that all the threads within a block can access. Each thread in the X dimension with $Y=0$ and $Z=0$ performs this load into shared memory copying one element of arrays x and y into arrays `sh_x` and `sh_y`, respectively (lines 22–25). These last arrays have been allocated in the shared memory in line 13. Upon completion of the loop in line 29, all the terms of the sum assigned to that thread have been calculated and stored in the register variable `a`. Now, this value is stored in shared memory (line 30). Therefore, a three-dimensional array `sh_A` of size `BLKSZ_X`×`BLKSZ_Y`×`BLKSZ_Z` has been allocated in shared memory in line 14.

We need to imagine the shared data `sh_A` as a three-dimensional cube where each position has a partial sum of the total sum. There is one sum for each element $r \times c$

Algorithm 3. CUDA Kernel.

```

1: #define BLKSZ_X    128
2: #define BLKSZ_Y    2
3: #define BLKSZ_Z    2
4:
5: __global__ void kernel( double *A, double *x, double *y,
6:                       int s, int n, int N ) {
7:     int k = blockIdx.y * blockDim.y + threadIdx.y;
8:     int l = blockIdx.z * blockDim.z + threadIdx.z;
9:     int X = threadIdx.x;
10:    int Y = threadIdx.y;
11:    int Z = threadIdx.z;
12:    double a = 0.0;
13:    __shared__ double sh_x[BLKSZ_X], sh_y[BLKSZ_X];
14:    __shared__ double sh_A[BLKSZ_X][BLKSZ_Y][BLKSZ_Z];
15:
16:    if( k<N && l<N ) {
17:        int exp1 = (k/s)+(l/s);
18:        int exp2 = (k%s)+(l%s);
19:        for( int K=0; K<n; K+=BLKSZ_X ) {
20:            int i = X+K;
21:            if( i<n ) {
22:                if( Y == 0 && Z == 0 ) {
23:                    sh_x[X] = x[i];
24:                    sh_y[X] = y[i];
25:                }
26:                __syncthreads();
27:                a += pow( sh_x[X], exp1 ) * pow( sh_y[X], exp2 );
28:            }
29:        }
30:        sh_A[X][Y][Z] = a;
31:        __syncthreads();
32:        if( X == 0 ) {
33:            a = 0.0;
34:            for( int i=0; i<BLKSZ_X; i++ ) {
35:                a += sh_A[i][Y][Z];
36:            }
37:            A[k+N*1] = a;
38:        }
39:    }
40: }

```

of matrix A . In other words, elements $sh_A[i][Y][Z]$, for all i , contain the partial sums corresponding to a given element $r \times c$, taking into account the parity between the matrix element and the thread coordinates set in lines 7–11. Thus, it is necessary now to add all the partial sums in the X dimension for all the sums. This operation (lines 32–38) is performed only by threads such that $X=0$. Once the sum has been computed, the result is saved in, global memory (line 37).

We use synchronization points within the code (`__syncthreads()`) to make sure data in shared memory is saved before read. The use of shared memory is restricted to a small size that must be statically allocated (at compilation time). The size of our target GPU is 48KB. The maximum number of threads per block is limited to 1024. However, the total amount of shared memory is what really determines the size of the threads block. Anyway, the limitation in the number of threads per block is easily overcome by the number of blocks that can be run concurrently. Typical values for the threads block dimensions are the ones defined in lines 1–3. We experimentally checked that dimensions Y and Z should be equal. Somehow there are proportional to N (size of matrix A) and dimension X should be related to n (size of arrays x and y) and so much longer. Values of N range from 9 to 441, while values of n , range between $1, 3 \times 10^6$ and $25, 4 \times 10^6$ in our experiments. Given this relationship between N and n , it is clear that the opportunity for concurrency spreads in the X dimension of the block.

Just as a simply note to say that we chose the first dimension as the “largest” one due to the GPU limits, the last dimension of the threads block to 64, allowing up to 1024 the number of threads in the other two dimensions. In addition, it is possible to say that the three-dimensional grid of blocks has really been limited to an effective two-dimensional grid since the first dimension is set to 1. More blocks in coordinate X means that data computed by each block in that dimension and stored in the shared memory should be also shared among the thread blocks. This can only be done through global memory resulting in a performance penalty.

4 Experimental Results

4.1 Characterization of the Execution Environment

The computer used in our experiments has two Intel Xeon X5680 at 3.33Ghz and 96GB of GDDR3 main memory. Each one is a hexacore processor with 12MB of cache memory. It contains two GPUs NVIDIA Tesla C2070 with 14 stream multiprocessors (SM) and 32 stream processors (SP) each (448 cores in total), 16 load/store units, four special functions, a 32K-word register file, 64K of configurable RAM, and thread control logic. Each SM has both floating-point and integer execution units. Floating point operations follow the IEEE 754-2008 floating-point standard. Each core can perform one double precision fused multiply-add operation in each clock period and one double-memory. The installed CUDA toolkit is version 4.0. We use library MKL 10.3 to perform BLAS operations in the CPU subsystem.

4.2 Landform Attributes Representation Analysis

In order to validate the presented methodology and derived equations, it will be applied computing techniques for efficient solution of two dimensional polynomial regression model to represent the landform attributes of an area of São Francisco river valley region. The data source of the chosen area comes from Digital Terrain Models (DTM) [12], in the form of a regular matrix, with spacing approximately 900 meters in

the geographic coordinates. The statistical analyses of the elevations indicate a dispersion from 1 to 2,863 meters. The DTM with 1,400 points has only 722 points inside the region, the other points are outside the area. Using all the points representing the landform attributes of the area and, by Equation 12, we estimate the polynomial coefficients for representing terrain altitude variation. The time to estimate such a polynomial in high degree needs great computer power and a long time of processing. However, the higher the degree of the polynomial is more accuracy in the description of landform attributes representation we have, thus achieving a more satisfactory level of details.

Using the DTM data source, the solution of the model shows an elevation map generated in 3D vision (Figure 3) and a 2D projection in gray tones (Figure 4). It can also be observed that São Francisco river valley region has a heavily uneven topography so a high degree of the adjusted polynomial is needed to attain an accurate representation of the surface. Figure 3 shows the elevation map generated with the coefficients of polynomials with degrees 2, 4, 6 and 20, respectively. Therefore, by fitting a high degree polynomial to the data a better landform attributes representation and a more accurate extrapolation is obtained.

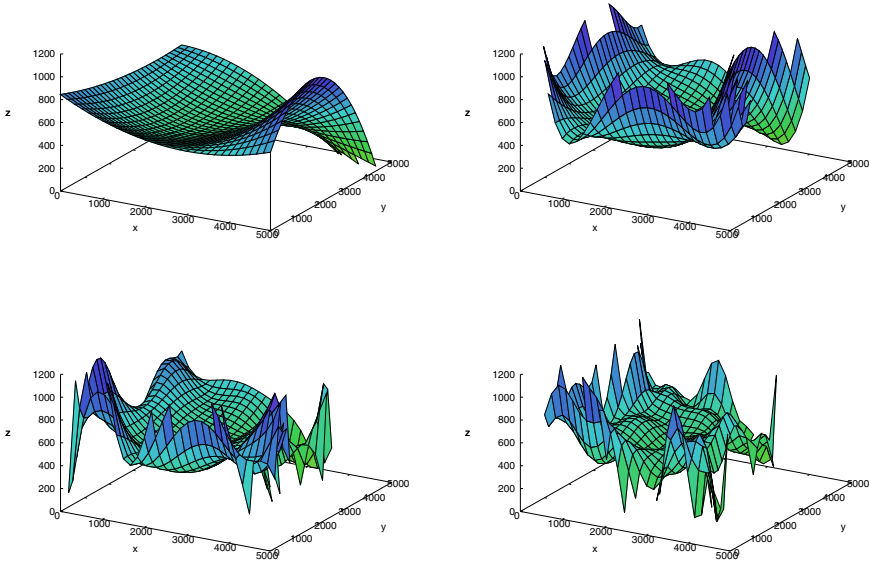


Fig. 3. 3D Vision landform attributes representation of São Francisco river valley region for polynomial degrees 2, 4, 6 and 20

4.3 Experiments Using Double Precision Data

We have implemented a parallel algorithm in CUDA, based on landform attributes representation by using the parallel scheme proposed in Section 3 to build the surface mapping with a global fitting using the polynomial regression technique. The

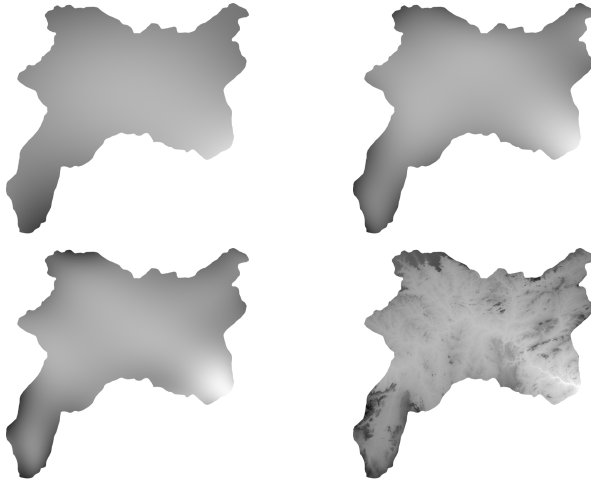


Fig. 4. Gray tones landform attributes representation of São Francisco river valley region for polynomial degrees 2, 4, 6 and 20

benchmarks were compiled with *nvcc*. In the experiments, we first increased the number of CPU threads from 1 to 24 (Hyper-Threading is set) to obtain the number that minimizes time. Then we add 1 and 2 GPUs to the number of threads obtained in the former test. The input sizes of the problem (degree of a polynomial) for the experiments were 2, 4, ..., 40. The algorithm performance is analyzed in Figure 5.

The execution with one thread is denoted by “Sequential” in the figure while “OMP” denotes the use of several CPU threads. The OMP version distributes the matrix calculation among the threads and each thread is run exclusively on a CPU core. Versions denoted by 1GPU and 2GPU represent executions in one single and two devices, respectively. The Parallel Model (“Model”) uses all cores available in the heterogeneous system. In this model the threads are executed by all the elements of the machine, the suitable number of CPU cores and the two GPUs. The results of the experiments show that the parallel CPU algorithm (OMP) reduces the execution time significantly. As can be seen in Figure 5 the maximum speedup is around 12, matching the number of cores. The second figure shows Gflops, presenting a difference in performance that can be observed more clearly. It must be noted that, for small polynomial degrees, the performance of OMP is larger than the performance with 1 GPU (size ≤ 10). This is due to the data transfer between CPU and GPU. Similarly, the performance of 1 GPU is larger than the performance with 2 GPUs (size ≤ 20). In this case, this is due to the setup time needed in the selection of the devices, which is high in our target machine (4.5 sec.) and is not necessary if just one GPU is used. The best result has been obtained with every resource available in the heterogeneous system. The speedup increases with the problem size reaching the theoretical maximum of 78, a number that has been obtained by comparing the computational power of one GPU with the CPU. The use of GPU as a standalone tool provides benefits but does not allow to reach the potential performance that could be obtained by adding more GPUs and/or the CPU subsystem.

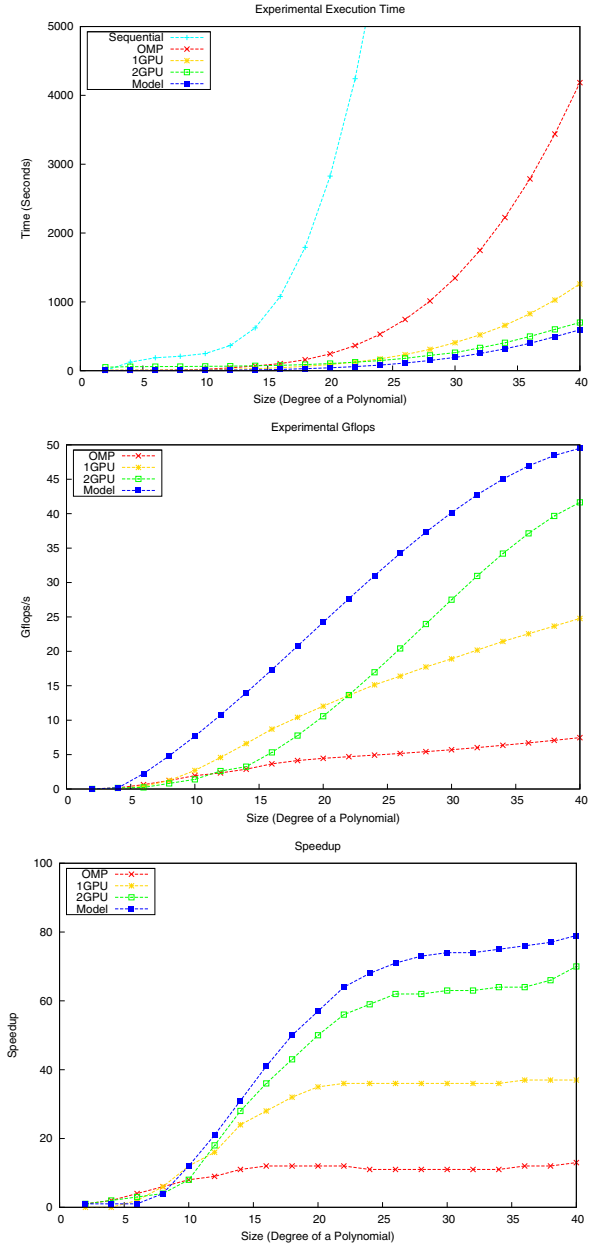


Fig. 5. Graphical representation of the execution time (in seconds), Gflops and Speedup rates by varying the size of the problem (degree of the polynomial)

Table 1. Comparative performance analysis of execution time (in seconds)

Degree Polynomial	Sequential	OMP	1GPU	2GPU	Model
8	84.49	12.32	12.44	14.19	13.61
12	386.17	41.85	21.36	19.39	18.04
16	1, 166.88	114.55	43.31	31.48	25.53
20	2, 842.52	268.32	90.57	57.03	49.29
24	5, 916.06	544.93	172.71	101.08	88.86
28	11, 064.96	1, 011.42	310.53	176.88	156.72
32	24, 397.66	1, 777.25	521.63	285.07	256.62
36	30, 926.82	2, 700.00	828.50	450.67	404.25
40	46, 812.70	4, 252.69	1, 261.09	666.77	600.90

5 Conclusion and Future Works

The experimental results obtained in this work indicate that our approach to the solution of the mathematical model for representing landform attributes is efficient and scalable. The built application exploits the computing power of current GPUs leveraging the intrinsic parallelism contained in the algorithm. Furthermore, our solution is designed so that tasks in which the building matrix is partitioned can be either been dispatched to a GPU or a CPU core. The high computing cost of the application and the way in which we performed the solution in this paper motivate us to extended this algorithm further to other hierarchically higher levels such as clusters of nodes like the one we used in these experiments. To this end, we propose for the future an auto-tuning method to determine the best tile size that will be computed by each subsystem in order to attain load balancing among all possible computational resources available.

Acknowledgment. We would like to thank The Generalitat Valenciana for PROMETEO/2009/2013 project.

References

1. Bajaj, C., Ihm, I., Warren, J.: Higher-order interpolation and least-squares approximation using implicit algebraic surfaces. *ACM Transactions on Graphics* 12, 327–347 (1993)
2. Ballard, G., Demmel, J., Gearhart, A.: Communication bounds for heterogeneous architectures. Tech. Rep. 239, LAPACK Working Note (February 2011)
3. Barnat, J., Bauch, P., Brim, L., Ceska, M.: Computing strongly connected components in parallel on CUDA. In: *Proceedings of the 25th IEEE International Parallel & Distributed Processing Symposium (IPDPS 2011)*, pp. 544–555. IEEE Computer Society (2011)
4. Chapman, B., Jost, G., van der Pas, R.: *Using OpenMP: portable shared memory parallel programming (scientific and engineering computation)*. The MIT Press (2007)
5. Golub, G.H., Loan, C.F.V.: *Matrix Computations*, 2nd edn., Baltimore, MD, USA (1989)
6. Marr, D.T., Binns, F., Hill, D.L., Hinton, G., Koufaty, D.A., Miller, J.A., Upton, M.: Hyper-threading technology architecture and microarchitecture. *Intel Technology Journal* 6(1), 1–12 (2002)

7. Namikawa, L.M., Renschler, C.S.: Uncertainty in digital elevation data used for geophysical flow simulation. In: *GeoInfo*, pp. 91–108 (2004)
8. Nogueira, L., Abrantes, R.P., Leal, B.: A methodology of distributed processing using a mathematical model for landform attributes representation. In: *Proceeding of the IADIS International Conference on Applied Computing (April 2008)*
9. Nogueira, L., Abrantes, R.P., Leal, B., Goulart, C.: A model of landform attributes representation for application in distributed systems. In: *Proceeding of the IADIS International Conference on Applied Computing (April 2008)*
10. Rawlings, J.O., Pantula, S.G., Dickey, D.A.: *Applied Regression Analysis: A Research Tool*. Springer Texts in Statistics. Springer (April 1998)
11. Rufino, I., Galvão, C., Rego, J., Albuquerque, J.: Water resources and urban planning: the case of a coastal area in brazil. *Journal of Urban and Environmental Engineering* 3, 32–42 (2009)
12. Rutzinger, M., Hofle, B., Vetter, M., Pfeifer, N.: Digital terrain models from airborne laser scanning for the automatic extraction of natural and anthropogenic linear structures. In: *Geomorphological Mapping: a Professional Handbook of Techniques and Applications*, pp. 475–488. Elsevier (2011)
13. Sengupta, S., Harris, M., Zhang, Y., Owens, J.D.: Scan primitives for GPU computing. In: *Proceedings of the 22nd ACM SIGGRAPH/EUROGRAPHICS Symposium on Graphics Hardware*, pp. 97–106. Eurographics Association, Aire-la-Ville (2007)
14. Song, F., Tomov, S., Dongarra, J.: Efficient support for matrix computations on heterogeneous multicore and multi-GPU architectures. Tech. Rep. 250, LAPACK Working Note (June 2011)

The Performance Model of an Enhanced Parallel Algorithm for the SOR Method

Italo Epicoco^{1,2} and Silvia Mocavero²

¹ University of Salento, Lecce, Italy
italo.epicoco@unisalento.it

² Euro-Mediterranean Center for Climate Change (CMCC), Lecce, Italy
silvia.mocavero@cmcc.it

Abstract. The Successive Over Relaxation (SOR) is a variant of the iterative Gauss-Seidel method for solving a linear system of equations $Ax = b$. The SOR algorithm is used within the NEMO (Nucleus for European Modelling of the Ocean) ocean model for solving the elliptical equation for the barotropic stream function. The NEMO performance analysis shows that the SOR algorithm introduces a significant communication overhead. Its parallel implementation is based on the Red-Black method and foresees a communication step at each iteration. An enhanced parallel version of the algorithm has been developed by acting on the size of the overlap region to reduce the frequency of communications. The overlap size must be carefully tuned for reducing the communication overhead without increasing the computing time. This work describes an analytical performance model of the SOR algorithm that can be used for establishing the optimal size of the overlap region.

Keywords: SOR, NEMO, Performance Model.

1 Introduction

The ocean engine of NEMO (Nucleus for European Modelling of the Ocean) [1] is a primitive equation model adapted to regional and global ocean circulation problems. It is a flexible tool for studying the ocean and its interactions with the other components of the earth climate system over a wide range of space and time scales. Prognostic variables are the three-dimensional velocity field, the sea surface height, the temperature and the salinity. In the horizontal direction, the model uses a curvilinear orthogonal grid and in the vertical direction, a full or partial step z-coordinate, or s-coordinate, or a mixture of the two. The model time stepping environment is a three level scheme in which the tendency terms of the equations are evaluated either centered in time, or forward, or backward depending on the nature of the term. The model is spatially discretized on a staggered grid (Arakawa C grid) masking the land points. Vertical discretization depends on both how the bottom topography is represented and whether the free surface is linear or not. Explicit, split-explicit and filtered free surface formulations are implemented for solving the prognostic equations for the active

tracers and the momentum. A number of numerical schemes are available for the momentum advection, for the computation of the pressure gradients, as well as for the advection of the tracers (second or higher order advection schemes, including positive ones). When the filtered sea surface height option is used, a new force that can be interpreted as a diffusion of the vertically integrated volume flux divergence is added in the momentum equation. The equation is solved implicitly and it represents an elliptic equation for which two solvers are available: the SOR and the Preconditioned Conjugate Gradient (PCG) schemes. The SOR has been retained because it is a linear solver very useful when using the adjoint model of NEMO. The NEMO model with the MFS16 [2] configuration has been evaluated on the MareNostrum platform at the Barcelona Supercomputing Center. The routine named *dyn_spg* is the most time consuming one; it computes the surface pressure gradient term using the SOR scheme.

The paper is organized as follows: next section introduces the SOR (Successive Over Relaxation) method. Section 3 describes our parallel approach, while the latter sections, 4 and 5, show respectively the analytical performance model of the parallel algorithm and the iso-efficiency analysis.

2 SOR Overview

The iterative methods for solving the linear equation systems $Ax = b$ iteratively generates a sequence $\{p_k\}$ of approximate solutions such that the residual vector ($r_k = b - Ap_k$) converges to 0. The Gauss-Seidel algorithm [3] is an example of iterative method for solving a linear equation system. The method can be applied only if the matrix A is strictly diagonally dominant. Each equation is solved by the unknown on the diagonal and the approximated values for the other unknowns are plugged in. The process is then iterated until convergence. The Gauss-Seidel method is easily derived by examining separately each of the n equations in the linear system. Let the i -th equation given by:

$$\sum_{j=1}^n a_{ij}x_j = b_i \quad (1)$$

At the iteration k , it can be solved by (2) for the value of $x_i^{(k)}$ assuming the approximation of the previous iteration ($x_{j \neq i}^{(k-1)}$) for the other unknowns $x_{j \neq i}$.

$$x_i^{(k)} = \frac{1}{a_{ii}} \left(b_i - \sum_{j=1}^{i-1} a_{ij}x_j^{(k)} - \sum_{j=i+1}^n a_{ij}x_j^{(k-1)} \right) \quad (2)$$

There are two important characteristics of the Gauss-Seidel method that should be noted. Firstly, the computation appears to be serial: since each component at the new iteration depends on all of the previously computed components, the updates cannot be done simultaneously as in the Jacobi method [4]. Secondly, the new iterate value $x^{(k)}$ depends upon the order in which the equations are

examined. If it changes, the values at the new iteration (and not just their order) change accordingly.

The definition of the Gauss-Seidel method can be expressed using the following matrix notation:

$$x^{(k)} = (D - L)^{-1}(Ux^{(k-1)} + b) \quad (3)$$

where the matrices D , $-L$, and $-U$ represent the diagonal, the strictly lower triangular, and the strictly upper triangular parts of A , respectively. The SOR [5] is an iterative method for solving a linear system of equations derived by extrapolating the Gauss-Seidel algorithm. This extrapolation takes the form of a weighted average between the previous iteration and the Gauss-Seidel component computed at the current iteration. Given a value for the weight ω the component at iteration k is given by:

$$x_i^{(k)} = \omega \bar{x}_i^{(k)} + (1 - \omega)x_i^{(k-1)} \quad (4)$$

where \bar{x} denotes a Gauss-Seidel approximation. The idea is to choose a value for ω within the interval $(0, 2)$ that will accelerate the rate of convergence to the solution. In general, it is not possible to compute in advance the value of ω that will maximize the rate of convergence of the SOR. Frequently, some heuristic estimate is used, such as $\omega = 2 - O(h)$ where h is the mesh spacing of the discretization of the underlying physical domain.

In matrix terms, the SOR algorithm can be written as follows:

$$x^{(k)} = (D - \omega L)^{-1}[\omega U + (1 - \omega)D]x^{(k-1)} + \omega(D - \omega L)^{-1}b \quad (5)$$

3 Parallel Algorithm

While the matrix notation for the SOR algorithm is useful for a theoretical analysis, a practical implementation requires an explicit formula to be defined [6]. Let's consider a general second-order elliptic equation in x and y , finite differenced on a square. Each row of the matrix A is an equation of the form:

$$a_{i,j}u_{i+1,j} + b_{i,j}u_{i-1,j} + c_{i,j}u_{i,j+1} + d_{i,j}u_{i,j-1} + e_{i,j}u_{i,j} = f_{i,j} \quad (6)$$

The iterative procedure is defined by solving the following equation for $u_{i,j}$.

$$u_{i,j}^* = \frac{f_{i,j} - a_{i,j}u_{i+1,j} - b_{i,j}u_{i-1,j} - c_{i,j}u_{i,j+1} - d_{i,j}u_{i,j-1}}{e_{i,j}} \quad (7)$$

Then, considering the (4), the $u_{i,j}^{new}$ is a weighted average given by:

$$u_{i,j}^{new} = \omega u_{i,j}^* + (1 - \omega)u_{i,j}^{old} \quad (8)$$

If we consider that the residual at any stage of the iteration is given by:

$$\xi_{i,j} = a_{i,j}u_{i+1,j} + b_{i,j}u_{i-1,j} + c_{i,j}u_{i,j+1} + d_{i,j}u_{i,j-1} + e_{i,j}u_{i,j} - f_{i,j} \quad (9)$$

we can calculate the new value at each iteration given by:

$$u_{i,j}^{new} = u_{i,j}^{old} - \omega \frac{\xi_{i,j}}{e_{i,j}} \quad (10)$$

This formulation is very easy to program, and the norm of the residual vector $\xi_{i,j}$ can be used as a criterion for terminating the iteration. The need to reduce the time spent by the SOR algorithm without increasing the number of iterations to reach convergence has been the main goal of several previous works. Different multi-color ordering techniques, such as the Red-Black [7] method for two dimensional problems, have been investigated; they allow the parallelization of operations on the same color. Other techniques, overlapping computation and communication or allowing an optimal scheduling of available processors, have been designed and implemented producing parallel versions of SOR [8]. Parallel SOR algorithms, suitable for use on an asynchronous MIMD computer, are presented since 1984 [9]. In the last years, the BPSOR [10], characterized by a new mesh domain partition and ordering, allows retaining the same convergence rate of the sequential SOR method with an easy parallel implementation on an MIMD parallel computing.

This work analyzes a parallel algorithm for the SOR based on the Red-Black method that supposes to divide the mesh into odd and even cells, like in a checkerboard. Equation (10) shows that the odd point values depend only on the even points, and vice versa. Accordingly, we can carry out one half-sweep updating the odd points and then another half-sweep updating the even points with the new odd values. The parallel algorithm uses a 2D domain decomposition based on checkerboard blocks. Let n_i and n_j be respectively the number of rows and columns of the global domain, and p_i and p_j respectively the number of processes along i and j directions, then each process will compute a subdomain made of $n_i/p_i \times n_j/p_j$ elements. If we consider only one overlap line between neighbors, each parallel process must exchange the computed values at the border at each iteration of the SOR. Two communication steps must be performed for each iteration (for the odd and for the even points). At each iteration, the generic process computes the odd points inside its domain, exchanges the odd points with its neighbors and updates the boundaries values, computes the inner even points and finally updates even points on the boundaries exchanging with neighbors (see Fig. 1). At each iteration, the generic parallel process will then communicate twice for each neighbor. In order to reduce the frequency of communication, the size of the overlap region could be increased [11]. In that case the neighboring processes would exchange a wider overlap region, but the values exchanged can be used for further iterations without the need of communication. Each process, after exchanging the data, computes a total number of lines given by $N_{inner} + N_{ol} - 1$, where N_{inner} and N_{ol} are respectively the total number of lines in the inner domain and the number of overlap lines. At each iteration only one line of the overlap expires so that the process has no need to exchange for $N_{ol} - 1$ iterations. The convergence rate of the algorithm does not change, since the ordering and partition is the same of the original SOR algorithm. The algorithm is explained by the following pseudo-code fragment.

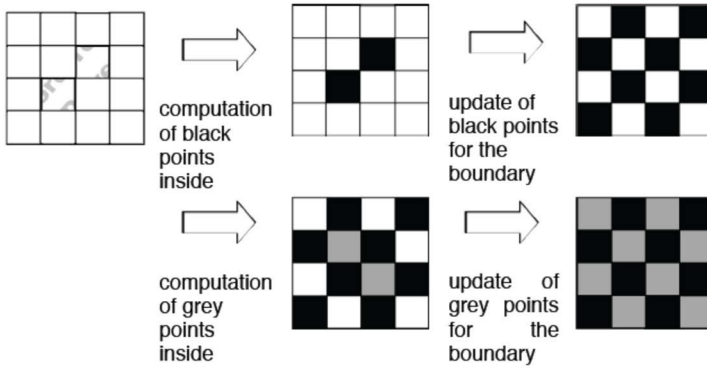


Fig. 1. SOR Red-Back computing algorithm

Require: u //result matrix with initial value
 a, b, c, d, e //coefficient matrix
 f //known term

$ol_exp \leftarrow ol$

while $\xi(i, j)$ is not enough small **do**

if $ol_exp == 0$ **then**

call data_exch //exchange odd points over the overlap

end if

for all even points **do**

$tmp \leftarrow (f(i, j) - a(i, j) * u(i, j - 1) - b(i, j) * u(i, j + 1) - c(i, j) * u(i - 1, j) - d(i, j) * u(i + 1, j)) / e(i, j)$

$\xi(i, j) \leftarrow tmp - u(i, j)$

$u(i, j) \leftarrow \omega * tmp + (1 - \omega) * u(i, j)$

end for

if $ol_exp == 0$ **then**

call data_exch //exchange even points over the overlap

$ol_exp \leftarrow ol$

end if

for all odd points **do**

$tmp \leftarrow (f(i, j) - a(i, j) * u(i, j - 1) - b(i, j) * u(i, j + 1) - c(i, j) * u(i - 1, j) - d(i, j) * u(i + 1, j)) / e(i, j)$

$\xi(i, j) \leftarrow tmp - u(i, j)$

$u(i, j) \leftarrow \omega * tmp + (1 - \omega) * u(i, j)$

end for

call convergence_test (ξ)

$ol_exp \leftarrow ol_exp - 1$

end while

A similar approach has been used by the HYCOM ocean model [12] where a maximum number of wide halo lines can be added to reduce the halo communication overhead.

4 The Analytical Performance Model

The SOR algorithm has been implemented in a test program made by the main *sor* routine that (i) calls the *data_exch* routine for exchanging the data between the neighbors and (ii) evaluates the convergence. Both the routines are then characterized by two kind of operations: computing and communication. *data_exch* performs some data buffering operations and the actual send and receive of the data on the boundaries. The size of the overlap region directly impacts on the frequency of the *data_exch* invocation. The *sor* routine computes the result matrix and performs a collective communication during the convergence test. If we increase the size of the overlap, the computation increases, while the time for collective communication does not change. The total time is the sum of these four components, three of them depending on the size of the overlap. Which is the best value of the overlap to get the best benefit? The optimal value is related to some architectural aspects (i.e. the processor speed and the network bandwidth and latency) and changes with both the number of parallel processes and the domain decomposition. A performance model for estimating the behavior of the SOR algorithm has been defined, such as in [13]. It takes into consideration the four above mentioned aspects. The total time spent by the solver (T_{sor}) is given by: (i) the communication time spent in the *sor* routine for the convergence test (T_{c_sor}); (ii) the computing time spent in the *sor* routine for evaluating the result matrix at each iteration (T_{u_sor}); (iii) the computing time spent in the *data_exch* routine for managing the data buffer used for the data transmission (T_{u_data}) and (iv) the communication time in the *data_exch* for the data transfer to the neighbors (T_{c_data}). The number of calls of *data_exch* depends on both the overlap size (l) and the number of iterations (m) needed to reach the convergence. The performance model is summarized as follows:

$$T_{sor} = T_{c_sor} + T_{u_sor} + \left(\frac{2m}{l} + 1 \right) (T_{c_data} + T_{u_data}) \quad (11)$$

The four timing components can be modeled as in (12) (13) (14).

The time spent by the collective communication depends only on the number of parallel processes ($p_i p_j$). The convergence test is performed after the first 100 iterations and has a frequency of 10 iterations through an *allreduce* MPI collective communication, where the maximum residual value is exchanged among all of the parallel processes. The amount of data exchanged is constant (it is independent from the subdomain dimension) and, considering the implementation of the *allreduce* with the butterfly parallel scheme, we have a number of communication steps logarithmic to the total number of processes.

$$T_{c_sor} = O\left(\frac{m - 100}{10} \log p_i p_j\right) \quad (12)$$

The computing time of the *sor* is related to the domain dimension: d_i and d_j are the dimensions of the biggest subdomain along the i and j directions respectively and they are given by $d_i = n_i/p_i$ and $d_j = n_j/p_j$. For each iteration of the SOR a complete sweep of the subdomain elements plus the overlap region is performed.

$$T_{u_sor} = O(m(d_i + l)(d_j + l)) \quad (13)$$

The communication is implemented with four point-to-point sends/receives hence the communication time is directly proportional to the number of exchanged elements. Here we consider a parallel process with four neighbors, but not all of the processes have four neighbors like those in the border of the global domain.

$$\begin{aligned} T_{c_data} &= O(L_i + L_j) \\ T_{u_data} &= O(L_i + L_j) \end{aligned} \quad (14)$$

L_i and L_j represent the total number of elements exchanged between neighbors, $L_i = (d_i + 2l)l$, $L_j = (d_j + 2l)l$.

Considering all of the previous equations, the parallel time of the whole algorithm can be expressed as follows:

$$T_{sor} = O\left(\frac{n_i n_j}{p_i p_j} + \frac{n_i l}{p_i} + \frac{n_j l}{p_j} + l^2 + \log p_i p_j\right) \quad (15)$$

If we consider a square global domain then $n_i = n_j = n$, we can also impose $p_i = p_j = \sqrt{p}$. The (15) can be simplified:

$$T_{sor} = O\left(\frac{n^2}{p} + \frac{nl}{\sqrt{p}} + l^2 + \log p\right) \quad (16)$$

The evaluation of the analytical equation for the performance model has been defined experimentally on an IBM Power6 cluster. It has 30 IBM p575 nodes, each of them equipped with 16 Power6 dual-core CPUs at 4.7GHz and 128GB of shared memory (4GB per core). The nodes are interconnected by an Infiniband network.

The minimum square method on a set of several runs, for which we fixed the global domain of 871x253 grid points and a predefined domain decomposition and modified the overlap size, has been used. For both the *data_exch* terms, when the overlap size changes, the number of exchanged element changes accordingly: figs. 2 and 3 show the communication and the computing time with the least square equation used to evaluate the multiplicative coefficients for the T_{c_data} and T_{u_data} terms. Regarding the analysis of the *sor* terms, we have taken into consideration only the trend of the computing time. Indeed, the communication time does not depend on the overlap size. Figure 4 shows the computing trend of the *sor* routine without considering the time spent calling the *data_exch*. The optimal value of the overlap size can be analytically defined setting at zero the derivate of the total execution time respect to the overlap size l , hence solving (17) by l .

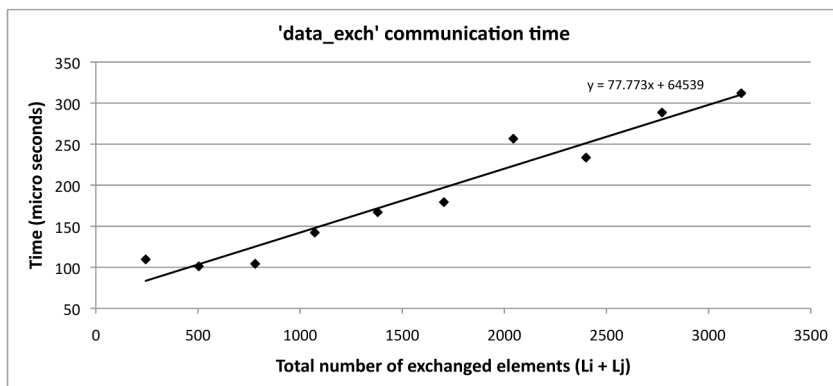


Fig. 2. *data_exch* communication time depending on the number of elements exchanged among all of the neighbors

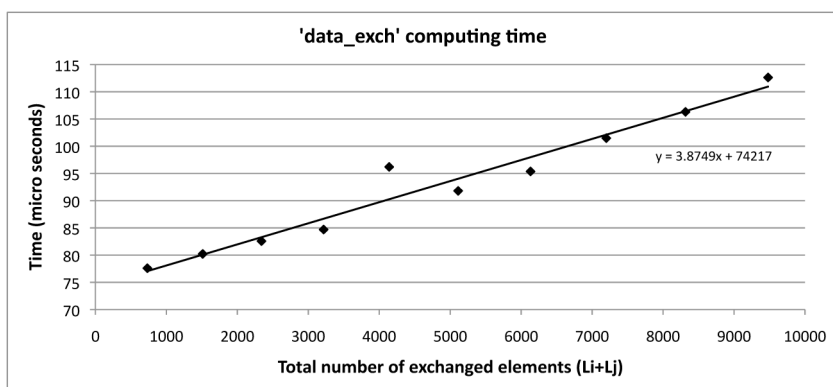


Fig. 3. *data_exch* computing time depending on the number of elements exchanged among all of the neighbors

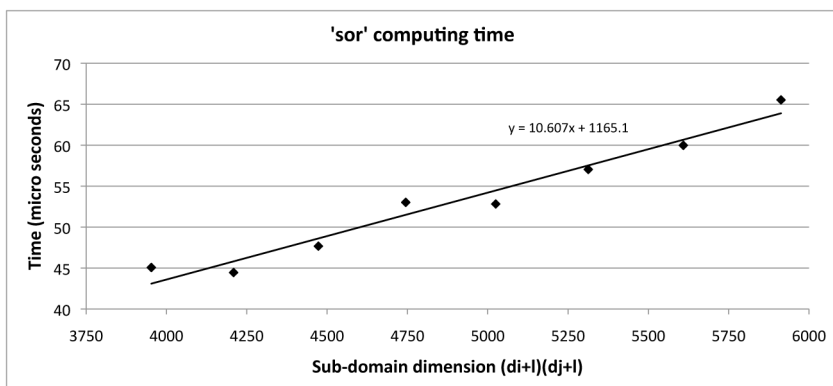


Fig. 4. *sor* computing time depending on the subdomain and the overlap size

$$\frac{dT_{sor}(n, p, l)}{dl} = 0 \quad (17)$$

As alternative we can easily derive the analytical expression of l considering that T_{u_sor} increases with l since the computation must be performed also on the elements of the overlap region (let T^+ be the positive delta time) while the communication start-up time decreases with l (let T^- be the negative delta time). The optimal value of l is such that $T^+ = T^-$. Considering that T^+ and T^- are given by the following two equations:

$$T^+ = 4(l-1) \left[\frac{n}{\sqrt{p}} + 2(l-1) \right] t_c \quad (18)$$

$$T^- = (l-1)t_s \quad (19)$$

where t_c denotes the time for executing the SOR operations on one matrix element and t_s is the communication start-up time. Hence the optimal overlap size is given by:

$$l = \frac{t_s}{8t_c} - \frac{n}{2\sqrt{p}} \quad (20)$$

and it is strictly dependent on the architectural parameters and namely on the ratio between the network latency and CPU speed. Moreover, l decreases with the subdomain perimeter increasing. Indeed when the subdomain perimeter grows up, the added time T^+ increases accordingly while T^- depends only on the number of communication steps.

4.1 Model Validation

The model has been tested and evaluated using three domain sizes: 871x253, 2Kx2K and 10Kx10K grid points. The first domain size has been chosen since it is used in the NEMO ocean model with MFS16. This is a production configuration of strategical scientific interest for the Euro-Mediterranean Center for Climate Change (CMCC) and it is employed for production experiments. Figure 5 reports a comparison between the model and the experimental data for the 871x253 domain size with a decomposition of 16x4 parallel processes. The theoretical model approximates accurately the real behavior with a deviation that is limited to the 5% of the execution time for $l > 1$. As we can notice, reducing the number of calls to *data_exch*, we consequently reduce the communication time. After a threshold, it is not convenient to increase the overlap size and the model helps us to define the value of this threshold when the decomposition changes. It depends on the domain decomposition, and more in particular on the balance between computing and communication time.

The parallel speedup of the algorithm has been evaluated: for each domain decomposition the optimal value for the overlap region has been applied.



Fig. 5. Validation of the analytical performance model

5 Iso-efficiency Analysis

Even if the main goal of this work is to find the optimal value of the overlap size, the analytical performance model also allows us to study the parallel efficiency of the SOR algorithm. Given a parallel algorithm with problem size n , executed on p processes, the iso-efficiency [14] relation is given by:

$$T(n, 1) \geq CT_o(n, p) \quad (21)$$

where $T(n, 1)$ is the execution time of the sequential algorithm and $T_o(n, p)$ is the time to execute all of those operations introduced by the parallelization, and namely is given by:

$$T_o(n, p) = (p - 1)\sigma(n) + pk(n, p) \quad (22)$$

where $\sigma(n)$ is the sequential part of the algorithm and $k(n, p)$ the communication time of each processor. The constant C is strictly related to the parallel efficiency. In order to maintain the same level of efficiency as the number of processes increases, the parallel system must be *cost-optimal* [15]. The SOR sequential algorithm has a computational complexity of $O(n^2)$. The sequential time is given by:

$$T(n, 1) = O(n^2) \quad (23)$$

The operations added by the parallel algorithm are: (i) the computing of the elements within the overlap region with a complexity of $O(nl\sqrt{p})$; (ii) the exchange of the overlap region values among neighbors with a complexity of $O(pnl/l\sqrt{p})$ and (iii) the communications for evaluating the convergence with a complexity of $O(\log p)$. The total overhead time is given by:

$$T_o(n, p) = O\left(nl\sqrt{p} + \frac{np}{\sqrt{p}} + \log p\right) \quad (24)$$

The logarithmic term can be ignored since it has a complexity lower than \sqrt{p} . The iso-efficiency relation is hence given by:

$$\begin{aligned} n^2 &\geq nl\sqrt{p} + n\sqrt{p} \\ n &\geq \sqrt{p}(l + 1) \end{aligned} \tag{25}$$

Considering for l the optimal value given by (20) we can rewrite the (25) as follows:

$$n \geq \frac{2\sqrt{p}}{3} \left(\frac{t_s}{8t_c} + 1 \right) = K\sqrt{p} \tag{26}$$

$n \geq f(p)$ denotes the iso-efficiency equation. The complexity of the problem (n^2) is proportional to the number of processes (p), then the parallel system is cost-optimal. The results, showed in Fig. 6, confirm that the parallel scalability is very poor for small problem sizes while it is good for bigger problems. The analytical results in Fig. 6 refer to some cases for which the matrix is not square and the matrix order (n) is not multiple of the number of processes (p). This could introduce a displacement from the iso-efficiency theoretical analysis.

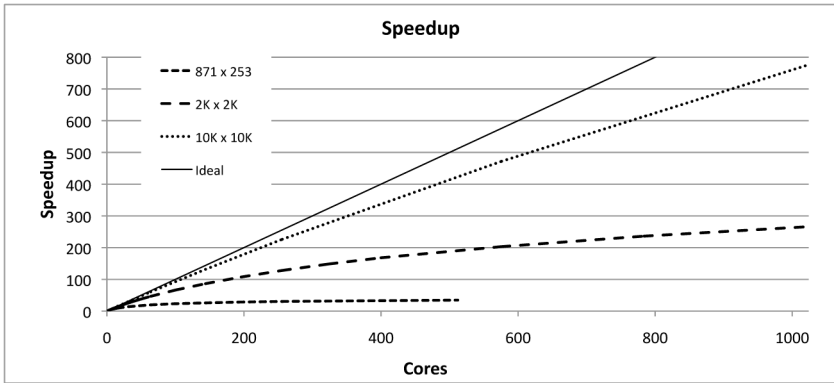


Fig. 6. Speedup of the SOR algorithm using the optimal size for the overlap region

The maximum problem size we can solve could be limited by the amount of the available main memory. Considering $M(n)$ the amount of the memory required to store the data for a problem of size n , the scalability function is given by $M(f(p))/p$. It indicates how the amount of memory used per process must increase as a function of p in order to maintain the same level of efficiency. For the SOR algorithm the amount of memory required is proportional to the number of elements in the following result matrix:

$$M(n) = O(n^2) \tag{27}$$

and hence we have:

$$M(f(p))/p = O((K\sqrt{p})^2/p) \tag{28}$$

hence $M(f(p))/p = O(1)$. This implies that the amount of memory required to solve problems with size that increases according to the iso-efficiency equation, is constant. The weak scalability is not limited by the given primary memory per process. We can conclude that the algorithm is perfectly scalable.

6 Conclusions

In this work, we presented the definition of an analytical performance model to establish the optimal overlap size for the SOR algorithm. The parallel algorithm can be optimally tuned acting on the size of the overlap region. The optimal value is given by a trade-off between computing and communication time. The use of the proposed performance model drives the user decision making strategies in the choice of the overlap size. An implementation of the algorithm has been evaluated on an IBM Power6 parallel architecture. The theoretical analysis of the parallel algorithm demonstrated a perfect weak scalability. Some criticality is evident when the number of parallel processes is so big that the dimension of the subdomain is smaller than the optimal value of the overlap region. For these cases a communication among processes that are not directly bordered is required. For the future, we plan to (i) modify the SOR parallel algorithm implementation in order to extend the exchange of data not only to the neighboring processes and (ii) introduce an overlapping between communication and computing operations leveraging on the Red-Black method.

References

1. Madec, G., et al.: NEMO ocean engine. Note du Pole de modélisation, Institut Pierre-Simon Laplace (IPSL), France, No 27 (2008) ISSN No 1288-1619
2. Tonani, T., Pinardi, N., Dobricic, S., Pujol, I., Fratianni, C.: A high-resolution free-surface model of the Mediterranean Sea. *Ocean Science* 4, 1–14 (2008)
3. Hageman, L., Young, D.: *Applied Iterative Methods*. Academic Press, New York (1981)
4. Bronshtein, I.N., Semendyayev, K.A.: *Handbook of Mathematics*, 3rd edn., p. 892. Springer, New York (1997)
5. Barrett, R., Berry, M., Chan, T.F., Demmel, J., Donato, J., Dongarra, J., Eijkhout, V., Pozo, R., Romine, C., Van der Vorst, H.: *Templates for the Solution of Linear Systems: Building Blocks for Iterative Methods*, 2nd edn. SIAM, Philadelphia, PA (1994)
6. Press, W.H., Flannery, B.P., Teukolsky, S.A., Vetterling, W.T.: *Successive Overrelaxation (SOR)*. *Numerical Recipes in FORTRAN: The Art of Scientific Computing*, 2nd edn., pp. 866–869. Cambridge University Press, Cambridge (1992)
7. Yavneh, I.: On Red Black SOR Smoothing in Multigrid. *SIAM Journal on Scientific Computing* 17(1), 180–192 (1994)
8. Niethammer, W.: The SOR method on parallel computers. *Numer. Math.* 56, 247–254 (1989)
9. Evans, D.J.: Parallel SOR iterative methods. *Parallel Computing* 1, 3–18 (1984)
10. Xie, D.: A New Block Parallel SOR Method and its Analysis. *SIAM Journal on Scientific Computing* 27(5), 1513–1533 (2006)

11. Benschila, R., et al.: Optimization of the SOR solver for parallel run. Technical report Version 1, LOCEAN-IPSL, France (2005)
12. Wallcraft, A.J., Chassignet, E.P., Hurlburt, H.E., Townsend, T.L.: 1/25° Atlantic Ocean Simulation Using HYCOM. DoD HPCMP Users (2005)
13. Meng, J., Skadron, K.: Performance modeling and automatic ghost zone optimization for iterative stencil loops on GPUs. In: Proceedings of the 23rd International Conference on Supercomputing, ICS 2009 (2009) ISBN: 978-1-60558-498-0, doi:10.1145/1542275.1542313
14. Grama, A.Y., Gupta, A., Karypis, G., Kumar, V.: Introduction to Parallel Computing, 2nd edn. Addison-Wesley, Harlow (2003)
15. Grama, A.Y., Gupta, A., Kumar, V.: Isoefficiency: measuring the scalability of parallel algorithms and architectures. IEEE Parallel Distributed Technology Systems Applications 1(3), 12–21 (1993) ISSN: 10636552

Performance Driven Cooperation between Kernel and Auto-tuning Multi-threaded Interval B&B Applications^{*}

Juan Francisco Sanjuan-Estrada¹, Leocadio Gonzalez Casado¹,
Immaculada García², and Eligius M.T. Hendrix²

¹ Department of Computer Architecture and Electronics, University of Almería,
Agrifood Campus of International Excellence (ceiA3), 04120, Spain
{jsanjuan,leo}@ual.es

² Department of Computer Architecture, University of Málaga,
Campus de Teatinos, 29017, Spain
igarcia@ual.es, Eligius@uma.es

Abstract. Dynamically determining the appropriate number of threads for a multi-threaded application may lead to a higher efficiency than predetermining the number of threads beforehand. Interval branch-and-bound (B&B) global optimization algorithms are typically irregular algorithms that may benefit from the use of a dynamic number of threads. The question is how to obtain the necessary on line information to decide on the number of threads. We experiment with a scheme following a SPMD (Single Program, Multiple Data) and AMP (Asynchronous Multiple Pool) model. This means that all threads execute the same code and they are consequently affected by the same types of blocked time.

There exist several methods to measure the blocked time of an application. The basis for the data to be obtained is the information provided by the Linux Operating System (O.S.) for tasks: `task_interruptible` and `task_uninterruptible` block time. We elaborate on this, to determine new metrics allowing kernel and applications to collaborate through system calls in order to decide on the number of threads for an application.

1 Introduction

Performance of a multi-threaded application executed on a multi-core system depends upon the number of used threads. The number of threads can be determined statically before running the application, or dynamically depending on the performance. It is a challenge to find the best number of threads at run time. It is often assumed that the number of threads should be equal to the number of cores. [15] shows that this is the best thing to do for systems with 4 or 8

^{*} This work has been funded by grants from the Spanish Ministry of Science and Innovation (TIN2008-01117), and Junta de Andalucía (P11-TIC-7176), in part financed by the European Regional Development Fund (ERDF). Eligius M. T. Hendrix is a fellow of the Spanish “Ramón y Cajal” contract program, co-financed by the European Social Fund.

cores. However, this is not the case for systems with larger number of cores. In that paper, this is shown by running eight PARSEC programs on a 24 cores system. The chosen number of threads is static during the execution and the runtime behaviour is input dependent. [15] also provides an interesting section with related work.

Our focus is on possibilities to decide on the number of used threads dynamically, also called "online creation of threads". The question is, how this influences performance for typically irregular codes. To achieve the dynamic allocation of threads, we do not use compilation techniques. Neither we modify the scheduler of the O.S. As a case, we focus on parallel Branch and Bound (B&B) algorithms. These algorithms perform irregular and unpredictable searches. They are considered one of the most challenging problems in the field of parallel computing. The basic code chosen for experimenting is called Local-PAMIGO and described in [3]. It concerns a parallel algorithm for interval B&B, which has shown a good speed up on multi-core systems. Local-PAMIGO uses dynamic threads creation at run time without explicit dynamic load balancing.

Some APIs, such as OpenMP [13], TBB [16] or Cilk [8], can obtain a good performance for parallel loops and nested parallelism. For instance, OpenMP allows the use of a dynamic number of threads with variable chunk size for loops. The corresponding task scheduling is not exposed to the users. To reduce the run time system overhead and achieve good performance, the excessive creation of tasks has to be avoided. Cut-off for task parallelism works for many applications but, unfortunately, it does not perform well for parallel B&B codes [5,11]. Instead of using a runtime system, we focus on the possibilities of the POSIX Thread NPTL library. This allows a stronger user control of the execution.

In order to control the number of threads, one also needs measurement of performance indicators (metrics) during execution for the current number of used threads. Linux O.S. collects information about the performance of the tasks. In [17] several approaches at application and kernel levels were compared. The best method appeared an approach that generates a new thread each time when none of the application threads has been in a sleeping state since the last check. The number of sleeping threads can be measured by the kernel "idle thread". This method was denoted as KITST-SC. Additionally, [18] shows how several instances of the same application running simultaneously self-adapt their number of threads in a simulated non-dedicated system. In the current paper, the KITST-SC model is used as a base. However, instead of the non existence of sleeping threads, the metric to determine the possible creation of a new thread is based on the measured interruptible and uninterruptible blocked time per thread.

The rest of this paper is organized as follows. Section 2 investigates ways to measure metrics at run time looking at alternatives provided by literature. Section 3 summarizes the case of the Local-PAMIGO application, which is used to compare several strategies. Section 4 shows how the application and Kernel communicate and how the number of threads of the application can be determined at run time taking into account the blocked times of the application. Section 5 shows the experimental results and finally, conclusions are shown in Section 6.

2 Measuring Thread Information

The question is how to obtain information about threads for an application at run time. We consider the Linux kernel 2.6 on a single multi-core computer. Information on threads for an application can be found in the directory `/proc/[pid]/tasks`. Only current values for a given thread are provided. Past values are not available. Moreover, every time the information is read, the O.S. not only updates information we are interested in, but also all information associated with the thread. How to obtain a better mechanism to extract information about threads? Notice that the Linux kernel not only stores the current states of threads, but also measures how long a thread has been in a certain state.

By using a system call which returns the current time in the system, an application is able to measure how much time is spent on selected sections of the code. The development of these measurements can be related to the variation in performance. The O.S. already stores the blocking, running, sleeping and waiting time of each thread. Therefore, it may be better to let the O.S. perform the monitoring of the application. In this way, the number of system calls is reduced and redundant computation at application and kernel levels is avoided. Decisions about different characteristics of the application can be made by the Kernel. The Kernel may need additional information from the application to make decisions depending on what is exactly monitored. A communication protocol between application and kernel is required. We come with a simple option in this paper.

The main aspect to be monitored is how blocked time of threads depends on the number of threads. As the number of threads increases, parallelism overhead increases mainly due to communications and competition for resources. If one gets hold of this relation at run time, one can determine the optimal number of threads in terms of performance.

Important factors to take into account are a) estimation of the remaining computational work in the application, b) metrics to determine the current performance of the application and c) frequency of metric evaluation and decision on creation of new threads.

Concerning a), most of the estimation methods found in literature are based on loop decomposition [10,20]. The case of interval branch-and-bound global optimization algorithms provides a challenging problem with respect to parallelization. These algorithms use a SPMD (Single Program Multiple Data) model, but the number of iterations, in terms of evaluated tree-nodes, and the computational work per node are not known beforehand. Additionally, these algorithms show search anomalies, i.e. the number of evaluated nodes can be different for parallel and sequential versions [4]. Some recent papers report that it is hard to achieve good parallel performance for automatic multi-threading in B&B algorithms [6,7,12]. Additionally, previous cited works use common runtime libraries that can suffer from large overheads [2].

Concerning b), the common used metric is the availability of an idle processor or core. Another factor is the power consumption in the system [19]. Few studies are found where system resources are shared by multiple programs [20,18]. In [14] it is said: *Portable parallel programs of the future must be able to understand*

and measure /any/ computer on which it runs so that it can adapt effectively, which suggests that hardware measurement should be standardized and processor performance and energy consumption should become transparent. In our opinion, the application should be able to request to the O.S. the values of parameters to be tuned and the O.S. should monitor the application to provide suitable values. This cooperation between application and O.S. will be beneficial for many applications with a computational pattern similar to B&B [1]. Specifically, we will distinguish and measure several types of blocked time and its influence on performance and availability of system resources, in order to decide if a new thread of the application should be created.

Concerning c), system and application changes have to be noticed as soon as possible. The objective is to maintain a good performance of the applications and system usage. Actions to achieve these goals, should only be done when they are needed. In our case, most statistics on (types of) blocked time are available due to the O.S. Decisions on the level of parallelism are taken only when there are idle processors.

Earlier studies on using the previous factors, can be found in [18,17]. In [17] a KIT model, denoted by KITST-SC, is compared with other decision models at application (ACW and AST-SF) and kernel levels (KST-SC), if only one application is running on the system. The KITST-SC model decides on thread creation if all threads of the application have performed some work and none of them are in sleeping state. No distinction was made on the types of blocked time. In [18], a similar comparison is made for the case where more than one instance of the same application is running on the system. In this work, the KITST-SC model is used as a base and we make the kernel distinguish between the different types of blocked time of the threads in order to decide on the number of threads.

3 Parallel B&B Application

We use B&B algorithms as a case to measure performance of the developed strategies. The algorithms are well known exhaustive search methods where the initial problem is partitioned into sub-problems until a solution is found. The method avoids the search in some branches of the search tree. The idea of using the power of parallel computers in B&B algorithms is not new. Many researchers have dedicated effort to obtaining efficient parallel implementations of this general framework. Some references in the field can be found in [3]. Here, we use a multi-threading interval B&B algorithm running on a multi-core system (Local-PAMIGO), as testbed for our experimentation [3]. Following the classification presented in [9], Local-PAMIGO has a parallelism that can be classified as AMP (Asynchronous Multiple Pool).

The programming model used in Local-PAMIGO is based on threads processing their own data structures. Threads cooperate by updating information stored in shared variables. Local-PAMIGO uses the concept of virtual process units (VPUs). The number of VPUs can be different from the number of available process units (PUs). The user sets the number p of VPUs to solve the problem.

To avoid idle VPU, a thread can generate a new thread assigning it part of its own pending work. In this way, the application tries to maintain the number of active threads (NTh) equal to p . A thread runs while it has nodes to evaluate. The algorithm collects results from shared memory and finishes when there is no thread running. Load balancing is inherent to the model. Local-PAMIGO adapts the number of running threads based on the pending work in the application and on the number of idle virtual process units. Most of the time $NTh = p$ for large size problems, but $NTh < p$ can also happen due to the irregularity of the B&B algorithm or the small size of the problems. Usually, the value of p is statically set to the number of PUs in the system as an input parameter. The optimum value of p , in terms of execution time of the application, will depend on the architecture, the level of parallelism of the algorithm, the size of the problem, etc.

If the value of p is too small, there is a possibility that the available parallelism of the algorithm and architecture is not exploited. On the other hand, if p is too large, even greater than the number of PUs in the system, overhead appears due to parallelism and to the management of such a number of threads by the scheduler of the O.S. Therefore, setting an appropriate value for p is a challenge for solving a given problem before execution of the algorithm.

4 Application-Kernel Communications

We describe the developed strategies and methods in order to have an application running in parallel in an efficient way, using information obtained at run time. Prototyping development and profiling of Local-PAMIGO show that this application is computationally intensive with few input and output operations. The blocked time is mainly due to accessing critical sections and dynamic memory allocation. For the latter, a *fast memory allocation library for multi-threaded applications*, called ThreadAlloc, taken from www.garret.ru/sal.html was used in order to reduce the number of memory requests to the system [3]. An important factor that affects blocked time is the number of threads of the application.

To achieve the communication between the threaded application and the kernel, every thread of the application performs the non-blocking system call *CheckDivideThread* at each iteration informing about the pending work to do.

CheckDivideThread returns the value of the variable *Create* which determines if a new thread can be created. After that, *Create* is set to *False*.

4.1 Kernel Idle Thread (KIT)

The Kernel Idle Thread (KIT) determines the value of the maximum number of threads (MNT) for the application, when there is an idle processor. Despite there is one idle thread associated with each processor, only one KIT is performing the MNT computation. In this way, resource utilization is low. Notice that the KIT has the lowest priority in the ready-to-run queue. For our investigation, the KIT has been modified to:

1. Check that $Create = False$ for each thread of the monitored application.
2. Check that all threads of the application did at least one iteration. If so, it performs the following steps.
3. Check for the existence of a processor with empty ready-to-run queue (execution of KIT is not a necessary condition to have an empty ready-to-run queue).
4. If conditions **1**, **2** and **3** hold
 - Calculate the value of MNT for the monitored application.
 - If the number of threads of the application is smaller than the value of MNT , the application will be rewarded with the possibility of creating a new thread, i.e. KIT sets the variable $Create$ to True in the struct $task_struct$ of the most loaded thread of the application.

All the counters are reset after positive or negative completion of step **4**. Notice that KIT execution and $CheckDivideThread$ system calls are asynchronous.

4.2 Blocked Times of the Threads of the Application

The performance of the application depends on the blocked time of its threads during execution. Examples of blocked time are: blocking in access to critical sections, input/output operations, dynamic memory allocation, cache misses, waiting in the ready-to-run queue, etc. We formalize the thread blocked time types.

- Block time (BT). This is the sum of two block time types:
 - Interruptible Block Time (IBT): time in state $task_interruptible$. For instance, blocked in access to critical sections, blocked in I/O operations, etc.
 - Non-Interruptible Block Time ($NIBT$): time in state $task_uninterruptible$. For instance, during dynamic memory allocation, during a cache miss, etc.
- Wait time (WT): time in the state $task_running$, i.e., waiting in the ready-to-run queue. This usually occurs when the number of ready to run threads is greater than the number of cores.

4.3 Determining the Maximum Number of Threads (MNT)

There are several ways to define the metric MNT based on the different types of blocked time. Consider the following possibilities:

- MNT based on $NIBT$ (MNT_NIBT): Let λ be the time required such that all the threads of the application finish at least one iteration. In this way all threads execute all the instructions that could provoke blocked time. We take

$$MNT_NIBT = \frac{\lambda}{\max_i\{NIBT_i\}}, \quad (1)$$

where $NIBT_i$ is the uninterruptible block time spent by thread i .

- *MNT* based on *IBT* (*MNT_IBT*): Let λ_{ini} be the time required by one thread of the application to carry out N iterations divided by N . So, λ_{ini} stores the average run time to carry out one iteration without blocked time due to the existence of other application's threads. We define

$$MNT_IBT = \frac{\lambda_{ini}}{\max_i \{IBT_i\}}, \quad (2)$$

where IBT_i is the interruptible block time spent by thread i .

- *MNT* based on *BT* (*MNT_BT*):

$$MNT_BT = \frac{\lambda}{\max_i \{NIBT_i + IBT_i\}}. \quad (3)$$

In the denominator, the \max_i operation is used, because it is supposed that with increasing number of threads, the maximum blocked time per thread also increases.

To measure the performance of the parallel algorithms with a dynamic number of threads, we define the efficiency as:

$$E_t(n) = \frac{t(1)}{n \cdot t(n)},$$

where $t(1)$ is the execution time with one thread and $t(n)$ is the execution time with n threads on average.

5 Experiments

The experiments have been carried out on a four quad-core AMD *Opteron*TM processor system, i.e., 16 processors with 64 GB of RAM. Linux Kernel 2.6.29 has been modified to perform the computational work described in Section 4. An interval B&B algorithm is coded in C and compiled with PThread and C-XSC libraries. To evaluate different versions of the algorithm, we have used a standard set of test problems in unconstrained Global Optimization: Kowalik, Griewank10, Ratz5, Ratz6, Neumaier2 and EX2. Descriptions can be found in [18,17]. The algorithms run up to a precision of 10^{-5} .

Two sets of experiments have been carried out to compare Local-PAMIGO and Local-PAMIGO-KIT. The first experiments use the ThreadAlloc memory allocation library while the second set uses standard C dynamic memory allocation.

5.1 Comparing Local-PAMIGO and Local-PAMIGO-KIT with ThreadAlloc Memory Allocation Library

Local-PAMIGO, which also uses a dynamic number of threads, has been described in Section 3. The most loaded thread, in terms of the number of pending nodes to evaluate, has the possibility of generating a new thread. The new thread

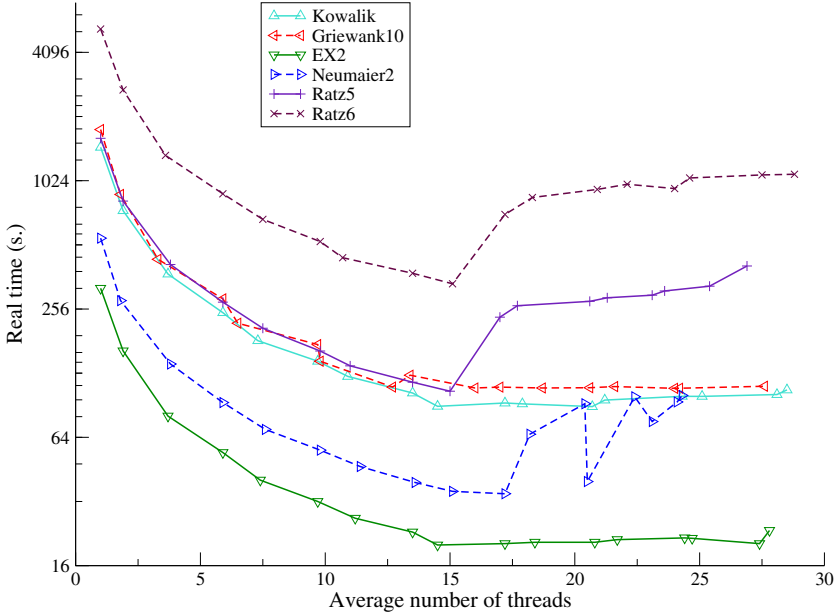


Fig. 1. Execution time of Local-PAMIGO using ThreadAlloc with default 4KB. pages

will process half of the pending nodes of its ancestor. The static maximum number of threads p is taken as input parameter. The algorithm has been run for $p = 1$ and even values of p in the set $\{2 \leq p \leq 32\}$. For each value of p , we have measured the execution time and the average number of threads during the running. Notice that the average number of threads n is always smaller than p .

Figure 1 shows the execution time for the set of test problems using ThreadAlloc with default page size of 4KB. It can be seen that increasing the value of p results in significant decreasing of the execution time only when p is less or similar to the number of cores in the system. For values of $p > 16$, the execution time keeps similar to the minimum for three test functions but for the other three functions increases significantly. The minimum value of the execution time are obtained in an interval around $p = 16$. A summary of the results in Figure 1 is given in Table 2, where the following header labels have been used:

- Function: Name of the problem to be solved.
- n : Average number of threads producing the minimum execution time.
- T_{min} : Minimum execution time.
- $E_t(n)$: Efficiency with an average of n threads.
- $[n_i, n_j]$: Interval of average number of threads giving about the same minimum time.
- $T_{av.}$: Average execution time for runs using on average a number of threads in interval $[n_i, n_j]$.
- Dev. (%): Percentage of deviation from $T_{av.}$.

Table 1. Real time for Local-PAMIGO, using ThreadAlloc with default 4KB. pages

Function	n	T_{min}	$E_t(n)$	$[n_i, n_j]$	$T_{av.}$	Dev. (%)
Kowalik	21	89.2	0.8	[15, 28]	95.0	5.1
Griewank10	24	108.7	0.7	[13, 24]	109.7	0.8
EX2	15	20.0	1.1	[15, 27]	20.8	2.9
Neumaier2	17	34.8	0.9	[14, 17]	36.6	6.5
Ratz5	15	105.3	1.0	[14, 15]	110.7	6.9
Ratz6	15	336.1	1.0	[14, 15]	356.4	8.0

Table 2. Real time for different versions of Local-PAMIGO-KIT, using ThreadAlloc with default 4KB. pages

Function	MNT_IBT			MNT_NIBT			MNT_BT		
	n	T(s.)	$E_t(n)$	n	T(s.)	$E_t(n)$	n	T(s.)	$E_t(n)$
Kowalik	17	90.4	1.0	17	90.5	0.9	17	90.6	1.0
Griewank10	18	111.5	0.9	15	111.2	1.1	16	110.2	1.0
EX2	16	20.6	1.0	16	20.7	1.0	16	20.3	1.0
Neumaier2	16	35.1	1.0	16	35.7	1.0	16	34.8	1.0
Ratz5	15	122.5	0.9	16	218.5	0.5	14	171.3	0.7
Ratz6	15	343.8	1.0	16	434.2	0.8	15	458.5	0.7

Table 1 shows that several values of n result into a small deviation from the minimum execution time. It also illustrates that the minimum execution time is not obtained when the average number of threads is equal to the number of cores (16). This follows from experimenting with different values of p . In general, Local-PAMIGO achieves a good efficiency for most of the instances.

Local-PAMIGO-KIT is a variant of Local-PAMIGO which communicates with the Kernel (see Section 4) adapting the number of threads to the performance of the application and the available resources. Three versions of Local-PAMIGO-KIT have been evaluated using the three estimators of the maximum number of threads (see Section 4.3). Experimental results for *MNT_BT*, *MNT_IBT* and *MNT_NIBT* are shown in Table 2, where $T(s.)$ shows the algorithms' execution time.

Local-PAMIGO-KIT auto-tune the number of threads avoiding the experimentation with different values of p . Local-PAMIGO-KIT obtains similar results to Local-PAMIGO for all problems apart from the Ratz5 and Ratz6 instances using *MNT_NIBT* and *MNT_BT*. These instances suffer from long *IBT* when the number of threads is larger than 16. Although Table 2 shows that, for Ratz5 and Ratz6 instances, the average number of threads is smaller or equal to 16 using *MNT_NIBT* and *MNT_BT* versions, the number of threads can be larger than 16 at run time. Adaptive methods allow the generation of a new thread if the performance criterion is satisfied. However, the new created thread can decrease the performance of the application. In the evaluated algorithms, the number of running threads decreases only when one thread finishes its work and the generated thread is not stopped when the performance is low. This deserves future research.

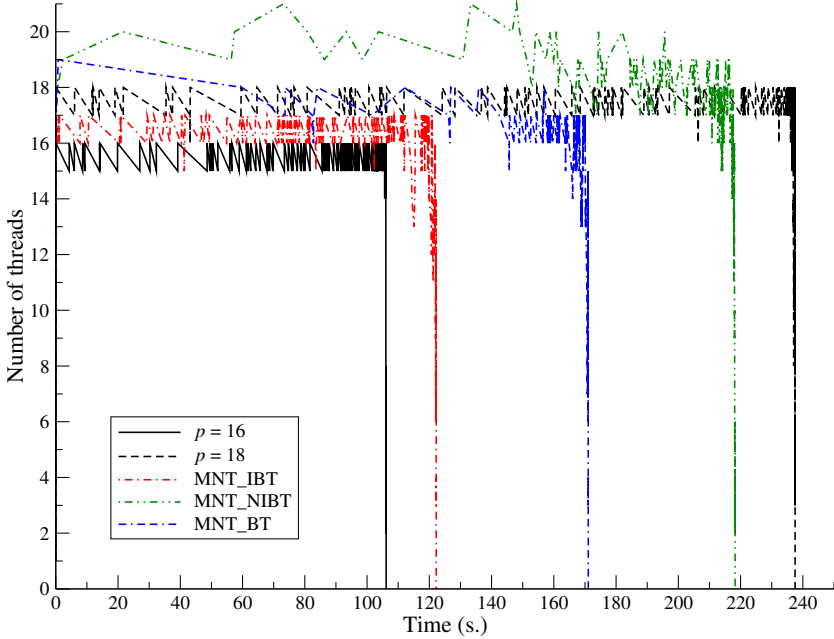


Fig. 2. Number of threads during algorithm executions for problem Ratz5. Local-PAMIGO with $p=16$ and 18, and Local-PAMIGO-KIT versions using ThreadAlloc with default 4KB. pages.

Figure 2 shows the number of threads during the execution of algorithms Local-PAMIGO with $p=16$ and 18, and Local-PAMIGO-KIT, for the Ratz5 instance. Local-PAMIGO with $p = 16$ shows that the number of threads grow very quickly up to 16 and when a thread finishes a new thread is generated, until the algorithm finishes. Local-PAMIGO with $p = 18$ behaves similarly, but suffering from long *IBT*. Local-PAMIGO-KIT using *MNT_IBT* has a good performance with a number of threads equal to 16. Therefore, it generates a new thread. The performance with 17 threads is not so good and a new thread is not generated. When a thread finishes, the performance of 16 threads is again good and a new thread is generated, and so on. Even for this difficult instance, the achieved result is near to the best Local-PAMIGO result. Local-PAMIGO-KIT using *MNT_NIBT* does not take into account *IBT* and the number of threads is too large, with the corresponding large execution time. *MNT_BT* is a trade-off between *MNT_IBT* and *MNT_NIBT*. A better decision for *MNT_BT* could be $MNT_BT = \min\{MNT_IBT, MNT_NIBT\}$ for this case.

5.2 Comparing Local-PAMIGO and Local-PAMIGO-KIT with the Standard C Dynamic Memory Allocation

This experimentation is used just to show how the auto-tuning versions of Local-PAMIGO-KIT adapt to a large *NIBT*. Experimental results for Local-PAMIGO

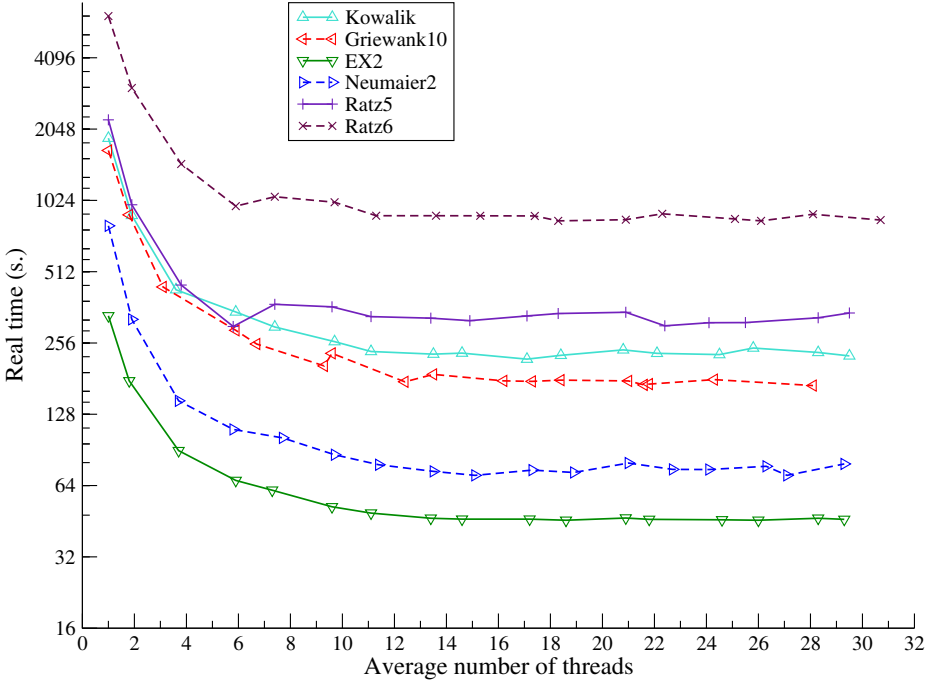


Fig. 3. Local-PAMIGO with standard C dynamic memory allocation

Table 3. Real time for Local-PAMIGO with standard C dynamic memory allocation

Function	n	T_{min}	$E_t(n)$	$[n_i, n_j]$	$T_{av.}$	Dev. (%)
Kowalik	17	218.8	0.5	[11, 30]	231.5	2.9
Griewank10	28	169.3	0.3	[12, 22]	175.0	2.1
EX2	{19, 26}	45.7	0.4	[13, 29]	46.2	0.8
Neumaier2	{15, 27}	70.7	0.7	[14, 27]	74.3	3.9
Ratz5	22	302.6	0.3	[13, 28]	324.8	4.2
Ratz6	{18, 26}	839.2	0.4	[11, 31]	868.0	2.6

have been drawn in Figure 3 where it can be seen that the values of execution time are always larger than those in in Figure 1. Table 3 shows similar information to Table 1. The minimum execution time for instances EX2, Neumaier2 and Ratz6 can be obtained with two different values of the average number of threads. Due to *NIBT* the efficiency is very low. Again, the minimum execution time for each instance is obtained with an different average number of threads, most of them larger, than the number of cores.

Table 4 shows similar information to Table 2. *MNT_IBT* obtains the smallest adaptive execution time at the cost of generating the largest average number of threads. This indicates that *IBT* is negligible compared to the execution time

Table 4. Real time for different versions of Local-PAMIGO-KIT with standard C dynamic memory allocation

Function	MNT_IBT			MNT_NIBT			MNT_BT		
	n	T(s.)	$E_t(n)$	n	T(s.)	$E_t(n)$	n	T(s.)	$E_t(n)$
Kowalik	35	225.2	0.2	8	269.4	0.8	8	283.7	0.8
Griewank10	19	172.2	0.5	15	232.0	0.5	8	231.5	0.9
EX2	23	45.3	0.3	16	57.5	0.4	8	56.3	0.7
Neumaier2	28	73.6	0.4	9	87.1	1.0	9	88.1	1.0
Ratz5	27	319.2	0.3	8	381.0	0.7	9	353.8	0.7
Ratz6	25	851.9	0.3	8	1025.7	0.7	8	1022.2	0.7

of the application with large *NIBT*. Although *MNT_IBT* obtains the smallest adaptive execution time it also produces the smallest adaptive efficiency.

MNT_NIBT produces the largest values of adaptive execution time, specially for the Griewank10 and EX2 instances. The average number of threads is smaller than those generated by the *MNT_IBT* variant but the efficiency is larger. In term of efficiency, *MNT_BT* makes the best decision on the number of threads.

6 Conclusions and Future Work

The general question that has been investigated is whether the dynamic decision on the number of threads at run time can lead to efficiency gain in applications with an irregular structure. To investigate this, information for controlling the number of threads was gathered by modifying the O.S. Kernel Idle Thread. In this way, one can measure blocked times: `task_interruptible` and `task_uninterruptible`, that already collected by the O.S. for scheduling purposes. The new way of allocating threads was tested on a multi-threaded interval B&B algorithm to adapt its level of parallelism. The application adapts its number of threads to the computational resources and to the achieved performance. Experiments show that the optimal average number of used threads does not equal the number of cores for several instances. There is a trade-off between the number of threads producing the minimum execution time and the achieved efficiency. Adaptive methods allow maintaining the efficiency of the application.

Another research question is due to the ability of the O.S. to delay the execution of some threads in order to maintain an acceptable level of performance of the applications in the system.

References

1. Asanovic, K., Bodik, R., Demmel, J., Keaveny, T., Keutzer, K., Kubiatowicz, J., Morgan, N., Patterson, D., Sen, K., Wawrzyniek, J., Wessel, D., Yelick, K.: A view of the parallel computing landscape. *Commun. ACM* 52, 56–67 (2009), doi:10.1145/1562764.1562783

2. Bhattacharjee, A., Contreras, G., Martonosi, M.: Parallelization libraries: Characterizing and reducing overheads. *ACM Trans. Archit. Code Optim.* 8, 5:1–5:29 (2011), doi:10.1145/1952998.1953003
3. Casado, L.G., Martínez, J.A., García, I., Hendrix, E.M.T.: Branch-and-bound interval global optimization on shared memory multiprocessors. *Optimization Methods and Software* 23(3), 689–701 (2008), doi:10.1080/10556780802086300
4. De Bruin, A., Kindervater, G., Trienekens, H.: Asynchronous Parallel Branch and Bound and Anomalies. In: Ferreira, A., Rolim, J. (eds.) *IRREGULAR 1995. LNCS*, vol. 980, pp. 363–377. Springer, Heidelberg (1995), doi:10.1007/3-540-60321-2_29
5. Duran, A., Corbalán, J., Ayguadé, E.: An adaptive cut-off for task parallelism. In: *SC 2008: Proceedings of the 2008 ACM/IEEE Conference on Supercomputing*, pp. 1–11. IEEE Press, Piscataway (2008), doi:10.1109/SC.2008.5213927
6. Duran, A., Corbalán, J., Ayguadé, E.: An adaptive cut-off for task parallelism. In: *Proceedings of the 2008 ACM/IEEE Conference on Supercomputing, SC 2008*, pp. 36:1–36:11. IEEE Press, Piscataway (2008), <http://portal.acm.org/citation.cfm?id=1413370.1413407>
7. Duran, A., Teruel, X., Ferrer, R., Martorell, X., Ayguadé, E.: Barcelona OpenMP Tasks Suite: A Set of Benchmarks Targeting the Exploitation of Task Parallelism in OpenMP. In: *38th International Conference on Parallel Processing (ICPP 2009)*, pp. 124–131. IEEE Computer Society, Vienna (2009), doi:10.1109/ICPP.2009.64
8. Frigo, M., Leiserson, C.E., Randall, K.H.: The implementation of the Cilk-5 multithreaded language. In: *PLDI 1998: Proceedings of the ACM SIGPLAN 1998 Conference on Programming Language Design and Implementation*, pp. 212–223. ACM, New York (1998), doi:10.1145/277650.277725
9. Gendron, B., Crainic, T.G.: Parallel branch-and-bound algorithms: Survey and synthesis. *Operations Research* 42(6), 1042–1066 (1994), doi:10.1287/opre.42.6.1042
10. Lee, J., Park, J.H., Kim, H., Jung, C., Lim, D., Han, S.: Adaptive execution techniques of parallel programs for multiprocessors. *Journal of Parallel and Distributed Computing* 70(5), 467–480 (2010), doi:10.1016/j.jpdc.2009.10.008
11. Olivier, S.L., Prins, J.F.: Evaluating openmp 3.0 run time systems on unbalanced task graphs. In: Müller, M.S., de Supinski, B.R., Chapman, B.M. (eds.) *IWOMP 2009. LNCS*, vol. 5568, pp. 63–78. Springer, Heidelberg (2009), doi:10.1007/978-3-642-02303-3_6
12. Olivier, S.L., Prins, J.F.: Comparison of openmp 3.0 and other task parallel frameworks on unbalanced task graphs. *International Journal of Parallel Programming* 38, 341–360 (2010), doi:10.1007/s10766-010-0140-7
13. OpenMP Architecture Review Board: OpenMP Application Program Interface, version 3.0. OpenMP (2008)
14. Patterson, D.A.: Software knows best: portable parallelism requires standardized measurements of transparent hardware. In: *Proceedings of the First Joint WOSP/SIPEW International Conference on Performance Engineering, WOSP/SIPEW 2010*, pp. 1–2. ACM, New York (2010), doi:10.1145/1712605.1712607
15. Pusukuri, K.K., Gupta, R., Bhuyan, L.N.: Thread reinforcer: Dynamically determining number of threads via os level monitoring. In: *Proceedings of the 2011 International Symposium on Workload Characterization, Austin, TX, USA*, pp. 116–125 (October 2011), doi:10.1109/IISWC.2011.6114208
16. Reinders, J.: *Intel Threading Building Blocks*. O'Reilly (2007)
17. Sanjuan-Estrada, J., Casado, L., García, I.: Adaptive parallel interval branch and bound algorithms based on their performance for multicore architectures. *The Journal of Supercomputing* 58(3), 376–384 (2011), doi:10.1007/s11227-011-0594-4

18. Sanjuan-Estrada, J.F., Casado, L.G., García, I.: Adaptive parallel interval global optimization algorithms based on their performance for non-dedicated multicore architectures. In: Proceedings of PDP 2011 - The 19th Euromicro International Conference on Parallel, Distributed and Network-Based Computing, Cyprus, pp. 252–256 (February 2011), doi:10.1109/PDP.2011.54
19. Suleman, M.A., Qureshi, M.K., Patt, Y.N.: Feedback-driven threading: power-efficient and high-performance execution of multi-threaded workloads on cmps. *SIGARCH Comput. Archit. News* 36, 277–286 (2008), doi:10.1145/1353534.1346317
20. Yu, C., Petrov, P.: Adaptive multi-threading for dynamic workloads in embedded multiprocessors. In: Proceedings of the 23rd Symposium on Integrated Circuits and System Design, SBCCI 2010, pp. 67–72. ACM, New York (2010), doi:10.1145/1854153.1854173

*k*NN-Borůvka-GPU: A Fast and Scalable MST Construction from *k*NN Graphs on GPU

Ahmed Shamsul Arefin, Carlos Riveros, Regina Berretta, and Pablo Moscato

Centre for Bioinformatics, Biomarker Discovery and Information-Based Medicine,
School of EECS, FEBE, The University of Newcastle, Australia

{Ahmed.Arefin, Carlos.Riveros, Regina.Berretta,
Pablo.Moscato}@newcastle.edu.au

<http://www.newcastle.edu.au/research-centre/cibm/>

Abstract. Computation of the minimum spanning tree (MST) is a common task in numerous fields of research, such as pattern recognition, computer vision, network design (telephone, electrical, hydraulic, cable TV, computer, road networks etc.), VLSI layout, to name a few. However, for a large-scale dataset when the graphs are complete, classical MST computation algorithms become unsuitable on general purpose computers. Interestingly, in such a case the *k*-nearest neighbor (*k*NN) structure can provide an efficient solution to this problem. Only a few attempts were found in the literature that focus on solving the problem using the *k*NNs. This paper briefs the state-of-the-art strategies for the MST problem and a fast and scalable solution combining the classical Borůvka's MST algorithm and the *k*NN graph structure. The proposed algorithm is implemented for CUDA enabled GPUs (*k*NN-Borůvka-GPU), but the basic approach is simple and adaptable to other available architectures. Speed-ups of 30-40 times compared with CPU implementation was observed for several large-scale synthetic and real world data sets.

Keywords: Minimum spanning tree, nearest neighbors, parallel computing, CUDA, GPU.

1 Introduction

The minimum spanning tree problem has a rich background history [14]. The earliest known MST algorithm was proposed by Otakar Borůvka [9], a Czech mathematician, to design an efficient electrical coverage for the *Moravia* region of Czech Republic, in 1926. Later, in the 1950s when the computer age just began, the MST problem drawn attention to several computational researchers. Among them, Joseph Kruskal and Robert Prim gave the two most commonly used MST algorithms and both of them mentioned Borůvka's approach as a ground work. Although it is an open problem whether a linear-time algorithm exists for finding the MST, the solution proposed by Chazelle (which is also Borůvka-based) is the fastest sequential algorithm to compute the MST up to date and runs in $\mathcal{O}(m\alpha(n))$ time, where α is the inverse of the *Ackermann's*

function, n and m are the number of vertices and edges, respectively. There are many other algorithms that claim to have lower asymptotic complexities but the hidden constants in those algorithm should also be considered before their application to real world data sets [21].

Interestingly, recent trends in solving this problem have moved to the domain of parallel and distributed computing. Although the MST computation on general graphs is an irregular problem that suits well on a sequential environment, a number of parallel and distributed implementations are proposed to tackle its run time complexity [25,24,30]. Most of these parallel formulations are actually based on known classical approaches like Borůvka’s, Prim’s and Kruskal’s or their combinations but they play vital roles in faster processing of the large data sets arising in several fields of research. Aside from the MST problems on general graphs, an important domain of solving the problem is on *complete graphs*, as these graphs are perfectly suitable for several network analysis approaches, such as feature set analysis, gene expression clustering etc. [18]. In such context, when the data sets get larger and the graphs get denser, traditional algorithms fall into the challenge of scalability [28]. One efficient way to solve this problem is to use a k NN structure instead of the complete graph. Bentley [8] proposed a solution when the vertices are points in a k -dimensional co-ordinate space. Murtagh [22] addressed the efficiency of the nearest neighbor structure in formulating an approximate MST of complete graphs. Tepper et al. [28] proposed an interesting variant of the Borůvka’s approach for complete graphs only by looking at the nearest neighbors, without formulating the complete graph structure. Although these methods can scale the computation by several orders of magnitude, they are only useful with low-dimensional datasets. We found no solution to this problem in the literature (on complete graphs) taking the advantage of parallel computation and the k NN graph structure and furthermore, being free from the *curse of dimensionality*. This gap in the literature influenced us to develop a scalable data parallel solution using the k NN graphs. Our approach (k NN-Borůvka-GPU) is based on Borůvka’s algorithm, but instead of concentrating only on the improvements of speed-ups on GPU, we worked on preserving the locality on each edge while constructing the tree, as one of our goals is to re-use the k NN annotated MST (or minimum spanning forests (MSFs), in most of the cases) for clustering of data [3].

In the rest of this paper, we discuss about the Borůvka’s approach to construct the MST along with a review of the existing parallel and distributed Borůvka-based approaches. Then, we introduce our **k NN-Borůvka-GPU** algorithm with a detailed illustration on a smaller version of the *84-into European Languages dataset* [13]. We also give directions to implement our algorithm on GPU and compare the performance of our algorithm against some other publicly available state-of-the-art parallel MST algorithms and finally, we give a brief concluding remark on our method.

2 Related Background

2.1 GPGPU Programming Model

The GPGPU is a powerful device that is devoted to parallel data processing rather than data caching and flow control as a general purpose CPU. The massive parallel processing capability of GPU makes it more attractive for algorithmic problem solving, when the processing of data (or a large block of data) can be handled in parallel. In general, the GPUs are organized in a streaming, data-parallel model in which the processors execute the same instructions on multiple data streams simultaneously. At the software level, there exist several application programming interfaces (APIs) that enable programmers to develop applications on GPU. NVidia's CUDA is one of the most widely adopted API that enables developing GPU-based applications using C/C++ programming language [1]. It exposes an abstraction to programmers that they can parallelize their tasks on GPU using concepts of threads, blocks and grids. CUDA supports a large number of threads (up to 512 or 1024, depending on the architecture) in a block and the maximum number of blocks in a grid can be up to $(2^{16} - 1)$, in at most 3 dimensions. Both the threads and blocks are referenced by their indices. A CUDA program typically consists of a component that runs on the CPU, or host, and a smaller, but computationally intensive component called *kernel*, that runs in parallel on the GPU. The kernel cannot access the main memory of the host directly and the input data for the kernel must be copied to the GPU's on-board memory prior to invoke the kernel and the output data also must first be written to the GPU's memory and then copied back to CPUs in-memory.

2.2 The k Nearest Neighbor (k NN) Graph

The nearest neighbor graph is a typical proximity graph that exploits nearest neighbor relation of any point in the ground set. The nearest neighbor or, in general, the k nearest neighbor (k NN) graph of a dataset is obtained by connecting each point to its k closest points, where a *distance metric* defines closeness. The k NN graphs can be produced using many different k NN search algorithms. In this work, we utilized the FS- k NN algorithm [4] to produce the k NN graphs and applied the *Pearson's correlation* as the similarity metric.

2.3 The Borůvka's MST Algorithm and Parallel Computing

The brief history of the Borůvka's MST algorithm can be found in [23]. After Borůvka, this classical algorithm was later re-discovered by Choquet (1938), Zubrzycki (1951), and Sollin (1965). The basic algorithm is simple, it finds the minimum outgoing edge for each vertex and merges the source with the target (of min edge). The connected vertices are considered as a *super-vertex*, the process continues until all the super-vertices become a single connected component (see Algorithm [1]). The run time complexity of the algorithm is $\mathcal{O}(m \log n)$.

Algorithm 1. Borůvka's Algorithm

Input : A connected undirected weighted graph $G(V, E)$ **Output**: A minimum spanning tree, G_{MST}

```

1 Initialize  $G_{MST}$  with  $V$ , as an isolated graph ;
2 while  $G_{MST}$  has less than  $|V| - 1$  edges do
3   foreach component  $C \in G_{MST}$  do
4     Select the lightest edge  $e$  between  $v \in C$  and
5     another vertex at  $C', C' \setminus C$ ;
6      $G_{MST} \leftarrow G_{MST} \cup e$ ;
7 Return  $G_{MST}$ ;

```

The main attraction of the Borůvka's Algorithm is its natural possibility of parallelization. Therefore, there exists a number of implementations using parallel and distributed computing environments. For example, the parallel MST computation algorithm proposed by Johnson and Metaxas [19] used the essence of Borůvka's in a *Exclusive-Read-Exclusive-Write Parallel Random Access Machine* (EREW PRAM) model of parallel computation which was theoretically faster, by a factor of $\sqrt{\log(n)}$, than other deterministic algorithms with no concurrent writing. Another variant of parallel Borůvka's algorithm was proposed by Chung and Condon [10] for asynchronous, distributed-memory machines that resulted in a four times speedup for sparse graphs over the sequential Borůvka's algorithm, using a total of 16 processors. Dehne and Götz [11] proposed the *Borůvka-Mixed-Merge* algorithm, where every processor sequentially computes the MST of the graph induced by the locally stored edges. They achieved six times speed on random dense graphs over the sequential algorithm, using a total of 16 processors. Bader and Cong [5] proposed four data structures for Borůvka's parallel variant (*Bor-EL*, *Bor-AL*, *Bor-ALM*, and *Bor-FAL*). Their algorithm *MST-BC*, combined the Prim's and Boruvka's algorithms and resulted in a five times speed-up for arbitrary random graphs, using 8 processors. Kang and Bader [20] designed a parallel minimum spanning forest (MSF) algorithm for transactional memory architecture addressing the complex data synchronization issues on the *MST-BC* algorithm [5] and achieved speedups of about eight times using 64 threads over a sequential single threaded version.

Aside from these parallel and distributed variants of Borůvka's algorithm, more recent trends moved to implement the algorithm on GPUs as they are commonly installed on today's home computers, workstations and gaming devices. For instance, Harish and Narayanan [15] proposed the first GPU-based variant of the Borůvka's algorithm using a divide-and-conquer approach similar to Johnson and Metaxas [19]. The basic approach is kernel-based and on sparse graphs their implementation achieved around ten-fold speed-ups. Vineet et al. [30] implemented another variant of GPU-based Borůvka's algorithm using similar concepts and the recursive framework of Harish and Narayanan [15], but employing a series of primitives, such as, *scan*, *segmented-scan*, *splits*, *sort* etc. Although the implementation performed 2 to 3 times faster than the previous

implementation [15], it turned out to be infeasible for graphs larger than six million vertices and weights larger than 1K because of the 32/64 bit restrictions of those primitive operations. Nobari et al. [24] proposed a data parallel variant of Borůvka’s approach that is based on the GPU-CPU synchronization at each iteration of the Borůvka’s step and achieved speedups of up to ten-folds. However, same as Harish and Narayanan [15] and Vineet et al. [30], they assumed that the entire data must reside into GPU’s memory that restricted the scalability of their approach. Rostrop et al. [25] proposed a memory-efficient MST, namely data parallel Kruskal’s that combined the Borůvka’s algorithm with Kruskal’s. Although they implemented their algorithm using primitives [17], the key benefit of their approach is a partitioning method that enabled them to process larger graphs. However, they do not employ any data streaming to one or multi-GPU similar to the external memory MST formulation in [2]. They achieved four times memory efficiency and around ten-fold speedups than other Borůvka’s GPU implementations. For complete graphs on very large datasets, there is no parallel/GPU-based formulation of the problem.

3 The Proposed Algorithm: k NN-Borůvka

The Borůvka’s algorithm naturally exploits maximal edge parallelism. However, for a very large dataset when the graphs are complete, the classical Borůvka’s algorithm can become very slow or incomputable on general purpose computers as the finding of the lightest edge outgoing from each vertex or super-vertex become time consuming [7]. In this work, a variant of the Borůvka’s algorithm is proposed that efficiently uses the k NN graph structure to construct the MST (or a set of MSF if the k NN is not connected). The proposed method is exact, as the k NN graph is pre-computed by using the exact method in [4]. It does not suffer from the *curse of dimensionality* also, as the above mentioned k NN computation can be efficiently performed for a large number of dimensions. Following restrictions are applied to the original Borůvka’s algorithm:

1. **Input graph:** The input is restricted to the k NN graph only. In addition, the edges are pre-sorted in an ascending order, first by vertex id and then by edge weights.
2. **Iteration:** The algorithm iterates only up to k , the number of nearest neighbors. Therefore, the resultant may not be a single component but rather a MSF, which can be further studied by clustering algorithms [3].

The proposed algorithm (**k NN-Borůvka-GPU**) is presented in Algorithm 2. We use a divide and conquer approach that is similar to the one employed in Harish and Narayanan [15]. However, the goal of our approach is different from them, instead of producing the MST our objective is to produce a partitioning of the MST, using the structure of nearest neighbors. Thus, we preserve the k NN ranks on edges while constructing the MST and employ a different strategy to implement the algorithm. The algorithm operates on four different steps. First, in the initialization step, a unique color (i.e., the vertex id) is assigned to each

vertex of the graph. Then, in the **Connect** step, colored trees are constructed by adding the minimum weighted outgoing edges from each of the colors and in the **Recolor** step, the connected components or the super-vertices are identified and re-colored. In the **Remove cycles** step, cycles are removed between any pair of colors and in the **Find min** step, the minimum outgoing edges from the super-vertices are identified. The algorithm terminates when the edge connected to the k -th nearest neighbor of each vertex has been examined.

Algorithm 2. k NN-Borůvka’s Algorithm

Input : G_k , the k NN graph

k , the number of nearest neighbors

Output: Atmost $(n-1)$ edges of the G_k will be selected.

- 1 Initialize the colors for each vertex and the minimum outgoing edge for each color;
 - 2 **for** $i \leftarrow 1$ **to** k **do**
 - 3 **Connect**: Mark the minimum outgoing edge from each colored super-vertex as an MST edge;
 - 4 **Recolor**: Recolor the vertices to find the super-vertex color;
 - 5 **Remove cycles**: Remove cycles between any pair of colored vertices;
 - 6 **Find min**: Find the minimum outgoing edge from each super-vertex ;
 - 7 Return the MST constructed from the marked edges of G_k .
-

Although this algorithm may compute the MSF for a given k NN graph embedded in a complete graph G , it is possible to extend the proposed algorithm to compute the MST of such G . In line 6 of Algorithm 2, (expanded in Algorithm 6 (Find min)), if for some vertex x the list of neighbors contains no different colored vertex to act as the target of minimum out going edge from x , then the NNs list needs to be extended and subsequently, minimum out going edge to the next different colored vertex needs to be identified. The **Find min** procedure will perform this computation of next bunch of k NN(x).

The parallel complexity of the algorithm can be computed as follows: each iteration of the Borůvka’s reduces the number of vertices by at least half, hence the iterations run at most $\log_2(n)$ times, as we restricted the outer loop by k , thus the complexity is $\mathcal{O}(k)$, where $k = \lfloor \ln(n) \rfloor$. Each edge in **Recolor/ Remove cycles** is checked by at most two parallel threads (from two end points), at most τ times, so the total work performed by can be seen as $\mathcal{O}(2\tau m)$, for a small constant τ . The **Find min** sequentially identifies the minimum outgoing edge from each color, which makes it to be the heaviest part of the algorithm with running time of $\mathcal{O}(\alpha)$, where α is a (decreasing) subset of n vertices that has the end points of all the min out edges. Putting them all together, the total work of Algorithm 2 is $\mathcal{O}(\alpha\tau mk)$.

The complete algorithm is demonstrated in Figure 1, on 16 Indo-European Language extracted from the 84 *Indo-European Language* data set [13]. Figure 1(a)-(b) show the input k NN graph (for $k=3$) and the initialization, respectively. Figure 1(c)-(d) show the outcome of the **Connect**, **Recolor** and **Remove cycles**

steps, during the 1st iteration. Figure 1(e) shows the Connect step of 2nd iteration, and Figure 1(d) shows the final results after 2nd iteration. Edges are annotated and directed by the *neighbor rank* of target vertices (see Section 4).

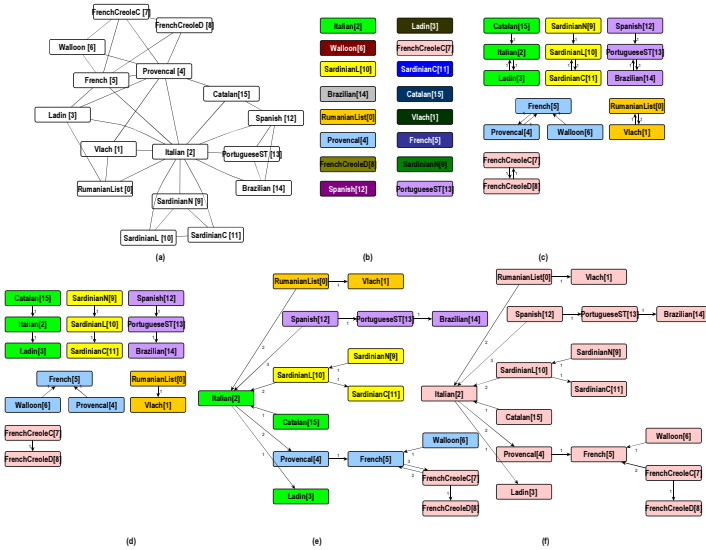


Fig. 1. Steps of the evolution of the algorithm on 16 Languages. The edges are annotated by their neighbor ranks and the arrows are the neighbor directions. Figure (b)-(d) illustrates the 1st iteration and the Figure (e)-(f) shows the of 2nd iteration.

4 Data Parallel Implementation on GPU

We implemented the proposed algorithm on NVidia GPUs utilizing the CUDA programming API [1] and following data structures. The k NN graph (G_k) is stored as an array of edge structure (Edge) that has five members (**source**, **target**, **weight**, **rank** and **candidate**). Additionally, an array of vertex structure (Vertex) is maintained to store three other attributes (**color**, **minIndex**, **minWeight**) for each vertex (v). Two other arrays, **color** and **neighborRank** store the color and the rank of the connecting neighbor of each vertex, respectively. The purposes of these arrays are to facilitate the search for the colors of the super-vertices and recoloring using the nearest neighbor ranks. The *neighbor rank* for a vertex is illustrated in Figure 2 in terms of ‘Spanish’ language of the the Indo-European dataset.

All of these variables and arrays are stored in the global memory of the device. We have not attempted to take advantage of device shared memory due to the irregularity of the problem and device’s workload imbalance between threads [15]. It should be possible to further optimize the algorithm in specific

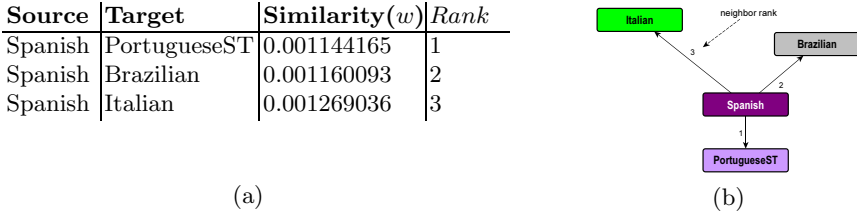


Fig. 2. Neighbor ranks for edges outgoing from the ‘Spanish’ Language

sections using data parallel primitives [17] and shared memory. However, in our implementation, we put an emphasis on stability and clarity, thus we chose not to use primitives and atomic operations. The algorithm is implemented using 1-dimensional orientation of CUDA threads and blocks. Each thread works on each vertex that leads to an execution of maximum $\mathcal{O}(n)$ parallel threads.

4.1 Implementation

First the algorithm initializes certain attributes associated with each vertex and edge. It initializes color ($vcolor$) of each vertex (v) by the vertex index and the index ($minIndex$) and weight ($minWeight$) of minimum out going edge for each vertex color. Additionally, for each edge it initializes the **candidate** attribute to **false** and **rank** attribute to the neighbor rank of the target vertex of each edge (see Figure 2). The **connect** kernel presented in Algorithm 3 marks the minimum outgoing edge from each super-vertex.

Algorithm 3. Connect Kernel Algorithm

Input : $Gk, v, color, neighborRank$
Output: The color and the $neighborRank$ arrays are initialized and the candidate attribute of the Gk is re-assigned

```

1 tid ← get thread identification;
2 if tid < n then
3   source ← v[tid].vcolor; index ← v[source].minIndex;
4   if index ≠ ∅ then
5     if tid = source then
6       target ← v[Gk[index].target].vcolor ;
7       rank ← Gk[index].rank; color[source] ← target;
8       neighborRank[source] ← rank; Gk[index].candidate ← true;

```

The main task in this step is equivalent to the *hooking* step in [19]. First, the vertex color and the index of the minimum outgoing edge from that color is determined by all the threads. Now, for each of these edge indices (if not *null*), only the threads that have the same identification as the source vertex

color initialize the `color` and `neighborRank` arrays and mark the edge as an tree edge.

The `Recolor` kernel presented in Algorithm 4 recolors all the vertices in each iteration. Our vertex recoloring approach is based on the nearest neighbor rank which is different from Harish and Narayanan [15]. First the vertices that created a cycle inside each of the super-vertex are identified. At least one cycle is expected to form in each super-vertex, as only the minimum weighted outgoing edge is chosen from each vertex. At this stage, the recoloring algorithm (namely, *color propagation*) in [15] uses the minimum color (i.e., the smallest vertex id) in the cycle to recolor the super-vertex. On the contrary, we choose the color of the vertex (in a cycle) that has the lowest nearest neighbor rank (Line 7-8). If the ranks on both the edges in a cycle are the same, only then the minimum color is chosen to recolor the super-vertex (Line 9-11). The purpose of doing this is to keep only the minimum ranked edges for each color to facilitate the k NN based partitioning.

Algorithm 4. Recolor Kernel Algorithm

Input : v , `color`, `neighborRank`

Output: The `vcolor` attribute of each vertex v is re-assigned

```

1 tid ← get thread identification;
2 if tid < n then
3   source ← tid;
4   while color [color [source]] ≠ source do
5     | source ← color [source];
6   target ← color[source];
7   if neighborRank [source] < neighborRank [target] then
8     | rootColor ← source;
9   else if neighborRank [source] = neighborRank [target] then
10    | if source < target then rootColor ← source;
11    | else rootColor ← target;
12  else
13    | rootColor ← target;
14  v [tid].vcolor ← rootColor;
```

The `Remove Cycles` kernel presented in Algorithm 5 removes all the cycles that are formed due the *connect step* of the algorithm. The cycles can occur exactly between two vertices that are in different colored super-vertices. As both edges in a cycle have equal weights (i.e, self-loops), only one edge per cycle need to be removed. Our cycle removal process is similar to our recoloring algorithm. Instead of removing an edge (in a cycle) from lower color to higher color (as in [15]), the edge annotated with higher nearest neighbor rank is removed (Line 6-7). The purpose of preserving the lower ranked edge is to facilitate the k NN based partitioning of the MST. When nearest neighbor rank on both the edges in a

Algorithm 5. Remove Cycles Kernel Algorithm

Input : Gk, v, color, neighborRank

Output: The candidate attribute of certain edge in the Gk is re-assigned

```

1 tid ← get thread identification;
2 if tid < n then
3   if tid = [color[color[tid]] then
4     source ← tid;
5     target ← color[tid];
6     if neighborRank[source] < neighborRank[target] then
7       index ← v[target].minIndex; Gk[index].candidate ← false;
8     if neighborRank[source] = neighborRank[target] then
9       if source < target then
10        index ← v[target].minIndex; Gk[index].candidate ← false;

```

cycle are the same then only the edge from lower color to higher color is removed (Line 8-10). An illustration is depicted in Figure 1(c) and (e), respectively.

Finding the minimum outgoing edge from each color is a crucial step in computing the MST using Borůvka’s approach. Harish and Narayanan [15] proposed to use several atomic operations to find the lightest edge from all the outgoing edges of a color. A slightly faster approach is suggested by Vineet et al. [30], as they employed the *segmented scan* primitive to perform this operation and the same approach is adapted by Rostrup et al. [25]. However, built-in primitives are not used in the proposed method to maintain the scalability and portability of the approach. As most of the readily available primitives are built for CUDA [17,27,16], on the other hand, we implemented a generic approach that can be adapted to any other available or upcoming APIs. Additionally, the k NN structure of the input graph makes the task of finding the lightest outgoing edge of each color easier than other approaches (the edges are already ordered by weights). The proposed Find Min method presented in Algorithm 6 first finds all the outgoing edges (`nextIndex`) from each vertex to a different colored vertex (the FindNext kernel) and then, sequentially identifies the index of minimum outgoing edge from each vertex color (the SetMin procedure). However, the Find min step can easily further be optimized in different ways. For instance, Nobari et al. [24] optimized this step by finding the the lightest edges from the previously found lightest edges of the identified colors. To achieve this, each color needs to be stored in an dynamic array (as the number of colors decrease in each iteration) and only the outgoing edges from each color to a different color (instead of from each vertex to a different colored vertex) need to be examined. Additionally, instead of the sequential lightest edge finding procedure a GPU-based sorting can be used to sort all the edges, first by color and then by weights. However, these improvements require CUDA primitives like sort [27] and reduction [16].

Algorithm 6. Find Min Algorithm

Input : $G_{k,v}$, nextIndex **Output**: The minIndex attribute of each vertex v is re-assigned

- 1 Call `FindNext` kernel;
 - 2 **Device** \rightarrow **Host** (v , nextIndex);
 - 3 Call `SetMin` Procedure; // on host
 - 4 **Host** \rightarrow **Device** (v);
-

5 Experimental Results

We implemented the k NN-Borůvka-GPU MST Algorithm using C/C++ and CUDA 4.0. We performed the computational tests on a Xenon Super micro server with $2 \times$ Dual Xeon E5620 2.4GHz processors, 32GB of DDR3 RAM, 800GB of HDD and $4 \times$ NVIDIA Tesla C2050 GPUs. The programs are written in C++ and CUDA Toolkit V4.0 and compiled using the g++ 4.4.4 and nvcc compiler on Linux, kernel 2.6.32. The computation times are obtained using CUDA timer utility.

5.1 Datasets

We applied our algorithm on several data sets ranging from synthetic to real world graphs. A brief description on each of these datasets are given below:

Synthetic Datasets: The synthetic graphs are produced using the Georgia Tech Graph Generator suite (GTGraph) [6]. These graphs are created using three available random distributions available in the suit: the Erdős-Rényi random model (RAND); the power law degree distribution model (R-MAT); and the hierarchical clique model (SSCA2). In each case, the average vertex degree is kept as $\lfloor \ln(n) \rfloor$, where n is the number of vertices.

The USA Road Network Datasets. We used a set of 12 USA road network datasets obtained from the 9th DIMACS challenge [12]. The goal of these datasets were to test the shortest path algorithms (such as, k -shortest paths, point-to-point, single-source, all-pairs etc.), but several other works on MST (such as, [15,30]) used the graphs from these datasets for performance evaluation. Each graph here has two different versions, one with weights as physical distances and the other with transit times. We used the graphs with physical distances as edge weights. However, the graphs are mostly sparse and each graph has only $m \approx 2 \times n$ number of edges. We transformed them on to the k NN graphs (first sorting by vertex id, then by weights and adding pad edges, if necessary), with $k = \lfloor \ln(n) \rfloor$ to make compatible with our proposed algorithm.

Biological Datasets. We used a data set from a renowned breast cancer study by Vijver et al. [29] and created a set of k NN graphs with different number of vertices. Artificial datasets are produced by filtering, refining and expanding them by using the concept of *metafeatures* (see details in Arefin et al. [3]). We employed the FS- k NN algorithm [4] to produce the k NN graphs.

5.2 Comparison Algorithms

We choose three comparison algorithms to compare the performance of our approach. The algorithms are: the sequential implementation of the Borůvka’s algorithm (termed as, **Boruvka-CPU1**) that is implemented using the Boost C++ library [26]. The parallel Borůvka’s algorithm (termed as, **Boruvka-CPU2**) suitable for multi-core processors. The implementation is obtained from the Parallel Boost Graph Library which is based on the *Borůvka_Mixed_Merge* algorithm in [11]. The GPU implementation of Borůvka’s algorithm (termed as, **Boruvka-GPU1**) in [15] which can be downloaded from the following web site of the author, <http://researchweb.iiit.ac.in/~harishpk/Codes/CUDAMST.zip> The GPU implementation of Borůvka’s algorithm (termed as, **Boruvka-GPU2**) by [30] which is obtained from the source code repository of the GPU Computing Gems, <http://www.gpucomputing.net/?q=node/5502>

5.3 Performances

In this section, we briefly discuss the performance of the proposed algorithm compared to the Borůvka’s sequential and other parallel implementations on the above mentioned synthetic and real-world data sets. Performances are demonstrated in Figure 3.

On the Synthetic Datasets. Figure 3(a)-(c) show the performance of the proposed algorithm on three synthetic datasets and Figure 3(d) shows the ratio of CPU and GPU works. For all the cases, both CPU implementations seem to scale with the number of vertices. In each plot, the parallel CPU implementation is faster on the smaller graphs than both the proposed and the Boruvka-GPU1 [15], however with the increase of graph size the performance slowed down dramatically on CPU. The reason for this behavior is the GPU’s memory access pattern (fixed performance penalty for scattered access) which than the CPU (see [25]). The performance on RAND (with many same degree vertices) and SSCA2 (with a number of varying sized cliques) model graphs (Figure 3(a) and (c)) are quite similar. Although the proposed method showed slightly better performance than the Boruvka-GPU1 [15], but both of them showed 3 to 4 times slower performance than the Boruvka-GPU [30]. Specially for R-MAT model graphs, the later seems to be the fastest, but it became infeasible when the graph size grew over six million nodes (details in [30]), thus in terms of scalability, it failed. Figure 3(d) shows the ratio of work for the proposed method on GPUs and CPU for these three graphs, each having one million vertices. Although for the RAND and SSCA2, the work distribution on CPU and GPU seems fair (more work on GPU compared to CPU), but for the R-MAT graph, which causes an uneven load balancing on the GPU, more work is transformed to CPU. This is because the R-MAT model creates graphs with a large number of vertices having smaller degree and a few vertices with larger degree (this behaviour is closer to

Table 1. Runtime of the algorithms on 9th DIMACS challenge graphs. The times are in milliseconds and the number of vertices and edges are in millions.

Datasets	n	m	Bvka CPU1	Bvka CPU2	Bvka GPU1	Bvka GPU2	k NN-Bvka GPU
San Francisco	0.32	0.80	840	68	88	50	85
California	1.89	4.65	9000	7850	450	145	405
Great Lakes	2.75	6.88	14500	720	685	210	620
Eastern USA	3.59	8.77	17255	1450	1280	250	1192
Western USA	6.26	15.24	35780	1800	1350	474	1200
Central USA	14.08	34.29	58605	4500	3890	infeasible	3655
Full USA	23.94	58.33	11560	7508	8945	infeasible	8850

the real world known as *scale-free*) which passes more work to CPU for finding the minimum outgoing edge for some of the components. The result is a slight slowdown in the performance.

On the USA Road Network Data Set. The performance of our approach compared with others on the DIMACS USA road network is given in Table 1. The performance of our approach is similar to Boruvka-GPU1 [15] and for smaller graphs their approach even performed better than ours. But for larger graphs, as we re-organised the structure of graph to our preferred format of k NN, our approach performed slightly better. Although, Boruvka-GPU2 [30] is nearly 2 to 3 times faster than any other approaches, but same as previous experiment, it could not handle all the graphs, specially those which have more than six million vertices. Figure 3(e) shows the performance of our approach in terms of speedups over the sequential implementation. We gained a speedup of around 20 to 30 times for some of the datasets. For smaller datasets, a significant amount of work performed on GPU but for larger ones, more work transformed to CPU that slowed down the performance (see Figure 3(f)). Overall, there is a fair ratio of work distribution ofn CPU and GPU.

On the Biological Datasets. The proposed approach is tested against the parallel Boruvka’s-MST Algorithm, on seven different variants of the breast cancer dataset [29]. Along with the original dataset of 24,158 probe sets, we created six other datasets containing 32,768, 65,536, 131,072, 262,144, 524,288, 1,048,576 metafeatures using the different operators and then, created a set of k NN graphs, for $k = \lfloor \ln(n) \rfloor$ from these data sets. The constructed graphs are not necessarily connected. Thus, we are unable to show the performance of the other GPU-based implementations on these graphs as they require graphs to be connected [15,30]. For smaller datasets, parallel Boruvka’s implementation on CPU (Boruvka-CPU2) showed better performance than ours but as the graph size grew over nearly 200K, our approach started showing better speedups (see Figure 3(g)).

For the k NN graph with 1 million vertices (and 10 million edges), our approach performed approximately 10 times faster than sequential CPU and 3 times faster than the Boruvka-CPU2. Figure 3(h) shows the amount of work performed by different kernels on the same graph.

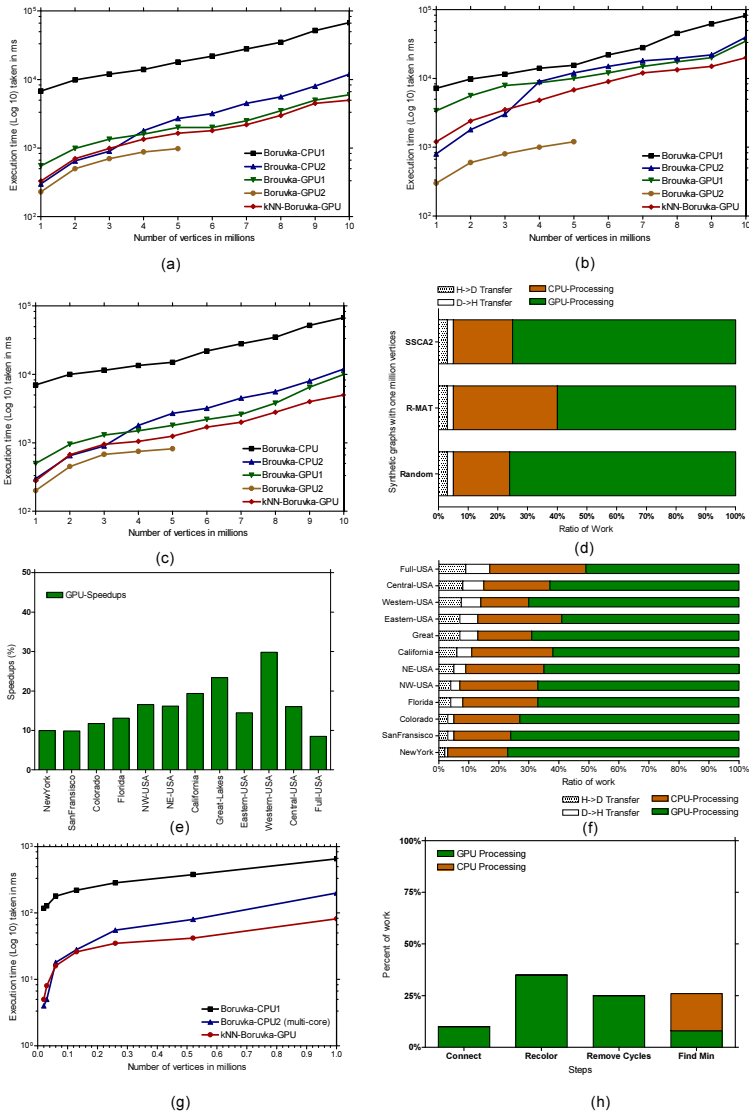


Fig. 3. Performance analysis on different graph models and data sets. Figure (a) to (c) show the running time comparisons on graphs for three different distributions, RAND, R-MAT and SSCA2. Figure (d) shows the ratio of work on the GPU and CPU for these graphs with one million vertices. Figure (e) shows the speedups of our approach USA Road Networks datasets with respect to sequential variant and Figure (f) shows the ratio of work on CPU and GPU for the same. Figure (g) shows the performance of our approach on the breast cancer datasets against sequential and parallel implementations. Figure (h) shows the distribution of works on CPU and GPU in different steps of our approach for a k NN graph of the breast cancer data set with 1 million nodes and 10 million edges.

Scalability and Limitation. The proposed approach is further scalable to larger datasets by dividing and distributing the input k NN graph to the multiple GPUs. Each device then independently constructs a part of the MST or a subset of the MSF and after recoloring and removing the cycles, the `color` and `neighborRank` arrays need to be synchronised on CPU for the next iteration. However, since CUDA supports a limited number of threads (256, 512 or 1024 varying the architecture) in each block, the current 1-D thread implementation can be extended to handle only up to 67 million vertices in the largest connected component.

6 Conclusions

We developed a scalable approach for constructing the MST from the pre-computed k NN graphs. This is a hybrid approach that uses both the CPU and GPU. The host or CPU is responsible for loading and distributing the data and determining the minimum outgoing edge from each component, where the device uses few kernel functions to construct the MST. The basic approach is simple, fast and scalable and easily portable to other parallel frameworks. Outcome of our proposed method can be integrated to other algorithms (such as [3]) and provide compelling benefits to several network analysis approaches such as clustering of gene expression networks, social networks, etc.

References

1. NVIDIA CUDA - Programming Guide (2007), <http://developer.nvidia.com/>
2. Abello, J., Buchsbaum, A.L., Westbrook, J.: A Functional Approach to External Graph Algorithms. In: Bilardi, G., Pietracaprina, A., Italiano, G.F., Pucci, G. (eds.) ESA 1998. LNCS, vol. 1461, pp. 332–343. Springer, Heidelberg (1998)
3. Arefin, A.S., Inostroza-Ponta, M., Mathieson, L., Berretta, R., Moscato, P.: Clustering Nodes in Large-Scale Biological Networks Using External Memory Algorithms. In: Xiang, Y., Cuzzocrea, A., Hobbs, M., Zhou, W. (eds.) ICA3PP 2011, Part II. LNCS, vol. 7017, pp. 375–386. Springer, Heidelberg (2011)
4. Arefin, A.S., Riveros, C., Berretta, R., Moscato, P.: Gpu-fs-knn: A fast and scalable knn computation technique using gpu. Faculty Postgrad Research Poster, The University of Newcastle, Australia (September 2011), <http://www.newcastle.edu.au/Resources/Faculties/Faculty%20of%20Engineering%20and%20Built%20Environment/Research/Arefin.pdf>
5. Bader, D.A., Cong, G.: Fast shared-memory algorithms for computing the minimum spanning forest of sparse graphs. *J. P. Dist. Comp.* 66, 1366–1378 (2006)
6. Bader, D.A., Madduri, K.: GTgraph: A suite of synthetic graph generators (2006)
7. Barr, R.S., Helgaon, R.V., Kennington, J.L.: Minimal spanning trees: an empirical investigation of parallel algorithms. *Parallel Computing* 12(1), 45–52 (1989)
8. Bentley, J.L., Friedman, J.H.: Fast algorithms for constructing minimal spanning trees in coordinate spaces. *IEEE Trans. Comput.* 27, 97–105 (1978)
9. Boruvka, O.: O Jistém Problému Minimálním (About a Certain Minimal Problem) (in Czech, German summary). *Práce Mor. Přírodoved. Spol. v Brne III* 3 (1926)

10. Chung, S., Condon, A.: Parallel implementation of boruvka's minimum spanning tree algorithm. In: Proceedings of the 10th International Parallel Processing Symposium, IPPS 1996, pp. 302–308 (1996)
11. Dehne, F., Götz, S.: Practical parallel algorithms for minimum spanning trees. In: Symposium on Reliable Distributed Systems, pp. 366–371 (1998)
12. Demetrescu, C., Goldberg, A., Johnson, D.: 9th DIMACS implementation challenge - shortest paths (2006), <http://www.dis.uniroma1.it/~challenge9/>
13. Dyen, I., Kruskal, J.B., Black, P.: An indoeuropean classification: A lexicostatistical experiment. *Trans. of the American Phil. Soc.* 82(5), iii–iv, 1–132
14. Graham, R.L., Hell, P.: On the history of the minimum spanning tree problem. *IEEE Ann. Hist. Comput.* 7, 43–57 (1985)
15. Harish, P., Narayanan, P.J.: Accelerating Large Graph Algorithms on the GPU Using CUDA. In: Aluru, S., Parashar, M., Badrinath, R., Prasanna, V.K. (eds.) *HiPC 2007. LNCS*, vol. 4873, pp. 197–208. Springer, Heidelberg (2007)
16. Harris, M.: Optimizing parallel reduction in cuda. *NVIDIA Developer Tech.* (2008)
17. Hoberock, J., Bell, N.: Thrust - a productivity-oriented library for cuda. Template library, Version 1.4 (2010), <http://code.google.com/p/thrust/>
18. Inostroza-Ponta, M.: An Integrated and Scalable Approach Based on Combinatorial Optimization Techniques for the Analysis of Microarray Data. Ph.D. thesis, School of Electrical Engineering and Computer Science, The University of Newcastle, Australia (2008)
19. Johnson, D.B., Metaxas, P.: A parallel algorithm for computing minimum spanning trees. In: Proceedings of the Fourth Annual ACM Symposium on Parallel Algorithms and Architectures, SPAA 1992, pp. 363–372 (1992)
20. Kang, S., Bader, D.A.: An efficient transactional memory algorithm for computing minimum spanning forest of sparse graphs. In: Proc. of the 14th ACM SIGPLAN Symp., Principles and Practice of Parallel Programming, PPOPP, pp. 15–24 (2009)
21. Moret, B.M.E., Shapiro, H.D.: An empirical assessment of algorithms for constructing a minimum spanning tree. *DIMACS Monographs* (1994)
22. Murtagh, F.: A survey of recent advances in hierarchical clustering algorithms. *Comput. J.* 26(4), 354–359 (1983)
23. Nesetril, J., Milkov, E., Nesetrilov, H.: Otakar boruvka on minimum spanning tree problem translation of both the 1926 papers, comments, history. *Discrete Mathematics* 233(1-3), 3–36 (2001)
24. Nobari, S.H., Bressan, S., Rassi, C.: A data parallel minimum spanning tree algorithm for most graphics processing units. In: Proc. of the Int. Con. ADPC (2010)
25. Rostrup, S., Srivastava, S., Singhal, K.: Fast and memory-efficient minimum spanning tree on the gpu (2011)
26. Siek, J., Lee, L.Q., Lumsdaine, A.: Boost random number library (June 2000), <http://www.boost.org/libs/graph/>
27. Sintorn, E., Assarsson, U.: Fast parallel gpu-sorting using a hybrid algorithm. *J. Parallel Distrib. Comput.* 68, 1381–1388 (2008)
28. Tepper, M., Mejail, M., Musé, P., Almansa, A.: Boruvka Meets Nearest Neighbors (2011), <http://hal.archives-ouvertes.fr/docs/00/58/31/20/PDF/preprint.pdf>
29. van de Vijver, M.J., He, Y.D., et al.: A gene-expression signature as a predictor of survival in breast cancer. *The New England JM* 347(25), 1999–2009 (2002)
30. Vineet, V., Harish, P., Patidar, S., Narayanan, P.J.: Fast minimum spanning tree for large graphs on the gpu. In: Proc. of Conf. on HPG, pp. 167–171. ACM (2009)

Global Hybrid Ant Bee Colony Algorithm for Training Artificial Neural Networks

Habib Shah, Rozaida Ghazali, Nazri Mohd Nawi, and Mustafa Mat Deris

Faculty of Computer Science and Information Technology
Universiti Tun Hussein Onn Malaysia (UTHM)
Parit Raja, 86400 Batu Pahat, Johor, Malaysia
Habibshah.uthm@gmail.com,
{rozaida,nazri,mmustafa}@uthm.edu.my

Abstract. Learning problems for Neural Networks (NNs) has widely been explored from last two decades. Population based algorithms become more focus by researchers because of its nature behavior processing with optimal solution. The population-based algorithms are Ant Colony Optimization (ACO), Artificial Bee Colony (ABC), and recently Hybrid Ant Bee Colony (HABC) Algorithms produced easy way for training NNs. These social based techniques mostly used for finding optimal weight values and over trapping local minima in NNs learning. Typically, NNs trained by a traditional and recognized algorithm called Backpropagation (BP) has difficulties such as trapping in local minima, slow convergence or might fail sometimes. In this research, the new method named Global Hybrid Ant Bee Colony (GHABC) algorithm used to train NNs to recover the BP gaps. The simulation result of a hybrid algorithm evaluates with ordinary ABC, Levenberg-Marquardt (LM) training algorithms. From the investigated results, the proposed GHABC algorithm did get better the learning efficiency for NNs using Boolean Function classification task.

Keywords: Swarm Intelligence, Ant Colony Optimization, Artificial Bee Colony, Hybrid Ant Bee Colony Algorithm, Global Hybrid Ant Bee Colony.

1 Introduction

Nowadays, neural networks are widely used in different functions such as linear and nonlinear modeling, prediction, forecasting and classification, mostly due to their property of generality [1-3]. It has powerful and flexible applications that have been successfully used in various applications such as statistical, biological, medical, industrial, mathematical, and software engineering. [4-6]. ANN learned their training techniques by parallel processing. NNs are capable of achieving many scientific research applications by providing best network architecture, activation function, input pre processing and optimal weight values.

NNs tools are the most interested and understandable to mathematical problems, statistical modeling by using different background of various data types. The accuracy makes this particular use of NNs as attractive to scientist analysts in various areas for

different task such as image processing, prediction, classification and other desired combinatorial task.

Many training techniques and NNs architectures for learning parity problem and other difficult boolean function's classification were accessible in [7–10]. These techniques are appropriate only for the parity problem and will not work for other complex problems. Biological NNs are able to solve quite complex learning problems inherent in optimization of intelligent actions. Finding general algorithm capable of solving a larger set of problems of similar complexity such as the XOR, Encoder Decoder and parity problems are still a challenge to the scientific scientists.

Traditionally, NNs models learn by changing the interconnection weights of their associated neurons. It can be trained by different approaches such as: BP, Improved BP algorithm, Evolutionary Algorithms (EA), Swarm Intelligence (SI), Differential Evolution (DE) and Hybrid Bee Ant Colony (HBAC), IABC-MLP and recently HABC Algorithms [11-16]. However, BP algorithm results in long training time and insufficient performance for the binary classification task. However, a BP learning algorithm has some difficulties; especially, it's getting trapped in local minima, where it can affect the NNs performance [17].

In order to overcome the weaknesses of standard BP, many approaches used, which are based on mathematical approach, local and global optimization and population techniques for training the NNs, These are: Particle Swarm Optimization (PSO), ACO, (ABC-LM), ABC-MLP, HABC, HBAC recently population-based and Evolutionary algorithms having reliable performance on training NNs [13-16,18,22,24,26].

In this study, the new hybrid populations based algorithm Global Hybrid Ant Bee Colony (GHABC) is used for training NNs for recovering the BP crack. The experimentation test is done by a Boolean Function while the result compared with different approaches such as ABC and BP (LM) algorithms.

The rest paper is organized as follows: Boolean function classification problems given in Section 2. A brief review on ANN and BP training is given in Section 3. Section 4 contains on swarm intelligence briefing with subsection ABC, ACO and HABC algorithms. The proposed hybrid technique GHABC algorithm is detailed in Section 5. Section 6 contains the simulation result with discussion. Finally, the paper concludes in Section 7.

2 Boolean Function Classification

A Boolean function “ f ” is a map $f: f\{0; 1\}^N \rightarrow f\{0; 1\}$, where N is the number of input bits. The function f is completely defined when the corresponding outputs for each of all the 2^N inputs are determined. Classification of data concern with the use of computers in order to create a structure that learns how automatically chooses to which of a predefined set of classes, a given object belongs. Boolean function classification is the most important issue until today how to decide the 0 and 1 or on or off separate classes by different techniques. These are Boolean functions such as XOR, 3-Bit Parity and Encoder Decoder problems. These are non-linear benchmark classification tasks consisting of 2^N patterns with N inputs and one output. Each input or output is either a 0 or a 1.

Definition (Function) If A and B are sets, a function from A to B is a rule that tells us how to find a unique $b \in B$ for each $a \in A$. We write $f(a) = b$ and say that f maps a to b . We also say the value of f at a is b .

We write $f: A \rightarrow B$ to indicate that f is a function from A to B . We call the set A the domain of f and the set B the range or, equivalently, co domain of f . To specify a function completely you must give its domain, range and rule.

Problem 1: XOR is a difficult classification problem mapping two binary inputs to a single binary output as $(0\ 0; 0\ 1; 1\ 0; 1\ 1) \rightarrow (0; 1; 1; 0)$.

Table 1. XOR classification table

P	q	f
F	F	F
F	T	T
T	F	T
T	T	F

The problem is taking the modulus 2 of summation of three inputs. In other words, if the number of binary inputs is odd, the output is 1, otherwise it is 0.

Table 2. 3-Bit Parity Problem

p	q	r	f
F	F	F	F
F	F	T	T
F	T	F	T
F	T	T	F
T	F	F	T
T	F	T	F
T	T	F	F
T	T	T	T

Table 3. 4-Bit Encoder/Decoder

p	q	r	s	f₁	f₂	f₃	f₄
F	F	F	T	F	F	F	T
F	F	T	F	F	F	T	F
F	T	F	F	F	T	F	F
T	F	F	F	T	F	F	F

4-Bit Encoder/Decoder is quite close to real world pattern classification tasks, where small changes in the input pattern cause small changes in the output pattern [19].

3 Learning Algorithms of Artificial Neural Networks

MLP is a universal approximate and mathematical model that contains a set of processing elements known as artificial neurons [20]. The network which is also known as feed forward neural network was introduced in 1957 to solve a non-linear XOR, and was then successfully applied to different combinatorial problems [20]. The basic building of MLP is constructed by neurons, which have some categories as input, hidden and output layers, as shown in Figure 1. The weight values between input and hidden nodes and between hidden and output, nodes are randomly initialized. The network is highly used and tested on a different job. Figure 1 shows the basic architecture Multilayer Perceptron [21].

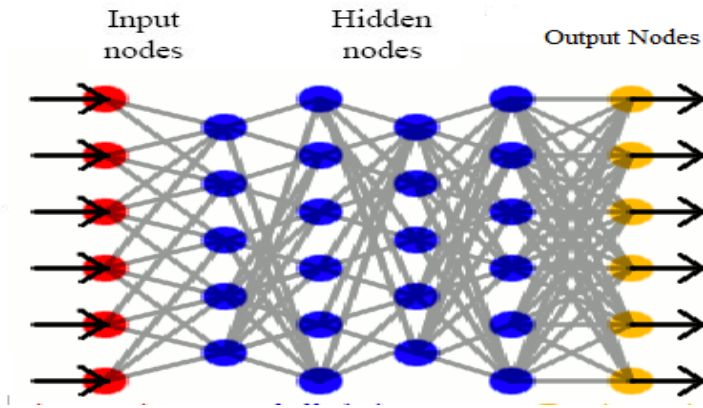


Fig. 1. Multilayer Perceptron Model

The output value of the MLP can be obtained by the following formula:

$$Y = f_i \left(\sum_{j=1}^n w_{ij} x_j + b_i \right) \tag{1}$$

Where Y is the output of the node x is the j_{th} input to the node, w is the connection weight between the input node and output node, b_i is the threshold (or bias) of the node, and f_i is the node transfer function. Usually, the node transfer function is a non-linear function such as: a sigmoid function, a Gaussian functions. Network error function E will be minimized as

$$E(w(t)) = \frac{1}{n} \sum_{j=1}^n \sum_{k=1}^k (d_k - o_t)^2 \tag{2}$$

Where $E(w(t))$ is the error at the t_{th} iteration; $w(t)$ is the weight in the connections at the t_{th} iteration; j shows training set, d_k is the desired output; o_t is the actual value of the k -th output node; K is the number of output nodes; and n is the no of patterns.

NN learning is a process of obtaining new knowledge or adjusting the existing knowledge through the training process. BP is currently the most widely and well known used algorithm for training MLP developed by Rumelhart [3]. The combination of weights which minimizes the error function is considered to be a solution of the learning problem. This step by step mathematical procedure adjusts the weights according to the error function. So, the adjustment of weights which decrease the error function is considered to be the optimal solution of the problem. In the input layer only inputs propagate through weights and passing through hidden layers and get output by some local information. For the BP error, each hidden unit is responsible for some part of the error.

Although the BP algorithm is a powerful technique applied to classification, combinatorial problems and for training, MLP. However, as the problem complexity increases, the performance of BP falls off rapidly because gradient search techniques tend to get trapped at local minima. When the nearly global minima are well hidden among the local minima, BP can end up bouncing between local minima, especially for those non-linearly separable pattern classification problems or complex function approximation problem [17]. A second shortcoming is that the convergence of the algorithm is very sensitive to the initial value. So, it often converges to an inferior solution and gets trapped in a long training time.

4 Swarm Intelligence (SI)

Since the last two decades, SI has been the focus of many researches because of its unique behavior inherent from the swarm insects [12]. Bonabeau has defined the SI as "any attempt to design algorithm or distributed problem-solving devices inspired by the collective behavior of nature insect colonies and other animal societies." He mainly focused on the behavior of social insects alone such as termites, bees, wasps, and different ant species. However, swarms can be considered as any collection of interacting agents or individuals. Ants are individual agents of ACO [22].

4.1 Ant Colony Optimization (ACO)

ACO is a meta-heuristic procedure for the solution of a combinatorial optimization and discrete problems that has been inspired by the social insect's foraging behaviour of real ant decision developed in 1990s [22]. Real ants are capable of finding Food Source (FS) by a short way through exploiting pheromone information, because ants leave pheromone on the ground, and have a probabilistic preference for trajectory with larger quantity of pheromone. Ants appear at a critical point in which they have to choose to get food, whether to turn right or left. Initially, they have no information about which is the best way for getting the FS.

Ants move from the nest to the FS blindly for discovering the shortest path. The above behavior of real ants has inspired ACO, an algorithm in which a set of artificial ants cooperate in the solution of a problem by sharing information. When searching for food, ants initially explore the area surrounding their nest in a random manner. As soon as an ant finds FS, it evaluates the quantity and the quality of the food and carries some of it back to the nest. The following is the ACO pseudo code.


```

Initialize Trail
Do While (Stopping Criteria Not Satisfied) - Cycle Loop
Do Until (Each Ant Completes a Tour) - Tour Loop
Local Trail Update
End Do
Analyze Tours
Global Trail Update
End Do

```

4.2 Artificial Bee Colony (ABC) Algorithm

ABC was proposed for optimization, classification, and NNs problem solution based on the intelligent foraging behavior of honey bee [23-24]. The three bees determine the objects of problems by sharing information to other's bees. The employed bees use multidirectional search space for FS with initialization of the area. They get news and all possibilities to find FS and solution space. Sharing of information with onlooker bees is performed by employed bees. Onlooker bees: Onlooker bees evaluate the nectar quantity obtained by employed bees and choose a FS depending on the probability values calculated using the fitness values. Onlooker bees watch the dance of hive bees and select the best FS according to the probability proportional to the quality of that FS. Scout bees: Scout bees select the FS randomly without experience. If the nectar quantity of a FS is higher than that of the old source in their memory, they memories the new position and forget the previous position. Whenever employed bees get a FS and use the FS very well again, they become scout bees to find a new FS by memorizing the best path.

5 Hybrid Ant Bee Colony Algorithm (HABC)

Hybrid Ant Bee Colony (HABC) technique was proposed for training NNs based on the intelligent foraging behavior of honey bee and ant swarms [14, 16]. The ABC algorithm has a strong ability to find the global optimistic results through most favorable weight's values by bee's representatives [23]. It is successfully trained the NNs for classification and prediction task [24].

HABC algorithm combines the ACO properties in the ABC algorithm which may accelerate the evolving speed of ANN and improve the classification precision of the well-trained networks. The hybrid algorithm is easily understandable, using an ABC algorithm to search the optimal combination of all the network parameters, and ACO used for selection best FS to find the accurate value of each parameter. HABC algorithm provides a solution in an organized form by dividing the agents into different tasks such as, employed bee, onlooker ant and scout bees. The algorithm of HBAC algorithm is shown as follows:

1. Load colony size and food Number

$$FN = \frac{SN}{2} \quad (3)$$

King Bee {

If

$$FN = SN \% 2 = 0 \quad (4)$$

Then

$$FN = \frac{SN + 1}{2} \quad (5)$$

2. Initialize of solutions x_i
3. Evaluate the fitness of the population
4. Cycle =1
5. Repeat
6. Produce a new solution v_i by using equation

$$v_{ij} = x_{ij} + \Phi_{ij}(x_{ij} - x_{kj}) \quad (6)$$

Calculate τ_i

$$\tau_{(i)} = \begin{cases} \tau \geq 0 & \text{for } \frac{Q}{1 + f_i} \\ \tau < 0 & 1 + \text{abs}(f_i) \end{cases} \quad (7)$$

$$Q = \frac{1 + FN}{\sum_{i=1}^{SN} (E + O)} \quad (8)$$

Apply greedy selection process

7. Calculate the probability values $P_{(i)}$ for the solution x_i by

$$P(i) = \frac{(0.09) * \tau(i)}{\sum_{1 \leq j \leq m} \tau(j)} \quad (9)$$

8. FOR each onlooker ant {
 - Select a solution x_i depending on P_i
 - Produce new solution v_i

$$v_{ij} = x_{ij} + \Phi_{ij}(x_{ij} - x_{kj}) \quad (10)$$

9. Calculate the value τ_i by eq (7)
10. Apply greedy selection process}
11. Determine the abandoned solution (source), if exists, replace it with a new randomly produced solution x_i for the scout using the following equation.

$$x_{ij}^{rand} = x_{ij}^{\min} + \text{rand}(0,1)(x_j^{\max} - x_j^{\min}) \quad (11)$$

12. Memories the best FS position (solution) achieved so far.
13. Cycle=cycle+1
14. Until the cycle= Maximum Cycle Number (MCN)

Where Q , E and O shows Numbers of Queen, Employed and Onlookers bees respectively. and x_i represents a solution is the fitness solution o , v_i indicates a neighbour solution of x_i , and p_i value of x_i . Also τ represents the fitness solution of trial, i which is not improved and j represents the improved solution. In the algorithm, first half of the colony consists of employed ant, and the second half constitutes the onlooker ant.

The Scout bee will be deciding the best values between onlookers and employed ant. In HABC algorithm, the position of a FS represents a possible solution to the optimization problem, and the nectar total of a FS corresponds to the fitness solution of the associated solution by King Bee. The King Bee initialized the colony size for employed and onlooker's ant. After initialization, the population of the positions (solutions) is subjected to repeated cycles, $C = 1, 2, \dots$ Maximum Cycle Number (MCN), of the search processes of the employed, onlooker and Scout Bee.

An employed ant produces a modification on the position in her memory depending on the local information (visual information) and tests the nectar total (accurate solution) of the new source. The King Bee will gather employed and onlooker ant for decision of fitness solution. After all employed ants around complete the search process; they combine the nectar information of the FS and their position information with the onlooker ant on the food's area. An onlooker ant evaluates the nectar amount taken from all employed ants and chooses a FS with a probability related to its nectar quantity. The onlooker ant chooses a FS depending on the probability value associated with that FS, and $P(i)$, calculated by the eq (9).

The King Bee initialized the colony size for bee. The FS will be divided into same quantity. King's bee will update the FS for equal division on employed and onlooker's bee. The number of FS equals the half of the colony size and after division on employed and onlooker ant the will start searching for finding optimal FS. The information sharing with onlooker ant is performed by employed. An employed ant produces a modification of the source position in her memory and discovers the unused FS position, which provided that the nectar quantity of the new source is higher than that of the previous source, the employed ant memorizes the new source position and forgets the old one.

The onlooker ants evaluate the nectar quantity obtained by employed ants and choose a FS depending on the probability values. For this purpose, a fitness-based selection technique can be used. Onlooker ants watch the dance of hive ants and select the best FS according to the probability proportional to the quality of that FS. Scout bees: Scout bees select the food source randomly without experience. If the nectar amount of a food source is higher than that of the previous source in their memory, they memorize the new position and forget the previous position. Whenever employed ants get. a food source and use the food source very well again, they become scout bees to find new food source by memorizing the best path.

6 Global Hybrid Ant Bee Colony (GHABC) Algorithm

Global Artificial Bee Colony Search (GABCS) Algorithm used for Numerical Function Optimization outperforms other algorithms in almost all of these experiments, especially multimodal benchmark functions [25]. Hybrid Ant Bee Colony (HABC) Algorithm successfully applied for training NNs using Boolean Function and Time-series data prediction task [14, 16]. HABC has powerful ability for finding best weight for NNs model. Here Global Hybrid Ant Bee Colony (GHABC) will combine the properties of HABC with intelligent behavior of GABCS algorithm [25, 16].

The GABCS will update the solution step and will convert to best solution based on neighborhood values. These modified steps will be in employed, Onlooker and Scout Section. Furthermore, in HABC algorithm, the employed ant and onlookers exploit their solutions based on the neighbor information of each individual with intensity of ant technique.

Usually, in bee swarm, the experienced foragers can use previous knowledge of position and nectar quantity of food source to regulate their group directions in the search space. Furthermore, in social insect's technique, the best foods can be find through experience or neighbor cooperation. So HABC agents employed, scout and onlookers can be improved by their best food source. The GABCS will merge their best finding approaches with HABC by the following steps.

Step 1: Modified the employed section as

$$v_{ij} = x_{ij} + \Phi_{ij}(x_{ij} - x_{kj}) + y \quad (11)$$

$$y = c_1 \text{rand}(0,1)(x_j^{\text{best}} - x_{ij}) + c_2 \text{rand}(0,1)(y_j^{\text{best}} - x_{ij}) \quad (12)$$

Step 2: Repeat the above formula with onlookers section

Where y shows Best_Food_Source, C_1 and C_2 are two constant, x_j^{best} is the j_{th} element of the global best solution found so far, y_j^{best} is the j_{th} element of the best solution in the current iteration, Φ_{ij} is a uniformly distributed real random number in the range $[-1, 1]$. The best values of c_1 and c_2 are 2.5 and -3.5 selected for the best performance for given problems.

Step 3: Modified the scout section as

$$x_{ij}^{\text{rand}} = x_{ij}^{\text{min}} + \text{rand}(0,1)(x_j^{\text{max}} - x_j^{\text{min}}) \quad (13)$$

If $\text{rand}(0, 1) \leq 0.5$,

$$x_{ij}^{\text{mutation}} = x_{ij} + \text{rand}(0,1) * (1 - \frac{\text{iter}}{\text{iter}_{\text{max}}})^b + (x_j^{\text{best}} - x_{ij}) \quad (14)$$

else

$$x_{ij}^{\text{mutation}} = x_{ij} + \text{rand}(0,1) * (1 - \frac{\text{iter}}{\text{iter}_{\text{max}}})^b + (y_j^{\text{best}} - x_{ij}) \quad (15)$$

Then comparing the fitness value of random generated solution x_i^{rand} and mutation solution $x_i^{mutation}$ the better one is chose as a new food source, where b is a scaling parameter which generally is a positive integer within the range of [2,5].

7 Simulation Results and Discussion

In this work, swarms intelligent-based combine technique based on Global Hybrid Ant Bee Colony algorithm is used to train feed-forward artificial neural networks. In order to calculate the performance of the GHABC with ABC and LM algorithms in terms of Mean Square Error (MSE), Standard Deviation (S.D) of Mean Square Error and success rate using boolean function for classification, where simulation experiments performed by Matlab 2010a software.

The Boolean function classifications are categorized in three phases as XOR, 3 bit parity and 4 bit Encoder Decoder problems. The stopping criteria minimum error is set to 0.0001 LM while ABC and GHABC stopped on MCN. During the experimentation, 30 trials were performed for training. The sigmoid function is used as activation function for network output. During the simulation, when the number of inputs, hidden and output nodes of the NNs and running time varies, the performance of training algorithms were stable, which is important for the designation of NNs in the current state. The value of c_1 and c_2 were selected 2.5 and -3.5 respectively. From the simulation experiment, the GHABC performance can be affected by c_1 and c_2 . So the best values selected for these two constant values.

Table 4. Parameters of the problems considered in the experiments. D: a Dimension of the problem, MCN: Maximum Cycle Numbers, NNs structure.

Problem	Colony Range	NN structure	D	MCN	Epoch
XOR6	[100,-100]	2-2-1	6	7500	32000
XOR9	[10,-10]	2-2-1+ Bias(3)	9	100	500
XOR13	[-10,10]	2-3-1+ Bias(4)	13	75	250
3-Bit	[-10,10]	3-3-1+bias(4)	16	1000	1600
Enc/Dec	[10,-10]	4-2-4+Bias(6)	22	1000	2100

From table4 the 2-2-1 NNs structure for XOR6 has six parameters including weights and without bias. The colony range is [100,-100] with 7500 MCN and dimension 6. The XOR9 problem has the same NNs structure included three biases with colony size [10,-10], where MCN and D are 100 and 9 respectively. The NNs 2-3-1+4 (bias) is set with MCN 75 and D 13 for the XOR13 classification task. The NNs 3-3-1+4 (bias) is set with MCN 1000 and D 16 for 3-bit parity problem with parameter [10,-10].

The 4-bit encoder/decoder problem was defined for 4-2-4 NNs shape with dimension 22, where 1000 MCN. The simulation runs thirty times with randomly foods

while the above information from table 4 is used for training NNs. The average of MSE for training NNs by the GHABC, ABC and LM algorithms are shown in table 5. From fig 3, the averages of MSE for XOR6, XOR9, XOR13, 3-bit Parity and 4-bit encoder/decoder are 0.0436906, 0.00122154, 0.00149476, 0.00016009, 0.000285367 respectively using GHABC algorithm.

The LM algorithm has averages of MSE are 0.1107, 0.0491, 0.0078, 0.0209 and 0.0243 for XOR6, XOR9, XOR13, 3-bit Parity and 4-bit encoder/decoder problems. The ABC has an average of MSE 0.007051, 0.006956, 0.006079, 0.006679 and 0.008191 for XOR6, XOR9, XOR13, 3-bit Parity and 4-bit encoder/decoder respectively.

The GHABC has outstanding MSE for XOR9, XOR13, 3-bit Parity and 4-bit encoder/decoder from ABC and LM, where ABC is less than GHABC for XOR6 only in terms of MSE.

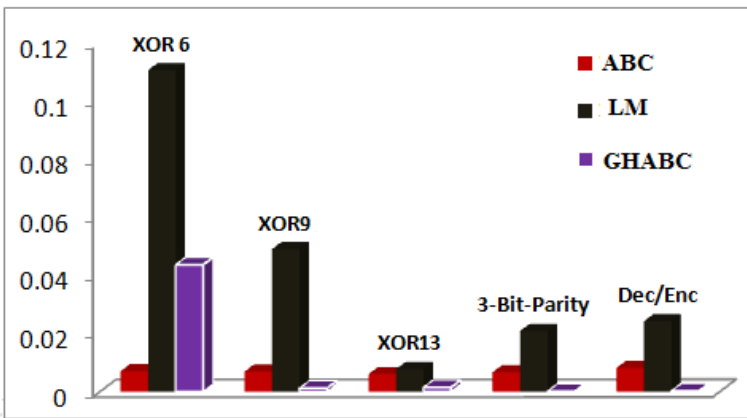


Fig. 2. Average of MSE for Training NNs by ABC, GHABC and LM

The S.D of MSE for GHABC, ABC and LM algorithms are given in fig 4.

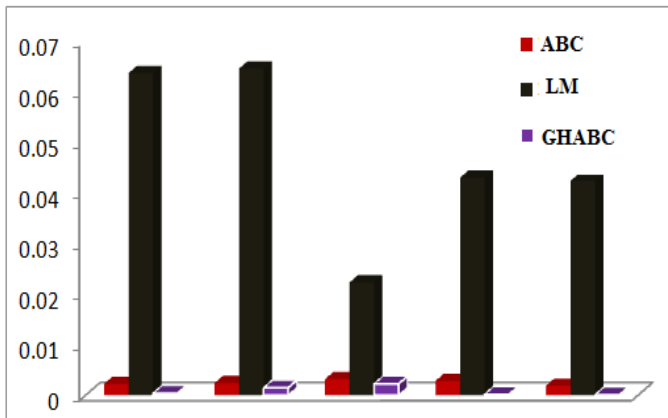


Fig. 3. Average of S.D for Training NNs by ABC, GHABC and LM

From fig 3, the SD of MSE for XOR6, XOR9, XOR13, 3-bit Parity and 4-bit encoder/decoder are 0.000391805, 0.00146855, 0.00223964, 0.00016729 and 9.91015E-05 respectively using GHABC algorithm. T

The LM algorithm has SD of MSE are 0.0637, 0.0646, 0.0223, 0.043 and 0.0424 for XOR6, XOR9, XOR13, 3-bit Parity and 4-bit encoder/decoder problems respectively. The ABC has the average of MSE 0.00223, 0.002402, 0.003182, 0.00282 and 0.001864 for XOR6, XOR9, XOR13, 3-bit Parity and 4-bit encoder/decoder respectively. The GHABC has outstanding S.D MSE for XOR9, XOR13, 3-bit Parity and 4-bit encoder/decoder from ABC and LM.

The success rate of GHABC, ABC and LM algorithms are given in fig 4. The GHABC has 100% success rate for XOR9, XOR13, 3-bit Parity and 4-bit encoder/decoder where LM has maximum 96.66 and minimum 6% only for Boolean function classification task.

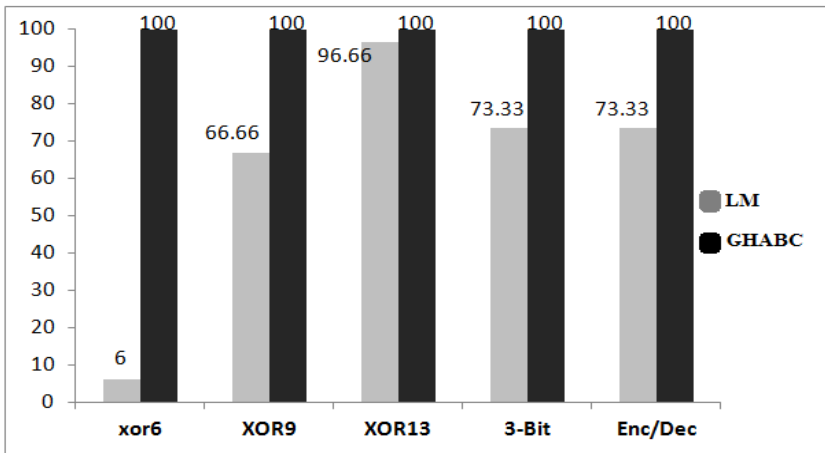


Fig. 4. Success Rates of BP (LM) and GHABC Algorithms

8 Conclusion

The GHABC algorithm combines the goods of three nature swarm’s techniques, are ACO, HABC and GABCS algorithms effectively, which are finding best solution so far so best, exploration and exploitation. The optimum possible weight values prove the high performance of the training MLP for boolean function classification using GHABC algorithm. GHABC has the great ability of searching global optimum solution in solution space. The optimal weights set of the algorithm may speed up the training process and improve the classification accuracy. The success rate of GHABC algorithm shows its high excellent association in training NN. The above simulation results show that the proposed GHABC algorithm can outstandingly learn the Boolean data, which further extends the quality of the given approach with lower prediction error. The GHABC approach will use for prediction and classification time-series data in the next project.

Acknowledgment. The authors would like to thank University Tun Hussein Onn Malaysia (UTHM) and Ministry of High Education (MOHE) for supporting this research under the FRGS.

References

1. Romano, M., et al.: Artificial neural network for tsunami forecasting. *Journal of Asian Earth Sciences* 36, 29–37 (2009)
2. Ghazali, R., Hussain, A.J., Liatsis, P.: Dynamic Ridge Polynomial Neural Network: Forecasting the univariate non-stationary and stationary trading signals. *Expert Systems with Applications* 38(4), 3765–3776 (2011)
3. Rumelhart, D.E., McClelland, J.L., The PDP Research Group: *Parallel Distributed Processing: Explorations in the Microstructure of Cognition*, vol. 1, 2. MIT Press, Cambridge (1986)
4. Osamu, F.: Statistical estimation of the number of hidden units for feedforward neural networks. *Neural Networks* 11(5), 851–859 (1998)
5. Shokri, A., Hatami, T., et al.: Near critical carbon dioxide extraction of Anise (*Pimpinella Anisum* L.) seed: Mathematical and artificial neural network modeling. *The Journal of Supercritical Fluids* 58(1), 49–57 (2011)
6. Thwin, M.M.T., Quah, T.-S.: Application of neural networks for software quality prediction using object-oriented metrics. *Journal of Systems and Software* 76(2), 147–156 (2005)
7. Iyoda, E., Nobuhara, H., Hirota, K.: A solution for the n-bit parity problem using a single translated multiplicative neuron. *Neural Processing Letters* 18, 233–238 (2003)
8. Stork, D., Allen, J.: How to solve the n-bit parity problem with two hidden units. *Neural Networks* 5, 923–926 (1992)
9. Wilamowski, B., Hunter, D.: Solving parity-n problems with feedforward neural network. In: *Proc. of the Int. Joint Conf. on Neural Networks (IJCNN 2003)*, Portland, Oregon, vol. I, pp. 2546–2551. IEEE Computer Society Press, Los Alamitos (2003)
10. Liu, D., Hohil, M., Smith, S.: N-bit parity neural networks: new solutions based on linear programming. *Neurocomputing* 48, 477–488 (2002)
11. Ilonen, J., Kamarainen, J.-K., et al.: Differential Evolution Training Algorithm for Feed-Forward Neural Networks. *Neural Processing Letters* 17(1), 93–105 (2003)
12. Bonabeau, E., Dorigo, M., Theraulaz, G.: *Swarm Intelligence: From Natural to Artificial Systems*. Oxford University Press, NY (1999)
13. Mendes, R., Cortez, P., Rocha, M., Neves, J.: Particle swarm for feedforward neural network training. In: *Proceedings of the International Joint Conference on Neural Networks*, vol. 2, pp. 1895–1899 (2002)
14. Shah, H., Ghazali, R., Nawi, N.M.: Hybrid Bee Ant Colony Algorithm (HBAC) for Classification and Prediction Mission. In: *2nd World IT Conference Turkey (Presented in Turkey, Procedia Computer Science Journal)* (2011)
15. Shah, H., Ghazali, R.: Prediction of Earthquake Magnitude by an Improved ABC-MLP, DESE, UAE (Presented in UAE, DESE 2011, to be published soon in IEEE) (2011)
16. Shah, H., Ghazali, R., Nawi, N.M.: Hybrid Ant Bee Colony Algorithm for Volcano Temperature Prediction. In: Chowdhry, B.S., Shaikh, F.K., Hussain, D.M.A., Uqaili, M.A. (eds.) *IMTIC 2012. CCIS*, vol. 281, pp. 453–465. Springer, Heidelberg (2012)
17. Gori, M., Tesi, A.: On the problem of local minima in back-propagation. *IEEE Trans. Pattern Anal. Mach. Intell.* 14(1), 76–86 (1992)

18. Yao, X.: Evolutionary artificial neural networks. *International Journal of Neural Systems* 4(3), 203–222 (1993)
19. Fahlman, S.: An empirical study of learning speed in back-propagation networks, Technical Report CMU-CS-88-162, Carnegie Mellon University, Pittsburgh, PA 15213 (September 1988)
20. Hornik, K., Stinchcombe, M., White, H.: Multilayer feedforward networks are universal approximators. *Neural Networks* 2(5), 359–366 (1989)
21. Rosenblatt, F.: A Probabilistic Model for Information Storage and Organization in the Brain. *Cornell Aeronautical Laboratory* 65, 386–408 (1958)
22. Dorigo, M., Di Caro, G., Corne, D., Dorigo, M., Glover, F.: The ant colony optimization meta-heuristic. *New Ideas in Optimization*, 11–32 (1999)
23. Karaboga, D., Akay, B., Ozturk, C.: Artificial Bee Colony (ABC) Optimization Algorithm for Training Feed-Forward Neural Networks. In: Torra, V., Narukawa, Y., Yoshida, Y. (eds.) *MDAI 2007. LNCS (LNAI)*, vol. 4617, pp. 318–329. Springer, Heidelberg (2007)
24. Ozturk, C., Karaboga, D.: Hybrid Artificial Bee Colony algorithm for neural network training. In: 2011 IEEE Congress on Evolutionary Computation, CEC (2011)
25. Peng, G., Wenming, C., et al.: Global artificial bee colony search algorithm for numerical function optimization. In: 2011 Seventh International Conference on Natural Computation, ICNC (2011)
26. Shah, H., Ghazali, R., Nawi, N.M.: Using Artificial Bee Colony Algorithm for MLP Training on Earthquake Time Series Data Prediction. *Journal of Computing* 3(6), 135–142 (2011)

The Effect of Intelligent Escape on Distributed SER-Based Search

Daniel S.F. Alves¹, Felipe M.G. França¹, Luiza de Macedo Mourelle²,
Nadia Nedjah³, and Priscila M.V. Lima⁴

¹ COPPE, Universidade Federal do Rio de Janeiro

² DESC, Universidade do Estado do Rio de Janeiro

³ DETEL, Universidade do Estado do Rio de Janeiro

⁴ DEMAT, Universidade Federal Rural do Rio de Janeiro

Abstract. Searching for intelligent escaping agents constitutes an interesting and hard problem. The use of multiple agents in the search involves decentralized coordination. This paper presents a novel solution for the problem of distributed search proposing SER^s, a variant for the mechanism of Scheduling by Edge Reversal. The mechanism was applied to search for agents with four different types of behavior. Experimental results are presented for the evaluation of efficiency and scalability of the mechanism according to the studied types of behavior and sensor range, among other parameters.

Keywords: distributed search, scheduling by edge reversal, intelligent agents.

1 Introduction

Solving the problem of searching an area by means of automated agents can yield beneficial results in many real-world applications. Automated search drones could help rescuing people in a disaster situation or patrolling forests in search for illegal wood extraction or fires, among other objectives. They can be more efficient yet cost-effective than human agents in performing this kind of activities.

Considering problems of scalability, a centralized solution would not be feasible. As the size of the region and amount of search agents increase, the costs associated with a central controller increase even faster. Therefore, an implementation of a distributed system is the most natural approach. Distributed solutions applied to related problems offer a good starting point.

The Scheduling by Edge Reversal (SER) algorithm applied to decontamination can be easily adapted to the search problem at hand [1]. A search process can be modeled as a decontamination process. In this case, the contamination represents the possibility that the searched target occupies an area, which must then be searched, i.e. decontaminated. Searching for static or even random roaming objects is rather trivial, it would be more interesting to concentrate on searching for objects with adversarial intelligence, such as illegal wood extractors in a protected forest. This article reports on an implementation of a SER-based

algorithm for searching purposes, with an analysis of the obtained results by the searching agents of different capabilities against targets of different behaviors.

In the remainder of this text, we first present an explanation of the settings in Section 2. There follows, in Section 3, a brief description of the main concepts behind the used mechanism, along with its application to the problem at hand. Section 4 describes the tests and analyses the obtained results. Finally, Section 5 withdraws some conclusions for the work and suggests further advancement steps.

2 Distributed Search

In the context of an agent-based searching environment, scalability constitutes an issue to be considered. Another important issue is that of agents coordination. The searching agents could have a central controller, but this solution usually does neither scale well nor be robust. Therefore it is better to opt for distributed control. By dividing the search space among agents, not only a wider area can be covered but the coverage can be performed in a more independent way.

As the agents operate autonomously, there must be some means of coordination among them. This coordination is necessary so that the efficiency of the search is preserved. Uncoordinated agents could, for example, investigate the same area, reducing thus their overall productivity.

Nevertheless, the coordination among searchers is not the only element that influences the efficiency of the search, the behavior of the target is also important. In general, a static target may be trivial to search, agents need only to cover exhaustively the entire region. A mobile target, however, may either improve or hinder the search. This work focuses on searching mobile targets that try to avoid search agents, while being limited to a known region.

A connection between search and the graph decontamination problem has been previously shown in [11], leading to the investigation of solutions in this area. Other works of distributed decontamination [6,7,10,11] are usually based on limited graph topologies. This work, instead, proposes a topology-independent approach for decontamination based upon the Scheduling by Edge Reversal mechanism [3,8].

3 SER^S : SER-Based Search and Intelligent Escape

The Scheduling by Edge Reversal (SER) is a distributed algorithm developed for resource sharing and to control concurrency in distributed systems [3], using directed edges, represented by tokens to control access to resources. It operates on graphs that are used as basis for the tokens dynamics. Each token configuration defines a digraph over the underlying graph. For this mechanism, it is considered a mapping of the processes into nodes of a graph, connected by edges representing shared resources. Each edge has a corresponding token, which is always at only one of the linked nodes: this provides the orientation of the edge.

In order to allow for operation, an acyclic orientation for the graph is generated, so that the orientation of directed edges dictates the priority to access the resources. The processes corresponding to the sink nodes¹ of the resulting digraph are able to operate for some time. After operation, all edges of a sink node are reverted, generating new sinks and thus, allowing new processes to run. This dynamic is illustrated by Fig. 1.

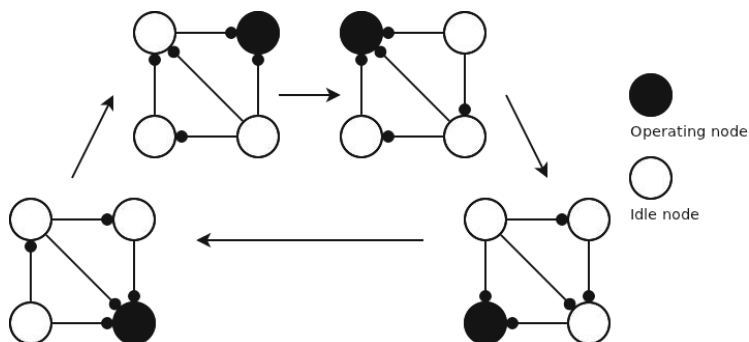


Fig. 1. Sample of SER execution

In order to have the structure of sinks working properly according to the SER mechanism it is necessary to have an initial acyclic digraph. Such initial orientation of the edges is of high importance to the algorithm, as it influences the amount of concurrency of the resulting SER dynamics [2]. Since finding the ideal orientation for this purpose is an expensive job, heuristics usually are adopted. Different heuristics serve different purposes while some attempt to maximize concurrency [2], others do the opposite [5][8]. Some heuristics can allow to reach a middle term [2], so that an heuristic should be chosen according to the application of SER [2].

The SER algorithm has been proven to run without deadlocks and starvation [3] and has been applied to the modeling of traffic intersections [4] and flexible manufacturing systems [9] and to the synchronous-to-asynchronous conversion of cryptographic circuits [5]. It has also been used as a graph decontamination algorithm [8]. This application can be adapted to be used with any number of decontamination agents, which can generate copies on demand [8], or to get them from a limited pool [1]. The principles of SER-based search are built on the idea of decontamination.

3.1 SER^D : SER-Based Decontamination

First, it is important to understand the concepts of contamination and decontamination applied to graphs. A node can be contaminated or not. When non-contaminated (or decontaminated) node has enough (pre-determined number of)

¹ Nodes of a digraph without diverging edges.

contaminated neighbors, according to some defined function of the graph and current node, it becomes contaminated too. A contaminated node stays so until an external agent renders it back into a decontaminated state. The processes of changing the nodes to the contaminated state and back to a decontaminated state are called *contamination* and *decontamination*, respectively.

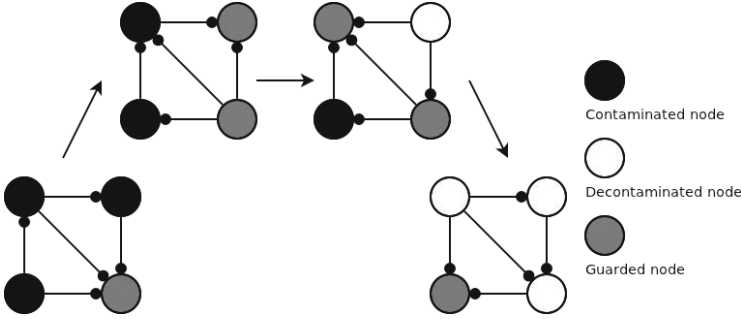


Fig. 2. Sample of SER-based decontamination

The SER^D algorithm needs only small modifications to the original SER formulation in order to model graph decontamination. At the start of operation the agents are sent to the sinks of the oriented graph. The agents operate, removing the contamination of sinks of their occupied nodes, then the edges of the sink nodes are reverted. Then they move themselves to new sinks, keeping copies in the previous nodes to avoid contamination. Of course, this is done with respect to availability of agents. The new nodes are decontaminated, repeating the same process until no more contaminated nodes can be found or in an endless process, in vigilance against resurgence of contamination.

3.2 SER Application to Search

A search can be modeled as a decontamination process with some relaxed conditions. In this situation, the nodes correspond to sub-areas of the limited region where the search happens. If the sub-areas of two nodes are adjacent, then there is an edge between them. A node is contaminated if it is possible that the target is located at the region covered by it. As the search agents investigate a node, verifying that it does not contain the target, they “clean” the node. In this manner it is possible to treat a search as a decontamination process.

Given the similarities between a SER-based decontamination and search processes, it is relatively simple to modify its operation to perform a search. Considering that it will take some time for the target to approach, as it can’t move instantly and an agent has already verified that the target is not present, the agents can leave a recently decontaminated node before another agent arrives to keep so. This allows for the agents to search the region faster and cover more ground. This mechanism is herein called SER^S .

Suppose that agents have sensors capable of covering a given region. The search area must be divided in sub-areas, each represented by a node, in such a way that an agent visiting all the nodes would be able to inspect the whole area. Such nodes will be called from now on, *nodes of coverage*. The optimal placement of nodes of coverage is a complex problem and will not be developed in this article. Fig. 3 presents an example of the resulting graph, for a region of width 32 and agents' sensor range 4. Dividing an area according to the sub-areas represented by the nodes of coverage, the search agents can be guided to the sinks. After verifying their surroundings, they can revert the edges and proceed to new sinks, as in a normal SER^D operation. Algorithm 1 presents an explanation of the mechanism operation in pseudo-code, for a situation of perpetual vigilance.

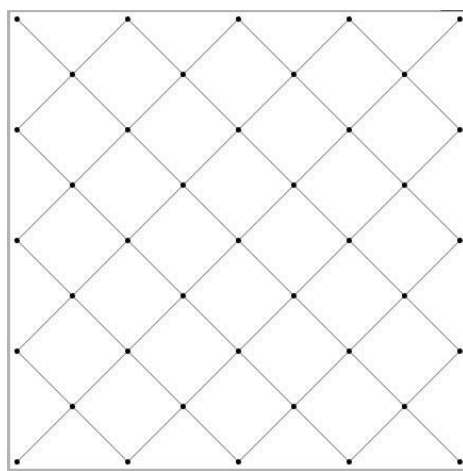


Fig. 3. Resulting graph after division of region in sub-areas

This algorithm, however, does not consider the behavior of the target. For the SER^S , the actions of the targeted agent are not even considered. The placing of the nodes and the initial orientation are important to ensure the detection. This work considers four kinds of behavior for a set of targets:

- stay in one location;
- wander randomly within the allowed area;
- actively avoid the agents;
- try to find the agents.

In order to simplify the model, the targets always know where all the searchers are, and also have knowledge of the nodes, including their states as contaminated or not.

Algorithm 1. SER-search algorithm

Variables:

target_node := null
digraph := initial orientation

▷ **Input:**

% Inner processing
msg = null

▷ **Action:**

```

if target_node = null then
  if there are available sinks then
    target_node := one of available sinks
  else
    target_node := one of previously inspected nodes
  end if
  if near target_node then
    inspects sub-area
    target_node := null
    if node is sink then
      % All edges from neighbors point to the node
      updates digraph reversing target_node
      sends(reversion_notice(target_node))
    end if
  else
    moves to selected target node
  end if
end if

```

▷ **Input:**

% Treats communication, by a fellow agent, of an edge reversal
msg = *reversion_notice*(*node*)

▷ **Action:**

updates *digraph* reversing *node*

The approaching behavior simply makes the target move in the direction of the closest agent. It was created to model the opposite of the avoidance intelligence, which is more interesting to study. The avoidance intelligence makes a target try to approach nodes already visited by agents, while keeping distance from the agents. This is achieved through a model that considers the agents as *repellers* and the decontaminated nodes as *attractors*, associating repeller with higher weights, in order to keep the targets moving through the region to sub-areas that have already been visited, i.e. probably will not be visited soon, but without approaching agents for that purpose. The linear combination of the normalized vectors from the repeller to the target and to the attractors from the target,

multiplied by their weights, results in a vector with the orientation of the target. The other two types of behavior, static and random, are trivial with the targets either not moving, or moving in random directions at a fixed speed.

4 Quantitative Results

4.1 Setup

The search algorithm was implemented in the NetLogo platform [12], which is a Logo-based system supporting parallel agents. Figure 4 shows the interface of the simulator. The nodes are in red, the search agents in green and the targets, yellow. All setups considered only a limited region, within which the targets are bound to stay. Nodes were placed in a simple two-dimensional grid pattern, towards covering the search region, i.e., if all nodes are occupied by agents, the targets cannot hide.

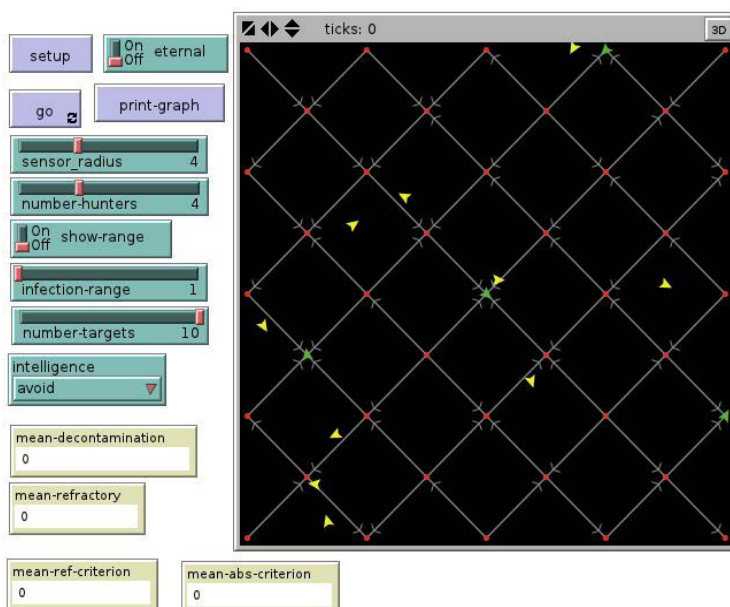


Fig. 4. Screenshot of the simulator

Tests were carried out varying the amount of searchers, targets, sensor range of the searchers and the behavior of the targets. All tests ran in a 32×32 region. The time step used to measure results in the tests was the time necessary for an agent or target to move by one unit, or $1/32$ of the side of the region. Nodes are created based on the sensor range. The initial orientation for the resulting graph

is randomly achieved with the help of the Alg-Edges heuristic [2], which offer a mid term between maximum and minimum concurrency. Search agents are then distributed in the sink nodes and targets are scattered through the region.

The search is then started; agents revert the sinks they occupy (becoming source nodes), then proceed to a new sink. To avoid underutilization of the agents, each one tries to find a sink that is not pursued by another agent. If no such sinks can be found, the agent will wander through recently decontaminated nodes. This process continues until all targets are found or a time limit is reached. The tests are repeated in total a hundred times.

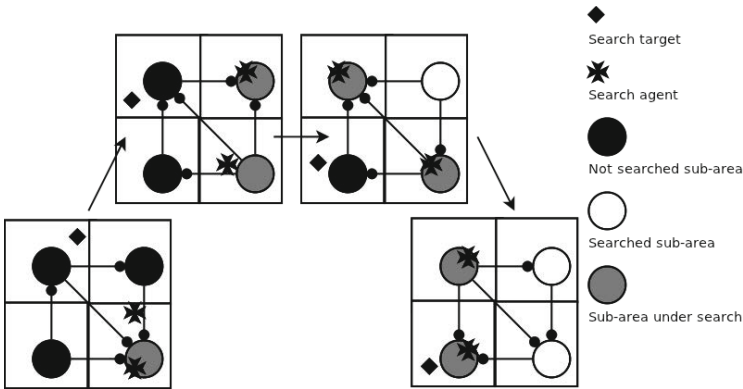


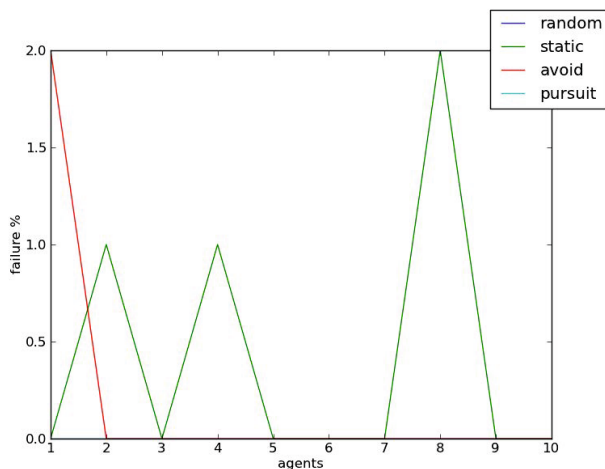
Fig. 5. Sample of SER^S

4.2 Results

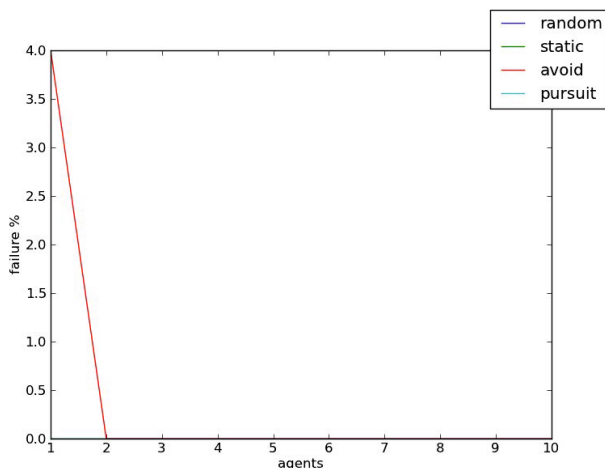
The results were grouped in order to obtain an average of the total time taken until all targets are found, as well as the failure rate. Some observations can be drawn from those results regarding impact of behavior, number of targets and searchers and overall efficiency of this approach.

Fig. 6 depicts failure rates of a setup with ten targets. The results were successful, with less than fifteen percent failure, considering any combination of parameters. Ignoring results for only one search agent, then the failure is less than five percent, often nonexistent.

Failures have two principal causes. Fig. 6a shows both kinds, while Fig. 6b shows only one. The most common one is caused by the avoidance of the target. It was only observed when there was only one search agent, and results of the incapacity of that agent to find the target in that situation. As the failure type is not constant, initial positions for agent and targets as well as digraph orientation are important. However, this is an extreme case and is not relevant for a distributed mechanism. It shows, though, that similarly extreme situations should be avoided in the application of this search mechanism.



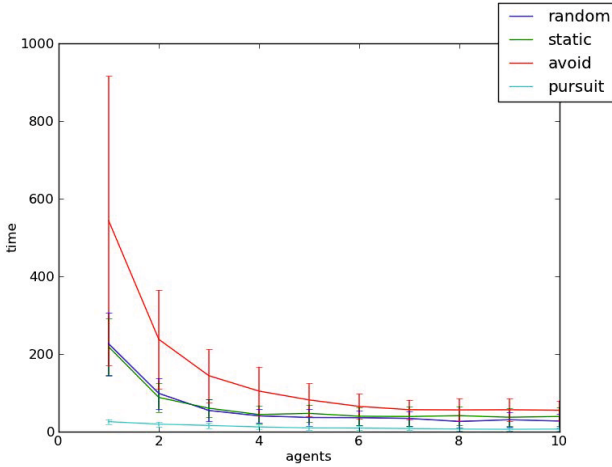
(a) sensor range 6



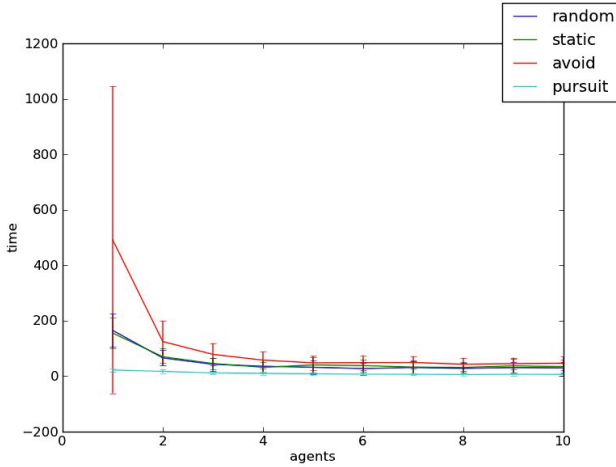
(b) sensor range 9

Fig. 6. Failure rates of a setup with ten targets

The other kind of failure results from imperfection due to the discretization carried out by the graph creation algorithm. Some values for the sensor range would result in a graph with blind spots at the corners of the region. Those zones without surveillance are minimal, relative to the total area, but as they are never seen a target that stops there will never be found. In the tests performed, only static targets that started in those corners escaped, targets that wandered the region were eventually caught. A better adjusted graph creation algorithm would remove this problem.



(a) sensor range 6



(b) sensor range 9

Fig. 7. Time averages to find all ten targets in the same scenarios as Fig. 6

The time averages, as exemplified in Fig. 7, show that higher sensor ranges as well as a larger number of agents tend to decrease the time needed to find all targets. With respect to both parameters, the improvement is sharper while the amount is relatively small. Further analysis of this improvement might lead to more tuned solutions.

The analysis of the behaviors conform to expectations. The pursuit behavior consistently presents the lowest time averages, while the avoidance usually

presented the highest. Static and random behaviors usually had very similar time averages, which is also expected. The graphics also show that, as the number of search agents increases, the average time for the avoidance behavior approaches the one needed for random and static targets.

Some tests also presented average times lower for the avoidance behavior than either random or static targets, for a small number of searchers. This happens with very short sensor range, relatively to the speed of the agents and targets. An explanation is that the weights for the avoidance behavior are based on the range of sensors and such a small range value might have minimized its effectiveness. As the avoidance intelligence guides the targets to decontaminated nodes, the targeted agents tend to get closer the search agents and might be cornered, while the others behaviors leave the targets scattered. This has a greater impact on the setup with minimal sensor range due to the high node density present in this configuration.

5 Conclusion

The performed tests confirm the possible application of the SER^S mechanism to search for targets in a limited area. With a good node planning, i.e. a combination of node placement and node coverage that leaves no regions out of the reach of the search agents, the targets can be found in a reasonable time interval with low failure rate. Some caution must be exercised with the amount of searchers and the placement of the nodes. If there are few searchers it is possible that some targets could avoid the agents indefinitely. Also, if portions of the search area are left uncovered, they may serve as sanctuary for the targets.

Future works could attempt to find solutions for the presented problems, such as a further analysis of the impact of the variations to the speeds of agents and targets or a deeper analysis of search in limitless regions. The solutions would probably involve better node placement. The impact of different speed between the agents and targets was not considered in this work and could present an interesting insight. Studies of a scenario wherein the targets could escape the searched region would also be a natural extension of the presented work and would involve enabling the search agents to pursue targets. When the movements of the target aren't limited by a region, its behavior plays a great role in detection. If it tries to avoid the searchers, it is often easy to leave the region, unless the initial placement of the search agents surrounds the target. In this case, it seems better to avoid the possibility that the target can leave the region or give the agents the capability to pursue targets.

The development of this work also offers some hints on the applicability of the middle term heuristics, i.e. heuristics that neither try to maximize nor minimize concurrency, in the distributed search. This topic and an adaptive mechanism to control against dispersion is subject of ongoing research.

References

1. Alves, D.S.F., Soares, E.E., de, M., Strachan, G.C., Carvalho, G.P.S., Xaud, M.F.S., Couto, M.V.B., Mendona, R.M., Freitas, R.S., Santos, T.M., Gonçalves, V.C.F., Mourelle, L.M., Nedjah, N., Maculan, N., Lima, P.M.V., França, F.M.G.: *Mobile Ad Hoc Robots and Wireless Robotic Systems: Design and Implementation*. IGI Global, Pennsylvania (to appear, 2012)
2. Arantes Jr., G.M., França, F.M.G., Martinhon, C.A.: Randomized generation of acyclic orientations upon anonymous distributed systems. *J. of Par. and Dist. Comp.* 69(3), 239–246 (2009)
3. Barbosa, V.C., Gafni, E.: Concurrency in heavily loaded neighborhood-constrained systems. *ACM Trans. Prog. Lang. Syst.* 11, 562–584 (1989)
4. Carvalho, D., Protti, F., De Gregorio, M., França, F.M.G.: A Novel Distributed Scheduling Algorithm for Resource Sharing Under Near-Heavy Load. In: Higashino, T. (ed.) *OPODIS 2004*. LNCS, vol. 3544, pp. 431–442. Springer, Heidelberg (2005)
5. Cassia, R.F., Alves, V.C., Besnard, F.G.-D., França, F.M.G.: Synchronous-to-asynchronous conversion of cryptographic circuits. *J. of Cir., Sys., and Comp.* 18(2), 271–282 (2009)
6. Flocchini, P.: Contamination and decontamination in majority-based systems. *J. Cell. Auto.* 4(3), 183–200 (2009)
7. Flocchini, P., Nayak, A., Schulz, A.: Cleaning an Arbitrary Regular Network with Mobile Agents. In: Chakraborty, G. (ed.) *ICDCIT 2005*. LNCS, vol. 3816, pp. 132–142. Springer, Heidelberg (2005)
8. Gonçalves, V.C.F., Lima, P.M.V., Maculan, N., França, F.M.G.: A Distributed Dynamics for WebGraph Decontamination. In: Margaria, T., Steffen, B. (eds.) *ISoLA 2010*. LNCS, vol. 6415, pp. 462–472. Springer, Heidelberg (2010)
9. Lengerke, O., Carvalho, D., Lima, P.M.V., Dutra, M.S., Mora-Camino, F., França, F.M.G.: Controle distribuído de sistemas job shop usando escalonamento por reversão de arestas. In: *Procs. of The XIV Latin Ibero-American Congress on Operations Research*, pp. 1–3. CLAIO (2008)
10. Luccio, F., Pagli, L.: Web Marshals Fighting Curly Link Farms. In: Crescenzi, P., Prencipe, G., Pucci, G. (eds.) *FUN 2007*. LNCS, vol. 4475, pp. 240–248. Springer, Heidelberg (2007)
11. Moscarini, M., Petreschi, R., Szwarcfiter, J.L.: On node searching and starlike graphs. *Congressus Numerantium* 131, 5–84 (1998)
12. Wilensky. U.: *Netlogo*. Netlogo. Center for Connected Learning and Computer-Based Modeling. Northwestern University, Illinois (1999), <http://ccl.northwestern.edu/netlogo/>

ACO-Based Static Routing for Network-on-Chips

Luneque Silva Jr.^{1,*}, Nadia Nedjah¹,
Luiza de Macedo Mourelle², and Fábio Gonçalves Pessanha¹

¹ Department of Electronics Engineering and Telecommunications
Faculty of Engineering
State University of Rio de Janeiro
luneque@hotmail.com, nadia@eng.uerj.br, pessanha1078@gmail.com

² Department of Systems Engineering and Computation
Faculty of Engineering
State University of Rio de Janeiro
ldmm@eng.uerj.br

Abstract. Network-on-Chip (NoC) have been used as an interesting option in design of communication infrastructures for embedded systems, providing a scalable structure and balancing the communication between cores. Because several data packets can be transmitted simultaneously through the network, an efficient routing strategy must be used in order to avoid congestion delays. In this paper, ant colony algorithms were used to find and optimize routes in a mesh-based NoC. The routing optimization is driven by the minimization of total latency in packets transmission. The simulation results show the effectiveness of the ant colony inspired routing by comparing it with general purpose algorithms for deadlock free routing under different traffic patterns.

Keywords: network-on-chip, packet routing, ant colony optimization.

1 Introduction

A System-on-Chip (SoC) is an integrated circuit composed by a full computer system. SoCs contains, within the same package, processors, memory, input-output controllers and specific application devices. This block structure follows a design methodology based on intellectual property (IP) cores. Components designed for a specific project can be reused in other SoCs, reducing design time. Thus, under an extremely simplified view, to increase the number of tasks performed by the SoC, just add more IP cores with different features.

The increase of SoC's scale raises new design challenges. Among them is communication between IP cores. The blocks of a SoC are interconnected by a communication infrastructure, such as buses or point-to-point links. However, each of these models have their limitations. Shared buses can cause high delays if

* The work of this author is supported by CAPES, the Coordination of Improvement of Higher Education Personnel of the Brazilian Federal Government.

multiple blocks need to transmit data simultaneously. This does not happen in point-to-point architectures. In turn, the communication structure need to be redesigned for each new system. For many SoC designs, it is desirable to use a framework scalable as buses and fast as point-to-point links. An architecture that includes these two features are the NoCs, *Networks-on-Chip* [1].

In a NoC architecture, *switches* are interconnected by point-to-point links, thus describing a network topology. An example of network topology is the mesh shown in Fig. 1. The switches are also connected to the IP cores that constitute the system, also called *resources*. Switches exchange information in the form of messages and packages. The information generated by a resource is divided into smaller parts and sent over the network. These packages are organized in the destination switch and then delivered to resource. This operation is similar to that performed by computer networks. The structure formed by a switch and a resource is called a *network node*.

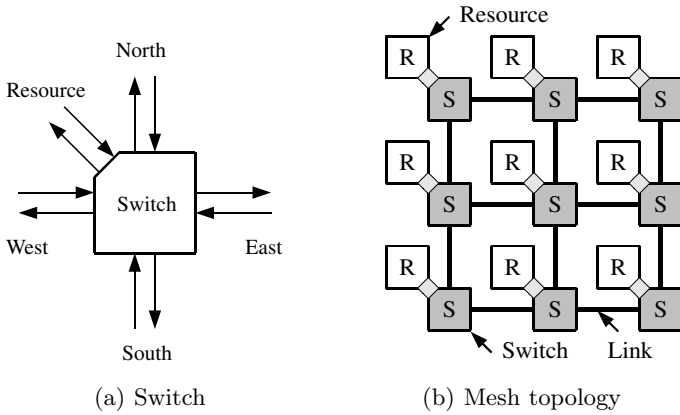


Fig. 1. Network-on-chip architecture

In the design of NoC-based systems, the communication infrastructure can be imported as a single configurable IP block. However, many are the ways to connect network and resources, in order to achieve the desired application. To assist the designer, computational tools for project assistance, or EDAs (Electronic Design Automation), are used. The purpose of EDAs is to optimize intermediate stages of SoC and NoCs project, in order to obtain a more efficient design implementation [2].

The EDA tool must be able to use information about the desired application (at a high level of abstraction) and, through successive stages of optimization, implement a solution that meets the design specifications. This optimization may include several steps, such as *task allocation*, *IP mapping* and *static routing*.

Delays in communication may occur in congestion situations, when multiple packets could be transmitted using the same switch at the same time. If the

routing algorithm adopted in the NoC's design is deterministic, the selection of the packet path from the source to the destination switch will not consider the load of intermediate switches - those between the source and destination switch. If these switches are under a heavy traffic, a given packet can only be transmitted after the end of congestion. This occurs even if other switches, not selected for routing, are free for transmission. On the other hand, adaptive routing algorithms can be used in order to avoid network congestion. These algorithms use not only the position of origin and destination nodes, but also the actual load condition of the network to calculate the route. When you find a region of network in use, the routing can set the package to follow another path. This congestion-free path may, however, be not minimal. These two situations are shown in Fig. 2.

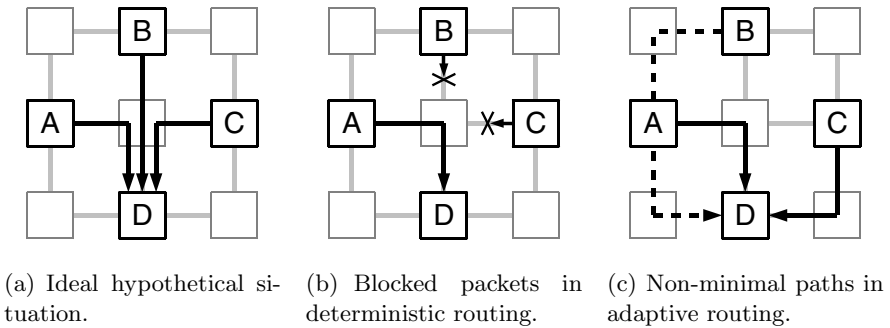


Fig. 2. Routing in a 3×3 mesh

In order to overcome the congestion problem, this paper proposes a route optimization step in the design of NoCs, or more precisely, an adaptive and static routing. In this routing, a network model provides the communication patterns required for application execution. The calculation of routes is accomplished by an optimization algorithm to minimize the communication time. The search is always for a shortest path between origin and destination. If the intermediate switches of this path are in use, the algorithm should be able to find another route, so that the contention effects does not affect the transmission.

In this paper, the algorithm used in the search for routes is the ant colony optimization (ACO) [3]. This is an example of swarm intelligence, where a group of individuals work together to find a solution to a given problem. We compared the results of the network using the proposed routing algorithms and literature widely adopted routing algorithms. As expected, the adaptive routing based on the ACO meta-heuristic obtained superior performance to others.

The reminder of this paper is organized as follows. In Section 2 we review the related work in routing algorithms. In Section 3, we do an overview on ACO meta-heuristic. The proposed routing is presented in Section 4. Simulation results are presented in Section 5. The paper closes with a conclusion and the description of future work in Section 6.

2 Related Work

There are several papers that study the efficient routing in parallel and distributed computing. For a broader reference, [4] presents a survey of routing techniques for direct networks.

Many of the techniques used for routing in NoCs, such as the XY algorithm, were originally developed for computer networks and multiprocessor systems. The XY algorithm is a routing technique widely used in 2D mesh networks with wormhole switching. It works by sending packets over the network first horizontally (X dimension), then vertically (Y dimension). In the context of NoCs, XY routing proves efficient due to its simplicity of implementation and because it is deadlock-free. Works that made use of this algorithm include the HERMES network [5] and the SoCIN network [6].

Glass and Ni have proposed the so-called Turn Model for adaptive, livelock and deadlock free algorithms [7]. A turn is a change of 90° in the direction of packet transmission. The main idea of this model is to restrict the amount of turns that a package can perform in order to avoid the formation of cycles that cause deadlocks. Following this concept, three routing algorithms were proposed by Glass and Ni: the West-First, the North-last and Negative-First. A related approach is the Odd-Even turn model [8] for designing partially adaptive deadlock-free routing algorithms. Unlike the turn model, which relies on prohibiting certain turns in order to achieve freedom from deadlock, this model restricts the locations where some types of turns can be taken. As a result, the degree of routing adaptiveness provided is more even for different source-destination pairs.

The work of Jose Duato has addressed the mathematical foundations of routing algorithms. His main interests have been in the area of adaptive routing algorithms for multicomputer networks. Most of the concepts are directly applicable to NoC. In [9], the theoretical foundation for deadlock-free adaptive routing in wormhole networks is given.

3 Ant Colony Optimization

Ant algorithms, also known as Ant Colony Optimization (ACO), are a class of heuristic search algorithms that have been successfully applied to solving NP hard problems [10]. Ant algorithms are biologically inspired in the behavior of colonies of ants, and in particular how they forage for food. One of the main ideas behind this approach is that the ants can communicate with one another through indirect means by making modifications to the concentration of highly volatile chemicals called pheromones in their immediate environment. The core ideas of ACO are (i) the use of repeated and concurrent simulations carried out by a population of artificial agents called “ants” to generate new solutions to the problem, (ii) the use by the agents of stochastic local search to build the solutions in an incremental way, and (iii) the use of information collected during past simulations (artificial pheromones) to direct future search for better solutions.

In the artificial ant colony approach, following an iterative process, each ant builds a solution by using two types of information locally accessible: problem-specific information, and information added by ants during previous iterations of the algorithm. In fact, while building a solution, each ant collects information on the problem characteristics and on its own performance, and uses this information to modify the representation of the problem, as seen locally by the other ants. The representation of the problem is modified in such a way that information contained in past good solutions can be exploited to build new better solutions. This form of indirect communication mediated by the environment is called stigmergy, and is typical of social insects. Several ant algorithms make use of the structure shown in the Algorithm [1](#) [\[11\]](#).

Algorithm 1. ACO meta-heuristic

```

1: initialize parameters and pheromone trails;
2: while termination condition not met do
3:   construct ant solutions;
4:   local search (optional);
5:   update pheromone trails;
6: end while;
```

4 ACO Based Routing

The Ant Colony Optimization, with the ability to search for paths, emerging as a powerful solution for routing problems. Thus, this paper presents the use of the ACO meta-heuristic in the construction of routing algorithms. Two models of static routing for NoCs are proposed.

4.1 Network Specification

The network model in this work uses switches with five communication ports. Four ports are responsible for communication with neighboring switches and one is for local communication with the resource. The switches are considered bufferless using no virtual channels. The network topology is a two dimension mesh, as shown in Fig [1](#). The switching technique adopted was the wormhole. In this method, packets are divided into smaller units called *flits* (flow-units). It is assumed that each communication channel has a width of a flit.

4.2 Proposed Routing Algorithms

In this paper, two algorithms perform routing using the ACO meta-heuristic. These algorithms were called REAS (routing based on Elitist Ant System [\[3\]](#)) and RACS (routing based on Ant Colony System [\[12\]](#)). Both algorithms search paths in an *architecture characterization graph* that represents the network 2D mesh topology. These algorithms make use of *multiple ant colonies*, where each

colony is responsible for searching the route of a package. In this approach, each colony has its own pheromone and ants. However, the colonies must exchange information in order to minimize the latency of their respective packages. Thus, the route found by an ant from a given colony is visible to the ants from other colonies, because these packets are being transmitted simultaneously and in the same network. A simplified pseudo-code of REAS is shown in Algorithm 2.

Algorithm 2. REAS algorithm

Require: network and ACO parameters;

- 1: **while** total of cycles **do**
- 2: **for** $k = 1 \rightarrow$ number of ants **do**
- 3: **for** $g = 1 \rightarrow$ number of packets **do**
- 4: $Ant_{k,g}$ constructs a solution
- 5: calculates $Ant_{k,g}$ pheromone;
- 6: **end for**
- 7: calculates the elitist pheromone;
- 8: accumulate the pheromone of actual ants;
- 9: **end for**
- 10: update the global pheromone;
- 11: **end while**
- 12: **return** best solution;

In the proposed algorithms, ants in a network node knows only two things. The first is the pheromone concentration in the surrounding nodes. The second is the load on a node, the waiting time in each of the four possible transmission directions.

The *Elitist Ant System* is directly inspired by the *Ant System* (AS), the first or ant algorithms [3]. The EAS is characterized mainly by the use of *elitism*, in order to differentiate the best ants. In the REAS algorithm, ants build paths through the network selecting the next node with base in Equation 1, where p_{ij}^k is the probability of the ant k go from the node i to the node j .

$$p_{ij}^k(t) = \begin{cases} \frac{\tau_j(t)^\alpha \cdot \eta_{ij}^\beta}{\sum_{k \in allowed_k} \tau_k(t)^\alpha \cdot \eta_{ik}^\beta} & \text{if } j \in allowed_k \\ 0 & \text{otherwise} \end{cases} \quad (1)$$

The probability of selecting a particular direction is function of pheromone concentration and network load in this direction. These two parameters are weighted by their importance constant α and β . The network load is used indirectly by η_{ij} , defined by:

$$\eta_{ij} = 1/C_{ij} \quad (2)$$

where C_{ij} is the load in transmission from i to j .

At the end of each iterative cycle, the pheromone of all colonies is updated according to Equation 3. Part of the pheromone of the previous iteration is reduced by evaporation rate ρ , and then reinforced by the contribution of all

m ants in the current cycle. The pheromone also receives the reinforcement of elitist ants: those that achieve the best solutions deposit their pheromone in every cycle, directing the search in subsequent cycles.

$$\tau_{t+1} = (1 - \rho) \cdot \tau_t + \sum_{k=1}^m \Delta\tau^k + \tau_{elite} \quad (3)$$

The pheromone in the path found by a single ant k is defined by:

$$\Delta\tau^k = Q/L_k \quad (4)$$

where Q is a constant and L_k represents the total latency of the solution. It is easy to see that the ants with the worst results provide a smaller amount of pheromone.

The second ant algorithm used in this work is described below. The RACS is very similar to REAS, with the same structure of *multiple colonies* being used. The algorithm on which the RACS was inspired, called *Ant Colony System* [12], differs from others ant algorithms by:

- the selection method of next nodes in solutions building, and
- the use of a different pheromone update.

Because these two mechanisms, ACS improves over AS by increasing the importance of exploitation of information collected by previous ants with respect to exploration of the search space.

Thus, the RACS uses the so-called *pseudo-random proportional* rule.

$$j = \begin{cases} \operatorname{argmax}_{j \in [1,4]} \{ \tau_j \cdot \eta_{ij}^\beta \} & \text{if } q \leq q_0, \\ S & \text{otherwise} \end{cases} \quad (5)$$

As shown in Equation 5, the probability for an ant to move from node i to node j depends on a random variable q , uniformly distributed over $[0, 1]$, and a parameter q_0 . If $q \leq q_0$, then the next node is directly selected by $\operatorname{argmax}_{j \in [1,4]} \{ \tau_j \cdot \eta_{ij}^\beta \}$, i.e., the direction with the largest value of $\tau_j \cdot \eta_{ij}^\beta$. Otherwise, the next node is defined by S , that uses a selection method similar to that employed by EAS (Equation 1).

The RACS algorithm also uses a double pheromone update. The *offline update* is applied at the end of each iteration only by the *best-so-far* ant.

$$\tau_{t+1}^j = \begin{cases} (1 - \rho) \cdot \tau_t^j + \rho \cdot \Delta\tau_j & \text{if } j \text{ belongs to best path} \\ \tau_t^j & \text{otherwise} \end{cases} \quad (6)$$

The offline update is given by Equation 6, where $\Delta\tau_j$ is the reinforcement of the best ant pheromone. As said, the offline update perform a strong elitist strategy. The best ant can be the iteration-best ant, that is, the best in the current iteration, or the global-best ant, that is, the ant that made the best tour from the start of the trial.

The *local update* is performed by all ants in each step of construction of a solution.

$$\tau_{t+1} = (1 - \rho) \cdot \tau_t + \rho \cdot \tau_0 \quad (7)$$

This local update is defined by Equation 7, where ρ is the evaporation constant, and τ_0 is the initial pheromone at each node. In practice ACS ants “eat” some of the pheromone trail on the edges they visit. This has the effect of decreasing the probability that a same path is used by all the ants (i.e., it favors exploration, counterbalancing this way the above-mentioned modifications that strongly favor exploitation of the collected knowledge about the problem).

5 Evaluation Experiments and Results

A cycle-accurate network simulator was implemented in Matlab, supporting 2D mesh networks with wormhole switching. To estimate the performance of the proposed methods, networks were simulated with four different routing algorithms: REAS, RACS, XY and Odd-Even (OE). The efficiency of each type of routing is evaluated through *latency/packet* \times *injection rate* curves. The time unit adopted is the *simulator cycle*, where one cycle is the transmission time of one flit. The performed tests uses synthetic patterns of packet generation, which vary the number of packets, the packet injection rate and the spatial arrangement of the nodes of origin and destination.

All algorithms were executed with Matlab Version 7.7.0.471 (R008b). The simulations were performed on PCs with Intel Core i7 950 3GHz, 8Gb RAM and Microsoft Windows 7 Home Premium operating system.

Table 1. Simulation parameters

Routing algorithms	REAS, RACS, XY, OE
Traffic pattern	Uniform, Hots-pot, Local, Complement, Transpose 1, Trans. 2
Injection rate	10%, 20%, 30%, 40%, 50%, 60%, 70%, 80%, 90%, 100%
Number of packets	10, 20, 30, 40, 50, 60, 70, 80, 90, 100

5.1 Tests with Synthetic Traffic Patterns

The network was simulated with size of 5×5 , a square of 25 nodes. The set of simulation tests were performed varying the network routing algorithm, the pattern of traffic generation, the rate of injection and the number of packets. These parameters are shown in Table 1. The source-destination pairs are generated following six different distribution patterns, as shown in Fig. 3. These patterns are based on models widely used in the evaluation of communication in multiprocessor and distributed systems [13]. The *uniform*, *hot-spot* and *local* were called random patterns, because both the source and destination nodes are chosen in a randomly way. In the uniform pattern, all nodes have the same probability of

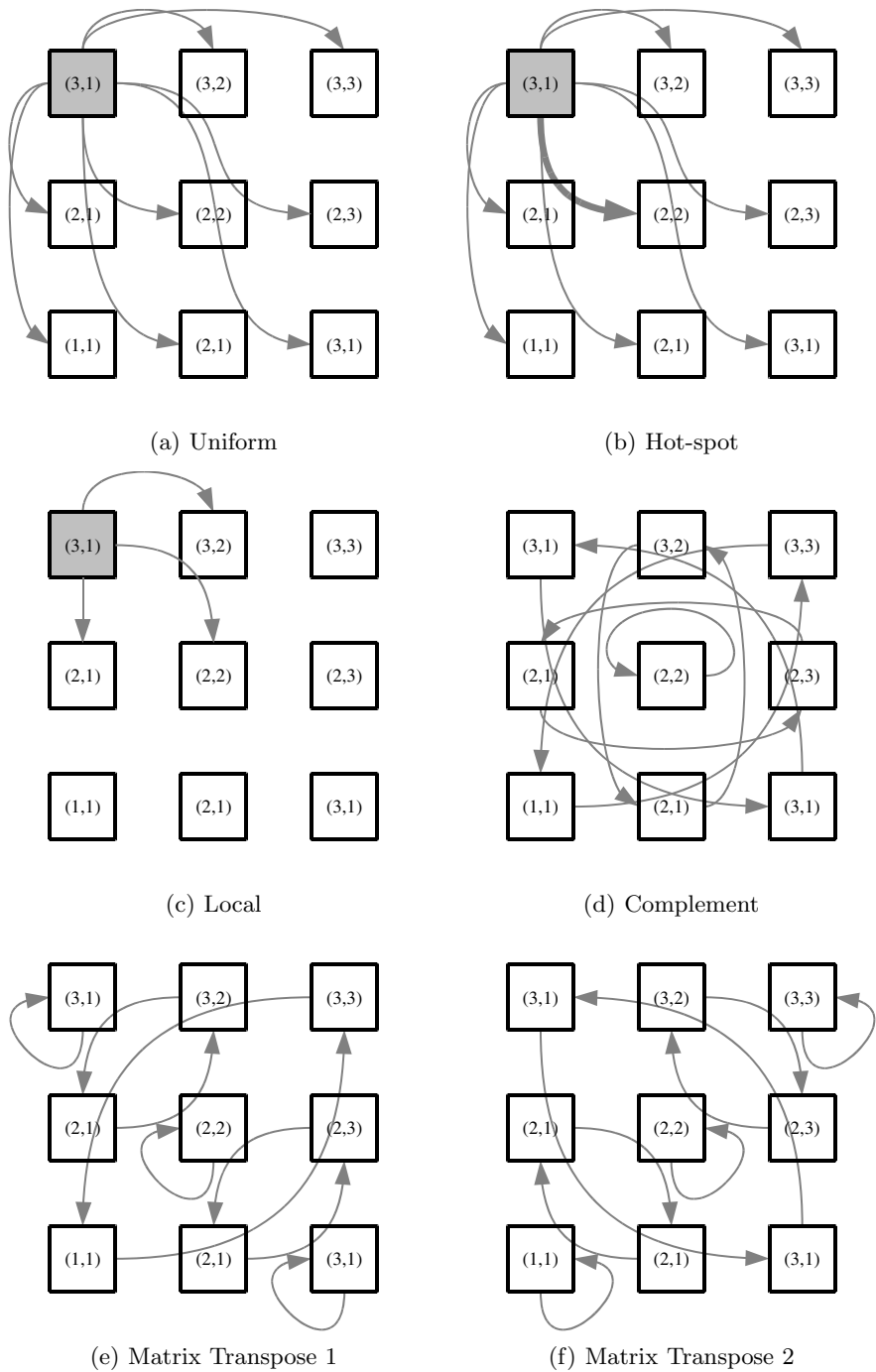
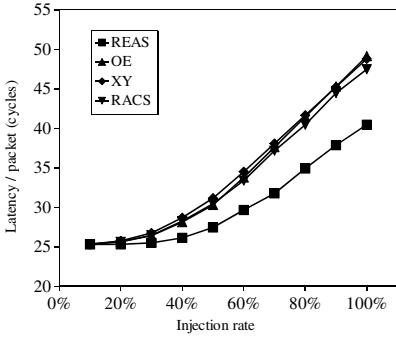
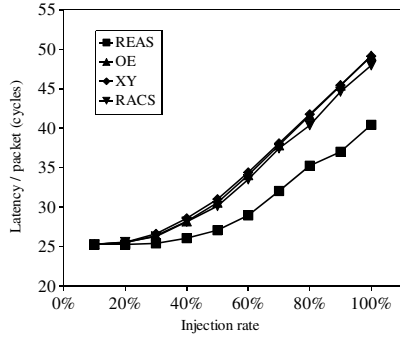


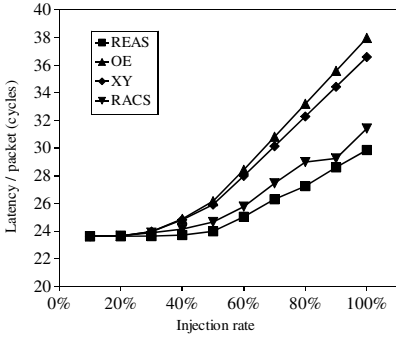
Fig. 3. Possible communication pairs in a 3×3 mesh



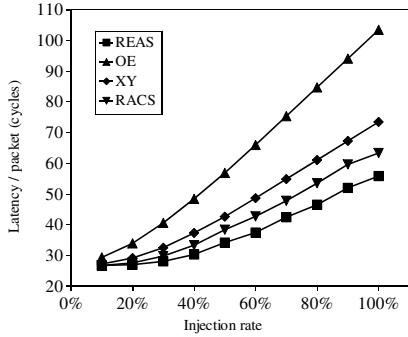
(a) Uniform



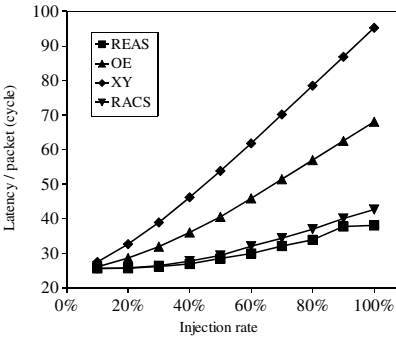
(b) Hot-spot



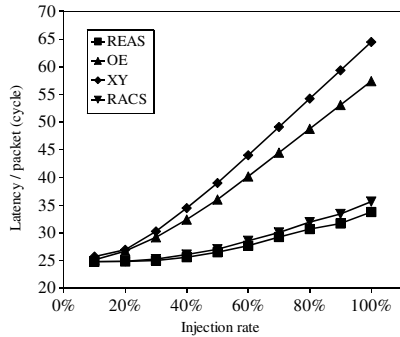
(c) Local



(d) Complement



(e) Matrix Transpose 1



(f) Matrix Transpose 2

Fig. 4. Results for the network under six different traffic patterns

being selected. The hot-spot pattern is similar to uniform. However, for the destination nodes, a particular node has a higher probability of selection. In local pattern, only nodes around the source node can be selected as a destination. The *complement*, *matrix transpose 1* and *matrix transpose 2* were called deterministic patterns. Although the selection of source nodes is random (following the uniform distribution), the destination nodes are selected according to the position of the source nodes. In the complement pattern, for a source node in the position (x, y) , the destination node is in the position $(size - x + 1, size - y + 1)$, where *size* is the number of nodes in a column or row of the mesh. For patterns matrix transpose 1 and 2, the destination nodes are respectively in the positions $(size - y + 1, size - x + 1)$ and (y, x) .

5.2 Simulation Results

For each simulation, we obtained the total latency and the average latency per packet. The total latency is the sum of the individual latency of all packets being transmitted on the network. The individual latency is the amount of simulation cycles that have elapsed since the injection of the first flit of a packet until the beginning of injection of the next packet of the same message. The average latency is the latency value obtained divided by the total number of packets. The general purpose of these tests is to verify the variation of latency under different injection rates.

Results are shown in the Fig. 4. The curves of *latency/packet* \times *injection rate* are, in fact, a mean of the values obtained for different quantity of packets. Each graph illustrates these curves for the four routing algorithms adopted.

For all traffic patterns, the latency curve of REAS is located below the curves of the other methods, indicating its ability to search for routes that provide a shorter transmission time. This performance is slightly better than the others at low injection rates, becoming more evident in rates above 50%. The RACS has a latency curve similar to the obtained by XY and OE algorithms for the uniform and hot-spot traffic patterns. For Local and Complement patterns these curves differ, with RACS getting lower latency values compared to the XY and OE. In matrix transpose patterns, the RACS achieved similar results to those obtained by REAS.

6 Conclusions

Static routing is an efficient solution in NoCs designed to run always the same set of applications. This is because the communication paths need only be defined one time. In this paper we propose the use of ACO-based algorithms in the optimization of paths in the static routing step in NoC design. The REAS and RACS algorithms proved to be effective in search of routes. Results of simulations with the network under different synthetic traffic patterns show the ant algorithms being able to find routes with latency less than that obtained with XY and OE algorithms. Future work may study the behavior of ant algorithms in packet

routing for applications mapped on the network, showing its use in examples closer to real world NoCs.

Acknowledgments. We are grateful to the Brazilian agencies CAPES, CNPq and FAPERJ, for their continuous financial support.

References

1. Benini, L., Micheli, G.D.: Networks on chips: A new soc paradigm. *Computer*, 70–78 (2002)
2. Edwards, S., Lavagno, L., Lee, E., Sangiovanni-Vincentelli, A.: Design of embedded systems: Formal models, validation, and synthesis. *Proceedings of the IEEE* 85(3), 366–390 (1997)
3. Dorigo, M., Maniezzo, V., Colorni, A.: Ant system: optimization by a colony of cooperating agents. *IEEE Transactions on Systems, Man, and Cybernetics, Part B: Cybernetics* 26(1), 29–41 (1996)
4. Ni, L.M., McKinley, P.K.: A survey of wormhole routing techniques in direct networks. *IEEE Tran. on Computers* 26, 62–76 (1993)
5. Moraes, F., Calazans, N., Mello, A., Moller, L., Ost, L.: Hermes: an infrastructure for low area overhead packet-switching networks on chip. *Integration, the VLSI Journal* 38(1), 69–93 (2004)
6. Zeferino, C.A., Susin, A.A.: Socin: A parametric and scalable network-on-chip. In: *Proceedings of the 16th Symposium on Integrated Circuits and Systems Design (SBCCI 2003)*, pp. 169–174. IEEE Computer Society, Washington, DC (2003)
7. Glass, C.J., Ni, L.M.: The turn model for adaptive routing. In: *Proceedings of the 19th Annual International Symposium on Computer Architecture (ISCA 1992)*, pp. 278–287. ACM, New York (1992)
8. Chiu, G.: The odd-even turn model for adaptive routing. *IEEE Transactions on Parallel and Distributed Systems* 11(7), 729–738 (2000)
9. Duato, J.: A new theory of deadlock-free adaptive routing in wormhole networks. *IEEE Trans. Parall. Distrib. Syst.* 4(12), 1320–1331 (1993)
10. Bonabeau, E., Dorigo, M., Theraulaz, G.: *Swarm Intelligence From Natural to Artificial Systems*. Oxford University Press, New York (1999)
11. Dorigo, M., Birattari, M., Sttzle, T.: Ant colony optimization - Artificial ants as a computational intelligence technique. *IEEE Computational Intelligence Magazine* 1(4), 28–39 (2006)
12. Dorigo, M., Gambardella, L.: Ant colony system: A cooperative learning approach to the traveling salesman problem. *IEEE Transactions on Evolutionary Computation* 1(1), 53–66 (1997)
13. Duato, J., Yalamanchili, S., Lionel, N.: *Interconnection Networks: An Engineering Approach*. Morgan Kaufmann Publishers Inc., San Francisco (2002)

A Genetic Algorithm Assisted by a Locally Weighted Regression Surrogate Model

Leonardo G. Fonseca¹, Heder S. Bernardino², and Helio J.C. Barbosa²

¹ Dept. of Computational & Applied Mechanics, Federal University of Juiz de Fora, Juiz de Fora, Brazil

² National Laboratory for Scientific Computing, Petrópolis, Brazil

Abstract. In this paper we compare two strategies using locally weighted regression as a surrogate model to improve the efficiency of a real-coded generational genetic algorithm where a fixed budget of simulations is imposed. Only a fraction of the candidate solutions are evaluated exactly, allowing for more generations to evolve the population (the number of generations increases according to a user defined parameter). We test the proposed strategies on a set of benchmark optimization problems from the literature. The results show that the surrogate strategies can improve the performance of the GA depending on the user defined parameter. We suggest a threshold value to this parameter so that the locally weighted regression can be used to enhance the efficiency of genetic algorithms, when the number of calls to the expensive simulation is limited.

1 Introduction

Although Genetic Algorithms (GAs) have obtained satisfactory solutions in several hard problems, they normally depends of a large number of objective function evaluations, similarly to other evolutionary algorithms. This demand normally limits the application of GAs to optimization problems which require computationally expensive simulations. An effective strategy to tackle this problem is to build a surrogate (approximate) model for the objective function to be used in the solution process of the given optimization problem.

The idea of reducing the number of computationally expensive function evaluations appeared early in the evolutionary computation literature [1] and efforts in this direction continue [2,3]. We mention also some additional reasons for using surrogate models in evolutionary algorithms: (a) to reduce complexity [4] and smooth the fitness landscape [5], (b) to alleviate user fatigue in interactive design systems [6], and (c) in noisy environments [7].

Many surrogate models are available in the literature, such as polynomial models [1], artificial neural networks [8], Kriging or Gaussian processes [9], Radial Basis Functions [10], support vector machines [11], and nearest neighbors approximation and interpolation [12,13]. Alternatively, a surrogate may be derived from physical or numerical simplifications of the original model [14], or *ad hoc* approaches can replace expensive simulations [15,16]. Furthermore, such techniques can also be combined and used as an ensemble [17,18].

Polynomial models are very simple and easy-to-build surrogates. However, the use of surrogate models based on global function approximation, such as polynomial regression, even for moderate dimension, can be hindered due to the curse of dimensionality [19]. An interesting alternative is the local regression, which is capable of producing accurate approximations even for nonlinear functions. The locally weighted regression appears as a suitable surrogate model in some papers from the literature. In [20] a local regression surrogate is used to estimate the fitness of candidate solutions in noisy landscapes. Reference [21] uses locally weighted regression models to enhance the efficiency of evolution strategies in the optimization of computationally expensive problems.

A surrogate modeling system based on locally weighted regression is presented in [22] for the simulation of tissue and movement. In [23] a locally weighted regression is employed to enhance the performance of a clonal selection algorithm when a fixed budget of expensive evaluations is imposed.

In this paper we use two evolutionary computing frameworks to explore the use of a locally weighted regression model to extend the number of generations of a real-coded genetic algorithm in order to (hopefully) obtain a final solution which is better than the one the baseline algorithm would find using only that fixed number of expensive simulations.

2 Surrogate-Assisted Evolutionary Framework

Surrogate modeling, or metamodeling, can be viewed as the process of replacing the original evaluation function (a complex computer simulation) by a cheaper approximation. The surrogate model should be simple, general, and keep the number of control parameters as small as possible [24]. In this section we describe the surrogate modeling approaches, and the surrogate-assisted evolutionary algorithm.

2.1 Extended Generations Approach

We will consider that a fixed budget of (expensive) exact simulations N_f is prescribed and only a fraction $0 < p_{sim} \leq 1$ of the population is to be evaluated by the exact model. In the strategy implemented here, both the initial and the final populations are entirely evaluated by the exact model so that the total number of evaluations by the simulation model (N_f) is equal to

$$N_f = 2\lambda + p_{sim}(N_G - 2)\lambda \quad (1)$$

where λ is the population size and N_G is the total number of generations.

An interesting approach is to use the surrogate model within the evolutionary cycle, in order to allow the GA to perform more generations. We distribute the budget of N_f simulations along a number of N_G generations according to:

$$N_G = \left\lceil \frac{N_f - 2\lambda(1 - p_{sim})}{p_{sim}\lambda} \right\rceil. \quad (2)$$

This approach will be referred to as *Extended Generations (EG)*. As the surrogates are introduced into the GA, the number of generations can be increased as given in Eq. (2). For the baseline generational GA, $N_f = \lambda N_G$ holds, and the number of generations allowed is given by $N_G = N_f / \lambda$. In the evolutionary context, a greater number of generations implies longer evolution time, with potentially better final solutions. However, although more generations are available, the evaluations performed by the surrogate model may be inaccurate. In fact, there is a trade-off between the number of generations and the frequency of use of the simulation model. In addition, when the number of generations is strongly increased (which corresponds to low frequency of use of the simulation model), poor results may be expected since few simulations are performed per generation.

2.2 Surrogate Model Management

We introduce the surrogate model into the evolutionary cycle using two surrogate model management strategies: Random Selection (RS) and Deterministic Selection (DS) [7].

Random Selection (RS): Considering a population of λ individuals, a parameter $0 < p_{sim} \leq 1$, and the offspring previously evaluated by the surrogate model, the RS model management consists in randomly choosing, with probability p_{sim} , λ^* individuals to be re-evaluated by the exact function. The remaining $\lambda - \lambda^*$ individuals keep their fitness from the surrogate evaluation. Clearly, by setting $p_{sim} = 1$, the standard GA is recovered.

Deterministic Selection (DS): The deterministic selection (DS) strategy chooses the individuals according to the pre-evaluation using the surrogate model. The offspring population is entirely evaluated by the surrogate model and then sorted in decreasing order of quality. Then, the $p_{sim}\lambda$ highest ranked individuals (according to the surrogate model) are evaluated by the original (expensive) model, and the remaining $\lambda - p_{sim}\lambda$ individuals maintain their objective function predicted by the surrogate model.

2.3 Locally Weighted Regression Surrogate Model (LWR)

Locally weighted regression (LWR) computes an approximation around a point of interest using only data in the neighborhood of that point [25]. A general form of a simple linear regression is given by [23]

$$\hat{f}(x^h) = \theta_0 + \theta_1 x_1^h + \dots + \theta_n x_n^h = (x^h)^T \boldsymbol{\theta} \quad (3)$$

or, in matrix format,

$$\hat{f}(x^h) = (x^h)^T \boldsymbol{\theta} \quad \text{with } x_0^h = 1, \quad (4)$$

where the superscript T denotes transposition, $x_0^h = 1$ and one must compute $\boldsymbol{\theta} \in R^{n+1}$. Given a matrix X with a set of candidate solutions and \mathbf{y} their corresponding objective function values, the least squares estimation leads to

$$\boldsymbol{\theta} = (X^T X)^{-1} X^T \mathbf{y}, \quad (5)$$

where $(X^T X)$ must be non-singular.

It is assumed that given the set of a query point's neighbors it is possible to obtain a linear approximation $\hat{f}(x) \approx f(x)$. The number of neighbor points used by the model is the minimum number of nearest neighbors such that $(X^T X)$ is a non-singular matrix. Considering that the closest points/solutions should contribute more to the surrogate model, then we also used the weighted version of the linear regression. In this case, the model is weighted using a diagonal matrix W with elements given by

$$w_{ii} = \frac{1}{d_E(x^h, x^i)} \quad (6)$$

where $d_E(\cdot, \cdot)$ is the Euclidean distance. We notice that for all surrogate models considered here, x^h is searched in the database set before its fitness value is calculated by the surrogate model. Thus $d_E(x^h, x^i) \neq 0$ and w_{ii} can always be calculated.

The weighted least squares estimator reads now

$$\hat{\theta} = (X^T W X)^{-1} X^T W \mathbf{y}, \quad (7)$$

and

$$\hat{f}(x^h) = (x^h)^T \hat{\theta} \quad \text{with } x_0^h = 1. \quad (8)$$

2.4 Surrogate-Assisted GA

The next crucial step is to define how the surrogate model will be incorporated into the search mechanism. Some possibilities discussed in the literature include incorporating the surrogate models as (i) local approximators [26], (ii) surrogate-guided evolutionary operators [27], (iii) surrogate-assisted local search [19][28], and (iv) a pre-selection technique [10][29].

Figure 1 shows the proposed surrogate-assisted GA for computationally expensive optimization problems, which implements either the RS or the DS model management.

It is assumed that for complex real-world applications the cost of a surrogate model evaluation is negligible when compared to that of a simulation, hence total computational time will be only slightly increased due to the extra surrogate evaluations.

3 Numerical Experiments

In order to assess the performance of the surrogate model and strategies we consider a set of minimization problems shown in Table 1. We adopted $n=10$ for all test-problems.

The parameters for the baseline and surrogate-assisted GA were: population size of $\lambda = 40$, two-point crossover and non-uniform mutation applied with probability 85% and 5%, respectively; rank-based selection, and elitism (the two highest ranked individuals are copied to the next generation). The computational budget was limited to $N_f = 6000$ exact (expensive) fitness evaluations, resulting in 150 generations in the baseline GA. For the surrogate-assisted GA, the parameter p_{sim} was tested for the values $p_{sim} \in [0.2, 1.0]$ in steps of 0.1, and the number of generations is set according

```

1: procedure SURROGATE ASSISTED GA
2:    $t = 0$ 
3:   Set  $p_{sim}$ 
4:   Generate a initial population  $P_t$  with  $\lambda$  individuals
5:   Evaluate  $P_t$  using the simulation model
6:   Set  $N_G$  according to Eq. (2)
7:   while  $t \leq N_G$  do
8:     Generate a population  $G_t$  from  $P_t$ 
9:     Evaluate all individuals in  $G_t$  by LWR surrogate
10:    Select  $\lambda^*$  individuals in  $G_t$  using RS or DS
11:    Evaluate  $\lambda^*$  individuals in  $G_t$  by simulation
12:     $P_{t+1} = G_t$ 
13:     $t = t + 1$ 
14:   end while
15:   Return the best solution in  $P_t$ 
16: end procedure

```

Fig. 1. Surrogate-assisted GA. P_t is the parent population, G_t is the offspring population, and p_{sim} is the fraction of individuals evaluated by the original (expensive) model. λ is the population size and N_G in the number of generations according to Eq. (2). RS and DS are the Random Selection and Deterministic Selection surrogate model management.

Table 1. Minimization problems: x^L is the lower bound and x^U is the upper bound. The dimension n is set to 10.

#	Objective function	$[x^L, x^U]$
F ₁	$\sum_{i=1}^n x_i^2$	$[-5.12, 5.12]$
F ₂	$\sum_{i=1}^n (x_i^2 - 10 \cos(2\pi x_i) + 10)$	$[-5.12, 5.12]$
F ₃	$20 + e - 20e^{-0.2\sqrt{\frac{\sum_{i=1}^n x_i^2}{n}}}$ $-e^{\frac{\sum_{i=1}^n \cos(2\pi x_i)}{n}}$	$[-32.768, 32.768]$
F ₄	$\sum_{i=1}^n \frac{x_i^2}{4000} - \prod_{i=1}^n \frac{\cos x_i}{\sqrt{i}} + 1$	$[-600, 600]$
F ₅	$\sum_{i=1}^n i x_i^4 + U(0, 1)$	$[-4.28, 4.28]$

to Eq. (2). A total of 25 independent runs were performed for each experiment. When $p_{sim} = 1$ the baseline GA is recovered (which uses only the exact fitness function). We remark that all results, independent of the value of the parameter p_{sim} were obtained using the same number of expensive simulations (up to small fluctuations due to the stochastic nature of the procedures).

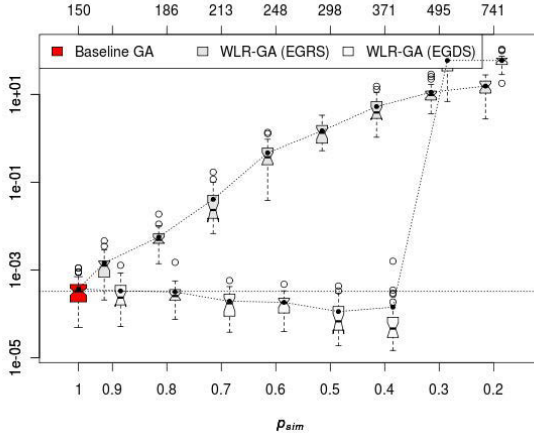


Fig. 2. Results for F_1 (in log scale). Comparison of the results obtained by the surrogate assisted GA using EGRS and EGDS strategies. The horizontal bottom axis displays the values of the the probability of evaluation by the simulation model p_{sim} , and the horizontal top axis displays the number of generations N_G . Filled circles indicate the average (mean) values.

We use boxplots to display relevant statistical measures such as median, minimum, maximum, interquartiles values, and also possible outliers. The average performance is shown with a filled circle and dotted lines. The box size denotes the dispersion of the results: the smaller the box, the better is the algorithm’s performance.

Figure 2 shows the results for function F_1 . We observe that EGRS does not contribute to improve the search: the baseline GA outperforms the surrogate-assisted GA in all experiments. However, significant improvements were obtained when using the EGDS strategy. For function F_1 the baseline GA produced fitness values with median values about 10^{-3} , while for surrogate assisted GA the median is about 10^{-5} for $p_{sim} = 0.4$. The boxplots indicate for EGDS a threshold value for p_{sim} (about 0.4) beyond which the results could not be improved, and the performance of the surrogate-assisted GA is considerably affected. The same behavior (for both EGRS and EGDS strategies) can be seen in the results for functions F_2 , F_3 and F_4 , as depicted in Figures 3, 4 and 5. The threshold $p_{sim} = 0.4$ appears in those functions, except for F_3 , where $p_{sim} = 0.5$.

From boxplots in Fig. 6 we can observe that both EGRS and EGDS strategies do not improve the final solutions in problem F_5 . It is interesting to notice that, unlike previous test-problems, the EGRS does not present poor quality results and EGDS does not improve the final solutions for any value of p_{sim} . We suggest that the noise term in this function renders the surrogate-assisted strategies ineffective in producing good results when compared to the baseline GA.

One can see that in all tests considered objective function values are non-negative. However, the LWR surrogate model can predict a negative fitness value, depending on the point to be predicted and the neighbors of the point to be approximated (see Eq. (3)). As a result, any solution with negative fitness is better than any solution evaluated by the exact model, including the optimum. In this case, a sub-optimal solution may appear

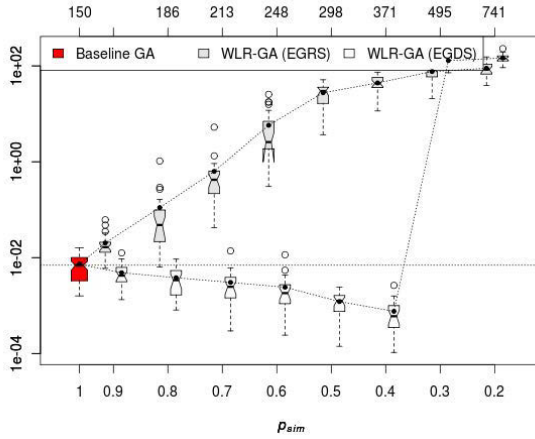


Fig. 3. Results for F_2 (in log scale). Comparison of the results obtained by the surrogate assisted GA using EGRS and EGDS strategies. The horizontal bottom axis displays the values of the the probability of evaluation by the simulation model p_{sim} , and the horizontal top axis displays the number of generations N_G . Filled circles indicate the average (mean) values.

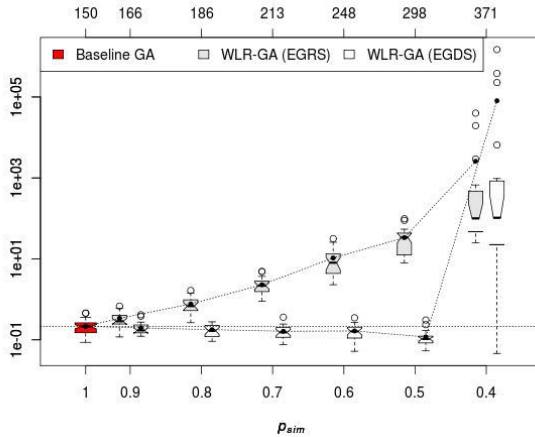


Fig. 4. Results for F_3 (in log scale). Comparison of the results obtained by the surrogate assisted GA using EGRS and EGDS strategies. The horizontal bottom axis displays the values of the the probability of evaluation by the simulation model p_{sim} , and the horizontal top axis displays the number of generations N_G . Filled circles indicate the average (mean) values.

as the best one, and degenerate the search towards the global optimum. In this way, since the RS strategy chooses individuals to be evaluated by the simulation model at random, it requires an accurate surrogate, in order to avoid values out of the range of the fitness function. For example, in the RS strategy the worst solution may have a negative fitness value assigned to it, and then it becomes the best solution in the generation. The

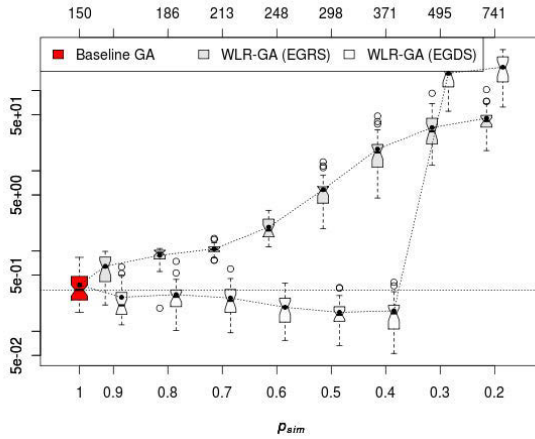


Fig. 5. Results for F_4 (in log scale). Comparison of the results obtained by the surrogate assisted GA using EGRS and EGDS strategies. The horizontal bottom axis displays the values of the the probability of evaluation by the simulation model p_{sim} , and the horizontal top axis displays the number of generations N_G . Filled circles indicate the average (mean) values.

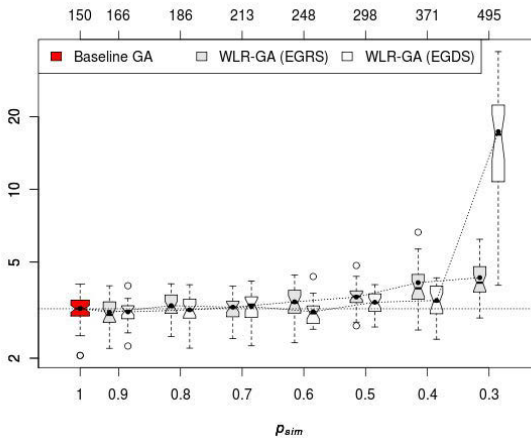


Fig. 6. Results for F_5 (in log scale). Comparison of the results obtained by the surrogate assisted GA using EGRS and EGDS strategies. The horizontal bottom axis displays the values of the the probability of evaluation by the simulation model p_{sim} , and the horizontal top axis displays the number of generations N_G . Filled circles indicate the average (mean) values.

accuracy of the surrogate model plays an important role in the search process of the RS strategy: as the GA implements elitism (the 2 best solutions are copied to the next generation), the worst individual is immediately copied to the parent population and has a great chance to be selected to be a parent in the next generation.

We noticed however that the accuracy of the surrogate model is not crucial in the EGDS strategy. Even when the surrogate is inaccurate, but preserves the ranking, the fitness landscape may be altered, but it will have the same overall shape. In the DS approach, surrogate solutions are compared and the best one is selected. Therefore, in the DS strategy it is important to use a surrogate that preserves the ranking of the solutions with respect to the original function. A discussion on rank preserving properties of surrogates can be found in [30].

Of course it is clear that the application of the proposed techniques will be really more effective for real-world problems with an expensive fitness evaluation, when the number of computational simulations allowed may be quite limited. For example, consider $p_{sim} = 0.5$ and running the GA using 40 individuals with a budget of 6000 expensive evaluations. Let the relative cost of the surrogate model be 0.005 (200 times cheaper than exact evaluation). We have 298 generations and 11920 surrogate evaluations (all individuals are evaluated by the surrogate model and then re-evaluated by the simulation model). With these values, the surrogate evaluations correspond to $11920 \cdot 0.005 \approx 60$ exact evaluations, resulting in an increase of only 1% of the total computational time.

4 Conclusions

The study in this paper compares two selection strategies and the locally weighted regression surrogate model as alternatives to improve the final solutions in a genetic algorithm. From the results derived here, we can say that the best approach to be used is the Deterministic Selection (DS) strategy. Except for the noisy function F_5 , the results suggest that EGDS with p_{sim} about 0.5 is the safest choice. In addition, we suggest that the EGDS works well when the surrogate captures the main trends in the exact model, preserving the ranking even when the approximation is not accurate.

Investigation on the use of the LWR surrogate in real-world applications, as well as a detailed study of the effect of noise on the performance of the surrogate-assisted strategies, remain as future work.

Acknowledgments. The authors acknowledge the support from CNPq (grants 308317/2009-2 and 300192/2012-6) and FAPERJ (E-26/100.308/2010). The first author also thanks FAPEMIG for the financial support.

References

1. Grefenstette, J., Fitzpatrick, J.: Genetic search with approximate fitness evaluations. In: Proceedings of the International Conference on Genetic Algorithms and Their Applications, pp. 112–120 (1985)
2. Forrester, A.I., Keane, A.J.: Recent advances in surrogate-based optimization. Progress in Aerospace Sciences 45(1-3), 50–79 (2009)
3. Jin, Y.: Surrogate-assisted evolutionary computation: Recent advances and future challenges. Swarm and Evolutionary Computation 1(2), 61–70 (2011)

4. Ong, Y., Nair, P., Keane, A.: Evolutionary optimization of computationally expensive problems via surrogate modeling. *AIAA Journal* 41(4), 687–696 (2003)
5. Yang, D., Flockton, S.J.: Evolutionary algorithms with a coarse-to-fine function smoothing. In: *IEEE International Conference on Evolutionary Computation*, vol. 2, pp. 657–662 (1995)
6. Sun, X.Y., Gong, D., Li, S.: Classification and regression-based surrogate model-assisted interactive genetic algorithm with individual's fuzzy fitness. In: *Proceedings of the 11th Annual Conference on Genetic and Evolutionary Computation, GECCO 2009*, pp. 907–914. ACM, New York (2009)
7. Jin, Y., Branke, J.: Evolutionary optimization in uncertain environments – a survey. *IEEE Transactions on Evolutionary Computation* 9(3) (2005)
8. Ferrari, S., Stengel, R.F.: Smooth function approximation using neural networks. *IEEE Transactions on Neural Networks* 16(1), 24–38 (2005)
9. Emmerich, M., Giannakoglou, K., Naujoks, B.: Single- and multiobjective evolutionary optimization assisted by gaussian random field metamodels. *Evolutionary Computation* 10(4), 421–439 (2006)
10. Giannakoglou, K.C.: Design of optimal aerodynamic shapes using stochastic optimization methods and computational intelligence. *Progress in Aerospace Sciences* 38(1), 43–76 (2002)
11. Kecman, V.: Learning and soft computing: support vector machines, neural networks, and fuzzy logic models. In: *Complex Adaptive Systems*. MIT Press, Cambridge (2001)
12. Fonseca, L.G., Barbosa, H.J.C., Lemonge, A.C.C.: A similarity-based surrogate model for enhanced performance in genetic algorithms. *OPSEARCH* 46, 89–107 (2009)
13. Fonseca, L.G., Barbosa, H.J.C., Lemonge, A.C.C.: On similarity-based surrogate models for expensive single- and multi-objective evolutionary optimization. In: *Computational Intelligence in Expensive Optimization Problems. Adaptation, Learning, and Optimization*, vol. 2, pp. 219–248. Springer, Heidelberg (2010)
14. Noronha Jr., D.B., Martins, R.R., Jacob, B.P., de Souza, E.: Procedures for the strain based assessment of pipeline dents. *International Journal of Pressure Vessels and Piping* 87(5), 254–265 (2010)
15. Salami, M., Hendtlass, T.: A fast evaluation strategy for evolutionary algorithms. *Applied Soft Computing* 2, 156–173 (2003)
16. Pilato, C., Tumeo, A., Palermo, G., Ferrandi, F., Lanzi, P.L., Sciuto, D.: Improving evolutionary exploration to area-time optimization of FPGA designs. *Journal of Systems Architecture* 54(11), 1046–1057 (2008)
17. Goel, T., Haftka, R., Shyy, W., Queipo, N.: Ensemble of surrogates. *Structural and Multidisciplinary Optimization* 33(3), 199–216 (2007)
18. Acar, E., Rais-Rohani, M.: Ensemble of metamodels with optimized weight factors. *Struct. Multidisc Optim.* 37(3), 279–294 (2009)
19. Lim, D., Jin, Y., Ong, Y.S., Sendhoff, B.: Generalizing surrogate-assisted evolutionary computation. *IEEE Transactions on Evolutionary Computation* 14(3), 329–355 (2010)
20. Branke, J., Schmidt, C., Schmeck, H.: Efficient fitness estimation in noisy environment. In: Spector, L., et al. (eds.) *Proceedings of Genetic and Evolutionary Computation*, pp. 243–250. Morgan Kaufmann (2001)
21. Kern, S., Hansen, N., Koumoutsakos, P.: Local Meta-models for Optimization Using Evolution Strategies. In: Runarsson, T.P., Beyer, H.-G., Burke, E.K., Merelo-Guervós, J.J., Whitley, L.D., Yao, X. (eds.) *PPSN 2006. LNCS*, vol. 4193, pp. 939–948. Springer, Heidelberg (2006)
22. Halloran, J.P., Erdemir, A., van den Bogert, A.J.: Adaptive surrogate modeling for efficient coupling of musculoskeletal control and tissue deformation models. *Journal of Biomechanical Engineering* 131(1), 011014 (2009)

23. Bernardino, H.S., Barbosa, H.J.C., Fonseca, L.G.: Surrogate-assisted clonal selection algorithms for expensive optimization problems. *Evolutionary Intelligence* 4, 81–97 (2011)
24. Blanning, R.W.: The source and uses of sensitivity information. *Interfaces* 4(4), 32–38 (1974)
25. Ruppert, D., Wand, M.P.: Multivariate locally weighted least squares regression. *The Annals of Statistics* 22(3), 1346–1370 (1994)
26. Regis, R.G., Shoemaker, C.A.: Local function approximation in evolutionary algorithms for the optimization of costly functions. *IEEE Trans. Evolutionary Computation* 8(5), 490–505 (2004)
27. Rasheed, K., Vattam, S., Ni, X.: Comparison of methods for using reduced models to speed up design optimization. In: *Proceedings of Genetic and Evolutionary Computation Conference*, pp. 1180–1187. Morgan Kaufmann, New York (2002)
28. Wanner, E.F., Guimaraes, F.G., Takahashi, R.H.C., Lowther, D.A., Ramirez, J.A.: Multiobjective memetic algorithms with quadratic approximation-based local search for expensive optimization in electromagnetics. *IEEE Transactions on Magnetics* 44(6), 1126–1129 (2008)
29. Praveen, C., Duvigneau, R.: Low cost PSO using metamodels and inexact pre-evaluation: Application to aerodynamic shape design. *Computer Methods in Applied Mechanics and Engineering* 198(9–12), 1087–1096 (2009)
30. Diaz-Manriquez, A., Toscano-Pulido, G., Gomez-Flores, W.: On the selection of surrogate models in evolutionary optimization algorithms. In: *2011 IEEE Congress on Evolutionary Computation (CEC)*, pp. 2155–2162 (2011)

Swarm Robots with Queue Organization Using Infrared Communication

Rafael Mathias de Mendonça¹, Nadia Nedjah¹, and Luiza de Macedo Mourelle²

¹ Department of Electronics Engineering and Telecommunications
Faculty of Engineering
State University of Rio de Janeiro
`rmathias.mendonca@gmail.com`, `nadia@eng.uerj.br`

² Department of Systems Engineering and Computation
Faculty of Engineering
State University of Rio de Janeiro
`ldmm@eng.uerj.br`

Abstract. This paper describes the implementation of a swarm of E-Puck robots with autonomous behavior of queue via a communication process that uses the infrared sensors of the robots. Each robot has the ability to identify other robots in seeking a collective formation of queue. Everyone can identify and avoid obstacles in the environment while maintaining the collective queue organization. A digital filter was implemented to inhibit the effects of external light interference during the measurements done by the infrared sensors. The project was implemented in the Webots prototyping software, while thoroughly and physically tested on a swarm of E-Puck robots. The tests proved the efficiency of the implementation to yield the expected behavior. We included in this paper the observed behaviors during the testing process with the robots.

Keywords: Infrared communication, swarm intelligence, queue formation, IR sensors, E-Puck, Webots.

1 Introduction

The expression *swarm intelligence* and *collective intelligence* has been proposed in the late 1980 from the observation of social behavior at species of insects and birds [1]. These species perform collective tasks with the objective of implementing more complex tasks and impossible to be done by only one individual. The approach of a swarm of robots appeared via this observation extended to groups of mobile robots with limited processing capability.

This paper presents a swarm of robots with the behavior of queue organization. Initially, the robots have random positions and seek the queue organization using the infrared communications (IR). This unidirectional communication uses the eight IR sensors of the robot hardware to capture the excitement of light provided by another robot in the characteristic frequency of 70Hz.

This captured signal is treated by a bandpass filter (BP) centered on this characteristic frequency that inhibits interference from other frequencies. After filtering, the signal is validated and interpreted to generate the robot's movement. Similarly, the robots are also able to identify and avoid obstacles.

Thus, a more complex behavior of queue organization is implemented for a group of robots with limited processing power and limited hardware. This process characterizes a side of swarm intelligence, normally called swarm robotics [2]. The code was developed in C language, tested on the Webots prototyping software PRO 6.2.4 [3], [4] and extensively tested on mobile E-Puck robots. At the end of this paper the results obtained with the E-Puck robots are shown. (A tutorial about Webots in Portuguese can be found at [5].)

This paper includes the following sections: First, in Section 2 we discuss the physical constitution of the E-Puck robot. In Section 3 we discuss the composition of the algorithm generated. Then, in Section 4 we discuss the signal processing by a digital filter. Finally, we present the results in Section 5, while in Section 6 we draw some conclusions.

2 Hardware - IR Sensors and LEDs

The collaboration between the *Autonomous Systems Laboratory* (ASL), the *Swarm-Intelligent Systems Group* (SWIS) and the *Laboratory of Intelligent Systems* (LIS) resulted in the development of a new small-scale robotic platform called E-Puck [6]. The robot has a diameter of 75mm and is basically composed of a plastic body with various embedded devices, as shown Fig. 1. Located on the circuit board of the E-Puck there is an E-Puck dsPIC microcontroller model 30F6014A [7], [8], [9]. This microcontroller has a limited processing capability and is responsible for managing all information between devices.

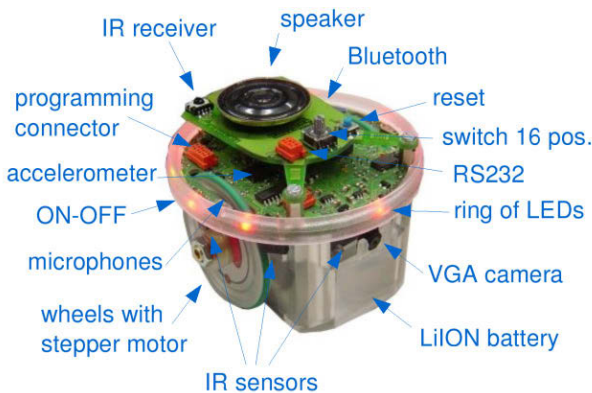


Fig. 1. Devices present on the E-Puck's hardware

The eight sensors and eight IR LEDs, shown in Fig. 2, are arranged around the robot's body and will be used in the process of communication between the group. The IR sensors [10] are responsible for identifying: (i) the light generated by LEDs of other robots and (ii) the proximity of obstacles. Thus, the IR sensors provide the needed information for the actions of following another robot (i) and avoiding obstacles (ii).

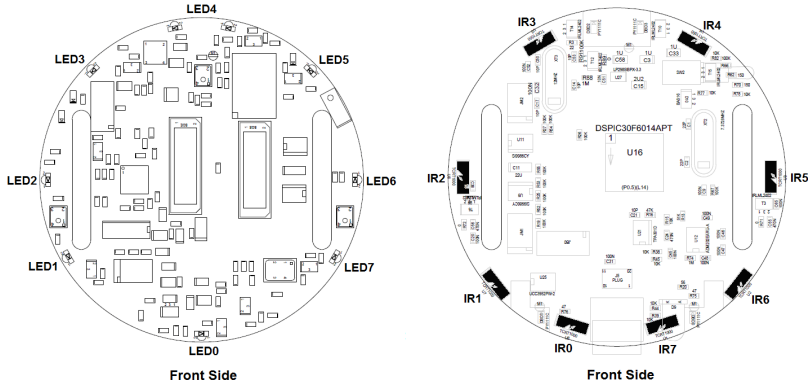


Fig. 2. Arrangement of LEDs (left) and IR sensors (right) of the E-Puck robot

The rear LEDs, described as LED3, LED4 and LED5, are excited in the characteristic frequency and describe the behavior of “blink”. This light signal is used for the communication between the robots.

3 Processes and Algorithms

The digital values, referring to the IR sensor, are sampled by the dsPic during the analog to digital conversion (A/D) at a frequency of 400Hz. Thus, a sub-sampling is done at a frequency of 200Hz. So, for every two samples obtained by the A/D conversion process, we can ensure that one sample is used.

The reading process, sampling and storage of the values of IR sensors for the filtering process is shown in the following Algorithm 1:

Algorithm 1. Process for the values of IR sensors

Require: *Vd* (value of digital sensors), *Vector* (vector with the *Vd* values), *Filtering* (function that performs the complete filtering process);

- 1: **for** $i = 0 \rightarrow 7$ **do**
 - 2: read *Vd* from sensor(*i*);
 - 3: *Vector*(*i*) $\leftarrow Vd$;
 - 4: **end for**
 - 5: run *Filtering*;
-

The choice of frequency of 70Hz for blinking the rear E-Puck LED is based on some restrictions. Firstly, the upper frequency is limited to 100Hz for Sampling Theorem [11] because of the 200Hz sub-sampling arbitrated. We chose to avoid low frequencies, very close to the DC level, and frequency of 60Hz, strongly present in the local power grid. These restrictions have the objective of avoiding unwanted interference from external sources known during the measurement process from IR sensors.

So, the process of blinking rear LEDs was carried out by the Algorithm 2 shown below:

Algorithm 2. Process for blink rear LEDs

Require: LED3 (logic state of LED number 3), LED4 (logic state of LED number 4), LED5 (logic state of LED number 5);

- 1: $LED3 \leftarrow notLED3$;
- 2: $LED4 \leftarrow notLED4$;
- 3: $LED5 \leftarrow notLED5$;

3.1 Avoiding Obstacles

The process for avoiding obstacles enables the robot to identify and avoid obstacles close to the IR sensors. This process changes the speed of its motors thus changing the speed and the direction of its displacement.

The process of value generation to drive the motor for the avoid action is shown by the Algorithm 3 described below:

Algorithm 3. Avoiding action

Require: Vector (vector with the Vd values), K (vector with the constant weights of the sensors), Vmotor (calculate variable), Vlimit (threshold value for the motor drive);

- 1: **for** $i = 0 \rightarrow 7$ **do**
- 2: read Vector(i);
- 3: $Vmotor \leftarrow Vmotor + k(i) \times Vector(i)$;
- 4: **end for**
- 5: /* Generation of the value for driving the motor */
- 6: **if** $Vmotor > +Vlimit$ **then**
- 7: $Vmotor \leftarrow +Vlimit$;
- 8: **end if**
- 9: **if** $Vmotor < -Vlimit$ **then**
- 10: $Vmotor \leftarrow -Vlimit$;
- 11: **end if**
- 12: /* Limiting the value for driving the motor between $\pm Vlimit$ */
- 13: $Motor \leftarrow Vmotor$;
- 14: **return** Motor;
- 15: /* Return value for driving the motor */

Basically, the function avoiding obstacles receives the values read by the IR sensors and multiplies them by constants according to the position of the sensors on the robot. Thus, the weighted values will generate a new value for driving the motor. Therefore, the front sensors will have a greater influence on the composition of the robot motion when compared with other sensors. This value can assume both positive and negative values.

After the generation of this value, a limitation will be made between the two extremes: maximum and minimum. This limitation is required to prevent the stepper motors from physical damage caused by excessive speeds.

3.2 The Following the Light Process

This process enables the robot to identify a light source by modifying the speed of their motors according to their intensity. This action allows to follow the light source generated by the rear LEDs of another robot. In addition to this action a filtering process of the values provided by the IR sensors is previously performed. This topic will be better discussed in the Section 4.

Initially, in order to start the process of following, the values received from the IR sensors are checked whether they have gone through the filtering process. If not, the values will be considered invalid and the execution of the function will be finished. After receiving of the filtered values, the execution of the function begins, attributing the values received as invalid. This attribution forces the passage of the values again through the filtration process, ensuring that the values will be updated and validated to be used by the function in the next cycle. Subsequently, the filtered values will be multiplied by constants making the weighting according to the position of the IR sensor on the robot, similar to the action of avoiding obstacles.

At this point, there will be a preliminary assessment of the value generated to adjust the distance between the robots in the queue. A constant concern during the following process is to keep a regular distance between the sensor and the light source. We must regulate this distance in an appropriate value because a very long distance can represent the loss of contact with the forward robot and a very short distance can cause an unwanted impact with the robot. This assessment consists of two tests: (i) for small distances and (ii) for large distances.

The first situation (i) is indicated by a high value of the front sensors. Thus, a slowdown is performed in 10% of the generated value to avoid a collision with the forward robot. Similarly, for the second situation (ii), we performed the acceleration at 25% of the generated value based on the analysis of the last three front values. If the values are in decreasing order we will have an increase of the distance and the acceleration process is started to correct this action. After this evaluation stage, the process is similar to that performed by the function to avoid obstacles. Where we will make a limitation of the generated values to prevent the stepper motors from physical damage caused by excessive speeds.

The process of value generation that will drive the motor for the action of following the light is then described by Algorithm 4:

Algorithm 4. Following the light action

Require: **Signal** (signal that indicates when the filtering process has been completed), **K** (vector with the constants of the sensors), **Vmotor** (calculate variable), **Vlimit** (threshold value for the motor drive), **VectorF** (vector with the filtered values from the sensors), **Front_Sensors** (values corresponding to the front sensors), **Ref** (reference value);

- 1: read **Signal**;
- 2: **if** $Signal = 1$ **then**
- 3: finish program;
- 4: **end if**
- 5: /* Checks if the values are valid ($Signal = 1$) */
- 6: $Signal \leftarrow 0$;
- 7: /* Assignment of values for invalid ($Signal \neq 1$) */
- 8: **for** $i = 0 \rightarrow 7$ **do**
- 9: read **VectorF**(i);
- 10: $Vmotor \leftarrow Vmotor + k(i) \times VectorF(i)$;
- 11: **end for**
- 12: /* Generation of the value for driving the motor */
- 13: read **Front_Sensors**;
- 14: **if** $Front_Sensors > Ref$ **then**
- 15: $Vmotor \leftarrow 0.9 \times Vmotor$;
- 16: **end if**
- 17: **if** **Front_Sensors** are decreasing **then**
- 18: $Vmotor \leftarrow 1.25 \times Vmotor$;
- 19: **end if**
- 20: /* Evaluation of distance with the forward robot */
- 21: **if** $Vmotor > Vlimit$ **then**
- 22: $Vmotor \leftarrow +Vlimit$;
- 23: **end if**
- 24: **if** $Vmotor < -Vlimit$ **then**
- 25: $Vmotor \leftarrow -Vlimit$;
- 26: **end if**
- 27: /* Limiting the value for driving the motor */
- 28: $Motor \leftarrow Vmotor$;
- 29: **return** **Motor**;
- 30: /* Return value for driving the motor */

3.3 Using Agendas

The execution routines of the functions that perform the displacement of the robot (follow and avoid), and the functions of sub-sampling and rear flashing LEDs are managed by a cycle of processes called *agendas*. Each agenda is responsible for executing a function in a period of preset time called cycle.

Thus, agendas are interconnected so that the execution of an agenda starts soon after the end of its ancestor. Fig. 3 shows the block diagram for a process of four agendas. In this project, a process for four agendas is executed, with their respective cycles: avoid (15ms), follow (20 ms), blink (14.3 ms) and filtering (5ms).

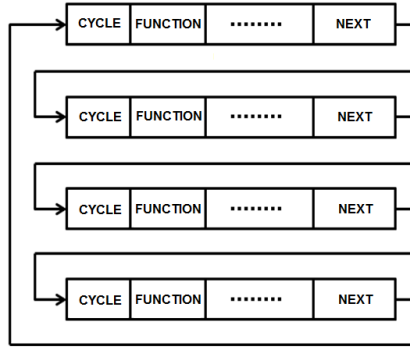


Fig. 3. Block diagram of the operation of four agendas

4 Digital Filter

For the design of the digital filter an analogical Butterworth filter of first order [11], [12], [13] was originally designed. This approach was chosen due to its ease of construction aggregating a low computational complexity to the program. Fig. 4 shows the Bode Diagram (magnitude and phase) of the analog filter designed by the Equation 1:

$$T(s) = \frac{1257s}{s^2 + 1257s + 1934X10^5}, \tag{1}$$

where the variable s represents the continuous time. The filter has a selective characteristic because of its BP configuration, in order to directing a proportionately greater gain to the vicinity of its center frequency.

Next, the discretization of the BP filter is performed by the method of *bilinear numerical integration* [14]. Subsequently, a compensation is applied for the linear distortion of phase *warping* caused by this method. Thus we have the discrete transfer function $T(z)$ shown in Equation 2:

$$T(z) = \frac{0.5361z^2 - 0.5361}{z^2 + 0.5453z - 0.07224}, \tag{2}$$

where the variable z represents the discrete time, which will provide us the difference equation $Y[n]$, shown in Equation 3:

$$Y[n] = -0.54531y[n - 1] + 0.07224y[n - 2] + 0.536u[n] - 0.536u[n - 2], \tag{3}$$

where n is a variable. Equation 3 represents the filter and was implemented in the program.

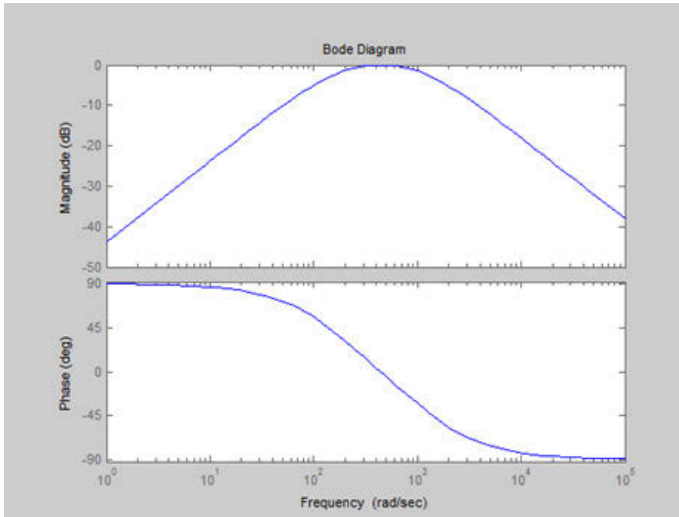


Fig. 4. Bode diagram for the analogical filter

The complete filtering function for the sensor zero is shown in Algorithm 5 below:

Algorithm 5. Filtering algorithm for the sensor 0

Require: `Vector_Sensors` (vector which containing the values of the eight sensors),
`Vsensor0` (value of sensor 0), `Filter` (function that performs filtering);

- 1: `Vsensor0` \leftarrow `Vector_Sensors(0)`;
- 2: /* Stores the value of the sensor before the filter */
- 3: run `Filter`;
- 4: update `Vector_Sensors`;
- 5: **return** `Vsensor0_af`;
- 6: /* value of sensor 0 after the filter */

After the filtering, the signal goes through stages of rectification and linearization [15]. In the rectification stage, the filtered signal is rectified so that it has only positive values. Next, in the linearization stage, the arithmetic average of last values is performed. This stage aims to: (i) minimize the influence of discrepant random values and (ii) linearize the resulting signal seeking to smooth the movement performed by the robot motors.

The process of implementing these three steps is shown as an example for the sensor zero by the Algorithm 6.

Algorithm 6. Steps of the filtering process

Require: `Vector_Sensors` (vector which containing the values of the eight sensors), `Vsensor0` (value of sensor 0), `Filter` (function that performs filtering), `Absolute` (function that performs the absolute value of the sensor value), `Average` (functions that executes the average the value of the sensor with some of their previous values);

- 1: read `Vector_Sensors`;
- 2: read `Vsensor0`;
- 3: run `Filter`;
- 4: update `Vector_Sensors`;
- 5: read `Vector_Sensors`;
- 6: read `Vsensor0`;
- 7: run `Absolute`;
- 8: update `Vector_Sensors`;
- 9: read `Vector_Sensors`;
- 10: read `Vsensor0`;
- 11: run `Average`;
- 12: update `Vector_Sensors`;
- 13: /* Generates a new value for the sensor 0 */
- 14: `Signal` \leftarrow 1;
- 15: **return** `Signal`;
- 16: /* Indicates that the filtering process has been completed */

5 Results

The tests were conducted for a group of up to five robots E-Puck with the code developed. The objectives of the tests were: (*i*) to achieve the original objective of queue formation and (*ii*) to obtain a behavioral analysis of the code for an interaction with multiple robots.

The main objective (*i*) of queue organization for a group of robots was achieved with good results. In these tests, the robots were placed in random positions on the environment and during the tests are showed the behavior of approach and formation of a single group with queue organization. Some behaviors were observed during the test of the group:

- Exchange of position between robots with queue formation during the action of deviation;
- Temporary cyclical behavior with a queue formation connecting the first to the last robot during the action of deviation.

Fig. 5 shows the results of tests for the main objective (*i*) of this project. In this example, a group of four robots starts their movements with random positions. After, they perform the actions of grouping and getting closer to each other, to form a queue.



(a) Initial random locations



(b) Pairs of robots attempting to achieve sub-formation



(c) Reaching a partial objective with 2 queues



(d) Sub-groups formed getting closer



(e) Sub-groups getting even more closer while avoiding obstacle



(f) Improving global objective



(g) Improving global objective by getting closer while avoiding obstacle



(h) Achieving global queue formation

Fig. 5. Example of initial queue organization

6 Conclusions

In this work, successful tests were shown with a group of E-Puck robots in the context of swarm robotics. The collective behavior of queue organization was observed, using IR communication.

The digital filter to treat the signal received by the IR sensors represented a major difference in the results. The filtered data improved the communication between the robots, yielding an increase in final speed of the robot. The linearization stage led to an improvement in the quality of movements performed by the stepper motors, making the robot's movements smoother and more natural.

Unlike most papers founded in the literature, we chose to use a one-way communication process. This choice represented a low computational cost for the E-Puck's dsPIC microcontroller. A demonstrative video is available at <http://www.youtube.com/watch?v=nFG1JpaxUPw>.

Acknowledgments. We are grateful to FAPERJ (*Fundação de Amparo à Pesquisa do Estado do Rio de Janeiro*, <http://www.faperj.br>) and CNPq (*Conselho Nacional de Desenvolvimento Científico e Tecnológico*, <http://www.cnpq.br>) and CAPES (*Coordenação de Aperfeiçoamento de Pessoal de Ensino Superior*, <http://www.capes.gov.br>) for their continuous financial support. The author thanks Jan Dyre Bjercknes of the Bristol Robotics Laboratory for his help in studying the development of digital filters.

References

1. Bonabeau, E., Dorigo, M., Theraulaz, G.H.: *Swarm Intelligence: From Natural to Artificial Systems*. Oxford University Press Inc., New York (1999)
2. Ddriche, O.: La prise de dcision au sein d'un groupe de robots: Conception et dveloppement d'une plateforme de travail libre et gratuite pour lesrobots e-puck destination de la communaut acadmique, et tude d'un comportement collectif auto-organis via une tache d'agrgation en robotique en essaim. Universite Libre de Bruxelles, Brussels (2007)
3. Olivier, M., Rohrer, F., Heiniger, N.: *Cyberbotics' Robot Curriculum*. Technical report, Cyberbotics Ltd. (2009), <http://www.cyberbotics.com>
4. Mondada, F., Bonani, M.: Tutorial for programming the e-puck robot using the bootloader via Bluetooth. Technical report, EPFL - cole polytechnique fdrale de Lausanne, Autonomous Systems Laboratory (2006), <http://www.e-puck.org>
5. Ferreira, D.S.M., Junior, J.M.T.: *Webots*. Universite Libre de Bruxelles, Brussels, Federal University of Grande Dourados (2010)
6. Mondada, F., Bonani, M., Raemy, X., Pugh, J., Cianci, C., Klaptoz, A., et al.: The e-puck, a Robot Designed for Education in Engineering. In: 9th IEEE/RAS Conference on Autonomous Robot Systems and Competitions, vol. 1(1), pp. 59–65. IEEE Press (2009)
7. Microchip Technology Inc., Technical report, dsPIC30F6014A (2006), <http://www.microchip.com>
8. Microchip Technology Inc., Technical report, Getting Started with CCS C in MPLAB IDE (2005), <http://www.microchip.com>

9. Microchip Technology Inc., Technical report, MPLAB Starter Kit for Serial Memory Products User's Guide (2008), <http://www.microchip.com>
10. Siegwart, R., Nourbakhsh, I.R.: Introduction to Autonomous Mobile Robots, 2nd edn. MIT Press Inc. (2004)
11. Hayes, M.H.: Processamento Digital de Sinais. Artmed Editor, Schaum collection (2006)
12. Daryanani, G.: Principles of Active Network Synthesis and Design. John Wiley and Sons Editor, Bell Telephone Laboratories
13. Ogata, K.: Modern Control Engineering, 4th edn. Pearson Education International Editor (2002)
14. Smith, S.W.: The Scientist and Engineer's Guide to Digital Signal Processing. Independent edn. (2002)
15. Bjercknes, J.D.: Scaling and fault tolerance in self-organized swarms of mobile robots. Phd thesis, University of the West of England, Bristol (2010)

Swarm Grid: A Proposal for High Performance of Parallel Particle Swarm Optimization Using GPGPU

Rogério M. Calazan¹, Nadia Nedjah², and Luiza de Macedo Mourelle³

¹ Department of Communication and Information
Technology of Brazilian Navy, Brazil
rgc.moraes@gmail.com

² Department of Electronics Engineering and Telecommunications

³ Department of Systems Engineering and Computation
Faculty of Engineering
State University of Rio de Janeiro, Brazil

Abstract. The Particle Swarm Optimization or PSO is heuristics-based optimization, in which the solution candidates of a problem go through a process that simulates a simplified model for social adaptation. Of course, parallel implementations of PSO can provide better performance. However, this depends on heavily on the number and characteristics of the exploited processors. With the advent and large availability of General Purpose Graphics Processing Units and the development and straightforward applicability of the Compute Unified Device Architecture platform, several applications are being benefited by the reduction of the computing time. In this paper, we propose a massively parallel algorithm of PSO and implement it using a GPGPU-based architecture, aiming at improving the performance of computationally demanding optimizations. We show that, for identifiable specific mapping parameters, one can reduce total execution time drastically and also, improve greatly the optimization process convergence. These parameters include the number of swarms and that of particles per swarm, together with their mapping into blocks and threads, respectively. All the swarms and particles therein operate in parallel and synchrony.

Keywords: PSO, GPGPU, CUDA.

1 Introduction

Swarm Intelligence is a field of artificial intelligence wherein a decentralized collective behavior of individuals, that interact with each other as well as with the environment, is at the basis to infer an intelligent decision with respect to a given problem.

PSO was introduced by Kennedy and Eberhart [1] and is based on collective behavior, social influence and learning. Many successful applications of PSO are reported, in which this algorithm has shown many advantages over other algorithms based on swarm intelligence, mainly due to its robustness, efficiency and

simplicity. Moreover, it usually requires less computational effort when compared to other evolutionary algorithms [2].

The PSO algorithm maintains a swarm of particles, where each of which represents a potential solution. In analogy with the evolutionary computation paradigms, a *swarm* can be identified as the population, while a *particle* with an individual. In general terms, the particle flows through a multidimensional search space, where the corresponding position is adjusted according to its own experience and that of its neighbors [2].

In recent years, the use of Graphic Processing Units, or GPUs, has been exploited for some general purpose computing applications. GPUs have shown great advantages on applications that require intensive yet independent computations. Despite the fact that GPU-based architectures require an additional CPU time to assign tasks to the available units, the speedup obtained by the former in relation to simple CPU architectures is higher for applications, wherein the processing effort is much more focused on floating-point and matrix handling operations. The major benefit of a PSO implementation using a GPU-based architecture is the possibility to reduce the execution time. It is actually quite probable since the fitness evaluation and the update processes of the particles are somehow independents and so can be parallelized and executed simultaneously via different threads.

Several works show that PSO implementation in GPGPU provide a better performance than CPU-based implementations [10] [11] [12]. In contrast, the purpose of this paper is to implement the Global Best version of PSO, which will be explained later on, in GPGPU. The proposed implementation first splits the search domain into a grid of smaller cell spaces. Then, it forms and assigns swarms to search their respective cells. However, within each swarm, particles act in parallel until a synchronization point, during which they exchange knowledge acquired so far, individually. This should favor the resolution of optimization problems of high dimensionality as threads that simulate particles keep iterating the same process fitness computation according to each dimension. A analysis that results in identifying the number of swarms and particle per swarm as well as how to map the swarms into blocks and particles into threads, respectively as to maximize performance. Furthermore, we study the impact of the grid resolution on the convergence time. The grid resolution is defined by the number of cells used. It coincides with the number of swarms invested in the search.

This paper is organized as follows: First, in Section 2, we present some related works; Then, in Section 3, we sketch briefly the PSO process and the algorithm; After that, in Section 4, we introduce some background information and concepts about GPU-based computing; Thereafter, in Section 5, we describe an implementation of the massively parallel PSO proposed algorithm suitable for GPGPU platform; Subsequently, in Section 6, we present and analyze the obtained results; Finally, in Section 7, we draw some concluding remarks and point out directions for future work.

2 Related Works

In [10], the authors report on an implementation of the particle swarm optimization algorithm in CUDA. The algorithm is tested on a well-known benchmark optimization problems and the computing time is compared with same algorithm implemented in C and Matlab.

In [11], the authors present an approach to run standard particle swarm optimization on GPU. The results was compared with CPU and third party GPU implementations. The implementation on GPU showed special speed advantages on large swarm population applications and high dimensional problems. The ring topology was used.

An alternative GPGPU PSO implementation is present is [12]. The authors show performance analysis for high dimension problems. Unlike the work presented here, only the fitness evaluation is executed by the GPU while the PSO main steps are performed in the host CPU.

In [13], the authors present a SIMT-PS² model that combines CPU and GPU codes in the particles best solution updates. The authors carried out the analysis for a ring topology. A pattern search improvement phase is added to the traditional PSO steps to speed up convergence. Unlike this implementation, our goal is to increase the convergence using the star global topology while maximizing the execution time within the GPU. We expect an improvement of the performance due to the mapping of swarms into blocks and particles into threads.

3 Particle Swarm Optimization

The main steps of the PSO algorithm are described in Algorithm 1. Note that, in this specification, the computations are executed sequentially. In this algorithm, each particle has a *velocity* and an *adaptive direction* [1] that determines its next movement within the search space. The particle is also endowed with a memory that makes it able to remember the best previous position that it passed by.

3.1 Global Best PSO

In this variation of the PSO algorithm, the neighborhood of each particle is formed by all the population particles. Thus, it can be viewed as the star topology, as shown in Fig. 1. Using this strategy, the social component of the particle velocity is influenced by all other particles [2] [3]. The velocity is the element that promotes the capacity of particle locomotion and can be computed as described in (1) [1] [2], wherein w is called *inertia weight*, r_1 and r_2 are random numbers in $[0,1]$, c_1 and c_2 are positive constants, y_{ij} is the best position $Pbest$ found by the particle i so far w.r.t. dimension j and y_j is the best position $Gbest$ w.r.t. dimension j , found so far, considering all the population particles.

The position of each particle is updated according as described in (2). Note that $x_{ij}(t+1)$ is the current position and $x_{ij}(t)$ is the previous position.

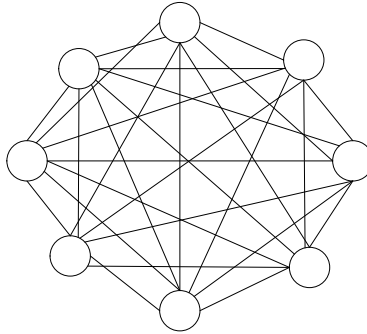
$$v_{ij}(t+1) = wv_{ij}(t) + c_1r_1(y_{ij} - x_{ij}(t)) + c_2r_2(y_j - x_{ij}(t)) \quad (1)$$

Algorithm 1. PSO

```

for  $i = 1$  to  $n\_particles$  do
  Initialize the information of particle  $i$ 
  Randomly initialize position and velocity of particle  $i$ ;
end for;
repeat
  for  $i = 1$  to  $n\_particles$  do
    Compute the  $Fitness_i$  of particle  $i$ ;
    if  $Fitness_i \leq Pbest$  then
      Update  $Pbest$  using the position of particle  $i$ ;
    end if;
    if  $Fitness_i \leq Gbest$  then
      Update  $Gbest$  using the position of particle  $i$ ;
    end if;
    Update the velocity of particle  $i$ ;
    Update the position of particle  $i$ ;
  end for;
until Stopping condition is true
return  $Gbest$  and corresponding position;

```

**Fig. 1.** Star social topology

$$x_{ij}(t+1) = v_{ij}(t+1) + x_{ij}(t) \quad (2)$$

The velocity component drives the optimization process, reflecting both the experience of the particle, and the exchange of information between the particles. The particle experimental knowledge is referred to the cognitive behavior, which is proportional to the distance between the particle and its best position found w.r.t. its first iteration [3].

The maximum velocity is defined for each dimension i of the search space, and can be formulated as a percentage of the domain, according to Equation 3 where x_{max} and x_{min} are respectively the maximum and minimum value of the domain and $\delta \in [0, 1]$.

$$v_{i,max} = \delta(x_{i,max} - x_{i,min}) \quad (3)$$

4 GPU Computing

Because of a growing market demand for real-time applications for high-definition 3D graphics, the programmable Graphic Processor Unit or GPU has evolved into a highly parallel, multi-threaded, many-core processor with tremendous computational power and very high memory bandwidth [6].

The GPU is especially well-suited to address problems that can be expressed as data-parallel computations, i.e. the same program is executed on many data elements in parallel, with high arithmetic intensity, i.e. large ratio of arithmetic operations to memory operations. Because the same program is executed for each data element, there is a lower requirement for sophisticated flow control. Moreover, because it is executed on many data elements and has high arithmetic intensity, the memory access latency can be overcome with calculations instead of big data caches [8] [6].

NVIDIA CUDA technology is a C language environment that enables programmers to develop software that solve complex computational problems by investing into the many-core parallel processing power of GPUs [6] [9].

In the CUDA programming model, all threads in a grid execute the same kernel function. Thus, each thread is assigned a unique identifier to distinguish it from others. Besides, groups of threads are organized into blocks and, hence, have access to a fast local shared memory and can be synchronized using a barrier synchronization function. On the other hand, threads in different blocks cannot be synchronized via barriers. Each block is also assigned a unique identifier.

Once a block is assigned to an SM, it is split into *warps*, which are groups of 32 threads with consecutive identifiers. Each block can include up to 1024 threads. A *warp* is scheduled for execution by a *Warp Scheduler*. Thus, if the instruction, say i , that is being executed is waiting for a previous one whose completion is delayed due to a required long-latency operation, then a different *warp* may be selected for execution. This allows for a better exploitation of SM the resources. The technique is called *latency hiding*.

CUDA's hierarchy of threads is mapped to an hierarchy of processors on the GPU. A GPU executes one or more kernel grids. The streaming multiprocessor executes one or more blocks of threads. CUDA cores and other execution units in the SM execute threads [6].

5 Implementation of PSO on GPGPU

The purpose of this paper is to implement the Global Best PSO in GPGPU. The main novel idea is to subdivide the search space into as um grid of cells, where each cell is searched by a swarms in order to find out the solution of high dimension optimization problems. We study the impact of the number and size of the swarms on the optimization process, in terms of the execution time, convergence and quality of the solution found. The swarm size is defined in terms of the number of invested particles.

The dimension and size of blocks per grid and the dimension and size of threads per block are both important factors. The number of blocks in a grid

should be at least the same or larger than the number of streaming multiprocessors so that all available SM have at least one block to execute. Furthermore, there should be multiple active blocks per SM so that blocks that are not waiting for a `_syncthreads()` can keep the hardware busy. This recommendation is subject to resource availability. Therefore, it should be determined in the context of the second execution parameter, which is the number of threads per block, or block size as well as shared memory usage.

Higher occupancy of the infrastructure of the GPU does not always lead a better performance of the process being executed by the GPU. For example, improving occupancy from 66% to 100% generally does not translate into a similar increase in performance. A lower occupancy kernel will have more registers available per thread than a higher occupancy one, as the former case may result in less register spilling to local memory.

5.1 Swarm Grid Parallel PSO

Aiming at improving the performance of the PSO, Algorithm 1 has been parallelized as shown in Fig. 2, where the domain of problem is subdivided between many swarms and each particle performs its fitness velocity and position computation, independently and in parallel with the other particles until the election of $Gbest$. In order to synchronize the process and prevent using incorrect values $Gbest$, the velocity and position computations can only commence once $Gbest$ have been chosen among $Pbest$ of all particles of the respective swarm [4] [5].

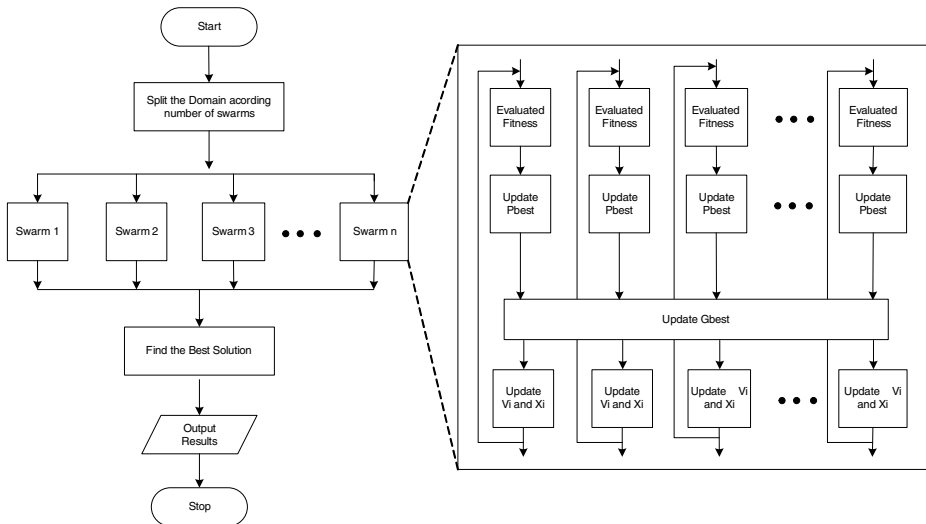


Fig. 2. Illustration of Swarm Grid

The global topology is the structure proposed in the first PSO approach and is still used. It uses a global neighborhood mechanism. Particles can share information globally through a fully-connected structure. This arrangement leads to a fast convergence, since the information spreads quickly.

In Parallel implementation, the maximum velocity $v_{i,max}$ with respect to dimension i is formulated as a percentage of the sub-domain Sd_i for that dimension, as defined in (4), where $x_{i,max}$ and $x_{i,min}$ are the maximum and minimum value of the whole search domain and $0 \leq \delta \leq 1$.

$$\begin{aligned} Sd_i &= (x_{i,max} - x_{i,min}) / \text{number of swarms} \\ v_{i,max} &= \delta * Sd_i \end{aligned} \quad (4)$$

In order to increase the efficiency of the algorithm in high dimensions, we use dynamic update of the inertia weight, w in equation 11.

5.2 PSO Implementation in CUDA

In order to implement the algorithm using CUDA, we opted to exploit two kernels. The first kernel generates random numbers and stores them in the GPU global memory. The second kernel runs all the remaining steps of the parallel PSO. This way, the host CPU, after triggering the PSO process, becomes totally free. Using a single kernel for the whole PSO, excluding the random number generation, allows us to optimize the implementation as there is no need for host/device communications. Recall that the PSO (kernel) implementation updates the inertia weight dynamically.

As introduced earlier, the problem search domain is organized into a grid of swarms, wherein each swarm is implemented as a block and each particle as a thread. The grid size is the number of swarms and block size is the number of particles. So, population size can be defined as the product of the grid size and block size, and this coincides with the total number of threads run by the GPU infrastructure. In this implementation, the position, velocity and $Pbest$ of all the particles are kept in the global memory on the GPU chip. Nonetheless, the $Gbest$ obtained for all the grid's swarms are stored in the shared memory of respective SM. The CUDA pseudo-code for swarm grid PSO is shown in Algorithm 2.

5.3 Random Number Generation

During the execution of optimizations, the algorithm PSO needs a considerable amount of random numbers for velocity updates. In order to generate random numbers efficiently in GPGPU, we used the CURAND library [7]. The CURAND library provides facilities that focus on the simple and efficient generation of high-quality pseudo-random and quasi-random numbers. This implementation generates random numbers in GPU and store them in global memory. This way, we keep the CPU free and thus, avoid host/device data transfer.

Algorithm 2. CUDA Swarm Grid PSO

```

// host code
set the blocksize and gridsize
initialize domain information
initialize random number generator on GPU

// device code
generate random number

// host code
initialize domain information
transfer data from CPU to GPU
// device code
split the domain according to number of Swarms
initialize the information of all particle
Randomly initialize position and velocity of all particle
repeat
  compute fitness of all particles with respect to n dimensions
  update Pbest of each particle
  update Gbest of each particle
  update velocity and position of each particle;
until stopping condition
transfer result back to CPU

// host code
return Gbest and corresponding position;

```

5.4 Fitness Functions

Three functions are implemented in order to assess the execution time and performance of the proposed implementation. These are shown in Table 1. The f_1 defines a Sphere, f_2 is Griewank function and f_3 is the Rastrigin function.

Table 1. Fitness Functions

Function	n	Domain	f_{min}
$f_1(x) = \sum_{i=1}^n (x_i^2)$	30	$(-100, 100)^n$	0
$f_2(x) = 1 + \frac{1}{4000} \sum_{i=1}^n x_i^2 - \prod_{i=1}^n \cos\left(\frac{x_i}{\sqrt{i}}\right)$	30	$(-600, 600)^n$	0
$f_3(x) = \sum_{i=1}^n (x_i^2 - 10\cos(2\pi x_i) + 10)$	30	$(-10, 10)^n$	0

6 Results and Analysis

The architecture was implemented on a NVIDIA GeForce GTX 460 GPU [6]. This GPU contains 7 SMs with 48 CUDA cores each, hence a of total 336 cores.

Three classical benchmark functions, as listed in Table 1, are used to evaluate the implementation performance.

In the following, we report on the experiments performed to analyze the impact of the swarm grid size and the particle numbers per swarm on the execution time while keeping the total number of particles constant. Then, we study the impact of these parameters while increasing the total number of particles. Recall that the swarm grid size and the particle numbers per swarm coincide with the block number and size, respectively. In both experiments, we always run the PSO algorithms for 2000 iterations.

6.1 Changing the Swarm Number

Using the CUDA Occupancy calculator [6], the GPU occupancy, which depends on the number of threads per block and that of register as well as the size of the kernel shared memory, amounts to 67%. Note that in all verified cases of different pairs of number and size of blocks per SM, the total number of 7168 threads was kept constant. Nonetheless, the disposition of block and thread numbers had significant impact on the performance. Table 2 shows the combinations of grid size and particle numbers and the optimization time for the benchmark functions in Table 1. Fig. 3 shows that despite the fact that the total number of particle is the same in all checked dispositions of number of swarms and particles per swarm, the combination 56×128 lead to the lowest execution time.

The increase of execution time can be explained by the work granularity level that each block of threads is operating at. Parallel computation of position coordinates and the subsequent velocity are performed by all threads within a block, but conditional branches, used to elect P_{best} and G_{best} as well as loops that allow the iteration of the work for each one of the problem dimension dominate most part of the thread computation. It is well-known that conditional constructions are not well suited for the Stream Processing model.

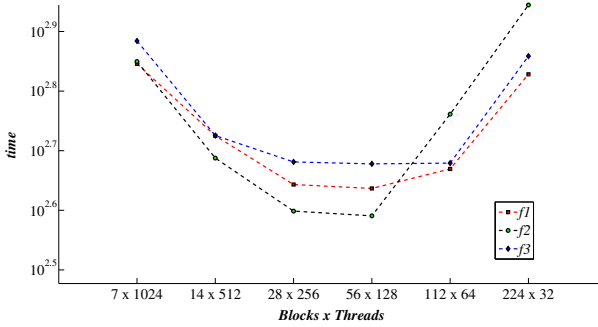
Also, the performance degenerates because more blocks of threads are competing the resources available to the SMs. A GPU offers a limited amount of CUDA memory, which limits the number of threads that can be simultaneously executed in the SM for a given application. In general, the more memory each thread requires, the fewer the number of threads that can reside in the processor [8]. Therefore, the choice of pair (block number and block size) has the kind of effect on the execution time illustrated in Fig. 3.

6.2 Changing the Swarm Size

In large dimension problems, it is expected that the number of particles influences positively the convergence speed of the optimization process, yet it has a negative impact on the corresponding processing time. Increasing the number of particles can be achieved by either increasing the number of swarms and/or the number of particles per swarm. We opted to keep the number of particles in a given swarm constant, i.e. 128, and increase the number of swarms.

Table 2. Disposition of number of swarms and particles per swarm together with the achieved execution time (ms) of the optimization of f_1 , f_2 and f_3

#Swarms \times #Particles	f_1	f_2	f_3
7×1024	707.42	701.15	765.83
14×512	487.04	530.95	531.35
28×256	396.84	439.78	479.88
56×128	389.65	433.21	476.28
112×64	577.24	467.01	477.69
224×32	879.94	673.23	722.12

**Fig. 3.** Execution Results

The latter was set as a multiple of the available streaming multiprocessors. Recall that the GPU used here includes 7 SMs. Table 3 shows the results for different configurations of total swarm size. It includes the total processing time as well as the reached pseudo-optimal solution for f_1 , f_2 and f_3 .

The charts of Fig. 4 illustrates of the optimization time comparison for the different studied configurations, w.r.t the three used functions while the chart of Fig. 5 depicts the comparison of the quality of the found optimal solution. Considering both charts, it is easy to note that for at most 56 swarms, which entails $56 \times 128 = 7168$ particles at most, the increase in terms of processing time is justified as the quality of the best solution is improved proportionally. However, for the case of 112 swarms, i.e. 14336 particles, the found solutions has not improved much whilst the execution time has worsened considerably. This kind of behavior is due the fact that the GPU used presents 7 SMs that can run 32 warps, each of which of 32 threads, simultaneously tracked and scheduled. Thus, this GPU can run $7 \times 32 \times 32 = 7168$ threads in parallel. The case wherein 56 swarms are used makes a good trade-off between the execution time and optimal solution quality. The convergence behaviors for the studied cases w.r.t. f_1 , f_2 and f_3 are shown in Fig. 6.

Table 3. Number of swarms and with the achieved Fitness result of the optimization of f_1 , f_2 and f_3

F	7 swarms*		14 swarms*		28 swarms*		56 swarms*		112 swarms*	
	time	solution	time	solution	time	solution	time	solution	time	solution
f_1	191.12	0.000598	218.11	0.000168	265.60	0.000014	571.85	0.000002	1130.17	0.000002
f_2	194.30	0.003830	201.47	0.045672	251.19	0.000735	455.30	0.000074	970.76	0.000010
f_3	279.15	0.010572	298.71	0.032246	335.04	0.000493	483.73	0.000008	1066.17	0.000004

*Each swarm has 128 particles.

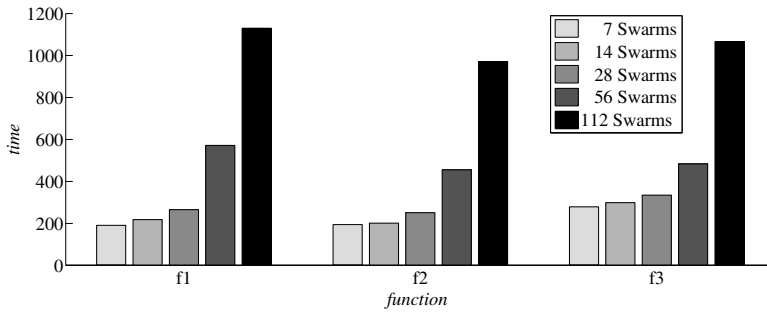


Fig. 4. Impact of the Swarm size on the total optimization time

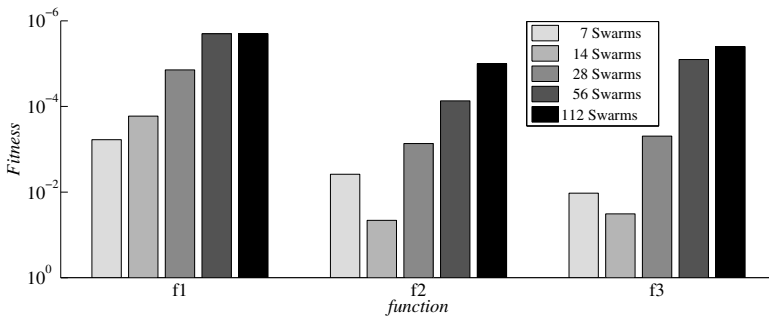


Fig. 5. Impact of the Swarm size on the optimization result

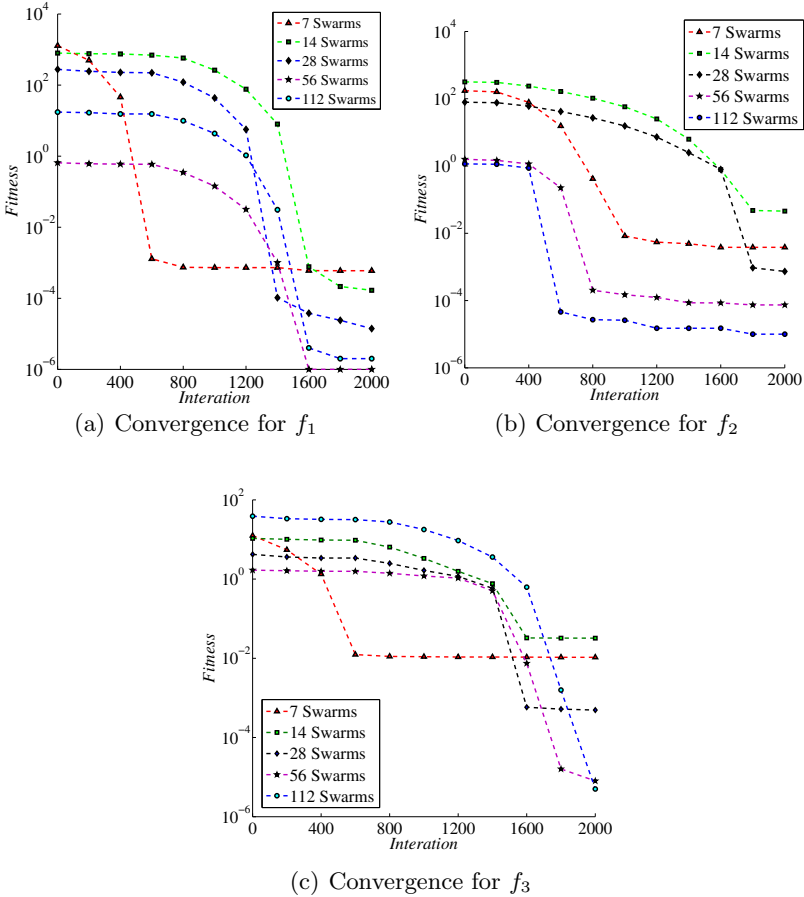


Fig. 6. Convergence f_1 , f_2 and f_3

7 Conclusion

This paper presents an implementation of parallel PSO using GPGPU. Aiming at high performance optimization of large dimension problems, the algorithm implemented divides the search space into a grid of sub-domains and assigns a particle swarm to each and every one of them. The implementation exploits the parallelism of the particle computation of the corresponding positions and velocities as well as the fitness value of the solution associated to the particle. This is performed independently of the others particles of the swarm. A swarm of particles was implemented as a block of threads, wherein each thread simulates a single particle. A two-fold analysis was carried on to evaluate the performance of the proposed parallel implementation: first, the impact of the number of invested swarms; then the impact of their size. The social structure used in this study is the star network.

The results show that the execution time can be optimized for a specific grid size and block size. We also observed that an increase in the total number of particle w.r.t. all swarms for the large dimensions problems used as benchmarks is important for finding better optimal solutions in less time. The scalability of the implementation depends solely, on the number of SMs and CUDA Cores of the device.

Future works include the evaluation of the swarm grid organization with other social network structure, such as ring and clusters. Moreover, we intend to investigate the parallelism within the computation of the particle position and velocity, considering each dimension of the search space.

References

1. Kennedy, J., Eberhart, R.: Particle Swarm Optimization. In: IEEE International Conference on Neural Network, pp. 1942–1948. IEEE Press, Australia (1995)
2. Engelbrecht, A.P.: Fundamentals of Computational Swarm Intelligence. John Wiley & Sons Ltd., New Jersey (2005)
3. Nedjah, N., Coelho, L.S., de Macedo Mourelle, L.: Multi-Objective Swarm Intelligent Systems – Theory & Experiences. Springer, Berlin (2010)
4. Calazan, R. M., Nedjah, N., de Macedo Mourelle, L.: Parallel co-processor for PSO. *Int. J. High Performance Systems Architecture* 3(4) (2011)
5. Calazan, R.M., Nedjah, N., de Macedo Mourelle, L.: A Massively Parallel Reconfigurable Co-processor for Computationally Demanding Particle Swarm Optimization. In: 3rd International Symposium of IEEE Circuits and Systems in Latin America — LASCAS 2012. IEEE Computer Society Press, Los Alamitos (2012)
6. NVIDIA: NVIDIA CUDA C Programming Guide, Version 4.0 NVIDIA Corporation (2011)
7. NVIDIA: CURAND Library, Version 1.0, NVIDIA Corporation (2010)
8. Kirk, D.B., Hwu, W.-M.W.: Programming Massively Parallel Processors. Morgan Kaufmann, San Francisco (2010)
9. Sanders, J., Kandrot, E.: CUDA by Example, An Introduction to General-Purpose GPU Programming. Addison-Wesley, San Francisco (2010)
10. Veronese, L., Krohling, R.A.: Swarm’s flight: accelerating the particles using C-CUDA. In: 11th IEEE Congress on Evolutionary Computation, pp. 3264–3270. IEEE Press, Trondheim (2009)
11. Zhou, Y., Tan, Y.: GPU-based parallel particle swarm optimization. In: 11th IEEE Congress on Evolutionary Computation (CEC 2009), pp. 1493–1500. IEEE Press, Trondheim (2009)
12. Cádenas-Montes, M., Vega-Rodríguez, M.A., Rodríguez-Vázquez, J.J., Gómez-Iglesias, A.: Accelerating Particle Swarm Algorithm with GPGPU. In: 19th Euro-micro International Conference on Parallel, Distributed and Network-Based Processing (PDP), pp. 560–564. IEEE Press, Cyprus (2011)
13. Zhu, W., Curry, J.: Particle Swarm with graphics hardware acceleration and local pattern search on bound constrained problems. In: IEEE Swarm Intelligence Symposium, SIS 2009, pp. 1–8. IEEE Press, Nashville (2009)

An Artificial Immune System Approach to Associative Classification*

Samir A. Mohamed Elsayed**, Sanguthevar Rajasekaran, and Reda A. Ammar

Computer Science Department, University of Connecticut

Abstract. Associative Classification (AC) mining is a promising approach that uses association rules discovery techniques to construct association classifiers. However, traditional AC algorithms typically search for all possible association rules to find a representative subset of those rules. Since the search space of such rules may grow exponentially as the support threshold decreases, the rules discovery process can be computationally expensive. One effective way to tackle this problem is to directly find a set of high-stakes association rules that potentially builds a highly accurate classifier. This paper introduces AC-CS, a novel AC algorithm, inspired by the clonal selection of the immune system. The algorithm proceeds in an evolutionary fashion to populate only rules that are likely to yield good classification accuracy. Empirical results on real datasets of different sizes show that the approach generates dramatically less rules than traditional AC algorithms. Hence, the proposed approach is indeed significantly more efficient than traditional AC algorithms while achieving good competitive accuracy.

1 Introduction

The Natural Immune System (NIS) is a distributed, multi-layered, adaptive, dynamic, and life-long learning system. The Artificial Immune System (AIS) is a computational system inspired by the principles and processes of the NIS. The field of AIS has obtained some degree of success as a branch of computational intelligence since it emerged in the 1990s. There have been several successful applications of AIS in computer security, optimization, anomaly detection, and data mining.

Data mining is the process of discovering patterns from large data sets. One of the branches of data mining is Associative Classification (AC). AC algorithms integrate association rules discovery and classification to build a classifier from a training data for predicting the class of unforeseen test data. AC algorithms typically build a classifier by discovering the full set of Class Association Rules (CARs) from the training dataset and then select a subset to form a classifier. CARs are association rules of the form $iset \Rightarrow c$, where $iset$ is an item-set and

* This work is partially supported by the following grants: NSF0829916 and NIH-R01-LM010101.

** The author is partially supported by Helwan University, Cairo, Egypt.

c is a class. Despite achieving high accuracy compared to other classification approaches such as C4.5 [26], the approach suffers from the overhead of exhaustive search through a large pool of candidate rules. Moreover, the rule discovery process in traditional AC algorithms is not well integrated with the classification process.

The main contribution of this paper is **AC-CS**, a new AC algorithm inspired by the Clonal Selection (CS) mechanism of the NIS. Unlike traditional AC algorithms, the algorithm doesn't search for all association rules and then select a subset of them. Rather, **AC-CS** directly populates high quality rules through an evolutionary process. This evolutionary process follows the clonal selection process of cloning, mutating, and pruning populations of rules based on both their support and confidence measures. The process is repeated until the generated rules cover all the training data.

The rest of the paper is organized as follows. Section 2 gives a background about the immune system processes and algorithms as well as the associative classification problem. Section 3 describes the proposed algorithm in details. Experimental results are reported in Section 4. Section 5 concludes with some possible future work.

2 Background

In this section, a brief description of the immune system principles and processes, that computer scientists draw inspiration from when designing AIS algorithms, is presented. A brief summary of one of the major AIS algorithms namely, the clonal selection algorithm, is also presented. In addition, the associative classification approach along with issues of traditional algorithms are discussed.

2.1 The Immune System

The Natural Immune System (NIS) is a complex network of tissues, organs, and chemicals. Its main function is to defend the body against foreign *pathogens* such as bacteria or viruses. NIS recognizes pathogens via a smaller portion on top of them called *antigens*. The main organs of the NIS where the immune cells develop, includes the lymph system, the thymus, and the bone marrow. The immune system protects the body from infection with layered defenses. Physical barriers (e.g., skin) prevent pathogens from entering the body. If a pathogen breaches these barriers, the innate immune system provides an immediate but non-specific response. In many cases, it is able to successfully defend the body. If the innate immune system fails to handle the attack, then the adaptive immune system takes over. The adaptive response is more specific yet slower, resulting in a more effective response. The adaptive immune system can remember past encounters with antigens such that the next time the antigen appears, a more specific and effective response is deployed (the main idea of vaccination).

The main component of the adaptive immune system is lymphocytes which are blood white cells. Lymphocytes consist of two types, namely: *B-cells* and

T-cells. B-cells get produced and develop in the bone marrow. While the T-cells get produced in the bone marrow and then migrate to the thymus to develop.

There are two main types of B-cells, namely: plasma B-cells and memory B-cells. Plasma B-cells are cells that have been exposed to antigens and produce large amounts of *antibodies* (i.e., Y-shaped receptor molecules bound on the surface of a B-cell with the primary role of recognizing and binding, through a complementary match, with an antigen [8]). While *memory* B-cells created in response to high affinity match with antigens, live for a very long time and provide faster future response. B-cells require co-stimulation from other immune cells (e.g., helper T-cells) in order to activate. B-cells undergo a process called *clonal selection*.

AIS is a relatively young field. The first paper by Farmer et al. [14] in the field was published in 1986. However, it was only in the mid-90's that AIS has become a subject area in its own right. There are several works that form the foundation of AIS. Examples of such works include the work by Forrest et al. [15] in 1994 as well as the work by Bersini [6]. There are five major AIS algorithms that have been popular in the literature, namely: negative selection [15,21], clonal selection [11,9], artificial immune networks [20,27], dendritic cells [17], and danger theory algorithms [25].

2.2 The Clonal Selection (CS)

According to Burnet's 1959 clonal selection theory, activation of lymphocytes occurs on binding with a matching antigen [1]. Once activated, *clones* of the lymphocyte are produced in large numbers with identical receptors of the original lymphocyte that encountered the antigen. Any lymphocytes that bind to self's cells are set to die. During the clonal selection of B-cells, the average antibody affinity increases for the antigen that triggered the process. This phenomenon is called *affinity maturation* and is responsible for the fact that upon a subsequent exposure to the antigen, the immune response is more effective due to the antibodies having a higher affinity for the antigen. Affinity maturation is facilitated by a *somatic hyper mutation* and selection mechanisms that occurs during the clonal expansion of B-cells. Somatic hyper mutation alters the specificity of antibodies by introducing random changes to them.

Researchers have tried to draw some inspiration from the clonal selection process, in particular, the antigen driven affinity maturation process of B-cells along with the hyper mutation mechanism. In [10], the authors highlight two features of affinity maturation in B-cells that can be exploited from a computational point. First, the proliferation of B-cells is proportional to the affinity of the antigen that binds it, the higher the affinity, the more clones are produced. Second, the mutations suffered by B-cells are inversely proportional to the affinity of the antigen it binds. Utilizing these two features, De Castro and Von Zuben [11] developed one of the most popular clonal selection inspired algorithm, CLONALG.

There are different variations of clonal selection algorithms in the literature. [9] presents a comparative case study of a handful of such algorithms.

2.3 Associative Classification (AC)

Agrawal, et al. [3] proposed association rules mining for market basket data patterns. Association rules identify correlations among a set of items found in transactions. The input to the association rules mining problem is a set of transactions where each transaction is a set of items. A set of items is also referred to as an *item-set*. A k -item-set is an item-set of size k . There are two measures proposed in [3] that quantify the significance of an association rule, namely, support and confidence ratio. An association rule is an implication $x \Rightarrow y$ where x and y are item-sets in a dataset. The *support* of the rule is the ratio of the number of transactions containing both x and y to the total number of transactions. The *confidence* of the rule is the ratio of the number of transactions that contain y to the number of transactions containing x . The mining of association rules from a set of transactions is the process of identifying all rules having a pre-specified minimum support and confidence. This involves several phases in processing transactions. A k -item-set is said to be *frequent* if the ratio of the number of transactions containing all the items of the k -item-set to the total number of transactions is greater than or equal to the user specified minimum support. Algorithms for finding frequent item-sets typically require multiple passes over the entire dataset.

There are many algorithms for mining association rules in the literature. Apriori [3] is possibly the well-known and most cited algorithm. It uses a breadth-first search strategy and generates candidate item-sets and tests if they are frequent. The key to its success over older algorithms such as AIS [2] and STEM [19] is the fact that it exploits an important property (commonly referred to as Apriori property or downward closure property). This property is the observation that no superset of an infrequent item-set can be frequent. However, generation of candidate item-sets is expensive both in space and time. In addition, support counting involves multiple dataset scans which heavily impact performance. Apriori as well as Apriori-inspired algorithms (e.g., [5]) typically perform well on sparse (i.e., short frequent item-sets) such as the market basket data. However, they perform poorly on dense (i.e., long frequent item-sets) datasets such as census data. This degradation is due to the fact that these algorithms perform as many passes over the database (i.e., high I/O overhead) as the length of the longest frequent pattern [31].

While many algorithms including Apriori use the traditional horizontal data layout, Eclat [32] is probably the first algorithm to introduce a vertical data layout. Eclat is more efficient for long item sets than for short ones. In this algorithm, data is represented as lists of transaction identifiers (one per item). Support counting is performed by simply intersecting these lists. Compared to Apriori and other algorithms, Eclat often performs better on dense rather than sparse datasets. A variation of the algorithm depicted dEclat can be found in [31].

Liu et al. [23] introduced the Classification Based on Associations (CBAs) algorithm which laid the foundation of the AC approach and other algorithms as well (e.g., [22], [24]). The basic idea is to mine the full set of association rules from

a training dataset into Class Association Rules (CARs) in the form of $iset \Rightarrow c$ where $iset$ is an item-set (i.e., body of the rule) and c is a class (i.e., head of the rule). Rules with high confidence are then selected to form the classifier. During the classification process, all test data that match the rule with the highest confidence are assigned the class of that rule.

AIS data mining applications include classification [33,18,13], clustering [8], and rule induction [4]. Most AISs for classification use an instance-based representation. This includes AIRS [30,29,28] and CLONALG [11,12]. In this representation, the candidate solutions considered by the classification algorithm take the form of a subset of the original data instances, each of them with all its attribute values [16]. Another type of representation is the rule-based one. This representation is used, for instance, in IFRAIS [4]: an AIS for discovering fuzzy classification rules. In this representation, the candidate solutions considered by the algorithm take the form of IF-THEN classification rules, where each rule typically contains a conjunction of a few attribute values [16]. Both representations have pros and cons. In [16], the authors argue that it all depends on the nature of the data being mined, the requirements of the application domain, and how important knowledge comprehensibility is to the user.

In [13] the authors propose an algorithm that employs the clonal selection of the immune system to directly find a subset of rules to form the classifier. Empirical results show that the algorithm is particularly efficient when the support threshold is low. In addition, reported accuracy appears to be competitive with a traditional AC algorithm. The approach in this paper is similar to this work.

3 The AC-CS Algorithm

The AC-CS algorithm is inspired by the clonal selection process, in which rules are populated as if they are B-cells that can be cloned, mutated, and pruned as well. Affinity measurements are determined by the confidence of those rules. The objective is to avoid an exhaustive search for all possible rules in an explosive search space as it is the case in traditional AC algorithms.

Prior to describing the algorithm in details, necessary notations and concepts are defined as follows:

- A *class rule* r can be defined as $iset \Rightarrow c$ where $iset$ is an item-set (i.e., body of the rule) and c is a class (i.e., head of the rule).
- The support of r , $support(r)$, is the ratio of the number of transactions that contain all items in both the head and body of the rule, to the the total number of transaction of the data set. This measure helps remove low-stakes rules.
- The confidence of r , $confidence(r)$, is the ratio of the number of transactions that contain the body item-set to the number of transactions that contain both the body and head item-sets of the rule.
- The coverage of r , $coverage(r)$, is the ratio of the number of transactions that are covered by the generated rules to the total number of transactions. The coverage measure has been previously used in [23] to filter the discovered

rules. We use the coverage measure as a termination check to the algorithm. Indeed, if the generated rules managed to cover the whole training data set, then there would be no need to proceed further.

- The clonal rate of r is dictated by the following equation, borrowed from [13]:

$$cloneRate(r) = \frac{n \cdot clonalRate}{\sum_{i=1}^n confidence(r_i)} \cdot confidence(r)$$

where n denotes the number of rules at the current generation, and *clonalRate* is a user defined parameter. The clone rate of the rule is proportional to its confidence (i.e., the higher the confidence, the higher the clone rate).

The proposed algorithm AC-CS, depicted in figure 1, accepts a training dataset of transactions and outputs a set of high quality rules that potentially yield a good accuracy classifier. The algorithm starts off by initializing a few data structures namely: the rule populations P , the frequent singleton items I , and finally the memory pool M that contains the high quality rules found throughout the algorithm (line 1). User-defined parameters are initialized at line 2. At lines (3-11), rules with only single item in the head and have higher support than the given *minSupport* are added to P . In addition, only items that turn out to be frequent are added to the new set of items I . From now on, AC-CS doesn't use the full set of singleton items \mathcal{I} . Rather, it uses the refined set I . Note that I is a subset of \mathcal{I} .

The algorithm proceeds in generations. In each generation, remaining rules from previous generations are cloned in proportional to their confidence (i.e., affinity) which is calculated using the *cloneRate* function above (line 16). For each new cloned rule, the items in the body of the rule are extended (i.e, mutated) by adding one more *new* item (line 19). Only rules with high support are retained (lines 20-21). Next, the remaining rules go through a pruning phase in which redundant rules are removed. For instance, given two rules $r_1 : iset_1 \Rightarrow c$ and $r_2 : iset_2 \Rightarrow c$:

$$iset_2 \subseteq iset_1 \wedge confidence(r_1) > confidence(r_2) \Rightarrow prune(r_2)$$

Upon pruning all the redundant rules, only remaining rules with high confidence are added to the memory pool M (lines 26-30). The process is repeated until either the rules in M cover the entire training dataset or the number of generations exceed the maximum allowed (line 32).

Note that the whole process is repeated for each class in the dataset. Upon completion, all rules in the memory pool M are sorted in a decreasing order of confidence. Sorted rules are then applied one by one to a test data and the accuracy is reported accordingly.

4 Experimental Results

Experiments were performed on real datasets of different sizes obtained from the UCI Machine Learning Repository [1]. These datasets are shown in table 1

¹ <http://archive.ics.uci.edu/ml/datasets.html>

```

1  $P = \{\}; I = \{\}; M = \{\};$ 
2 initialize  $cloneRate, currentGeneration, maxGenerations;$ 
3 foreach item  $i \in \mathcal{I}$ 
4 {
5   set rule  $r = \{i \Rightarrow c\};$ 
6   if( $support(r) \geq minSupport$ )
7   {
8     set  $P = P \cup r;$ 
9     set  $I = I \cup i;$ 
10  }
11 }
12 do
13 {
14   foreach rule  $r \in P$ 
15   {
16     repeat  $cloneRate(r)$  times
17     {
18       set  $\bar{r} = r;$ 
19       set  $\bar{r}.items = r.items \cup i$  where  $i \in I \wedge i \notin r.items;$ 
20       if( $support(r) \geq minSupport$ )
21         set  $P = P \cup \bar{r};$ 
22     }
23   }
24   prune  $P$ 
25   foreach rule  $r \in P$ 
26   {
27     if( $confidence(r) \geq minConfidence$ )
28        $M = M \cup r;$ 
29   }
30 }
31  $currentGeneration = currentGeneration + 1;$ 
32 while( $coverage(M) < 100\% \wedge currentGeneration < maxGenerations$ )
33 return  $M;$ 

```

Fig. 1. The AC-CS Algorithm

along with their parameters. A few pre-processing steps were performed on the datasets. Continuous data were discretized into intervals using the entropy methods with the MLC++ tool². Any transactions with missing fields were removed. Data were converted into a vertical layout for efficient support counting. A hash table for item transactions were implemented for easy and efficient access. In addition, items in the body of rules were implemented as sets.

The proposed algorithm AC-CS is compared against AC-Apriori, an Apriori based AC algorithm. We use a publicly available implementation of Apriori by

² <http://www.sgi.com/tech/mlc/>

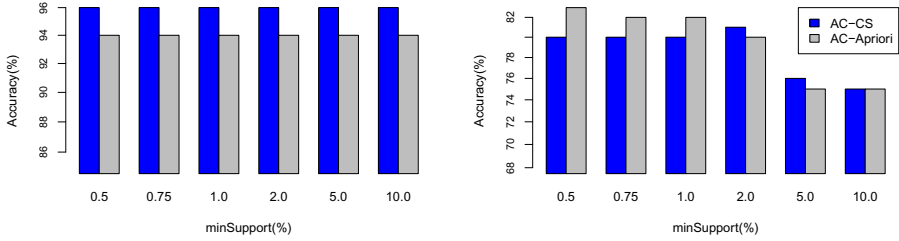


Fig. 2. Accuracy results, in log-scale, for datasets (from left) Iris & Adult

Borgelt³. This implementation is widely used for academic and commercial purposes.

Execution times are reported in both milliseconds and minutes as appropriate. They include both the time to extract and apply the generated rules. The minimum support ratios used are 0.5%, 0.75%, 1%, 2%, 5%, 10%. All experiments were performed on a Windows 7 machine with processor speed at 2.80GHz and 3.0GB memory.

Table 1. Datasets & Parameters

Dataset	Instances	Classes	Training	Testing
Adult	45,222	2	30,162	15,060
Iris	150	3	100	50

Figure 2 illustrates the accuracy of both the AC-Apriori and AC-CS algorithms on two datasets with different support thresholds. Clearly, for the smaller dataset Iris, AC-CS has a higher accuracy than that of AC-Apriori in every single case. Meanwhile, for the larger dataset Adult, AC-CS's accuracy is approaching and sometimes rivaling that of AC-Apriori. Similar results were obtained for other values of support.

Similarly, figure 3 shows the execution times of the two algorithms. For both datasets, AC-CS has outperformed AC-Apriori in all cases. This is probably due to the significant reduction of rules required as a result of not discovering all possible rules as it is the case with AC-Apriori. Figure 4 shows the dramatic reduction in rules. The reduction is particularly apparent in the case of the larger dataset Adult. While the rules used by AC-CS grow slowly with lower minSupport, the rules generated by AC-Apriori grows exponentially in some cases. In addition, the AC-CS algorithm appears to be more efficient than the algorithm proposed in [13].

The AC-CS algorithm is able to integrate the rule discovery along with the rule selection processes. A clear advantage that traditional AC algorithms lack.

³ <http://www.borgelt.net/apriori.html>

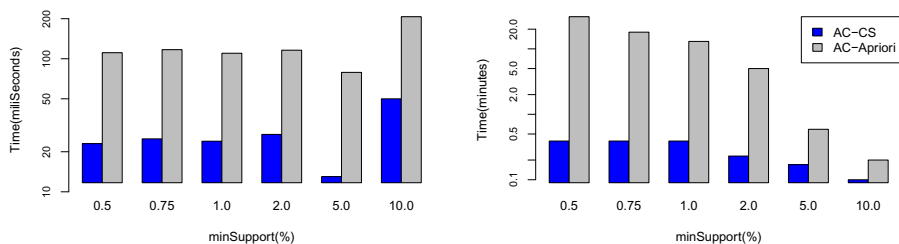


Fig. 3. Execution times, in log-scale, for datasets (from left) Iris & Adult

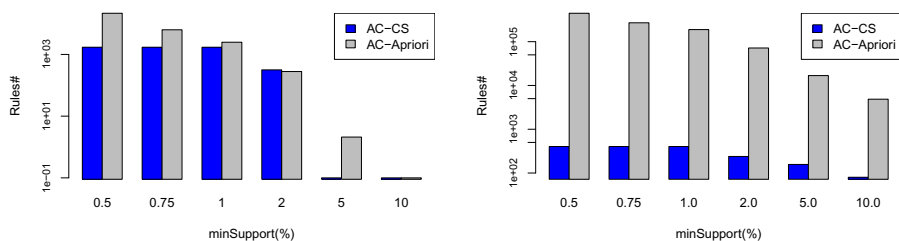


Fig. 4. Rules count in, log-scale, for datasets (from left) Iris and Adult

Moreover, unlike Genetic Algorithms (GA), the employed CS algorithm performs proportionate selection as well as affinity inversely proportional hypermutation with no crossover operation [7]. Moreover, the authors in [11] show that unlike GA, CS algorithm can reach a diverse number of local optimal solutions.

5 Conclusions and Future Work

In this paper, we have introduced AC-CS, a novel AC algorithm inspired by the clonal selection algorithm. The algorithm begins with a small population of frequent single item rules. These rules then go through a process of cloning, mutating, and pruning for several generations. Only high quality rules are added to the memory pool. These rules are applied in turn to classify a testing dataset. Empirical results show that the approach outperforms traditional AC algorithms in running time and quite competitive in accuracy as well. Possible future research directions for this work include: drawing more inspiration from the NIS processes; optimizing the algorithm to improve the running time while keeping the accuracy as high as possible; and more extensive testing with both synthetic & real datasets.

References

1. <http://www.artificial-immune-systems.org>
2. Agrawal, R., Imieliński, T., Swami, A.: Mining association rules between sets of items in large databases. In: Proceedings of the 1993 ACM SIGMOD International Conference on Management of Data, SIGMOD 1993, pp. 207–216. ACM, New York (1993)
3. Agrawal, R., Srikant, R., et al.: Fast algorithms for mining association rules. In: Proc. 20th Int. Conf. Very Large Data Bases, VLDB, vol. 1215, pp. 487–499 (1994)
4. Alves, R., Delgado, M., Lopes, H., Freitas, A.: An Artificial Immune System for Fuzzy-Rule Induction in Data Mining. In: Yao, X., Burke, E.K., Lozano, J.A., Smith, J., Merelo-Guervós, J.J., Bullinaria, J.A., Rowe, J.E., Tiño, P., Kabán, A., Schwefel, H.-P. (eds.) PPSN 2004. LNCS, vol. 3242, pp. 1011–1020. Springer, Heidelberg (2004)
5. Bayardo Jr., R.J.: Efficiently mining long patterns from databases. In: Proceedings of the 1998 ACM SIGMOD International Conference on Management of Data, SIGMOD 1998, pp. 85–93. ACM, New York (1998)
6. Bersini, H., Varela, F.: Hints for adaptive problem solving gleaned from immune networks. In: Parallel Problem Solving from Nature, pp. 343–354 (1991)
7. Castro, L., Timmis, J.: Artificial immune systems as a novel soft computing paradigm. *Soft Computing-A Fusion of Foundations, Methodologies and Applications* 7(8), 526–544 (2003)
8. Castro, L.N.D., Zuben, F.J.V.: An evolutionary immune network for data clustering. In: Brazilian Symposium on Neural Networks, pp. 84–89 (2000)
9. Cutello, V., Narzisi, G., Nicosia, G., Pavone, M.: Clonal Selection Algorithms: A Comparative Case Study Using Effective Mutation Potentials. In: Jacob, C., Pilat, M.L., Bentley, P.J., Timmis, J.I. (eds.) ICARIS 2005. LNCS, vol. 3627, pp. 13–28. Springer, Heidelberg (2005)
10. De Castro, L., Timmis, J.: Artificial immune systems: a new computational intelligence approach. Springer (2002)
11. De Castro, L., Von Zuben, F.: The clonal selection algorithm with engineering applications. In: Proceedings of GECCO 2000, Workshop on Artificial Immune Systems and Their Applications, vol. 3637 (2000)
12. De Castro, L., Von Zuben, F.: Learning and optimization using the clonal selection principle. *IEEE Transactions on Evolutionary Computation* 6(3), 239–251 (2002)
13. Do, T.D., Hui, S.C., Fong, A.C.M., Fong, B.: Associative classification with artificial immune system. *IEEE Transactions on Evolutionary Computation* 13, 217–228 (2009)
14. Farmer, J., Packard, N., Perelson, A.: The immune system, adaptation, and machine learning. *Physica D: Nonlinear Phenomena* 22(1-3), 187–204 (1986)
15. Forrest, S., Perelson, A., Allen, L., Cherukuri, R.: Self-nonself discrimination in a computer. In: Proceedings of the 1994 IEEE Computer Society Symposium on Research in Security and Privacy, pp. 202–212. IEEE (1994)
16. Freitas, A.A., Timmis, J.: Revisiting the Foundations of Artificial Immune Systems: A Problem-Oriented Perspective. In: Timmis, J., Bentley, P.J., Hart, E. (eds.) ICARIS 2003. LNCS, vol. 2787, pp. 229–241. Springer, Heidelberg (2003)
17. Greensmith, J., Aickelin, U., Cayzer, S.: Introducing Dendritic Cells as a Novel Immune-Inspired Algorithm for Anomaly Detection. In: Jacob, C., Pilat, M.L., Bentley, P.J., Timmis, J.I. (eds.) ICARIS 2005. LNCS, vol. 3627, pp. 153–167. Springer, Heidelberg (2005)

18. Gu, F., Feyereisl, J., Oates, R., Reys, J., Greensmith, J., Aickelin, U.: Quiet in Class: Classification, Noise and the Dendritic Cell Algorithm. In: Liò, P., Nicosia, G., Stibor, T. (eds.) ICARIS 2011. LNCS, vol. 6825, pp. 173–186. Springer, Heidelberg (2011)
19. Houtsma, M., Swami, A.: Set-oriented mining of association rules. In: International Conference on Data Engineering (1993)
20. Ishida, Y.: Fully distributed diagnosis by pdp learning algorithm: towards immune network pdp model. In: 1990 IJCNN International Joint Conference on Neural Networks, pp. 777–782. IEEE (1990)
21. Ji, Z., Dasgupta, D.: Revisiting negative selection algorithms. *Evolutionary Computation* 15(2), 223–251 (2007)
22. Li, W., Han, J., Pei, J.: Cmar: Accurate and efficient classification based on multiple class-association rules. In: IEEE International Conference on Data Mining, pp. 369–376 (2001)
23. Liu, B., Hsu, W., Ma, Y.: Integrating classification and association rule mining. In: Knowledge Discovery and Data Mining, pp. 80–86 (1998)
24. Liu, B., Ma, Y., Wong, C.: Classification using association rules: weaknesses and enhancements. *Data Mining for Scientific Applications*, 1–11 (2001)
25. Matzinger, P.: The danger model: a renewed sense of self. *Science* 296(5566), 301–305 (2002)
26. Quinlan, J.: C4. 5: programs for machine learning. Morgan Kaufmann (1993)
27. Timmis, J., Neal, M., Hunt, J.: An artificial immune system for data analysis. *Biosystems* 55(1-3), 143–150 (2000)
28. Watkins, A.: Exploiting immunological metaphors in the development of serial, parallel and distributed learning algorithms. PhD thesis, University of Kent, Computing Laboratory (2005)
29. Watkins, A., Timmis, J.: Exploiting Parallelism Inherent in AIRS, an Artificial Immune Classifier. In: Nicosia, G., Cutello, V., Bentley, P.J., Timmis, J. (eds.) ICARIS 2004. LNCS, vol. 3239, pp. 427–438. Springer, Heidelberg (2004)
30. Watkins, A., Timmis, J., Boggess, L.: Artificial immune recognition system (airs): An immune-inspired supervised learning algorithm. *Genetic Programming and Evolvable Machines* 5(3), 291–317 (2004)
31. Zaki, M.J., Gouda, K.: Fast vertical mining using diffsets. In: Proceedings of the Ninth ACM SIGKDD International Conference on Knowledge Discovery and Data Mining, KDD 2003, pp. 326–335. ACM, New York (2003)
32. Zaki, M.J., Parthasarathy, S., Ogihara, M., Li, W.: New algorithms for fast discovery of association rules. In: Knowledge Discovery and Data Mining, pp. 283–286 (1997)
33. Zheng, H., Du Jiaying, Z., Wang, Y.: Research on vehicle image classifier based on concentration regulating of immune clonal selection. In: Fourth International Conference on Natural Computation, pp. 671–675. IEEE (2008)

A Review on Delaunay Refinement Techniques

Sanderson L. Gonzaga de Oliveira

Universidade Federal de Lavras, 37200-000 Lavras-MG, Brazil

sanderson@dcc.ufla.br

<http://algot.dcc.ufla.br/~sanderson>

Abstract. Delaunay refinement is a technique for generating triangulations. Triangulations produced by algorithms in this class of techniques guarantee bounds on angles, edge lengths, the number and the grading of triangles in theory and practice. This paper is a brief review of point insertion techniques in Delaunay triangulations. Important works on the insertion of vertices in Delaunay triangulations and its dual graph, the Voronoi diagram, are described as a start point for one who needs to build a quality mesh using adaptive triangular-mesh refinement.

Keywords: mesh generation, Delaunay triangulation, Voronoi diagram.

1 Introduction

Triangles are considered the most versatile and the simplest space-filling configurations in which spaces can be partitioned. Any polygonal domain can be discretized using only triangles (see Frey [29] for details). Consequently, triangular meshes, or triangulations, are typical geometric discretizations in many scientific applications, such as geographic information systems, engineering simulations, visualizations, and many applications in Computational Fluid Dynamics. Specifically in the numerical solution of partial differential equations, common inputs to numerical methods to solve them, such as finite volume and element methods, are in the form of triangles that fill all the computational space domain.

In a triangulation, the preferred shape of the triangles depends on the application. However, theoretical and experimental analysis of numerical methods that are used in conjunction with triangulations suggest that triangles with no large angles and/or small angles serve well in most applications (see, e.g. Babuzka and Aziz [2] for details). According to Erten and Üngör [25], “in general, the better the shape of the triangles, the smaller the interpolation and approximation errors are in their use”. Moreover, there are geometric criteria in which the triangulation should be smooth and the triangles should be of somewhat uniform shape and size. Generally, triangulations comprised of long and *skinny* triangles do not provide accurate approximations to the solution of the mathematical model being studied. There were proposed many ways to measure the quality of a triangle. A usual one is that a skinny triangle presents *circumradius* r to *shortest-edge* s ratio larger than a threshold B (see Miller et al. [43] for details). The ratio is related to the minimum triangle angle θ by: $r/s = 1/(2\sin(\theta))$. This value is $r/s = 1/(2\sin(\theta)) = 1/\sqrt{3} \cong 0.58$ for an equilateral triangle.

In addition, the simulation time is generally proportional to the number of triangles, and therefore, one needs to balance the minimum number of triangles with reasonably accurate results, usually by using an *irregular* (or *unstructured*) mesh. Note that irregular meshes do not exhibit a uniform topological structure and the location of the neighbors of any vertex must be explicitly stored; whereas regular meshes exhibit a uniform topological structure and indices of the neighbors of any vertex can be calculated using a simple increment.

An approach in order to provide adaptive triangular mesh refinement with adequate quality can use algorithms based on a automatic point insertion strategy on the Delaunay triangulation. A planar Delaunay triangulation [19] for a point set P is a triangulation $DT(P)$ such that no point in P is inside the circumcircle of any triangle in $DT(P)$.

The Delaunay triangulation and its duals Voronoi diagram [73] and medial axes have been applied in many different fields, such as the ones earlier cited, including numerical methods and computer graphics. Inserting a new point into an existing Delaunay triangulation can be a local operation. Consequently, this operation can be inexpensive, except in uncommon applications (see [65] for details). Delaunay triangulations have been extensively studied, and very good algorithms are available. The reader is referred to Barth [5] for properties and algorithms in order to build Delaunay triangulations. Shewchuk ([63] and [64]) presented aspects of the Delaunay mesh generation and algorithms. Edelsbrunner [21] provided a theoretical review on Delaunay triangulation. Erten and Üngör [25] is another survey on this context of providing a good triangulation.

This review was motivated when the author searched techniques to adaptively insert points into an existing Delaunay triangulation and the approach must maintain the Delaunay triangulation characteristics. The techniques to improve a mesh scan the triangulation searching for bad quality triangles. On the other hand, a solution to a partial differential equation by finite element or volume discretizations may require to insert a new point into specific regions, even if it is comprised of good quality triangles. In addition, the new mesh must be a Delaunay triangulation. The techniques reviewed on this note can be used as part of a mesh generation stage of a solver of partial differential equations.

This review extends a previous one [31]. This review only presents the description of the ideas without providing pseudo-codes and details that can be better understood in the original papers. As a outline of this note, a freely-available package in order to implement a Delaunay triangulation is briefly described in Section 2. The Voronoi diagram is described in Section 3. Choices of point insertions are described in Section 4. In the following, a brief review of schemes for point insertion in an existing Delaunay triangulation in the context of providing an adaptive mesh refinement is provided. Incremental approaches are described in Section 5. The Ruppert technique, the Chew techniques and the Üngör off-center solutions and improvements are explained in Sections 6, 7, and 8, respectively. The Hierarchical Delaunay Triangulations is presented in

Section 9. The longest-edge based triangle partition within Delaunay triangulation are described in Section 10. Other approaches are commented in Section 11. Finally, some future directions are given in Section 12.

2 Freely-Available Computational Codes to Implement a Delaunay Triangulation

An excellent example where the reader can obtain freely-available computational codes to implement a Delaunay triangulation is the mesh generation software Triangle (see Shewchuk [61] for details). Triangle's high-quality mesh-generation package is based on Chew [12] and Ruppert [57] Delaunay refinement techniques. Shewchuk surveyed both techniques in [65]. In addition, Shewchuk described Ruppert's Delaunay refinement technique in [66]. These algorithms evolved from a first technique proposed by Chew [11] and Bern et al. [6]. The Chew and Ruppert Delaunay refinement techniques are modified in Triangle to handle domains with small angles, following a idea of Miller et al. [42] and [44]. It also incorporates a modification by Üngör [71] that reduces the number of generated triangles. Triangle's implementation of the divide-and-conquer and incremental Delaunay triangulation algorithms follows closely the elegant $O(n \lg n)$ divide-and-conquer algorithm promoted by Guibas and Stolfi, which was originally developed by Lee and Schachter [41]. Dwyer [20] showed that the Guibas and Stolfi's algorithm is improved by using alternating vertical and horizontal cuts to divide the vertex set. Moreover, Triangle uses a triangle-based data structure instead of Guibas and Stolfi's quad-edge data structure. Triangle uses an expected $O(n^{1/3})$ time point location scheme proposed by Mücke [45]. Triangle's $O(n \lg n)$ sweepline algorithm for Delaunay triangulation is due to Fortune [27], and relies upon Sleator and Tarjan's splay trees [68]. Details of the earlier description can be obtained in the Triangle's website [61].

Given a Delaunay triangulation, one is allowed to insert Steiner points in order to compute high quality triangulations. A Steiner point is the one that is not part of the input point set or a point with a particular geometric relation to a triangle. Inserting new points into the triangulation, however, may increase the number of triangles in the triangulation, which is a key factor in the running time of the model it is applied. After briefly describing the Voronoi diagram, some point insertion techniques are surveyed in the following.

3 Voronoi Diagram

The Voronoi diagram was proposed in [73]. As cited by Watson in [74], Boots [7] was apparently the first one to observe that the Voronoi diagram computation can be greatly simplified by performing its dual mesh, the Delaunay triangulation. Moreover, Shamos [60] was the first to argue that the Voronoi diagram can be used as a tool to provide efficient algorithms for a wide variety of geometric problems. The Delaunay triangulation is formed by connecting two points

if and only if their Voronoi regions have a common border segment. If no four or more points are cocircular, then the vertices of the Voronoi diagram are the triangle circumcenters. Moreover, Voronoi vertices represent locations that are equidistant to three or more points. Barth [5] presents details of the Delaunay triangulation and Voronoi diagram duality.

Consider the Delaunay triangulation of a set V of planar points. The Voronoi diagram describes the proximity relationship among the points of V . The Voronoi diagram of a set V of n points is a planar subdivision into n convex polygonal regions. Consider a region R belonging to a Voronoi diagram. Consider that R is associated to a point $p \in V$. Each Voronoi region is the set of planar points that lie closer to a certain point of V than to any other point in V . For example, each point of R is closer to $p \in V$ than any other point $q \in V$, in which $p \neq q$. Two points of V are neighbors when the corresponding Voronoi regions are adjacent.

Voronoi diagrams are fairly used within finite volume discretizations. Furthermore, in such approach, the finite volumes are not the triangles themselves, but the Voronoi regions, i.e. parts of certain triangles. A triangulation edge orthogonal to the segment between two control-volume centroids facilitates finite-volume approximations because the cosine between these segments does not need to be calculated. Namely, one just needs to apply the basic finite volume method as in a regular quadrangular mesh. Moreover, it improves the solution accuracy and reduces the computational effort to approximate a solution of a partial differential equation; though having some problems in boundary in certain applications, e.g. viscous flow problems. Note that for the finite volume method, the mesh must be truly Delaunay, i.e. not just *constrained* Delaunay and the circumcenter of each triangle must lie within the triangulation. The constrained Delaunay triangulation is the best approximation of the Delaunay triangulation containing the set of given segments among its edges. In the following, techniques of point insertion into an existing Delaunay triangulation are surveyed.

4 Point Insertion into a Delaunay Triangulation

Consider that one recognized the triangle t of the mesh to be divided. A fundamental decision is the location of the vertex to be inserted, i.e. a central idea in any Delaunay refinement algorithm is where should the next vertex be inserted. One could simply insert a point into the triangle barycenter and link the barycenter to the vertices of the triangle t . However, this process quickly degenerates the triangulation quality, specially along boundaries and even considering non-conforming meshes. This occurs even when carrying out global refinement. A triangle could be divided by trisecting the edges of t , joining the barycenter to those points and also to the vertices of t . However, this results in poor-quality triangles as well. In another example, Plaza and collaborators [47] proposed the 7-triangle Delaunay partition. This refinement scheme also propagates the refinement and inserts non-similar triangles. Farrashkhalvat and Miles [26] provided a description of point insertion strategies. According to these authors, there are two main approaches to the insertion of new points into a Delaunay triangulation:

- Inserting new interior points at the circumcenters of the triangles. Clearly, new inserted points should not be too near to existing vertices, i.e. it is reasonable to insert the new vertex as far from other vertices as possible. Insertion at the circumcenter results in the inserted point being equidistant from the three vertices of the triangle t ; though the triangle that contains the new point should be sought because the circumcenter may not lie inside the triangle t . Anyway, after the point insertion, the mesh must be retriangulated. The remaining decisions to be performed are which triangles to select for the insertion of new points. The idea is to devise a set of rules for identifying unsatisfactory triangles.
- Known as Voronoi-segment point insertion (Rebay, 1993 [49]), new points are inserted along Voronoi edges. Rebay's algorithm tends to generate approximately equilateral triangles of the target circumradius after a few steps.

The literature is rich in approaches to introduce points into the Delaunay triangulation. As alternatives to circumcenter insertion, incenter and barycenter have the advantage for always being inside the triangle. However, those points are not as adequate as the circumcenter insertion because, as described, the inserted point should be equidistant from the three vertices of the triangle. Incenter always lies near to the shortest side of the triangle. Frey [29] weighted the triangles choosing either circumcenter or other points. Weatherill [75] also inserted centroids as new vertex into triangulations. In the following, schemes that provide high-quality Delaunay triangulations are described.

5 Incremental Approaches

The Green-Sibson [32] and Bowyer-Watson ([9] and [74]) algorithms are commonly related to the creation of a Delaunay triangulation. Besides, the algorithms of Cline-Renka [14] and the Sloan [69] follow the incremental approach. Mainly the Bowyer-Watson algorithm is used in some way as part of techniques to: insert a new point into an existing Delaunay triangulation; triangulate the vertices maintaining the Delaunay triangulation characteristics. Before describing Green-Sibson and Bowyer-Watson algorithms, the Lawson's technique is briefly described in the following.

5.1 Lawson's Technique

The Lawson [40] approach is also known as Flipping Edge or Diagonal Swapping algorithm. It is an algorithm to generate a Delaunay triangulation from a existing triangulation by flipping edges. More specifically, if a point p is inserted into a triangle t clearly belonging to an existing triangulation, edges are also inserted linking the new point p to the vertices of t . If any of the vertex neighbors lie inside the circumcircle of any new triangle, then a quadrilateral is formed comprised of the triangle and its neighbor. The diagonals of this quadrilateral are swapped and this process is continued till a Delaunay triangulation is reached. In special,

a Lawson's result is that a Delaunay triangulation maximizes the minimum angle among all possible triangulations of a set of points.

Joe ([38] and [39]) and Rajan [48] generalized this flip-based technique to arbitrary dimensions. The reader is referred to Seidel [59] for the $O(n \lg n)$ analysis of the Lawson's algorithm.

5.2 Green-Sibson Algorithm

This algorithm was proposed by Green e Sibson [32] for Voronoi diagram generation. According to Aurenhamer e Klein [1], this algorithm runs in $O(n^2)$ time, in which n is the number of vertices. It is similar to the Lawson's technique. Commonly, the input of this algorithm is a Delaunay triangulation. There is two cases: if the inserted point p lies on an existing edge \overline{ab} and supposing \overline{ab} is part of $\triangle abc$ and $\triangle abe$, then \overline{ab} is removed, and new edges are inserted linking p to the vertices of the quadrangle $abce$; otherwise, p lies into a triangle, say $\triangle abc$, and edges linking p to the vertices a , b , and c are inserted.

In both cases, tests are performed to verify if the the new mesh is a Delaunay triangulation. These tests are based on verifying if some vertex is inside to the circumcircle of some triangle, a basic characteristic of the Delaunay triangulation. If a vertex is inside a circumcircle triangle, a flip edge is performed. The algorithm terminates when all the vertices are satisfied by these tests.

5.3 Bowyer-Watson Algorithm

This algorithm was proposed by Bowyer [9] for Voronoi diagrams and Watson [74] for Delaunay triangulation. In this $O(n^{1.5})$ time algorithm, with an existing Delaunay triangulation, it verifies all the triangles where a new point p lies on their circumcircles. The edges of these triangles are removed, resulting in a polygon. Afterwards, edges are inserted linking p to the vertices of the resulting polygon.

As described by Farrashkhalvat and Miles [26], the initial Delaunay triangulation of a domain, based on a selection of boundary points joined with the application of the Bowyer-Watson algorithm, can often yield a poor-quality mesh. A mesh improvement must then be sought by inserting new points into the mesh, and the resulting triangulations are judged according to various geometric and physical criteria.

6 Ruppert's Technique

Ruppert's technique [57] is also known as Delaunay refinement; though similar techniques are all called Delaunay refinement algorithms by some authors, such as Tournois et al. [70]. Ruppert's technique triangulates *planar straight-line graphs*; or in dimension higher than two, a piecewise linear system. *Planar straightline graph* is an embedding of a planar graph in the plane such that its edges are mapped into straight line segments. According to Shewchuk [66], the

2D Ruppert quality mesh generation technique was probably the first theoretically guaranteed scheme to be “truly satisfactory in practice”. The idea is either to refine a small angled triangle by the Delaunay insertion of its circumcenter; or to modify the boundary if the circumcircle is external to the domain.

The technique starts with a Delaunay triangulation of the input vertices. Then, consisting of two main operations, the technique inserts into the triangulation: the midpoint of a segment (restricted edges) with non-empty diametral circles; the circumcenter of a poor-quality triangle. If this point lies in the diametral circle of some edge, then the technique splits the *encroached* segment. During refinement, an edge is *encroached* if a point, except its endpoints, is on or inside its diametral circle.

These operations are repeated until no poor-quality triangle exists and all edges are not encroached. This algorithm results in a strict conforming Delaunay triangulation comprised of quality triangles. Ruppert’s technique produces a size-optimal nonuniform mesh. It is also size-optimal to within a constant factor.

Shewchuk [65] showed that this algorithm terminates within a finite number of Steiner points and generates a quality mesh for non-acute input and any poor-quality threshold less than about 20.7° . Besides, Ruppert’s algorithm allows the density of triangles to vary quickly over short distances. Various improvements have been proposed in order to relax these restrictions. For example, Miller et al. [44] extended the technique to handle any straightline input by relaxing the quality requirement of small input angles. Curved input can also be meshed using techniques proposed by Pav and Walkington [46]. Ruppert’s technique can be naturally extended to 3D; however its output ensures are weaker because the sliver type tetrahedron. An extension of Ruppert’s algorithm in two dimensions is implemented in the freely available Triangle package. Two variants of Ruppert’s techniques in this package are guaranteed to terminate for a poor-quality threshold of about 26.5° (see Shewchuk [65] for details).

7 Chew’s Techniques

In his first scheme, Chew [11] proposed a Delaunay improvement technique that triangulates a given polygon into a uniform mesh with all angles between 30° and 120° . It guarantees that the output mesh is size-optimal within a constant factor amongst all uniform meshes.

The input of the Chew second technique is a piecewise linear system, namely, the technique begins with a constrained Delaunay triangulation of the input vertices. At each iteration, the technique inserts a point in the circumcenter of a poor-quality triangle with one exception. If the circumcenter lies on the opposite side of an input edge as the poor-quality triangle, then the segment midpoint is inserted. Moreover, the technique removes all previously inserted circumcenters inside the diametral circle of the original edge, i.e. before being split. Chew’s second technique is guaranteed to terminate. The circumcenter insertion process is repeated until no poor-quality triangle exists. It returns a constrained Delaunay triangulation totally comprised of good quality triangles. Note that

the *quality* of a triangle is defined by the minimum angle of a triangle. Chew's second technique produces a local feature size-graded and size-optimal mesh and ensures that all angles are between 26.5° and 126.9° . Without those features, Chew's second technique produces triangulations with about 30° as the minimum angle. The reader is referred to Shewchuk ([63] and [65]) for details. The Chew [12] second algorithm produces a mesh that is not guaranteed to be a truly Delaunay triangulation. The Chew second technique was proposed to generate a *constrained* Delaunay triangulation. This technique presents the same basis of the Ruppert scheme [57]. Although the Chew second technique was proposed for 3D meshing surfaces, it has been adopted as a 2D mesh generator due to practical advantages over Ruppert's scheme [57] in certain cases: Chew second Delaunay refinement algorithm offers an improved guarantee of grading in theory, and splits fewer subsegments in practice. This means that, depending on the edge lengths of the input planar straightline graph, Chew's second algorithm generates fewer triangles than Ruppert's algorithm. Besides, Chew's second algorithm leads to better bounds on the minimum angle, the edge lengths, and the mesh cardinality, than Ruppert's algorithm. The Chew [12] second technique is the default quality mesh generator implemented in the freely available Triangle package of Shewchuk [61]. However, Ruppert's algorithm should be preferred if a truly Delaunay triangulation is required.

Shewchuk [63] proposed several modifications to the Delaunay refinement algorithms that improve the quality of the triangulation, such as improving the quality bound in the interior triangles of the mesh; and both Ruppert's and Chew's techniques were modified to make it possible to apply a quality bound of $B=1$ to all triangles of the mesh, although there is no accompanying guarantee of good grading, in which all the triangles presents circumradius-to-shortest edge ratio no larger than B . Shewchuk [65] presented a framework for analyzing Delaunay refinement algorithms that unifies the mesh generation algorithms of Chew and Ruppert. The Shewchuk's framework improves Chew's and Ruppert's techniques in several ways, and also helps to solve the difficult problem of meshing non-manifold domains with small angles.

8 Üngör's Off-Center Solutions and Improvements

Üngör ([71] and [72]) presented an algorithm based on the *off-center* insertion. In the former case, the off-center of a triangle with the shortest edge \overline{pq} is a point o on the bisector of \overline{pq} furthest from p (or q) such that the angle among the three points is a user-specified constraint angle. The idea of using *off-centers* led Har-Peled and Üngör [34] to the design of the first time-optimal Delaunay refinement algorithm. Erten and Üngör [24] proposed algorithms that improve the off-center performance with respect to the mesh size and a minimum angle tolerance. This is performed by using point selections depending on some triangle cases. Erten and Üngör [23] published a Delaunay refinement algorithm that generally terminates for constraint angles up to 42° .

Erten and Üngör [25] proposed two algorithms to improve the performance of Delaunay refinement. The first one uses the Voronoi diagram and unifies previously suggested Steiner point insertion schemes (circumcenters of Chew [11], Ruppert [56], Shewchuk [65], sink of Edelsbrunner and Guoy [22], off-center of Üngör [71]) together with a proper strategy. The second algorithm integrates a local smoothing strategy into the refinement process. For a given input domain and a constraint angle α , the Delaunay refinement algorithms aim to compute triangulations with angles at least α . Chernikov and Chrisochoides [10] generalized and improved Üngör's off-center solution. They showed that choosing any Steiner point inside the *selection disk* eliminates a poor-quality triangle t , and that the algorithm terminates. The authors proposed an example of a new Steiner point inside the selection disk showing that their refinement technique, in general, inserts fewer points than using off-centers.

9 The Hierarchical Delaunay Triangulations

The Hierarchical Delaunay triangulations (HDT) was proposed by De Floriani and Puppo in [17] and [18]. It is based on a hierarchy of triangle-based surface approximations, in which each node, except the root, is a triangulated irregular network refining a triangle face belonging to its parent in the hierarchy.

This method is similar to the proposed by Scarlatos and Pavlidis [58]; however, the triangle subdivision is more general. The subdivision inside every macrotriangle is locally a Delaunay triangulation; whereas a global expanded subdivision of the whole domain generally is not. The triangle partition is performed by an iterative application of a selector process that, at each step, updates the current Delaunay triangulation by introducing the point having the maximum error. Moreover, in order to subdivide a triangle for a given hierarchical level, they used a curve approximation algorithm (see Ballard and Brown [4] for details) in order to insert points along the edges. Afterwards, points are added into the inner triangle until an error threshold is met throughout the triangle and so the inner triangle is retriangulated using Delaunay triangulation properties.

The constructing algorithm basis for a HDT must be an on-line approach that incrementally builds a Delaunay triangulation through iterative point insertion (see De Floriani et al. [16] for details). According to Heckbert and Garland [35], the HDT seems to present nearly identical flexibility and speed compared to the one proposed by Scarlatos and Pavlidis [58]. However, for a given error threshold, the HDT likely yields slightly better simplification.

10 The Longest-Edge Based Triangle Partition within Delaunay Triangulation

Rivara [50] presented the backward longest-edge refinement (BLER) algorithm based on the longest-edge propagation path (LEPP) in order to conform the mesh in the finite element context. Briefly, the LEPP keeps a path of n triangles

that have also to be refined for each triangle of the mesh. For example, consider that the triangle t_0 is marked to be refined. The LEPP indicates that the triangles t_1, t_2, \dots, t_n also must be refined in order to maintain a conforming good-quality mesh. It propagates the list until the longest-edge shared by triangles t_{n-1} and t_n . This edge is either larger than the one of its previous neighbor or t_n is in the boundary.

The BLER is a partition procedure that extended both the pure longest-edge refinement algorithms for general non-Delaunay triangulation (see Rivara and collaborators [54], [55] and the references therein) and the longest-edge refinement algorithm for Delaunay triangulations proposed by Rivara and Inostroza [53]. Specifically, the algorithm proposed by Rivara and Inostroza [53] guarantees that meshes of analogous quality to the input reference-mesh are built.

Rivara and collaborators (see [52] and [67]) presented the LEPP-Delaunay midedge algorithm. It generalized and improved both previous longest-edge algorithms for the Rivara's refinement of general non-Delaunay triangulations, and the longest-edge algorithm for the refinement of Delaunay meshes of Rivara and Inostroza [53]. In the LEPP-Delaunay midedge algorithm, only considering local information associated to the terminal triangle that contains a constrained edge allows a constrained Delaunay triangulation. The LEPP-Delaunay midedge algorithm avoids the interaction with the entire set of constrained items. This algorithm is not a nested partition procedure because it changes the previously existing points. Moreover, it replaces previous triangles by Delaunay triangles due to the circumcircle test of $DT(P)$. In addition, it suffers of a looping case for angle tolerance greater than 22° . Namely, in certain cases, the triangles are not improved during the refinement. Nevertheless, it is interesting since it provides meshes with triangles which the smallest angle is greater than or equal to $\pi/6$, including triangle along boundaries. Hitschfeld and Rivara [36] introduced a automatic construction of non-obtuse triangles in boundary for LEPP-Delaunay triangulations within control volume methods. Each 1-edge obtuse boundary triangle is eliminated by the Delaunay insertion of midedges.

Consider that α is the smallest angle of the triangle. In the case that $\alpha \geq 25.4^\circ$, any isolated 1-edge obtuse triangle and isolated pairs of neighbor 1-edge obtuse triangles sharing their longest edge demand the insertion of only one point. When $\alpha \geq 15.4^\circ$, the Delaunay insertion of at most three boundary/interface points eliminates any isolated 1-edge boundary triangle and isolated pairs of neighbor 1-edge boundary triangles sharing a longest edge. An obtuse angle in each isolated 2-edge boundary triangle having medium-size edge l and longest-size edge L over the boundary is eliminated by building an isosceles triangle of boundary edges of lengths $l/2$ followed by the Delaunay insertion of N (clearly, a finite number) points, in which $N \leq 2.14/\sin(\alpha/2)$. A generalization of those approaches solves more complex patterns of obtuse triangles, i.e. chains of 2-edge constrained triangles forming a saw diagram and clusters of triangles that have boundary/interface edges sharing a common vertex [36]. Hitschfeld and collaborators [37] presented the LEPP algorithm for Delaunay mesh and its dual

Voronoi diagram, without obtuse angles opposite to the boundary and interfaces for semiconductor device simulation using Box-method Delaunay meshes.

Rivara and Calderon [51] presented the LEPP-Delaunay centroid algorithm. They proved that the centroid version of the LEPP-Delaunay algorithm produces triangulations both with average smallest angles greater than those obtained with the midedge version and with larger smallest edges without suffering from the looping case associated to the midedge method. In addition, the centroid version terminates for high-quality threshold angle, i.e. up to $\pi/5$. They also showed that the centroid version behaves better than the off-center algorithm for quality threshold angle larger than 25° . Because the finite-element conformity requirement, most of those previous articles describe algorithms that propagate the refinement in neighbors of the triangle marked to be refined and/or modify the points of the current mesh. As an example, Rivara and Inostroza [53] pointed out that numerical experiments performed with their 2D algorithm have shown that the number of points inserted by propagation is approximately \sqrt{N} , where N is the number of points in the mesh.

If an algorithm modifies the positions of the refined-triangle points, the data-structure nodes that represent those triangles also have to be changed. A process that operates strict local changes (a nested mesh) is desirable. Guibas and Stolfl [33], De Florian [15], and Sloan [69] described algorithms that perform the circumcircle test of DT(P) without locally destroying the current triangulation.

11 Other Approaches

Fowler and Little [28] proposed the *vertex insertion* in conjunction with the Delaunay triangulation. A Delaunay criterion localizes the position of a potential point to be inserted. This could affect the fit to the circumscribed circle about the triangle. The authors argued that it is sufficient to perform series of domain-limited searches in each triangle of the model; rather than carrying out global searches for the global “worst-fit” points. In this approach, adding a point removes the original triangle and introduces new ones. The inserted point is a vertex of the new triangles. In Figure 11a, a point is inserted and the region is triangulated. The reverse operation, known in computer-graphic context as *decimation*, is performed in order to unrefine the region. In a variation, a point is inserted, the set of triangles on its neighborhood are deleted and the region is retriangulated (Figure 11b). The inverse operator, the *vertex removal*, deletes a point together with its incident triangles and constructs new triangles in the region. Clarkson and Shor [13] showed that if the order of the vertex insertion is randomized, each vertex can be inserted in $O(n)$ time, without counting point location. The reader is referred to Shewchuk [61] for details.

Baker [3] published a comparison of edge and circumcenter based refinements. Properties of mesh improvement for iterative Delaunay refinement based on inserting a point in the circumcenter of triangles to be refined was also established by Shewchuk [62]. A combination of edge refinement and Delaunay point insertion was described by Borouchaki and George ([8] and [30]).

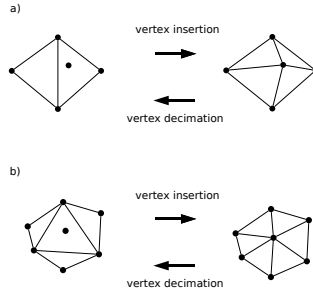


Fig. 1. Vertex insertion and vertex decimation

Tournois et al. [70] proposed to triangulate a domain into large and well-shaped triangles by interleaving Delaunay refinement and optimization. They aimed to generate large triangles by performing refinement by inserting a subset of the Voronoi vertices batch-wise in each refinement step. By applying the Lloyd iteration, the constraints are ensured to be preserved during mesh optimization. Although they did not present theoretical bounds on the triangle angles, they showed experiments that, for the required sizing, their algorithm produces, on average, meshes with 25% fewer Steiner points and of better quality than a standard Delaunay refinement algorithm.

12 Final Considerations

The Delaunay triangulation may not be satisfactorily applied in certain problems, such as problems involving viscous flows. Specifically about advancing front techniques with Delaunay triangulation, the reader can obtain details in Farrashkhalvat and Miles [26].

Besides point insertion, the mesh can be improved by smoothing techniques or topological transformations. These schemes shall be reviewed in future studies. The reader is referred to Shewchuk [63] for an introduction about this subject. In addition, the 3D review shall be provided.

Currently, the Ruppert technique is being adapted to refine a Delaunay triangulation (with Voronoi diagram) for finite volume discretizations of partial differential equation solutions. In addition, the proposal of Chernikov and Chrisochoides [10] and the LEPP-Delaunay centroid algorithm of Rivara and Calderon [51] shall be implemented for partial differential equation solutions by finite volume discretization. These solutions shall be compared in a future work.

The purpose of this article is to survey the approaches and not to evaluate them. Probably other schemes exist. However, such schemes may be either variations of the ones cited in this article or are not known to the author. Although the limited space for explaining details of the techniques, the author hopes that this review and the references cited serve to consolidate the ideas, principles and schemes that constitute the state-of-art in this subject. Moreover, the

author hopes that the list of references and descriptions to the large body of work on this issue can provide a useful starting point for one faced with the task of adaptively constructing a Delaunay triangulation.

Acknowledgments. The author gratefully acknowledges FAPEMIG and CNPq for the financial support.

References

1. Aurenhammer, F., Klein, R.: Handbook of Computational Geometry, ch. 5, Voronoi diagrams, from SFB Report F003-092, TU Graz, Austria, 1996, pp. 201–290. Elsevier Science Publishing (2000)
2. Babuka, I., Aziz, A.K.: On the angle condition in the finite element method. *SIAM Journal on Numerical Analysis* 13, 214–226 (1976)
3. Baker, T.J.: Triangulations, mesh generation and point placement strategies. In: Caughey, D. (ed.) *Computing the Future*, pp. 61–75. John Wiley (1995)
4. Ballard, D.H., Brown, C.M.: *Computer Vision*. Prentice Hall, Englewood Cliffs (1982)
5. Barth, T.J.: Aspects of unstructured grids and finite-volume solvers for the Euler and Navier-Stokes Equations. Von Karman Institute for Fluid Dynamics Lecture Series, NASA Ames Research Center, 1994-05 (February 1995)
6. Bern, M., Eppstein, D., Gilbert, J.R.: Provably good mesh generation. *Journal of Computer and System Sciences* 48(3), 384–409 (1994)
7. Boots, B.N.: Delaunay triangles: An alternative approach to point pattern analysis. *Proc. Assoc. Am. Geogr.* 6, 26–29 (1974)
8. Borouchaki, H., George, P.L.: Aspects of 2-d Delaunay mesh generation. *International Journal for Numerical Methods in Engineering* 40, 1957–1975 (1997)
9. Bowyer, A.: Computing dirichlet tessellations. *The Computer Journal* 24(2), 162–176 (1981)
10. Chernikov, A.N., Chrisochoides, N.P.: Generalized delaunay mesh refinement: From scalar to parallel. In: *Proceedings of the 15th International Meshing Roundtable*, pp. 563–580 (2006)
11. Chew, L.P.: Constrained Delaunay triangulation. *Algorithmica* 4, 97–108 (1989)
12. Chew, L.P.: Guaranteed-quality mesh generation for curved surfaces. In: *Proceedings of the Ninth Annual ACM Symposium on Computational Geometry*, pp. 274–280. ACM Press, San Diego (1993)
13. Clarkson, K.L., Shor, P.W.: Applications of random sampling in computational geometry ii. *Discrete & Computational Geometry* 4(1), 387–421 (1989)
14. Cline, A.K., Renka, R.J.: A storage-efficient method for construction of a thiesen triangulation. *Rocky Mountain Journal of Mathematics* 14(1) (1984)
15. De Floriani, L.: Surface representation based on triangular grids. *The Visual Computer*, 27–48 (1987)
16. De Floriani, L., Bussi, S., Magillo, P.: Triangle-based surface models. In: *Intelligent Systems and Robotics*, ch. 9, pp. 340–373. Breach Science Publishers (2000)
17. De Floriani, L., Puppo, E.: A Hierarchical Triangle-Based Model for Terrain Description. In: Frank, A.U., Formentini, U., Campari, I., et al. (eds.) *GIS 1992*. LNCS, vol. 639, pp. 236–251. Springer, Heidelberg (1992)
18. De Floriani, L., Puppo, E.: Extrating contour lines from a hierarchical surface model. *Computer Graphics Forum (Proc. Eurographics 1993)* 12(3), 249–260 (1993)

19. Delaunay, B.: Sur la sphère vide. *Izvestia Akademii Nauk SSSR, Otdelenie Matematicheskikh i Estestvennykh Nauk* 7, 793–800 (1934)
20. Dwyer, R.A.: A faster divide-and-conquer algorithm for constructing delaunay triangulations. *Algorithmica* 2(2), 137–151 (1987)
21. Edelsbrunner, H.: *Geometry and Topology for Mesh Generation*. Cambridge Monographs on Applied and Computational Mathematics. Cambridge University Press, New York (2001)
22. Edelsbrunner, H., Guoy, D.: Sink insertion for mesh improvement. In: *Proceedings of the 17th ACM Symposium on Computational Geometry*, pp. 115–123 (2001)
23. Erten, H., Üngör, A.: Computing acute and non-obtuse triangulations. In: *Canadian Conference on Computational Geometry (CCCG)*, pp. 205–208 (2007)
24. Erten, H., Üngör, A.: Triangulations with locally optimal Steiner points. In: Belyaev, A., Garland, M. (eds.) *Eurographics Symposium on Geometry Processing*, pp. 143–152 (2007)
25. Erten, H., Üngör, A.: Quality triangulations with locally optimal steiner points. *SIAM Journal of Scientific Computing* 31(3), 2103–2130 (2009)
26. Farrashkhalvat, M., Miles, J.P.: *Basic Structured Grid Generation with an introduction to unstructured grid generation*. Butterworth-Heinemann (2003)
27. Fortune, S.: A sweepline algorithm for voronoi diagrams. *Algorithmica* 2(2), 153–174 (1987)
28. Fowler, R.J., Little, J.J.: Automatic extraction of irregular network digital terrain models. *ACM Computer Graphics (SIGGRAPH 1979 Proceedings)* 13(3), 199–207 (1979)
29. Frey, W.H.: Selective refinement: a new strategy for automatic node placement in graded triangular meshes. *International Journal for Numerical Methods in Engineering* 24, 2183–2200 (1987)
30. George, P.L., Borouchaki, H.: *Delaunay triangulation and meshing*. Hermes (1998)
31. Gonzaga de Oliveira, S.L.: A survey of point insertion techniques in bidimensional delaunay triangulations. *INFOCOMP Journal of Computer Science* 10(2), 1–7 (2011)
32. Green, P.J., Sibson, R.R.: Computing Dirichlet tessellations in the plane. *The Computer Journal* 21(2), 168–173 (1977)
33. Guibas, L.J., Stolfi, J.: Primitives for the manipulation of general subdivisions and the computation of Voronoi Diagrams. *ACM Transactions on Graphics* 4(2), 74–123 (1985)
34. Har-Peled, S., Üngör, A.: A time-optimal delaunay refinement algorithm in two dimensions. In: *Proceedings of the 21st ACM Symposium on Computational Geometry, Pisa, Italy*, pp. 228–236 (2005)
35. Heckbert, P.S., Garland, M.: Survey of polygonal surface simplification algorithms. Technical report, Carnegie Mellon University - Department of Computer Science, May 1 (1997)
36. Hitschfeld, N., Rivara, M.C.: Automatic construction of non-obtuse boundary and/or interface Delaunay triangulations for control volume methods. *International Journal for Numerical Methods in Engineering* 55, 803–816 (2002)
37. Hitschfeld, N., Villablanca, L., Krause, J., Rivara, M.C.: Improving the quality of meshes for the simulation of semiconductor devices using LEPP-based algorithms. *International Journal for Numerical Methods in Engineering* 58, 333–347 (2003)
38. Joe, B.: Construction of three-dimensional triangulations using local transformations. *Computer Aided Geometric Design* 8, 123–142 (1991)
39. Joe, B.: Construction of -dimensional delaunay triangulations using local transformations. *SIAM J. on Scientific Computing* 14(6), 1415–1436 (1993)

40. Lawson, C.L.: Software for C^1 surface interpolation. In: Rice, J.R. (ed.) *Mathematical Software III*, pp. 161–164. Academic Press (1977)
41. Lee, D.-T., Schachter, B.J.: Two algorithms for constructing the delaunay triangulation. *International Journal of Computer and Information Science* 9(3), 219–242 (1980)
42. Miller, G.L., Pav, S.E., Walkington, N.J.: When and why Ruppert's algorithm works. In: *Twelfth Int. Meshing Roundtable*, pp. 91–102 (September 2003)
43. Miller, G.L., Talmor, D., Teng, S.-H., Walkington, N.: A delaunay based numerical method for three dimensions: Generation, formulation, and partition. In: *Proceedings of the Twenty-Seventh Annual ACM Symposium on the Theory of Computing, Las Vegas, Nevada* (May 1995)
44. Miller, G.L., Pav, S.E., Walkington, N.J.: When and why Ruppert's algorithm works. *International Journal of Computational Geometry and Applications* 15(1), 25–54 (2005)
45. Mücke, E.P., Saias, I., Zhu, B.: Fast randomized point location without preprocessing in two- and three-dimensional delaunay triangulations. In: *Proceedings of the Twelfth Annual Symposium on Computational Geometry* (May 1996)
46. Pav, S.E., Walkington, N.J.: Delaunay refinement by corner lopping. In: *Proceedings of the 14th International Meshing Roundtable*, pp. 165–181 (2005)
47. Plaza, A., Márquez, A., Moreno-González, A., Suárez, J.P.: Local refinement based on the 7-triangle longest-edge partition. *Mathematics and Computers in Simulation* 79, 2444–2457 (2009)
48. Rajan, V.T.: Optimality of the Delaunay triangulation in R^d . In: *Proceedings of the 7th ACM Symposium on Computational Geometry*, pp. 357–363 (1991)
49. Rebay, S.: Efficient unstructured mesh generation by means of delaunay triangulation and bowyer-watson algorithm. *Journal of Computational Physics* 106, 125–138 (1993)
50. Rivara, M.C.: New longest-edge algorithms for the refinement and/or improvement of unstructured triangulations. *International Journal for Numerical Methods in Engineering* 40, 3313–3324 (1997)
51. Rivara, M.C., Calderon, C.: LEPP terminal centroid method for quality triangulation. *Computer-Aided Design* 42, 58–66 (2010)
52. Rivara, M.C., Hitschfeld, N., Simpson, B.: Terminal-edges Delaunay (small-angle based) algorithm for the quality triangulation problem. *Computer-Aided Design* 33, 263–277 (2001)
53. Rivara, M.C., Inostroza, P.: Using longest-side bisection techniques for the automatic refinement of Delaunay triangulations. *International Journal for Numerical Methods in Engineering* 40, 581–597 (1997)
54. Rivara, M.C., Iribarren, G.: The 4-triangles longest-side partition of triangles and linear refinement algorithms. *Mathematics of Computation* 65(126), 1485–1502 (1996)
55. Rivara, M.C., Venere, M.: Cost analysis of the longest-side (triangle bisection) refinement algorithms for triangulations. *Eng. with Computers* 12, 224–234 (1996)
56. Ruppert, J.: A new and simple algorithm for quality 2-dimensional mesh generation. In: *Proceedings of the Fourth ACM-SIAM Symposium on Discrete Algorithms*, pp. 83–92 (1993)
57. Ruppert, J.: A Delaunay Refinement Algorithm for Quality 2-Dimensional Mesh Generation. *Journal of Algorithms* 18(3), 548–585 (1995)
58. Scarlatos, L., Pavlidis, T.: Hierarchical triangulation using cartographic coherence. *CVGIP: Graphical Models and Image Processing* 54(2), 147–161 (1992)

59. Seidel, R.: Backwards analysis of randomized geometric algorithms. Technical Report TR-92-014, International Computer Science Institute, Berkeley, California (February 1992)
60. Shamos, M.I.: Computational geometry. PhD thesis, Yale University, New Haven, Conn. (1977)
61. Shewchuk, J.R.: Triangle: A two-dimensional quality mesh generator and delaunay triangulator, <http://www.cs.cmu.edu/~quake/triangle.html>
62. Shewchuk, J.R.: Triangle: Engineering a 2D quality mesh generator and Delaunay triangulator. In: First Workshop on Applied Computational Geometry, pp. 124–133. ACM (1996)
63. Shewchuk, J.R.: Delaunay Refinement Mesh Generation. PhD thesis, Carnegie Mellon University, Computer Science Department (1997)
64. Shewchuk, J.R.: Lecture notes on Delaunay mesh generation (1999)
65. Shewchuk, J.R.: Delaunay refinement algorithms for triangular mesh generation. *Computational Geometry* 22, 21–74 (2002)
66. Shewchuk, J.R.: Ruppert's delaunay refinement algorithm. website (July 2005) (accessed September 2011)
67. Simpson, B., Hitschfeld, N., Rivara, M.C.: Approximate shape quality mesh generation. *Engineering with Computers* 17, 287–298 (2001)
68. Sleator, D.D., Tarjan, R.E.: Self-adjusting binary search trees. *Journal of the ACM* 32(3), 652–686 (1985)
69. Sloan, S.W.: A fast algorithm for constructing Delaunay triangulation in the plane. *Advances in Engineering Software* 9, 34–55 (1987)
70. Tournois, J., Alliez, C.W.P., Desbrun, M.: Interleaving delaunay refinement and optimization for practical isotropic tetrahedron mesh generation. *ACM Transactions on Graphics - Proceedings of ACM SIGGRAPH 2009* 28(3), article no. 75 (2009)
71. Üngör, A.: Off-centers: A new type of Steiner points for computing size-optimal quality-guaranteed Delaunay triangulations. In: *Proceedings of the Latin American Symposium on Theoretical Informatics*, Buenos Aires, Argentina, pp. 152–161 (April 2004)
72. Üngör, A.: Off-centers: A new type of steiner points for computing size-optimal guaranteed-quality delaunay triangulations. *Computational Geometry: Theory and Applications (CGTA)* 42(2), 109–118 (2009)
73. Voronoi, G.: Nouvelles applications des paramètres continus à la théorie des formes quadratiques. *J. für die Reine und Angewandte Mathematik* 133, 97–178 (1907)
74. Watson, D.F.: Computing the n-dimensional delaunay tessellation with application to voronoi polytopes. *The Computer Journal* 24(2), 167–172 (1981)
75. Weatherill, N.P.: Delaunay triangulation in computational fluid dynamics. *Computers and Mathematics with Applications* 24(5/6), 129–150 (1992)

Axis-Parallel Dimension Reduction for Biometric Research

Kushan Ahmadian and Marina Gavrilova

CPSC Department,
University of Calgary, Canada
{kahmadia,mgavrilo}@ucalgary.ca

Abstract. The objective of this research is to present a novel methodology based on the axis-parallel dimension reduction technique and chaotic neural network to improve the performance and circumvention of multi-modal biometric system. The proposed methodology for dimensionality-reduction and chaotic neural network learner on example of face, ear and fingerprint biometric was presented in the methodology section. This paper validates the proposed methodology by providing experimentation results. First subsection showcases advantages of chaotic neural network for fingerprint recognition (accuracy and circumvention). Next subsection compares results of the proposed multi-biometric system based on axis-parallel dimensionality reduction. The experiments demonstrate that the proposed dimensionality reduction and associative memory training methodology outperforms other commonly used techniques in both FAR (False Accept Rate) and FRR (False Reject Rate) both individually and if used together. Finally, the last section proposes the alternative multimodal system architecture with additional features that can further improve system performance in terms of accuracy and circumvention.

Keywords: geometry, axis-parallel, Voronoi diagram, dimensionality-reduction, biometrics.

1 Introduction

The current trend in design of security systems is optimization and efficiency. These goals can be achieved by variety of means, including high-capacity resources, parallelization, reducing costs, limiting functionality, increasing training, or changing acceptable error rate thresholds. High complexity and high-dimensionality of data has been for a long time a key hurdle in achieving desired results in terms of accuracy and circumvention (resistance to noisy data). However, fairly recently, advances in data mining and geometric data analysis have paved new ways to deal with this problem.

This paper presents the outcomes of research on using axis-parallel dimensionality reduction method in biometric optimization, specifically for fingerprint and face and ear biometric systems. We start with fingerprint processing which possesses nice geometric and topological properties which can be represented through Voronoi diagram and Delaunay triangulation, and then proceed to axis-parallel dimensionality

reduction for any image-based geometric data. The overall architecture of multi-biometric system based on selected geometrical features is presented next, with specific emphasis on a case of missing or unreliable data.

The outline of this paper is as follows. In the second section, we provide a general discussion on geometric methods in biometric research. Fingerprint optimization using Voronoi diagrams and neural networks is described in Section 3. Section 4 is dedicated to dimensionality-reduction method and Section 5 presents new multi-modal system architecture which can deal with missing or unreliable data. Section 6 concludes the paper and presents some views on possible future research.

2 Biometric Security and Optimization

2.1 Biometric Security

The idea behind geometric security spans from the natural way people recognize each other – through familiar facial features, eyes, voice, style of walk or even way they communicate. Biometric security systems thus rely on physiological characteristics of humans or their behavioral patterns to identify individuals in cases where secure access or verification of identity is required (Ross et al 2006). A number of biometric security systems has span to life over last decade, with major government organization and consumer corporations supporting the trend. Thus, majority of airports now have biometric security systems, banks have pattern recognition surveillance systems, and consumer products have biometric recognition devices (fingerprint readers, voice recognition, facial image capturing camera etc) (Yanushkevich et al 2006).

Constraints with system performance when biometric data is not reliable or of poor quality, however, inspired research into more complex systems where a combination of factors is taken into account to make access granting decision. The systems combine data at different source levels (raw source data, pre-processed images, extracted features, ranked preliminary outcomes or final decisions individually made) and arrives to final authentication answer –to grant or not to grant an access. The examples of various systems are found in (Monwar and Gavrilova 2010).

2.2 Biometric Optimization

The concept of mathematical optimization of a system is based on arriving at optimum solution (local minimum or maximum) with as little time or as little resources as possible under given constraints. In biometric systems, the constraints might be *physical* (data availability), *resource based* (availability of certain sensor), *algorithm based* (existence of optimal algorithms for biometric feature extraction or data processing), *cost based* (amount of available funds for equipment), *personnel based* (amount of training and support for day to day operation), or *acceptability based* (how accepting public would be of particular biometric system in light of privacy concerns). In this paper, we concentrate on **neural-network based**

optimization, which takes care of biometric system learning processes being optimal, and **processing optimization for multi-modal biometric system**, which relies on finding new ways to reduce amount of data while selecting the most important features for subsequent recognition. The both tasks are performed simultaneously in the system, while keeping accuracy high and impact of circumvention (poor quality noisy data or missing data) low.

3 Geometric Methods and Neural Networks in Biometrics

One of the earlier research provided the background and the methodology for combining topology-based computational geometry methods, such as Voronoi diagrams and Delaunay triangulation, with state-of-the-art biometric research. The results were more than optimistic. The original paper (Wang and Gavrilova 2006) introduced one of the highest precision fingerprint recognition methods based on representing biometric patterns through building Delaunay triangulation on minutiae points. There were numerous advantages to this approach. Not only the position of minutiae points was taken into account during pattern matching of input sample to closes stored biometric fingerprint pattern in the database, but also the length of Delaunay edges, the area of triangles, the proportions of angles were taken into account, thus reducing FAR (False Acceptance Error) rate to less than 1% on commercial fingerprint database. In addition, performing both local and global matching and applying non-linear transformations to the fingerprint surface image allows to reduce the error to 0.18% with False Rejection Rates around 6%.

In (Ahmadian and Gavrilova 2010), experimental results to showcase advantages of combining Chaotic Neural Network (CNN) with Delaunay Triangulation (DT) matching method for fingerprint recognition in both accuracy and circumvention (resistance to errors). The test database contained both high and very low quality fingerprint images, thus if high level of accuracy, it is confirmed that the system possesses both precision and circumvention. After normalization, thinning and minutiae extraction, the Delaunay Triangulation is built for the minutiae point set, and the neural network is being trained to identify the closest stored pattern to the input fingerprint. The experiments were performed on the database from the University of Bologna, containing 21*8 fingerprint images of 256*256 sizes. The size of the neural network was set to 64*64. The performance of the proposed method in comparison with traditional method such as DT matching, DT matching with additional ridge geometry features and standard minutiae method. For the provided samples, the false rejection rate (FRR) was the smallest for the combination of CNN and DT. It show improvement in FRR to 0.047% over Wang's method which is one of the best recent algorithms based on rigid Delaunay triangulation with 5.46% FRR rate. The false acceptance rate remains very low, at 1.17%. The convincing quality of these experimental results is the result of using a combination of minutia, singular points and ridge features. The experiments show that application of the proposed neural network improves the FRR rate significantly while keeping FAR at a very low rate.

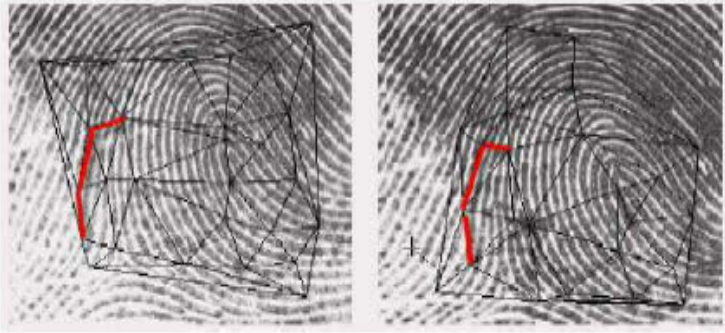


Fig. 1. Matched Delaunay triangle edges for fingerprint

4 Chaotic Neural Networks and Dimensionality Reduction

Another recent paper from our lab by (Gavrilova and Ahmadian 2011) studied if neural networks combined with dimension reduction improve biometric system accuracy and circumvention, i.e. resistance to low quality data or absence of one of biometric traits all together.

In that work from, we aimed to find the subset of biometric features derived from the original dataset which is most representative of the unique and distinctive features of given biometric dataset. As the primary biometric sample, we chose face and ear images due to significant variability of image quality and also popularity of the biometric. Each face image in the training set is then represented as a linear combination of the original images. The number of possible classes is equal to the number of face image groups in the training set. The faces are then approximated using only the most characteristic features which account for the most variance and thus distinctiveness within the set of face images. This approach allows not only move compact space representation, but also a convenient tool for subsequent clustering and learning of common patterns.

Next, we use neural networks as a fast and reliable way for a biometric system to learn the pattern from the previously extracted subspaces. The neural network approach is based on chaotic noise injection strategy which is the leading strategy for neural network training. Reported experimental results show that the advantages are the ability to learn and later recognize new biometric samples in an unsupervised manner and that method is easy to implement using the proposed neural network architecture.

The novelty of the proposed system relies on the representation of the feature space, which is not limited to single biometrics and neither to the number of dimensions. While the system is capable of handling large number of feature vectors, it makes it also capable of learning complex biometric patters faster using neural network learner. The nature of associative network is based on minimizing the energy function assigned to the neural network. The energy function simply shows the distance of the stored pattern to the introduced pattern. The lower the energy function gets the network is more stable. On the other side, patterns are stored as the weights

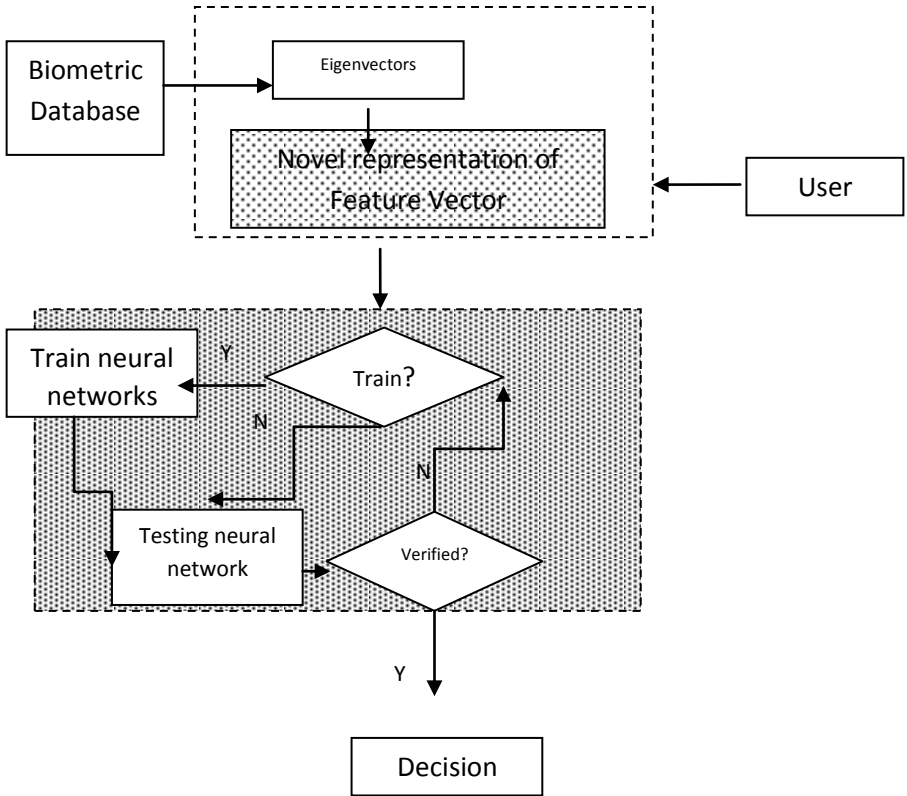


Fig. 2. Neural Network learner based biometric system architecture

between pairs of neurons. By other means when two values are changing with a high correlation, the weights between the neurons corresponding to those values gets higher. The learner system then converges the given set of vectors to the stored pattern to perform matching.

In the introduced above approach, amount of input data, database size and number of features have direct correlation with system complexity and performance. Clustering aims at dividing datasets into subsets (clusters), where objects in the same subset are similar to each other with respect to a given similarity measure, whereas objects in different clusters are dissimilar. If clusters of biometric features are identified in advance, the number of features from selected clusters can be reduced and NN training can be accomplished faster and to higher accuracy. When clustering high- dimensional data of biometric features, we face a variety of problems. The presence of irrelevant features or of correlations among subsets of features heavily influences the appearance of clusters in the full-dimensional space. The main challenge for clustering is that different subsets of features are relevant to different clusters, that is, the objects cluster in subspaces of the data space but the subspaces of the clusters may vary. Additionally, different correlations among the attributes may be relevant for different clusters. This assumption implies that different biometric

features or a different correlation of biometric features may be relevant for varying clusters the local feature relevance or local feature correlation. A common way to overcome problems of high-dimensional data spaces where several features are correlated or only some features are relevant is to perform feature selection before performing any other data mining task. Due to the problem of local feature relevance and local feature correlation, usually no global feature selection can be applied to overcome the challenges of clustering high-dimensional biometric data.

Instead of a global approach to feature selection, (Gavrilova and Ahmadian 2011) proposed to use a local approach accounting for the local feature relevance and/or local feature correlation problems. Since traditional methods, like feature selection, dimensionality reduction, and conventional clustering, do not solve the previously sketched problems, new method based on axis-parallel subspace clustering has been introduced. The main idea of the method is to project d-dimensional vector of biometric feature points in the parameter space represented through a (d-1)-dimensional hyperplane. In order to detect those linear hyperplanes in the data space, the task is to search for points in the parameter space where many sinusoidal curves intersect. Since computing all possibly interesting intersection points is too expensive, we discretize the parameter space by some grid and search for grid cells with which many sinusoidal curves intersect. For that purpose, for each grid cell the number of intersecting sinusoidal curves is aggregated. Due to this discretization of the parameter space, exact intersections are no longer considered. Rather, a slight impreciseness is allowed in modeling a certain degree of jitter given by the grid resolution. The higher the grid resolution is, the more accurate the recognition of the line segments. With the proposed concepts, we transform the original subspace clustering problem (in data space) into a grid-based clustering problem (in parameter space) where similar features are now located on the same hyperplane spanning the set.

The proposed methodology was tested extensively with testing cases design diagram depicted in Figure 3. Specifically, it shows that clustering methods can be substituted with alternatives, and learning mechanism can be chosen (one of which is naturally new CNN method). As experimentation outcome, the combination of subspace clustering and CNN learner produces best possible result – less than 0.2% Equal Error Rate (where FAR and FRR are equal).

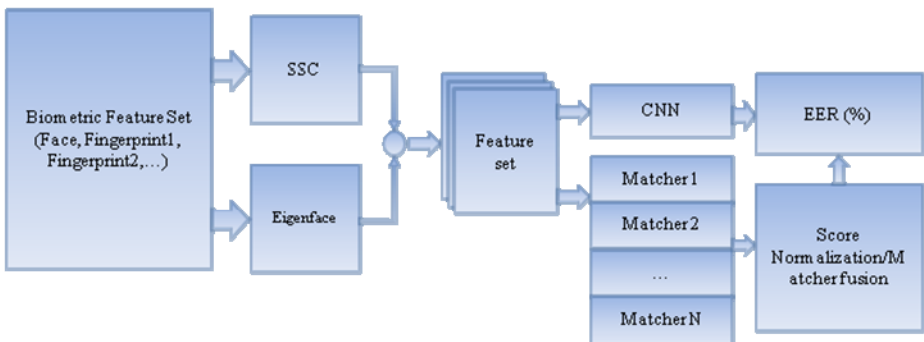


Fig. 3. System testing design for both subspace clustering and CNN learner

5 New Multi-biometric System Architecture

The performance of the multi-modal biometric system based on the above architecture is shown in Figure 4. The system has been tested on separate ear and face biometrics and their combinations. As it can be seen in Figure 4, for a FAR rate of 1.5%, the usage of ear biometric solely results in 5.4% false rejection rate error, while this rate reduces to 2.3% for face database. When the biometrics are combined together, the resulting system benefits from very low 1.7% rejection rate. Since the neural network is trained by the ear and face samples concurrently, however, a special attention must be given to the case when only one of the patterns are presented to the neural network. The architecture of the system with missing biometric is shown in Figure 5.

Experiments confirm that in that case, for a FAR rate of 2.5% the FRR is dropped to 5%. By removing the ear features the FRR rate for the same FAR value increases to 20%. The results were predictable due to the nature of neural network which used to utilize all the vectors in the training phase. By eliminating any of the feature sets, the network would experience confusion in convergence patterns. We thus propose a modified system, which tends to overcome the described issue. In the new architecture, the feature vectors of different biometrics are treated separately. By other means, instead of one large vector which contains the features of all the biometrics, there are several vectors as:

$$\begin{aligned} \mathbf{x} &= (x_1, \dots, x_d)^T \\ \mathbf{u} &= (u_1, \dots, u_m)^T \\ &\dots \\ \mathbf{v} &= (v_1, \dots, v_n)^T \end{aligned}$$

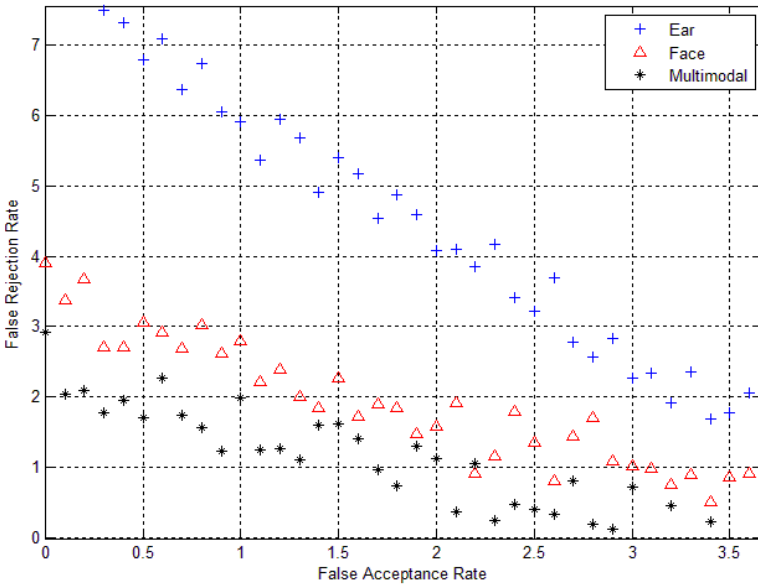


Fig. 4. FAR-FRR graphs for multimodal biometric system with CNN

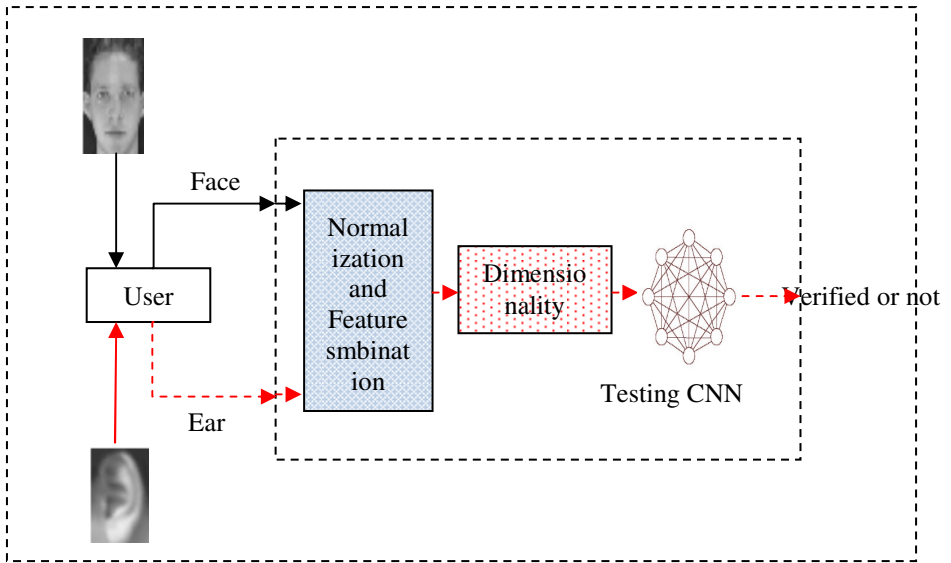


Fig. 5. Absence of one of the biometric features

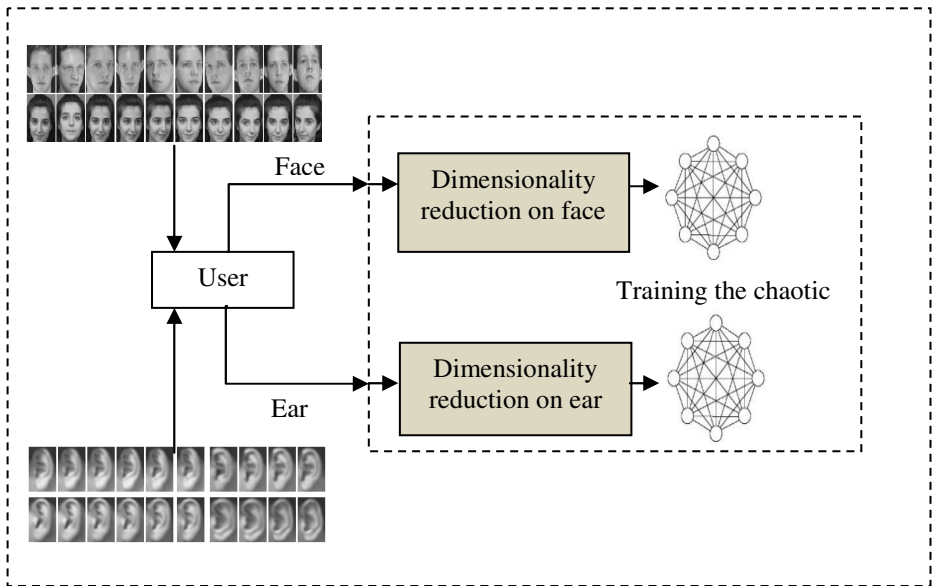


Fig. 6. Proposed multi-biometric system architecture

and for each vector, a separate neural network is trained. Within the testing phase and when a new pattern is introduced into the system, once the normalization phase is passed, each pattern is fed into its corresponding learner system as shown in Figure 6.

In case of verification, each neural network returns the closest distance between the new pattern and one of the stored pattern in the database. If the distance is greater than the FAR-FRR ratio threshold, then the pattern is simply classified as imposter. Once the system obtains the yes/no results from all its neural subsystems, it performs a simple majority voting mechanism to verify/reject the user. The main advantage of the new architecture is to avoid system crashes during the absence of some of the input biometrics. Meanwhile, we sacrifice the correlation between many of the features from different biometrics. In order to evaluate the new architecture, we compare a similar set of face and ear samples and their corresponding FAR-FRR graph, which is shown in Figure 7. As it can be seen, the system 1 architecture has slightly better performance compared to the new one, where approximately 2% more accuracy. However, making the separate feature sets and training separate classifiers based on each set results is highly advantageous if one biometric is missing. When one of the resources is eliminated or highly unreliable, the original system performance is worse than that of a new system. According to the results, the new architectures is affected only slightly - e.g. for FAR of 2% the FRR rate is increased from 3.5% to 6%. The original architecture is affected to a much bigger degree with error rate reaching 20%.

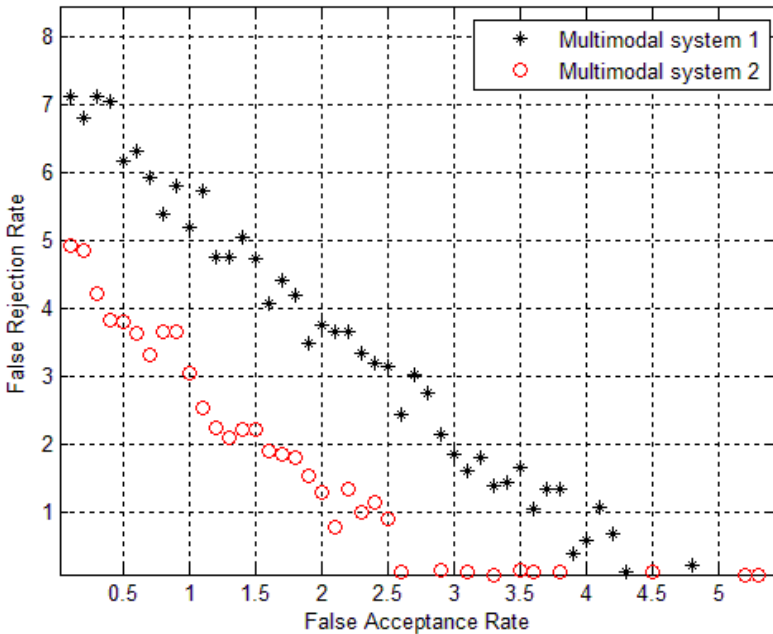


Fig. 7. Performance of proposed multi-biometric system2 vs original system1

6 Conclusions

In this paper, we have presented a brief overview of neural network based and geometric optimization in biometric systems, and presented a new multi-modal

system architecture based on neural network learner that can handle noisy or very low quality data. Extensive experimentation showed that high accuracy rates are preserved while system is resistant to errors and even absence of some data sources. The future research includes developing alternative mechanisms for decision making in the context of the proposed system and looking at geometry-base pattern matching as a basis for neural network learner.

Acknowledgment. Authors of the paper acknowledge partial support of the project form NSERC, NATO and Alberta Ingenuity.

References

- Aihara, K., Takabe, T., Toyoda, M.: Chaotic neural networks. *Phys. Lett. A* 144(6,7), 333–340 (1990)
- Ahmadian, K., Gavrilova, M.: Transiently Chaotic Associative Network for Fingerprint Image Analysis, *SI on Intelligent Computing for Multimedia Assurance. International Journal of Neural Network World* 20(3), 389–403 (2010)
- Gavrilova, M., Ahmadian, K.: Dealing with Biometric Multi-Dimensionality through Novel Chaotic Neural Network Methodology. Issue on "Advances and Trends in Biometrics" of the *International Journal of Information Technology and Management, Inderscience* 11(1/2) (2011)
- Monwar, M., Gavrilova, M.L.: A Multimodal Biometric System Using Rank Level Fusion Approach. *IEEE Transactions on Man, Systems and Cybernetics TSMC Part B, Special Issue on Cognitive Informatics and Cybernetics* 39(5), 867–878 (2009)
- Ross, A., Nandakumar, K., Jain, A.: *Handbook of Multibiometrics. International Series on Biometrics, vol. 6* (2006)
- Yanushkevich, S., Gavrilova, M., Wang, P., Srihari, S.: *Image Pattern Recognition: Synthesis and Analysis in Biometrics. Machine Perception and Artificial Intelligence, vol. 67. World Scientific*
- Yamada, T., Aihara, K., Kotani, M.: Chaotic neural networks and the travelling salesman problem. In: *Proc. Int. Joint Conf. Neural Networks*, pp. 1549–1552 (1993)
- Wang, C., Gavrilova, C., Delaunay, M.: Triangulation Algorithm for Fingerprint Matching. In: *IEEE-CS Proceedings, ISVD 2006, Banff*, pp. 208–216 (2006)

An Overview of Procedures for Refining Triangulations

Sanderson L. Gonzaga de Oliveira

Universidade Federal de Lavras, 37200-000 Lavras-MG, Brazil

sanderson@dcc.ufla.br

<http://algot.dcc.ufla.br/~sanderson>

Abstract. In this paper, a list of procedures for refining triangulations and other related issues is presented. The wide variety of processes in order to refine triangles in a meshed geometry is placed in perspective. Moreover, the focus of this overview is strictly on adaptive triangle partition and collapse operators using mesh refinement procedures and some associated algorithms.

Keywords: Triangulations, triangle subdivision, mesh generation, computational geometry.

1 Introduction

Modeling a surface within a finite set of sampled discrete places is fundamental in many disciplines. This includes meshes for numerical methods in order to solve partial differential equations, computer graphics, computer vision, virtual reality, flight simulation, computer-aided design and geographic data processing. Non-uniform and/or irregular triangular computational meshes are quite used in those areas. Irregular triangulations can provide advantages in relation to other meshes. Usually, triangulations provide less computational cost than using other polygonal shapes, allow points on curved boundaries of irregularly shaped domains and to be distributed inside the domain as desired for variable resolution (see Thacker [58] for details). Roughly speaking, a triangular mesh is a 2D simplicial complex that is widely applied in order to represent geometric models. One can consider *triangulation* the act of transforming a non-triangular mesh into a triangular one. On the other hand, *triangular mesh* and *triangulation* are interchangeably used here since an initial mesh comprised only of triangles is considered.

Rivara and Inostroza [50] explains that the creation of the triangular discretization should not be a separate step of the solution process, but an adaptive process. Managing local refinement of the discretization is important in order to obtain low computational cost solutions. Moreover, algorithms in mesh discretizations that maintain the non-degeneracy of the triangles and smoothness of the mesh are desirable (see [50] for details). Clearly, different approaches exist for aspects of improvement of the mesh quality. Those approaches have been

proposed in a great variety of disciplines and similar lines of research in disparate fields into a unique text can facilitate a cross-fertilization.

Researchers from different disciplines have provided excellent surveys, tutorials and textbooks in this issue. Examples are cited in the following.

- Jones and Plassmann [25] reviewed processes for using adaptive refinement of non-uniform finite-element triangular meshes.
- Heckbert and Garland [21] reviewed methods for simplifying and approximating polygonal surfaces. Methods from a wide range of disciplines were practically and theoretically classified, summarized, and compared by these authors. In addition, the piecewise-linear curve simplification was also briefly surveyed.
- Puppo and Scopigno [46] reviewed and discussed simplification methods, level of detail (LOD), multiresolution models for surface meshes, and their applications.
- Garland [16] surveyed techniques for the automatic simplification of polygonal models.
- Zorin and collaborators [62] covered the basic principles of subdivision, and how its rules are constructed, among other aspects in this issue.
- Ivriissimtzis and collaborators [24] provided a complete classification of possible subdivision schemes. These authors classified subdivision schemes in terms of the base mesh and of how mesh primitives (vertices, face centers, midedges) map to one another from one subdivision pass to the next.
- Warren and Weimer [61] published a textbook in this issue. Since subdivision is based on repeated refinement, LOD ideas can be incorporated.
- Luebke and collaborators [33] covered a wide gamut of LOD topics in the computer-graphic context. They categorized and discussed work on derefining the mesh, known as *mesh simplification* in computer-graphic context. In addition, they emphasized the underlying similarities and differences among the most important algorithms. They also discuss issues of mesh topology, since modifying a topology can permit simplification in the mesh, but can also lead to poor fidelity.
- Sabin [54] also provided a survey on this subject.
- De Floriani and collaborators [10] surveyed data structures for encoding LOD models. They classified LOD data structures according to the dimensionality of the basic structural element that they represent based on point, triangle, and tetrahedron. Within each class, they reviewed single-level and general data structures for LOD models based on non-uniform meshes. In addition, they reviewed specialized data structures that assume a certain data (semi-) regularity.
- Ma [34] provided a subdivision surface modeling overview. Moreover, basic topics, such as scheme construction, property analysis, parametric evaluation and subdivision surface fitting, were addressed.
- Danovaro and collaborators [8] presented a historical overview of LOD models highlighting the contributions of the work of their group during more than twenty years.

Those surveys were written within different focus. Since they were written, the repertoire of available adaptive triangle partition techniques has grown in different disciplines. So a more up-to-date list is provided here. In addition, differently from those works, the focus of this *overview* is strictly on adaptive triangle partition (and collapse) operators using mesh refinement procedures (and some associated algorithms). The adaptive refinement of triangulations is a very well known problem. However, a beginner could have some difficulty in learning about the subject because the huge number of works in this topic. The purpose of this article is to provide an overview of the approaches and the techniques are not evaluated. In this sense, this overview is far from being exhaustive.

Researchers have been improving local mesh refinement/derefinement schemes mainly to improve the numerical solution of partial differential equations. In this issue, the mesh adaptation is based on a posteriori error estimator or error indicator that is evaluated in function of the current numerical solution at each discrete place of the mesh. In addition, the analysis of the convergence of the numerical solution along the sequence of the refinement steps is important. Moreover, the number of degrees of freedoms and time of the simulation comparing to the error for each strategy should be compared to evaluate the better algorithm. Besides, the easiness of the mesh conformity, the treatment of transient discrete places, i.e. if they are used to conform the mesh, the propagation of the scheme, the complexity of the refinement and derefinement algorithms, the construction of a sequence of nested meshes versus re-meshing, and the mesh degeneration are characteristics that should be analyzed in the context of adaptive mesh refinement. Although these aspects are fundamental to decide which refinement algorithm is better, they are not discussed in this paper because the enormous number of applications and each one may have its specific characteristics.

Heckbert and Garland [21] explain that the objective in approximation theory is often to characterize the error in the limit as the mesh becomes more and more fine. In computational geometry, specifically in mesh generation, the goal is typically to find algorithms that generate approximations either with optimal or near-optimal compactness, error, or speed or to prove bounds on these. Usually, these features receive more attention than both the implementation of algorithms and low level practical optimizations. So no comparisons are provided in this paper neither practical examples are shown. The reader should study those aspects of the procedures related to the intended application and its specific features. Besides, Delaunay refinement techniques are not described in this article. Although this paper is far from being exhaustive and its limitations, it may serve as a list of schemes for one who is starting studying adaptive mesh refinement schemes. The discussion is intended solely as a general and undetailed introduction to the approaches, with the expectation being that a reader wishing to pursue particular topics in technical detail will do so by consulting the cited references. Namely, since the mathematical theory behind those procedures is very technical, this overview does not deal with mathematical details for simplicity, clarity, and the limited space. So the cited references should be followed by those interested in the theory underlying each procedure.

Prior to discussing the partition processes themselves, high-quality mesh features for finite calculations as well as characteristics of partition processes are described in Section 2. Powell-Sabin splits are presented in Section 3. The longest-edge triangle partition process and its variations are briefly explained in Section 4. The centroid point insertion is briefly described in Section 5. Afterwards, the *vertex split* approach is presented in Section 6. The $\sqrt{3}$ -subdivision is discussed in Section 7. Laves nets are commented in Section 8. The stellar subdivision grammar is commented in Section 9. The 7-triangle trisection partition processes are presented in Section 10. The RGB subdivision is commented in Section 11. Finally, some future directions are given in Section 12.

2 Some Features for Refinement in High-Quality Triangulations

Zorin and collaborators [62] defined subdivision as “a smooth curve or surface as the limit of a sequence of successive refinements” of a polyhedra. The basic procedures are quite simple. A given triangle is split through the insertion of new vertices. The new vertices are computed as weighted averages of nearby existing vertices. Few assumptions are made about the global nature of the domain to be modeled and data structures only need to support operations such as graph neighbor findings. The reader can obtain details about this subject in papers of Schröder and collaborators [7, 31], and references therein.

In this sense, a process that inserts points into the mesh partitioning only an individual triangle is desirable since it demands only strict local updates of the data structure that represents the mesh. Namely, *nesting* is an important characteristic of the refinement algorithm, i.e. the triangles in the refined mesh are nested within the previous mesh level. Moreover, *nesting* means that a unique discrete place generates others without changing the edges and coordinates of its neighbors in a refinement process. This process may provide low computational cost because few nodes of the data structure should be traversed and updated in order to correctly represent the new mesh. It is worth noting that accessing the main memory of a RAM-model computer system is still currently a bottleneck in terms of performance. The strict local triangle partition is difficult to reach in the Finite Element Method (FEM) because the *conformity* problem. Conformity refers to the requirement that the intersection of adjacent triangles is either a common point or a common edge. For instance, in Fig. 1 a conforming mesh is sketched on left and a non-conforming mesh is sketched on right. However, conformity is not a concern in the Finite Volume Method (FVM). Thus, non-conforming meshes with finite-volume discretizations may result in competitive approaches.

Babuska and Aziz [1] demonstrated that the finite-element approximation accuracy degrades as the maximum angle of the triangle approaches π . Moreover, small angles should be avoided because the condition number of the resulting linear-system matrix that arises from the finite-element discretization grows $O(1/\theta_{min})$, in which θ_{min} is the minimum angle in the triangulation (see the

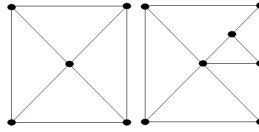


Fig. 1. Simple examples of conform mesh on left and non-conform mesh on right

discussion in Fried [15] for details). So when dividing a triangle, the essential is that no angle be too close to 0 or π : triangulations which minimize the maximum angle (or maximize the minimum angle) are desirable.

3 Powell-Sabin Splits

Powell and Sabin [41] presented four types of subdivisions, currently known as Powell-Sabin splits among computer-graphic researchers. In Fig. 2a, I is any interior point of the triangle. This split operation connects I to the three vertices and to a point from each edge of the triangle. Then, the original triangle is replaced by six triangles. In the operation shown in Fig. 2b, the authors considered that the inserted point E can be in any position of the longest-edge. The point E is connected to the opposite vertex and to a point of each other two edges. Then, the original triangle is replaced by four triangles. These authors did not provide profound study about this subdivision because they considered the lack of symmetry unattractive and that it is not suitable for providing overall first derivative continuity when the data triangles are put together. Another Powell-Sabin split, shown in Fig. 2c, connects the midedges and traces the medians generating twelve triangles that replace the original one.

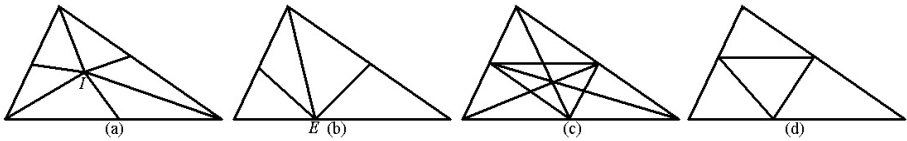


Fig. 2. Powell-Sabin splits

The split operation of Fig. 2d is another 1-to-4 split. It connects points from any position of each triangle edge generating four triangles that replace the original one. If the points are adequately inserted, then the new triangles are improved. This split operation is used in the Butterfly [12] and Loop [32] schemes. The latter is one of the simplest subdivision schemes. It is based on a spline basis function called the three-directional quartic box spline.

Gómez and Guzmán [17] used the approach shown in Fig. 2d. They divided a triangle by adding a “significant” point (chosen in some unspecified way) near each midedge generating four new triangles that replace the original one.

Moreover, each triangle is recursively subdivided into four sub-triangles until meeting a maximum error tolerance. It is known as *quaternary subdivision* among geographic information system researchers.

If one chooses to divide a triangle by adding the three midedges generating four new triangles that replace the original one, finite-element researchers call this approach as 4-triangle self-similar (4T-SS). This fixed approach maintains the quality of the original triangle.

In order to avoid non-conformity (or *T-vertices*), Bank and collaborators [5] introduced edges according to the *red-green triangulation* rules. An adaptive non-conforming mesh from the 4T-SS (red) partition is made conforming by splitting some triangles by a 2-triangle (green) partition (see Bank and Sherman [3] and [4] for details), depending on their neighbor level. Moreover, green edges are those inserted in order to conform the mesh. More specifically, green triangles are those made by joining each non-conforming point with the opposite vertex of the non-conforming triangle. The green edges can be removed before the next level of refinement.

A variant of red-green triangulations was used by Zorin and collaborators [63] in order to support *multiresolution editing of meshes* based on the Loop subdivision scheme [32]. Zorin [62] explains that multiresolution mesh editing extends subdivision by including detail offsets at every subdivision level. In addition, it unifies patch based editing with the flexibility of high-resolution polyhedral meshes. In the approach of Zorin and collaborators [63], a reverse subdivision computes adaptive meshes. It begins at the finest level and prunes overrefined triangles. It computes a restricted non-conforming mesh. Then some triangles are bisected in order to conform the mesh. A hierarchical data structure deals with the correct relocation of points.

The *incremental subdivision* (Pakdel and Samavati [37]) is another variant of both the Loop [32] and the butterfly [12] schemes. A large support area for refinement deals with the correct geometric computation of control points. The reader is referred to Puppo and Panozzo [45] for a description of works related to adaptive subdivision.

Puppo [42] provided a general framework for multiresolution meshes called Multi-Triangulation. The general idea underlying the it is that any multiresolution mesh can be construct through local processes that progressively change an initial mesh through refinements or simplifications.

4 Bisecting the Longest Edge of Triangles and Variations

One of the first proposal in order to adaptively refine triangles was the triangle bisection process sketched in Fig. 3a. Let $\triangle ABC$ be a triangle with vertices A , B and C . $\triangle ABC$ is bisected choosing its longest edge (say \overline{AB}). Let D be the midpoint of \overline{AB} . Then replace $\triangle ABC$ by two triangles $\triangle ACD$ and $\triangle BCD$. This two-triangle longest-edge partition is denoted here as 2T-LE.

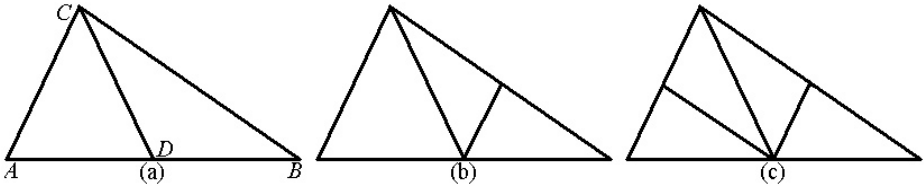


Fig. 3. Triangle partition processes: (a) 2-triangle longest-edge (2T-LE); (b) 3-triangle longest-edge (3T-LE); (c) refinement by successive bisections - 4-triangle longest-edge (4T-LE)

Let \triangle_{01} be a given triangle. Bisect \triangle_{01} into two triangles \triangle_{11} and \triangle_{12} . Afterwards, bisect them forming four new ones \triangle_{2i} , $i = 1, 2, 3, 4$. Continue thus, forming an infinite sequence $T_j = \{\triangle_{ji} : 1 \leq i \leq 2^j\}$, $j = 0, 1, 2, \dots$, of triangle sets. Rosenberg and Stenger [53] proved that the interior angles of \triangle_{ji} do not go to zero as $j \rightarrow \infty$. It was a conjecture of finite-element users and the result was demanded for convergence. Specifically, if α is the smallest interior angle of \triangle_{01} and θ is any interior angle of \triangle_{ji} , then $\theta \geq \alpha/2$. Stynes [57] demonstrated that the shapes produced by the 2T-LE tend to be closer to an equilateral triangle than the original \triangle_{01} . In addition, Stynes proved that the resulting triangles satisfy a shape regularity property. These properties hold for all partition processes based on the triangle bisection, e.g. 3T-LE and 4T-LE, described in the following. In order to conform a finite-element mesh, when using the 2T-LE partition process, the other triangle that shares the divided edge must also be refined unless it is in the boundary of the domain. Velho and Zorin [60] presented a 4-8 subdivision using bisection. Moreover, a new $\sqrt{2}$ -scaled mesh comes from a single refinement pass.

Rivara [47] proposed to process successive bisections into a single triangle, i.e. the longest-midedge is always chosen. Rivara chose to divide the triangle into three or four new ones. Moreover, based on the works of Rosenberg and Stenger [53] and Stynes [57], Rivara [47] proposed the 3-triangle longest-edge (3T-LE) partition process depicted in Fig. 3b, which principles have been firstly described by Kearfott [26] and [27]. Furthermore, it is obtained by joining the longest-midedge of the triangle with the opposite vertex and the other midedge (that can be the second longest edge) of the triangle. This partition process is used in order to conform the mesh when applying the 4T-LE partition approach. Also based on the works of Rosenberg and Stenger [53] and Stynes [57], Rivara [47] proposed the 4-triangle longest-edge (4T-LE) partition process sketched in Fig. 3c. It is obtained by joining the longest-midedge of the triangle with the opposite vertex and the two remaining midedges. In order to obtain a conforming mesh when applying local 4T-LE refinement into a triangle t , a 2T-LE is applied into the neighbor of t that shares the longest edge; in addition, either an additional 2T-LE or 3T-LE partition is applied into the other two neighbors of t . The Rivara's refinement maintains the feature that any interior angle of the resulting

triangles is bounded away from 0 or π and the resulting triangles satisfy a shape regularity property. Particularly, Rivara proposed solutions to the smoothness and conformity problems without using green triangles.

Stamm and collaborators [56] applied the 2T-LE approach; however, they applied the 4T-SS approach in an acute triangle. Padrón and collaborators [36] also applied the hybrid *4T-LE-SS* partition process. Specifically, they invoked 4T-LE on obtuse triangles and 4T-SS on acute ones. A related partition approach, the 4-triangle shortest-edge refinement, was studied by Plaza and Rivara [40].

Rivara [49] presented the backward longest-edge refinement (BLER) algorithm based on a scheme to conform the mesh: the longest-edge propagation path (LEPP). The LEPP keeps a path of n triangles that have also to be refined for each triangle of the mesh. It propagates the list until the longest-edge shared by the last two considered triangles. Such edge is larger than the one of its previous neighbor or the last considered triangle in the boundary. The BLER is a partition procedure that extended both the pure longest-edge refinement algorithms for general non-Delaunay Triangulation (see Rivara and collaborators [51], [52] and the references in these papers for details) and the longest-edge refinement algorithm for Delaunay Triangulations proposed by Rivara and Inostroza [50]. Specifically, the algorithm presented by Rivara and Inostroza [50] guarantees that meshes of analogous quality to the input reference-mesh are built.

Regarded to the derefinement process, the refinement and derefinement algorithms proposed by Rivara [48] work together; whereas the ones proposed by Plaza and collaborators [39] are independent modules. Namely, they are set by the user when choosing the particular adaptive strategy.

5 Centroid Point Insertion

De Florian and collaborators [9] published the hierarchical ternary triangulation method. The points are inserted into triangle interiors and each triangle is split into three sub-triangles by adding edges to its vertices. Moreover, no edge swapping is done (Fig. 4a). Hence, all of the initial edges remain in the triangulation. Faugeras and collaborators [14] developed a similar technique; however, it does not present persistent long edges.

Related to the centroid point insertion shown in Fig. 4a, one can see that the same triangle degeneration can occur to the 6-triangle partition process shown in Fig. 4b, that traces the triangle medians. Similarly, degeneration can occur in the 9-triangle partition process shown in Fig. 4c that: trisects each edge; joins the centroid with those points inserted; and also joins the centroid with the vertices of the triangle (see Plaza and Rivara [40] for details).

Scarlatos and Pavlidis [55] developed a hierarchical triangulation algorithm for height fields. It employs a recursive triangulation approach.

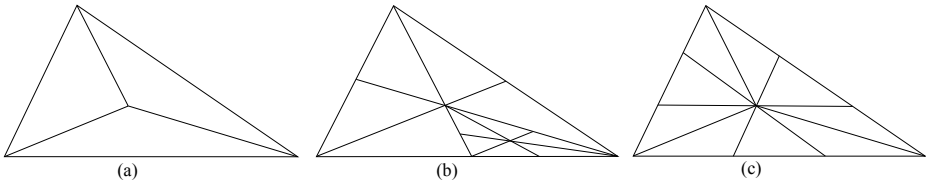


Fig. 4. Triangle partition processes: (a) *ternary subdivision* - refinement by simple centroid insertion; (b) refinement by centroid insertion and adding midedges - a second refinement is performed in the bottom right triangle; (c) trisection of the edges, joining the centroid to those points and also to the vertices

6 Splitting Points

Hoppe [22] proposed the *vertex split*, an operator that splits a single point A into points A_1 and A_2 . This simplification algorithm for progressive mesh construction is a simplified version of the algorithm presented in [23]. The vertex split inserts the edge $\overline{A_1A_2}$ as well as the triangles spanning that edge. Its inverse operator is an *edge collapse*. Moreover, the edge collapse operator simplifies a mesh and the vertex split operator adds details to the mesh. A single point can be expanded to a triangle and the region triangulated. Reversely, a triangle collapses into a single point and edges are introduced among the neighbor points and the new point (*triangle decimation*).

Guéziec [18] and Guéziec and Hummel [20] developed a method for simplifying orientable manifolds that also employs this *edge-decimation* approach. The authors defined the edge collapse, or edge contraction, operator in order to delete an edge and merge its two endpoints into a single vertex. An algorithm performs edge collapses where legal. Moreover, in the Simplification Inside a Tolerance Volume method, Guéziec [19] adopts an edge collapse scheme to decimate meshes. Furthermore, candidate edges receive an increasing order performed by their length. In addition, four tests are carried out in order to check for edge decimability: to prevent changes in the mesh topology; to avoid the sliver face generation; to reduce surface normals variation; and to maintain a bounded error. This approach is detailed explained by Heckbert and Garland [21] and Puppo and Scopigno [46]. Guéziec [19] defined a triangle compactness measured in terms of its area and edges length. The quality $q(t)$ of a triangle t was defined as $q(t) = 4\sqrt{3}a(l_1^2 + l_2^2 + l_3^2)$, in which t has area a and side lengths l_1 , l_2 and l_3 . The function $q(t)$ is normalized to be equal one for an equilateral triangle and for triangles with small angles to approach zero. This measure is applied by Bank [2]. Moreover, this author uses $q(t) \geq 0.6$ for a high-quality triangulation.

7 The $\sqrt{3}$ -Subdivision

In the Kobbelt's $\sqrt{3}$ -subdivision [28], based on a split operation, the number of triangles increases in every step by a factor of 3. Firstly, it inserts a point into

the triangle barycenter and flips the original edges. Applying the $\sqrt{3}$ -subdivision twice leads to a 1-to-9 refinement of the original triangle as shown in Fig. 5. Its name is because applying the subdivision operator twice causes a uniform refinement with trisection of every original edge. Although it provides natural conforming meshes, it does not improve the quality of the selected triangle and degrades triangles around the one selected to be refined.

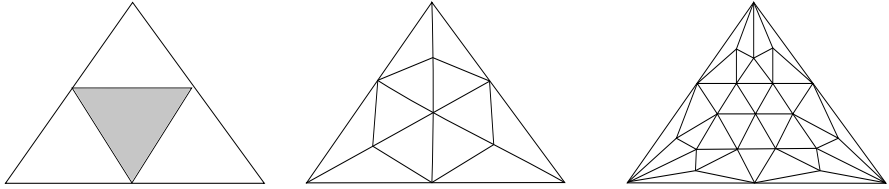


Fig. 5. Two $\sqrt{3}$ -subdivisions into the shaded triangle

Lapsik and Greiner [29] proposed the interpolatory $\sqrt{3}$ -subdivision. The difference of this procedure to the Kobbet’s $\sqrt{3}$ -subdivision is that, in the scheme presented in [29], the triangle neighbors’ barycenters are also connected to the midedges. This forces to refine also the neighbors that share those edges (see Fig. 6). It presents the same features of the Kobbet’s $\sqrt{3}$ -subdivision.

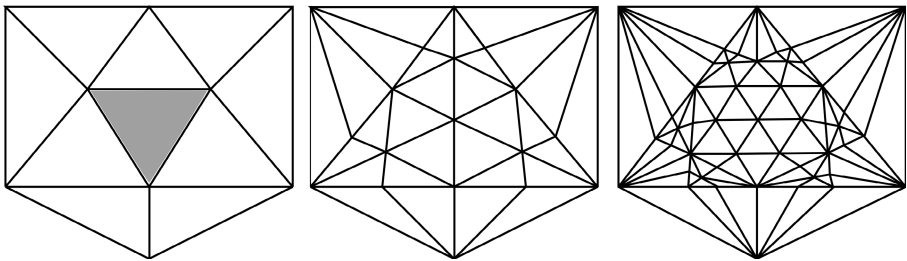


Fig. 6. Two interpolatory $\sqrt{3}$ -subdivisions into the shaded triangle

The reader is referred to Dodgson and collaborators [11] for a minutely investigation of the dual $\sqrt{3}$ -subdivision characteristics. Ivriissimtzis and collaborators [24] defined dual subdivision schemes as those where points at one level of subdivision map to face centers at the next.

8 Laves Nets

A partition scheme comes from the study of general lattice structures. Bell and collaborators [6] cited work on crystal lattice structures by Laves [30] that defined four uniform planar meshes. Those authors named them as Laves nets.

A tessellation is named isohedral, or Laves, if all pieces are identical, and for any point the angles between successive edges meeting at the point are equal [62]. Zorin and collaborators [62] showed the general 11 plane Laves nets. As examples, Laves net of type $[4^4]$ is a quadrilateral mesh (in Fig. 7a, discrete places with four 4-valent vertices), Laves net of type $[3^6]$ is a hexagonal mesh (in Fig. 7b, discrete places with six 3-valent vertices), Laves net of type $[6^3]$ is an equilateral mesh (in Fig. 7c, discrete places with three 6-valent vertices), Laves net $[4 \cdot 8^2]$ is comprised of right triangles (in Fig. 7d), Laves net $[4 \cdot 6 \cdot 12]$ (Fig. 7e) is also a triangulation comprised of right triangles in which each vertex is either 4-valent, 6-valent or 12-valent. Evans and collaborators [13] presented a non-uniform partition based on the $[4 \cdot 6 \cdot 12]$ Laves net.

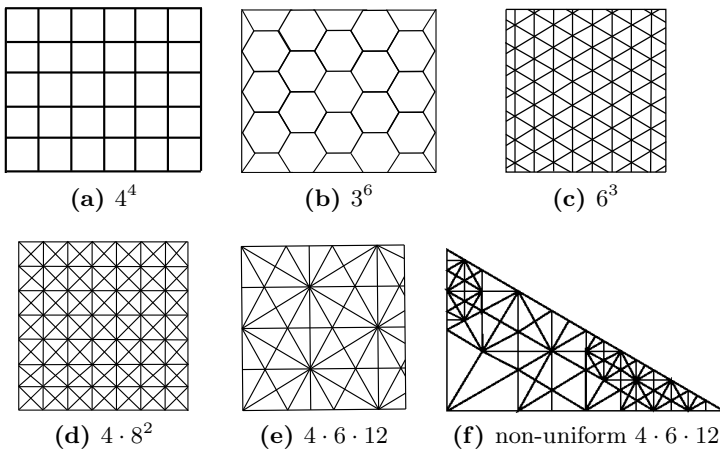


Fig. 7. Pieces of uniform Laves net

9 Stellar Subdivision Grammar

Velho [59] described subdivision surfaces based on a graph grammar formalism. The subdivision approaches are specified by a context sensitive grammar so that the rules of production represent geometrical and topological transformations to the control mesh of the surface.

Stellar subdivision operators define topological modifications; whereas linear maps specify geometrical modifications. Velho claims that his methodology can be used to describe all known subdivision surface approaches. The advantages of stellar subdivision grammars include: it provides how to unambiguously specify a subdivision approach; it provides an effective representation with simple implementation; and it is suitable for adaptive computations. Moreover, switch subdivision approaches without recoding is possible through it. This eases experimentation with other subdivision approaches.

10 7-Triangle Trisection Partition Processes

Márquez and collaborators [35] proposed the 7-triangle longest edge (7T-LE) partition approach. In this approach, two equally spaced points per edge are introduced and then are joined using parallel segments to the edges. In the following, each interior point of the original triangle longest edge is joined to the base point of the opposite sub-triangle in such a fashion that the new edges do not intersect. Finally, it triangulates the interior quadrangle by the shortest diagonal. As a result, the interior of the triangle is divided into seven sub-triangles. Three new triangles are similar to the original, two are similar to the new triangles also generated by the 4T-LE partition, and the other two triangles are, in general, better shaped. Some aspects should be studied in this approach since its disadvantages are due to the difference among the areas of the subdivided triangles, the increasing of the mesh adaptation complexity, and the possibility of introducing an unnecessary number of discrete places.

In order to conform the mesh after a 7T-LE partition process applied to a selected triangle, Plaza and collaborators [38] proposed to refine the neighbors as follows. Consider the 7T-LE partition process applied to $\triangle ABC$ in Fig. 8: *i*) since \overline{AB} is the longest edge of $\triangle ABD$, join the trisecting points of \overline{AB} to the opposite vertex (D) of the triangle $\triangle ABD$ forming three new triangles; *ii*) since \overline{AC} is the second longest edge of $\triangle ACE$, trisect the longest edge (\overline{AE}), consider G the closest new point to A and H the other one, join G to the trisecting points of the second longest edge (\overline{AC}), join H to its closest trisecting point of (\overline{AC}) and to C , forming five new triangles; *iii*) since \overline{BC} is the shortest edge of $\triangle BCF$, trisect the longest edge (\overline{CF}), join the closest trisecting point of \overline{CF} to the trisecting points of \overline{BC} and join B to the trisecting points of \overline{CF} , forming five new triangles. Plaza and collaborators [38] also proposed the derefinement process of this scheme.

Márquez and collaborators [35] also proposed the 7-triangle Delaunay (7T-D). It introduces two equally spaced points per edge and triangulate the points using the DT. Both 7T-LE and 7T-D partition processes resulted in meshes with

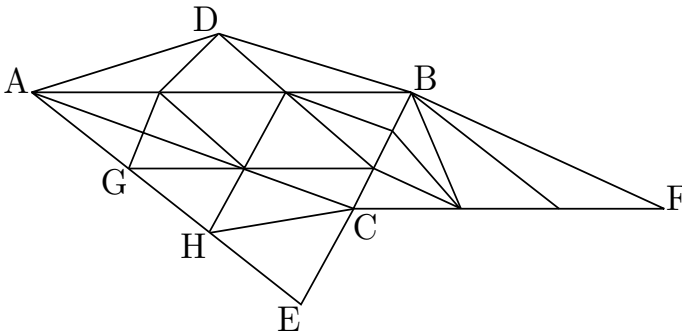


Fig. 8. The 7T-LE partition process propagation

better quality in tests showed in [35] in relation to the 4T-LE partition process. Moreover, the 7T-LE partition scheme presented even better results than the 7T-D in relation to the mesh quality after several refinement levels. Furthermore, the 7T-LE with its $O(n)$ running time in beats the 7T-D, whose running time is $O(n \lg n)$, in which n is the number of points in the mesh.

11 RGB Subdivision

Puppo and Panozzo [43], [44] and [45] introduced the RGB subdivision, an adaptive subdivision scheme for triangular meshes. It is based on the iterative application of local refinement and coarsening operators. It “generates the same limit surface of the Loop subdivision [32], independent of the order of local operator application” [45]. This scheme supports dynamic selective refinement, as in continuous level of detail models. This is performed by plugging faces inside the triangulation, according to rules encoded in tables. In addition, it generates conforming meshes at all intermediate passes.

The authors claimed that RGB subdivision scheme has several advantages over classical and adaptive subdivision schemes, as well as over continuous level of detail models. Moreover, the authors argued that it is better adaptive than previously known approaches based on the 1-to-4 triangle split pattern. Besides, it does not require hierarchical data structures. The reader is referred to Puppo and Panozzo [45] for details.

12 Concluding Remarks

Plaza and collaborators [38] provided several open problems related to their 7-triangle partition approaches. So did Puppo and Panozzo [45] related to their RGB subdivision. Besides, there is a lot of open problems related to 3D. For example, see the descriptions in Danovaro and collaborators [8] for details.

Probably other schemes exist, which either are variations of the ones shown in this article or are not known to the author. However, the author hopes that this overview serves to introduce the ideas, principles and schemes that constitute the state-of-art in this subject. In addition, the author also hopes that the list of references and descriptions to the large body of work on this issue can provide a useful starting point for one faced with the task of constructing an irregular triangulation.

Acknowledgments. The author gratefully acknowledges FAPEMIG and CNPq for the financial support.

References

1. Babuska, I., Aziz, A.K.: On the angle condition in the finite element method. SIAM Journal on Numerical Analysis 13, 214–226 (1976)

2. Bank, R.E.: PLTMG: A Software Package for Solving Elliptic Partial Differential Equations Users' Guide 10.0. Department of Mathematics, University of California at San Diego (September 2007)
3. Bank, R.E., Sherman, A.H.: The use of adaptive grid refinement for badly behaved elliptic partial differential equations. In: *Advances in Computer Methods for Partial Differential Equations III*. IMACS, pp. 33–39 (1979)
4. Bank, R.E., Sherman, A.H.: An adaptive, multilevel method for elliptic boundary value problems. *Computing* 26, 91–105 (1981)
5. Bank, R.E., Sherman, A.H., Weiser, A.: Refinement algorithms and data structures for regular local mesh refinement. In: Stepleman, R.S. (ed.) *IMACS Conference, Scientific Computing*, vol. 1, pp. 3–17. North Holland, Amsterdam (1983)
6. Bell, S.B.M., Diaz, B.M., Holroyd, F., Jackson, M.J.: Spatially referenced methods of processing raster and vector data. I. and V. *Comp.* 1(4), 211–220 (1983)
7. Bolz, J., Schröder, P.: Rapid evaluation of catmull-clark subdivision surfaces. In: *Proceeding of the Seventh International Conference on 3D Web Technology*, pp. 11–17. ACM Press (2002)
8. Danovaro, E., De Floriani, L., Magillo, P., Puppo, E., Sobrero, D.: Computer Graphics in Italy - Level-of-detail for data analysis and exploration: A historical overview and some new perspectives. *Computers & Graphics* 30, 334–344 (2006)
9. De Floriani, L., Falcidieno, B., Nagy, G., Pienovi, C.: A hierarchical structure for surface approximation. *Computers & Graphics* 8(2), 183–193 (1984)
10. De Floriani, L., Kobbelt, L., Puppo, E.: A Survey on Data Structures for Level-Of-Detail Models. In: Dodgson, N.A., Floater, M., Sabin, M. (eds.) *Advances in Multiresolution for Geometric Modelling*. Series in Mathematics and Visualization, pp. 49–74. Springer, Heidelberg (2004)
11. Dodgson, N.A., Ivrişimtzis, I.P., Sabin, M.A.: Characteristics of dual triangular $\sqrt{3}$ subdivision. In: Cohen, A., Merrien, J.-L., Schumaker, L.L. (eds.) *Curve and Surface Fitting: Saint-Malo*, pp. 119–128 (2002)
12. Dyn, N., Levin, D., Gregory, J.A.: A butterfly subdivision scheme for surface interpolation with tension control. *ACM Trans. on Graph.* 9(2), 160–169 (1990)
13. Evans, W., Kirkpatrick, D., Townsend, G.: Right-triangulated irregular networks. *Algorithmica* 30, 264–286 (2001)
14. Faugeras, O., Hebert, M., Mussi, P., Boissonnat, J.-D.: Polyhedral approximation of 3-d objects without holes. *Comp. Vision, Graph., and I. Proc.* 25, 169–183 (1984)
15. Fried, I.: Condition of finite element matrices generated from nonuniform meshes. *American Institute of Aeronautics and Astronautics Journal* 10, 219–221 (1972)
16. Garland, M.: Eurographics 99. In: *Multiresolution Modeling: Survey & Future Opportunities*. In State of the Art Report, pp. 111–131 (September 1999)
17. Gómez, D., Guzmán, A.: Digital model for three-dimensional surface representation. *Geo-Processing* 1, 53–70 (1979)
18. Guéziec, A.: Surface simplification with variable tolerance. In: *Second Annual International Symposium on Medical Robotics and Computer Assisted Surgery (MR-CAS 1995)*, Baltimore, MD, pp. 132–139 (November 1995)
19. Guéziec, A.: Surface simplification inside a tolerance volume. Technical report, RC 20440, I.B.M. T.J. Watson Research Center (1996)
20. Guéziec, A., Hummel, R.: Exploiting triangulated surface extraction using tetrahedral decomposition. *IEEE Transactions on Visualization and Computer Graphics* 1(4), 328–342 (1995)
21. Heckbert, P.S., Garland, M.: Survey of polygonal surface simplification algorithms. Technical report, Carnegie Mellon Univ.-Dep. of Comp. Sc., May 1 (1997)

22. Hoppe, H.: Progressive meshes. In: SIGGRAPH 1996 Proc., pp. 99–108 (1996)
23. Hoppe, H., De Rose, T., Duchamp, T., Mc-Donald, J., Stuetzle, W.: Mesh optimization. In: Computer Graphics, SIGGRAPH 1993 Proc., pp. 19–26 (1993)
24. Ivriissimtzis, I.P., Dodgson, N.A., Sabin, M.A.: A generative classification of subdivision schemes with lattice transformations. Technical Report 542, University of Cambridge Computer Laboratory (2002)
25. Jones, M.T., Plassmann, P.E.: Adaptive refinement of unstructured finite-element meshes. *Finite Elements in Analysis and Design* 25(1-2), 41–60 (1997)
26. Kearfott, R.B.: Computing degree of maps and a generalized method of bisection. PhD thesis, University of Utah (1977)
27. Kearfott, R.B.: An efficient degree-computing method for a generalized method of bisection. *Numerische Mathematik* 32, 109–127 (1979)
28. Kobbelt, L.: $\sqrt{3}$ subdivision. In: Proc. of the SIGGRAPH 2000, pp. 103–112 (2000)
29. Labsik, U., Greiner, G.: Interpolatory $\sqrt{3}$ subdivision. *EUROGraphics 2000, Computer Graphics Forum* 19(3), 131–138 (2000)
30. Laves, F.: Ebenenteilung und koordinationszahl. *Zeitschrift für Kristallographie* 5, 68–105 (1931)
31. Litke, N., Levin, A., Schröder, P.: Fitting subdivision surfaces (2001), <http://www.multires.caltech.edu/pubs> (accessed January 2011)
32. Loop, C.: Smooth subdivision surfaces based on triangles. Master's thesis, University of Utah, Department of Mathematics (1987)
33. Luebke, D., Reddy, M., Cohen, J.D., Varshney, A., Watson, B., Huebner, R.: Level of Detail for 3D Graphics. Morgan Kaufmann (2003)
34. Ma, W.: Subdivision surfaces for CAD - an overview. *Computer-Aided Design* 37, 693–709 (2005)
35. Márquez, A., Moreno-González, A., Plaza, A., Suárez, J.P.: The seven-triangle longest-side partition of triangles and mesh quality improvement. *Finite Elements in Analysis and Design* 44, 748–758 (2008)
36. Padrón, M.A., Suárez, J.P., Plaza, A.: Refinement based on longest-edge and self-similar four-triangle partitions. *Math. and Comp. in Sim.* 75, 251–262 (2007)
37. Pakdel, H., Samavati, F.: Incremental subdivision for triangle meshes. *International Journal of Computational Science and Engineering* 3(1), 80–92 (2007)
38. Plaza, A., Márquez, A., Moreno-González, A., Suárez, J.P.: Local refinement based on the 7-triangle longest-edge partition. *Mathematics and Computers in Simulation* 79, 2444–2457 (2009)
39. Plaza, A., Montenegro, R., Ferragut, L.: An improved derefinement algorithm of nested meshes. *Advances in Engineering Software* 27, 51–57 (1996)
40. Plaza, A., Rívara, M.C.: On the adjacencies of triangular meshes based on skeleton-regular partitions. *J. of Comp. and Applied Math.* 140, 673–693 (2002)
41. Powell, M.J.D., Sabin, M.A.: Piecewise quadratic approximations on triangles. *ACM Transactions on Mathematical Software* 3(4), 316–325 (1977)
42. Puppo, E.: Variable resolution triangulations. *Comp. Geometry* 11, 219–238 (1998)
43. Puppo, E.: Selectively refinable subdivision meshes. In: Polthier, K., Sheffer, A. (eds.) *Eurographics Symposium on Geometry Processing*, pp. 153–162 (2006)
44. Puppo, E., Panozzo, D.: RGB subdivision. *IEEE Transactions on Visualization and Computer Graphics*, 1–14 (2008)
45. Puppo, E., Panozzo, D.: RGB subdivision. *IEEE Transactions on Visualization and Computer Graphics* 15(2), 295–310 (2009)
46. Puppo, E., Scopigno, R.: Simplification, LOD and multiresolution principles and applications. In: *EUROGRAPHICS 1997 Conference Proc.*, vol. 16(3). Blackwell (1997)

47. Rivara, M.C.: Algorithms for refining triangular grids suitable for adaptive and multigrid techniques. *Int. J. for Numerical Methods in Eng.* 20, 745–756 (1984)
48. Rivara, M.C.: Selective refinement/derefinement algorithms for sequences of nested triangulations. *International Journal for Numerical Methods in Engineering* 28, 2889–2906 (1989)
49. Rivara, M.C.: New longest-edge algorithms for the refinement and/or improvement of unstructured triangulations. *International Journal for Numerical Methods in Engineering* 40, 3313–3324 (1997)
50. Rivara, M.C., Inostroza, P.: Using longest-side bisection techniques for the automatic refinement of delaunay triangulations. *International Journal for Numerical Methods in Engineering* 40, 581–597 (1997)
51. Rivara, M.C., Iribarren, G.: The 4-triangles longest-side partition of triangles and linear refinement algorithms. *Mathematics of Computation* 65(126), 1485–1502 (1996)
52. Rivara, M.C., Venere, M.: Cost analysis of the longest-side (triangle bisection) refinement algorithms for triangulations. *Eng. with Computers* 12, 224–234 (1996)
53. Rosenberg, I.G., Stenger, F.: A lower bound on the angles of triangles constructed by bisecting the longest side. *Math. of Computation* 29, 390–395 (1975)
54. Sabin, M.: Recent Progress in Subdivision: A Survey. In: Dodgson, N.A., Floater, M., Sabin, M. (eds.) *Advances in Multiresolution for Geometric Modelling*, pp. 203–230. Springer, Heidelberg (2004)
55. Scarlatos, L., Pavlidis, T.: Hierarchical triangulation using cartographic coherence. *CVGIP: Graphical Models and Image Proc.* 54(2), 147–161 (1992)
56. Stamm, C., Eidenbenz, S., Pajarola, R.: A modified longest side bisection triangulation. In: *Proceedings of the 10th Canadian Conference on Computational Geometry 1998*, pp. 1–6 (1998)
57. Stynes, M.: On faster convergence of the bisection method for all triangles. *Mathematics of Computation* 35(152), 1195–1201 (1980)
58. Thacker, W.C.: A brief review of techniques for generating irregular computational grids. *International Journal for Numerical Methods in Engineering* 15, 1335–1341 (1980)
59. Velho, L.: Stellar subdivision grammars. In: Kobbelt, L., Schröder, P., Hoppe, H. (eds.) *Proceedings of the 2003 Eurographics/ACM SIGGRAPH Symposium on Geometry Processing. ACM International Conference Proceeding Series*, vol. 43, pp. 188–199 (2003)
60. Velho, L., Zorin, D.: 4-8 subdivision. *Comp. Aided Geom. Des.* 18, 397–427 (2001)
61. Warren, J., Weimer, H.: *Subdivision Methods for Geometric Design*. Morgan Kaufmann (2002)
62. Zorin, D., Schröder, P., De Rose, T., Kobbelt, L., Levin, A., Sweldens, W.: *Subdivision for Modeling and Animation, SIGGRAPH 2000 Course Notes*. Organizers: Zorin, D., Schröder, P. (2000)
63. Zorin, D., Schröder, P., Sweldens, W.: Interactive multiresolution mesh editing. In: *Proceedings of ACM SIGGRAPH 1997*, pp. 259–268 (1997)

DEM Interpolation from Contours Using Medial Axis Transformation

Joonsoo Choi, Jaewee Heo, Kwang-Soo Hahn, and Junho Kim

School of Computer Science, Kookmin University, Republic of Korea
{jschoi, jwheo, kshahn, junho}@kookmin.ac.kr

Abstract. Contours and digital elevation model (DEM) are the most commonly used digital terrain models. In this paper, we propose a technique for constructing a DEM from contours. The elevation of each ground point in DEM is computed by interpolating the heights of the two adjacent contours of the point. The technique decomposes each sub-domain between adjacent contours into a set of sub-regions using medial axis transformation. Each sub-region in the decomposition is classified into a variety of terrain features like hillsides, valleys, ridges, canyons, peaks, pits, etc. The elevations of points are interpolated with different methods according to terrain features they belong to. The interpolation is conducted on the approximate steepest or shortest slope lines constructed based on medial axis. The univariate monotone rational Hermite spline and convex rational Hermite spline are used for the interpolation.

Keywords: Contours, Digital Elevation Model (DEM), Medial Axis Transformation, Convex Hermite Interpolation, Monotone Hermite Interpolation.

1 Introduction

Large quantities of topological data stored in a digital form have been utilized in support of modeling, visualizing, and interrogating topographic features, and also been used to analyze terrain more efficiently and precisely. Three major digital terrain models (DTM) widely used are regular-grid, contour, and triangulated irregular network (TIN). A regular-grid model, or digital elevation model (DEM), stores elevations of ground positions sampled in the form of a raster grid over a specified area of terrain. A contour is a polygonal or smoothed line that passes through ground positions having the same elevation. A triangulated irregular network (TIN) is a mesh of triangulated facets to approximate the terrain surface.

DEM can be generated by automatic DEM extraction from stereo satellite scenes or stereo digital aerial photography, or constructed by involving interpolation from pre-existing digital contour maps which may have been produced by direct survey of the terrain. TIN can be created by converting from contours to DEM and then to a TIN or more directly from contours.

The DEM, TIN, or general surface reconstruction of three-dimensional object from a set of contours is to determine a surface that approximates an unknown surface using geometric information in the contours. The contours are usually terrain contours

or contours obtained from cross-sectional data of CT, MRI, or range sensors. The general surface reconstruction from contours can be broken into three subproblems: correspondence problem, branching problem, and tiling problem [1]. Correspondence problem is to determine which contours at a given level must be connected to which contours of adjacent levels. When a contour at a given level corresponds to a single contour of an adjacent level it is called one-to-one correspondence. When a contour corresponds to more than one contour at an adjacent level, it is called one-to-many correspondence. The branching problem occurs when there is a one-to-many, or many-to-many correspondence between adjacent levels. It is to determine how to connect the corresponding contours at adjacent levels. The tiling problem is to construct a surface connecting a set of corresponding contours with a triangular mesh.

In the terrain surface reconstruction from contours, only the cases of one-to-one or one-to-many correspondences occur since one contour encloses one or more adjacent contours [2, 3]. Various techniques to reconstruct terrain surface from contours using the Voronoi diagram or its dual, the Delaunay triangulation are developed [4-8]. The rather complicated many-to-many correspondence or branching structures do not occur in this problem. The problem of extracting DEM from contours is simpler than terrain reconstruction problem since the approximate surface does not need to be constructed and the problem can be solved with the correspondence and branching subproblems. A technique is also presented to create DEM from contours by constructing new intermediate contours in between existing contours [9].

In this paper, we propose a new algorithm to construct DEM from a set of terrain contours. The elevation of each ground point of DEM not belonging to a contour is computed by interpolation from two adjacent contours of the point. The algorithm consists of two steps. First, the terrain features (hillsides, ridges, valleys, canyons, pits, and peaks) are extracted from contours. These terrain features are the most significant regional features to characterize and extract from terrain models [10]. Secondly, the elevations of points are interpolated with different methods according to terrain features they belong to. For example, for a given point in hillside, we determine an approximate gradient line from a higher elevation position to a lower position that passes through the point. Gradient lines should intersect contour lines perpendicularly. The elevation of the point is interpolated from the known elevations of the two adjacent contours along the approximate gradient line. For the univariate interpolation method to compute heights of points on the gradient line, the monotone rational Hermite spline [2, 11] is used. For a point in a region of peak or pit, the height function along the gradient line passing the point is convex or concave, respectively. Convex rational Hermite spline [12] is used to interpolate the height of a point in a region of peak.

2 Geometric Preliminaries

2.1 Terrain Features

A preliminary step to terrain analysis is to extract terrain features from a topological data represented by DTMs. The terrain features could be point features like peaks, pits and saddle points, or linear features like ridge-lines and valley-lines, or area features

like ridges, valleys, canyons, etc. These features play the important role in the terrain analysis. For example, valley-lines can be used as drainage networks and ridge lines can be served as boundaries between different terrain regions. There are numerous ways to define terrain features since the different representations of terrain features on DTMs are to be reflected in the definition of terrain features [10]. In this paper, a ridge refers to an area feature posing a convex downhill shape along its cross profiles, a valley refers to an area feature showing a downhill concave pattern. Canyon is a narrow valley between two mountains or plateaus. Hillside is a flat or smoothed convex (or concave) surface which has a constant slope or increasing (or decreasing) slope on a slope-line of the surface, respectively.

2.2 Terrain Model by Contours

A contour is usually represented by a simple polygon and any point on a contour has the same height value. Contours modeling terrain has certain restrictions on the allowed geometrical configurations. Terrain is modeled as a strictly nested hierarchy of contours: Any contour encloses an arbitrary number of other contours, but is entirely contained within only one other contour at the next hierarchical level, and any contour does not intersect with other contours. Contour tree [13] is a data structure to describe the hierarchical relationship among contours. The correspondence problem to determine adjacent contours to be connected together can be solved by utilizing the contour tree [2, 3].

Suppose that we have a set of n contours $\{c_1, c_2, \dots, c_n\}$ in the plane where contour c_i has height value h_i and c_i lies inside some c_j with $j < i$ for $i \geq 2$. The outermost contour c_1 encloses all the other contours and it partitions the plane into two open sets, the unbounded domain Ω_0 and the domain bounded by c_1 which in turn partitioned by other contours into n disjoint open sets Ω_i . Each sub-domain Ω_i has c_i as an exterior boundary and k_i interior boundaries c_j with $j > i$. Fig. 1 (a) shows four nested contours and their corresponding sub-domains. For simplicity, we suppose that all k_i interior boundaries have the same height and the height is different from that of c_i . All the other special situations are treated in a similar way, and are not detailed here.

- If $k_i = 0$, then the sub-domain Ω_i has a local extremum point and the sub-domain is a *peak* or a *pit*. We differentiate them by considering the height relationship between h_i and h_j , where c_i is an interior boundary of sub-domain Ω_j . If $h_i > h_j$, then Ω_i is a peak and otherwise it is a pit.
- If $k_i = 1$, then a contour c_i corresponds to one contour c_{i+1} . In this case, the sub-domain Ω_i is a mixture of hillsides, ridges, or valleys. Just like the peak and pit cases, if $h_{i+1} > h_i$, then Ω_i is a mixture of outbound hillsides and ridges; otherwise it is a mixture of inbound hillsides and valleys.
- If $k_i > 1$, then a contour c_i corresponds to k_i contours. This case is called a one-to-many branching and it forms complex terrain. The sub-domain Ω_i is a mixture of hillsides, ridges, valleys, and canyons.

For example, Fig. 1 (b) shows area terrain features of the regions roughly subdividing the sub-domain Ω_1 .

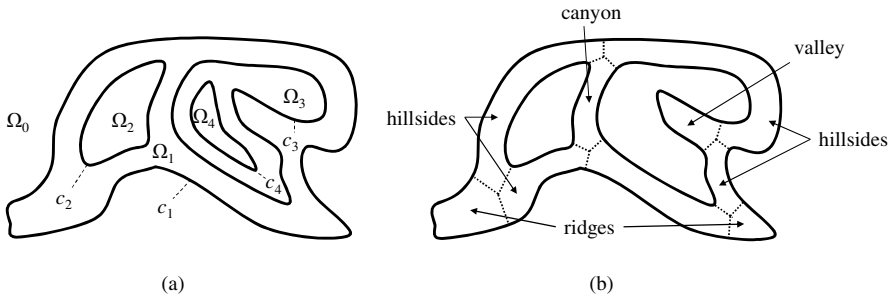


Fig. 1. (a) Nested contour sets and their corresponding sub-domains (b) Terrain features for regions roughly subdividing sub-domain Ω_1

2.3 Medial Axis of a Polygon

The *medial axis* of a simple polygon P is the locus of all centers of circles (called maximal circles) contained in P that are tangent to P in two or more points. The medial axis is a simple tree graph composed of vertices and edges, where edges are either parabolic arcs or straight line-segments. There exist optimal $O(n \log n)$ algorithms to compute the medial axis of a polygon with n vertices [14, 15]. For a simple polygon with polygonal holes, the medial axis of the polygon can be computed in $O(n(\log n + h))$ time, where n is the number of edges of the polygon and holes, and h is the number of holes [16]. The medial axis of a polygon with holes is a general planar graph with parabolic arcs or straight line-segments. Each hole of in the polygon is surrounded by a cycle in the medial axis.

The edges and concave vertices of a polygon that are touched by maximal circles are called active boundary elements. The number of active boundary elements touched by a maximal circle classifies the type of points on medial axis. The points of medial axis intersecting with the boundary of a polygon are called *end points*. The centers of maximal circles tangent to three or more active boundary elements are called *junction points*. *Regular points* are the centers of maximal circles tangent to two boundary elements. A *transition point* is a regular point where one of the active boundary element changes.

A *segment* of the medial axis is the maximal subset of the medial axis associated uniquely with two distinct active boundary elements. Therefore internal points of segments are regular points. The endpoints of a segment, which are vertices of a medial axis, are junction points, transition points or end points.

Therefore, in non-degenerate case, the degree of any vertex of a medial axis is at most three. The only vertices with degree three are junction points. For some junction vertex of a cycle, a tree of edges is connected to the vertex. A maximally connected subtree connected to some vertex of a cycle is called a *dangling subtree* and the junction vertex on a cycle is called the *root* of the dangling subtree (see Fig. 2). There are six dangle subtrees in the medial axis in Fig. 2.

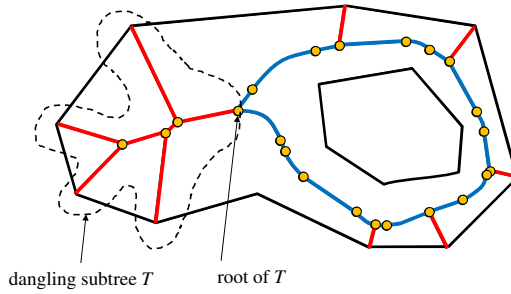


Fig. 2. Medial axis of a polygon with a hole, and a dangle subtree

3 Terrain Feature Extraction from Contours

For each sub-domain Ω_i defined in a hierarchy of terrain contours, the corresponding medial axis can be constructed. In this case, the exterior contour of Ω_i is the polygon to define the medial axis, and interior contours of Ω_i are holes in the polygon. Tang proposed a method to extract linear or point terrain features (ridge-lines, valley-lines, saddle points, etc.) from a raster contour line image [17]. It is based on raster operations and makes use of a medial axis derived from contours. Similar to the method proposed by Tang, we extract regional terrain features (ridges, valleys, hillsides, canyons, pits and peaks) using a medial axis transformation. For each sub-domain Ω_i , the corresponding medial axis decomposes Ω_i into a set of regions bounded by contours and medial axis edges (see Fig. 2). In sub-domain Ω_i , consider drawing line-segments connecting each junction point or transition point of medial axis to tangent points on contours of the maximal circle centered at the point. These line-segments decompose Ω_i into a set of regions and these regions are bounded by contours and the line-segments. Note that these regions are not bounded by edges of the medial axis. The decomposition of the sub-domain is called the *quasi-dual medial axis decomposition*. Each region in the quasi-dual decomposition contains and matches exactly one segment of medial axis and the region is called the corresponding *zone* of the segment (see Fig. 3 (a)).

In our approach, the identification of terrain feature is derived from the quasi-dual decomposition. This can be achieved by examining the structure of the medial axis. The medial axis of a sub-domain Ω_i is a general planar graph with cycles. A dangling subtree of the medial axis is a union of ridge-lines or a union of valley-lines depending on whether the relative height of internal and external contours of Ω_i . If the height of interior contour is greater than that of exterior, then the dangling subtree represents ridge-lines and otherwise it represents valley-lines. In the same way, the union of corresponding zones of all segments in a dangling subtree represents a ridge or a valley. The area feature to be identified depends on the relative heights of the bounding contours.

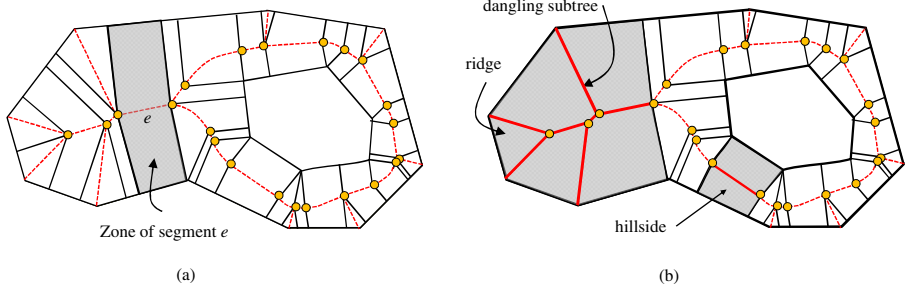


Fig. 3. (a) Quasi-dual medial axis decomposition (b) Dangling subtree of medial axis and its corresponding ridge

If there are no interior contours in Ω_i , then the exterior contour c_i is a terminal contour in the contour tree. There are peaks or pits in contour c_i depending on the relative height of the contour containing c_i . In this case, the medial axis is just a tree. If Ω_i contains peak points, then the medial axis represents a union of ridge-lines along the top of mountain where locally maximal heights points, peaks, are on the ridge-lines.

The zone of a segment not in dangling trees, i.e. in a cycle or in a path connecting two cycles, of medial axis may create a hillside, a ridge, or a canyon depending on the relative heights of the bounding contours. The zone of a segment of medial axis is classified according to the types of active boundary elements that define the segment. Suppose that the height of the exterior contour is smaller than the height of interior contours. Then,

- Zone bounded by two boundary elements, one on interior contour and one on exterior contour. The zone corresponds to a hillside (see Fig. 3 (b)).
- Zone bounded by two boundary elements on the same exterior contour. In this case the segment is on a path connecting two cycles in the medial axis. Therefore the zone corresponds to a ridge between two mountains represented by the two cycles and there may exist a saddle point on the ridge.
- Zone bounded by two boundary elements on different interior contours. The zone corresponds to a canyon (see Fig. 1 (b)).

In the case of when the height of exterior contour is greater than the height of interior one, the terrain features of zones can be defined similarly.

4 Interpolation Method

Various methods are proposed to interpolate the height of a point in a sub-domain of a set of contours [2, 6, 9, 18, 19]. Chai et al. proposed a method to obtain smooth terrain surface by solving partial differential equations with contour heights and gradient conditions [18]. They assumed that a terrain surface height function defined by contours is smooth so that the height function can be governed by PDEs. The method they proposed is based on the observation that terrain contour is very similar to the potential contour in the 2D electric field generated by some electrodes. Similar to the flux lines to describe the electric field distribution, they modeled the gradient lines

which describe the paths of slopes on the surface from high elevation points to low elevation points. The gradient lines are assumed to obey similar properties of flux lines in electric field;

1. (Orthogonality) The gradient lines and the contours are orthogonal each other everywhere.
2. (Non-intersection) Gradient lines do not meet nor branch out each other.
3. (Monotonicity) The height varies monotonously along a gradient line between two neighboring contours with different heights.

The usual interpolation method to compute the height of point between contours is based on the ratio of shortest distances from the point to both contours (see Fig. 4 (a)).

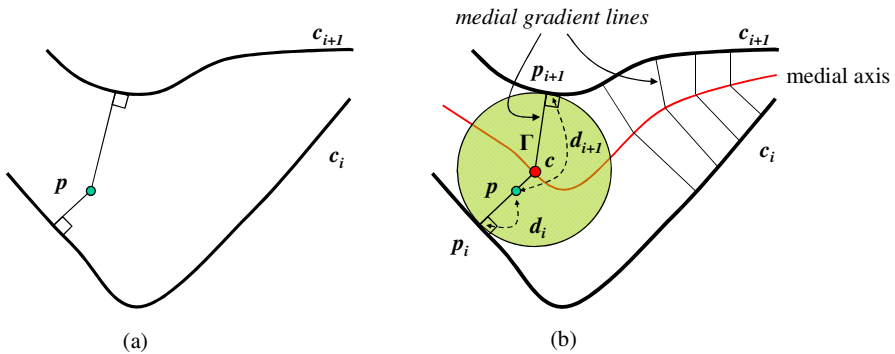


Fig. 4. (a) Shortest distances to contours from a point p in traditional slope line model (b) Medial gradient line Γ passing through a point p

The new method we propose to interpolate the height of a point between contours is done by computing an approximation of gradient line that passes through the point. For a point p between two consecutive contours, the nearest point p_i on one of the contours defines a maximal circle centered on medial axis and the circle touches on the other contour at p_{i+1} . The approximate gradient line, called *medial gradient line*, passing through p is defined by the two line segment $[p_i, c]$ and $[c, p_{i+1}]$, where c is the center of the circle on the medial axis (see Fig. 4 (b)). Therefore any medial gradient line touches contours orthogonally at everywhere. We can prove that medial gradient lines between two contours of different heights do not intersect by showing that the trajectories of two tangent points on contours of maximal circles moving one direction along medial axis segments move along the same and one direction along contours. To preserve the monotonicity of gradient lines, we use monotone Hermite interpolation method to compute the heights of points on the gradient line.

In the new method, to interpolate the height of a point in a sub-domain of a set of contours, the terrain feature they belong to has to be determined beforehand. For a point in a terrain feature of hillside, the height of the point can be interpolated as described in Fig. 4.

For a point p in an innermost contour c_i which has a peak, the medial gradient line Γ passing through p is defined by the two line segment $[p_i, c]$ and $[c, p_{i+1}]$, where c is

the center of the circle on the medial axis (see Fig. 5 (a)). Note that any medial gradient line in c_i touches the contour orthogonally at everywhere. We can also show that any two medial gradient lines in a peak do not intersect. To preserve the convexity of gradient lines, we use convex Hermite interpolation method to compute the heights of points on the gradient line. Similarly the height of a point in an innermost contour which has a pit can be interpolated.

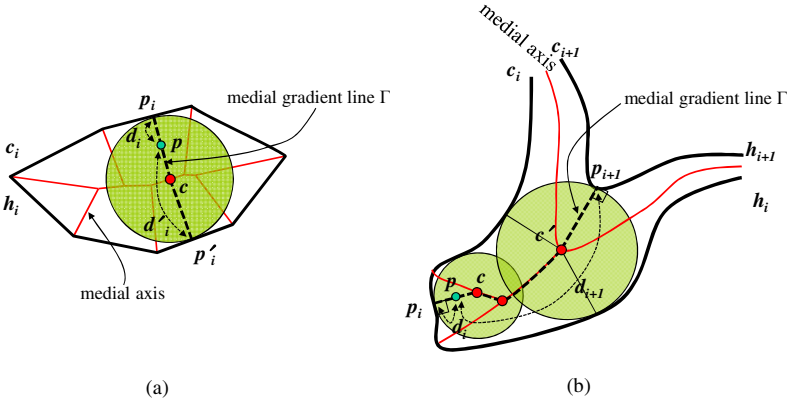


Fig. 5. (a) Medial gradient line Γ passing through a point p in a sub-domain having a peak or a pit (b) Medial gradient line Γ of a point p in a ridge or a valley

For a point p in a set of zones which is a ridge, the medial gradient line passing through p is defined as follows (see Fig. 5 (b)): Let T be the dangling subtree of medial axis defining the ridge and let $c \in T$ be the center of the maximal circle touching the contour c_i at p_i where the point p is on the line segment $[p_i, c]$. Let $c' \in T$ be the center of the maximal circle touching both contours c_i and c_{i+1} and let the maximal circle touch c_{i+1} at p_{i+1} . The point p_{i+1} is the root of T . The medial gradient line passing the point p consists of the line segment $[p_i, c]$, the path between c and c' on the dangling subtree T and the line segment $[c', p_{i+1}]$. Note that the medial gradient line touches the two surrounding contours c_i and c_{i+1} orthogonally. To preserve the monotonicity of gradient lines, we use monotone Hermite interpolation method to compute the heights of points on the gradient line. For two point p and q in the same set of zones which is a ridge, the corresponding medial gradient lines Γ_p and Γ_q passing through p and q may overlap or intersect each other on the dangling subtree T . This violates the non-intersection property of flux lines in electric field. By considering the two gradient lines Γ_p and Γ_q be close infinitesimally along T , we can make Γ_p and Γ_q not intersect each other and satisfy the non-intersection property of flux lines. Similarly the height of a point in a valley can be interpolated.

4.1 Monotone Hermite Interpolation

Suppose a medial gradient line Γ starts from a point p_{i+1} on contour c_{i+1} and ends at a point p_i on contour c_i (see Fig. 4 (b)). The height h of any point p on Γ can be

computed by univariate interpolation along the line Γ . Let d_i, d_{i+1} be distances from p to p_i, p_{i+1} along the line Γ , respectively. The simplest kind of univariate interpolation is linear interpolation defined as follows:

$$h = \frac{h_{i+1}d_i + h_i d_{i+1}}{d_i + d_{i+1}}$$

This linear interpolation results in undesirable artifacts caused by first derivative discontinuities at contours. To circumvent this problem and to produce a smoother behavior, cubic interpolation scheme can be used since it offers continuity at contours. But this interpolates heights outside the valid range $[h_i, h_{i+1}]$ of heights on the gradient line Γ . To preserve the monotonicity of height values and interpolate heights in the valid range $[h_i, h_{i+1}]$, monotone interpolation methods exploiting cubic Hermite spline [20], or rational two-point Hermite spline [2, 11], can be used. The spline proposed by Gregory and Delbourgo on the gradient line Γ is as follow:

$$h(t) = \frac{\Delta_i h_{i+1} t^2 + (h_i g_{i+1} + h_{i+1} g_i) t(1-t) + \Delta_i h_i (1-t)^2}{\Delta_i t^2 + (g_{i+1} + g_i) t(1-t) + \Delta_i (1-t)^2}$$

where $\Delta_i = (h_{i+1} - h_i) / (d_i + d_{i+1})$, and t is the local coordinate given by $t = d_i / (d_i + d_{i+1})$. The g_j are derivatives at p_j where the gradient line Γ intersects c_j (see Fig. 6). If c_j is not the outermost nor the innermost contour, Γ can extend to sub-domains Ω_j^+, Ω_j^- , where c_j is the exterior (interior) boundary of $\Omega_j^+ (\Omega_j^-)$, respectively. Let $h_j^+ (h_j^-)$ be the height of the interior (exterior) contour of $\Omega_j^+ (\Omega_j^-)$, and let $\ell_j^+ (\ell_j^-)$ be the length of the extended gradient line Γ in the sub-domain $\Omega_j^+ (\Omega_j^-)$, respectively. A suitable method for estimating the derivative is

$$g_j = \frac{h_j^+ - h_j^-}{\ell_j^+ + \ell_j^-}$$

which is a central difference around p_j when $j > 1$. At the boundary points on contours c_l or c_n , the derivatives can be estimated by

$$g_1 = \frac{h_1^+ - h_1}{\ell_1^+}, \quad g_n = \frac{h_n - h_n^-}{\ell_n^-}.$$

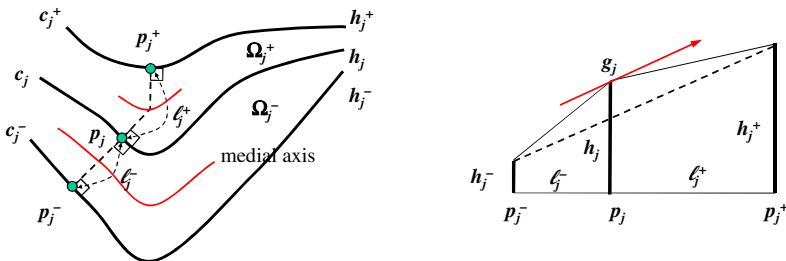


Fig. 6. Derivative at a point on an interior contour

4.2 Convex Hermite Interpolation

When a medial gradient line Γ is in a region of peak, pit, canyon, or ridge-peak (which is a dual of canyon), the height h of any point p along the line Γ can be computed by convex (or concave) univariate interpolation (see Fig. 7). If line Γ is in a region of peak, pit, canyon, or ridge-peak (which is a dual of canyon), the height h of any point p along the line Γ can be computed by convex (or concave) univariate interpolation. If line Γ is in a region of peak or ridge-peak, the height function along Γ must be concave, and if line Γ is in a region of pit or canyon, the height function along Γ must be convex. To preserve the convexity of height values, convex rational Hermite spline [12] can be used. The spline proposed by Delbourgo on the gradient line Γ is as follow:

$$h(t) = h_{i+1}t + h_i(1-t) - \frac{1}{\frac{1}{(d_i+d_{i+1})t(\Delta_i-g_i)} + \frac{1}{(d_i+d_{i+1})(1-t)(g_{i+1}-\Delta_i)}} \tag{1}$$

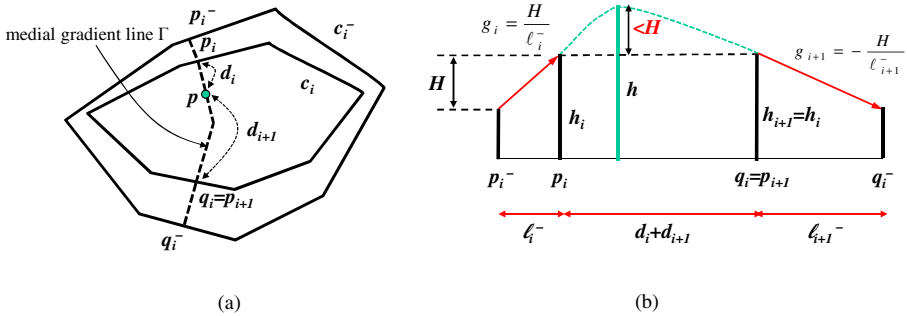


Fig. 7. (a) Medial gradient line passing through a point in a sub-domain of peak (b) Derivative at the point

Since contour data is convex (i.e., $g_i \leq \Delta_i \leq g_{i+1}$), near to pit or canyon, the second derivative of $h(t)$ is shown to be nonnegative for all $t \in [0,1]$. Hence $h(t)$ is C^1 -continuous.

Suppose a medial gradient line Γ , in a region of peak bounded by a contour c_i of height h_i starts from a point p_i ends at a point q_i on the same contour (see Fig. 7 (a)). Since $h_i = h_{i+1}$ and $\Delta_i = 0$, the concave spline function (1) becomes:

$$h(t) = h_i + \frac{1}{\frac{1}{(d_i+d_{i+1})t(-g_i)} + \frac{1}{(d_i+d_{i+1})(1-t)(g_{i+1})}} \tag{2}$$

Determination of the first derivative of $h(t)$ yields the maximum value of $h(t)$:

$$\max_{0 < t < 1} h(t) = h_i + H \frac{(d_i + d_{i+1})}{4\sqrt{\ell_i^-} \sqrt{\ell_{i+1}^-}}$$

where H is the height gap between two adjacent contours c_i and c_i^- . By assuming $d_i + d_{i+1} < 4\sqrt{\ell_i^-} \sqrt{\ell_{i+1}^-}$ in equation (2) which is a reasonable assumption for many contour data, the maximum value of $h(t)$ is $h_i + H$. This validates that there are no other contours within a contour c_i .

5 Experiments

We applied our algorithm to real world data. The contours of Woomyon mountain (located in Seoul) in Fig. 8 and Gwangnung mountain (near to Seoul) in Fig. 9 are provided by the National Geographic Information Institute of Korea. The interval distance of contours in both data is 5 meters. In the examples, there are several instances of contour branching with one-to-many correspondence. Terrain features like peaks, ridges, valleys and hillsides are well shown in the examples.

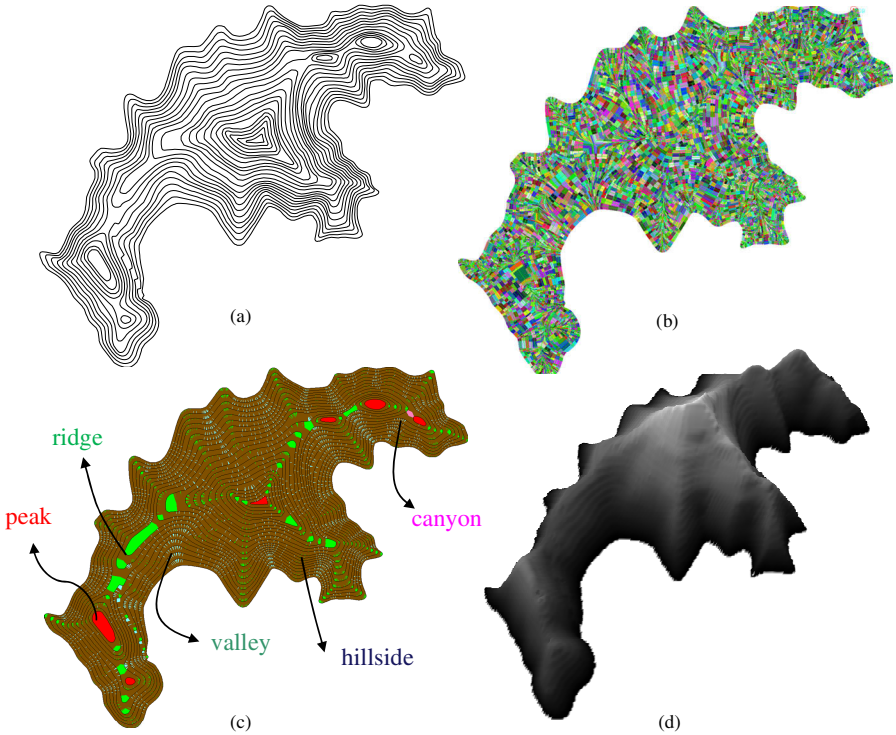


Fig. 8. (a) Contour set of Mt. Woomyon (in Seoul) (b) Zones colored randomly (c) Zones of the same terrain features colored the same color (d) Terrain model with DEM

Fig. 8(a) represents a contour set of Woomyon mountain. All sub-domains of the contours are subdivided into quasi-dual medial axis decompositions. Every zone corresponding to a segment of medial-axes has been computed and depicted with different, randomly generated, colors in Fig. 8(b). In Fig. 8(c), every zone having the same terrain features are depicted with the same color. Dark brown represents hillside, red represents peak region, sky blue represents valley, and pink represents canyon. Note that canyon in this figure represents a hollow region between two mountain areas. Fig. 8(d) represents the corresponding terrain constructed from the DEM converted from the contours.

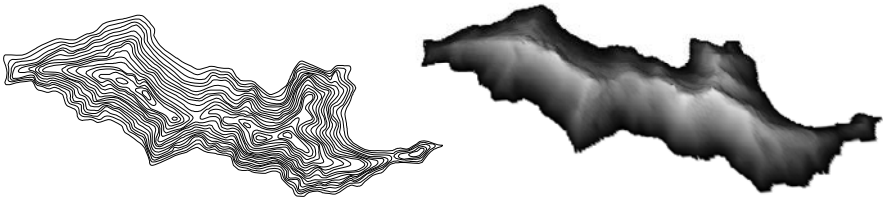


Fig. 9. Contours and DEM generated terrain model of Mt. Gwangnung

Table 1 shows the statistics for the real world contour examples used for the experiments. Note that the number of zones in each sub-domain of contours is the same as the number of edges in medial axis of the sub-domain. Ground points for DEM are counted if the points are within the outermost contour.

Table 1. Statistics for real world contour data

	Mt. Woomyon	Mt. Gwangnung
# contours	32	32
# contour points	5492	6280
# zones	31246	36167
DEM grid size	269×230	155×351
# DEM points	23700	21084

From the examples, we can see that the proposed algorithm is suitable to produce high quality DEM with gap distance of sub-contours from contour data.

6 Conclusion

In this paper a new technique for computing the elevation of a ground point to construct a digital elevation model (DEM) from contours is proposed. The elevation of a ground point of DEM not belonging to a contour is determined by interpolating the heights of the two adjacent contours of the point. The main contribution exists in the

decomposition of each sub-domain between adjacent contours into a set of sub-regions using medial axis transformation and classifying each sub-region into a variety of terrain features. The elevations of points are interpolated with different methods according to terrain features they belong to. The other contribution is that a gradient line which is an approximate shortest path passing through some point between two adjacent contours is defined using medial axis and the gradient line is used to interpolate the height of the point. For instance, in the case of hillside sub-region, a gradient line is approximated with two line segments touching each adjacent contour orthogonally and joining at medial axis of the sub-domain. This type of approximate gradient line satisfies similar properties of flux lines to describe electric field distribution. The univariate monotone rational Hermite spline is used to compute an approximate height of a point on the gradient line. In the case for a point in innermost contours, near to a pit or a peak, the univariate convex rational Hermite spline is used. We demonstrated the proposed algorithm by applying to some real world examples.

References

1. Meyers, D., Skinner, S., Sloan, K.: Surfaces from Contours. *ACM Transaction on Graphics* 11, 228–258 (1992)
2. Hormann, K., Spinello, S., Schröder, P.: C^1 -continuous Terrain Reconstruction from Sparse Contours. In: *Proceedings of Vision, Modeling and Visualization (VMV 2003)*, pp. 289–297 (2003)
3. Zhang, Z., Konno, K., Tokuyama, Y.: 3D Terrain Reconstruction Based on Contours. In: *The Ninth International Conference on Computer Aided Design and Computer Graphics (CAD-CG 2005)*, pp. 325–330 (2005)
4. Thibault, D., Gold, C.: Terrain Reconstruction from Contours by Skeleton Construction. *GeoInformatica* 4, 349–373 (2000)
5. Dakowicz, M., Gold, C.: Visualizing Terrain Models From Contours – Plausible Ridge, Valley and Slope Estimation. In: *Proceedings of the International Workshop on Visualization and Animation of Landscape (2002)*
6. Dakowicz, M., Gold, C.: Extracting Meaningful Slopes from Terrain Contours. *International Journal of Computational Geometry & Applications* 13, 339–357 (2003)
7. Gavrilova, M., Rokne, J.: Updating the Topology of the Dynamic Voronoi Diagram for Spheres in Euclidean d-Dimensional Space. *Computer Aided Geometric Design* 20, 231–242 (2003)
8. Liu, X., Rokne, J., Gavrilova, M.: A Novel Terrain Rendering Algorithm Based on Quasi Delaunay Triangulation. *The Visual Computer* 26, 697–706 (2010)
9. Gousie, M., Franklin, W.: Constructing a DEM from Grid-based Data by Computing Intermediate Contours. In: *Proceedings of the 11th ACM Int. Symp. on Advances in GIS*, pp. 71–77 (2003)
10. Mascardi, V.: Extraction of Significant Terrain Features from RSG and TIN: A Survey (1998)
11. Gregory, J., Delbourgo, R.: Piecewise Rational Quadratic Interpolation to Monotonic Data. *IMA Journal of Numerical Analysis*, 123–130 (1982)
12. Delbourgo, R.: Shape Preserving Interpolation to Convex Data by Rational Functions with Quadratic Numerator and Linear Denominator. *IMA Journal of Numerical Analysis*, 123–136 (1989)

13. Chen, J., Qiao, C., Zhao, R.: A Voronoi Interior Adjacency-Based Approach for Generating a Contour Tree. *Computers & Geosciences*, 355–467 (2004)
14. Lee, D.T.: Medial Axis Transformation of a Planar Shape. *IEEE Transactions on Pattern Analysis and Machine Intelligence* 4, 363–369 (1982)
15. Yap, C.K.: An Algorithm for the Voronoi Diagram of a Set of Simple Curve Segments. In: *Discrete and Computational Geometry*, pp. 365–393 (1987)
16. Srinivasan, V., Nackman, L.R.: Voronoi Diagram for Multiply-Connected Polygonal Domain I: Algorithm. *IBM Journal Research and Development* 31, 361–372 (1987)
17. Tang, L.: Automatic Extraction of Specific Geomorphological Elements from Contours. In: *Proceedings of the 5th International Symposium Spatial Data Handling*, pp. 554–566 (1992)
18. Chai, J., Miyoshi, T., Nakamae, E.: Contour Interpolation and Surface Reconstruction of Smooth Terrain Models. In: *Proceedings of the Conference on Visualization 1998*, pp. 27–33 (1998)
19. Choi, J., Cha, Y., Heo, J., Ryu, Y., Kim, C., Oh, S.: Generation of DEM from Contours for the Orthorectification of High-Resolution Satellite Images. In: *Proceedings of the International Symposium of Remote Sensing*, pp. 7–10 (2008)
20. Fritsch, F., Carlson, R.: Monotone Piecewise Cubic Interpolation. *SIAM Journal of Numerical Analysis* 17, 238–246 (1980)

Analysis of a High Definition Camera-Projector Video System for Geometry Reconstruction

José Luiz de Souza Filho, Roger Correia Silva, Dhiego Oliveira Sad,
Renan Dembogurski, Marcelo Bernardes Vieira,
Sócrates de Oliveira Dantas, and Rodrigo Silva

Universidade Federal de Juiz de Fora - DCC/ICE,
R. Lourenço Kelmer, 36036-330, Juiz de Fora-MG, Brazil
{jsouza,correia.roger,dhiegosad,ad.renan,
marcelo.bernardes,rodrigoluis}@ice.ufjf.br,
dantas@fisica.ufjf.br
<http://www.gcg.ufjf.br>

Abstract. The present work describes the development of a high definition camera-projector system (with resolutions up to 1920x1080 and 1280x720). The steps and processes that lead to the reconstruction of geometry, from system setup to triangulation, are detailed. A structured light coding scheme that offers a flexible number of stripes for projection was used. One of the objectives of this work is to estimate the limit number of stripes possible within the current resolutions of high definition video. This limit number is the one that provides dense geometry reconstruction with low accuracy and precision errors. To evaluate the reconstructions, we propose a protocol for error measurement. The geometry of general objects is also presented for qualitative evaluation. Our results show that low cost but effective 3D scanners can be built with high definition video devices providing compressed data.

Keywords: camera-projector system, 3D reconstruction, structured light, error evaluation.

1 Introduction

A 3d scanner is a device that captures 3D geometric information of objects and scenes from real world. A camera-projector scanner does that by projecting a structured light pattern over an object. The deformation of the projected light pattern allows the geometry reconstruction. Information obtained from high resolution devices provide detailed and dense generation of point clouds.

In this work we describe the development of a 3D scanner with high definition camera and projector. Our scanner uses the $(b, s) - BCSL$ structured light coding [1], which employs the projection of a sequence of colored vertical stripes on the scene. The higher the number of projected stripes is, more details the reconstructed geometry has. A good reconstruction is the one that recovers geometric details of objects or scenes with subpixel accuracy, has a high density number

of points and also has a low reconstruction error. Another major advantage of this type of color coding is that only a few number of complementary slides are needed for a complete new geometry shot. Our system provides a set of 3D points for each two consecutive frames.

There are other works that focus on acquiring high density of points as [2] and [3]. An extended overview of structured light reconstruction methods are presented in [4].

2 Structured Light Pattern and Camera-Projector Calibration

In this work, we chose the (b,s) -BCSL [1] as structured light pattern. This coding can obtain high resolution geometry without imposing strong restrictions on the scene dealing, for example, with reflection problems. Every transition of adjacent stripes has a unique code defined by the colors on its left and right. The parameter b denotes the number of colors to be used. There are six eligible colors: red (R), green (G), blue (B) and their respective complementary cyan (C), magenta (M) and yellow (Y). The number of stripes is defined by s and it is directly related to the coding and decoding.

The number of different possible codes for transitions is $[b(b-1)]^s$, considering that consecutive stripes cannot have the same colors. The (b,s) -BCSL coding uses slides with complementary colors to deal with photometric restrictions of a scene. Each projection of a slide S is followed by a complementary color slide \bar{S} . This allows robust transition identification with subpixel precision in $O(1)$.

The triangulation is obtained by calibrating the camera-projector system. There are many methods as seen on [5] and [6], but the one used in this paper is Tsai's with a global optimization [7]. Tsai's is an accurate calibration method and it models the distortion caused by the camera's lens. This turns the linear relations on a non-linear problem due to the radial distortion term in the system. To solve this problem we use an optimization scheme as the Levenberg-Marquadt algorithm [8] [9].

3 Geometry and Photometry Extraction

In this section we describe the steps of the pipeline from getting the initial images and outputting a 3D point cloud. An overview of the whole process is shown on Figure 1.

3.1 Pre-processing Images

The proposed pipeline has four images I_1, \bar{I}_1, I_2 and \bar{I}_2 as input. We also acquire a fifth image T lightened with a white projection for further texture mapping. First we use a 5x5 Gaussian low-pass filter to remove noise on each of the four images. Then we apply a color calibration matrix \mathbf{M} to each pixel [10]. As a result there are four color calibrated images C_1, \bar{C}_1, C_2 and \bar{C}_2 .

The next step is to subtract each image from its complementary image. For each pair of images we create a difference image D_n and a projected colors image P_n . The images D_1, D_2, P_1 and P_2 are the input of the boundary detection.

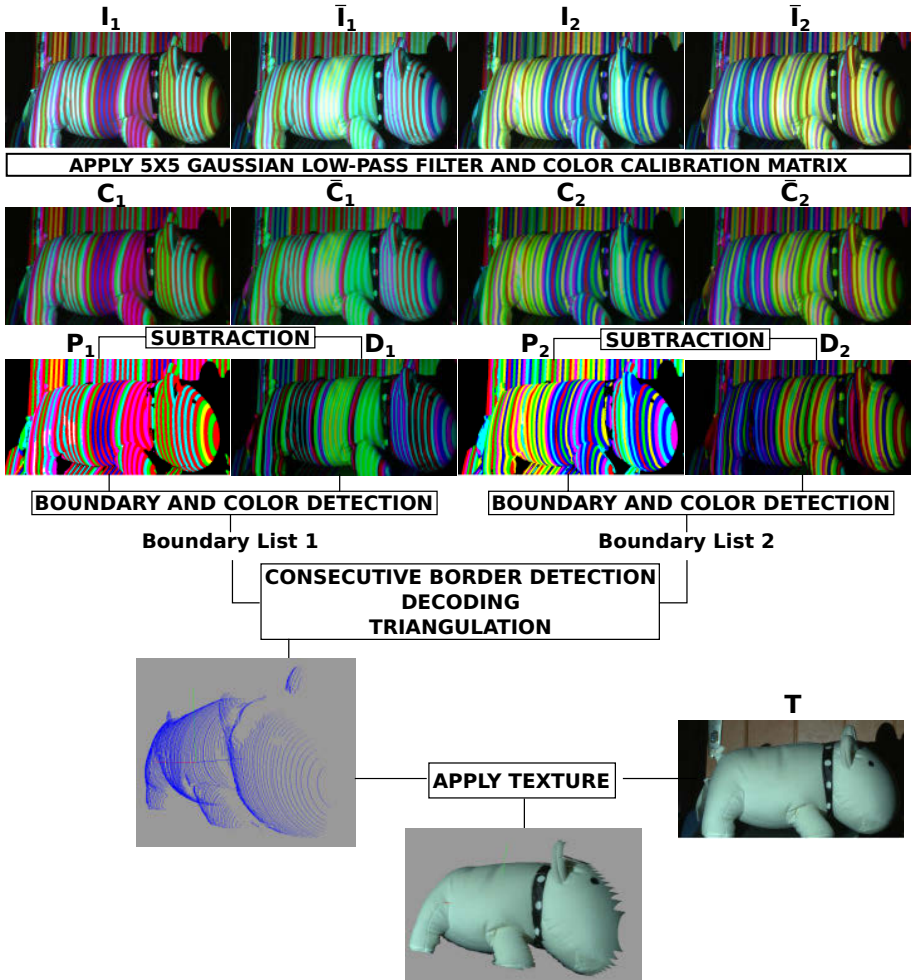


Fig. 1. Pipeline overview

3.2 Boundary Detection

The boundary positions are identified by looking for zero crossings at any of the Red, Green or Blue channels of the difference images. The left and right colors of a boundary correspond to the colors at that position on the projected colors images.

Let D_n^R, D_n^G e D_n^B be the color channels of a difference image D_n where $n = \{1, 2\}$. As the (b,s) -BCSL projected stripes are vertical we can process each

line of D_n individually. The pixels on the right and left of a zero crossing have opposite signs. Between them there is a high intensity variation. A zero crossing should satisfy, at least on one color channel K , the following restriction:

$$|D_n^K(i - \delta_1, j)| + |D_n^K(i + \delta_1, j)| \geq l, \quad (1)$$

where $K = \{R, G, B\}$.

On Equation 1, i and j are the columns and rows of the difference image respectively. The parameter l is a threshold which denotes the minimum intensity variation that characterizes a zero crossing. Empirically we assumed $l = 5$ in this paper. δ_1 is a parameter referred to a slightly offset describing the left and right neighbor pixels of a zero crossing. If Equation 1 is satisfied by any channels of D_n at a position (i, j) , a boundary is generated. Each boundary is defined as $b = (x, j, a, c_l, c_r)$, where $x \in \mathbb{R}$ is the horizontal coordinate of a zero crossing with subpixel precision, j is the row in which the zero crossing was found, a is the amplitude of the crossing, and c_l and c_r are respectively the left and right colors of the projected stripes where the boundary was identified. The amplitude a and coordinate x are

$$a = |D_n^K(i - \delta_1, j)| + |D_n^K(i + \delta_1, j)| \quad (2)$$

and

$$x = \frac{D_n^K(i + \delta_1, j) \cdot (i - \delta_1) + D_n^K(i - \delta_1, j) \cdot (i + \delta_1)}{a}. \quad (3)$$

If more than one boundary is found and the distance between the x coordinate of some of them are lower than a given distance δ_2 , these boundaries are linearly combined into a single boundary:

$$x_c = \frac{x_1 \cdot a_1 + x_2 \cdot a_2 + \dots + x_n \cdot a_n}{a_1 + a_2 + \dots + a_n}, \quad (4)$$

and the combined amplitude of the new boundary is

$$a_c = \frac{a_1^2 + a_2^2 + \dots + a_n^2}{a_1 + a_2 + \dots + a_n}. \quad (5)$$

In this paper we defined $\delta_2 = 3$ meaning there is no redundant transition in a 3 pixel region. High values of δ_2 could filter boundaries of distinct stripes transitions.

The next step is to filter the boundaries detected in all the color channels at once. For each row of the image we traverse the list of boundaries. For each boundary b_i we find the boundary b_h of highest amplitude in a δ_2 distance. The final computed zero crossing position x_f of this D_n region is

$$x_f = \frac{x_i \cdot a_i + x_h \cdot a_h}{a_i + a_h}. \quad (6)$$

After the boundaries are found we need to get the left and right colors to each of them. In order to do that we search the projected colors image P_n . Each color channel K of P_n is $P_n^K(i, j) = 0$ if $D_n^K(i, j) > 0$ and $P_n^K(i, j) = 1$ otherwise.

For a boundary $b = (x, j, a, c_l, c_r)$ the left and right colors are $c_l = P_n(x - \delta_2, j)$ and $c_r = P_n(x + \delta_2, j)$ respectively. If left and right valid colors are found and they are distinct, a complete boundary is formed. If not, this boundary is discarded.

3.3 Boundaries over Time

In the last detection stage we need to relate the boundaries found in both difference images D_1 and D_2 so we can reconstruct the 3D points. For every boundary $b_p = (x_p, j_p, a_p, c_{lp}, c_{rp})$ on the first list we look for a correspondent boundary $b_q = (x_q, j_q, a_q, c_{lq}, c_{rq})$ in a 7×7 region of the second one. If a correspondence is found and the colors c_{lp} , c_{rp} , c_{lq} and c_{rq} denote a valid (b, s) -BCSL code, its decoding is possible. Before that, the final x_p must be updated as

$$x_p = \frac{x_p \cdot a_p + x_q \cdot a_q}{a_p + a_q}. \quad (7)$$

With x_p , j_p and the boundary code defined, the depth of a zero crossing point can be calculated using the camera-projector calibration matrices.

3.4 Error Evaluation Protocol

One of the contributions of this work is an error evaluation protocol to analyze the geometry reconstruction. The analysis of the scanner with this protocol presents the experimental limits of reconstruction density with high definition video and stripe based, complementary color codes. High definition off-the-shelf video equipments provide compressed data. Even so, our results show that the reconstruction using these devices has reasonable precision and accuracy.

We capture planes with different orientations to evaluate and compare their reconstructions. By using least squares on each reconstructed plane set of points we get their equations. To compare the similarity between two planes $\pi_1 : a_1x + b_1y + c_1z = d_1$ and $\pi_2 : a_2x + b_2y + c_2z = d_2$ the following metric based on the distance in the projective space is proposed:

$$d = \sqrt{\left(\frac{a_1}{d_1} - \frac{a_2}{d_2}\right)^2 + \left(\frac{b_1}{d_1} - \frac{b_2}{d_2}\right)^2 + \left(\frac{c_1}{d_1} - \frac{c_2}{d_2}\right)^2}, \quad (8)$$

where each plane $\pi : ax + by + cz = d$ is considered a point $P = (a, b, c, d) \in \mathbb{RP}^3$ and $[a, b, c]$ is a unit vector in \mathbb{R}^3 .

3.5 Quantitative Analysis

The objective of this protocol is to measure the accuracy and precision of the developed scanner. Accuracy is the exactness of distance measures and precision is related to repeatability and its high values indicate low variations between the calculated distances.

A sequence of five reconstructions of a known planar object is performed for each fixed number of stripes evaluated (Fig. 6 and 7). A mean plane is estimated uniting all five point clouds. This plane minimizes the mean square error between all scanned points for a fixed number of stripes. The precision of the reconstruction is calculated as the standard deviation of the five planes' distances in relation to the mean plane. The accuracy is given by the correspondent mean distance.

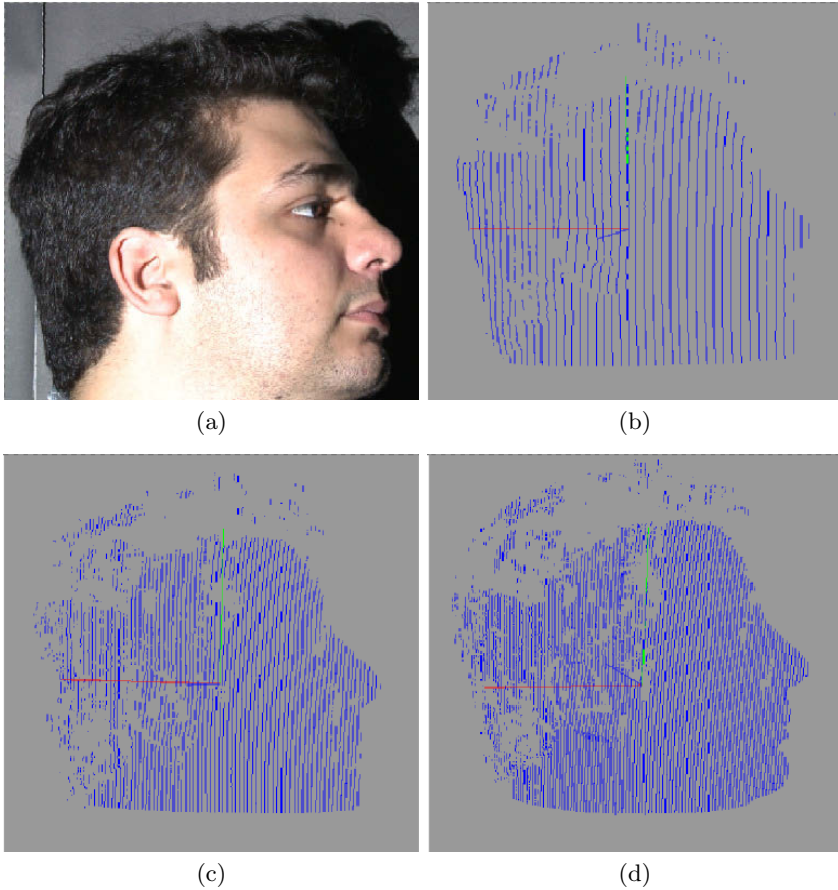


Fig. 2. Reconstruction of a face. (a) Captured scene. (b) 100 stripes; 16860 points. (c) 200 stripes; 29128 points. (d) 250 stripes; 56334 points.

To act as a reference, we create a base plane which is the mean plane of the reconstruction using 50 stripes. We have manually checked the distance given by our scanner for the marked points of the calibration pattern. Several measures were made using a ruler to validate this base plane.

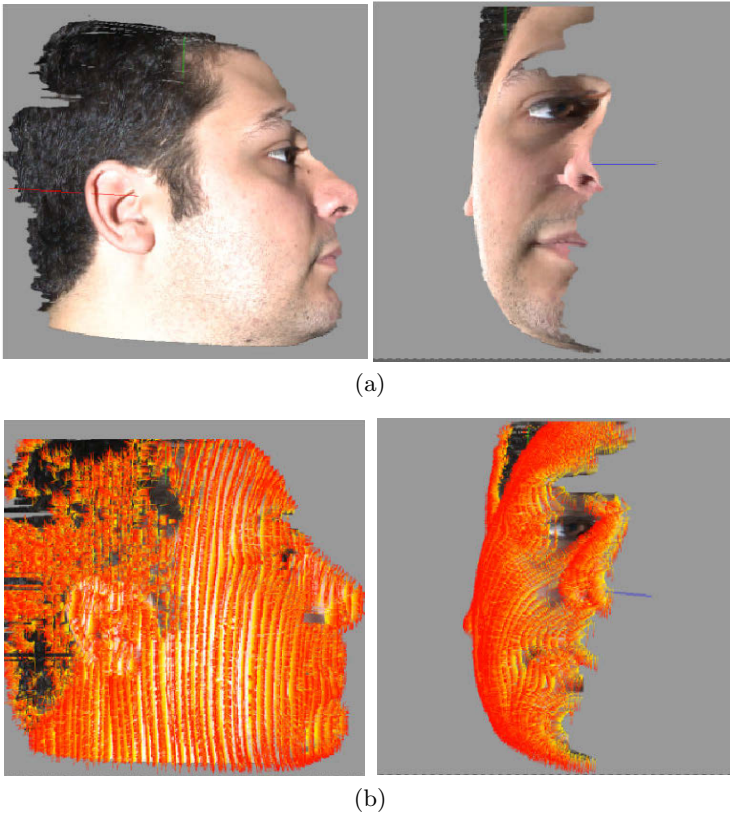


Fig. 3. Reconstruction of a face. (a) Textured surface and (b) its normals.

4 Experimental Results

In this section we show the results of the 3D reconstructions of our scanner. we also present the results that relate image's resolutions and number of projected stripes, realized with the developed error protocol.

Figure 2 shows three point clouds of a scanned face. Each of the clouds was generated with a different number of projected stripes: Figures 2 (b) and (c) have 100 and 200 stripes with a 1280x720 resolution. The one with 100 stripes generated 16860 points and the other with 200 stripes has 29128 points. Over Figure 2 (d), there are 250 projected stripes in a 1920x1080 resolution, resulting in 56334 points. Projecting more stripes results in more detailed acquired geometry. With 250 projected stripes we can see a better contour of the chin, mouth and details of the ear. One may see that there are only a few points acquired over the hair. It is a limitation of all active light reconstruction systems: the quality of the recovered geometry is sensitive to the materials that composes the scene and their interaction with projected light.

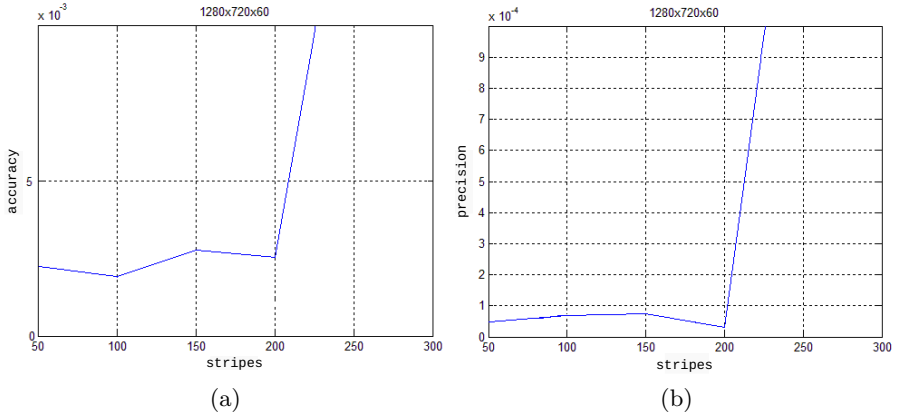


Fig. 4. (a) Accuracy and (b) precision for 1280x720x60

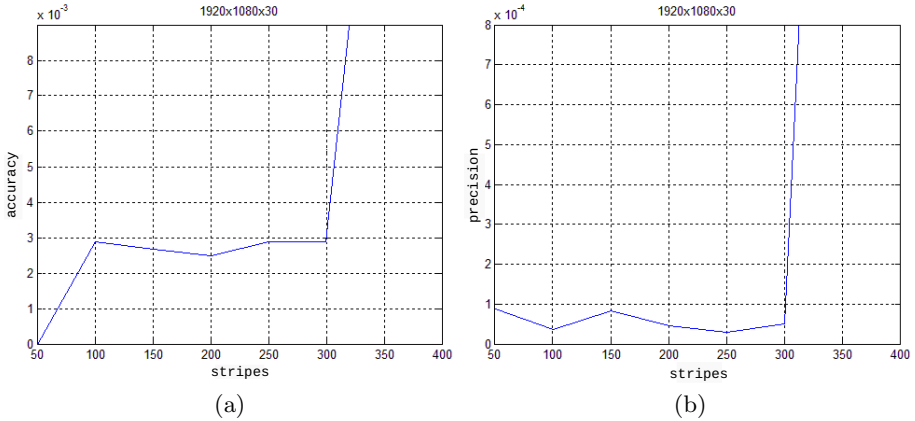


Fig. 5. (a) Accuracy and (b) precision for 1920x1080x30

In general, translucent, specular, and low reflection intensity materials are problematic. Figure 3 (b) shows the estimated normals for the 250 projected stripes reconstruction of a face and (a) its final result already with texture.

In this section we evaluate the relationship between the number of stripes and the resolution of the captures, using our error protocol. The objective is to estimate, for each resolution, a limit for the number of projected stripes.

The result of accuracy and precision for the configuration 1280x720, with a capture rate of 60Hz is shown on Figure 4. The measurements show a low error between 50 and 200 projected stripes. For 250 stripes though, this error significantly increases, showing that the safe limit of projected stripes for the 1280x720x60 configuration was exceeded. The precision measurement is similar to the accuracy. Low oscillations between 50 and 200 stripes and a high step for

the 250 error. These results indicate that similar reconstructions of the plane are repeated until 200 stripes. The accuracy and precision results shows that reliable reconstructions stands until projecting 200 stripes. This may be noticed on Figure 6. For 250 there are decoding errors and miscalculated depths.

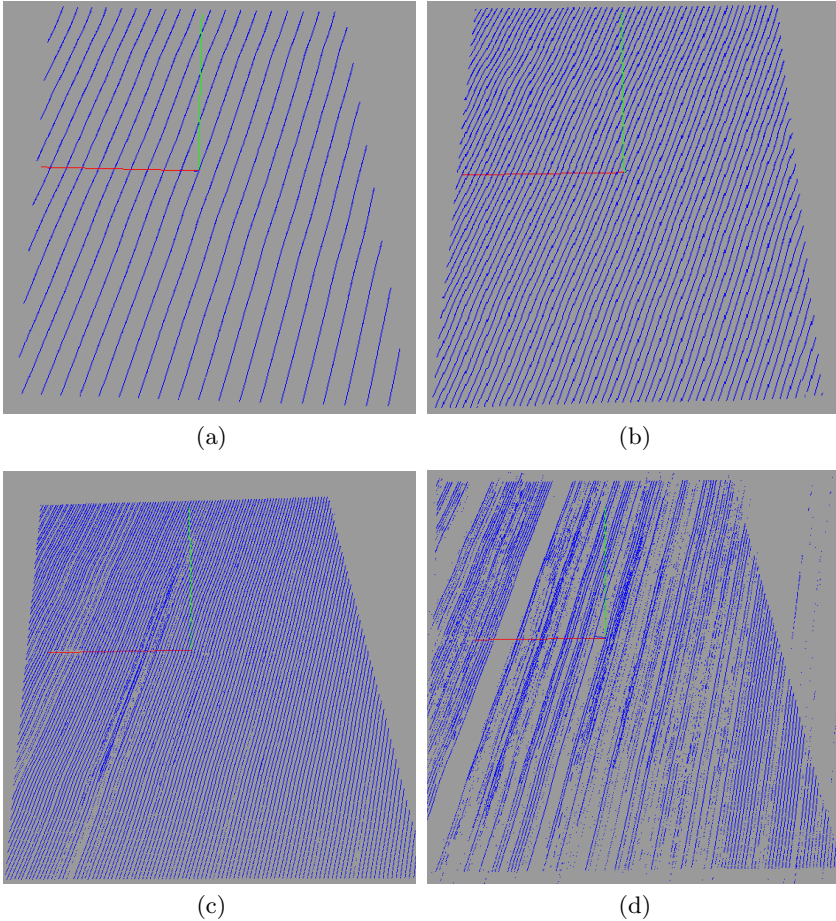


Fig. 6. Reconstructed planes for 1280x720x60. (a) 50 stripes; 13694 points. (b) 150 stripes; 40750 points. (c) 250 stripes; 67905 points. (d) 300 stripes; 78668 points.

The results for 1920x1080 with 30Hz configuration is presented on Figure 5. The accuracy error is stable, with low variations, up to 350 projected stripes. While for precision, an error increase is noted after 300 stripes. A safe reconstruction should have a maximum number of 300 projected stripes. Some reconstructions with different numbers of stripes for this resolution are shown on Figure 7. There, one may notice that for 350 stripes there are some miscalculated points at the middle left of the plane. For 400 stripes, in addition to the

points reconstructed outside the plane, there are lots of empty areas. Thus, this visual analysis accords with the graphics presented on Figure 5, indicating that for those number of stripes the precision and accuracy of reconstructions are compromised.

The use of planes with different orientations in this error analysis is sufficient to infer the maximum number of stripes for each resolution. Planes with more depth helps to estimate, as specified in Section 3.4 the method's behavior reconstructing more complex objects. With 1920x1080 pixels, 300 stripes is a safe limit for objects with non-null curvatures.

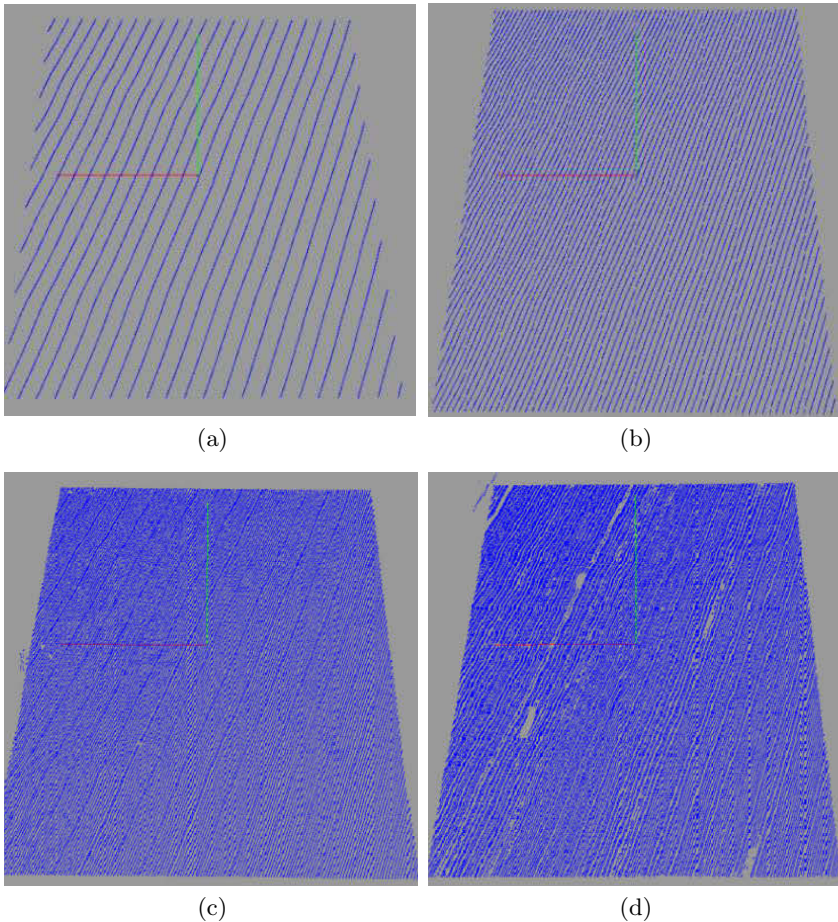


Fig. 7. Reconstructed planes for 1920x1080x30. (a) 50 stripes; 20383 points. (b) 150 stripes; 60963 points. (c) 350 stripes; 142225 points. (d) 400 stripes; 156776 points.

5 Conclusion and Future Work

A high resolution scanner, requiring few parameters, and a protocol for reconstruction error evaluation were shown in this paper. Objects of different shapes and materials were reconstructed generating dense point clouds. It was possible to identify points even in specular and black objects. However, active light scanners have limitations. Shadowed areas and some surfaces that have low reflection properties might result in reconstruction imperfections (Fig. 2).

The use of complementary slide patterns provide a robust identification of transition boundaries. Combined with the high speed and high image quality of off-the-shelf camera-projectors, the reconstruction results have reasonable precision and accuracy. Low cost but effective 3D scanners are possible to be constructed with high-definition cameras and projectors.

An error evaluation protocol to analyze precision and accuracy based on projective space distances was proposed. The objective of this protocol was to define an upper bound for the number of projected stripes, assuring a high number of points acquired with a minimal desired error.

A possible application could generate complete 3D models of objects or scenes, aligning point clouds acquired from different views [11][2].

Acknowledgment. The authors thank to FAPEMIG (*Fundação de Amparo à Pesquisa do Estado de Minas Gerais*), CAPES (*Coordenação de Aperfeiçoamento de Pessoal de Ensino Superior*) and UFJF for funding this research.

References

1. Sa, A., Carvalho, P.C., Velho, L.: (b, s)-bcsI: Structured light color boundary coding for 3d photography. In: 7th Int. Fall Workshop on Vision, Modeling, and Visualization (2002)
2. Guhring, J.: Dense 3-d surface acquisition by structured light using off-the-shelf components. In: Proc. Videometrics and Optical Methods for 3D Shape Measurement, pp. 220–231 (2001)
3. Fechteler, P., Eisert, P., Rurainsky, J.: Fast and high resolution 3d face scanning. In: Proceedings of the International Conference on Image Processing, ICIP 2007, September 16–19, pp. 81–84. IEEE, San Antonio (2007)
4. Salvi, J., Fernandez, S., Pribanic, T., Llado, X.: A state of the art in structured light patterns for surface profilometry. *Pattern Recogn.* 43, 2666–2680 (2010)
5. Zhang, Z.: A flexible new technique for camera calibration. *IEEE Transactions on Pattern Analysis and Machine Intelligence* 22, 1330–1334 (2000)
6. Coda, C., Velho, L., Lewiner, T., Peixoto, A.: Um sistema generico de calibracao de camera. In: Proceedings of SIBGRAPI (2007)
7. Tsai, R.: A versatile camera calibration technique for high-accuracy 3d machine vision metrology using off-the-shelf tv cameras and lenses. *IEEE Journal of Robotics and Automation* 3(4), 323–344 (1987)
8. Levenberg, K.: A method for the solution of certain nonlinear problems in least squares. *Quart. Appl. Math.* 2, 164–168 (1944)

9. Marquadt, D.: An algorithm for the least-squares estimation of nonlinear parameters. *SIAM J. Appl. Math.* 11, 431–441 (1963)
10. Vieira, M.B., Sa, A., Velho, L., Carvalho, P.C.: A camera-projector system for real-time 3d video. In: *IEEE Int. Workshop on Projector-Camera Systems*, vol. 3, pp. 96–100 (2005)
11. Rusinkiewicz, S., Hall-Holt, O., Levoy, M.: Real-time 3D model acquisition. *ACM Trans. on Graphics (Proc. SIGGRAPH)* 21(3), 438–446 (2002)
12. Besl, P., McKay, N.: A method for registration of 3-d shapes. *IEEE Transactions on Pattern Analysis and Machine Intelligence* 14, 239–256 (1992)

Video-Based Face Verification with Local Binary Patterns and SVM Using GMM Supervectors

Tiago F. Pereira, Marcus A. Angeloni, Flávio O. Simões,
and José Eduardo C. Silva

CPqD - Research and Development Center in Telecommunications,
Campinas - SP 13026-123, Brazil
tpereira@cpqd.com.br
<http://www.cpqd.com.br>

Abstract. The classification task has a relevant importance in face verification systems and there are many approaches proposed to solve it. This paper shows a new approach for the classification task in video-based face verification systems using Support Vector Machines (SVM) as classifier and Gaussian Mixture Models (GMM) working as its kernel. The use of Local Binary Patterns (LBP) for face description, in conjunction with the generation of Gaussian supervectors as input points for the classifier, describes the temporal information contained in a video by a unique feature point, which seems to be a very compact and powerful form of representation. Our experimental results, performed on MOBIO database and protocol, shows the advantages of the proposed technique.

Keywords: Face Verification, Local Binary Patterns, Support Vector Machines, Gaussian Mixture Models.

1 Introduction

Face recognition is one of the most important abilities that humans use in their daily lives [8]. On the last decades, methods for automatically recognizing faces have received significant attention owing, firstly because of the wide range of commercial and law enforcement applications, such as access control, surveillance and information security, and secondly due to the availability of feasible technologies to perform this task [21], [10].

Face recognition has several advantages over other biometric modalities: it is natural, non-intrusive, easy to use, and suitable for covert applications [8]. It can operate in two modes: identification or verification. In identification mode, the user provides his face image to the system, which makes a comparison between this sample and a set of biometric references stored in a database (i.e, a 1-to- N comparisons, where N is the number of users represented in the database) to determine his identity. In verification mode, on the other hand, the system verifies the claimed identity based on a one to one comparison between the biometric sample and the claimed user's biometric reference.

This paper focuses in face verification with video input. The main contribution of this work is to generalize the information of an entire video in one single

feature vector without lose of accuracy. Local Binary Pattern (LBP) is used as the face descriptor, and experimental results show that face verification based on a combination of Support Vector Machines (SVM) and Gaussian Mixture Models (GMM) supervectors overcomes face verification based solely on GMM or SVM.

In Section 2 face description using Local Binary Patterns is presented. In Section 3 the GMM-based classifier for face verification tasks is adressed. Section 4 discusses the use of Support Vector Machines for face verification. Section 5 presents the proposed approach, based on both SVM and GMM supervectors. Section 6 and 7 presents experimental results and, finally, Section 8 contains a conclusion for this work.

2 Face Description Using Local Binary Patterns

The Local Binary Pattern (LBP) operator was originally designed for texture description [13]. This operator is computed in a pixel level basis using a 3x3 kernel, thresholding the surroundings of each pixel with the central pixel value and considering the result as a binary value. The decimal form of the LBP code is expressed as:

$$LBP(x_c, y_c) = \sum_{n=0}^{N-1} f(i_n - i_c)2^n, \quad (1)$$

where i_c corresponds to the gray intensity of the center pixel (x_c, y_c) , N is the number of sampling points, i_n is the gray intensity of the n -th surrounding pixel, and $f(x)$ is defined as follows:

$$f(x) = \begin{cases} 0 & \text{if } x < 0 \\ 1 & \text{if } x \geq 0 \end{cases}. \quad (2)$$

Later, Ojala et al. [14] extended this operator to support surrounding points and radius of a pixel neighbourhood with different shapes and sizes, enabling handling textures at different scales. Fig. 1 illustrates the operator calculation and the points distribution in a circular neighbourhood with radius 2, where the pixel values are bilinearly interpolated whenever the sampling point is not in the center of a pixel.

Another important extension proposed by Ojala et al. [14] was the uniform patterns concept. A LBP operator is considered uniform if it contains at most two bitwise transitions 0-1 or 1-0 when viewed as a circular bits chain, and according to Ojala et al. [14], nearly 90 percent of LBP operators observed in images are uniform. In spacial terms, uniform patterns represent some patterns of a texture: spot, flat, area, edge and corner. With an 8-bit representation, there are 58 patterns with at most two bitwise transitions. Fig. 2, extracted from [6], describes all possible uniform patterns with 8 neighbours.

Ahonen et al. (see [1] and [2]) adopt the following notation for the LBP operator: $LBP_{P,R}^{u2}$, where the subscript represents the neighbourhood configuration

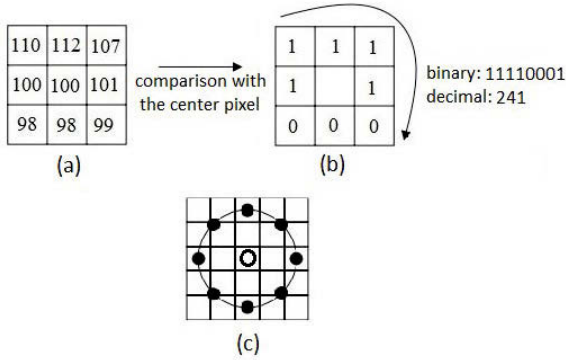


Fig. 1. LBP operator. (a) and (b) The basic LBP operator, where the neighbourhood of each pixel is thresholded and a binary number is obtained. (c) A circular neighbourhood example (with 8 neighbours point and radius 2). The pixel values are bilinearly interpolated whenever the sampling point is not in the center of a pixel.

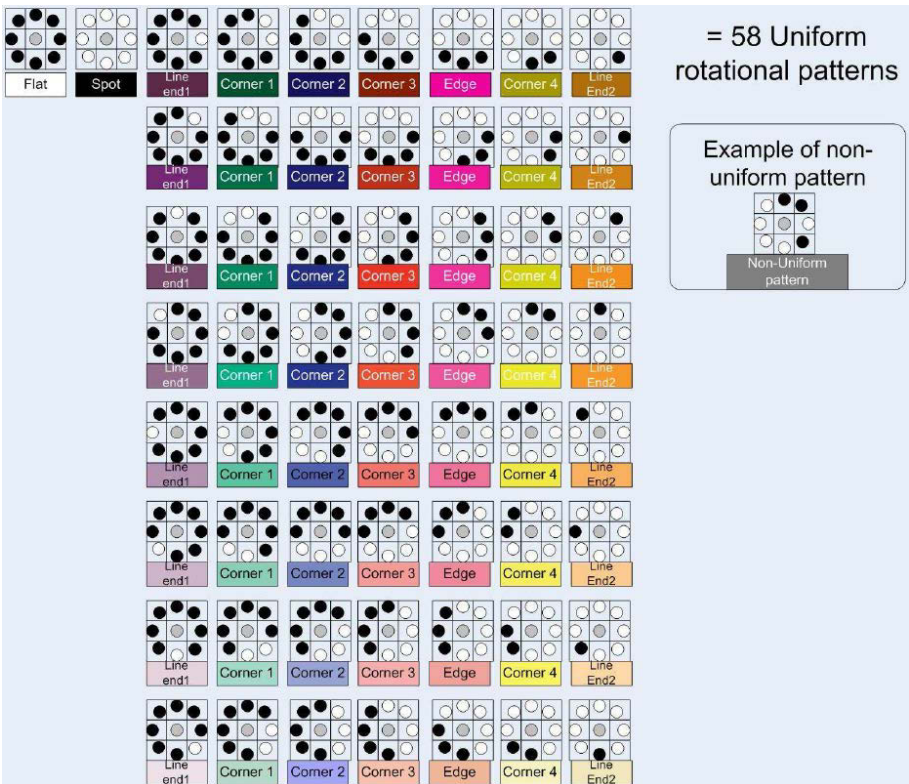


Fig. 2. (Color online) All uniform patterns for LBP with 8 neighbours [6]

with P sampling points on a circle of radius R , and the superscript $u2$ stands for using only uniform patterns and labelling all non-uniform patterns with a single label.

Recently, LBP have been applied to represent face images, yielding in promising results [1]. The face description using LBP consists in computing a histogram of LBP operators, and good results have been achieved using a configuration with 8 circular surrounding pixels and radius 2 (see [1], [2] and [16]). The LBP histogram-based approach for face description also takes advantage of the LBP operator extensions. As an example, when uniform patterns are used, the number of histogram bins is greatly reduced, since all non-uniform patterns are grouped into a single bin.

A relevant modification in the original LBP operator for face representation is the idea of splitting the face image in small blocks (which can be overlapped or not) and computing the LBP histogram for each block individually, thereby retaining spatial information. So, the face image is described in three different levels: a pixel level, with the calculation of each operator individually; the regional level, with the calculation of histograms for each block; and a global level, with the concatenation of all block histograms [16]. Fig. 3 shows all three levels of face description.

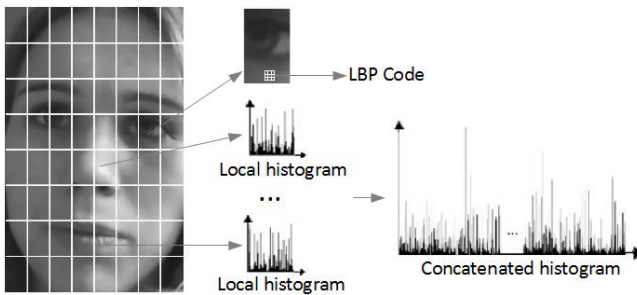


Fig. 3. Face description in three different levels: pixel level (LBP code), regional level (block histogram) and global level (concatenated histogram)

Although spatial information is preserved when the image is divided into blocks, some information is lost at the blocks' border. To avoid this, LBP operators are first calculated for the whole face image and later the resulting LBP matrix is divided into blocks. Thus, both spatial information and block edges are preserved.

3 GMM-Based Classifier

A Gaussian Mixture Model is a stochastic model that describes a generic probability density function as a product of multivariate Gaussian components.

The Gaussian Mixture Model (GMM) approach for face verification using LBP features is based on [16] and [5] and works as follows: given a sequence of LBP histograms derived from an individual, each one representing a video frame, we can calculate the probability of occurrence of this observed sequence by the following equation:

$$P(X|\lambda) = \prod_{t=1}^{N_v} p(\mathbf{x}_t|\lambda), \tag{3}$$

where $X = \{\mathbf{x}_1, \mathbf{x}_2, \dots, \mathbf{x}_{N_v}\}$ is the observation sequence, \mathbf{x}_t is a single observation, N_v is the number of observations, λ is the GMM model associated with an individual and $p(x)$ is the probability function associated with the GMM. This function describes the probability of observations and is given by:

$$p(\mathbf{x}_t|\lambda) = \sum_{j=1}^{N_G} m_j \eta(\mathbf{x}|\boldsymbol{\mu}_j, \boldsymbol{\Sigma}_j). \tag{4}$$

In equation 4, $\eta(\mathbf{x}|\boldsymbol{\mu}_j, \boldsymbol{\Sigma}_j)$ is a N-dimensional gaussian function with mean $\boldsymbol{\mu}_j$ and diagonal covariance matrix $\boldsymbol{\Sigma}_j$, N_G is the number of gaussians and m_j is the weight of a gaussian [5].

The GMM model parameters $(m_k, \boldsymbol{\mu}_k, \boldsymbol{\Sigma}_k)$ are estimated from training samples. The basic idea is to iteratively update the model parameters in order to maximize the probability of observation of the training samples. K-means [9] is used to initialize the model parameters; then the expectation-maximization (EM) algorithm [7] is executed to maximize the probability with respect to the training data.

Better performance of the GMM approach can be achieved if the individual models are derived from a common Universal Background Model (UBM). This model is trained with the procedure described above and the training data, in this case, consists of samples from hundreds of different individuals. This common model is the basis for a model adaptation procedure that is used to generate the individual models.

The algorithm used to adapt the individual models is a modification of the EM algorithm, known as maximum a posteriori (MAP) adaptation.

In this work, only the means of the N-dimensional gaussian functions of the UBM are adapted. The mean adaptation is described by the equation 5.

$$\mu_k = 1 - \alpha_k u_k^w + \alpha_k \frac{\sum_{t=1}^T P(k|\mathbf{x}_t) \mathbf{x}_t}{\sum_{t=1}^T P(k|\mathbf{x}_t)}, \tag{5}$$

where μ_k is the mean of the k-th gaussian, u_k^w is the correspondent mean in the UBM gaussian and α is an adaptation factor [5].

The value of the adaptation factor α follows a different strategy from that described in [16] and [5]. Following the idea presented by [15], the value of α is adapted for each gaussian, according to equation 6:

$$\alpha_k = \frac{n_k}{n_k + R}, \quad (6)$$

where n is a probabilistic measure that accounts for the number of times the gaussian k is activated by the training samples and R is a relevance factor fixed by the user. The use of this probabilistic count makes it possible for the algorithm to control the amount of adaptation of the mixtures. Mixture components with high probabilistic count are adapted towards the new data, whereas a low probabilistic count leads to small adaptation. The relevance factor R controls the importance of new data for adaptation.

In a verification task the score is calculated according to equation 7

$$\text{score} = \log(P(X|\lambda_c)) - \log(P(X|\lambda_w)), \quad (7)$$

where $P(X|\lambda_c)$ is the probability of X in the client model λ_c and $P(X|\lambda_w)$ is probability of X in the UBM. Since probabilities are in the log domain, the operation performed in equation 7 plays the role of a score normalization, making scores that came from different client models comparable.

4 SVM-Based Classifier

Support Vector Machines (SVM) have received a considerable attention in classification problems in the last decade. Differently from GMM, SVM is a discriminative classifier whose goal is to solve binary classifications problems.

Given a binary classification problem such as face verification with LBP face description, where Σ_1 is the positive class and Σ_2 is the negative class, the train step of an SVM classifier consists in finding the hyperplane \mathbf{w} that maximizes the separation between these two classes. The position of the hyperplane is defined by the support vectors.

The verification step is described by equation 8

$$\begin{cases} \mathbf{w} \cdot \mathbf{x} + b \geq 0, x \in \Sigma_1 \\ \mathbf{w} \cdot \mathbf{x} + b < 0, x \in \Sigma_2 \end{cases}, \quad (8)$$

where \mathbf{w} is the hyperplane normal vector, \mathbf{x} is the input data (LBP histogram) and b is a bias parameter.

To maximize the generalization power of the SVM classifier, a modification of the regular SVM so-called soft-margins SVM or C-SVM [17] was used in our simulations. In that approach, some classifications errors in the training stage are permitted in order to increase the value of the separation margin.

5 SVM-Based Classifier with GMM Supervectors

One video is composed by a large (and maybe not fixed) number of frames. It would be advantageous for a SVM classifier if the feature vector sequence corresponding to one video could be represented as a single vector, so the whole

video could be used as an individual input for the classifier. This single vector could carry the time varying information contained in the video, which could increase the discriminative power of this “sequence kernel SVM” [4].

GMM supervectors are a very effective way to map a variable length feature vector sequence into one single vector. A common UBM and the feature vector sequence representing the video of an individual are used as input for MAP adaptation, and a K-component UBM-adapted GMM of that individual is generated using the procedure described in section 3. Then a GMM supervector can be generated from the adapted GMM by stacking the N-dimensional mean vectors of GMM into one single $K \times N$ -dimensional vector. Note that the dimension of the GMM supervector is fixed and independent of the number of frames contained in the video.

Moreover, and most important, a GMM supervector has a much higher dimension compared to that of the original feature vectors. SVM classifiers usually make use of non-linear kernels to map the input data to a higher dimensional space, with the assumption that the mapped data are linearly separable in that new space. Since GMM supervectors already lie in a very high dimensional space, a simpler linear kernel could be used. To calculate the distance between two supervectors, an approximation of the Kullback-Leibler divergence is used. It can be shown that this approach satisfies the Mercer condition required in SVM optimization, and thus can be used as a Gaussian Supervector Kernel [4].

GMM supervectors are mostly used in speaker recognition tasks. In [3], a similar approach for face recognition is presented, where eigenfaces [19] are used to describe face information. In our work, the approach used in [4] and [3] is adapted, since Local Binary Patterns are now used to describe face information. The entire video is represented in a very compact form by a low cost and powerful descriptor, leading to an efficient classification procedure.

This section delineates the experiments that were carried out to test the three classification approaches described in the previous sessions. All tests were performed with the same set of LBP parameters, using the MOBIO database and protocol as a benchmark.

5.1 MOBIO Database and Protocol

Captured in a real-world scenario with mobile phones, the MOBIO database is a very large and challenging multimodal database [12]. Presented during the “Face and speaker verification evaluation” contest in ICPR 2010 [11], the MOBIO database is composed by 15,444 audio and video samples of 162 users (57 women and 105 men). For the experiments reported here, only the video part of the database was used. Fig. 4 presents some images extracted from the MOBIO database. These examples illustrate the amount of pose and illumination variability present in the database.

The MOBIO protocol defines 3 non-overlapped partitions (development, test and world) split in 6 non-overlapped sessions. The development set is used to estimate a threshold value to be used in the test set. In order to permit the



Fig. 4. (Color online) Images of MOBIO database

comparison of different face verification systems, the protocol employs the Half Total Error Rate (HTER) as a performance measurement:

$$HTER(\tau, D) = \frac{FAR(\tau, D) + FRR(\tau, D)}{2}, \quad (9)$$

where τ is a threshold, D is the dataset, FAR is the False Acceptance Rate and FRR is the False Rejection Rate.

5.2 Pre-processing, Segmentation and Feature Extraction

For each video, frames were selected with an uniform spacing of 5 frames (this value was chosen empirically). Faces in each frame of the training, world and test set videos were detected with the OpenCV¹ implementation of the Viola and Jones algorithm [20].

After the segmentation phase, the cropped image faces were converted to gray scale, resized to 108x108 pixels and processed using Tan & Triggs normalization [18] for illumination correction.

The $LBP_{8,2}^{\mu 2}$ operator was applied to the processed cropped faces, resulting in a 104x104 “LBP operator matrix”. This matrix was split into 64 blocks (sub-matrixes) with 13x13 LBP operators each. For each block, the LBP histogram was calculated to generate the local description of a face, and these histograms were concatenated to generate the face global description, with a dimensionality of 3776 (64×59).

5.3 GMM-Based Classifier Configuration

In this work, the implementation of the GMM classifier was based on an adaptation of the Speech Signal Processing Toolkit (SPTK²).

¹ <http://opencv.willowgarage.com>

² <http://sp-tk.sourceforge.net>

Two UBMs were generated, both trained with videos from the world set of the MOBIO database. The first one was trained only with videos of women (1,890 videos), whereas the second UBM used only videos of men (4,914 videos).

During the training phase, the selection of an UBM to initialize the GMM parameters (means, variances and weights) for MAP adaptation was based on genre. To train a male user GMM, the male UBM was selected, and the female UBM was used to train female models. The same idea was employed in the verification phase to select a UBM for score normalization.

The impostors used in the false acceptance tests were selected according to the division of the MOBIO database sets. To train users belonging to the development set, only impostors from the development set were used, while impostors from the test set were used to train users belonging to the test set.

The GMM number of mixtures and the R factor were chosen based on previous simulations. The selected values were 1 and 4 respectively.

5.4 SVM-Based Classifier Configuration

As described in section 4, SVMs are usually used as binary classifiers. Elements from both the positive class (user) and the negative class (impostor) are necessary for training. Videos from the development and test sets were used as positive class samples. The negative class, on the other hand, consists of videos from the world set. The idea of genre division was once again used in the training phase: videos of man were used as negative class samples when training male models and female videos were used to train female models.

The impostors used in the false acceptance tests were also selected according to the division of the MOBIO database sets. For users in the development set, only impostors in the development set were used, while impostors in the test set were used to train users in the test set.

Still at the train phase, the soft-margins (C-SVM) approach was employed. The value of the penalty parameter (C) used in the SVM loss function was set to 10^{-4} , based on previous simulations.

Since the face descriptor have a high dimension (\mathfrak{R}^{3776}), a simple linear kernel was used.

The LIBLINEAR Toolkit³ was employed to run all the simulations with C-SVM.

5.5 SVM-Based Classifier with GMM Supervectors

The UBMs used for the supervector approach were the same used for the GMM-based approach (section 5.3), and the penalty parameter of the SVM loss function was set to the same value used for the pure SVM classifier (section 5.4).

³ <http://www.csie.ntu.edu.tw/~cjlin/liblinear>

6 Results

Table 1 reports the comparative results of face verification experiments based solely on GMM and SVM, as well as our approach based on a combination of GMM supervectors and SVM.

Table 1. HTER performance in MOBIO Protocol

	Male	Female	Average
GMM	23.54%	25.54%	24.54%
SVM	22.84%	17.79%	20.31%
GMM + SVM	18.39%	18.78%	18.59%

The experiments have shown that our approach, on the average, performs better than GMM and SVM solely. Also, our method presented the best HTER in the male group. But, in the female class, it was overcome by the SVM strategy.

Another metric to analyse the results is using DET plots. Figures 5 and 6 show the DET plots on the test set of the MOBIO database. Using this metric, our approach (SVM + GMM) had the best performance in the male group too. In the female class, the method proposed had approximately the same behavior of the SVM approach.

A possible reason for this behavior could be explained by the different sizes of the male/female sets in the MOBIO database and the way of GMM and SVM classifiers work. The male set is approximately twice bigger than the female set. So, it is expected that GMM performs better in the biggest set, since it has more data to estimate its generative models. It explains why the GMM works better in the male set. On the other hand, the SVM reduces its performance as the number of classes in the same N-dimensional space is augmented, since it becomes harder to discriminate these classes. It could to explain the second line of the table 1. Our approach combines informations from the GMM and SVM. The GMM describes one video and the time-varying information in one single point to be input to the SVM classifier, explaining the results in the third line of the table 1.

It is important to highlight that the face segmentation step was completely automatic, based on the use of the OpenCV implementation of Viola-Jones algorithm. Problems with the performance of this algorithm have been previously reported [11], due to the pose variability and specular reflection present in the MOBIO database. Several videos were not segmented at all, and a lot of noise was introduced in the segmented faces, which certainly contributed to produce poorer classification results.

Face Verification on Test Set (male trials)

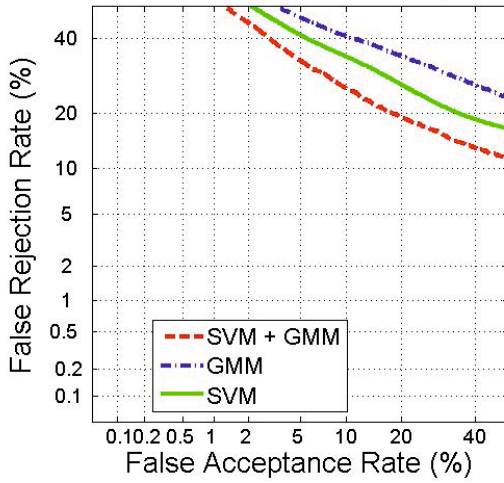


Fig. 5. (Color online) DET plot of face verification systems with different classifiers on test set (male trials)

Face Verification on Test Set (female trials)

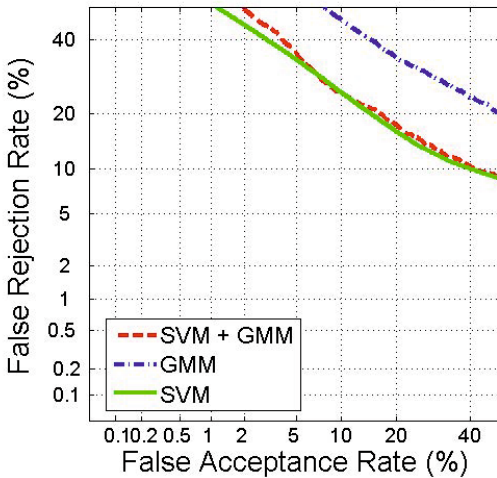


Fig. 6. (Color online) DET plot of face verification systems with different classifiers on test set (female trials)

7 Conclusion

In this paper, an approach for face verification using Local Binary Pattern (LBP) as a face descriptor and using a combination of SVM and GMM for classification was proposed. Experiments were performed using the MOBIO database and protocol. Experimental results have shown that, for the MOBIO database, the proposed approach performs better than pure GMM or SVM classifiers.

It is important to remark that the proposed method allows the representation of temporal information contained in a video input with one single point. The results drawn out from the experiments show that this form of representation is not only extremely compact, but also performs better when compared to classification approaches based solely on GMM or SVM classifiers operating on raw LBP data. We believe that the temporal information contained in the full video is better represented by the supervector, and its use introduces a significant improvement in face description.

Acknowledgements. The BIOMODAL project has financial support from FINEP (Studies and Projects Financing Agency), MCT (Science and Technology Ministry) and MC (Communications Ministry) with resources from FUNTTEL (Telecommunication Technological Development Fund).

References

1. Ahonen, T., Hadid, A., Pietikäinen, M.: Face Recognition with Local Binary Patterns. In: Pajdla, T., Matas, J(G.) (eds.) ECCV 2004. LNCS, vol. 3021, pp. 469–481. Springer, Heidelberg (2004)
2. Ahonen, T., Hadid, A., Pietikainen, M.: Face Description with Local Binary Patterns: Application to Face Recognition. *IEEE Trans. Pattern Anal. Mach. Intell.* 28, 2037–2041 (2006)
3. Bredin, H., Dehak, N., Chollet, G.: GMM-based SVM for face recognition. In: *International Conference on Pattern Recognition*, vol. (3), pp. 1111–1114 (2006)
4. Campbell, W., Sturim, D., Reynolds, D.: Support vector machines using GMM supervectors for speaker verification. *IEEE Signal Processing Letters* 13, 308–311 (2006)
5. Cardinaux, F., Sanderson, C., Bengio, S.: Face verification using adapted generative models. In: *IEEE International Conference on Automatic Face and Gesture Recognition*, pp. 825–830 (2004)
6. Chan, C.: Multi-scale Local Binary Pattern Histogram for Face Recognition. PhD thesis - University of Surrey (2008)
7. Dempster, A., Laird, N., Rubin, D.: Maximum likelihood from incomplete data via the EM algorithm. *Journal of the Royal Statistical Society*, 1–38 (1977)
8. Li, S., Jain, A.: *Handbook of Face Recognition*, 2nd edn. Springer (2011)
9. Linde, Y., Buzo, A., Gray, R.: An algorithm for vector quantizer design. *IEEE Transactions on Communications* 28, 84–95 (1980)
10. Luo, Y., Gavrilova, M.: 3D Facial Model Synthesis using Voronoi Approach. In: *3rd International Symposium on Voronoi Diagrams in Science and Engineering*, pp. 132–137 (2006)

11. Marcel, S., McCool, C., Matejka, P., Ahonen, T., Cernocky, J., Chakraborty, S., Balasubramanian, V., Panchanathan, S., Chan, C., Kittler, J., Poh, N., Fauve, B., Glembek, O., Plchot, O., Jancik, Z., Larcher, A., Levy, C., Matrouf, D., Bonastre, J., Lee, P., Hung, J., Wu, S., Hung, Y., Machlica, L., Mason, J., Mau, S., Sanderson, C., Monzo, D., Albiol, A., Nguyen, H., Bai, L., Wang, Y., Niskanen, M., Turtinen, M., Nolzco-Flores, J., Garcia-Perera, L., Aceves-Lopez, R., Villegas, M., Paredes, R.: On the results of the first mobile biometry (MOBIO) face and speaker verification evaluation. In: International Conference on Pattern Recognition, pp. 210–225 (2010)
12. McCool, C., Marcel, S.: MOBIO database for the ICPR 2010 face and speech competition. Idiap Research Institute, Technical Report (2009)
13. Ojala, T., Pietikainen, M., Harwood, D.: A comparative study of texture measures with classification based on featured distributions. *Pattern Recognition* 29, 51–59 (1996)
14. Ojala, T., Pietikainen, M., Maenpaa, T.: Multiresolution gray-scale and rotation invariant texture classification with local binary patterns. *IEEE Trans. Pattern Anal. Mach. Intell.*, 971–987 (2002)
15. Reynolds, D., Quatieri, T., Dunn, R.: Speaker verification using adapted Gaussian mixture models. *Digital Signal Processing* 10, 19–41 (2000)
16. Rodriguez, Y., Marcel, S.: Face Authentication Using Adapted Local Binary Pattern Histograms. In: Leonardis, A., Bischof, H., Pinz, A. (eds.) ECCV 2006. LNCS, vol. 3954, pp. 321–332. Springer, Heidelberg (2006)
17. Tan, P., Steinbach, M., Kumar, V., et al.: *Introduction to Data Mining*. Pearson Addison Wesley, Boston (2006)
18. Tan, X., Triggs, B.: Enhanced local texture feature sets for face recognition under difficult lighting conditions. *IEEE Transactions on Image Processing* 19, 1635–1650 (2010)
19. Turk, M., Pentland, A.: Eigenfaces for recognition. *Journal of Cognitive Neuroscience* 3, 71–86 (1991)
20. Viola, P., Jones, M.: Robust real-time face detection. *International Journal of Computer Vision* 57, 137–154 (2004)
21. Zhao, W., Chellappa, R., Phillips, P., Rosenfeld, A.: Face recognition: A literature survey. *ACM Computing Surveys* 35, 399–458 (2003)

GPU-Based Influence Regions Optimization*

Marta Fort and J. Antoni Sellarès

Dept. Informàtica i Matemàtica Aplicada, Universitat de Girona, Spain
{mfort,sellares}@ima.udg.edu

Abstract. In this paper we introduce an optimization problem, that arises in the competitive facility location area, which involves the maximization of the weighted area of the region where a new facility has influence. We consider a finite set of points S in a bounded polygonal region domain D subdivided into several non-negative weighted regions according to a weighted domain partition \mathcal{P} . For each point in S we define its k -nearest/farthest neighbor influence region as the region containing all the points of D having the considered point as one of their k -nearest/farthest neighbors in S . We want to find a new point s in D whose k -influence region is maximal in terms of weighted area according to the weighted partition \mathcal{P} . We present a GPU parallel approach, designed under CUDA architecture, for approximately solving the problem and we also provide experimental results showing the efficiency and scalability of the approach.

1 Introduction

The main objective of single facility location problems is to place a new facility with respect to a given set of customers optimizing a certain objective function [5,10]. Facilities can be attractive or desirable, in the sense that customers wish them as close as possible, like supermarkets and hospitals, or obnoxious or undesirable, so that customers wish to push them as far as possible, like garbage dumps and chemical plants. In the context of competitive facility location, the new facility competes with pre-existing facilities. Competitive location models have been studied in several disciplines such as geography, economics, marketing and operations research [6,12].

Next we present two motivational examples of the class of single competitive facility location problems that we want to solve:

Example 1. Suppose that we want to find the optimal location for a new opening restaurant so that it takes over as many customers as possible from the existing competitors. If we assume that clients, that are not equally distributed, eat at one of their 4 nearest restaurants, the new restaurant will be best located at the point having the biggest number of people living/working in the region having the new restaurant among their 4-nearest restaurants.

* Work partially supported by the Spanish Ministerio de Ciencia e Innovación under grant TIN2010-20590-C02-02.

Example 2. To fairly distribute undesirable garbage dumps, a new plant is best located where the number of people, that is not equally distributed, living/working in the region having the plant among their 4-farthest garbage dumps is maximum.

In this paper we address a single competitive facility location problem in which facilities and customers are modeled by points continuously dispersed over a planar domain, and so that customers can move without barriers. The location of a facility is chosen supposing that costumers select facilities depending on distance. Under the assumption that customers are indifferent when it comes to choose between their k -nearest/farthest facilities, we define the influence region of a facility as the set of points of the domain having the given facility among their k -nearest/farthest neighbors. Consequently influence regions are not disjoint regions. On the other hand, we partition the domain into regions so that each region has associated a non-negative weight which represents its potentiality, for example population density or buying capacity of the people living in the region. For any region included in the domain, we define its weighted area as the sum of the weighted areas of the subregions obtained intersecting the given region with the subregions of the domain partition. We want to solve the problem of locating a new facility in the domain maximizing the weighted area of its influence region.

Previous papers discussing maximizing the Voronoi region of a new facility include [4,3,2]. In [4] a pixel based solution obtained by using graphics hardware is presented. Dehne et al. [3] show that the area function has only a single local maximum inside a region where the set of Voronoi neighbors does not change and is in convex position and give an algorithm for approximately finding the optimal new facility placement based on Newton approximation. Cheong et al. [2] present a near-linear time algorithm, when the facilities are in general position, that locates a new facility whose Voronoi region approximates the maximum area up to a $(1 - \epsilon)$ factor. A discrete analogue to the problem of maximizing the Voronoi region was considered in [1], where the problem of placing a new facility in a location so that the number of nearest/farthest customers is maximum is studied.

The development of GPUs (Graphics Processing Units) hardware design, together with CUDA (Compute Unified Device Architecture) and some programming languages which use this architecture such as OpenCL, make them attractive to solve problems which can be treated in parallel as an alternative to CPUs in different computational demanding tasks, where a big amount of data or operations need to be done. Computations in General-Purpose GPU (GPGPU) are capturing the attention of researchers in many computational fields ranging from numeric computing operations and physical simulations to bioinformatics and data mining [11].

The difficulty of maximizing, either analytically or by a numerical optimization procedure, the function that gives the weighted area of the nearest/farthest influence region determined by the inclusion of a new facility has motivated

us to explore an alternative GPU parallel approach, designed under CUDA architecture, for solving approximately the problem. In this paper we describe the proposed solution and also provide experimental results obtained with our implementation that show the efficiency and scalability of the approach.

2 Preliminaries

2.1 Higher Order Voronoi Diagrams

Let S be a set of n points included in a bounded polygonal domain D of the Euclidean plane \mathbb{R}^2 . We will denote by $d(p, q)$ the Euclidean distance between points $p, q \in \mathbb{R}^2$.

Given a subset S_k of k points of S , $k \in \{1, \dots, n-1\}$, the nearest order- k Voronoi region $N(S_k, S)$ of S_k is the set, possibly empty, of points of D lying closer to each point of S_k than to any other point of S :

$$N(S_k, S) = \{q \in D \mid d(s', q) \leq d(s, q), \forall s' \in S_k, \forall s \in S \setminus S_k\}.$$

The nearest order- k Voronoi region $N(S_k, S)$ may not contain the points from S_k . Nearest order- k Voronoi regions are convex polygonal regions as they arise as the intersection of halfplanes bounded by perpendicular bisectors of the points in S . The number of such regions is $O(k(n-k))$ [8].

The nearest order- k Voronoi diagram of S , denoted $\mathcal{N}_k(S)$, is the set of the nearest order- k Voronoi regions $N(S_k, S)$ of all subsets S_k of k points:

$$\mathcal{N}_k(S) = \{N(S_k, S) \mid S_k \subseteq S, |S_k| = k\}.$$

The farthest order- k Voronoi region $F(S_k, S)$ of S_k is the set, possibly empty, of points of D lying farther to each point of S_k than to any other point of S :

$$F(S_k, S) = \{q \in D \mid d(s', q) \geq d(s, q), \forall s' \in S_k, \forall s \in S \setminus S_k\}.$$

The farthest order- k Voronoi diagram of S , denoted $\mathcal{F}_k(S)$, is the set of the farthest order- k Voronoi regions $F(S_k, S)$ of all subsets S_k of k points:

$$\mathcal{F}_k(S) = \{F(S_k, S) \mid S_k \subseteq S, |S_k| = k\}.$$

Farthest order- k Voronoi regions are convex polygonal regions that also arise as the intersection of halfplanes bounded by perpendicular bisectors of the points in S .

Directly follows from the definition that the farthest order- k Voronoi diagram of S coincides with the nearest order- $(n-k)$ Voronoi diagram of S :

$$\mathcal{F}_k(S) = \mathcal{N}_{n-k}(S).$$

From previous relation between the nearest and farthest order- k Voronoi diagrams of S , we have that the number of farthest order- k Voronoi regions is $O((n-k)k)$.

2.2 The Weighted Area of a Region

Let $\mathcal{P} = \{P_1, \dots, P_m\}$ be a partition of the bounded polygonal domain D in the plane into polygonal regions that do not intersect except possibly along their boundaries.

We associate with each region P_i a non-negative number w_i , called the weight of P_i , representing some characteristic of the region P_i , for example population density or buying power of people living in the region.

We define the weighted area of a subregion $R \subset D$, denoted $w(R)$, as:

$$w(R) = \sum_{i=1, \dots, m} w_i \mu(R \cap P_i)$$

where $\mu(\overline{R})$ denotes the area of the subregion \overline{R} .

2.3 CUDA and GPU Computing

CUDA is a parallel computing architecture that makes GPUs accessible for computation like CPUs. The CUDA processors, which can be executed in parallel, are referred to as threads, and each thread executes the instructions contained in the so-called kernels in parallel. Each thread computation is independent from the others, however, there exist some read-modify-write atomic operations called atomic functions. They read and return the value stored in a memory position, operate on it and store the result without allowing, during the whole process, any other access to that memory position. These operations allow the users to obtain global results when several threads access to the same memory position. For instance we can obtain a global sum, maximum or minimum in a specific position by using them.

Several types of memories can be used, data stored in global memory are accessible by every thread and are visible from the CPU, global memory is where more data can be allocated, but is the slowest access time memory. Registers are the fastest memory and store the local variables of each thread. Since the number of accesses to global memory are reflected in the execution times of the algorithms, ν readed, written or transferred values to global memory are represented by r_ν^g , w_ν^g and t_ν^g , in the complexity analysis.

Serial and parallel programming paradigms are focused on very different purposes making efficient serial algorithms unattractive candidates for GPUs [9]. When working with serial algorithms the total number of operations has to be minimized to guarantee time-efficiency, thus serial algorithms have to be work-efficient. When working in parallel, work-efficiency does not guarantee time-efficiency, and elaborated algorithms using complex data structures can not be built nor managed in parallel machines like GPUs.

2.4 Solving Multiple Proximity Queries on the GPU

The uniform grid is a simple and efficient data structure that can be used to solve proximity queries. For a given set of points S , Fort and Sellarès [7] build and

store an uniform grid over a bounding box of S on the GPU by using CUDA. They also design algorithms, that exploit the uniform grid structure, for solving multiple disk range searching queries and k -nearest/farthest neighbor queries. Since these two algorithms are used in the present work, we briefly overview them.

In a multiple disk range searching query we are given a family \mathcal{F} of disk ranges and we want to find the points in S located inside or outside each of the ranges in \mathcal{F} . A multiple disk range searching query is solved by using a uniform grid containing S , and considering a thread per disk. In a first step each thread solves a range counting query by determining the number of points of S located inside or outside its corresponding disk. Then the total output size is determined using the exclusive scan algorithm [13], and finally the points contained in the range are reported. To count or report the points contained in the range the grid cells intersecting the disk are explored and all the points of these cells are checked to determine whether they are contained in the disk.

Given a set Q of query points, an all k -nearest/farthest neighbor query finds the subset of k points of S which are nearest/farthest to each point of Q . To solve an all k -neighbor query a thread per query point is used. The thread locates its corresponding query point in the uniform grid containing S , and explores the grid cells in a spiral like search. The search works outwards starting at the cell containing the query point when the nearest case is handled, and looking inwards for the farthest case.

3 Order- k Influence Regions

The order- k nearest influence region of a point $s \in S$, denoted $NI_k(s, S)$, is the set of points of D having s among their k -nearest points in S (see Figure 1). For any point $q \in D$, let $d_k(q, S)$ denote the distance to the k -th nearest point to q in S . Clearly:

$$NI_k(s, S) = \{q \in D \mid d(s, q) \leq d_k(q, S)\} = \bigcup_{\substack{S_k \subseteq S \mid s \in S_k \\ |S_k|=k}} V(S_k, S).$$

Lemma 1

- a) $NI_k(s, S) \subset NI_{k+1}(s, S)$.
- b) Given k , for any $q \in D$ there exists a subset $S_k \subseteq S, |S_k| = k$, so that $q \in NI_k(s, S)$ for any $s \in S_k$.
- c) $NI_k(s, S)$ is a star-shaped polygonal region whose kernel contains s .

Proof

a) This follows from nearest influence regions definition.

b) Given $q \in D$, there exists a subset $S_k \subseteq S, |S_k| = k$, so that $q \in V(S_k, S)$, consequently $q \in \bigcap_{s \in S_k} NI_k(s, S)$.

c) We want to prove that for each point q in $NI_k(s, S)$ the segment sq lies entirely in $NI_k(s, S)$. Denote by $D_q(s)$ the disk of center q and radius $d(q, s)$. It

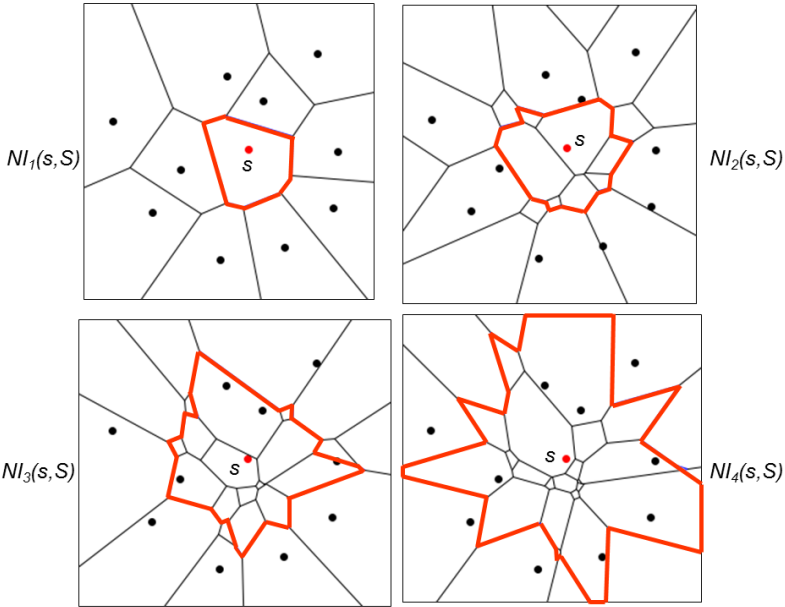


Fig. 1. Nearest influence regions of point s

is easy to see that $q \in NI_k(s, S)$ if and only if $|D_q(s) \cap S| \leq k$. Let q' be a point of segment sq , since $D_{q'}(s) \subset D_q(s)$, we have that $|D_{q'}(s) \cap S| < |D_q(s) \cap S| \leq k$, and consequently $q' \in NI_k(s, S)$.

The farthest order- k influence region of a point $s \in S$, denoted $FI_k(s, S)$, is the set of points of D having s among their k -farthest points in S . For any point $q \in D$, let $f_k(q, S)$ denote the distance to the k -th farthest point to q in S . Then

$$FI_k(s, S) = \{q \in D \mid d((s, q) \geq f_k(q, S)\} = \bigcup_{\substack{S_k \subseteq S \mid s \in S_k \\ |S_k| = k}} F(S_k, S).$$

Contrarily to what happens for the nearest case, a farthest order- k influence region may have more than one connex component, as it can be seen in $FI_4(s, S)$ in Fig. 2.

Lemma 2

- a) $FI_{k+1}(s, S) \subset FI_k(s, S)$.
- b) Given k , for any $q \in D$ there exists a subset $S_k \subseteq S, |S_k| = k$, so that $q \in FI_k(s, S)$ for any $s \in S_k$.
- c) $FI_k(s, S)$ and $NI_{n-k}(s, S)$ are complementary with respect to the domain D .

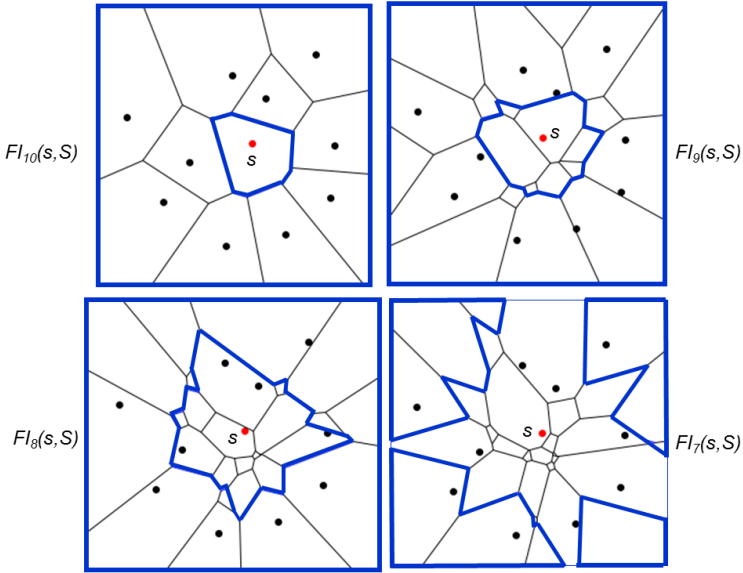


Fig. 2. Farthest influence regions for a set S of 11 points

Proof

a) This follows from farthest influence regions definition.

b) Given $q \in D$, there exists a subset $S_k \subseteq S, |S_k| = k$, so that $q \in F(S_k, S)$, and consequently $q \in \bigcap_{s \in S_k} FI_k(s, S)$.

c) Obviously, the set of points of D having s among their k -farthest points in S is the complementary of the set of points of D having s among their $(n - k)$ -nearest neighbor points in S (see Fig. 1 and Fig. 2).

4 Optimizing the Weighted Area of a New Influence Region

From now on, when a definition or statement holds for both criteria we skip the word nearest or farthest, thus we talk about an order- k influence region, denoted $I_k(s_i, S)$, without specifying the nearest or farthest criterion.

Given a set $S = \{s_1, \dots, s_n\}$ of points within the bounded polygonal domain D of the Euclidean plane \mathbb{R}^2 and a weighted partition $\mathcal{P} = \{P_1, \dots, P_m\}$ of D , we want to solve the following problem:

Find the positions for a new point s maximizing the weighted area $w(I_k(s, S \cup \{s\}))$ over all possible points $s \in D - S$.

According to Lemma 2.c) $FI_k(s, S \cup \{s\})$ and $NI_{n-k}(s, S \cup \{s\})$ are complementary with respect to the domain D . Consequently the point s maximizing $w(NI_k(s, S \cup \{s\}))$ is the one minimizing $w(FI_{n-k}(s, S \cup \{s\}))$ and similarly, the

one maximizing $w(FI_k(s, S \cup \{s\}))$ is the one minimizing $w(NI_{n-k}(s, S \cup \{s\}))$. Using this property it would be sufficient to be able to solve the nearest or farthest problem. However, we present algorithms to solve both problems, and in Section 5 we show how depending on the k value it is better to tackle the problem directly maximizing $w(I_k(s, S \cup \{s\}))$ or indirectly minimizing $w(I_{k'}(s, S \cup \{s\}))$ with $k' = n - k$.

For a given s , the value of $w(I_k(s, S \cup \{s\}))$ can be obtained by computing the overlay intersection of $I_k(s, S \cup \{s\})$, which is a starshaped polygonal region or a polygonal region with a starshaped hole, and the weighted partition \mathcal{P} . Since each maximal connected polygonal region of the resulting intersection is contained in a region of \mathcal{P} , it has univocally associated a weight. Consequently, the weighted area $w(I_k(s, S \cup \{s\}))$ can be written as a sum of functions that depends on the location of s .

4.1 Solving the Problem on the GPU Using CUDA

We approximately solve the optimization problem discretizing the polygonal domain D by superimposing on it an axis-parallel rectangular grid of size $G = H \times W$. We denote by Q the set of grid points corresponding to the geometric center of the grid cells. First, for each grid point q of Q we compute an estimation of the weighted area $w(I_k(q, S \cup \{q\}))$ from the weight of the grid points that are contained in $I_k(q, S \cup \{q\})$. Next we find the points q of Q optimizing $w(I_k(q, S \cup \{q\}))$.

In order to estimate the weighted areas $w(I_k(q, S \cup \{q\}))$ we consider for each $q' \in Q$ all the points $q \in Q$ such that $q' \in I_k(q, S \cup \{q\})$. In the nearest case we compute the distance of each grid point q' to its k -th nearest neighbor in S , $dn_k(q', S)$, and use the fact that $q' \in NI_k(q, S \cup \{q\})$ whenever $d(q, q') \leq dn_k(q', S \cup \{q\})$, or equivalently when $d(q, q') \leq dn_k(q', S)$. Thus, for each grid point q' we find the points $q \in Q$ contained in the disk of center q' and radius $dn_k(q', S)$. Concerning the farthest case, we compute the k -th farthest neighbor distance, $df_k(q', S)$, and use that $q' \in FI_k(q, S \cup \{q\})$ when $d(q, q') \geq df_k(q', S \cup \{q\})$, or equivalently when $d(q, q') \geq df_k(q', S)$. In this case we obtain the points $q \in Q$ contained outside the disk of center q' and radius $df_k(q', S)$.

The input of the process consists of the grid dimensions H, W , the coordinates of the points in S , and the weights associated to the grid points according to the weighted partition \mathcal{P} of D . This information is transferred from the CPU to the GPU storing the coordinates of the points in S and the weights of points of Q in 1D-arrays of size n and G , respectively. Notice that the grid points are not explicitly stored but obtained when needed from the grid dimensions and the domain vertices. The output contains the maximal value together with the possible optimal placements among the grid points of Q . All the 1D-arrays we use in the presented algorithm are stored in GPU global memory.

We start by computing the distance of each grid point q to its k -th neighbor in S , considering all the grid points in parallel and using the algorithm presented in 7. The obtained distances are stored in a 1D-array of size G .

Next, the weighted area $w(I_k(q, S \cup \{q\}))$ of the grid points q is estimated in parallel by using the precomputed distances from the grid points to their k -th neighbor and the weights associated to the grid points. Using the previously mentioned properties and considering all the grid points q' in parallel, for each $q' \in Q$ we find all the points $q \in Q$ such that $q' \in I_k(q, S \cup \{q\})$ by solving an in/out multiple disk range query. The multiple disk range query is handled using the ideas presented in [7]. The k -influence value of each grid point q is stored in an 1D-array of size G initialized to 0, its value is updated when $q' \in I_k(q, S \cup \{q\})$ by adding at the existing value the weight w' associated to q' with an atomic function.

Once the k -influence values of all the grid points are known, the optimal placements, among the considered ones, are determined by using a reduction type algorithm [13] to find the optimal k -influence value and the number of points where this optimal value is achieved. Then an array of the corresponding size is allocated to store in a second step the points where this optimal value is obtained.

4.2 Complexity Analysis

We only transfer from the CPU to the GPU the sites S and the weights associated to the grid points, which takes $O(t_{n+G}^g)$ time. No other CPU-GPU communication is needed. We read from global memory the weight and distance to the k -th corresponding neighbor of each grid point once, thus the number of reads is $O(r_{2G}^g)$. We update the k -influence values, which are stored in global memory, by using atomic functions I times, where I is the total number of grid points contained in all the considered k -influence regions, which takes $O(w_{\rho I}^g)$ time, ρ denotes writings done by using atomic functions. Thus we have a time complexity of $O(t_{n+G}^g + r_G^g + w_{\rho I}^g)$. The bigger term, $O(w_{\rho I}^g)$, is due to the use of atomic operations, however although atomic functions slow down the running time of the algorithm they are necessary to guarantee correct results.

Next we analyze the work complexity. We execute G parallel threads, each of them finds the k -th distance to S in $O(n)$ worst case time. Then the weighted areas are estimated using G threads executed in parallel. The number of grid points explored by each thread depends on the k -th neighbor distance of the corresponding grid point, however, the total work in both steps is $O(Gn + I)$. In the worst case each grid point will explore $O(G)$ grid points and $I = \Omega(G^2)$, yielding a work complexity of $O(G(G + n))$. In the case that the set S has all its points near a corner of the domain the influence regions of most of the grid points will contain at least $G/2$ points yielding to this $I = \Omega(G^2)$.

We use $O(n + G)$ space to store the coordinates of the n points of S and three arrays of size G . The GPU memory space limits the information that can be stored, which directly bounds the discretization size. However, if necessary, the domain can be partitioned into subdomains, the problem can be partially solved in each subdomain, and finally the solution of the problem can be obtained analyzing the results globally.

5 Experimental Results

In this section we present results obtained by our implementation of the presented algorithms. We used OpenCL and the executions are done using a Intel Core 2 CPU 2.13GHz, 2GB RAM and a GPU NVidia GeForce GTX 480. The provided times are obtained as the median of 10 executions and show the scalability of our algorithm for several grid sizes and n . In order to provide realistic inputs, we used small values of k .

In the presented execution times the CPU-GPU transferring times involved are not included and are 0.005(ms), 0.007(ms), 0.011(ms) and 0.062(ms) to transfer the coordinates of the points in S for $n = 10, 100, 1000$ and 10000 , respectively. The times needed to transfer the grid point weights when a grid of size $100 \times 100, 300 \times 300, 500 \times 500$ and 1000×1000 is considered are 0.025(ms), 0.3(ms), 1.33(ms) and 2.73(ms), respectively.

Table 1 provides the times needed to solve the problem for different k, n and G values considering the nearest criterion, and Table 2 contains the computational times obtained for the farthest one. All these times are obtained by considering the weight domain partition shown in Fig 3, which is given by the population density of USA.

Table 1. Nearest case computational times in *seconds*

G	100×100				300×300				500×500				1000×1000			
	$n \setminus k$	1	5	10	50	1	5	10	50	1	5	10	50	1	5	10
10	0.018	0.05	-	-	0.26	0.83	-	-	1.09	4.99	-	-	8.09	15.79	-	-
100	0.008	0.02	0.03	0.13	0.08	0.24	0.38	1.73	0.31	1.02	1.73	9.52	2.47	10.11	10.84	12.48
1000	0.006	0.01	0.01	0.06	0.04	0.07	0.10	0.45	0.12	0.23	0.35	1.42	0.59	1.14	2.46	7.65
10000	0.008	0.01	0.01	0.05	0.04	0.04	0.07	0.32	0.11	0.15	0.20	0.83	0.43	0.61	0.83	3.50

Table 2. Farthest case computational times in *seconds*

G	100×100				300×300				500×500				1000×1000			
	$n \setminus k$	1	5	10	50	1	5	10	50	1	5	10	50	1	5	10
10	0.064	0.09	-	-	1.70	2.84	-	-	8.15	14.62	-	-	16.62	-	-	-
100	0.056	0.07	0.08	0.17	1.12	1.79	2.10	4.08	6.36	10.45	12.8	15.3	18.7	17.7	18.4	19.2
1000	0.056	0.06	0.07	0.12	1.00	1.23	1.33	2.14	5.65	6.42	7.63	12.3	15.4	13.7	12.1	15.7
10000	0.089	0.91	0.09	0.17	1.22	1.28	1.34	1.95	5.74	6.04	6.47	8.67	14.0	14.0	16.1	20.7

Notice that the execution time tends to decrease when n increases because the influence regions become smaller and their weighted area is obtained with a smaller number of operations.

Comparing the nearest and farthest running times, the farthest case, for small values of k , is always slower because the number of grid points to handle is much bigger. For the farthest case we have to explore all the grid points not contained in the circle of radius equal to the k -th farthest neighbor, in fact, we start

exploring the grid boundaries and moving circularly inwards. However, for the nearest case we explore the grid starting from the actual grid point and moving circularly outwards until we have gone outside the circle. Thus, for small values of k the farthest case represents a much bigger number of points to explore than the nearest case.

In Table 1 and Table 2 we have presented results with what we consider realistic values of k , however we can also handle bigger k values. For instance, solving the problem with a grid of size 100×100 , $n = 1000$ and $k = 100, 200, 300, 400$ and 500 takes, respectively, $0.18(s), 0.56(s), 1.15(s), 1.94(s)$ and $2.94(s)$ for the nearest case, and $0.27(s), 0.62(s), 1.13(s), 1.79(s)$ and $2.71(s)$ for the farthest case. Consequently, and as it is expected, when $n = 1000$, if we are interested in solving a 600-nearest neighbor problem is better to minimize a 400-farthest problem instead, and viceversa, if we are interested in a 600-farthest problem it will be better to solve a minimization 400-nearest problem. Thus, in general, when $k > n/2$ the problem should be solved indirectly finding its complementary region $I_{n-k}(q, S \cup \{s\})$ and minimizing its weighted area, meanwhile when $k < n/2$ the problem is tackled directly finding the $I_k(q, S \cup \{s\})$ and maximizing its weighted area.

To end with we provide images obtained with our implementation of the algorithms in Fig 3 and Fig. 4. Fig. 3 shows the obtained weighted areas according to a color gradation together with the optimal placement of a new facility using a population density map of USA, a set S of $n = 100$ points and $k = 10$. On the left we find the corresponding images using a grid of 100×100 cells, and on the right the obtained solution for a 500×500 grid. Fig. 3 a) presents a map colored from dark to light green according to the increasing weight assigned to the regions of the domain. The weights associated to the domain points are integer weights varying from 0 to 255 depending on the region population density. Squared green points represent the 100 points of S . Fig. 3 b) presents the same map colored from dark to light red according to the increasing weight $w(I_{10}(q, S \cup \{q\}))$ of each grid point q . The orange point shows the optimal placement for a new facility. Fig. 3c) presents the farthest influence values again colored from dark to light blue. The orange point located on the top right is the one having its k -farthest influence region with maximal weighted area. As it happens in the presented images, in many cases the maximal weighted area is obtained in a single grid point. In general terms, to obtain optimal regions defined by more than a single point we should consider either big grids or k values nearby $n/2$.

Fig. 4 contains the obtained results when considering a grid of size 500×500 with $n = 100$ sites and $k = 50$. In this case $k = n - k$, consequently the k -nearest influence region of a point coincides with its k -farthest influence region complementary. In this specific case solving the nearest or farthest problem is equivalent, we only have to consider the appropriate optimization criterion. This can be easily seen by comparing Fig. 4a) and b), the smaller the weighted area in the nearest case, the bigger it becomes in the farthest one, and viceversa.

To end with just mention that the accurateness of the obtained solution directly depends on the grid resolution, the thinner the grid, the more accurate the

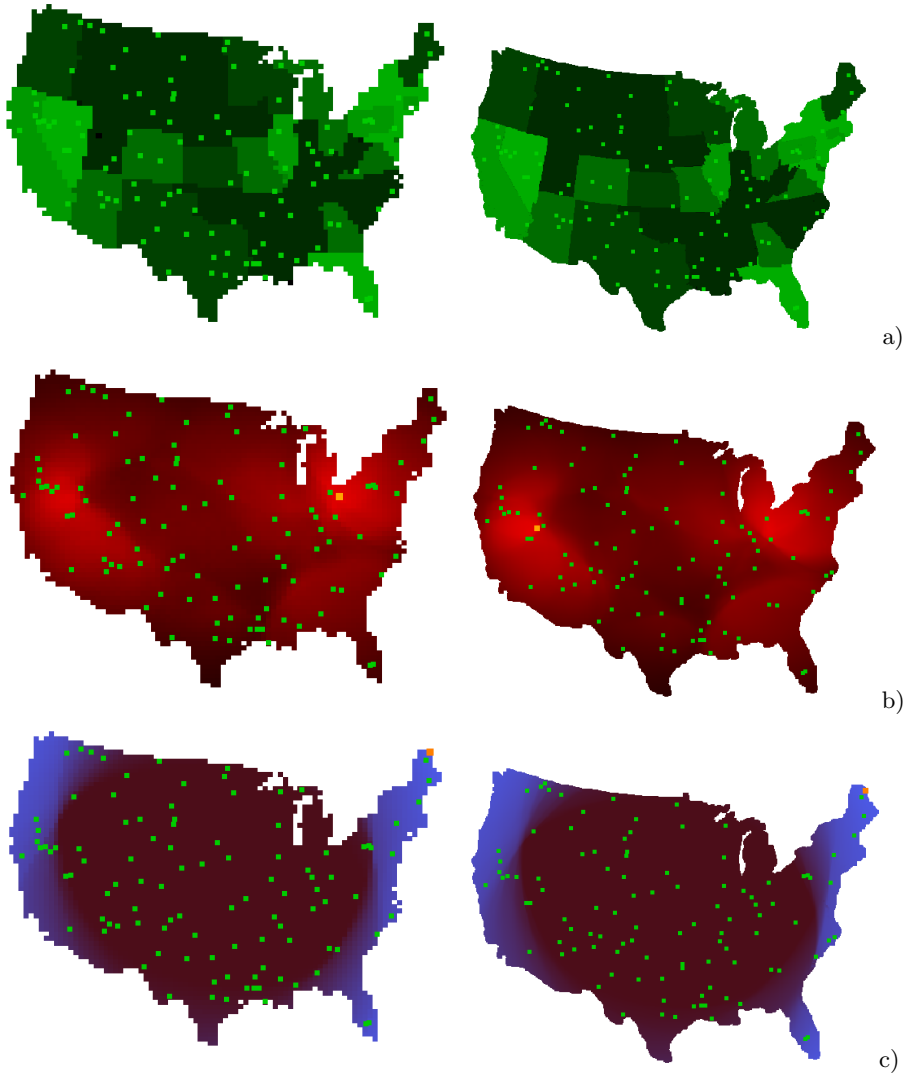


Fig. 3. Comparison between a grid of size 100×100 on the left and 500×500 on the right

obtained solution is. However the algorithm can not be used with any desired resolution by handling the whole domain at once. Those discretizations that can not be handled at once can be partitioned into several subdomains. Then the influence region of a point may not be contained in its subdomain region, and thus to estimate its weighted area we should explore all the subdomains with not empty intersection with the influence region.

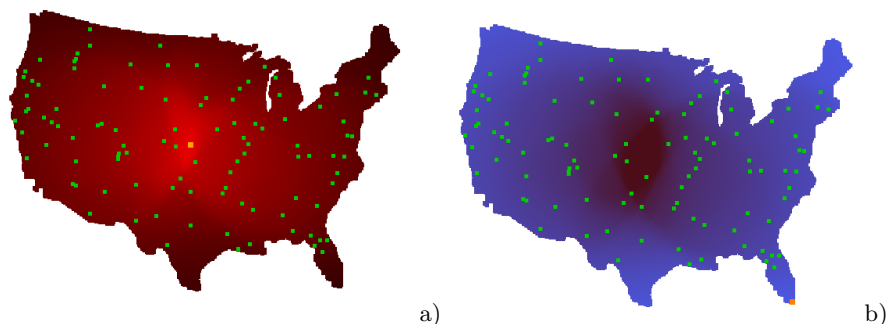


Fig. 4. k -influence values with a grid of size 500×500 , $n = 100$ and $k = 50$ considering the a) nearest, b) farthest criterion

6 Conclusions

In this paper we present an algorithm to approximately locate a new facility in such a way that its k -influence region, the set of points having this new facility as one of the k -neighbors, has maximal weighted area.

Two different strategies can be used to solve the problem, when $k < n/2$ we maximize the k -nearest/farthest influence region weighted area, meanwhile when $k > n/2$ we should minimize the $(n - k)$ -farthest/nearest influence region weighted area. It can be done using the fact that the k -nearest and the $(n - k)$ -farthest influence regions are complementary regions with respect to the domain.

We presented the complexity analysis of our algorithm, together with some experimental results concerning execution times and images of the obtained results. To end with we have given a brief idea on how the domain can be subdivided into several subdomains to consider big grids that can not be handled in a single step.

References

1. Cabello, S., Díaz-Báñez, J.M., Langerman, S., Seara, C., Ventura, I.: Facility location problems in the plane based on reverse nearest neighbor queries. *European Journal of Operational Research* 202(1), 99–106 (2009)
2. Cheong, O., Efrat, A., Har-Peled, S.: Finding a guard that sees most and a shop that sells most. *Discrete Comput. Geom.* 37(4), 545–563 (2007)
3. Dehne, F.K.H.A., Klein, R., Seidel, R.: Maximizing a Voronoi region: the convex case. *Int. J. Comput. Geometry Appl.* 15(5), 463–476 (2005)
4. Denny, M.: Solving geometric optimization problems using graphics hardware. *Comput. Graph. Forum* 22(3), 441–452 (2003)
5. Drezner, Z., Hamacher, H.W.: *Facility location - applications and theory*. Springer (2002)
6. Eiselt, H.A., Laporte, G., Thisse, J.F.: *Competitive location models: A framework and bibliography*. *Transportation Science* 27, 44–54 (1993)

7. Fort, M., Sellarès, J.A.: A parallel GPU-based approach for solving multiple proximity queries in 2d and 3d euclidean spaces (submitted)
8. Lee, D.-T.: On k-nearest neighbor Voronoi diagrams in the plane. *IEEE Transactions on Computers* 31(6), 478–487 (1982)
9. Lieberman, M.D., Sankaranarayanan, J., Samet, H.: A Fast Similarity Join Algorithm Using Graphics Processing Units. In: *International Conference on Data Engineering*, pp. 1111–1120 (2008)
10. Nickel, S., Puerto, J.: Location theory - a unified approach. *Mathematical Methods of Operations Research* 66(2), 369–371 (2009)
11. Owens, J.D., Luebke, D., Govindaraju, N., Harris, M., Krüger, J., Lefohn, A.E., Purcell, T.J.: A survey of general-purpose computation on graphics hardware. *Computer Graphics Forum* 26(1), 80–113 (2007)
12. Plastria, F.: Static competitive location: an overview of optimisation approaches. *European Journal of Operational Research* 129, 461–470 (2001)
13. Sengupta, S., Harris, M., Garland, M.: Efficient Parallel Scan Algorithms for GPUs. NVIDIA Technical Report NVR-2008-003 (2008)

Fast and Simple Approach for Polygon Schematization

Serafino Cicerone and Matteo Cernignani

Dept. of Electrical and Information Engineering,
University of L'Aquila, L'Aquila, Italy
serafino.cicerone@univaq.it, mat.cernignani@gmail.com

Abstract. The schematization of simple polygons into octilinear polygons is a computational problem arising in the context of electronic CAD systems. In particular, it appears when the generation and propagation of electromagnetic noise into real-world multi-layer PCBs has to be detected. In this paper we provide a fast and simple heuristic for solving such a problem. Experimental evaluations over real-world data show the efficiency and the good performance of the proposed approach.

Keywords: Computational geometry, polygon schematization, CAD applications, algorithm engineering, experimental analysis.

1 Introduction

Currently, microprocessors and application-specific integrated circuits have thousands of gates switching simultaneously. The impulsive and repetitive current drawn by these active devices from the power delivery network (PDN) is a challenging issue for a correct and reliable PDN design and a severe source of electromagnetic noise generation [21]. The PDN for modern medium-to-high-speed digital printed circuit boards (PCBs) is usually formed from one or more pair of conducting parallel planes used as “power“ and “ground”. The PDN for digital circuitry has evolved over time, as signal and clock speeds have increased, from discrete power supply wires, to discrete traces, to area fills and ground islands on single/two-layer slow-speed boards, to the planar power bus structure used extensively in today’s multi-layer high-speed PCBs.

Noise generated in the power bus can be easily propagated throughout the board. Propagated noise can affect the operation of other active devices (signal integrity) [19]. Among the possible techniques to study the generation and propagation of noise there is the so called Cavity Model [16] in which facing portions of power bus are considered electromagnetic resonant cavities. Given a real-world board’s layout, one of the primary requirements for the application of this technique is the geometrical identification of all the cavities and their connectivity. Then, a suitable processing of the geometrical cavities’ boundaries is requested for a correct and not over-detailed electromagnetic modeling. After these actions, the geometry dataset (containing also the electrical parameters) is ready for being input to the cavity model solver.

From a geometrical point of view, a power bus corresponds to a polygon. Two facing polygons P_1 and P_2 located at parallel layers L_1 and L_2 form a cavity; this cavity is geometrically defined as a polyhedron having the polygon $P = P_1 \cap P_2$ as base area and the distance from L_1 and L_2 as height. The currently available cavity model solvers require that such a polygon P must be *octilinear*, i.e. a polygon whose angles are all multiple of 45° . This constraint implies that each polygon forming the base of a cavity must be *simplified into an octilinear polygon* according to an error criterion (defined later). Requiring an octilinear polygon as output results in a “schematised” simplification of the original polygon. In this work we address this specific problem of polygon schematization.

Related Work: The general problem of approximating a given polygon (or a polygonal path) P by another coarser one Q is important task in many fields, such as computer graphics, CAD, pattern recognition, GIS, shape analysis, vector data compression and more. As a consequence, this problem has been explored very intensively for the last 30 years.

Two versions of the problem exist: if it is required that the points of Q are a subset of those of P then we are considering the *Polygon Approximation* problem (PA), otherwise we have the *General Polygon Approximation* problem (GPA), which in general gives a better solution to the approximation problem. The PA problem has been studied extensively, and probably the most popular polygonal path simplification algorithm is the Douglas Peucker algorithm [12]. Imai and Iri [14] formulated the problem as a graph problem. They constructed an unweighted directed acyclic graph and then used a breadth-first search to compute a shortest path in this graph. The same approach has been used by many algorithms devoted to this problem (e.g., [4,6]). Several results exist also for the GPA problem: for instance, Kurozumi and Davis [15] used a *minimax method* to provide optimal solutions.

Numerous error criteria have been proposed for the approximation. In [7,14] the so-called *tolerance zone* criterion was used. Other measurements are the *infinite beam* criterion [6], the *uniform measure* criterion [3], *distance preserving* criterion [13], and the *area preserving* criterion [4].

Some authors restricted their attention to the *polygonal path schematization* problem. In this case, given an input polygonal path P and a finite set \mathcal{C} of given directions, it is required to simplify P into a polygonal path Q such that every link of Q is parallel to an orientation $c \in \mathcal{C}$. A path conforming to this restriction is called a \mathcal{C} -oriented path. Of course, this is a GPA problem.

Concerning the polygonal path schematization problem, Neyer [20] proposed an algorithm that uses a minimum number of edges to compute Q . Furthermore, Q must have Fréchet distance at most ε from P . For a constant-size set \mathcal{C} , this algorithm requires $O(mn^2 \log n)$ time, where n is the number of vertices of P and m is the number of vertices of Q . Merrick and Gudmundsson [17] studied a slightly relaxed version of the same problem and gave an $O(n^2|\mathcal{C}|^3)$ -time algorithm to compute a \mathcal{C} -oriented simplification of P that is within Hausdorff distance at most ε of P . Delling et al. [10] presented an efficient two-steps approach for schematizing x - or y -monotone polygonal paths.

Our Contribution: Our aim is to provide a fast and simple algorithm for solving the polygon schematization problem such that it can be efficiently applied to process the geometrical cavities' boundaries computed over real PCBs. Such PCBs are composed of thousands of polygons, and each polygons is composed of hundreds of vertices. In turn, it follows that the optimal algorithms proposed by [20] and by [17] cannot be used, while [10] consider x - or y -monotone polygonal paths only. Hence, we defined a fast and simple heuristic called ORSA for solving the polygon schematization problem with \mathcal{C} containing octilinear or rectilinear directions only. This solution combines classical approaches (sequential approaches and graph theory algorithms) with the algorithm engineering approach [11,18] (a combination of theoretical algorithm design with experiments on real-world data). The proposed solution has been implemented by using CGAL [2] and tested over a medium-size real PCB consisting of 16 layers and 923 "large enough" polygons (having 40685 points in total). The performed experiments witnessed that the heuristic is fast and computes near-optimal solutions. To assess the quality of the provided solutions, for each polygon we compared the number of points computed by ORSA and those computed by MM, i.e. our implementation of the minimax method proposed by Kurozumi and Davis [15] for computing optimal solutions for the general (non-oriented) case.

2 Preliminaries

A n -vertex simple polygon P is specified by an ordered set $\{p_0, p_1, \dots, p_{n-1}\}$ of vertices, such that $\overline{p_i p_{i+1}}$, for $0 \leq i \leq n-1$, are all line segments in \mathbb{R}^2 (in the subscript of vertices, the operator $+$ is always meant as modulo n).

Let $\mathcal{C} = \{\alpha_1, \alpha_2, \dots, \alpha_t\}$ be a set of angles with respect to the x -axis that represents the admissible line segment orientations. We consider two possible schematizations: either \mathcal{C} contains the multiples of 90° exactly (rectilinear case), or \mathcal{C} contains the multiples of 45° exactly (octilinear case).

Concerning the error criterion to be used in the schematization of P , we use the so called *tolerance zone criterion* [9,14]. Formally, if $P = \{p_0, p_1, \dots, p_{n-1}\}$ is a simple polygon, then call a circle with radius ε and center p_j the ε -circle C_j of p_j . The convex hull of two ε -circles C_j and C_{j+1} from two consecutive vertices p_j and p_{j+1} is called the *tube* T_j . The tolerance zone for P is defined as $\mathcal{T}(P) = \bigcup_{j=0}^{n-1} T_j$. Clearly, each point in $\mathcal{T}(P)$ has distance at most ε to the polygon P . We require that the simplification of P lies in $\mathcal{T}(P)$ and uses only orientations in \mathcal{C} .

There are two types of optimization problems concerned with polygonal approximation:

- min-#:** given P , find an approximating polygon Q that has the minimum number m of line segments so that the approximation error does not exceed a given maximum tolerance ε ;
- min- ε :** given P , find an approximating polygon Q with a given number m of line segments so that the approximation error ε is minimized.

In this work we are interested in the following optimization problem:

(ORPS) OCTILINEAR/RECTILINEAR POLYGON SCHEMATIZATION

GIVEN: A simple polygon P , a set \mathcal{C} containing octilinear or rectilinear directions only, and a maximum tolerance ε .

PROBLEM: Find a simplification of P consisting of a \mathcal{C} -oriented polygon Q having the minimum number of line vertices and lying in $\mathcal{T}(P)$.

Concerning this problem, notice that:

1. it belongs to the class min-#,
2. it is a GPA problem,
3. in general, $|Q| \geq |P|$.

Moreover, according to the practical relevance of this problem in the context of electronic CAD systems, we are interested in defining *practical* and *fast* algorithms, even if they compute sub-optimal solutions.

3 The Algorithm

In this section we provide a fast and simple heuristic named ORSA (Octilinear/Rectilinear Schematization Algorithm) for finding sub-optimal solutions for the ORPS problem. The main idea underlying this approach is to perform a discretization of the plane in order to define a new discrete reference system.

Definition 1. Given the origin point $\sigma = (x, y) \in \mathbb{R}^2$ and a quantum $\gamma \in \mathbb{R}^+$, $\mathbb{D}_{\sigma, \gamma} \subseteq \mathbb{R}^2$ is a discrete coordinate system defined by points $\{(x \pm \gamma \cdot k_1, y \pm \gamma \cdot k_2) \mid k_1, k_2 \in \mathbb{N}^+\}$.

The proposed algorithm uses only points in $\mathbb{D}_{\sigma, \gamma}$ for finding a sub-optimal solution for the ORPS problem. The parameters σ and γ define a general discrete reference system: in Section 4 they will be specialized to provide a custom implementation of ORSA. The following main steps represent a high level description of the proposed algorithm:

ORSA

INPUT: A simple polygon P , a set \mathcal{C} containing either octilinear or rectilinear directions, and a maximum tolerance ε .

OUTPUT: A \mathcal{C} -oriented polygon $Q = \{q_0, q_1, \dots, q_{m-1}\}$ lying in $\mathcal{T}(P)$.

1. APPROX POINTS: for each vertex $p_i \in P$, compute the set $\text{AP}(p_i)$ containing the *approximation points* of p_i . A point q is an approximation point for p if $q \in \mathbb{D}_{\sigma, \gamma}$ and $d(p, q) \leq \varepsilon$.

2. APPROX SEGMENTS: for each line segment $\ell_i = \overline{p_i p_{i+1}} \in P$, compute the set $AS(p_i)$ containing the *approximation segments* of ℓ_i . A line segment $\ell' = \overline{q' q''}$ is an approximation segment for ℓ_i if $q' \in AP(p_i)$, $q'' \in AP(p_{i+1})$, and $\overline{q' q''}$ is a \mathcal{C} -oriented line segment. All the computed approximation segments $AS(p_i)$, $0 \leq i \leq n-1$, are stored, in order according to the index i , in a list denoted as \mathcal{AS} .

- 2.1. BRESENHAM APPROX SEGMENTS: It is possible that for a given vertex p_i , $AS(p_i)$ is empty. This means that there are no \mathcal{C} -oriented line segments between points of $AP(p_i)$ and points of $AP(p_{i+1})$.

In such a case, by using the well known Bresenham's algorithm [5] for line rasterization [1] the algorithm determines a new set of approximation points $AP_{j_1} \equiv AP(p_i), AP_{j_2}, AP_{j_3}, \dots, AP_{j_t} \equiv AP(p_{i+1}), t > 2$. Fig. 1 show an example of how to get each $AP_{j_k}, 1 \leq k \leq t$. This sequence of approximation points features the following property: AP_{j_k} , for each $1 \leq k \leq t-1$, is not empty - i.e. there are \mathcal{C} -oriented line segments between points of AP_{j_k} and points of $AP_{j_{k+1}}$.

All the approximation segments connecting points in $\bigcup_{k=1}^{t-1} AP_{j_k}$ are inserted, in order according to the index k , into \mathcal{AS} . Notice that, at the end of the step APPROX SEGMENTS the size of \mathcal{AS} may be larger than n , i.e. the size of the input polygon P .

3. COLLINEAR MERGE: for each two consecutive approximation sets AS_1 and AS_2 in \mathcal{AS} , test the existence of collinear segments $\ell' = \overline{q' q''} \in AS_1$ and $\ell'' = \overline{q'' q''' } \in AS_2$ with a common endpoint q'' . If so, remove ℓ' from AS_1 , remove ℓ'' from AS_2 , and insert the new approximation segments $\overline{q' q'''}$ into AS_2 . This step may reduce the whole number of approximation segments (see Fig. 2), and, in turn, it may reduce the size of some approximation point set AP (even, all approximation points having no more adjacent segments are removed).
4. CLOSE GAP: it is possible that there is a "gap" in some approximation set $AP(p_i), p_i \in P$. This means that approximation segments ending at $AP(p_i)$ and approximation segments starting from $AP(p_i)$ have no points in common. In this case the algorithm "closes the gap" by inserting all the possible useful \mathcal{C} -oriented segments between points in $AP(p_i)$ (see blue line segments at Figs. 3 and 4).

¹ The Bresenham's line algorithm determines which points in an n -dimensional raster should be plotted in order to form a close approximation to a straight line between two given points. It is very simple and fast, since it uses only integer addition, subtraction and bit shifting.

The algorithm is used in hardware such as plotters and in the graphics chips of modern graphics cards. It can also be found in many software graphics libraries. Because the algorithm is very simple, it is often implemented in either the firmware or the graphics hardware of modern graphics cards. The label "Bresenham" is used today for a whole family of algorithms extending or modifying Bresenham's original algorithm.

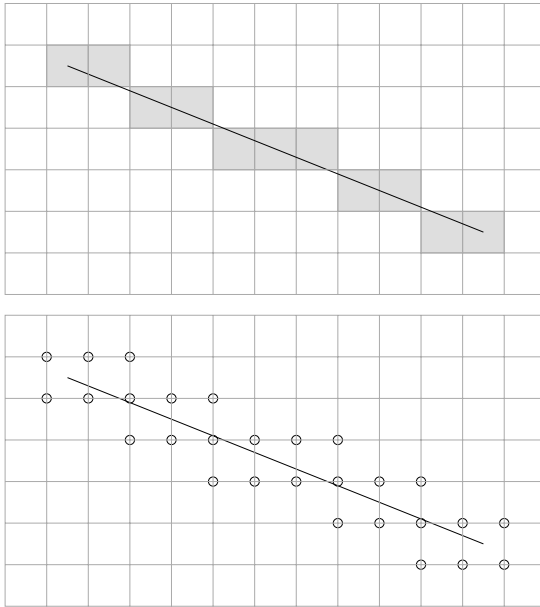


Fig. 1. Illustration of the result of Bresenham’s line algorithm (top figure, where the filled squares represent the computed raster points to be plotted), and its modification to get a sequence of approximations points in $\mathbb{D}_{\sigma,\gamma}$ (bottom)



Fig. 2. An example for the COLLINEAR MERGE step. Circles highlight approximation points, the polyline represents (part of) the input polygon P , and the long straight line represents an approximation segment computed by the COLLINEAR MERGE step.

5. POLYGON CHOICE: after the CLOSE GAP step, the set of computed approximation segments \mathcal{AS} can be seen as an unweighted undirected connected graph $G_{\mathcal{AS}} = (V, E)$ defined as follows: E is formed by all the approximation segments in \mathcal{AS} and V contains all the endpoints of edges in E .

According to the observation at the end of COLLINEAR MERGE step, the approximation point sets $AP(p_i)$, $p_i \in P$, may have different size. Now, among such approximation point sets takes the one (say AP) having the minimum size, and let V_{AP} the subset of V containing all the vertices corresponding to points in AP .

Take an arbitrary vertex $v \in V_{AP}$ and consider a shortest path tree T_v , rooted at v , that provides the edges on a shortest path from v to each vertex $u \in V \setminus \{v\}$. Select the vertex $v' \in N(v)$ such that v' is a leaf in T_v and $d_G(v, v')$ is minimum. It follows that the shortest path v, \dots, v' in T_v

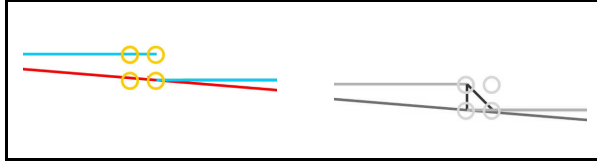


Fig. 3. Example of “gap” at some approximation set $AP(p_i)$, $p_i \in P$. On the left, an approximation point set formed by 4 points in which a gap occurs. On the right, two \mathcal{C} -oriented segments are inserted by the CLOSE GAP step.

along with the edge (v', v) form a cycle in G_{AS} that induces a \mathcal{C} -oriented polygon Q_v .

Q_v is the approximating \mathcal{C} -oriented polygon with the minimum number of segments among all the polygons passing through the vertex/point v . By performing the above approach for each possible vertex in V_{AP} , and computing

$$\min \{|Q_v| : v \in V_{AP}\},$$

then we get the best approximating \mathcal{C} -oriented polygon in \mathcal{AS} for the input polygon P that lie in $\mathcal{T}(P)$. Fig. 4 shows some examples for the POLYGON CHOICE step.

4 Experimental Evaluation

In this section, we report the results of our experimental study. In detail, we describe: how ORSA has been specialized for the implementation, the implementation platform, the executed tests, and the final results of our study (assessment of efficiency and performance of ORSA).

The proposed algorithm has been implemented by specializing its general behavior as follows:

- \mathcal{C} contains the octilinear directions;
- concerning the Step 1, parameters σ and γ have been set such that $\sigma \equiv p_0$ (p_0 is the first vertex of the input polygon P), and $\gamma = \varepsilon$ (ε is the tolerance error). So, in the implementation, the discrete reference system is $\mathbb{D}_{p_0, \varepsilon}$, and $|AP(p_i)|$, $0 \leq i \leq n - 1$, contains either 5 or 4 points (according whether p_i coincides with a point in $\mathbb{D}_{p_0, \varepsilon}$ or not).
- concerning the step 5, the shortest paths computation has been performed not for each possible vertex in the selected set V_{AP} , but only for one arbitrary vertex $v \in V_{AP}$. Since G_{AS} is unweighted, we used a breadth-first search (BFS) algorithm to compute the shortest path tree T_v .

The approximation algorithm presented in the previous section has been implemented by using CGAL [2] and BOOST [1]. Both provide free peer-reviewed

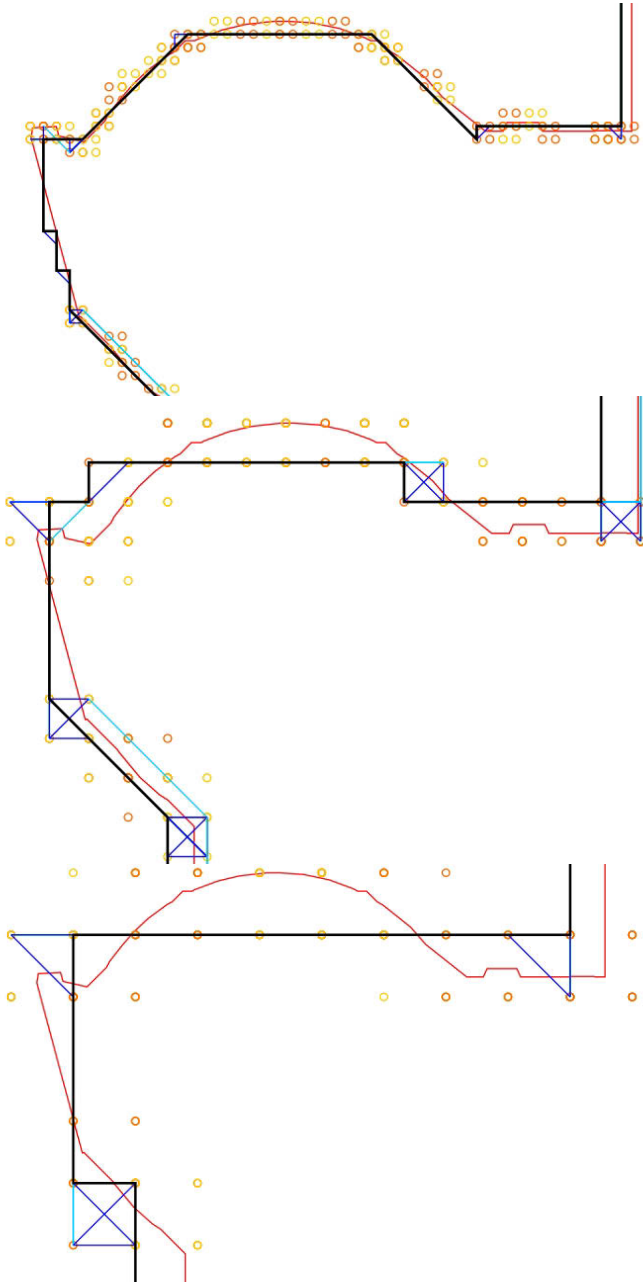


Fig. 4. Approximation of a polygon P with errors equals to 10, 30, and 50 (only part of P is shown). The thin polyline represents (part of) P , circles highlight approximation points, and some approximation segments (those connecting circles) are shown. The bold line segments represent (part of) the octilinear polygon Q computed by ORSA.

portable C++ source libraries; in addition, CGAL provides an easy access to efficient and reliable geometric algorithms. The experiments of such an implementation has been performed over the following platform: a PC equipped with an Intel Dual Core E2140 @ 2800 MHz, RAM 2GB DDR2 800 MHz, GNU/Linux Kernel 2.6 x86_64, and GCC 4.2.3.

By using this implementation we performed an experiment by running the tool over a real PCB consisting of 16 layers. The PCB polygons have been extracted from a Cadence® Allegro® PCB editor project file. We did not consider all the polygons in the board (≈ 13.000), but only the relevant ones with respect to the cavities identification problem. Disregarding all the polygons that have the area under a given threshold we got just 923 “large enough” polygons. These resulting polygons have 40.685 points in total. The dimensions of the board are 15.000 mils (width) and 9.000 mils (height) (1 mil = 10^{-3} inch). In the remainder, each number referring to some board measure is expressed in mils (e.g., the error measure ε).

Efficiency: The first experiment aims to provide a measure of how good is the approximation of the proposed algorithm with respect to real world data. This task is performed empirically by comparing the number of points obtained by ORSA with the number of points obtained by MM, the implementation of the *minimax method* defined by Kurozumi and Davis [15] for the GPA problem. We recall that MM computes the optimum approximating polygon and not a \mathcal{C} -oriented polygon. This means that the solution computed by MM is always better than the solution provided by ORSA.

Table 1. Five experiments for approximating a polygon consisting of 332 vertices. From left to right, the columns report: the input error, the number of vertices of the polygon computed by the minimax method, the number of points of the \mathcal{C} -oriented polygon, the ratio (%) between the previous two values.

error	points MM	points ORSA	MM/ORSA (%)
10	122	142	85.9
20	81	106	76.4
30	67	83	80.7
40	52	71	73.2
50	47	56	83.9
<i>average</i>			80.2

Table 1 provides numerical results related to such a comparison with respect to a single input polygon P_{332} that belongs to the considered PCB and consists of 332 vertices. The table shows that, in average, MM finds an optimum approximated polygon having the 80.2% points of the \mathcal{C} -oriented polygon computed by ORSA. Fig. 5 shows the solution computed by ORSA for the polygon P_{332} with respect to a tolerance error $\varepsilon = 50$.

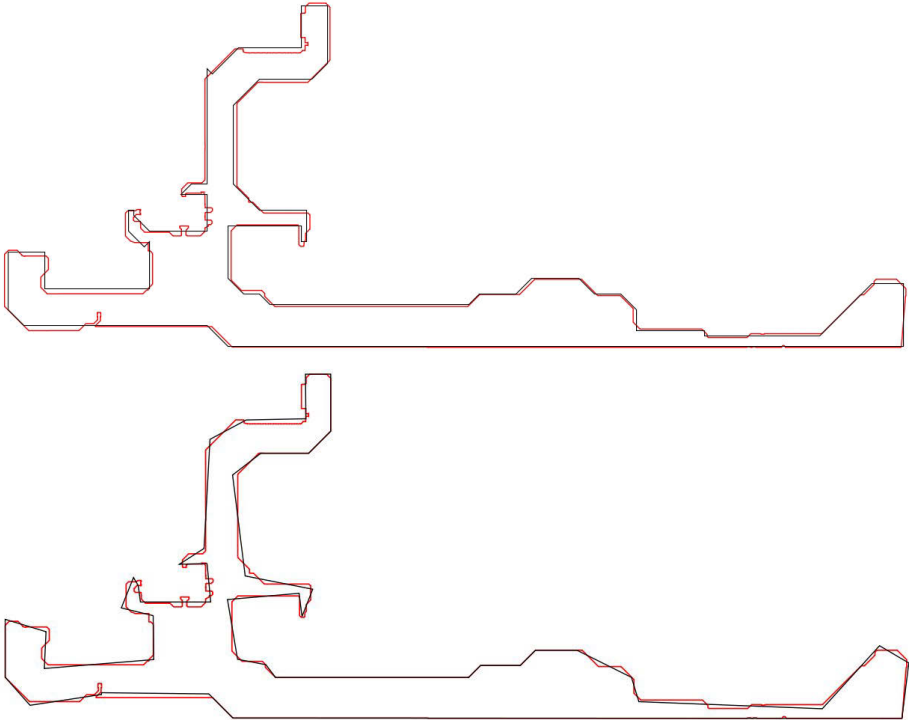


Fig. 5. Example of approximating a polygon taken from the real PCB and consisting of 332 vertices: the figure on the top represents the input (332 vertices) and the octilinear polygon obtained by using the **ORSA** algorithm (56 vertices). The figure on the bottom shows the optimal approximating polygon obtained by **MM** (47 vertices). In both cases, the tolerance error is $\varepsilon = 50$.

After performing a similar comparison for *all* the polygons of the PCB we got that **MM** finds optimum approximated polygons having, in average, the 77.9% of points of the \mathcal{C} -oriented polygon computed by **ORSA**.

Performance: Here we report the performance of the proposed algorithm with respect to the elaboration of the entire board (i.e., using **ORSA** to approximate all the 923 large polygons of the PCB, having 40685 vertices in total). Table 2 shows the number of resulting polygons, the total number of vertices of the resulting polygons, and the overall execution time (in seconds). These values are reported for 5 different approximations of the entire board, according to different values of the input error.

4.1 Self-adapting Error

Table 1 shows that, if we use **ORSA** for the simplification of the entire board, the quality of the result heavily depends on the input choice of the tolerance error ε .

Table 2. Numerical results obtained by executing ORSA over the whole board consisting of 923 large polygons and 40685 vertices. Different tests, according to 5 different values of the input error (the same error has been used for all the input polygons), have been performed. With larger values of the error, the algorithm may produce no results, since the approximation of a small polygon may result in a *degenerated* polygon consisting of zero or one vertex.

error	polygons	vertices	time (sec)
10	763	11833	20.89
20	675	8045	14.37
30	574	6112	10.06
40	526	5146	9.40
50	478	4371	8.71
<i>average</i>			12.68

For instance, choosing a small value for ε (with respect to the quantum γ in the definition of the discrete coordinate system $\mathbb{D}_{\sigma,\gamma}$) it is possible that each $AP(p_i)$ is empty, and hence the input polygon P cannot be schematized into an octilinear polygon. In general, a not careful choice of the tolerance error may lead to loose a large part of the board geometrical dataset.

To overcome this drawback we have extended the proposed approach by introducing a *self-adapting error*. It consist of a preprocessing of the current polygon P to be approximated so that the algorithm determines a “good” tolerance error for it.

Let us denote the height and the width of the bounding-box of P by h and w , $h \leq w$, respectively. Experimentally we observed that when P is a polygon with a large number of vertices and such that $h/w \approx 1$, then P is nicely approximated by an error defined as $h/100$. If we adjust the value $K = h/100$ according to the ratio h/w as reported in Table 3, then we get the numerical results reported in Table 4. By comparing Tables 4 and 2 we see that the self-adapting approach is able to approximate almost all the board with a small increase in the execution time.

Table 3. How to determine a self-adapting value of the tolerance error ε for a given polygon P . Symbols h and w represent the height and the width of the bounding-box of P , respectively. We assume $h \leq w$ and denote $r = \frac{h}{w}$, $R = \frac{h}{K}$, and set $K = 100$.

r	ε
$0 < r \leq 0.10$	$7.5 \cdot R$
$0.10 < r \leq 0.20$	$6 \cdot R$
$0.20 < r \leq 0.33$	$5 \cdot R$
$0.33 < r \leq 0.67$	$1.67 \cdot R$
$0.67 < r \leq 1$	$1 \cdot R$

Table 4. Numerical results showing the usage of the self-adapting error. The processed board contains 923 polygons and 40685 vertices.

K	polygons	vertices	time (<i>sec</i>)
100	860	12237	25.32

5 Conclusion and Future Work

In this paper we provided **ORSA**, a fast and simple heuristic for the schematization of simple polygons into octilinear polygon. This problem arises in the context of electronic CAD systems when it is necessary to detect the generation and propagation of electromagnetic noise into real-world multi-layer PCBs. The proposed algorithm has been implemented and tested over a real PCB. The performed experiments revealed that **ORSA** is fast and computes near-optimal solutions.

According to such good performances, **ORSA** has been included in a software application named Cavity Identification Tool [8], whose purpose is the full computation and processing of the geometry dataset from real-world multi-layer PCBs. This tool has been designed as a client-server application. The client is written in **Java** and implements a GUI that allows the user to provide the input and to perform shapes and cavities visualization. The server is responsible for implementing all the **C++** algorithms by using **CGAL**.

Some further remarks are the following:

- the discrete reference system $\mathbb{D}_{\sigma,\gamma}$ could be also used by letting $\gamma = \varepsilon/k$, with some natural number $k > 1$. In this way we get approximation sets with more points than in used system $\mathbb{D}_{p_0,\varepsilon}$. This approach could be used any time a closer approximation is needed;
- the **ORSA** algorithm could be used for graph drawing problems, such as the road and metro map layout problems [10,17].

References

1. BOOST, Peer-reviewed portable c++ source libraries, <http://www.boost.org>
2. CGAL, Computational Geometry Algorithms Library, <http://www.cgal.org>
3. Agarwal, P.K., Varadarajan, K.R.: Efficient algorithms for approximating polygonal chains. *Discrete & Computational Geometry* 23(2), 273–291 (2000)
4. Bose, P., Cabello, S., Cheong, O., Gudmundsson, J., van Kreveld, M.J., Speckmann, B.: Area-preserving approximations of polygonal paths. *J. Discrete Algorithms* 4(4), 554–566 (2006)
5. Bresenham, J.E.: Algorithm for computer control of a digital plotter. *IBM Systems Journal* 4(1), 25–30 (1965)
6. Chen, D.Z., Daescu, O.: Space-efficient algorithms for approximating polygonal curves in two-dimensional space. *Int. J. Comput. Geometry Appl.* 13(2), 95–111 (2003)

7. Chen, D.Z., Daescu, O., Hershberger, J., Kogge, P.M., Mi, N., Snoeyink, J.: Polygonal path simplification with angle constraints. *Comput. Geom.* 32(3), 173–187 (2005)
8. Cicerone, S., Orlandi, A., Archambeault, B., Connor, S., Fan, J., Drewniak, J.L.: Cavities' identification algorithm for power integrity analysis of complex boards. In: 20th Int. Zurich Symposium on Electromagnetic Compatibility (EMC-Zurich 2009), pp. 253–256. IEEE Press (2009)
9. Daescu, O.: New results on path approximation. *Algorithmica* 38(1), 131–143 (2004)
10. Delling, D., Gemsa, A., Nöllenburg, M., Pajor, T.: Path Schematization for Route Sketches. In: Kaplan, H. (ed.) SWAT 2010. LNCS, vol. 6139, pp. 285–296. Springer, Heidelberg (2010)
11. Demetrescu, C., Finocchi, I., Italiano, G.F.: Algorithm engineering, algorithmics column. *Bulletin of the EATCS* 79, 48–63 (2003)
12. Douglas, D.H., Peucker, T.K.: Polygonal path simplification with angle constraints. *The Canadian Geographer* 10(2), 112–122 (1973)
13. Gudmundsson, J., Narasimhan, G., Smid, M.H.M.: Distance-preserving approximations of polygonal paths. *Comput. Geom.* 36(3), 183–196 (2007)
14. Imai, H., Iri, M.: Computational-geometric methods for polygonal approximations of a curve. *Computer Vision, Graphics, and Image Processing* 36(1), 31–41 (1986)
15. Kurozumi, Y., Davis, W.A.: Polygonal approximation by the minimax method. *Computer Graphics and Image Processing* 19, 248–264 (1982)
16. Lei, C.T., Techentin, R.W., Gilbert, B.K.: High-frequency characterization of power/ground plane structures. *IEEE Trans. Microwave Theory Tech.* 47, 562–569 (1999)
17. Merrick, D., Gudmundsson, J.: Path Simplification for Metro Map Layout. In: Kaufmann, M., Wagner, D. (eds.) GD 2006. LNCS, vol. 4372, pp. 258–269. Springer, Heidelberg (2007)
18. Müller-Hannemann, M., Schirra, S.: Chapter 1. Foundations of Algorithm Engineering. In: Müller-Hannemann, M., Schirra, S. (eds.) *Algorithm Engineering*. LNCS, vol. 5971, pp. 1–15. Springer, Heidelberg (2010)
19. Na, N., Choi, J., Chun, S., Swaminatham, M., Srinivasan, J.: Modeling and transient Simulation of planes in electronic packages. *IEEE Trans. on Advanced Packaging* 23(3), 340–352 (2000)
20. Neyer, G.: Line Simplification with Restricted Orientations. In: Dehne, F., Gupta, A., Sack, J.-R., Tamassia, R. (eds.) WADS 1999. LNCS, vol. 1663, pp. 13–24. Springer, Heidelberg (1999)
21. Swaminathan, M., Joungho, K., Novak, I., Libous, J.: Power distribution networks for system-on-package: status and challenges. *IEEE Trans. on Advanced Packaging* 27(2), 286–300 (2004)

On Counting and Analyzing Empty Pseudo-triangles in a Point Set

Sergey Kopeliovich¹ and Kira Vyatkina²

¹ Department of Mathematics and Mechanics, Saint Petersburg State University,
28 Universitetsky pr., Stary Peterhof, St. Petersburg 198504, Russia
burunduk30@gmail.com

² Algorithmic Biology Laboratory,
Saint Petersburg Academic University, Russian Academy of Sciences,
8/3 Khlopina str., Saint Petersburg 194021, Russia
kira@math.spbu.ru

Abstract. We address the problems of counting and analyzing empty pseudo-triangles defined by a set of points in the plane. First, we assume that the three convex vertices are fixed, and provide algorithms, which solve the counting problem in quadratic time using linear space, for the cases when the pseudo-triangles can be arbitrary or must be star-shaped. In addition, we demonstrate that our approach leads to a fairly simple method for retrieving empty pseudo-triangles optimal in a certain sense in cubic time and linear space. The relaxation of our assumption increases the time complexity by factor n^3 in each case.

Keywords: pseudo-triangles, finite planar point sets, counting problems, optimization problems.

1 Introduction

The problem of counting empty polygons in a planar point set has been studied in the literature for a few decades. A polygon is *contained* in a set P of points if all its vertices reside at the points from P , and is *empty* if no point from P falls inside it. The goal is usually to determine or to bound the number of empty polygons contained in P , or to answer some related questions.

In 1978, Erdős [8] asked for the smallest number $n(k)$, such that any set of $n(k)$ points in the plane contains a convex empty k -gon. The results obtained in this respect are surveyed in [2]. Certain bounds on the number of convex empty polygons in a point set can be found in [6,7,11].

Analogous questions can be stated for non-convex polygons. They were first addressed by van Kreveld and Speckmann [10], and applied to empty pseudo-triangles in a planar point set.

A *pseudo-triangle* is a planar polygon with precisely three convex vertices, which are often referred to as *corners*.

In 2007, van Kreveld and Speckmann [10] provided tight asymptotic bounds on the minimum and maximum number of arbitrary empty pseudo-triangles in

a point set, and of star-shaped ones. Two years later, Ahn et al. [4] examined the problem of generating such pseudo-triangles optimal in a certain sense—and namely, those with the minimum perimeter, the maximum area, or the minimum longest convex chain. (As a matter of fact, Ahn et al. [4] used a more general definition of a pseudo-triangle, allowing its corners to be connected by concave *curves*, and not necessarily polygonal chains. However, the respective optimization problems immediately reduce to those of finding an optimal *polygonal* pseudo-triangle, defined as above.) A year ago, Aichholzer et al. [3] investigated non-convex *4-holes* in a point set, which essentially represent non-convex quadrilaterals, and can be viewed as a special case of pseudo-triangles. Finally, very recently, Ahn et al. [5] have further elaborated and extended the results from [10] and [4] and summarized them in a joint paper.

In [5], Ahn et al. are looking, in particular, for an empty pseudo-triangle with the maximum perimeter or the maximum area. Thereby, their algorithms actually enumerate all the empty pseudo-triangles defined by P . In addition, the asymptotic bounds by van Kreveld and Speckmann [10] imply that those algorithms fulfil the mentioned enumeration task in worst-case optimal time.

The main goal of the present research is to develop simple and maximally efficient algorithms for counting empty pseudo-triangles in a point set. Of course, the method by Ahn et al. [4,5] allows accomplishing this task; however, we demonstrate that the counting problem can be solved at a lower computational cost than the enumerating one. Moreover, our proposed approach extends to finding an empty pseudo-triangle with the maximum perimeter or the maximum area, resulting in a simpler and clearer algorithm than the one described by Ahn et al. [5].

We shall follow the scheme suggested by van Kreveld and Speckmann [10] and further adopted by Ahn et al. [4,5], and first restrict our attention to the case when some three points from P are selected, and we are interested only in the empty pseudo-triangles with the corners at those points. Then the worst-case number of general and of star-shaped empty pseudo-triangles is known to be $\Theta(n^3)$ and $\Theta(n^2)$, respectively [10], and the method by Ahn et al. [4,5] adapted for solving the corresponding counting problems will require $O(n^3)$ time and $O(n)$ space in either case. In this work, we propose algorithms, which accomplish this task in $O(n^2)$ time and linear space in either case. In addition, we demonstrate that our approach leads to a very transparent method for retrieving pseudo-triangles optimal in either sense mentioned above in $O(n^3)$ time and linear space. Through the arguments provided in [10,5], our results immediately extend to the general case, when the pseudo-triangle corners are not fixed; the computational time is thereby slowed down by a factor of n^3 in each case, while the working storage always remains linear. All our algorithms exploit only the most common data structures like arrays or linked lists.

A preliminary version of this paper appeared as [9].

In the next section, we introduce main observations and ideas needed to develop and justify our methods. In Section 3, the algorithms for counting empty pseudo-triangles with fixed corners are provided, for the cases when the pseudo-triangles

can be arbitrary or must be star-shaped, respectively. Section 4 addresses the two optimization problems. In Section 5, we eliminate the restrictions on the corner location. We conclude with a few brief remarks.

2 Preliminaries

Let P be a set of n points in the plane. To simplify the exposition, let us assume that no three points from P are collinear. In addition, we shall first assume that some three points $a, b, c \in P$ have been selected, and restrict our attention to empty pseudo-triangles, the corners of which reside at a, b , and c . Clearly, only the points from P lying inside $\triangle abc$ may become the vertices of such an empty pseudo-triangle. Since we are mainly interested in the worst-case behavior of our algorithms, we shall suppose that a, b , and c constitute the set of vertices of the convex hull of P , which is thus the triangle $\triangle abc$.

Without loss of generality, let us assume that the segment ab is horizontal, a is its leftmost endpoint, and c lies above ab (Fig. 1a).

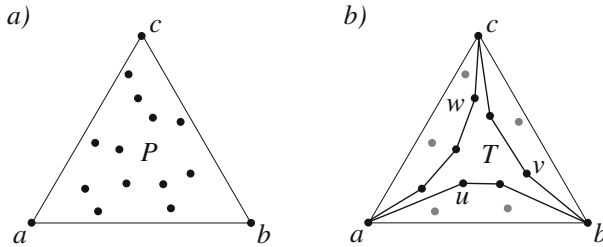


Fig. 1. a) The convex hull of the set P of points is the triangle $\triangle abc$. b) In the boundary of the empty pseudo-triangle T , the vertices u, v , and w follow the corners a, b , and c , respectively, in the counterclockwise order of vertices.

Let T be an empty pseudo-triangle, and let u, v , and w be its three vertices immediately following a, b , and c , respectively, in the counterclockwise order of vertices (Fig. 1b). Note that u, v , and w may coincide with b, c , and a , respectively; yet all the three coincidences occur simultaneously if and only if $P = \{a, b, c\}$.

We shall use the following fact proved in [10].

Lemma 1. *Let T and T' be two distinct empty pseudo-triangles with the corners at a, b , and c . Let u, v , and w (resp. u', v' , and w') denote the vertices of T (resp. T') immediately following a, b , and c , respectively, in the counterclockwise order of vertices. Then the triples (u, v, w) and (u', v', w') are necessarily distinct.*

The converse is obviously not true: for example, if some two of the segments au, bv , and cw —which are supposed to be pseudo-triangle edges—intersect, then the triple (u, v, w) does not correspond to any pseudo-triangle.

For any two points p and q in the plane, we shall denote by l_{pq} the line through p and q .

We shall make use of the following observation [104]. Suppose that a triple (u, v, w) does define a (unique) empty pseudo-triangle T . Then the lower concave boundary chain of T , which connects a and b , can be obtained as follows: compute the convex hull of the set of points consisting of a, b, u , and all the points from P lying below l_{au} and l_{bv} , take its boundary, and remove from it the edge ab (Fig. 2).

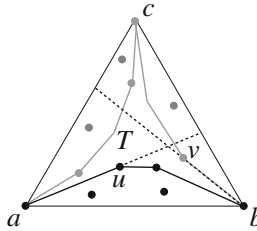


Fig. 2. The concave chain connecting a and b in the boundary of T represents the boundary of the convex hull of the black points, from which the edge ab has been eliminated

Since u and v fully determine the concave boundary chain between a and b , we shall further denote it by C_{uv} .

Our algorithms for counting empty pseudo-triangles will examine all the (valid) candidate pairs (u, v) of points from P , and for each of them determine the number of choices for w , which would result in a triple (u, v, w) defining either an arbitrary or a star-shaped empty pseudo-triangle. To obtain such a pair (u, v) , we shall first choose u , and then appropriately select v .

3 Counting Problems

3.1 General Empty Pseudo-triangles

Obviously, any point from $P \setminus \{a, c\}$ can be selected as u , while a and c cannot (Fig. 3a). Suppose that u and some two points v and w form a triple defining an empty pseudo-triangle T . Since C_{uv} must lie strictly below l_{bv} , we conclude that v must lie strictly above l_{bu} . On the other hand, any point from P residing above l_{bu} can be chosen as v (Fig. 3b).

It remains to select w . First, let us assume that $v \neq c$. Since C_{vw} must lie strictly to the right of l_{cw} , w must lie strictly to the left of l_{cv} . Moreover, C_{wu} must lie above l_{au} , and share with it a single point a ; therefore, w must either be a or lie strictly above l_{au} (Fig. 4a). Finally, our choice of w must ensure that the triangle bounded by the lines l_{au} , l_{bv} , and l_{cw} is empty (see Fig. 4b), since this triangle would be contained in the pseudo-triangle having the edges au , bv and cw , and thus, any point from P lying inside the former would also fall inside the latter.

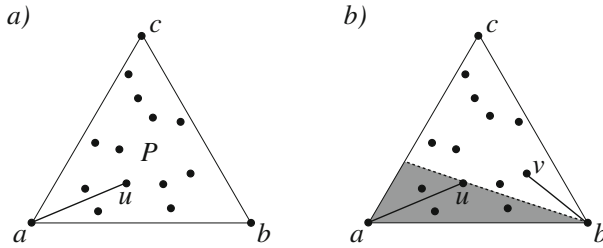


Fig. 3. a) Any point from $P \setminus \{a, c\}$ can be chosen as u . b) Any point lying above l_{bu} can be chosen as v .

Let $o = l_{au} \cap l_{bv}$, and let $x = l_{bv} \cap ac$ (Fig. 4b). Moreover, let r be the point from P lying inside $\triangle aox$, which maximizes the angle $\angle acr$. First, suppose that v lies to the right of l_{cr} . Then the valid candidate points to be selected as w are represented by r and the subset P' of points from P lying strictly between l_{cr} and l_{cv} and above l_{bv} (in the white triangle, according to Fig. 4b). Note that P' can be alternatively viewed as the subset of points from P lying strictly between l_{cr} and l_{cv} and above l_{au} (due to the fact that the interior of the light-gray triangle must be empty, according to Fig. 4b).

Observe that v may happen to lie to the left of l_{cr} (Fig. 4c). If so, no point from P is a valid candidate for w .

Finally, note that for $v = c$ (and any fixed u), precisely one empty pseudo-triangle corresponds, and this pseudo-triangle is star-shaped (Fig. 5).

Now let us outline an algorithm, which allows to efficiently compute the number of empty general pseudo-triangles in P .

Algorithm EmptyGeneral(P, a, b, c)

Input: P – set of points with a convex hull $\triangle abc$

Output: Num – the number of empty general pseudo-triangles in P with the corners at a, b, c

1. Let P_b be a set of points composing $P \setminus \{a, b\}$ sorted in a cw order w.r.t. b .
Let P_c be a set of points composing $P \setminus \{b, c\}$ sorted in a ccw order w.r.t. c .
2. $Num \leftarrow 0$
3. **for each** point $u \in P \setminus \{a, c\}$
4. Let $P_u \subset P_c$ consist of the point a and all points from P_c lying strictly above l_{au} .
5. **for each** point $q \in P \setminus \{c\}$
6. Let $left[q]$ be the number of points from P_u lying strictly to the left from l_{cq} .
7. $r \leftarrow a$
8. **for each** point $v \in P_b \setminus \{c, u\}$
9. **if** v lies above l_{bu} and to the right of l_{cr}
/* v is a valid candidate, and allows for at least one choice for w . */

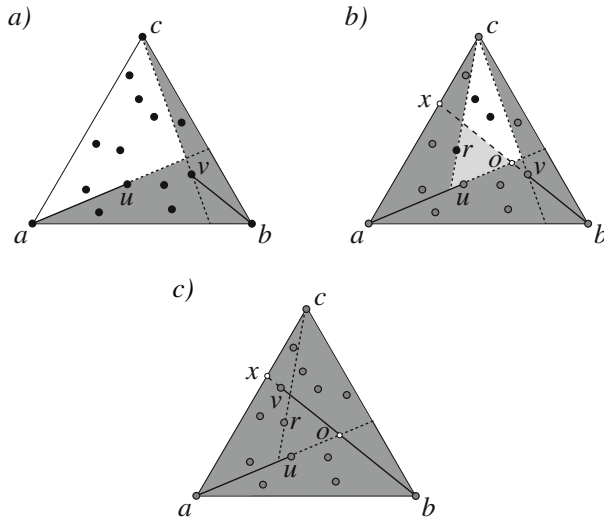


Fig. 4. a) A candidate point w cannot lie in the gray area. b) Since the interior of the light-gray triangle bounded by the lines l_{au} , l_{bv} , and l_{cw} must be empty, w must be one of the three black points (here, $w = r$). c) If v lies to the left of l_{cr} , no point can be selected as w .

```

/* Increment Num by the number of valid candidates for w. */
10.  Num ← Num + left[v] − left[r]
/* Update r for the next iteration, if needed. */
11.  if v lies above  $l_{au}$  and  $\angle acv > \angle acr$ 
12.    r ← v
13.  Num ← Num + 1
/* Account separately for (unique) the empty pseudo-triangle
    defined by u and v = c.*/
14. return Num

```

Correctness of the proposed algorithm is guaranteed by the discussion carried out above. The time complexity of the preprocessing stage (Steps 1 and 2) is $O(n \log n)$. It is easy to see that for each point u , the respective iteration of the cycle “for” (Steps 4–13) is accomplished in linear time. Obviously, linear storage is sufficient for any auxiliary data structures. We conclude that the algorithm **EmptyGeneral** runs in $O(n^2)$ and $O(n)$ space.

Theorem 1. *Let P be a set of n points in the plane, such that its convex hull is a triangle $\triangle abc$, and no three its points are collinear. The number of empty general pseudo-triangles in P with the corners at a, b, c can be computed in $O(n^2)$ time using $O(n)$ space.*

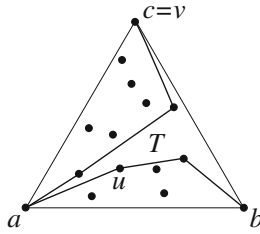


Fig. 5. For any fixed u and $v = c$, a unique empty pseudo-triangle T with corners at a, b, c corresponds, which is star-shaped

3.2 Empty Star-Shaped Pseudo-triangles

To count the empty star-shaped pseudo-triangles in P , we follow essentially the same scheme. The only distinction is that w now needs to be chosen more carefully.

Suppose we have selected the points u and v as described in Section 3.1 (see Fig. 3). Consider the triangle Δaox and the point r defined as above (see Fig. 4b). As in the case of general empty pseudo-triangles, if v lies to the left of l_{cr} , no point can be selected as w (see Fig. 4c). Otherwise, w again must either be r or lie strictly between l_{cr} and l_{cv} , and above l_{bv} . However, if $o \notin bv$, this does not yet guarantee that the pseudo-triangle defined by the triple (u, v, w) would be star-shaped: to this end, we must require w to lie strictly to the left of the line l_{co} , which is a stronger condition (Fig. 6a). Observe that the set of points lying strictly inside the triangle bounded by l_{cr}, l_{co} and l_{bv} is identical to that lying strictly inside the triangle bounded by l_{cr}, l_{co} and l_{au} . Consequently, in this case, w can be either r or any point lying strictly inside the triangle bounded by the lines l_{cr}, l_{co} and l_{au} .

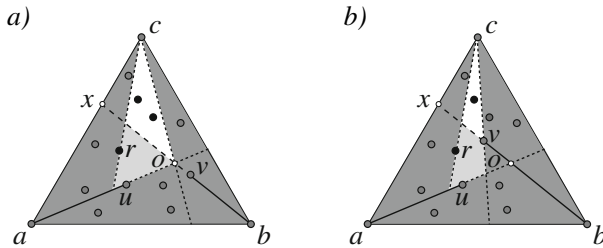


Fig. 6. The set of valid candidates for w (black points) consists of r and the points lying strictly inside the triangle bounded by a) l_{cr}, l_{co} and l_{au} , if $o \notin bv$; b) l_{cr}, l_{cv} and l_{au} , if $o \in bv$ but $cr \cap bv = \emptyset$

If $o \in bv$ but v lies to the right of l_{cr} (that is, $cr \cap bv = \emptyset$), then the condition that w lies strictly to the left of the line l_{cv} must hold, and w can be either r or any point lying strictly inside the triangle bounded by the lines l_{cr}, l_{cv} and l_{au} (Fig. 6b).

Now it should become clear that the method for counting empty star-shaped pseudo-triangles in P is fully similar to the one for counting general ones. The most important distinction is that throughout the algorithm, we should maintain the number of points from P lying strictly to the left of l_{co} . However, since the point o moves along the line l_{au} constantly to the right, this is easy to incorporate without affecting the complexity.

Theorem 2. *Let P be a set of n points in the plane, such that its convex hull is a triangle $\triangle abc$, and no three its points are collinear. The number of empty star-shaped pseudo-triangles in P with the corners at a, b, c can be computed in $O(n^2)$ time using $O(n)$ space.*

4 Optimization Problems

In order to retrieve in P an empty pseudo-triangle with the maximum perimeter or the maximum area, we shall analyze each empty pseudo-triangle present in P using the same framework as described above. That is, we shall first choose u , then select v , and finally, examine one-by-one all the valid candidates for w —instead of simply retrieving the number of those,—and for each triple (u, v, w) defining an empty pseudo-triangle, retrieve the needed information on the latter. Having examined all such triples, we shall be able to indicate the desired optimal pseudo-triangle.

The perimeter of a pseudo-triangle defined by a triple (u, v, w) equals the sum of the lengths of the three concave chains C_{uv} , C_{vw} , and C_{wu} , and its area can be computed by subtracting from the area of $\triangle abc$ those of three convex polygons, each bounded by a concave chain and the edge of $\triangle abc$ connecting two its endpoints. Thus, for our purposes, it is sufficient to keep track of the lengths of the three concave chains, and of the areas of the convex polygons they cut off from $\triangle abc$, throughout the algorithm.

We shall iterate through the triples (u, v, w) that define empty pseudo-triangles, thereby efficiently updating concave boundary chains C_{uv} , C_{vw} , and C_{wu} , along with the necessary information associated with them. Let us now analyze when and how each of those chains should be updated.

First, consider the chain C_{uv} . Assuming that at a current step, the point v is being included in the triple, let v_{prev} denote the point, which has played this role just before (Fig. 7a,b). Observe that C_{uv} needs to be updated if and only if v_{prev} falls inside the triangle bounded by l_{au} , l_{bv} , and ab . If this is the case, v_{prev} should be inserted in C_{uv} right before b , and then its preceding vertex should be iteratively removed as long as C_{uv} makes at it a left turn (Fig. 7b). Evidently, this is essentially the famous Graham’s scan, which maintains the convex hull of the point set composed of a, b, u , and certain points from P processed in a clockwise order with respect to b . This implies that for a fixed u , all the updates of C_{uv} are performed in total $O(n)$ time.

Now let us reuse the notation introduced in Section 3.1 (Fig. 8; see also Fig. 4). The chains C_{vw} and C_{wu} get modified as w moves counterclockwise with respect to c from the point r to the last valid candidate (Fig. 8a,b). Observe that the

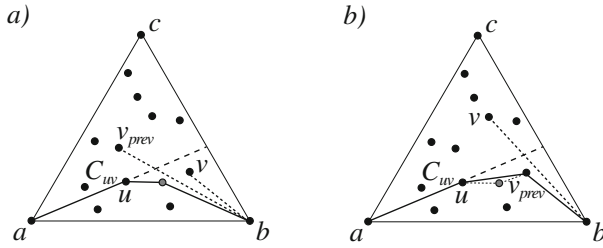


Fig. 7. Two consecutive iterations on v for a fixed u . The point v has been included in the triple at the current step; v_{prev} represents the previous choice of v . The chain C_{uv} after v has been processed is shown bold. a) The point v_{prev} lies above l_{au} , and, thus, is not present in C_{uv} . b) The point v_{prev} lies below l_{au} , and is present in C_{uv} . The gray point has been eliminated from C_{uv} at the current step.

point preceding c in C_{vw} is always the one following w in P_u , unless w represents the last candidate, in which case the point preceding c in C_{vw} is v . At each iteration, C_{wu} is updated analogously to C_{uv} : the point newly selected as w is inserted in the former chain right after c , and its successive vertex is iteratively removed while C_{wu} makes at it a left turn. Consequently, for a fixed pair (u, v) , all the updates of C_{wu} are accomplished in total linear time.

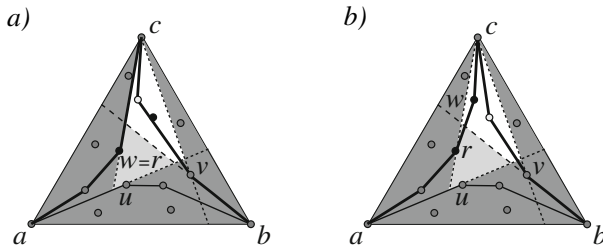


Fig. 8. The first two iterations on w for a fixed pair (u, v) . The point w and its successive point (white) in P_u are the vertices following c in C_{vw} and preceding c in C_{vw} , respectively. The chains C_{vw} and C_{wu} are depicted bold. a) At the first step, w coincides with r . b) At the second iteration, the new candidate for w has been deleted from C_{vw} and inserted into C_{wu} .

On the contrary, from C_{vw} , the vertex preceding c is removed as w is updated. Conceptually, the whole process of updating C_{vw} can be viewed as a “reversed” Graham’s scan, which also requires $O(n)$ time in total.

Below we outline an algorithm, which iterates over all the triples (u, v, w) that define empty pseudo-triangles, thereby maintaining the three concave chains C_{uv} , C_{vw} , and C_{wu} .

Algorithm EmptyGeneral-ConcaveChains(P, a, b, c)**Input:** P – set of points with a convex hull $\triangle abc$

1. Let P_b be a set of points composing $P \setminus \{a, b\}$
sorted in a cw order w.r.t. b .
Let P_c be a set of points composing $P \setminus \{b, c\}$
sorted in a ccw order w.r.t. c .
2. **for each** point $u \in P \setminus \{a, c\}$
3. **if** $u \neq b$ **then**
4. $C_{uv} \leftarrow (a, u, b)$
5. **else**
6. $C_{uv} \leftarrow (a, b)$
7. $v_{prev} \leftarrow u$
8. Let $P_u \subset P_c$ consist of the point a and
all points from P_c lying strictly above l_{au} .
9. $r \leftarrow a$
10. **for each** point $v \in P_b \setminus \{u\}$
11. **if** v lies above l_{bu} and to the right of l_{cr}
12. $C_{wu} \leftarrow$ boundary chain of the convex hull of the set of points
composed of c, a , and the subset of points from P_u lying
non-strictly to the left of l_{cr}
13. $C_{vw} \leftarrow$ boundary chain of the convex hull of the set of points
composed of b, c, v , and the subset of points from P_u lying
strictly to the right of l_{cr}
14. **if** $v \neq c$ **then**
15. $l \leftarrow l_{cv}$
16. **else**
17. $l \leftarrow l_{cb}$
18. **for each** point $w \in P_u$, starting from r , lying to the left of l
19. **update** C_{wu}
20. **update** C_{vw}
 / Now C_{uv}, C_{vw} , and C_{wu} together form the boundary of
 the empty pseudo-triangle defined by the triple (u, v, w) . */*
21. **if** $v = c$ **then**
22. **break**
 / Terminate the loop on v . */*
23. **if** v lies above l_{au} **and** $\angle acv > \angle acr$
24. $r \leftarrow v$
25. **if** v_{prev} lies non-strictly below l_{au}
26. **update** C_{uv}
27. $v_{prev} \leftarrow v$

Essentially, it represents a modification of the algorithm **EmptyGeneral** developed in Section 3.1. The above discussion implies that the updates of the concave chains performed at Steps 19, 20, and 26 increase the running time by factor n . Initialization of C_{uv} at Step 4 or 6 is accomplished in constant time,

while C_{vw} and C_{wu} are initialized at Steps 12 and 13 in $O(n)$ time each, which does not further affect the running time.

It is easy to see that along with modifying the concave chains, we may appropriately update the information on both their lengths and the area of the convex polygons they cut off from $\triangle abc$. Knowing the triple (u, v, w) , which defines the optimal pseudo-triangle, we can easily reconstruct the latter in linear time and space. Consequently, we may summarize our results in the following theorem.

Theorem 3. *Let P be a set of n points in the plane, such that its convex hull is a triangle $\triangle abc$, and no three its points are collinear. An empty pseudo-triangle in P with the corners at a, b, c , which has the maximum perimeter or the maximum area, can be computed in $O(n^3)$ time using $O(n)$ space.*

Clearly, many other characteristics may be proposed, such that an optimal pseudo-triangle with respect to them can be retrieved in the same fashion.

We emphasize once again that though the asymptotic complexity of our method is the same as of that by Ahn et al. [45], it does have a substantial advantage—and namely, it does not need to store any intermediate results other than the triple of points defining the best pseudo-triangle encountered so far, and its “cost”. On the contrary, Ahn et al. introduced special tree-like data structures, which accumulate the needed information, but require a more serious effort to be computed and maintained.

5 Empty Pseudo-triangles with Arbitrary Corners

To relax the assumptions that the convex hull of P is a triangle, and the corners of the pseudo-triangles being counted reside at its three vertices, we simply note that in a general set of points, there are $O(n^3)$ distinct triples of those. To count all the empty general or star-shaped triangles for a given set of points, it is sufficient to handle each triple separately using the algorithms described in Section 3. Consequently, the running time in both cases will increase up to $O(n^5)$, while the amount of storage will remain linear.

Similar observations apply to the case of optimal empty pseudo-triangles addressed in the previous section. Having dropped our two assumptions, we shall be able to solve analogous optimization problems using our approach in $O(n^6)$ time and linear space.

6 Conclusion

An open question that arises immediately is whether it is possible to develop faster algorithms for solving the counting problems addressed in this paper. Another potential direction for future research is generalizing the results obtained for empty pseudo-triangles in a point set to the case of empty pseudo-quadrilaterals and other polygonal figures.

Acknowledgment. The second author highly appreciates discussions with Hee-Kap Ahn and Iris Reinbacher carried out when she was visiting Geometric Computing Lab at Pohang University of Science and Technology (POSTECH) in July 2009.

References

1. Clarke, F., Ekeland, I.: Nonlinear oscillations and boundary-value problems for Hamiltonian systems. *Arch. Rat. Mech. Anal.* 78, 315–333 (1982)
2. Aichholzer, A.: [Empty] [colored] k -gons - Recent results on some Erdos-Szekeres type problems. In: *Proc. XIII Encuentros de Geometria Computacional*, Zaragoza, Spain, pp. 43–52 (2009)
3. Aichholzer, O., Fabila-Monroy, R., González-Aguilar, H., Hackl, T., Heredia, M.A., Huemer, C., Urrutia, J., Vortenhuber, B.: 4-Holes in Point Sets. In: *Proc. the 27th European Workshop Comp. Geom. (EuroCG 2011)*, pp. 115–118 (2011)
4. Ahn, H.-K., Bae, S.W., Reinbacher, I.: Optimal empty pseudo-triangles in a point set. In: *Proc. the 21st Canadian Conf. Comp. Geom. (CCCG 2009)*, pp. 5–8 (2009)
5. Ahn, H.-K., Bae, S.W., van Kreveld, M., Reinbacher, I., Speckmann, B.: Empty pseudo-triangles in point sets. *Discr. Appl. Math.* 159(18), 2205–2213 (2011)
6. Bárány, I., Valtr, P.: Planar point sets with a small number of empty convex polygons. *Studia. Sci. Math. Hungar.* 41, 243–266 (2004)
7. Dumitrescu, A.: Planar sets with few empty convex polygons. *Studia. Sci. Math. Hungar.* 36, 93–109 (2000)
8. Erdős, P.: Some more problems on elementary geometry. *Austral. Math. Soc. Gaz.* 5, 52–54 (1978)
9. Kopeliovich, S., Vyatkina, K.: On Counting Empty Pseudo-Triangles in a Point Set. In: *Proc. the 28th European Workshop Comp. Geom. (EuroCG 2012)*, pp. 261–264 (2012)
10. van Kreveld, M.J., Speckmann, B.: On the number of empty pseudo-triangles in point sets. In: *Proc. the 19th Canadian Conf. Comp. Geom. (CCCG 2007)*, pp. 37–40 (2007)
11. Pinchasi, R., Radoicic, R., Sharir, M.: On empty convex polygons in a planar point set. *J. Comb. Theory, Ser. A* 113, 385–419 (2006)

Quantum Reactive Scattering Calculations on GPU

Leonardo Pacifici¹, Danilo Nalli², and Antonio Laganà¹

¹ Department of Chemistry, University of Perugia, via Elce di Sotto, 8, 06123 Perugia, Italy

² Department of Mathematics and Informatics, University of Perugia, via Vanvitelli, 1, 06123 Perugia, Italy

Abstract. An atom diatom time dependent reactive scattering code has been implemented on a platform made of a CPU and a GPU. The detailed analysis of the implemented code led to its restructuring to exploit the architectural features of graphic processors. Resulting gains of efficiency of the code when used for a prototype case study are compared.

1 Introduction

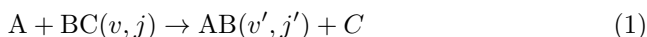
As part of our effort to build a virtual Research Community [1] we have developed a Grid Empowered Molecular Simulator (GEMS) [2] that can be used to simulate on the Grid [3,4,5] *ab initio* molecular and materials processes. To exploit the availability on the Grid of the innovative GPU (Graphic Processing Unit [6,7]) architecture we have implemented some components of GEMS on a machine made by an Intel PC-QuadCore i7 with 6 GB of DRAM memory, equipped with a NVIDIA GTX 285 GPU, which communicates with the CPU via a PCI Express bus. Such machine is part of a larger cluster assembled as a science specialized platform made of many cores highly-parallel shared-memory units used by the virtual organization COMPCHEM [8] of EGI [9]. The NVIDIA architectural solution belongs to the SIMD (Single Instruction Multiple Data) [10] class performing concurrent executions of the same instruction flow over large sets of data. From a functional point of view the NVIDIA architecture is based on *Stream Processors* (SM), which are processors with a large number of elaboration units working in parallel.

The GPU utilized in our laboratory is a NVIDIA GTX 285 whose architecture is based on the NVIDIA SPA (Scalable Processor Array) and is equipped with a DRAM (Dynamic Random Access Memory) of 1 GB [11]. The characteristic feature of this architecture is the use of a large amount (240) of SIMD (Single Instruction Multiple Data) computing cores connected to a shared small on-chip memory that allows a program to organize data as streams and express computations as *kernels*. In particular, the SPA is made up of a certain number (depending on the the GPU model) of *Texture Processor Clusters* (TPC). A single TPC contains a *Geometry Controller* (GC), a *Streaming Multiprocessor Controller* (SMC) and three *Streaming Multiprocessor* (SM) executing computing instructions.

To enable GPUs to efficiently solve scientific problems, the NVIDIA CUDA [12] programming environment has been introduced allowing the use of programs written in the C (or C++) language and a better debugging. CUDA supports C/C++ high level programming language and is based on a thread-based execution model, shared memory mechanisms and synchronization mechanisms which can be managed by the user thanks to some extensions and additional constructs of the C programming language. These extensions provide the user with the possibility of partitioning the problem into decoupled subproblems which can be solved separately, thanks to cooperating threads (different concurrent execution threads for the same computation).

A CUDA application is made of sequential sections (generally executed by the *host*), and parallel sections (called *kernels* and executed by the *device*). In particular, a GPU *kernel* is written like a standard C function. C for CUDA, in fact, extends C by allowing the programmer to define C functions which are executed N times in parallel by N different CUDA *threads*, as opposed to the single execution in regular C functions. A *kernel* is organized as a grid of *blocks*, in which each *block* contains the same number of *threads*. These *blocks* are assigned sequentially to the *Stream Processors* in a coarse grained parallel fashion. At the same time the *threads* are dealt at a very fine grained parallel level. A *thread* belongs to a single *block* and is identified by a unique (among the *kernel*) index. Only *threads* of the same *block* can access the same shared memory. In particular, CUDA provides the possibility of labeling the *block* (using a two-dimensional index) and the *threads* (using a three-dimensional one). Therefore, while, as already mentioned, different *kernels* are executed sequentially, the *threads* and the *blocks* are executed concurrently. In particular, for a given computation the number of active *threads* depends on their organization inside the *blocks* as well as on the *device* available resources. Moreover, thanks to the CUDA primitives the GPU can access its *global memory* and the *host* can transfer data to/from it. However, while each SM can access its shared memory this is not possible for the *host* that can not manage this kind of memory: data allocated on the shared memory can be accessed only by a single *block* of *threads*.

This paper reports on the porting on a GPU of a time-dependent (TD) quantum reactive scattering program based on a wavepacket method that was recently ported on the Grid [5]. The program considered for that purpose is RWAVEPR [13], a Fortran code representing molecular systems as quantum wavepackets evolving in time under the effect of the system Hamiltonian. The code integrates the time-dependent Schrödinger equation for the generic atom diatom reaction



having a reduced mass μ and the diatomic molecule in the v and j (for reactants) and v' and j' (for products) vibrational and rotational states, respectively. The related numerical procedure propagates the complex wavepacket in discrete time starting from an initial wavepacket $\Psi(R, r, \Theta)$ with R being the atom diatom distance, r the diatom internuclear distance and Θ the angle formed by the R

and r vectors set at a value of R (R_0) large enough to consider the system in its asymptotic state. Comprehensive reviews of the time-dependent method have been published in refs. [14] and [15] while the application has been described in detail in a previous work [16].

The paper is articulated as follows: in section II the structure of RWAVEPR is described; in section III how the RWAVEPR code restructured for CUDA implementation on the GPU is discussed; in section IV the results obtained for a case study are analyzed.

2 The Basic CUDA Implementation of RWAVEPR

In the first phase of RWAVEPR, after the input file is read, several calls to functions of the linear algebra routine library are issued. During the second phase, that represents the computational core of the overall procedure, instead, recursive calls to functions carrying out the propagation of the wavepacket through a repeated use of the Fast Fourier Transform subroutines are issued. Because of this significant effort was initially spent in implementing the mathematical libraries of the Basic Linear Algebra Subroutines (BLAS) provided in CUBLAS [17] and the Fast Fourier Transform operations provided in CUFFT [18]. It is important to recall here that RWAVEPR is entirely written in Fortran 77 and works on very large multidimensional matrices, often of the complex type. On the contrary, both the CUDA programming environment and the libraries provided by the CUDA toolkit are written in standard C and therefore adopt a different way of storing matrix elements. In order to cope with such difference and maximize the compatibility with existing Fortran environments, CUBLAS uses column-major storage and 1-based indexing. Unfortunately, Fortran to C calling conventions are not standardized and depend on the platforms and toolchains used for symbol naming and arguments passing.

Then, a profiling of the code was carried out. The results of the profiling is given in Fig. 1 and shows that the main time consuming routines are `miham` (66.36%) and `lowpass` (17.06%) which are repeatedly called by the propagation loop. In our RWAVEPR runs 2159 calls to `miham` are typically performed. The remaining execution time is mainly spent for the `pass` (8.98%) and the `tfft2d` (4.62%) subroutines. For this reason we focused our work on the analysis and restructuring of the `miham` subroutine. The pseudo code of the `miham` subroutine given in Fig. 2 shows how the two 4-dimensional double precision complex valued matrices, `psi` and `hampsi`, representing pointwise the partial wavefunction ψ in which Ψ has been decomposed (for sake of simplicity quantum labels are omitted) and the application to ψ of an appropriate function f of the Hamiltonian $f(\hat{H})\psi$, respectively, are manipulated. The figure shows also how the subroutine makes use of other 2D and 3D matrices, `gob` and `angc`, containing respectively the information needed to absorb the wavepacket at the boundaries of the R , r domain and to integrate over the Θ angle domain. In particular, it shows how the four nested loops implementing the runs over the indices of the involved matrices are the central structure of the routine. For sake of completeness it

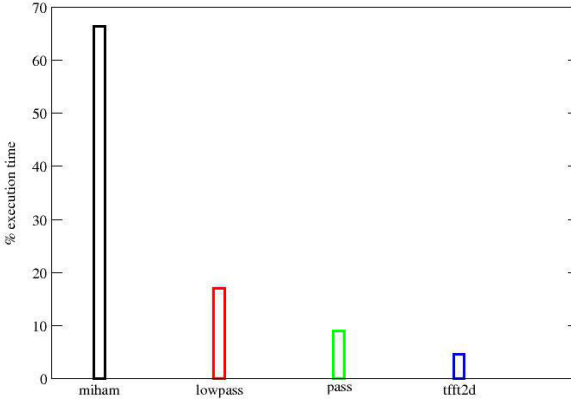


Fig. 1. RWAVEPR profiling histogram

has to be pointed out that `miham` calls other two routines: `tfft2d` and `lowpass`. The `tfft2d` subroutine iterates `jmax2` (that is the parameter related to the Θ Jacobi angular coordinate) times on the `tpsi` array (in which the `psi` matrix is initially stored) of dimension `npoinx*npoiny` (respectively, the number of grid points of R and r). `tfft2d` calls the `pass` subroutine that performs the FFT on a set of data not having power of 2, using a working array called `cw`. The `lowpass` subroutine performs a `hampsi` low angular pass filter. As shown in Fig. 2, the `lowpass` routine is external to the mentioned nested cycles while the Fast Fourier Transform subroutine `tfft2d` is repeatedly called inside them. Accordingly, the `miham` basic scheme reads as follows:

1. calculations on the `hampsi` matrix related to the `gob` matrix and `tpsi` array;
2. calculations on the `hampsi` matrix related to the `vpot` and `angc` matrices;
3. 2D FFT calculation on `tpsi` and update on the `hampsi` matrix.

The crucial step of the basic implementation of the various nested loops of the `miham` subroutine over the dimensions of the `psi` and `hampsi` matrices on the GPU is the distribution of the mentioned matrix calculations among the `threads` of different `blocks`. It is worth pointing out here that, although the matrices involved in the calculations, like `psi` and `hampsi`, are 4-dimensional, the iterations run only over 3 indices because one index, `is1`, specifying which of the `nsr` total number of potential energy surfaces is employed in the calculation, is always 1 in the case study considered. On the basis of the structure of the various matrices involved in the calculations the most natural partition scheme is the distribution of the 2-dimensional sub-matrices on the CUDA `blocks` following the execution flux of the original algorithm. In this case, we have `jmax2` `blocks` each of which contains a `npoinx*npoiny` sub-matrix. Accordingly, each `block thread`

```

subroutine miham (psi,hampsi,lgob)
! variable declarations and initialization
if(condition) rfc = 2.0d0/delte
else rfc = 1.0d0/delte
do is1 = 1, nsr
  do ith = 1, jmax2
    isk=0
    do iy = 1, npoiny
      do ix = 1, npoinx
        bcon = rfc * (bkb(ix) + bks(iy))
        isk=isk+1
        tpsi(isk) = psi(ix,iy,ith,is1)
        if(condition)
          hampsi(ix,iy,ith,is1)= -gob(ix,iy)*hampsi(ix,iy,ith,is1)
        else
          hampsi(ix,iy,ith,is1)=0
        do is2 = 1, nsr
          tempv = tempv + vpot*psi
          tempr = 0
          do ithp = 1, jmax2
            tempr = tempr + angc(is1,ith,is2,ithp)*psi(ix,iy,ithp,is2)
            if (condition1 .or. condition2) then
              hampsi(ix,iy,ith,is1)= hampsi(ix,iy,ith,is1)+bcon*tempr
            tempr = 0
            endif
          enddo
        enddo
        hampsi(ix,iy,ith,is1)=hampsi(ix,iy,ith,is1)+rfc*tempv
      enddo
    enddo
    call tfft2d(tpsi,cw,npoinx,npoiny)
    isk=0
    do l = 1, npoiny
      do i = 1, npoinx
        isk = isk + 1
        hampsi(i,l,ith,is1) = gob(i,l)*(hampsi(i,l,ith,is1)+rfc*tpsi(isk))
      enddo
    enddo
  enddo
enddo
call lowpass(hampsi)
return
end

```

Fig. 2. The miham pseudo code

is assigned a row of the sub-matrix of dimension **npoinx**. Using this distribution scheme and exploiting the *thread* parallelism we obtain a drastic decrease in the complexity of the algorithm. As a matter of fact, in the original algorithm the total number of iterations is **nsr(=1)*npoinx*npoiny*jmax2** while in the CUDA algorithm the only loop is the one running over **npoinx**.

In particular, the 2D sub-matrices of **hampsi**, **psi** and **vpot** are distributed to the various CUDA *blocks* and each *thread* is assigned one row per sub-matrix. On the other hand, the 2D **gob** matrix is replicated into every *block* global memory (each *thread* works on one row of this matrix) while the 2D **angc** matrix is partitioned by distributing one row to each *block* because of the distribution of the relevant 3D matrices aimed at preserving the use of the matrix indices in the algorithm.

In distributing these matrices, we used the primitives of the CUDA programming environment. In particular, we made use of the following relevant functions:

- `cudaMallocPitch(void**, devPtr, pitch, ...)`: this function allocates in memory a 2D data structure pointed by `devPtr`. Moreover, the `pitch` output parameter contains the length that each stored row should have in order to decrease the memory transactions in accessing global memory data. This is particularly suited for allocating 2-dimensional matrices because this function allows the padding of the matrix guaranteeing the correct data alignment.
- `cudaMalloc3D(struct cudaPitchedPtr* pitchedDevPtr, struct cudaExtent extent)`: this function allocates memory resources for 3-dimensional matrices. The out parameter `pitchedDevPtr` contains the pointer to the allocated memory. It returns also the same `pitch` parameter as above.

It is important to point out here that, in addition to the just mentioned matrices, the `miham` subroutine makes use of other data structures initialized into the main program, the `common` variables. In order to preserve the same "programming philosophy", we created, for each `common` variable, external C structures which keep the same Fortran name and have the same variable ordering of Fortran to avoid possible memory disalignments.

3 The Restructured CUDA Implementation of RWAVEPR

After distributing all matrices and creating and initializing the data structures, we have defined the *kernel* structure, in which every *thread* acts on its own sub-matrix partitions. At the very beginning of the calculation, each *thread* is assigned a global index (`idx`) in order to identify it in the *block* grid. This index is also used to identify the matrix partitions assigned to each *thread* in the GPU global memory. In this way each *thread* partition is stored into the *thread* local memory guaranteeing a decrease in the access to the stored elements. The result is a fine grained parallelism because each *thread* works on the assigned partitions only. In this way, in fact, the four nested loops of the original algorithm are collapsed into a single loop in the CUDA implementation whose dimension corresponds to the `rowH` array dimension (`npoiny=npoinx`) (as shown in the CUDA *kernel* of Fig. 3 the main loop now runs on the dimension `npoiny` only). Moreover, all the calculations are carried out locally (with the same operation flux described above for the native Fortran code) on the elements of the array `rowH` and, only at the end of the loops, global memory locations are updated. On the other hand, the `tpsi` array is initialized using again the `idx` global index in order to guarantee that each *thread* writes the proper (assigned) `tpsi` row values (`tpsi[idx*dim+c] = rowH[c]`, in which `dim` is the row dimension and `c` the loop counter). In the final part of the pseudocode, the `tpsi` array is Fast Fourier transformed by all the *threads* concurrently.

The last phase of the `miham` procedure is represented by the `hampsi` update whose Fortran pseudocode reads:

```

__global__ void kernelMiham (params1, params2, ...) {
if (idx < npoinx*jmax2) {
// row assignment
for (c == 0 ; c <= npoiny ; c++) {
tpsi[idx*dim+c]=rowH[c]
if(condition) {
bcon = rfc*(d_bks[threadIdx.x]+d_bkb[c])
rowH[c]= -row_g[c]*rowH[c]
}
else {
rowH[c]=0
}
// array angc calculation for each block
tempv = tempv + rowV[c]*rowPsi[c]
tempr = 0
for (m == 1 ; m <= jmax2 ; m++) {
// psi element calculation
tempr = tempr + rowA[m]*elementPsi
if (condition1.or.condition2) {
rowH[c] = rowH[c] + bcon*tempr
tempr = 0
}
}
}
// Hampsi update
}
}

```

Fig. 3. The CUDA miham pseudo code

```

do ithp = 1, jmax2
  tempr = tempr + angc(is1,ith,is2,ithp)*psi(ix,iy,ithp,is2)
  if (condition1.or.condition2) then
    hampsi = hampsi + bcon*tempr
    tempr = 0
  endif
enddo

```

in which the **angc** matrix is distributed one row per *block* while the **psi** one is distributed by partitioning it into 2-dimensional sub-matrices. For this purpose the **psi** matrix is read along the third dimension, the angular one (a time consuming operation of the GPU algorithm), for a given pair of R and r values. To access the relevant elements inside a single *block* in the proper *threads* (each *thread* receives only one row of the 2D partition) the fact that 3D matrices are allocated in the global memory linearly is exploited and the statement: `(myType)((char*)data)[x*sizeof(myType)+y*pitch+z*slicePitch]` is used. In the statement `myType` is the data-type, `(char*)data` gives the base address of the data structure, `pitch` is the number of elements in each row, `z*slicePitch` is the pointer to the third dimension of the matrix. In this way, the last part of the *miham* CUDA loop takes the form:

```

typedef cufftDoubleComplex cplx;
...
double *rowA = (double*)((char*)d_angc + blockIdx.x*pitch_angc);
for(int m = 1; m <= extent.depth ;m++){
  cplx element =*((cplx*)((char *)devPtr
+ (c*sizeof(cplx) + threadIdx.x*pitch

```

```

+ (m-1)*pitch *extent.height));
tempr.x+=rowA[m-1]*element.x;
tempr.y+=rowA[m-1]*element.y;
if( (m==10*(m/10)) ||m==extent.depth ){
    rowH[c].x+=tempr.x*bcon;
    rowH[c].y+=tempr.y*bcon;
    tempr.x=0.0;tempr.y=0.0;
}
}
...

```

where, `cufftDoubleComplex` represents the data-type, the casting to `char*` by `DevPtr` allows to recover the base address of `psi`, `c` identifies the row element, `threadIdx.x` labels the matrix row to be considered for calculation, and, finally, the value `((m-1)*pitch*extent.height)` represents the matrix third dimension size. Then, data local to each *thread* are copied into the **hampsi** matrix stored in the GPU global memory. Finally, the FFT 3D is applied to the **tpsi** matrix (already calculated inside the *kernel*) making use of the CUFFT library primitives. Then, in order to enhance the performances by limiting the use of PCI Express for communication between the *device* and the *host*, the normalization procedures are directly performed on the GPU using the developed *kernel*. Instead, the **hampsi** matrix is updated on the *host* side using the coefficients worked out by CUFFT.

The algorithm outlined above has been implemented first by allocating at each call of the procedure the computational resources and afterwards by allocating the computational resources only once at the beginning of the calculation (data preload version). The goal of the second version is both to exploit in depth the potentialities offered by the GPU (as well as by the CUDA environment) and to improve the overall performance of the algorithm, by trying to reduce the data transfers between the GPU and the CPU thanks to an initial allocation of the relevant matrices and their subsequent use by means of pointers when feeding input parameters to the `miham` subroutine. In order to implement the data preload it has been necessary to split the `miham` execution with respect to the remaining calculations (overlap calculation, S matrix elements update etc.). To this end a new module (`miham_module`) and an associated C external function performing all the operations described above were implemented for execution after every call to `miham`. The associated C function is responsible for allocating the resources at the beginning of the calculation while the various calls inside the loop deal with the resources allocated on the GPU using the pointers. In this way the original code structure has been preserved.

4 The Case Study Cl + H₂

The Cl + H₂(*v*, *j*) is a prototype atom-diatom reaction extensively studied in the past [19,20,21,22,23,24], for which large amounts of computing time are typically required to calculate its detailed properties. In our case the state to state

reactive probabilities of the $\text{Cl} + \text{H}_2(v, j)$ reaction were calculated for a range of energy of 0.5 eV and several initial states. For this purpose calculations were carried out using a standard grid of dimensions (120x120x100), corresponding to 12000 active *threads* (calculated as **npoinx*jmax2**), as is typical of atom diatom reaction production runs. The elapsed times measured using the standard input for $v = 0$ and $j = 0$ are given in Table [1](#)

Table 1. Elapsed time of Serial (CPU) vs Parallel (GPU) execution of the RWAVEPR program for $\text{Cl} + \text{H}_2$ system (DP stands for Data Preload)

Sequential	GPU (without DP)	GPU (with DP)
3690 s	1502 s	1340 s

As can be seen from the table, a computing time decrease of a factor 2 was obtained when running the code on the GPU. Time gains further improved when using the data preload mechanism. We measured also the elapsed times for the execution of the `miham` routine only. In passing from the serial CPU to the parallel GPU execution time reduces of about a factor 2 and 3, respectively (see Tab. [2](#)). It is very important to point out here that in both GPU versions

Table 2. Elapsed time of Serial (CPU) vs Parallel (GPU) execution of the `miham` routine

Routine	Sequential	GPU (without DP)	GPU (with DP)
<code>miham (including lowpass)</code>	1.561 s	0.984 s	0.620 s
<code>miham (not including lowpass)</code>	0.842 s	0.685 s	0.340 s

(without and with data preload) the execution of the `miham` routine is affected, as already mentioned, by the serial (CPU) execution of the `lowpass` routine, that represents a clear bottleneck to the calculation. In fact, the elapsed time measured to execute the pure `miham` *kernel* (obtained by excluding the execution of `lowpass` as shown in the table) tells us that the GPU execution of `miham` is shorter of about 200 ms when data is not preloaded and of about 600 ms when data is preloaded (in other words, the preload mechanism increases the efficiency).

In order to confirm the results obtained we carried out further calculations by varying the grid dimension and, consequently, the number of active *threads* for each computation. The elapsed times measured when using the data preload version of the GPU algorithm are compared with those of the CPU in Fig. [4](#)

They clearly show that the algorithm scales quite well with the number of active *threads* (or equivalently with the matrix size) as confirmed by the first large portion of the corresponding speedup plot of Fig. [5](#).

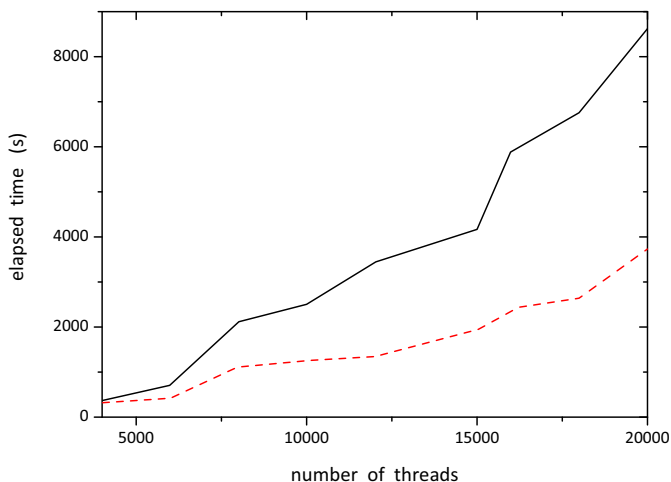


Fig. 4. Elapsed time comparison between the CPU code (solid black line) and the GPU implementation (dashed red line)

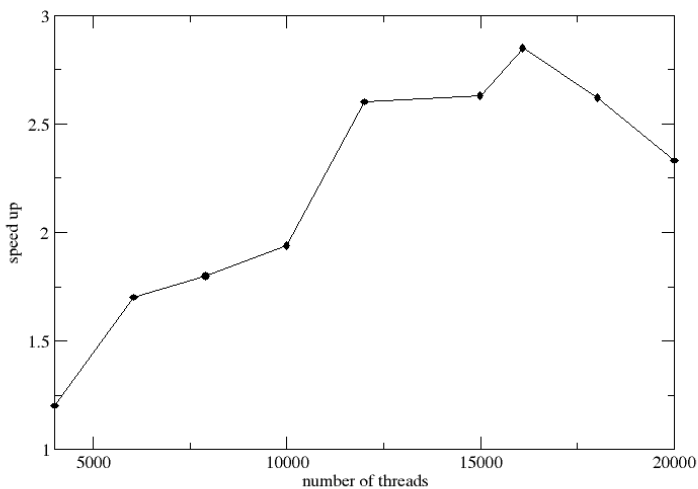


Fig. 5. Calculated GPU speedup for the Cl + H₂ reaction

The decrease of the speedup in the last portion of the plot can be attributed to the fact that the dimension of the associated matrices becomes so large to saturate the bandwidth of the PCI Express bus during the *host-device* (and vice-versa) data transfers. For the same reason when using a larger number of *threads* for the same matrix dimensions the speedup should not be expected to decrease.

5 Conclusions

In this work we have described a simple implementation of the time dependent quantum reactive scattering code RWAVEPR on a machine made by a CPU and a NVIDIA GPU connected by a PCI Express bus. The code had to be restructured to exploit the innovative architectural features of the platform used. For this reason, it has been implemented in the NVIDIA CUDA programming environment and has been used for the study of the prototype $\text{Cl} + \text{H}_2$ reaction. The GPU execution was found to be effective in reducing the overall execution time if the restructuring is properly performed, despite the fact that we are dealing with tightly coupled quantum dynamics calculations. The study has in fact demonstrated that good performances are obtained when:

1. a large number of *blocks* and *threads* are involved in every step of the computational procedure;
2. an appropriate use is made of the GPU shared memory;
3. an improved support to the mathematical CUDA libraries is provided using for example CUFFT, preloading data and including `lowpass`;
4. a fine computational grain is adopted for the distribution of the heavily used matrices.

Moreover, the use of GPUs is not alternative to other HPC and HTC approaches. They instead provide an important platform improvement for all of them.

Acknowledgements. This research was supported by the EGI-Inspire project (contract 261323), the MIUR PRIN 2008 (contract 2008KJX4SN 003), the ESA-ESTEC contract 21790/08/NL/HE, the Phys4Entry (Planetary Entry Integrated Models) FP7/2007-2013 project (contract 242311). The authors also wish to acknowledge CASPUR (IT) for computing time on the FERMI platform.

References

1. De Roure, D., Goble, C., Stevens, R.: The design and Realisation of the Virtual Research Environment for social sharing of workflows. *Future Generation of Computer Systems* 25, 561–567 (2009)
2. Costantini, A., Gervasi, O., Manuali, C., Faginas Lago, N., Rampino, S., Laganà, A.: COMPCHEM: progress towards GEMS a Grid Empowered Molecular Simulator and beyond. *Journal of Grid Computing* 8(4), 571–586 (2010)
3. EGI-InSPIRE project RI-261323, <http://www.egi.eu> (last access: September 26, 2011)
4. Gervasi, O., Laganà, A.: SIMBEX: a portal for a priori simulation of crossed beam experiments. *Fut. Gen. Comp. Syst.* 20, 703–715 (2004)
5. Gervasi, O., Manuali, C., Laganà, A., Costantini, A.: On the restructuring of a molecular simulator as a Grid service in Chemistry and Material Science Applications on Grid Infrastructure. In: ICTP. *Lecture Notes*, vol. 24, pp. 63–81 (2009)
6. NVIDIA, NVIDIA GeForce GTX 200 GPU architectural overview, second generation unified GPU architecture for visual computing, Tech. Rep. (2008), www.nvidia.com/docsIO/55506/GeForce_GTX_200_GPU_Technical_Brief.pdf

7. Richardson, A., Gray, A.: Utilisation of the GPU architecture for HPC, Technical Report from the HPCx Consortium (2008)
8. COMPCHEM website, <http://compchem.unipg.it> (last access October 14, 2011)
9. EGI website, <http://uf2011.egi.eu/> (last access October 14, 2011)
10. Flynn, M.: Some computer organizations and their effectiveness. *IEEE Trans. Comput.* 21, 948–960 (1972)
11. http://www.nvidia.com/object/product_geforce_gtx_285_us.html (last access: September 26, 2011)
12. CUDA ZONE website, http://www.nvidia.it/object/cuda_home_new_it.html (last access October 14, 2011)
13. Skouteris, D., Pacifici, L., Laganà, A.: Time-dependent wavepacket calculations for the $N(^4S) + N_2(^1\Sigma_g^+)$ system on a LEPS surface: inelastic and reactive probabilities. *Mol. Phys.* 102, 2237–2248 (2004)
14. Balakrishnan, N., Kalyanaraman, C., Sathyamurthy, N.: Time-dependent quantum mechanical approach to reactive scattering and related processes. *Phys. Rep.* 280, 79–144 (1997)
15. Althorpe, S.C., Clary, D.C.: Quantum scattering calculations on chemical reactions. *Ann. Rev. Phys. Chem.* 54, 493–529 (2003)
16. Pacifici, L., Nalli, D., Skouteris, D., Laganà, A.: Time Dependent Quantum Reactive Scattering on GPU. In: Murgante, B., Gervasi, O., Iglesias, A., Taniar, D., Apduhan, B.O. (eds.) ICCSA 2011, Part III. LNCS, vol. 6784, pp. 428–441. Springer, Heidelberg (2011)
17. NVIDIA BLAS Library, http://developer.download.nvidia.com/./CUBLAS_Library_2.0.pdf (last access September 30, 2011)
18. NVIDIA FFT Library, http://developer.download.nvidia.com/./CUFFT_Library_1.1.pdf (last access September 30, 2011)
19. Bian, W., Werner, H.-J.: Global ab initio potential energy surfaces for the ClH_2 reactive system. *J. Chem. Phys.* 112, 220–230 (2000)
20. Skouteris, D., Werner, H.-J., Aoiz, F.J., Banares, L., Castillo, J.F., Menendez, M., Balucani, N., Cartechini, L., Casavecchia, P.: Experimental and theoretical differential cross sections for the reactions $Cl + H_2(D_2)$. *J. Chem. Phys.* 114, 10662–10673 (2001)
21. Aoiz, F.J., Banares, L., Castillo, J.F., Menendez, M., Skouteris, D., Werner, H.-J.: A quantum mechanical and quasi-classical trajectory study of the $Cl + H_2$ reaction and its isotopic variants, Dependence of the integral cross sections on the collision energy and reagent rotation. *J. Chem. Phys.* 115, 2074–2082 (2001)
22. Alexander, M.H., Capecchi, G., Werner, H.-J.: Theoretical Study of the Validity of the Born-Oppenheimer Approximation in the $Cl + H_2$ reaction. *Science* 296, 715–718 (2002)
23. Skouteris, D., Laganà, A., Capecchi, G., Werner, H.-J.: Wave packet calculations for the $Cl + H_2$ reaction. *Int. J. Quant. Chem.* 96, 562–567 (2004)
24. Skouteris, S., Laganà, A., Capecchi, G., Werner, H.-J.: Rotational and alignment effects in a multisurface wavepacket calculation for the $Cl + H_2$ reaction. *Phys. Chem. Chem. Phys.* 6, 5000–5006 (2004)

Tuning Heme Functionality: The Cases of Cytochrome *c* Oxidase and Myoglobin Oxidation

Vangelis Daskalakis^{1,*}, Stavros C. Farantos², and Constantinos Varotsis¹

¹ Department of Environmental Science and Technology
Cyprus University of Technology
Limassol, Cyprus, P.O. Box 50329

{evangelos.daskalakis,c.varotsis}@cut.ac.cy

² a. Institute of Electronic Structure & Laser, Foundation for Research and Technology, Hellas
71 110 Heraklion, Greece P.O. Box 1527

b. Department of Chemistry, University of Crete
71 003 Heraklion, Greece
farantos@iesl.forth.gr

Abstract. The (Fe-O) moiety of Cytochrome *c* oxidase ferryl intermediate of the dioxygen activation reaction and the oxy-myoglobin (Mb-O₂) structure have been probed by QM/MM (hybrid quantum mechanical/ molecular mechanical) calculations using Density Functional Theory (DFT)/MM to elucidate the effect of the heme propionates and the protein matrix on the chemistry of heme Fe-O moieties. On this line, we have probed the role of His97 in various protonation states of the heme propionate-6 in Mb and compared the results to that of the Cytochrome *c* oxidase chemistry.

Keywords: heme tuning, propionates, myoglobin, cytochrome *c* oxidase, autoxidation.

1 Introduction

The biological function of heme proteins consists in the transport of electrons (e.g. cytochromes), the transport or sensing of oxygen (e.g. myoglobin, hemoglobin, HemAT), and the catalysis of redox reactions (e.g. cytochrome *c* oxidase, CcO). Protoporphyrin IX (heme) is the common prosthetic group in the majority of heme proteins, while the amino acids surrounding the heme appear to control the protein functionality (1). Theoretical computational studies are routinely used to probe complex biological systems in atomistic details. These studies include, among others, Density Functional Theory (DFT), Molecular Mechanics (MM) and Dynamics (MD), as well as combined Molecular Mechanics/Quantum Mechanics (QM/MM) methodologies.

1.1 The Case of Cytochrome *c* Oxidase

DFT at the BLYP level of theory, QM/MM and MD (OPLS force field) calculations have been applied previously to models of the Cytochrome *c* oxidase (CcO) including

* Corresponding author.

the Fe-Cu_B binuclear center, where dioxygen is bound and subsequently is reduced to water (2-4). Cytochrome *c* oxidase (CcO), the terminal respiratory enzyme, catalyzes the transfer of electrons from the reduced cytochrome *c* to the molecular oxygen and translocates protons vectorially across the mitochondrial inner membrane. Four redox active metal centers are present in the enzyme: two hemes a and three associated copper atoms. In eukaryotes, the electrons coming from the substrate cytochrome *c* enter the homo-dinuclear copper center, Cu_A, and then they are transferred, via the low-spin heme a, to the binuclear center containing a high-spin heme a₃ and a Cu_B complex. The latter two metal sites constitute the active catalytic site, where oxygen is reduced to water by four electrons and four protons and is depicted in Fig.1. The properties of several intermediates of the CcO dioxygen reaction have been investigated in these studies and mechanisms of action have been proposed.

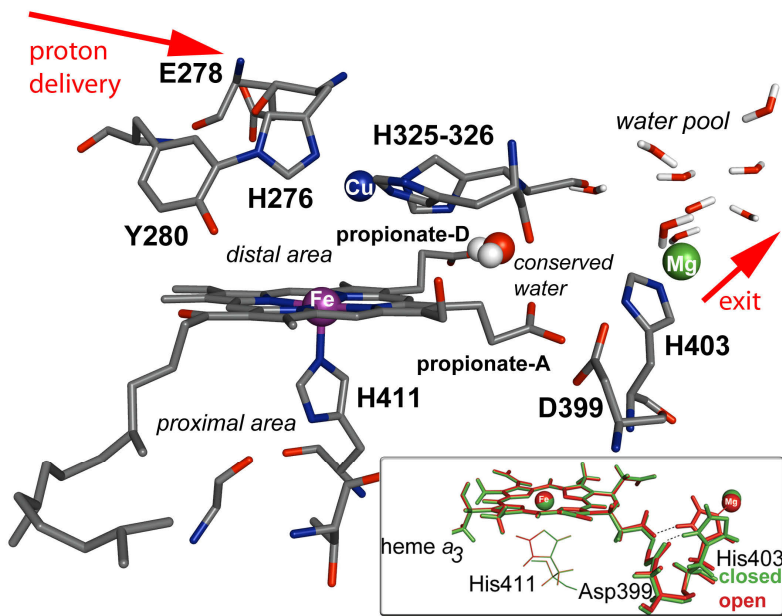


Fig. 1. Active site of aa₃ Cytochrome *c* Oxidase from *P. denitrificans*. His403 (H403) conformations are shown in the inset. Most important surrounding amino acids are also visible, like the Asp399 (D399).

His403 residue of CcO plays a role, as a valve, controlling the flow of protons in the region. By substantially changing the pK_a values of the heme a₃ propionate-A (prop-A) or Asp399, a proton is trapped or released by prop-A. When His403 is at the closed conformation (strong hydrogen bonding with Asp399) the proton is trapped on the prop-A site (4). Starting from a structure where a single proton is shared between the latter pair, in the oxy intermediate, and the closed His403 conformation, the proton resides 'locked' on the prop-A side. Active site oxidation will trigger the release

of that proton as it becomes loosely bound (between prop-A/ Asp399) in the rest of the oxidation states and the His403 closed conformation. A conserved water molecule in the area could easily abstract the labile proton. Deprotonation of the prop-A/ Asp399 pair increases the presence of negative charges in the area, reallocating Cu_B closer to heme a_3 iron, accommodating also half spin on prop-A. Heme a_3 $\text{Fe(II)} \rightarrow \text{Fe(III)}$ is oxidized upon protonation of the prop-A/ Asp399 pair via the proton delivery D-pathway (4). Electron transfer should occur from heme a, concurrently to the previous proton transfer to quench the half spin population on prop-A. This should eventually trigger cycles of the further oxidation of the active site to the peroxy a_3 - $\text{Fe(III)}/\text{Cu}_B(\text{II})$ and ferryl a_3 - $\text{Fe(IV)}/\text{Cu}_B(\text{II})$ intermediates. Protonation should change the His403 conformation, in this case trapping the proton on the Asp399 site (His403 open conformation). Another release of a proton to the propionates area via the proton delivery D-pathway is able to neutralize the prop-A/ Asp399 charges and protons become loosely attached to the pair, in this way (His403 closed conformation). A water molecule out of the active site can be a possible proton carrier, as well as a trigger for the neutralization of the prop-A/ Asp399 pair and the His403 conformational change. In each case, a loosely bound carboxylic proton residing on prop-A/ Asp399 is released to the water pool via Mg coordinated to His403 and later or immediately to the solvent when His403 changes conformation from open to closed.

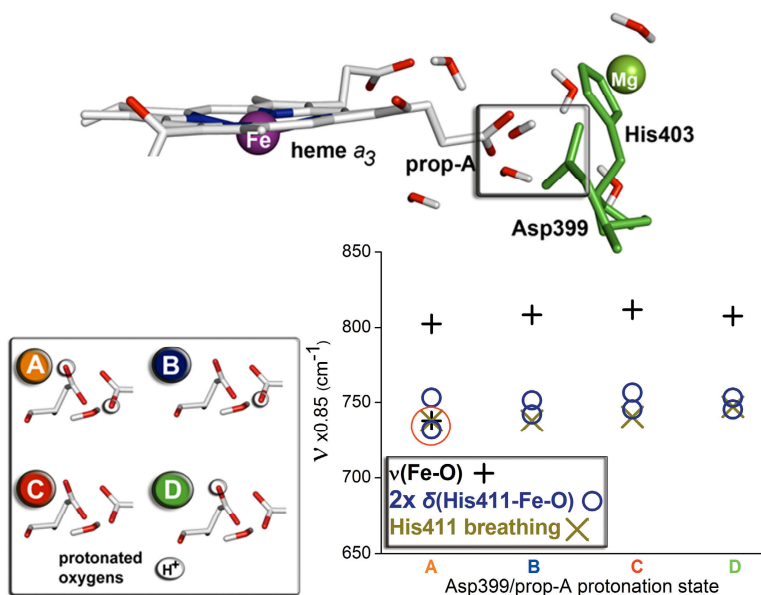


Fig. 2. Different protonation states of the prop-A/Asp399 pair are depicted as A, B, C and D in the inset. These protonation states influence the spectroscopic characteristics of the Fe-O moiety of the heme a_3 , such as the stretching $\nu(\text{Fe-O})$, the bending $\delta(\text{His411-Fe-O})$ and the His411 imidazole breathing.

Different control points have been identified for the transition from one intermediate to the next. In these studies of CcO we found that the protonation state of the heme propionates, as well as the conformational changes and protonation states of amino acids in their vicinity can control the redox chemistry and spectroscopy of the heme groups in such proteins (2-4). Positive or negative charges near the heme group seem to affect strongly its functionality, while proton motion responsible for the appearance of such charges can be identified in the experimental spectroscopic data of the heme a_3 -Fe=O moiety in CcO (2), as it can be seen in Fig. 2. $\nu(\text{Fe-O})$ vibrational frequency is calculated at 744 cm^{-1} (less negative charges around heme a_3) or around 800 cm^{-1} (more negative charges around heme a_3), as seen on the latter figure, based on the protonation states A, B, C and D.

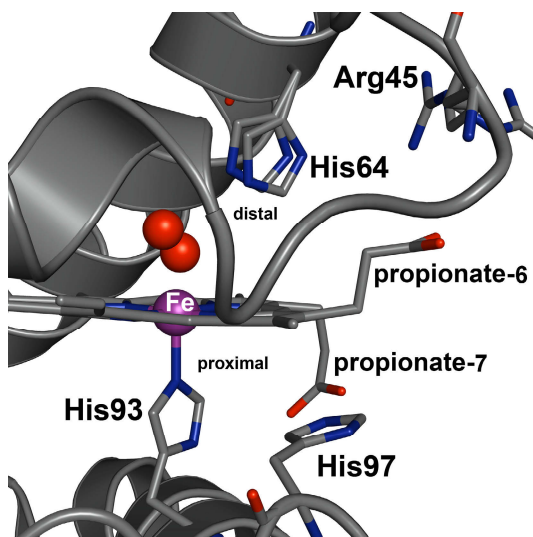


Fig. 3. The crystal structure of myoglobin (Mb) from sperm whale (pdb code 2Z6S)

1.2 The Case of Myoglobin Oxidation

In this paper we extend the research of Cytochrome *c* Oxidase to another heme protein; we probe the tuning of heme functionality in Myoglobin (Mb) and we compare it to that in the CcO enzyme. We are focused on the effects of the protein matrix and protonations around the heme group. For this, we built models of the protein which are varied at the heme environment. This variability is based on hydrogen bonding interactions or amino acid protonation states.

For the rest of the article, we will use the terms ‘external’ and ‘inner’ Histidines that refer to the Histidines of Mb easily accessible, or not from the solvent, respectively. The term ‘deprotonated’ His97 refers to an histidine deprotonated only at the N_δ site, while a ‘fully deprotonated’ His97 refers to an histidine deprotonated at both N_δ and N_ϵ sites.

The oxygen coordination site in Myoglobin (Mb) lies on the distal side of the heme pocket, while a proximal histidine residue (His93) serves as the axial iron ligand (Fig. 3) (5-7). Distal histidine (His64) stabilizes the O₂ binding through a hydrogen-bonding interaction, as well as it strengthens the Fe^{III}-O₂⁻ character. This Fe-O bond arises by electron transfer from heme-Fe^{II} to O₂ for the formation of a singlet state Fe^{III}-O₂⁻ Mb oxidized species that possesses a $\sigma(\text{Fe-O})$ bond and a weakly coupled $\pi(\text{Fe-O}_2)$ bond pair (8). How does this Mb-O₂ oxidation occur *in vivo*? For example, copper mediated Mb oxidation is of great interest, as this redox reaction plays a major role in the damage of the myocardium upon and after an ischemic shock (9-10).

Metals are essential for the normal function of several biological species, while they exert toxicity when they are present in excess. In a recent publication, Postnikova et al. (11) have proposed that the interaction of a Cu ion, in its hydrated or complex form, with the inner His97, and possibly with the distal His64, exerts a high contribution to the Mb oxidation reaction. His97 interacts with the heme propionate-7, while His64 is involved in a hydrogen bonding interaction at the distal site with the bound to the heme O₂. His97 is present in all animal myoglobins and the β chains of hemoglobin (Hb), which are all oxidized by copper ion, but absent in the Hb α chains resistant to the oxidation (12-13). In spite of the fact that the oxidation of respiratory proteins catalysed by copper ion has long been studied, its molecular mechanism is still unclear. The clarification of the role of the His97 residue in controlling the chemical properties of the Fe-O₂ bonding is of great importance for elucidating such mechanisms.

This work is focused on the role of His97 and heme propionate-6 in controlling Mb oxidation. We vary the protonation states of both His97 and propionate-6 in order to increase the amount of negative charges in the vicinity of the Fe-O₂ moiety and introduce some local conformational changes in the area (see refs. 3-4 for CcO inter-comparison). We describe the relationship between these negative charges, His97 conformational change and the Fe-O₂ bonding properties. The results show that His97 and the propionate-6 undertake a role with their involvement in determining Mb reactivity. DFT/MM methodology is used to probe different Mb-O₂ structures and their spectroscopic characteristics (8).

2 Computational Details

2.1 Computational Methods

The DFT/MM calculations were performed using QSite module of Schrödinger 2009 Suite of Programs (14). B3LYP functional and lacvp* basis set were used for the QM (Quantum Mechanical) part, while the OPLS2005 force field (FF) for the MM (Molecular Mechanical) part throughout this work. We prepared initial structures for the QM/MM calculations, by varying the protonation state of the propionate-6 or fully deprotonating His97. Starting coordinates were derived from the X-ray structure of the oxy sperm whale Mb (PDB code 2Z6S) (7). We have built complete models of the solvated Mb-O₂ protein by adding missing hydrogen atoms and an at least 14Å water buffer (TIP3P FF) between the protein matrix and the boundaries of the simulation box. Crystallographic waters, inside the protein structure, were retained before and after the solvation.

For each protein system, an initial minimization/ relaxation process was performed by Desmond Software of Schrödinger Suite 2009, before each QM/MM calculation, and it was based on the default protocol proposed in the Desmond manual (14). For the QM/MM geometries, after the minimization/ relaxation, we reduced the water buffer significantly by excluding every solvent molecule beyond a distance of 8 Å off the protein matrix and froze those waters beyond a 20 Å layer around the heme iron to their minimized positions. A cutoff distance of 100 Å was also set. The entire QM/MM system consisted of around 7640 atoms, including 5130 atoms in the solvent. The Hydrogen-cap approach was used for the covalent QM-MM boundary region, where hydrogen atoms are used to “cap” the QM cut/ unsaturated bonds. Gaussian charges were implemented to provide the electrostatic contribution from the MM part to the QM Hamiltonian. For the QM/MM calculations, our chosen QM part was comprised of the iron-oxy porphyrin complex (including all the side chains of heme), His64, His93 and His97, while the rest of the protein was treated by the empirical potential (OPLS2005 FF). The distal His64 formed a hydrogen bond with the O₂ coordinated to the heme iron. Propionate-7 was kept deprotonated for all structures. The ground state of oxy-Mb was set as an open-shell singlet state (8).

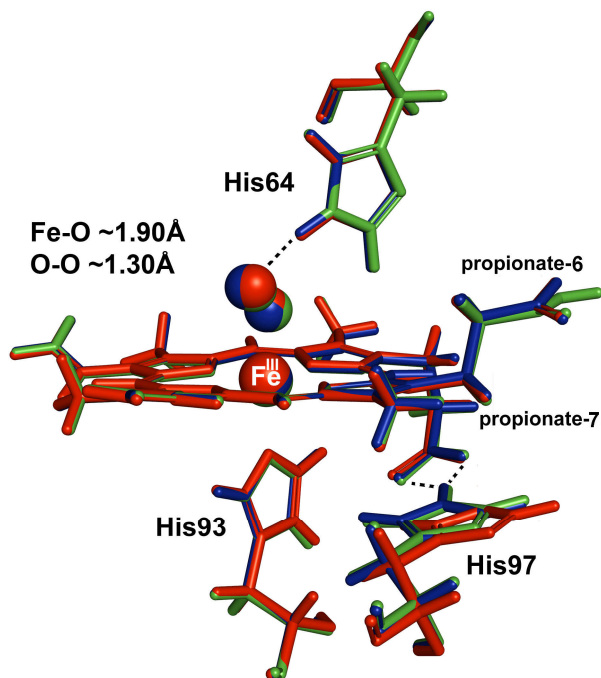


Fig. 4. Overlapping QM parts of QM/MM geometry optimized structures of Mb-O₂ with varying propionate-6/ His97 protonation states: green structure/ Propionate-6 protonated and His97 deprotonated, red structure/ both propionate-6 and His97 fully deprotonated, blue structure/ both propionate-6 and His97 deprotonated

2.2 Computational Efficiency

Simulated Systems contain more than 30K atoms with around 2000 basis sets for the quantum QM part (QM/MM methodology), while in certain cases (MD methodology) more than 80K atoms. This required 16-20 CPUs running in parallel per calculation for the QM/MM and the Molecular Dynamics package used. A common QM/MM simulation to be completed required around (20 days) \times (16 or 20 CPUs) = 320 or 400. This means (320 or 400) \times 24= 7680 or 9600 total core hours per calculation. This significant amount of computational time has to be multiplied by 16 QM/MM simulations. The computational time per MD simulation was half that of the QM/MM, nevertheless, concerning the number of MD runs (more than 50), this raised significantly the total computational time.

Schrodinger Suite of programs (14) (QSite for QM/MM and Desmond for MD) is adequately parallelized and runs on multiple architectures. The storage per calculation needed was around 10 GB per MD run and around 30 GB per QM/MM run, while the amount of memory per core allocated from the system was around 3GB.

QSite was using a large amount of storage space per run, as the code required a different copy of every input/ output file for each core used, generating multiple copies of the same file on the same storage device. A more efficient communication of the input/ output files between each core and a better storage algorithm would favor our highly parallelized run. The multiple file-copies communicated between each core were slowing down significantly not only our calculations, but also the overall performance of the computational cluster.

Desmond is a software package developed at D. E. Shaw Research (23) to perform high-speed molecular dynamics simulations of large systems on conventional commodity clusters. The code uses novel parallel algorithms and numerical techniques to achieve high performance and accuracy on platforms containing a large number of processors, but may also be executed on a single computer. Desmond and its source code are available without cost for non-commercial use by universities and other not-for-profit research institutions. The code uses novel parallel algorithms and numerical techniques to achieve high performance and accuracy on platforms containing a large number of processors. The parallelization is through MPI architecture. MD calculations were run on a Linux cluster combining 8 SunFire X4200 (2x Dual Core AMD Opteron 280 2.3 Ghz, 8x 4GB RAM) and 10 Dell PowerEdge 1950 (2x Quad Core Intel Xeon X5355 2.66Ghz 10x 16GB RAM) nodes, resulting in a total of 116 CPUs with the performance discussed earlier.

After scalability tests for both QSite and Desmond packages we found that the number of CPUS (16-20) for the QM/MM and MD calculations was the optimum run configuration for the systems under study, as a further increase on that number resulted in slower calculations. To obtain a better scalability for the MD Simulations we will compile the Desmond Software package for GRID application based on an efficient parallelization algorithm we have developed on EGEE-GRID (24).

3 Results and Discussion

The QM areas of the geometrically optimized QM/MM models, with varying protonation states of the propionate-6 and His97 sites, are shown in Fig. 4 in an overlapping scheme. A main structural distortion (at the His97 site), from the initial Mb x-ray crystal structure, appears on the case where His97 is fully deprotonated (total model charge of -3). This is observed by comparing Fig. 3 and 4. The above distortion is expected, as the accumulation of negative charges, in close proximity, strongly repel each other.

In order to study the properties of the Fe-O₂, we focus on the spectroscopic character of the Fe-O₂ bond. When vibrational frequencies are calculated by electronic structure theory, they can be improved by scaling factors. Such scaling factors depend on the level of electronic structure theory and the one-electron basis set. It has been established that calculated frequencies may be scaled in various ways (15). For example, one scaling factor is applied to reproduce the true harmonic frequencies, the true fundamental frequencies, or the zero point energy. A scaling factor of 0.85 has been applied to our QM/MM level derived frequencies (3). This lowers the absolute calculated numbers to the experimental ones from the literature (16). Evaluation of the Hessian and calculation of the vibrational frequencies at the same level of theory (b3lyp/lacvp* QM/ OPLS2005 MM region) showed two spectroscopically distinct Mb-O₂ species, dependent on the protonation states of propionate-6 and His97 with bands at a) $\nu(\text{Fe-O})=560\text{ cm}^{-1}$, $\nu(\text{O-O})=1200\text{ cm}^{-1}$ (both propionate-6 and His97 deprotonated, total model charge of -2) and b) $\nu(\text{Fe-O})=620\text{ cm}^{-1}$, $\nu(\text{O-O})=1160\text{ cm}^{-1}$ in all the other cases (green and red) of Fig. 4. The blue structure on Fig. 4, where both propionate-6 and His97 appear deprotonated with a total model charge of -2, exerts spectroscopic characteristics at 560 and 1200 cm⁻¹. This blue structure would be the main structure giving the experimental vibrational spectra observed at pH range 5-8. Although the structures (green and red, Fig. 4) giving rise to the same bands are significantly different, the calculated vibrational frequencies are affected by several factors like charges, conformational changes and resonances (see below). Enhancement or suppression of different factors could lead to the same spectrum.

We utilized the broken symmetry methodology (17) for the calculation of the spin populations on the Fe^{III}-O1-O2- moiety, while the NBO (Natural Bond Orbital) methodology for the charge population analysis (18). We observed that spin population on the oxygens is independent on the protonation states of the propionate-6 and His97 (O1=0.40/ O2=0.60). On the other hand, the heme iron spin population decreases from 1.05 (Fe charge +0.64) for the green structure of Fig. 4, with a total model charge of -1, down to 0.80 (Fe charge +1.14), when all sites appear fully deprotonated for the red structure of Fig. 4. In addition, the O-O bond becomes more polarized, with the O1-O2 charge separation ($\Delta Q=Q_{O1}-Q_{O2}$) to increase when we move to the fully deprotonated propionate-6/ His97 case which appears as the red structure on Fig. 4 with a model total charge of -3. In this latter case the distal oxygen exerts a $\Delta Q= -0.8$ compared to the directly bound on Fe oxygen.

The above results are consistent to the experimental study by Harada et al. (19), where it was proposed that the lack of the propionate-6, in a Mb heme mutant, induces

conformational changes in the area of the heme group and stabilizes the Fe-O₂ bond, while the removal of the propionate-7 does not cause a significant structural change in the residues of the distal and proximal sites. The latter exerts, instead, an electronic effect on the heme group and the properties of the Fe-His93 bond. The lack of the propionate-6, in the Mb heme mutant, accelerated the autoxidation from the oxygenated heme. In accordance to this, we have shown that by varying the protonation state of propionate-6, there are shifts on the Fe-O₂ spin and charge populations.

As mentioned before, we induced a deformation in the His97 area by choosing extreme deprotonation state of the His97 (fully deprotonated). This resulted in the His97 conformational change in the vicinity of Fe-O₂ in the red structure of Fig. 4. From the crystal structure, it seems that His97 stabilizes the heme position by hydrogen bonding interaction to propionate-7, but the mutation of propionate-7 to a -CH₃ group did not induce any significant conformational changes in the area (19). Another contribution to the stability of the heme cavity derives from the fact that its imidazole ring is parallel to the heme pyrrole rings. This interaction seems to be more important than that of the His97/ propionate-7. Both interactions are perturbed when His97 appears fully deprotonated as shown in Fig. 4. It should be noted that the perturbation on the His97 imidazole ring orientation may have induced the change in heme iron spin population and charge. Additionally, a deprotonated His97 as shown on our structures could be an extreme case, although it represents the polarization of the N δ -H imidazole bond in the cases where a positively charged metal ion (like Cu) would interact with that residue. Moreover, we have showed that the deprotonation of propionate-6 induced a stabilization of this Fe-O bond, by increasing the charge separation between Fe-O and O-O.

Compared to previous studies (8,20), we go further by fully deprotonating His97 residue. This enables us to observe enhanced changes in the electronic structures and charge distribution of the heme group, otherwise suppressed. Although such protonation states would not be easily observed in experimental results, there exist several theoretical studies on the normal pH range relevant to the pKa values observed for Mb (21). Nevertheless, it is important to follow the flow of such enhanced electronic density and the effects it has in the vicinity of His97. By enhancing the presence of negative charges from the deprotonation of His97, we make it easier to clarify the interactions in Mb. In theory we can probe extreme protonation cases, observe the charge and spin density changes, use the results to identify crucial, key interactions. These interactions are sometimes suppressed and are not easily observed when probing normal protonation states.

Our study shows that the Mb oxidation state is vulnerable to the His97 protonation state and/ or consequent conformational changes in the area. This indicates a possible target of Cu ion in the Cu mediated oxidation, adding to the proposed binding of the metal to His97 (11). His97 which is near the proximal His93 is capable of being titrated in the pH 5-8 range and partly accessible from the solvent. pK values of His97 have been reported in the literature at 5.55-5.9 (22). At pH < 6, when there is an increase of the oxidation rate at the presence of a Cu ion, the external histidines are protonated and His97 possibly, as proposed, takes action by binding the Cu ion (11). That local conformational change would possibly be disrupting the interaction of

His97 imidazole with the heme group, destabilizing the interaction. While we observe no significant effect on heme or His64 conformations, when His97–heme interaction is disturbed (Fig. 4) there is a spin population change on heme iron and a further effect on the Fe, O–O charges leading to the stabilization of the Fe^{III}-O₂⁻ species.

4 Conclusions and Comparison between CcO and Mb

In this study we have probed the effect of different protonation states of heme propionate-6 and His97 on the chemistry of Fe-O₂ of the oxy-myoglobin species. We follow the flow of the electronic density between key residues in Mb and also identify key sites as important switches to control Mb oxidation state. We provide a theoretical evidence for possible control points in Mb auto-oxidation. The heme propionate-6, as well as the His97 residue were found to play a key role in heme Fe oxidation, providing an indication of a target site of species controlling heme oxidation. In this study, we provide information on the role of His97 having a direct effect on the stabilization of the Fe^{III}-O₂⁻ moiety. Future work will be focused on QM/MM calculations with the QM part to include a Cu ion in different positions (coordination states) and oxidation levels in the Myoglobin, near the heme group.

Heme groups in Cytochrome *c* Oxidase and Myoglobin show a strong dependency on the protonation events in their vicinity. Protein matrix interactions with these heme groups, although different, show a similar spectroscopic effect. As negative charges increase around the heme groups, the $\nu(\text{Fe-O})$ modes appear at higher frequencies.

Acknowledgment. The work has been performed under the HPC-EUROPA2 project (number: 228398) with the support of the European Commission – Capacities Area - Research Infrastructures. V. D. is grateful to Prof. Guallar and to his research group for their hospitality and help at the Barcelona Super Computing Center, Life Sciences Department.

References

1. Ozaki, S.-I., Roach, M.P., Matsui, T., Watanabe, Y.: Investigations of the Roles of the Distal Heme Environment and the Proximal Heme Iron Ligand in Peroxide Activation by Heme Enzymes via Molecular Engineering of Myoglobin. *Acc. Chem. Res.* 34, 818–825 (2001)
2. Daskalakis, V., Farantos, S.C., Varotsis, C.: Assigning Vibrational Spectra of Ferryl-Oxo Intermediates of Cytochrome *c* Oxidase by Periodic Orbits and Molecular Dynamics. *J. Am. Chem. Soc.* 130, 12385–12393 (2008)
3. Daskalakis, V., Farantos, S.C., Guallar, V., Varotsis, C.: Vibrational Resonances and Cu_B Displacement Controlled by Proton Motion in Cytochrome *c* Oxidase. *J. Phys. Chem. B* 114, 1136–1143 (2010)
4. Daskalakis, V., Farantos, S.C., Guallar, V., Varotsis, C.: Regulation of Electron and Proton Transfer by the Protein Matrix of Cytochrome *c* Oxidase. *J. Phys. Chem. B* 115, 3648–3655 (2011)
5. Chu, K., Vojtchovsky, J., McMahon, B.H., Sweet, R.M., Berendzen, J., Schlichting, I.: Structure of a ligand-binding intermediate in wild-type carbonmonoxy myoglobin. *Nature* 403, 921–923 (2000)

6. Schotte, F., Lim, M., Jackson, T.A., Smirnov, A.V., Soman, J., Olson, J.S., Phillips Jr., G.N., Wulff, M., Anfinrud, P.A.: Watching a Protein as it Functions with 150-ps Time-Resolved X-ray Crystallography. *Science* 300, 1944–1947 (2003)
7. Unno, M., Chen, H., Kusama, S., Shaik, S., Ikeda-Saito, M.: Structural Characterization of the Fleeting Ferric Peroxo Species in Myoglobin: Experiment and Theory. *J. Am. Chem. Soc.* 129, 13394–13395 (2007)
8. Chen, H., Ikeda-Saito, M., Shaik, S.: Nature of the Fe–O₂ Bonding in Oxy-Myoglobin: Effect of the Protein. *J. Am. Chem. Soc.* 130, 14778–14790 (2008)
9. Berenshtein, E., Mayer, B., Goldberg, C., Kitrossky, N., Chevion, M.: Patterns of Mobilization of Copper and Iron Following Myocardial Ischemia: Possible Predictive Criteria for Tissue Injury. *J. Mol. Cell. Cardiol.* 29, 3025–3034 (1997)
10. Gunter, M.R., Sampath, V., Caughey, W.S.: Potential roles of myoglobin autoxidation in myocardial ischemia-reperfusion injury. *Free Radic. Biol. Med.* 26, 1388–1395 (1999)
11. Postnikova, G.B., Moiseeva, S.A., Shekhovtsova, E.A.: The Main Role of Inner Histidines in the Molecular Mechanism of Myoglobin Oxidation Catalyzed by Copper Compounds. *Inorg. Chem.* 49, 1347–1354 (2010)
12. Rifkind, J.M., Lauer, L.D., Chiang, S.C., Li, N.C.: Copper and oxidation of hemoglobin: a comparison of horse and human hemoglobins. *Biochemistry* 15, 5337–5343 (1976)
13. Christova, P.K., Devedzhiev, Y.D., Atanasov, B.P., Volkenshtein, M.V.: [Study of electron transfer in hemoproteins. IV. Oxidation of sperm whale oxymyoglobin catalyzed by copper ions]. *Mol. Biol. (Mosk.)* 14, 1088–1097 (1980)
14. <http://www.schrodinger.com>
15. Pople, J., Scott, A., Wong, M.: Scaling Factors for Obtaining Fundamental Vibrational Frequencies and Zero-Point Energies from HF/6-31G* and MP2/6-31G* Harmonic Frequencies. *Isr. J. Chem.* 33, 345–350 (1993)
16. Hirota, S., Li, T., Philips Jr., G.N., Olson, J.S., Mukai, M., Kitagawa, T.: Perturbation of the Fe–O₂ Bond by Nearby Residues in Heme Pocket: Observation of $\nu(\text{Fe-O}_2)$ Raman Bands for Oxymyoglobin Mutants. *J. Am. Chem. Soc.* 118, 7845–7846 (1996)
17. Noodleman, L.J.: Valence bond description of antiferromagnetic coupling in transition metal dimers. *Chem. Phys.* 74, 5737–5743 (1981); Noodleman, L., Peng, C.Y., Case, D.A., Mouesca Coord, J.M.: Orbital interactions, electron delocalization and spin coupling in iron-sulfur clusters. *Chem. Rev.* 144, 199–244 (1995)
18. Reed, A.E., Weinstock, R.B., Weinhold, F.: Natural Population Analysis. *J. Chem. Phys.* 83, 735–746 (1985)
19. Shibata, T., Nagao, S., Fukaya, M., Tai, H., Nagatomo, S., Morihashi, K., Matsuo, T., Hirota, S., Suzuki, A., Imai, K., Yamamoto, Y.: Effect of Heme Modification on Oxygen Affinity of Myoglobin and Equilibrium of the Acid–Alkaline Transition in Metmyoglobin. *J. Am. Chem. Soc.* 132, 6091–6098 (2010); Shikama K.: The Molecular Mechanism of Autoxidation for Myoglobin and Hemoglobin: A Venerable Puzzle. *Chem. Rev.* 98, 1357–1374 (1998); Allen, K.E., Cornforth, D.P.: Myoglobin Oxidation in a Model System as Affected by Nonheme Iron and Iron Chelating Agents. *J. Agric. Food Chem.* 54, 10134–10140 (2006); Murakami, T., Morishima, I., Matsui, T., Ozaki, S.-I., Hara, I., Yang, H.-J., Watanabe, Y.: Effects of the Arrangement of a Distal Catalytic Residue on Regioselectivity and Reactivity in the Coupled Oxidation of Sperm Whale Myoglobin Mutants. *J. Am. Chem. Soc.* 121, 2007–2011 (1999); Grunwald, E.W., Richards, M.P.: Mechanisms of Heme Protein-Mediated Lipid Oxidation Using Hemoglobin and Myoglobin Variants in Raw and Heated Washed Muscle. *J. Agric. Food Chem.* 54, 8271–8280 (2006)

20. Harada, K., Makino, M., Sugimoto, H., Hirota, S., Matsuo, T., Shiro, Y., Hisaeda, Y., Hayashi, T.: Structure and Ligand Binding Properties of Myoglobins Reconstituted with Monodepropionated Heme: Functional Role of Each Heme Propionate Side Chain. *Biochemistry* 46, 9406–9416 (2007)
21. Bashford, D., Case, D.A., Dalvit, C., Tennant, L., Wright, P.E.: Electrostatic calculations of side-chain pKa values in myoglobin and comparison with NMR data for histidines. *Biochemistry* 32, 8045–8056 (1993)
22. Carver, J.A., Bradbury, J.H.: Assignment of proton NMR resonances of histidine and other aromatic residues in met-, cyano-, oxy-, and (carbon monoxy) myoglobins. *Biochemistry* 23, 4890–4905 (1984)
23. <http://www.deshawresearch.com>
24. Daskalakis, V., Giatromanolakis, M., Porrini, M., Farantos, S.C., Gervasi, O.: Grid Computing Multiple Shooting Algorithms for Extended Phase Space Sampling and Long Time Propagation in Molecular Dynamics. *Computer Physics* 4, 1–18 (2011)

Theoretical and Experimental Study of the Energy and Structure of Fragment Ions Produced by Double Photoionization of Benzene Molecules

Marzio Rosi^{1,2}, Pietro Candori¹, Stefano Falcinelli^{1,*},
Maria Suelly Pedrosa Mundim³, Fernando Pirani⁴, and Franco Vecchiocattivi¹

¹ Department of Civil and Environmental Engineering,
University of Perugia,
Via Duranti 93, 06125 Perugia, Italy
marzio@unipg.it,
{atomo, stefano, vecchio}@dyn.unipg.it

² ISTM-CNR, University of Perugia,
Via elce di sotto 8, 06123 Perugia, Italy

³ Instituto de Física, Universidade Federal da Bahia,
40000 Salvador, Brasil
spedrosa@unb.br

⁴ Department of Chemistry, University of Perugia,
Via Elce di Sotto, 8, 06123 Perugia, Italy
pirani@dyn.unipg.it

Abstract. Theoretical calculations of the energy and structure of dissociation product ions have been performed to provide detailed information about the dynamics of the charge separation reactions following the photoionization event of benzene molecules. The calculations are in agreement with the experimental results obtained in a study where a time-of-flight mass spectrometer with a position sensitive ion detector has been used in the dissociative double ionization of benzene by UV synchrotron radiation.

Keywords: ab initio calculations, potential energy surfaces, fragmentation dynamics, photoionization.

1 Introduction

The properties of molecular dications are rather different from those of both singly charged ions and neutral molecules. In a solution, molecular dications are often stabilized by solvent interactions, however, in the gas phase they remain unstable in most cases. This is due to the strong coulombic repulsion between the two charges that can induce the dissociation of the molecular dication in two singly charged ions. However, in some cases the couplings by charge transfer effects can produce the formation of metastable states [1-5]. It follows that the dynamics and the lifetimes of these

* Corresponding author.

doubly charged metastable states can selectively affect several microscopic and macroscopic phenomena.

These doubly charged species play an important role in plasma chemistry and physics: a plasma may contain many molecular ions, and, under some conditions, molecular dications can be present in not negligible concentrations. Molecular dications are also present in the ionosphere [6] of the earth or of other planets and are of interest in interstellar clouds and in hot material surrounding star forming regions [7]. Theoretical calculations of the properties of molecular dications are far more difficult than similar calculations for neutral molecules or singly charged ions with equivalent numbers of electrons and nuclear masses. In fact, computing the properties of molecular dications typically requires full configuration interaction calculations using very large basis sets. The study of the dynamical characteristics of the dissociation reactions of these species, carried out at a molecular level, involves a detailed evaluation of the relative role of fundamental components of intermolecular interactions, with their strength, selectivity and anisotropy, that can strongly affect the stability, the energy barriers in the dissociation channels, the dication lifetime and the kinetic energy release of ion products. In particular, these characteristics depend not only on the coulombic repulsion, that is the dominant interaction component, but also on the critical balancing of other non covalent contributions, like size repulsion, induction, and dispersion attraction, and chemical contributions due to charge transfer effects. This aspect has been investigated in detail for relatively simple systems, like hydrogen halide dications as, for instance, HCl^{2+} [3,8], HBr^{2+} [5,9,10], HI^{2+} [11]. In these systems the metastability increases on going from HCl to HI because of the larger role of charge transfer coupling [4]. Very recently, we have also experimentally investigated the dissociation of N_2O [12,13], CO_2 [14,15], and benzene [16] dications, passing from simple diatomic to small polyatomic and aromatic molecules. The simplest mechanisms by which gas phase molecular dications can be produced are electron impact ionization, or double photo-ionization. Synchrotron radiation provides the possibility of studying the double-photo-ionization of molecules by a single photon, with high intensity light, allowing the observation of rather detailed features of the spectroscopy and dynamics of the parent ion and its fragments. For the systems mentioned above, the double ionization has been studied as a function of the photon energy, by measuring the ion products with time-of-flight mass spectrometry and, in the case of charge separation processes, by detecting in coincidence the two fragment ions. For HBr, we have also measured in coincidence the two threshold photoelectrons [10], obtaining interesting information about the low lying electronic and vibrational states of the molecular dication. In a recent paper [16] we have studied the benzene case, finding that the dication, once formed by double photoionization, that occurs with a threshold of 24.65 eV, it remains undissociated up to 27.8 eV, when the charge separation reaction



starts to occur. The second dissociative channel



opens at 29.5 eV, while a third process



starts at 30.2 eV. It has been observed, in early investigations [17,18], that the following symmetric dissociation



can also occur. However, in our recent experiment [16] we have been unable to clearly resolve this channel because the dication and the fragments provide in the mass spectrometer the same signal. Moreover, in such experiment it has been observed that channel (1) occurs also through a metastable state. The features of the coincidence data related to such a reaction can provide the lifetime of the metastable state by a statistical analysis. To do this, three main methods are presently available: one is based on a fit with some analytical functions [19], another one exploits a Monte Carlo simulation [19], while a generalized simulated annealing statistical method has been very recently proposed by our laboratory [20]. In order to provide additional information on the above mentioned charge separation reaction dynamics, we present in this paper an investigation of the double photoionization by synchrotron radiation of mono-deuterated benzene molecules. The analysis of this new set of photoelectron-photoion-coincidence data confirms the threshold and energy dependence of the processes (1), (2) and (3), and provide information on the isotopic variants of reaction (4). Moreover, we have analyzed the characteristics of the coincidence data related to reaction (1), with its isotopic variants, in order to obtain the lifetime of the benzene dication when dissociates *via* metastable states. In the previous recent paper [16] we have also reported on some theoretical calculations about the energetics and structure of involved molecular ions for the first three reactions. In the present study we have extended such a calculation also to the channel (4). The combination of experimental and theoretical data allow a deeper characterization of the dissociation dynamics of the benzene dication.

2 Experimental

The experiment has been carried out at the synchrotron light laboratory ELETTRA (Trieste, Italy) using the ARPES end station of the Gasphase Beamline. Details about the beamline, the end station and the used apparatus have been previously reported [12-15]. Only a brief description is given below. The energy selected synchrotron light beam crosses an effusive molecular beam of a helium/benzene gaseous mixture. The product ions are detected in coincidence with photoelectrons. The photon energy resolution provided by the grating-monochromator has been between 1.5 and 2.0 meV in the investigated 26-33 eV energy range. In order to avoid spurious effects, due to the ionization by high order diffraction photons, a magnesium film filter was placed in the synchrotron radiation beam. The molecular beam, the light direction and the ion detection axes are mutually perpendicular. The ion extraction and detection system has been assembled following the design described by Lavollée [21]. Such an arrangement allows the detection of the ion arrival position on the detector plate. Benzene is supplied to a needle beam source from a container kept at room temperature, where the vapor above the liquid is mixed with helium. This allows us to normalize all ion signals, at each photon energy, to the total ion yield of helium at that energy.

In Fig. 1 is reported the coincidence plot for monodeuterated benzene at 32.0 eV photon energy. Several similar plots have been obtained in the whole photon energy range investigated. The presence of a deuterium atom in the molecule produces the splitting of some of the mass spectrum peaks because the isotopic variants of product ions. This makes more complicated the analysis of such data, with respect to what it has been done in the previous work [16]. However, the reaction (4) is here quite evident (see location A in the lower panel of Fig. 1) and the analysis in terms of threshold and energy dependence becomes now possible. It has to be noted that in the case of the process (4) there is not a tail, indicating that the dissociation occurs only as “instantaneous”, that is within about 50 ns, as already discussed. The consistency of these data with those of the experiment with C_6H_6 has been checked, and we have done it for the energy threshold of processes (1), (2) and (3), obtaining values that are consistent, within the experimental uncertainty (± 0.1 eV), with those that we have very recently published for the non-deuterated benzene [16]. The thresholds have been extracted by the use of a Wannier function [24-26].

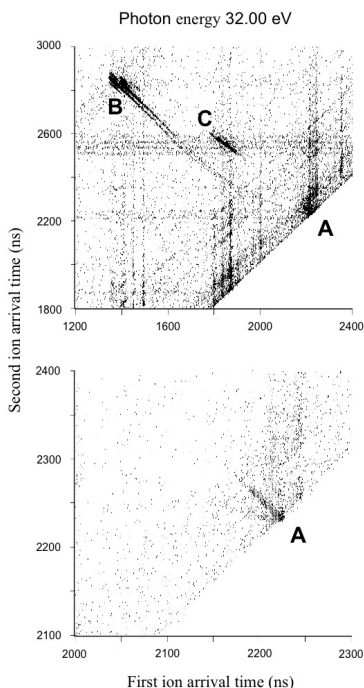


Fig. 1. In the upper part plot of coincidences at 32.0 eV photon energy for monodeuterated benzene. In the lower part: the coincidences around the location A are reported in an expanded scale. The points at the location A are a mixture of $C_3H_2D^+/C_3H_3^+$ coincidences and of the $C_6H_5D^{2+}$ dications. The points at the location B are the $C_5H_2D^+/CH_3^+$ coincidences, while those at C are $C_2H_2D^+/C_4H_3^+$ and $C_2HD^+/C_4H_4^+$ coincidences.

As an example, in Fig. 2 the cross sections measured for the channel (1) are reported. In this case two sets of products are formed: $\text{CH}_2\text{D}^+ + \text{C}_5\text{H}_3^+$ (open circles) and $\text{CH}_3^+ + \text{C}_5\text{H}_2\text{D}^+$ (full circles). In the figure it appears rather evident that the two isotopic variants show a very similar behavior, indistinguishable within the experimental uncertainty, that indicates a not appreciable isotopic effect for this dissociation reaction.

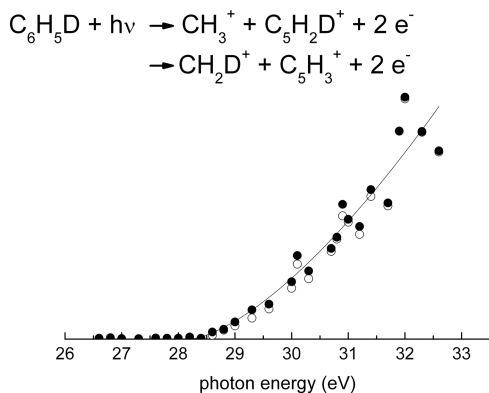


Fig. 2. Measured cross sections for the dissociation of $\text{C}_6\text{H}_5\text{D}^{2+}$ leading to $\text{CH}_2\text{D}^+ + \text{C}_5\text{H}_3^+$ (open circles) and $\text{CH}_3^+ + \text{C}_5\text{H}_2\text{D}^+$ (full circles). The two isotopic variants of products show a very similar behaviour. The line is the Wannier analysis for obtaining the threshold energy.

In Fig. 3 the cross sections for the process (4) are plotted as a function of the photon energy. The threshold is also in this case obtained by the use of a Wannier function [24-26], and a value of 30.1 ± 0.1 eV has been found, which is a value very close to that of reaction (3).

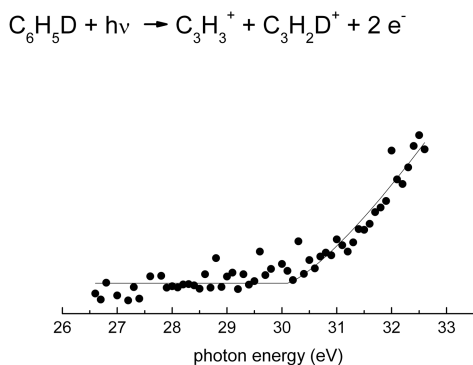


Fig. 3. Measured cross sections for the dissociation of $\text{C}_6\text{H}_5\text{D}^{2+}$ leading to $\text{C}_3\text{H}_2\text{D}^+ + \text{C}_3\text{H}_3^+$. The line is the Wannier analysis for obtaining the threshold energy.

However, one has to point out that all the threshold energies for these four channels are smaller than those reported by Richardson *et al.* [17] more than twenty years ago, as summarized in Table I where the present results, those of our recent paper [16] and the early ones [17], are compared. Moreover, the KER for reaction (4), obtained here by a vector analysis, as it has been done in our previous work [16], results to be 3.8 ± 0.1 eV (see Table 2).

Table 1. Dissociation reactions of the benzene dication

Products ^a	Appearance energy (eV)		
	<i>Ref. 17</i>	<i>Ref. 16</i>	<i>present work</i>
$C_3H_3^+ + CH_3^+$	28.4 ± 0.5	27.8 ± 0.1^b	28.0 ± 0.1
$C_4H_3^+ + C_2H_3^+$	31.3 ± 0.5	29.5 ± 0.1	29.6 ± 0.1
$C_4H_4^+ + C_2H_2^+$	---	30.2 ± 0.1	30.2 ± 0.1
$C_3H_3^+ + C_3H_3^+$	32.2 ± 0.5	---	30.1 ± 0.1

^a In the case of the present work, the monodeuterated benzene has been used and the products contain a deuterium atom.

^b This value is in agreement with Ref. 18.

For obtaining the lifetime of the metastable dication states leading to the dissociation (1), it is necessary to analyze the distribution of coincidence points along the tails connecting the spots in the location B and the dication peak at the location A in the results relative to the non deuterated and those for the monodeuterated, as reported in figure 1. However, in the case of the monodeuterated benzene, the tail becomes double, because the isotopic peaks, in the vicinities of the spot in B, merging in a single one in the vicinities of A.

Table 2. Kinetic Energy Released for dissociation reactions of the benzene dication

Products ^a	kinetic energy release - KER (eV)		
	<i>Ref. 17</i>	<i>Ref. 18</i>	<i>present work</i>
$C_3H_3^+ + CH_3^+$	3.0 ± 0.1	3.1	2.9 ± 0.1
$C_4H_3^+ + C_2H_3^+$	3.8 ± 0.1	---	3.2 ± 0.1
$C_4H_4^+ + C_2H_2^+$	---	---	3.5 ± 0.1
$C_3H_3^+ + C_3H_3^+$	4.2 ± 0.1	---	3.8 ± 0.1

In Fig. 4, the lifetimes as a function of the photon energy, obtained by the use of Monte Carlo analysis [19], are reported. Such results do not exhibit, within the experimental uncertainty, any energy dependence, being the average value of 0.75 ± 0.22 μ s.

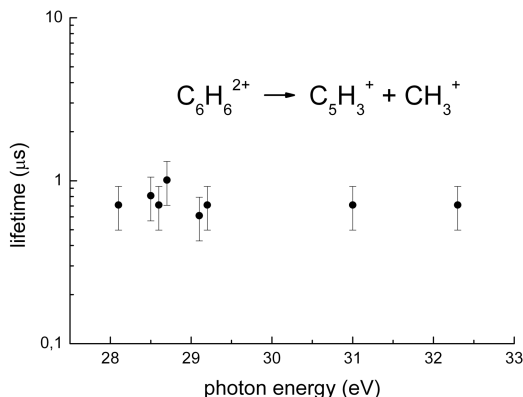


Fig. 4. Photon energy dependence of the lifetime for the dissociation of the metastable $C_6H_6^{2+}$ dication

3 Computational

The potential energy surface of the system $C_6H_6^{2+}$ and its fragmentation products was investigated by locating the lowest stationary points at the B3LYP [27] level of theory in conjunction with the 6-311+G(d) basis set. At the same level of theory we have computed the harmonic vibrational frequencies in order to check the nature of the stationary points, *i.e.* a minimum if all the frequencies are real, saddle point if there is one, and only one, imaginary frequency. The energy of all the stationary points was computed also at the higher level of calculation CCSD(T) [28] using the 6-311++G(3df,3pd) basis set. The B3LYP and the CCSD(T) energies were corrected to 298.15 K by adding the zero point energy correction and the thermal correction computed using the scaled harmonic vibrational frequencies evaluated at the B3LYP/6-311+G(d) level. All calculations were done using Gaussian 03 [29] while the analysis of the vibrational frequencies was performed using Molekel [30].

Early theoretical work suggested that the lowest energy level of the $C_6H_6^{2+}$ dication is a triplet state, although the singlet state is located just above, separated by only 0.02 eV [31]. A more recent evaluation found that the singlet state is the most stable one [32]. We have accurately investigated this point by appropriately extending the basis set and have found that the singlet state is the most stable one, although very close to the triplet. However, looking at the total spin multiplicity of the two product ions, we observe that this is a singlet, in all dissociation reactions observed in this work. This indicates that such reactions are more likely to originate from a singlet state dication, since the conservation of the total spin state can be assumed. In Fig. 5 the energy levels of the ionic products of the reactions that we have studied are reported for the various possible structures of the heavier products. Actually, the calculation provided the energy levels with respect to the ground state of the $C_6H_6^{2+}$ dication. The values listed in the figure are obtained by the assumption that the dication ground energy level is given by the experimental value of 24.65 eV [33]. These energy levels allow us to obtain further insight into the energetics of these dissociation reactions, when

they are considered together with the threshold energies and the kinetic energy released into the ionic products (see Tables 1 and 2). For the reaction (1) an internal energy of the products of about 0.9 eV can be obtained. For the reaction (2) the value of the internal energy appears to be over-estimated when the heavier product ion is assumed to be formed in the ground state geometry, while it appears to be more reasonable when the product is assumed to be formed in the highest energy structure. However, it is difficult to draw similar conclusions for the reaction (3) since the calculated structures are close in energy (see Table 2 and Fig. 5).

In order to study the dissociation reactions of $C_6H_6^{2+}$ into $C_5H_3^+ + CH_3^+$ and $C_3H_3^+ + C_3H_3^+$ we performed an optimization at B3LYP/6-311+G(d) level of the stationary points involved. The schematic reaction coordinate of these two dissociation reactions is shown in Fig.6, where we have reported the relative enthalpies at 298.15 K computed at CCSD(T)/6-311++G(3df,3pd) level. TS_3 and TS_4 which are true saddle points on the potential energy surface having only one imaginary frequency, lie slightly under the respective reactants when we include the zero point energy and the thermal corrections. The optimized structures, with the main geometrical parameters, of the minima and the saddle points are reported in Fig.6. For the sake of simplicity, in the following discussion we will consider only the more accurate CCSD(T) energies. Reaction (4) $C_6H_6^{2+} \rightarrow 2 C_3H_3^+$ is strongly exothermic being the $\Delta H^\circ_{298.15}$ computed to be -3.17 eV at CCSD(T)/6-311++G(3df,3pd) level. This dissociation proceeds with the opening of the $C_6H_6^{2+}$ ring which gives rise, through the saddle point TS_1 , to an open intermediate, which evolves to the products through the saddle point TS_2 . This mechanism is in agreement with the one previously reported by Anand and Schlegel [34]. The highest barrier is the second one which is 3.53 eV above $C_6H_6^{2+}$. Also reaction (1) $C_6H_6^{2+} \rightarrow C_5H_3^+ + CH_3^+$ is exothermic but its $\Delta H^\circ_{298.15}$ is much smaller, in absolute value, being -0.668 eV. However this reaction shows a lower barrier compared with the first one. Also this reaction starts with the opening of the $C_6H_6^{2+}$ ring through saddle points TS_1 , but after this initial process the reaction mechanism involves several intermediates. However the highest saddle point is the first, TS_1 , which is 2.70 (2.74) eV above $C_6H_6^{2+}$.

4 Discussion

It is possible to draw some important insights by joining the recent experimental results [16] about the double photoionization of C_6H_6 , the present ones, about C_6H_5D , and the theoretical calculations here reported. It appears that the benzene molecule is doubly ionized and remains undissociated from 24.65 eV up to about 28 eV, on the time scale of our experiment. At photon energies higher than 28 eV, the dissociation (1) producing $C_5H_3^+/CH_3^+$ occurs, involving also a metastable channel. *Ab initio* calculations indicate that all dissociation channels in this range of energy involve an opening of the $C_6H_6^{2+}$ ring. The metastability of reaction (1) could be attributed to the fact that, during the ring opening and rearrangement, two hydrogen nuclei must be transferred to form the final dissociation products. It is interesting to note that the present results appear consistent with the lower probability for the CH_2D^+ formation channel, a slight trend also shown by our data. The lifetime of the metastable channel

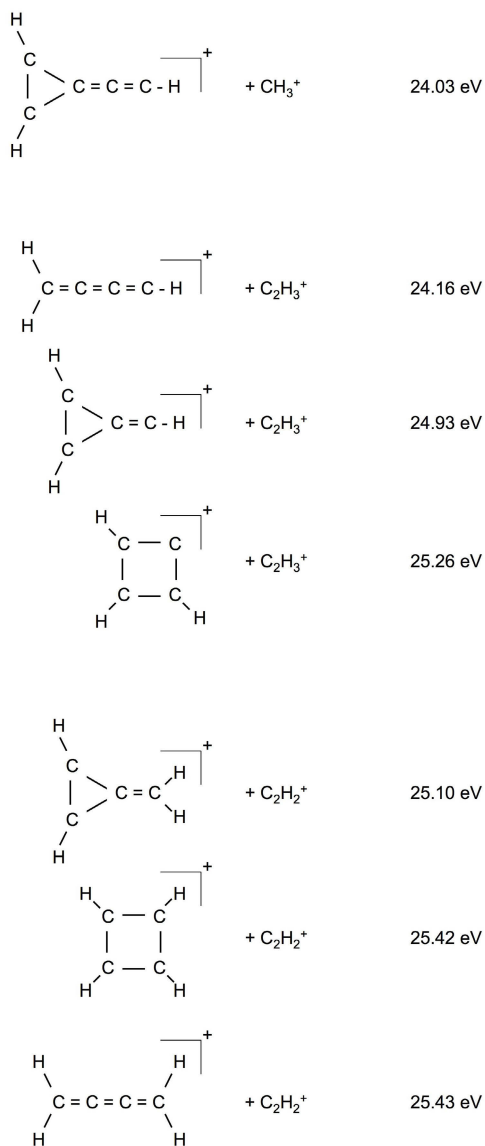


Fig. 5. Energy and structure of the product ions as obtained by theoretical calculations. The energy was calculated with respect to the benzene dication ground state and scaled by the use of the experimental value of 24.65 eV.

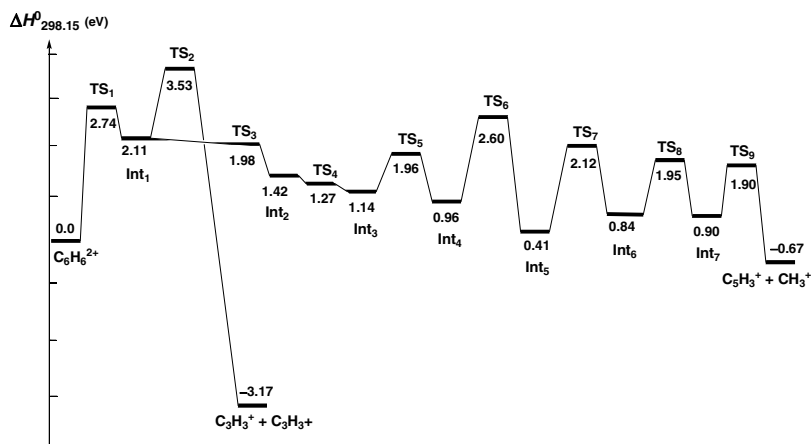


Fig. 6. Profile of the enthalpy changes at 298.15 K, computed at CCSD(T)/6-311++G(3df,3pd) level, for the two dissociation reactions $C_6H_6^{2+} \rightarrow C_3H_3^+ + C_3H_3^+$ and $C_6H_6^{2+} \rightarrow C_5H_3^+ + CH_3^+$. For the labels of saddle points and minima, see Figs. 7 and 8.

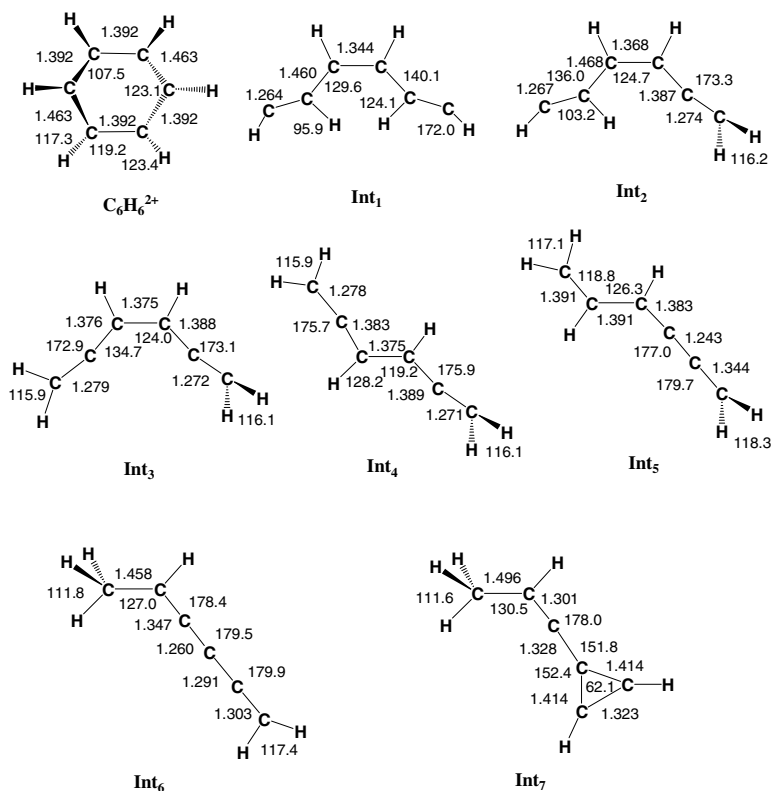


Fig. 7. B3LYP/6-311+G(d) optimized geometries (in Å and degrees) of the main stationary points investigated: minima

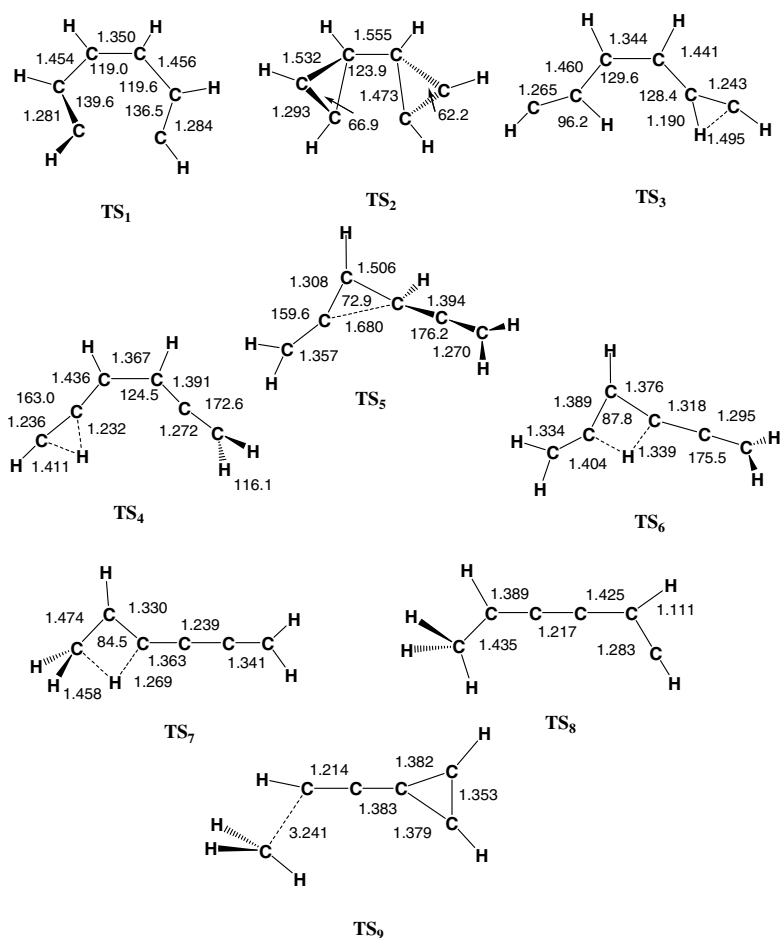


Fig. 8. B3LYP/6-311+G(d) optimized geometries (in Å and degrees) of the main stationary points investigated: saddle points

of this reaction has been found to be not affected by the photon energy. This observation suggests that this channel could be dominated by a vertical transition, leading to the dissociation of the dication. At a photon energy of about 29.5 eV a dissociation leading to $C_4H_3^+/C_2H_3^+$ also occurs, while at about 30.1 eV the two channels leading to $C_4H_4^+/C_2H_2^+$ and $C_3H_3^+/C_3H_3^+$ start to open. The first two processes are instantaneous, *i.e.* occurring in a time shorter than ~ 50 ns, while a contribution of metastable states to the third channel cannot be excluded based on our data. It has to be noted that the experimental threshold energies cannot be compared with the features of the calculated minimum energy path: as it is well known, the experimental values are the average over energy distributions connected with the many possible dissociations paths. However, a comparison of the energy levels of final products, provided by *ab initio* calculations, with the experimental threshold energies and with the product ion KER values, strongly suggests that the dissociation ion products are formed with an

high internal energy content, that can be structural, electronic, vibrational and rotational. As an example, the reaction (4) exhibits an exothermicity of -3.17 eV, a threshold of 5.5 eV and a KER of 3.8 eV, with respect to the molecular dication. This leads to an excess energy of 4.9 eV, which cannot be only vibrational and rotational. As already noted above, channels (1) and (2) require the movement of respectively two and one hydrogen nuclei. The channels (3) and (4) do not require instead any atom migration and they are simply promoted by the removal of two electrons from one of the two degenerate HOMOs of benzene. It is interesting to note that when two electrons are removed from the HOMOs, if they are from each one of the two orbitals, a triplet state is formed, with an almost planar structure. On the other side, if the two electrons are spin coupled, they are removed from one of the two degenerate orbitals and a singlet state, with the formation of a distorted ring structure. In a recent paper [33], Eland reports the spectrum of benzene dication produced by double photoionization. The analysis of such a spectrum, when combined with some calculated energy levels [31], appears to be consistent with the formation of the dication in a triplet ground state.

However, other more recent theoretical works [32,34] found that the ground state is a singlet. In all calculations the low lying triplet and singlet states appear to be very close in energy [31,32,34]. The present theoretical results confirm that the most stable state is a singlet one. It has also to be noted, when looking at the spin of product ions, that the dissociative channels here studied are consistent with a precursor dication in a singlet state. Obviously, triplet and singlet states can be formed in the investigated photon energy range, but only the singlet is involved in the dissociation channels. We believe that all this information is important for a better understanding of the phenomena where double photoionization and fragmentation of benzene are involved.

5 Conclusions

The double photoionization of benzene molecules has been studied in the 26-33 eV energy range. The dissociative channel leading to $\text{CH}_3^+ + \text{C}_5\text{H}_3^+$ opens at 27.8 eV, while the onset for channels leading to $\text{C}_2\text{H}_3^+ + \text{C}_4\text{H}_3^+$ and $\text{C}_2\text{H}_2^+ + \text{C}_4\text{H}_4^+$ are at 29.5 and 30.2 eV, respectively. The first channel remains dominant in the whole investigated energy range, while the third appears to be always the least effective one. These reactions have also been characterized by studying theoretically energy, structure and spin multiplicity of the dication and of the dissociation product ions.

Combining these results with the observed kinetic energy release into the products it has been possible to obtain new information about the most probable structure and internal energy of final ions. The main dissociation channel, namely the one producing $\text{CH}_3^+ + \text{C}_5\text{H}_3^+$, appears to proceed via "metastable" ion formation, with the precursor dication $\text{C}_6\text{H}_6^{2+}$ exhibiting a lifetime longer than the characteristic detection time of our instrument (~50 ps). The lifetime is shorter in both the other two dissociation reactions. This can be easily rationalized considering that such a "metastable" dissociation channel requires a rearrangement of two C-H bonds with a following transfer of two hydrogen atoms.

The measurement of the same processes also with mono-deuterated benzene allowed us not only an improvement of the statistics of the collected data, in order to better study the precursor dication lifetime, but also the investigation of the symmetric dissociation leading to $C_3H_2D^+ + C_3H_3^+$, a channel not resolved in the previous work [16]. It appears that the benzene molecules are doubly ionized and remain undissociated from 24.65 eV up to about 28 eV. At photon energies higher than the latter one, the dissociation (1) producing $C_5H_3^+ / CH_3^+$ occurs, involving also a metastable channel. The *ab initio* calculations indicate that all dissociation channels, in this range of energy, involve an opening of the $C_6H_6^{2+}$ ring. The metastability of reaction (1) could be attributed to the fact that, during the ring opening and rearrangement, two hydrogen nuclei must be transferred to form the final dissociation products. It is also interesting to note that the present results do not exhibit isotopic effects, appreciable under the experimental conditions that we have exploited. The lifetime of the metastable channel of this reaction has been found to be not affected by the photon energy. This observation suggests that this channel could be dominated by a vertical transition, leading to a dissociating dication. At a photon energy of about 29.5 eV a dissociation leading to $C_4H_3^+ / C_2H_3^+$ also occurs, while at about 30.1 eV the two channels leading to $C_4H_4^+ / C_2H_2^+$ and $C_3H_3^+ / C_3H_3^+$ start to be open. All these three processes are instantaneous, *i.e.* occurring in a time shorter than ~ 50 ns. A comparison of the energy levels of final products, provided by *ab initio* calculations, with the experimental threshold energies and with the product ion KER values, strongly suggests that the dissociation ion products are formed with an high internal energy content, that can be structural, electronic, vibrational and rotational. As an example, the reaction (4) exhibits an exothermicity of -3.17 eV, a threshold of 5.5 eV and a KER of 3.8 eV, with respect to the molecular dication. This leads to an excess energy of 4.9 eV, that cannot be only vibrational and rotational. All these informations can be useful for understanding the phenomena where double photoionization and fragmentation of benzene can be of importance as they are mentioned in the introduction. An interesting development can be the study, for C_6H_6 and C_6D_6 , of the threshold photoelectron-photoelectron coincidence spectrum, as we have already done recently for other molecules [10], in order to characterize the internal states of the benzene dication.

Acknowledgment. Financial contributions from the MIUR (Ministero dell'Istruzione, dell'Università e della Ricerca) are gratefully acknowledged. We acknowledge partial travel support by the "Sincrotrone Trieste S.C.p.A.". We wish to thank the "Fondazione Cassa di Risparmio di Perugia" for financial support. The authors are grateful to Prof. S. Fornarini, Università di Roma "La Sapienza", who, very kindly, provided us with mono-deuterated benzene and to the ION-CNR TASC Laboratory for financial support at Gasphase beamline. P.C. gratefully acknowledge financial support by Regione Umbria, project POR UMBRIA FSE 2007-2013 Asse II "Occupabilità", Obiettivo specifico "e" - Asse IV "Capitale Umano", Obiettivo specifico "I".

References

1. Pauling, L.: J. Chem. Phys. 1, 56 (1933)
2. Cox, S.G., Critchley, A.D.J., Kreymin, P.S., McNab, I.R., Shiellx, R.C., Smith, F.E.: Phys. Chem. Chem. Phys. 5, 663 (2003)

3. Moix-Teixidor, M., Pirani, F., Candori, P., Falcinelli, S., Vecchiocattivi, F.: *Chem. Phys. Lett.* 379, 139 (2003)
4. Candori, P., Falcinelli, S., Pirani, F., Tarantelli, F., Vecchiocattivi, F.: *Chem. Phys. Lett.* 436, 322 (2007)
5. Alagia, M., Brunetti, B.G., Candori, P., Falcinelli, S., Moix-Teixidor, M., Pirani, F., Richter, R., Stranges, S., Vecchiocattivi, F.: *J. Chem. Phys.* 120, 6985 (2004)
6. Prasad, S.S., Furman, D.R.: *J. Geophys. Res.* 80, 1360 (1975)
7. Rosner, S.D., Cameron, R., Scholl, T.J., Holt, R.A.: *J. Mol. Spectrosc.* 189, 83 (1998)
8. Alagia, M., Biondini, F., Brunetti, B.G., Candori, P., Falcinelli, S., Moix-Teixidor, M., Pirani, F., Richter, R., Stranges, S., Vecchiocattivi, F.: *J. Chem. Phys.* 121, 10508 (2004)
9. Alagia, M., Boustimi, M., Brunetti, B.G., Candori, P., Falcinelli, S., Richter, R., Stranges, S., Vecchiocattivi, F.: *J. Chem. Phys.* 117, 1098 (2002)
10. Alagia, M., Brunetti, B.G., Candori, P., Falcinelli, S., Moix-Teixidor, M., Pirani, F., Richter, R., Stranges, S., Vecchiocattivi, F.: *J. Chem. Phys.* 120, 6980 (2004)
11. Alagia, M., Brunetti, B.G., Candori, P., Falcinelli, S., Moix-Teixidor, M., Pirani, F., Richter, R., Stranges, S., Vecchiocattivi, F.: *J. Chem. Phys.* 124, 204318 (2006)
12. Alagia, M., Candori, P., Falcinelli, S., Lavollée, M., Pirani, F., Richter, R., Stranges, S., Vecchiocattivi, F.: *Chem. Phys. Lett.* 432, 398 (2006)
13. Alagia, M., Candori, P., Falcinelli, S., Lavollée, M., Pirani, F., Richter, R., Stranges, S., Vecchiocattivi, F.: *J. Chem. Phys.* 126, 201101 (2007)
14. Alagia, M., Candori, P., Falcinelli, S., Lavollée, M., Pirani, F., Richter, R., Stranges, S., Vecchiocattivi, F.: *J. Phys. Chem. A* 113, 14755 (2009)
15. Alagia, M., Candori, P., Falcinelli, S., Lavollée, M., Pirani, F., Richter, R., Stranges, S., Vecchiocattivi, F.: *Phys. Chem. Chem. Phys.* 12, 5389 (2010)
16. Alagia, M., Candori, P., Falcinelli, S., Pirani, F., Pedrosa Mundim, M.S., Richter, R., Rosi, M., Stranges, S., Vecchiocattivi, F.: *Phys. Chem. Chem. Phys.* 13, 8245 (2011)
17. Richardson, P.J., Eland, J.H.D., Lablanquie, P.: *Org. Mass Spectrom.* 21, 289 (1986)
18. Holland, D.M.P., Shaw, D.A., Sumner, I., Bowler, M.A., Mackie, R.A., Shpinkova, L.G., Cooper, L., Rennie, E.E., Parker, J.E., Johnson, C.A.F.: *Int. J. Mass Spectrom.* 220, 31 (2002)
19. Field, T.A., Eland, J.H.D.: *Chem. Phys. Lett.* 211, 436 (1993)
20. Alagia, M., Candori, P., Falcinelli, S., Mundim, K.C., Mundim, M.S.P., Pirani, F., Richter, R., Stranges, S., Vecchiocattivi, F.: *Chem. Phys.* (2011), doi:10.1016/j.chemphys.03.031
21. Lavollée, M.: *Rev. Sci. Instrum.* 70, 2968 (1999)
22. Hsieh, S., Eland, J.H.D.: *J. Phys. B: At. Mol. Opt. Phys.* 30, 4515 (1997)
23. Slattery, A.E., Field, T.A., Ahmad, M., Hall, R.I., Lambourne, J., Penent, F., Lablanquie, P., Eland, J.H.D.: *J. Chem. Phys.* 122, 084317 (2005)
24. Wannier, G.H.: *Phys. Rev.* 90, 817 (1953)
25. Eckhardt, B., Sacha, K.: *Europhys. Lett.* 56, 651 (2001)
26. Denifl, S., Candori, P., Ptasinska, S., Limão-Vieira, P., Grill, V., Märk, T.D., Scheier, P.: *Eur. Phys. J. D* 35, 391–398 (2005)
27. Becke, A.D.: *J. Phys. Chem.* 98, 5648 (1993); Stephens, P.J., Devlin, F.J., Chabrowski, C.F., Frisch, M.J.: *J. Phys. Chem.* 98, 11623 (1994)
28. Bartlett, R.J.: *Annu. Rev. Phys. Chem.* 32, 359 (1981); Raghavachari, K., Trucks, G.W., Pople, J.A., Head-Gordon, M.: *Chem. Phys. Lett.* 157, 479 (1989); Olsen, J., Jorgensen, P., Koch, H., Balkova, A., Bartlett, R.J.: *J. Chem. Phys.* 104, 8007 (1996)

29. Frisch, M.J., Trucks, G.W., Schlegel, H.B., Scuseria, G.E., Robb, M.A., Cheeseman, J.R., Montgomery Jr., J.A., Vreven, T., Kudin, K.N., Burant, J.C., Millam, J.M., Iyengarms, S.S., Tomasi, J., Barone, V., Mennucci, B., Cossi, M., Scalmani, G., Rega, N., Petersson, G.A., Nakatsuji, H., Hada, M., Ehara, M., Toyota, K., Fukuda, R., Hasegawa, J., Ishida, M., Nakajima, T., Honda, Y., Kitao, O., Nakai, H., Klene, M., Li, X., Knox, J.E., Hratchian, H.P., Cross, J.B., Bakken, V., Adamo, C., Jaramillo, J., Gomperts, R., Stratmann, R.E., Yazyev, O., Austin, A.J., Cammi, R., Pomelli, C., Ochterski, J.W., Ayala, P.Y., Morokuma, K., Voth, G.A., Salvador, P., Dannenberg, J.J., Zakrzewski, V.G., Dapprich, S., Daniels, A.D., Strain, M.C., Farkas, O., Malick, D.K., Rabuck, A.D., Raghavachari, K., Foresman, J.B., Ortiz, J.V., Cui, Q., Baboul, A.G., Clifford, S., Cioslowski, J., Stefanov, B.B., Liu, G., Liashenko, A., Piskorz, P., Komaromi, I., Martin, R.L., Fox, D.J., Keith, T., Al-Laham, M., Peng, C.Y., Nanayakkara, A., Challacombe, M., Gill, P.M.W., Johnson, B., Chen, W., Wong, M.W., Gonzalez, C., Pople, J.A.: Gaussian 03, Revision D.01, Gaussian, Inc., Wallingford, CT (2004)
30. Flükiger, P., Lüthi, H.P., Portmann, S., Weber, J.: Molekel, 4.3, Swiss Center for Scientific Computing, Manno (Switzerland) (2000-2002); Portmann, S., Lüthi, H.P.: *Chimia* 54, 766 (2000)
31. Tarantelli, F., Sgamellotti, A., Cederbaum, L.S., Schirmer, J.: *J. Chem. Phys.* 86, 2201 (1987)
32. Rosi, M., Bauschlicher Jr., C.W., Bakes, E.L.O.: *Astrophys. J.* 609, 1192 (2004)
33. Eland, J.H.D.: *Chem. Phys.* 345, 82 (2008)
34. Anand, S., Schlegel, H.B.: *J. Phys. Chem. A* 109, 11551 (2005)

Theoretical Study of Reactions Relevant for Atmospheric Models of Titan: Interaction of Excited Nitrogen Atoms with Small Hydrocarbons

Marzio Rosi^{1,2,*}, Stefano Falcinelli¹, Nadia Balucani³,
Piergiorgio Casavecchia³, Francesca Leonori³, and Dimitris Skouteris³

¹ Department of Civil and Environmental Engineering,
University of Perugia, Via Duranti 93, 06125 Perugia, Italy
marzio@unipg.it, stefano@dyn.unipg.it

² ISTM-CNR

³ Department of Chemistry, University of Perugia, Italy
nadia.balucani@unipg.it,
{piro,leonori}@dyn.unipg.it,
dimitris@impact.dyn.unipg.it

Abstract. The potential energy surface of the systems $N(^2D) + CH_4$, C_2H_4 , and C_2H_6 have been investigated at B3LYP/aug-cc-pVTZ//CCSD(T)/aug-cc-pVTZ level in order to assist the interpretation of available experimental information very relevant for its implication for the chemical models of the atmosphere of Titan, and possibly of objects where both N_2 and small hydrocarbons like methane are present, such as Triton and Pluto.

Keywords: ab initio calculations, potential energy surfaces, atmospheric models.

1 Introduction

Chemical reactions involving atomic nitrogen are of relevance in a variety of natural environments, such as the upper terrestrial atmosphere [1] and the atmospheres of other planets [2], in particular Titan, the largest moon of Saturn, which is the only solar system body to have a dense atmosphere mainly composed of molecular nitrogen like the Earth [3-5]. The second most abundant molecule in the atmosphere of Titan is methane [5, 6]. In those conditions, it is intuitive that the formation of nitriles (observed in trace amounts by the Cassini-Huygens mission) is initiated by some reactions of active forms of nitrogen – such as nitrogen atoms or ions – which can be produced in the upper atmosphere from the dissociation of the abundant parent molecule N_2 . Nitrogen ions are expected to play a significative role in the ionosphere of Titan [7, 8], which has recently revealed a rich chemistry [9], but below that, since there are practically no radicals that are able to react with undissociated N_2 molecules, a major role in the formation of C–N bonds has to be played by atomic nitrogen. In particular, atomic

* Corresponding author.

nitrogen can be produced by several N_2 dissociation processes. Detailed information about the predissociation probabilities and product state distributions for the excited states of N_2 is therefore fundamental to establish the role of these processes in producing atomic nitrogen in the atmosphere of Earth and of other N_2 dominated atmospheres. The production of N atoms in the 2D state is an important fact, because $N(^4S)$ atoms exhibit very low reactivity with closed-shell molecules and the probability of collision with an open-shell radical is small. On the contrary the reactions of $N(^2D)$ with several molecules identified in the atmosphere of Titan (including the relatively abundant CH_4) can give an important contribution to the chemical evolution of the atmosphere. The reactions involving atomic nitrogen are of relevance also for applied processes, where molecular nitrogen is deliberately introduced or present because it is the main component of air. Although kinetic studies are available [1,10] and reaction mechanisms have been speculated from rate constants, a better knowledge of the reactive behavior of atomic nitrogen requires an investigation of the reaction dynamics of these processes. The dynamics of the H-displacement channels in the reactions $N(^2D) + CH_4$ [11], $N(^2D) + C_2H_4$ [12] and $N(^2D) + C_2H_6$ [13] have been investigated by the crossed molecular beam technique with mass spectrometric detection and time-of-flight analysis at different collision energies. In order to assist the interpretation of these scattering results *ab initio* electronic structure calculations of the ground state doublet potential energy surfaces (PES) of the systems CH_4N , C_2H_4N and C_2H_6N have been performed.

2 Computational Details

The potential energy surfaces of the systems $N(^2D) + CH_4$, C_2H_4 and C_2H_6 were investigated by locating the lowest stationary points at the B3LYP [14] level of theory in conjunction with the correlation consistent valence polarized set aug-cc-pVTZ [15]. At the same level of theory we have computed the harmonic vibrational frequencies in order to check the nature of the stationary points, *i.e.* minimum if all the frequencies are real, saddle point if there is one, and only one, imaginary frequency. The assignment of the saddle points was performed using intrinsic reaction coordinate (IRC) calculations [16]. The energy of all the stationary points was computed at the higher level of calculation CCSD(T) [17] using the same basis set aug-cc-pVTZ. Both the B3LYP and the CCSD(T) energies were corrected to 0 K by adding the zero point energy correction computed using the scaled harmonic vibrational frequencies evaluated at B3LYP/aug-cc-pVTZ level. The energy of $N(^2D)$ was estimated by adding the experimental [18] separation $N(^4S) - N(^2D)$ of 230.0 kJ/mol to the energy of $N(^4S)$ at all levels of calculation. Thermochemical calculations were performed at the W1 [19] level of theory for the most relevant stationary points. All calculations were done using Gaussian 03 [20] while the analysis of the vibrational frequencies was performed using Molekel [21].

3 Results and Discussion

3.1 $N(^2D) + CH_4$

The lowest stationary points localized on the potential energy surface of $N(^2D)+CH_4$ have been reported in Figure 1, where the main geometrical parameters (distances/

Å and angles/°) are shown together with the energies computed at B3LYP/aug-cc-pVTZ, CCSD(T)/aug-cc-pVTZ and W1 level, relative to that of N(²D) + CH₄. A schematic representation of the potential energy surface of the N(²D)+CH₄ system is shown in Figure 2. For the sake of simplicity in Figure 2 we have reported only the relative energies computed at CCSD(T) level. Many of the stationary points which are of interest in this work have been previously reported by Kurosaki *et al.* [22] and Jursic [23]. Kurosaki *et al.* optimized the geometries at MP2(full)/cc-pVTZ level of theory and computed the energies at PMP4(full,SDTQ)/cc-pVTZ level, while Jursic performed mainly CBS-Q calculations. The agreement of our work with their results is generally good, the small differences being due to the different methods employed. In the following paragraph we will discuss our results; for simplicity we will refer only to the CCSD(T) results. From Figure 2 we can see that the interaction of N(²D) with CH₄ gives rise to the species CH₃NH which is more stable than the reactants by 427.6 kJ/mol. For this insertive approach we have found a saddle point which is, however, below the reactants both at B3LYP and CCSD(T) level of calculation. The presence of saddle points below the reactants has already been observed for very exothermic reactions, in particular involving methane [24]. However, since we were not successful in localizing a stable initial complex, the energy of this saddle point does not seem to be very meaningful. We tried also to localize this saddle point at MP2 level of calculations, but we did not succeed. Notably, this saddle point was computed at several levels of calculations by Takayanagi *et al.* [22, 25] and their best estimate for the barrier height was calculated to be only 5.3 kJ/mol above the reactants. More recently, Ouk *et al.* [26] computed a barrier of 3.86 ± 0.84 kJ/mol with a multi-state multi-reference configuration interaction method. Once formed after N(²D) insertion into a C-H bond, CH₃NH can either isomerize to species CH₂NH₂, which is the most stable isomer of the CH₄N PES, with a barrier of 154.2 kJ/mol or can directly dissociate to CH₂NH and H products through a slightly lower barrier of 141.4 kJ/mol. The other CH₃NH dissociation channels, *i.e.* those leading to CH₃+NH or CH₃N+H, are both barrierless, but they are very endothermic with respect to CH₃NH, being the dissociation energies 306.9 and 343.0 kJ/mol, respectively. The products CH₃ + NH can be reached also directly from N(²D) + CH₄ through an hydrogen abstraction process with a saddle point which lies 60.4 kJ/mol below the reactants. Also in this case we were not able to localize any stable initial complex. The geometry of this saddle point is comparable to that obtained by Jursic [23]. In principle, CH₃N can be formed either in a triplet or in a singlet state. According to the present calculations, however, only the triplet state can be formed, because the singlet methylnitrene (\tilde{a}^1E) is too high in energy ($\Delta E=130.4\pm 1.1$ kJ/mol) [27]. Once formed by CH₃NH isomerization, CH₂NH₂ can also lose one H atom giving rise to the isomers CH₂NH (with an exit barrier of 163.8 kJ/mol) or CHNH₂ (in a very endothermic, 299.0 kJ/mol, barrierless process). CH₂NH₂ can also dissociate into CH₂(³B₁, ¹A₁)+NH₂: these barrierless dissociation channels are endothermic by 404.5 and 443.6 kJ/mol for the triplet and singlet CH₂ formation, respectively. Finally we have located a small barrier (34.2 kJ/mol) for the reaction of the CH₂NH product with its co-fragment H to produce CHNH + H₂. This reaction is exothermic by 34.7 kJ/mol.

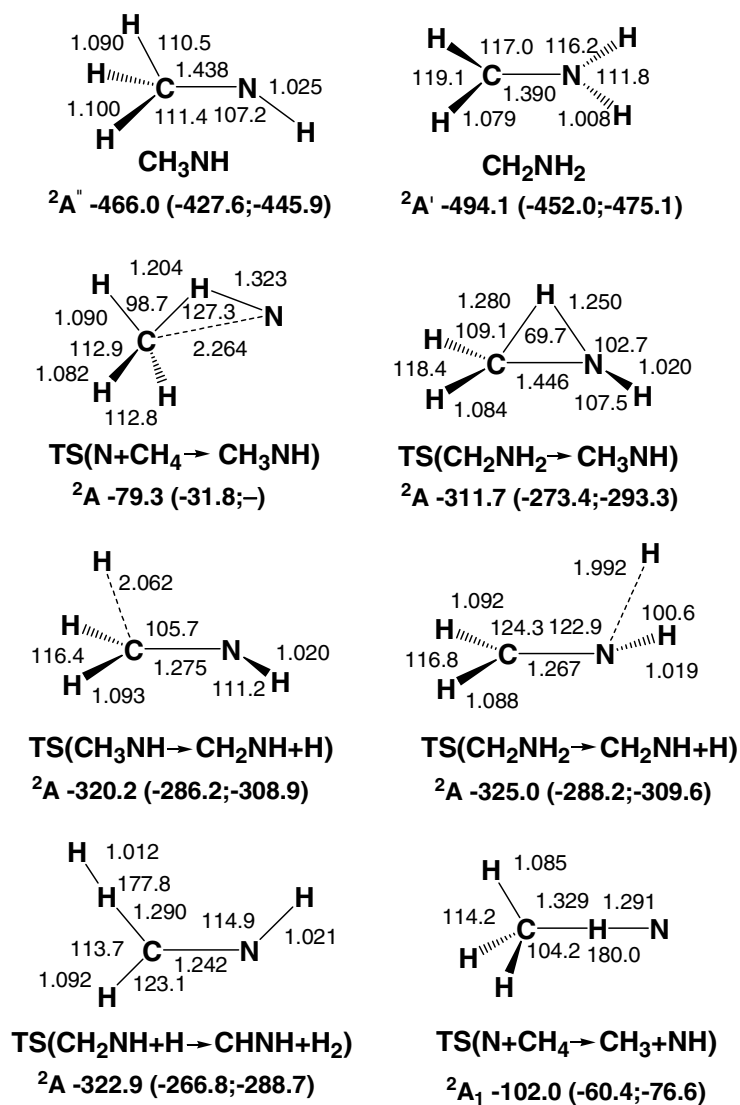


Fig. 1. B3LYP optimized geometries (Å and °) and relative energies with respect to N(²D) + CH₄ (kJ/ mol) at 0 K of minima and saddle points localized on the PES of N(²D) + CH₄; CCSD(T) and W1 relative energies are reported in parentheses

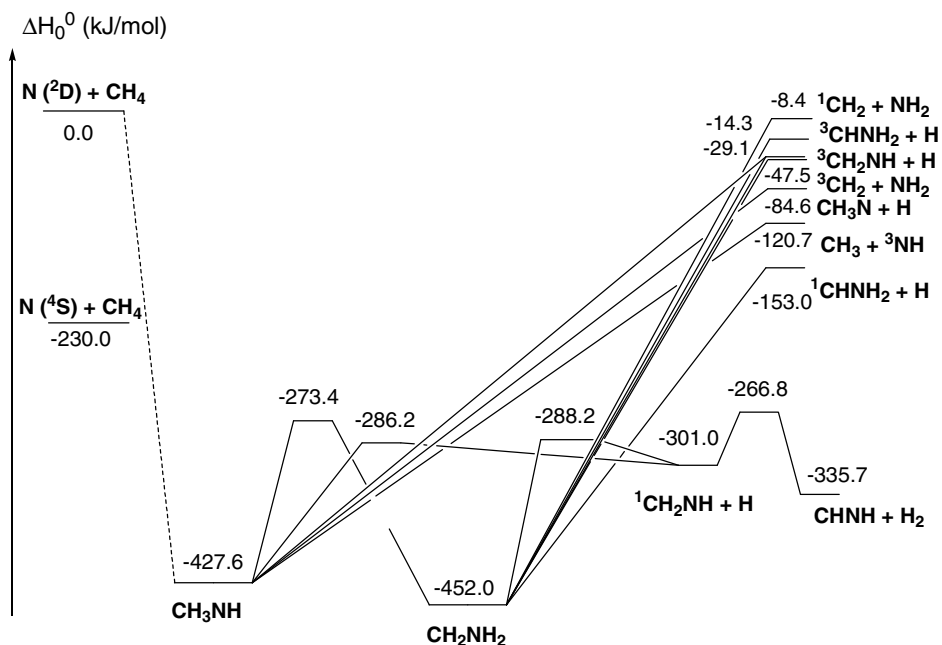


Fig. 2. Schematic representation of the $\text{N}(^2\text{D}) + \text{CH}_4$ potential energy surface. For simplicity, only the CCSD(T) relative energies (kJ/mol) are reported.

3.2 $\text{N}(^2\text{D}) + \text{C}_2\text{H}_4$

The lowest minima localized on the potential energy surface of $\text{N}(^2\text{D}) + \text{C}_2\text{H}_4$ have been reported in Figure 3, where the main geometrical parameters (distances/Å and angles/°) are shown together with the energies computed at B3LYP/aug-cc-pVTZ, CCSD(T)/aug-cc-pVTZ and W1 level, relative to that of $\text{N}(^2\text{D}) + \text{C}_2\text{H}_4$. As expected, CCSD(T) relative energies are in better agreement with the W1 values than the B3LYP ones; for this reason we will consider only CCSD(T) values in the following discussion. A schematic representation of the potential energy surface of the system $\text{N}(^2\text{D}) + \text{C}_2\text{H}_4$ is shown in Figure 4. For the sake of simplicity in the upper panel we have reported only the isomerisation processes, while in the lower panel we have shown the main dissociation processes. From Figure 4 we can see that the interaction of $\text{N}(^2\text{D})$ with C_2H_4 gives rise to the species $\text{CH}_2(\text{N})\text{CH}_2$ (**1**) in agreement with the previous investigations of Takayanagi *et al.* [28] and Lee *et al.* [29]. (**1**) is more stable than the reactants by 428.9 kJ/mol and is formed without any barrier at least at B3LYP level.

The cyclic species (**1**) can isomerize to the other cyclic isomer $\text{CH}_2(\text{NH})\text{CH}$ (**3'**) through the transfer of an hydrogen atom from carbon to nitrogen with a barrier of 189.2 kJ/mol, or to the open structure CH_2NCH_2 (**2**) with a barrier of 116.9 kJ/mol, due to the opening of the ring through the breaking of the C—C bond. The transfer of an hydrogen from one carbon atom to the other implies the isomerisation of (**1**) to CH_3NCH (**7'**) with a barrier of 206.6 kJ/mol. The breaking of a C—H bond with

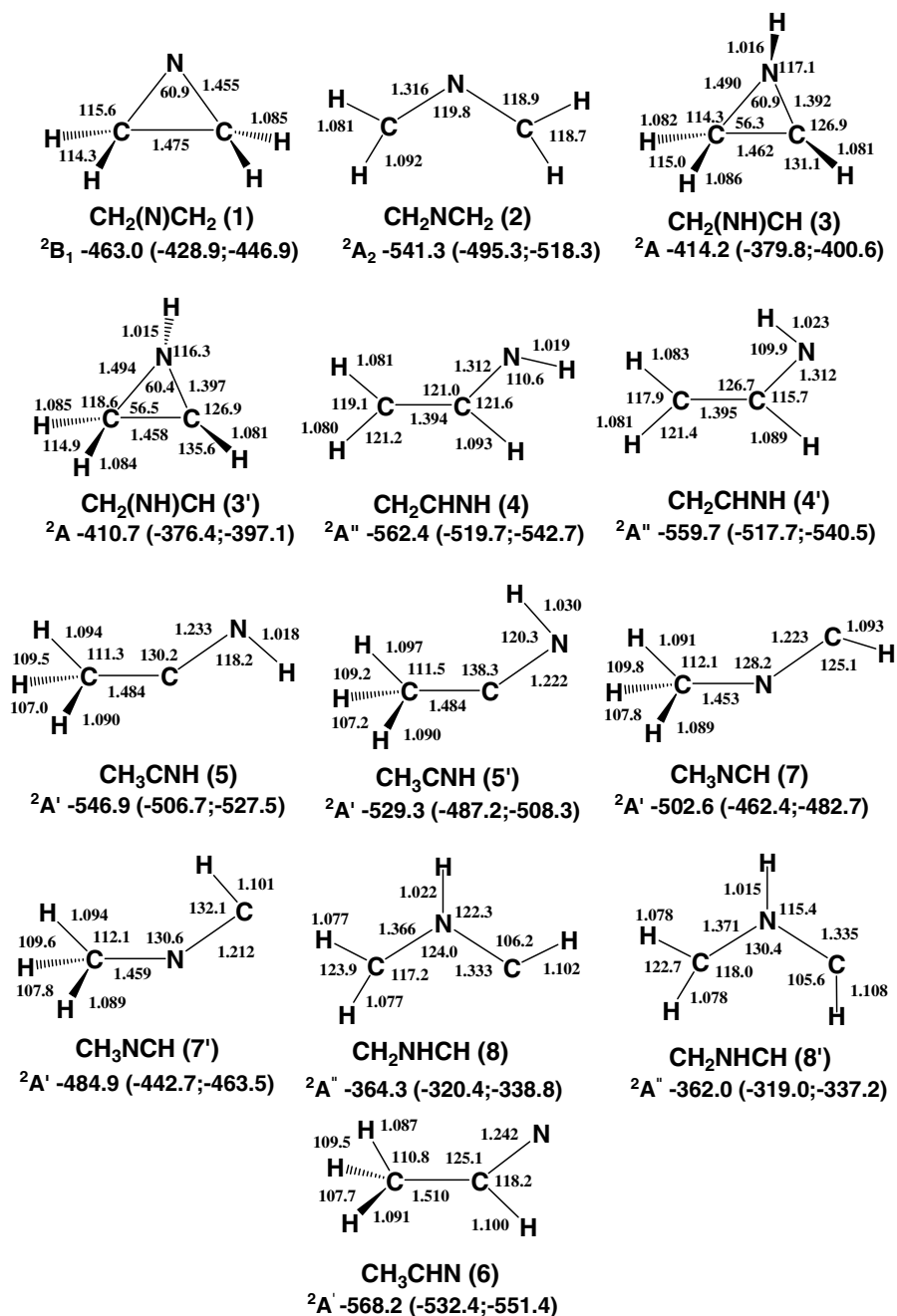


Fig. 3. B3LYP optimized geometries (Å and °) and relative energies with respect to $\text{N}(^2\text{D}) + \text{C}_2\text{H}_4$ (kJ/mol) at 0 K of minima localized on the PES of $\text{N}(^2\text{D}) + \text{C}_2\text{H}_4$; CCSD(T) and W1 relative energies are reported in parentheses

formation of *2H*-azirine $\text{CH}_2(\text{N})\text{CH}$ is an endothermic reaction with a ΔH_0^0 of 184.8 kJ/mol and a barrier of 198.6 kJ/mol. The formation of the corresponding triplet product $^3\text{CH}_2(\text{N})\text{CH}$ is a barrierless process but is much more endothermic being ΔH_0^0 476.9 kJ/mol. The breaking of a C—H bond in (**2**) implies the formation of $\text{CH}_2\text{NCH} + \text{H}$ in a reaction endothermic by 289.1 kJ/mol; this reaction shows a barrier almost equal to the endothermicity of the reaction at B3LYP level (286.2 kJ/mol vs 286.1 kJ/mol) which disappears at CCSD(T) level. For simplicity this barrier has not been reported in Figure 4. The formation of the corresponding triplet product $^3\text{CH}_2\text{NCH}$ is barrierless but much more endothermic being ΔH_0^0 406.4 kJ/mol. (**2**) can dissociate also to $\text{CH}_2\text{NC} + \text{H}_2$ in a reaction endothermic by only 116.8 kJ/mol but with a barrier as high as 343.3 kJ/mol. The dissociation of (**2**) into $\text{CH}_2\text{N} + ^3\text{CH}_2$ is a barrierless reaction endothermic by 376.5 kJ/mol. We could not find any pathway towards the formation of $\text{CHNCH} + \text{H}_2$ from (**2**) in contrast with Takayanagi *et al.* [35]. Species $\text{CH}_2(\text{NH})\text{CH}$ (**3'**) can isomerize to the similar species (**3**) through a very low barrier of 42.4 kJ/mol or to the open species *cis* CH_2CHNH (**4'**) through a barrier of 87.2 kJ/mol. This last reaction is exothermic by 141.3 kJ/mol. The cyclic species (**3**) can isomerize to the more stable open species *trans* CH_2CHNH (**4**) through a barrier of 85.6 kJ/mol. (**3**) can also lose an hydrogen giving rise to the *2H*-azirine $\text{CH}_2(\text{N})\text{CH}$ with a barrier of 149.2 kJ/mol or to the *1H*-azirine $\text{CH}(\text{NH})\text{CH}$; for this last reaction we found a very small barrier at B3LYP level almost equal to the endothermicity of the dissociation, which disappears at CCSD(T) level. Also in this case for simplicity we have not reported this barrier in Figure 4. The dissociations of (**3**) towards the corresponding triplet products $^3\text{CH}_2(\text{N})\text{CH} + \text{H}$ or $^3\text{CH}(\text{NH})\text{CH} + \text{H}$ are barrierless reactions very endothermic (427.7 kJ/mol and 427.1 kJ/mol, respectively). Also (**3'**) can dissociate in barrierless reactions to the triplet products $^3\text{CH}_2(\text{N})\text{CH} + \text{H}$ or $^3\text{CH}(\text{NH})\text{CH} + \text{H}$; however both these reactions are strongly endothermic being ΔH_0^0 424.3 kJ/mol and 423.7 kJ/mol, respectively. We were not able to find transition states for the dissociation towards the corresponding singlet products. However, the variational calculations show the presence of a barrier for these reactions, but any attempts to localize these transition states lead to the corresponding barriers of species (**3**); this means that these transition states should be very similar. *cis* CH_2CHNH (**4'**) can isomerize to *trans* CH_2NHCH (**4**) through a low barrier of 63.8 kJ/mol. *cis* CH_2CHNH (**4'**) can isomerize also to species CH_3CNH (**5'**) but the barrier is 232.6 kJ/mol. *trans* CH_2CHNH (**4**) isomerizes to the species CH_3CNH (**5**) with a barrier of 218.4 kJ/mol. *trans* CH_2CHNH (**4**) can dissociate into $\text{CH}_2\text{CN} + \text{H}_2$; however the barrier for this reaction is as high as 403.0 kJ/mol. Also the dissociation of *trans* CH_2CHNH (**4**) into keteneimine $\text{CH}_2\text{CNH} + \text{H}$ shows a barrier which is however much lower (212.7 kJ/mol). The dissociation reactions of both the *trans* CH_2CHNH (**4**) and *cis* CH_2CHNH (**4'**) towards a triplet product are all barrierless.

The species CH_3CNH (**5'**) can isomerize to CH_3CNH (**5**) with a small barrier of 48.0 kJ/mol. CH_3CNH (**5**) can isomerize also to species CH_3CHN (**6**) which is the most stable isomer localized on the PES of $\text{N}(^2\text{D}) + \text{C}_2\text{H}_4$; this isomerisation shows a barrier of 149.6 kJ/mol. (**5'**) can dissociate into acetonitrile $\text{CH}_3\text{CN} + \text{H}$ with a barrier of 79.6 kJ/mol and into $\text{CH}_3 + \text{HNC}$ with a barrier of 114.2 kJ/mol. (**5**) can dissociate into keteneimine $\text{CH}_2\text{CNH} + \text{H}$ with a very small barrier which disappears at CCSD(T) level. The dissociation of both (**5**) and (**5'**) into $^3\text{CH}_3\text{CN} + \text{H}$ and $^3\text{CH}_2\text{CNH} + \text{H}$ are all barrierless. Species (**6**) can dissociate into *2H*-azirine + H with a barrier

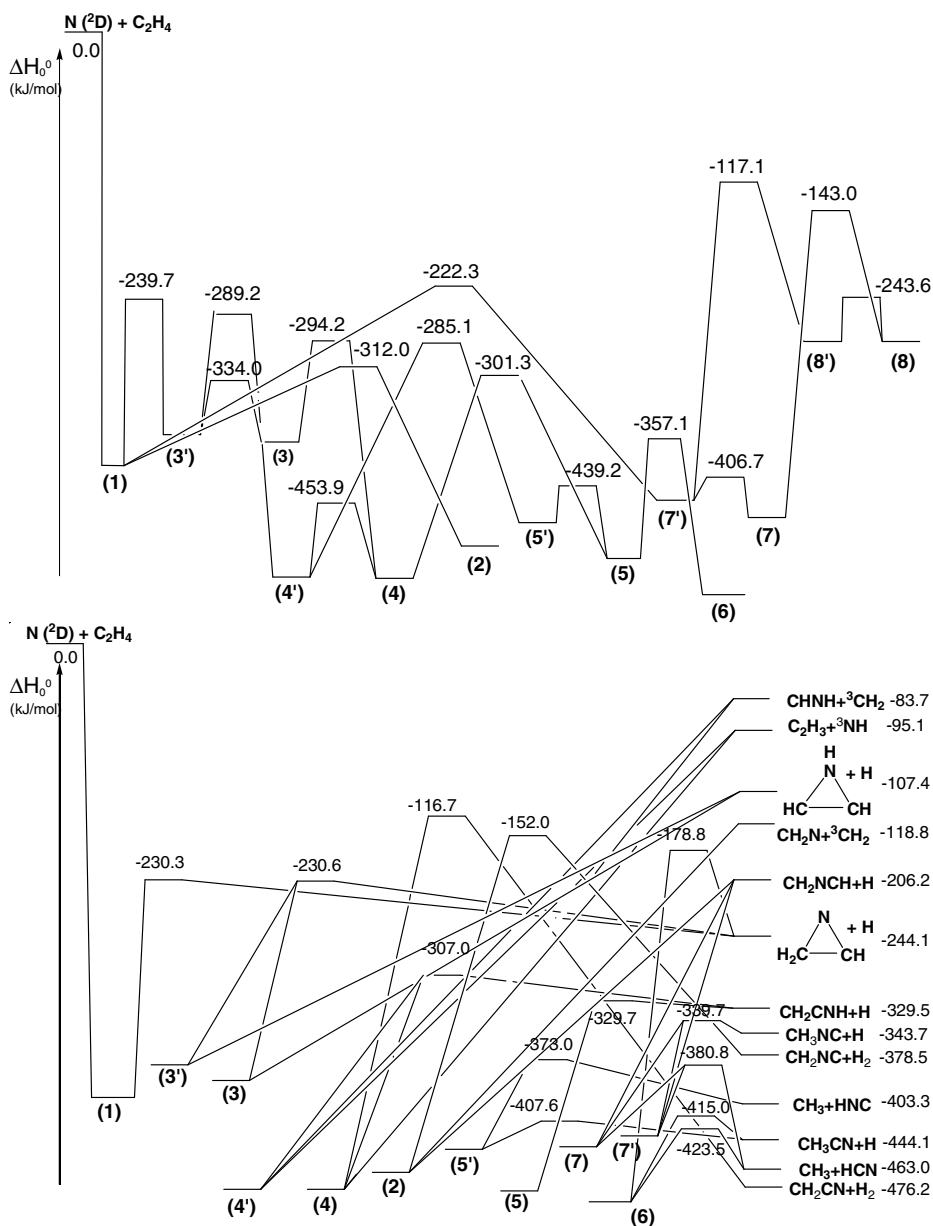


Fig. 4. Schematic representation of the $N(^2D) + C_2H_4$ potential energy surface. Only the CCSD(T) relative energies (kJ/mol) are reported. In the upper panel, for simplicity, only the isomerization reactions are reported, while, in the lower panel, only the main dissociation processes are reported.

of 353.6 kJ/mol, into acetonitrile $\text{CH}_3\text{CN} + \text{H}$ with a barrier of 117.4 kJ/mol, and into $\text{CH}_3 + \text{HCN}$ with a barrier of 108.9 kJ/mol. The dissociation of (6) into ${}^3\text{CH}_3\text{CN} + \text{H}$ is barrierless and very endothermic (532.8 kJ/mol). Species CH_3NCH (7') can isomerize to CH_3NCH (7) with a very low barrier of 36.0 kJ/mol or to the less stable species CH_2NHCH (8') with a very high barrier of 325.6 kJ/mol. Also species (7) can isomerize to the corresponding species CH_2NHCH (8) with a still high barrier of 319.4 kJ/mol. (8') can isomerize to (8) with a small barrier of 75.4 kJ/mol. Since both (8') and (8) show very high barriers for their formation, we will not consider anymore these isomers. Species CH_3NCH (7') can dissociate into $\text{CH}_3 + \text{HCN}$ with a barrier of 61.9 kJ/mol and into $\text{CH}_3\text{NC} + \text{H}$ with a barrier of 103.0 kJ/mol. Species CH_3NCH (7) can dissociate into $\text{CH}_2\text{NCH} + \text{H}$ with a very small barrier which disappears at CCSD(T) level. For (8) and (8') we have considered only the dissociation into $\text{CH}_2\text{NCH} + \text{H}$, for the relevance of this product. The dissociation of CH_2NHCH (8) into $\text{CH}_2\text{NCH} + \text{H}$ is an endothermic process with a relatively high barrier.

3.3 $\text{N}({}^2\text{D}) + \text{C}_2\text{H}_6$

The lowest stationary points localized on the potential energy surface of $\text{N}({}^2\text{D}) + \text{C}_2\text{H}_6$ have been reported in Figure 5, where the main geometrical parameters (distances/Å and angles/°) are shown together with the energies computed at B3LYP/aug-cc-pVTZ and CCSD(T)/aug-cc-pVTZ (in parentheses), relative to that of $\text{N}({}^2\text{D}) + \text{C}_2\text{H}_6$. For simplicity we will consider only CCSD(T) values in the following discussion. A schematic representation of the potential energy surface of the system $\text{N}({}^2\text{D}) + \text{C}_2\text{H}_6$ is shown in Figure 6. In order to have a clear picture of the exit channels we have reported in two different panels the exit channels with and without a barrier. From Figure 6 we can see that the interaction of $\text{N}({}^2\text{D})$ with C_2H_6 gives rise to the species $\text{CH}_3\text{CH}_2\text{NH}$ which is more stable than the reactants by 447.0 kJ/mol. For this reaction we have found a saddle point which is, however, below the reactants both at B3LYP and CCSD(T) level of calculation. The presence of saddle points below the reactants has already been observed for very exothermic reactions [24]. However, since we were not successful in localizing a stable initial complex, the energy of this saddle point does not seem to be very meaningful. $\text{CH}_3\text{CH}_2\text{NH}$ can isomerize to species CH_3NHCH_2 , with a relatively high barrier of 253.6 kJ/mol or to species CH_3CHNH_2 , which is the most stable isomer on the $\text{N}({}^2\text{D}) + \text{C}_2\text{H}_6$ PES, with a barrier of 146.3 kJ/mol. $\text{CH}_3\text{CH}_2\text{NH}$ can also dissociate to CH_3CHNH and H with a slightly lower barrier of 131.0 kJ/mol or to the more stable products CH_3 and CH_2NH with an even lower barrier of 113.6 kJ/mol. A schematic representation of the potential energy surface of the system $\text{N}({}^2\text{D}) + \text{C}_2\text{H}_6$ is shown in Figure 6. In order to have a clear picture of the exit channels we The other channels, *i.e.* the dissociation of $\text{CH}_3\text{CH}_2\text{NH}$ to $\text{CH}_3\text{CH}_2 + \text{NH}$, $\text{CH}_3\text{CH}_2\text{N} + \text{H}$, $\text{CH}_3 + \text{CH}_2\text{NH}$ in its excited triplet state, and $\text{CH}_2\text{CH}_2\text{NH}$ in its excited triplet state + H are barrierless, but they are very endothermic, being the dissociation energies 311.4, 348.2, 352.6, and 415.4 kJ/mol, respectively. CH_3NHCH_2 can isomerize to CH_3NCH_3 with a barrier of 172.2 kJ/mol or can dissociate to $\text{CH}_3 + \text{CH}_2\text{NH}$, $\text{CH}_3\text{NCH}_2 + \text{H}$, *c*- $\text{CH}_2(\text{NH})\text{CH}_2 + \text{H}$, or $\text{CH}_2\text{NHCH}_2 + \text{H}$ with barriers of 125.2, 140.2, 268.7, 276.7 kJ/mol, respectively. CH_3NHCH_2 can dissociate also to $\text{CH}_3 + \text{CH}_2\text{NH}$ in its excited triplet state, $\text{CH}_3\text{NH} + \text{CH}_2$, CH_2NHCH_2 in its

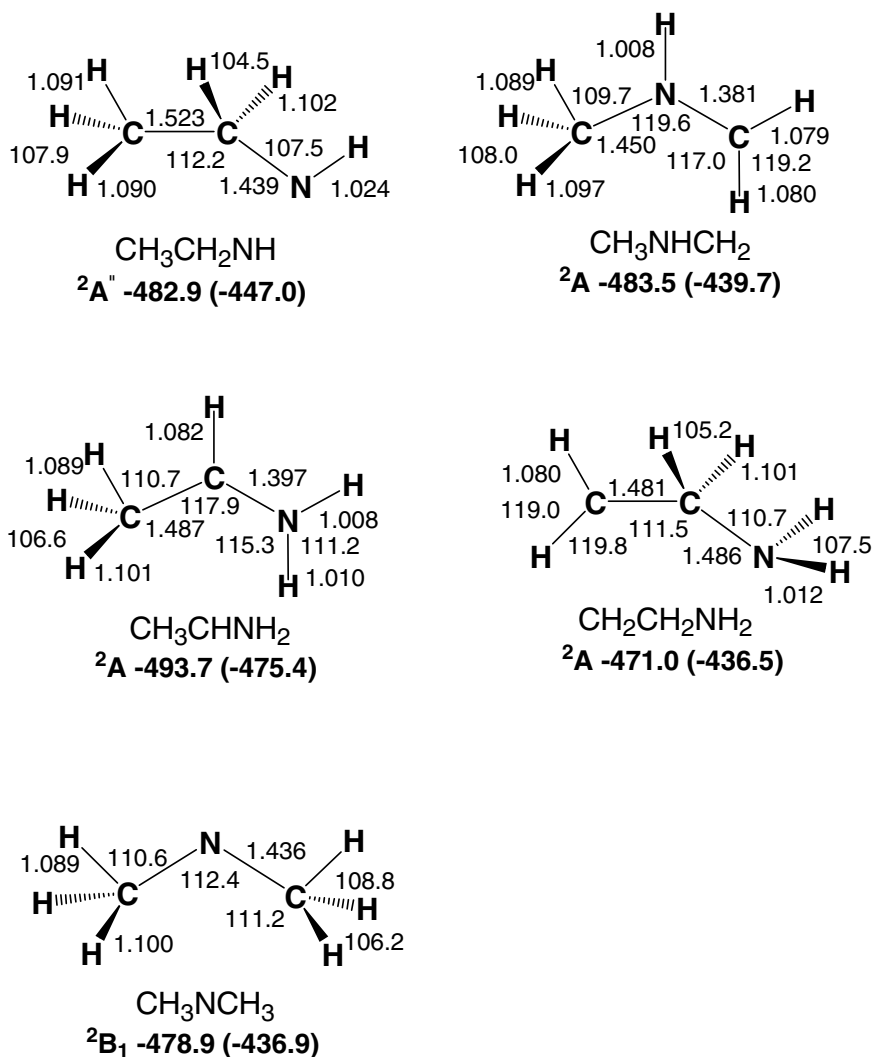


Fig. 5. B3LYP optimized geometries (Å and °) and relative energies with respect to $\text{N}({}^2\text{D}) + \text{C}_2\text{H}_6$ (kJ/mol) at 0 K of minima localized on the PES of $\text{N}({}^2\text{D}) + \text{C}_2\text{H}_6$; CCSD(T) relative energies are reported in parentheses

excited triplet state + H, and CH_3NCH_2 in its excited triplet state + H. All these processes are barrierless but they are very endothermic, being the dissociation energies 345.4, 396.4, 401.6, and 402.1 kJ/mol, respectively. The most stable isomer CH_3CHNH_2 can isomerize to $\text{CH}_2\text{CH}_2\text{NH}_2$ with a relatively low barrier of 193.6 kJ/mol or can dissociate to $\text{CH}_3\text{CHNH} + \text{H}$, $\text{CH}_2\text{CHNH}_2 + \text{H}$, $\text{CHNH}_2 + \text{CH}_3$, $\text{CH}_3\text{CNH}_2 + \text{H}$ with barriers of 148.3, 154.1, 258.9, 280.9 kJ/mol, respectively. CH_3CHNH_2 can dissociate also to CH_3CNH_2 in its excited triplet state + H, $\text{CH}_3 + \text{CHNH}_2$ in its excited triplet state, $\text{NH}_2 + \text{CH}_3\text{CH}$ both in its ground state or in its

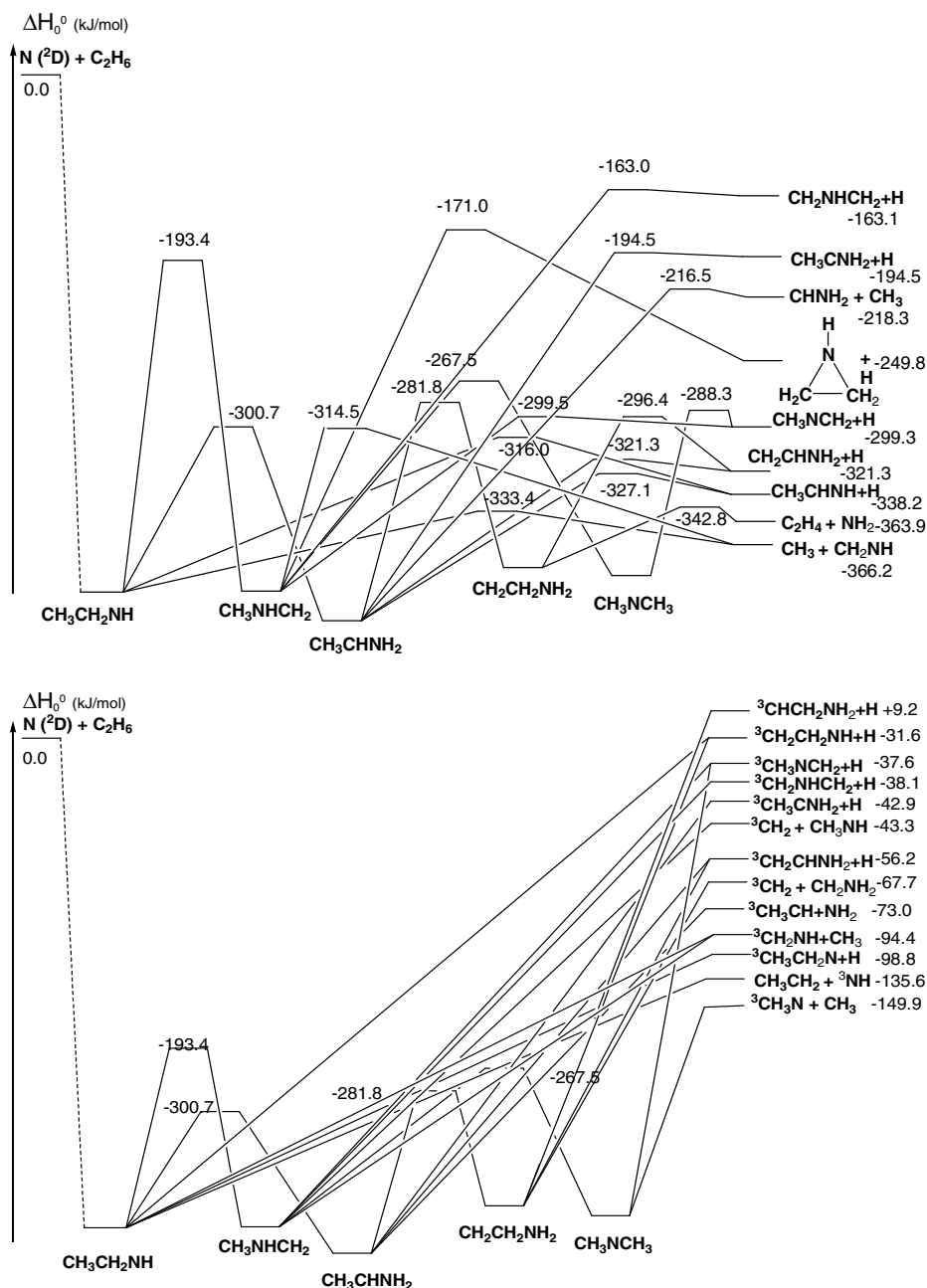


Fig. 6. Schematic representation of the $\text{N}(^2\text{D}) + \text{C}_2\text{H}_6$ potential energy surface. Only the CCSD(T) relative energies (kJ/mol) are reported. In the upper panel, for simplicity, only the reaction channels which are characterized by an exit barrier are reported. In the lower panel, for simplicity, only the reaction channels which are not characterized by an exit barrier are reported. The energy scale has been expanded in the upper part of the lower panel.

excited singlet state, and CH_2CHNH_2 in its excited triplet state + H; all these processes are barrierless but very endothermic being the dissociation energies 376.6, 395.8, 402.4, 416.7, and 419.2 kJ/mol, respectively. $\text{CH}_2\text{CH}_2\text{NH}_2$ can dissociate to C_2H_4 + NH_2 or to CH_2CHNH_2 + H with relatively low barriers of 93.7 and 140.1 kJ/mol, respectively. $\text{CH}_2\text{CH}_2\text{NH}_2$ can dissociate also to CH_2 + CH_2NH_2 , CH_2CHNH_2 in its excited triplet state + H, $\text{CH}_2\text{CH}_2\text{NH}$ + H, and CHCH_2NH_2 + H; all these processes are barrierless but very endothermic being the dissociation energies 368.8, 380.3, 404.9, and 445.7 kJ/mol, respectively. CH_3NCH_3 can dissociate to CH_3NCH_2 + H with a barrier of 148.6 kJ/mol or to CH_3N + CH_3 in a barrierless process endothermic by 287.0 kJ/mol. The dissociation of CH_3NCH_3 to CH_3NCH_2 in its excited triplet state + H is much more endothermic (399.3 kJ/mol).

4 Conclusions

In summary, we have investigated the potential energy surfaces of the reactions of $\text{N}(^2\text{D})$ with methane, ethene and ethane at *ab initio* level. This study provides a complete understanding of the behavior of the involved systems, intermediates as well as fragment products, which is of primary importance in order to explain the available experimental information. The calculations allowed the localization of the main stationary points (*i.e.* minima and transition states) of the systems investigated and the evaluation of the most relevant product energetics. In all the investigated systems the insertion pathway, which is the first process observed, has been found to be barrierless at all levels of theory employed in the present calculations. The computed PESs, together with RRKM calculations performed for all the systems, allow to discriminate among the possible reaction channels, in agreement with the experimental information. In particular, for the $\text{C}_2\text{H}_6\text{N}$ system the dominant reaction channel is the one leading to methanimine and CH_3 .

Acknowledgment. We acknowledge financial support from the Italian MIUR (Ministero Istruzione Università Ricerca) under project PRIN 2009SLKFEX_004.

References

1. Chemical Kinetics and Photochemical Data for Use in Atmospheric Studies, Evaluation No. 15; JPL. Publication 06-2, Jet Propulsion Laboratory; Pasadena, CA (2006)
2. Yung, Y.L., DeMore, W.B.: Photochemistry of Planetary Atmospheres. Oxford University Press, New York (1998)
3. Coustenis, A., Lellouch, E., Sicardy, B.: In: Brown, R.H., Lebreton, J.-P., Waite, J.H. (eds.) Titan from Cassini-Huygens, ch. 2, pp. 9–34. Springer, Dordrecht (2009)
4. Strobel, D.F., Atreya, S.K., Bezar, B., Ferri, F., Flasar, F.M., Fulchignoni, M., Lellouch, E., Muller-Wodarg, I.M.: In: Brown, R.H., Lebreton, J.-P., Waite, J.H. (eds.) Titan from Cassini-Huygens, ch. 10, pp. 235–257. Springer, Dordrecht (2009)
5. Niemann, H.B., Atreya, S.K., Bauer, S.J., Carignan, G.R., Demick, J.E., Frost, R.L., Gautier, D., Haberman, J.A., Harpold, D.N., Hunten, D.M., Israel, G., Lunine, J.I., Kasprzak, W.T., Owen, T.C., Paulovich, M., Raulin, F., Raaen, E., Way, S.H.: Nature 438, 779 (2005)

6. Coustenis, A., Salama, A., Schulz, B., Ott, S., Lellouch, E., Encrenaz, T., Gautier, D., Feuchtgruber, H.: *Icarus* 161, 383 (2003)
7. Vuitton, V., Yelle, R.V., McEwan, M.J.: *Icarus* 191, 722 (2007)
8. Carrasco, N., Alcaraz, C., Dutuit, O., Plessis, S., Thissen, R., Vuitton, V., Yelle, R., Perrot, P.: *Planet. Space Sci.* 56, 1644 (2008)
9. Cravens, T.E., Robertson, I.P., Waite, J.H., Yelle, R.V., Kasprzak, W.T., Keller, C.N., Ledvina, S.A., Niemann, H.B., Luhmann, J.G., McNutt, R.L., Ip, W.H., De La Haye, V., Mueller-Wodarg, I., Wahlund, J.E., Anicich, V.G., Vuitton, V.: *Geophys. Res. Lett.* 33, L07105 (2006)
10. Baulch, D.L., Bowman, C.T., Cobos, C.J., Cox, R.A., Just, T., Kerr, J.A., Pilling, M.J., Stocker, D., Troe, J., Tsang, W., Walker, R.W., Wamatz, J.: *J. Phys. Chem. Ref. Data* 34, 757 (2005)
11. Balucani, N., Bergeat, A., Cartechini, L., Volpi, G.G., Casavecchia, P., Skouteris, D., Rosi, M.: *J. Phys. Chem.* 113, 11138 (2009)
12. Balucani, N., Leonori, F., Petrucci, R., Skouteris, D., Casavecchia, P., Rosi, M.: (to be submitted)
13. Balucani, N., Leonori, F., Petrucci, R., Stazi, M., Skouteris, D., Rosi, M., Casavecchia, P.: *Faraday Discussions* 147, 189 (2010)
14. Becke, A.D.: *J. Chem. Phys.* 98, 5648 (1993); Stephens, P.J., Devlin, F.J., Chabalowski, C.F., Frisch, M.J.: *J. Phys. Chem.* 98, 11623 (1994)
15. Dunning Jr., T.H.: *J. Chem. Phys.* 90, 1007 (1989); Woon, D.E., Dunning Jr., T.H.: *J. Chem. Phys.* 98, 1358 (1993); Kendall, R.A., Dunning Jr., T.H., Harrison, R.J.: *J. Chem. Phys.* 96, 6796 (1992)
16. Gonzales, C., Schlegel, H.B.: *J. Chem. Phys.* 90, 2154 (1989); *J. Phys. Chem.* 94, 5523 (1990)
17. Bartlett, R.J.: *Annu. Rev. Phys. Chem.* 32, 359 (1981); Raghavachari, K., Trucks, G.W., Pople, J.A., Head-Gordon, M.: *Chem. Phys. Lett.* 157, 479 (1989); Olsen, J., Jorgensen, P., Koch, H., Balkova, A., Bartlett, R.J.: *J. Chem. Phys.* 104, 8007 (1996)
18. Moore, C.E.: *Atomic Energy Levels. Natl. Bur. Stand (U.S.) Circ. N. 467. U.S., GPO, Washington, DC* (1949)
19. Martin, J.M.L., de Oliveira, G.: *J. Chem. Phys.* 111, 1843 (1999); Parthiban, S., Martin, J.M.L.: *J. Chem. Phys.* 114, 6014 (2001)
20. Frisch, M.J., Trucks, G.W., Schlegel, H.B., Scuseria, G.E., Robb, M.A., Cheeseman, J.R., Montgomery Jr., J.A., Vreven, T., Kudin, K.N., Burant, J.C., Millam, J.M., Iyengar, S.S., Tomasi, J., Barone, V., Mennucci, B., Cossi, M., Scalmani, G., Rega, N., Petersson, G.A., Nakatsuji, H., Hada, M., Ehara, M., Toyota, K., Fukuda, R., Hasegawa, J., Ishida, M., Nakajima, T., Honda, Y., Kitao, O., Nakai, H., Klene, M., Li, X., Knox, J.E., Hratchian, H.P., Cross, J.B., Bakken, V., Adamo, C., Jaramillo, J., Gomperts, R., Stratmann, R.E., Yazyev, O., Austin, A.J., Cammi, R., Pomelli, C., Ochterski, J.W., Ayala, P.Y., Morokuma, K., Voth, G.A., Salvador, P., Dannenberg, J.J., Zakrzewski, V.G., Dapprich, S., Daniels, A.D., Strain, M.C., Farkas, O., Malick, D.K., Rabuck, A.D., Raghavachari, K., Foresman, J.B., Ortiz, J.V., Cui, Q., Baboul, A.G., Clifford, S., Cioslowski, J., Stefanov, B.B., Liu, G., Liashenko, A., Piskorz, P., Komaromi, I., Martin, R.L., Fox, D.J., Keith, T., Al-Laham, M.A., Peng, C.Y., Nanayakkara, A., Challacombe, M., Gill, P.M.W., Johnson, B., Chen, W., Wong, M.W., Gonzalez, C., Pople, J.A.: *Gaussian 03, Revision B.04. Gaussian, Inc., Wallingford CT* (2004)
21. Flükiger, P., Lüthi, H.P., Portmann, S., Weber, J.: *MOLEKEL 4.3. Swiss Center for Scientific Computing, Manno (Switzerland)* (2000-2002); Portmann, S., Lüthi, H.P.: *Chimia* 54, 766 (2000)

22. Kurosaki, Y., Takayanagi, T., Sato, K., Tsunashima, S.: *J. Phys. Chem. A* 102, 254 (1998)
23. Jursic, B.S.: *Int. J. Quantum Chem.* 71, 481 (1999)
24. Fokin, A.A., Shubina, T.E., Gunchenko, P.A., Isaev, S.D., Yurchenko, A.G., Schreiner, P.R.: *J. Am. Chem. Soc.* 124, 10718 (2002); Schreiner, P., Fokin, A.A., Schleyer, P.v.R., Schaefer III, H.F.: *Fundamental World of Quantum Chemistry*. In: Bründas, E.J., Kryachko, E.S. (eds.), vol. II, pp. 349–375. Kluwer, The Netherlands (2003)
25. Takayanagi, T., Kurosaki, Y., Yokoyama, K.: *Int. J. Quantum Chem.* 79, 190 (2000)
26. Ouk, C.-M., Zvereva-Loëte, N., Bussery-Honvault, B.: *Chem. Phys. Letters* 515, 13 (2011)
27. Travers, M.J., Cowles, D.C., Clifford, E.P., Ellison, G.B.: *J. Chem. Phys.* 111, 5349 (1999)
28. Takayanagi, T., Kurosaki, Y., Sato, K., Tsunashima, S.: *J. Phys. Chem. A* 102, 10391 (1998)
29. Lee, S.-H., Chin, C.-H., Chen, W.-K., Huang, W.-J., Hsieh, C.-C.: *PCCP* 13, 8515 (2011)

Efficient Workload Distribution Bridging HTC and HPC in Scientific Computing

Carlo Manuali¹, Alessandro Costantini^{2,3}, Antonio Laganà¹, Marco Cecchi³,
Antonia Ghiselli³, Michele Carpené⁴, and Elda Rossi⁴

¹ Department of Chemistry, University of Perugia, via Elce di Sotto, 8, 06123
Perugia, Italy

{carlo,lag}@unipg.it

² Department of Mathematics and Informatics, University of Perugia, via Vanvitelli,
1, 06123 Perugia, Italy

³ INFN-CNAF, viale Berti-Pichat, 4/3, 40127 Bologna, Italy

{alessandro.costantini,marco.cecchi,antonia.ghiselli}@cnaf.infn.it

⁴ CINECA, via Magnanelli, 8, 40033 Casalecchio di Reno, Italy

{m.carpen,e.rossi}@cineca.it

Abstract. GriF is a Workflow Management System designed to support users of the Molecular and Materials Sciences and Technologies COMPCHEM Virtual Organization. In particular, GriF manages the results of the parameter sweeping studies submitted to the Grid. This service has been recently extended to implement seamless access to both High Performance and High Throughput Computing architectures. To this end, the Workflow execution is splitted into single blocks whose execution is most suited to one or the other platform. This has been obtained by implementing a communication channel allowing interoperability between the gLite middleware operating on the Italian Grid Initiative segment accessible to COMPCHEM and the software stack operating on the CINECA machines. As a prototype application a high level ab initio calculation of the potential energy surface of few atom system has been implemented.

1 Introduction

Computational researchers of several scientific communities make heavy usage of the resources of the accessible computing facilities. The advent of High Performance Computing (HPC) networks and large grids of off-the-shelf High Throughput Computing (HTC) elements can provide these scientists with increasing processing power. HPC and HTC platforms, however, pursue different approaches to massive computing. Namely:

- HPC networks (like PRACE [\[1\]](#) in Europe and TeraGrid [\[2\]](#) in the United States) offer a suitable distributed infrastructure for tightly coupled calculations requiring large memory sizes, MPI libraries [\[3\]](#), a high speed interconnection network, large and high throughput storage devices. The interconnection of the different supercomputers is mainly intended in this case for facilitating the job management and offering unified resources (like storage).

- HTC grids (like that of the European Grid Infrastructure EGI [4]) offer a highly cost-effective computational platform exploiting the concurrent elaboration of a huge number of small-middle sized computers most often of the rackable CPU cluster type. The typical job exploiting the advantage of this infrastructure consists of a huge amount of substantially uncoupled computational tasks that can be distributed on independent CPUs.

The HPC and HTC computing paradigms have developed separately, and sometimes even conflictingly, to enable two totally different approaches to concurrent computing. As a consequence, they are also managed by middlewares quite different in nature and target different classes of applications, numerical algorithms and computational methods. Yet, from the researchers' point of view, the different infrastructures implementing HPC and HTC may result difficult to be directly handled. In many scientific fields, in fact, researchers would greatly benefit from combining the two HPC and HTC paradigms altogether, so as to enable the accurate modeling of real-like systems and virtual reality simulations based on multi-scale and multi-physics approaches. Despite that, little effort has been spent, up to date, to promote a seamless integration of the two infrastructures. Yet, in the recent INFRA-2011 [5] call of the 7th Framework Programme, the European Community has prompted for actions and projects to let PRACE and EGI converge into a harmonized system and related scientific communities to develop interoperable applications.

This is also, indeed, the main scope of the presented paper that reports on the work made to extend GriF (Grid Framework) [6,7] that is a Workflow Management System (WfMS) designed to support users of the COMPCHEM [8] Virtual Organization (VO), mainly, in optimizing the return of their parameter sweeping studies submitted to the Grid, to split the Workflow execution into single blocks whose execution is most suited either to HPC or HTC platforms. The implementation of such a High Performance Grid (called HIPEG) has requested a tight collaboration among experts of IGI (the Italian Grid Initiative) [9] for what concerns the gLite middleware, of CINECA (the largest Supercomputing Center of Italy) [10] for the UNICORE software stack and of COMPCHEM the virtual community of the Molecular and Materials Science and Technologies research area. COMPCHEM, in fact, is engaged in designing and implementing accurate realistic multi-scale applications like the Grid Empowered Molecular Simulator (GEMS) [11], involving coordinated utilization of HPC and HTC resources. This is meant to overcome the shortcomings of the present somewhat unsatisfactory situation whereby none of the available resources is suited for complex requests, in terms of the diversity of requested computations, such as the ones required by GEMS. What is lacking, in fact, is the coordination of different systems, such as HPC and HTC, to interoperate via a single Workflow Management System that properly isolates into known patterns the user Workflow and dispatches such building blocks so as to send each of them to the most suitable resource. This would allow a more efficient execution of complex applications.

The paper is organized as follows. Section 2 provides a high level description of the work. Section 3 describes the prototype case study. Section 4 illustrates

the approach tackling the problem. Section 5 reports the GriF implementation. Section 6 indicates the further developments lines opened by the work done. Section 7 draws some conclusions.

2 High Level Description of the Work

The main objective of the work presented in this paper is the design and development activities aimed at equipping GriF with the ability to use HPC machines (provided by CINECA in the case study considered in the paper), so as to enhance its Grid submission engine and also to refine its Quality evaluation features that is a crucial step in enabling the implementation on the Grid of highly realistic complex collaborative (in terms of expertise and platforms) scientific applications. A high level description of the work carried out is sketched in Fig. 1 in which the two levels of development to implement a proper Distributed Computing Infrastructure (DCI) framework are singled out.

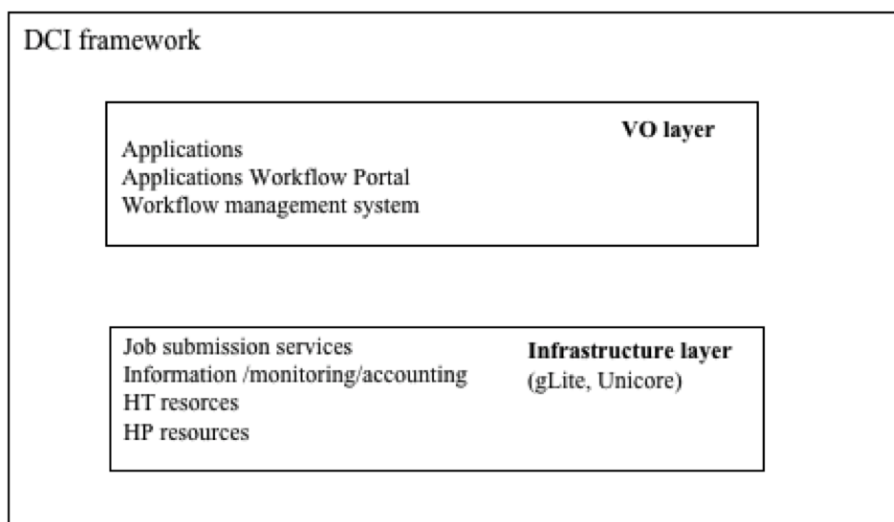


Fig. 1. Composition of the DCI framework

As a prototype application we considered a particular implementation of the first block of GEMS devoted to the ab initio calculation of the electronic structure of molecular systems (in our case we considered a high level few atom one). To this end use has been made of the package GAMESS US [12] and GriF has been structured so as to allow the launch on both the Grid and the IBM SP6 machine of CINECA. The assembled tool, however, has the more general target of allowing interoperability between HPC and HTC platforms that is the first step towards the possibility of carrying out accurate realistic simulations of

several environmental phenomena. In order to distribute grid-oriented GAMESS-US jobs on a HPC platform, monitor their evolution and gather the results back to the user, the whole package was implemented as a service offered by the SP6 machine of CINECA that makes use of MPI and OpenMP libraries. Furthermore, GriF has been designed in a modular way so as to allow, in the near future, to utilize the so called EMI [13] Execution Service [14], under development in the european FP7 project EMI, that will offer a new, common interface for job submission, specifically conceived with the intent of encompassing both HTC and HPC environments. Basing GriF on EMI-ES will allow for a cleaner and more complete solution, with respect to the pragmatic approach that is described in the present paper. This new interface, whose definition has already taken place and is being implemented by the major european middleware providers, has been enriched with a variety of features that include multiple job submission and the possibility to retrieve information about multiple activities in one single call. This choice was motivated by the benefits of the mission of the EMI project, aimed at delivering a consolidated and sustainable set of middleware products based on the four major middleware providers in Europe ARC, dCache, gLite and UNICORE by providing a unified, standardized, easy to install, software for deployment on a distributed computing infrastructure, like for example EGI and PRACE.

Although the triggering problem and related solutions attain to the specific realm of Molecular and Materials Sciences and Technologies users and in particular to COMPCHEM, various science domains will benefit from the work made. Moreover, on the resource providers side there are also good reasons for coordinating the use of HPC and HTC infrastructures and interoperate large computational applications allowing an optimization of the different computing resources usage. It is, in fact, not infrequent the case in which a user utilizes HPC platforms not as such but as a bunch of loosely coupled processors underutilizing their fast dedicated network. At the same time, HTC users may utilize massively distributed HTC platforms to solve tightly coupled computational tasks ending up by wasting a large amount of time in transferring data. A coordination of the two types of platforms to interoperate via a single Workflow and properly manage the various components on the most suitable of them, would instead allow a clever composition of complex applications that optimizes the use of the various computing resources and offers to the users the best level of performance. A typical discriminant in this respect is, for example, the different efficiency of MPI on the two platforms.

3 The Prototype Case Study

The practical goal of the work reported here is the provisioning, involving both execution and management of the mentioned scientific application GAMESS-US to the COMPCHEM community in such a way to be made available, in a near future, in a general-purpose Science Gateway. In order to be able to compose the computational case study of different level of complexity, the project focused in

the creation of a tool allowing the chained execution of a HTC calculation following a HPC one and vice-versa. The prototype applications representing these execution patterns (that we will call *HTPC skeletons*) typically consist of two COMPCHEM codes which combine iteratively an HPC and an HTC computing task until an exit condition is satisfied. These HTPC skeletons are, indeed, typical of several Computational Chemistry applications of the COMPCHEM VO. Yet they are of much more general validity since their building blocks constitute the basic components of many of the presently used computational applications developed not only in Chemistry and Materials Sciences but also in several other disciplines.

The first skeleton (HTPC1) is the one inspired to the implementation of the mentioned GAMESS-US package that is based on an execution flow distributing a large quantity of independent tasks on a HTC platform whose results are individually passed as input to a set of strongly coupled treatments implemented on a HPC platform (see Fig. 2).

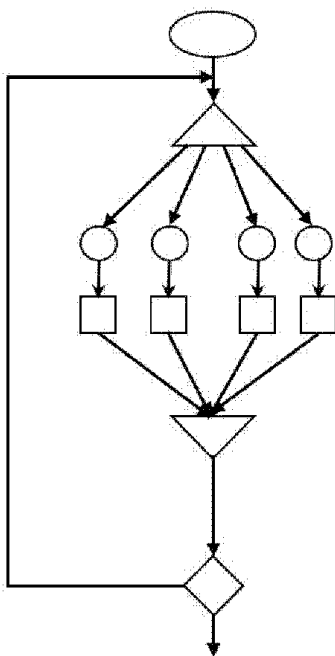


Fig. 2. Skeleton HTPC1: a HPC computation following a parallel execution of HTC jobs

In the first section of the HTPC1 skeleton (that is of the HTC type) an emitter (triangle) generates a (large) number of independent events (circles) each of which provides the input for a HPC highly coupled calculation (square). The outcomes of the distributed HPC tasks are returned (lower layer of arrows)

and gathered together by a collector (inverted triangle). In case the information collected is insufficient the sequence is further iterated a certain number of times.

The second skeleton (HTPC2) is the one inspired to the MCTDH program [15] that is based on a scheme performing a strongly coupled treatment implemented on a HPC platform first followed by the distribution of a large quantity of independent tasks to be calculated on a HPC platform. Also in this case the sequence of the two sections is checked against convergence and further iterations are performed (with the associated switch between the two platforms) until either convergence or a predefined maximum number of iterations has been reached (see Fig. 3).

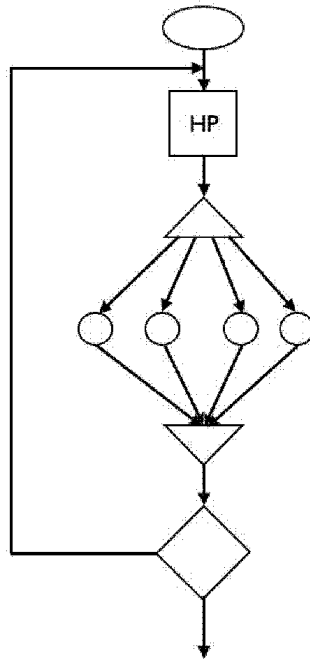


Fig. 3. Skeleton HTPC2: a HPC computation preceding a parallel execution of HTC jobs

A pragmatic implementation of these skeletons has been accomplished utilizing the technology offered by the various middleware providers and by implementing in GriF the logic needed to deal with the aforementioned use cases. This will be presented with more details in the next section.

4 The Service-Oriented Approach to the Problem

The approach followed by us is the Service Oriented Architecture (SOA) one that is emerging as the premier integration and architecture framework in complex and heterogeneous computing environments for building software applications by making use of services available in a public network [16]. In this respect, a service is an implementation of a well-defined functionality that can be consumed by clients in different applications or automatic processes. Therefore, SOA allowed us to reuse existing assets when creating new services from an existing IT infrastructure. As a matter of fact, we built applications in SOA on services thanks to the fact that SOA helps organizing streamline processes by promoting loose coupling among software components to allow an easy and efficient reuse. The SOA approach provides, in fact, the users with an unprecedented higher level of flexibility relying on the fact that:

1. Services are software components with well-defined independent interfaces. An important aspect of SOA is the separation of the service interface (the what) from its implementation (the how): such services, in fact, are consumed by clients (called Consumers) which are not concerned with the way these services will execute their requests;
2. Services are self-contained (perform predetermined tasks), loosely coupled (for independence) and can be dynamically discovered;
3. Composite services (e.g. Workflows) can be built from aggregation of other services.

In particular, SOA has allowed us to adopt the *find-bind-execute* paradigm [17]. According to this paradigm, in GriF service Providers register their services in a public registry. This registry is consulted by Consumers to find the services matching certain criteria. If the registry has such a service, SOA provides the Consumer with a contract (Service Level Agreement, or SLA) and an endpoint address for that service. In general, SOA-based applications are distributed multi-tier applications articulated into Presentation, Business Logic and Persistence layers. This has been, indeed, important in extending GriF because although services are the building blocks of SOA applications and any functionality can be rendered as a service, the real challenge is to well define service interfaces bearing the right level of abstraction (in other words, services should provide coarse-grained functionalities). As expected, interoperability is a key feature of SOAs. A simple way of ensuring interoperability has been the use of Web Services which run on a variety of different software platforms and hardware architectures. Therefore, although SOA cannot be confused with Web Services, it is usually based on them.

As a matter of fact, Web Services can be considered, in general, software systems designed to support interoperable machine-to-machine interaction (providing a common approach for their definition, publication and use) ensured through a set of XML-based open standard protocols such as Web Service Definition Language (WSDL) [18], Simple Object Access Protocol (SOAP) [19] and Universal Description, Discovery and Integration (UDDI) [20]. In the present

work the Apache eXtensible Interaction System (AXIS) has been used as SOAP engine. AXIS is, in fact, an open source framework for constructing SOAP processors (such as clients, servers and gateways) which plugs into servlet engines (e.g. Apache Tomcat [21]) and supports Java Web Services (JWS)s. As mentioned before, Web Services are the leading technology of choice for Internet-based applications with loosely coupled clients and servers and are, therefore, an obvious choice as building blocks also for developing the next generation of Grid-based applications.

Accordingly, starting from plain Web Services (as currently specified by W3C [22]), formally Grid Services are Web Services with improved characteristics and additional enhanced capabilities (as for example security and persistency). This was firstly introduced in Open Grid Services Infrastructure (OGSI) that was the first recommendation meant to provide a layer for the Open Grid Services Architecture (OGSA) describing an architecture for a service-oriented Grid computing environment. The description was derived from [23] and then developed within the Open Grid Forum (OGF) [24]. As a matter of fact, OGSI has taken into account the statelessness issues (along with others [25]) by essentially extending Web Services to allow Grid computing resources that are both transient and stateful. At present, the Web Services Resource Framework (WSRF) [26] has superseded OGSI providing a set of Web Service specifications developed by the Organization for the Advancement of Structured Information Standards (OASIS) [27] with the specific goal of defining a generic and open framework for modeling and accessing stateful resources using Web services and for describing how these mechanisms can be extended to groups of Web services. Accordingly, in our work we considered a Grid Service as a set of secure and collaborative Web Services implementing a particular high-level atomic function on the Grid middleware.

5 The GriF Implementation

In this respect, GriF [6,7] is a Java-based SOA Grid Framework aimed at running on the Grid multi-purpose scientific applications. The basic goal of GriF is to provide the users with a high-level and user friendly tool allowing them to exploit the innovative features of Grid computing with no need for mastering the low-level Grid environment. This means that there is no need for using specific Grid operating system dependent commands to manage all the Grid operations (as, for example, running Grid and/or HPC jobs, checking their status and retrieving related results) when building applications of higher level of complexity (e.g. Workflows). Accordingly, GriF makes HTC and HPC applications black-box like pushing the Grid Computing to a higher level of transparency. This makes GriF a tool of extreme importance for enhancing the VO activities. Its utilization, in fact, leads to higher memory usage, reduced cpu and wall times consumption as well as to an optimized distribution of parallel (e.g. MPI and OpenMP) tasks over the various computing platforms made available. To this end, GriF has been recently extended for distributing the various serial and

parallel computational applications (under the form of a service) on the most suited HTC or HPC platform [28] according to the simplified architecture shown in Fig. 4. In particular, the Java server called YP acts as a container providing

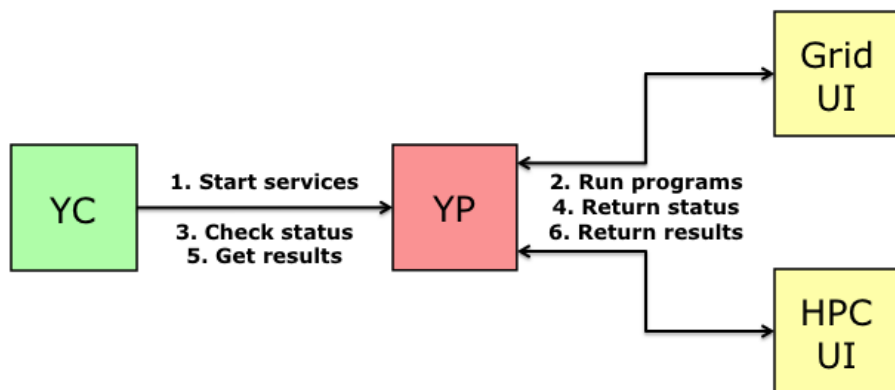


Fig. 4. Section of the GriF architecture bridging HTC and HPC

serial and parallel applications under the form of Grid Services. The Java client YC, instead, takes care of running the various HTC and HPC jobs on one of the associated User Interface (UI) and supports the correct interfacing of the Grid Services offered by GriF.

Another important extension of GriF, prompted by the use case described in detail in [28], is specifically tailored to take care of multi-executions of the computational tasks on the Grid following a user-defined operation logic providing a global path for the whole computational experiment to be carried out. As a matter of fact, the user has, in general, to upload first a set of instructions (say a kind of main procedure) chaining for example a given application (say A) to a following one (say B) by uploading the initial input and both A and B binary programs separately. Then the user can define, when is the case, the output of A as an input to B combining the Collection [29] modality within the Workflow feature of GriF to run in parallel several subjobs using different initial input files and following the same operational logic. In the same way, results generated by different Grid subjobs are channeled via the mentioned main procedure and eventually gathered in the final result file under the form of a compressed package. On top of all, this means that a general Workflow supported by GriF can make use of all the available programming language constructs and produce complex sequential, conditional and iterative paths.

As a matter of fact, this version of GriF allowing the running of complex concurrent Workflows has been tested for running part of the GEMS Workflow [28,30,31]. While running it, we faced, for example, the need for launching, as already mentioned, several concurrent tasks which are themselves Workflows (say up to 500) to be managed as they were a single Grid job splitted into

independent Grid subjobs. Accordingly, a parametrization of the application allowing to interoperate via a "multiple Workflows" approach has enabled us to properly tackle the diverse nature of multi-scale Molecular and Materials applications based on concurrent paths starting from different initial inputs leading to a faster composition and to a better chaining of data results.

In this respect, for the last two months (November 2011 - January 2012) COMPCHEM users have conducted 51 Workflow-based experiments corresponding to a total of 6231 Workflow-based jobs run on the EGI Grid middleware for a total of about 911 and 100 days of, respectively, wall time and cpu time elapsed and of about 114 GB of real memory consumed.

6 Headings for Future Evolution

As anticipated, the ability to process mixed HPC/HTC skeletons composed of simpler building blocks can be considered expressive enough to be adopted in a wider context, other than the COMPCHEM community. Therefore, although at present GriF is still limited to a predefined number of patterns specialized, in a pragmatic way, to accommodate requirements of COMPCHEM, its structure is ready to accommodate the applications of generic users. GriF allows, in fact, a generic user to describe, through an e-Science Portal and using an abstract formalism, the Workflow structure and to provide it as input to the WfMS, that, by interoperating with a job submission service (like the gLite Workload Management System [32]), will submit HTC or HPC computing tasks to the most suitable resource available in the various distributed computing infrastructures. The experience accumulated during the work reported here will mandate to keep the Workflow Engine (WfE) as general purpose as possible, so as to accommodate for a wide range of present and future needs, other than the typical uses-cases for Computational Chemistry applications that have been shown. In doing so, attention will be placed at the definition of a well-suited formalism for process description, which is basically what will be passed as input to the WfE. Another design principle is the neutrality towards the underlying infrastructure for task execution and data handling, to allow for interoperability with such heterogeneous computing paradigms as the two that this proposal addresses. A layered architecture is foreseen in such a way to abstract from both the Virtual Organization and the infrastructure frameworks, which stand at opposite ends in the proposed scenario, as shown in Fig. 5.

Proceeding bottom-up, at the very bottom lies the fabric level, for example an unorganized collection of heterogeneous computing and storage resources which are managed by some Local Resource Management Systems (LRMS)s. These resources can be abstracted, within the scope of a single infrastructure by a Grid middleware layer which sits on the LRMS layer providing consistent and homogeneous access to them. Since two different and specific Computing paradigms must be taken into account, an overall Grid Abstraction Layer (GAL) needs to be defined in order to abstract high level functionality such as job submission, data transfer, information retrieval, job tracking and monitoring. GAL services

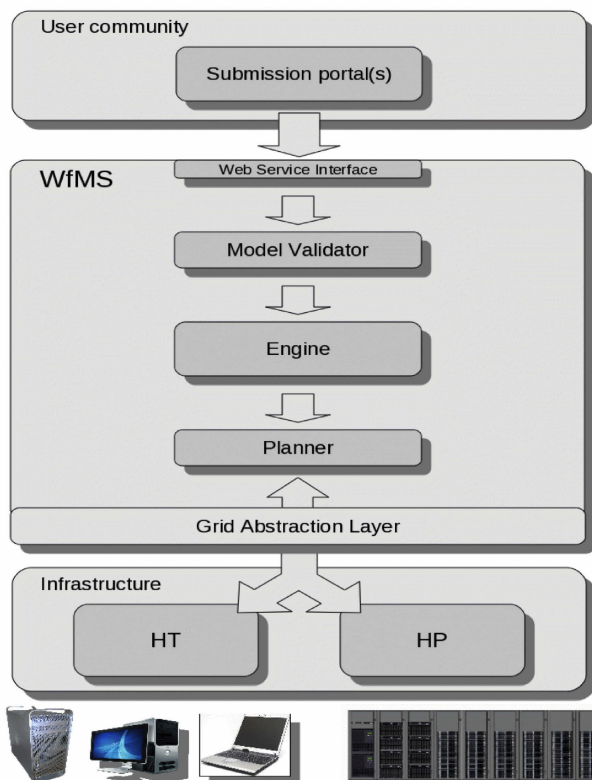


Fig. 5. A sketch of the architecture to process high-level Workflows in both HPC and HTC

and their interfaces with the underlying Grid systems will be decided through a collaborative endeavour of the researchers of the involved laboratories.

7 Conclusions

Scientific frameworks have always been targeted towards one single computing paradigm, typically HPC or HTC. The Grid middleware, in fact, requires a non-trivial level of skills and training to deal with its complexity, and the present situation typically sees only one kind of specialization addressed at a time. As a matter of fact, this led to suboptimal choices. There are cases, such the aforementioned multi-scale Molecular and Materials applications, in fact, where the nature of the Workflows is so diverse that it would hardly be managed by a single environment in an efficient way. Computations that can be split into multiple, relatively short and independent jobs are well suited on HTC, whereas single, huge computations requiring a high degree of parallelization can only be solved

on HPC supercomputers. Due to the fact that GEMS Workflows need both, the existent GriF architecture was extended to interoperate with the two paradigms. In the present phase, this has been implemented by specifically writing connectors to the different software stacks, in a pragmatic way. Future work will be devoted at developing a fully-fledged framework, also relying on mainstream technology providers such as EMI, built upon a set of standard and consolidated middleware services.

Acknowledgements. The research leading to the results presented in this paper has been possible thanks to the Grid resources and services provided by EGI and IGI. The authors also acknowledge financial support from the European Community's Seventh Framework Programme (FP7/2007-2013) under grant agreement No. 242311, from the project EGEE III and from the COST CMST Action D37 "CHEMGRID" in particular for building the collaborative distributed network. Thanks are also due for funding to the project "Fundamental Issues on the Aerothermodynamics of Planetary Atmosphere Re-entry" (AO/1-5593/08/NL/HE), the ESA-ESTEC contract 21790/08/NL/HE and MIUR. Computer time allocation has been obtained through the COMPChem VO of EGI.

References

1. PRACE Research Infrastructure, <http://www.prace-project.eu> (cited February 13, 2012)
2. TeraGrid Archives, <https://www.xsede.org/tg-archives> (cited February 13, 2012)
3. The Message Passing Interface (MPI) standard, <http://www.mcs.anl.gov/research/projects/mpi> (cited February 13, 2012)
4. European Grid Infrastructure, <http://www.egi.eu> (cited February 13, 2012)
5. ICT research in FP7, http://cordis.europa.eu/fp7/ict/e-infrastructure/calls_en.html (cited February 13, 2012)
6. Manuali, C., Rampino, S., Laganà, A.: GriF: A Grid Framework for a Web Service Approach to Reactive Scattering. *Comp. Phys. Comm.* 181, 1179–1185 (2010)
7. Manuali, C., Laganà, A.: GriF: A New Collaborative Framework for a Web Service Approach to Grid Empowered Calculations. *Future Generation Computer Systems* 27, 315–318 (2011)
8. CompChem Virtual Organization, <http://www3.compchem.unipg.it> (cited February 13, 2012)
9. Italian Grid Infrastructure, <http://grid.infn.it> (cited February 13, 2012)
10. CINECA, <http://www.cineca.it> (cited February 13, 2012)
11. Costantini, A., Gervasi, O., Manuali, C., Faginas Lago, N., Rampino, S., Laganà, A.: COMPChem: progress towards GEMS a Grid Empowered Molecular Simulator and beyond. *Journal of Grid Computing* 8(4), 571–586 (2010)
12. The General Atomic and Molecular Electronic Structure System (GAMESS) ab initio quantum chemistry package, <http://www.msg.ameslab.gov/games> (cited February 13, 2012)

13. European Middleware Initiative, <http://www.eu-emi.eu> (cited February 13, 2012)
14. EMI Execution Service page, <https://twiki.cern.ch/twiki/bin/view/EMI/EmiExecutionService> (cited February 13, 2012)
15. Costantini, A., Faginas Lago, N., Laganà, A., Huarte Larranaga, F.: A Grid Implementation of MCTDH Rate Coefficients. In: Gervasi, O., Taniar, D., Murgante, B., Laganà, A., Mun, Y., Gavrilova, M.L. (eds.) ICCSA 2009. LNCS, vol. 5593, pp. 104–114. Springer, Heidelberg (2009)
16. Manuali, C.: A Grid Knowledge Management System aimed at Virtual Research Communities Sustainability based on Quality Evaluation. Ph.D. Thesis, Department of Mathematics and Informatics, University of Perugia (IT), February 14 (2011), http://www.unipg.it/carlo/PhD_Thesis.pdf (cited February 13, 2012)
17. SOA and Web Services, <http://www.oracle.com/technetwork/articles/javase/index-142519.html> (cited February 13, 2012)
18. Web Service Description Language (WSDL) 1.1, <http://www.w3.org/TR/wsd1> (cited February 13, 2012)
19. Simple Object Access Protocol (SOAP) 1.2, <http://www.w3.org/TR/soap> (cited February 13, 2012)
20. Universal Description, Discovery and Integration (UDDI) 3.0.2, <http://www.oasis-open.org/standards#uddiv3.0.2> (cited February 13, 2012)
21. Apache Tomcat, <http://tomcat.apache.org> (cited February 13, 2012)
22. Web Services Activity, <http://www.w3.org/2002/ws> (cited February 13, 2012)
23. Foster, I., Kesselman, C., Nick, J.M., Tuecke, S.: The Physiology of the Grid: An Open Grid Services Architecture for Distributed Systems Integration, Open Grid Service Infrastructure WG, Global Grid Forum (GGF), <http://www.globus.org/alliance/publications/papers/ogsa.pdf> (cited February 13, 2012)
24. The Open Grid Forum (OGF), <http://www.ogf.org> (cited February 13, 2012)
25. What is a Grid Service?, <http://gdp.globus.org/gt3-tutorial/multiplehtml/ch01s03.html> (cited February 13, 2012)
26. OASIS Web Service Resource Framework (WSRF) TC, http://www.oasis-open.org/committees/tc_home.php?wg_abbrev=wsrf (cited February 13, 2012)
27. OASIS: Advancing Open Standards for the Global Information Society, <http://www.oasis-open.org> (cited February 13, 2012)
28. Manuali, C., Garcia, E., Laganà, A.: On the Enhancing of GriF a Workflow-oriented Grid Framework combining High-level Services. Journal of Grid Computing (submitted)
29. Job Collection - EGEE SEE ROC Wiki, http://wiki.egee-see.org/index.php/Job_Collection (cited February 13, 2012)
30. Gervasi, O., Dittamo, C., Laganà, A.: A Grid Molecular Simulator for E-Science. In: Sloot, P.M.A., Hoekstra, A.G., Priol, T., Reinefeld, A., Bubak, M. (eds.) EGC 2005. LNCS, vol. 3470, pp. 16–22. Springer, Heidelberg (2005)
31. Laganà, A., Gervasi, O.: A Priori Molecular Virtual Reality on EGEE Grid. International Journal of Quantum Chemistry 110, 446–453 (2009)
32. Marco, C., Fabio, C., Alvise, D., Antonia, G., Francesco, G., Alessandro, M., Moreno, M., Salvatore, M., Fabrizio, P., Luca, P., Francesco, P.: The gLite Workload Management System. In: Abdennadher, N., Petcu, D. (eds.) GPC 2009. LNCS, vol. 5529, pp. 256–268. Springer, Heidelberg (2009)

Taxonomy Management in a Federation of Distributed Repositories: A Chemistry Use Case

Sergio Tasso¹, Simonetta Pallottelli¹, Michele Ferroni¹,
Riccardo Bastianini¹, and Antonio Laganà²

¹ Department of Mathematics and Computer Science, University of Perugia
via Vanvitelli, 1, I-06123 Perugia, Italy
{simona,sergio}@unipg.it, micheleferroni@aruba.it,
riccardo@bastianini.org

² Department of Chemistry, University of Perugia
via Elce di Sotto, 8, I-06123 Perugia, Italy
lagana05@gmail.com

Abstract. The increasingly popular Learning Object-based didactic approach has been investigated by considering related activities of the European Chemistry Thematic Network. Learning Objects specific interoperability and reusability properties have been considered for building a didactic-scientific repositories federation. For this reason international standards have been adopted to solve interoperability problems among the different computing elements of the adopted platforms and a module has been created to effectively manage taxonomy to classify Learning Objects via ontology-based criteria.

Keywords: repository, taxonomy, learning objects.

1 Introduction

The process of assembling the educational material of a virtual campus for Chemistry and Molecular Science and Engineering teaching and learning within the EC2E2N [1] project has progressed via the definition of a common syllabus, an accreditation mechanism of the curricula for the various cycles, a procedure for carrying out internet based self evaluation sessions, and various other instruments designed and implemented by the European Chemistry Thematic Network Association (ECTNA) [2]. Other components of the virtual campus are still in their design and prototyping phase according to a roadmap that was designed in the recent past [3,4]. Among them, the one on which the efforts of an ad hoc workpackage (WP5) of the EC2E2N has focused is the assemblage of a distributed repository [5,6] aimed at storing, identifying, localizing and reusing educational information in science.

Accordingly, part of the teaching and learning materials has been packed into units (called Learning Objects or shortly LOs) which not only represent consistently a well defined topic in teaching and learning practices but also bear a specific pedagogical background and embody a significant amount of multimedia and interactivity.

LOs, also defined as “any digital resource that can be reused to support learning”[7,8], often bear such an extent of modularity, availability, reusability and interoperability it is convenient to store them in a repository (LOR [9]) and employ them in different contexts (thanks also to the recent developments of instruments like Web 2.0 [10] and other ICT products [11]).

The dramatic development of Grid and cloud technologies has prompted the multiplication of such LORs and their empowering by federating them on the network as we did when developing G-LOREP [5,6] into a distributed and collaborative LOR. After all, the building of a system of distributed LORs exploiting the collaborative use of metadata has already been shown to play a key role in the success of physical sciences teaching and learning (see for example ref. [12]).

A key feature of G-LOREP is, indeed, its focus on Virtual Organizations (VO)s and large distributed communities along the stream of activities of the involved research groups within the European Grid Infrastructure (EGI) [13] and the Computational Chemistry (COMPCHEM) [14] VO. As a matter of fact the already mentioned EC2E2N community involving more than 100 University Chemistry Departments is already a candidate itself as the educational component of the Virtual Research Community (VRC) named e-Chemist [15]. Unfortunately e-Chemist was not funded in the INFRA-10 call of the 7th Framework program of the European Commission.

Despite such failure the work of the EC2E2N WP5 has gone farther than the objectives of the project with a subset of its original 12 groups¹. The experimenting reported in the present paper has, in fact, involved mainly the Mathematics and Computer Science Department of the University of Perugia, Perugia (Italy) and the Chemistry Departments of the same University and, though to a lower extent, the University of Thessaloniki, Thessaloniki (Greece) and CPE, Lyon (France).

Already at the initial stage of the WP5 activities, the variety of EC2E2N teaching and learning subjects overflow the traditional chemistry discipline classification schemes and prompted the development of efficient mechanisms for filing and retrieving the distributed information stored in the related LOR. The illustration of such a development process is, indeed, the aim of the present publication.

¹ The groups (with the name heading each line being the local coordinator) directly involved in the virtual campus workpackage coordinated by one of the authors (A.L.), are:

Marina Rui, marina@frecy.chimica.unige.it, University of Genova, Genova, Italy,
Hazel Wilkins, h.wilkins@rgu.ac.uk, Aberdeen University, Aberdeen, United Kingdom,
Pita Vanderveelde, pita.vanderveelde@plantijn.be, Antwerp University, Antwerp, Netherland,
Carol Mathe, Carole.Mathe@univ-avignon.fr, Avignon University, Avignon, France,
Mariano Fajardo, mariano.fajardo@urjc.es, Rey Juan Carlos University, Mostoles, Spain,
Gino Paolucci, paolucci@unive.it, Ca Foscari University, Venezia, Italy,
Ioannis Kozaris, ikozaris@chem.auth.gr, Aristotle University, Thessaloniki, Greece,
Johannes Froehlich, johannes.froehlich@tuwien.ac.at, Technical University, Vienna, Austria,
Marek Frankowicz, marek.frankowicz@gmail.com, Jagiellonian University, Krakow, Poland,
Kristiina Wahala, Kristiina.Wahala@helsinki.fi, Helsinki University, Helsinki, Finland,
Stuart Bennett, s.w.bennett@open.ac.uk, Open University, United Kingdom,
Paul Peijzel, P.S.Peijzel@uu.nl, Utrecht University Utrecht, Netherland.

Accordingly, the paper is structured as follows:

- In section 2 the G-LOREP architecture is described and the importance of making use of suitable ontologies and taxonomies is pointed out;
- In section 3 the implementation of an appropriate taxonomy management is addressed;
- In section 4 the details of the functioning of the ad hoc developed Dis_Cat Drupal module are given;
- In section 5 a Chemistry use case is presented;
- In section 6 conclusions and future developments are discussed.

2 The G-LOREP Federation and LOR Taxonomies

Despite the large amount of work carried out on Learning Object Repositories there is not yet an agreed definition of LOR. The most popular definition of LOR [11] is “a database characterized by specific functions of searching, browsing, memorizing, indexing and digital distributing LOs”. The LORs are of two main types:

- Repositories containing Learning Objects and Metadata;
- Repositories containing only Metadata.

and can be implemented in two ways:

- **Centralized Repositories** containing objects on a single server or website;
- **Distributed Repositories** containing objects on multiple servers or websites connected with a peer-to-peer architecture.

The original version of our G-LOREP LOR designed for a local campus distribution was strictly centralized. At present, instead, because of the highly distributed nature of the EC2E2N WP5 members, it has been found more convenient, as already mentioned, to convert it into a federation of distributed repositories with the peculiarity of having also a central database for the purpose of making some operations quicker and easier to perform. As detailed in [6] the new G-LOREP allows the registered users to create and/or download learning contents, automatically makes such content shareable among the federation servers and enables dependency management and Software Attachment (SA) creation. That version of G-LOREP is entirely built on web technologies: it is based, in fact, on Drupal [16], a powerful Content Management System (CMS) which only requires a database and the PHP hypertext preprocessor to run.

Once Drupal had been set up, the federation was established by installing a few more modules which enable Drupal to access the shared database and to communicate to the other federates. The same procedure was required to join an existing federation, provided that the federation is set to accept new members and that the new repository is authorized to join. G-LOREP takes care of forwarding LO metadata updates to the federation, enforcing user access control on such data, compressing and transferring SA cache files and maintaining the federation in synch. Every time an object is created by a specific federate user, G-LOREP makes this action synchronized with the whole federation.

However, after we began feeding federates with new content, we quickly realized that Drupal is unable to handle content organization satisfactorily in the distributed

environment. Among the core functionalities of Drupal lies the Taxonomy module which allows a user to easily classify content and subsequently search for it. Such a module ,however, fails when moved in a distributed environment. The Taxonomy module though, is very functional and widely used in Drupal sites over the Web: for this reason we decided to extend its capabilities and adapt it to the distributed structure of G-LOREP, instead of writing a new classification system. In order to achieve this, we developed a new CMS module aimed at synchronizing the Learning Object Taxonomy. The module comes pre-loaded with a broad list of categories² and with a simple help-choice-assistant to assist the user while cataloguing new Learning Objects[17] .

Unfortunately, most of the LORs do not adopt a simple to use reference ontology to catalogue and search LOs in appropriate categories although several Learning Object Repository projects pay particular attention to the definition of the metadata standard structure. For this purpose the Dublin Core schema has been adopted by several projects to describe Learning Objects. Moreover, a workgroup (DCMI Education Community) [18] has been purposely created to adapt the standard to the *e-learning* community requirements. However, the Dublin Core schema is still too general to match the specific needs of a community. For this reason the IEEE (Institute of Electrical and Electronics Engineers), in particular the Learning Technology Standards Committee section (LTSC), created a new Learning Object Metadata standard (LOM) [19]. The IEEE/LOM standard defines the minimum set of attributes to manage, localize and evaluate Learning Objects.

Such a definition, however, still lacks an Ontology reference that would make possible a unique use of the keywords. Several projects have attempted to design a valid Ontology (ALOCoM Ontology [20,21], OntoDNA [22], Ontolingua [23]), though all of them hardly found a valid application.

The repository interface, in fact, must provide LOs with search and catalog tools able to simplify the user fruition. The most popular of such tools are either those based on the use of keywords, or the more advanced ones utilizing specific metadata information. The peculiar feature of G-LOREP is that it adopts a third search method: the distributed search, that extends over all the federation repositories [24] and operates through the use of keywords. The keyword control management is dealt with by organizing the keywords in a Taxonomy resulting from a combination of specialized Thesauri.

Several repositories prompt users to add content using metadata. Such method has the advantage of being highly flexible and adaptable. Yet it has the disadvantage of making the information too heterogeneous. The problem is partially solvable, though, by choosing a limited vocabulary to restrict the usable group of keywords during the indexing of the resources of each repository. Then the overall Vocabulary is assembled by gathering all the federation taxonomy keywords and the user-view Taxonomy is organized on a tree forest schema.

Each tree element (a category) represents a scientific subject that can be differently evaluated depending on its tree level. Categories are built out of the Dewey Decimal Classification (DDC) schema [25,26] for the following reasons:

² By category we mean a well defined knowledge area.

- ⤴ DCC is an updated international standard;
- ⤴ DCC is a multi-discipline classification that covers all the relevant fields;
- ⤴ DCC allows to associate a describing label to the subject numeric code (in order to create lists, or small word search);
- ⤴ DCC makes it possible to define classes and subclasses on different specialization levels.

A first level DCC structure for chemical subjects (the ones of our use case) is shown in Fig. 1.

Name
+ 540 - Chemistry & allied sciences
+ 541 - Physical chemistry
+ 542 - Techniques, equipment & materials
+ 543 - Analytical chemistry
+ 546 - Inorganic chemistry
+ 547 - Organic chemistry
+ 548 - Crystallography
+ 549 - Mineralogy

Fig. 1. The first level DCC Chemistry structure

3 Implementation of the Taxonomy Management

As already mentioned G-LOREP adopts the Drupal CMS. Drupal is a free and open-source CMS that does not require specific programming skills to be used. It is written in PHP and distributed under the GNU General Public License. The 6.x release of Drupal we used includes a "core" containing basic features common to most CMSs. These allow to create pages, stories, authentication rules and permissions. Moreover, they allow the adding of several custom features by installing "modules" created by the Drupal community members. Drupal treats most content types as variants of the same concept that is called node. A node is a PHP object that can be a page, a digital object (photo, video, etc.), or just a piece of information. Each node is linked to multiple DB Tables containing all its characterizing information like its ID, title, author, date of creation, type of content, subversion, the path allowing its easy attainment, etc..

In order to manage the object catalogs, Drupal provides "Taxonomy", a dormant module that belongs to the Drupal core. By activating the Taxonomy module, it becomes possible to associate categories and objects. Moreover Drupal provides a Taxonomy manager panel where the user can edit the taxonomy architecture by either creating or deleting categories. In order to deal with the G-LOREP architecture made of non-centralized repositories in which each node is both a client and a server, a new module has been designed that allows the interaction between the federation and the

Drupal local categories module. Such "Dis_Cat" module (alias of Distributed Categories) makes the taxonomy federation management possible. In the presence of "Dis_Cat", "Taxonomy" becomes another synchronized component of the G-LOREP federation.

At first we tried to build a module allowing each federate to catalog its LOs according to its own categories. However, in doing so we met organization and implementation problems associated with the fact that by inserting in the same federation objects catalogued using different criteria the material of the repository ends up being heterogeneous both in terms of contents and in terms of cataloguing mechanisms. Moreover, the implementation of the policies of editing new categories in such context was making the structure scarcely intuitive, the selection of a management standard difficult and the handling of the categories developed by the other federates unmanageable.

The problem was solved by developing a cataloguing standard enabling the sharing of categories among all the federated repositories. This makes it the cataloguing of the various LOs simpler and their fruition easier. As a matter of fact the DCC standard provides a wide range of disciplines for a large choice of associations with the federation objects. Drupal has a particular type of object to represent categories (named "term"). Term is designed to contain discipline information as name, description, classification ID, and also possible synonyms.

As a matter of fact using the term structure, a thesaurus containing subject keywords has been assembled.

Each category has a group of associated synonyms, useful for the module to work.

An example of the category "Chemistry Data processing" and its DCC structure is given in Fig. 2, where also a view of the synonyms list is shown.

Edit term

▼ Identification

Term name: *

542.85 - Chemistry Data processing

The name of this term.

▼ Advanced options

Parents:

<root>
 540 - Chemistry & allied sciences
 -541 - Physical chemistry
 -542 - Techniques, equipment & materials
 -542.8 - Auxiliary techniques and procedures, electrical and electronic equipment
 -543 - Analytical chemistry
 -546 - Inorganic chemistry
 -547 - Organic chemistry
 -548 - Crystallography

Parent terms.

Synonyms:

Computational Chemistry
 Chemistry data processing
 Cheminformatics

Synonyms of this term, one synonym per line.

Fig. 2. The DCC Chemistry Data Processing structure

The Drupal taxonomy is designed as a tree structure, in which each category (called term inside Drupal) is an element of a tree. Using "Dis_Cat" every tree of the federation taxonomy represents a master discipline (like Chemistry, Computer Science, Math, etc.), and every other node is one of its sub-categories.

To make the G-LOREP project as simple as possible, instead of using a different node type for each file type, a new Drupal node type called "Linkable Object" was created to store federation-related data along with common object information. The Learning Object information is organized in a Metadata structure that "Dis_Cat" expands with further details about object cataloging.

The "Dis_Cat" installation, does not change the architecture balance of the federation. All federation data structures become simply predisposed also for the federation taxonomy management. When "Dis_Cat" is installed, every federate receives a preloaded disciplines catalog in which the user can choose Learning Objects categories.

When an authenticated user wants to create a new Learning Object in a federate where "Dis_Cat" is installed, he/she has also to choose one or more categories for its classification. Only after making such choice the Object is loaded in the federate server. When the object upload is complete, the newly created Learning Object Metadata (containing also the new Taxonomy information) are broadcast to all the online federates as well as to the shared database. The federates which receive such Metadata, update their local databases to add the new Learning Object.

On the contrary, the temporary unavailable federates (as well as the new federates) can still read later the shared database to update local information.

4 The Taxonomy Assistant

In the preliminary trials of the Module "Dis_Cat" a lack of intuitivity while creating a LO was pointed out. The shown form of the Taxonomy module was of little help in cataloguing the LO to be created if one had not already a clear idea of what it was about. This prompted the creation of a compilation assistant.

Creating a Learning Object, requires the choice of a title, the writing of an exhaustive description of the material that is going to be shared. After the "Dis_Cat" installation, the LO creation also requires a classification to be chosen.

The "Dis_Cat" module, via the Drupal core feature AHAH (Asynchronous HTML over HTTP [27]), is able to read in real-time the object description before its actual creation. Once the description is written, the taxonomy assistant, using a customized search algorithm, produces an advice (Vocabulary Hint) about the choice of the most appropriate discipline. In this way the user receives important information about the right category association, even before sharing the Learning Object among the federation.

The implemented search algorithm, analyzes the Learning Object description by exploring the categories' forest and searching for the best match between category and object.

The Taxonomy Assistant work could be computationally optimized. For example, it would be appropriate to make that the Learning Object creator chooses a preliminary category before writing the description. If the user does so, the search algorithm explores the category tree containing the preliminarily chosen subject first and then either confirms the user's choice or searches for a better match. The implemented algorithm takes care of finding the best match between the available thesaurus and the subjects mentioned in the LO title and description. The union of both the interesting words of the title and of the description are the first elements of comparison. Meaningful words (MWs) are extracted from the LO by difference against a stopwords vocabulary [28].

Let us begin with a concept that better illustrates how terms are related to our category forest: the deeper a node is in one of our category trees, the more specific are its associated keywords.

Beginning with the category preliminarily chosen by the user, a set of keywords, resulting from the union of those belonging to the preselected category and those of its ancestors, up to the root, is assembled. With this set we are able to evaluate the relevance of the LO for the chosen category.

Fundamental to the evaluation of the relevance of a search is the matching tolerance, which is also strictly related to the tree structure of the category being explored. The tolerance threshold of a solution varies depending on the number of branching levels of the category and on its positioning on the tree. Usually it is taken to be inversely proportional to the Minimum Threshold of Acceptance (MTA) that represents the percentage of words which satisfy the matching.

In fig. 3 an example of the MTA percentage of a three level tree is shown.

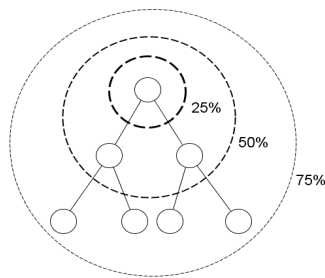


Fig. 3. MTA of a three level tree

Our algorithm considers these different detail levels while searching for the best match, as shown in fig. 4 where a macro schema of the Dis_Cat flow is illustrated.

To carry out checks between CAT and MTA (in the schema) our algorithm performs a comparison between MWs and keywords sets. After checking the affinity between the user text and the preliminary category thesaurus, the keywords of the user's suggested category are removed from the set, and those related to a sibling category are added in their place (see fig. 5, e.g. switching between CAT A to CAT B the keywords set is modified from {A+E+G} to {B+E+G}) searching for a best match. This procedure continues until there are no more sibling categories, if there is one or more of such categories satisfying the MTA, the algorithm keeps the best matching.

If the current CAT has children, these steps are applied also to them until a level with no categories satisfying the MTA is reached.

When both the preliminary choices do not satisfy the MTA, the exploration takes another direction, going upward: the current CAT becomes the father of the already examined one, and the keyword set becomes less specific and smaller (e.g. from {A+E+G} to {E+G}, see Fig. 5). As a consequence, the matching tolerance increases, while the MTA percentage decreases. In this case the search may also change tree to explore. The algorithm checks the root categories searching for the one which satisfies MTA (see fig. 6).

The algorithm terminates as soon as the best MTA is satisfied. When the search ends, a suggestion is displayed on the webpage to let the user know that either a better match has been found, or his/her preliminary choice is confirmed. The user can then accept the suggestion or discard it if he/she believes the choice made is appropriate.

There is also the possibility that the Taxonomy Assistant does not provide any feedback. In that case, a warning message is issued to the webpage advising the user to add further information about the LO.

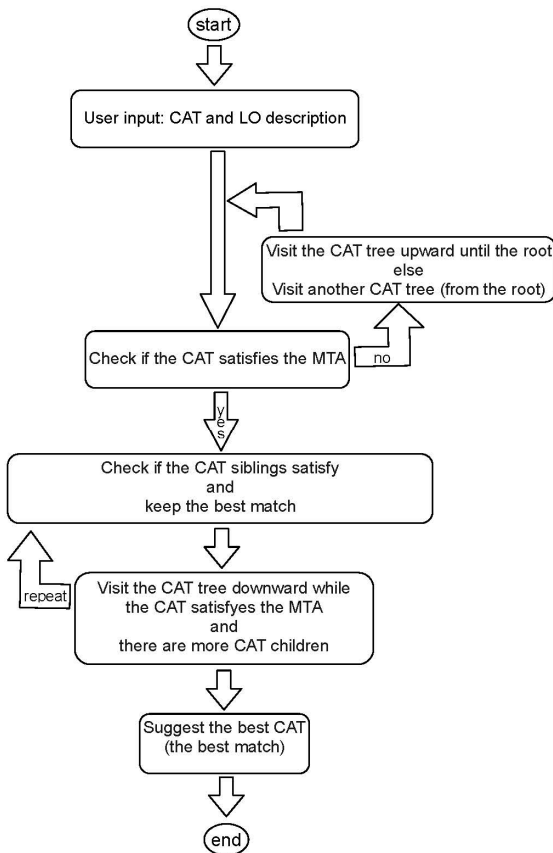


Fig. 4. The macro schema of Dis_Cat algorithm

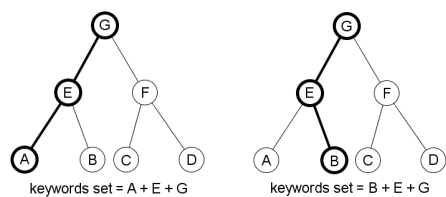


Fig. 5. Category tree horizontal exploration

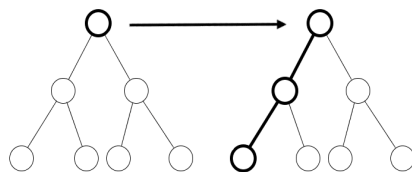


Fig. 6. Taxonomy forest exploration

5 A Chemistry Use Case

As already mentioned, we considered as a use case the handling of the teaching and learning material of the Joint Interface Third Cycle Degrees in Chemistry [29] coordinated by the University of Thessaloniki with the participation of the Computational Dynamics and Kinetics group of the Department of Chemistry of the University of Perugia.

In particular we considered the material used by the group to illustrate the research lines of the project and we show here an example of creation of the Learning Object containing the slides illustrating the relationships between Molecular and Computer Science.

To this end the user fills the required fields by writing the title and the description of the Learning Object, moreover he/she chooses a category to manually catalog the LO.

The object title is “Computational Chemistry: A doctorate at the interface between molecular and computer science”, and its description is “These slides talk about items interfacing molecular and computer science. In particular they describe several applications implemented in the virtual organization COMPCHEM of the EGI GRID” (see fig.7).

In the first instance, for example, the preliminary category selected by the user (by purpose a wrong choice was made) was, say, “Halocarbons”. When the Taxonomy Assistant is activated to the end of helping the user, its algorithm reads the input and works out other tentative categories.

At first, the taxonomy assistant removes stopwords from the text found. Then, starting from the preliminary category, the taxonomy assistant begins to analyze the reworked LO text comparing it with the keyword set that is being prepared.

In this case, the comparison between the thesaurus of the preliminary category and the user input, does not meet the threshold of acceptance (MTA). For this reason, the search moves to consider other alternatives.

The first categories analyzed are the siblings of the chosen category. The algorithm performs a comparison between the text and the keyword set of each of them. After analyzing the aforementioned categories, the algorithm heads up, since none of them meets the minimum acceptance level.

The Assistant compares then the text with the keyword-set of the father (that, being at a higher level, has a higher acceptance threshold). As the control is not yet

successful as described above, the next comparisons are made between the father's siblings, which in this case all have negative feedback, except for the branch of "Chemistry: Techniques, procedures, apparatus, equipment, materials". The outcome of the comparison between the heading of the chosen branch and the text extracted from the user input, now meets the threshold of acceptance.

Create Linkable Object

Name: *

Computational Chemistry: A doctorate at the interface between molecular and computer science

500 - Natural Sciences and Mathematics:

---547.02 - Halocarbons

—▶ [Menu settings](#)

Description:

These slides talk about items interfacing Molecular science and Computer Science, in particular they describe several applications implemented in the virtual organization COMPCHEM of the EGI GRID

Vocabulary Hint:

The recommended category is : 542.85 - Chemistry data processing

Fig. 7. A chemistry use case

At this point, the algorithm makes sure that there are no child categories which meet the higher ranking MTA. In this case the feedback is positive because in the lower level there is a child category that meets a higher threshold of acceptance, "Chemistry Data Processing". At this point the message "Vocabulary Hint" shows up on the webpage displaying the results of its search to prompt the user to change the category, by adopting the one with best relevance to its description.

6 Conclusions and Future Work

The present paper shows the progress made in organizing the content and synchronizing the taxonomy in the G-LOREP distributed federation. It also explains how a user who is not familiar with the Dewey Decimal Classification can be guided during the selection of a suitable category for a new content.

This paves the way for future work aimed to improve the algorithm in working out its suggestions by learning new keywords-category associations from LO descriptions and titles and paying attention to avoid the possibility that the tree does not lose its keyword-category balance. Due to the encouraging results obtained (further checks are being carried out), work will also be devoted to the refinement of selection criteria and terms for their coupling, even with respect to precedence. This will involve the

development of a suitable algorithm which couples the extracted terms significantly and contextually [30].

We shall address also the problem of making data transfer amongst federates instantaneous (from the user perspective)[31, 32]. However, in an attempt to make the G-LOREP modules easy to install, the communication between repositories is carried out by Drupal itself through XMLRPC and the Services module. Unfortunately, the latest versions of this module break compatibility with the older ones and lack of some functionalities (such as user authentication). For this reason we decided to rewrite the communication portion of our code and to implement it in another multiplatform language such as Java or Python. Because of the Services module compatibility issues, this part of our project will have now the highest priority.

Acknowledgements. The work has been carried out within the EC2E2N project. Thanks are due to Evangelia Varela and Ioannis Kozaris (Department of Chemistry, University of Thessaloniki, Greece), as well as to EGI and IGI.

References

1. EC2E2N European Chemistry and Chemical Engineering Education Network, <http://ectn-assoc.cpe.fr/network/ec2e2n> (last access January 2011)
2. ECTN European Chemistry Thematic Network, <http://ectn-assoc.cpe.fr/network/index.htm> (last access January 2011)
3. Laganá, A., Riganelli, A., Gervasi, O., Yates, P., Wahala, K., Salzer, R., Varela, E., Froehlich, J.: ELCHEM: A Metalaboratory to Develop Grid e-Learning Technologies and Services for Chemistry. In: Gervasi, O., Gavrilova, M.L., Kumar, V., Laganá, A., Lee, H.P., Mun, Y., Taniar, D., Tan, C.J.K. (eds.) ICCSA 2005. LNCS, vol. 3480, pp. 938–946. Springer, Heidelberg (2005)
4. Laganá, A., Manuali, C., Faginas Lago, N., Gervasi, O., Crocchianti, S., Riganelli, A., Schanze, S.: From Computer Assisted to Grid Empowered Teaching and Learning Activities in Higher Level Chemistry Education. In: Eilks, I., Byers, B. (eds.) Innovative Methods of Teaching and Learning Chemistry in Higher Education. RCS Publishing (2009)
5. Pallottelli, S., Tasso, S., Pannacci, N., Costantini, A., Lago, N.F.: Distributed and Collaborative Learning Objects Repositories on Grid Networks. In: Taniar, D., Gervasi, O., Murgante, B., Pardede, E., Apduhan, B.O. (eds.) ICCSA 2010. LNCS, vol. 6019, pp. 29–40. Springer, Heidelberg (2010)
6. Tasso, S., Pallottelli, S., Bastianini, R., Laganá, A.: Federation of Distributed and Collaborative Repositories and Its Application on Science Learning Objects. In: Murgante, B., Gervasi, O., Iglesias, A., Taniar, D., Apduhan, B.O. (eds.) ICCSA 2011, Part III. LNCS, vol. 6784, pp. 466–478. Springer, Heidelberg (2011)
7. Falcinelli, E., Gori, C., Jasso, J., Milani, A., Pallottelli, S.: E-studium: blended e-learning for university education support. *International Journal of Learning Technology* 4(1/2), 110–124 (2009)
8. Wiley, D.A.: Connecting Learning Objects to Instructional Design Theory: A Definition, A Metaphor, and A Taxonomy. In: Wiley, D.A. (DOC) (ed.) *The Instructional Use of Learning Objects: Online Version* (2000), <http://reusability.org/read/chapters/wiley.doc>
9. Smith Nash, S.: Learning Objects, Learning Object Repositories, and Learning Theory: Preliminary Best Practices for Online Courses. *Interdisciplinary Journal of Knowledge and Learning Objects* 1 (2005)

10. Stephens, M., Collins, M.: Web 2.0, Library 2.0, and the Hyperlinked Library. *Serials Review* 33(4), 253–256 (2007)
11. Regueras, L.M., Verdu, E., Perez, M.A., De Castro, J.P., Verdu, M.J.: An applied project of ICT-based active learning for the new model of university education. *Int. J. of Continuing Engineering Education and Life-Long Learning* 17(6), 447–460 (2007)
12. Schweik, C.M., Stepanov, A., Grove, J.M.: The open research system: a web-based metadata and data repository for collaborative research. *Computers and Electronics in Agriculture* 47(3), 221–242 (2005)
13. EGI (European Grid Infrastructure), <http://www.egi.eu/> (last access January 2011)
14. COMPCHEM (Computational Chemistry), <http://compchem.unipg.it> (last access January 2011)
15. e-Chemist, proposal n. 283678 submitted to Call FP7-INFRASTRUCTURE-2010-2 funding schema Integrating activities/e-infrastructures/Preparatory phase – CP – CSA – INFRA activity INFRA-2011-1.2.1 e_Science – e-Science environment
16. drupal.org, Documentation, <http://drupal.org/handbooks> (accessed November 2011)
17. Che, L.M., Hua, T.K., Cheng, H.T.: A multi-strategy knowledge interoperability framework for heterogeneous learning objects. *Journal: Expert Systems With Applications* 38(5), 4945–4956 (2011)
18. DCMI Education Community, <http://dublincore.org/groups/education/> (accessed January 2012)
19. Draft Standard for Learning Object Metadata, http://ltsc.ieee.org/wg12/files/LOM_1484_12_1_v1_Final_Draft.pdf (accessed January 2012)
20. Verbert, K., Duval, E.: ALOCOM: a generic content model for learning objects. *International Journal on Digital Libraries* 9(1), 41–63 (2008)
21. ALOCOM framework, <http://hmdb.cs.kuleuven.be/alocom/> (accessed November 2011)
22. Kiu, C.-C., Lee, C.-S.: OntoDNA: Ontology Alignment Results for OAEI (2007), <http://ceur-ws.org/Vol-304/paper17.pdf> (accessed November 2011)
23. Farquhar, A., Fikes, R., Rice, J.: The Ontolingua Server: a Tool for Collaborative Ontology Construction, http://www.vhdl.org/rassp/documents/.../KSL_96a.pdf (accessed November 2011)
24. Chu, H.-C., Chen, M.-Y., Chen, Y.-M.: A semantic-based approach to content abstraction and annotation for content management. *Expert Systems With Applications* 36(2), 2360–2376 (2009)
25. Dewey, M.: Dewey Decimal Classification and relative index / devised. In: Mitchell, J.S., et al. (eds.), 23th edn., vol. 4. Dublin, Ohio: OCLC (2011)
26. Dewey, <http://www.oclc.org/dewey/> (accessed January 2012)
27. Introduction to AHAH Forms in Drupal, <http://drupal.org/node/348475> (accessed January 2012)
28. Default English stopwords list, <http://www.ranks.nl/resources/stopwords.html> (accessed January 2012)
29. Joint Interface Third Cycle Degrees in Chemistry (Project n. 502271-LLP-1-2009-1-GR-ERASMUS-ECDSP)
30. Sanz-Rodriguez, J., Doderio, J.M., Sanchez-Alonso, S.: Metrics-based evaluation of learning object reusability. *Software Quality Journal* 19(1), 121–140 (2011)
31. Milani, A., Poggioni, V.: Planning in Reactive Environments. *Computational Intelligence* 23(4), 439–463 (2007)
32. Ukey, N., Niyogi, R., Singh, K., Milani, A., Poggioni, V.: A Bidirectional Heuristic Search for web service composition with cost. *IJWGS* 6(2), 160–175 (2010)

Grid Enabled High Level *ab initio* Electronic Structure Calculations for the N_2+N_2 Exchange Reaction

Marco Verdicchio, Leonardo Pacifici, and Antonio Laganà

Department of Chemistry, University of Perugia,
via Elce di Sotto, 8, 06123 Perugia, Italy

Abstract. A Grid enabled implementation of the first two blocks of an *ab initio* simulator of molecular systems is described by considering as a benchmark case the $\text{N}_2(^1\Sigma_g^+) + \text{N}_2(^1\Sigma_g^+)$ system. Following the related workflow and thanks to the use of the Grid, first a potential energy surface allowing the N atom reactive exchange has been generated by performing high level *ab initio* (MP2 and Coupled Cluster) calculations for a large number of geometries, then a global fit of the *ab initio* points has been performed.

1 Introduction

Significant theoretical and experimental work has been reported on weakly bound molecular clusters and complexes [1, 2]. Some of these studies have been performed in order to better characterize the dynamics of formation of highly symmetric simple molecular clusters (like the dimer $(\text{H}_2)_2$) and their main properties. Recently, growing efforts have been devoted to the determination of the interaction energy of two nitrogen molecules, $(\text{N}_2)_2$, a system that is important in high temperature atmospheric chemistry of Earth (like that occurring in spacecraft reentry [3, 4]). Moreover, due to the importance of $(\text{N}_2)_2$ in astrochemistry (it has been found, for example, that the N_2 dimer plays an important role in the atmospheric chemistry of Titan, the largest moon of Saturn), the investigation of $(\text{N}_2)_2$ has also been extended to low temperature [5].

The first attempt to model an empirical potential for the nitrogen dimer was carried out by fitting a Lennard-Jones potential to the second virial coefficient and solid state data [6–10]. Recently, by combining *ab initio* and experimental data, alternative representations of the Potential Energy Surface (PES) of $(\text{N}_2)_2$ have been proposed [11–13].

A first (partial) *ab initio* PES was assembled by Van der Avoird, Wormer and Jansen (AWJ) [14] by combining *ab initio* estimates of the short range $(\text{N}_2)_2$ interaction with long range electrostatic and dispersion terms. However, the accuracy of such PES went rapidly under scrutiny due to its inability to reproduce some experimental and theoretical findings [15, 16].

The first full *ab initio* PES of $(\text{N}_2)_2$ was developed by Stallcop and Partridge [17] by combining CCSD(T) (coupled cluster using single and double

substitutions, together with a perturbative treatment of triple excitations) calculations with second virial coefficients evaluations aimed at determining the interaction energy in the van der Waals region. In the next years, further theoretical investigations were performed in order to better characterize the interaction and formulate a new PES [18–21].

However, despite the interest shown in the past for the characterization of the $(\text{N}_2)_2$ dimer its intermolecular structure still remains a subject of controversy. The system is optically inactive (for this reason it is unsuitable for experimental investigations) and the potential strongly depends on both the distance and the reciprocal orientation of the two molecules.

The specific focus of the paper is to go through the first two blocks of GEMS (Grid Empowered Molecular Simulator) [22] that allows to determine in an *ab initio* fashion the electronic energy of several arrangements of the $\text{N}_2(^1\Sigma_g^+) + \text{N}_2(^1\Sigma_g^+)$ system all the way through from the reactant to the product arrangements of a nitrogen atom exchange reaction [23]. In the paper we describe the steps of the development of a PES for $\text{N}_2 + \text{N}_2$ by carrying out a campaign of *ab initio* calculations of the potential energy values (exploiting in a combined way both the High Throughput (HTC) and the High Performance (HPC) computing capabilities offered by the GRID [24–28]). Accordingly, in Section 2 we present low level MP2 *ab initio* calculations, in Section 3 we discuss higher level *ab initio* calculations and in Section 4 we illustrate the work done for their fitting.

2 A First Grid Based *ab initio* Investigation of the Potential Energy

The evaluation of the potential energy of a four atom system is computationally very demanding because one has to repeat the calculations (that is already heavy for a single geometry) for a large number of nuclear arrangements (10^4 if one wants 10 values per internuclear distance) with high accuracy. This type of calculations make use of a large quantity of memory and high amounts of CPU time. In our case we have been able to manage the problem by exploiting the symmetry of the system, reducing the sampling of the reactive channels and using the accessibility of both High Throughput and High Performance platforms on the Grid.

2.1 The Coordinate System and the Investigated Arrangements

A first aspect we had to take care of was the formulation of a coordinate framework tailored to preferentially describe the subspace relevant to the investigated processes. In this work we adopted a space fixed axis system with the z axis passing through the centers of mass of the two nitrogen molecules. Using such coordinates the relative positions of the nuclei of a 4 atom system, like the N_4 one considered in this paper, can be uniquely defined using the 6 variables (three radial and three angular) illustrated in Figure 1. In this scheme the orientation

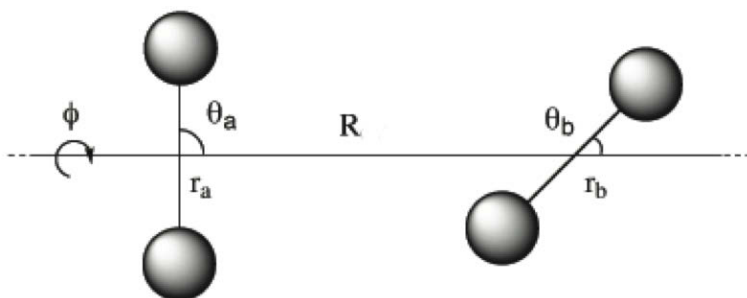


Fig. 1. Schema of the adopted coordinate system for $(\text{N}_2)_2$

of the internuclear axis of the two molecules with respect to the z axis is specified by the angles θ_a and θ_b , while the dihedral angle, ϕ , is the one formed by the planes defined by each of the N-N bonds and the z axis. The distance between the centers of mass of the two nitrogen molecules is given by R , while r_a and r_b represent the two intermolecular distances. The sampling of the various reaction channels was carried out by calculating the potential energy value at four different θ_a , θ_b , ϕ triples for R varying from 1 to 8 Å and setting the bond length of the two monomers at the equilibrium distance of 1.094 Å [29] (each $(\theta_a, \theta_b, \phi; R)$ combination will be called arrangement hereinafter). The five arrangements belong to different symmetry groups (namely: D_{2h} (90, 90, 0; R), D_{2d} (90, 90, 90; R), $D_{\infty h}$ (0, 0, 0; R), C_{2v} (0, 90, 0; R), C_{2h} (45, 45, 0; R)) and are labeled also H (parallel), X (X-shaped), L (linear) and T (T-shaped) and Z (Z-shaped), respectively, as illustrated in Figure 2.

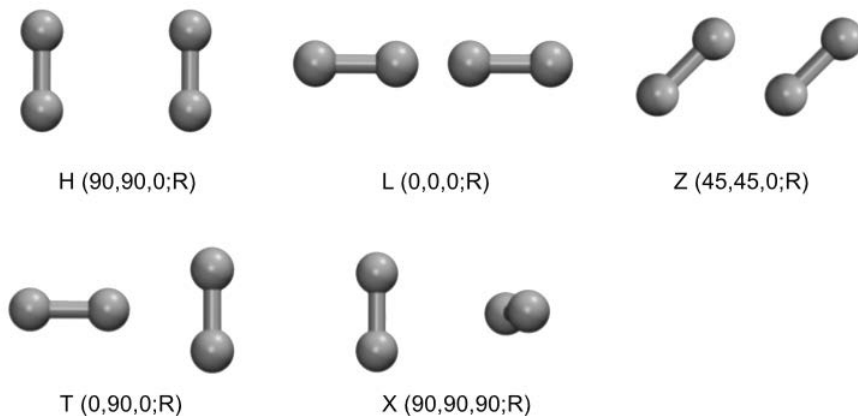


Fig. 2. Summary of the investigated arrangements

2.2 The Lower Level of Theory Calculations

To obtain a first systematic lower level *ab initio* evaluation of the electronic energies of N_4 we adopted a relatively small basis set called cc-pVTZ (correlation consistent polarized triple valence) involving 140 gaussian functions retrieved from the EMSL public database [30, 31] that is too small for the system considered and the final desired accuracy. Using such basis set we carried out extended MP2 (Second order Møller-Plesset perturbation theory) [32] *ab initio* calculations by correcting the BSSE (Basis Set Superposition Error) via the full counterpoise procedure (FCP) [33] as well as CCSD(T) (Coupled Cluster with Single and Double excitations and perturbative correction to the Triple) [34–36] ones. They were both carried out using the serial version of GAMESS-US [37, 38] offered as a Grid service by the COMPCHEM Virtual Organization [27], that thanks to its limited usage of memory and cpu time was run on the typical Grid single-core machines.

The potential energy values computed for the L, T, H and X arrangements are plotted as a function of R in Figure 3 for the short range interaction region (from $R=1$ to $R=3$ Å). Obviously, the plots of Fig. 3 can be used only as a

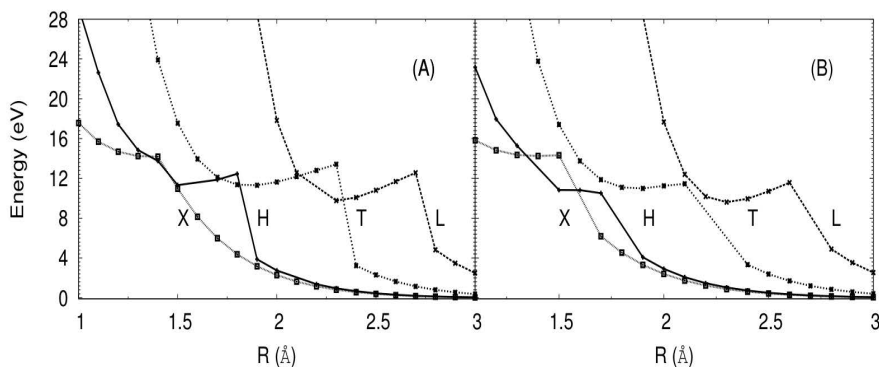


Fig. 3. MP2 (panel A) and CCSD(T) (panel B) short range (R) potential energy values (connected by straight segments) for the H, L, T and X arrangements (see text for more details) plotted as a function of R . Distances are given in Angstrom, energies in eV with the zero set at total dissociation of the two nitrogen molecules.

qualitative guide to the actual reaction path because the diatomic bond lengths are not relaxed to search for an energy minimum [39]. The plots show a close similarity between X and H (there is also a close similarity between T and Z not shown here) as well as a clearly decreasing repulsive behavior of the potential energy along the series L, T, H, X indicating that collinear encounters are quite unlikely to drive the system to likely reactive close encounters. The calculations show also that close encounters are difficult to occur (though less difficult than for linear geometries) for perpendicular approaches. For H and X arrangements,

instead, the repulsive barrier is located at such a small value of R to suggest as possible the formation of a stable $(\text{N}_2)_2$ adduct and an opening of a side (relaxed bond length) window allowing reaction. Indeed, the formation of bound states on the singlet ($^1\Sigma_g^+$) PES was already pinpointed by previous theoretical studies [40]. These are two relative minima of symmetry D_{2h} and T_d (the D_{2d} is the largest Abelian subgroup of the T_d) that favourably shape the potential channel for an exchange process.

3 The Supercomputer Based Higher-Level of Theory Calculations

After having investigated on the Grid at a lower level of theory the arrangements more relevant for understanding reaction, we turned our efforts into using a higher level *ab initio* CCSD(T) approach and the cc-pV5Z basis set that makes use of a total of 420 gaussian contractions. This suppresses the large BSSE that unphysically lowers the energy in the short range region (with respect to the long range one).

3.1 The Supercomputer Based Calculations

Using the larger cc-pV5Z basis set we repeated the calculations for the H, X, T, L and Z arrangements. The use of the cc-pV5Z basis set led to matrices of much larger dimensions that while significantly improving the accuracy of the calculations made the cost of the related computations three orders of magnitude larger and prompted the use of supercomputers. This motivated the development by our research group, in collaboration with people of INFN-CNAF and CINECA, of a tool [28, 41] allowing, though still experimentally, cross submission from the EGI Grid (using gLite middleware) to the PRACE supercomputer platform of CINECA (using Unicore middleware) on which parallel versions of electronic structure *ab initio* packages like GAMESS-US 2009 matching our calculation requirements are available. This allowed us to extend our investigation to better characterize the angular dependence of the potential energy by regularly varying the ϕ angle from 0° (H shape) to 90° (X shape), in steps of 15° . At the same time, to better sample the effect of stretching the bonds, further calculations were performed by varying the internuclear distances r_a and r_b as follows: $r_a = 1.094 \text{ \AA}$, $r_b = 1.694 \text{ \AA}$; $r_a = 1.494 \text{ \AA}$, $r_b = 1.694 \text{ \AA}$; $r_a = 1.694 \text{ \AA}$, $r_b = 1.694 \text{ \AA}$. The calculations provided us with a more accurate and a more detailed picture of the interaction of the $(\text{N}_2)_2$ system.

3.2 The Analysis of the Improved Results

The calculated intermolecular pair potential of $\text{N}_2\text{-N}_2$ for the H, X, T, L and Z arrangements considered by us are shown in Figures 4-8, in which the improved long range interaction energy is plotted as a function of R in the range 3-8 \AA . As can be seen from the long range curves shown in Figure 4, which confirm the close

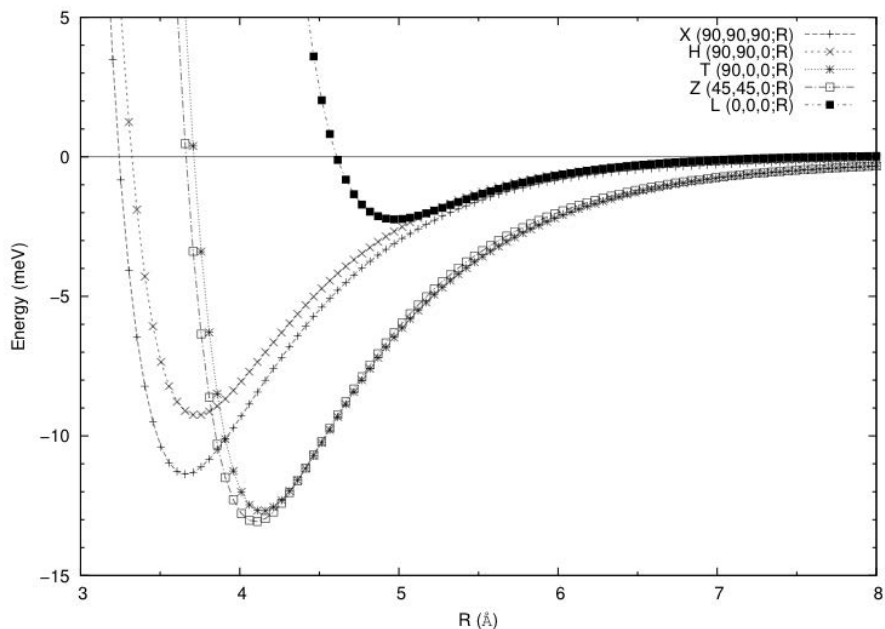


Fig. 4. Long range CCSD(T) potential energy curves plotted as a function of R for the H-shape, X-shape, T-shape, Z-shape and L-shape arrangements

similarity between the H and X and T and Z arrangements, all the investigated arrangements form van der Waals clusters having the energy minimum in the interval of R values ranging from ca. 3.5 Å (for the H-shape) to ca. 5 Å (for the L-shape). In order to get a more accurate estimate of these well depths the five curves were interpolated in the region close to the minimum, using a cubic function. In this way we obtained that for the T and Z arrangements the most stable geometries have a stabilization energy of 11.55 and 12.83 meV, respectively. On the contrary, the less stable bound geometry, the linear one, has a stabilization energy of 2.29 meV. In addition to a comparable energetic stability, T and Z structures show also a very similar position of the minimum that is for both located at about 4.1 Å. These results are in good agreement with the study of Wada et al. [18] aimed at investigating the in-plane rotation of the two N_2 monomers.

Due to their importance for the reactive exchange processes, as singled out by the lower level *ab initio* preliminary investigation, we focused our attention on the parallel (H-shape) and crossed (X-shape) arrangements. These lead to wells deep 9.38 and 11.55 meV (less deep than for the T and Z-shape arrangements) which minimum is located at $R=3.74$ Å (for H) and $R=3.64$ Å (for X), respectively. Further information can be obtained from Figure 5, where the long range potential energy curves for the arrangements obtained by varying the Φ angle value from 0 (H-shape) to 90 (X-shape) degree have been reported. As can be clearly seen

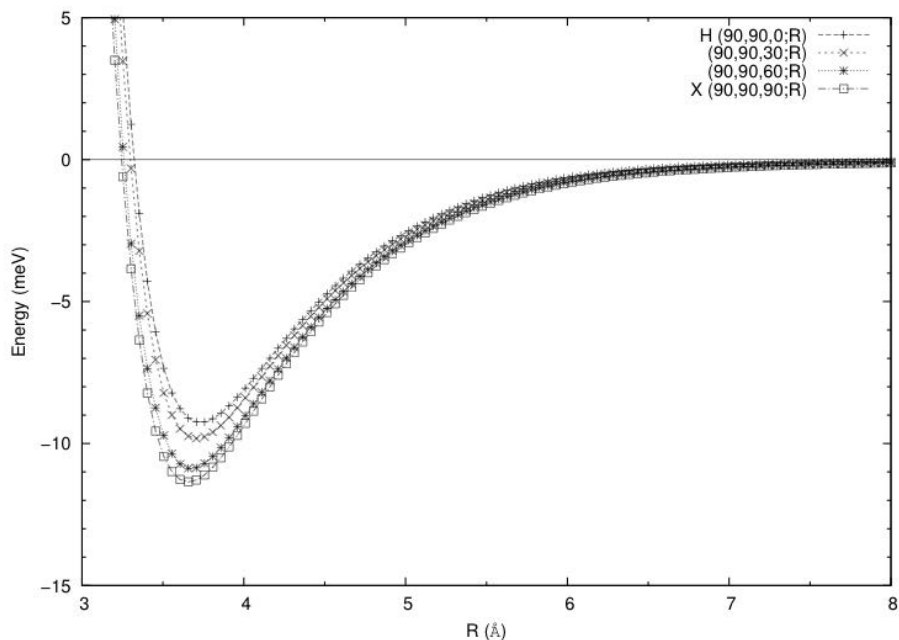


Fig. 5. Long range CCSD(T) potential energy curves plotted as a function of R at different values of Φ

from the Figure, in going from the H to the X arrangement the location on R of the minimum lowers gradually with Φ and the well depth deepens.

In order to better analyze that region of the PES, we also compared the behavior of the H and X arrangements when one or both intermolecular distances are stretched with respect to the N_2 equilibrium distance [42]. For illustrative purposes, we plot in Figure 6 the values of the potential energy for the considered arrangements as a function of R while stretching the internuclear distances from 0.4 to 0.6 Å. The potential energy curves of the H and X arrangements show a well defined minimum also with the stretching of the intermolecular bonds. As we can see from the interpolated values reported in Table 1 the position of the minimum does not change appreciably when varying r_a and r_b whereas the related energy difference decreases significantly.

However, when the intermolecular distance is increased from equilibrium the role of non-dynamical correlation energy becomes important and the wavefunction of the system cannot be properly described by a single determinant. Following the diagnostic method proposed by Lee and Taylor [43] we found that for our system a multireference electron correlation approach is needed. Unlike the long range region, the short range one does not show any stable structures. Figure 7 suggests that when R shrinks, the potential energy increases although a channel is likely to open to allow exchange reaction via a change of arrangement. The X, T and L arrangements exhibit a local minimum that follows (as R decreases)

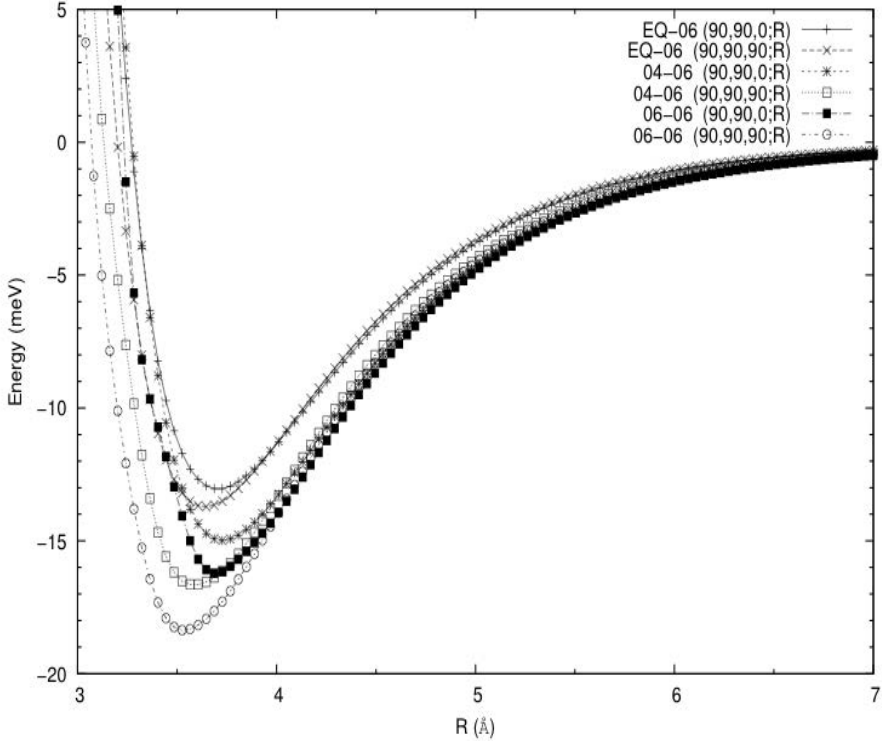


Fig. 6. CCSD(T) Van der Waals potential energy curves plotted as a function of R of the three stretched geometries for the H and X arrangements. The plus and cross symbols refer to the arrangements with one intermolecular distance at the equilibrium and the other one stretched by 0.6 \AA (EQ-06); the star and white-square symbols refer to the arrangements with one distance stretched by 0.4 \AA and the other one by 0.6 \AA (04-06) whereas the circle and the black-square symbols refer to the arrangements with both intermolecular distances stretched by 0.6 \AA (06-06).

Table 1. Interpolated positions and energy variations for H and X arrangements minima. The internuclear distances of each monomer are stretched.

	$r_a \mid r_b$ 1.094 1.694	$r_a \mid r_b$ 1.494 1.694	$r_a \mid r_b$ 1.694 1.694
$R_H \text{ [\AA]}$	3.72	3.74	3.72
$R_X \text{ [\AA]}$	3.63	3.60	3.55
$\Delta E_{H-X} \text{ [meV]}$	0.7541	1.7300	2.3175

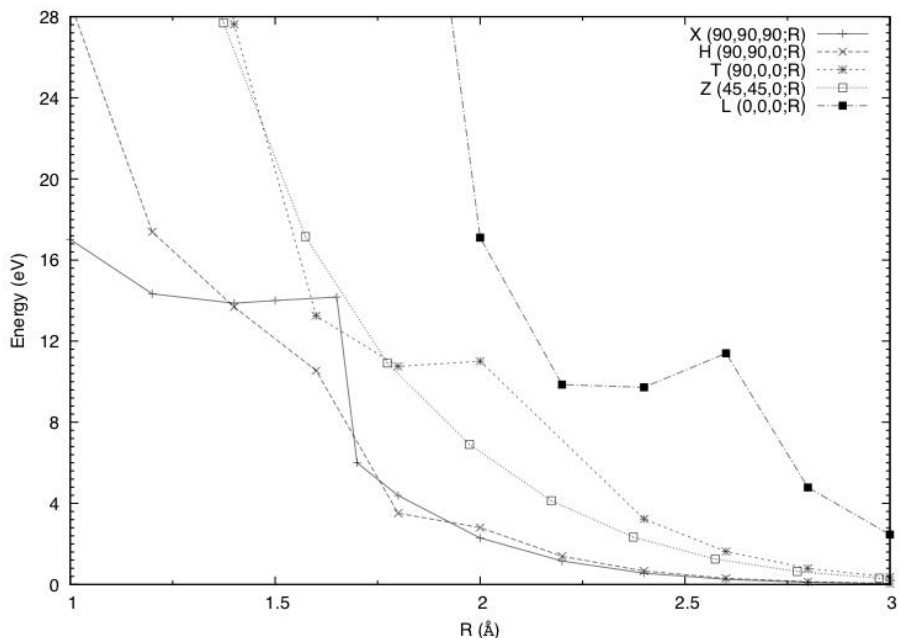


Fig. 7. Short range CCSD(T) potential energy values plotted as a function of R , like in panel (B) of Fig. 3

a first maximum (located at larger distances) and moves to lower R values in going from L to X, while this is not true for the H and Z ones which exhibit only a repulsive wall. The dependence of the potential energy value from Φ in the same short range interval of R values is plotted in Figure 8.

4 The Fit of the *ab initio* Potential Energy Values

The last part of the work has been concerned with the fitting of the calculated CCSD(T) results using a suitable functional form in order to allow a fast evaluation of the potential energy and its derivatives at any given geometry accessed during dynamical calculations for the $N_2(^1\Sigma_g^+) + N_2(^1\Sigma_g^+)$ reaction. A further clear advantage of adopting the procedure of fitting the *ab initio* points using a functional form is associated with the fact that this allows the incorporation of corrections when the values of the *ab initio* points are found to be inadequate either during the fitting process or during dynamical calculations.

4.1 The Adopted Fitting Procedure

The functional form adopted for this purpose is made of polynomials in physical coordinates. The theoretical ground for such representation is the Many Body

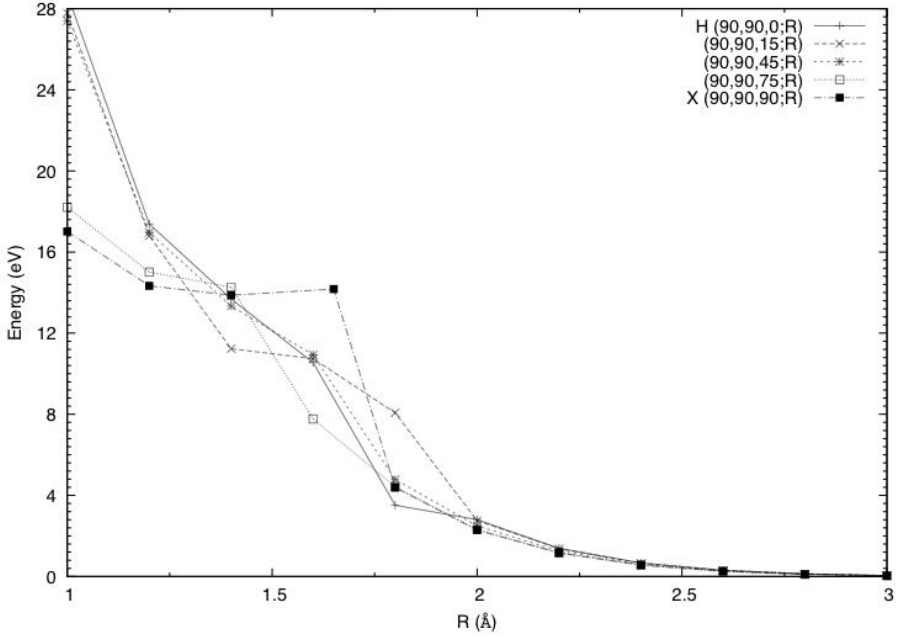


Fig. 8. Short range CCSD(T) potential energy curves plotted as a function of R for different values of Φ

Expansion (MBE) method developed by Sorbie and Murrell [44]. The MBE method is able, in principle, to fit potential energy surfaces for systems made of any number of atoms. The expression of the many-body expansion for a four-atom system is given as a sum of one-body (1), two-body (2), three-body (3) and four-body (4) terms as follows:

$$\begin{aligned}
 V(r_a, r_b, \theta_a, \theta_b, \Phi, R) = & V_A^{(1)} + V_B^{(1)} + V_C^{(1)} + V_D^{(1)} + \\
 & V_{AB}^{(2)}(\xi_{AB}) + V_{AC}^{(2)}(\xi_{AC}) + V_{BC}^{(2)}(\xi_{BC}) + \\
 & V_{AD}^{(2)}(\xi_{AD}) + V_{BD}^{(2)}(\xi_{BD}) + V_{CD}^{(2)}(\xi_{CD}) + \\
 & V_{ABC}^{(3)}(\xi_{AB}, \xi_{BC}, \xi_{AC}) + V_{ABD}^{(3)}(\xi_{AB}, \xi_{BD}, \xi_{AD}) + \\
 & V_{ACD}^{(3)}(\xi_{AC}, \xi_{AD}, \xi_{CD}) + V_{BCD}^{(3)}(\xi_{BC}, \xi_{CD}, \xi_{BD}) + \\
 & V_{ABCD}^{(4)}(\xi_{AB}, \xi_{AC}, \xi_{AD}, \xi_{BC}, \xi_{BD}, \xi_{CD}) \quad (1)
 \end{aligned}$$

in which for sake of simplicity the four N atoms are called A, B, C, D and ξ is an appropriate function of the relative positions of the nuclei. The one-body terms $V^{(1)}$ are the electronic energies of the atoms in the appropriate dissociation configuration. For the N_2+N_2 electronic ground state potential energy surface these terms were set equal to zero. In the Paniagua approach embodied in the `gfit4c` routines [45] adopted by us, ξ is defined as a function of the internuclear

distances r_{ij} and the two-body components (say $V_{AB}^{(2)}(\xi_{AB})$) of the potential are expressed as:

$$V_{AB}^{(2)}(\xi_{AB}) = \frac{c_{0AB}e^{-\alpha_{AB}r_{AB}}}{r_{AB}} + \sum_{s=1}^S c_{sAB}\rho_{AB}^s \quad (2)$$

in which ρ_{AB} is a Rydberg-like variable formulated as:

$$\rho_{AB} = r_{AB}e^{-\beta_{AB}^{(p)}r_{AB}}, p = 2, 3, \text{ or } 4 \quad (3)$$

with p being chosen as in [46]. The c_{sAB} coefficients (including $s=0$) as well as the non linear parameters $\beta_{AB}^{(p)}$ were evaluated by fitting the two-body *ab initio* values and S is the chosen order of the polynomial. The three-body terms (say $V_{ABC}^{(3)}(\xi_{AB}, \xi_{AC}, \xi_{BC})$) were expressed in terms of polynomials of order N in the same Rydberg-like variables (ρ_{AB} , ρ_{AC} and ρ_{BC}):

$$V_{ABC}^{(3)}(\xi_{AB}, \xi_{AC}, \xi_{BC}) = \sum_{lmn}^N d_{lmn}\rho_{AB}^l\rho_{AC}^m\rho_{BC}^n \quad (4)$$

with the d_{lmn} coefficients being evaluated by fitting the three body ABC *ab initio* values. Finally, also the functional form chosen to express the four-body term $V_{ABCD}^{(4)}(\xi_{AB}, \xi_{AC}, \xi_{AD}, \xi_{BC}, \xi_{BD}, \xi_{CD})$ was written, similarly to what has been done for the three-body term, in terms of a polynomial of order N in the Rydberg-like variables (ρ_{AB} , ρ_{AC} , ρ_{AD} , ρ_{BC} , ρ_{BD} and ρ_{CD}):

$$V_{ABCD}^{(4)} = \sum_{ijklmn}^N e_{ijklmn}\rho_{AB}^i\rho_{AC}^j\rho_{AD}^k\rho_{BC}^l\rho_{BD}^m\rho_{CD}^n \quad (5)$$

where appropriate constraints are imposed on the indices in order to guarantee the right behavior of the polynomial in all regions of the configuration space.

4.2 The Actual Fit of the PES

As already mentioned, the fitting procedure of the global PES for the $N_2(^1\Sigma_g^+) + N_2(^1\Sigma_g^+)$ system has been based on three different sets of *ab initio* points: 1440 two-body values, 4320 three-body values and 1917 four-body values. Moreover, by exploiting the total symmetry of the system data were replicated to enforce symmetry under atom permutations. Whenever possible *ab initio* values were also corrected using experimental information. This has been possible for both the two and three body terms thanks also to the work previously performed for the assemblage of the PES for the $N + N_2$ system [47, 48]. Moreover, all the *ab initio* values were scaled with respect to the dissociation energy of the dimer. The scaling values were calculated at CCSDT(T) level of theory. In particular, we calibrated the calculated potential energy values with respect to the single energy point obtained by increasing R till its convergency and comparing the

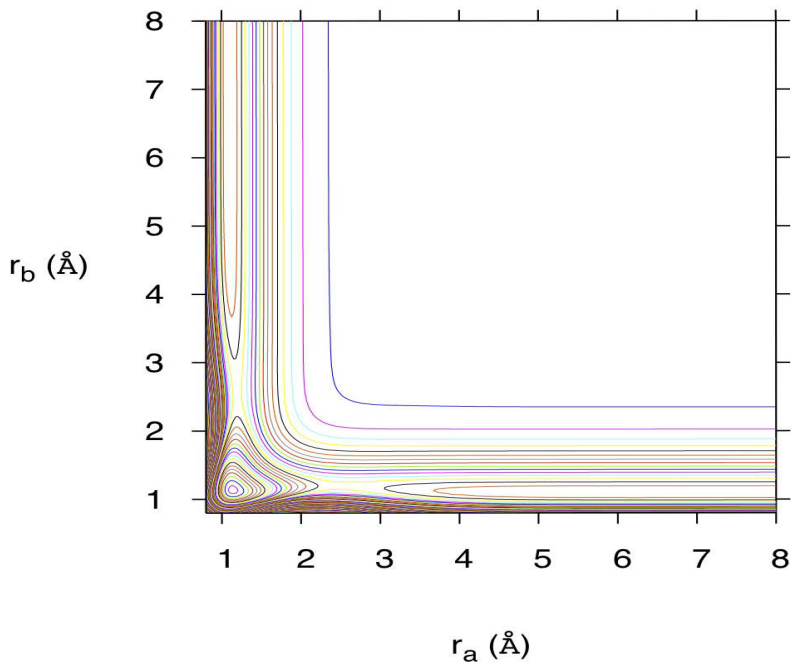


Fig. 9. $N_2 + N_2$ isoenergetic contours of the fitted potential energy surface calculated for the H arrangement at $R=6$. The contours are spaced of about half eV.

obtained value with the one obtained for an isolated nitrogen molecule (the value used is -218.82612523 Hartree).

The root mean square deviation of the fitted two and three body terms are of 0.005 and 0.05 eV, respectively. It is important to point out here that because the *gfit4c* procedure does not include the possibility of specifying that the system is made of all atoms of the same type (say AAAA), but only of ABCD, AABB and ABBB systems, we have been able to work with N_4 using the AABB class of systems thanks to the already mentioned procedure of replicating data. Moreover, a further analysis of the *ab initio* electronic energy values obtained by plotting them for each arrangement (X, H, etc.) versus R showed some unphysical points characterized by a large rms. These points have then been excluded from the final fit and, in some cases, replaced by values interpolated from their neighbors. As a result, we reduced the total number of *ab initio* points to 1870 (that, taking into account the symmetry permutations, become 11220) and carried out the fit using a polynomial of order 8. The overall calculated rms is about 0.2 eV with a maximum error of 2 eV in highly repulsive regions. For illustrative purposes in Figure 9 we plot the isoenergetic contours of the fitted PES for the $N_2 + N_2 \rightarrow N_2 + N_2$ exchange reaction calculated for the H arrangements, are taken at $R=6$ Å with the contours being spaced of about half eV. The figure clearly shows a reactive channel to exchange going through a double barrier of a few eV with interposed a well at short internuclear distances stabilizing the N_4 complex.

5 Conclusions

Thanks to the exploitation of the increasing versatility of the Grid empowered molecular simulator GEMS implemented on the section of the European Grid Initiative accessible to the members of the virtual organization COMPCHEM we have tackled the problem of building the Potential Energy Surface for the $N_2 + N_2$ exchange reaction. To this end in the first block of the simulator devoted to *ab initio* calculations the package GAMESS-US was used at different levels of theory and by exploiting via the Grid both HTC and HPC platforms. The calculated *ab initio* potential energy values were, when possible, cleared from the results of anomalous runs, modified to ensure the reproduction of the basic properties of a potential energy surface (continuity, symmetry, etc.) and fitted using a Many Body method and the numerical procedure of Paniagua. The process has involved a first step of lower level of theory investigation on the Grid devoted to the analysis of the main qualitative features of the PES for the most important arrangements. Then, the calculations were pushed to a higher level of theory by exploiting an ad hoc open communication channel of the Grid to the CINECA supercomputer. The resulting potential energy values were fitted in the second block of the simulator using a proper functional form. This has allowed us to investigate in detail the reaction channel. Despite the fact that the calculated rms for the fit of the 4-body component of the overall potential for some arrangements (in particular, those characterized by small values of R) still remains above the usually accepted limit of chemical accuracy, the produced PES behaves properly and before upgrading the calculations to a MRSCF level we are planning to explore its suitability for dynamical calculations.

Acknowledgments. This research was supported by the EGI-Inspire project (contract 261323), the MIUR PRIN 2008 (contract 2008KJX4SN 003), the ESA-ESTEC contract 21790/08/NL/HE, the Phys4Entry (Planetary Entry Integrated Models) FP7/2007-2013 project (contract 242311) and INSTM. The authors also wish to acknowledge CINECA (IT) and CESGA (ES) for computing time on their parallel platforms. The research leading to the results presented in this paper has been supported by the use of the Grid resources and services provided by the European Grid Infrastructure (EGI) and the Italian Grid Infrastructure (IGI) For more information, please reference the EGI-InSPIRE paper (<http://go.egi.eu/pdnon>) and the IGI web server (<http://www.italiangrid.it>)

References

1. Nesbitt, D.J.: High-resolution infrared spectroscopy of weakly bound molecular complexes. *Chem. Rev.* 88, 843–870 (1988)
2. Weber, A.: *Structure and Dynamics of Weakly Bound Molecular Complexes* (NATO Science Series C) (1987)
3. Capitelli, M.: *Non-equilibrium vibrational kinetics*. Springer, Berlin (1986)

4. Armenise, I., Capitelli, M., Garcia, E., Gorse, C., Laganà, A., Longo, S.: Deactivation dynamics of vibrationally excited nitrogen molecules by nitrogen atoms. Effects on non-equilibrium vibrational distribution and dissociation rates of nitrogen under electrical discharges. *Chem. Phys. Lett.* 200, 597 (1992)
5. Knauth, D.C., Andersson, B.G., McCandliss, S.R., Moos, H.W.: The Interstellar N₂ Abundance toward HD 124314 from Far-Ultraviolet Observations. *Nature* 429, 636 (2004)
6. Raich, J.C., Gillis, N.S.: The anisotropic interaction between nitrogen molecules from solid state data. *J. Chem. Phys.* 66, 846 (1977)
7. MacRury, T.B., Steele, W.A., Berne, B.J.: Intermolecular potential models for anisotropic molecules, with applications to N₂, CO₂, and benzene. *J. Chem. Phys.* 64, 1288 (1976)
8. Cheung, P.S.Y., Powles, J.G.: The properties of liquid nitrogen V. Computer simulation with quadrupole interaction. *Mol. Phys.* 32, 1383 (1976)
9. Cheung, P.S.Y., Powles, J.G.: The properties of liquid nitrogen. *Mol. Phys.* 30, 921 (1975)
10. Evans, D.J.: Transport properties of homonuclear diatomics I. Dilute gases. *Mol. Phys.* 34, 103 (1977)
11. Cappelletti, D., Vecchiocattivi, F., Pirani, F., Heck, E.L., Dickinson, A.S.: An Intermolecular potential for Nitrogen from a multi-property analysis. *Mol. Phys.* 93, 485 (1998)
12. Aquilanti, V., Bartolomei, M., Cappelletti, D., Caramona-Novillo, E., Pirani, F.: The N₂-N₂ system: An experimental potential energy surface and calculated rovibrational levels of the molecular nitrogen dimer. *J. Chem. Phys.* 93, 485 (1998)
13. Gomez, L., Bussery-Honvault, B., Cauchy, T., Bartolomei, M., Cappelletti, D., Pirani, F.: Global fits of new intermolecular ground state potential energy surfaces for N₂-H₂ and N₂-N₂ van der Waals dimers. *Chem. Phys. Lett.* 445, 99–107 (2007)
14. van der Avoird, A., Wormer, P.E.S., Jansen, A.P.J.: An improved intermolecular potential for nitrogen. *J. Chem. Phys.* 84, 1629–1635 (1986)
15. Cappelletti, D., Vecchiocattivi, F., Pirani, F., McCourt, F.R.W.: Glory structure in the N₂-N₂ total integral scattering cross section. A test for the intermolecular potential energy surface. *Chem. Phys. Lett.* 248, 237–243 (1996)
16. Huo, S.W.M., Green, S.: Quantum calculations for rotational energy transfer in nitrogen molecule collisions. *J. Chem. Phys.* 104, 7572–7589 (1996)
17. Stallcop, J.R., Partridge, H.: The N₂-N₂ potential energy surface. *Chem. Phys. Lett.* 281, 212–220 (1997)
18. Wada, A., Kanamori, H., Iwata, S.: Ab Initio MO studies of van der Waals molecule (N₂)₂: Potential energy surface and internal motion. *J. Chem. Phys.* 109, 9434–9438 (1998)
19. Couronne, O., Ellinger, Y.A.: An ab initio and DFT study of (N₂)₂ dimers. *Chem. Phys. Lett.* 306, 71–77 (1999)
20. Leonhard, K., Deiters, U.K.: Monte Carlo Simulations of Nitrogen Using an Ab Initio Potential. *Mol. Phys.* 100, 2571–2585 (2002)
21. Karimi Jafari, M.H., Maghari, A., Shahbazian, S.: An improved ab initio potential energy surface for N₂-N₂. *Chem. Phys.* 314, 249–262 (2005)
22. Costantini, A., Gervasi, O., Manuali, C., Lago, N.F., Rampino, S., Laganà, A.: COMPCHEM: progress towards GEMS a Grid Empowered Molecular Simulator and beyond. *Journal of Grid Computing* 8, 571–586 (2010)

23. Laganá, A., Balucani, N., Crocchianti, S., Casavecchia, P., Garcia, E., Saracibar, A.: An Extension of the Molecular Simulator GEMS to Calculate the Signal of Crossed Beam Experiments. In: Murgante, B., Gervasi, O., Iglesias, A., Taniar, D., Apduhan, B.O. (eds.) ICCSA 2011, Part III. LNCS, vol. 6784, pp. 453–465. Springer, Heidelberg (2011)
24. EGI-InSPIRE project RI-261323, <http://www.egi.eu> (last access: January 11, 2012)
25. EGI, <http://uf2011.egi.eu/> (last access December 14, 2011)
26. IGI, <http://grid.infn.it/> (last access December 14, 2011)
27. COMPCHEM, <http://compchem.unipg.it> (last access November 14, 2011)
28. Manuali, C., Costantini, A., Laganà, A., Cecchi, M., Ghiselli, A., Carpené, M., Rossi, E.: Efficient Workload Distribution Bridging HTC and HPC in Scientific Computing. In: Murgante, B., et al. (eds.) ICCSA 2012, Part I. LNCS, vol. 7333, pp. 345–357. Springer, Heidelberg (2012)
29. Hay, P.J., Pack, R.T., Martin, R.L.: Electron correlation effects on the N₂-N₂ interaction. *J. Chem. Phys.* 81, 1360–1372 (1984)
30. Feller, D.: The Role of Databases in Support of Computational Chemistry Calculations. *J. Chem. Phys.* 17, 1571–1586 (1996)
31. Schuchardt, K., Didier, B., Elsethagen, T., Sun, L., Gurumoorthi, V., Chase, J., Li, J., Windus, T.: Basis Set Exchange: A Community Database for Computational Sciences. *J. Chem. Inf. Model.* 47, 1045–1052 (2007)
32. Møller, C., Plesset, M.S.: Note on an Approximation Treatment for Many-Electron Systems. *Phys. Rev.* 46, 618 (1934)
33. Boys, S.F., Bernardi, F.: The calculation of small molecular interactions by the differences of separate total energies. Some procedures with reduced errors. *Mol. Phys.* 19, 553–566 (1970)
34. Piecuch, P., Kucharski, S.A., Kowalski, K., Musial, M.: Efficient computer implementation of the renormalized coupled-cluster methods: The R-CCSD[T], R-CCSD(T), CR-CCSD[T], and CR-CCSD(T) approaches. *Comput. Phys. Comm.* 149, 71–96 (2002)
35. Bentz, J.L., Olson, R.M., Gordon, M.S., Schmidt, M.W., Kendall, R.A.: Coupled cluster algorithms for networks of shared memory parallel processors. *Comput. Phys. Comm.* 176, 589–600 (2007)
36. Olson, R.M., Bentz, J.L., Kendall, R.A., Schmidt, M.W., Gordon, M.S.: A Novel Approach to Parallel Coupled Cluster Calculations: Combining Distributed and Shared Memory Techniques for Modern Cluster Based Systems. *J. Comput. Theo. Chem.* 3, 1312–1328 (2007)
37. Schmidt, M.W., Baldridge, K.K., Boatz, J.A., Elbert, S.T., Gordon, M.S., Jensen, J.J., Koseki, S., Matsunaga, N., Nguyen, K.A., Su, S., Windus, T.L., Dupuis, M., Montgomery, J.A.: General atomic and molecular electronic structure system. *J. Comp. Chem.* 14, 1347–1363 (1993)
38. Gordon, M.S., Schmidt, M.W.: Theory and Applications of Computational Chemistry, the first forty years (2005)
39. Laganà, A.: Potential surface graphical study for chemical reactions. *Computer and Chemistry* 4, 137–143 (1980)
40. Lee, T.J., Rice, J.E.: Theoretical characterization of tetrahedral N₄. *J. Chem. Phys.* 94, 1215–1221 (1991)
41. Manuali, C., Laganà, A.: A New Collaborative Framework for a Web Service Approach to Grid Empowered Calculations. *Future Generation of Computer Systems* 27(3), 315–318 (2011)

42. Hay, P.J., Pack, R.T., Martin, R.L.: Electron correlation effects on the N_2-N_2 interaction. *J. Chem. Phys.* 81, 1360–1372 (1984)
43. Lee, T.J., Taylor, P.R.: A Diagnostic for Determining the Quality of Single-Reference Electron Correlation Methods. *Int. J. Quant. Chem.* S23, 199–207 (1989)
44. Sorbie, K.S., Murrell, J.N.: Analytical potentials for triatomic molecules from spectroscopic data. *Mol. Phys.* 52, 1387 (1975)
45. Aguado, A., Tablero, C., Paniagua, M.: Global fit of ab initio potential energy surfaces: II.1. Tetraatomic systems ABCD. *Comput. Phys. Comm.* 134, 97 (2001)
46. Aguado, A., Suarez, C., Paniagua, M.: Accurate global fit of the H_4 potential energy surface. *J. Chem. Phys.* 101, 404–4010 (1994)
47. Garcia, E., Saracibar, A., Gomez-Carrasco, S., Laganà, A.: Modelling the global potential energy surface of the $N + N_2$ reaction from ab initio data. *Phys. Chem. Chem. Phys.* 10, 2552–2558 (2008)
48. Caridade, P.J.S.B., Galvao, B.R.L., Varandas, A.J.C.: Quasiclassical Trajectory Study of Atom-Exchange and Vibrational Relaxation Processes in Collisions of Atomic and Molecular Nitrogen. *J. Phys. Chem. A* 114, 6063–6070 (2010)

A Bond-Bond Portable Approach to Intermolecular Interactions: Simulations for N-methylacetamide and Carbon Dioxide Dimers

Andrea Lombardi¹, Noelia Faginas Lago^{1,*}, Antonio Laganà¹,
Fernando Pirani¹, and Stefano Falcinelli²

¹ Dipartimento di Chimica,

Universita' di Perugia, Perugia, Italy

² Department of Civil and Environmental Engineering,

Universita' di Perugia, Perugia, Italy

{ebiu2005,piovro,lagana05}@gmail.com, {pirani,stefano}@unipg.it
<http://www.chm.unipg.it/gruppi?q=node/48>

Abstract. In this paper we present two applications of a recently developed method for obtaining analytical potential energy surfaces describing the intermolecular interaction of pairs of molecules made up of three or more atoms. The method is based on an empirical formulation of the intermolecular terms of the potential based on the idea that pairwise interaction terms, usually appearing in the many-body expansion of the potential energy, must be referred to pairs of interacting centers (group of atoms and/or bonds) of the molecular monomers, rather than, as traditionally done, to atomic centers. Such representation is incorporated in a grid empowered molecular simulator and coupled with dynamical calculations to evaluate observable properties of a simple CO₂ dimer and a more complex chemical system (the N-methylacetamide dimer).

Keywords: Intermolecular interaction, molecular dynamics, classical dynamics, H-bonds, carbon dioxide.

1 Introduction

The detailed theoretical and experimental investigation of intermolecular (weak and non-covalent) forces is of crucial importance to understand their nature, to model their behavior, and to define their influence on many observed phenomena both in gaseous and condensed phases [1, 2]. Following the scheme of our grid empowered molecular simulator [3] we have assembled a suitable representation of the Potential Energy Surface (PES) and then performed on it dynamical calculations. The calculations were aimed at reproducing observable properties of the title chemical systems and were made possible by the exploitation of the innovative computational features of the European and Italian segment of the grid [4] available to the computational chemistry COMPChem Virtual Organization [5].

* Corresponding author.

Intermolecular interactions determine the equilibrium geometry of molecular aggregates and strongly affect the dynamics of their components, so influencing transport properties, energy exchange and chemical reactivity. Small molecules, though with a sufficiently complex structure, can serve as prototypes for understanding patterns and common features of the mentioned observable properties as well as to test theoretical approaches and empirical descriptions of the interactions. For this purpose we have chosen the $\text{CO}_2 + \text{CO}_2$ system as representative of the role that intermolecular interaction plays in collision dynamics. In particular, rotovibrational energy exchange, associated in rarefied gas phase with bimolecular collisions which are selectively driven by non-covalent intermolecular forces, are largely responsible for energy relaxation and state population of the involved molecules. Such energy relaxing and population altering effects play a key role in determining the energy balance of several chemical processes. At the same time, however, due to fact that also properties of aggregates of more complex molecules can be reconducted to those of simpler molecular building blocks, the approach can be applied to larger molecular structures. For this reason we considered in our study also the N-methylacetamide (NMA), which presents interactions typical of biological molecules (e.g. $\text{N-H} \cdots \text{O}=\text{C}$ and $\text{C-H} \cdots \text{O}=\text{C}$) [6–8], both in its dimer and solvated form.

The availability of transferable descriptions of the intermolecular interaction, is of fundamental importance in biological systems and life science. However, in principle, the only truly transferable approach to the description of the intermolecular interaction is the high level *ab initio* one. Yet, even for the relatively simple systems considered here, high level *ab initio* calculations are computationally so demanding that an adequate investigation of their full configuration space is still, in practice, out of reach. For this reason, high level *ab initio* calculations are still confined to the most stable geometries of the monomers (the so called strong or intramolecular interaction region) and are seldom extended to molecule-molecule (the so called weak or intermolecular) interaction regions, which are often governed by long range non-covalent forces.

Ab initio calculations have been performed in refs. [9] for CO_2 and in refs. [10–16] for NMA. The study of the interaction for $\text{CO}_2\text{-CO}_2$ is relevant to the modeling of spacecraft atmospheric reentry [17] while those for NMA-NMA are important for the rationalization of structures and properties of proteins and nucleic acids as well as of the behaviour of various solvent systems [18]. In particular, the H-bonds formed either between the oxygen of the carbonyl group of NMA and the hydrogen atom of the amide group ($\text{N-H} \cdots \text{O}=\text{C}$) or between the oxygen atom and the hydrogen atom from methyl group ($\text{C-H} \cdots \text{O}$) offer an important example of the role that this type of bond plays in stabilizing intermolecular aggregates [19–23]. In this paper we report a generalization of the atom-bond pairwise additivity approach [24–26] and illustrate applications to the $\text{CO}_2\text{-CO}_2$ dimer case (for which collision dynamics is considered) and to the more complex NMA-NMA one.

The paper is organized as follows. In section 2, the background theory underlying the proposed approach is sketched. Section 3 describes the formulation of the

intermolecular interaction for the systems chosen as example applications whose results are presented in Section 4. In section 5 conclusions and perspectives are discussed.

2 The Intermolecular Interaction: Background Formulation

In our approach the total potential energy of two interacting molecules is splitted into an intermolecular (V_{inter}) and an intramolecular (V_{intra}) potential energy term (namely the potential energy of the two isolated molecules) as follows:

$$V = V_{intra} + V_{inter}. \quad (1)$$

V_{inter} depends on the internal coordinates of the two individual molecules and varies as their internal configuration deforms. When the internal configuration deforms, the physical properties of the isolated molecule, like polarizability and charge distribution, change affecting the calculated value of the intermolecular interaction. This means that the two terms of Eq. 1 are not strictly separable even if in most of the applications V_{inter} is considered to largely coincide with its value at the equilibrium geometry. Yet, there are cases, indeed, for which explicit account of the dependence of V_{intra} on the internal structure of the interacting molecules has to be taken. In turn the intermolecular part of the interaction, V_{inter} , can be formulated as a combination of two effective interaction components:

$$V_{inter} = V_{vdW} + V_{elect} \quad (2)$$

where V_{vdW} and V_{elect} represent the van der Waals (size repulsion plus dispersion attraction) and the electrostatic interaction components, respectively. V_{elect} originates from the anisotropic molecular charge distributions of the two bodies which asymptotically tend to the permanent quadrupole-permanent quadrupole interaction. Both V_{vdW} and V_{elect} depend in general on the distance R between the centers of mass of the two molecules (say a and b), plus the necessary additional coordinates (in general taken as angular coordinates) defining the mutual orientation of the two molecules.

2.1 The Van der Waals Component

The van der Waals term, V_{vdW} of Eq. 2 is expressed as a sum over the contributions V_{vdW}^i of all the possible interaction center pairs between the two monomers

$$V_{vdW}(R, \gamma) = \sum_i^N V_{vdW}^i(R_i, \gamma_i) \quad (3)$$

where R_i is the distance between the reference points of the two interacting centers of the i -th pair, γ_i denotes collectively the angular coordinates defining the related mutual orientation and N is the number of interaction pairs. Note that, as explicitly exemplified later on, the interaction centers can be atoms, group of atoms or even bonds, depending on the structure of the monomers. Such representation exploits the additivity of the various bond polarizability components in forming the overall molecular polarizability that is a fundamental feature of the van der Waals interactions. Moreover, it also indirectly accounts for three body effects [24], as testified by the fact that each bond polarizability component differs from the sum of the free atom contributions.

The V_{vdW}^i term is given a functional form that generalizes the atom-bond pairwise additivity discussed in Refs [24, 25] with each of the interacting centers being considered to be an independent sub-unit having a definite polarizability and a given electronic charge distribution (it can be, for example, of nearly cylindrical symmetry when the center is a bond).

The formulation adopted for V_{vdW}^i is of the Improved Lennard-Jones (ILJ) type [26]:

$$\frac{V_{vdW}^i(R_i, \gamma_i)}{\varepsilon_i(\gamma_i)} = f(x_i) = \left[\frac{m}{n(x_i) - m} \left(\frac{1}{x_i} \right)^{n(x_i)} - \frac{n(x_i)}{n(x_i) - m} \left(\frac{1}{x_i} \right)^m \right] \quad (4)$$

where x_i is the reduced distance defined as

$$x_i = \frac{R_i}{R_{mi}(\gamma_i)} \quad (5)$$

and $n(x_i)$ is an indirect function of both the distance R_i and the angles γ_i via the empirical equation [25]:

$$n(x_i) = \beta + 4.0x_i^2 \quad (6)$$

in which β is a parameter that depends on the nature and hardness of the interacting centers and introduces as well an ambient-like metric (that can be named as the hardness of the interacting partners [25, 26]) by modulating the repulsion and controlling the strength of the attraction. The introduction of this modulation (absent in the classical Lennard-Jones potential function) provides the ILJ expression with the possibility of indirectly taking into account induction, charge transfer and atom clustering effects. Further parameters of Eq. 4 are ε_i and R_{mi} (the well depth of the interaction potential and the related equilibrium distance, respectively) as well as the parameter m that takes pair specific values (e.g. it is equal to 6 for neutral interacting centers). All this makes the ILJ function [26] definitely more realistic than the original Lennard-Jones(12,6) one because it represents more accurately both the size repulsion (first term within the square brackets) and the long range dispersion attraction (second term within the square brackets) [27].

2.2 The Electrostatic Component

The V_{elect} term of Eq. 2 has been formulated as a sum of Coulomb potential terms for a pair $a - b$ of interacting molecules. For a given pair V_{elect} reads as:

$$V_{elect}(R, \gamma) = \sum_{jk} \frac{q_{ja}q_{kb}}{r_{jk}} \quad (7)$$

where q_{ja} and q_{kb} are the point charges located on the interacting molecules with r_{jk} being their distance. Such formulation improves considerably the description of V_{elect} over the usual expression that depends on the product of the molecular quadrupoles Q (see Eq. 9 of Ref. 28) because the charge distributions, associated by Eq. 7 with each molecular monomer, are compatible with the corresponding calculated molecular quadrupoles (see below). This formulation of V_{elect} must be necessarily used for cases in which the molecular dimensions are not negligible with respect to the intermolecular distance R 2. The choice of the spatial distribution of the charge is not a problem for relatively simple molecules (e.g. triatoms), especially when the dominant role of strongly charged atoms (e.g. oxygen in H_2O) is evident 29. The choice of the charge centers has instead a certain extent of arbitrariness for more complex systems (see e.g., ref. 30).

3 Prototypical Applications

To show the versatility of the adopted semiempirical portable model potential, we considered, as already mentioned, the CO_2-CO_2 and NMA-NMA dimers. The CO_2-CO_2 dimer is important for the modeling of the earth and planetary atmospheres and is considered here as a suitable prototype for gas dynamics and energy transfer studies. The more complex NMA-NMA dimer is a convenient testing ground for the application to biological molecules and is considered here as an example of configuration study useful to understand the dynamics of the hydrogen bonds, using molecular dynamics (MD) simulations.

3.1 The CO_2-CO_2 System

As anticipated in the introduction, in the CO_2-CO_2 gas phase system the internal vibrations and rotations of the molecule have to be taken in great care because they affect polarizabilities and charge distributions. This is in particular the case of collision dynamics or critical temperature plasma conditions in which high internal energy levels can be significantly populated and energy exchange between different degrees of freedom can lead to significant internal excitation. In order to give a realistic description of the intermolecular interaction for these cases, the dependence of the parameters on the internal molecular structure has been explicitly included in the representation of the PES. This dependence has been derived in ref. 31 where it has been shown that internal excitation (namely the stretching and the bending of CO_2) affects the value of the parameters of

the proposed formulation of V_{vdW} and V_{elect} . These values depend respectively on the C-O bond polarizability α and on the monomer charge distribution. In particular the modification of the bond length, r , and of the monomer bending angle, δ , is linked both to the bond polarizability and to the positions and values of the point charges localized on the O and C atoms. As a matter of fact, for the C-O bond stretching and shrinking, an empirical radial dependence of α on r was adopted and, for the charge distribution, a multipole moment formulation was tailored on the *ab initio* results using appropriate analytical functions linking the radial dependence of the point charges to the bond length of each monomer. In order to take into account the displacement of the dispersion center with r , the ratio r_{disp}/r (where r_{disp} is the distance of the dispersion center from the carbon atom) is kept constant and equal to 0.61, while a differentiation between bond shortening and bond lengthening has been adopted for CO₂ monomers undergoing asymmetric stretching.

The effect of the bending angle variation on the polarizability is taken into account by assuming that the components of the interaction are modeled as those of an ‘effective’ linear molecule whose bond length r is shorter than the actual one and whose total electronic charge, responsible for the molecular polarizability, is reduced along the molecular axis and increased on the perpendicular one with respect to the unbent molecule (for each value of the monomer bending angle δ , we have considered the interaction averaged over oscillation and rotation around the main molecular axis).

3.2 The NMA-NMA System

Due to the more complex structure of the NMA-NMA dimer and to the prevailing biological focus of the investigations concerned with such system, no detailed labeling of initial and final states was introduced.

Accordingly the term V_{elect} of Eqs. 2 and 7 is formulated as a sum of coulombic potentials associated with a set of punctual charges (AMBER 32) localized on the atoms of the corresponding molecule having a defined spatial distribution. For the V_{vdW} term five effective interaction centers 33 were considered for an adequate description of the intermolecular dimer interaction (see Fig.1). In particular, two of such centers are associated with the CH₃ groups and were placed on the related C atoms. Two other interaction centers are associated with (and placed on) the C and O atoms of the carbonyl group. The last interaction center is associated with the NH group and the related lone pair, and was placed on the N atom. The values of the polarizability contributions of the interacting centers have been derived by properly combining the polarizabilities of the involved atoms following the rules given in ref. 24.

As a result, for the NMA-NMA dimer the V_{vdW} term is expressed as a sum of 15 effective interaction pairs, with each effective pair contribution being evaluated by Eq. 4. The values of ε_i , R_{mi} and m for each interacting center are given in Table 1. The value of β of Eqs. 4 and 6 are linked to the the cubic root of the polarizability of the involved partners 34.

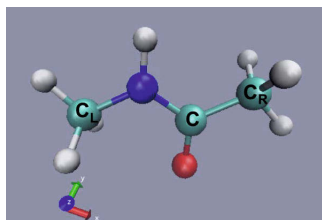


Fig. 1. The trans NMA molecule with the dispersion centers indicated by the letters C_L (lhs C), C_R (rhs C), C (central C), N, O (see text)

Table 1. The values of the well depth (ε_i), equilibrium distance (R_{mi}) and m parameters for the NMA-NMA system

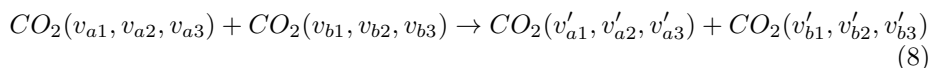
NMA-NMA			
Pairs	ε_i / meV	R_{mi} / Å	m
C_R-C_R	12.64	3.952	6.0
C_R-C_L	12.64	3.952	6.0
C_L-C_L	12.64	3.952	6.0
C-C	6.52	3.628	6.0
O-O	5.16	3.398	6.0
N-N	9.12	3.773	6.0
C_R-C	8.81	3.805	6.0
C_L-C	8.81	3.805	6.0
C_R-O	7.28	3.721	6.0
C_L-O	7.28	3.721	6.0
C_R-N	10.64	3.867	6.0
C_L-N	10.64	3.867	6.0
C-O	5.64	3.521	6.0
C-N	7.66	3.704	6.0
O-N	7.51	3.670	6.0

4 Dynamical Calculations and Results

In the second step of the simulation dynamical calculations of the two systems were performed by targeting for CO_2 - CO_2 on collisional vibrations excitation/decitation processes whereas for NMA - NMA on conformation analysis.

4.1 CO_2 - CO_2

The dynamics calculations were performed using the quasiclassical trajectory (QCT) method to evaluate state-to-state probabilities and cross sections for the processes:



where the $v_{a(b)i}$ ($i = 1, 2, 3$) are the quantum labels of a normal-mode model for symmetric stretching (1350 cm^{-1}), bending (678 cm^{-1}) and asymmetric stretching (2388 cm^{-1}) respectively, before (unprimed) and after (primed) the collision event. At equilibrium CO_2 is a linear molecule, with degenerate (ground) bending states. Bending excitation generates rotation around the O–C–O molecular axis and an additional (l) quantum number is needed to label the discretized total molecular angular momentum projection on the quantization axis z . However, in our model treatment of the CO_2 monomer, the associated amount of energy is neglected because it is in general small and, in any case, smaller than the statistical error of the QCT calculations (that amounts up to 5 %). Accordingly, to allow separability between rotations and vibrations, the CO_2 molecule is approximated as a linear rigid rotor (yet dynamical effects induced by the modification of the molecular shape occurring during the collision are in any case properly taken into account by computing the true intermolecular potential V_{inter} , as described in Sec. 2). QCT calculations were performed using the VENUS96 program [35] which has been modified to incorporate the CO_2 – CO_2 potential energy routine.

The initial conditions of the batches of trajectories run for the study reported here were selected as follows: the collision energy E was given a fixed value; the initial rotational angular momenta of the two molecules, were selected through a uniform random sampling of the Boltzmann distribution corresponding to the rotational temperature T_{rot} (that for our calculations was set equal to the translational one, as usually done for this type of massive computational campaigns [36]); the initial vibrational states of the two molecules were defined by choosing two triples of integer numbers (one for each molecule) corresponding to the $v_{a(b)1}, v_{a(b)2}, v_{a(b)3}$ quantum numbers. Then initial coordinates and momenta for the relative motion were set by assigning a random value to the impact parameter b in the range $[0, b_{max}]$, where b_{max} , the maximum impact parameter, was taken as a truncation limit. The molecules were then randomly oriented, with the initial distances being large enough to make the interaction between them negligible and the rotation of each of them that of a linear rigid rotor, with no coupling between rotations and vibrations. A number of 60000 trajectories were run for each batch calculation. According to the QCT method, the final states of the two molecules collected from the trajectories can be “quantized” by a binning procedure and from the obtained ensemble of quantum states the probabilities of reaching upon collision a given final state from the initial one can be calculated. The corresponding cross sections are directly obtained by multiplying probabilities by a factor $2\pi b_{max}$.

A first study of the vibrational energy transfer upon collision of CO_2 with CO_2 has been carried out at collision energy $E=86.7\text{ meV}$ (2 kcal/mol), with the colliding molecules initially set in the ground vibrational state (0,0,0) and an initial rotational energy distribution corresponding to that of a temperature of 1000 K. Related detailed probabilities and cross sections are shown in Table 2. In this case vibrational excitation is almost exclusively confined to the first two symmetric stretching modes (for both molecules). Cases of excitation to the first

level of bending are also observed while no excitation at all is observed for asymmetric stretching. Further calculations were carried out at collision energy equal to 2.17 eV (50 kcal/mol), with both colliding molecules initially excited to the state (9,0,0) and an initial rotational energy distribution corresponding to that of

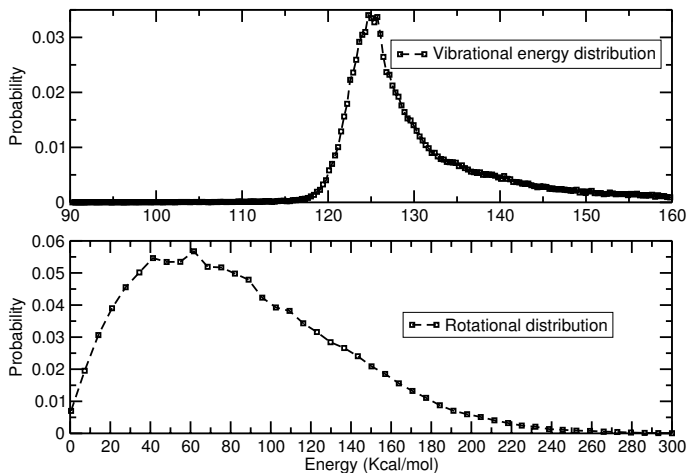


Fig. 2. Final vibrational and rotational energy distributions, for collisions at $E=50$ kcal/mol and symmetric stretching initially excited at (9,0,0) for the two molecules

Table 2. Probabilities and cross sections for CO_2+CO_2 collisions at a collision energy $E= 86.7$ meV (2.0 kcal/mol), initial angular momenta of the molecules sampled randomly from a Boltzmann distribution at a rotational temperature $T_{rot}=1000$ K. The initial vibrational state of CO_2 is (0,0,0) for both molecules.

v'_{a1}	v'_{a2}	v'_{a3}	v'_{b1}	v'_{b2}	v'_{b3}	Prob.	Cross section (\AA^2)
1	0	0	1	0	0	0.34100	466.91652
0	0	0	0	0	0	0.24527	333.49738
0	0	0	1	0	0	0.20754	281.18675
1	0	0	0	0	0	0.20521	277.78731
0	0	0	2	0	0	0.00022	0.20047
1	0	0	2	0	0	0.00012	0.14733
2	0	0	1	0	0	0.00018	0.14623
0	1	0	0	0	0	0.00010	0.10199
2	0	0	0	0	0	0.00008	0.09862
1	0	0	0	1	0	0.00004	0.06878
1	0	0	0	0	1	0.00008	0.06639
0	1	0	1	0	0	0.00006	0.05661
0	0	1	1	0	0	0.00004	0.04291
0	0	0	0	1	0	0.00002	0.03955
1	0	1	0	0	0	0.00002	0.03464
1	0	0	1	0	1	0.00002	0.03456

Table 3. Probabilities and cross sections for CO₂+CO₂ collisions at a collision energy $E= 2.17$ eV (50.0 kcal/mol), initial angular momenta of molecules sampled randomly from a Boltzmann distribution at a rotational temperature $T_{rot}=25000$ K. The initial vibrational state of CO₂ is (9,0,0) for both molecules (symmetric stretching excited).

v'_{a1}	v'_{a2}	v'_{a3}	v'_{b1}	v'_{b2}	v'_{b3}	Prob.	Cross section (Å ²)
4	7	1	5	6	1	0.00036	0.49265
2	8	1	3	7	1	0.00036	0.45404
5	6	1	3	7	1	0.00032	0.44874
3	7	1	4	6	1	0.00030	0.43726
3	7	1	3	7	1	0.00036	0.43623
3	8	1	2	8	1	0.00031	0.43405
4	7	1	3	8	1	0.00030	0.43202
5	6	1	4	7	1	0.00034	0.42869
5	6	1	3	9	0	0.00033	0.41667
3	7	1	5	6	1	0.00030	0.41365
2	9	1	4	7	1	0.00027	0.41316
8	5	1	8	5	1	0.00027	0.41139
4	7	1	3	7	1	0.00030	0.40453
4	8	0	4	7	1	0.00028	0.40347
3	7	1	4	7	1	0.00031	0.40201
4	7	1	7	5	1	0.00030	0.39356
4	8	0	5	6	1	0.00028	0.39331
3	9	1	5	6	1	0.00026	0.39304
3	9	0	5	6	1	0.00027	0.39125
4	7	1	4	7	1	0.00028	0.38810
2	9	0	5	6	1	0.00026	0.38792
2	9	0	3	7	1	0.00027	0.37744
3	9	0	3	9	0	0.00026	0.37706
3	8	1	6	7	0	0.00027	0.37529
5	8	0	3	7	1	0.00028	0.37352
6	6	1	7	5	1	0.00026	0.37290
6	5	1	3	7	1	0.00024	0.37105
5	7	1	6	7	0	0.00026	0.36915
4	7	1	5	7	0	0.00026	0.36708
7	5	1	3	8	1	0.00026	0.36555

a temperature of 25000 K. Fig. 2 shows the computed vibrational and rotational energy distributions with the latter corresponding to a Boltzmann rotational distribution. Table 3 shows, instead, the first 30 more likely vibrational transition probabilities and cross sections for the case of $E= 2.17$ eV (50 kcal/mol). As it can be seen from the Table, a larger number of transitions take place at this higher value of collision energy, evidencing a large collision induced energy transfer effect. The vibrational and rotational distributions (Fig. 2) confirm the broad range covered by the product energies.

4.2 NMA-NMA

To calculate the equilibrium conformations of the NMA dimer the DL_POLY code [37] was used. Initially, the trans-NMA monomers were arbitrarily placed without imposing boundary conditions. The system was equilibrated before beginning a data collection run of 10 ps. To this end the trajectories were integrated for a period of 1.5 ns using a time step of 0.1 ps. The NVE ensemble was adopted to ensure total energy conservation. Batches of calculations were carried out at many values of total energy corresponding to a temperature of 100 K. The geometries of the most stable isomers were selected as initial configurations for further runs at decreasing values of the temperature to 0 K.

For the NMA dimer, a careful inspection of the dynamical results indicates the formation of only one stable conformer or of two different conformers having similar energies. The *Ab initio* calculations for the stable conformers of the NMA dimer are compared with the same results obtained from our MD calculations carried out using the AMBER charge distribution and setting the value of the parameter β (see Eqs. 4 and 6) equal to 8 for all the interacting center pairs (see Sec. 2.1 and Eq. 3). The comparison is shown in Table 4. The literature suggests -0.3 eV as a suitable reference value for the NMA dimer binding energy D_e .

Table 4. Comparison of the binding energies calculates from MD calculations with the *ab initio* ones for the NMA-NMA system. *when making a counterpoise correction.

	D_e / eV
Our result	-0.3123
Ref. [38]	-0.2885
Ref. [38]	-0.2746*
Ref. [7]	-0.4193

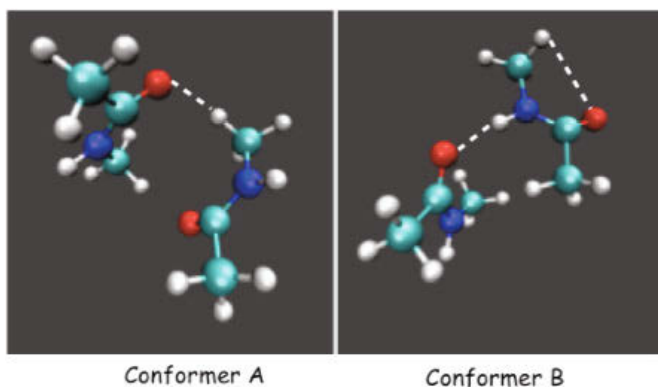


Fig. 3. Two conformers of the NMA dimer. On the left hand side panel, the most stable conformer, denoted as A. On the right hand side panel the less stable conformer, denoted as B. The dotted white lines represent the possible H-bonds.

Table 5. The values of binding energy, D_e , and selected geometry data for the NMA-NMA^a system (Conformer B)

D_e / eV	r_{OH} / Å	r_{NO} / Å	$r_{O-H(CH_3)}$ / Å	\widehat{NHO} /degrees	\widehat{COH} /degrees	Reference
-0.3123	1.844	2.860	2.701	171.3	131.2	present
-0.2550	-	3.028	-	-	-	ref.[39]
-0.3777	1.82	-	-	-	-	ref.[40]
-0.4193	2.035	2.949	2.685	148.1	106.3	ref.[7]

^aAMBER charge distribution has been used to calculate the electrostatic interaction.

Both conformers and their structures, as obtained from the above mentioned MD simulations, are shown in Fig. 3.

The figure shows that for Conformer A the oxygen atoms of the carbonyl group of both the NMA molecules form H-bonds with one of the H atoms in the CH₃ group. In conformer B (nearly perpendicular configuration) the O atom of the carbonyl group forms a H-bond with the H atom in the NH group, with a small additional contribution of the C=O \cdots H(CH₃) interaction. The conformer A results to be more stable, having a binding energy of -0.3507 eV (lower than the -0.3123 eV value of conformer B). This is due to the higher number of H-bonds of conformer A, while the H-bond distance is 1.84 Å for conformer B and 1.90 Å for conformer A. Geometry and binding energy are compared for conformer B with results taken from the literature in Table 5 (while no comparison can be made for the more stable conformer A, due to the unavailability of published *ab initio* results).

5 Conclusions

This paper intended to illustrate the validity of the bond-bond approach for the construction of intermolecular potential energy surfaces also exploiting its portability based on the additivity of polarization components, suited for both small and medium-large size molecules, and the properties of an innovative Grid empowered molecular simulator. The procedure has been applied to both the NMA and the CO₂ dimers. For the CO₂ dimer for which the dependence of the intermolecular interaction part on the internal geometry of the two molecules has been explicitly included in the PES, the gas phase calculations pointed at the importance of the various degrees of freedom in channelling energy into product states. The results confirm that for light systems the PES is feasible enough to well describe dimers of deformable molecules and to induce significant energy exchange when the various internal modes are selectively excited.

For the NMA-NMA dimer, the stable conformers have been studied by molecular dynamics simulations and results show that the adopted formulation of the van der Waals interaction is sufficiently flexible thanks to the modulation of the β parameter of the V_{ILJ} function. The calculations predict the existence of two conformers, of which the less stable one, not referenced in the literature, has similar geometrical characteristics and binding energies as the most stable

one, but different charge distribution. The proposed applications show that the bond-bond method can be applied to a wide range of systems (from small to large size molecules) and that it is of perspective use in different types of chemical problems, such as collision dynamics and energy transfer, and conformational studies.

Acknowledgments. The authors acknowledge financial support from MIUR PRIN 2008 (contract 2008KJX4SN_003), Phys4entry FP72007-2013 (contract 242311) and EGI Inspire. Thanks are also due to IGI and the COMPCHEM virtual organization for the allocated computing time as CASPUR and CINECA.

References

1. Hirschfelder, J.O.: Intermolecular Forces. *Adv. Chem. Phys.* 12 (1967)
2. Maitland, G.C., Rigby, M., Smith, E.B., Wakeham, W.A.: Intermolecular Forces. Clarendon Press, Oxford (1987)
3. Laganà, A., Costantini, A., Gervasi, O., Faginas-Lago, N., Manuali, C., Rampino, S.: *J. Grid Computing* 8, 571 (2010)
4. EGI (European Grid Infrastructure), <http://www.egi.edu>; IGI (Italian Grid Infrastructure), <http://www.italiangrid.it> (last visited on January 19, 2012)
5. Laganà, A., Riganelli, A., Gervasi, O.: *LNCS*, vol. 3980, p. 665 (2006), <http://www3.compchem.unipg.it/compchem/> (last visited on January 20, 2012)
6. Buck, M., Karplus, M.: *J. Phys. Chem. B* 105, 11000 (2001)
7. Vargas, R., Garza, J., Friesner, R.A., Stern, H., Hay, B.P., Dixon, D.A.: *J. Phys. Chem. A* 105, 4963 (2001)
8. Whitfield, T.W., Crain, J., Martyna, G.J.: *J. Chem. Phys.* 124, 094503 (2006)
9. Oakey, M.T., Wheatley, R.J.: *J. Chem. Phys.* 130, 034110 (2009)
10. Katz, J.L., Pst, B.: *Acta Crystallogr.* 13, 624 (1960)
11. Itoh, K., Shimanouchi, T.: *Biopolymers* 5, 921 (1967)
12. Fillaux, F., De Loze, C.: *Chem. Phys. Lett.* 39, 547 (1976)
13. Fillaux, F., Baron, M.H.: *Chem. Phys.* 62, 275 (1981)
14. Zanni, M.T., Asplund, M.C., Hochstrasses, R.M.: *J. Chem. Phys.* 114, 4579 (2001)
15. Woutersen, S., Mu, Y., Stock, G., Hamm, P.: *Chem. Phys.* 266, 137 (2001)
16. Schmidt, J.R., Corcelli, S.A., Skinner, J.L.: *J. Chem. Phys.* 121, 8887 (2004)
17. Capitelli, M., Ferreira, C.M., Gordiets, B.F., Osipov, R.: *Plasma kinetics in atmospheric gases*. Springer (2000)
18. Vargas, R., Garza, J., Dixon, D.A., Hay, B.P.: *J. Am. Chem. Soc.* 122, 4750 (2000)
19. Dixon, D.A., Dobbs, K.D., Valentini, J.J.: *J. Phys. Chem.* 51, 13435 (1994)
20. Nandini, G., Sathyanarayana, D.N.: *J. Mol. Struct.: THEOCHEM* 579 (2002)
21. Kang, Y.K.: *J. Mol. Struct.: THEOCHEM* 546, 183 (2001)
22. Eckert, J., Barthes, M., Klooster, W., Albinati, A., Aznar, R., Koetzle, T.: *J. Phys. Chem.* 105, 19 (2001)
23. Akiyama, M., Torii, H.: *Spectrochim. Acta, Part A* 56, 137 (1999)
24. Pirani, F., Cappelletti, D., Liuti, G.: *Chem. Phys. Lett.* 350, 286 (2001)
25. Pirani, F., Albertí, M., Castro, A., Moix Teixidor, M., Cappelletti, D.: *Chem. Phys. Lett.* 37, 394 (2004)
26. Pirani, F., Brizi, S., Roncaratti, L., Casavecchia, P., Cappelletti, D., Vecchiocattivi, F.: *Phys. Chem. Chem. Phys.* 10, 5489 (2008)

27. Lombardi, A., Palazzetti, F.: *J. Mol. Structure (THEOCHEM)* 852, 22 (2008)
28. Cappelletti, D., Pirani, F., Bussery-Honvault, B., Gomez, L., Bartolomei, M.: *Phys. Chem. Chem. Phys.* 10, 4281 (2008)
29. Faginas Lago, N., Huarte-Larrañaga, F., Albertí, M.: *Eur. Phys. J. D* 55, 75 (2009)
30. Albertí, M., Aguilar, A., Lucas, J.M., Pirani, F., Coletti, C., Re, N.: *J. Phys. Chem. A* 113, 14606 (2009)
31. Bartolomei, M., Pirani, F., Laganà, A., Lombardi, A.: A full dimensional Grid empowered simulation of the CO₂+CO₂ processes. *J. Comp. Chem.* (submitted)
32. Cornell, W.D., Cieplak, P., Bayly, C.I., Gould, I.R., Merz Jr., K.M., Ferguson, D.M., Spellmeyer, D.C., Fox, T., Caldwell, J.W., Killman, P.A.: *J. Am. Chem. Soc.* 117, 5179 (1995)
33. Albertí, M., Faginas Lago, N., Laganà, A., Pirani, F.: *Phys. Chem. Chem. Phys.* 13, 8422 (2011)
34. Capitelli, M., Cappelletti, D., Colonna, G., Gorse, C., Laricchiuta, A., Liuti, G., Longo, S., Pirani, F.: *Chem. Phys.* 338, 62 (2007)
35. Hase, W.L., Duchovic, R.J., Hu, X., Komornicki, A., Lim, K.F., Lu, D.-H., Peshherbe, G.H., Swamy, K.N., Vande Linde, S.R., Zhu, L., Varandas, A., Wang, H., Wolf, R.J.: *J. Quantum Chemistry Program Exchange Bulletin*, 16, 671 (1996)
36. Laganà, A., Crocchianti, S., Piermarini, V.: *LNCS*, vol. 422, p. 3044 (2008); García, E., Sánchez, C., Saracibar, A., Laganà, A., Skouteris, D.: *Phys. Chem. Chem. Phys.* 11, 11456 (2009); Rampino, S., Skouteris, D., Laganà, A.: *Int. J. Quantum Chem.* 358, 110 (2010)
37. http://www.stfc.ac.uk/CSE/randd/ccg/software/DL_POLY/25526.aspx (last visited January 12, 2012)
38. Köddermann, T., Ludwig, R.: *Phys. Chem. Chem. Phys.* 6, 1867 (2004)
39. Trabelsi, S., Bahri, M., Nasr, S.: *J. Chem. Phys.* 122, 024502 (2005)
40. Jorgensen, W.L., Duffy, E.M., Essex, J.W., Severance, D.L., Blake, J.F., McDonald, N.A., Tirado-Rives, J.: *Computational Studies of Molecular Recognition from alkane dimers to protein-ligand complexes*. In: Seddon, K.R., Zaworotko, M. (eds.) *Crystal Engineering: The Design and Application of Functional Solids*. *Nato Series. Series C: Mathematical and Physical Sciences*, vol. 539, p. 113 (1996)

A Grid Execution Model for Computational Chemistry Applications Using the GC3Pie Framework and the AppPot VM Environment

Alessandro Costantini^{1,2,3}, Riccardo Murri⁴,
Sergio Maffioletti⁴, and Antonio Laganà⁵

¹ INFN-CNAF — National Institute of Nuclear Physics, Bologna, Italy

² IGI — Italian Grid Infrastructure, Italy

³ Department of Mathematics and Informatics, University of Perugia, Italy

`alessandro.costantini@cnafe.infn.it`

⁴ Grid Computing Competence Centre, University of Zürich, Switzerland

`riccardo.murri@gmail.com`, `sergio.maffioletti@gc3.uzh.ch`

⁵ Department of Chemistry, University of Perugia, Italy

`lag@unipg.it`

Abstract. This paper describes and discusses the implementation, in a high-throughput computing setting, of a chemoinformatics tool oriented to quantum mechanics scattering calculations.

The developed workflow tackles some technical problems, typical of some legacy applications, that cannot be solved with a static workflow specification and are therefore unsuitable for running on the most common workflow engines.

The tool has been validated by re-running published calculations carried out using those same applications and procedures, and the outcomes have been discussed and compared with previous attempts at porting the same applications on computational grids.

1 Introduction

The increasing availability of computing power on Grid platforms has prompted the implementation of complex computational chemistry applications on distributed systems and, at the same time, the development of appropriate frameworks allowing to define event-related dependencies between them (which may involve different computer environments) in a workflow-like fashion. More specifically, part of the work of the Working Group 3 (WG3) of the COST Action CM1002 named CODECS [1] pursues the goal of designing and developing collaborative tools aimed at integrating the different applications used by the Molecular Science community. This is, indeed, the case of the Grid-empowered versions of the molecular system simulation workflows SIMBEX (SIMulation of Molecular Beam EXperiments) [2] and GEMS (Grid Empowered Molecular Simulator) [3,4], developed by the University of Perugia. The work presented here is the result of a collaboration among the Italian Grid Initiative (IGI) [5], the COMPCHEM Virtual Organization (VO) [6] of the European Grid Initiative (EGI) [7], and the Grid Computing Competence Center, University of Zurich (GC3) [8].

The purpose of the presented work is twofold:

- create chemoinformatics tools aimed at facilitate the porting of complex computational chemistry application on distributed infrastructures.
- provide efficient mechanisms to run high throughput data analysis with the ported applications.

The prototypical workflow presented in this paper has been tested for the calculation of the time independent quantum probabilities of the $\text{H} + \text{H}_2$ benchmark reaction.

It involves the use of two applications: GFIT3C [9] and ABC [10]. The first is a routine performing the global fitting of the potential energy surfaces in triatomic systems; the latter is a quantum mechanical atom-diatom reactive scattering program. Both codes belong to the set of computational applications in which GEMS is articulated.

In a typical use case the *ab initio* points of the Potential Energy Surface (provided by running *ab initio* electronic structure calculations or searched in web repositories) are fitted using GFIT3C. The output carried out by such global fitting routine (“fitting file”) is then merged into the source code of the ABC application, and compiled to obtain the ABC executable which can be then distributed on the Grid in a parameter study fashion. It is clear that the compiling step introduces a very specific software dependency between the two programs, which is not easily handled with some workflow engines. For addressing this issue, we leveraged a grid-based virtualization mechanism called AppPot [11] to distribute the entire application-specific environment as part of the workflow execution. For the orchestration of the workflow instances, including the supervised high throughput ABC execution, we used the GC3Pie framework [12]. The Swiss National Grid Infrastructure [13] has been used for running initial high throughput tests with the proposed solution.

The paper is structured as follows. In Section 2 we recap results from previous and related work; in Section 3 and 4 an illustration of our new approach using GC3Pie and AppPot is given; in Section 5 the two blocks of GEMS ported in the grid environment and considered as benchmark use cases are described; in Section 6 the articulation of the developed workflow is described, and finally in Section 7, performance data of a sample run is analyzed. Our conclusions are summarized in section 8.

2 Previous and Related Work

A first attempt to build a suitable workflow has been described in Ref. [14] and [15]. A more detailed account of the running of the ABC code on a computational grid using a workflow approach has been given in Ref. [16] using the P-GRADE Grid Portal [17,18]. P-GRADE allows to define a parameter study application structure in a graphical environment and, based on this description, it generates the scripts and commands which actually carry out the execution on the distributed grid platform. Unfortunately the software dependency of the

computational codes from specific libraries and compilers, rarely available in the most common Linux distributions over the grid, can not be easily handled with P-GRADE with the result that the execution of such codes turns out to be strictly dependent from the machinery where the calculation is performed.

More recently an attempt of porting the ABC code on a grid infrastructure, has been carried out using the GriF [19] framework, developed at the University of Perugia.

GriF framework aims to build user friendly interfaces to run scientific applications on the EGI infrastructure.

GriF has been designed to make Grid applications black-box like enabling an easy access and a GriF enables CPU and memory usage optimization of Grid resources; it also offers a way for evaluating the enhance collaborative work [20] and to evaluate Quality of Services and Quality of Users for enhancing Virtual Research Community sustainability [21]. Yet GriF is still insufficiently equipped to implement a workflow-like logic.

3 The GC3Pie High-Throughput Framework

GC3Pie is a library of Python classes for running large job campaigns (high throughput) on diverse batch-oriented execution environments, including ARC-based computational grids [22]. It also provides facilities for implementing command-line driver scripts, in the form of Python object classes whose behavior can be customized by overriding specified object methods.

At the heart of the GC3Pie model is a generic *Application* object, that provides a high-level description of a computational job: list of input/output files, what command to run, resource requirements and limits, etc. GC3Pie translates this information into the job description format needed by the actual execution back-end selected, e.g., xRSL for ARC-based Grids, or a submission script for direct execution on a batch-queuing system. *Application* objects can be adapted to provide behavior customized to a specific use case as for the AppPot Virtual Machine approach described later.

3.1 Workflow Composition

GC3Pie provides composition operators, that allow treating a collection of tasks as a single whole [23]: compositions operators can be arbitrarily nested, allowing the creation of complex workflows, including workflows with cycles in them, and dynamic workflows whose structure is created at runtime by the script itself. Two base composition operators are provided, upon which others can be created (by subclassing).

The *ParallelTaskCollection* operator takes a list of tasks and creates a task that executes them all independently and, compatibly with the allowed degree of job parallelism, concurrently.

The *SequentialTaskCollection* operator takes a list of tasks and creates a task that executes them in the sequence; a decision method is invoked in between

each step, which can terminate execution early (e.g., in case of errors), but also alter the list of planned tasks.

See section 6 for an overview of how these composition operators are applied to the GFIT3C+ABC workflow.

3.2 Command-Line Scripts

GC3Pie provides template command-line scripts for frequently-occurring use cases, in the form of reusable Python objects. The most used command-line pattern, and also the one we chose for the GFIT3C+ABC workflow, is called a *SessionBasedScript*. This template script manages a collection (“session”) of tasks (where each task can be itself a collection, see above); tasks in the session are submitted to the grid and monitored until they have ended execution; the output from completed tasks is retrieved and stored in a configurable location. The *SessionBasedScript* also ensures the session is persisted to disk and correctly restored in case the program is interrupted or crashes and restarted later.

4 The AppPot Virtual Machine

AppPot [11] is a software system comprising a standard Linux Virtual Machine (VM) image and a set of auxiliary programs that make the AppPot software self-contained so that it can be deployed by just copying a few files. AppPot provides a way to run commands inside the VM, possibly in a non-interactive fashion, and to copy files in and out of the VM filesystem.

AppPot is based on the User-Mode Linux [24, 25] virtualization technology. User-Mode Linux (UML) provides a way to run a Linux VM inside a Linux host using only a code that runs in “user space” and thus requires no “root” privileges or any other form of systems administrator support or consent. Only two files are needed for running a UML Virtual Machine: the UML kernel and the VM disk image. The UML kernel is a single executable file consisting basically of a regular Linux kernel modified to run as a process in a Linux host. It is possible to compile the UML kernel statically, so that it can run on a wide spectrum of Linux systems.

Combining the features above, one can run Linux-based VMs as grid jobs and implement user-initiated, generic application deployment on a computational grid. Indeed, users can install a new application into a copy of an AppPot VM, and then package the modified VM as a job’s input data; the job control script can make use of the `appot-start` script to run any command inside the AppPot VM.

5 Overview of the Considered Computational Applications

5.1 The Grid Empowered Molecular Simulator

Accordingly, the design of GEMS [3] has been founded on the following sections: INTERACTION, DYNAMICS and OBSERVABLES.

INTERACTION is the first section of GEMS and carries out the theoretical step of the calculations which determine the electronic structure of the system. The calculated energies (usually called potential energy values) can be used directly (on the fly) as soon as they are produced. Most often, instead, they are first performed for a large set of geometries of the system and then properly adjusted to reproduce some known molecular properties. Finally they are interpolated using appropriate functional forms. In this way an accurate easy to use Potential Energy Surface is created.

DYNAMICS is the second section of GEMS and carries out the theoretical calculations determining the dynamics of the nuclei of the system. Most frequently these calculations are based on classical mechanics approaches. Elective approaches should be instead the quantum ones yet, at present, they are feasible in a rigorous way, only for three and four atom systems because the related computational machinery is extremely heavy. Because of this the efficient implementation of the related computational procedures on the computing grid is an extremely active field of research.

OBSERVABLES is the final section of GEMS and carries out the necessary statistical and model treatments of the outcomes of the theoretical calculations to provide an a priori estimate of the monitored (measured) properties of the system. Obviously, theoretical calculations may be confined only to a mere geometrical analysis of the molecular system or to an exploration of the Potential Energy Surface (PES). In the most rigorous approaches both the calculation of the potential energy surface and the integration of nuclear dynamics equations are performed and use is made of suitable computational packages. The procedures to calculate the observable properties of the system are, instead, specifically designed for the final application of interest and are most often entirely handled by the final users.

5.2 GFIT3C

As discussed above, the starting point of GEMS is the assemblage of a suitable PES providing an analytical representation of the interaction characterizing the electronic structure of the considered system. When a PES is not available neither from web repositories, *ab initio* electronic structure values for a suitable set of molecular geometries covering all the energetically important regions of the arrangements are best fitted to a suitable functional form.

In principle, the functional form of this function is chosen so as to provide a good picture of the interaction at stationary points and at all the asymptotic limits having the correct symmetry properties of the system. This function should connect smoothly the asymptotic and interaction regions in a physically sound way and should behave in a physically reasonable manner in those parts of the interaction region for which no theoretical data is available. The typical root-mean-square (r.m.s.) values of analytical PES useful for reliable scattering calculations are of the order of fractions of kcal/mol.

GFIT3C is, indeed, a computer program implementing the method proposed by Aguado et al. [9] to fit a PES and is based on the formulation of the

three-atom (A , B , C) potential as a many-body expansion [26] of the internuclear distances as follows:

$$\begin{aligned}
 V_{ABC}(R_{AB}, R_{AC}, R_{BC}) &= V_A^{(1)} + V_B^{(1)} + V_C^{(1)} \\
 &+ V_{AB}^{(2)}(R_{AB}) + V_{AC}^{(2)}(R_{AC}) + V_{BC}^{(2)}(R_{BC}) \quad (1) \\
 &+ V_{ABC}^{(3)}(R_{AB}, R_{AC}, R_{BC})
 \end{aligned}$$

As shown by eq. (1), the potential is written as a sum of three monoatomic terms ($V_A^{(1)}$, $V_B^{(1)}$, $V_C^{(1)}$), three diatomic terms ($V_{AB}^{(2)}$, $V_{AC}^{(2)}$, $V_{BC}^{(2)}$), plus one triatomic term ($V_{ABC}^{(3)}$). The one-body terms are the energies of the separated atoms in their corresponding electronic state (three constant values). The two-body terms correspond to the diatomic potential energy curves, including the nuclear repulsions which are formulated as polynomials of variables ξ_{AB} , ξ_{AC} and ξ_{BC} defined as $\xi_{IJ} = R_{IJ} \exp(-\beta_{IJ} R_{IJ})$ (with I and J being one of the three A , B , C atoms) in which ξ_{IJ} is optimized to represent the long-range term of the two-body potential. The three-body term corresponds to the residual interaction due exclusively to three atoms forces. The advantage of this development is that, if we impose the proper restrictions on the internuclear distances, the correct asymptotic limits are obtained.

In this context, the GFIT3C program fits the three-body term $V_{ABC}^{(3)}$ using an expansion of order M of ξ_{AB} , ξ_{AC} and ξ_{BC} as follows:

$$V_{ABC}^{(3)}(R_{AB}, R_{AC}, R_{BC}) = \sum_{ijk}^M d_{ijk} \xi_{AB}^i \xi_{AC}^j \xi_{BC}^k. \quad (2)$$

5.3 ABC

ABC is the code of the third block of GEMS that carries out exact and approximate quantum dynamical calculations for reactive atom-diatom systems. To this end, the ABC program integrates the Schrödinger equation for an atom-diatom reactive scattering problem using the Delves hyperspherical coordinates [27] and a coupled channel method. The program makes use of a time independent technique to integrate the atom-diatom nuclear Schrödinger equation:

$$[\hat{H} - E]\psi = 0 \quad (3)$$

on a single PES according to a Born-Oppenheimer approach.

In eq. (3), ψ is the nuclear wavefunction (depending on nuclear coordinates only) and \hat{H} is the related electronically adiabatic Hamiltonian of the nuclei. In the approach adopted by ABC ψ is expanded in terms of the hyperspherical arrangement channel τ basis functions $B_{\tau v_{\tau} j_{\tau} K_{\tau}}^{JM}$. The basis functions $B_{\tau v_{\tau} j_{\tau} K_{\tau}}^{JM}$, which are also labeled after J (the total angular momentum quantum number), M and K_{τ} (the space- and body- fixed projections of \mathbf{J}), v_{τ} and j_{τ} (the τ asymptotic vibrational and rotational quantum numbers), depend on the three Euler α , β , γ , the Jacobi Θ_{τ} angle and the internal Delves hyperspherical angle

$\theta_{D\tau}$ at a given ρ value. In order to carry out the propagation of the solution from small (strong interaction region) to large values (the asymptotic region) of the hyperradius ρ , ABC integrates the equations linking the second derivative of the matrix of the coefficients (\mathbf{g}) of the expansion of ψ (see eq. (4)) to the overlap matrix \mathbf{O} and the coupling matrix \mathbf{U} as follows:

$$\frac{d^2\mathbf{g}}{d\rho^2} = \mathbf{O}^{-1}\mathbf{U}\mathbf{g}. \quad (4)$$

where the \mathbf{O} matrix elements are formulated as:

$$O_{\tau v_\tau j_\tau K'_\tau}^{\tau v'_\tau j'_\tau K'_\tau} = \langle B_{\tau v_\tau j_\tau K_\tau}^{JM} | B_{\tau v'_\tau j'_\tau K'_\tau}^{JM} \rangle, \quad (5)$$

and the coupling \mathbf{U} matrix elements are formulated as:

$$U_{\tau v_\tau j_\tau K_\tau}^{\tau v'_\tau j'_\tau K'_\tau} = \langle B_{\tau v_\tau j_\tau K_\tau}^{JM} | \frac{2\mu}{\hbar^2}(\bar{H} - E) - \frac{1}{4\rho^2} | B_{\tau v'_\tau j'_\tau K'_\tau}^{JM} \rangle, \quad (6)$$

in which μ is the reduced mass of the system and \bar{H} is the part of the Hamiltonian not containing derivatives with respect to ρ .

To integrate the set of coupled differential equations given in eq. (4), the interval of ρ is divided into various sectors, and solve for local (sector) bound state functions by diagonalizing a Hamiltonian which describes related $\theta_{D\tau}$ -dependent motions using a carefully chosen reference potential. After integrating the coupled-channel equations by propagating the solution from small values of ρ to the asymptotes, the solutions are matched to product states and the scattering matrix \mathbf{S} is evaluated. From this, the quantum scattering probability matrix \mathbf{P} ($\mathbf{P}_{v_j, v'j'}(E) = |\mathbf{S}_{v_j, v'j'}(E)|^2$) is determined.

6 Implementation of the Grid-Based Workflow

6.1 Workflow Description

The considered workflow has emerged from the primary need of running large ABC analysis campaign from a set of input *ab initio* points of the PES. The workflow is centered around the building of ABC binary and its execution.

The steps involved in the workflow are described as follows:

- (A) The *ab initio* points of the PES are passed as input to GFIT3C which produces a Fortran file (“fitting file”) containing the PES routine for the considered system.
- (B) The fitting file is then merged into the ABC source code, which is compiled into an executable binary.
- (C) The resulting ABC binary is distributed and executed for computations.

On this basis we considered in our work three different use cases:

- (1) The user provides the *ab initio* points of the Potential Energy Surface; this executes steps (A), (B), and (C).

- (2) The user provides the *fitting file* (produced by a previous run of GFIT3C or by any other means); only steps (B) and (C) need to be executed.
- (3) The user provides his/her version of the ABC executable for distribution in a parameter study fashion: only step (C) is executed.

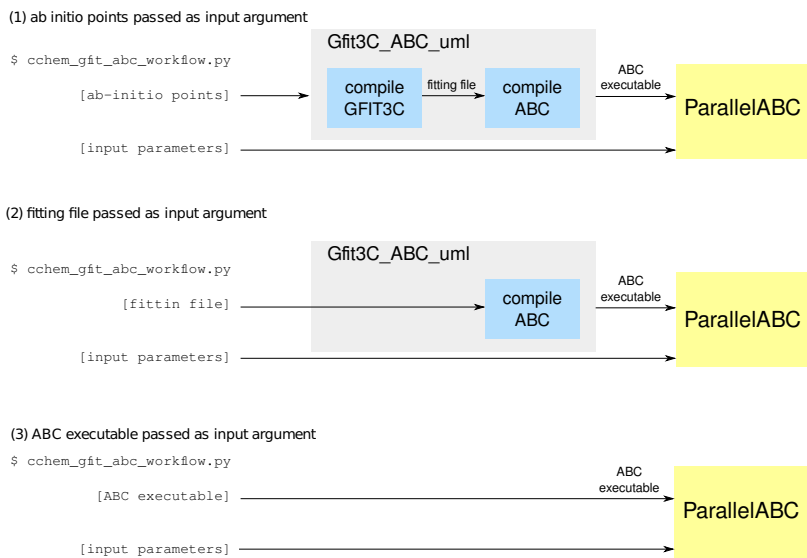


Fig. 1. Sketch of the developed workflow showing its components and the connections between them

Out of the three different use cases, of which a graphical illustration is provided in Fig. 1, the first one is the most complex and complete. For its porting, in fact, different factors needed to be taken into account like the dependencies from libraries and compilers used. The ABC code, for example, is only compiled correctly by using the G95 Fortran compiler [28]. As this compiler is not natively available in any of the most common Linux distributions, step (B) cannot be normally executed on the computational nodes available on a grid infrastructure. A traditional approach to this problem would require users to negotiate the installation of the dependent software on a substantial fraction of the execution nodes. A simpler solution to this, however, comes from a VM-based approach: workflow steps are run within a Virtual Machine that provides a controlled and uniform execution environment, including all software dependencies. The AppPot software runs a Linux VM as a Grid job, allowing to roll out the planned solution on a Grid infrastructure without prior negotiations with Grid systems administrators. Moreover, the ABC code is rarely evaluated for a single set of parameters: in step (C) and, in general, in any parameter-sweep study, the program must be executed several times, consuming a large amount of CPU time. This justifies the use of an “embarrassingly parallel” style of execution, where many instances of ABC run independently and results are collected at the end.

6.2 Implemented Application Classes

The workflow driver has been implemented as a command-line script using GC3Pie *SessionBasedScript* template (an abstract of the script invocation syntax and help text can be seen in Fig. 2). The script searches for ABC input files by scanning an input directory (provided by the user in the command-line) and for each combination of ABC input files and *ab initio* points or fitting file (depending on command-line options), a workflow task is created and executed through completion.

```
$ cchem_gfit_abc_workflow.py --help
usage: cchem_gfit_abc_workflow [OPTIONS] [INPUT]

OPTIONS:
[...]
--g3c G3CFILE           GFIT3C input file.
--dim DIMENSIONS       Surface file.
--pes FORTRAN_PES      Fortran file for the potential energy surface.
```

Fig. 2. Extract from the help text of the workflow driver script. Depending on the input provided by the user, a specific workflow task is created and executed.

Following the GC3Pie development model, most of the coding effort consisted in creating appropriate classes for specifying the workflow logic and the relation between the parts (see Fig. 1 for details).

The *ABC_Workflow* class represents the top level logic of the workflow: it conditionally enables the *MainSequentialABC* class (responsible for the source compiling stage) or the *ParallelABC* class (responsible for the ABC execution stage) for every input file and parameter combination provided by the user through the command line interface, defining the sequence of tasks to be executed.

If a compiling stage is needed, the *MainSequentialABC* creates an instance to the *Gfit3C_ABC_umLApplication* class (a *SequentialTaskCollection* according to the GC3Pie nomenclature) responsible for controlling steps (A) and (B). The script is able to build an AppPot VM, with the required software environment, in any of the execution nodes available on the Grid infrastructure and compile the source code of both GFIT3C and ABC (or only ABC depending on the provided parameters). At the end of this step, the statically compiled ABC executable and the related log files are transferred back to the user account in the client machine and are made available for a control check.

The management of single and multiple ABC instances are delegated to different *Application* classes called *ABC_Application* and *ParallelABC* (a *SequentialTaskCollection* and a *ParallelTaskCollection* class, respectively, according to the GC3Pie nomenclature). The first class makes use of the GC3Pie libraries to submit and control the ABC execution as a single job in a grid environment. The second class, instead, manages the submission of multiple instances of the first class according to the number of input files provided by the user (see Fig. 3 for graphical details).

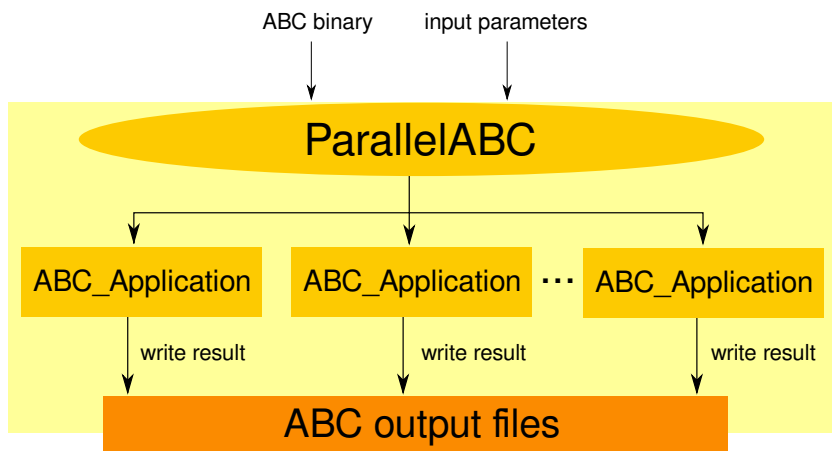
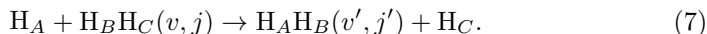


Fig. 3. Sketch of the Workflow portion developed to distribute the ABC code into a grid environment making use of the GC3Pie framework

Also in this case the results carried out by each computation, together with the file logs, are saved on the client machine. Attention has been paid to the need that different output files must be stored in different directories to facilitate checks and further utilization by the end-user. Alternately, GC3Pie can leverage features of ARC and upload the output files to a specified Storage Element (ARC supports the GridFTP and SRM protocols). In this case, output files are not downloaded to the local directory: GC3Pie specifies an output location in the job description and the ARC server will upload the output files to the specified SE when the job is finished.

7 Experimental Results and Performance

To the end of testing the computational machinery and the validity of the developed workflow, we executed on the Swiss Multi-Science Computational Grid (SMSCG) infrastructure the complete workflow for the calculation of the time independent quantum probabilities of the following atom-diatom reaction:



In the test we assumed that the *ab initio* points are those calculated by Rampino et al. in [14]. In this approach [1] therefore, the first step of the workflow is devoted to run the GFIT3C routine to the fitting of the *ab initio* points. From the fit a r.m.s. of 0.19 kcal/mol was obtained using a polynomial of degree 7 for the two

¹ For the same benchmark calculation, alternative solutions aimed at carrying out an update of the current workflow are being studied. More precisely, we are developing a new library able to search on the web for suitable *ab initio* points or, if they are not available, start the *ab initio* calculations for the investigated system.

body term and a polynomial of degree 10 for the three body. These values are completely in line with those obtained by Rampino et al.

In the second step of the workflow the PES Fortran routine, obtained by the GFIT3C fitting of the *ab initio* points, was integrated into the ABC code. To compare and validate the present case study, all calculations were performed by varying the scattering energy from 0.4 eV to 1.4 eV at zero total angular momentum and diatomic parity +1.

The calculated $v = 0$, $j = 0$ state specific reaction probability is plotted in Fig. 4 as a function of the total energy. The agreement with the results of [14] provides a solid validation test of the two workflow approaches. For a more detail, in Fig. 5 a decomposition in the state to vibrational states $v' = 0$ and $v' = 1$ is plotted by using different lines and colors.

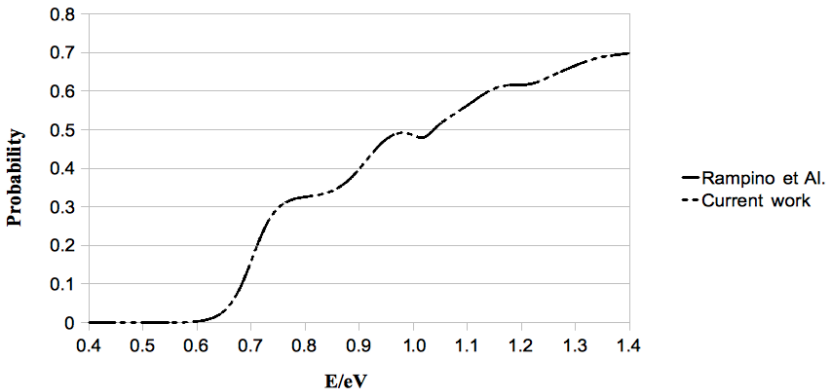


Fig. 4. Comparison between the reactive probabilities as a function of total energy calculated on the present study with those obtained by Rampino et al. [14]. As expected by the adoption of the same set of *ab initio* points, the calculations of the reactive probabilities lead to the same results.

7.1 Performance

Application porting and the validation runs were initially performed on the Swiss National Grid infrastructure (SMSCG, see [13]), which runs on the Advanced Resource Connector (ARC) middleware [22]. The GC3Pie client script was run from a user interface machine at the GC3.

In our validation tests for the $\text{H} + \text{H}_2$ reaction we submitted 1000 jobs in the above mentioned energy interval in order to have a regular grid of results of 10^{-3} eV.

GC3Pie allows to programmatically set the number of simultaneous jobs concurrently “in flight” (i.e., either running or submitted to a remote system and waiting to run); this is a feature used to better cope with the availability and responsiveness of the underlying infrastructure (no need to submit all possible jobs at once if the infrastructure cannot serve them).

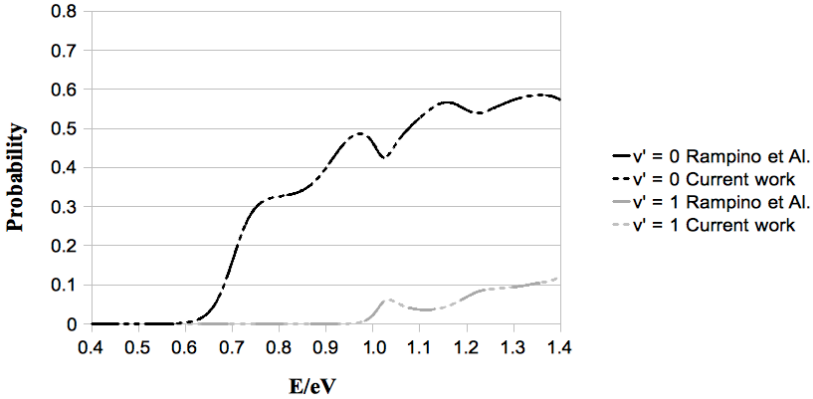


Fig. 5. A detail of the reactive probabilities at $v' = 0$ and $v' = 1$ as a function of total energy calculated on the present study and compared with those obtained by Rampino et al. [14]

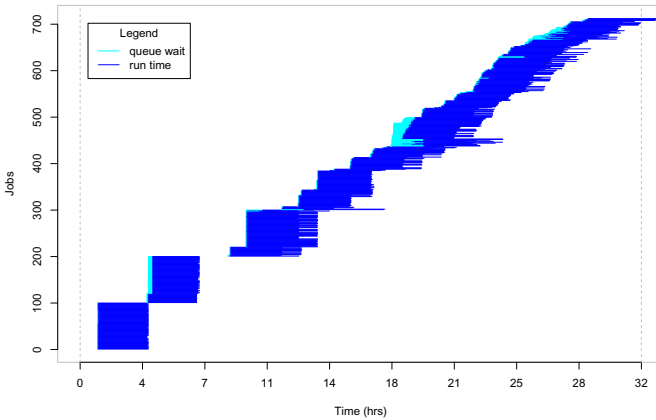


Fig. 6. Representation of running and waiting times for the successful jobs in the SMSCG workflow submission experiment. Each horizontal segment represents a job; the light- and dark- colored portions measure the waiting time (in the remote batch system queue) and the actual running time, respectively. The gaps should be interpreted as a concentration of failures in a certain time span.

For the validation test we set this number to 100 concurrent jobs.²

After about 32 hours, we were able to collect the results coming from 712 successful job submissions, for a grand total of about 138000 min of computation time, i.e., about 2300 CPU-hours. The remaining jobs failed due to hardware

² This is an empirical value we chose mostly due to the limited number of sites supporting the AppPot application tag at the time we run the whole validation test.

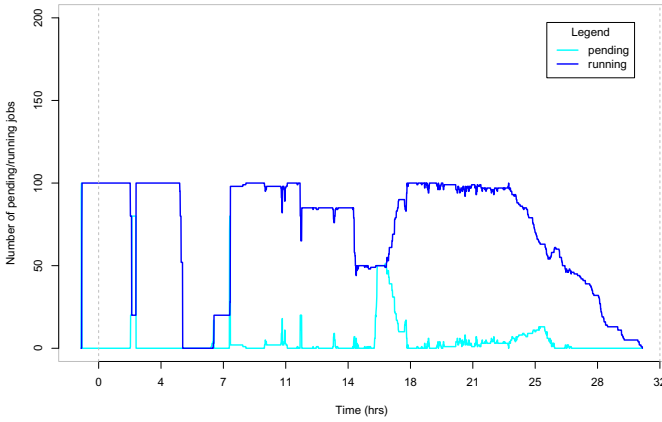


Fig. 7. Number of running (dark color) and pending (light color) jobs as a function of time in the SMSCG infrastructure submission. The GC3Pie client was configured to check job status every 45 seconds, and try to keep a total of 100 jobs in submitted or running status at any time.

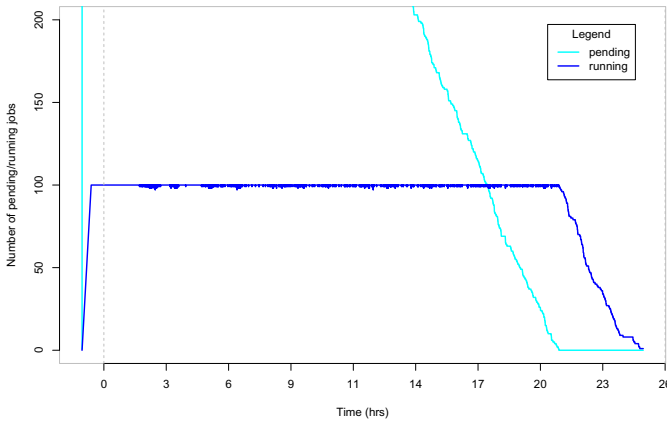


Fig. 8. Number of running and pending jobs as a function of time in a simulated “ideal” situation. In this simulation, all jobs are submitted at the onset, and then are executed on a dedicated cluster of 100 independent CPUs; it is further assumed that no other jobs are contending the use of the cluster. The solid blue line clearly shows that the number of running jobs is roughly constant until the end, when there are not enough pending jobs to fill the cluster.

and/or software related problems that need to be investigated. The average run time of successful jobs was thus of about 190 min, or little more than 3 CPU-hours. Fig. 6 provides a pictorial representation (carried out by using the code provided by Panse [29]) of the running and waiting time for each individual job.

The gaps in the visualization should be interpreted a concentration of failed jobs in a short time span; a cross-analysis of the job error messages show that two clusters of SMSCG had a malfunction and acted as “black holes”.

In Fig. 7 the number of running and pending jobs as a function of time in the current grid submission are shown. A simulation of an ideal submission of 100 jobs constantly running and no queue wait time (see Fig. 8) takes about 26 hours to complete. According to our simulations, the grid execution model added less than 25% overhead for a realistic use case, involving significant waiting time at remote clusters and important malfunctions.

8 Conclusions

The porting of legacy computational chemistry applications onto the Grid infrastructure, together with the development of the related workflows, has been tackled as part of a more general effort to build a solid platform for assembling accurate multi-scale realistic simulations and for establishing an advanced molecular and material science research environment.

In particular our efforts were aimed at building a library of molecular dynamics codes to be offered to the users of the COMPCHEM Virtual Organization, to implement related computer codes on the production Grid infrastructure. On this ground the adoption of the framework GC3Pie allowed us to define event-related dependencies between different applications and execute them simultaneously on a large-scale distributed computing infrastructure. The main difference with other popular workflow systems is the programmatic approach to workflows. There is no fixed and pre-defined structure of the workflows: the entire execution schema is assembled at runtime and steps can be added and removed dynamically as the program progresses, adapting to the outcome of individual computations. The implemented case study demonstrates the validity of this approach by following different routes depending on the availability of outcomes of previous investigations. Such a feature of GC3Pie paves the way to further work on better embodying workflows in molecular simulators.

The possibility of porting the workflow on the portion of the EGI Grid available to the COMPCHEM VO has been also evaluated by the GC3 (at present the accessible Swiss National Grid Infrastructure is entirely based on the ARC middleware). Interface to gLite [30] (the other main middleware in the EGI infrastructure), is not yet available through the GC3Pie framework. Preliminary results indicate that the direct submission to CREAM-CE is possible due to the common APIs used by the two middleware and implemented in GC3Pie. However no submission through gLite’s WMS is possible yet and, for this reason, a specialized set of GC3Pie libraries need to be developed and tested.

Acknowledgments. The first author would like to acknowledge the financial support of the COST CMST Action CM1002 CODECS, through the activities of Working Group 3; EGI-Inspire contract 261323; MIUR PRIN 2008 contract 2008KJX4SN_003; ESA ESTEC contract 21790/08/NL/HE; Phys4entry

FP7/2007-2013 contract 242311; Fondazione Cassa di Risparmio di Perugia and ARPA Umbria. This work was supported by the AAA/SWITCH funded Swiss Multi Science Computing Grid project (<http://www.smsgc.ch>) with computational infrastructure and support.

References

1. CODECS (COncurrent Distributed Environment for Computational Spectroscopy), http://www.cost.esf.org/domains_actions/cmst/Actions/CM1002
2. Gervasi, O., Laganà, A.: SIMBEX: a Portal for the a priori simulation of crossed beam experiments. *Future Generation Computer Systems* 20, 703–715 (2004)
3. Gervasi, O., Crocchianti, S., Pacifici, L., Skouteris, D., Laganà, A.: Towards the Grid design of the Dynamics engine of a molecular simulator. *Lecture Series in Computer and Computational Science*, vol. 7, pp. 1425–1428 (2006)
4. Costantini, A., Manuali, C., Faginas Lago, N., Rampino, S., Laganà, A.: COMPCHEM: progress towards GEMS a Grid Empowered Molecular Simulator and beyond. *Journal of Grid Computing* 8(4), 571–586 (2010)
5. IGI (Italian Grid Infrastructure), <http://www.italiangrid.it/>
6. Laganà, A., Riganelli, A., Gervasi, O.: On the Structuring of the Computational Chemistry Virtual Organization COMPCHEM. In: Gavrilova, M.L., Gervasi, O., Kumar, V., Tan, C.J.K., Taniar, D., Laganà, A., Mun, Y., Choo, H. (eds.) ICCSA 2006. LNCS, vol. 3980, pp. 665–674. Springer, Heidelberg (2006), <http://www.eu-egce.org/compchem>
7. European Grid Initiative, <http://www.egi.eu>
8. GC3 (Grid Computing Competence Center), <http://www.gc3.uzh.ch/>
9. Aguado, A., Tablero, C., Paniagua, M.: Global fit of ab initio potential energy surfaces I. Triatomic systems. *Computer Physics Communications* 108(2-3), 259–266 (1998)
10. Skouteris, D., Castillo, J.F., Manolopoulos, D.E.: Abc: a quantum reactive scattering program. *Comp. Phys. Comm.* 133, 128–135 (2000)
11. AppPot website, <http://code.google.com/p/appot/>
12. GC3Pie website, <http://code.google.com/p/gc3pie/>
13. SMSGC website, <http://www.smsgc.ch>
14. Rampino, S., Monari, A., Rossi, E., Evangelisti, S., Laganà, A.: A priori modeling of chemical reactions on computational grid platforms: Workflows and data models. *Chemical Physics* (2011), doi:10.1016/j.chemphys.2011.04.028
15. Rampino, S.S., Monari, A., Evangelisti, S., Rossi, E., Ruud, K., Laganà, A.: A priori modeling of chemical reactions on a grid-based virtual laboratory. In: Cracow 2009 Grid Workshop, pp. 164–171 (2010)
16. Skouteris, D., Costantini, A., Laganà, A., Sipos, G., Balaskó, Á., Kacsuk, P.: Implementation of the ABC Quantum Mechanical Reactive Scattering Program on the EGEE Grid Platform. In: Gervasi, O., Murgante, B., Laganà, A., Taniar, D., Mun, Y., Gavrilova, M.L. (eds.) ICCSA 2008, Part I. LNCS, vol. 5072, pp. 1108–1120. Springer, Heidelberg (2008)
17. Farkas, Z., Kacsuk, P.: P-GRADE Portal: A generic workflow system to support user communities. *Future Generation Computer Systems* 27, 454–465 (2011)
18. Kacsuk, P., Sipos, G.: Multi-Grid, Multi-User Workflows in the P-GRADE Portal. *Journal of Grid Computing* 3, 221–238 (2005)

19. Manuali, C., Laganà, A., Rampino, S.: GriF: A Grid framework for a Web Service approach to reactive scattering. *Computer Physics Communications* 181, 1179–1185 (2010)
20. Manuali, C., Laganà, A.: New Collaborative Framework for a Web Service approach to Grid empowered Calculations. *Future Generation Computer Systems* 27, 315–318 (2011)
21. Manuali, C., Laganà, A.: A Grid Credit System Empowering Virtual Research Communities Sustainability. In: Murgante, B., Gervasi, O., Iglesias, A., Tanar, D., Apduhan, B.O. (eds.) *ICCSA 2011, Part III*. LNCS, vol. 6784, pp. 397–411. Springer, Heidelberg (2011)
22. ARC middleware website, <http://www.nordugrid.org/arc/>
23. Maffioletti, S., Murri, R., Jonen, B., Scheuring, S.: Computational workflows with GC3Pie, <http://gc3pie.googlecode.com/svn/wiki/posters/euroscipy2011/gc3pie-euroscipy2011.pdf>, Poster Presented at the EuroSciPy 2011 Conference
24. Dike, J.: *User Mode Linux*. Prentice Hall (April 2006)
25. UML website, <http://user-mode-linux.sourceforge.net>
26. Murrell, N.J., Carter, S., Farantos, S.C., Huxley, P., Varandas, A.J.C.: *Molecular Potential Energy Functions*. John Wiley & Sons, New York (1984)
27. Schatz, G.C.: Quantum reactive scattering using hyperspherical coordinates, results for $H + H_2$ and $Cl + HCl$. *Chem. Phys. Lett.* 150, 92–98 (1998)
28. The G95 Project, <http://www.g95.org/>
29. Panse, C.: Cloud Util Plots, <http://cran.r-project.org/web/packages/cloudUtil/index.html>
30. gLite middleware website, <http://glite.web.cern.ch/glite>

The MPI Structure of Chimere

Antonio Laganà¹, Stefano Crocchianti¹,
Giorgio Tentella¹, and Alessandro Costantini²

¹ Department of Chemistry, University of Perugia, 06123 Perugia, Italy

² INFN-CNAF - National Institute of Nuclear Physics, Bologna, Italy

IGI - Italian Grid Infrastructure, Italy

Department of Mathematics and Informatics, University of Perugia, Italy

`alessandro.costantini@cnafe.infn.it`

Abstract. The multiscale three dimensional Chemistry and Transport Model (CTM) package Chimere has been ported onto the segment of the European Grid Initiative platform available to the Virtual Organization COMPCHEM as part of the MPI parallelization activities of the European project EGI-Inspire. The model adopted by the package, its structure, the parallel restructuring made to execute it on EGI and an analysis of some of the main factors affecting its parallel performances are illustrated and discussed.

Keywords: ozone production, Chimere, domain partitioning, grid computing, Chemistry and Transport Model.

1 Introduction

The present trend of chemical research is moving out of per se theoretical investigations into service oriented approaches. To this end complex computational applications are increasingly being ported on the Grid[1] using Service Oriented Architecture (SOA)[2] approaches. Grid empowered SOA approaches are, in fact, a significant step forward to sustainability and pave the way to higher level multi-scale scientific research and innovation. As a matter of fact, Grid computing opens the access to virtually unlimited computing capabilities right when needed by the researchers without any filters or conditions once the computational applications have been properly structured. This requires, however, a detailed analysis of the structure of the considered programs, the decoupling of the execution of their independent tasks, the measurements of the performances achieved for some prototype cases.

This is indeed the focus of the activities that our research group is carrying out within the European project EGI-Inspire[3] by experimenting the use of Message Passing Interface (MPI)[4] on the segment of the EGI infrastructure[5] available to the Molecular and Materials science Virtual Organization (VO) called COMPCHEM[6] initiated in the precursor Grid project EGEE[7]. As a first part of this effort we have already structured for MPI on the Grid some basic linear algebra routines and some quantum reactive scattering programs[8]. As a second

part of this effort we have concentrated our work on the MPI structuring on the Grid of some complex applications and in particular of the package Chimere[9].

Chimere is the multiscale three dimensional Chemistry and Transport Model (CTM) package, owned by French institutes INERIS, LISA, CNRS, modeling the transformations of chemical species and the production of secondary pollutants in the atmosphere. Chimere, originally implemented on our machines in Perugia within a research agreement signed with the Regional Agency for the Environment (ARPA[10]) of the Umbria Region, is believed to be one of the modellistic packages better suited to deal with the chemistry nature of pollutants transformation like the physico-chemical processes concerned with diffusion, transport, deposition and photochemistry. It is in fact based on mechanisms combining a large family of chemical processes and the transport eulerian model. Chimere is designed to provide daily predictions of Ozone (O_3), sulphur oxides (SO_x), nitrogen oxides (NO_x), carbon monoxide (CO), all the volatile organic compounds but Methane (COVNM), particulate matter (PM_k with k being the maximum value of the diameter of the particulate for the considered class) and other important atmospheric pollutants.

The paper is structured as follows: in section 2 the implementation of the Chimere application is described; in section 3 the parallel structure of the code is presented; in section 4 the analysis of the execution time of the MPI parallelized version is discussed; in section 5 the effect of subdomain partitioning is examined; in section 6 some conclusions are drawn.

2 The Implementation of the Chimere Application

The adopted version of Chimere (the V200606A one, written in FORTRAN 77 and later converted into FORTRAN 90, originally structured to run on x86 processors and Linux operating systems) has been installed on a cluster of 8 Intel nodes (Xeon 3 GHz, 4 GB ram, RedHat 8.0 operating system, Intel Ifort 3.1.036 compiler, Gbit network) connected to the distributed computing grid[11] of EGI. This version of the package has a Multiple Program Multiple Data (MPMD) structure that is suited for use in MPI and needs in any case the running of at least two concurrent processes. The machine used to measure the parallel performances of Chimere is a multicomputer made of 8 nodes and a *front-end*, each of which has 4 Intel Xeon cores of 2 GHz, 4 GB ram, Scientific Linux 5.2 operating system, OpenMPI 1.2.5 and GNU gfortran compiler. Complementary computing power is provided by a local network of RISC nodes and UltraSPARC-IIIi processors equipped with SUN SOLARIS 9 operating system, FORTRAN SUN STUDIO 11 compiler and SUN HPC5.0 parallel environment.

The work performed goes from the analysis of the program structure, to its debugging using a high level SUN debugger (useful for spotting bugs undetected by the Intel and GNU compilers[12]) and to the design and implementation of improved scripts to set up the environment and execute the programs. The use of double (SUN and x86 processor) platforms has been tested by reproducing the

¹ As is the case of attempts to modify constants given as functions' arguments.

heat wave that hit Europe in the period July 30 - August 3 of the year 2003. Such run required the installation of the parallel libraries LAM/MPI and OpenMPI. Later on, the MPICH1 library was also implemented. Yet, for the study of the parallel performance we adopted the OpenMPI library because native of the base operating system.

To measure the parallel performances of Chimere we implemented several parallel profiling tools on our Scientific Linux 64bit platform. We started using the `-pg` profiling option of `gfortran`, to be used in combination with the GNU `gprof` utility. After a few tests on a simple serial code, we compiled the entire model source tree with the `-pg` option. Yet, the related execution core dumped giving a segmentation fault error. While debugging the code we found that it assumes an automatic initialization of local variables to zero. Aside from contradicting the general programming rule of not relying on the compiler to assign initial values, the assumption is indeed invalid for the installed version of the `gfortran` compiler (4.1.2). We decided, therefore, to implement the last version of the compiler by first downloading and testing precompiled binaries and then completing the user installation of the `gcc-4.5.2` sources. The new version of the `gfortran` did support the automatic initialization to zero of all local variables (`-finit-local-zero`). The execution of the model did not fail but created a single `gmon.out` profiling output file showing (seemingly undocumented) data relative to just one of the parallel processes. For this reason we switched to different MPI profiling libraries and installed the Fast Profiling library for MPI (`fpmpi`), version 2.1g. In this way we compiled the model including the `fpmpi` libraries and evaluated the response, which focuses on MPI calls giving good timing informations but difficult to work out connections to specific processes bottle necks.

As already mentioned, in the implemented execution chain Chimere is launched on two different concurrent platforms by an initial script. The used V200606A version of the code is, in fact, parallel and parallel runs on an increasing number of processor have been performed. A typical run on our 8 processor Intel cluster needs 124 hours to handle a simulation covering 120 days and collecting 30 *GB* of result data. A distribution of Chimere over the Grid is the most effective way of exploiting concurrency and gaining in computing throughput. As a matter of fact the input section of the program is already designed in a way that collects data of distributed provenance. However, in order to effectively exploit concurrency and achieve significant computing throughput a proper distribution model was adopted. More in detail, this consists of an iterative structure of independent cycles to be executed a large number of times. Such a model exploits the fact that the dependence of the simulation relative to a given day does only partially (for a few hours) depend on the initial concentrations (i.e. the values of the previous day) since they rapidly converge to the actual solution regardless of the starting values. Accordingly, we have restructured Chimere so as to run concurrently several simulations for subsets of days the first of which replicates the last day calculations of another (arbitrary) subset. Then the results obtained using various subsets are glued together by discarding the starting day of each

subset. The procedure was checked by comparing with an actual serial calculation and no significant difference was found.

Such a restructuring has allowed us to implement a prototype version of Chimere on the segment of the EGEE production grid available to COMPCHEM within the activities of the European project EGI-Inspire. The porting was performed by making use of the User Interface (UI) machine available in COMPCHEM. From the UI the user is able to compile and test the code, submit it on the Grid environment for execution, control the status of the submitted work and, finally, retrieve the results of the performed calculations.

The procedure is articulated as follows: first, the code is compiled using the Intel Fortran Compiler, the NetCDF libraries [11] with the support of the MPI libraries in order to maximize the performance of the multi processor Working Nodes (WNs) of the segment of the production EGI grid available to the COMPCHEM VO. Second, the files necessary for the execution are uploaded to the Grid environment on one of the Storage Elements (a remote machine for the data storing that supports, via the gridftp protocol, the data transfer between the machines interconnected into the Grid) which supports the VO (in our case for example the se.grid.unipg.it, SE) before submitting the job. Third, the script is launched for execution.

Chimere is structured as a *task farm* concurrent model in which a main process (master) rules a certain number of processes (workers) working for it. The master sends to the workers the work to carry out and collects and stores the returned results. The master is the only process accessing input data and writing results to the disk. Such scheme makes extended use of messages to communicate with and transfers data among the various processes. A detailed description of the communications exchanged among workers will be given later. However we can anticipate that the size of exchanged data is proportional to the total length of the boundaries between the subdomains. Therefore, execution time depends on several parameters like the number of workers used, the type of connections linking the workers to the master, the maximum communication speed of the machine. Some of them depend on the features of the machine while others depend on the operating system or the software used, and others depend on how and which options have been adopted for their execution.

3 Parallel Structure of the Code

The execution of Chimere is launched by the initial script `chimere-mm5` that is articulated in two parts: *a)* the execution of the preprocessors; *b)* the execution of the program `chimere.e` that represents the heavy computational duty of the package. With the launch of the initial script `chimere-mm5` the calculation parameters are set and the script `chimere-mm5.sh` is executed to compile and run the preprocesses and finally launch the main program. At this point it is important to emphasize that only the second part is considered for parallel execution. For this reason our analysis is concerned only with `chimere.e` that bears a tight interdependence among the various components: at each time step (one hour long) several iterations are performed for each of the N continuity equations of the CTM model.

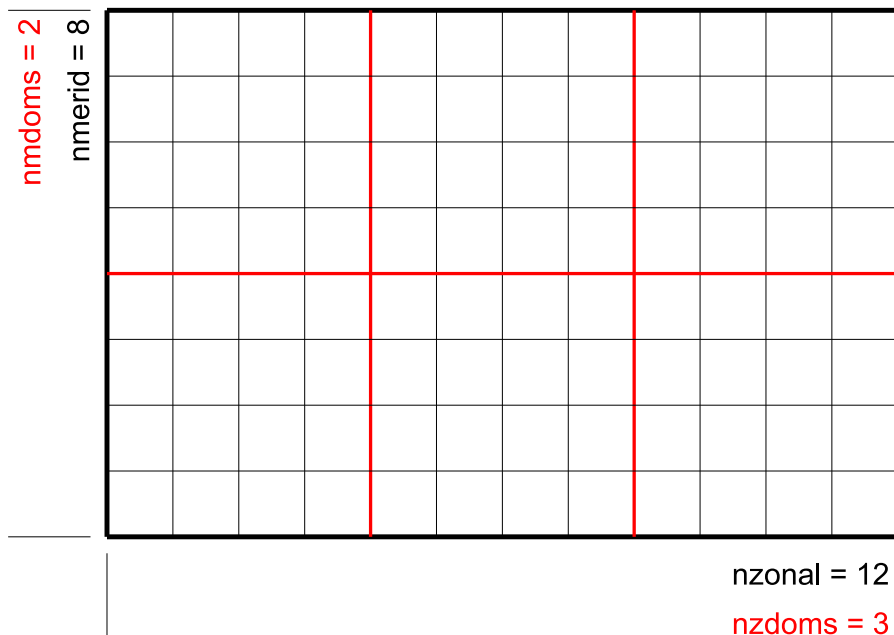


Fig. 1. Example of the domain division in subdomains

The method adopted by the developers to distribute the work among the workers is the so called *domain decomposition*. This method partitions the grid of the domain and assigns part of it to each process. The $nzonal \times nmerid$ bi-dimensional grid associated with each of the lowest eight layers of the troposphere (computing domain) is then partitioned into rectangular subdomains characterized by the two user defined variables $nzdoms$ e $nmdoms$ (with $nzdoms$ indicating the number of subdomains in the direction west-east and $nmdoms$ that in the direction south-north as shown in Fig. 1). The number of needed workers will be, therefore, $nzdoms \times nmdoms$.

The work flow is such that the master sends to every worker the proper set of data to be processed whereas the workers return to the master the results obtained. After writing the results received the master sends another set of data to be processed. Such cycle is iterated for each time step allowing each processor to get its slice of work to carry on. Workers, however, are partially coupled: the process calculating data for the cell (i, j) , for example, makes use of data of cells $i - 3, i - 2, i - 1, i, i + 1, i + 2, i + 3$ in the direction west-east and of cells $j - 3, j - 2, j - 1, j, j + 1, j + 2, j + 3$ in the direction south-north. It also receives from the master data belonging to its own subdomain together with a set of data of certain surrounding regions as illustrated in Fig. 2. Moreover, at the end of the integration of the chemistry mechanisms terms, the workers update their own surroundings by communicating with neighbor workers and

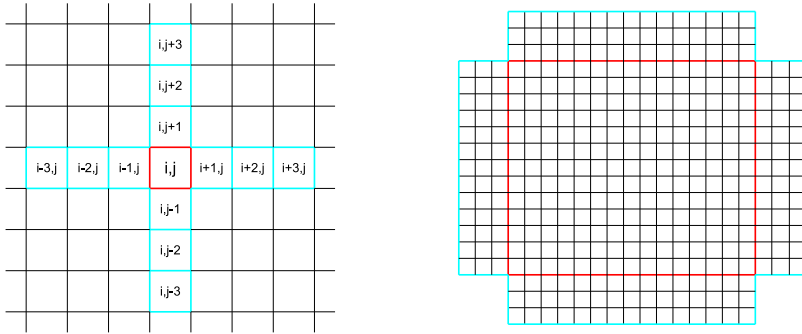


Fig. 2. Left hand side: cells of the computational domain and its internal regions. Right hand side: a subdomain and its surroundings.

fishing relevant data. Further coupling is requested by the fact that in order to compute a given value in cell i at time t , the process needs values belonging to cells $i-3$, $i-2$, $i-1$ though computed at time $t-1$, and values belonging to cells i , $i+1$, $i+2$, $i+3$ calculated instead at time t . This coupling could be satisfied by sending actual values of the last three cells of each row of each subdomain to the worker taking care of the adjacent rhs domain (obviously, the same scheme could be adopted also for the columns, bottom up). However, as stated in the Chimere documentation [12], this would imply that each worker should start working only after the workers taking care of the three domains to its left hand side (and underneath it) have ended their job. This would require a strictly sequential execution inhibiting full parallelization of Chimere. The problem has been bypassed by (arbitrarily) assuming that each row of the subdomain division does not depend on the others (while the above and below ones do and are, therefore, updated after each iteration). The adoption of such simplified parallel method led to a significant enhancement of the parallelism and a consequent clear reduction of the computing duty of the master. A practical validation of such approximate scheme is provided by the negligible difference obtained between results calculated using such parallel implementation and the sequential ones [12].

4 Execution Time Analysis

To carry out the execution time analysis we have performed several tests varying the domain decomposition. As already mentioned, we find first of all that the execution time of Chimere appreciably depends on the number of workers used. This seems quite reasonable due to the fact that the partitioning of the computational domain among an increasing number of workers makes the amount of work per processor decrease. However, it is all but clear what is the effect of an increase of workers on the utilization of the various components of a distributed computing platform. We have therefore monitored, in the various runs carried

out to the end of measuring performances, *real time* (in seconds) values returned by the system command `time` at the end of the execution of `chimere.e`. Such a quantity indicates the net usage of the CPU inclusive of the time necessary to the system to meet the requests of the process (*system time*).

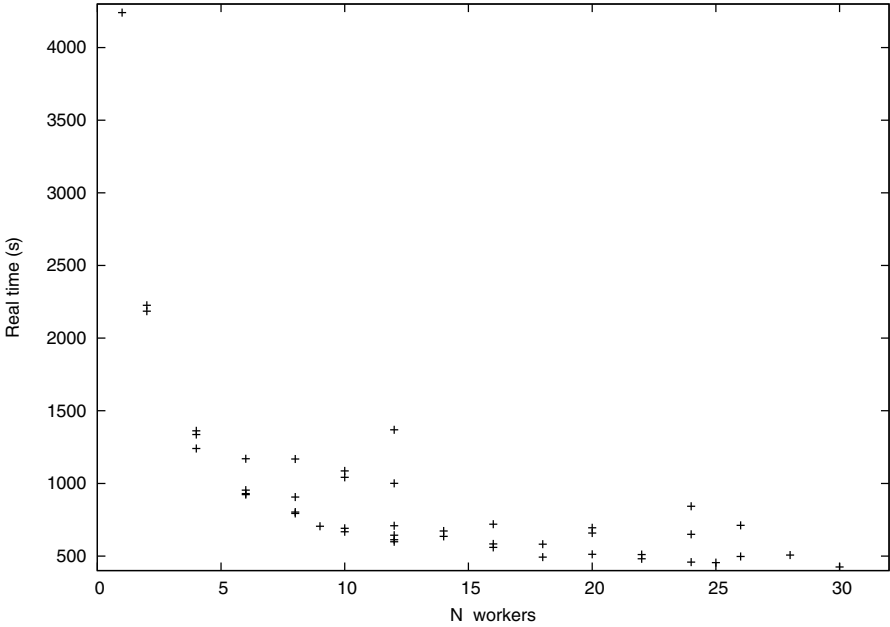


Fig. 3. Dependence of the real time as a function of the number of workers

In Fig. 3 the graph plotting the execution time of `chimere.e` as a function of the number of workers employed is shown. The runs were performed by executing the Chimere benchmark on the parallel machine. The most apparent feature of such graphs is the decrease of the execution time from a maximum of about 70 minutes and 41 seconds for a single worker to a minimum of 7 minutes and 4 seconds for 30 workers². The time gain, however, decreases significantly with the number of workers although runs with the same amount of workers do not automatically lead to an even consumption of time. The reason for such behaviour can be traced back to the fact that the spatial domain in `chimere.e` is partitioned according to the value of the two variables `nzdoms` and `nmdoms` and that there may be different combinations of `nzdoms` and `nmdoms` leading to the same number of workers (in the graph these are the values having the same abscissa).

² We prevented the same processor from acting at the same time as master and worker to the end of minimizing its overload when all the workers send their results.

To the end of evaluating the corresponding gain of time obtained when increasing the number of processes, the usually plotted quantity is the speedup (i.e. the ratio between the real time associated with the use of a single worker and the one associated with the use of a given number of workers). Such plot is

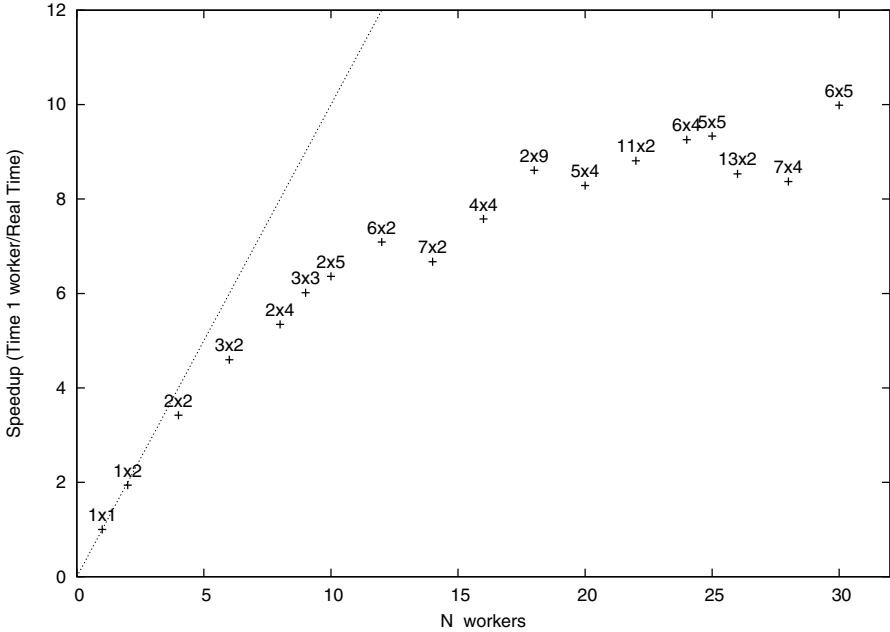


Fig. 4. Best speed up value (+ symbols) plotted as a function of the number of workers. The corresponding $nzdoms \times nmdoms$ combination of values are quoted above the symbol. The dotted line indicates the ideal trend.

shown in Fig. 4, in which the best (shortest) times for a given number of workers are plotted. The plot has an initial increasing trend starting from 1 (single worker) and keeps rising (though more smoothly) to reach a speedup close to 10 when 30 workers are used. Plotted values show large deviations from what can be extrapolated from the first ones (see Fig. 4). As a matter of fact, already with a number of workers slightly larger than 10, the deviation nears 100% with the speedup curve approaching a plateau (though still keeping a residual positive slope). Such behaviour is typical of parallel schemes requiring significant communication between the master and the workers that prevents additional gains. As the number of workers increases, the competition of workers to communicate with the master increases too because it faces almost contemporary requests which queue to be met, prolonging accordingly idle times. Moreover, the structure of `chimere.e`, requests that workers taking care of adjacent sub-domains exchange data necessary for calculating in addition to receiving initial

data and returning results. The need for communicating among workers requires a synchronous execution obtained through an insertion of "barriers" within the code lines to force the worker to wait until all processes have ended the current phase and start at the same time the next phase. Obviously these barriers subtract time to computing because they force the processes having completed their work to wait for the others still busy in carrying out the assigned calculations. The larger the difference in cells' number assigned to the processes is, the longer is the waiting for a new assignment.

5 The Effect of Subdomain Partitioning

Table 4 singles out also how the division of the domain into subdomains impacts the execution time (in seconds) of `chimere.e` by quoting its value as a function of the variable `nzdoms` along the columns and of the variable `nmdoms` along the rows. An even number of subdivisions has been always adopted in all but the run with one worker (that has been taken as the reference value to calculate the speedup) and in other few cases. The limited number of processors available has confined our analysis to a number of workers not exceeding 30 (though we can reasonably expect that the time gain obtainable from the addition of further workers would be in any case modest). As a general indication we find that the minimum time is associated with the combination $nzdoms = 6 - nmdoms = 5$ (indicated as 6×5)³. The lowest times are located in the central part of the table and refer to the cases with the highest number of workers having more "regular" subdomains.

In the upper left part of the Table are collected, on the contrary, the highest times associated with a small number of used workers. It is important to notice here that going along a row (see for example $nmdoms = 1$ or $nmdoms = 2$) or a column (see for example $nzdoms = 1$ or $nzdoms = 2$), times generally tend to decrease first and then, after reaching a minimum, to increase. In addition, the minimum reached on row $nmdoms = 2$ is lower than the minimum obtained on row $nzdoms = 2$. By looking, however, at that row one can notice that, from a certain point on, an oscillating trend shows up (as it also occurs along the columns) if we consider, as an example, the one for $nzdoms = 2$. When going down along that column by increasing $nmdoms$, at the beginning time lowers. Afterwards, in going from $nmdoms = 5$ to $nmdoms = 6$ time increases while it decreases again in going from $nmdoms = 6$ to $nmdoms = 7$. A similar trend can be seen also at higher values of $nmdoms$. This makes the speedup plot oscillate as shown in Fig. 5.

Such oscillatory trend suggests that factors other than the extent of occupation of the last node come into play when determining the execution time. The criterion adopted in assigning the processes to the quad-core nodes has been that of minimizing the number of partially active ones to reduce communications external to the nodes. As a result of having decided to utilize an even number of subdomains it follows that, apart from the first node in which there are at most

³ The 5×6 combination (not shown in the table) takes a few seconds more.

Table 1. Real time values (in seconds) for different combinations of *nzdoms* and *nmdoms*

nmdoms	nzdoms												
	1	2	3	4	5	6	7	8	9	10	11	12	13
1	4241	2226		1362		954		906		1042		1000	
2	2186	1240	923	803	691	598	636	583	582	659	481	649	497
3		930	705	643									
4	1336	793	612	560	512	458	507						
5		667			454	425							
6	1170	709											
7		672											
8	1168	719											
9		493											
10	1086	695											
11		510											
12	1369	842											
13		711											

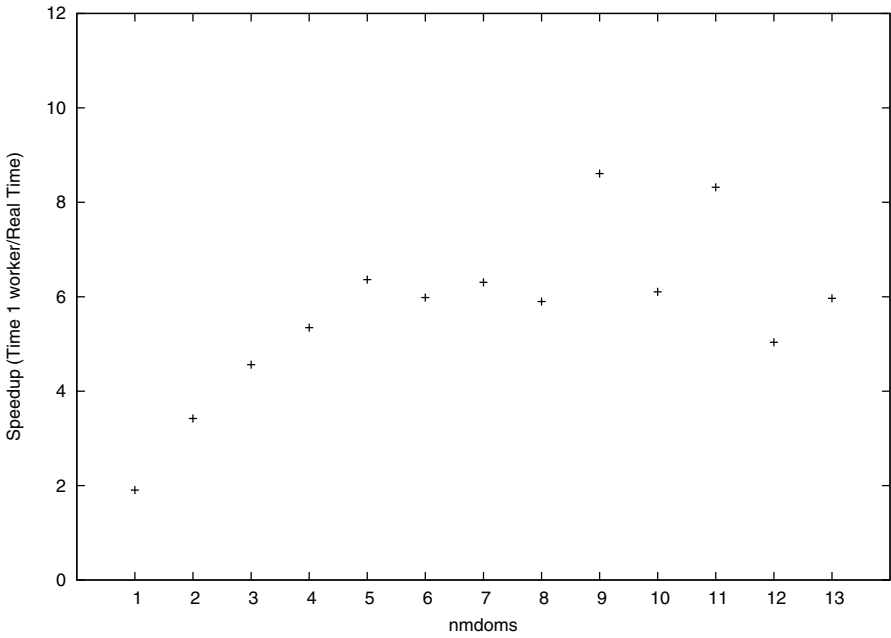


Fig. 5. Plot of the Speedup as a function of *nmdoms* only for combinations at *nzdoms* = 2

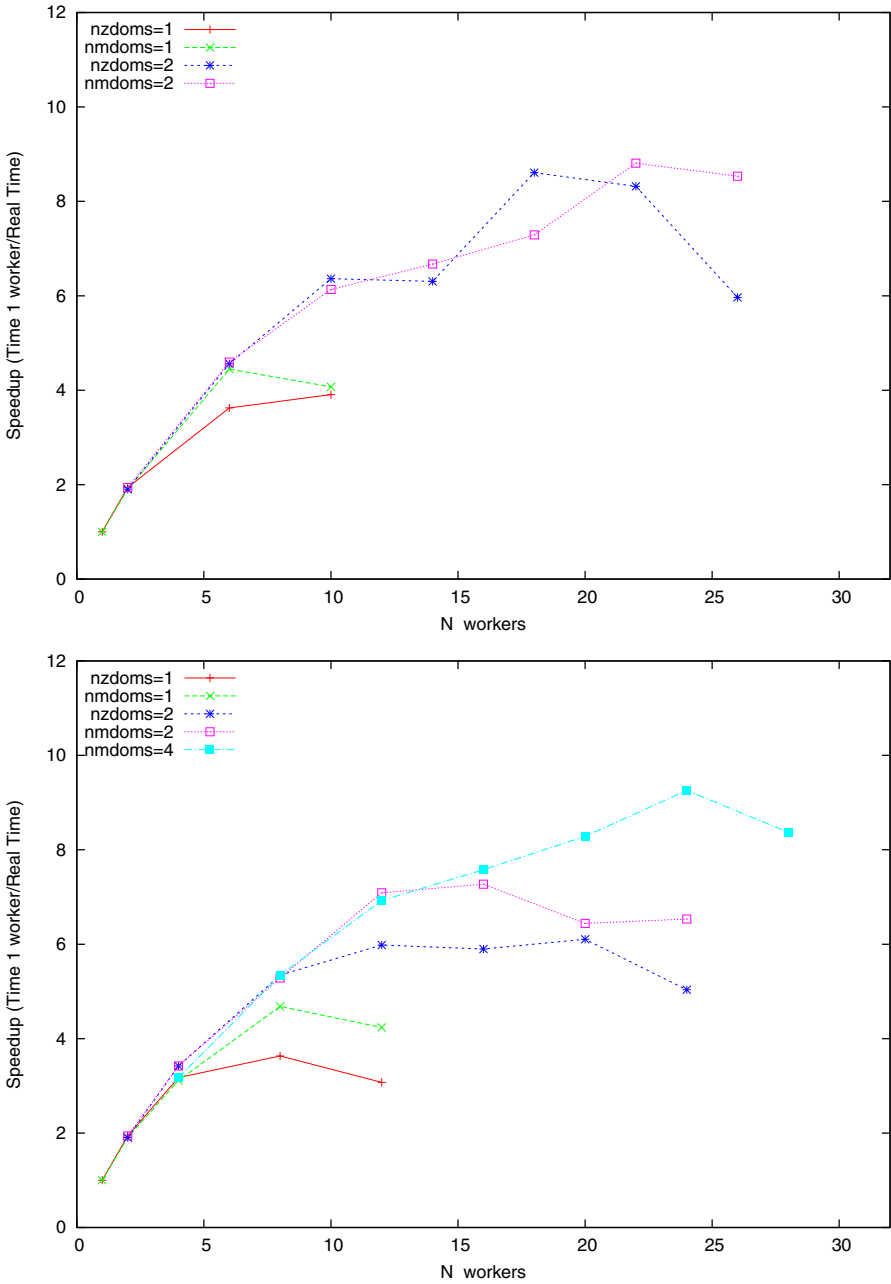


Fig. 6. Plot of the speedup as a function of the number of workers when the last node is fully occupied (above) and the last node is partially occupied (below). In the two graphs constant *nzdoms* or *nmdoms* series have been evidenced.

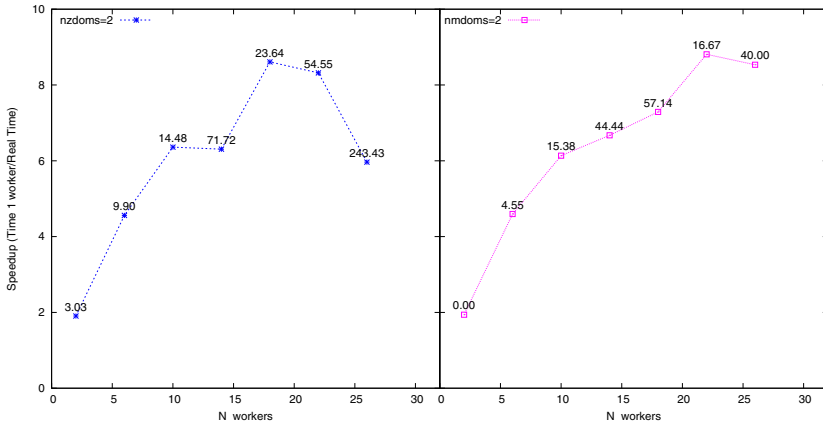


Fig. 7. Plot of the speedup as a function of the number of workers when the last node is fully occupied. Above the points related cell percentual deviations are given.

one master and two workers, all the other nodes are fully occupied (with the exception of the last that is partially occupied). In the combination 2x6 with 12 workers, for example, the last node is only half occupied. This means that only 2 processors out of 4 are engaged. In fact, on the first node there is always a processor engaged by the master task and of the remaining 3 processors one is left inoccupied while the other two are engaged to run as workers. By following the criterion of maximum occupation, the other workers are 4 on the second node and 4 on the third node so that they are fully occupied. The remaining 2 workers run on the 4th node that results, therefore, half occupied. In the combination 2x5 with 10 workers, instead, the last node is totally occupied. In going from the 2x5 to the 2x6 combination the execution time increases suggesting that the best times are those in which the last node is fully occupied (as confirmed by the analysis of the other cases).

To better single out such effect, two plots (see Fig. 6) show the speedups achieved in the cases of a fully occupied (upper plot) or a partially occupied (lower plot) last node. In the graphs we have connected results corresponding to the same value of *nzdoms* or *nmdoms* obtaining, again, the typical trend in which the speedup smoothly increases before reaching a maximum and decreases again afterwards. The final decrease could be rationalized in terms of an increase of the time devoted to communications. However, it should be noted that the plots are not free of "anomalous" values (see for example the value corresponding to 14 and 18 workers in the series with *nzdoms* = 2). A reasonable explanation could be given in terms of the non homogeneous partition of the cells in subdomains. As a matter of fact, when subdomains are created, the cells of the computational domain are partitioned by the subroutine `master_init_mpi` and seldom the cells are evenly divided among the subdomains. This makes the remainder of the division to be unevenly partitioned among the various subdomains. The criterion adopted by the

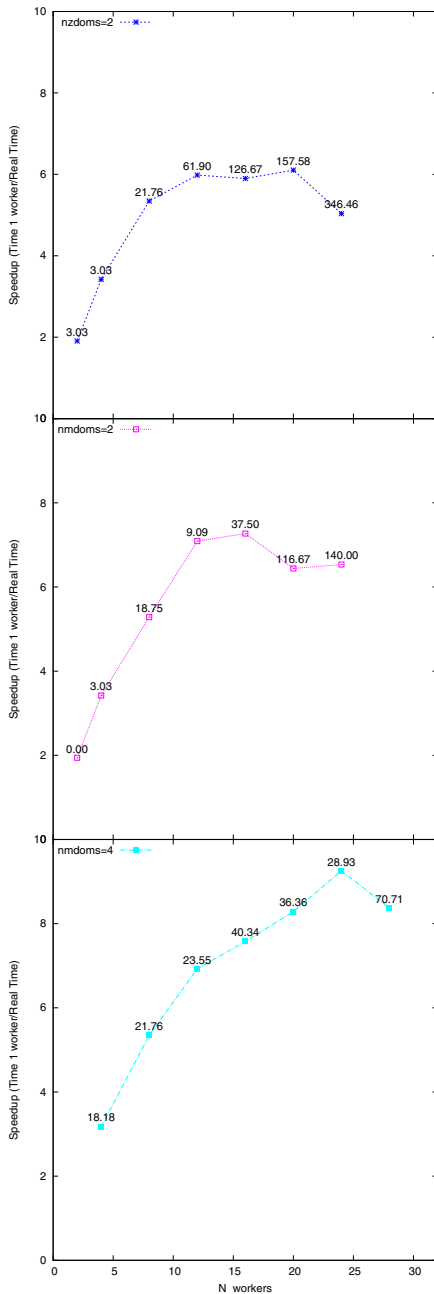


Fig. 8. Plot of the speedup as a function of the number of workers when the last node is partially occupied. Above the points related cell percentual deviations are given.

developers is to add remaining cells to the last subdomain whose worker might end up by dealing with a larger number of cells slowing down all the others because of the effect of the synchronization barriers⁴.

To verify the dependence of the execution time on the domain partitioning, the relative deviation of the number of cells in the various subdomains has been considered. Given the maximum C and the minimum c number of cells in the subdomains of a particular combination of $nzdoms$ and $nmdoms$, the percentual deviation in cells is quantified as: $(C - c) * 100/C$. By quoting in the plot the deviation together with the speedup values (Fig. 7 and Fig. 8) it becomes apparent how its increase corresponds to a larger imbalance of the load among the workers that usually causes a decrease of the speedup and an increase of computing time. Obviously the effect is larger in the rightmost part of the graph in which the speedup increase is milder than in its first part. This is clearly visible in the whole series like, for example, in the one with $nzdoms = 2$ (the last node is fully occupied in the last 5 points) or in that with $nmdoms = 4$ (the last node is partially occupied in the last three points). This confirms the correlation between the load imbalance and the execution times. However, in this case too there are points not fulfilling such rule especially when percentages do not increase significantly. In the series with $nzdoms = 2$ and the last node partially occupied, as in Fig. 8 for example, between the fifth and the sixth point the percentage of increase of the cells increases (yet also the speedup increases rather than decrease). An explanation of this could be associated with the shape of the plot: usually speedup plots increase steadily at the beginning and then flatten to decrease further out. Here, instead, we notice that plots tend only to flatten unless there is a clear effect of load imbalance.

6 Conclusions and Possible Developments

In this paper we discuss the problems met when executing the MPI parallelized version of Chimere. The main goal of the work has been that of carrying out a critical implementation of Chimere targeted to the development of loosely coupled distributed structures suited to run on the computing grid. Our efforts led to the assemblage of a prototype distributed version of the code that has been effectively implemented on the EGI production computing grid and has been used for modeling the production of secondary pollutants in the Umbria region during the summer (which means a particular attention to the ozone concentration) by exploiting the information obtainable from the appropriate distributed sources.

Such grid implementation and the related parallel execution show that the efficiency of the code is significantly affected by the way the work is assigned to computing nodes and pave the way for further improvements like:

⁴ For the sake of completeness, such inefficiency has been fixed in the last version (2011a+) of the code that we are currently implementing.

- optimization of the distributed version of Chimere for a high throughput utilization in routine usage;
- improvement of the chemical mechanisms with the linking of Chimere with GEMS^[13] the grid empowered simulator of molecular processes allowing to use ab initio estimates of the efficiency of the intervening chemical processes;
- a better integration of Chimere with output statistical analysis and further graphical tools supporting a better understanding and a multimedia dissemination of the results.

Acknowledgments. Thanks are due to the French Institutes Pierre-Simon Laplace (C.N.R.S.), INERIS and LISA (C.N.R.S.) for distributing the version of Chimere used for our investigation; to the Italian ARPA Emilia Romagna and Lombardia for sharing meteorological and biogenic emission data. Thanks are also due to COMPCHEM, IGI, EGI-Inspire, the Fondazione Cassa di Risparmio of Perugia and Arpa Umbria for financial support.

References

1. Kesselman, C., Foster, I.: The Grid: Blueprint for a Future Computing Infrastructure. Morgan Kaufmann Publisher, USA (1998)
2. Erl, T.: Service-Oriented Architecture: Concepts, Technology, and Design. Prentice Hall PTR, Upper Saddle River (2005) ISBN:0131858580
3. <http://www.egi.eu/projects/egi-inspire>
4. Gropp, W., Lusk, E., Doss, N., Skjellum, A.: A high-performance, portable implementation of the MPI message passing interface standard. *Parallel Computing* 22, 789–828 (1996)
5. <http://www.egi.eu>
6. Laganá, A., Riganelli, A., Gervasi, O.: On the Structuring of the Computational Chemistry Virtual Organization COMPCHEM. In: Gavrilova, M.L., Gervasi, O., Kumar, V., Tan, C.J.K., Taniar, D., Laganá, A., Mun, Y., Choo, H. (eds.) ICCSA 2006. LNCS, vol. 3980, pp. 665–674. Springer, Heidelberg (2006), <http://compchem.unipg.it/start.php>
7. EGEE: Enabling Grids for E-Science in Europe, <http://www.eu-egee.org>
8. Laganà, A., Costantini, A., Pacifici, L.: UNIPG: The research cluster of the University of Perugia. MPI on Grid, <http://www3.compchem.unipg.it/newsletter/?q=articles>
9. The Chimere Chemistry-Transport Model. A multi-scale model for air quality forecasting and simulation. © Institut Pierre-Simon Laplace, INERIS, LISA, C.N.R.S (2004), <http://euler.lmd.polytechnique.fr/chimere>
10. <http://www.arpa.umbria.it/>
11. Network Common Data Form: a set of software libraries and machine-independent data formats that support the creation, access, and sharing of array-oriented scientific data, <http://www.unidata.ucar.edu/packages/netcdf>
12. Documentation of the Chemistry - Transport model Chimere, version V200606A, <http://euler.lmd.polytechnique.fr/chimere/>
13. Costantini, A., Gervasi, O., Manuali, C., Faginas Lago, N., Rampino, S., Laganà, A.: COMPCHEM: progress towards GEMS a Grid Empowered Molecular Simulator and beyond. *Journal of Grid Computing* 8(4), 571–586 (2010)

A New Statistical Method for the Determination of Dynamical Features of Molecular Dication Dissociation Processes

Maria Suely Pedrosa Mundim¹, Pietro Candori², Stefano Falcinelli^{2,*},
Kleber Carlos Mundim³, Fernando Pirani⁴, and Franco Vecchiocattivi²

¹Instituto de Física, Universidade Federal da Bahia,
40000 Salvador, Brasil
spedrosa@unb.br

²Department of Civil and Environmental Engineering,
University of Perugia,
Via Duranti 93, 06125 Perugia, Italy
atomo@dyn.unipg.it,
{stefano, vecchio}@dyn.unipg.it

³Instituto de Química,
Universidade de Brasília, Caixa Postal 4478,
70904-970 Brasília, Brazil
kcmundim@unb.br

⁴Department of Chemistry,
University of Perugia,
Via Elce di Sotto, 8, 06123 Perugia, Italy
pirani@dyn.unipg.it

Abstract. A new statistical and stochastic method for the determination of dynamical features of the molecular dication dissociation processes, following the single photon double ionization has been developed. The method is based on an extension of the generalized simulated annealing statistical methodology, previously applied in other fields. The results are consistent with previous determination of the metastable lifetime of the dication, but the analysis also provides additional information about the dynamics of the reaction.

Keywords: statistical method, stochastic method, fragmentation dynamics, photoionization.

1 Introduction

The physical and chemical properties of molecular dications are rather different from those of both singly charged ions and neutral molecules. In solution dications can be stabilized by solvent interactions, however, in the gas phase they are unstable in

* Corresponding author.

most cases. This is due to the coulombic repulsion between the two charges that can produce a dissociation of the molecular dication in two singly charged ions. Moreover, in some cases the couplings by charge transfer effects can produce the formation of a metastable state [1-5].

It follows that the dynamics and the lifetimes of these doubly charged metastable states can selectively affect several microscopic and macroscopic phenomena.

These doubly charged species have an important role in plasma chemistry and physics: a plasma may contain many molecular ions, and under some conditions molecular dications are present in significant concentrations. Molecular dications are also present in the ionosphere [6] of the earth or of other planets and are of interest in interstellar clouds and in hot material surrounding star forming regions [7].

Theoretical calculations of the properties of molecular dications are far more difficult than similar calculations for neutral molecules or singly charged ions with equivalent numbers of electrons and nuclear masses. In fact, computing the properties of molecular dications typically requires full configuration interaction calculations using very large basis sets.

The simplest mechanisms by which gas phase molecular dications can be produced are electron impact ionization, or double-photo-ionization. Synchrotron radiation provides the possibility of studying the double-photo-ionization of molecules by a single photon, with high intensity light, allowing the observation of rather detailed features of the spectroscopy and dynamics of the parent ion and its fragments.

In recent years, we have investigated the double photo-ionization of some simple molecules, like HCl [3,8], HBr [5,9], HI [10], N₂O [11-12], CO₂ [13,14], and benzene [15]. For these systems, the double ionization has been studied as a function of the photon energy, by measuring the ion products with time-of-flight mass spectrometry and, in the case of charge separation processes, by detecting in coincidence the two fragment ions. For HBr, we have also measured in coincidence the two threshold photoelectrons [16], obtaining interesting information about the low lying electronic and vibrational states of the molecular dication.

The typical experimental scheme for measuring photoelectron-photoion-photoion coincidences is sketched in Fig. 1. The photo-ionization events occur in the scattering volume *s*, where the ultraviolet synchrotron light crosses the molecular beam formed of ABC molecules. The grids *g*₁ and *g*₂ establish an electric field that sends the photoelectron towards the electron detector and the ions in the opposite direction. The latter are then extracted and, after acceleration due to the field of grid *g*₃, enter into the drift tube where they fly to the ion detector. The pulses generated by the ions arriving at the detector are recorded as a function of the delay time with respect to the photoelectron.

The typical results of a photoelectron-photoion-photoion-coincidence measurement, in the dissociative ion-ion formation reaction following the double photoionization of molecule, are usually reported in an ion-ion coincidence plot, also shown schematically in the upper part of Fig. 1.

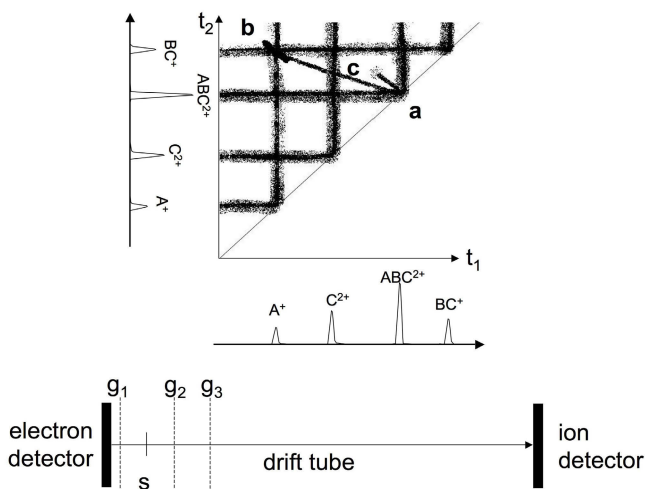


Fig. 1. In the lower part shows the schematics of a typical time-of-flight mass spectrometer. Ions are formed by photoionization in the location *s*, inside the grid system g_1 , g_2 and g_3 . In the upper part, a typical coincidence plot for the double photoionization of a molecule *ABC* is shown. In the plot, the t_1 and t_2 time-of-flight values for ions produced in coincidence with the same electron are reported as points. The photoion peaks are represented by horizontal and vertical ribbons of high intensity points. The location **a** is where ABC^{2+} dication are recorded, while the spot in **b** represents A^+ and BC^+ ions in coincidence, *i.e.* produced in the same ionization event. The tail **c**, connecting the locations **a** and **b**, represents pairs of ions produced by the same dication, after a dissociation occurring along the path from *s* to the ion detector. Therefore we can say that in **a** stable dications, in **b** pairs of ions produced by instantaneous dissociations, and in **c** pairs of ions from metastable dications are recorded.

In such a plot one reports the delay time between the pairs of ions arriving at the detector correlated with the same photoelectron. The vertical and horizontal ribbons, due to high density of points, indicate the ions correlated with the start pulse of the photoelectron. The position **a** refers to the signal produced by the molecular ABC^{2+} dication, while the spot in the position **b** indicates the t_1 - t_2 region for the observation of A^+/BC^+ coincidences, in other words ions correlated with the same photoelectron. The tail **c** connecting positions **a** and **b**, represents pairs of ions produced by the ABC^{2+} dication dissociating into $A^+ + BC^+$ along the drift tube. Considering the time scale, we can assert that ions dissociating during a very short time, given by the difference between the t_1 and t_2 limits in the spot **b**, are enclosed in that spot. Dications with a lifetime longer than the characteristic ion flight time along the drift tube are detected in the position **a**. The ions detected along the tail are those produced by metastable dications with a lifetime comparable to the dication flight time along the drift tube. It is important to stress that the characteristic times for the definition of an instantaneous dissociation, the metastability of the dication, or the formation of a stable doubly charged ion, are depending on the geometrical characteristics of the experimental device and on the applied electrical potentials. These conditions also determine the time resolution of the experiment.

In order to better describe the matter reported above, we discuss the results of two real experiments. In Fig. 2 the plot of coincidences, as measured for the double photoionization of CO_2 at 44 eV photon energy, is reported [13,14]. The formation of a stable CO_2^{2+} dication is quite evident, as well as the instantaneous dissociation into O^+ and CO^+ , but also the same dissociation via a metastable dication.

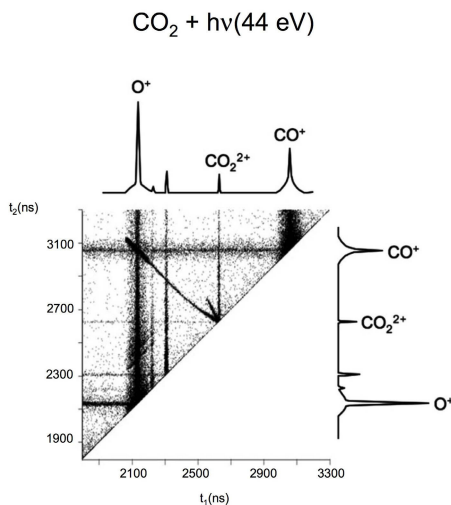


Fig. 2. Ion coincidence plot of the double photoionization of CO_2 as measured at 44 eV photon energy (see Fig. 1 and text)

From the size of the O^+/CO^+ coincidence spot we can define that the instrument (described below) recognizes as instantaneous dissociations those occurring in a time shorter than 50 ns, while the dications seen as stable are those living for a time longer than 2.5 μs . Therefore, dissociations occurring *via* metastable dication states must happen in the times interval between 50 ns-2.5 μs . In Fig. 3 the plot of coincidences, as measured for the double photoionization of N_2O at the photon energy of 39 eV, is shown [11-12]. In this case, we observe two instantaneous charge separation channels, one leading to the formation of N_2^+ and O^+ , while another produces NO^+ and N^+ . For the latter it is evident that also dissociation via a metastable dication occurs, but a stable N_2O^{2+} dication is not formed.

From the two examples described above it emerges that the coincidence plots contain detailed qualitative information about the dynamics of processes promoted by the double photoionization of molecules. In order to extract also quantitative information a numerical analysis of the distribution of coincidences is necessary. In previous experiments a procedure, based on approximated expressions, obtained from a previous kinematical analysis [17], has been exploited by Field and Eland [18].

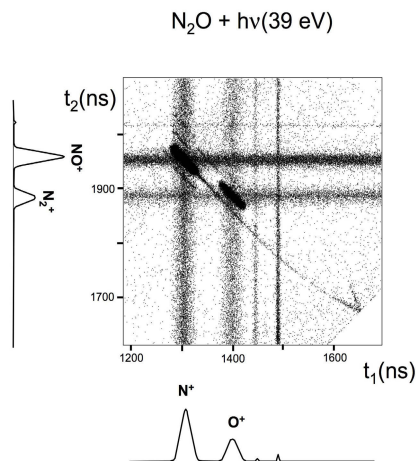


Fig. 3. Ion coincidence plot for the double photoionization of N_2O recorded at 39 eV photon energy (see Fig. 1 and text)

In other cases, a Monte Carlo trajectory simulation of the ion flight inside the instrument has been used [13,18,19]. We have used both methods [13], obtaining consistent results for the lifetime of the metastable dication and the kinetic energy release (KER) into the two product ions.

The extension and generalization of those methods to other systems appear somewhat difficult, especially because their mathematical basis has never been explicitly published and therefore the application to data obtained under different conditions is not immediate. In this paper we report on a new general stochastic method for the analysis of coincidence plots in order to extract details of the dynamics of charge separation processes of the type described above, especially for obtaining the relevant lifetimes. Such an analysis includes the definition of the geometry and the relevant electric fields in the time of flight mass spectrometer. In the next section the instrument used in our experiments is described in order to define conditions and parameters employed in the CO_2^{2+} and N_2O^{2+} experiments. Then the new method is illustrated in a following section, together with the algorithms used for the analysis. In the final section the results of its application are reported and discussed.

The apparatus exploited to obtain the coincidence plots of the type in Fig. 2 and Fig. 3 is operating at the synchrotron light laboratory ELETTRA (Trieste, Italy), in the ARPES end station of the Gasphase Beamline. Details about the beamline and the end station have been previously reported [11-14].

The energy selected synchrotron light beam crosses an effusive molecular beam of target molecules. In most cases, this target gas is mixed with a rare gas employed for calibration reference measurements. The product ions are detected in coincidence with photoelectrons. The photon energy resolution provided by the monochromator is between 1.5 and 2.0 meV in the energy range recently investigated (25-55 eV). In order to avoid spurious effects due to the ionization by higher-order diffraction photons, a magnesium film filter is placed along the synchrotron radiation beam path. The molecular beam, the light direction and the ion detection axes are mutually

perpendicular. The ion detection system has been assembled following the design described by Lavollée [20]. Such a time-of-flight spectrometer, with an ion position sensitive detector, is designed specifically to measure the spatial momentum components of the dissociation ion products. The electron detector, located just below the interaction volume, consists of a stack of three micro-channel-plates followed by a copper anode. The ion detector also consists of a stack of three-micro-channel plates located at the end of a drift tube. The signals are read by an array of anodes arranged in 32 rows and 32 columns. Such an arrangement allows the detection of the ion arrival position on the detector plate. In our experiments the photoelectron signals are used as start pulses, and then ions are counted as a function of their arrival time and position on the detector. All experiment components are controlled by a computer that also records experimental data.

As already mentioned above, the target gas is supplied to a needle beam source kept at room temperature, where it is also mixed with helium or argon. This allows us to normalize all ion signals, at each photon energy, to the total ion yield of the rare gas signal measured at that energy. An adjustable leak valve along the gas inlet line is used to control the gas flow, which is monitored by recording the pressure in the main vacuum chamber. The incident photon flux and the gas pressure are monitored and stored in separate acquisition channels. Ion yields are then corrected for pressure and photon flux changes while varying the photon energy.

2 Time-of-Flight Mass Spectrometry Generalized Simulated Annealing Method

In this paper we present and apply a new method to obtain a global optimization of an objective function, defined as chi-square between experimental and theoretical data. This method exploits an extension of the temperature concept, used to define the width of the distribution function of each physical variable. In the present case the temperature is permitted to vary to reach the lowest value, defining the most probable distribution of the examined variable. When the objective function represents the energy, the temperature concept assumes the thermodynamic meaning, while in other cases corresponds to a measure of the external noise. Therefore, the present method contains the Monte Carlo procedure, often exploited in the analysis of experimental data, as particular case where the temperature is maintained constant.

The Time-of-Flight Mass Spectrometry Generalized Simulated Annealing (TOFMS-GSA) methodology, employed to characterize the metastability of dications by using experimental data obtained by TOFMS technique, is based on an *inverse problem* that can be formulated by mapping the model parameters on experimental data, through physical considerations. In our case the physical model consists of a set of charged particles moving under the influence of external electrostatic fields. Inverse problems are often formulated in infinite dimensional spaces. However, limitations due to a finite number of measurements, and the practical considerations of recovering only a finite number of unknown parameters, may lead to the problems being recast in discrete form. In this case the inverse problem will typically be conditioned, but the regularization may be used to introduce mild assumptions about the solution and prevent *overfitting*. Many instances of regularized inverse problems can be interpreted as special cases of Bayesian inference.

In our procedure the inverse problem is formulated through an objective function f , defined in a multi-dimensional parameter space as follows

$$f(E_{KER}, \tau, v_0, S_0, \theta) = \sum_{i=1}^2 \left(t_{i_{exp}} - t_{i_{theo}} \right)^2 + \Delta p_z^2 + \Delta E_T^2 \approx 0 \tag{1}$$

where E_{KER} , τ , v_0 , S_0 are the kinetic energy released, the dication time of flight, the initial velocity and position, respectively. θ is the fragmentation angle of the ion momenta with respect to the detector axis. On the right side of Eq.(1), the first term is the chi-square deviation between the experimental and theoretical time of flights for the two ionic fragments obtained by solving, stochastically, the classical motion equation through the GSA procedure. Δp_z^2 is the chi-square deviation of the z component of the linear momentum, that is parallel to the detector axis, while ΔE_T^2 is the total energy chi-square deviation. Δp_z^2 and ΔE_T^2 are constrains to ensure linear momentum and total energy conservation. The ΔE_T^2 term is taken into account only if the ejected electron energy is known. The parameters representative of the analyzed systems are obtained by using classical mechanics to describe trajectories and energy properties of ionic fragments and comparing predictions with measured time of flight mass spectrometry data. The TOFMS-GSA procedure consists in solving, stochastically, the Newton's equations in order to map the set of parameters E_{KER} , τ , v_0 , S_0 , θ that minimize the objective function f defined by Eq. (1).

The main purpose of TOFMS is to collect a population of ions (fragments) moving in the direction of the detector and having a distribution of masses (M_i), charge (q_i), kinetic energy and velocities, the latter being inversely proportional to $\sqrt{M_i / q_i}$. When the fragment ions, under the influence of an external electric field and starting from the rest at the same time, are accelerated in the detector direction, their times of flight, following the usual TOF model [21], at the detector will be distributed according to $\sqrt{M_i / q_i}$. As shown in Fig. 4, our TOF mass spectrometer consists of two acceleration regions, 1 and 2, followed by one field free region, 3, and two small acceleration region, 4 and 5, up to the detector. The values of potentials and the dimensions of each region, as used in the CO₂ experiments, are also given in the figure.

The detailed analysis of the experimental TOF requires no more than Newtonian physics, as shown by the equations reported in the following. The positions S of the i_{th} fragment (di- or mono-cation) in the sector n of the TOF tube is described by,

$$S_{n_i} = S_{n-1_i} + v_{n-1_i} \Delta t_{n_i} + \frac{1}{2} a_{n_i} \Delta t_{n_i}^2 \tag{2}$$

where the time of flight difference is $\Delta t_{n_i} = \frac{-v_{n-1_i} + \sqrt{v_{n-1_i}^2 + 2\Delta S_{n_i} a_{n_i}}}{a_{n_i}}$ and the fragment

velocity is $v_{n_i} = v_{n-1} + v_{KER_i} + a_{n_i} \Delta t_{n_i}$. The acceleration of the i_{th} fragment, in sector n , due the electric field is $\frac{V_n - V_{n-1}}{dS_{n_i}}$, is given by

$$a_{n_i} = \frac{2 \times 1.602 \times 10^{-19}}{M_i \times 1.660 \times 10^{-27}} \frac{V_n - V_{n-1}}{dS_{n_i}} \quad (3)$$

where $V_n - V_{n-1}$ and dS_{n_i} are respectively the electrical potential difference and the dimension of the n^{th} sector. The velocity (z component) of the fragments, parallel to the detector axis, and due to the kinetic energy release (E_{KER}), is equal to

$$v_{z_{KER_A}} = \sqrt{\frac{E_{KER}}{M_A \left(1 + \frac{M_A}{M_B}\right)}} \cos \theta \quad (4)$$

$$v_{z_{KER_B}} = \sqrt{\frac{E_{KER}}{M_B \left(1 + \frac{M_B}{M_A}\right)}} \cos(\theta - \pi) \quad (5)$$

θ is the fragmentation angle in the TOF equipment diagram as shown in Fig. 4. The partial time of flight that the i^{th} ion spends in each region n , is t_{in} and the total time $t_{i_{esime}}$ will be defined as

$$t_{i_{esime}} = \sum_{i=1}^5 t_{in} \quad (6)$$

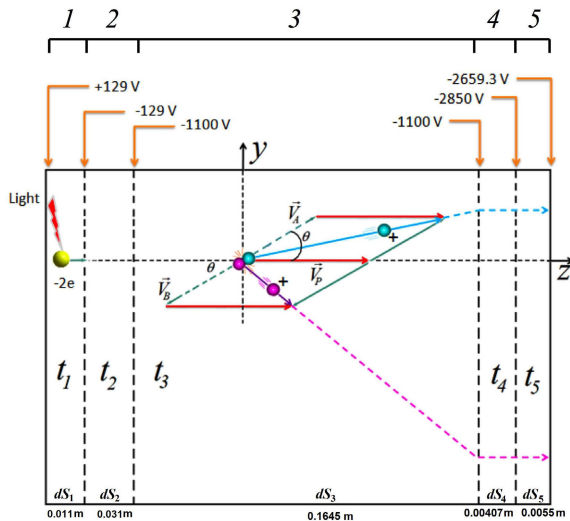


Fig. 4. Definition of the distances dS_i , the applied potentials and the time-of-flight t_i in the sectors i of the TOFMS instrument. The kinematic variables of ions are also indicated.

3 Global Optimization and Discussion

The global optimization problem is a subject of intense research and current scientific interest. Finding the optimal solution for a complex problem is of great importance in a variety of fields, such as image restoration, microprocessor circuitry design and protein folding [22] among others. In this context, we present an alternative methodology, based on the GSA global optimization method to analyze data from TOF experiments.

The simulated annealing (SA) corresponds to a stochastic method used in global procedures and it was proposed by Kirkpatrick and collaborators [23,24]. As stressed above, differently from the Monte Carlo and Metropolis methods [25], in SA the temperature T_{qv} is time dependent and the “temperature” term used does not refer to the thermodynamic concept and the “time” is the number of cycle, n , in the GSA procedure. In this technique, the concept of artificial temperature is introduced and gradually cooled, in complete analogy with the well known annealing technique frequently used in metallurgy, when a molten metal reaches its crystalline state (global minimum of thermodynamic energy). In the literature, the SA algorithm is also referred to as classical simulated annealing (CSA) and its visiting distribution, i.e. the procedure to map the range of variability of the parameter, is a Gaussian function, $g(x) \propto e^{-x^2/T_1(n)} / T_1(n)$. Geman and Geman [26] show that the necessary and sufficient condition for reaching convergence is that the temperature decreases logarithmically with time, that is $T_1(n) = T_0 / \log(I+n)$, where T_0 is the initial temperature.

Szu and Hartley [27] propose to use a Cauchy-Lorentz visiting distribution function $g(x) \propto T_2(n) / (T_2^2(n) + x^2)^{\frac{D+1}{2}}$, instead of a Gaussian one. D is the dimension of parameter space and, in our case, $D = 5$. This algorithm is referred to as fast simulated annealing (FSA) or Cauchy machine. In the reference [27] it is shown that, for a Cauchy-Lorentz visiting type of distribution function, the convergence procedure will reach a global minimum if temperature $T_2(n)$ decreases inversely with time, that is, $T_2(n) = T_0 / (I+n)$. On the other hand, the GSA or Tsallis machine approach [28], which closely follows the recent statistical mechanics for non-extensive systems, has been proposed and applied in quantum chemistry [28,29]; GSA generalizes both the FSA and CSA procedures. So, as introduced in reference [28], instead of using a Gaussian or Cauchy-Lorentz visiting distribution function, the new one is defined as

$$g_{qv}(x) = \frac{\left(\frac{q_v - 1}{\pi}\right)^{D/2} \left[\Gamma\left(\frac{1}{q_v - 1} + \frac{D-1}{2}\right) / \Gamma\left(\frac{1}{q_v - 1} - \frac{1}{2}\right) \right] \left(\frac{\pi - \theta}{2}\right) \times [T_{qv}(n)]^{\frac{D}{3-q_v}}}{\left\{ 1 + \frac{(q_v - 1)x^2}{[T_{qv}(n)]^{\frac{2}{3-q_v}}} \right\}^{\frac{1}{q_v - 1} + \frac{D-1}{2}}} \tag{7}$$

which has the following limits:

$$\lim_{q_v \rightarrow 1} g_{q_v}(x) = g^{CSA}(x) = \frac{e^{-\frac{x^2}{T_{q_T}(t)}}}{\left[\pi T_1(n)\right]^{D/2}} \tag{8}$$

$$\lim_{q_v \rightarrow 1} g_{q_v}(x) = g^{FSA}(x) = \frac{\Gamma\left(\frac{D+1}{2}\right)}{\pi^{\frac{D+1}{2}}} \cdot \frac{T_2(n)}{\left[T_2(n)^2 + x^2\right]^{\frac{D+1}{2}}}$$

CSA and the FSA visiting distributions, respectively. The present approach defines the acceptance probability function as

$$A_{acc} = \left[1 + (q_A - 1) \frac{f(\bar{P}_{n+1}) - f(\bar{P}_n)}{T_{q_T}(n)} \right]^{1 - q_A} \tag{9}$$

which has the following limit if $q_A \rightarrow 1$

$$\lim_{q_A \rightarrow 1} A_{acc} = e^{-\frac{[f(P_n) - f(P_{n-1})]}{T_{q_T}(n)}} \tag{10}$$

The latter is the same acceptance probability function introduced in the CSA and FSA [27] procedures. In the usual GSA methodology, the new temperature is defined as

$$T_{q_v}(n) = T_0 \frac{2^{q_v - 1} - 1}{(1+n)^{q_v - 1} - 1} \tag{11}$$

Taking into account the limits $q_v \rightarrow 1$ and $q_v \rightarrow 2$ we obtain the temperature functions for the CSA and FSA procedures, respectively, as follows

$$\lim_{q_v \rightarrow 1} T_{q_v}(n) = T_1(n) = T_0 \frac{\ln 2}{\ln(1+n)} \tag{12}$$

$$\lim_{q_v \rightarrow 2} T_{q_v}(n) = T_2(n) = \frac{T_0}{n}$$

It has to be stressed again that the GSA approach has been used with success in predicting new three-dimensional protein structures and protein folding [22], in fitting the potential energy surface for reaction pathways and chemical reaction dynamics [30,31], gravimetric problems [32], mechanical properties in alloys [33,34] and the study of molecular electronic structure properties [35,36].

It has to be noted that in the previous equations q_v , q_A , q_T are parameters derived from the generalization of Boltzmann statistical mechanics. In particular, when $q_v = q_A = q_T = 1$ and T is constant, the method reduces to the Monte Carlo procedure.

When using the GSA procedure, proof of convergence to the absolute minimum can be obtained in the same way as was established by Szu and Hartley in the ref. [27].

The TOFMS-GSA procedure, proposed here, starts with a given solution (combination of variables), then random changes are made in a typical "suck-it-and-see" approach. If an improvement is obtained, the old solution is always abandoned in favor of the new one. But if a worse result is obtained, the old solution may still be abandoned in the hope of getting a marked improvement after few steps. This check prevents the algorithm from being stuck in a local minimum, a state which has a value which larger than the global minimum, but smaller than any of its neighbors. However, the frequency with which this is done, decreases as time goes on (this is equivalent to gradually lowering the temperature), so that we should eventually end up at the global optimum, i.e. the best possible solution. While, to reach an acceptable solution could require a large number of trials, simulated annealing is extremely flexible in that rules can easily be devised to obtain new solutions of any kind, including those involving structural changes. More details on the methodology and on the presently suggested procedure are given elsewhere [37].

Concerning computational details of our work, the whole TOFMS-GSA algorithm for mapping and searching the global minimum of the objective function f is composed by the following steps: first we fix the q_A , q_V , and q_T parameters relative to the acceptance and visitation probability-distributions and to the temperature function, respectively; then we start the iterative process with an arbitrary initial guess vector of parameters $P(E_{KER}, \tau, v_0, S_0, \theta)$ and an high enough value for the "temperature" $T_{qT}(n)$ at the GSA loop n ; we calculate the objective initial function $f(P_n)$ by using Eq. (1) and a new "temperature" in the GSA loop $n+1$ [37]; next, by using the visiting probability distribution $g_{qV}(T_{qTn+1}, X)$ as defined in Eq.(7), we calculate the new set of parameters P_{n+1} and $D(E_{KERn}, t_n, v_{0n}, S_{0n}, q_n)$ [37] and finally, at the GSA step $n+1$ and by using these new set of parameters over the Newton's equations, we calculate, in sector k , the main physical properties [37].

Another difference from traditional GSA is that we use a version exploiting in the algorithm also the q_T parameter, introduced in the ref. [36]. This makes the overall procedure more efficient, allowing convergence with a smaller number of cycles, when compared to the usual GSA process. However, when dealing with the traditional GSA algorithm, the proof of convergence to the absolute minimum, as established in the references [28,29], only includes the case of two independent q_A and q_V parameters. While, in the paper [36], by using a modified form of the distribution function, $g_{qV, qT}$, a proof of convergence was introduced for the absolute minimum, which is based on the alternative GSA [38] and defined with three independent parameters q_A , q_V and q_T .

As a check of the procedure proposed in this paper, we have analyzed the CO₂ coincidence plot that has been already investigated with different methods [13]. In order to minimize the simulation computational time, we excluded the fragment time of flights or events, $t_1 \times t_2$, that are not first order correlated, which are usually contained in the experimental data. In the case of the CO₂ system, after the simulation, we have imposed that the chi-square deviation between experimental and theoretical ion time of flights and the linear momentum conservation,

$$\chi^2 = \sum_{i=1}^2 (t_{i_{exp}} - t_{i_{theo}})^2 + (p_{A_z} - p_{B_z})^2, \text{ must be } \chi^2 < 10^{-4} \text{ for each event. After the}$$

simulation and using the Newton's equation we have evaluated some physical

features of the dissociation dynamics, like the kinetic energy release (KER), the fragmentation time, the position in the spectrometer or sector where the fragmentation occurs, the velocity of the dication and that of fragments and their angular orientation.

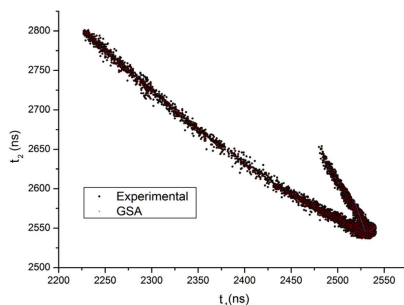


Fig. 5. Coincidence plot shown in Fig. 2, cleaned up of false coincidences and used for analysis. In the plot, the points produced by the simulation procedure are also reported (black points), but are overlapping the experimental dots (open circles) and therefore almost indistinguishable.

In the Fig. 5 the experimental data (open circles) of the coincidence plot for the double photoionization of CO_2 at 44 eV, are reported and compared with the simulation results (black points). It is practically impossible to distinguish the two kinds of results, because the convergence of the simulation has been stopped when the chi-square deviation is really very small. As stressed above, from the analysis of the trajectories produced in the simulation, it is now possible to extract important dynamical features of the dissociation reaction under investigation. In Fig. 6 some of these features are plotted. In particular, the (a) panel reports the initial transversal velocity of the dication, at the beginning of the flight, while panel (b) gives the position where ions are produced by the VUV light; dications then fly up to the location, along the path, where dissociation occurs and panel (c) provides the distribution of such positions. In the panel (d) the KER in the dissociation, exhibiting a distribution around the most probable value, is reported, while in the (e) panel the angular distribution of the direction of the two ion products is displayed. The (f) panel shows the number of dications as a function of the flight time along the path in the drift tube. It is evident their decrease with time, caused by the dissociation reaction.

This last distribution contains the average lifetime of the metastable dication and this information can be easily extracted by using a simple first order kinetic law. However, in this analysis is important to separate the portions of the plot referring to different sectors of the TOFMS: a simple $e^{-t/\tau}$ function applies only in the free field region of the drift tube, as discussed and indicated in the Sect. 2. In the present case a result of lifetime τ of the order of magnitude of the μs is obtained. Following the discussion by Field and Eland [18], one has to consider that CO_2 is a particular case, because when the CO_2^{2+} dication is formed in a metastable state, the spread of lifetimes is large due to a manifold of vibro-electronic states, formed in the photoionization and leading to the opening of several different dissociation channels. Therefore,

the measurements evidently yield average values of τ which depend on the time window over which the observations have been made [13,18] and also on the method used for the analysis of data. Actually, these different methods can attribute different weights to the several possible channels and to the regions of the ion path where dissociation can occur. Nevertheless, it is interesting to note that the τ and KER values here derived are comparable, as order of magnitude, with those that we have already obtained with alternative methods [13,14].

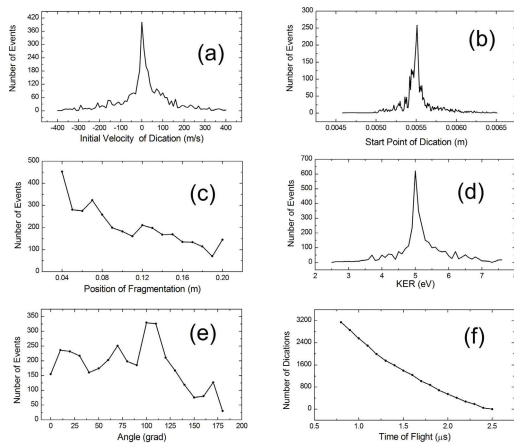


Fig. 6. Dynamical features extracted by the simulation trajectories on the CO_2^{2+} dication. Number of events observed in the simulation as a function of the variables. Panel (a): initial velocity. Panel (b): start point. Panel (c): position where dissociation occurs, along the drift tube. Panel (d): kinetic energy release (KER) of the two fragments. Panel (e): angular distribution of the fragment ions. Panel (f): number of dications along the ion flight path.

One has to emphasize that the distributions in Fig. 6, panels from (a) to (e), must not be confused with the experimental ones, because they are the distributions generated by the procedure, in order to minimize the chi-square of the coincidence plot data in the simulation. The KER distribution, that has been measured separately in the experiment [13,14], although larger, exhibits very similar most probable value. Also the lifetime extracted here is of the same order of magnitude of the one obtained [13] exploiting different methodologies of analysis.

We expect that the methodology presented here can be used, with further improvements, for the analysis of many other systems, like the double photoionization of N_2O [11,12], and of benzene molecules [39] that we have recently investigated. Moreover the same methodology, appropriately extended and modified, could be used also for the analysis of angular distribution of products [12].

Acknowledgment. Financial contributions from the MIUR (Ministero dell’Istruzione, dell’Università e della Ricerca) are gratefully acknowledged. We acknowledge partial travel support by the “Sincrotrone Trieste S.C.p.A.”. We wish to thank the

“Fondazione Cassa di Risparmio di Perugia” for financial support. The authors are grateful to Prof. S. Fornarini, Università di Roma “La Sapienza”, who, very kindly, provided us with mono-deuterated benzene and to the ION-CNR TASC Laboratory for financial support at Gasphase beamline. P.C. gratefully acknowledge financial support by *Regione Umbria*, project *POR UMBRIA FSE 2007-2013Asse II “Occupabilità”, Obiettivo specifico “e”- Asse IV “Capitale Umano”, Obiettivo specifico “I”*. Part of this project has been supported by the Brazilian Ministry of Education and KCM is grateful and wish to thank the CAPES for this grant.

References

1. Pauling, L.: J. Chem. Phys. 1, 56 (1933)
2. Cox, S.G., Critchley, A.D.J., Kreyin, P.S., McNab, I.R., Shiellx, R.C., Smith, F.E.: Phys. Chem. Chem. Phys. 5, 663 (2003)
3. Moix-Teixidor, M., Pirani, F., Candori, P., Falcinelli, S., Vecchiocattivi, F.: Chem. Phys. Lett. 379, 139 (2003)
4. Candori, P., Falcinelli, S., Pirani, F., Tarantelli, F., Vecchiocattivi, F.: Chem. Phys. Lett. 436, 322 (2007)
5. Alagia, M., Brunetti, B.G., Candori, P., Falcinelli, S., Moix-Teixidor, M., Pirani, F., Richter, R., Stranges, S., Vecchiocattivi, F.: J. Chem. Phys. 120, 6985 (2004)
6. Prasad, S.S., Furman, D.R.: J. Geophys. Res. 80, 1360 (1975)
7. Rosner, S.D., Cameron, R., Scholl, T.J., Holt, R.A.: J. Mol. Spectrosc. 189, 83 (1998)
8. Alagia, M., Biondini, F., Brunetti, B.G., Candori, P., Falcinelli, S., Moix-Teixidor, M., Pirani, F., Richter, R., Stranges, S., Vecchiocattivi, F.: J. Chem. Phys. 121, 10508 (2004)
9. Alagia, M., Boustimi, M., Brunetti, B.G., Candori, P., Falcinelli, S., Richter, R., Stranges, S., Vecchiocattivi, F.: J. Chem. Phys. 117, 1098 (2002)
10. Alagia, M., Brunetti, B.G., Candori, P., Falcinelli, S., Moix-Teixidor, M., Pirani, F., Richter, R., Stranges, S., Vecchiocattivi, F.: J. Chem. Phys. 124, 204318 (2006)
11. Alagia, M., Candori, P., Falcinelli, S., Lavollée, M., Pirani, F., Richter, R., Stranges, S., Vecchiocattivi, F.: Chem. Phys. Lett. 432, 398 (2006)
12. Alagia, M., Candori, P., Falcinelli, S., Lavollée, M., Pirani, F., Richter, R., Stranges, S., Vecchiocattivi, F.: J. Chem. Phys. 126, 201101 (2007)
13. Alagia, M., Candori, P., Falcinelli, S., Lavollée, M., Pirani, F., Richter, R., Stranges, S., Vecchiocattivi, F.: J. Phys. Chem. A 113, 14755 (2009)
14. Alagia, M., Candori, P., Falcinelli, S., Lavolleé, M., Pirani, F., Richter, R., Stranges, S., Vecchiocattivi, F.: Phys. Chem. Chem. Phys. 12, 5389 (2010)
15. Alagia, M., Candori, P., Falcinelli, S., Mundim, M.S.P., Pirani, F., Richter, R., Stranges, S., Vecchiocattivi, F.: J. Chem. Phys. 135, 144304 (2011)
16. Alagia, M., Brunetti, B.G., Candori, P., Falcinelli, S., Moix-Teixidor, M., Pirani, F., Richter, R., Stranges, S., Vecchiocattivi, F.: J. Chem. Phys. 120, 6980 (2004)
17. Hsieh, S., Eland, J.H.D.: J. Phys. B: At. Mol. Opt. Phys. 30, 4515 (1997)
18. Field, T.A., Eland, J.H.D.: Chem. Phys. Lett. 211, 436 (1993)
19. Slattery, A.E., Field, T.S.A., Ahmad, M., Hall, R.I., Lambourne, J., Penent, F., Lablanquie, P., Eland, J.H.D.: J. Chem. Phys. 122, 084317 (2005)
20. Lavollée, M.: Rev. Sci. Instrum. 70, 2968 (1999)
21. Wiley, W., McLaren, I.: Rev. Sci. Instr. 26, 1150 (1955)
22. Moret, M.A., Bisch, P.M., Mundim, K.C., Pascutti, P.G.: Biophys. J. 82, 1123 (2002)

23. Kirkpatrick, S., Gelatt, C., Vecchi, M.: *Science* 220, 671 (1983)
24. Kirkpatrick, S.: *J. Stat. Phys.* 34, 975 (1984)
25. Metropolis, N., Ulam, S.: *J. Am. Stat. Assoc.* 44, 335 (1949)
26. Geman, S., Geman, D.: *IEEE Transactions on Pattern Analysis and Machine Intelligence* 6, 721 (1984)
27. Szu, H., Hartley, R.: *Phys. Lett. A* 122, 157 (1987)
28. Mundim, K.C., Tsallis, C.: *Int. J. Quant. Chem.* 58, 373 (1996)
29. Tsallis, C., Stariolo, D.: *Physica A* 233, 395 (1996)
30. Vilela, A.F.A., Neto, J.J.S., Mundim, K.C., Mundim, M.S.P., Gargano, R.: *Chem. Phys. Lett.* 359, 420 (2002)
31. Esteves, C.S., de Oliveira, H.C.B., Ribeiro, L., Gargano, R., Mundim, K.C.: *Chem. Phys. Lett.* 427, 10 (2006)
32. Ellis, D.E., Mundim, K.C., Fuks, D., Dorfman, S., Berner, A.: *Mat. Sci. Semicond. Proc.* 3, 123 (2000)
33. Dorfman, S., Fuks, D., Malbouisson, L.A.C., Mundim, K.C.: *Comput. Mat. Sci.* 27, 199 (2003)
34. de Oliveira, H.C.B., Esteves, C.S., Gargano, R., Chaer do Nascimento, M.A., Malbouisson, L.A.C., Mundim, K.C.: *Int. J. Quant. Chem.* 108, 2540 (2008)
35. de Andrade, M.D., Mundim, K.C., Malbouisson, L.A.C.: *Int. J. Quant. Chem.* 103, 493 (2005)
36. Alagia, M., Candori, P., Falcinelli, S., Mundim, K.C., Mundim, M.S.P., Pirani, F., Richter, R., Stranges, S., Vecchiocattivi, F.: *Chem. Phys.* (2011), doi:10.1016/j.chem.phys.2011.03.031
37. Dall'igna, A., Silva, R., Mundim, K.C., Dardenne, L.: *Gen. Mol. Biol.* 27, 616 (2004)
38. Alagia, M., Candori, P., Falcinelli, S., Pirani, F., Pedrosa Mundim, M.S., Richter, R., Rosi, M., Stranges, S., Vecchiocattivi, F.: *Phys. Chem. Chem. Phys.* 13, 8245 (2011)

SWOT Analysis of Information Technology Industry in Beijing, China Using Patent Data^{*}

Lucheng Huang¹, Kangkang Wang¹, Feifei Wu¹,
Yan Lou¹, Hong Miao¹, and Yanmei Xu²

¹Economics & Management School, Beijing University of Technology, Beijing 100124, China
hlch@bjut.edu.cn

²Management School of Graduate University, Chinese Academy of Sciences,
Beijing 100080, China

Abstract. At present the analysis of emerging industry, especially the strategy researches on high-tech emerging industries lack of quantitative analysis and micro-level approaches. This paper sets the information technology(IT) industry in Beijing as the object of study. Combine the methods of authorized ratio, R&D capability, patent technical-value, technology opportunity, technology advantage with patent mapping analysis. Based on the patent data of China and worldwide, analyze the strengths, weaknesses, opportunities and threats in the IT industry in Beijing by SWOT model. By the comparative analysis of Beijing and other regions, find the IT industry development direction for Beijing. Finally put forward the development strategy for promoting IT industry. The results show that the ideas and analysis methods in this study can add value to the emerging industries researches in China and worldwide.

Keywords: SWOT analysis, Beijing, Information Technology Industry, Patent Data.

1 Introduction

Information technology (IT) is the major driver of the research, innovation, growth and social change. IT industry has a significant role to play in increasing the competitiveness and sustainability (in all senses of the world) of the entire economy. OECD survey results make clear that after economic crisis governments regard ICTs and the Internet as a major platform for research and innovation across all economic sectors [1]. Supports for IT research and development (R&D) and provision of venture finance to innovative entrepreneurs are seen as key components of the economic recovery [2]. Patents by industry make it possible to see the link between technology and industries' economic performance. As a measure of output of S&T activities, patents by industry provide valuable information about industries' technological strengths.

A few of studies have applied patent analysis to explore the industry issues such as R&D inputs and outputs, technical abilities and strategies in different countries and

^{*} This paper was granted by National Social Science Research Funds (11&ZD140).

regions. For example, in two researches, patent analysis techniques were used to measure the technological changes in Canada and Germany respectively [3,4]. Li identified key technologies in Saskatchewan, Canada by analyzing patent information [5]. Tseng et al. analyzed trends and the technological strategies of the amorphous silicon thin-film solar cell industry using patent data [6].

At the same time, SWOT analysis is a methodology allowing an industry to understand and plan to use their strengths to exploit opportunities, to recognize and repair or avoid their weaknesses, and to defend against or sidestep any known threats. The method has been widely used as a strategic planning tool and found it was effective[7]. More recently, researchers have applied this method to the assessment of biomass power generation industry, energy sector and Greek mining and mineral industry, which with some basic statistical data [8-10].

The present study is an attempt to apply SWOT analysis by using patent data in the capital of China, Beijing. Beijing is the leading city to promote the development of strategic emerging industries, especially the IT industry. During the last few years, Beijing has increased its investment in R&D on IT industry, and several large research facilities such as cloud computing base, software center and interspaces technology information platform have been established. Because patents are often considered as an indicator of technology output and R&D performances [11], and IT Industry is a typical high-tech industry, this study will analyze patent activities of IT industry in Beijing with SWOT method, hoping to not only find out the technological strengths and opportunities for IT industry development in Beijing, but also provide evidence for future policy directions.

2 Research Structure

2.1 Sources of Patent Data

There are two kinds of patent data used in this study, patents filed in State Intellectual Property Office of the P.R.C.(SIPO patents) and patents under PCT treaty(PCT patents). State Intellectual Property Office of the P.R.C (SIPO) database and World Intellectual Property Organization (WIPO) PATENTSCOPE database were searched to identify patents held by Beijing organizations (including individual).The field searched was “Applicant Address” because it provides locations of assignees.

There are three types of patents: invention patents, utility model patents and design patents. It is generally agreed that only invention patents represent real inventive or innovative activities, therefore, only invention patents were included in this study.

Patents in IT Industry are identified using the International Patent Classification (IPC) system: one or several classification codes are attributed to the patent during the examination process. A list of IT technology IPC codes developed by OECD was used [12]. We improved this list based on some other studies on IT technology. Finally, the IPC codes search list of IT industry technology was conducted, which listed in Appendix.

2.2 Research Framework

In this paper, S, W, O and T factors involved in the IT industry in Beijing are proposed to be analyzed with patent data. Specifically, the framework of this study is showed as Figure 1.

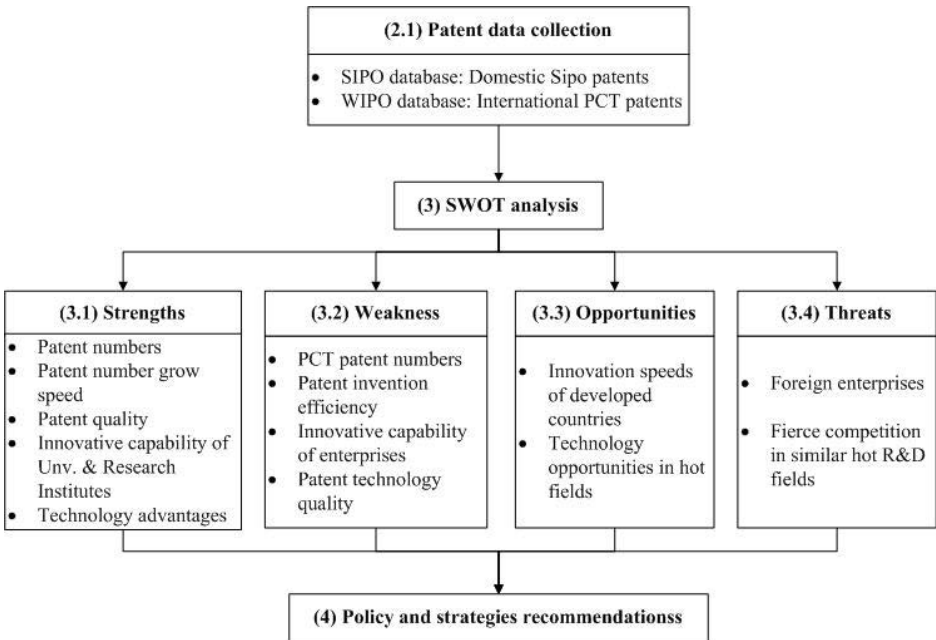


Fig. 1. Research flowchart of this study

3 SWOT Analysis Based on Patent

3.1 Strengths

3.1.1 Large Share of Total IT Patent Numbers in China

Figure 2 shows the distributions of IT patent applications in China in 2010. Shenzhen, Beijing and Shanghai are the leading regions with the most SIPO and PCT patent applications in China. Beijing owns the second most numbers of IT patents, which only less than Shenzhen, but much more than other domestic regions. With the large share of total IT patent numbers, Beijing take a technology advantage for developing IT industry.

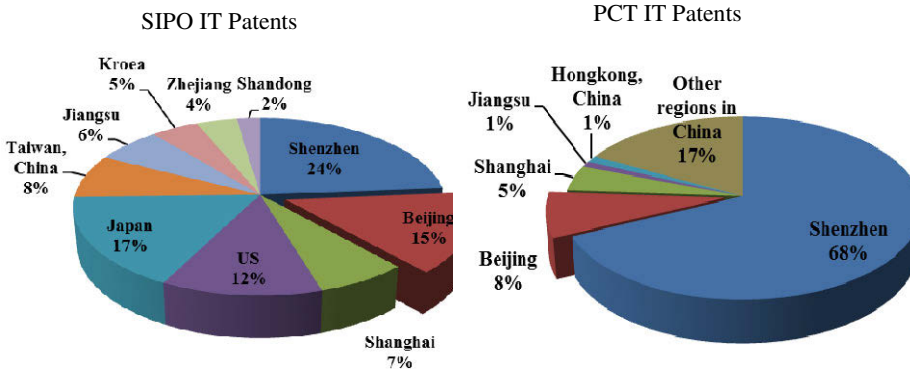


Fig. 2. IT Patent count distribution in China, 2010

3.1.2 Patent Applications and Grants Continue Grow Fast

Numbers of IT patent applications in China are keep growing from 2001 to 2011, especially from 2006. Because of the large share of patents distribution, taking Shenzhen, Shanghai and US as the comparison example, figure out the average annual growth rate of their SIPO applications, SIPO grants and PCT applications from 2006 to 2010 (Table 1). Among the 4 regions, the SIPO application average annual growth rate of Beijing is the highest, and the PCT application grow rate ranks the second. It indicates that Beijing has great potential for the development of IT industry.

Table 1. Growth rates of IT patents of 4 regions, 2006-2010

Region	Average annual growth rate		
	SIPO Applications	SIPO Grants	PCT Applications
Shenzhen	18.80%	48.87%	38.24%
Beijing	23.10%	36.47%	12.43%
Shanghai	16.36%	29.93%	2.31%
US	1.20%	22.18%	-1.84%

3.1.3 Quality of Patents Improves Steadily

Patent granting rate and validity rate are the indicators of patent quality. Patent granting rate is the ratio of obtained number divided by application number in the same issuing period. Higher the granting rate is, better the quality of patent is, stronger the R&D capability of patentee is. Recording to the statics of SIPO IT patent applications number and grants number from 2006 to 2010, we can figure out the 4 regions' granting rates (show as Figure 3). Figure 3 shows that the IT patent granting rates of the 4 regions has kept growing in recent years, and the quality of patents improves steadily. In 2010, Beijing's IT patent granting rate ranks the second in China, is 36.8%. But there is a gap between Beijing and US, whose patent granting rate is 63.4%.

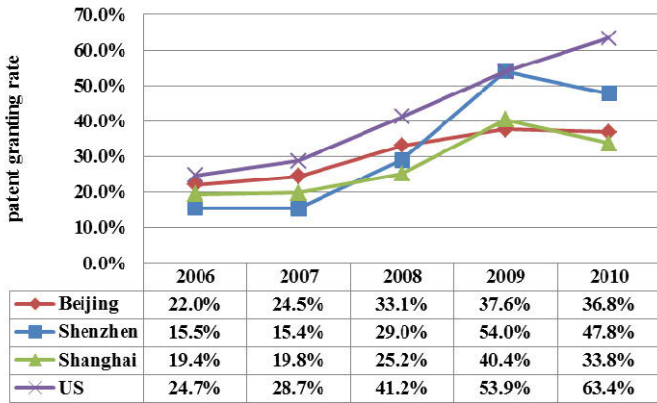


Fig. 3. SIPO IT patent granting rates of 4 regions, 2006-2010

Patent validity rate is the ratio of valid patents number divided by grants number. Patent validity rate indicates the market value of patent. Higher the patent validity rate is, longer the patent duration is, larger the patent creates economic benefits. Figure 4 shows the SIPO IT patent validity rates of Beijing, Shanghai, Shenzhen and US during the period from 2001 to 2011. The IT patent validity rate of Beijing is 85%, only lower than Shenzhen, which indicates Beijing owns the good economic performance and high quality patents.

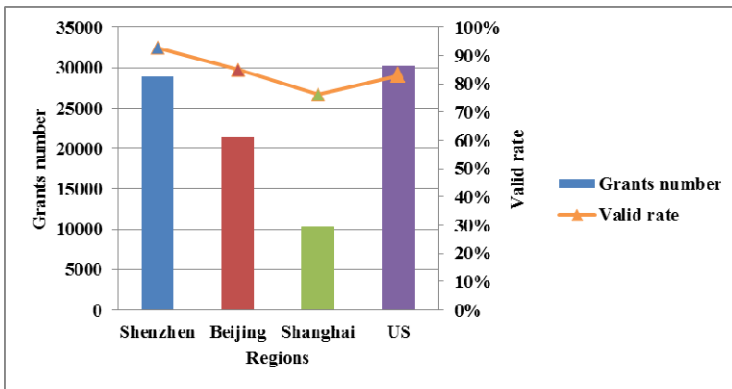


Fig. 4. SIPO IT patent validity rates of 4 regions, 2001-2011

3.1.4 Universities and Research Institutes Innovate Actively

Universities and research institutes play an important role in innovation activities in Beijing. Their innovation mainly embodied in strong R&D capabilities and high patent grants rate. Activity years, Inventors number and patent average valid years are 3 indicators of R&D capabilities. Activity years and Inventors number can reflect the R&D input level. Average valid year's equals total valid patent years divided by patent number, which indicates the monopolistic advantage of the patentee. The R&D

capacities comparison of Top 10 IT patent assignee in Beijing from 2001 to 2011 is showed as Table 2. There are 5 universities or research institutes (gray marked) in the Top 10, which with the characteristics of long activity years, large inventors' number and short average valid years. Besides, SIPO IT granting rates of universities and research institutes usually are high. Institute of Computing Technology, Chinese Academy of Sciences has the highest IT patent granting rate 60.44%. This suggests that universities and research institutes assure patents quality as well as R&D actively.

Table 2. R&D capabilities of major IT patent assignee of Beijing, 2001-2011

Rank	Patent Assignee	SIPO Application No.	SIPO Granting Rates	Activity Years	Inventors No.	Average valid years
1	Tsinghua University	4028	54.92%	14	5152	4
2	Datang Mobile Communications Equipment Co., Ltd.	2748	24.49%	10	1049	3.18
3	Beijing University of Aeronautics and Astronautics	2671	46.91%	12	3781	2.77
4	LG Electronics (China) Research and Development Center Co., Ltd.	1630	27.48%	8	1088	5.81
5	Beijing Zhongxing microelectronics Co., Ltd.	1608	50.68%	11	375	3.95
6	China Mobile Communications Corporation	1575	28.44%	9	1420	3.18
7	Beijing University	1561	48.43%	12	2030	3.53
8	Beijing University of Posts and Telecommunications	1417	31.55%	12	2371	3.02
9	Lenovo (Beijing) Co., Ltd.	1282	50.16%	9	876	5.24
10	Institute of Computing Technology, Chinese Academy of Sciences	1125	60.44%	12	1225	4.36

3.1.5 Technology Advantages in Key Fields

Technology advantages mean owing large number of patents in key technology fields and having the upper hand in the future competition. Technology Correlation Analysis is an effective method for identification of key fields. Technology Correlation Analysis embraces 2 aspects of depth and breadth, which figured out by Correlation Degree and Correlation Scoter Number respectively. Take Technology Correlation Analysis of Top 10 SIPO IT IPC sector with the most patent number from 2001 to 2011 in China. Table 3 and Figure 5 show the results.

In breadth aspect, the technology sectors with more patent number are better than those with small patent number, as G06F is the IT key field. While the technology with small patent number, as H04B, H04Q, H04M and G06K, although their breadth influences are not so good as G06F, they have advantages in depth which with the characteristic of technology professional. The results show that Beijing accounts for

high proportion of the IT key fields, especially in G06F (Electric Digital Data Processing). At the same time, Beijing sets a rational distribution in other technology sectors with depth or breadth feature. It helps Beijing to take up positions in the competition and have advantages in key technology fields.

Table 3. Technology correlation analysis of IT industry

No.	IPC	Patent No.	Correlation Patent No.	Correlation Degree	Correlation Sector No.
1	H04L	21338	6560	30.7%	89
2	G06F	11459	4999	43.6%	157
3	H04W	9502	2047	21.5%	56
4	G01N	7545	1487	19.7%	171
5	H01L	6788	1329	19.6%	127
6	H04N	6088	2316	38.0%	100
7	H04B	4988	3276	65.7%	87
8	H04Q	4704	3178	67.6%	76
9	H04M	4504	2891	64.2%	97
10	G06K	2714	1514	55.8%	107

Note: Technology Correlation Degree is patent number with one main IPC and other sub IPC divided by the total patent number with this main IPC. Correlation Sector Number is the sector number with one main IPC and other sub IPC.

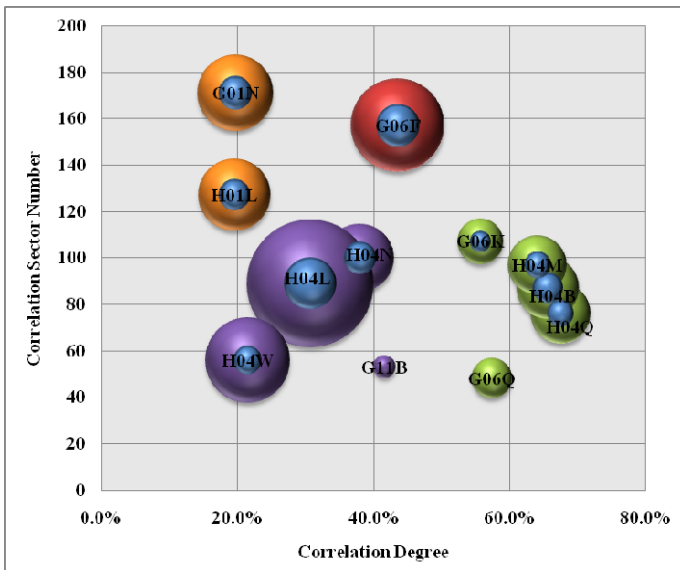


Fig. 5. Bubble chart of IT industry technology relevance. Note: The size of bubble on behalf of patent number. Different colors represent different types of depth and breadth. The blue bubbles represent patents of Beijing.

3.2 Weaknesses

3.2.1 Lack of PCT Patent Applications

The international competition in IT is very fierce. The one obtains most PCT patents will take advantage in the competition. In 2010, there are 32030 SIPO patent applications and 5826 PCT applications in China, with the PCT/SIPO ratio of 18.2%. In 2010, the PCT/SIPO ratio of Beijing is 12.4% (PCT number is 458, SIPO number is 3700), while this ratio of Shenzhen is 64.7%, Shanghai is 14.6%. Recording the PCT patent applications number, application ratio and grow speed analysis above in Section 3.1, there is a huge gap between Beijing and Shenzhen. It indicates that Beijing lacks of attention to the technology R&D facing the international competition.

3.2.2 Low Efficiency of Patent Invention

The efficiency of patent invention can be figured out by the inputs and outputs of patent activities. The patent inputs include patent research institutions and inventors; the output is the granted patents. The Granted Patents Number per Hundred Inventors is the indicator of the patent invention efficiency. The IT patent inputs and outputs of patent institutions (granted patent number \geq 5) in Beijing, Shenzhen, Shanghai and US in 2010 are showed in Table 4. The number of patent institutions in Beijing is the most. The inventors number in Beijing is little less than US. However Beijing is the leader in China. This goes to Beijing has paid attention to R&D inputs in IT, including lots of research institutions and inventors, which contributing to the fast-growing patents invention in Beijing. However, the patent number per hundred inventors of Beijing is much less than Shenzhen, and in the same level with Shanghai whose inputs are much less. This suggests Beijing needs to move up to a new level of IT patent invention efficiency.

Table 4. R&D inputs and outputs of IT patents of 4 regions, 2010

Region	Institutions No.	Inventors No.	Patent Grants No.	Patent number per hundred inventors
Beijing	141	9505	4306	45.30
Shenzhen	61	8958	7097	79.23
Shanghai	67	3781	1741	46.05
US	121	10387	3983	38.35

3.2.3 The Shortage of Innovative Capability of Enterprises

Enterprise innovation ability is the engine of the emerging strategic industry and the driver of the core competition. The IT enterprise innovation ability depends on the patent invention activities. Table 5 shows the major SIPO and PCT IT patent assignees (Top 10) of Beijing from 2001 to 2011. Among these SIPO IT patentees, there are 5 universities and research institutes, 2 state-owned enterprises, 2 private enterprises and 1 foreign enterprise. Among these PCT IT patentees, there are 5 foreign enterprises and 3 domestic enterprises. The universities and research institutions in Beijing innovate actively while domestic enterprises lack of patent innovation

capabilities. It's disadvantageous for Beijing to boost competitiveness in IT industry. Because it is more difficult and time-consuming for universities and research institutes to industrialize research findings than enterprises do.

Table 5. Major IT patent assignee of Beijing, 2001-2011

Rank	SIPO Patent		PCT Patent	
	Patent Assignee	Application No.	Patent Assignee	Application No.
1	Tsinghua University	4028	China Academy of Telecommunications	203
2	Datang Mobile Communications	2748	Nokia Corporation	166
3	Beijing University of Aeronautics and Astronautics	2671	Thomson Licensing	137
4	LG Electronics (China) Research and Development Center Co., Ltd.	1630	China Mobile Communications	137
5	Beijing Zhongxing microelectronics Co., Ltd.	1608	Samsung Electronics Co., Ltd.	105
6	China Mobile Communications	1575	Tsinghua University	95
7	Beijing University	1561	Datang Mobile Communications	92
8	Beijing University of Posts and Telecommunications	1417	Intel Corporation	88
9	Lenovo (Beijing) Co., Ltd.	1282	Lenovo (Beijing) Co., Ltd.	71
10	Institute of Computing Technology, Chinese Academy of Sciences	1125	Linkair Communications INC	61

3.2.4 Gap in Patent Quality between Foreign and Domestic Patentee

At Section 3.1.3, it takes patent granting rate and validity rate as the indicators of patent quality. In order to measure the technology value of patents further, add the indicators of patent description pages number and duration years.

Patent description pages number can reflect the technology complexity of patents. Patents with more description pages usually contain more claims and technology contents. H04W (Wireless Communication) is a mushrooming field in IT industry. The static of H04W patent description pages numbers of Beijing, Shanghai, Shenzhen and US in 2010 is showed in Figure 6. There is no more less of average patent description pages numbers between the domestic institutions in Beijing, Shanghai and Shenzhen. However, there is a huge gap between domestic and foreign institutions in patent technology value.

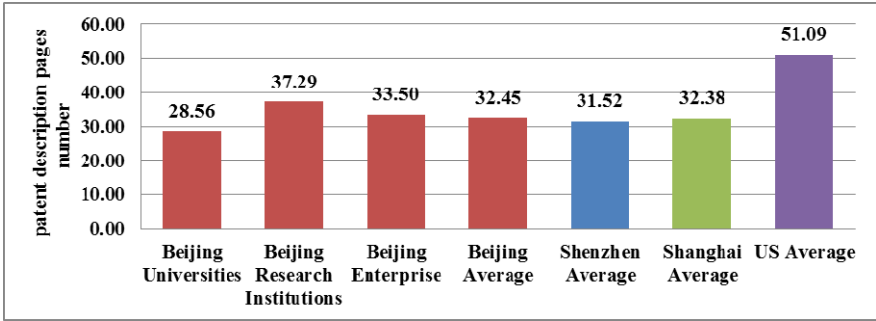


Fig. 6. H04W patent description pages number of 4 regions, 2010

Patent duration year is the two-dimensional form of patent validity rates. It's more explicit to represent the distribution of valid patents with time axis. Figure 7 shows the comparison of Beijing and US in SIPO IT patent duration years. The most patents duration of Beijing is about 2 to 6 years while US is 4 to 10 years. There are little patents over 10 years of Beijing. The patentees give up maintaining patents suggests the low value of patents.

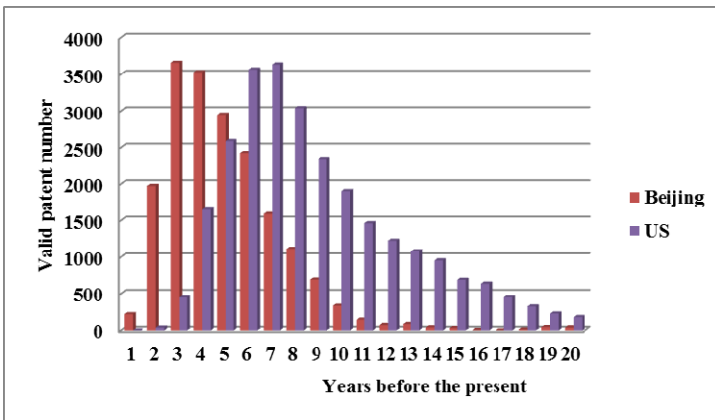


Fig. 7. Duration of SIPO IT patents of Beijing, US

3.3 Opportunities

3.3.1 Innovation Speeds of Developed Countries Slow Down

As Table 1 above showed the growth rates of SIPO and PCT IT patents of 4 regions from 2006 to 2010, the average annual grow speed of US much slower than domestic regions. US stands for the IT developed countries which apply for most patents in China. But its SIPO IT patent grow speed is only 1.2%, and PCT IT applications decreased from 2006 to 2011. Take US as example, the developed countries have slowed down innovation speeds in recent years with the influence of financial crisis [13]. As developed countries reduce the R&D inputs and patent applications decrease, it

provides opportunities for China and other developing countries to intensify IT R&D to leapfrog ahead of the West.

3.3.2 Technology Opportunities in Hot Fields

The technology strength of a country or region can be reflected in the obtained patents number of a certain IPC class. By the comparison of the obtained patents number of different regions in certain technology fields, we can identify the technology strength and opportunities. Set the Top 10 IT IPC class with the most SIPO granted patents number from 2001 to 2011 as the hot technology fields. With the grants patent numbers of Beijing, Shenzhen, Shanghai and US, make the comparison of their technology strength as Figure 8. Recording the figure, Beijing takes technology advantage in G01N and G06K compared with US, Shanghai and Shenzhen. Meanwhile, Beijing is stronger than Shanghai and US in H04W. As a result, Beijing should keep on research on G01N and G06K, and seize the opportunity to cross license to enhance the R&D capability.

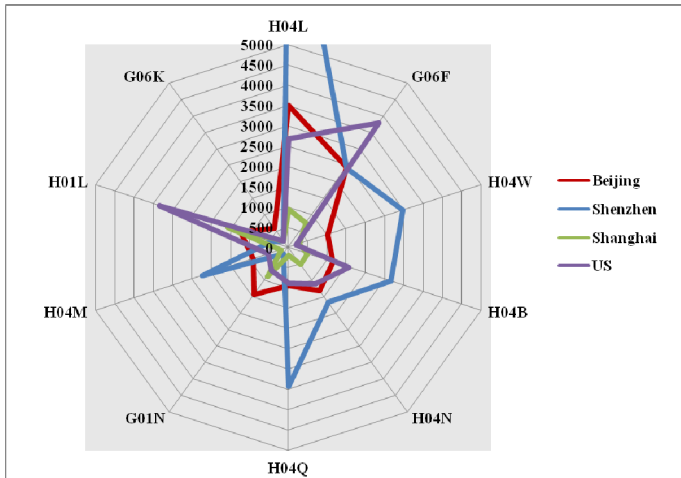


Fig. 8. Comparison of 4 regions' IT technology strength (top 10 IPC class with the most SIPO granted patents number), 2001-2011

3.4 Threats

3.4.1 Foreign Enterprises Have Strong Competitive Strength

There are only Huawei and ZTE 2 domestic corporations in China Top 10 IT patent assignees in 2010 (Table 6). Among the Top 10 IT patent assignees in Beijing from 2001 to 2011, there are over half foreign enterprises which make threats of competition to domestic. The foreign old well-known enterprises will be the strongest rival of domestic institutions when Beijing develop IT industry.

Table 6. Major IT patent assignees in China, 2010

Rank	SIPO Patent		PCT Patent	
	Patent Assignee	Applications No.	Patent Assignee	Applications No.
1	Huawei Technologies Co., Ltd.	2668	ZTE Corporation	1861
2	ZTE Corporation	2232	Huawei Technologies Co., Ltd.	1507
3	Samsung Electronics Co.,Ltd.	1344	Panasonic Corporation	1452
4	Sony Corporation	1081	Qualcomm Incorporated	1213
5	Panasonic Corporation	963	LG Electronics Corporation	973
6	International Business Machines Corporation	855	Sharp Corporation	957
7	Canon Corporation	642	NEC Corporation	652
8	Intel Corporation	475	Konikligke Philips Electronics N.V.	621
9	Sharp Corporation	469	Nokia Corporation	604
10	LG Electronics Corporation	467	LimiEricsson(pubication)	599

3.4.2 Fierce Competition in Similar Hot R&D Fields

The number of patents can indicate the general situation and trends in a particular field. Hot R&D fields are the technology fields with the most patent grants numbers. Table 7 shows the comparison of IT hot R&D hot fields of Beijing and world from 2001 to 2011 (Different fields of Beijing and word are marked gray). There are only 3 different IT hot R&D fields between Beijing and world. It indicates that the IT R&D tendency of Beijing is closed to the world, and the technology structures are similar. As a result of the similar hot R&D fields, the competition in IT industry will be much fiercer in the future.

Table 7. Comparison of IT hot R&D hot fields of Beijing and world, 2001-2011

Rank	IT Hot R&D Fields of Beijing			IT Hot R&D Fields of World	
	Field (IPC)	SIPO Application No.	PCT Application No.	Field (IPC)	PCT Application No.
1	Transmission Of Digital Information (H04L)	11421	709	Electric Digital Data Processing (G06F)	84230
2	Electric Digital Data Processing (G06F)	7575	583	Transmission Of Digital Information (H04L)	57362
3	Wireless Communication (H04W)	4489	504	Semiconductor Devices; Electric Solid State Devices (H01L)	48304
4	Transmission (H04B)	3748	340	Investigating Or Analyzing Materials By Determining Their Chemical Or Physical Properties (G01N)	42369
5	Pictorial Communication (H04N)	3627	207	Pictorial Communication (H04N)	28496

Table 7. (Continued)

6	Selecting (H04Q)	3576	37	Transmission (H04B)	26518
7	Investigating Or Analyzing Materials By Determining Their Chemical Or Physical Properties (G01N)	3523	185	Data Processing Systems Or Methods, Specially Adapted For Administrative, Commercial, Financial, Managerial, Supervisory Or Forecasting Purposes (G06Q)	25888
8	Telephonic Communication (H04M)	3330	83	Wireless Communication (H04W)	23004
9	Semiconductor Devices; Electric Solid State Devices (H01L)	2662	100	Information Storage Based On Relative Movement Between Record Carrier And Transducer (G11B)	16317
10	Recognition of Data; Presentation of Data; Record Carriers; Handling Record Carriers (G06K)	1913	63	Optical Elements, Systems, Or Apparatus (G02B)	14731

4 Policy and Strategies Recommendations

4.1 Further Actions on Improving Quality and Efficiency of IT Industry

Beijing had strong R&D capability in the IT industry with a large share of IT patents number and high growth potential. As a whole, the patent situation of Beijing IT industry is developing in the good direction. However, as the international R&D hot spots become similar, the competition in IT industry will be fiercer and fiercer. To improve patent quality and invention efficiency is the key way to maintain the competition advantage. Through the patent analysis above, there is a huge gap between the domestic and foreign patentees both in patent quality and efficiency. Beijing lacks of high-value added patents. So, further actions need to be taken on improving the patent technology quality and market value while maintaining the high granting rate & validity rate.

4.2 Based on the R&D Advantages of Universities and Research Institutes, and Award for Enterprises Technology Innovation

The universities and research institutes in Beijing innovate actively while enterprises lack of invention abilities. There are lots of universities and research institutes in Beijing, which should benefit the University Industry Collaboration and enhance the research on generic technology. On the other hand, enterprises should take the advantage from the university industry collaboration and enhance R&D abilities. During the development of IT industry in Beijing, the major patent assignees should change from universities and research institutes to enterprises. It's important to promote the patent industrialization and turn patent number advantage into market advantage.

4.3 Strengthen the Obtained Technology Advantages, and Grasp the Future Technology Opportunities

Carry on key deployment to the important technical realm. Beijing owns advantage in IT hot fields and key fields, especially in the electric digital data processing and wireless communication which with complete and high-quality patents. It offers the good technology base for Beijing to develop the internet of things sector and 4G sector. At the same time, the competitors' weaknesses (relatively Beijing's strength) provide a chance for Beijing to step up technology R&D and take cross license. Must seriously implement the information technology patent topology strategy. Encourage the independent innovation while actively launch the technical collaboration, and strive to participate in the information technology domain in the international standard project.

4.4 Pay More Attention to International Patents, and Broaden the International Cooperation Ways

As competition tends to be intense, China will enter the much hair period that an international trade chafes. Patent rights play a more and more important role in protecting the export products and enhancing the export products technological competitiveness. The lack of international patents leads to the passive status in patent litigation and the risk to economic losses. In the obtained PCT patents aspect, Beijing has little enterprises which can compare with world-class enterprises. In order to close the gap with developed countries, it's a pressing task for the patent assignees to master the international roles like PCT treaty, and enhance the ability to manage intellectual property. At the same time, focus on improving the environment for investment and strengthening cooperation in training talents. Encourage foreign companies to set up R&D center in Beijing, and increase the communication and cooperation between international.

5 Conclusion

This paper has combined the methods of authorized ratio, R&D capability, patent technical value, technology opportunity, technology advantages with the general patent mapping analysis. Based on the patent data of China and worldwide, analyze the strengths, weakness, opportunities and threats in the information technology industry in Beijing by SWOT model. By the comparative analysis of Beijing and other regions, find the development direction. Finally put forward the development strategy for promoting information technology industry in Beijing. The results show that the ideas and analysis methods in this study can add value to the emerging industries researches in China and worldwide.

However, the results presented here must be taken with caution. It should be noted that patent data alone does not give a comprehensive assessment of the importance of a technology in a region, other indicators such as employment data, number of companies, or R&D expenditure should be considered as well. Future studies are needed

in this regard to provide a more robust assessment of innovation and technological performance in this region in conjunction with patent data.

Appendix: IPC Codes Search List

Patents taken in the IT industry can be listed as the following IPC codes:

G01S,G08C,G09C,H01P,H01Q,H01S3/(025,043,063,067,085,0933,0941,103,133,18,19,25),H1S5,H03B,H03C,H03D,H03H,H03M,H04B,H04J,H04K,H04L,H04M,H04Q,G11B,H03F,H03G,H03J,H04H,H04N,H04R,H04S,B07C,B41J,B41K,G02F,G03G,G05F,G06,G07,G09G,G10L,G11C,H03K,H03L,G01B,G01C,G01D,G01F,G01G,G01H,G01J,G01K,G01L,G01M,G01N,G01P,G01R,G01V,G01W,G02B6,G05B,G08G,G09B,H01B11,H01J(11/13/15/17/19/21/23/25/27/29/31/33/40/41/43/45/),H01L,H04W.

References

1. OECD, *The OECD Innovation Strategy: Getting a Head Start on Tomorrow*, Paris (2010)
2. OECD *Information Technology Outlook 2010*. OECD Publishing (2010), http://dx.doi.org/10.1787/it_outlook-2010-en
3. Yegul, M.F., Yavuz, M., Guild, P.: Nanotechnology: Canada's position in scientific publications and patents. In: *Portland International Conference on Management of Engineering & Technology*, Cape Town, South Africa, pp. 704–713 (2008)
4. Grupp, H., Lacasa, I.D., Schmoch, U.: Tracing technological change over long periods in Germany in chemicals using patent statistics. *Scientometrics* 57, 175–195 (2003)
5. Zhang, L.: Identifying key technologies in Saskatchewan, Canada: Evidence from patent information. *World Patent Information* 33, 364–370 (2011)
6. Tseng, F.-M., Hsieh, C.-H., Peng, Y.-N., Chu, Y.-W.: Using patent data to analyze trends and the technological strategies of the amorphous silicon thin-film solar cell industry. *Technological Forecasting & Social Change* 78, 332–345 (2011)
7. Zhao, Z.Y., Shen, L.Y., Zuo, J.: Performance and strategy of Chinese contractors in the international market. *Journal of Construction Engineering and Management* 2, 108–118 (2009)
8. Zhao, Z.-Y., Yan, H.: Assessment of the biomass power generation industry in China. *Renewable Energy* 37, 53–60 (2012)
9. Nikolaou, I.E., Evangelinos, K.I.: A SWOT analysis of environmental management practices in Greek Mining and Mineral Industry. *Resources Policy* 35, 226–234 (2010)
10. Markovska, N., Taseska, V., Pop-Jordanov, J.: SWOT analyses of the national energy sector for sustainable energy development. *Energy* 34, 752–756 (2009)
11. OECD. *OECD patent statistics manual* (2009)
12. OECD. *Compendium of patent statistics* (2008), <http://www.oecd.org/dataoecd/5/19/37569377.pdf>
13. People.com.cn, <http://hn.people.com.cn/GB/195700/214999/14068252.html>

Using 3D GeoDesign for Planning of New Electricity Networks in Spain

Francisco-Javier Moreno Marimbaldo¹, Federico-Vladimir Gutiérrez Corea²,
and Miguel-Ángel Manso Callejo

¹ Red Eléctrica de España S.A.U., Paseo del Conde de los Gaitanes, 177. Alcobendas 28109,
Madrid, Spain

fmoreno@ree.es

² Universidad Politécnica de Madrid (UPM), ETSI en Topografía, Geodesia y Cartografía,
Ctra de Valencia Km7. Madrid 28031, Spain

{fv.gutierrez,m.manso}@upm.es

Abstract. Power supply plays a fundamental role in society to boost development in some nations and maintain the standard of living in others. The development of an electricity transmission network involves the planning of a new infrastructure and subsequent construction which entails the creation of new conditions in the territory. This article proposes a new workflow in which the GeoDesign principles are applied, so that the actors share their interests and work together to develop a new electrical infrastructure and thus achieve the planned objectives. We present a consistent method to describe the context, requirement analysis, identification of constraints and relationship stages, a proposed workflow, a web-based GeoDesign tool prototype and tools for 3D visualisation and GoogleEarth interaction as well as other tools to generate reports for administration processing. The first available results related to GeoDesign in administration processing are encouraging in terms of productivity growth and costs and timeframes reduction.

Keywords: GeoDesign, ARR (Affected Assets and Rights Report), Owners, Plots, Affections.

1 Introduction

Electric power supply is essential for our society since it “plays a prominent role in maintaining the standard of living” [1]. Electric power is the engine of growth of any developing country; in fact no major economic activity can be sustained without adequate and reliable power supply [2]. The electric energy sector may play a key role in competitiveness among many other economic sectors [2], in addition to its specific own challenges of supply, provision of services and production which represent by themselves an important industrial sector.

It is assumed and widely accepted that electric energy should be a dynamising factor for the entire economy and infrastructures [2] and there should never be any barrier to its growth. For this reason the energy policy of governments should ensure energy supply under optimal conditions of safety, quality and price as an unwaivable

goal. Thus on May 2008 the Spanish Ministry of Industry, Tourism and Trade approved an electricity/gas planning document for 2008-2016 [3] with the purpose of ensuring the safety and quality of the power supply. This plan contemplates an important programme of construction of new electric installations which will allow anticipation of the future needs based on the increasing demand seen in recent years. The Spanish Electric Network Company (Red Eléctrica de España – REE), is the manager of the transmission network, is in charge of the maintenance, development and expansion of the infrastructure at the national level.

In the construction of a new electrical installation –which is likely to reach hundreds of kilometres– a large amount of different conditioning factors and interest profiles exert an influence over the design. All those factors do not necessarily coincide from the viewpoint of all the intervening interest profiles, although they should be studied as a whole through the project to take the pertinent decisions. For instance, a cork tree forest is not meaningful from the viewpoint of the electrical infrastructure but it has a great environmental value. Presently it is not possible to achieve concurrently a pooling and sharing of views in this type of projects. Neither administrations nor agencies/companies in charge of executing the planning of electrical transmission infrastructures have the tools that would allow them dealing with the needs, restrictions, limitations and wishes of every interest profile. The use of the PSS and DSS allows us thinking of reorienting the development of these projects towards a methodology that will enable to take decisions based on the reality of the territory, therefore more solid, organised, efficient, and allowing us advancing new projects nimbly. The possibility of representing in the same environment the different requirements or viewpoints of all actors involved, creates spontaneously a collaborative framework that allows the consensus decision making. This is the objective we pursue.

The purpose of this paper is to aid in the systematisation of that work of development and expansion and to facilitate the Planning Support Systems (PSS), Decision Support Systems (DSS) [4][5] and Participatory Geographic Information Systems (PGIS) [6] through the design and proposal of a workflow for the planning of new electrical infrastructures that integrates the principles of GeoDesign. The relationships and interactions among the different actors (interest profiles) and the constraints (requirements to be complied with) will be identified. The objective is to overcome the hurdles of every phase of the present working method and to take advantage of the characteristics of this type of projects with particular reference to territories and Geographic Information. These systems that try to put together the aids relative to GI-based information and decision-taking are known as GeoDesign [7].

This paper provides detailed information about some important issues regarding the development of new electrical infrastructures using a collaborative environment based on the information and knowledge of the territory as the backbone. The main reflections on the results of the implementation developed so far are gathered and new lines of work are proposed for the future.

1.1 Related Works

There are many recent references about the GeoDesign concept. Some try to take up the use of tools provided by the Geographic Information Systems (GIS) for the purpose of making sketches that would subsequently allow users to interact in virtual

environments. Others try to bind the GI field to the helping tools/systems in decision taking/planning. Next we present a brief state of the art concerning DSS, PSS, PGIS and GeoDesign.

For McHarg [8] "...a simple sequential scan of the place ... shows an interactive system a warehouse and a value system. From this information it is possible to suggest what are the potential uses of the land?, understood not as isolated activities, but as associations between them". Steinitz [9] emphasizes a collaborative approach to design that he says transcends traditional landscape architecture curricula: the notion that a designer makes the design. The biggest problems of the foreseeable future—population growth, landscape preservation and water quality, to name a few—do not fit that model. Rather, these require collaboration among the design professions and the geographic sciences in design. Steinitz says. "Most of the time, design schools teach on the basis of a client, a site and program," he says. "But what if there's no client, no site, and no program?"

Harris [10] defined PSS as appropriate models for combining a range of computer-based methods into an integrated system enabling spatial planning. Later Vonk [4] carried out a study with 100 PSS experts to find the main bottlenecks blocking the widespread use of PSS in spatial planning. Kumar [2] proposed an integrated multimedia environment based on intelligent systems of group decision taking for the electric energy distribution networks. Concerning the PSS, Geertman and Stillwell [5] stress the capability of the computer-based geo-information instruments to enable the participation of the different involved agents in planning, decision-taking and anticipated visualisation of the effects of the adopted policies or decisions.

For Abukhater and Walker [7] planning has been done historically by experts on behalf of the communities they serve, but a new paradigm replaces planning for people with planning with people. Aditya [6] proposes PGIS for assessments and investigating potentials of maps and visual methods to support bottom-up and top-down approaches in participatory decision-making. He remarks that potentials can include: potential use of maps and visual PGIS methods to facilitate explicit communication, to facilitate information gathering, to enable shared access, to facilitate transfer, and to be used as decision-support tools.

For Artz [11] GeoDesign expands the role of geospatial technologies in design workflows and formalises this role, and finally for Ball [12], it involves a more interactive interface to geospatial layers with the means for sketching and design upon those layers in a collaborative way while contributing and interacting with an evolving intelligent model. Finally Dangermond [13] in *The Third GeoDesign Summit Focuses on Creating Our Future* said that GeoDesign is not just a concept, it can be thought of as a process to measure, model, interpret, create plans, measure impacts and influence decisions. GeoDesign is an evolution where we connect the dots and understand the connections. It will range across all fields, from agriculture to urban planning and other infrastructure disciplines.

2 Method

To develop a 3D GeoDesign method we used the Spanish electricity network as a case study. We conformed to the following research steps:

1. Context: case study of the Spanish electrical network planning: general description, rationale for case studies.
2. Requirement analysis (current planning method) from policy documents.
3. Modelling constraints and relationships. We analysed the actors' restrictions and their relationships.
4. Workflow proposal and prototype implementation. We proposed and implemented a GeoDesign-based workflow.
5. Visualisation and interaction tools. We provided a 3D visualisation and interaction based on SDI technology and Google Earth TM virtual globe for result representation.

2.1 Context

The development and improvement of the electric energy transmission network brings on an interaction with the environment: generation centres, international connections, industrial use, distribution companies, affected institutions and enterprises, social agents, rural and urban environment, administrations and owners of the affected plots by new installations, as can be appreciated in Figure 1.

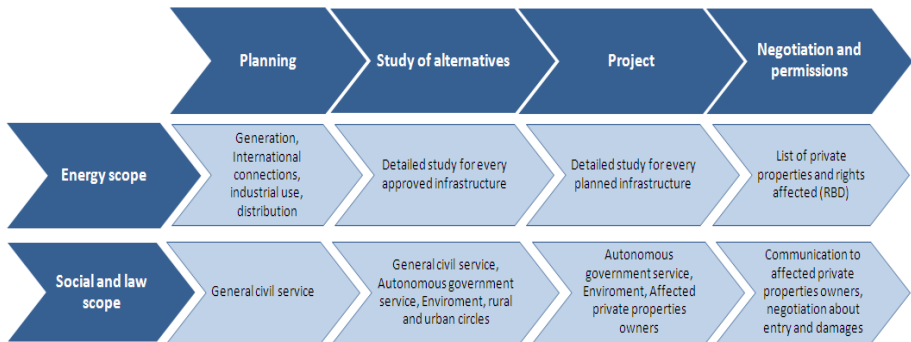


Fig. 1. Actors and phases in an electric power transmission line

The realisation of an infrastructure on a territory implies implementation of the different types of projects making up the activities of environmental impact assessment and engineering. In each electric power transmission infrastructure project, several phases may be distinguished, namely, planning, start, preparation, design (preliminary draft and final project), building and placing into service. The planning defines the real need for the new infrastructures and it designs them schematically. However, the existence of different interest groups related to the new infrastructure compels us to a pooling and sharing of technical, social, urban, political and economic needs, the study of alternatives, the choice of the most favourable alternatives or the ones with the least social and environmental impact, negotiation, to finally reach a consensus.

The study of the different alternatives requires knowledge of the territory and its management as well as environmental constraints, terrain characteristics, climate and

local culture and habits. Only by being aware of the territory can the most appropriate corridors be determined for the technical design of the new infrastructure. The importance of GI in the decisions and interactions between the different involved actors and agents in this type of planning, studies and projects prompted us to evaluate and propose a GeoDesign-based workflow for this type of infrastructures.

2.2 Requirement Analysis

We identified four basic phases in the development of the electric power transmission network prior to construction during which the new installations were detailed more accurately step by step.

Planning Phase. The Act 54/97 is the regulatory framework for the Spanish electricity sector; its purpose is to ensure the power supply, its quality and its least possible cost while respecting the environment. In order to reach these objectives the planning of the sector is needed in such a way that: a) availability of generation, transmission and distribution infrastructures be assured to guarantee power supply; b) enough information be provided to the business fabric so that free initiative on the part of companies is supported; c) coordination between public administrations in terms of energy, town planning, land use and environmental protection; and finally d) maintenance and improvement of the electrical system, shoring up the networks and coordinating the supply activities. In addition, this regulatory framework provides for effective freedom to install new generation plants –complying with the current legislation– without restricting market access or location to any installation.

At this first planning phase no restrictions, constraints, factors conditioning the layout of the facilities or the working mapping scales (which do not allow determining their exact drawing) are considered. After planning is approved, the next step is the detailed study of every planned installation.

The legislation of the sector intends to liberalise the generation and marketing activities while keeping network activities regulated and under a binding planning. In this sector two types of planning are differentiated: indicative and binding. The first gathers data and information for the administration, promoters and private customers about the evolution and expectations regarding demand behaviour, needed resources to meet demand, market developments, etc. with criteria of environmental protection and security of supply among others.

The binding planning establishes the development of the transmission network within a certain period of time to meet the needs identified by the indicative planning. Both plans should be coordinated jointly with the remainder of the planning instruments (especially urban and land use) depending on the scope of application.

Phase of Study of Alternatives. Every installation approved in the planning process should be studied by the different administrative, social, environmental, energetic and technical parties involved. All of them shall try to profile with the greatest detail possible the corridor with the least impact where the engineering project will be designed. At this second phase a consensus among the different actors should be

reached. Since the final objective is the geographic demarcation of the region through which the electrical circuit has to be subsequently designed, the use of GI, besides being an indispensable requirement to delineate the corridor, helps understand or analyse the terrain, the environment, the infrastructures and properties that will be affected and will allow considering different alternatives as well. Every alternative is discussed by both the administration, which is responsible for monitoring compliance with the current regulation, and the technical area which ensures the technical and financial feasibility of the project. Figure 2 illustrates the manner in which different restrictions defined by the different actors –socio-economic, historical heritage, wildlife, etc.– modify the tracing of the infrastructure.

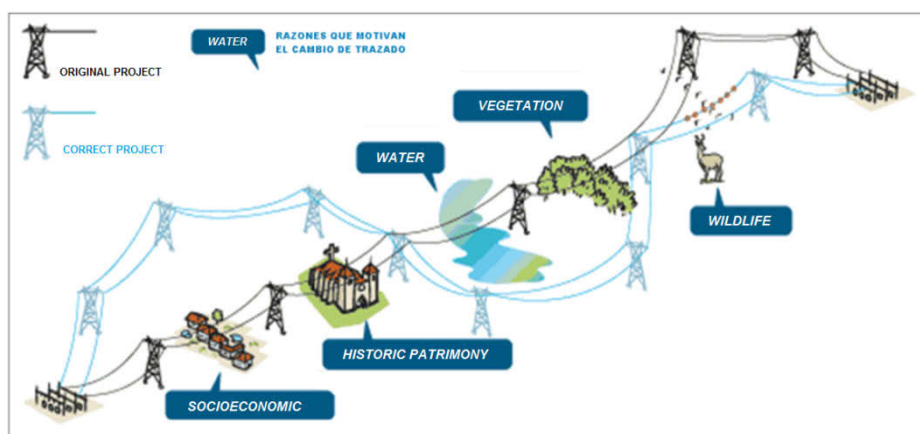


Fig. 2. Alternatives to the initial planning motivated by different constraints

Project Phase. After having agreed on the corridor, the detailed project phase begins with the study of alignments. Every vertex of the tracing is studied in detail as well as every support that will sustain the wiring of the future electrical line, the technical profile being prevailing.

Also at this phase the large-scale GI (1:2.000-1:5.000) and its analysis plays an important role. The aerial or underground electrical circuits bring on different types of affections on the territory: need to cement and reinforce a support, ditches to bury a power line, safety streets with felling of trees and removal of shrub vegetation, temporal occupation necessary to manoeuvre machinery, storage of materials and building of the installation, access pathways or any other aspect that somehow modifies the original condition of the terrain. After having accurately defined the tracing and the project, it will be possible to calculate and draw a set of layers, one for each type of affection.

The possibility of studying the layers conveying the different types of affections, together with the plot map, will allow getting information helping decision-taking, necessary at the beginning of the construction or when carrying out a variant of the original project.

Processing Phase. The analysis of the different properties affected by the new installation allows quantifying the surfaces requiring some type of occupation, either temporal or permanent, associated to the need to anchor the pylons that sustain the power lines, access to the machinery, safety area around conductors, need for tree cutting or removal of shrub vegetation, etc. As a result of this analysis, a document is obtained named affected Assets and Rights Report (ARR) that contains the type and magnitude of each type of affection for every plot, together with their owners' data.

2.3 Modelling Constraints and Relationships

The workflow that comprises the four phases (planning, design of alternatives, project design and negotiation) has been designed following the GeoDesign principles, so that the phases are developed on a participatory and collaborative basis. To that effect the relationships between the different actors and the constraints that the actual process imposes were analysed. The analysis was carried out in four steps. In the first step the actors, the conditions and the stages of each of the four phases of the electrical infrastructure project are identified. In the second step the relationships between actors, conditions and stages were identified. In the third step the relationships representing collaboration and participation were identified. Finally these relationships requiring collaboration were associated to the GeoDesign principles, thus strengthening that collaboration with this methodology.

Thus in the planning phase four actors were identified: generation centres, transmission (transmission nodes), distribution/consumption, and administration /environment.

Table 1. Relationships between actors in the planning phase

	Generation Centres	Transmission	Distribution and Consumption
Generation Centres	/		
Transmission	↖	/	
Distribution and Consumption		↖	/
Administration and Environment	↑	↑	↑

In Table 1 is shown the relationships identified between actors; the direction of the arrows indicates the influence between actors. For example, the relationship between administration and environment on the generation centres, on transmission or on distribution/consumption is unidirectional; the first one conditions the others.

In the phase of study of alternatives, four actors were also identified: administration, social actors, environment and energy scope. In this case the relationships identified between actors are unilateral between the energy scope and the remainder. Table 2 shows those relationships formulated as objectives. The

administration intends to maximise the short and long-term development of the energy scope. The social actors try to maximise the short-term development as well and finally, the environment intends to minimise the impact of the energy scope.

Table 2. Relationships between actors in the phase of study of alternatives

Actor: Energy Scope	
Administration	Maximize the Long- and Short-term Development
Social Actors	Maximize the Short-term Development
Environment	Minimise the Environmental Impact

From the viewpoint of collaboration and participation, at least two iterations in the previous working method have been identified. In the first iteration each actor puts forward his (her) proposals and positions. In the second iteration each actor tries to maximise the energy scope criterion on the basis of the minimal approaches defined by the remainder of actors. The result of this phase is the definition of a swath of territory (corridor) where the electrical installation project will have to be designed.

In the phase of project design a significant number of actors have been identified, several of them belonging to the REE: environment, line engineering, surveying, others belonging to the administration: cadastre, local administration, cultural and rural heritage, flora and fauna, and finally, the owners of the plots that will be affected. As a previous condition in this phase, a corridor is needed to determine the limits of implantation of the project. In this phase two stages or processes may be distinguished: the detailed design of the project and the analysis of the affections. The first process consists of the exact drawing of the new installation within the corridor defined in the phase of study of alternatives, and the position and distribution of supports are determined. At this stage it is possible to carry out slight modifications to the solution proposed by the technical-energy scope, especially suggested by the local administration and the plot owners. In the analysis of the affections (pylons, forest fellings, conductor flights, accesses, etc.) their form and magnitude are determined in such a way as to minimise the effect they would produce on the territory.

In the processing phase three actors have been identified: the administration, the processing department of REE and the owners. As a previous condition the Assets and Rights Report (ARR) table is needed with information about the affections for each plot and the owners' data. The main relationships are established between the processing department and the owners with the purpose of reaching an economic agreement on the issue of the affections. At this point the graphic representation of the infrastructure on the affected properties plays a very important role since the owners can then interact visually and contextualise spatially the object of the occupation. Likewise the generation of digital or printed cartographic documentation of the affections helps the administration in the cognitive communication processes and in the legal acts.

After having identified the actors, conditions, stages, relationships and collaborations or participation, many similarities with the GeoDesign principles have been found; different GI sources, sketching of the planning –primarily the binding

planning, joint design of the corridor for the electric wiring taking into account the various interests of the actors at stake, availability of 3D visualisation tools of the infrastructure project to be able to promote discussion, study of unpredictable situations, etc. By considering these similarities between the phases of the infrastructure design workflow and the GeoDesign principles, a number of needs to be developed in the new workflow were defined. These needs and the main ideas exposed in this section are shown in Figure 3.

2.4 Workflow Proposal and Prototype Implementation

The proposed workflow integrates the GeoDesign principles to promote collaboration between actors, providing for tools allowing them to express their viewpoints both graphically (sketching) and textually (annotations) and carry out modifications in the corridor proposal.





Step	Planning	Study of alternatives	Project	Negotiation and permissions
Inputs	Needs from: generation, infrastructures, High velocity train	New infrastructure plans, Topographic and environmental information and urban planning information.	Corridors for infrastructure approved, Topographic, Cadastral, weather and aeronautical restrictions information, etc.	Affection table(RBD) and its related geographic information
Process	Proposals 	Collaborative work 	Collaborative work and informative 	Informative work and negotiation 
GeoDesign Needs	Draw and Annotation tools 2D visualization capabilities	Draw, Annotation, and Editon tools, versioning capabilities 2D y 3D visualization capabilities	Analysis Capabilities: aggregation, intersection, buffers, etc. 3D visualization capabilities, Reporting capabilities.	2D y 3D visualization
Outputs	New infrastructure plans.	Hallways/Corridors for infrastructure approved	Detailed layout of the electrical infrastructure. Affection table(RBD)	Entry and occupation permissions to the affected properties

Fig. 3. GeoDesign needs to support the workflow

These tools consist of a Web environment allowing GI visualisation provided through standardised services ISO [14], OGC [15] coming from different sources, with the capability to carry out graphic editing and annotations (GeoEditor) and to interact with the proposals on a 3D virtual globe (GeoExplorer). In order to support the needs of the GeoDesign environment, we have designed three-tier architecture, as shown in Figure 4, which allows eliminating dependency of the data on the services and applications that act as clients. It may be appreciated in this figure how the different data sources may be exploited through the Portrayal and Data Edition Services in the GeoEditor and GeoExplorer applications. It may also be observed how the data generated by the GIS tools are made accessible through conventional or

geospatial Web services to facilitate their exploitation on 3D virtual globes or in the generation of Assets and Rights Reports (ARR).

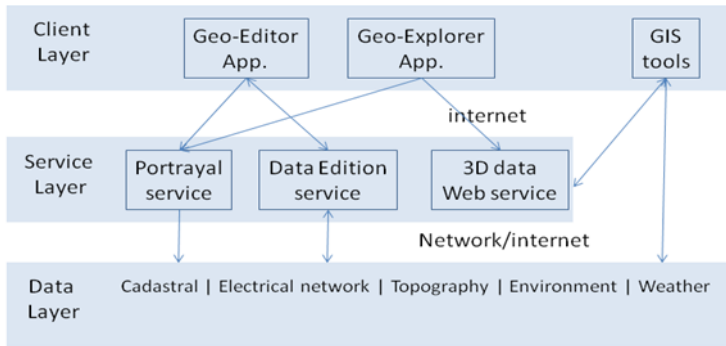


Fig. 4. Proposed three-tier architecture to support GeoDesign workflow

2.5 Visualisation and Interaction Tools

In the planning phase the different actors may select different GI sources in catalogues (through the descriptive metadata) and they may navigate through the territory by using a GeoEditor and combine the different data sources. By means of the GeoEditor they may introduce alphanumerical annotations in support of their proposals, draw the starting point, make the pertinent considerations, etc. In addition, thanks to the GeoEditor, new installation proposals may be generated that will be represented on the territory as new electric lines independently of their aim, i.e. to maximise the power evacuation capacity of the generation plants, to maximise the housing of generation into the distributors or to introduce redundancy into the interconnections to assure the availability of the infrastructures.

In the phase of study of alternatives, by means of the collaborative GeoEditor and GeoExplorer, it is possible to show simultaneously the information about the previously proposed installations and the more detailed data of historical heritage, water bodies, vegetation, fauna, etc. By means of the GeoEditor it is possible to generate and adapt the geometry of a first polygon in the shape of a corridor around the trace defined in the planning. Thus, later on the different actors may modify graphically the corridor and introduce simultaneously annotations in support of different decisions. The actors of the energy scope may also adjust and modify the corridor in order to maximise the benefit of the energetic performance (minimisation of costs, energy losses, etc.), indicating or justifying every change introduced for the general knowledge of the different actors. Finally the actors will review the conformity with their constraints in the new version of the corridor. In the event of disagreement on the part of one or more actors, revision and redefinition of the corridor is possible by providing the pertinent justifications. Figure 5 shows the capability of the GeoEditor application to add and modify the graphic and alphanumerical information associated to the project. It can also be observed how different GI sources justifying or conditioning the trace may be overlaid.

In the project phase a corridor is generated in a collaborative way and the different pertinent information sources are combined, i.e. surveying, cadastre, meteorology, etc. and the engineering project is started by defining the location of the supports, the terrain, the boundaries of the plots, the communication pathways, the forested areas, etc. The result of this study comprises a layer of point information and a set of geographic polygon information representing the different types of occupations and affections that the new infrastructure will cause on the territory. This set of GI generated with GIS tools is stored in an appropriate format for its 3D visualisation in KML format [16], and is shared on the Web for exploitation by the GeoEditor and the GeoExplorer. Figure 6 illustrates the capability of GeoExplorer to show in 3D the planning information, the annotations and the corridors of the new structure over the GI of the territory.



Fig. 5. GeoEditor: drawing, annotation, edition and modification tools

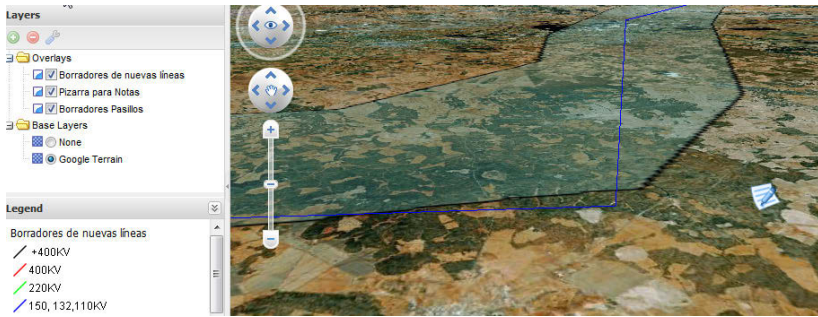


Fig. 6. GeoExplorer: 3D visualisation tools

If there were several alternative proposals for the tracing, this type of tools might be very useful since they allow analysing the advantages and inconveniences of every one of them. Figure 7 illustrates two alternatives for the same planning as well as the aspect a new infrastructure would have before being implanted on the territory after having carried out the project.



Fig. 7. Two different alternatives for the same planning and Google Earth 3D representation for final infrastructure planning and her affections

In the processing phase the developed GIS tools automate the calculations, the generation of the ARR document and the generation and publication of the polygon that delineate each affection in each plot. After having published this data, they may be exploited on GeoExplorer and on a Web application developed to facilitate queries. This application allows selecting an installation and the plot identifier that is defined by the administration in charge (Cadastral), i.e the cadastral reference (CR). Once the plot was identified, a 2D GeoViewer was used so that the owner may look up the cartography, navigate on it, and activate or deactivate the different layers with the affections. Figure 8 shows the Web application that allows navigation over the affections of a plot.

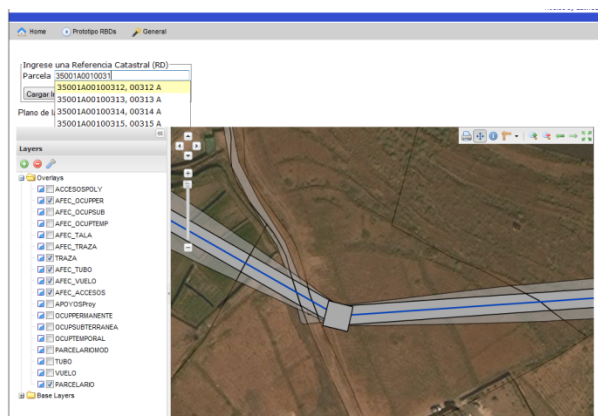


Fig. 8. GeoExplorer: 3D visualisation tools

In this same Web environment a tool was developed that automatically generates digital reports containing quantitative data relative to the affections and their graphic representations.

3 Summary, Conclusions and Future Works

Collaborative environments provide the necessary tools for people of different agencies may be able to work as a team as propose Geertman and Stillwell [5]. All the actors involved in the design of a new installation of electric power transmission are somehow compelled to collaborate through pooling and sharing of criteria, needs and relevant alphanumeric and geographic information for every project, as propose Abukhater & Walker [7] enabling: Sketching, Spatially informed models, Fast feedback supporting collaboration or a brainstorming and Iteration or highlight Dangermond [13]. At this point working groups are spontaneously formed in which the profile of each actor is not a constraint.

The primary advantage of GeoDesign is that it is a single environment based on the spatial reference provided by the GI; this allows georeferencing of all the included, analysed and discussed information. It enables the actors to take responsibility for their information and to translate their needs, priorities and requirements when they enter the collaborative environment as Kumar [2] or Aditya [6] proposed. The use of a single symbology will enable their understanding.

We assumed the hypothesis that we should first identify the collaboration between actors through analysis of the relationships, objectives and constraints conditioning them in each project phase and their relationship/application on the basis of the GeoDesign principles. Through this analysis we detected four phases: planning, study of alternatives, project and negotiation/management of permits. The actors, relationships and constraints were identified as well as the need for graphic tools for drawing, annotation, visualisation and computing of the affections on the properties.

In the phase of implementation of solutions, a three-tier architecture was proposed in which the data become independent of the services and the applications, facilitating the interconnection and interoperability that standard services provide. Several desktop and web applications were developed for calculations, data publishing and report generation in the final phases (project and management of permits). For the early phases, available Open-Source solutions (GeoEditor y GeoExplorer) were integrated and different web services were put in place that allowed interacting with a geographic data warehouse that will give support to these phases as described in the previous section.

As far as results is concerned, it is worth stressing that the early phases of planning and study of alternatives of each project were especially slow and involved many actors belonging to different organisations; they were not tried with all the actors.

In contrast, we do have available the results of the last phase of management of permits and notifications. The development of GIS tools for the calculation of affections has allowed increasing the number of types of affections to be calculated, the reliability of the data-result, the number of projects to be managed per year and on the other hand it has allowed cutting down remarkably on deadlines, cost of project and cost of preparation of data, as can be seen in Figure 9. The results of this new methodology have been compared with the results of the traditional way, where automatic processes were almost nonexistent. The source of these data is the Environment department, Engineering lines department and Procedures department of Spanish Electric Network Company (Red Eléctrica de España – REE).

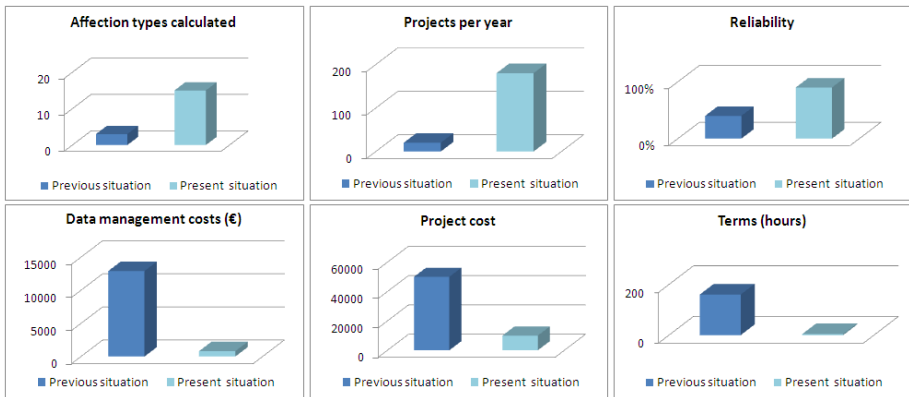


Fig. 9. Results of the phase of management of permits and notifications

In this same phase the Web tool for querying affections and the application for the generation of reports was developed. These tools had been considered of great usefulness by the actors involved in the processing and management of permits since they allowed the owners to communicate graphically and quantitatively the magnitude and location of their affections.

As a future line of work we intend to put into practice the whole process, engaging all the actors around the set of developed GeoDesign applications to analyse the experience of collaboration in this type of environments. We rely on the willingness of participation of the actors involved in this type of environments who will undoubtedly help us advance in the e-administration toward transparency of negotiation and decision-taking, the protection of the environment and the development of the national energetic sector.

Acknowledgements. The research and technology developed in this piece of work have been supported in part by Red Eléctrica de España S.A.U. through the collaborations under the Ide-REE and RBD Projects (2009-2011).

References

1. Ramachandra, T., George, V., Vamsee, K., Purnima, G.: Decision support system for regional electricity planning. *Energy Education Science and Technology* 17(1), 17–25 (2006)
2. Kumar, A., Bhatnagar, S.D., Saxena, P.K.: Integrated multimedia based intelligent group decision support system for electrical power network. *AJIS (Australasian Journal of Information Systems)* 9(2) (May 2002)
3. MITYC, Planificación de los sectores de electricidad y gas 2008-2016: Desarrollo de las redes de transporte. Secretaría General de Energía, Ministerio de Industria, Turismo y Comercio (2008)
4. Vonk, G., Geertman, S., Schot, P.P.: Bottlenecks blocking widespread usage of planning support systems. *Environment and Planning A* 37(5), 909–924 (2005)

5. Geertman, S., Stillwell, J. (eds.): *Planning Support Systems in Practice*. Springer, Berlin (2003b)
6. Aditya, T.: Usability Issues in Applying Participatory Mapping for Neighborhood Infrastructure Planning. *Transactions in GIS* 14, 119–147 (2010), doi:10.1111/j.1467-9671.2010.01206.x
7. Abukhater, A., Walker, D.: Making Smart Growth Smarter with GeoDesign. *Directions Magazine*, July 19 (2010)
8. McHarg, I.: *Design with Nature* (1969) ISBN 0-471-11460-X
9. Steinitz, C.: *Alternative Futures for Changing Landscapes* (2003)
10. Harris, B.: Beyond geographic information-systems-computers and the planning professional. *Journal of the American Planning Association* 55, 85–90 (1989)
11. Artz, M.: GeoDesign: New Concept or New Name? *Geospatial Today* (January 2010); Geertman, S., Stillwell, J.: Planning support systems: an inventory of current practice. *Computers, Environment and Urban Systems* 28(4), 291–310 (2004) ISSN 0198-9715, doi:10.1016/S0198-9715(03)00024-3
12. Ball, M.: Is GeoDesign an activity, a practice or a software-enabled modeling approach? *Spatial Sustain Blog*, March 12 (2010)
13. Dangermond, J.: The Third GeoDesign Summit Focuses on Creating Our Future (2012), <http://www.vector1media.com/spatialsustain/the-third-geodesign-summit-focuses-on-creating-our-future.html>
14. International Standards for Business, Government and Society. Geographic information – Spatial referencing by coordinate, http://www.iso.org/iso/iso_catalogue/catalogue_tc/catalogue_detail.htm?csnumber=26016
15. Open Geospatial Consortium, <http://www.opengeospatial.org> (accessed January 2012)
16. KML documents, <http://code.google.com/intl/es-ES/apis/kml/documentation> (accessed January 2012)

Assessment of Online PPGIS Study Cases in Urban Planning

Geisa Bugs

PROPUR - Programa de Pós-Graduação em Planejamento Urbano e Regional
UFRGS - Universidade Federal do Rio Grande do Sul, Porto Alegre, Brazil
geisabugs@gmail.com

Abstract. The paper assesses newest study cases in PPGIS in order to contribute to tools development that would be able to establish more appropriate practices for public participation in urban planning. By adopting previously applied comparison methodology, it assesses the usability, interactivity and functionalities of four selected online PPGIS study cases. It concentrates on online PPGIS assuming that the combination of traditional participatory methods with GIS, ICT, and the interactivity of the Web nowadays, can be of great value to make the participatory debate more democratic and consistent and, eventually, improve the levels of public participation in urban planning, strengthening the role of citizens in decision making. However, the assessment shows that online PPGIS applications are, in some aspects, limited. It is still an open question how online PPGIS should be built to face the difficulties of traditional methods and provide the proposed benefits.

Keywords: PPGIS, GIS, urban planning, public participation.

1 Introduction

GIS – Geographic Information System is a computer environment used to collect, store, manipulate, analyze, produce and disseminate geographic information [1]. It is considered the best tool for dealing with any problem related to space. In other words, it is an essential platform for urban planning [2].

Since the 90's, the knowledge area called Public Participation Geographic Information Systems – PPGIS researches and develops a set of applications designed to exploit the potential of GIS to promote community goals [3]. As the name suggests, PPGIS uses GIS tools for public participation, connecting the technical capacity of GIS to local knowledge. Rather than using GIS resources in a traditional way, as in spatial analysis, they are used for production of maps and spatial stories that help to characterize the local space [4]. The goal is not to turn participation into GIS, but present and organize relevant information that would not become visible through other methods [5].

In a broad sense, public participation can be understood as a decision making process open to citizens, involving issues that directly or indirectly affect their lives in the use and ownership of a specific urban territory [6]. The participation is an

important planning component that leads to different solutions than might have been achieved otherwise, once the citizens know the reality and the local problems better than anyone else and can provide detailed insights into local space description that are not normally available from other sources [7].

Urban planning can be understood as an ongoing work that aims to systematically organize resources to achieve goals that will help to improve a given situation, which in the case of urban planning regards to the city [8]. It deals with problems of the built, natural, and social environments, where a wide range of factors have to be balanced against each other to reach solutions. Urban problems are incomplete, contradictory and changeable, with solutions often difficult to recognize because of the interdependence of factors [9]. There is no single planning solution, but an infinite number of possible solutions, where public participation is one of the factors involved.

A significant research number has examined the use GIS in public participation processes, recognizing: the importance of a better understanding of participatory processes to build relevant PPGIS projects, need for further evidence to assess whether the technological advances will promote the improvements suggested by GIS experts, lack of documental research on how users are making use of online PPGIS, and necessity of more studies investigating how Web GIS could be a PPGIS component [10] [11] [12].

In order to contribute to the development of tools that would be able to establish more appropriate participation channels, and assuming that participatory planning should take advantage of the Internet and PPGIS, this paper assesses four projects, applying a methodology developed by Steinmann [13]. The objective is to find indications on how online PPGIS could be developed to face the difficulties pointed by the literature. Which GIS tools and interaction levels are adequate? How to balance complex tolls and usability? How to promote the use of GIS tools by the lay public?

Before exploring the study cases, the following subsections provide an overview about novel tools available for public participation and its adoption on decision making to urban planning purposes.

1.1 Public Participation in Urban Planning

Everywhere, the participatory processes receive much criticism, carrying an ineffectiveness connotation [14] [15]. This occurs, in part because the term public participation is widely used to refer to a number of different methods with distinct levels of participation [16]. But also because building an urban planning solution by means of public participation is a complicated progression, in which solutions should emerge gradually, through continuous judgment and consensus building between experts and no experts [17].

Each participant has the prospect of their interests or function: general citizenry, private sector actors, civil society, politicians, and technicians, among others. Interested parties may participate only if there is information, which must be true, complete and objective. If the available information is sufficient and is well communicated, everyone should be able to understand it in order to make known their vision, and also understand the views of other participants, establishing a consistent debate [18].

The legitimacy of the participatory process necessarily involves accessibility to the different levels of information. The population heterogeneous characteristics require techniques and methodologies that create the conditions for debate consistent. The public hearings are not sufficient to make people with entrenched attitudes of submission over the years or that were severely discriminated, talk [19]. One must establish alternative and inclusive forms of participation in all decision making stages. Public involvement in planning requires an information system and services provided by the authorities accessible to all, and this system is, supposedly, configured by the effective use of Information and Communication Technologies - ICT and GIS [20].

1.2 Online Participatory Planning Tools

The Internet is already the dominant platform used for communication, mobilization and collaboration, as exemplify the recent episodes in the Arab countries. The Internet is being more strongly associated with civic engagement than the consumption of television and printed media, as well as face to face discussion [21]. Changes in how people are using the Internet to their own interests reflect in great changes in society and their forms of organization [22]. The content construction by more than one person (the wisdom of crowds) is an example of these social transformations.

The ICT can be understood as all the technical information used to treat and assist communication. ICT has been part of the planning system since the introduction of the mainframe in the 1960s. Its use for public participation, however, is a relatively new phenomenon, which focuses on visualization and analysis using the GIS [20]. Much of the literature recognizes the communication possibilities of ICT and its ability to mediate the relationship between citizens and government, resulting in significant changes in the operation mode of contemporary politics [23]. The mass adoption of ICT in all areas of society requires that government, particularly at the local level, turns more citizen-oriented, allowing the organized inclusion of various sectors in the process of the public policy setting [18] [21] [23].

Among the Internet technological advances, one must highlight the interaction offered by social media, the ease of access to information and knowledge, the sophisticated tools freely available, and the increased interactivity between users and systems [24]. The Internet has also become a collaborative platform, known as Web 2.0 [25], in which people not only consume content (downloading), but also contribute and produce new content (uploading) [26]. Nowadays, an increasing information amount that we consume digitally is created by users [27]. The interaction and collaboration promoted by the Web 2.0 converge with the ideal of participatory construction of decisions through a democratic process of consensus building (collaboration) with intensive communication and discussion (interaction) between the participants [17].

The ubiquity of geographic information services bound to online maps and its use for content creation by the public, are also Web 2.0 consequences [28]. Geographic information and tools that were once exclusively used by experts are now available to anyone on the Web. The online mapping services are used by a variety of Web applications to create new services, the called mashups. The users, in turn, use these

services to create and distribute their own geographic information. The terms Neogeography [29] and Voluntary GIS [30] refer to this growing use of geographic tools and techniques by lay people, enabled by recent advances in the Internet.

Differently from the past when institutions were the mainly responsible for geographic information creation and distribution, now anyone can easily produce a map and publish it online. Therefore, even unintentionally, there is an increase on geographic information awareness by the general public. This phenomenon can be considered a revolution in the geographic information world, because GIS tools can be learned quickly and effectively without the need of immersion in professional activities [27].

The internet is also the dominant platform to the PPGIS projects. Some authors consider this combination an evolution of the classical participation methods [7]. Online Maps and GIS tools supposedly bring more freedom for the public explore the problem and create solutions that represent their perception. They can examine existing information, test possible solutions, see and compare ideas, and share visions with the community [7]. The key is in the easiness that the users have to identify points of interest that connect the mind map with the system map. Users can base themselves on different types of media such as photos, videos, and 3D models [4].

Some authors use the term e-planning referring to the provision of planning information on the Web for population use: "The term e-planning has become common in this area, and identifies several applications (...) that allow strengthening the understanding and communication of actions and policies to the public through publicity and consultation of legislation, plans and projects, surveys, discussion rooms, in addition to online voting on proposals. These proposals may include multimedia communication resources (images and virtual reality) to an efficient representation of planning information to society [31]."

There are a number of benefits that the online participatory planning would have in comparison to presential methods [7]: there is no restriction to geographic location or time, providing opportunities to more people participate. When compared with meetings in which participants have to make comments in front of a group of strangers, the online system allows them to do so in a relatively anonymous way. The Internet could also overcome the atmosphere of confrontation and avoid the domination by individuals whose views do not necessarily represent the majority.

In short, it seems clear that Internet and the PPGIS tools have potential to improve public participation into decision making. However, evidences show that there are not many experiences taking place focusing on urban planning, implemented for real, or that the results have been adequately evaluated [20] [21].

1.3 PPGIS Applications

Some bottom-up initiatives to facilitate citizen participation are already emerging on Internet. Projects like the Urbanias [32] that proposes to "promote activism, providing mechanisms and tools that facilitate and encourage individual enterprise and improvement of all aspects related to quality of life in the city". But in general, public institutions have failed to incorporate the technology in a satisfactory manner.

A research evaluated the degree of democratic participation in Internet usage in Brazil and showed that there is predominance, more or less structured, of the quite elementary function: information delivery [23]. In the few cases where there is provision of public services, these are mainly oriented to the tributary relationship between citizen and government. There is an underuse of Internet possibilities.

In Australia, a survey with local councils evaluated the willingness and openness of government on the Internet usage to create spaces of discussion and exchange of information with the citizenry [20]. It found that approximately 15% of councils are willing to embrace online planning tools, other 15% at least in opinion polls level, and 70% in online discussions. Almost all councils see the Internet as an inevitable technology for the provision of services to the population.

Virtual Slaithewaite [33] is a pioneer PPGIS for urban planning purpose, but it is a quite simple system if compared with the services capabilities of today's online maps. Other applications focus on environmental planning [34], agrarian reform [35], and self-management community [10], for example. But, in general, it can be said that PPGIS are not yet a concern among decision-makers and planners. Also, the existing initiatives regarding participatory planning still need to be assessed [35].

Online information technologies are becoming essential tools for urban planning. It represents a new threshold for the discipline of planning, as it creates a new operation platform, which increases the opportunities for public participation, providing continuous public access on the records of the evolution and adoption of proposals and policies planning [20].

2 Study Cases

The study cases generally have a dual purpose, firstly try to understand who are the members of the group and secondly, try to develop general theoretical statements about regularities of the process [36]. The latter is the case of this research. Given the complexities of all possible observations, one should restrict the evaluation to some relevant issues through the observation of evaluation criteria. Finally, we seek generalizations about the phenomena studied, which provides answers to theoretical questions of the study.

2.1 Selection

The selected study cases meet the following requirements:

1. Link accessible and operational at the time of the survey, for better investigation;
2. Project published in the last five years and quoted by other research on the topic, to find newest and relevant studies;
3. Have subsequent work evaluation or have been used in a practical situation with real users, in order to provide elements for the usability assess;
4. Have been designed with the aim of helping some kind of decision making or planning purpose, to filter only PPGIS project related with planning.

Accordingly, the following four projects were selected, which are helpful to develop general statements about the PPGIS projects. These statements, in turn, could be used

for PPGIS improvements, and thus contribute to the development of more interactive and innovative participation methods in the framework of collaborative planning and decision making.

2.2 Description

ParticipatoryGIS is a collaborative Web GIS based on MCDA (Multicriteria Decision Analysis) developed during 2010 by researchers of the Department of Geography, The University of Western Ontario [37]. The motivation was that the process of spatial planning requires collaboration and distribution over an extended period of time, and there are relatively few spatial planning and decision making tools available to the general public. In their words: “implementing GIS within the WWW environment and integrating its capabilities with MCDA methods can provide a mechanism for bridging the gap between the experts and the public [37].”

The application sets the “best” location for building a new parking in Canmore, Alberta, Canada (Fig. 1). It consists of two components: the deliberative part based on the argumentation map concept [38] and the analytic component based on MCDA methods. ParticipatoryGIS combines each individual judgment with the group preferences, in order to identify the best alternative. The analysis involves two stages: the decision rules to combine the maps according to the preferences of each individual (analytical structure), and the rules of collective choice that transforms individual preferences into a group decision, building consensus (deliberative structure).

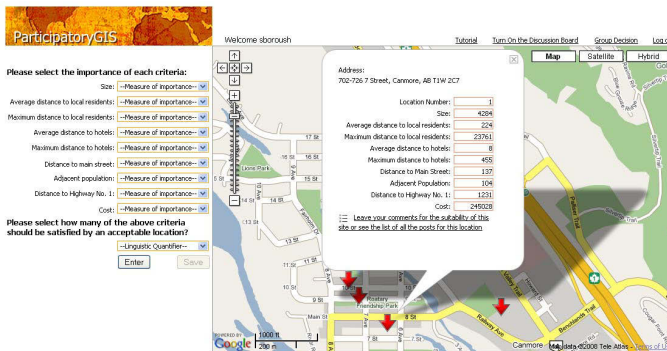


Fig. 1. ParticipatoryGIS interface < www.participatorygis.com>

Users must register, read and accept the terms of use. By completing the registration, users are referred to the tutorial. After that, users are directed to the main map where there are four alternative sites for parking. By clicking on each alternative a window displays its properties. Users can then enter with their preferences on the relative importance of each suitability criterion using a set of terms (none, low, low, medium, high and very high). In addition, users must define how many of the evaluation criteria must be satisfied for the site to be considered adequate. The criteria relate to distance from the city center location, and land area, for instance.

By submitting the preferences, users can see their individual map with the final classification of each alternative location and also the collective results.

SoftGIS is a Finnish initiative, held by researchers from the Aalto University [39]. It is a tool for assessing environmental quality perceived by the residents. SoftGIS collects the resident’s perceptions in a systematic way, questioning them about their experiences and everyday behavior within the cities. The information is gathered mainly for the scientific purposes but also for the support of planning and decision making.

The knowledge generated form a special GI database to be used in planning. The environment quality can be approached in two ways: based on official data and/or as perceived by the residents. The latter challenges the traditional top-bottom practices. SoftGIS was designed to be easy to use for all age groups. To participate, the user follows a step by step through the application, filling up a questionnaire. There are questions, among others, about appearance, functionality and social life of places where they live.

SoftGIS first version was used in the city of Järvenpää, in Finland, between 10/2004 and 12/2004 (Fig. 2). The questionnaire was available on the municipality website during three months. The research was advertised in newspapers and local libraries. 427 inhabitants, aged between 13 and 73, filled out the online questionnaire. At the end of the application, the respondents gave feedback about the research and the application to the researchers, 28% were positive, 20% were general comments about the city, and 24% reported technical problems. The greatest difficulty reported concerned about the use of the map tool, which was found to be difficult to use or the map hard to orientate. Many users were suspicious about the data security. For this reason, information concerning data security was added in the application already during the data collection. Subsequent work has already made applications in various situations, as for example on how to evaluate the mobility of children.



Fig. 2. SoftGIS interface <http://opus.tkk.fi/softgis/>

Participatory Geographic Information Systems for Transportation - PGIST is an Internet GIS-based portal to support public participation in transportation

decision- making. It was developed by researchers from the Department of Geography, University of Washington [11]. The research principal question was: “What Internet platform designs and capabilities involving participatory modeling, particularly including GIS technology, can enable public participation in analytic-deliberative transportation decision making within large groups? [11].”

The survey generated the tool called Let’s Improve Transportation (LIT) (Fig. 3), employing the notion of ideas generation, synthesize, and reach a decision on the best-case scenario. It is an asynchronous participatory methodology, in which all activities can be exploited alternately by various actors. The online activities include: i) to receive information on projects, learning about the proposals, ii) to categorize and prioritize ideas, considering the potential impacts of these changes on communities, and iii) to determine which projects should be supported by working in collaboration with other residents.

The study took place in the central Puget Sound region of Washington State and its object is a transportation improvement program that allocates resources to implement a transportation plan via project selection. It is a complex decision making process involving various stakeholder groups, in which US law requires public participation. 135 residents of King, Pierce and Snohomish participated, during four weeks in 2007, of the online experience. The task was to determine which transportation improvement projects should be constructed and what funding mechanisms (such as taxes) should be used to pay for these improvements. The end result contains 27 projects with total cost of 11.8 billion U.S. dollars, approved by 61% of the participants. Participants also had the opportunity to review the report and suggest revisions. 50 participants endorsed the final report, while 12 rejected.

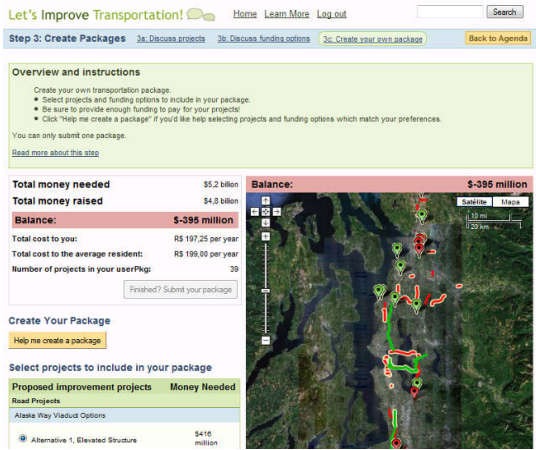


Fig. 3. Lets Improve Transportation interface <www.letsimprovetransportation.org>

Canela PPGIS prototype's was developed as a dissertation project during 2009 at the University Jaume I, Castellon, Spain [40]. It takes advantage of the interactive-collaborative Web 2.0 aspect, and uses the Google Maps API. Users can view spatial

data organized by urban planning aspects (housing or equipment, for instance), post comments in text form geographically referenced to the object of interest (schools and streets, for example), classify the comment (as hint, complaint and so on.), and see all the contributions posted by other users on the map (Fig. 4).



Fig. 4. Canela PPGIS interface < <http://geoportal.dlsi.uji.es/pgis/>>

The system stores the comments in a database that, once consulted by planners and technicians, may assist spatial analysis that eventually reveal patterns and/or trends according to the community point of view. The comments are saved along with its "context" (coordinates, zoom level, driven layers, and so on), which allows the specialist to get a better understanding of the "thrill of the user."

Local actors performed a usability test in January, 2009. The results showed, according to the authors, that there is public interest in using a web application like this for participation in urban planning and management. The public stressed very easy access to information about their city. The comments posted were pertinent to planning issues and the users have not had great difficulty in using the tool.

2.3 Assessment Criteria

The study cases were evaluated by using methodology previously applied in a study that developed a framework for PPGIS analysis [13]. The comparison criteria adopted here are: 1) Interactivity, 2) Functionality and 3) Usability.

Interactivity: Arnstein's participation ladder [16] is a useful analogy for levels of public participation. The base represents zero opportunity to take part in, with successive rungs representing increased levels of participation until total citizen control. Based on it, [7] proposed the e-participation ladder, where the involvement increases with the access to information. The bottom rung represents online delivery of public services such as payment of rates. Further up, the communication becomes bidirectional making participation more interactive by sharing information and ideas until the public involvement in decision making. Again, the e-participation ladder was adapted by [13] to assess the degree of interactivity.

In a PPGIS application, interactivity refers to the user interaction with the application using a computer. There are four stages of interactivity:

a) *Information Delivery*: bottom stage, passive participation, one-way flow of information, only from the system to the user;

b) *Online Discussion*: two-way flow of information exchange, since it includes discussion between participants, planning offices and planning authorities;

c) *Map-based Discussion*: user communicates on the basis of an online map, through graphical expressions or comments on specific objects of the selected map. Participants can submit to the planning authorities their personal versions of maps, but are not actively involved in decision making through processes that include the return of their participation;

d) *Involvement in Decision Making*: highest stage, when participants contribute actively to the decision making process.

Functionality: the following GIS functionalities are standard in all GIS and are usually needed for PPGIS applications [13]:

a) *Topological Overlay*: different layers can be combined in a customized map;

b) *Information Retrieval*: the user may retrieve attribute data describing characteristics about a selected object with a mouse click on a spatial element;

c) *Query*: the user can retrieve the data according to the related terms, phrases or features chosen;

d) *Data Selection*: enables the user to select spatial objects on the specified thematic data layer;

e) *Zoom and Pan*: enable the users to change their view and the level of detail by clicking on a location or by dragging a box to define a particular extent;

f) *Distance Measure*: enables the user to measure the distance between two locations or the total distance of a route, with multiple stops, for example.

Usability is a part of the Human Computer Interaction discipline, which refer to evaluating whether an application works and has met its design goals according to the user's needs [40]. Usability testing with real users involves watching target users or existing users of a system interact with it by performing a set of real or representative tasks. Involves the analysis of the extent to which a computer technology supports to users to achieve specific objectives in an effective, efficient and satisfactory. PPGIS studies have been criticized for stressing more technological rather than usability aspects [41].

2.4 Assessment

Analyzing the study cases comparison on Table 1, based on the assessment criteria developed by [13], it is verified that, currently, PPGIS projects uses little functionality of GIS: none of them make available query or data selection. The two-way communication is not fully established yet. And it's also observed that the two applications with higher levels of involvement in decision making are more complex, which consequently compromises its usability. Finding this balance is a challenge to be overcome.

ParticipatoryGIS, regarding the interactivity degree, achieves a high stage, because the participants contribute to the decision making. Although the intermediate steps are not guaranteed. Information retrieval is restricted to the land location suitability. The online discussion tool was not used by most users according to usability test [42], indicating that the two parts, discussion and multicriteria analysis, are not totally integrated. It aims only to produce the multicriteria evaluation map. The functionalities available are information retrieval and zoom and pan.

Regarding usability, [42] performed a test and concluded that this depends significantly on the previous participants experiences with GIS and Web. The multicriteria concepts turn it into a tool designed to an audience with some basic statistics understanding. It is not an easy tool, given that there are several criteria to be considered.

Table 1. Study cases comparison

		Participatory GIS	SoftGIS	PGIST	Canela PPGIS
Interactivity	Information delivery				
	Online discussion				
	Map-based discussion		x		x
	Involvement in decision making	x		x	
Functionality	Topological overlay				x
	Information retrieval	x	x	x	x
	Query				
	Data selection				
	Zoom and Pan	x	x	x	x
Usability			x		x
	Distance measure				

SoftGIS, although is a tool whose usefulness was positively evaluated, even being used by children and elderly, the degree of interactivity achieved is not high. Communication is primarily one-way, but not as often occurs from the system to the user, but as a questionnaire answered from the user to the system. So, the user communicates map-based, however, unilaterally. Discussions among participants do not occur. And there is no evidence that the research findings had been used effectively in decision making. Regarding the functionalities, users can recover information and uses the zoom and pan. SoftGIS differential is to be a permanent tool for public opinion collection, since it is not a decision support system for a specific question.

PGIST reaches the highest interactive stage, where participants contribute to decision making. Provision of information occurs in both directions and discussion among participants is made possible through the forums. However, it is not a map-based discussion. The map serves only as a means of information communication that subsidize participation. The available tools are basically the same as for other projects: information retrieval on objects in the map and navigation.

By enabling detailed analysis of alternative scenarios and aiming to prioritize proposals, it is a tool that requires a degree of dedication to be used correctly, even though the authors advocate that the site is designed to properly orient any citizen interested in the process.

Canela PPGIS archives the third stage on interactivity, with user communication on the basis of an online map, through comments on specific objects of the selected map. Regarding the functionalities it provides, differently from others, the topological overlay of layers. Its usability was evaluated as satisfactory during a usability test developed in 2009 with local actors [40]. But participants are not actively involved in decision making through processes that include the return of their participation, mainly because it was not implemented as a government tool.

3 Final Considerations

The article starts from the hypothesis that participatory planning should take advantage of ICT and GIS online tools to create novel interactive channels for collaboration and emancipation in order to achieve higher participation levels. For various reasons, a large portion of the population is excluded from the current participatory processes - usually public hearings and consultations. The combination of Internet and GIS tools encompasses new methodological possibilities for participatory urban planning. Online PPGIS make possible combine three key aspects: interaction (ICT), technology (GIS), and local knowledge (capital/people).

However, the study cases show that online PPGIS applications are also unilateral in many ways. Although PPGIS aims primarily to support the bottom-up decision making, this level was not yet reached. It is still unclear how Online PPGIS must be built to face the difficulties of traditional methods and provide information for both sides: residents and planners. This is not an easy goal to achieve, because there are many weaknesses in the participatory planning process that persist, such as the use of knowledge of the population and their effective integration in decision making, and mediation of conflicts inherent to the urban planning. The virtual increases participation, but the key issue is to improve participatory processes so that it's worth the public effort to attend [37].

The paper concludes that the expectation that these technologies can reverse the gap between citizens and decision making in urban planning has yet to be proven, indicating that perhaps should be based on new empirical experiences. Should be evaluated more closely the relevance of their use, and which is the effective potential of the contributions collected to intervene in urban planning decisions.

In time, it should be noted that it is not the apologia of the Internet or the GIS as a panacea that would be the redemption of all the public participation difficulties. It is about understanding that the technologies are available, must be assimilated by both experts and no experts, and, especially, about how to do it properly.

References

1. Goodchild, M.F.: What is Geographic Information Science? NCGIA Core Curriculum in GIScience (1997), <http://www.ncgia.ucsb.edu/giscc/units/u002/>
2. Batty, M.: Apresentação. In: Almeida, C.M., Câmara, G., Monteiro, A.M.V. (eds.) Geoinformação em urbanismo: cidade real x cidade virtual, pp. 7–11. Oficina de Textos, São Paulo (2007)

3. Sieber, R.: Public Participation and Geographic Information Systems: A Literature Review and Framework. *Annals of the American Association of Geographers* 96, 491–507 (2006)
4. Elwood, S.: Critical Issues in Participatory GIS: Deconstructions, Reconstructions, and New Research Directions. *Transactions in GIS* 10, 693–708 (2006)
5. Sieber, R.: Rewiring for a GIS/2. *Cartographica: The International Journal for Geographic Information and Geovisualization* 39, 25–39 (2004)
6. Pozzobon, R.M.: Participação e planejamento urbano: o processo de elaboração do plano de desenvolvimento urbano ambiental de Porto Alegre. Dissertação de Mestrado PROPUR-UFRGS, Porto Alegre (2008)
7. Carver, S.: Participation and Geographical Information: a position paper. In: ESF-NSF Workshop on Access to Geographic Information and Participatory Approaches Using Geographic Information Spoleto, pp. 9–15 (2001)
8. Ferrari Júnior, J.C.: Limites e Potencialidades do Planejamento Urbano. *Estudos Geográficos: Revista Eletrônica de Geografia* 2, 15–28 (2004)
9. Webber, M.M., Rittel, H.: Dilemmas in a General Theory of Planning. *Policy Sciences* 4, 155–169 (1973)
10. Rattray, N.A.: User-Centered Model for Community-based Web-GIS. *URISA Journal* 18, 25–34 (2006)
11. Nyerges, T., Patrick, M.: Rethinking public participation as instant access to virtual meetings. In: Miller, H.J. (ed.) *Societies and Cities in the Age of Instant Access*, pp. 331–342. Springer (2007)
12. Craig, W.J., Harris, T.M., Weiner, D. (eds.): *Community participation and geographic information systems*, pp. 3–16. CRC Press (2002)
13. Steinmann, R., Krek, A., Blaschke, T.: Can Online Map-Based Applications Improve Citizen Participation? In: Böhlen, M.H., Gamper, J., Polasek, W., Wimmer, M.A. (eds.) *TCGOV 2005. LNCS (LNAI)*, vol. 3416, pp. 25–35. Springer, Heidelberg (2005)
14. Villaça, F.: *As Ilusões do Plano Diretor*. São Paulo (2005)
15. Hansen, H.S., Reinau, K.H.: The Citizens in E-Participation. In: Wimmer, M.A., Scholl, H.J., Grönlund, Å., Andersen, K.V., et al. (eds.) *EGOV 2006. LNCS*, vol. 4084, pp. 70–82. Springer, Heidelberg (2006)
16. Arnstein, S.R.: A Ladder of Citizen Participation. *Journal of the American Planning Association* 4, 216–224 (1969)
17. Tang, T., Zhao, J., Coleman, D.J.: Design of a GIS-enabled Online Discussion Forum for Participatory Planning. In: *Proceedings of the 4th Annual Public Participation GIS Conference* (2005)
18. Centelles, J.C.P.: *El buen gobierno de la ciudad: Estrategias urbanas y política relacional*. La Paz, Plural editors (2006)
19. das Cidades, M.: *Plano Diretor Participativo: Guia para a elaboração pelos municípios e cidadãos* (2004)
20. Yigitcanlar, T.: Australian Local Governments' Practice and Prospects with Online Planning. *URISA Journal* 8, 7–17 (2006)
21. Rothberg, D.: Por uma agenda de pesquisa em democracia eletrônica. *Opinião Pública, Campinas* 14 (2008)
22. Castells, M.: *Conversation with Manuel Castells: Entrevista concedida a Harry Kreisler*. Institute of International Studies, UC Berkeley, California (2001)
23. Silva, S.P.: Graus de participação democrática no uso da Internet pelos governos das capitais brasileiras. *Opinião Pública, Campinas* XI, 450–468 (2005)
24. Jazayeri, M.: Some Trends in Web Application Development. In: *Future of Software Engineering (FOSE 2007)*, Minneapolis, pp. 199–213 (2007)

25. O'Reilly, T.: *What is web 2.0: Design Patterns and Business Models for the Next Generation of Software* (2005)
26. Vossen, G., Hagemann, S.: *Unleashing Web 2.0: From Concepts to Creativity*. Morgan Kaufmann, Burlington (2007)
27. Hudson-Smith, A., Crooks, A.: *The Renaissance of Geographic Information: Neogeography, Gaming and Second Life*. UCL Working Papers 142 (2008)
28. Haklay, M., Weber, P.: *OpenStreetMap: User-generated Street Maps*. *IEEE Pervasive Computing* 7, 12–18 (2008)
29. Turner, A.: *Introduction to Neogeography*. O'Reilly Media (2006)
30. Goodchild, M.F.: *Citizens as Voluntary Sensors: Spatial Data Infrastructure in the World of Web 2.0*. *International Journal of Spatial Data Infrastructures Research* 2, 24–32 (2007)
31. Almeida, C.M.: *O diálogo entre as dimensões real e virtual do urbano*. In: Almeida, C.M., Câmara, G., Monteiro, A.M.V. (eds.) *Geoinformação em urbanismo: cidade real x cidade virtual*, São Paulo, Oficina de Textos, pp. 19–31 (2007)
32. Urbanias, <http://www.urbanias.com.br>
33. Kingston, R., Carver, S., Evans, A., Turton, I.: *Web-based public participation geographical information systems: an aid to local environmental decision making*. *Computers, Environment and Urban Systems* 24, 109–125 (2000)
34. Brown, G.G., Reed, P.: *Public Participation GIS: A New Method for Use in National Forest Planning*. *Forest Science* 55, 166–182 (2009)
35. Weiner, D., Harris, T.M.: *Community-integrated GIS for Land Reform in South Africa*. *URISA Journal* 15 (2003)
36. Becker, H.S.: *Métodos de pesquisas em ciências sociais*. Hucitec, São Paulo (1999)
37. Boroushaki, S., Malczewski, J.: *ParticipatoryGIS.com: A WebGIS-based Collaborative Multicriteria Decision Analysis*. *Urisa Journal* (2010)
38. Keßler, C., Rinner, C., Raubal, M.: *An Argumentation Map Prototype to Support Decision making in Spatial Planning*. In: *Proceedings of AGILE*, pp. 26–28 (2005)
39. Kahila, M.: *Possibilities of Web-based softGIS Method in Revealing Residents Evaluation Knowledge of the Living Environment*. In: *FUTURE - Future Urban Research in Europe, The Electronic City Conference*, Bratislava (2008)
40. Bugs, G., Granell, C., Fonts, O., Huerta, J., Painho, M.: *An assessment of Public Participation GIS and Web 2.0 technologies in urban planning practice in Canela, Brazil*. *Cities* 27, 172–181 (2010)
41. Nielsen, J.: *Usability Engineering*. Morgan Kaufmann, San Diego (1993)
42. Meng, Y., Malczewski, J.: *Usability evaluation for a web-based public participatory GIS: A case study in Canmore, Alberta*. *Cybergeo: European Journal of Geography, Cartographie, Imagerie SIG* 483 (2010)

e-Participation: Social Media and the Public Space

Gilberto Corso Pereira¹, Maria Célia Furtado Rocha², and Alenka Poplin³

¹ Federal University of Bahia, Architecture and Urbanism, Salvador, Brazil
corso@ufba.br

² PRODEB, Salvador, Brazil
mariacelia.rocha@prodeb.ba.gov.br

³ HafenCity University Hamburg, Germany
alenka.poplin@hcu-hamburg.de

Abstract. Today many initiatives bring groups and individuals together by using social media. They amplify their voice and make their expectations, desires and frustrations public. Some of these initiatives have demonstrated the competence to mobilize people and networks and push government for action. Internet enables connection of various networked local events to occur in different parts of the world; the network is global while events are local. Thus new geographies are formed exploding contextual limits and boundaries between localities and previous hierarchies of scale. We can say that the public sphere has become hybrid as it incorporates virtual and geographical spaces, and traditional and social media. This paper argues that social media can amplify the public space. The categories of "public", "public space" incorporate the possibilities of collaboration and participation in everyday life that portable devices such as smartphones or cell phones already enable.

Keywords: e-Participation, social media, public space.

1 Introduction

Today many initiatives bring groups and individuals together by using social media. They amplify their voice and make their expectations, desires, and frustrations public. Some of these have demonstrated competence to mobilize people and networks and push government for action. The United Nations have incorporated public participation as an element of e-Government. In 2010 they published the result of an assessment carried out in 2009 analyzing the tools for citizen participation available on online channels at the national level (United Nations, 2010).

The United Nation report recognized the relevance of e-Participation in all its aspects; e-information, e-consultation and e-decision making. It assessed how governments interact with citizens by using blogs, chats, SMS, Facebook, Twitter and others. The same report concluded that Web 2.0 tools and social networks have created a new environment that should be incorporated into the day-to-day activities for politicians and decision makers.

According to the results of research in this report, the Republic of Korea achieved the best results in e-Participation, followed by Australia, Spain and New Zealand. Good

practices of government-citizen interaction were observed in Chile, Croatia, Cyprus and Mongolia. The most often activities observed in these countries included input from citizens and extensive use of blogs, forums, social networks and questionnaires. European countries dominated the list of the top thirty-five countries (with around 50% of them), followed by Asia (more than 30% of them) followed by the North- and South America and Oceania. Africa failed to qualify among the top thirty-five list.

In 2012, some developing countries were included on the e-Participation top list, among them Egypt, the United Arab Emirates, Colombia, and Chile (United Nations, 2012). Considering the type of e-Participation (e-information, e-consultation, e-decision making) the UN 2012 Survey showed that though e-Participation was adopted among many countries, the top seven countries provide more than 70 per cent of the assessed services (United Nations, 2012). The survey also reports that Twitter and Facebook are increasingly being deployed by governments as a consultation tool. It also provides examples of Web 2.0 tools use, e.g. the online discussion forums on the Hungarian e-democracy site (<https://edemokracia.magyarorszag.hu>) and Mozambique websites (Ministry of Education's - <http://www.mec.gov.mz> - and Ministry of Health's - <http://www.misau.gov.mz>).

In the urban sphere there are many examples of Internet usage for interaction and collaboration using geographic information where the government and citizens are involved. Examples include Sanpablog (www.sanpablog.it/?page_id=111), a hyperlocal blog from a San Paolo quarter in Turin (Italy); Porto Alegre.cc (www.portoalegre.cc/) state capital of Rio Grande do Sul (Brazil); e-Part (www.epart.it), a citizen social network (Italy), and Nexthamburg (www.nexthamburg.de), a think-thank initiative in which the citizen's and planners discuss the future development of the city, (Germany).

There are also non-governmental initiatives that incorporate views and information provided by citizens related to problems and issues faced by cities and their inhabitants. Many of them work as platforms for complains, claims or demands, taking geographic location as the main reference. Examples include Whatif (<http://whatif.es/en/>) an auto-denominated participatory and collective creativity digital tool, Fix-my-Street (<http://www.fixmystreet.com/>) on which the citizens can point out to the needed repair work on the streets, and Urbanias (www.urbanias.com.br/) in São Paulo City. Some initiatives serve as the connecting node e.g. the central portal for information about public participation and stakeholders involved in participatory processes. Such examples include the European Institute for Public Participation (www.participationinstitute.org/) created in Germany, and People & Participation Online (www.peopleandparticipation.net/display/Involve/Home), created by a non-profit organization Involve, and an innovative new media company Headshift, in the United Kingdom.

A collaborative mapping is often used for strengthening the participants' identification with their own cultural background. Wikimapa Project (<http://wikimapa.org.br/>) stimulates Rio de Janeiro slum's residents to see their territory, and themselves as well, in a new and more positive way. A social cartography project funded by Ford Foundation in Amazon provides another example of community active involvement in mapping its territory, in this case with fruitful outcome for the official recognition of the indigenous territory limits (<http://vimeo.com/24234784>).

In an increasingly urbanized world in which cities are becoming larger and larger agglomerations, the complexity of variables that influence the analysis of these cities increases as urban societies become more diverse and gain more mobility. Planning and managing cities growth necessarily involves a series of diverse knowledge and use of sophisticated tools and processes. Ideas like Participatory Budgeting were developed in order to bring people and decision-makers together. “Participatory Budgeting is a process of direct, voluntary and universal democracy, where the people can debate and decide on public budgets and policy. The citizen’s participation is not limited to the act of voting to elect the executive or the legislators, but also decides on spending priorities and controls the management of the government. Presently, at least three-hundred cities worldwide have adopted this method of public administration and participation” (UN-HABITAT, 2004).

A number of technologies are available today to produce a large amount of information about the city from both perspectives; human activities and automated systems. Information and communication technologies allow analysis of urban realities, and communication between various social actors - citizens, organizations, corporations - enabling access and use of information. They provide an opportunity for engagement of individuals in participatory activities through the Internet by allowing users interaction with representations of the physical environment and extensive exchange of information between them.

2 Urban Public Space, Place and Digital Space

Urban public spaces have always been places of movement and activities of various types and, once connected, enable the mobility of citizens - the streets, avenues, passages, squares - linking markets, houses, and offices. The cities in the new millennium “are characterized by a growing provision of urban places, appearing in the most diverse forms: shopping malls, historical settings, restaurants, entertainment places, sport complexes, hybrid complexes – places which copy qualities found in other places, or which create what is believed to attribute quality to the urban space” (Castello 2010).

Some key concepts of dominant theories about the global economy suggest that the place does not matter anymore. Sassen (2001) disagrees: she notes that the public space of cities accommodates a wide range of political activities, many of them visible on the streets. Their visibility can be amplified by the digital media circulating in local and global networks. In her book titled *The Sociology of Globalization* (2007) she seeks to understand how this phenomenon articulates by the local inhabitants. Most of the urban politics are concrete, focused on the local issues and lead by the local people. The people are becoming aware of the power of their voice which enable political subjects to express their opinions even without being part of the formal political system. For Sassen (2007) these are signs of new kinds of political opportunities. Today we face new possibilities to act, and people that are “not authorized” can be active and present in a global city.

In the globalized world processes of formation of a global civil society emerge: there is a shift of public spheres anchored in national institutions and societies territorially limited to a public sphere formed by systems of media. “This media system includes television, radio, and the print press, as well as a variety of multimedia and communications systems, among which the Internet and horizontal

networks of communication now play a decisive role” (Castells, 2008, p. 89-90). It includes the mass self-communication, that is, “networks of communication that relate many-to-many in the sending and receiving of messages in a multimodal form of communication that bypasses mass media and often escapes government control” (Castells, 2008, p. 90).

Internet allows connection for various networked local events occur in different parts of the world – network is global while events are local. The new initiatives include the Occupy Wall Street initiative, and Stuttgart 21, both supported and initiated by the new social media. The Occupy Wall Street spread around the Northern America (Occupy Florida, Occupy Washington) with similar initiatives created in numerous European cities (Occupy London, Occupy Frankfurt, Occupy Hamburg). Stuttgart21 is an urban development transportation project initiated by the politicians to modernize the link between Paris, Vienna, and Budapest. Since 2009 numerous protests against the disputed project have taken place in the city of Stuttgart, Germany. New geographies are formed exploding contextual limits and boundaries between localities and previous hierarchies of scale (Sassen, 2007).

We may consider that the public sphere is not limited to media or public places for sociospatial interaction, but as Castells (2008) states, it is the cultural / informational repository for ideas and projects that feed the public debate, where the interaction between citizens, civil society and the state happens. The public sphere has become hybrid as it incorporates virtual and geographical spaces and traditional and social media. In digital culture, the distance is measured differently: access to digital spaces where transactions, social and political interaction, academic and cultural activities occur, is measured by "clicks" or "at the touch of a button" (Devriendt et al. 2008).

The process of cultural convergence and technological progress, made possible by the emergence of portable devices, with unlimited access to cyberspace and sensitive location, brings side by side virtual geographies and physical arrangements of cities, one influencing the other. In this case the citizen is in the real city, but also in cyberspace, since the devices allow her to access the digital world and send information about her activities or perceptions of the physical world into the virtual world. In other words, in the “real world” now, there are no separations between digital / virtual and physical / real as the citizens use these two social environments simultaneously.

At the same time the citizens are able to register and disclose their impressions that can be anchored in the city itself. Planners must recognize that now the citizens’ urban experience is not only influenced by urban form but by different media and forms of communication with which they interact daily.

In this context, Internet is not only a support element and technological mediation. It also works as an environment for information, communication and action within multiple and heterogeneous systems (Palacios, 2006). For their part, cellphones provide movements that are born and flow into physical encounters, spreading information and feelings exponentially, a kind of effect from "small worlds". Networks of trust are formed instantly as the person who receives the message identifies its source and starts to distribute it based on its own address book - the "small world" doing the big movements we have seen also on the streets of our cities (Castells, 2009).

This hybridism, an imbrication between geographical space and cyberspace, affects the concepts of public space and public sphere whatever definition we give to the terms. Social networks are now the space in which people connect, communicate,

exhibit themselves, interact, and invite other to flock to the streets, squares, every public or almost-public spaces, like shopping centers that Bauman (2001) named as public but not civic spaces.

3 Creating Spaces for Collaboration and Citizenship

The categories of "public", "public space" may incorporate the possibilities of collaboration and participation in everyday life that portable devices such as smartphones or cell phones already enable. Technologies that add layers of data and information to the urban areas of large cities are already available: geotagging, municipal public WiFi, augmented reality, mobile social networks, intelligent infrastructures. What still needs to be improved are the concepts and applications which city dwellers can design and implement for their needs. The main current use of these technologies is intended for consumption, and marketing. The so-called "locative media", an association of data and digital information in specific areas, have been used to deliver advertising and consumer associated place. This includes some personal information as well as location: who are you (your preferences or history of consumption) and where are you (what do you can consume and where). Besides receiving data, people also transmit data - location, messaging, diverse media. These data and information, in addition to increasing individual consumption, can expand to support the processes of participation and social interaction.

The emergence and consolidation of a digital technology culture brings new discussions about forms of representation of urban space (Sassen, 2001) that should address the representation of contemporary economic, political and cultural events and processes that exist either in real or in virtual world by putting into question the establishment of boundaries between physical and digital.

An urban digital model faces the question of time, because the model is a portrait of the city at a given time and the cities are dynamic organizations that grow and transform, so the model becomes a picture dated and increasingly distant from reality unless it was updated on an ongoing basis, what could be done by sensors, volunteering geoinformation (VGI) or crowdsourcing. Digital serious games (Michael and Chen, 2005) can potentially add new dimensions in the representation of the reality, and aim to educate and support learning about the environment and urban planning initiatives. The majority of them use highly dynamic and interactive virtual spaces in which the participants take on different roles; they can be immersed in the system and suddenly part of the digital reality in a completely new way. The reality is often represented in 3D or sometimes 4D spaces. Incentives such as awards, money, collected points are integrated in the concept of a game to motivate the participants to get involved and to participate in the game environment. Digital serious games are a novel, innovative research area in urban planning and participation and their potentials still need to be explored, in research as well as in the practical implementations (Poplin, 2011).

Digital representation of the world is now available on handheld devices that can be carried in the pocket and accessed (almost) anywhere providing ease collaborative mapping and crowdsourcing, use of geographical and social networking applications on mobile devices, applications of Augmented Reality, to name a few possibilities.

Nowadays we can find platforms developed to promote easy navigation through data, maps and services, as in case of Urbanflow Helsinki (<http://helsinki.urbanflow.io/>) or to create a big database with environmental data automatically collected associated to individual subjective perceptions about it, as does the European EveryAware project. (<http://www.everyaware.eu/>), both can improve interaction with and within the public urban space, whether physical or digital.

The representations of social and demographic aspects in cities are traditionally based in aggregation of individuals or households in areas defined and evenly represented (census tracts, for example) or physical addresses of individuals (commercial databases). They are topographical representations that provide the basis for the social representations.

Digital representations based on the geometric description of physical aspects of cities have enormous importance for a large number of activities in architecture, engineering and urban planning. They capture important aspects of everyday life and the emergence of new types of public space. Although they seem not be enough anymore.

For Bruno Latour (2010), traditional forms of representation of the social start from the idea that the whole is greater than the parts, the society is more complex than the individual. Thus, from atomic individuals they imagine a second level where collective phenomena take place (Latour, 2010). The reason was the previous lack of information, the discontinuity in available data, says Latour. The multiplication of digital data has rendered collective existence traceable (back and forth), micro and macro being just two faces of the same coin (Latour, 2010).

In face of this, now, although the usual forms of treatment of data and information remain relevant, contemporary digital social networks begin to play a structural role in society and must be incorporated in urban social representations. That can be viewed for instance at <http://twittervision.com/> where tweets are mapped in real time, overlapping a cyberspace representation with a topographical representation.

Focusing on online platforms, it's worth seeing some results of the research project "Web platforms and collective action: the complementary roles of proprietary and non-proprietary platforms", from University of Westminster (Parker, 2011). They pointed out that proprietary social networking platforms like Facebook are not enough to widespread political mobilization. They have been complemented by platforms tailored for activists' needs (Parker, 2011). The project guided by Anastasia Kavada from Communication and Media Research Institute verified that the possibility of accessing personal data seems to be a problem for political groups. These tools are also limited in establishing conversation between persons that are not connected as "friends" but share commons political interests.

On the other hand, platforms specialized to deliver functionalities for discussions, collaborative editing of documents and decision making, as the open source platform Craggrass (<http://craggrass.riseuplabs.org/>) are not able, alone, to spread the political mobilization (Parker, 2011).

Some of these platforms incorporate functionalities that aim to support the process of participation via Internet: Infotoolkit (www.infotoolkit.org/) includes the community communication management and ePart (www.epart.it/) provides monitoring of public administration actions to respond to the citizen demand. The initiative Protect the Human (www.protectthehuman.com/) initiated by International Amnesty includes the two concepts: the concept of social networks and the concept of group organization.

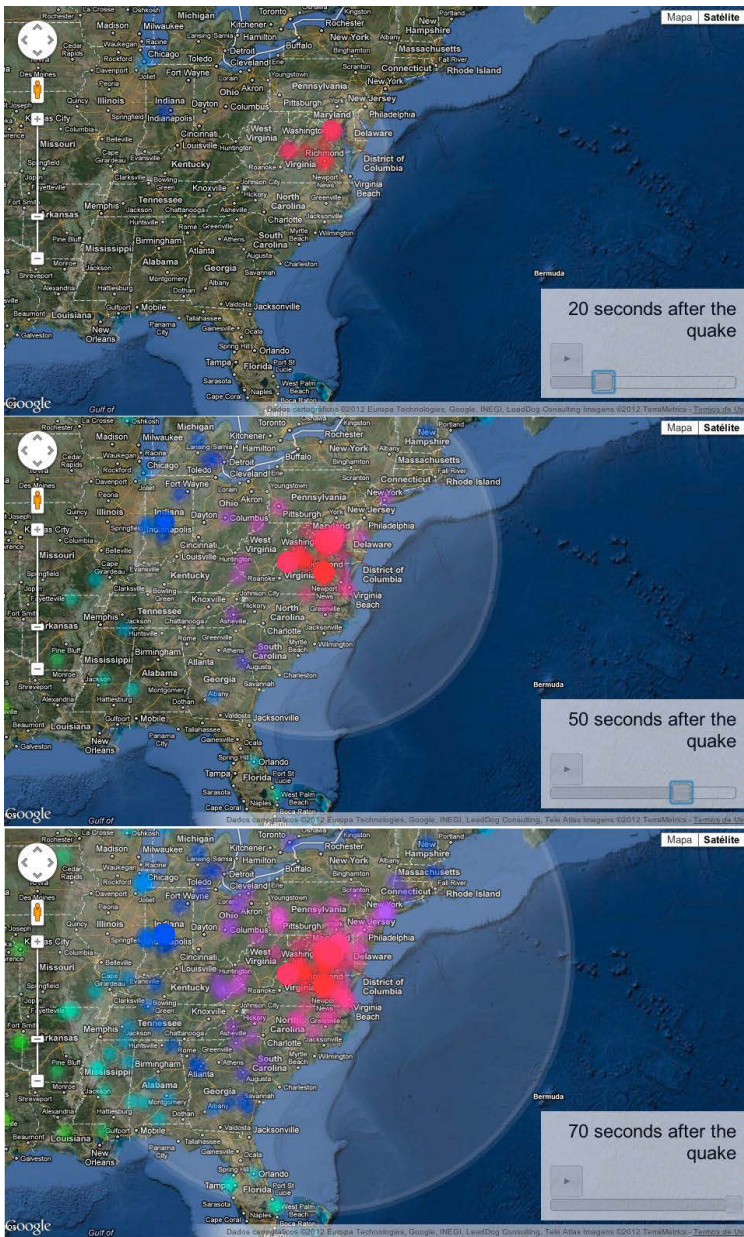


Fig. 1. Tweets after the earthquake in Virginia (http://online.wsj.com/article/SB10001424052970204138204576598942105167646.html?mod=ITP_review_0#articleTabs=interactive&project=TwitterVerse1001)

Crowdsourcing has established as an exemplary way for collecting and sharing valuable information with relevant social purposes, as seen in the climate and

environmental disasters monitoring – Haiti, Rio de Janeiro and Fukushima are examples. Other example can be seen on the map of tweets about the earthquake from Virginia in August 2011 (<http://blog.socialflow.com/post/7120244132/all-shook-up-mapping-earthquake-news-on-twitter-from-virginia-to-maine>) and on Figure 1.

Vis-à-vis the present emphasis in collaborative collective movements we are tempted to relate the notion of open knowledge with a civic use of the cyberspace. In this way public participation today may be guided by a model of open citizenship involving spaces shared with the aid of social media's use.

Faced with this we must also consider the limitations of platforms for online participation related to the views of those who develop them. In her blog, Smith Catherine Howe (2011) brings the opinion of Lawrence Lessig in Code v2 about three generations of these platforms on the Internet. The first one did not have commercial objectives; it was created by researchers and hackers focusing on building network. The second one was built by the people or organizations with commercial interests. The third could be a government product. Lessig already posed these questions: Which of these regulators do we prefer? Which of them should be controlled and by whom?

Today we have more to worry about. Currently online search engines are configured according to the user's participation, albeit unconsciously, through the popularity of terms, the relevance of keywords linked to other sites that the user uses in the process of participation. Not to mention the action taken by Google since December 2009 to filter search results for the same term according to what it considers to be the most adequate for each user, even choosing the language of the presentation and information on behalf of the user. We face the situation in which the corporation decides in the name of the individual user which information to hide, and which content may be displayed for her.

Despite the lack of transparency and control over the code embedded in the commercial software, people are still populating the cyberspace and creating civic spaces online – spaces that support the user's motivation to speak and collaborate with her community or with a wider public space with which she identifies herself. To make these civic spaces truly open and democratic, the government would have to start thinking not only in its own interest in governing (Howe, 2011), but also about the citizens and their wishes and needs.

4 Emergent Initiatives, New Opportunities

Everything involving access and mobility in the city is correlated with power of individuals and groups derived from their social, economic and politic position. The assessment of real impacts of the web citizenship and an assessment of the power of groups and individuals is a subject of empiric studies.

Some recent initiatives in public participation concentrate in attracting specific groups. They consider the differences in the perception and interests among different groups. We can observe the differentiation of the goals and concepts of such initiatives trying to attract specific groups addressing their particular needs and wishes. For example, the "British Youth Council" has launched its new platform "Youth on Board Awards" (<http://byc.org.uk/get-active/youth-on-board-awards.aspx>) and an award scheme that encourages young people and the organizations to participate. Their aim is to encourage young people to participate and express their opinions. Voice,

Inclusion, Participation, Empowerment, Research (Viper) is a project which aims to identify the best ways for young disabled people to participate in decision making about their lives and the services they can use in public spaces (www.councilfordisabledchildren.org.uk/what-we-do/work-themes/participation/viper). The virtual spaces designed for specific groups differ from the spaces designed for the general audience; the advantage is that they can potentially address the needs and wishes of this particular group better than some generic approaches.

The emergent initiatives can amplify and diversify opportunities for people to engage in actions that positively influence the public administration towards a better quality of life. It may be that these online experiences will accommodate various subjective dimensions and establish a new public space multifaceted based on phenomena of a “small world” as those exposed by Castells (2009).

Each case of participation and creation of new virtual spaces and networks must be examined according to its own characteristics. Serge Proulx (2011) suggested that we should deconstruct stereotypical ideas about a supposed “revolution 2.0”, and we should not deterministically assume that Internet has a supposedly liberating function, as so-called “cyberutopists” would do. Anyway we can say that developed platforms with ever more ubiquitous technologies, easy to use and economical, together with the emergence of a digital culture brought about by the advent of the so-called Web 2.0, are powerful auxiliary instruments of participatory planning, allowing the user to view and interact with contexts, with the data, and may incorporate the temporal dimension in the analysis of space. Therefore, it is possible to use such resources in the assessment of scenarios, discussion of alternatives in favor of sharing ideas and even to experience their ability to stimulate citizens to establish social, civic and democratic interactions, as a kind of Internet-mediated governance.

During the Future e-Democracy Forum, in London, in December 2010, Catherine Smith Howe, talking about government and crowdsourcing, challenged the widespread idea that crowdsourcing is always good. According to her, the crowd is reduced down to the lowest common denominator, the government is slow and does not perform well in the network society (Digital Government & Society, 2010). Furthermore crowdsourcing is not good “at longitudinal effects as citizens respond more to present issues” (Digital Government & Society, 2010). According to her, the crowdsourcing per se does not necessary lead to good solutions. Gez Smith, on the other hand, said that it could possibly work, as in case of public consultation, but it is “important to know how to set the questions, how to handle and make sense of the data that come in” (Digital Government & Society, 2010).

Collaboration between government and society seems more common today, particularly in case of emergency mapping. In the case of USGS (<http://earthquake.usgs.gov/>), the American geological service seems to be able to take advantage of data provided by citizens. Unfortunately this kind of collaboration is not always successful in other fields. It might be emerging from public services devoted to environment because of the already long tradition in discussing climate changes, supported above all by a wide network of scientists well connected to the environmental activists and celebrities that easily get the attention of the media and the audience as Castells (2009) exposed in the book titled *Communication Power*. Even e-Participation platforms that are simple murals of complaints may turn into civic spaces for web citizenship providing a creative space of shared practices thus becoming a place for the open knowledge construction and democratic improvement.

It can be argued that the current characteristics of the new online spaces may be an incentive more than an obstacle for promotion of social interactions and social actions, in part due to the architecture of the software used. In any case, social networks and other social media give chance to retrace the way how actors and social movements are associated over the territory. Individual and collective, micro and macro actions are visible in this way, showing how the world behaves at a certain time.

Practices of collective creation, sharing of ideas, creation based on quotes, remix culture, commons (something that everyone owns and can be used by everyone) that are held and used by many people, are impregnated with value and ethics which are the fundamentals of networked communities. Those fundamentals and practices can be spread by social networks through digital space improving cultural openness.

Sons and daughters of immigrants are now using the multimedia features present on the Internet to make themselves heard, to show how they are integrated and claim their right to full citizenship. In the post "Sono già connessi i nuovi nostri concittadini", Giampaolo Colletti (2011) shows how web radio and web TV are being used to promote the positive identification of the immigrant community in Italy. Radio Asterisco (www.asterisradio.com) deals with Bologna city services and predominantly uses the Italian language, but also inserts in French, Chinese and Spanish languages. Rete G2 (www.secondogenerazioni.it) was born in Rome in 2005 and spread to other Italian cities. It asserts itself as a nonpartisan network of "world citizens" from several continents. It promotes physical and virtual meetings, bringing together people working for the recognition of Italian citizenship of sons and daughters of immigrants and refugees.

Considering that local interactions can influence the overall network as the actor-network theory proposes (Latour, 2011), we could have expectations about a plausible scenario where many people – mainly supported by social media – are able to choose ideas coming from different cultures and take what they find most appropriate for each situation. We are all immigrants now, says Peter Burke (2009), borrowing the idea of Néstor Canclini that says "the border is everywhere".

Knowledge produced in a new way – pervasive, contextualized and unplanned – will help to develop social activism even further. This gives an opportunity to a higher level of public participation. Largest groups will be able to access larger sets of data and information, of knowledge and shared experiences, using geography as a way to organize information and also search and view information with a geographic footprint (Craglia et al., 2008). In this way we might experience a citizenship model where local government and public administration represent just nodes in a decentralized network whose topology responds to demands for greater public participation and democracy.

Acknowledgements. Gilberto Corso Pereira work were partially supported by Coordenação de Aperfeiçoamento ao Pessoal de Nível Superior.

References

1. Bauman, Z.: *Liquid Modernity*. Polity Press, Cambridge (2001)
2. Burke, P.: *Cultural Hybridity*. Polity Press, UK (2009)

3. Castello, L.: *Rethinking the Meaning of Place, Conceiving Place in Architecture-Urbanism*. Ashgate Publishing Limited, England (2010)
4. Castells, M.: *The New Public Sphere: Global Civil Society, Communication Networks, and Global Governance*. The ANNALS of the American Academy of Political and Social Science 616, 78–93 (2008)
5. Castells, M.: *Communication Power*. Oxford University Press, New York (2009)
6. Colletti, G.: Sono già connessi i nostri nuovi concittadini,
<http://www.apogeeonline.com/webzine/2011/07/26/sono-gia-connessi-i-nostri-nuovi-concittadini> (access in: January 25, 2012)
7. Craglia, M., et al.: Next-Generation Digital Earth. *International Journal of Spatial Data Infrastructures Research* 3, 146–167 (2008)
8. Devriendt, L., Derudder, B., Witlox, F.: Cyberplace and Cyberspace: Two Approaches to Analyzing Digital Intercity Linkages. *Journal of Urban Technology* 15, 5–32 (2008)
9. *Digital Government & Society: Future e-Democracy*, London (2010),
<http://digitalgovernment.wordpress.com/2010/12/17/future-e-democracy-london-2010> (access in: October 5, 2011)
10. Howe, C.: Lex Informatica. Curiouscatherine's Blog. Blog. (July 03, 2011),
<http://curiouscatherine.wordpress.com/2011/07/03/lex-informatica/> (access in: August 7, 2011)
11. Howe, C.: Space, Place and an exploration of term hyperlocal. Curiouscatherine's Blog. Blog. (August 30, 2010), <http://curiouscatherine.wordpress.com/2010/08/30/space-place-and-an-exploration-of-the-term-hyperlocal/> (access in: January 4, 2011)
12. Latour, B.: Networks, Societies, Spheres: Reflections of an Actor-network Theorist. *International Journal of Communication* 5, 796–810 (2011)
13. Michael, D., Chen, S.: *Serious games: Games that educate*. Train and inform: Course Technology PTR (2005)
14. Palacios, M.: A Internet como mídia e ambiente. Reflexões a partir de um experimento de rede local de participação. In: Maia, R., Castro, M.C.P.S. (org.) *Mídia, esfera pública e identidades coletivas*, pp. 229–244. Editora UFMG, Belo Horizonte (2006)
15. Parker, T.: Mix of Tools Needed For Online Activism, Research Finds. *e-government Bulletin* (May 16, 2011), <http://www.headstar.com/egblive/?p=879> (access in: January 24, 2012)
16. Poplin, A.: Playful Public Participation in Urban Planning: A Case Study for Online Serious Games. *Journal: Computers, Environment and Urban Systems* 36(3), 195–206 (2012), <http://www.sciencedirect.com/science/article/pii/S0198971511001116>
17. Sassen, S.: The City: Between Topographic Representation and Spatialized Power Projects. *Art Journal* 60(2), 12–20 (2011)
18. Sassen, S.: *A Sociology of Globalization*. W.W. Norton, New York (2007)
19. United Nations: E-Government Survey 2010. Leveraging e-government at a time of financial and economic crisis. UN Publishing Section, New York (2010), http://www2.unpan.org/egovkb/global_reports/10report.htm (accessed in: September 20, 2010)
20. United Nations: United Nations E-Government Survey 2012. E-Government for the People. United Nations, New York (2012), http://www2.unpan.org/egovkb/global_reports/12report.htm (accessed in: March 16, 2012)
21. UN-HABITAT. 72 Frequently Asked Questions about Participatory Budgeting, United Nations Human Settlements Program, UN-HABITAT (2004), <http://www.internationalbudget.org/themes/PB/72QuestionsaboutPB.pdf> (accessed: January 15, 2012)

Ubicomp and Environmental Designers: Assembling a Collective Work towards the Development of Sustainable Technologies

Renato Cesar Ferreira de Souza

School of Architecture of Federal University of Minas Gerais - Brazil, Rua Paraíba 697,
Bairro Funcionários, Belo Horizonte, CEP 30130-140
rcesar@pesquisador.cnpq.br

Abstract. Case studies are presented pointing out problems that probably slower the development of UbiComp and Environmental Computing. A place-theoretical framework was developed in order to correlate both creativeness and technical routine for helping Computer Scientists, Mechatronic Engineers and Environmental Designers such Urban Designers and Architects to work together, overcoming their different languages of their fields. Future research is drawn aiming to improve the framework as to achieve more sustainable products and services concerning the urban scene.

Keywords: UbiComp, Urban Design, Architecture, Environmental Computing, Computing Science.

1 Introduction

By the 1990s most of the Designers of UbiComp Systems was guided either by commercial opportunities or simply technological and industrial conditions to create new but useless gadgets, as pointed out by Thackara [1]. In that moment, the technology seemed to be boosted by itself. It looked as being always easy to evolve a step forward with some new innovation in the design. According to Thackara that was a dilemma, because what was created was based only in the fact that the Technology and industries permitted it. However, it had nothing to do with real life necessities. Concerning the improvement of qualities of urban and architectural places, the question was: how users could use spaces and common daily objects designed as interfaces to access computational capabilities installed in the places as to improve activities and user's lives?

Recognizing the difficulty of integrating Information Technology (IT) and Urban Design, Eamon O'Neil [2] stated that to build UbiComp systems for cities, "*we have no fundamental theory, knowledge base, principle methods or tools for designing and building ubiquitous computing systems as integral elements of the urban landscape.*" He claimed to extend and adapt the understanding and practice of both Urban Design and IT Design solutions through new research works. A systematic approach to IT Design in the urban environment, such as an integrated system of physical

Architecture and IT would demand an amalgamation of disciplines as Architecture, Urban Design, Computer Science, Geography, Engineering, among others. But the key to this interdisciplinary integration was the concept of space, not only in terms of physical location or volume but also taking into account the social phenomena, and the conventions and values attached to a particular physical place.

Since 2004 I have researched the possibility of developing a place-theoretical framework for applying Ubiquitous Computing (Ubicomp) in urban spaces [3]. This theory intended to inspire professionals in the early stages of projects supported with IT components and services as UbiComp systems. It should provide two main tools: first, it should give a common language to Environmental Designers, Computers Scientists and others Engineers and professionals involved who hypothetically should work together. Secondly, it should focus on how Information Technology devices and services could solve spatial conflicts between human activities and missing spatial elements in places.

With the support of the School of Architecture of The University of Sheffield, United Kingdom, I started the research with two considerations: in the last 15 years, a growing crisis in the concept of space and place had caused poor contributions of Environmental Designers for the UbiComp debate; secondly, the mechanical paradigm in the understanding of what Information is had embarrassed the thinking about the correlations between place and IT.

2 Crisis of the Concepts of Place and Space

To Malcolm McCullough [4], Environmental Designers should become aware of the challenges and opportunities raised by UbiComp, and they need to be discerning when it comes to the spurious terminology that has spread across this field. To that author, the physicality of places is the context that supports the application of computational resources in the space. However, as it happened with many other words in the field, the term 'Ubiquity' has become overexposed and had come to mean just about anything having to do with universal connectivity. Thus, UbiComp was assumed directly to cause social and spatial change in a simple and linear way. Since information would be available anytime and everywhere, and the entire world will be connected through networks, physical distance, as a socio-economic and cultural constraint, will disappear. Consequently, a geographical dispersal of metropolitan regions will happen, or even the effective dissolution of the city [5]. As the life and fluxes of the urban centres are gradually substituted by some universalized and interactive technique of communication, large metropolitan nuclei will gradually become a technological anachronism. In addition, the convergence of virtual reality technologies (VR) associated with powerful networks will transform all the relations that were once made through place-base interactions with 'virtual' ones, decreasing the importance of real places. Thus, immersive technologies will create electronic spaceless cities in which VR will allow the construction of life-like 3D environments. 'Virtual spaces' will finally substitute physical places. In conclusion, human societies, cultures and economies will migrate into the electronic environment, where it will be possible to construct identities with flexibility, accessing all services from any location, at anytime, sharing the

experience of endless fantasy worlds. The very concepts of material space, place, time and body are irrelevant from this point of view.

Therefore, the universalist understanding of that term overlooked the value of Architectural and Urban Design contexts. The importance of the real space has been reduced and Environmental Designers has been conditioned into an outlook that marginalized the new operations and requirements that IT brings to the built environment.

By 1990s, 'techno-futuristic' waves of enthusiasm had created many lame metaphors for IT pervasiveness - for instance, the idea related to the anytime-anywhere uniformity of services resulting from Ubicomp. Since those metaphors are now outmoded, Environmental Designers can finally contribute to the evolution of the field through research into new approaches that allow for the inclusion of located peculiarities without detracting from physical characteristics and user requirements.

Regarding the buildings as interfaces between place and information, Pawley [5, 6] appealed to Architects for a new way of applying IT in their projects, focusing on the real interactions required by people's activities. Taking the same perspective, Shafer [7] stated that the search for an IT Design process that considers meaningful interactions with people and places is the central problem for this emerging field. Similarly, Sengers [8] argues that the design of IT solutions for urban areas requires an understanding of spatial and social organization in order to incorporate the meanings engaged.

To break with the crisis of the concept of space and place, I took two thoughts as contributions: the ideas from the German Philosopher Heidegger about space [9] and the ontology of place's qualities, developed by the Brazilian Professor Maria Lúcia Malard [10]. First, however, I would like to connect them with Mark Weiser [6] thoughts, once was he who created the term Ubicomp by 1990s and in that time gave clues about the relation between space and Technology.

Weiser summarized the idea of Ubiquitous Computing deeming that the most profound technologies are those that disappear in our consciousness. *"They weave themselves into the fabric of the everyday life until they are indistinguishable from it"*[11], explained. He exemplified it using trivial facts as machines which are integrating our lives nowadays, as cars, phones and others. This concept allows us to understand, specifically through Heidegger's thoughts, the consequences of a common vision about Technology, at the same time helping us to review spatial implications for the human being associated with the built environment [9]. To Heidegger [12], the term *"ready-to-hand"* points out a kind of entity that was turned into equipment by means of human labour. On the other hand, elements of nature are *"present-at-hand"*, which means they are not for a specific purpose, but when human being applies over them some labour, they are turned, then, into equipment. The essence of equipment is being for something, which means, its essence is its finality. If we consider places as a result of human labour in the space, we can say that they are equipment and their essence is being for dwelling.

When *"ready-to-hand"* object is genuinely effective, it becomes *"transparent"* [13] and unnoticed for us. In this situation, we are not busying our mind with its immediate presence and our consciousness becomes a whole with the utensil we are using exactly by means of the usage. However if it breaks down and stop functioning, it starts occupying again our mind instead. Thus, it becomes visible for us again, conspicuous, requiring our attention to fix it. In the same way, dwelling is an activity

that, when the spatial elements work fine, the feeling caused in the dwellers can be compared with freedom as mentioned by Heidegger and quoted by N-Schulz[14-16]. A good manner to improve the place is looking for what kind of elements are missing or broken down, for they will be visible to us as “*present-at-hand*” objects. Therefore, we need to ask how concrete spatial elements play incorrectly in order to detect how they can really qualify places. But beforehand we will do describe the ontology of the place in general terms.

According to Mallard [10], it is possible to understand the qualities of places and its correlation with spatial elements as those that appear in the founding circumstances of it, when men/women differentiate space from place applying their labour on the former.

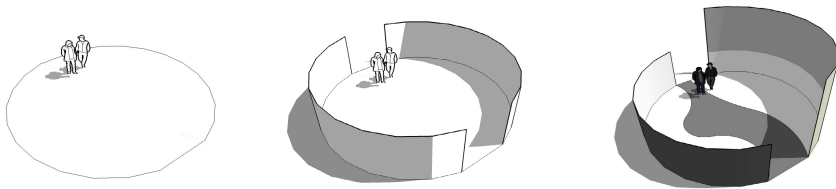


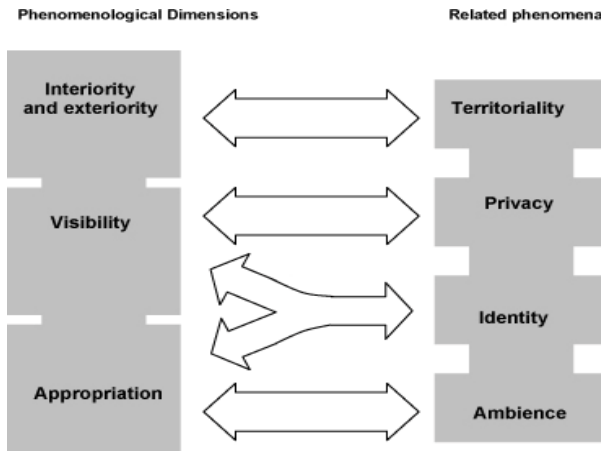
Fig. 1. Phenomenological dimensions in qualification of the space: inside/outside, visibility of limits and appropriation

The setting up of an inside/outside is a question of establishing boundaries that qualify space. Dwelling is to be inside (in a place) as opposed to being outside (the infinite space). From this opposition (inside/outside) emerges the characteristic of visibility. Any dwelling can be both, closed or open, visible or concealed, at the same time. Doors and windows make it visible and enable views to be enjoyed from within it. Walls conceal the dwelling but also impede the views that can be enjoyed from it. Finally, appropriation is the process of fully experiencing the phenomenon of dwelling, acting in manners that order the interior, when the dwellers take care of the place. These basic experiences are expressed by subjective phenomena that occur in the dwelling process, e.g., by behavioural issues such as privacy, territoriality, identity and ambience. Those four are, in fact, the qualities that I will consider in the place. If we are concerned to use places as interfaces to deploy UbiComp and use UbiComp to improve places, those qualities are the goals that the Designers should address to. I will summarize the relations between physical elements and the qualities of places in the Table 1 below.

Korošec-Serfaty [17] commented that the dwelling’s qualities corresponds to the result of the spatial changes made in the place to differentiate it from the abstract space. The differentiation process concerns of choosing, defining, marking and building. It is achieved by bringing up physical aspects of the place such as, for instance, building walls, positioning signals, indicating the demarcation of limits with spatial elements by means of fences and trees, and organizing the physical aspects of the interior. The qualification of the space corresponds to adding it up with all the spatial resources that enable human activities to be performed better. Therefore,

qualification corresponds to the involvement of the place with people’s activities and vice-versa. Once we understood this, we can try to establish a correlation between spatial elements and Information, but firstly we need to roughly draw a generic topology to specify types of spatial elements and how they can bring up the qualities as territoriality, privacy, identity and ambience, concretely.

Table 1. Physical characteristics and related qualities in dwelling



As in Figure 2, bellow, the interiority of a place is defined when enclosures (5) delimitate an internal area (2), which has a centrality (1). These elements qualify the place, turning its interior into territory. Simultaneously, the association of enclosures plus the entrances (6) control the manner through which the place is connected to the exterior, specifying its privacy and the way it can be visually identified from outside (identity). Human actions inside the delimited internal area in both horizontal and vertical directions (4, 3) would define simultaneously the identity and the appropriation, showing off how people care about that place, giving it attention and making its ambience.

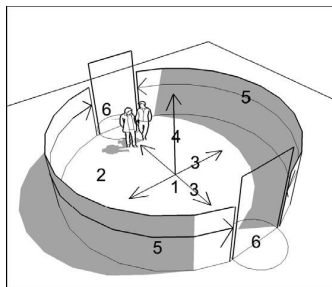


Fig. 2. Topology of spatial elements of places

This topology turns possible to explain how built places can be analyzed through similar categories of their elements, such as enclosures, centres, internal directions, and the others.

Accordingly to what was said before, this analysis put out how those elements can be correlated to the qualities as territoriality, privacy, identity and ambience (Table 1 and Figure 3). But we also need to correlate the components of Information Technology with this topology in order to use an Ubicomp system as to improve these qualities in places.

3 Changing the Paradigm of Information

Using the paradigm formulated by Humberto Maturana, who pointed out that the modifications that living systems do in the environment belong to a linguistic domain [18], it is possible to understand that the term “information” should not be used as its mechanical conception in Shannon [19], to whom it is a simply conveyer of meanings.

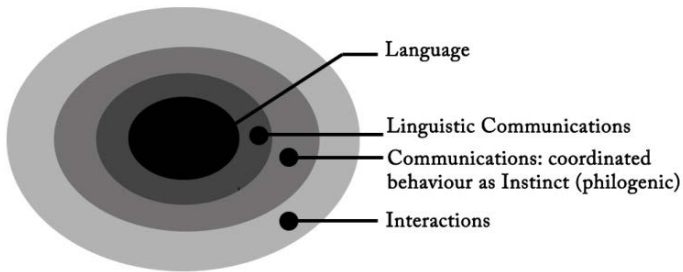


Fig. 3. Linguistic domains in the interaction between living systems and their environment [20]

Quite the opposite, spatial organization created by living systems in the environment is tied up with their skill to co-operate among them and adapt themselves to each other and to the environment. It is a kind of linguistic domain. Thus, the language, a human privilege, depends upon the concrete environment to create meanings [21]. Maturana [20] has exemplified the linguistics domains of living systems as shown in Figure 4. Hence, it is possible to infer that, by an external point of view, the physical characteristics of the environment, summed up with the history of its transformations, could be considered as part of a linguistic domain by an external observer.

The skill of a living system to modify its environment as to adapt it and survive could be understood as a particular kind of communicative behaviour, specified through the spatial interactions. Since the environment is modified by the systems that live on it, also could be said that this situation is “*communication*”. But does not mean that the space conveys “*information*”: rather, a spatial element is, itself, information [21].



Fig. 4. Illustrative comparison of the structure of different places. The topology explained beforehand, its interposed elements over St. Peter's Square, Vatican, and over a meeting in a park.

By “*spatial element*” we meant types of elements grouped into the topological categories compounding the places. A monument in a centre of a square could be a “*centrality*”. Also a man speaking loud, claiming for something, rounded by others hearing him could be considered a “*centrality*”. Thus, we are dealing with the phenomenon, the concrete happening of communication. Therefore, it would be possible to wonder how spatial elements could be correlated to IT components when we intent to reinforce the qualities of places.

4 Elements of Ubicomp

Components and functions of generic Ubiomp system, considering their spatial attributes (Figure 5), were firstly clarified by Steve Shafer in his seminal paper “Ten Dimensions of Ubiquitous Computing”[7]. Years later, McCullough [4], inspired by Shafer’s list, has enumerated ten essential components and functions by which Ubiomp can be studied. His description is a means to facilitate to Ubiomp Designers how they could refer to IT applied in the environment. The components of Ubiomp are a)microprocessors; b)sensors; c)process and devices for tagging; d)links to communicate; e)actuators; f)control process; g)displays; h)determination of fixed locations; i)software models; j) and tuning process.

Analyzing both classifications of McCullough and Shafer in terms of spatial characteristics it was possible to list their properties considering four space related categories, according to the relationship between IT components or service and the place.

So, an Ubiomp system has *1) elements to sense the place; 2) elements to modify and actuate in the place; 3) elements to represent the place; 4) the place itself, as a referential matrix, which should also be considered.*

In my research each Ubiomp component and service was analyzed accordingly with their potential applicability, by the study of their technical features and how they can modify spatial instances or topology of the places. In doing so, the spatiality of Ubiomp was described, putting out each component and relating its features to the topology of the place and describing how one of each can potentially be tied up with the qualities of territoriality, privacy, identity and ambience. The brief following summarization can exemplify it:

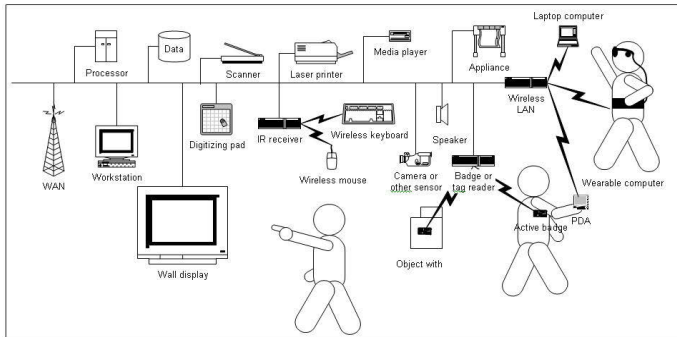


Fig. 5. Representative Elements of Ubiquitous Computing according to Shaffer[17]

Components to sense the place are all components and processes that sense modifications in the environment in terms of changes in some type of energy, transforming it into processed data and dispersing it to connected servers. Those components include microprocessors, sensors, tags, and communication links and all the spatial procedures where they are organized. To exemplify this category, we refer to the sensors, which function is to detect action in the place. They are electronic devices used to measure a physical quantity such as temperature, pressure or loudness and convert it into an electronic signal of some kind. They can act on place's territoriality by detecting when moveable elements are inside or outside of pre-established delimitations. They can act on privacy by sensing proximity, invasion, or permitting surveillance and informing when an action is needed to react against invasion. They can interfere on place's identity when they provide visual identification of users, according with user's status given by electronic tags. They can also permit users to visually identify specific elements according to embedded electronic tags. In terms of appropriation, sensors can act on Identity by sensing mechanical movements in the adjustment process when people tune the system, permitting to know the user preferences while appropriating the place. Also modifying the ambience, they can help to collect information about changes in temperature, pressure, light, permitting automatically trigger action to tune the system.

Components to modify the place are a group of elements to physically actuate in the place. They intervene in the environment physically by delivering some types of energy, and are named actuators, controls process and displays. To exemplify this category we mention the actuators. Probably, the idea of actuators is the most popular among Architects who sometimes dare including robots and programmed mechanisms in their projects. An actuator is the mechanism by which an agent acts upon an environment. The agent can be either an artificial intelligent agent or any other being, autonomous or connected online. They can interfere on territoriality by the servo mechanic adjustment of territorial enclosure such as doors, walls, ceilings and canopies, floors, directions in the internal area, fences, and delimiters. Openness and visual barriers also can be controlled by servomechanisms, providing adjustments in privacy. With the adjustment of the visibility of some elements, they can act on the identity by changing enclosure shapes and textures. Adjustments of physical elements according to conditions demanded by user's occupation, weight, physical efforts,

movements, can also act on identity, interfering on appropriation of the place. Finally, when they act providing self cleaning functions and self adjustment of comfort conditions, like openness, wind and sound barriers, they interfere on the ambience.

Components to represent the place are a group of elements that exhibit the place in terms of model to adjust the whole system by processing data collected on it, simulating and predicting patterns of modifications in the place. They include the techniques related to determining fixed locations, designing and using software models and all tuning process of the system. Fixed locations correspond to strategic positions in the place through which information will be strategically gathered or delivered. They are referential points in physical world important to the geo-reference of the whole IT system. Software model is a list of prescribed behaviours (algorithms) that the system can deal with. It informs mainly how sensing and acting has a closed correspondence, prescribing expected outcomes. Some models can include artificial intelligence, accumulating information about the environment and the users by learning them and exchanging data online. The tuning process refers to all sorts of services and devices that enable tuning the IT gears in the place. Such adjustment comprises defining scales of sensitiveness, accuracy of software models to represent the phenomena (events), and adjusting the physical presence of gadgets in located positions.

The place itself is a geo-referential matrix, with the aforementioned components. It includes the events organized though the topology of the place. It consists of a set of parameters that guide this analysis.

Table 2. A sample of correlation between an IT component and the qualities of a place[3]

	Territoriality	Privacy	Identity		Ambience
	Interiority and exteriority	Visibility	Visibility	Appropriation	Appropriation
Sensors detect action, measure physical quantities such as temperature, pressure or loudness and convert it into an electronic signal of some kind.	Related to interiority, for instance, when they are able to sense whether a moveable element is inside or outside a pre-established territorial delimitations.	Sensors are related to privacy by sensing proximity, invasion, thus permitting surveillance, and informing when an action is needed to react against invasion.	Sensors could permit Identification of visible users according their tag. They could also Permit users to identify specific elements according to specific concerns.	By the use of 'gesture sensing' technology, they could Sense mechanical movements, adjustments in order to tune the system, distinguishing how the user appropriates the place.	These could integrate systems in order to sense changes in temperature, pressure, light, when the user tunes the system, allowing information about how the user appropriates the place to be gathered. These would permit the creation of collections of info about those variables in order to trigger actions.

Using the previous concepts, the framework was accomplished as to help Designers deploying IT components and services within the place while dealing with Ubicomp design. Used in the early stages of urban projects, the framework consisted by asking the Designers to identify conflicts between spatial elements and the

activities that those elements should support. For instance, while identifying how a missing element plays as part of the topology of the place, it was possible to interpret how it was interfering in the four qualities. Then, the Designers established how it could be articulated to the space within a system to support the affected activities, improving the qualities of place.

5 Supporting Projects in Brazil

By the years of 2005 to 2007, three projects of urban refurbishments were made by Architects in UK using the described framework that I had developed. I studied which limits were imposed to qualitative solutions when the approach here described was partially used or used in its integrity by the Designers' groups. The analyses of the outcomes has demonstrated that, when entirely applied, the framework permitted the creation of solutions with less physical interferences, less intrusive spatial recasts, with the reduction of physical and expensive refurbishments. Ubicomp systems designed also were robustly supported and embedded accordingly to local characteristics.

Those experiments confirmed Mark Weiser's ideas: when an Ubicomp system is designed according to the logic of activities and spatial structure of a place, then physical interferences can be minimized and the technology applied tends to "disappear" in our consciousness. Otherwise, when this not happen, the solutions look only as an exhibition of the technological apparatus without a logic concerning local qualities, and so they imprint a feeling of discontinuation in the environment, ruining the function and fruition of the activities in the place.

Since 2008 I have ran a module in the Architectural Master Degree course at University Federal of Minas Gerais using the described framework. It is called "IT applied in Urban Design". The Architects are called to create Ubicomp systems to provide solutions in housing refurbishment projects, which they choose within the county of Belo Horizonte.

After deciding which area they would study, they should identify conflicts between local activities and missing or malfunctioning spatial elements. After that, they should interpret the conflicts according to following table:

Table 3. Interpreting conflicts

Categorization/ name	Conflicts description	Affected qualities				Spatial elements	Documents References	Frequency (M,A,E)	Location (P,S)
		T	P	I	A				
a	b	c				d	e	f	g

Each field should be fulfilled with:

“a” field: Categorization or name of the identified conflict. It is a name given as in the expression ‘spatial element X (versus) activity’. According to Malarð [10], this ordination is to emphasize that the analysis should focus on spatial elements and activities only, avoiding interpretations that consider conflicts between two or more activities or considering the conflict as a social category only. Activities cannot be interpreted as being in conflict with other activities; otherwise the analysis does not reveal the missing spatial element;

“b” field: This field contains the description of the conflict. It consists of an interpretation of the evidence for the stated conflict. That interpretation is made based on documents gathered in loco, such as reports, photos, video-footages, and interviews with the users and so on. All the registers indicating the conflict may be regarded as important to the interpretive activity.

“c” field: This corresponds to the four fields as to specify affected qualities of place. Once one conflict is described, it will be analysed in terms of how it affects territoriality, privacy, identity and ambience, by means of an analysis of how it is related to the components of place (i.e., enclosure, internal areas, internal directions, centrality and entrances). More than one quality could be interpreted as being affected by just one conflict. The register of that interference is made by ticking one or more of the columns. The four categories of qualities of place are a means to simplify and organize the interpretive method and are based on an analytical ontology of the place as an organization given by the interiority/exteriority, visibility and appropriation phenomena;

“d” field: Field to state the spatial element missing or malfunctioning. This corresponds to the realization that either a spatial element is missing or a spatial condition is obstructing the activities;

“e” field: Fields to relate documents to the analysed conflict. These are organized by indexing the records of the conflict, and constitute the basis for interpretation of that conflict. They could be pictures, interviews, reports or other documents, gathered in the period of the project;

“f” field: Field to interpret the frequency of a conflict. It reveals the period of the day time in which the activity is being affected by the conflict (morning, afternoon or evening);

“g” field: Field of location of the conflict. Considering the possible existence of internal areas hierarchically organized in the place, this column tells whether the observed conflict takes place diffusely or occurs punctually. This is meaningful when it comes to analysing urban precincts, as they can be taken to be portions of a bigger area.

After, the students were given the Table 4, casting some IT components according to the classification of Ubicomp by McCullough[4]. IT components and the elements of the place (enclosure, centrality, internal area, directions and entrances) were, thus, analysed within the context of the same principle that is expressing their spatiality in terms of the same spatial conditions (interiority/exteriority, visibility and appropriation). Consequently, this method has permitted interpretations on how those components of Information Technology could be potentially and positively involved with the qualities of the place (territoriality, privacy, identity and ambience).

Of course this framework is not a mechanic method that automatically provides a solution just because those previous tables are supporting the process of thinking about Ubicomp components in the space concerned. Actually, the whole process consists of thinking about information in the space and it clarifies spatial correlations with information exchanged across local and non local activities. Once again, it is possible by using those tables to provide support, even considering the flexibility implied in any process of design.

Table 4. Information analysed according to the qualities of the place

		Territoriality	Privacy	Identity		Ambience
		Interiority / exteriority	Visibility	Visibility	Appropriation	Appropriation
Section A: Components to Sense the place	Microprocessors					
	Sensors					
	Tags					
	Communication links					
Section B: Components to act in the place	Actuators					
	Processes of control					
	Displays					
Section C: Components to represent the place	Fixed locations					
	Software models					
	Tuning					
Section D: Place Components	Enclosure					
	Horizontal directions					
	Vertical directions					
	Centrality					
	Internal Area					
	Entrances					

6 Examples

I will now roughly introduce some systems created in the Master Course of Architecture, by Brazilians Architects, highlighting some special features obtained by them. The Architects worked in the following urban places:



Fig. 6, 7 and 8. Views of PAMALS Village, some houses, the entrance and a touch screen to identify cars and pedestrians (from www.keypass.com.br).

PAMALS Village (aeronautic park and Military Village), at Lagoa Santa County: the place was built by 1940s and militaries and soldiers are the current dwellers. The Architects identified problems mainly related to territorial security and interior identity. The repetition of house formal patterns and the bad state of conservation of them also interfered in the ambience.

To provide identity in the façades it was proposed the use of coloured lights to illuminate them accordingly through an online system programmed by the owners. Also other simple devices to control security were used to make possible alternatives for surveillance online.

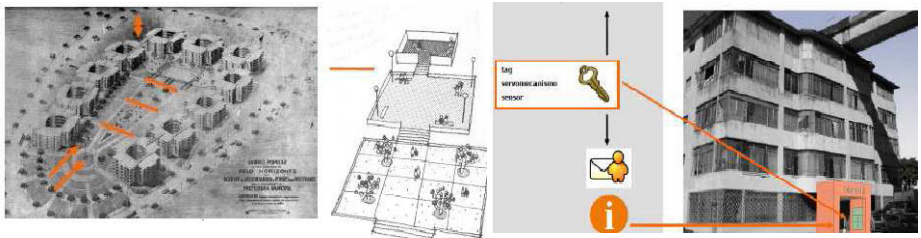


Fig. 9. At IAPI: physical recast to promote desobstruption and hierarchy in the external space, with a strategic surveillance; **Fig. 10.** Entrances to the buildings with a “Torii” Portal

IAPI Housing, at Belo Horizonte City: this is a massive Housing (Figures 9 and 10) built by the 1940s. It is plenty of conflicts, and the main problem described was the territorial definitions. Since the buildings’ design was opened to outside through

many entrances, the dwellers were exposed to strangers. Various solutions were developed by the Architects, since an Electronic Portal, with features to identification using online resources, until the recast of physical space with strategic online surveillance.

Estrela D'alva Housing, at Belo Horizonte City: built by the 1980s, this popular housing as well shown many problems, since those referring to territorial security until the collective parking. One of the solutions to this latter was tagging the cars with a chip and establishing a fixed sensor, connected online with a central of information in order to manage general resources of the housing.

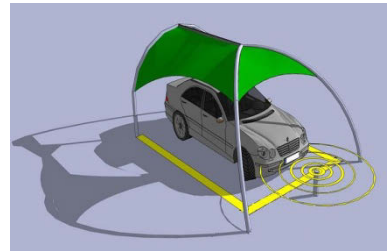


Fig. 11. View of the Estrela D'alva Housing **Fig. 12.** Parking with sensors and electronic tags

Columbia Housing, at Belo Horizonte: is another massive housing built by 1980s. The problems identified were too much complex than the others, once the social-economic levels were lower than the others. The solutions covered a wide range of devices and services accessed locally and through internet and mobiles, being probably the lesser physically intrusive project. The main problem addressed to was the path finding inside the territory, together with the lack of identity of the façades.

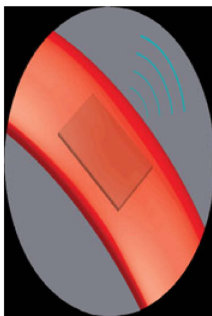


Fig. 13. A ring with sensor to locate children inside the territory; **Fig. 14.** a schematic view of the Columbia housing; **Fig. 15.** among others, pavements signals and bollards were designed with sensors and leds connected online, able to indicate paths.

7 Conclusions

It seems to have plenty of research to be done related to the application of the developed framework. The results here presented were timid if compared with those obtained in the Master Course at The University of Sheffield, UK, as it is described in the book “*Information Technology in Urban Places - A Theoretical Framework for the Development of IT applied in Urban places*” [21].

Dealing with the classroom, with the students and Architects involved, I could identify some causes for this timidity: the lack of time to get the concepts properly, as to use them to facilitate the design of Ubicomp Systems in early stages of the work. Another problem was the Designer’s incapacity of abstraction while designing manners to represent graphically their ideas and solutions. In my point of view, this problem demands an urgent and deep research about how to complement the theoretical framework in terms of the representation of Ubicomp interfaces. Also the student’s knowledge of electronic components and services was a problem, for the most of IT stuff belongs to international factories, demanding a research about the innovation to permit roughly specifying updated parts of a system.

In an attempt to accomplish the developed framework, presently I am developing an online Database about Brazilian IT components and services [22] to provide an analyses of their potential to improve the qualities of places, as it has been discussed in this paper.

Finally it seems clear that the research aiming the amalgamation of the disciplines related to Ubicomp needs to continue beyond the theory presented here in order to better engage the fields of knowledge involved, in a useful, powerful way as to be applied in true Urban Design challenges.

Acknowledgements. This study has been supported by FAPEMIG (Agency to Support Research in Minas Gerais County) and CNPQ (National Council to support Brazilian Research) Author are grateful to all members of his research team on Contextual Computing in Brazilian Architecture and Urban Design (<http://dgp.cnpq.br/buscaoperacional/detalhegrupo.jsp?grupo=03336049IU4BLW#indicadores>).

References

1. Thackara, J.: The design challenge of pervasive computing. In: Computer Human Interaction Forum (CHI 2000), The Hague (2000)
2. O’Neil, E.: Foothill Project: Ubiquitous Computing and the Urban Environment (2006), <http://www-dse.doc.ic.ac.uk/Projects/UbiNet/GC/Manifesto/fp-urbanenvironment.html> (cited March 2006)
3. Souza, R.C.F.: A Place-Theoretical Framework for the Development of IT in Urban Places, in School of Architecture of The University of Sheffield, p. 365. The University of Sheffield, Sheffield (2008)

4. McCullough, M.: *Digital Ground: architecture, pervasive computing and environmental knowing*. Massachusetts Institute of Technology - MIT Press (2004)
5. Graham, S.: The end of geography or the explosion of place? Conceptualizing space, place and information technology. In: *Progress in Human Geography*, pp. 165–185 (1998)
6. Weiser, M.: *Ubiquitous Computing*. Nikkei Electronics Magazine, 137–143 (1993)
7. Shafer, S.A.N.: *Ten Dimensions of Ubiquitous Computing*. Vision Technology Group, Microsoft Research (1999),
<http://research.microsoft.com/easyliving/Documents/1999%2012%20Ten%20Dimensions.doc> (cited January 2007)
8. Sengers, P., et al.: Culturally embedded computing. *IEEE Pervasive Computing* 3(1), 14 (2004)
9. Malpas, J.: *Heidegger's Topology - Being, Place, World*. MIT Press (2007)
10. Malard, M.L.: *Brazilian Low Cost Housing: Interactions and Conflicts between Residents and Dwellings*. In: *Architectural Studies*, p. 239. University of Sheffield, Sheffield (1992)
11. Weiser, M.: *The computer for the 21st Century*. ACM SIGMOBILE: Mobile Computing and Communications Review (1999)
12. Heidegger, M.: *Being and Time*. SCM Press, London (1962)
13. Dreyfuss, H.L.: *Being-in-the-World: A Commentary on Heidegger's Being and Time*. MIT Press, Massachusetts (1991)
14. Heidegger, M.: *Poetry, Language, Thought*, p. 230. Harper and Row, New York (1975)
15. Norberg-Schulz, C.: *Genius loci: towards a phenomenology of architecture*. Rizzoli, New York (1980)
16. Norberg-Schulz, C.: *Genius loci: towards a phenomenology of architecture*. In: *Architectural Design 1980*. John Wiley & Sons, Inc., London (1980)
17. Korosec-Serfaty, P.: *Experience and Use of the Dwelling*. In: Altman, I.A.C.M.W. (ed.) *Home Environments*, pp. 65–83. Plenum Press, New York (1985)
18. Maturana, H.: *Biology of Language: The Epistemology of Reality*. In: Miller, G.A., Lenneberg, E. (eds.) *Psychology and Biology of Language and Thought: Essays in Honor of Eric Lenneberg*, pp. 27–63. Academic Press, New York (1978)
19. Shannon, C., Weaver, W.: *The Mathematical Theory Of Communication*. University of Illinois Press, Urbana (1949)
20. Maturana, H.: *Autopoiesis and Cognition: The realization of the Living*. Reidel Publishing Co., Boston (1980)
21. Souza, R.C.F.: *Information Technology in Urban Places - A Theoretical Framework for the Development of IT applied in Urban places*, 1st edn., vol. 1, p. 304. Lambert Publishing (2010)
22. Souza, R.C.F.: *CCB - Banco de Dados de Computação Contextual Brasileira*, Database / site (2010/2012), <http://www.mom.arq.ufmg.br/rcesar/>

Sustainable Micro-business in Environmental Unsustainability and Economic Inefficiency

José G. Vargas-Hernández

University Centre for Economic and Managerial Sciences, University of Guadalajara,
Department of Administration
Periférico Norte 799 Edif G-201-7, Núcleo Universitario Los Belenes, Zapopan, Jalisco,
México 45100
jvargas2006@gmail.com

Abstract. This paper analyzes sustainability and efficiency of organizations committed to the exploitation' activities of *tule Thypha spp* at the Zapotlán's Lake taking into consideration the socioeconomic and environmental impact in the municipalities of Gómez Farías and Zapotlán el Grande. The initial hypothesis departs from the consideration of the scarce social capital of organizations that limits development's sustainability. The research method employed is the ethnographic complemented with field work supported by informal interviews, documental and bibliographic research. The hypothesis of this research is proved empirically and confirms similar findings by the research conducted on the mainstream theory of social capital and its implications on economic development. The outcomes of the application demonstrate that the drama of economic efficiency and sustainable development of micro-business is tied to constrain of social capital. This finding has implications for the design and implementation of economic and social policies oriented towards the improvement of economic growth and sustainable development.

Keywords: Economic efficiency, organizational social capital, organizational sustainability.

1 Introduction

The new conditions of globalization underlie life conditions and the importance of a generational future as a component of competitiveness. What constitutes globalization is the interaction that changes the scenarios for the individuals, organizations and society, who are constantly hounded by contradictory forces and uncertainties. The appropriate use of natural resources can meet present and future interests, having a change in current practices. In comparison to the economic rationality's logic that drives the functioning of organizations and has as a lead obtaining maximum present return, before that if natural resources yield greater benefit under their exploitation than taking care of them, they are sacrificed. Thus, the immediate economic profit is the current enemy of the environment.

The ecological proposal in organizations, widen its model of interactions which can integrate the environmental paradigm to the organizational system. An approaching to

sustainability of organizations is affected by the combination of ambiguous environmental economic policies, the abrupt adoption of production technologies and market practices. Sustainability in business organizations as an implementation strategy of process reengineering and the adoption of production technologies are oriented toward avoiding waste materials, recycling trash and eliminating toxics.

Lacking acceptance of the role that business organizations play in sustainability, it influences the global debate questioning real causes of pollution which poses safeguards to organizations and justify poverty as the main cause generating environmental degradation. It also suggests as a consequence of deterioration the inadequate economic policies that allow for business actions less friendly with the environment.

This paper sets as aims, firstly to determine the level of organizational sustainability for the environmental and economic development of cutting treatment and exploitation activities of the grass called *tule thypa spp* from the Zapotlán Lake. Similarly, the paper pretends to analyze potentialities and economic benefits derived from a marketing orientation of international business in the making of art craft out of *tule* and *palmilla* (a kind of palm) that growth spontaneously in the Zapotlán Lake.

2 Different Aspects of Sustainable Development

2.1 Sustainable Development

Sustainability is one of the major things that every organization is involved. Sustainable development has been defined in many ways, but the most frequently quoted definition is from World Commission on Environment and Development [1] "Sustainable development is development that meets the needs of the present without compromising the ability of future generations to meet their own needs. It contains within it two key concepts:

- The concept of needs, in particular the essential needs of the world's poor, to which overriding priority should be given; and
- The idea of limitations imposed by the state of technology and social organization on the environment's ability to meet present and future needs." (p.43).
- Every development if wants to be continuous should be systematic i.e. development should be in all parts and aspects (Economic, environment and society).

2.2 Economic Sustainability

The modern concept underlying economic sustainability wants to maximize the flow of income that could be generated while at least maintaining the stock of assets (or capital) which yields this income [2]. Fisher [3] had defined capital as "a stock of instruments existing at an instant of time", and income as "a stream of services flowing from this stock of wealth". Hicks [4] argued that people's maximum

sustainable consumption is “the amount that they can consume without impoverishing themselves”. Economic efficiency plays a key role in ensuring optimal consumption and production.

Problems arise in defining the kinds of capital to be maintained (for example, manufactured, natural, human and social capital have been identified) and their substitutability. Many argue that unrestrained economic growth is unsustainable, and point out practical limitations in applying the economic sustainability rule without additional environmental and social safeguards.

In the organizations all assets are not tangible and some are intangible for a sustainable development organization should note to this fact and to be sustainable economic development the organization should develop tangible and intangible (both) assets. Often, it is difficult to value these assets and the services they provide, particularly in the case of ecological and social resources [5]. Even key economic assets may be overlooked – e.g., where non-market transactions dominate. Uncertainty, irreversibility and catastrophic collapse also pose difficulties [6].

2.3 Environmental Sustainability

As we know every sustainable development should consider the environmental development as well. The environmental interpretation of sustainability focuses on the overall viability and health of living systems – defined in terms of a comprehensive, multi-scale, dynamic, hierarchical measure of resilience, vigor and organization [7].

These ideas apply to either natural (or wild) and managed (or agricultural) systems, and cover wilderness, rural and urban areas. Resilience is the potential of a system state to maintain its structure/function in the face of disturbance [8]. An ecosystem state is defined by its internal structure and set of mutually re-enforcing processes. Holling [9], Holling and Walker [10] originally defined resilience as the amount of change that will cause an ecosystem to switch from one system state to another. Resilience is also related to the ability of a system to return to equilibrium after a disruptive shock [11], [12], [13].

A sustainable organization integrates the ecological vision and the institutional theories in organizational systemic values. The acquisition of a common sense in the production of goods and services is utilized as a stronghold to promote the eco-efficiency as a friendly culture of organizations with their environments to achieve emission reductions and rational exploitation of natural resources.

The environmental variable in organizational culture is inserted as a rational interpretation of the functioning for the environmental protection, reducing insecurity and context’s social pressure. Environmental protection is a technical variable composed by other environmental values such as the promotion of environmental caring, environmental risk control, adequate relationship between organizations, and integration of working groups, orientation and permanent staffing on sustainability.

In addition, it is necessary economic instruments to tie sustainable development to micro and small business enterprises. Instruments such as governmental policies, low market tariffs to diminish costs, promotion and incentive of employment opportunities, detection of opportunity areas, etc. are required. Also, it is convenient to have the

diagnostic of adaptable enterprises to sustainability because not all of the micro and small business enterprises are capable to form an environmental internal culture.

From the point of view of general theory of organizations, Portes [14] studies social capital to gain a greater insight, comprehension and understanding of market competitiveness mechanisms, while Joyce [15] focuses his analysis of social capital in the leadership phenomena. Either the organization or each one of its members can be incorporated as public and private issues to social capital. Thus, from social capital emerge two patterns, the emphasis on public goods and the emphasis on private goods.

Leana y Van Buren III [16] define organizational social capital as a resource which reflects the character of social relations within the organization, achieved through the levels of members' orientation by collective objectives and shared trust. Social capital is a collective attribute more than aggregation of individual social connections. It is a byproduct of other organizational activities and thus, it constitutes an indispensable component for the collective action. Social organizational capital is an asset whose joint possession between members and the organization benefits both.

A new organization has the advantage to create its own organizational social capital in such a way that can maintain optimum equilibrium between stakeholders, individual and other organizational interests in spite of their contingent nature. This is to say, different situations and persons in their relation to organizational performance. A community accounts on social organizational capital when their organizations are characterized by relationships of trust that develop and make predictable their behavior. The capacity of a community is reflected in its level of endogenous development.

The organizations are concrete reality with resources' rules and ordinances for the pursuit of objectives. Members of an organization have as expectations to solve problems of collective action to get supply of some goods and services. Organizations that follow general strategies and the ones that follow strategies of niches occupy different environmental resources to produce innovative responses that form inter-dependent connections with other specialized organizations in other industries such as structures of community support. Processes of economic structural change in a local economy require profound changes in trust levels and inter-relationships of cooperation fomented by arrangements of institutions and organizations. Thus, local government must define action lines which function as a catalytic converter of the community efforts.

Finally, population ecologists suggest that the environment selects the organizations which structural features provide the highest values for adjustment, emphasizing the competitive process as a driver of institutional change. Besides, population ecology suggests that organizations founded in a specific organizational form, combined with differences on the surviving rates between organizations with different organizational forms, produce institutional change.

3 The Case of Micro and Small Business Enterprises Involved in the Exploitation of *Tule typha spp* from the Lake of Zapotlán

Similarly to the great majority of aquatic bodies localized in closed basins of Mexican national territory, the Zapotlán Lake is the natural receptacle, dump and outlet where

converge the sewage, trash and black waters from the human settlements of Cd. Guzmán and San Sebastián del Sur (Southern San Sebastián)

The presence of these natural elements form a nutrients mix that facilitates the growth and development of an abundant aquatic mix which has achieved to cover almost the totality of the mirror's surface of the lake and it extends further beyond the shores while penetrating humidity. The transformations of the environment's lake of Zapotlán has a strong impact on the population's socio-economic issues, mainly in San Sebastián del Sur in the municipality of Gomez Farías, and to a lesser extent to the settlers of Cd. Guzmán in the municipality of Zapotlán el Grande, despite the higher levels of pollution in which it is actually found

Deterioration of this lake-body has achieved alarming levels as a consequence of the increasing population and its corresponding enlarging urbanization processes, industrial, farming and agricultural activities. Specifically, one of the natural resources offered by the lake of Zapotlán, the aquatic *tule typha spp* has been benefiting the settlers and inhabitants of San Sebastián del Sur mainly for its exploitation through the crafting of several products and handicrafts. Thus, the exploitation of the *tule* and the elaboration of handicrafts create direct employments and constitute the income base for around 300 families and their members, a roughly estimation of one thousand and five hundred individuals making a living out of these activities in the municipality of Gomez Farías.

However, more are the benefits obtained from the *tule* chubby and plump those other kinds, followed by the one known as *palmilla* (palm). In its natural habitat, the *palmilla tule* harms the *tule* chubby's growing and development. This problem, among others, added to the problems derived from environmental degradation which transforms nature of the Zapotlán's lake, limit the economic activities derived from the extraction of *tule*, whose tendency, if it is going to continue in the future, and threatens the disappearance of an important employment's source for living sustainability of the inhabitants in San Sebastian del Sur.

To aggravate this problem, The Pan-American Olympic Games has chosen the Zapotlán's Lake as the location where the aquatic games will take place the year 2011. For that reason, the lake is having a profound transformation which implies the clearance and cleaning of the lake's mirror from any type of grass and bush, including the cutting off and taking out of the *tule*.

Other factors contributing to limit the environmental and economic sustainability of development and the scope of benefits from economic activities and exploitation of *tule* are the following:

- a) Null orientation toward a sustainable exploitation of the *tule* as a natural resource.
- b) Lack of organization between the cutters of *tule* and the handcrafters'
- c) Weak infrastructure for the development of a more advanced handcrafted production.
- d) Excessive interest of hoarders and middlemen in the processes of commercialization and distribution of elaborated products.
- e) Lack of mechanisms of governmental institutions to foster and develop economic activities, such as credits, training and technical assistance.
- f) Null knowledge of techniques and systems to export their products to the international markets where more acceptances have.

Until now, handcrafted products derived from the *tule* as the main raw material, are elaborated with a strong artistic content to attend local, regional, national and international markets, which traditionally consume because there is a strong historic presence in Mexican culture since the pre-colonial times.

In order to be organized to attend the regional market, a group of 42 craftsmen acting as partners integrating the Association of Craftsmen (Asociación de Artesanos) initiated the construction of the “House of Craftsmen” in the early nineties to operate as an outlet for selling their products. This business still operates until now having only six partners, although it can be inferred from simple observation that the partners are undergoing heavy conflicts, dividing the building and infrastructure in small areas to operate their own personal business.

Most of the craftsmen deliver their production to middlemen who always perform as hoarders being a link in the distribution channel and contributing to the commercialization of the handcrafted products in the local, regional and national markets an incipiently in the international markets. These middlemen are precisely who hold the greater percentage of profits. By the same talking, a production oriented to meet the fundamental needs and wishes of our own local, regional and national markets, the craftsmen do not perform product design and product development activities. The crafted products implicitly have a higher craftsmanship content to meet a more sophisticated demand of international markets which value and appreciate the artistic sensibility and good taste of the skillful craftsmen. These craftsmen work the *tule* as a raw material for the creation of handcrafts.

The exploitation of *tule* from the Zapotlán’s lake has followed irrational patterns which affect not only the environmental sustainability and equilibrium, but also generate problems of low family income and in the running time lesser employment for manpower. The rehabilitation of the Lake requires a more rational exploitation of the *tule*, in such a way that does not affect the environmental sustainability and the economic activity derived and the treatment of *tule*, while on the other hand, also it is required to improve the family income who work the *tule* and inclusive to generate new employments.

4 Discussion and Comments on Organizational Sustainability Based on the Research Results

4.1 Environmental Sustainability

The presence of bundles of *tule* covering around one third of surface at the Zapotlán’s Lake [17] it is important for the nesting, refuge and protection of several species of fishes, tilapia, and carps and also for several species of birds. The *tule*’s plant serves as the food for some species beginning from the organic material which become detached from the roots, regulates water’s temperature thus the environmental temperature.

In the following months after November, the *tule*’s plant is affected by a bundles of birds know as zanates that nest, recognize to sleep and to protect against the bundles of *tule* that the same birds break down. The biggest problem that face the *tule* is that

the proper bundles of *tule palmilla* (tule palm) used to weave chairs are flouting and invading the chubby *tule* used to manufacture matting and bedrolls and impede its normal growth and development. Thus, the bundles of *tule* need cleaning or to the contrary, the *tule palmilla* damage to the chubby *tule*. This problem has a solution. If there are extracted the bundles of *tule palmilla* that walk soils when the level of water goes up and cover the chubby *tule*.

The cutters of *tule* signal that, among other problems, they do not count on the support and back up of any governmental dependence or institution through the expedition of permits to cut and exploit the *tule*, none support in credits for the creation of infrastructure to facilitate to carry on their activities and increase their productivity, as for example, the acquisition of launch, cutters or motorboats to facilitate the cut of *tule* or the conditioning of plots of land (patios or country yards) adjacent to the Zapotlán's Lake to facilitate the dry of the cut *tule*. This situation always represents problems when the *tule* is green. When the *tule* is spread out and lay out in a country yard or patio for the processing of drying, it last from 3 to 4v days. There are some spells; mainly during the period of ebb tide in which the *tule* is dried without it has been cut, stating a little bit green. However, ecologically and environmentally this processes have some serious consequences which affect the economics and environment.

4.2 Economic Benefit

Cultivation and exploitation of *tule* constitutes an important economic activity, mainly for the community of San Sebastian del Sur because it provides economic support to around three hundred families. About 80 families are economically benefited with the income received from the cutting, drying and transport of *tule*. Around 140 families are benefited from the handcrafted production of goods made of both varieties of *tule*, the *palmilla tule* and the chubby *tule* as the main raw material. Out of these 140 families, 120 are self-considered handcrafters of matting and bedrolls (petateros).

Around half of the 55 handcrafters registered in the Association trade have their own workshops, while the other half only work in assembling plant because they do not count on the instruments of a workshop properly equipped. Around 70 families receive income from intermediation, hoarding, stockpiling and commercialization activities of products derived from *tule*

The cutters of *tule* dry their raw material and make even up to two bunches per one day that sells at an average price of 75-80 pesos each one. The income from the selling contributes to the daily family income that averages 160 pesos per day. The *tule palmilla* used for the manufacturing of chairs is sold to intermediaries; most of them are owners of small stores who stockpile it. The *tule* chubby is sold to the craftsmen at a price a little bit less expensive to be used in the manufacturing of matting and bedrolls (petites).

Most part of manpower employed in the cutting of *tule* is permanent and their trade was inherited from antecedent generations. According to the conducted field research, and due to the ongoing changes taking place in the Zapotlán's Lake, every year there are less cutters, thus, in the years before, the cutting of *tule* was an activity which

generated more employment than nowadays. In the years before, the cutters formed a group and became a formal association of tule's cutters. Some of the actual cutters are temporarily workers in this activity, more specifically when they do not find a better remunerated employment.

The craftsmen produce different goods using as the main raw material the *tule*, such as matting, bedrolls, hats, chiquihuites (containers in form of wide baskets), shadows, traditional chairs, high chairs, seamstresses, etc. From a roll to a bunch or bundle of *tule* handcraft up to seven matting which the craftsmen sell to a price of 30 pesos each one, an equivalent of two USA dollars and 40 cents, obtaining up to 210 pesos (almost 17 USA dollars) with an original investment averaging 80 pesos, the cost of one bunch of *tule*. A bunch of *tule* is formed with 5 or 6 big hands (manotadas) of *tule*.

The cost of one big hand is approximately 20 pesos and it is the base to manufacture one chair which is sold at a price of 50 pesos to the intermediary or middleman. The cost of materials of one chair also includes besides the big hand, a wood branch of pine whose costs is up to 15 pesos, a cost that has been increasing when used to be 1.50 pesos several years ago. In one workshop where regularly work five craftsmen achieve to produce up to 70 chairs per week which are sold to the intermediaries and middlemen at a price of 70 pesos as an average. This price can improve depending on negotiations and trading with intermediaries and middlemen.

Many cutters supply raw material to their own families who are in charge of the crafting of handcrafted products, widening with this situation the economic benefits and adding value. In other cases, there are conducted some practices of half by half ("medieros") between the cutters and the handcrafters. This is to say, after the selling of products; both cutter and handcrafter share the benefits in the same proportion, half and half.

Actually, the relationship among handcrafters of tule registered in one association at the location of San Sebastian del Sur is 55. 16 years ago, the association was formed by 42 partners and set as the main aim the founding and building of the craftsman's house (Casa Del Artesano) as the market place in which their handcrafted production can be exhibited and sold. The three levels of government, Federal, State and Municipal contributed with donations of materials for the construction, while the partners made manpower contributions.

However, most of the craftsmen members of the Association do not made any contributions of manpower and finally only six partners did it, and who nowadays exhibit and sell their handcrafted products in a separated way at the craftsman's house. This craftsman's house is located at one side of the Federal Highway Guadalajara- Cd. Guzman, in an adjacent location to the Municipal Cemetery.

Leovigildo Bautista de la Cruz is the person who is at the front of the Association and he is also the ownership of land and building. Originally the land was signaled by the Municipal Government of Gomez Farías for the construction of the craftsman's house. However, lately it was found that this land did not have any proprietorship according to the archives of the Public Register of Ownership.

Thus, nowadays, the ownership of the craftsman is the "apple of discord" and the cause of several conflicts due to the other craftsmen wants to participate of the

benefits with the support of the municipal government. One of the former municipal President intended to benefit to a group of craftsmen who do neither exhibit nor sell their products at the craftsman's house, had sent official letters to the Public Notary requesting change of ownership regime and claiming that it is municipal's ownership. Despite of this, there is not one organization of craftsmen to whom it may classify among these who count on their own workshops, approximately half of the 55 registered members, and those who sell or "maquilan" their own manpower for the former. Thus, those who sell their own manpower, they do not have their own equipment, tools and facilities to establish their own workshop.

According to our own research, the interviewed assure that sales are declining. Today, they argue, sell less than 10 years ago. The middlemen and intermediaries are who more profits obtain from the commercialization of the handcrafted products. In order than a handcrafted product reaches the final consumer, it is required at least a three level's distribution channel, and this is to say that at least there are two intermediaries between producers and consumers. The intermediaries are the ones who attend national markets and to a lesser extent they export the handcrafted products to some parts of United States, Canada, Puerto Rico, England and Japan. The terrorist actions of September 11, 2001 had affected missing some orders of handcrafts.

Some of the problems that the craftsmen face are those related to the lack of training programs to develop and preserve handcrafter techniques, financial support, and obtaining credits to extend basic production infrastructure, and of course, staffing and consultancy for direct exports of their products to the international markets. All these actions will benefit the economic income of more than 300 families in San Sebastián del Sur, Jalisco.

5 Conclusion

The exploitation of *tule* represents an economic activity that provides income to approximately three hundred families living at the settlement of San Sebastian del Sur. Nevertheless, in the last few years the income has been decreasing due to the environmental changes and to the rehabilitation of the Zapotlan's Lake to host the Pan-American Games in 2011. Both, the environmental changes and rehabilitation of the lake represent a serious threat to the economic efficiency and environmental sustainability.

To achieve equilibrium between environmental sustainability and economic sustainability must be one of the main goals of the rehabilitation programs. Thus, it is required the best indicators under a systematic study to determine the most adequate levels of environmental sustainability and economic efficiency.

The limited social organizational capital and the lack of adequate forms of organization for the productivity, contribute to limit the scope and economic benefits that must provide an adequate exploitation of *tule* from the Zapotlan's Lake. Disorganization of cutters and craftsmen of *tule* is the source of profound and increasing conflicts that not only block and limit the scope of better levels of productivity and family income, but also make difficult the pacific coexistence and living together and spoil the community's quality of life.

Lacking a consultancy program to exports of handcrafted products has an impact on lower income to the families of cutters and craftsmen, because who actually obtain the greater part of profits are the intermediaries who take part on the commercialization processes and distribution channels.

Some characteristics of specificity and appropriateness of social and human capital involve economic, social and political relationships among individuals who are members of organizations, making complex their effects. Market is a social construction that makes operational social relations. Both capitals can be important resources of the competitive advantage, assuming that reside in the members or it is specific to the organizations as integral parts of resources that are unique and that are no observables. Organizations with higher levels of social and human capital generate more competitiveness than those with lower levels. A sustainable and competitive Economy requires programs aimed to improve social and human capital.

6 Recommendations

Some recommendations after this research are formulated below:

- Design a program to promote handcrafted activities derived from the exploitation of tule that in a parallel form to the rehabilitation program of Zapotlán's Lake, establish the right indicators to achieve equilibrium between economic efficiency and environmental sustainability.
- To set a program of export consultancy with the support and technical staffing from students of international business at University of Guadalajara that provide the knowledge, skills and contacts in such a way that the *tule's* craftsmen directly commercialize and market their own handcrafted products in the international markets.
- To propose a program for development of organizational and social capital and new forms of organization aimed to increase productivity and competitiveness of the craftsmen, thus increasing their family income and promoting employment creation and improve the quality of life of the whole community of San Sebastian del Sur.

References

1. World Commission on Environment and Development (1987). Address by the Chairman at the Closing Ceremony of the 7th - Eighth and Final Meeting of the World Commission on Environment and Development. 27, Tokyo (February 1987)
2. Solow, R.: On the intergenerational allocation of natural resources. *Scandinavian Journal of Economics* 88(1), 141-149 (1986)
3. Fisher, I.: *The Nature of Capital and Income*. Augustus M. Kelly, New York (1906) (reprinted 1965)
4. Hicks, J.: *Value and Capital*, 2nd edn. Oxford University Press, Oxford (1946)
5. Munasinghe, M.: *Environmental Economics and Sustainable Development*. Paper Presented at the UN Earth Summit, Rio de Janeiro, Environment Paper No.3. World Bank, Wash. DC, USA (1992)

6. Pearce, D.W., Tuner, R.K.: *Economics of Natural Resources and the Environment*, 1st edn. Harvester Wheatsheaf, Hemel Hempstead (1990)
7. Costanza, R.: Ecological sustainability, indicators and climate change. In: Munasinghe, M., Swart, R. (eds.) *Climate Change and its Linkages with Development, Equity and Sustainability*. IPCC, Geneva (2000)
8. Pimm, S.L.: The complexity and stability of ecosystems. *Nature* 307, 322–326 (1984); Pimm 1991. *The Balance of Nature?* University of Chicago Press, Chicago, Illinois, USA
9. Holling: Resilience and stability of ecological systems. *Annual Review of Ecology and Systematics* 4, 1–23 (1973)
10. Holling, C.S., Walker, B.: Resilience Defined. In: *Internet Encyclopedia of Ecological Economics*. International Society for Ecological Economics (2003)
11. Ludwig, et al.: Sustainability, stability, and resilience. *Conservation Ecology* 1(1), 7 (1997)
12. Pimm, S.L.: The complexity and stability of ecosystems. *Nature* 307, 322–326 (1984); Pimm 1991. *The Balance of Nature?* University of Chicago Press, Chicago, Illinois, USA
13. Petersen, G.D., Allen, C.R., Holling, C.S.: Diversity, ecological function, and scale: resilience within and across scales. *Ecosystems* 1 (1998)
14. Portes, A.: *Capital social: Sus orígenes y aplicaciones en la sociología moderna*. Carpio, Jorge y Novaconovsky, Irene (comp.), *De igual a igual. El desafío del Estado ante los nuevos problemas sociales*, Fondo de Cultura económica-Siempro-Flacso, Ciudad de México (1999)
15. Joyce, P.: Management and innovation in the public services. *Strategy Change* 7 (1998)
16. Leana, R.C., Van Buren III, H.: Organizational social capital and employment practices. *Academy of Management Review* 24(3) (1999)
17. Universidad de Guadalajara, *Ordenamiento Ecológico de la Cuenca de la Laguna de Zapotlán el Grande Jalisco*, Gobierno municipal, Cd. Guzmán, Jalisco (1995)

Efficient Visualization of the Geometric Information of CityGML: Application for the Documentation of Built Heritage

Iñaki Prieto¹, Jose Luis Izkarra¹, and Francisco Javier Delgado del Hoyo²

¹ Construction unit, Tecnalia Research & Innovation, C/ Geldo Edificio 700, Parque tecnológico de Bizkaia, Derio, Spain
{inaki.prieto, joseluis.izkarra}@tecnalia.com

² MoBiVAP Research Group, Parque Científico Universidad de Valladolid, Paseo de Belén, 11, Valladolid, Spain
franciscojavier.delgado@uva.es

Abstract. CityGML is a standard data model for the representation, storage and exchange of 3D city models issued by the OGC (Open Geospatial Consortium). CityGML represents a very attractive solution that combines 3D information and semantic information in a single data model. The efficient visualization of the geometric information contained in the CityGML data model is still an open challenge. A survey of the state of the art shows that current approaches have to be improved. In this paper we introduce a new approach for efficient web visualization of CityGML without plugins based on the use of X3D and web services. The approach has been evaluated with an implementation applied to built heritage at urban scale based on an extended CityGML model.

Keywords: CityGML, 3D visualization, built heritage, 3D visualization on the Web, Web Services.

1 Introduction

A georeferenced virtual 3D model represents an increasingly accepted solution for storing and displaying information at urban scale. CityGML represents a very attractive solution that combines 3D information and semantic information in a single data model.

The efficient display of the geometric information in CityGML is still a big technological challenge. Stakeholders involved in process around city models demand rapid access to information anywhere at anytime. The visualization of CityGML geometry is a critical issue because there is not an appropriate/efficient format for visualization since the file size (around hundreds of megabytes), the structure of the data model (XML-based) and the geometry representation (in GML) are not designed taking in mind the exchange of information in the web.

The goal of this paper is to introduce the key technologies and open standards needed to implement a solution for efficient visualization of geometric information of CityGML in the Web 3D framework. In order to achieve this goal some steps have to

be performed. Firstly, the CityGML file is stored in a relational database to be able to retrieve and manage the information efficiently. Then, the information is exported based on the required level of detail to enable a progressive visualization of different pieces. For this, several requests are made to our custom implementation of the W3DS (Web 3D Service) so the geometric information is accessible via web. Finally, X3D file is visualized in a web browser without plugins by means of the X3DOM framework which has been adapted to our needs.

The rest of this paper is decomposed in the following sections. Section 2 makes a review of the state of the art. Section 3 presents a technological review about standards and technologies for 3D visualization on the Web. Section 4 briefly describes CityGML. Section 5 covers the details about the implementation of our approach. Finally, section 6 summarizes the conclusions extracted from our work.

2 State of the Art

CityGML, issued by the OGC, is an open standard for store and exchange virtual 3D city models [1] and is an application schema for version 3.1.1 of GML. GML [2] is an extensible international standard for spatial data exchange issued also by the OGC and ISO TC211.

The aim of the development of CityGML is to reach a common definition of basic entities, attributes and relationships of a 3D city model. CityGML defines the classes of objects in city models which have been identified as necessary or relevant in many applications in different areas. CityGML also includes different LoDs (Levels of Detail) to join concepts from the scale of a city or district to a building, joining GIS (Geographic information system) and BIM (Building information modelling) concepts in a single data model.

The visualization of CityGML is a critical issue as it is denoted by the number of publications. The main author of CityGML, T.H. Kolbe, said [3] that "CityGML is not optimized with respect to efficient visualization" [4], "It is not a good idea to render the 3D scenes directly from the CityGML files". Several formats are available to represent CityGML geometry such as VRML/X3D, SketchUp, 3DMax and KML. CityGML requires more bytes to represent the same geometry [5]. The agreement between the OGC and Web3D to use X3D with OGC standards for improving location-based 3D visualization means a significant advance [6]. As a consequence, several research groups are studying how to adapt X3D for CityGML.

There exist several approaches in the literature to tackle 3D visualization of CityGML. The first approach is to visualize CityGML files in desktop viewers such as Aristoteles [7] or FZKViewer. Another approach is to develop specific viewers combining the citygml4j library and a low level graphics library like OpenGL [8]. The main drawback of this approach is that GML is not efficient for visualization.

Another approach consists of exporting the geometry of the CityGML object to a more efficient file format, like X3D, where the export has to be done offline because a lot of time is needed to export an entire city model [4]. Even when the export process is finished, specific tools or plugins are needed to visualize X3D files.

The natural evolution of this approach is the visualization of parts of the CityGML model selected using bounding boxes such that the export can be done online. The retrieval of these virtual city objects is performed using the W3DS which is a standard web service that returns the geometry in an output format such as KML, VRML or X3D. In [9] CityGML file is requested to a W3DS that returns VRML file which is visualized using the XNavigator viewer [10]. This approach makes still necessary the use of specific tools or plugins to visualize the X3D files.

In order to visualize the geometry of CityGML files directly on a web browser without using plugins, some approaches visualize pre-rendered images from different viewpoints in the server side. For this purpose, [11] shows a review of different client/server configurations where a thin client combined with the Web Perspective View Service (WPVS) were finally chosen. They developed a graphical interface to visualize geographic data in a browser by requesting images to a WPVS for the viewpoint selected by the user. A comparison between the advantages/disadvantages of WPVS against W3DS was done in [12], showing an improvement of the solution introduced in [13] where a pre-generated set of images from different viewpoints was stored and then visualized in a web browser. The main drawback of both approaches is that images do not allow navigating the model because the views are fixed. Still, depending on the user's needs it might be a sufficient solution.

Another approach for 3D visualization on web applications without plugins is explained in [4]. The Xj3D library is used in desktop visualization while the CityGML content is exported to X3D and visualized in a web browser using the X3DOM framework. The main advantage is the interoperability of the visualization but the main drawback is that the whole model needs to be exported to visualize it.

In this paper we propose a solution which combines the efficiency of representation of the geometry through X3D with the flexibility of using web services (W3DS) without requiring plugins for the visualization in a web browser.

3 Technological Review

3.1 3D Representation Standards

As previously explained, it is not efficient to visualize 3D content directly from CityGML. In this section we will analyse different 3D standards to which export the geometry and the appearance of CityGML.

The implementation of CityGML in XML facilitates the transformation into other 3D representation standards. CityGML is based on GML, which is aimed to exchange spatial data. The most relevant open formats which can interoperate with CityGML are KML, X3D, VRML and Collada. KML is another OGC standard, focused on providing structures to represent multimedia content associated with a 3D model. KML is also the standard format for data exchange adopted by the popular application Google Earth. It has a similar structure to GML and allows attaching COLLADA models. COLLADA was designed to facilitate sharing and reuse of 3D content between different tools and content creators. VRML describe interactive three-dimensional objects and worlds; while the purpose of X3D, its successor, is the creation and transmission of 3D content between web applications.

X3D [14] is an open standard to represent and communicate 3D scenes and objects based on XML. It is an ISO standard to store, access and play 3D content in real time over the Internet. Its main advantages are the simplicity and the possibilities to import/export from/to X3D from most known 3D representation standards.

There are also other 3D representation technologies like O3D [15] or Universal 3D [16]. The disadvantages of these standards are that they are designed only for certain tools and they are not international standards supported by different communities.

Fig. 1 presents a comparison between different 3D representation standards. It also details what features each standard supports. These features have to be analyzed to choose a standard depending on the application too. Fig. 1 shows that CityGML supports all the features and that X3D supports most of CityGML features such as geometry, textures, levels of detail and georeferencing.

In summary, we can say that KML and Collada are designed for 3D world browsers, so the export from CityGML is more limited. X3D has a geospatial component [18] and represents different levels of detail [19] which are nearer to the GIS philosophy of CityGML. Thus, X3D is the best option to represent 3D models on the Web since it is designed to be compatible with HTML and sent across the network. However, because of X3D was designed to represent geometry, CityGML semantics are lost in this conversion.

	DXF	SHP	VRML	X3D	KML	Collada	IFC	CityGML	3D PDF
Geometry	++	+	++	++	+	++	++	+	++
Topology	-	-	0	0	-	+	+	+	-
Texture	-	0	++	++	0	++	-	+	+
LOD	-	-	+	+	-	-	-	+	-
Objects	0	+	+	+	-	-	+	+	+
Semantic	+	+	0	0	0	0	++	++	+
Attributes	-	+	0	0	0	-	+	+	+
XML based	-	-	-	+	-	-	+	+	-
Web	-	-	+	++	++	+	-	+	0
Georef.	+	+	-	+	+	-	-	+	+
Acceptance	++	++	++	0	++	+	0	+	++

- not supported; 0 basic; + supported; ++ extended

Fig. 1. Comparison between different 3D exchange standards [17]

3.2 Web 3D Visualization

Plugins have been the predominant way of visualizing 3D content on the Web in recent years. However they have some clear disadvantages. On the one hand the user has to install the plugin, with the distrust that means and they can have security or incompatibility problems. On the other hand, the developer has to learn how to work

with the plugin to develop applications. As it is said in [20], "these plugins include their own runtime-systems which control all the visualization, interaction, communication and distribution issues internally".

Until recently, 3D graphics on the Web was visualized using APIs such as Flash, O3D, VRML or X3D, but always using a specific browser and installing plugins. Currently, WebGL allows the integrations of 3D contents in the browser without plugins or additional software.

WebGL [21] is a Javascript API for rendering interactive 3D graphics on any compatible browser without plugins by binding JavaScript with OpenGL ES [4]. It has been developed by the WebGL Working Group. Currently, some of the browsers supporting WebGL are: Mozilla Firefox (desktop and mobile), Google Chrome, Safari and Opera (desktop and mobile). Some smartphones are: Nokia N900, BlackBerry playbook, Sony Ericsson Xperia. WebGL renders the 3D content in the new HTML5 canvas element [23]. Its main drawback is that WebGL is a low level API so several frameworks have been developed in order to simplify application development such as the X3DOM framework.

X3DOM is an experimental, WebGL-based, open source framework to support the discussion between W3C and Web3D communities on how to integrate the HTML5 specification and 3D content [25]. The aim of X3DOM, as said in [20], "is to ease the integration of X3D in modern web applications by directly mapping and synchronizing live DOM elements to an X3D scene mode". However, until now all browsers do not support X3DOM; only Google Chrome, Firefox and Safari support it natively and Internet Explorer using Flash. Furthermore, X3DOM does not implement all features which are traditionally found in a 3D graphics engine.

4 CityGML

The aim of CityGML is to store and exchange virtual 3D city models which are decomposed thematically into a core and other thematic modules. The core module covers the basic concepts in the background of a CityGML model. The other modules cover specific subject areas within the 3D virtual city model, such as appearance, topography, vegetation, city furniture, buildings, land use, transportation, etc.

CityGML defines five LoD to represent concepts from the scale of city or district to a building. Thus, the same object can be represented in different LoD simultaneously which allows to analyse and visualize the same object with different degrees of resolution. Fig. 2 shows the five LoDs defined by CityGML. LoD0 represents the digital terrain model in two dimensions and a half. LoD1 is the block model of buildings using prisms with flat roofs. LoD2 differentiates roof structures and thematically differentiated boundary surfaces. LoD3 denotes architectural models detailing walls, roofs, balconies, etc. LoD4 completes LoD3 with interior structures such as rooms, doors, stairs and furniture. However, these LoDs are not necessarily valid for all projects.

The standard also enables a mechanism to allow extending CityGML semantics taking into account the different requirements of CityGML based applications. Thus, developers are encouraged to design their own extensions in order to include some required concepts and properties which are not reflected in basic CityGML. These extensions are called ADE (Application Domain Extension).

One of the main features of CityGML is the interoperability. Generated models can be easily reused in other standard and applications. We have analyzed multiple tools, technologies and standards to visualize, edit, parse, store, import/export, etc. CityGML files (see Fig. 3).

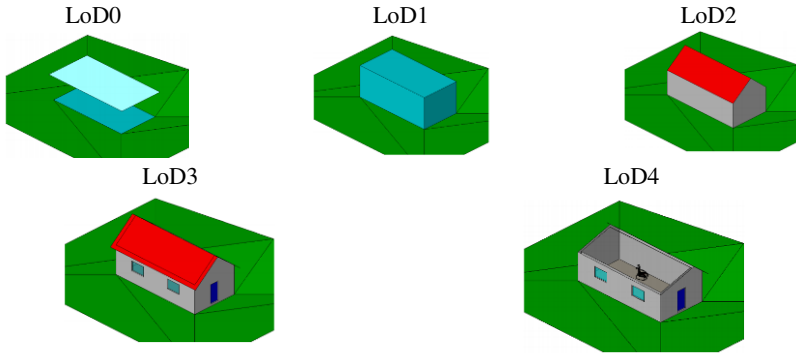


Fig. 2. Different Levels of Detail defined by CityGML [1]

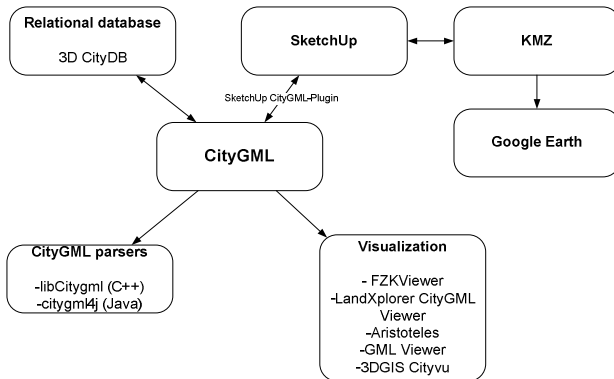


Fig. 3. Tools, technologies and standards around CityGML [26]

5 Implementation

This section presents the implementation of a documentation system for built heritage at urban scale based on a CityGML data model. The main use case which motivates the development introduced in this section is the historic city of Segovia in Spain which contains a large amount of historic buildings, monuments and other cultural assets. In fact, cultural tourism is one of the main revenues of Segovia and they lack of technologies to improve the management and enhance the value of its cultural heritage. Thus, there are two different kinds of target user and, as a consequence, two different kinds of applications from two points of view: there is a need of tools to

manage cultural heritage but there is also a need of tools to market cultural assets in tourism sector. Since both tools are fed by the same information, a common data model for city information is required which can be shared in real time by different users. More details about the concrete needs of these users are provided in Section 5.1

The rest of the section is divided as follows. Firstly, end user requirements are presented distinguishing two complementary tools. Then, the architecture of the system is described where the following subsections are defined: data storage backend, web services and end user applications. The first one details the developments performed to store information represented in CityGML (extensions and database). The second one describes the Web Services implemented for retrieving data. Finally, the last one advances implementation details of the user applications.

5.1 End User Requirements

The following section details the main requirements of user applications (the urban management tool and the application for the citizen) which motivate the implementation of the solution given below. Both applications access to the same stored data using web services.

The main goal of these applications is an efficient visualization of the geometric information of CityGML. Thus, some requirements for the solution are mandatory: a) progressive visualization is required such that instead of exporting the whole model, just the necessary objects are exported; b) taking into account the zoom level of the scene different LoDs of the model are visualized, it is also possible to show different LoD at the same time allowing to keep the attention of the end-user in a single building/set of buildings; c) users can select which different thematic layers are visualized according to their needs; d) the visualized geometry can be filtered with certain parameters from CityGML semantics; e) a bounding box can be selected in the viewer to spatially filter the visualized CityGML objects.

Urban Management Tool

This tool is intended for the agents responsible of the management and preservation of historic heritage in charge of maintaining and updating the data model. These agents need tools for helping them in decision making processes taking into account the peculiarities of historic urban environments from a territorial scale. The tool must be able to navigate the model, to select different thematic layers of information, levels of detail and 3D objects. It will be deployed as a desktop application and it includes the ability to view and manage the set of attributes of the selected objects in the 3D viewer. The tool also allows semantic searches to filter city objects by a set of parameters. After, these objects will be highlighted using a different colour.

Application for the Citizen

This application is intended for citizens or visitors to the city area so it will be developed as a web application supporting multiple devices. It visualizes the information about the 3D model of the city and it queries the semantic information of CityGML in a mobile device. This tool retrieves the value of the attributes of the building by selecting the building in the 3D viewer. It allows selecting different layers to show different thematic information.

5.2 Architecture

The architecture has been developed taking into account the following features: flexibility, reusability and scalability. Furthermore, the logic and workflow is distributed between several computers such that information can be accessed and shared by different agents using open standards. Fig. 4 shows the three-layer designed architecture where presentation, business logic and data storage are distributed. The first one will be implemented on the client side, the second one will be shared between the client side and server side, and the third one will be on the server side. Communications will take place through standard OGC web services.

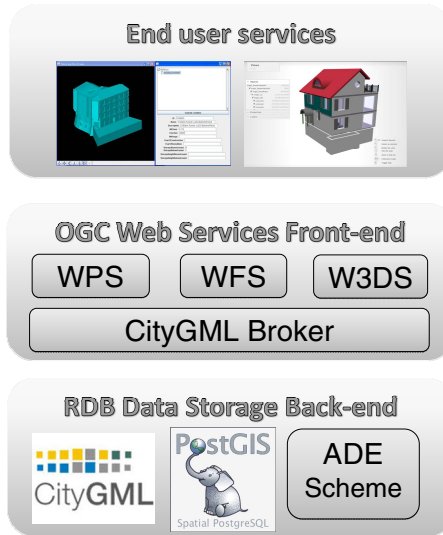


Fig. 4. Overview of the system architecture [27]

5.3 Data Storage

Extensions

As it was explained in Section 4, CityGML is a generic city object model which can be extended by ADEs. Thus, since CityGML do not represent well the documentation requirements in the fields of architectural and historical heritage, energy efficiency parameters and interventions in buildings, we have designed and developed three custom ADEs whose UML diagrams are represented by Figs. 5-7. The Cultural Heritage ADE models information such as monuments and sites by their name, location, functional type, date, history, physical condition and protection status. The Energy Efficiency ADE represents information about physical properties of materials such as conductivity, reflectivity, emissivity, transmittance, etc. Finally, the Intervention ADE allows representing what organization and actors are involved in the intervention processes to accomplish the maintenance and the rehabilitation of the cultural heritage city objects. With these three extensions it is possible to document

our needs on these areas. Figs. 5-7 show the relationships between these new concepts and with CityGML classes [27].

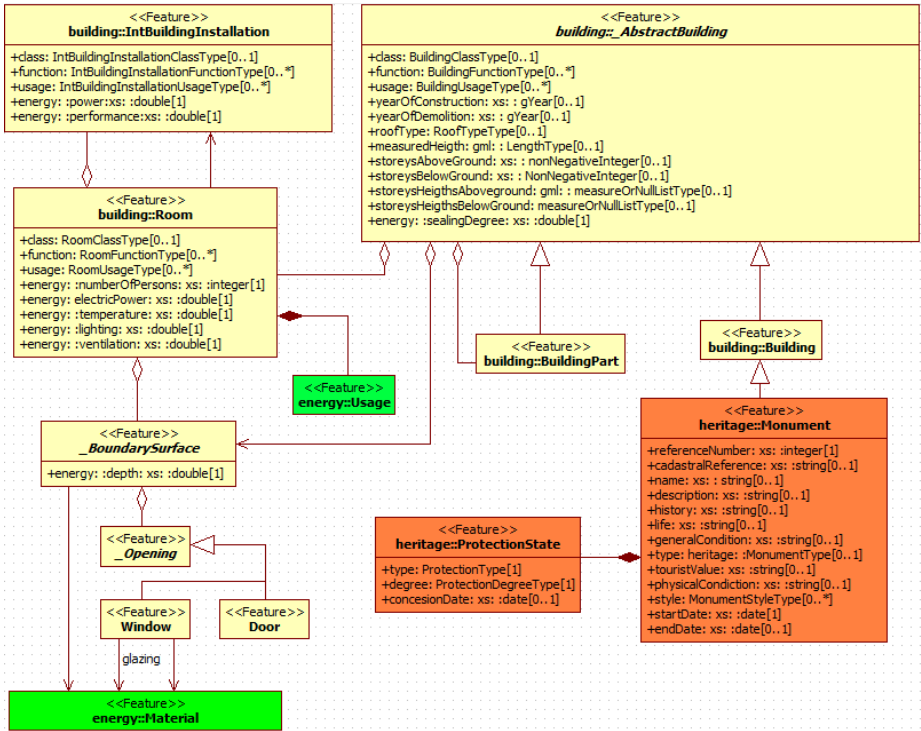


Fig. 5. Cultural Heritage Extension for CityGML

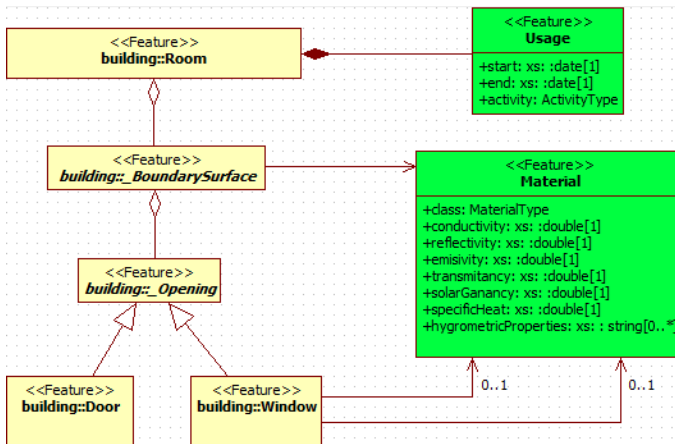


Fig. 6. Energy Efficiency Extension for CityGML

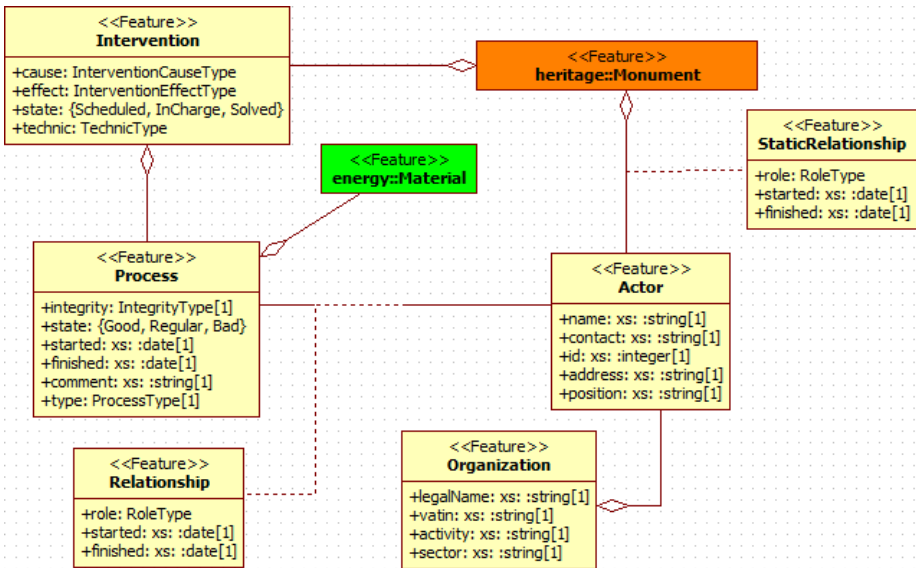


Fig. 7. Intervention Extension for CityGML

Storage

CityGML is intended to represent the semantic and geometric information of city objects. XML is the recommended format to exchange this information but it is not suitable for storing and retrieving complex city models where hundreds or thousands of objects can be involved. These files can take up to several gigabytes. Some other drawbacks of using XML are that redundant information is stored unnecessarily, data is more difficult to access and manage, there is no atomicity and integrity and the security level is lower. The alternative is to store the same information in a relational database system extended with spatial capabilities.

Dollner et al. [28] explain the new policy that has begun in Germany to create 3D models of cities. They developed a complex database scheme called 3D City Database [29] to represent and store the same information modeled by CityGML. This database has been complemented with an Importer/Exporter tool whose main objective is to process, store and retrieve efficiently and quickly CityGML dataset. More details about the import and export processes can be found in [30, 31]. One of the most recent improvements in this tool is the export to Collada and KML [31, 32]. The main drawback of this approach is the use of Oracle Spatial which is a proprietary and close-source relational database management system. Alternatively, we have developed and adapted the original database scheme to a PostgreSQL database extended by PostGIS [33]. However, the importer/exporter of 3D City Database does not work properly with PostgreSQL so we have also patched the original source code of the importer tool in order to work over a PostgreSQL database.

In order to support the storage of ADEs information mentioned above, we have designed and developed the necessary database scheme extensions which include a set of new tables, constraints and indices. We have also modified the importer/exporter

tool to adapt it with our new extensions. Thus, we have achieved the inclusion of the CityGML data model together with its extensions stored in PostgreSQL database and the tool ready to import/export CityGML files to the underlying database.

5.4 Web Services

The access to the stored city objects is made through Web Services since it allows retrieving particular pieces of the whole city model and different stakeholders or applications share the same information. Thus, city models taking up to various gigabytes can be accessed and shared in real time.

Since one of our objectives is to improve interoperability, instead of creating new web services interfaces we have taken the standard Web service interfaces defined by the OGC such as the W3DS (Web 3D Service) and the WFS (Web Feature Service). W3DS allows retrieving geometric information and the second one the semantics.

W3DS

The W3DS (Web 3D Service) [34] allows to retrieve the geometry and appearance of three-dimensional models for visualization. It is still in draft phase as a previous step to final approval by the OGC. There is a reference implementation developed in OSM3D-Germany project [35] which implements almost all features of the standard specification. However, the software has not been open sourced, so we have developed our own implementation.

The W3DS accesses to the stored information and returns a KML or X3D file [34]. The client is responsible for rendering the model in contrast to the Web Feature Service where client has to generate the scene graph or the Web Perspective View Service where the server sends rendered images to the client.

Our implementation only serves the *GetScene* requests using parameters such as *Service*, *Request*, *Version*, *Format*, *BoundingBox*, *Layers* and *LoD*. Only *Service*, *Request*, *Version* and *Format* have always a fixed value while *BoundingBox*, *LoD* and *Layers* parameters can be changed. By the moment, our implementation of *GetScene* request only includes the features required by our end user applications.

The request is done using a REST style call. REST is a philosophy of design for Web Services which tries to mimic the HTTP primitives to manipulate remotely allocated resources. GET retrieve a resource, POST creates a new resource, PUT modify or update a resource and DELETE remove the resource. The main advantage of REST is that it is based on open Web standards such as URI to represent the resources, HTTP to provide access to resources, and XML, HTML, etc. Finally, requests are done by means of a well-formed URL (Uniform Resource Locator).

GetScene request involves performing the following steps in the server side:

1. The ID of the building within the bounding box is retrieved. Fig. 8 represents the requested bounding box (P) and the building bounding box (Q). The following conditions must be met when a building is within the bounding box: $P_1 < Q_1$, $P_2(x) > Q_2(x)$ and $P_2(y, z) < Q_2(y, z)$, $P_3 > Q_3$, $P_4(x) < Q_4(x)$ and $P_4(y, z) > Q_4(y, z)$, $P_1 = P_5$ and $Q_1 = Q_5$

2. A query statement is generated for each building, layer and LoD to achieve a more efficient visualization and selection of layers. Several files will be created for each layer and LoD of a building. These layers are the next ones: Wall Surface, Ground Surface, Closure Surface, Roof Surface, Interior Wall Surface and Ceiling Surface.
3. A SQL query is run against the database.
4. The cache of X3D files is queried such that if the file already exists it is not generated again by exporting from CityGML to X3D.
5. A main X3D file is generated with an *Inline* element for each one of the previously generated X3D files.
6. The files are streamed to the client.

WFS

WFS allow exchanging, sharing and managing georeferenced information between different agents. There exists several implementations of this service such as GeoServer project [36], which allow to publish geographic data developing an adapter that allow communicate with the database. Another alternative is the Deegree3 [37] environment which is more simple and flexible and offers an implementation of other OGC Web Services. We have selected Deegree3 because it can be easily integrated with PostGIS too. This service allows getting and modifying the semantic information of the CityGML model such that we can separate the access to the geometry (W3DS) and semantics (WFS). Communication with the service (requests and responses) is done via XML files according to the XML schema specifications of the OGC.

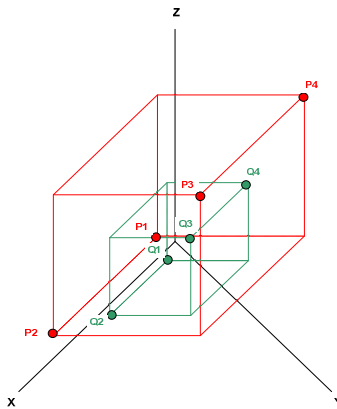


Fig. 8. Bounding boxes used in W3DS implementation

5.5 End User Applications

Urban Management Tool

3D visualization is an important part of the interface of this tool which allows the user to navigate the model and picking individual objects. The tool retrieves the level of detail of 3D models according to the zoom level selected by the user using W3DS and X3D format. Xj3D [38] graphics engine has been used to develop the 3D viewer.

The selection of different layers is done manipulating *Inline* element in the main X3D file. Semantic searches and retrieval of building attributes are performed through the WFS. There are two ways of visualizing these attributes by selecting the building in the list or selecting the building in the 3D viewer. Fig. 9 shows a screenshot of the urban management tool running.

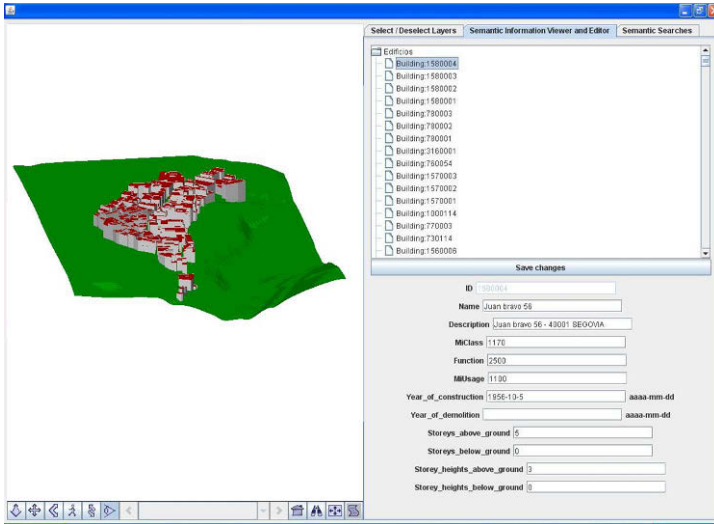


Fig. 9. Screenshot of the Urban Management Tool

Application for the Citizen

Fig. 10 shows the methodology to visualize the 3D model. Geometries are retrieved through W3DS and exported to X3D which is visualized in a web browser without plugin using the X3DOM framework.

The 3D viewer allows the navigation of the model and the selection of the heritage buildings, parking, etc. which have been defined by the heritage manager previously. The rendering and the interaction with model components are implemented using X3DOM. This application uses the strategies about object attributes, levels of detail and layer visibility which was shown for the Urban Management Tool.

The use of a web browser without plugins allows citizens to perform visual and textual queries or navigate the 3D model (see Fig. 11) by means of a mobile device with traditional features such as GPS, network access and gyroscope.

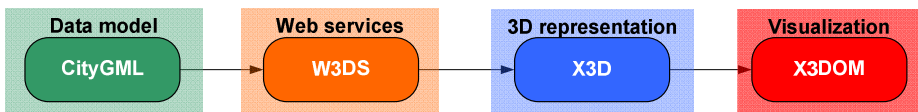


Fig. 10. Methodology for visualizing the geometry of CityGML [26]

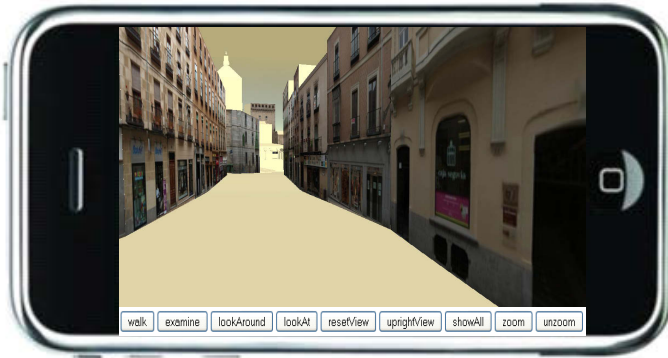


Fig. 11. Screenshot of the application for the citizens

6 Conclusions

This paper introduces an implementation of an efficient solution for visualization of the geometric information of CityGML. Our proposal improves performance in terms of file size and rendering time, using X3D for the representation of geometric information. In terms of file size, the X3D file represents almost a third of the size of the original model in CityGML. In terms of rendering time, the file structure and the way of representing the geometric primitives make X3D faster than CityGML. At the same time, a city model can be accessed via web by components, using the lower level of detail on large areas (urban level) and the higher level of detail in small regions (building level). The information is retrieved via W3DS and WFS, which guarantees interoperability with other implementations. Furthermore, only a web browser is necessary to render the model which facilitates the access to information from any device (PC, tablets and smartphones). However, 3D Web visualization still presents some limitations in performance regarding the size of models and speed of rendering which are more noticeable in mobile devices with a low bandwidth.

The use of an extended CityGML data model enables the development of a documentation system for the built heritage based on a common and shared model. The information is accessible in a standard way through web services defined by the OGC, allowing management and access to information shared by different users.

Future developments include new navigation functionalities with different camera perspectives and walking modes, as well as the enhancement of interaction capabilities by triggering animations of CityGML objects with semantic information.

Acknowledgment. The work of this paper has been done as part of the project "Analysis, Digitization and Interoperability between Systems for Architectural Heritage" (ADISPA) with reference BIA-2009-14-254-0C2-01 which has been funded by the Spanish "Ministerio de Economía y Competitividad" - MINECO (former MICINN).

References

1. OpenGIS® City Geography Markup Language (CityGML) Encoding Standard, document 08-007r1, version 1.0.0 (2008), <http://www.opengeospatial.org/standards/citygml>
2. OpenGIS Geography Markup Language (GML) Encoding Standard (2007), http://portal.opengeospatial.org/files/?artifact_id=20509 (2008)
3. Kolbe, T.H.: Representing and exchanging 3D city models with CityGML. In: 3D Geo-Information Sciences. Springer, Berlin (2008)
4. Mao, B.: Visualization and Generalization of 3D City Models, Doctoral Thesis, Royal Institute of Technology (2011)
5. Alizadehashrafi, B., Abdul-Rahman, A.: Enhancing textures of 3D building façade. In: 10th International Symposium & Exhibition on Geoinformation (ISG 2011) & ISPRS Commission II/5 & II/7 Conference, pp. 181–190. ISPRS (2011)
6. Havele, A.: Web3D and OGC to build cohesive standards for location-based 3D Web visualization services (2010), <http://www.web3d.org/press/detail/Web3D-and-OGC-to-build-cohesive-standards-for-location-based-3D-Web-visuali/>
7. Kumke, H., Hoegner, L., Meng, L., Stilla, U.: Visualization of Building Models and Factual Data integrated by CityGML. In: International Conference on Communications 2007 (2007)
8. Rakip, I., Abdul-Rahman, A., Atila, U.: Automatic Generation of 3D Networks in CityGML via MUSCLE Model. In: Joint ISG 2011 & ISPRS 2011 Conference (2011)
9. Over, M., Schilling, A., Neubauer, S., Zipf, A.: Generating web-based 3D City Models from OpenStreetMap: The current situation in Germany. In: Computers, Environment and Urban Systems, GeoVisualization and the Digital City - Special issue of the International Cartographic Association Commission on GeoVisualization, vol. 34(6), pp. 496–507 (November 2010)
10. XNavigator, <http://xnavigator.sourceforge.net>
11. Willmes, C., Baaser, U., Volland, K., Bareth, G.: Internet based distribution and visualization of a 3D model of the university of cologne campus. In: 3rd ISDE Digital Earth (2010)
12. Hagedorn, B., Döllner, J.: Web Perspective View Service – Overview and Initiative. In: OGC TC Meeting, Potsdam, June 04 (2008)
13. Béjar, R., Gayán-Asensio, D., Eced-Cerdán, J., López-de-Larrínzar, J., Muro-Medrano, P.P.: Un visualizador web de mapas 3D teselados basados en modelos de CityGML. In: Actas de las II Jornadas Ibéricas de Infraestructuras de Datos Espaciales, IIIDE 2011 (2011)
14. X3D, <http://www.web3d.org/x3d/specifications/x3d/>
15. O3D, <http://code.google.com/p/o3d/>
16. U3D, <http://sourceforge.net/projects/u3d/>
17. Oosterom, P.V., Zlatanova, S.: 3D Cadastre Modelling in Russia, G2G10/RF/9/1 Report Work Package 2, 3D-cadastral model for data generation, storage and distribution (2011)
18. X3D Geospatial Component, <http://www.web3d.org/x3d/specifications/ISO-IEC-19775-1.2-X3D-AbstractSpecification/Part01/components/geodata.html>

19. X3D Navigation Component, <http://www.web3d.org/x3d/specifications/ISO-IEC-19775-1.2-X3D-AbstractSpecification/Part01/components/navigation.html>
20. Behr, J., Eschler, P., Jung, Y., Zöllner, M.: X3DOM – A DOM-based HTML5/ X3D Integration Model. In: Web3D 2009 (2009)
21. WebGL, <http://www.khronos.org/webgl/>
22. OpenGL GLSL, <http://www.opengl.org/documentation/glsl/>
23. HTML5 specification, <http://dev.w3.org/html5/spec/Overview.html>
24. HTML5 Recommendation, <http://www.web3d.org/x3d/content/html5/HTML5RecommendationAdditionsForX3D.html>
25. X3DOM Homepage, <http://www.x3dom.org/>
26. Prieto, I., Egusquiza, A., Delgado, F.J., Martínez, R.: CityGML como modelo de datos para la representación, intercambio y visualización de información sobre el patrimonio arquitectónico, *Arqueológica 2.0 – 2011* (2011)
27. Delgado, F.J., Martínez, R., Prieto, I., Izgara, J.L., Egusquiza, A., Finat, J.: A common framework for multidisciplinary information management in historic urban districts. In: EuroGEOSS 2012 Conference (2012)
28. Döllner, J., Kolbe, T.H., Liecke, F., Sgouros, T., Teichmann, K.: The virtual 3D city model of berlin - managing, integrating and communicating complex urban information. In: 25th International Symposium on Urban Data Management UDMS 2006 (2006)
29. The 3D City Database, <http://www.3dcitydb.net/>, <http://opportunity.bv.tu-berlin.de/software/projects/3dcitydb>
30. Stadler, A., Nagel, C., König, G., Kolbe, T.H.: Making interoperability persistent: A 3D geo database based on CityGML. In: 3D Geo-Information Sciences, vol. 2, pp. 175–192 (2009)
31. Herrerueta, J., Kolbe, T.H.: KML/COLLADA Export - 3DCityDB Import/Export Tool extension, 100% CityGML - TU Delft, March 14 (2011)
32. Herrerueta, J., Kolbe, T.H., Nagel, C., König, G.: CityGML DBMS storage (2011)
33. PostgreSQL, <http://www.postgresql.org/>
34. Draft for Candidate OpenGIS® Web 3D Service Interface Standard, doc. OGC 09-104r1 (2010), http://portal.opengeospatial.org/files/?artifact_id=36390
35. Osm-3D Europe, <http://www.osm-3d.org/>
36. GeoServer, <http://www.geoserver.org>
37. Deegree3, <http://wiki.deegree.org/deegreeWiki/deegree3>
38. Xj3D X3D Developer Toolkit, <http://www.xj3d.org/>

ICT to Evaluate Participation in Urban Planning: Remarks from a Case Study^{*}

Francesco Rotondo and Francesco Selicato

Department of Architecture and Town Planning of Bari Polytechnic,
via Orabona 4, 70126, Bari, Italy
{f.rotondo, f.selicato}@poliba.it

Abstract. The paper study the ICT available to evaluate participation in urban planning, starting from a relevant experience made in Italy inside a funding programme of the Italian Ministry for Innovation and Technology. It starts describing the state of the art of methods and techniques to evaluate participation in urban planning and the informatics tools available to support these participation processes, before the arrival on the scene of the social networks such as Facebook or Twitter. In the following paragraph the paper describes the case study: a participation process in the South of Italy, made to design the master plan of a medium sized city. In the following paragraph ICT used in the case of study are discussed and revised. In the last paragraph conclusions are made on this relevant subject for urban planning and design offering some general reflections.

Keywords: e-democracy, collaborative planning, ICT evaluation, urban planning.

1 Evaluating Participation in Urban Planning

It is considered valuable, as an initial step, to briefly examine the significance of participation, in order to better understand its meaning within a given decision-making process. Participation implies, in this context, two distinct meanings: to be part of and to take part in. In the first, the "part" is understood as belonging to a system able to make collective decisions. In the second, "part" is understood as involvement in the action itself. The advantage of participation in political action is, therefore, broadly expressed in its own explicit meaning: political in the sense that it engages individuals in the management of the city as a place of belonging for a collective, closing the gap between the "managed city" (institutions, public bodies and elected representatives in the strict sense) and the "living city" (experienced by citizens in their daily lives). This dual meaning of participation, albeit with an implied weight oscillating every so often between the two extremes, is ever more frequently located in the context of decision-making processes within the field of planning. Indeed, ever-changing urban and regional dynamics have led to a gradual shift of

^{*} The paper is the result of a joint work of the authors. Nonetheless, section 1 has been written by Selicato F. and section 2, 3, 4 by Rotondo F.

focus in terms of how best to manage a planning process, from the formulation of almost deterministically defined choices to the construction of scenarios according to a procedural and interactive conception, dynamic and evolutionary in nature. Urban and regional planning is, in this context, characterized as a more collaborative process in which actors of different cultural and professional backgrounds must collaborate as the bearers of, often conflicting, interests [1] [2] [3].

On the other hand, forms of participation accessible to all are, to an ever-greater extent, the subject of active trials, in which collaborative practices aim to encourage cohesiveness in social relations, stimulating institutional learning and social change. In all cases, the dynamism of learning is linked to that of social processes, deriving the effective involvement of stakeholders from participatory practices, contributing to "community development" and improving institutional processes [4] as well as nourishing and constructively influencing the planning process.

The effective involvement of stakeholders in the planning process requires, in particular, planners and public administrators skilled in managing participatory practices who possess the ability to listen and dialogue and are able to make others more aware of potential risks and opportunities [5]. Learning thus results, as is widely documented in the literature, in deliberation and negotiation in policy-making [6] [7] [8] [9] [10] [11] [3]. It is therefore necessary to consider and, consequently, evaluate, not only the essential factors and/or associated conditions that may influence the effectiveness of participation but also methods of managing the collaborative process and, specifically, the role assessment plays in the learning process.

In the view of some authors [11] [12] strategies for collaborative planning processes must be defined according to the specific nature of the case, considering routine procedures as generally expensive, often contradictory and possibly even detrimental when their effectiveness is considered in relation to the actions for which they are intended. Such solutions cannot be defined as simple or generalized; they may, at best, provide suggestions in order allow planners and public administrators to face up to the challenges of public participation or better grasp opportunities [13] [5].

In this perspective:

- a) planners must work proactively in order to go beyond the dissatisfaction of members of the community [14] [15] [9] [16] [17] [18];
- b) in the case of mutual recrimination with stakeholders, planners may use indirect strategies in order to explore issues, enable learning and simultaneously build relationships [2]. Stakeholders may, in particular, reformulate issues from other angles, attempting to identify the key issues and practices under discussion and, only at a later stage, attempt to negotiate agreements [19] [20] [7];
- c) when, during public meetings promoting collaborative paths, those taking part only serve to fuel suspicion, it may be useful to employ qualified mediators [5];
- d) planners must be highly skilled and able to identify appropriate strategies for coping with conflict [5];
- e) mediation in participation may be more effective when building on previous experience in order to consciously deal with future opportunities [12];
- f) mediation in participation means building mutually beneficial and workable agreements in order to take action. Planners must therefore be able to recognize discussion that encourages moderation and mediated agreement within dialogues [21].

With regards to the role of evaluation, it should be noted that assessing participation is unquestionably a demanding task, not only in relation to the considerations mentioned above but above all, to its multi-dimensional, pluralistic and often conflicting character. Nevertheless, evaluation has long been recognised as fundamental in providing a general and essential enrichment of the planning process [22].

An epistemological analysis of evaluation as a cognitive process and creator of social realities reveals, however, its value and significance, not merely as a set of judgments at the conclusion of a process, but, rather, the construction of meaning by participants, developing a self-reflective learning process, discovering unknown meaning in actions and building networks (of people, actions and thoughts). This occurs when evaluation equates to an opportunity for the recognition on the part of participants of having worked alongside one another, enjoyed the experience, and recognized their own commitment, potential difficulties, as well as critical points and weaknesses. In this perspective evaluation may be considered not only in terms of a final outcome or an administrative procedure, intended to validate, or otherwise, participatory activities but, rather, as a working method, a "process of gradual learning" which makes sense, even when developed through small steps or partial experimentation. The purpose of evaluation is, in fact, not simply, or solely, making judgments of eligibility but increasing, within the decision-making process, an awareness of choices made. Evaluation is, in this sense, revealed as an innovative feature of a learning process and, therefore, becomes a critical research task generating increased awareness and responsibility in terms of choices to be made [23], especially in the case of social and institutional interaction that is both concrete and continuous.

2 ICT to Evaluate Participation in Urban Planning

2.1 The Evaluation of Participation in Urban Planning

Examining the considerations outlined of the previous paragraph, building upon the knowledge accumulated over forty years experience in evaluation processes in urban planning (from the early works of Lichfield, Kettle and Whitbread [22] to the later work of Faludi [24] and Seasons [25]), the following section summaries various basic elements of evaluation within participatory urban planning pathways. The ever-greater attention paid towards participation in urban planning has not been matched by similar focus in terms of paths chosen in applying such evaluation and eventual results, leading to a relative lack of disciplinary debate on the nature of the relationship between evaluation and urban planning.

Influential authors in the field of urban planning regulations such as Healey [26], argue that however evaluation is defined and implemented it remains, nevertheless, a key activity in urban planning. Others, such as Faludi [24], consider evaluation in planning as a complex, yet necessary practical exercise. The theory of communicative action has become a mainstay of planning [2] [27] [28]. Few, however, have attempted to understand how to evaluate the effectiveness and efficiency of participatory practices in urban planning [29].

The assessment of urban planning may be considered, in general, a means to represent and communicate a project, a plan, program or policy as an object open to judgment as well as an opportunity for capacity building [25]. Assessing public action is to judge its value in a perspective of collective interest with explicit criteria and targeted information (both common and different from those used for the development of an action plan, [30]). Assessment in this context should, in the opinion of the authors, seek to highlight whether and how a plan may facilitate the development of capacities of affected communities (both local and connected), without responding exclusively to declared or detected needs. A plan is therefore defined as neither right nor wrong due merely to the effects or impacts it may produce or to a theory that proposes its execution but, above all, to the capacities that it is capable of creating and implementing in settled, interested communities. A plan thus becomes a social occasion, and evaluation a means to recognizing its importance.

The evaluation of participatory processes in urban planning thus becomes not only an adequately constructed opportunity in order to generate expert judgement (scientific knowledge, importance of method, etc.) but, rather, the means to supporting informed dialogue between players and forms of knowledge (the dialogue between expert knowledge and the ordinary [31]). The need to evaluate plans and the desire to analyse the outcomes of participatory pathways should carefully consider the difficulties of this task, both in terms of its entirety as well as its various divisions: a link between modes of evaluation and the products or processes under evaluation; the range of possible definitions of the issues to be evaluated; the multiple criteria and indicators to be used; the search for data sources; the presentation of evaluation results; monitoring activities of activities evaluated.

Alexander [32] argues that the complexity of assessment in planning schemes is largely due to three fundamental issues:

1. The complexity of objects and subjects of evaluation such as policies, plans, projects, local contexts, key-players, stakeholders and, at the same time, the complexity of the evaluation process involving different disciplines, theories, methods, tools and techniques;
2. The inter-subjectivity that somehow undermines the legitimacy of findings and objectively derived conclusions;
3. The uncertainty of planning actions concerning the prediction of an unknown future.

Lichfield [33] outlines certain key issues of assessment in urban planning:

- The assessor should be a member of the planning group from the outset;
- Evaluation criteria should be identical to urban planning criteria;
- Information necessary for evaluation should be identified at the beginning of the planning process;
- On-going evaluation methodologies should be able to integrate and improve the implementation of a plan and provide the necessary adjustments throughout the urban planning process;
- Ex-post evaluation should analyse whether the policies and objectives of the plan were carried out, reviewing the ex-ante and contributing to their improvement if necessary.

The position of Lichfield on the need for the evaluator as part of the working group of planners is not always shared in the literature and, in the opinion of the authors, should be combined with an independent internal evaluation able to report any negative results arising from the process.

2.2 The Possible Support of ICT in the Evaluation of Participation in Urban Planning

There is a widespread necessity for governments to rethink analysis methods of citizen participation, requested or otherwise. It is immediately clear that such an issue is fundamentally cultural and organizational in nature, not resolved through the simple introduction of technology into participatory processes. Technology is capable, however, of assisting in change. As previously highlighted, the complex task of analyzing large amounts of unstructured information can be supported by technology. This is demonstrated, for example, through the possibilities offered by information and communication technologies in online forums in the storage of data collected and contextualized during their insertion by participants themselves, a process which naturally lends itself to content analysis. In order to assess, however, the support levels offered by ICT in participatory pathways, the following key issues must be addressed:

- who is to define criteria for the analysis of participant contributions;
- how contributions collected online can be integrated in decision-making;
- how evaluation is carried out in terms of contributions received online and those collected traditionally;
- how, and to what extent technology can assist in highlighting possible areas of agreement and disagreement;
- to what extent technology can adequately support the synthesis and analysis of the content of the contributions gathered.

As previously mentioned, one of the central characteristics of participatory pathways conducted online is the tracking of contributions. Eventual dialogue between participants is visible to all in precisely the same terms used by participants, without the need for interpretation by a facilitator, thus rendering several modes of analysis. There exists a range of well-known methods for qualitative analysis aimed at developing interpretative categories in participatory processes as, for example, the analysis of ethnographic content [34] [35]. Each approach shares the objective of interpreting large amounts of text in order to produce a narrative summary. It is therefore possible within online participatory processes to examine the number of comments posted, the average and total number of words used to describe the same concept as well as the number of response levels (the number of question/answer exchanges). The values of such data may provide an indication of which issues stimulated participants and which were better able to provoke debate.

It should be noted that forms of evaluation of policies, programs and plans are, generally speaking, relatively rare (indeed, only since 2008 has it become obligatory in Italy to accompany planning projects or proposals with a Strategic Environmental

Assessment - SEA¹) and that, more often than not, such assessment is carried out ex-ante, in certain cases is on going yet almost never ex-post. The support offered by ICT in the evaluation of participatory processes in urban planning suffers, therefore, from the lack of a comprehensive evaluation framework of participation within decision-making processes in general. Furthermore, it is necessary to establish whether evaluation is carried out from the standpoint of governing bodies or citizens.

Governments now routinely employ ICT in supporting processes of political action, as is highlighted by the case study presented below. E-mail, online discussion forums and message boards now appear on a range of government websites at various levels, interested in urban planning and territorial cohesion, and have recently been joined by tools such as the social networks Facebook and Twitter, increasingly employed in political life to develop and manage the social networks that accompany participative processes. Relations, however, between the development of information technology and participation in democratic processes have yet to be systematically explored. Before carrying out assessment it is therefore necessary to identify the aim of the online involvement of citizens.

Whyte and Macintosh [36] argue that in order to assess the effectiveness of online participation in engaging a wider audience and to improve deliberation in order to inform and influence decision-making, an analytical framework must be developed that takes into account overlapping political, technical and social viewpoints.

The political perspective asks: has consultation followed guidelines for conducting consultations issued by the government and are stakeholders satisfied by the process?

The technical perspective addresses: to what extent did the design of ICTs directly affect e-consultation outcomes? In designing the e-consultation there is a need to take into account technical skills, the target audience and the location of participants.

The social perspective asks: were the contributions relevant to the policy topic, were they informed contributions and were the contributions debated and supported (or not) by others? This perspective is concerned with the extent to which the social conditions of those being consulted affect the communicative skills of citizens, their capability to contribute and consultation outcomes.

From a technical standpoint, the extent to which the design of ICT has directly influenced the results of participatory process should be examined along with the capacity and location of target participants.

From the social point of view, contributions concerning political themes must be examined. When attempting to render such questions as concretely located within urban planning practices, the complexity of such an operation is emphasized as assessment must take into account the interdependencies between the design of computer systems, the implementation of urban policy and communication practices between citizens and governmental agencies. Assessing the tangible impact of participatory process on choices made within a plan is a particularly challenging issue that may prove difficult to resolve.

¹ Legislative Decree No. 152/2006 coming into force through Legislative Decree No. 4/2008, implemented in European Directive 42/2001/EC.

3 “PartecipaPUG”: A Participation Process in the South of Italy

3.1 “PartecipaPUG” in Brief

The goal of the collaborative process was that of gathering and formalizing the views and wishes of residents and stakeholders in order to define a new local development plan (see table 1) in the city of Monopoli² in the South of Italy.

In 2003, based on the successful results achieved according to public opinion from previous experiences in collaborative planning, various sections of the town council decided to accompany the creation of the new municipal development plan with a public participation process, integrating the knowledge of citizens with the techniques of planners through a logic of mutual learning. The town, and its administrative staff, was thus able to learn more about their own territory, designing ways in which to implement development hypotheses.

The process was finally initiated in 2006 following a successful proposal in a national request for tender from the Italian Ministry for Innovation and Technology aimed at funding projects supported by experimental e-democracy tools, combining the use of traditional participation methods with ICT support techniques within collaborative processes (see table 2).

Table 1. Significant aspects of the collaborative process in the “partecipaPUG” process

The collaborative process of the General Urban Plan of the Council of Monopoli

The collaborative process of the General Urban Plan of the Council of Monopoli					
<i>Body</i>	<i>Territorial coverage</i>	<i>Objectives of the collaborative process</i>	<i>Participative methodologies</i>	<i>IT support tools</i>	
Council authorities	Council	Understanding with each group of key players:	On-line and off-line public forums	Web, videos	
Environmental groups				On-line forums	
Schools		Needs, opportunities, actions and initiatives to be undertaken through the new development plan	On-line and off-line workshops	Blogs	
Representatives of other economic, social and third sector bodies				On-line and off-line brainstorming	Electronic Meeting Systems
Representatives of professional bodies (architects, engineers, planners)				Define ex-ante objectives of the plan in a shared manner, allowing participants to evaluate documentation and the choices made by designers ex-post	Questionnaires distributed on-line and off-line
		Virtual online scenarios	Electronic voting		

² 50.000 Inhabitants, distributed on a territorial surface of about 156 km².

To date, until the first half of 2007, around 1200 questionnaires have been collected, the majority according to traditional data gathering methods and around 200 online; 12 "brainstorming" sessions have been carried out off-line with the video format available on-line along with a total of around 1400 geo-referenced data records in a data base.

The initial results of the experience have included the promotion, within the local community, of the concept of an open and democratic planning process to which any individual may contribute [1].

Around 1,000 individual have participated in Web-based or traditional meetings, work sessions and online forums. The web provided an office environment open 24

Table 2. The table shows the manner in which the various ICT tools were employed during the process

ICT support tools	Software	Capacity of tool	Mode of use
Web page: www.partecipapug.it	Microsoft Explorer®	The web allowed for communication and informed all stakeholders of the process; acted as the portal from which all site services could be accessed	Different times / different places Same times / different places
On-line forums	Microsoft Explorer®, Access®	Acted as the virtual discussion space	Different times / different places
Blogs	Microsoft Explorer®, Access®, Blogit software®	Diary of views on issues of the plan	Different times / different places
Electronic Meeting Systems	Meetingworks®	Allowed for the management, analysis and recording of online brainstorming sessions, synthesized through the development of tables, graphs and final reports	Same times / same places Same times / different places Different times / different places
Cognitive maps on WebGIS	Map Guide®, Access®	Represented the views and perceptions of residents on issues of value to the local area	Different times / different places
Electronic voting	Microsoft Explorer®, Access®	Allowed for voting on proposed scenarios for the future of the municipal area in several key issues (including the port, coast, rural- agriculture, historical centre, tourism)	Different times / different places

hours a day, where data and information on the collaborative planning process could be easily tracked, including conceptual designs of the plan, even before their adoption by the Town Council.

The cognitive maps, developed with the results of questionnaires and interactive maps, highlighted social consensus through a geographic database, making the basic themes of the Plan clearly available for political decision-makers and citizens themselves. Confirming results found in the literature [37] [38], it should be noted that in the case presented, politicians did not use the web in order to interact with participants and that users had no means of communicating up until the point of facilitator-promoted involvement.

The only means to improving the level of web-based participation was through an on-line facilitator at certain times of day. Indeed, participation levels proved to be higher during those periods. It is therefore of significance that those attempting to utilize forms of interactive dialogue at the same time while in different places aim to reproduce the actual mechanics of virtual socialization to a greater degree than those interacting at different times as well as from different places.

PartecipaPUG - Incontri sul web - Mappa interattiva della Città [torna alla home](#)

sei in questa zona...

Questionario con mappa interattiva

domanda 1

"Seleziona sulla mappa i luoghi che ritieni più belli"

Per rispondere ...

scegli di... spostarti nella mappa oppure... clicca sulla zona di tuo interesse

sei in ... Settore Sud-Est

irretta navigazione si consiglia di **NON utilizzare** i tasti **Avanti** e **Indietro** del browser

credits Progetto PartecipaPUG - Città di Monopoli - Ufficio URP Numero Verde 800253735 - P. IVA 00371620722 best view 1024x768

Fig. 1. Interactive map published through WebGIS (Autodesk MapGuide®). The user was able to associate a response to a SWOT analysis for the identification of dominant environments in the council area to a map.

3.2 Assessing Participation in the “PartecipaPUG” Process

As noted in paragraph 2.2, following on from considerations offered by Whyte and Macintosh (2002), assessment was carried out in terms of the effectiveness of online

participation in engaging an extensive audience and in improving deliberations in order to inform and influence decision-making, taking into account three overlapping perspectives: the political, technical and social. In the political perspective, consultation followed guidelines for the carrying out of consultations published by the Ministry of Innovation and Technology. The participatory process involved all areas of the city and participating citizen groups stated their general satisfaction with the process with the exception of certain individuals who considered participation in the preliminary phase (drawing up of general guidelines) as ineffective, considering participation more relevant during the definition of planning choices phase, particularly decisions regarding the identification of locations. From the technical point of view, key points arising from web-based activities were represented by evaluating the number of daily visits, as demonstrated in the figure 2. Evaluation was made of the most commonly travelled web routes followed in accessing the project web site, noting that 80% of visitors gained access the web portal of the town council (www.comune.monopoli.ba.it). The “anchor” effect could have been greater still, given the high number of visitors regularly using the web site of the council (around 1000 per day). However, the site is lacking in terms of both an independent identify and an adequate number of links from other sites. While open site access has seen peaks of up to 200 visitors per day, access to the forums and blogs of the project, available through a registration process, saw the registration of 228 participants over the entire year of project activity.



Fig. 2. Daily number of visits to www.partecipapug.it

The range of information and documentation published on the “partecipaPUG” site included:

- Documentation on the existing urban master plan as well as the new plan in its development phase.
- Audio and video resources and written accounts of 12 live meetings as well as the entire town council meeting during which the Preliminary Planning Document was adopted.

It was not possible to identify the number of unregistered users downloading the above documents, while registered users data showed around 67% of users

downloading the draft Preliminary Planning Document (a document outlining the main issues relevant to the creation of the plan itself), demonstrating the usefulness of e-democracy when conceived as a virtual bulletin board, constantly available to citizens through information and communication technology. In addition, the “participaPUG” site functioned as a common platform hosting several electronic participation tools over time including:

- 2 open access blogs including 1 multimedia blog;
- 1 forum accompanying the live meetings;
- 5 themed multimedia forums open to all in read-only mode (with registration required in order to contribute);
- 1 interactive *geoblog* map providing navigation through a detailed geographical map allowing for comments associated with specific areas of the town;
- various web pages allowing access to and/or the downloading of information and documentation.

The first open dialogue toolbox, in May 2006, had a forum structure in which anyone could submit a contribution either to open a new discussion, join a discussion with a comment or attach multimedia files. A total of 39 discussions were instigated by an initial contribution, generating a total of 105 comments, distributed with 7 contributions receiving no comments and 16 contributions receiving 3 or more comments. The maximum number of comments on any discussion was 9 and 4 messages were accompanied by photographs. Few contributions went unacknowledged and most messages actually opened group discussion. The multimedia nature of the experience, carried forward until the end of 2007, does not yet appear mature (user behaviour must be assessed with more recent data) and most participants preferred to express themselves verbally. The collection tools used lend themselves to both shorter comments and more articulate reflections. The registration process seems to hinder extemporaneous posts to a greater extent than in-depth reflections, while discouraging the operation of novice users. The five thematic forums began in November of 2006 with the aim of pursuing the following objectives:

- Focusing on four priority areas (*port, coast, countryside, historical centre and city centre*) identified by the designers of the PUG, which saw the later addition of *tourism*, proposed by a citizen;
- Allowing citizens to express their preference for certain strategic choices (scenarios) presented in the Preliminary Planning Document, identifying possible decision options.

The complex web pages contained:

- Multimedia documentation (text, attachments, photographs, maps);
- Discussion forums moderated and reserved for registered users;
- Survey to rate favourite scenarios.

A total of 50 messages were received: the growing number of thematic definitions and the wealth of content does not seem to operate in favour of participation. Only the forum focusing on the port attracted real interest, generating 25 messages and representing the only real discussion on specific scenarios. Evaluating the results, it

can be argued that opening discussion forums on predefined themes can capture the attention of citizens if the issue is significant, and if participants are able to express opinion on real existing alternatives. The registration process may have discouraged potential participants yet most users, in any case, chose a pseudonym rendering them anonymous. Similarly, in this case the opportunity to express opinions through multimedia language was not grasped, remaining limited to textual interventions.



Fig. 3. The access page to the five city scenarios forum for 2020 (www2.comune.monopoli.ba.it/partecipapug.it)

The forum may have played a further positive role in terms of creating a better understanding of the parts of the Preliminary Planning Document that sought to stimulate discussion. The interactive map tool (see figure 1) allowed visitors to navigate to different scales in a map of the entire council area divided into sectors, followed by macro-areas and then into square cells with an edge equal to 100 meters. Citizens had the opportunity to associate comments with the above-mentioned spatial entities, responding to one or more questions through an online questionnaire. From a purely quantitative point of view, the response of citizens must be considered remarkable when compared to similar initiatives carried out in Italy during the same period (2006-2007) and, indeed, the survey by the CENSIS Institute of Social Surveys (www.censis.it) published in 2006 on behalf of the Italian Ministry for Reforms and Innovation in Public Administration. The civic network of the town of Monopoli is assigned a score summary of 52, placing the town at 16th place in national rankings of municipalities of more than 40,000 inhabitants that are not provincial capitals and at 1st place among towns in the Apulia Region of the same size category. Excellent results have been achieved on a cultural level: a number of individuals now have a basic grasp of what the new urban town plan entails, a good number of individuals have actively discussed the issue, with the majority of those involved or, at least, informed, expecting the council to pursue the same process of participation and transparency in future initiatives. E-democracy as the provision of innovative services by a public authority (best defined as e-government) would seem, therefore, to have worked effectively in the case of Monopoli, although further efforts are needed in order to open up actual decision-making and implementation processes. Real dialogue

(at least web-based) has been lacking between decision makers and citizens and, with a few notable exceptions, politicians (both from the majority and opposition), officials and technicians did not make use of their interactive tools. The town council put faith in “partecipaPUG” in order to communicate their initiatives and gauge public opinion on specific urban issues. Questions were raised, from the social point of view, regarding what participative contributions were made to planning choices. Potential explanations are complex as distinguishing participative contributions from those of participating technicians and politicians is not clear-cut, even if some elements are unquestionably related to the outcomes of participatory process. Among such elements, significant choices relate to structures in rural contexts in which the aim is that of strengthening the presence of small, traditional community settlements; choices regarding the port and the nineteenth-century city centre focused on protection in order to avoid “museification”.

4 Conclusions

It is evident that generalizations cannot be made regarding the particular experiences as outlined above. Indeed, consistent with the scientific rigor under examination, it is necessary to conduct further studies in order to analyse the specificities of all results observed from a socio-cultural perspective. It would, for the moment, seem appropriate to draw attention to the large-scale e-democracy projects being carried out on a global scale, both in terms of their techniques and approaches used, and in terms of social consequences resulting from their employment. The collaborative planning experiences in the town of Monopoli are related to certain circumstances rarely found in other contexts in the south of Italy such as:

- The existence of a relationship of trust between citizens and experts;
- The existence of a reciprocal relationship (and conflict management) between technical expertise and political will;
- The development within the public authority of a particular aptitude for planning, namely the ability of public institutions to recognize the complexity of problems, and willingness to overcome potential deadlocks, to build relationship networks and encourage public debate.

In the transition from regional to local, private interests and personal claims prevail. The project therefore loses its strategic dimension and becomes more operational and detailed. The role of the various tools used also varies, thus altering the specific form of a participative process, from information to communication between expert and common knowledge. Information technologies prove most effective in the problem identification stage and brainstorming than in the project phase itself. Furthermore, the same technical planner takes on different roles at different stages of the participation process through the use of ICT. The planner uses the network infrastructure as a means of delivery and content distribution. Communication is “one-to-many” in nature and, at least in theory, one planner may communicate the same content to an unlimited number of recipients. In the decision making phase, the technician/planner becomes part of the dialogue that develops between individuals. The interaction is typically “many-to-many”. It therefore follows that the technical

planner is not necessarily the most central point of reference for action, but tends to take on such a role among a number of players. Eventually, the planner will be charged with the task of translating the results of the participatory process into more technical planning language by assessing the participants - the authority and the key players involved - as well as the consistency with the objectives of the entire territorial project. The use of information technology in participatory processes surely implies a pathway with numerous pitfalls, but also a range of challenges in which a different way of interacting with others may be discovered which are neither better nor worse than traditional "face to face" methods, simply different. The net is undoubtedly intended as a space in which the interaction between citizen-citizen or citizen-planner or institution-citizen may be enriched by new modes of communication. ICT clearly provides immense opportunities. The advantages that such technologies possess when compared to more traditional forms of face-to-face participation are considerable (low cost, easy access to information, flexibility of space and time, resource sharing, increased users, ease of management of informative content, measurement of results, etc.). They are, at least in theory, highly democratic tools, providing everyone with the same opportunity to choose whether, when and how to intervene. While it may be true that such methods lack human contact with relationships "mediated" by the computer, a range of other aspects including the opportunity to reflect on what was said/written by others offsets such "deficiencies". Such reflection also applies to exposure in the first person, which is not necessarily less spontaneous, but, perhaps, less impulsive, as the experience of the urban plan in Monopoly demonstrates though the comparison between on-line questionnaires and traditional responses. Such methods also provide individuals with the possibility to "play" with their personality, posing as someone different from their everyday persona, abandoning masks and spontaneously offering ideas, sometimes uncomfortable and difficult to externalize when in physical proximity to others. It is clear that even computer-mediated communication presents a number of risks: among them being misunderstood or not fully understood, due, perhaps, to the lack of the visual smile or a sullen face that "supports" the language produced. However, if such risks and pitfalls are shared and clearly defined from the start, perhaps more attention may also be paid to interpretation and judgment. Diachronic communication can gain in terms of the reflexivity of interventions and proposals within a participatory process but may remain liable to lose spontaneity. In this case, ICT would tend to reduce or even remove disputes (conflicts) that, despite their intense involvement in the processes of traditional face-to-face processes, can lead to learning and the construction of new knowledge. The need to communicate through texts at different times within a group involves an effort in terms of synthesis and greater clarification than face-to-face communication. Processes of meta-reflection on what is being written are thus developed with ICT able to provide learning environments in which individuals construct new knowledge through negotiation and the sharing of meanings. Difficulties associated with the use of ICT are frequently connected with finding the right motivation to work with such methodologies rather than understanding how such systems may work in a technical sense. Evaluating ICT capacity to support the assessment of participation in planning process still remains a need in its different political, technical and social aspects. The case of "participaPUG" has shown that ICT could simplify this evaluation.

References

1. Healey, P.: Collaborative Planning. Shaping Places in Fragmented Societies. Macmillan Press Ltd., London (1997)
2. Forester, J.: The deliberative practitioner. The M.I.T. Press, Cambridge (1999)
3. Duany, A., Zyberk, E.: Nine Questions About the Present and Future of Design. *Harvard Design Magazine* 20, 5–52 (2004)
4. Wenger, E.: Communities of practice: learning, meaning, and identity. Cambridge University Press, Cambridge (1998)
5. Forester, J.: Making participation work when interests conflict. *Journal of the American Planning Association* 72(4), 447–456 (2006)
6. Arnstein, S.: A ladder of citizen participation. *Journal of the American Institute of Planners* 34(4), 216–224 (1969)
7. Schön, D.: The reflective practitioner: How professionals think in action. Basic Books, New York (1983)
8. Hoch, C.: What planners do: Power, politics, and persuasion. Planners Press, Chicago (1994)
9. Baum, H.: The organization of hope. Albany, State University of New York (1997)
10. Innes, J.E., Booher, D.E.: Consensus building as role playing and bricolage: Towards a theory of collaborative planning. *Journal of the American Planning Association* 65(1), 9–26 (1999)
11. Susskind, L., McKernan, S., Thomas-Larmer, J. (eds.): The consensus building handbook: A comprehensive guide to reaching agreement. Sage, Thousand Oaks (1999)
12. Susskind, L.: Activist mediation and public disputes. In: Kolb, D.M. (ed.) *When Talk Works: Profiles of Mediators*, pp. 309–354. Jossey Bass, San Francisco (1994)
13. Moore, M.: Creating public value. Harvard University Press, Cambridge (1995)
14. Marris, P.: Loss and change. Routledge, London (1986)
15. Baum, H.: Why the rational paradigm persists: Tales from the field. *Journal of Planning Education and Research* 15(2), 127–135 (1996)
16. Susskind, L., Field, P.: Dealing with an angry public. Free Press, New York (1996)
17. Umemoto, K.: Walking in another's shoes: Epistemological challenges in participatory planning. *Journal of Planning Education and Research* 21(1), 17–31 (2001)
18. Sandercock, L.: *Cosmopolis II: Mongrel cities in the 21st century*. Continuum Books, New York (2003)
19. Laws, D., Rein, M.: Reframing practice. In: Hajer, M., Wagenaar, H. (eds.) *Deliberative Policy Analysis: Governance in the Network Society*, pp. 172–206. Cambridge University Press, Cambridge (2003)
20. Lewicki, R., Gray, B., Elliot, M.: Making sense of intractable environmental conflicts. Islands Press, Washington, DC (2003)
21. Reardon, K., Welsh, J., Kreiswirth, B., Forester, J.: Participatory action research from the inside: A profile of Ken Reardon's community development practice in East St. Louis. *American Sociologist* 24(1), 69–91 (1993)
22. Lichfield, N., Kettle, P., Whitbread, M.: *Evaluation in the Planning Process*. Pergamon, Oxford (1975)
23. Fusco Girard, L., Nijkamp, P.: *Le valutazioni per lo sviluppo sostenibile della città e del territorio*. Franco Angeli, Milano (1997)
24. Faludi, A.: Evaluating plans: the application of the European Spatial Development Perspective. In: Alexander, E. (ed.) *Evaluating and Planning, Evolution and Prospects*, pp. 119–143. Ashgate, Aldershot (2006)

25. Seasons, M.: Monitoring and evaluating in urban planning. Chapter 9 in the UN-Habitat Global Report: revisiting urban planning. Nairobi, UN-Habitat (2009), <http://www.unhabitat.org>
26. Healey, P.: Evaluation in planning. In: Pinho, P., Oliveira, V. (eds.) *Citta 1st Annual Conference on Planning Research*. FEUP edições FCT Citta, Porto (2009)
27. Healey, P.: Transforming governance: challenges of institutional adaptation and a new politics of space. *European Planning Studies* 14(3), 299–320 (2006)
28. Innes, J.E., Booher, D.E.: *Planning with complexity: an introduction to collaborative rationality for public policy*. Routledge, London (2010)
29. Rotondo, F., Selicato, F.: E-Democracy in Collaborative Planning: a Critical Review. In: Murgante, B., Gervasi, O., Iglesias, A., Taniar, D., Apduhan, B.O. (eds.) *ICCSA 2011, Part II. LNCS*, vol. 6783, pp. 199–209. Springer, Heidelberg (2011)
30. Alexander, E.: Evaluation and status: where is planning evaluation today and how did it get here? In: Alexander, E. (ed.) *Evaluating and Planning, Evolution and Prospects*, pp. 3–16. Ashgate, Aldershot (2006a)
31. Patton, M.: *Qualitative research and evaluation methods*. Sage, Thousand Oaks (2002)
32. Alexander, E.: Problems and prospects: dilemmas in evaluation and directions for the future. In: Alexander, E. (ed.) *Evaluating and Planning, Evolution and Prospects*, pp. 267–276. Ashgate, Aldershot (2006b)
33. Lichfield, N.: Where do we go from here? In: Voogd, H. (ed.) *Recent Developments in Evaluation*, pp. 7–15. Geopress, Groningen (2001)
34. Altheide, D.: Ethnographic Content Analysis. *Qualitative Sociology* 10(1), 65–77 (1987)
35. Strauss, A., Corbin, J.: *Basics of Qualitative Research: Grounded Theory Procedures and Techniques*. Sage, London (1990)
36. Whyte, A., Macintosh, A.: Analysis and Evaluation of e-Consultations. *E-Service Journal* 2(1), 9–34 (2002)
37. Coleman, S., Götze, J.: *Bowling Together: Online Public Engagement in Policy Deliberation*. Hansard Society and BT (2001)
38. Rotondo, F.: Utility of web and electronic meeting systems supporting collaborative planning. In: Bucher, U., Finka, M. (eds.) *The Electronic City*, pp. 219–240. *Berliner Wissenschafts - Verlag BWV*, Berlin (2008)

A Spatial Data Infrastructure Situation-Aware to the 2014 World Cup

Wellington Moreira de Oliveira^{1,2}, Jugurta Lisboa Filho¹,
and Alcione de Paiva Oliveira¹

¹ Universidade Federal de Viçosa (UFV),
Departamento de Informática
36570-000 Viçosa - MG, Brazil

² Instituto Federal de Educação,
Ciência e Tecnologia do Sudeste de Minas Gerais,
Campus Rio Pomba,
Departamento Acadêmico de Ciência da Computação
36180-000 Rio Pomba, MG, Brazil
wellington.moreira@ifesudestemg.edu.br,
jugurta@ufv.br, alcione@dpi.ufv.br

Abstract. World events as the 2014 World Cup not only need a good physical infrastructure, but also need a virtual infrastructure consisting of intelligent information systems that can assist users in locating games, drills, interviews, among other events and services associated with the Cup and their preferences. Spatial Data Infrastructure (SDI) context information associated with the mapped ontology is presented as a solution to the search and location of events and services for the World Cup intertwined with the "interests" of the user and can be replenished by him voluntarily.

Keywords: SDI, TSDI, Situation-Aware, Ontology, World Cup.

1 Introduction

The World Cup to be held in Brazil in 2014 will bring together millions of people from different cultures, different nationalities and with different objectives. Each of these people (athletes, spectators, journalists, etc.) has different interests that are directly or indirectly related to this event.

To provide adequate infrastructure to carry out the World Cup, the Brazilian government in partnership with the private sector, has undertaken several initiatives. Most of these initiatives are linked to physical infrastructure, such as the construction of stadiums, airports, public transport, hotels, among others. The Brazilian government foresees an investment of about US\$ 26 billion to meet the demands of physical infrastructure for the World Cup which includes the modernization of airports, football stadiums, telecommunications, security, professional training, safety, urban mobility, energy and health, generating an "indirect impact" of about US\$ 105 billion [1]. Moreover, beyond any physical structure, there will be a great demand for

information related to events (games, drills, interviews, etc.) and information relating to other personal needs such as food, lodging, clothing, etc. In all these information notices the presence of two important attributes in common that should be considered: the location of events and/or services and the relevance of these events and/or services to particular user.

Currently many services and applications on the Web GIS (Geographic Information System) allow you to find information about many different locations. However, to maintain a GIS with data from multiple vendors and distribute them in a transparent way in the network is necessary to use a Spatial Data Infrastructure [2].

Spatial Data Infrastructure (SDI) has provided adequate support to numerous projects and projects where the use and ease of access to spatial information and associated services are their main requirements. This infrastructure can meet the different levels that can be global, national, regional or local [3]. In Brazil there are many regional and local initiatives beyond the INDE (National Spatial Data Infrastructure) which is defined as:

“Integrated set of technologies, policies, procedures and mechanisms for coordination and monitoring, standards and agreements necessary to facilitate and organize the generation, storage, access, sharing, dissemination and use of geospatial data source federal, state, district and municipal level.”[4]

The INDE is maintained by the National Commission for Cartography (CONCAR) [5] and has several spatial data sets about the Brazilian territory, documented through metadata. These metadata follow the profile MGB (Brazilian Geographical Metadata) in accordance with ISO 19115:2003 and its catalog is managed by an open source system called GeoNetwork.

This article describes the creation of a Spatial Data Infrastructure situation-aware that will benefit visitors and professionals involved with the 2014 World Cup. The system also allows them to find the location of events and/or services according to their personal preferences. Finally it collects data obtained by the user's browsing to feed a database of information based on the concept of VGI (Volunteered Geographic Information).

2 Related Works

The development of SDI involves technical and nontechnical elements for the exchange, distribution and sharing of spatial data in an ongoing process of negotiations and alignments between heterogeneous actors within a specific context [6]. An SDI is not something that can deliver as a finished product or an artifact, rather it should be considered as an ongoing process [6]. Figure 1 shows the configuration and performance of SDIs.

Among the various components of SDIs shown in figure 1 (geomatics, public administration, sociology of organizations, laws and economics) one occupies a prominent position to be the basis of all SDI: geographical information.

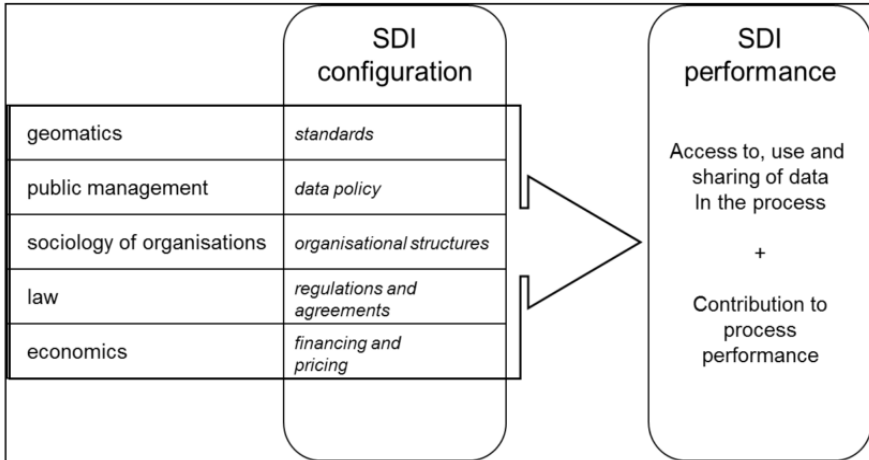


Fig. 1. Configuration and performance of an SDI [7]

The human characteristics include geographic information, environmental information, measures of air quality, place names, cultural information, etc. This type of information cannot always be detected by remote sensing devices. Volunteered geographic information (VGI) presents itself as a solution with greater coverage. This information has more than 6 billion of sensors: the whole terrestrial population spread across the globe [8]. A good example is the use of VGI in the project Open Street Map (<http://www.openstreetmap.org/>) which has tens of thousands of fonts provided by citizens with or without previous experience in geographic information. There are still mechanisms to ensure the quality of this information, remove errors and constitute some level of confidence on the other hand shows how volunteering is the only solution for the decline in the supply of geographic information worldwide [8].

In creating an infrastructure that takes into account user preferences, which is the objective of this work, is necessary to make use of the mapping environment through an ontology. According to [9], from the standpoint of computer science, ontology "is a formal explicit specification of a shared concept." This type of mapping is essential to model the environment of each user, allowing them to access the geographic information of interest.

The ontology-based computing has recently shown a tendency to develop a model for processes situation-aware based on computer [10]. Currently, few languages have been standardized to formalize ontologies. Only the Semantic Web languages such as Resource Description Framework (RDF) and Web Ontology Language (OWL), which is based on RDF, support logic to formalize ontologies [10]. The OWL has been widely used as a language formalization of ontological concepts and was standardized by W3C [11].

An SDI also provide access to data also offers various services, from a simple query to a metadata geoprocessing services, such as viewing maps and location of entities based on coordinates. To ensure that these services are available to a larger

number of people and systems in distributed and collaborative it is necessary to use Web Services. This technology not only provides independent services it also supports a collaborative work where components (Web Services) designed for a given service can be connected to form a greater service [12].

Aiming at interoperability of geoprocessing services Open Geospatial Consortium (OGC) [13] standardized specifications for Web services that handle data on geographic information and services, known as OWS (OGC Web Service). This standard allows the connection of multiple Web services that together form a dynamic application [12]. Figure 2 illustrates the main OGC standards.



Fig. 2. Main OGC standards [14]

Some works have been developed for problems relating to other major events like the Olympic Games 2008 in Beijing. Working in context of this event, Weißenberg [15] developed a platform (FLAME 2008) for mobile devices, which provides services to the user, based on information in your environment.

In [16], Lamas et al. propose a GIS situation-aware mobile system to assist students, faculty, staff and visitors to find events at university sectors. In his work models were developed and architectures to support location services also based in the user environment.

Rodrigues [17], in his work on GIS in public transport, developing a proposal for an SIU (System User Information) that allows users to receive and interact with systems that display information about public transport, georeferenced and contextualized for your environment.

All works presented above deal with situation-aware GIS that can even be improved and applied to other major events like the World Cup 2014. However, none of them makes use of data availability, services or metadata of SDIs, or proposes to issue an IDE such as situation-aware solution to the demand for spatial information that take into account the user's environment.

According to [18], an SDI aimed at a specific community of users (e.g. tourists and professionals involved with the World Cup in 2014) with thematic data (information about this event) is called Thematic Spatial Data Infrastructure (TSDI).

3 Architecture for Situation-Aware SDIs

The SDI issue described in this paper uses an interface as a Web application that makes use of a GPS and failing to ask the user to define its geographical position. The information processing is performed by Web services following the OGC standards. Figure 3 shows the architecture of the SDI in layers with their respective components.

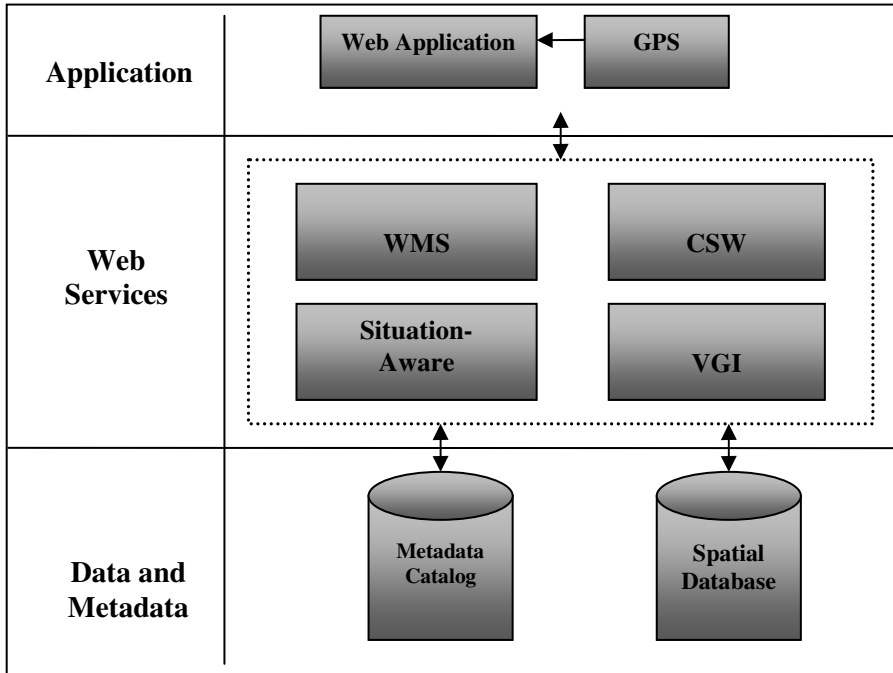


Fig. 3. Architecture of a situation-aware SDI

The three layers of the architecture of the SDI proposal with their respective components are described below:

- *Application Layer:* The application layer consists of the Web application and the GPS device.

- *Web Application:* it consists of an interface with support for multiple languages that prompts the user for a username and password to access and display information about its location and other context information as events or services of interest. The user can at any time to update your list preferences, or to search on other events or services.

- *GPS (Global Position System):* global positioning system that provides the geographic coordinates through a point receiver. If the computer, laptop or mobile device does not have GPS, the user can enter his/her current location using the interface.

- *Web Services layer*: a Web services layer consists of the WMS, and CSW VGI.
- *WMS (Web Map Service)*: Web services responsible for creating and/or display of maps.
- *CSW (Catalogue Service for the Web)*: Web services responsible for searching for metadata in the catalog.
- *Situation-Aware*: This ontological mapping based on Web service provides information relevant to user preferences.
- *VGI (Volunteered Geographic Information)*: the user can at any time provide new information about a particular place or about events and services related to a location. These data are filtered to increase the geographic database of the World Cup 2014.
- *Data and Metadata Layer*: This layer is composed by Metadata Catalog and the Spatial Database.
- *Catalog Metadata*: A set of metadata (data about data) that describe the available data, including description of VGI.
- *Spatial Database*: This database stores information about the spatial locations where the events take place in the World Cup 2014 and also manage the data about the preferences of each user.

3.1 Context Model

An ontological domain is an abstraction of reality to be shown and may contain concrete entities and abstract [19]. Each of these entities is described using concepts that can have properties and relationships.

To formalize the concepts that are part of the World Cup environment a domain ontology was developed. This led to a formal context model, here called OntoCopa. This domain ontology provides the necessary support to the SDI in the treatment of requests and preferences. Using OWL as the language of the ontological model, is possible generate an XML output that is used in the SDI to map the environment according to user profiles. Thus, the SDI will provide services for search and retrieval of geographic information based on context information, mapped by the ontology OntoCopa. In the ontology development, the Protégé ontology editor was used which offers facilities for editing, viewing and using ontologies [20]. Figure 4 displays the editing tool for class concepts.

Classes, subclasses and their objects properties were created for each concept related to the World Cup using Protégé, as is shown in figure 5.

The concepts formalized as classes, subclasses and their objects properties are described below:

- *Abstract*: class that corresponds to the concept of intangible entities. The “Time” class is its subclass.
- *Time*: class that represents the changes in space. It has a subclass “Interval”.
- *Interval*: subclass of “Time” class that represents a time period between an initial and a final time.
- *Coaching_Staff*: class that comprises a set of auxiliary football team.

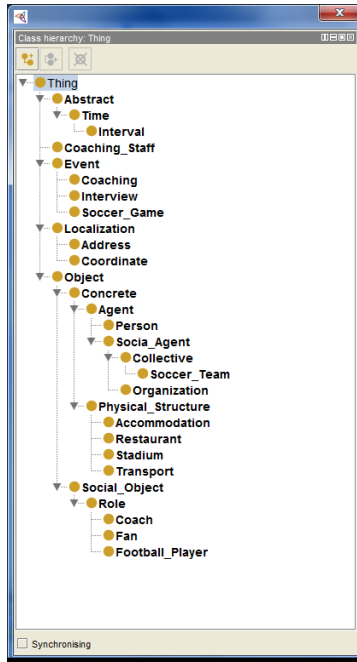


Fig. 4. Edition of the OntoCopa ontology classes with Protégé

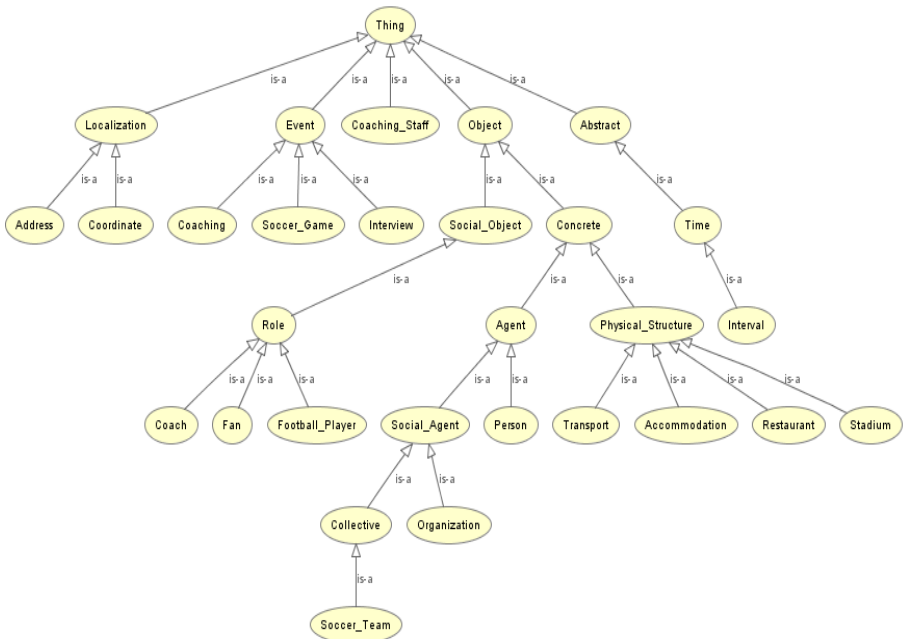


Fig. 5. OntoCopa Concepts Hierarchy

- *Event*: class that denotes some phenomenon that happens in a given place and time, or not being able to have the participation of a person. Its subclasses are: “Interview”, “Coaching” and “Soccer_Game”.

- *Coaching*: subclass of “Event” class that denotes an interval in space and time that is used to exchange information between players, coaches and other related professionals.

- *Interview*: subclass of “Event” class that represents the concept of scheduled events in a place and time for questioning media players and other professionals involved.

- *Soccer_Game*: subclass of the “Event” class that represents the concept of holding a competition between two teams from different clubs and countries scheduled for a given time and place.

- *Localization*: class that represents the geographical position of some person, an event or physical structure. Its subclasses are: “Address” and “Coordinate”.

- *Address*: subclass of “Localization” class which expresses the location of people, events or structures in the host cities Cup, through a textual description of the street, neighborhood, city, state and mailbox.

- *Coordinate*: subclass of “Localization” class composed of the values of latitude, longitude and altitude to determine the location of people, events or structures.

- *Object*: class that represents the abstracts concepts tangible and intangible perceived by man. The classes “Concrete” and “Social_Object” are its subclass.

- *Concrete*: subclass of the class object that represents the concept of tangibles entities. The classes “Physical_Structure” and “Agent” are its subclass.

- *Agent*: class that calls the active object that performs some action. The classes “Social_Agent” and “Person” are its subclasses.

- *Person*: class that represents all human beings who can participate in some form of events. Its subclasses are: “Role”, “Fan”, “TouristFan”, “LocalFan”, “Professional”, “SoccerTeam”, “Coach”, “Athlete” and “Journalist”.

- *Social_Agent*: class that represents actors participated in a social environment. Its subclasses are: “Collective” and “Organization”.

- *Collective*: class that corresponds to the set of social agents. “Soccer_Team” is its subclass.

- *Soccer_Team*: subclass of “Collective” that identifies the group of professionals who play together representing their country.

- *Organization*: class that represents the concept of a set of social actors, united by common goals and objectives.

- *Physical-Structure*: represents the concept of support for people. Its Subclass are: “Accommodation”, “Restaurant”, “Transport” and “Stadium”.

- *Accommodation*: class that consists of hotels, hostels, lodging, and others structures that can accommodate people.

- *Restaurant*: subclass of the class “Physical_Structure” representing the structures where meals is supplied to the people.

- *Stadium*: class that denotes the arena which hosts football matches.

- *Transport*: subclass of class “Physical_Structure” that represents the service of locomotion for various locations.

- *Social_Object*: class that represents the objects that play a role in the social a world. The "Role" class is its subclass.

- *Role*: subclass of "Social_Object" that perform a particular function in a specific domain.

- *Coach*: subclass of class "Role" which represents the professional responsible for the training of athletes.

- *Fan*: subclass of class "Role" that identifies tourists or people residing in the city which hosts event sand cheer for one team.

- *Football_Player*: subclass of class "Role" that identifies professionals who play in a team.

4 Final Considerations

A Spatial Data Infrastructure is aimed at providing spatial information allowing an easier access to them. But the complexity of information and its large volume can be an obstacle for nontechnical users. So this paper proposes an SDI that takes into account the environment and user preferences to filter the information and report only data that is of interest through a Web interface.

With the context information can not only deliver information relevant to the user in question, but also motivate you to bring new geographic information about places and events of his knowledge. Thus, the proposed SDI facilitates access to and use of spatial information by inexperienced users from different countries and cultures and also tackles the problem of lack of spatial data using the VGI.

As future work can be made in the implementation of Web services, metadata catalog and web application.

More information about the SDI to the 2014 World Cup can be obtained in <http://www.dpi.ufv.br/projetos/geocopa2014>.

Acknowledgments. Project partially supported by the agencies CNPq, Fapemig and CAPES. The authors also thanks for the financial support from the company Gapso.

References

1. Blog do Planalto. Copa do Mundo 2014, <http://blog.planalto.gov.br/copa-do-mundo-2014-tera-impacto-indireto-de-r-185-bilhoes-preve-ministro/> (2011) (in Portuguese)
2. Noguera, I.J., Zarazaga, S.F.J., Ruro, M.P.R.: Geographic information metadata for spatial data infrastructures. Springer, New York (2005)
3. SDI Cookbook (2012), http://www.gsdi docs.org/GSDIWiki/index.php/Main_Page
4. Decreto n° 6.666, de 27 de novembro de (2008) (in Portuguese), http://www.planalto.gov.br/ccivil_03/_Ato2007-2010/2008/Decreto/D6666.htm

5. Comitê de Planejamento da Infraestrutura Nacional de Dados Espaciais INDE. Plano de Ação para implantação da INDE (2010) (in Portuguese), <http://www.concar.ibge.gov.br/arquivo/PlanoDeAcaoINDE.pdf>
6. Man, E.: Spatial Data Infrastructuring: praxis between dilemmas. *International Journal of Spatial Data Infrastructures Research* 6, 261–289 (2011)
7. Dessers, E., Crompvoets, J., Janssen, K., Vancauwenberghe, G., Vandenbroucke, D., Vanhaverbeke, L., Hootegem, G.V.: A multidisciplinary research framework for analysing SDI in the context of business processes. *International Journal of Spatial Data Infrastructures Research* 7 (2012)
8. Goodchild, M.F.: Citizens as Voluntary Sensors: Spatial Data Infrastructure in the World of Web 2.0. *International Journal of Spatial Data Infrastructures Research* 2, 24–32 (2007)
9. Gruber, T.R.: Towards principles for the design of ontologies used for knowledge sharing. *Int. J. Hum.-Comput. Stud.* 43, 907–928 (1995)
10. Kokar, M.M., Matheus, C.J., Baclawski, K.: Ontology-based situation awareness. *Information Fusion* 10, 83–98 (2009)
11. OWL - Web Ontology Language Reference (2009), <http://www.w3.org/TR/owl-ref>
12. Doyle, A., Reed, C.: Introduction to OGC Web Services. White Paper. OGC (2001)
13. OGC. OGC Reference Model, v. 2.0 (2011), https://portal.opengeospatial.org/files/?artifact_id=47245
14. OGC Standards, <http://blog.geoprocessamento.net/tag/ogc/>
15. Weißenberg, N., Gartman, R., Voisard, A.: An Ontology-based Approach to Personalized Situation-aware Mobile Service Supply. *GeoInformatica* 10, 55–90 (2006)
16. Lamas, A.R., Lisboa Filho, J., Oliveira, A.P., Júnior, R.M.A.B.: A mobile geographic information system managing context-aware information based on ontologies. *Ubiquitous Computing and Communication Journal* 4, 718–727 (2009)
17. Rodrigues, M.L.: GIS no Transporte Público Urbano: Aplicações do GIS como suporte aos sistemas de informação ao usuário. *MundoGEO* 66, 60–61 (2012)
18. Orshoven, J.V., Bamps, C., Beusen, P., Hall, M., Janssen, K., Vandenbroucke, D.: Spatial Data Infrastructures in Europe: State of Play Spring 2003. Summary report of Activity 3 of a study commissioned by the EC (EUROSTAT & DGENV) in the framework of the INSPIRE initiative. K.U. Leuven (2003), <http://www.ec-gis.org/inspire/reports/stateofplay/rpact3v4.pdf>
19. Murgante, B., Tilio, L., Lanza, V., Scorza, F.: Using participative GIS and e-tools for involving citizens of Marmo Platano - Melandro area in European programming activities. *Journal of Balkan and Near Eastern Studies* 13, 97–115 (2011)
20. Knublauch, H., Fergerson, R.W., Noy, N.F., Musen, M.A.: The Protégé OWL Plugin: An Open Development Environment for Semantic Web Applications. In: McIlraith, S.A., Plexousakis, D., van Harmelen, F. (eds.) *ISWC 2004*. LNCS, vol. 3298, pp. 229–243. Springer, Heidelberg (2004)

Towards a Two-Way Participatory Process

António Silva and Jorge Gustavo Rocha

Departamento de Informática,
Universidade do Minho,
4710-057 Braga, Portugal
ajfsilva@gmail.com, jgr@di.uminho.pt

Abstract. In less than a decade, several millions of articles have been written in Wikipedia and several million roads have been traced out on Open Street Map (OSM). In the meantime, the authorities have still not been able to understand and use the power of crowd sourcing. In this paper, we present the design principles of a new Public Participation Geographic Information System (PPGIS). We aim to eliminate the typical limitations of previous unsuccessful platforms, that have mostly failed due to conceptual design issues.

We argue that two fundamental changes must exist in new PPGIS platforms: there is a shift from hierarchies to increased equal rights platforms; improved communication, more transparency, and bi-directionality.

The role of the authority in former platforms was really an authoritarian role: having all the power and only partly knowing and controlling the entire platform. This is completely different from the crowd source platforms we know to be successful. So, one fundamental change is to diminish hierarchies and prevent people from hiding themselves behind the institution.

The second major conceptual design issue is related to transparency and communication. While former platforms use mechanisms to prevent citizens from seeing each other's participation, we aim to enable people to see the participation of others. That's a fundamental feature in social networks. We will also design it to be a two-way communication platform. If citizens are requested to participate, the administration must use the same platform to communicate with them. Not only to provide feedback, but also to publish useful information for the citizen.

In this paper we describe how social media meets our design principles. We decide to implement our case study, the "Fix my Street" application, on top of a social engine, to take advantage of all social media features. Two necessary extensions to the social engine are briefly described, to capture the core logic of our application.

Keywords: VGI, PPGIS, Government, Social Media.

1 Motivation

Under names like neogeography, volunteered geographic information (VGI), wiki-mapping, GIS 2.0, crowd sourcing, citizens as sensors, collaborative mapping,

community mapping, among others, innovations and new applications of on-line geospatial technologies and crowd sourced spatial data continue their rapid expansion [3].

Users and therefore companies were the first to understand this power in the Web 2.0 age. Complex geographic information started to be produced by complete amateurs, using low cost GPS enabled phones. In less than a decade, several million roads were traced out on OpenStreetMap (OSM). This has revolutionized the way maps are made. It is thus possible to obtain updated data about the territory, made by those who know it best: the citizen. However, even with the budget and human resources constraints that many governments are facing, they were not able to take advantage of the huge potential of VGI. No alternative opportunities to collect, update, analyze and use geographic information are being explored. Using VGI in government is not a technological limitation. The problem is really a *communication problem* between parts not at the same level (not equal parts). We know from our experience in PPGIS projects, that the use of sophisticated interfaces does not guarantee massive public participation. On the contrary, the lack of sophisticated data models and tools does not prevent, for example, OSM users from creating detailed maps.

In this work, we have the opportunity to study how VGI can be used in government and how PPGIS projects can benefit with it. In the context of a collaboration with the AMA (Administrative Modernization Agency) public agency, we were challenged to connect the world of VGI and government. But these are two different worlds and we can point out some evident difficulties:

1. Although public authorities could benefit from geographic information provided by citizens, these public bodies still gather data from traditional sources, and it is legally difficult to accept data from non-trusted sources;
2. Although the legal framework for participation in all democratic countries has enshrined the right to participate, public participation is almost zero in practice;
3. Although public participation is very low, we have never had so many people participating in social networks and in open data projects.

The use of VGI in local and central administration is also a new challenge and the initial focus is mostly dedicated to content creation. We want to fully explore the new and updated data from citizens, in order to facilitate, speed up and improve government decision-making processes.

2 Introduction

2.1 VGI

Early on, researchers realized the need to find a name that clearly identifies this concept of spatial or geographic user-generated content. Several names have been appearing at the speed with which the various works were being published, each one emphasizing, in most cases, their area of interest, or research. Since

2006 various papers and examples of applications have presented us many terms that tried to describe and define this phenomenon.

In 2006, Andrew Turner introduced the concept of neogeography, which might be defined as geography for the masses, even as mapping for the masses [9]. One year later, Michael Goodchild termed volunteer geographic information (VGI), a special case of user-generated content where participants are private citizens, mostly untrained, and their actions are almost always voluntary [6]. Song et al, defines VGI as a human side of the sensor revolution, while pointing some paths for the future saying that “it could be useful to enhance the information used by professionals as well as decision makers” with the advantage that some information cannot be sensed remotely such as local knowledge [12]. This term has been adopted by many researchers since then. Both VGI and neogeography are terms that draw our attention to a new way to produce geographic information in opposition to the classical methods. In fact, this could be a new paradigm for the production of maps, with great impact on Geographic Information Systems (GIS), and a very important means for developing the relationship of the citizen with geographical information.

However, other terms have appeared with the same basic idea even though they differ slightly in the focus. Ostlaender presented in 2010 the term Geowikis, “the confluence of two social computing trends: user-contributed content and map-based interactive Web applications” [11] very similar to the wikification of GIS concept presented by Sui in 2008 and GIS 2.0 by McHaffie in the same year. These names suggest the Web 2.0 modes of interactivity, user-generated content, the iterative mutability of wikis, and their implications for the processes and relationships of knowledge making. Terms like collaborative mapping, community mapping or ubiquitous cartography are terms where the emphasis is on the technological side and its influence on a interactive way to create geographic information and knowledge [3].

VGI Issues. Despite the already discussed advantages and the enormous potential recognized by all, there are still doubts about using VGI data, particularly by government, who have always been accustomed to using geographic information collected through traditional methods, with standards and specifications that are usually assured by experienced and qualified technicians in cartography. Due to the amateur nature of VGI, one of the major issues of using it in organizations is how to assess the reliability of contributors and the confidence of their actions [1, 5]. This is not a new issue, or exclusive to VGI, in many other projects related to the Web 2.0 movement, including Wikipedia among others, questions were being raised about the accuracy and correctness of the information provided [13]. As a result, several researchers have been studying the quality of VGI in recent years. Between 2008 and 2010 Zielstra et al in Germany, Haklay et al in England and François-Girres et al in France, performed exhaustive tests to assess the quality of OSM data in their respective countries. The overall results were quite similar, pointing to a significantly higher quality (positional and completeness accuracy) in larger cities than in inner-cities and rural areas,

which can be explained by the presence of more active members of the project in larger cities [4, 7, 13]. Beside quality issues, there are other issues that can arise regarding the use of VGI. These issues can be related with:

- the lack of will among people to contribute to government compared with social networks;
- how do organizations attract new volunteer contributors and how do they keep existing volunteers “engaged”;
- what are the motivations of volunteers;
- the recognition of the contributors;
- the lack of adoption of VGI data in organizations, especially in public organizations;
- will individuals remain interested in making contributions.

2.2 Traditional One-Way PPGIS

In a 1998 specialist meeting on “Empowerment, Marginalization and Public Participation GIS” at the National Centre for Geographic Information and Analysis (NCGIA) (Santa Barbara) Craig et al established some basic assumptions related to what a PPGIS should contain and look like [2]. These are:

- equal access to data and information is a key component of a Web-based PPGIS;
- PPGIS should have the capability to empower the community and its members by providing the necessary data and information;
- establishing and maintaining community trust is key for people working with PPGIS.

Despite these basic assumptions, until now traditional PPGIS applications have been governed by an almost legal obligation imposed by government on citizens to participate by providing input on various matters of public interest, involving citizens on the one hand and government on the other. Unfortunately traditional PPGIS have very low participation rates. With this traditional one-way PPGIS, citizens do not feel comfortable in the role of information givers, without receiving anything in return, often without even a “thank you message” from the promoter of the participation. The public, as many polls have shown, typically believes that government is unresponsive to their concerns or when it is responsive it is solely for special interests. Most often these methods discourage most individuals from wasting their time going through what appear to be nothing more than rituals designed to satisfy legal requirements. In fact, traditional PPGIS do not usually achieve genuine participation in planning or other decisions; they do not satisfy the members of the public that they are being heard; they seldom can be said to improve the decisions that agencies and public officials make; and they do not incorporate a broad spectrum of the public [10].

Although, as stated above, the legal framework for participation in all democratic countries has enshrined the right to participate, it is only in theory and not in practice. Sophisticated platforms have been designed and developed for

participation in regional and urban planning, for example, but these tools and similar ones do not ensure massive participation. Several techniques have been used in an attempt to increase participation by the citizen, apparently without great success. Techniques such as images, videos, 3D maps, simulation games, or even virtual and augmented reality systems [8] were used to capture the attention of citizens and to drive public participation. This finding confirms that the problem of low participation is not technological but certainly more related with how citizens are invited to participate and what they get when they do participate.

To illustrate what was said above, last year the municipality of Águeda, Portugal, launched a traditional PPGIS platform to collect opinions from citizens regarding a new urban plan for the entire county. This platform was on-line for a 3-month period and allowed the citizen to draw a point, a line or an area on a map and write a comment on the proposed land use stated in the plan for that area. In return, the citizen received a message of gratitude from the local authority. At the end of the three months, there were only seven contributions out of a universe of 50,000 inhabitants. This is a very poor level of participation, we may even say that it is insignificant.

Roles. There are always two parts: the “administration” on one side and the citizen on the other. So, from the conceptual point of view, that’s a problem because they both have different interests, purposes, backgrounds, views and most importantly, different privileges for the same platform. In traditional PPGIS platforms this conceptual understanding usually tends to result in a departure of the most disadvantaged elements, because they feel like they aren’t playing with the same weapons.

Lessons Learned from Social Networks. Social networks have given us some valuable lessons that we believe to be important to implement in this platform, since contrary to what happens as regards participation in traditional PPGIS projects, the participation and involvement of people in social networks is increasingly growing.

One of the most interesting things that happens on social networks is the equality with which all participants are treated, without distinction of any kind, that leads people to participate for various reasons, mostly without reward other than recognition among their peers. Because of this equality of treatment, social networks teach us another important lesson, that is the decrease of hierarchies, and they prevent people from hiding behind an institution, thus bringing more transparency to the process.

2.3 Goal

The main goal of this work is to develop a PP GIS platform where all participants are treated equally in access to information, i.e. a platform that places the citizen, government and companies at the same level concerning access to information.

3 Designing a Two-Way PPGIS

3.1 The Case Study

“Fix my Street” is a service that is already running on the web, allowing citizens to report problems in their neighborhood. All reports are routed to the corresponding local or central authority in charge.

But since some requirements were not initially identified, technological limitations are present, and the actual participation is low (with about 4 reported situations per day, for a population of 10 million), we are redesigning the service. Besides just improving the minimal geographical support and solving the technological problems, we are going further and designing it to change and enhance communication between the citizen and the administration, a new paradigm of participation that assumes the collaboration of all stakeholders [10] in order to achieve equal access to data and information as a key component of a Web-based PPGIS.

Beside the web interface, we also propose that participation must be enabled when the citizen sees the problem. So, new applications for smart phones are being developed, enabling simple and fast reports on the go. We will also support an innovative interface, on the TV suppliers’ power box, trying to reach audiences not so familiar with computers and the internet.

The test and development cycles of this “Fix my Street” service will provide us with valuable feedback on public participation, reward mechanisms, etc.

Despite the relative success demonstrated by this platform, we believe it may have other capabilities which will benefit central and local government, businesses and citizens. The basic idea is based on a platform where government and citizens have equal access to the generated information, where it is possible for both to create added value from that data.

We believe that this, the equal access to information with a policy based on the availability of services, is the only way possible to truly engage citizens, businesses and government, providing evident gains for all. From the beginning, open and service oriented architectures will be adopted. This might enable private companies to take advantage of VGI. For example, a missing one-way street restriction reported by a citizen can be used simultaneously by the local municipality, the OSM community and by a transportation company.

3.2 Design Principles

In this section, we will mention some new features, while remaining focused on the fundamental design principles that should drive the way we design the new PPGIS.

Cutting Back on the Hierarchy and Improving Relations. Everybody should care about their neighborhood. The people living there, local authorities and all the companies providing services in that area. Even existing neighborhood associations, which join neighbors and business owners together to work

for changes and improvements in all different aspects of our daily life, such as neighborhood safety, parking, beautification and promoting social activities. Since local authorities are not the only ones caring about the neighborhood, they must talk to citizens in a different way.

Using the lessons learned from social networks and open source projects, we definitely need to reduce the hierarchy and improve relations between all stakeholders. The local authority must be represented by people working there, and not by an anonymous worker. Local authorities must participate under the user name of actual employees. Any kind of relationship established with citizens is desirable and healthy.

The user from the local government must have the same rights as citizens on the platform. Even if he or she can tag and partially hide any non-sensical participation, every user must be able to see the hidden participations and have the right to understand why there were rejected, for example.

Reducing the hierarchy also has another major advantage - no external regulation is needed. Regulation would be needed to ensure that local authorities are answering in time and not disregarding any problems raised by citizens. But if local authorities can not delete and change the rules, the platform tends to auto-regulate. The participation volume is also important to achieve the auto-regulation and we definitely need to raise the participation level to achieve this auto-regulation.

In social networks, the relationships between nodes are driving their growth. Social network platforms are essentially designed to enable and promote relationships. We should promote the establishment of relationships. While the relationships on social networks can result from one or more specific types of interdependency, on our platform the relationships will be mostly based on geography (street, parish, county, city, etc).

Bi-directionality. One of the most, or even the most important conceptual goal that we want to achieve is bi-directionality. We think this new platform, “Fix my Street”, could also serve as a privileged channel of communication, and not only in the traditional direction from citizens to authorities. It should be used for communication from the city council and other authorities with the citizen. The idea is to reward every citizen with customized and timely information about what is happening in his neighborhood or close to it. As citizens can exactly indicate where they live (and work), we can provide them with just the necessary information about what is or is going to happen in that neighborhood.

For example, tree pruning, public facilities maintenance, road maintenance, etc. can all be announced in advance. Citizens will feel that they are not the only ones contributing to the neighborhood. Citizens will feel their participation rewarded if others are also participating and if authorities are also making an effort to give timely notice of any change to the neighborhood.

Greater Return for Participation. The more active users (either citizens, people from local business or local authority employees) should be highlighted in

some way. Open source projects are based on meritocracy. In such communities, people have more important roles simply based on their participation. The rules to achieve such status are well known by all, and only the ones working harder will be rewarded. There are no discussions at all when people are rewarded following this method, since it is based on merit. All the other users can check and confirm the merit of each other.

Every participation counts as something for the user. Simple rewarding mechanisms, like the one adopted by the <http://stackexchange.com> are easy to implement. Such mechanisms are really important in demonstrating the dynamics of equity.

More Emphasis on the Geographic Component. It is important to provide the service with a greater geographical component. Based on the lessons learned from social networks, we need to improve the relations among users, and the most natural relationship between users will be based on geography. The focus on this component is also important in ensuring greater participation since users tend to participate and interact more when they are reporting issues from the local world surrounding them. The better knowledge they have of their local environment makes them feel more confident.

To accomplish that, users can select one or more locations that they care about. It can be their home, work place, their parents' home or any other place they care about. All those places will be considered to implement the notion of "near me".

This geographic approach is important to enable an instant view of all reports near me. With lots of contributions from citizens and local authorities, we must only provide the most important information for each user, and not all the available information. With less, more suitable information, it is easy for users to review each other's participation. Users can subscribe and reinforce another's participation with a "+1" mechanism. These interactions can be made in a tabular fashion, and also over the street map.

We will also take advantage of the geographic information to develop suitable visualizations on all platforms, especially for smart phones, as we explain in the next section.

Enable and Increase Participation in Mobile Devices and TV Boxes.

We cannot ignore the benefits of participation using mobile devices that streamline the process of participation, based on an image, a video, a pair of coordinates and one or two tags. This method is not only easier, but it allows immediate on-site participation, without the disadvantage of having to wait to get home or to work to participate. We hope to significantly increase participation by providing a smart phone application. Applications of this kind are already available. "Fix my Street", available in the UK, and "Fix it Plano", in the USA, are just two examples of this kind of applications.

Mobile applications can be very useful not only for reporting occurrences. They can be used as a tool to allow local authorities to go around and visit all reported sites. The same tool used for participation can be used in a different

manner by local authorities to visit each site, confirm the reported problem, and change its status. With such an interface, local authorities can quickly review all participations from a certain area and send immediate feedback to the users.

Another interface we want to explore are the new capabilities offered by TV boxes. Everyone can work the TV remote control. The software and hardware capabilities of TV boxes make it possible to participate while comfortably sitting on the sofa at home watching TV.

4 Developing a Social Media Strategy

As we have already stated, there is already one “Fix my Street” application running that we should improve. Rather than improve it from the technological point of view, we wanted to rethink how web-based services for public participation in local management should be conceived. We identify the design principles that this kind of applications should comply with, prior to any implementation, as stated in the previous section. The principles enumerated must be enabled by the tools.

In this section, we will discuss that social media tools meet these principles. While some are held back by the uncertainties of such media usage, we argue that crowded source projects have already proven to us that this is the way to go. We would say that the last 5 years of Wikipedia and Open Street Map have removed our uncertainties. People are definitely available to participate.

4.1 When Social Media Meets Our Requirements

The very first paragraph of Wikipedia’s “social media” definition says: “Social media includes web-based and mobile technologies used to turn communication into interactive dialogue”. Since we definitely want to move from the traditional governmental monologue to interactive dialogue, social media seems to promise that, while also complying with our other requirements as well. So, we must ask ourselves: Should we move to social media to support participation in local management? Should we use existing tools or should we develop our own?

For some, our relationship with technology is still in its infancy, and we still don’t know how to mindfully and meaningfully interact over social media. For others, it is a just a matter of when we are to adopt such an approach, since the use of social media in our communication with public authorities seems almost inevitable.

4.2 Implementing the “Fix my Street” as a Social Network

We decided to move from a traditional web application where citizens can report problems, to a social network where dialogues occur between citizens and public servants. This dialogue is open. The problems reported are open, and the feedback is also open as well. Public servants not only answer problems reported by citizens, but also will publish information that might affect citizens daily life.

The existing tools, such as Twitter, YouTube or Facebook are public, hosted social networks for individuals to create user accounts. Since we want communication around people's neighbourhood problems, we need to develop our own social network tool to integrate, among other smaller things, the concept of 'problem' and 'neighbourhood'.

Instead of developing such a social network from scratch, we select one of the many social engines available. We needed an engine that already has the typical social network features implemented, such as user registration, user profile management, user groups, friendship support, messaging, discussions, etc. We chose Elgg because it has all such features already implemented and it is open source.

To extend the social engine to support the "Fix my Street" application, we started by implementing the notion of 'problem' that can be reported by the citizen. To submit a problem, the user publishes a slightly different post, since the problem's location and its type must be specified. The location can be pinpointed on the map. The type of problem is chosen from a closed domain. After choosing the problem type, the user can add more information (and media) concerning the problem being reported. The reported problem is displayed like any other user's post. Other users can see the reported problem and can say if the problem also affects them, as well as post additional media about it.

Another extension of the social network engine is related to the spatial component. In the "Fix my Street" application, the location is very important. It is important to know where the problems are, but it is also important to create relationships and engage communities around their neighbourhood. In the user profile, users can add one or more locations, like their place of work and their residence. Accordingly, users can define more than one neighbourhood they care about. These locations are used to filter problems for those areas related to the user. These areas are also used to filter the information published by the authorities. As soon as users log on, they can see all the recent information about their friends and group activities, as well as things that have been reported and fixed in their neighbourhood(s). Location is a key component to implement this thematic social network.

Finally, parallel to the core social network back office tools must exist to keep track of all the problems being reported. Internally, as soon as the problem is reported, this information is routed to the corresponding municipality and assigned to a specific public servant accordingly to its type. We need to know what problems are still pending solution, their duration, which problems have been partially addressed, how long it takes for their solution, etc. Various statistics are collected and the performance of each municipality is openly published.

5 Conclusions

We described the overall process to move from a traditional "Fix my Street" web application to a "Fix my Street" social network-oriented communication platform. In this process, we started by acknowledging the limitations of the existing implementation. The lack of success of the existing tool is not technological. The

embedded features of the tool implement just one-way communication between parties with unequal rights.

To overcome such limitations, we started by enumerating some design principles that should be presented for the relationships and communication between authorities and citizens, in section 4.2. These principles are absolutely essential. Some of these principles are the result of existing crowd source platforms. We have made a review of VGI literature to highlight that people are massively participating in such projects. It is obvious, for example, that platforms such Open Street Map are technologically very limited but can engage thousands of participants.

Having stated the principles, the next step was to decide how to implement them. Two major options could be followed. We could develop another application that includes the design principles we mentioned. But since social media enable our own principles, we chose to focus on the implementation of a “Fix my Street” social network. We opted for this because it embeds our design principles, not just because it’s in vogue. We also started by stating a specific tangible reason for using social media. This is important because since we define the need, it’s easier to select the tools to use and develop the necessary extensions. It is also important to measure success. Even before we power the social network around the “Fix my Street”, we can establish metrics to measure the impact of the tools in achieving our goals.

There are also risks involved. We are aware that this social network will only work if the AMA agency is committed to its maintenance and operation, by continuously monitoring and improving its operation. The lack of experience of public servants with social media can also be a problem. We will need to give additional support to the users, whether by specific training in addition to developing guidelines that can help them.

References

- [1] Coleman, D.J., Eng, P.: Volunteered Geographic Information in Spatial Data Infrastructure: An Early Look At Opportunities And Constraints, pp. 1–18
- [2] Craig, W., Harris, T., Weiner, D.: Empowerment, Marginalization and Public Participation GIS Report of Varenius Workshop Compiled by. Number (February 1999)
- [3] Elwood, S.: Geographic information science: emerging research on the societal implications of the geospatial web. *Progress in Human Geography* 34(3), 349–357 (2009)
- [4] Girres, J.-F., Touya, G.: Quality Assessment of the French OpenStreetMap Dataset. *Transactions in GIS* 14(4), 435–459 (2010)
- [5] Goodchild, M., Alan Glennon, J.: Crowdsourcing geographic information for disaster response: a research frontier. *International Journal of Digital Earth* 3(3), 231–241 (2010)
- [6] Goodchild, M.F.: Citizens as sensors: the world of volunteered geography. *GeoJournal* 69(4), 211–221 (2007)
- [7] Haklay, M., Basiouka, S., Antoniou, V., Ather, A.: How Many Volunteers Does it Take to Map an Area Well? The Validity of Linus Law to Volunteered Geographic Information. *The Cartographic Journal* 47(4), 315–322 (2010)

- [8] Hanzl, M.: Information technology as a tool for public participation in urban planning: a review of experiments and potentials. *Design Studies* 28(3), 289–307 (2007)
- [9] Hudson-smith, A., Batty, M., Crooks, A., Milton, R.: Mapping for the Masses: Accessing Web 2.0 through Crowdsourcing. *Analysis* 44(0), 0–18 (2008)
- [10] Innes, J.E., Booher, D.E.: Reframing public participation: strategies for the 21st century. *Planning Theory & Practice* 5(4), 419–436 (2004)
- [11] Ostlaender, N., Smith, R.S., De Longueville, B., Smits, P.: What Volunteered Geographic Information is (good for)-designing a methodology for comparative analysis of existing applications to classify VGI and its uses. *Remote Sensing* 817, 1422–1425 (2010)
- [12] Song, W., Sun, G.: The Role of Mobile Volunteered Geographic Information in Urban Management. *Context*
- [13] Zielstra, D., Zipf, A.: A comparative study of proprietary geodata and volunteered geographic information for germany. In: 13th AGILE International Conference on Geographic Information Science (2010)

An Automatic Procedure to Select Areas for Transfer Development Rights in the Urban Market

Carmelo Maria Torre, Pasquale Balena, and Romina Zito

Department of Civil Engineering and Architecture
Polytechnic of Bari,
Via Orabona 4, Bari Italy
torre@poliba.it

Abstract. The first part of the paper provides an overview of urban rent recapture and equalization today and the application of Transfer Development Rights (TDR) mechanism. Below, in the second part, starting from the definition of spatial data infrastructure you try to give an account of the importance that has the support of GIS in planning, and consequently in the analysis of possible forms of compensation in terms of equalization. Finally the third part will provide information on the sources necessary for the construction of automatic procedures for the analysis of transfer of building rights. The last part is devoted entirely to the illustration of a case study, and some hypotheses for implementation. It is provided of specifications for the routines used for analysis in a GIS environment, and explains the process of decision, which, once supported the findings of gis routines, lead towards a prelude to Transfer Development Rights. C. Torre wrote the first, the second and the last paragraph, R. Zito wrote the third and the fourth paragraph, and P. Balena wrote the fifth paragraph.

Keywords: TDR, Equalisation, GIS, Spatial data infrastructure, Zoning.

1 Introduction: Equalisation: Why?

The land plusvalue is the advantage enjoyed by the owner of a soil. Such advantage is linked to the productive capacity of the soil, which in today's world stems primarily from the ability to generate an annuity-due to the discharge of agricultural production, industrial-commercial, and residential-tertiary.

In urban areas the value of an area, “*ceteris paribus*”, depends on its building rights, expressed by the indices of land and / or territorial buildability. Other factors that affect the rent of land and buildings in general are the proximity to urban services, accessibility etc.

In other words, planning instruments create differential rents from ground to ground and building from property to property. With equalization you can manage the planning processes of construction and regeneration of the city without incurring the criticality due to unsteady soil. The mechanism on which the size of the plan, which determines which inequality can only increase, with urban sprawl. Therefore, higher rates are higher earnings and profits of the landlord of a soil to new construction.

So the urban evolution of the city has created income for both companies and property developers involved in the transformation of urban expansion, useful to the land owners, compensated by the private sector for the private urban renewal, and discharged as debt on local authorities for expropriation must the transformation of urban public.

The progressive growth, favoured by the oversized plans, has seen increasingly widening the gap between urban income private, urban and public debt.

A further element of inequality due to such gap among public and private, it is added because of the issue of recovery of the built environment, and then of the theme of regeneration and environmental protection.

The introduction of these two criticalities has caused the need to establish the configuration of the offer, not only on the planning system of buildable soils, but also on the management of land wholly or partially built, to be recovered or reprocessed, or, finally redistributed in the aspect of rent, by a form of equalization or compensation.

2 Equalisation: How?

The compensation can be implemented using the following models [1] [2]:

1. Acquisition costs of compensation from the private (in the philosophy of the recapture of surplus value) [3][4]
2. Construction of a plafond equalization in order to [5]:
 - a. Acquire from the partial sale of land from the private to the compensatory award of a building index in residual soils [6]
 - b. Transferring title to real estate (Transfer Development Right) from a soil of departure (sending site) to a landing ground (receiving site) [7]
 - c. To compensate expropriation.

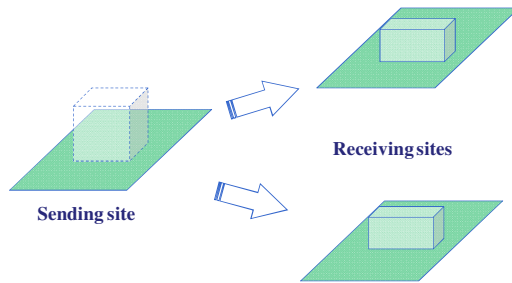


Fig. 1. A typical TDR process

Let's consider two sub-areas of a given area to be set up and it is assumed that:

- one of the two sub-areas have a lower carrying capacity than the other
- for the entire area the state of environmental resources depends only on the transformation of the first sub-area,
- the two sub-areas are subject to unified planning and the least amount of construction is realized in the sub-area to be preserved.

It is possible to transfer volume from one sub-area to another by the use of a compensatory principle, provided that the volume should not exceed those of the entire area. In this way you can keep the natural heritage, because it makes a settlement with limited environmental impact and landscape and preserve the rights acquired through the transfer of volumes by means of equalization.

The development rights transferred are distributed among the owners as a function of soil properties, and are marketed as rights that can be bought and sold. In the second case, the compensation is based on a sale made voluntarily by the private areas and compensated with a "bonus volume" that owners can implement in the remaining areas, earmarked for development. The measurement of this limit represents the plafond.

The plafond reflects the state of affairs (urban characteristics of the site) and the rule of law (intended use and title owner).

The revenue equalization in Italy hold on behalf of:

- seniority of building products
- there are restrictions to building arising from provision of law
- need for urban destinations other than the residence

Established the scope in which to operate will identify the areas designated for urban transformation.

The determination is based on the "Plafond" of the building areas that is to say the equivalent of rent value of land in buildable volume. If we neglect the time of execution of works and the placing on the market for buildings made of an area, and the agricultural value of land, the value of building rights that are dependent on:

1. volume / floor area achievable;
2. costs of building production
3. consistency of building rights
4. market value of the built property
5. unitary market values and cost

Finally let's give:

A = surface area of building

Valu = unit value per square meter market

Cu = unit production cost per square meter of gross floor area paved

$\Delta u = \text{Valu} - \text{Cu} = \text{differential value-unit cost per square meter}$

Iff = land building index

H = height of plane

If the total value of the VA is the value processing unit $VAU = VA / \text{In area, ceteris paribus}$, it will depend only on the index of building rights according to the following relationship:

$$VAU = \frac{VA}{A} = \frac{\Delta u \times A}{H} Iff \tag{1}$$

The “plafond” is represented by a right of building equivalent to the total value of the area. Then coincides with the building index, as a function of the unit value of the area:

$$Plafond = \frac{H}{A \times \Delta u} VAu \quad (2)$$

A main question in managing compensation and in attributing a right to buildability by a correct plafond is regarding the quality of information about suitable rent of soils and fabrics. An incorrect information about land values is the main cause of inefficiency of the compensation system from an economic point of view. In addition, the set of rules and norms maintain since forty years a difficulty to fix a correct balance among private rights and public needs.

3 The Infrastructure of Data in Town Planning

To better understand the information deficit that affect the identification of a correct compensatory system of building rights and land value recapture, we need to better understand what kind of information sources area available, and are ready to be networked in a system of spatial data. The first source is represented by the set of information represented in the land use plans, and inside their geographic information systems [8].

In Italy the General Municipal Plan (PRGC) is defined as an instrument that regulates the activity of traditional building in a municipality. It is a tool written by a single municipality or several neighboring municipalities (General Inter) and contains information on the possible use or protection of portions of the territory to which it relates.

The P.R.G. was founded in 1942 as a regulatory tool of urban growth, but around the 70 becomes a management tool for spatial planning.

It had as its purpose the growth of cities and urban management increase, its scope is the entire municipality.

Requires an additional level of implementation; delegated to the Implementation of Detailed Plans and plotting plans. It has no expiration of validity, but for the expropriation constraint exists that requires safeguarding the expropriations start within five years after approval of the plans.

On the basis of the planning regulations of 1942, the doctrine is used to distinguish between zoning and locations. The zoning indicates the division of land in areas of homogenous character: they affect the legal status of property in the sense that the building, which according to the traditional doctrine of the inherent right to property is subject to discipline, on grounds of public character General (Conditions of heights, volumes in relation to the maximum permitted building lots, compared to the distances between buildings and boundaries, etc..).

The locations for network services and infrastructure for the general user: the prediction of new structures gives rise to constraints on time with content substantially expropriation, as already stated, set time horizon of five years.

The zones are (as provided by some decrees of 1968), homogeneous as regards the land use. There is a prevailing land use and the maximum and minimum relative to other uses for each area are adjusted by law and plans (eg land to neighbourhood facilities in a residential area)

Information to be used for the infrastructure of data from forms and sizes of uses, the qualitative and quantitative aspects connected with the construction, preservation and retrieval of soils are given to the planning parameters and classified uses by zones

A: Old Town and urban areas of environmental and cultural landscape

B: consolidated area for residential use

C: area of new buildings for residential use

Q: areas intended for business, industrial, artisanal, commercial, tourist

E: areas for productive, agriculture, food activities

F: areas intended for urban services

For each zone the plan provide a set of variable parameter that identify the suitability for transformation (maximum admitted volumes for buildability, shape parameters, such as height, distances and so on).

4 The Infrastructure of Data in Property Archives

The Land Registry is the set of documents - maps and values - which list and describe the property, indicating the location and boundary, as the holders, annuities, the latter must be calculated on taxes .

The land is in force in Italy, as stated in the first article of its founding law, "geometric", particle and not "evidence": Although there are records in his notes relating to changes of ownership of the assets counted, contrary to opinion that there is widespread popularly value of these do not have full proof of ownership.

The register has a function purely tax, that serves to establish a uniform taxable income on which taxes will be calculated and property taxes.

The transfer of ownership of land or property (for purchase or inheritance) is reported immediately to the local Conservatory and after some months or even longer to register.

In a broad sense, the term register can be used for any systematic survey of homogeneous objects, typically accompanied by a map and from a register.

In the '80s all the paper material of the old register was computerized and digitized. The existing cadastral maps on huge sheets often wasted, were scanned by special ultra large format scanner and cleaned up from staining, folds and lines due to dirt.

The project that lasted several years, brought the domestic deployment of 93 data centers (one in each provincial capital) containing maps and information relating to the province.

By the year 2000, access to information was also made possible via the Internet, both institutional (surveyors, organizations) and individual persons.

Today, the "land" is managed by the Land and the municipalities that have chosen to act as land allocated to them by special conventions.

The register divides the urban area in cadastral census zones and micro-zones.



Fig. 2. A typical cadastral map, (referring to the case of study)

The microzone represents a portion of the municipality or, in the case of areas consisting of groups of municipalities, an entire municipality that has consistency in the characters of location, zoning, historical and environmental, socio-economic, as well as in terms of provision of services and urban infrastructure.

In each microzone residential units are uniform typological characteristics, destination and time of construction prevalent.

At the same time the definition of micro-zones based on geographical areas of homogeneous market, and is performed particularly taking into account the impact on these areas of the positional characteristics of the building units.

The articulation of the municipality in microzones, generally, must meet the following conditions:

a) within each microzone, the ratio of unit values of maximum and minimum market of the building units, must not be greater than two, except for those building units that have unique characters for the microzone considered

b) the percentage deviation between the average values per square meter of ordinary reference housing units belonging to two adjacent micro-zones and homogeneous urban point must not be less than 30%.

In the presence of specific and objective conditions of the territory, which make it difficult to respect the limits of variability, the limits themselves can take the value of 3 to 1 for maximum and minimum gap, and 20% for similar units belonging to adjacent microzones.

The second source of information is the Real Estate Market Watch (Osservatorio Mercato Immobiliare or OMI) base on the collection and compilation of technical and economic information, relating to real estate values, the rental market and annuity rates and the publication of studies and statistical processing and exploitation of the archives of the Agency Territory.

Among its activities are also the analysis, research, development and testing of theoretical profiles, applications and innovation in institutional matters, with specific reference to the definition of property values.

The database of the Centre is an important source of information on the housing market, serving as a useful tool for all market participants, researchers and scholars of the real estate sector, for public and private research institutions, for public administration and, more generally, for the individual citizen.

The values in the database of property prices Observatory Agency of the housing market area can not meant to substitute the appropriate "estimate"; they refer to the ordinary buildings with particular reference to the main state of conservation and fabric use prevailing in each zone.

The use of OMI quotations in the estimation process does provide indications of large maximum values.

The basic hypothesis of the OMI is that positional factors are explaining the differences in value between similar various units, particularly those for residential use. It is therefore considered that in order to reduce the sampling variability it is useful to divide the land into portions that express similar levels of market, according to common characteristics (urban, socio-economic, equipment services, etc..).

Therefore, each district is segmented into one or more homogeneous areas. The homogeneous area OMI reflects a homogeneous segment of the local property market, in which there is substantial uniformity of appreciation for environmental and socio-economic conditions. It 's been established that the maximum deviation of the range of values found in each area and should not normally be higher than 1.5.

The quotations identify a range of minimum and maximum values with reference to ordinary residential units having a given intended use (residential, office, shop, etc.), located in a given homogeneous area. The minimum and maximum values represent the ordinariness and therefore prices are excluding those related to property damage, or particularly valuable or that have characteristics not common for the building type of zone.

The OMI areas, finally, have been grouped into bands, which are areas with territorial precise geographic position in the community and reflect, in general, a consolidated urban location (central, semi-central, peripheral, Suburban, Rural).

Types of intended use of buildings OMI, the most frequently found in the database that correspond to destinations according to the rules of the Plan are listed below:

1. Luxury habitation.
2. Civil habitation.
3. Economical habitation.
4. Villas and Chalets.
5. Private garage.
6. Box.
7. Covered parking spaces.
8. Uncovered parking spaces.
9. Shop.
10. Warehouse.
11. Laboratory.
12. Typical warehouse.
13. Industrial warehouse.

Figure 3 shows in the first map the land classification according land use zoning and in the second map according OMI zones, in the municipality if the case of study. Note that the fragmentation of land use zoning is deeper than he Estate Market values fragmentation. The highly generic identification of the real estate value is a proof of the difficulty of building accurate data infrastructure about.

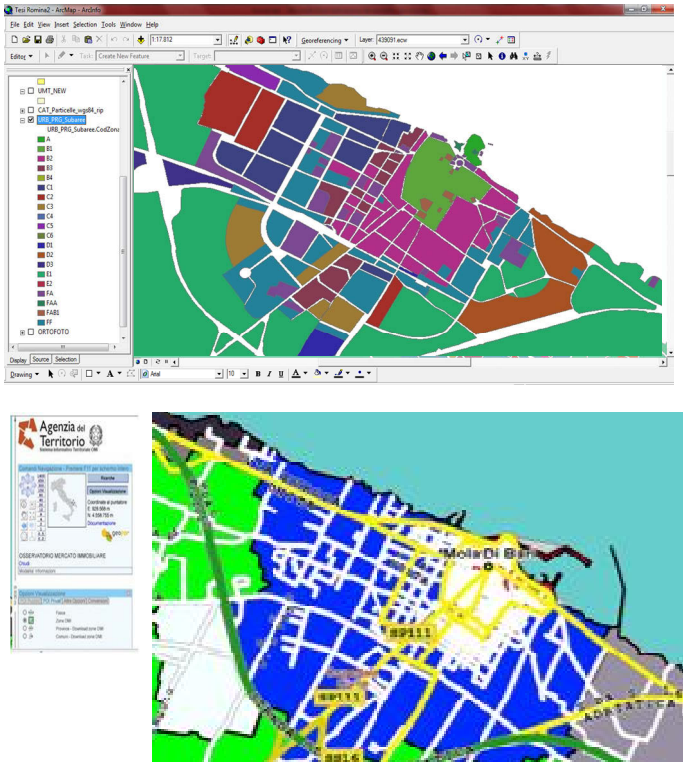


Fig. 3. Zoning of land use planning and the zones of Real Estate Survey (OMI)

5 A Case Study of GIS Supported TDR Application to Improve Local Land Use Planning

The town of Mola di Bari initiated a number of years preparing the PUG, in collaboration with the Department of Architecture at the Polytechnic of Bari. The instrument currently in force is PRGC of Eighties', prepared according with a rational distribution and radiocentric homogenous areas, with low-value green belts [9] and land for community services for the more concentrated towards the outside and other areas which are wedged into the interior.

The City of Mola has also effected the creation of a GIS devoted to drafting the Plan.

The geographic information system that supported the analysis in the case study was constructed as described in the following pages.

Starting from the existing urban plan seeking to understand what new needs should form the basis of the redirection of rights building variation in the Plan.

In areas under study have identified the buildable portions of territory but not yet built, has identified the urban load to be transferred to another place, from typing and from the urban belt (urban, suburban, middle, etc.) identified by OMI.

It is established that the volume of the instrument by means of equalization will be transferred to another area and the relevant building index.

The volume and type (high, medium low density) in some way determine the value, if matched to the OMI types (Civil buildings, economic, villas etc.).

The building index expressed for each zone of the Plan represents the amount of building volume for each square meter. A high index values for the same area is an extensive building, which generally corresponds to a higher real estate value per share (in € / m² of gross floor area paved) [5].

This is because in areas where the index is low you typically plan settlements housing type family, such as villas and / or villas.

These are assigned a unit value deduced from the proper sources OMI, higher than other building types.

In defining the new areas (the receiving sites of this volume), we consider the characteristics of the current zoning. The situations are possible:

1. the receiving area is partially free;
2. the receiving area is completely free;
3. the receiving area is guaranteed clear for the presence of any external constraint.

In the event of an area partially or completely free, there are of the boundary conditions which require a limit of urban load hospitable, higher than that corresponding to the existing urban density.

It then checks if the new area will exceed the maximum load capacity of volume following the transfer of the rights of building rights, if that were the case we shall be directed towards new and more landing areas of the residual portion of the airspace associated with the initial reception area .

The load capacity is variable and may be derived from requirements for environmental, morphological, architectural and urban planning.

The receiving area may have an urban destination other than the "starting" (eg an area falling in the area F can be a receiving area of rights of building from residential areas).

At this point it is checked whether the consequent reduction of soil typed with urban destinations "arrival" of the law contravenes the minimum size (such as for areas of services): If so it would be necessary to define a new area.

In the case of constraint due to reasons of protection in building the free area can not accommodate new volume.

The spatial databases used refer to:

- Cadastral System
- Together with the intended use of urban PRG
- Georeferenced ortho-photos
- Regional Technical Map (CTR) of Apulia and related information layers.

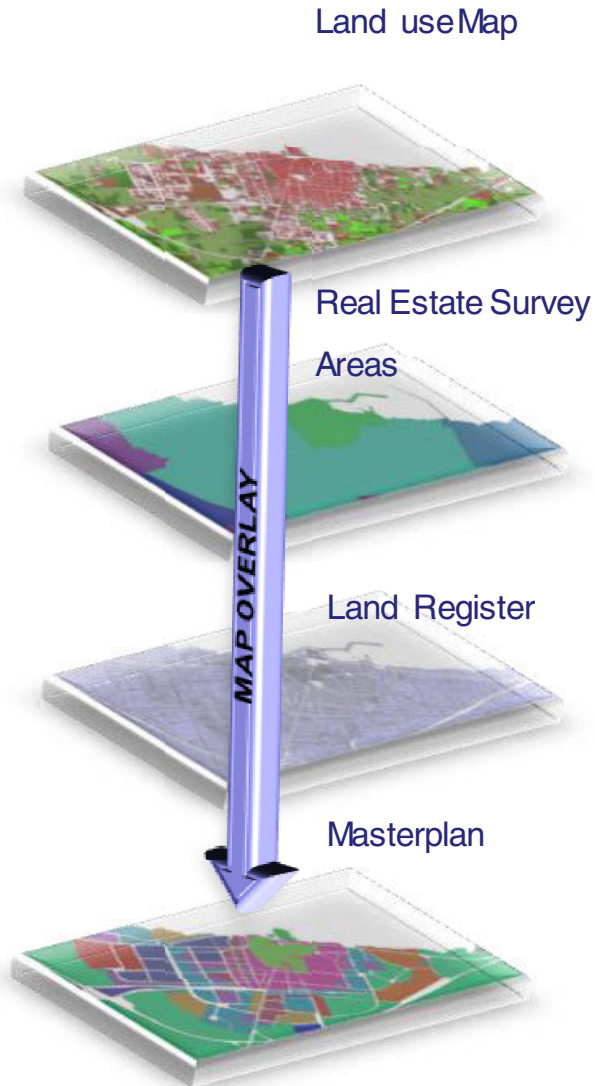


Fig. 4. The overlay

The GIS collects information base used for many purposes. In the primary case study using the following purposes [8]:

- Identification of free areas, which may represent areas in which urban form claims or rights of building rights, typed in the current urban structure;
- Identification of free areas, which may represent areas of acceptance of claims or rights of urban building rights, already typed in the current urban structure;
- Identification of the free areas not currently typed in the urban plan, which may represent reservoirs of soil to be used in case of a new destination, as host sites for additional rights building
- identification of the "state of fact and law of land", ie the set of capabilities already made settlement, potentially expressible by the residual capacity of settlements, through the junction between the layers of information related to the urban use of land use and texture, the intended use and the cadastral income.

Once created, the GIS will be designed so equalizing the opportunities associated with all construction-free zones. This work is done by overlaying the General Urban Plan (which indicates destinations and parameters), the Regional Technical or Aero-photogrammetric Hall (which identify the provisions of volumes, soils, infrastructure etc.), the Land Registry and / or the Observatory Real Estate Market (which define the values referred to the areas examined and the types established). The overlay creates a micro segmentation in areas that differ from each other just to look from any of the states listed above.

Micro areas are defined in the Territorial Unit Minimum (UMT). The procedure creates overlap around 9000 UMT. The transfer volume from one area to another can happen to move within the same area OMI.

The preliminary steps are as follows.

Acquisition of regional technical cartography on the municipal territory of Mola di Bari, and its consolidation into a single information layer: once acquired the so-called "plaques" that make up the regional technical paper relating to the town of Mola di Bari, has proceeded to mosaic them, returning them all to a single reference system. The overlay with the administrative boundaries has allowed us to "cut" the information layer of the technical paper, until the municipal boundaries.

In the third phase was given all the land boards, and related map sheets for an additional overlay showing the overall picture of the properties and land uses, with its revenues.

If you are within the same area OMI, and are characterized simultaneously by the same urban typing, checked the load capacity can proceed with the transfer of the volume defined above. In case of not belonging to the same area OMI transfer volumes would be correct in increments / decrements the corresponding values in the presence of inferior / superior in the landing area is necessary to identify the new values and redefine the new indices.

By doing so you ensure that you are dealing with a variation to the floor, always compatible with the logic dictated by the urban settlement and the plan itself and the context. Also in this case occurs in transferring this volume is not exceeded the maximum load volume and continues to maintain in the area intended to receive the volume a morphologically uniform appearance, or at least coherent.

In searching for new areas that can accommodate the volumes defined "mobile", it may be considered appropriate to transfer these volumes in areas not defined by the building floor, and so this procedure would require a variation of planning.

Defined non-building areas, or better with a different intended use-for example the area F of the Plan - which are designed to accommodate community services, may change their destination, passing through areas zoned C2 F (zone expansion).

The variation is taken to be urbanized context of a different design dimension. By defining new types and densities will set new values. Obviously in the database layer or OMI these areas will be anchored to the average values of agricultural and residential agricultural uses. Due to the absence of reference to these areas, property values related to urban settlements, we will assume for the present value of new building sites in areas OMI existing settlement patterns attributed to the most similar to those to be realized.

The cycle develops and eventually repeats the above steps, downstream of a project proposal:

1. Check areas of OMII and Land use Plan
2. Check if the landing area is vacant or partially built
3. Check if you exceed the maximum load building
4. Check the area in which the Plan will fall
5. Check the limits of building rights
6. Define the minimum territorial unit
7. Check which zone you fall Omi
8. Check if you have persistent values Omi,
9. Any estimation of new values
10. Check to see if it falls into the same area of the Land use Plan
11. Verification of compatibility of the new urban load
12. If you should fall in the same area we assume a variant of the Land use Plan and assign the new area the intended use by the operator.

It is at this point defined the themes to be considered in the case study and then proceed to their relocation from the layers of information hitherto obtained.

The shown example concerns an area taken into consideration in order to protect the coastline from those that may be environmental impacts from development.

The area in question corresponds to the current regulator according to the plan area C5, intended to accommodate construction of hotels and / or pensions.

The area is currently devoid of buildings, this can be up to the building with the TDR, in favor of sustainability

By the rules of PRG is clear that in the area C5 is provided for a maximum height of buildings to eight meters and a maximum number of levels equal to two.

The corresponding building type according to the OMI may therefore be that of the houses "in residence". After reviewing this area, the sending site, you must identify the receiving site, or the landing area of development rights packed up the coast. This is an area adjacent to C2 of the Plan area to be preserved.

Queries the system to know the data on property values: both the sending site and receiving site fall into the D1 zone (peripheral). The zone data are shown to follow OMI.

Table 1. The zoning of land use planning in the City Masterplan

Zone	Min-max buildability (m ³ /m ² built/area)		% coverage (m ² / m ²)	Hmax (m)	Hmin (m)
A (Historic)	5	0	0	0	0
B1 (residential)	5	0	75/100	0	0
B2 (residential)	5	2,5	60/100	12	8
B3 (residential)	5	3,5	50/100	18	11,5
B4 (residential)	0,3	0,2	6,6/100	4,5	0
C1 (residential)	4	2	33/100	15	9,5
C2 (residential)	2,4	1,5	30/100	12	8
C3 (residential)	1,8	1,25	25/100	7,5	0
C4 (residential)	0,5	0,35	6,6/100	7,5	0
C5 (residential)	1	0,75	12,5/100	8	0
C6 (residential)	0,15	0,1	0	4,5	0
D1 (productive)	4	2	40/100	12	0
D2 (productive)	2,5	1,5	50/100	8	0
D3 (productive)	3	1,75	60/100	8	0
E1 (productive)	0,03	0	0,75/100	4	0
E2 (productive)	0,01	0	2,5/100	4	0
F (City services)	0	0	0	0	0

The starting area in addition to their intended from the plane was given the maximum buildable volume expected, the total surface area and the index of manufacturability.

Starting area of rights, the building volume consists of about 26000 cubic meters, a floor area equal to about 34600 square meters. The index of the corresponding building is equal to 0.75 m³/m².

Similar considerations are also made for the C2 zone, where land will be made to the volume.

In the arrival of the rights, the building volume consists of about 163500 cubic meters, a floor area equal to about 109000 square meters. The index of the corresponding building is equal to 1,5 m³/m². In this area we formulate two hypotheses of transfer.

In the former case the whole volume of 26000 cubic meters of area C5, highlighted in green in the figure, C2 is transferred to the area with a density corresponding to the indices of urban manufacturability maximum of departure. It remains therefore a density of 0.75 m³/m², and the C2 zone is an area removed from pariah to the sending of the sites, that is 34600 square meters

Table 2. Real estate value of building type in the external urban zone (OMI)

Building Type	Quality Level	Estate value (€/m ²)		Monthly Rent value (€/m ²)	
		Min	Max	Min	Max
Ordinary Housing	NORMAL	1450	1900	4,8	6,4
Popular Housing	NORMAL	1150	1450	3,8	4,8
Garages	NORMAL	475	610	1,6	2,1
Box	NORMAL	700	1050	2,4	3,5
Covered Parkings	NORMAL	410	570	1,4	2
Open Parking	NORMAL	260	310	0,9	1,1
Luxury homes	NORMAL	1450	1950	4,8	6,6

At the landing surface, C2 zone, is not expected to build residential PRG an area corresponding to that of the C5 area. It verifies the sustainability of the transfer of all rights of residential construction in the area of residual volumes, which has an area of about 74400 square meters [10].

The calculations performed through the use of ArcMap can know all the information necessary to perform the verification.

If you want to keep the residual in the entire volume of the entire building area C2 of departure, the local index of buildability becomes equal to about 2.2 m³/m².

In this way the remaining area allocated for residential switching from one type of building semi-intensive (building multi / single family, such as townhouses or villas) to a type of intensive housing (multi-family housing, such as buildings in line, or tower) with indices and consequently property values typical of the C1 area of the current land use Plan.

It should be considered a possible increase in volume due to the change of housing type in the residual.

The area OMI has intermediate values almost identical villas and bungalows and houses. Therefore you need not provide volumetric bonus.

To preserve the coastal zone and therefore the area C5 can also take a second method of transfer of development rights [10].

Notwithstanding that the whole volume is transferred to the afferent area C5, this will come in the C2 zone through a different procedure.

It is considered an index of manufacturability of the C5 area equal to twice that required by the existing Master Plan, which in our case from 0.75 m³/m² becomes 1.5 m³/m².

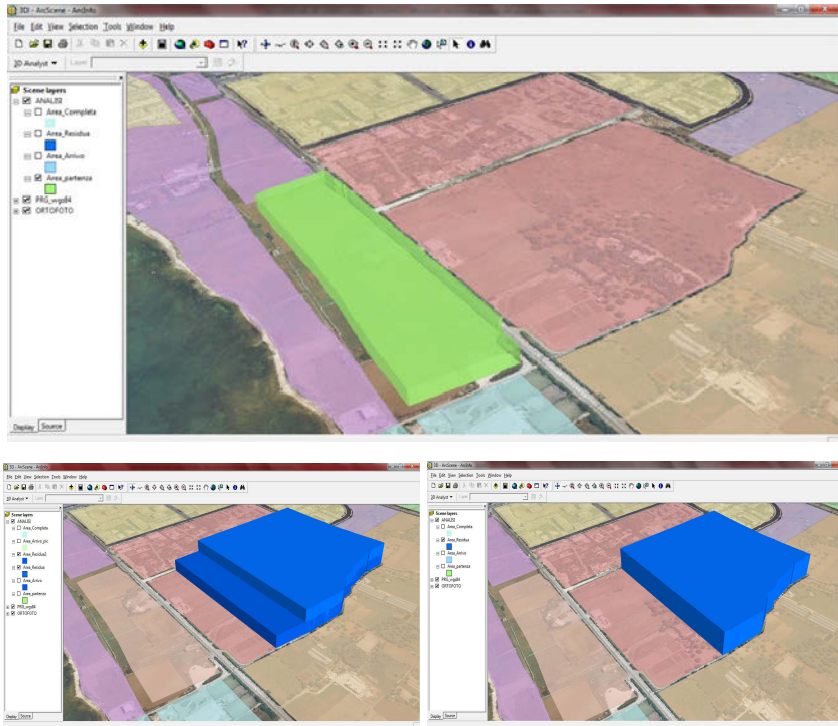


Fig. 5. The volume to be shifted by TRD is referring to the coast area. Two different Hypotheses have been assessed.

In this case the corresponding building area will be equal to half that of departure, ie about 17,300 square meters. This new surface, the smaller will be found in the landing area of the building volumes, which remain equal to 26000 cubic meters. The volumes on the area well represent the transferred urban load [11].

It can be observed as the area reserved to accommodate the construction hotel will have an index of manufacturability equal to twice the original and a final surface equal to half.

The area remaining residential this time will have a surface area equal to the difference between the initial 109,000 m² less, this time 17,330 m²rs. The residue for the residence will have an area of 91700 m². On this surface the resulting index will be (163500/91700) m³/m² approximately equal to 1.8 m³/m². The project is more sustainable. The residential real estate have remained faithful to their value. The project will provide the plant with the connections to the beach, and the reclaimed area will be earmarked for additional equipment.

With regard to the primary residences, the index allows the coexistence of single- and multi-family types, although with a higher incidence of the latter. The gap in terms of property values will diminish.

6 Final Remarks

The approach has proven useful in providing an idea of urban loads generated by the transfer of building rights. The opportunities provided by the application now in 3D GIS make it communicated the result of the analysis.

It should be noted, however, limit design experience. The areas covered are relevant extension. One use for a scale project involves the ability to cross not only the urban areas OMI ii data, but with each parcel of land, to highlight the potential of each locality of private and public property affected by the conversion plan. This is not now possible because of the well-known limitations of our current and supports land trust.

The perspective is thus linked to future developments of databases and infrastructure of data.

References

1. Conrad, J.M., LeBlanc, D.: The Supply of Development Rights: Results from a Survey in Hadley, Massachusetts. *Land Economics* 55, 269–276 (1979)
2. Alterman, R.: Takings International: A Comparative Perspective on Land Use Regulations and Compensation Rights. American Bar Association Publications, Chicago (2010)
3. Daniels, T.L.: The Purchase of Development Rights: Preserving Agricultural Land and Open Space. *Journal of the American Planning Association* 57, 421–431 (1991)
4. Levinson, A.: Why Oppose TDRs: Transferable Development Rights Can Increase Overall Development. *Regional Science and Urban Economics* 27, 283–296 (1997)
5. Macheimer, P.L., Kaplowitz, M.D.: A Framework for Evaluating Transferable Development Rights Programmes. *Journal of Environmental Planning and Management* 45(6), 773–795 (2002)
6. Fusco Girard, L.: Perequazione: principio e strumento della pianificazione sostenibile. In: Carbonara, S., Torre, C.M. (eds.) *Urbanistica e Perequazione, dai principi all'attuazione*, Franco Angeli, Milano (2008)
7. Micelli, E.: Development Rights Markets to Manage Urban Plans in Italy. *Urban Studies* 39, 141–154 (2002)
8. Lake, I.R., Lovett, A.A., Bateman, I.J., Day, B.H.: Improving Land Compensation procedures via GIS and hedonic pricing. *Environment and Planning C: Government and Policy* 18, 681–696 (2000)
9. Correll, M.R., Lillydahl, J.H., Singell, L.D.: The Effect of Greenbelts on Residential Property Values: Some Findings on the Political Economy of Open Space. *Land Economics* 54, 207–217 (1978)
10. Brown, G.M., Pollakowski, H.O.: Economic Valuation of Shoreline. *Review of Economics and Statistics* 59, 272–278 (1977)
11. ESRI, ArcGIS 3D Analyst: Three Dimensional Visualization, Topographic Analysis and Surface Creation, ESRI White Papers (January 2002), The publication is available at this date at http://www.esri.com/library/whitepapers/arcgisxt_lit.html#whitepapers

Magnetic Net and a Bouncing Magnetic Ball

Haiduke Sarafian

The Pennsylvania State University
University College
York, PA 17403, USA
has2@psu.edu

Abstract. Motivated by observing a tennis ball bounce off of a tennis racket we envision a parallel scenario where a magnetic ball bounces off a virtual magnetic net. A steady DC current in a closed horizontal loop casts the invisible elastic magnetic net. Contrary to a mechanical net the magnetic net continuously stays in contact with the magnetic ball. By adjusting the relevant parameters we seek for steady bounces. The equation describing the oscillation is a highly nonlinear differential equation and is symbolically unsolvable. Deploying *Mathematica* [1] we solve the equation numerically conducive to kinematics. Inclusion of viscosity generalizes the scope of the analysis resulting modified kinematics. We include also a 3D animation simulating the nonlinear oscillations of the magnetic ball.

1 Objectives

In our previous work we investigated the kinematics of a loose cylindrical permanent magnet dipole within the magnetic field of an electromagnet [2]. A glass tube containing the dipole is placed horizontally through the center and perpendicular to the circulating DC current. Aligning the axes of the tube and the loop makes the setting symmetrical. A DC looping current produces a uni-directional stationary magnetic field along the common symmetry axis on both sides of the loop. A stationary dipole with its magnetic moment aligned with the magnetic field gets attracted to the loop. The inner layer of the tube counter balances the dipole's weight making it free to slide. The speedy dipole passes the center of the loop slowing to a momentary halt on the other side of the loop. The magnetic field once again attracts the stationary dipole and the frictionless tube causes the dipole to oscillate symmetrically about the center of the loop.

In conjunction with our previous study and motivated by observing a bouncing tennis ball off of a racket we extend our previous work to considering a vertical glass tube. Contrary to the horizontal setting gravity pulls on the dipole making it continually fall. However, in our current work we justified that it would be plausible by adjusting the relevant parameters making the dipole rebound even when it is fallen beneath the center of the invisible magnetic net. Therefore, similar to the horizontal case, the dipole performs up and down oscillations about the center of the loop.

To address the relevant issues of interest we compose our work as follows. In section 2, by applying basic physics principals we formulate the problem conducive to equation of motion. Because of the non-linearity of the magnetic force we fail to solve the corresponding differential equation symbolically, as did *Mathematica*. We deploy *Mathematica* numeric scheme and solve the equation numerically. Utilizing the solution we then address the relevant kinematics of the motion. In section 3, to make our theoretical model compatible with reality we include viscosity. Solution of the modified equation of motion addresses the impact of the viscosity. For comprehensive visual understanding we display a pair of 3D animations simulating the free as well as the damped oscillations. We conclude our investigation with a few closing remarks.

2 Analysis

We assume the electric current is the source of the magnetic field. We then consider a looping DC current through a flat circle of radius R. Along the symmetry axis of the loop, the axis that passes through the center and perpendicular to the loop the magnetic field is a one-component vector field. The field according to Biot-Savart law [3] is,

$$\vec{B} = k'i \int \frac{d\vec{\ell} \times \vec{r}}{r^3} \tag{1}$$

Here i is the conduction current running through the loop, \vec{r} is the vector position connecting the current element $id\vec{\ell}$ to a point along the symmetry axis, and $k' = \frac{\mu_0}{4\pi} \equiv 10^{-7} \frac{T.m}{Amp}$, with μ_0 being the permeability of the vacuum. Equation (1) for a counter-clockwise looping current in a horizontal coil of radius R along the symmetry z -axis of a right-handed Cartesian coordinate system trivially evaluates,

$$\vec{B}(z) = \zeta \frac{1}{(R^2 + z^2)^{\frac{3}{2}}} \hat{k} \tag{2}$$

Here $\zeta = 2\pi R^2 ni$, with n being the number of turns. The current sets a unidirectional magnetic field along the z -axis. Figure 1 aside from the scaling factor ζ for a coil of radius 10.0 cm depicts the field vs. the distance from the center of the coil.

Figure 1 shows that the magnetic field along the symmetry axis is unidirectional, meaning it sustains its direction on both sides of the loop, and shows its value falls off rapidly vs. the distance from the center of the loop. A permanent magnet with magnetic dipole moment $\vec{\mu}$ placed within this field experiences a force. The force is subject to $\vec{F}_B = -\vec{\nabla}U$, where the magneto-static energy of the dipole is $U = -\vec{\mu} \cdot \vec{B}$, with \vec{B} , being the external field subject to eqn (2). Mathematically speaking, because the field is a function of z , $\vec{\nabla} \equiv \frac{d}{dz} \hat{k}$, therefore, $\vec{F}_B \simeq \frac{z}{(R^2+z^2)^{\frac{3}{2}}} \hat{k}$; in other words, the inhomogeneity of the field along the z -axis necessitates the force. Placing a permanent magnet with its moment parallel and aligned with the \vec{B} field experiences an attractive force towards the

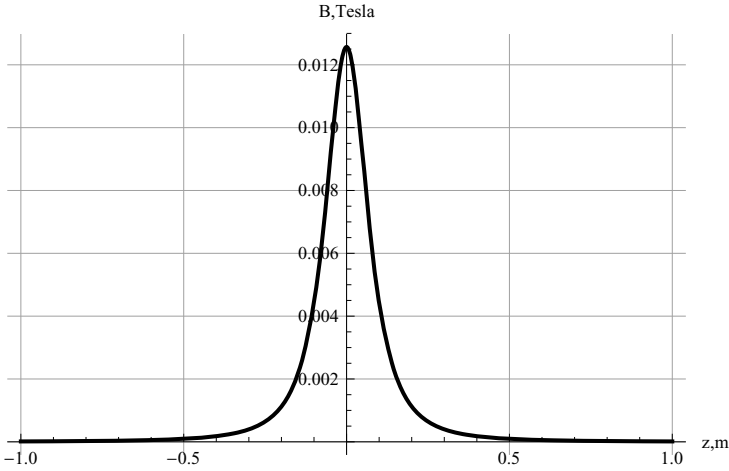


Fig. 1. Display of the magnetic field along the z -axis of the looping current vs. distance from the center of the loop

center of the loop. In addition to the attractive magnetic force gravity pulls on the dipole too. Given the scenario, the dipole falls and passes the center of the loop; depending on the parameters of the setting it may even fall considerably beneath the loop. Once underneath the loop the unidirectional magnetic field exerts a reversed magnetic force counteracting the gravity pull. Therefore, it is feasible by adjusting the relevant parameters to seek situations where these two forces balance each other making the dipole after a momentary halt to rebound rising to its initial height above the loop.

Applying Newton’s law of motion, $\vec{F}_{net} = m\vec{a}$ we form the equation of motion. Along the z -axis it yields, $m\ddot{z}(t) + F_B(t) + mg = 0$, with m and F_B being the mass of the dipole and the magnetic force, respectively. Utilizing the magnetic force the latter yields,

$$\ddot{z}(t) + \xi \frac{z(t)}{(R^2 + z(t)^2)^{\frac{3}{2}}} + g = 0 \tag{3}$$

Where $\xi = \frac{\mu}{m}\zeta$. This is a highly nonlinear differential equation. We were unable to solve this equation analytically, as did *Mathematica*.

We then deploy *Mathematica* numeric scheme. Assuming a set of practical initial conditions utilizing *NDSolve* we seek those solutions conducive to steady oscillations.

We provide the list of the relevant parameters in MKS units. These are: The magneto-static constant, radius of the loop, conduction current, number of turns, gravity acceleration, magnetic moment of the dipole, and the coefficient of viscosity, respectively.

Magnetic field and the force are shown in Fig 1 & 2, respectively.

```

values = {k → 1.0 × 10-7, R → 10.0 × 10-2, i → 10.0, n → 200.0, g → 9.8, μ → 1.75, γ → 3.0};
ξ := k 2 π n i R2 /. values
field[z_] = ξ * (1 / (R2 + z2)(3/2));
Plot[field[z] /. values, {z, -1, 1}, PlotRange -> All, PlotStyle -> {Black, Thick},
  AxesLabel -> {"z,m", "B,Tesla"}, GridLines -> Automatic];
forcez = (-μ) * D[-field[z], z];
Plot[forcez /. values, {z, -1, 1}, PlotRange -> All, PlotStyle -> {Black, Thick},
  AxesLabel -> {"z,m", "\!\{\*\SubscriptBox[\(F\), \(\B\)]\},N"}, GridLines -> Automatic]

```

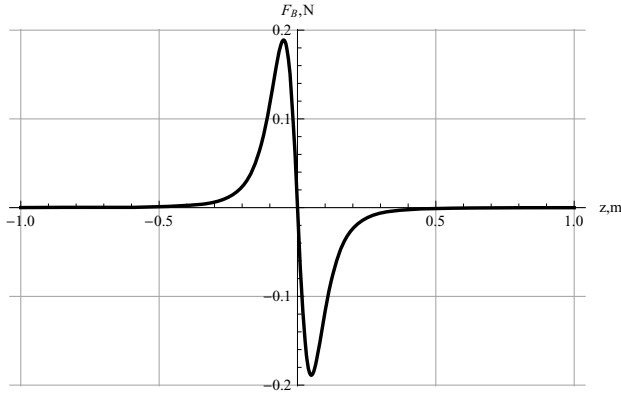


Fig. 2. Magnetic force on the dipole vs. the distance from the center of the loop

In forming the equation of motion we treat the mass of the dipole as an unknown variable. Consequently, for a chosen initial release height, we seek those masses conducive to oscillating solutions. For the given parameters listed in values, by inspection, we set the initial height at 0.9 m, this is nine times the radius of the loop! Shorter initial heights obviously do work as well.

```

solzm =
Table[NDSolve[{eqn[m] == 0, z[0.] == 0.9, z'[0.] == 0}, z[t], {t, 0.0, 10}, MaxSteps -> ∞],
  {m, 0.6 × 10-6, 1.0 × 10-6, 0.2 × 10-6}]

```

By inspection, we identify a range of masses fulfilling our objective. Figure 3, displays the position of the dipole vs. time for three different masses; $m = 0.6, 0.8$ and 1.0 mg .

The solid curve corresponds to the lightest mass and shows the dipole oscillating unevenly about the center of the loop. These oscillations are quite different vs. the vibrations of a harmonic oscillator. The reason is, the magnetic force is highly nonlinear. Also, one observes that the dipole spends a longer period of time underneath the loop. These are shown by the abscissa of the corresponding intersections of the oscillating function. As expected and confirmed by the short dashed curve, the oscillation of the second heavy mass is more uneven; the second heavier dipole spends longer periods underneath the loop. And finally, the heaviest dipole has a tendency of spending its time entirely underneath the loop (the gray curve); i.e. it breaks loose and never bounces off the net.

```
{positionz, velocityz, accz} = {z[t] /. solzm, D[z[t] /. solzm, t], D[z[t] /. solzm, {t, 2}];
Plot[positionz, {t, 0, 2}, PlotRange -> {-3, 1},
AxesLabel -> {"t,s", "z,m"}, GridLines -> Automatic,
PlotStyle -> {{Black, Thick}, {Black, Thick, Dashing[{0.015}]}, {Gray, Thick}}]
```

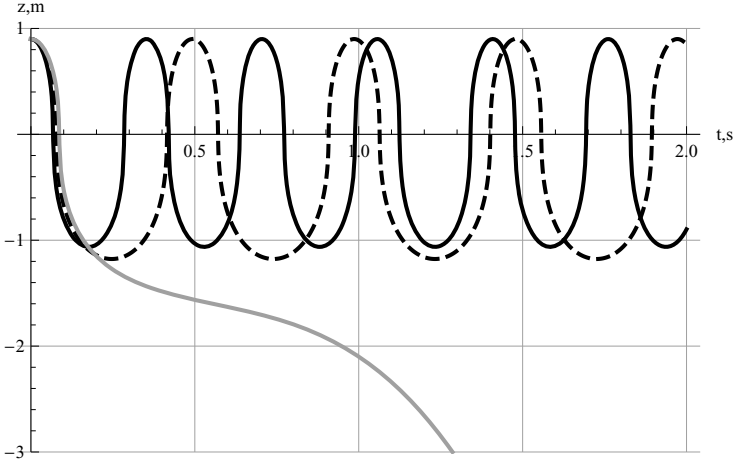


Fig. 3. Display of the position of the dipole vs. time

A magnified version of the oscillations of the first two oscillations are depicted in Fig 4.

```
Plot[{positionz[[1]], positionz[[2]]}, {t, 0, 2},
PlotRange -> All, AxesLabel -> {"t,s", "z,m"}, GridLines -> Automatic,
PlotStyle -> {{Black, Thick}, {GrayLevel[0.1], Thick, Dashing[{0.02}]}}
```

As expected, the lighter dipole (the solid curve) oscillates semi evenly about the center of the loop, while the heavier one (the dashed curve) drops deeper and spend longer underneath the loop.

By folding the time variable, we plot the associate phase diagrams for the set of three masses. We also extend our graphic phase analysis accordingly. Plots of $\{z(t), \dot{z}(t)\}$, $\{z(t), \ddot{z}(t)\}$ and $\{\dot{z}(t), \ddot{z}(t)\}$ i.e. $\{position, velocity\}$, $\{position, acceleration\}$ and $\{velocity, acceleration\}$, are depicted in Fig. 5-7, respectively.

Plots shown in Fig 5 are useful. For oscillating dipoles the plots are closed curves, while for non-oscillating case it is an open curve. The abscissa of the left plot is almost symmetric while the second plot shows a higher degree of asymmetry. The open curve of the last figure is a signature of non-oscillating dipole.

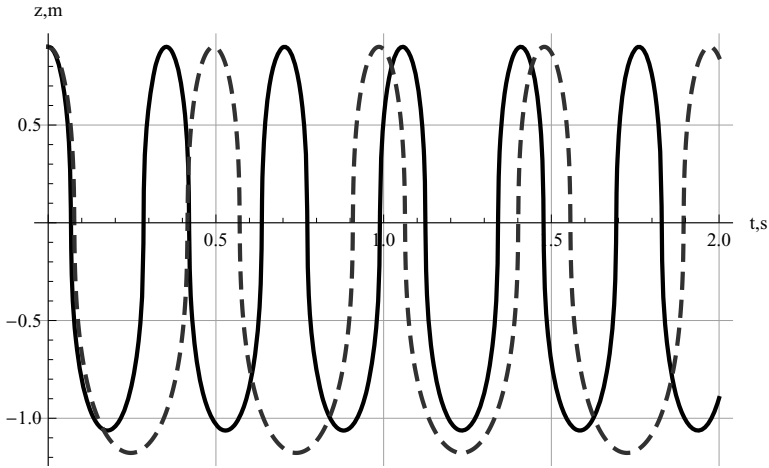


Fig. 4. Position of the oscillating dipoles vs. time. The solid and the dashed curves correspond to the light and semi-heavy dipoles, respectively.

```

tablem = Table[m 10^6, {m, 0.6 * 10^-6, 1.0 * 10^-6, 0.2 * 10^-6}];
plotparav = Table[ParametricPlot[Flatten[{positionz[n], 0.005 velocityz[n]}],
{t, 0, 1(*10*)}, PlotStyle -> {GrayLevel[0.1 (n - 1)], Thick, Dashing[{0.02 (n - 1)}]},
GridLines -> Automatic, AxesLabel -> {"z,m", "v,m/s"}, PlotRange -> All,
PlotLabel -> StringJoin["m=", ToString[tablem[n]]], {n, 1, Length[solzlm]}]

```

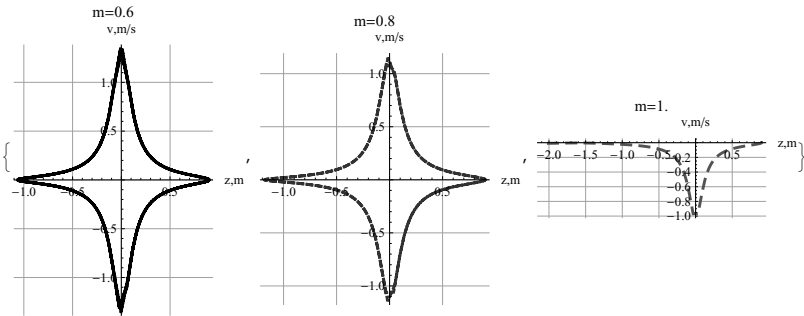


Fig. 5. Phase diagrams of the oscillating dipoles, masses are labeled on each graph

```

plotparav = Table[ParametricPlot[Flatten[{positionz[n], 0.00001 accz[n]}],
{t, 0, 1}, PlotStyle -> {GrayLevel[0.1 (n - 1)], Thick, Dashing[{0.02 (n - 1)}]},
GridLines -> Automatic, AxesLabel -> {"z,m", "a,m/s^2"}, PlotRange -> All,
PlotLabel -> StringJoin["m=", ToString[tablem[n]]], {n, 1, Length[solzlm]}]

```

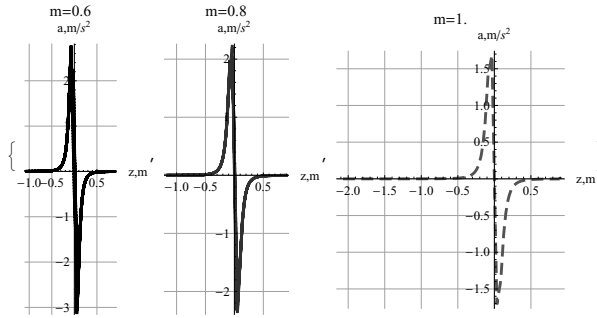


Fig. 6. Plots of position vs. acceleration for three different masses

Plots in Fig 6 show the falling dipoles are accelerating, and when they pass the center they reverse their direction.

```

plotparaa = Table[ParametricPlot[Flatten[{velocityz[[n]], 0.0002 accz[[n]]},
{t, 0, 1}], PlotStyle -> {GrayLevel[0.1 (n - 1)], Thick, Dashing[{0.02 (n - 1)}]},
GridLines -> Automatic, AxesLabel -> {"v, m/s", "a, m/s² n"},
PlotRange -> All, PlotLabel -> StringJoin["m=", ToString[tablem[[n]]],
PlotPoints -> 400], {n, 1, Length[solzm]}]
    
```

Plots depicted in Fig 7 are velocity vs. acceleration. The “bow-tie” loops, the first two plots are indicators of oscillating dipoles, and the last plot, the “half bow-tie” is a signature of a non-oscillator. These type of analyses are missing in literature.

To further our analysis, we pose a question: “In contrast to a linear oscillator, do we know how a nonlinear vibrator oscillates?” To answer this question we compose a *Mathematica* code simulating the oscillations. Figure 8 simulates the oscillations of the dipole in a 3D setting. Watching this animation helps to form an opinion about the nonlinear oscillations.

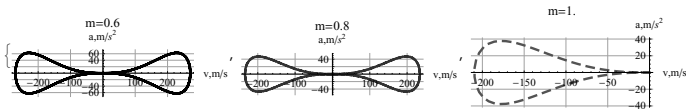


Fig. 7. Plots of velocity vs. acceleration for three different masses

```

plotlinex = ParametricPlot3D[{t, 0, 0}, {t, -3, 3}, PlotRange -> {{-1, 1}, {-1, 1}, {-1, 1}},
  PlotStyle -> {Black(*Red*), Dashing[0.02], Thick};
plotliney = ParametricPlot3D[{0, t, 0}, {t, -3, 3}, PlotRange -> {{-1, 1}, {-1, 1}, {-1, 1}},
  PlotStyle -> {Black(*Red*), Dashing[0.02], Thick};
plotlinez = ParametricPlot3D[{0, 0, t}, {t, -3, 3},
  PlotRange -> {{-1, 1}, {-1, 1}, {-1, 1}}, PlotStyle -> {Black, Thickness[0.015]};
Manipulate[Show[{ParametricPlot3D[{x, Sqrt[1-x^2], 0},
  {x, -1, 1}, PlotStyle -> {Black(*Red*), Thick},
  PlotRange -> {{-2, 2}, {-1, 1}, {-2, 2}}, AxesLabel -> {"x", "y", "z"}],
  ParametricPlot3D[{x, -Sqrt[1-x^2], 0}, {x, -1, 1}, PlotStyle -> {Black(*Red*), Thick},
  PlotRange -> {{-2, 2}, {-2, 2}, {-2, 2}}, AxesLabel -> {"x", "y", "z"}],
  plotlinex, plotliney, plotlinez,
  ParametricPlot3D[{t, 0, 0}, {t, -3, 3}, PlotRange -> {{-1, 1}, {-1, 1}, {-1, 1}},
  PlotStyle -> {GrayLevel[0.2](*Red*), Dashing[0.02], Thick}],
  ParametricPlot3D[{0, 0, t}, {t, -3, 3}, PlotRange -> {{-1, 1}, {-1, 1}, {-1, 1}},
  PlotStyle -> {Dashing[0.02], Thick}],
  Graphics3D[{GrayLevel[0.2](*Blue*), Cylinder[
    {{0, 0, positionz[[1, 1]] /. t -> t}, {0, 0, positionz[[1, 1]] + 0.08 /. t -> t}], 0.08}
    (*Sphere[{positionx[[1]] /. t -> t, 0, 0}, 0.05]*)}],
  Graphics3D[{Opacity[0.4], Specularity[White, 5],
  Tube[{{0, 0, -2}, {0, 0, 2}], 0.1}], Boxed -> False},
  ParametricPlot3D[{-8 forcez /. values /. t -> t, 0, z}, {z, -2.0, 2.0},
  PlotStyle -> {(*Green*) GrayLevel[0.5], Thick}, PlotRange -> All]
}], FaceGrids -> {{0, 0, 1}, {0, 0, -1}}, FaceGridsStyle ->
  Directive[Black, Dashed, Thickness[0.003]], {{t, 0, "t"}, 0, 2, 0.01}]

```

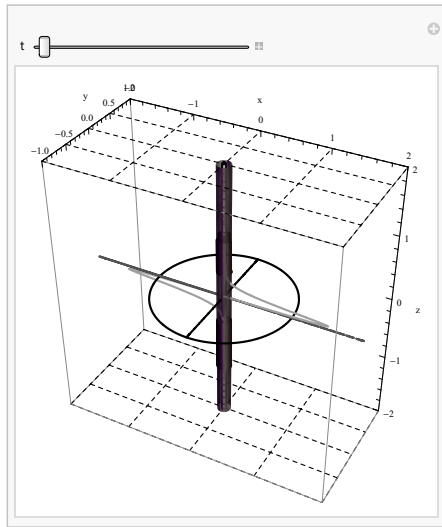


Fig. 8. A display of the 3D setting and simulation of a nonlinear oscillator

In this figure, the circular looping current, the vertical glass tube, the magnetic dipole and the nonlinear force are shown. Simulating this active 3D plot shows how a massive magnetic dipole falls underneath the loop and then bounces off the invisible magnetic net. It also shows how the non-linear force makes the dipole oscillate in an unorthodox fashion.

3 Impact of the Viscosity

In the previous section we assume the dipole falls freely in the tube. However, in reality the tube contains air and its fluid resistance damps the oscillations. The impact of the air resistance can be quantified by including the viscosity. As we have previously explored [4] viscosity is velocity dependent and is formatted as $\Gamma\dot{z}(t)$, where Γ is the viscosity constant. Accordingly, the equation of motion modifies,

$$\ddot{z}(t) + \xi \frac{z(t)}{(R^2 + z(t)^2)^{\frac{5}{2}}} + \gamma\dot{z}(t) + g = 0 \tag{4}$$

where $\gamma = \frac{\Gamma}{m}$. Corresponding *Mathematica* code reads,

```
eqnγ[m_] = zγ''[t] -  $\left(\frac{1}{m} \text{forcez} /. \text{values} /. z \rightarrow z\gamma[t]\right) + (g + \gamma z\gamma'[t]) /. \text{values};$ 
```

As we exercised in the viscose free case, we explore scenarios conducive to damped oscillations. Applying the same mass range as previous section we obtain the corresponding solutions. Utilizing these solutions we construct the kinematics of interest.

```
solzγm = Table[NDSolve[{eqnγ[m] == 0, zγ[0.] == 0.9, zγ'[0.] == 0},
  zγ[t], {t, 0.0, 10}, MaxSteps -> ∞], {m, 0.6 × 10-6, 1.0 × 10-6, 0.2 × 10-6};
{positionzγ, velocityzγ, acczγ} = {zγ[t] /. solzγm,
  D[zγ[t] /. solzγm, t], D[zγ[t] /. solzγm, {t, 2}]};
Plot[positionzγ[[1]], {t, 0, 0.4}, PlotRange -> All, AxesLabel -> {"t,s", "z,m"},
  GridLines -> Automatic, PlotStyle -> {Black, Thick}]
```

Figure 9 is to be compared to the solid curve of Fig 4. The impact of the viscosity is clearly shown. For clarity the first few dozen of such oscillations are graphed. In practice the dipole oscillates and damps to its final resting position at the center of the loop; for the given parameters it takes about two seconds. We also display the phase diagrams similar to the ones shown in Fig 5-7. These are shown in Fig 10.

The differences between graphs depicted in Fig 5-7 vs. the ones in Fig 10 are to be contributed to the viscosity. The asymmetry of the phase plots in the first row of Fig 10 is attributed to damping. The loops have open ends, however, because of the chosen time span only the start off open ends are shown. Had we graphed them for a two-second time span we could have shown the other open end as well. The third row of the Fig 10 shows similar features, the fuzzy, multi-loop “bow-ties” are indicative of the damping feature. For the damped oscillations, even the heaviest of three masses shows a “bow-tie” behavior.

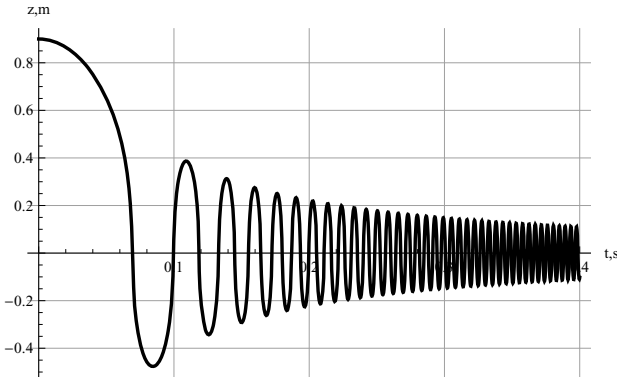


Fig. 9. Display of the damped oscillations of the lightest dipole

```

plotparaz = Table[ParametricPlot[Flatten[{positionzγ[[n]], 0.005 velocityzγ[[n]]},
{t, 0, 0.2(*10*)}, PlotStyle -> {GrayLevel[0.1 (n - 1)], Dashing[{0.02 (n - 1)]}},
GridLines -> Automatic, AxesLabel -> {"z,m", "v,m/s"}, PlotRange -> All,
PlotLabel -> StringJoin["m=", ToString[tablem[[n]]], {n, 1, Length[solzγm]}]
plotparav = Table[ParametricPlot[Flatten[{positionzγ[[n]], 0.00001 acczγ[[n]]},
{t, 0, 0.4}, PlotStyle -> {GrayLevel[0.1 (n - 1)], Dashing[{0.02 (n - 1)]}},
GridLines -> Automatic, AxesLabel -> {"z,m", "a,m/s^2"}, PlotRange -> All,
PlotLabel -> StringJoin["m=", ToString[tablem[[n]]], {n, 1, Length[solzγm]}]
plotparaa = Table[ParametricPlot[Flatten[{velocityzγ[[n]], 0.0002 acczγ[[n]]},
{t, 0, 0.3}, PlotStyle -> {GrayLevel[0.1 (n - 1)], Dashing[{0.02 (n - 1)]}},
GridLines -> Automatic, AxesLabel -> {"v,m/s", "a,m/s^2"},
PlotRange -> All, PlotLabel -> StringJoin["m=", ToString[tablem[[n]]],
PlotPoints -> 400], {n, 1, Length[solzγm]}]
(*Show[{plotparax}, ImageSize->700]*)
    
```

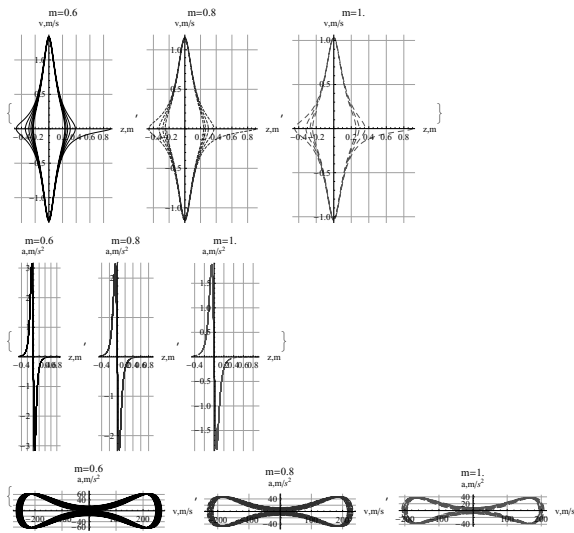


Fig. 10. Description of these plots are similar to those shown in Fig 5-7

4 Conclusions

Comparing the characters of a bouncing tennis ball off of a tennis racket to a bouncing magnetic dipole off of a magnetic net is novel. It is intriguing envisioning a situation where a massive permanent magnet with its dipole moment aligned with the external magnetic field in the presence of gravity to perform steady oscillations. The equation describing the oscillations of the problem on hand is a highly nonlinear differential equation. Solving this equation analytically poses challenges, deploying *Mathematica* numeric scheme eases the situation. Not only we solve the equation, we explore a suitable range of parameters making the solutions conducive to desired set of oscillations. By including the viscosity we further the computation making the analysis compatible with reality. We emphasize the distinct differences between the mechanical and its counterpart magnetic forces. The former is effective only at the contact, yet the latter continuously acts at a distance. Interestingly, for the case at hand the dipole stretches the magnetic net beyond its mechanical counter example, as if it is tied with nonlinear rubber bands to the rim of the loop. Currently the oscillations of a magnetic dipole with reversed magnetic moment is under investigation.

References

1. Wolfram, S.: The Mathematica Book, 5th edn. Cambridge University Publications, Cambridge (2003); and Mathematica software V8.0 (2011)
2. Sarafian, H.: Nonlinear Oscillations of a Magneto Static Spring-Mass. *J. Electromagnetic Analysis & Applications* 3, 133–139 (2011)
3. Jackson, J.D.: Classical Electrodynamics, 3rd edn. Wiley, Hoboken (2005)
4. Sarafian, H.: Dynamic Dipole-Dipole Magnetic Interaction and Damped Nonlinear Oscillations. *J. Electromagnetic Analysis & Applications* 1, 195–204 (2009)

Autonomous Leaves Graph Applied to the Simulation of the Boundary Layer around a Non-symmetric NACA Airfoil

Sanderson Lincoln Gonzaga de Oliveira¹ and Mauricio Kischinhevsky²

¹ Universidade Federal de Lavras, 37200-000 Lavras-MG, Brazil
sanderson@dcc.ufla.br

<http://algot.dcc.ufla.br/~sanderson>

² Universidade Federal Fluminense, 24210-240 Niterói-RJ, Brazil
kisch@ic.uff.br

<http://www.ic.uff.br/~kisch>

Abstract. The Boundary Layer is a fluid layer in the neighborhood of a surface. It is important in many disciplines related to Physics and Fluid Mechanics, which aerodynamics is an example. This paper presents a 2D numerical simulation of this problem considering an incompressible laminar flux in steady state with non-slip condition. An adaptive mesh refinement is carried out by the Autonomous Leaves Graph with finite volume discretizations. The Modified Hilbert Curve is implemented to traverse and provide the total ordering of the finite volumes. Flux simulations are presented around a non-symmetric airfoil NACA2415 shape. The results show evidences that the adaptive mesh refinement scheme is adequate for numerical solution of this type of problem.

Keywords: Finite Volume Method, Boundary Layer Problem, NACA airfoil, adaptive mesh refinement, Hilbert space filling curve.

1 Introduction

Different techniques are being proposed to solve differential equations. Examples are Yanchuk et al. (2001) [12] that presented simulation of partial synchronization in diffusively coupled arrays of identical chaotic oscillators with periodic boundary conditions and Respondek (2010) [10] that describes simulation of partial differential equations by the so-called controllable attainable sets. On the other hand, numerical solution of partial differential equations may require the use of a mesh refinement strategy that concentrates more discrete places where the solution and/or its derivatives change rapidly. The Autonomous Leaves Graph [3] was proposed to implement the adaptive mesh refinement with low computational cost in numerical solution of partial differential equations by quadrangular finite volume discretizations. The Autonomous Leaves Graph is a data structure coupled to a solver of systems of linear and non-linear equations. The reader is referred to Burgarelli et al. [3] for details of the adaptive mesh refinement strategy and the Autonomous Leaves Graph.

Using the Autonomous Leaves Graph, all modifications in the graph data structure are merely local. In addition, an algorithm based on the Hilbert Curve construction is used in order to implement the numbering of the control-volume nodes. More specifically, the control-volume total-ordering is provided by the Modified Hilbert Curve. Again, the reader is also referred to Burgarelli et al. [3] for details of this space-filling curve.

The Autonomous Leaves Graph has begun to be applied in the numerical solution of partial differential equations in different contexts. For example, Unfer et al. [11] applied a simplified version of the Autonomous Leaves Graph in the plasma analysis when interacting with gas flux. In this present work, all the Autonomous Leaves Graph resources are applied in the numerical modeling of a aerodynamic problem. Specifically, the Autonomous Leaves Graph represents the adaptive mesh refinement in the study of the Boundary Layer Problem. Prandtl [9] demonstrated the existence of a fine layer in the flow of fluids very close to the surface of an object. This permitted to simplify the Navier-Stokes fluid flow equations, dividing the flow field in two areas:

- one inside the boundary layer, where the viscosity is dominant and occurs the larger part of the drag experimented by an object immersed in a flow;
- the other area lies outside the boundary layer, where the viscosity can be neglected without relevant effects in the solution.

The thickness of the velocity boundary layer is commonly defined as the distance from the object at which the flow velocity is 99% of the freestream velocity. The freestream velocity is represented by u_∞ in this paper. In the top of the boundary layer, the molecules move in the same velocity of the molecules outside of the boundary layer. The velocity that is calculated at the surface of the body in an inviscid flow solution. The no-slip condition requires that the flow velocity at the surface of a solid object be zero. The flow velocity will then increase rapidly within the boundary layer, governed by the boundary layer equations (the boundary layer equations are described in the following). This means that there is a large velocity variation inside the boundary layer flux.

In this context, the numerical solution needs to refine the mesh with a large number of discrete places inside the boundary layer in order to adequately represent it. However, a fine mesh outside the boundary layer results in unnecessary computational effort because the *variation* of the flow velocity in this area is small or even null. In this problem, a numerical scheme that uses the adaptive mesh refinement can provide a solution with lower computational cost than using a uniform mesh. For those reasons, the Boundary Layer Problem has characteristics to be simulated with the Autonomous Leaves Graph and the coupled numerical methods.

The Boundary Layer Problem has already been simulated using the Autonomous Leaves Graph. The flat plate version of this problem was simulated in [5] and this problem was simulated with a *symmetric* NACA0012 airfoil shape in the computational domain in [6]. In addition, a simulation was also provided in a *symmetric* NACA0009 airfoil shape in the computational domain by in [7].

In this note, the non-symmetric NACA2415 airfoil shape is simulated in the computational domain. This non-symmetric NACA four-digits airfoil-shape simulation aims to give new evidences that the Autonomous Leaves Graph can be applied to study complex problems, such as in aerodynamics. Specifically, the Boundary Layer Problem is studied.

In the following sections, the Boundary Layer Problem is presented in Section 2. A discretization by the finite volume method is shown in Section 3. Experimental results are given in Section 4. Finally, the conclusions are addressed in Section 5.

2 Boundary Layer Problem

The Boundary Layer is a very fine region adjacent to an object immersed in a fluid flow. The molecules that directly touch the object surface are virtually without movement.

Each layer of molecules inside the boundary layer moves faster than the layer closer to the object surface. In the top of the boundary layer, the molecules move in the same velocity than the molecules outside the boundary layer, represented by u_∞ in this note.

Inside the boundary layer, the velocity of the molecules depends on the object shape, the fluid mass in the direction of the object, the viscosity, and the fluid compressibility. Those characteristics provide to the boundary layer a shape not necessarily similar to the physical shape of the object.

The equations of a bidimensional incompressible steady Boundary Layer Problem in rectangular coordinates are given in the following.

$$\text{Moment: } u \frac{\partial u}{\partial x} + v \frac{\partial u}{\partial y} = -\frac{1}{\rho} \frac{dp}{dx} + v \frac{\partial^2 u}{\partial y^2} \quad (1)$$

$$\text{Continuity: } \frac{\partial u}{\partial x} + \frac{\partial v}{\partial y} = 0, \quad (2)$$

in which p is the pressure, u is the dependent variable of the partial differential equation, ρ is the fluid density, and v is the cinematic viscosity. The reader is referred to Anderson et al. [1] for details of this mathematical modeling of the Boundary Layer Problem.

3 A Finite Volume Discretization of the Boundary Layer Problem

The following discretization was presented in [7]. One can integrate equation (1) in the control-volume yielding

$$\int \int u \frac{\partial u}{\partial x} + v \frac{\partial u}{\partial y} dx dy = -\frac{1}{\rho} \int \int \frac{dp}{dx} dx dy + \int \int v \frac{\partial^2 u}{\partial y^2} dx dy \quad (3)$$

Applying the Divergence Theorem yields

$$\int uu|_e - uu|_w dy + \int vu|_n - vu|_s dx = \quad (4)$$

$$-\frac{1}{\rho} \int \int \frac{dp}{dx} dx dy + \int v_n \frac{\partial u}{\partial y}|_n - v_s \frac{\partial u}{\partial y}|_s dx.$$

Considering that the flow in the middle of an edge of a control-volume represents the average of the variation in the edge of the control-volume, equation 5 can be written as

$$\Delta y(uu|_e - uu|_w) + \Delta x(vu|_n - vu|_s) = \quad (5)$$

$$-\frac{1}{\rho} \int \int \frac{dp}{dx} dx dy + \Delta x(v_n \frac{\partial u}{\partial y}|_n - v_s \frac{\partial u}{\partial y}|_s)$$

in which Δx and Δy represent the size of a control-volume in horizontal and vertical directions, respectively.

An interpolation function evaluates the value of the dependent variable u in the interface of a control-volume. Considering the flow from west to east and from south to north and using the *Upwind Difference Scheme* from Courant et al. [4] yields

$$u_P u_P - u_P u_W + v_P u_P - v_P u_S = -\frac{1}{\rho} \int \int \frac{dp}{dx} dx dy + \frac{v}{h} (u_N - 2u_P + u_S), \quad (6)$$

in which $h = \Delta x = \Delta y$ and $v = v_n = v_s$.

Equation [6] is divided by u_P for clarity. Besides, u_W is considered in the previous iteration and algebraic manipulations provide

$$u_P^{k+1} - u_N^{k+1} \frac{v}{hu_P^k} - u_S^{k+1} \frac{v_P^k + \frac{v}{h}}{u_P^k} = -\frac{1}{\rho} \int \int \frac{dp}{dx} dx dy + u_W^k - 2\frac{v}{h} - v_P^k, \quad (7)$$

in which (u_W, v_W) , (u_N, v_N) and (u_S, v_S) are the neighbors of the control-volume (u_P, v_P) in west, north and south directions, respectively.

According to Anderson [2], usual boundary conditions can be applied since $u(x, y) = u_b(x)$, in which the subscript b refers to the border of the Boundary Layer. Namely, the gradient pressure term in the equation [1] is evaluated in the boundary-layer border.

Since $u_b(x)$ is estimated, $\frac{dp}{dx}$ can be evaluated with the application of equations that model the inviscid flow outside the boundary layer (Euler equations) given by $\frac{dp}{dx} = -\rho u_b \frac{du_b}{dx}$. Again, the reader is referred to Anderson et al. [1] for details. The moment equation is estimated as a semi-implicit numerical approximation given by

$$u_P^{k+1} - u_N^{k+1} \frac{v}{hu_P^k} - u_S^{k+1} \frac{v_P^k + \frac{v}{h}}{u_P^k} = u_W^k - 2\frac{v}{h} - v_P^k + u_{bP} \frac{u_{bP}^k - u_{eW}^k}{hu_P^k} \quad (8)$$

Considering the same approach, equation 2 is discretized as

$$v_P^{k+1} - v_S^{k+1} = u_W^{k+1} - u_P^{k+1}. \quad (9)$$

The equations 8 and 9 are semi-implicit finite volume approximations of the equations 1 and 2, respectively.

4 Experimental Tests

For practical purposes, the following tests were accomplished with the cinematic viscosity of the air $\nu = 1.5 \cdot 10^{-5} m^2/s$ and freestream velocity set as $u_\infty = 300$. The adopted refinement criteria was the relative difference of the quantity of interest in both horizontal and vertical directions between adjacent control-volumes larger than a threshold. This threshold is defined by the user in the implemented computational project.

In the experimental tests, the NACA2415 shape was simulated in the computational domain. The NACA2415 is a kind of NACA¹ four-digit airfoil shape. As an example, the NACA2415 airfoil shape is visualized with 45° angle of attack in Figure 1.

A simulation with control-volumes refined until two levels is shown in Figure 2. In this figure, the space-filling curve, i.e. the Modified Hilbert Curve, is also shown. The Modified Hilbert Curve is a Hamiltonian path that begins at the most superior right control-volume and terminates at the most inferior right control-volume.

In Figure 3, a simulation with control-volumes refined until five levels is provided. In this figure, the Modified Hilbert Curve is also provided. Including, the quantity of mass in each control-volume centroid can be visualized in this figure.

Control-volumes totally inside the airfoil shape are inactive and they are not considered in the numerical solution. This means that inactive control-volumes are not considered while traversing each control-volume by the Modified Hilbert Curve in order to set up the system of linear equations from the finite volume discretizations.

Vortices can appear close to the above surface of the airfoil shape in these kind of simulations. In the simulation shown in Figure 3, vortices are represented by the quantity of mass close to zero in the control-volumes that discretize the above airfoil-shape surface.

The molecules move in the same velocity than the molecules outside the boundary layer in the top of the boundary layer. This is represented by the freestream velocity set as $u_\infty = 300$. Clearly, the quantity of mass of each control-volume is less than $u_\infty = 300$ inside the boundary layer. On the other hand, the quantity of mass is close to $u_\infty = 300$ in the control-volumes that discretize the bottom airfoil-shape surface in the simulation shown in Figure 3 because this mesh is coarse. Namely, the approximated numerical solution is not adequate because this coarse mesh and the mesh should be improved so that the simulation

¹ NACA stands for National Advisory Committee for Aeronautics (from USA).

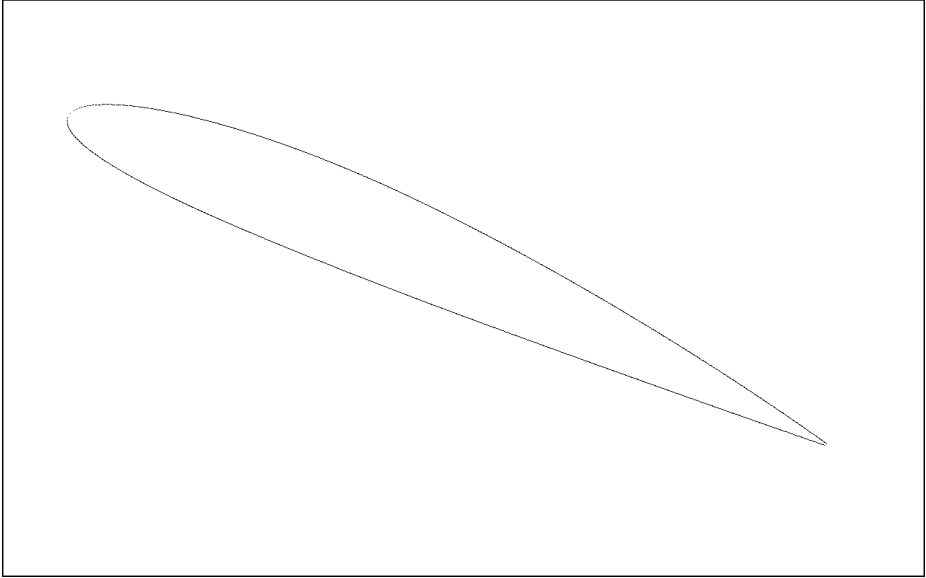


Fig. 1. A NACA2415 airfoil shape with 45° angle of attack in the computational domain

may provide a better solution to the problem than the one shown in Figure 3. On the other hand, the control volumes outside the boundary layer do not to be refined.

A simulation with control-volumes refined until 10 levels is shown in Figure 4. The Modified Hilbert Curve is also shown in this figure. Most of the control-volumes lies close to the airfoil-shape surface where the boundary layer occurs: the solution varies quicker inside the boundary layer than in the other regions of the mesh.

In Figure 5, a simulation with 12 as the maximum level of refinement can be visualized. In this figure, the mesh is comprised of 19288 control-volumes. This mesh is still coarse; however, this simulation is obtained in seconds in a simple workstation.

Most of the computations of these simulations are solving the systems of linear equations. Furthermore, all the simulations resulted in symmetric positive-definite systems of linear equations. For this reason, there are strong evidences that this scheme always results in systems of linear equations with those characteristics and the Conjugate Gradient Method from Hestenes and Stiefel [8] was used.

In Figure 5, again, most of the control-volumes lies inside the boundary layer region. The region outside the boundary layer is not refined as the region inside the boundary layer. This leads to a smaller system of linear equations than using a uniform refinement of the mesh.

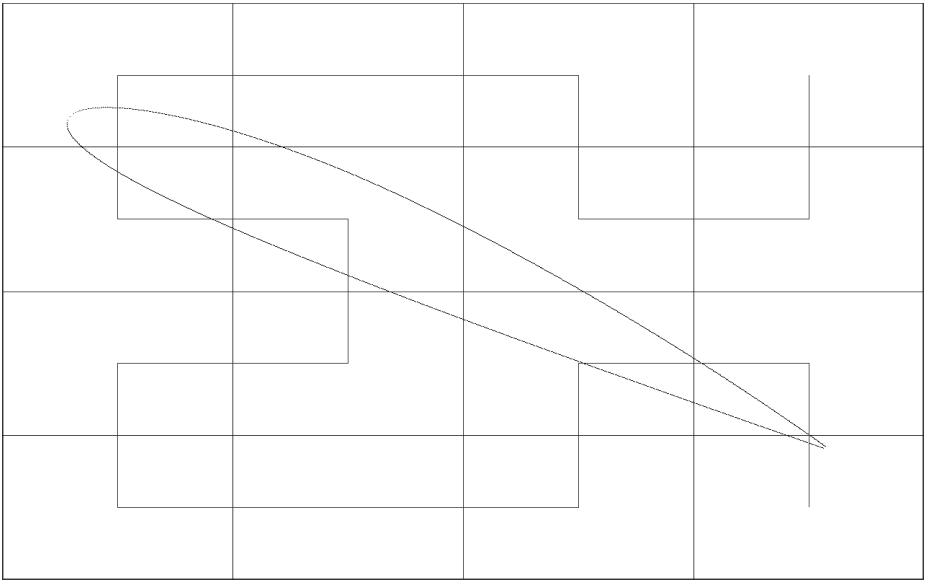


Fig. 2. A mesh with 16 control-volumes with a NACA2415 airfoil shape in the computational domain in 45° angle of attack and the Modified Hilbert Curve ordering the control-volumes. The Modified Hilbert Curve is a Hamiltonian path that begins at the most superior right control-volume and terminates at the most inferior right control-volume.

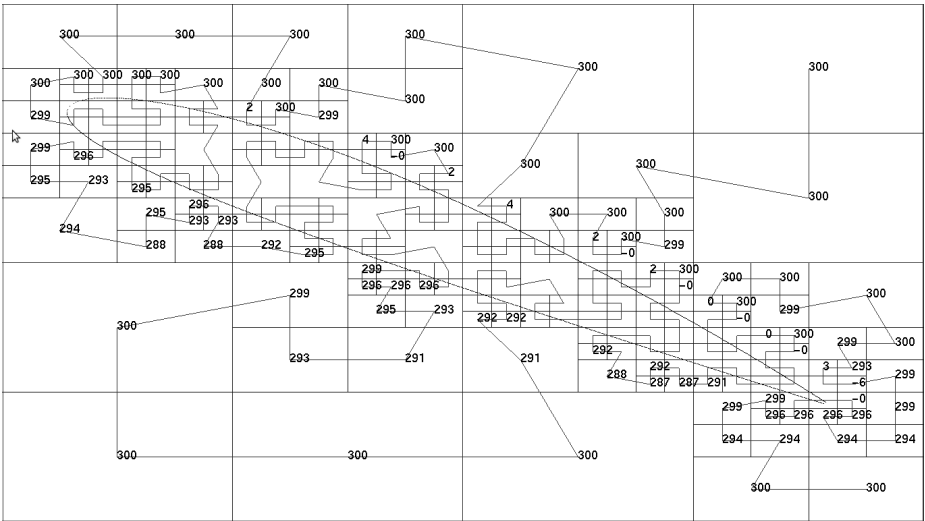


Fig. 3. NACA2415 airfoil shape in the computational domain with 45° angle of attack and five levels of refinement. The quantity of mass in the centroids of the control volumes and the Modified Hilbert Curve are also shown.

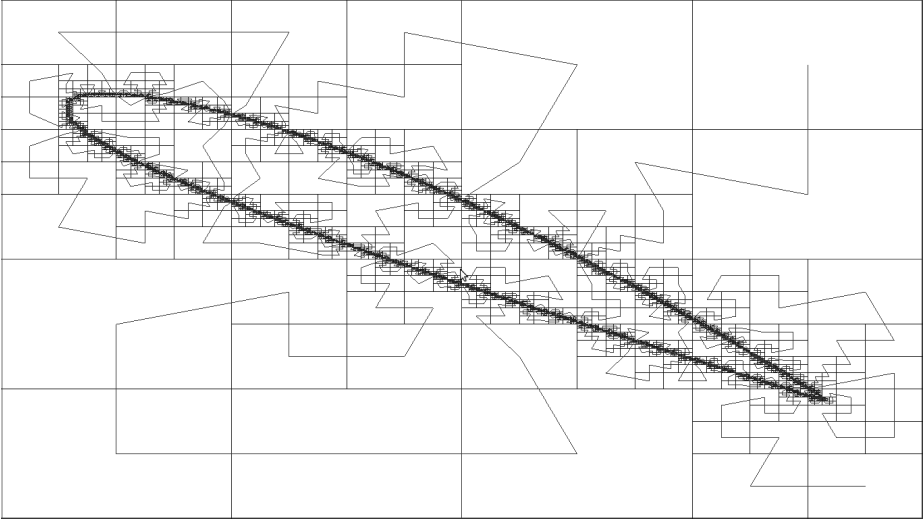


Fig. 4. NACA2415 airfoil shape in the computational domain with 45° angle of attack, 10 levels of refinement, and 7618 control-volumes. The Modified Hilbert Curve for control-volume ordering is shown. The Modified Hilbert Curve begins at the most superior right control-volume and terminates at the most inferior right control-volume.

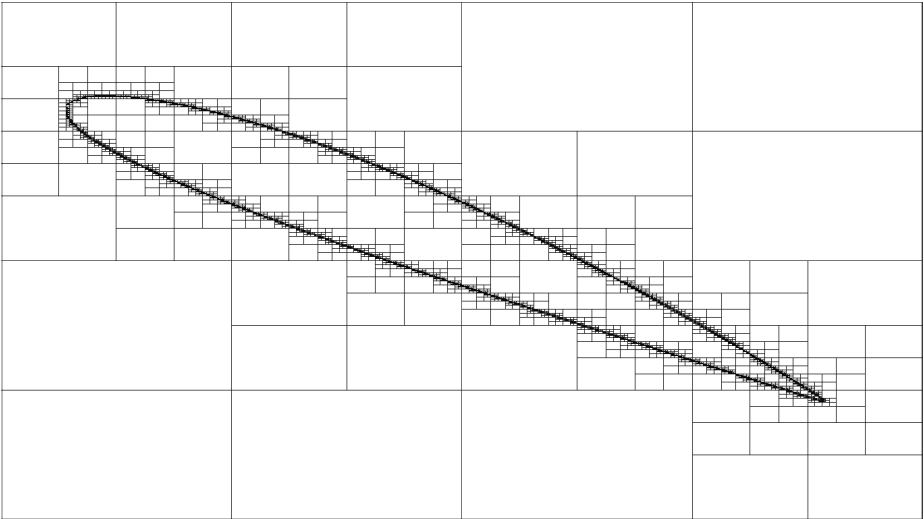


Fig. 5. NACA2415 airfoil shape in the computational domain with 45° angle of attack, 12 levels of refinement, and 19288 active control-volumes in the mesh

The adaptive mesh refinement is performed pursuing for a simulation with lower computational cost than using a uniform refinement of the mesh. In addition, the simulation using the adaptive mesh refinement should result in an approximation with similar (equal or better) precision than using a uniform refinement of the mesh.

5 Conclusion

This work presented numerical simulations of the Boundary Layer Problem with adaptive mesh refinement applying finite volume discretizations and Autonomous Leaves Graph. The finite volumes total-ordering is given by the Modified Hilbert Curve. Simulations with the non-symmetric NACA2415 in the computational domain were presented. The experimental tests show that the numerical scheme refines more the mesh inside the boundary layer letting a coarse mesh outside of the boundary mesh. Those simulations aim to provide evidences and disclose that the Autonomous Leaves Graph can be applied to study complex problems, such as in aerodynamics.

Detailed analysis shall be provided in a future work. Moreover, the presented approach shall be compared against other methods and some numerical comparison shall be added in a future work.

Acknowledgments. The author gratefully acknowledges FAPEMIG, CNPq, and FAPERJ for the financial support.

References

1. Anderson, D.A., Tannehill, J.C., Pletcher, R.: Computational Fluid Mechanics and Heat Transfer. Hemisphere, New York (1984)
2. Anderson, J.D.: Fundamentals of Aerodynamics. McGraw-Hill Inc., New York (1991)
3. Burgarelli, D., Kischinhevsky, M., Biezuner, R.J.: A new adaptive mesh refinement strategy for numerically solving evolutionary PDE's. *Journal of Computational and Applied Mathematics* 196, 115–131 (2006)
4. Courant, R., Isaacson, E., Rees, M.: On the solution of nonlinear hyperbolic differential equations by finite differences. *Communications on Pure and Applied Mathematics* 5, 243–255 (1952)
5. Gonzaga de Oliveira, S.L., Guedes, M., Kischinhevsky, M.: Método dos Volumes Finitos com refinamento adaptativo de malhas aplicado ao problema da camada limite. In: XXIX CILAMCE - Congresso Ibero Latino Americano de Métodos Computacionais em Engenharia (June 2007)
6. de Oliveira, S.L.G., Kischinhevsky, M.: Autonomous Leaves Graph Applied to the Boundary Layer Problem. In: Allen, G., Nabrzyski, J., Seidel, E., van Albada, G.D., Dongarra, J., Sloot, P.M.A. (eds.) ICCS 2009. LNCS, vol. 5544, pp. 560–569. Springer, Heidelberg (2009)
7. de Oliveira, S.L.G., Kischinhevsky, M., Burgarelli, D.: Refinamento adaptativo de malhas de volumes finitos baseado em grafo aplicado ao problema da camada limite. *Revista do IEEE América Latina* 9(1), 102–108 (2011)

8. Hestenes, M.R., Stiefel, E.: Methods of conjugate gradients for solving linear systems. *Journal of Research of the National Bureau of Standards* 49(6) (December 1952)
9. Prandtl, L.: Über flüssigkeitsbewegung bei sehr kleiner reibung. In: Krazer, A. (ed.) *Verhandlungen des dritten internationalen Mathematiker-Kongresses in Heidelberg*, pp. 484–493. Teubner, Leipzig (1905)
10. Respondek, J.S.: Numerical simulation in the partial differential equation controllability analysis with physically meaningful constraints. *Mathematics and Computers in Simulation* 81, 120–132 (2010)
11. Unfer, T., Boeuf, J.-P., Rogier, F., Thivet, F.: Multi-scale gas discharge simulations using asynchronous adaptive mesh refinement. *Computer Physics Communications* 181, 247–258 (2010)
12. Yanchuk, S., Maistrenko, Y., Mosekilde, E.: Partial synchronization and clustering in a system of diffusively coupled chaotic oscillators. *Mathematics and Computers in Simulation* 54, 491–508 (2001)

Sinimbu – Multimodal Queries to Support Biodiversity Studies

Gabriel de S. Fedel, Claudia Bauzer Medeiros, and Jefersson Alex dos Santos

Institute of Computing, University of Campinas, Brazil
gabrielfedel@gmail.com, {cmbm, jsantos}@ic.unicamp.br

Abstract. Typical biodiversity information systems can only solve a small part of user concerns. Available query mechanisms are based on traditional textual database manipulations, combining them with spatial correlations. However, experts need more complex computations – e.g., using non-textual data sources. This involves a considerable amount of manual tasks, to obtain the needed information. This paper presents the specification and implementation of Sinimbu – a framework to process multimodal queries that support both text and images as search parameters, for biodiversity studies, thus providing support for subsequent complex simulations. Sinimbu was validated with real data from our university’s Zoology Museum, which houses one of the largest zoological museum collections in Brazil. Not only can users interact with the system in several modes, but query possibilities (and answers) vary according to the user’s profile. Query processing in Sinimbu combines work in database management, image processing and ontology construction and management.

Keywords: Biodiversity data management, CBIR, Ontologies.

1 Introduction

The goal of biodiversity information systems is to help experts manage information on live organisms and their relationships with each other and the environment. This forms the basis for complex computational processes and simulations. From a high level point of view, one can say that there are two main kinds of primary data handled by such systems – (a) data on observations of species, and (b) data about the (geographical) environment in which these species were observed. Observation data contains information about *what* species were observed *where, when, how, and by whom*.

Queries and models in biodiversity systems require correlation of these data, using many kinds of knowledge on geographic, biologic and ecological issues. Available biodiversity systems can only cope with part of these factors, and scientists must perform several manual tasks to derive the desired information, e.g., because of semantic mismatches among data sources, or lack of appropriate operators. Data extraction for model construction, on such systems, is made via queries that are basically of two kinds: (a) those that require textual input (e.g.,

species’ taxonomic classifications) and (b) those that allow direct interaction with some kind of cartographic representation (usually resulting from a textual-based query). There are however many other kinds of data that are used by scientists in their analyses, but which are not taken advantage of in biodiversity systems. Examples include images (in particular, photos of animals or plants), sound recordings (of animals), sketches, etc.

This paper presents *Sinimbu* – a multimodal query processing framework that extends queries on observation data by combining standard text-based queries with ontology manipulation (for semantic enhancement) and query by image content. *Sinimbu* means *chameleon* in tupi-guarani¹, indicating that the system supports several interaction modes and accommodates distinct user profiles – both scientists and non-experts. Once relevant data are identified and retrieved, scientists use the corresponding records in their simulations – e.g., to study species’ interactions in a given region,

Sinimbu uses real data, and was implemented within the BioCORE project², a joint research effort from computer scientists and biologists to design tools to support biodiversity studies. Previous results of ours within this effort include the construction of an ontology service that supports several kinds of operations on ontologies, the development of a set of tools that allow querying [8], the development of a set of tools that allow querying inter-species relationships [9], a query expansion toolkit for species occurrence data, also based on ontological knowledge [19], and an infrastructure for content-based image retrieval, tested on fish image collections [7].

This work is being developed at the Laboratory of Information Systems, Institute of Computing at the University of Campinas, Brazil. The main contributions of this paper are: (1) it shows how to combine distinct query processing techniques and special purpose data structures to explore multiple modalities, for biodiversity purposes, thereby filtering and restricting relevant data for biodiversity applications; (2) it presents design details and implementation choices, thereby helping those who want to implement similar functionality; (3) it discusses design and implementation challenges associated with these choices.

The rest of this paper is organized as follows. Section 2 presents the concepts needed to understand the text. Sections 3 and 4 present *Sinimbu*’s architecture and implementation. Section 5 discusses related work, and reviews our contributions. Section 6 presents conclusions and ongoing work.

2 Basic Concepts

2.1 Observations and Occurrence Records

Observations of live organisms are at the core of biodiversity studies. In biodiversity systems, such information is stored in so-called *occurrence* or *collection* records. The terms designate any digital record that describes “when, where

¹ South America native group of languages.

² <http://www.lis.ic.unicamp.br/projects/biocore>

and how” a species (or a set thereof) was observed or collected, and by “whom”. One record may refer to several individuals, or even several species, if different organisms were observed at a certain geo-spatial location (e.g., when insects are collected by means of a trap).

Besides biodiversity systems, data on such records can also be obtained from portals, in which institutions publish information about their collections. Such portals play an important role in contributing to biodiversity studies (even though they cannot be considered as biodiversity information systems). Some of these portals belong to museums, where records are frequently connected with a “physical” object, in the sense that the corresponding organism (a “specimen”) was actually collected from the field and preserved. Some experts distinguish between “occurrence” (in which observations do not require collecting an organism) and “collection” (associated with some kind of catalog structure). For this reason, from now on this paper will use the term “collection” to denote data on species.

2.2 Content-Based Image Retrieval and Multimodal Queries

Image data can be processed and retrieved in several ways – e.g., considering metadata (such as device used), image captions (and hopefully semantics) or, in our case, image content. In the so-called “Content-based image retrieval” (CBIR), the query predicate is an image, and the result is a set of images that are computed to be “most similar” to the input image. CBIR relies on the use of algorithms that can describe and distinguish images based on their content via *descriptors*. A descriptor [7] extracts feature vectors that represent image visual properties (e.g., color, texture, shape) and defines a distance function that is used to determine how similar two images are, given the distance of their feature vectors. From a high level point of view, a descriptor is a pair $\langle f, v \rangle$ where v is the feature vector, and f the distance function used to compare two vectors. Given a query pattern (usually an image), descriptors can be used to rank sets of images according to their similarity to the query pattern.

Multimodal queries are those that involve more than one mode for defining query parameters, and normally require processing distinct kinds of data types. The goal is to improve the quality of the result, through the combination of distinct kinds of information. Research in multimodal interfaces is increasing, with a conference entirely dedicated to this subject, already in its 13th edition [14]. This conference covers a wide range of subjects, involving multidisciplinary research on multimodal human-human and human-computer interaction, interfaces, and system development. This paper concentrates on system development issues, considering the modalities of textual and image parameters.

3 Multimodal Search in Sinimbu

3.1 Overview

Sinimbu parameters combine text and/or images. Textual input can be of the following kinds: (a) species’ common names, and (b) fields from occurrence records,

e.g., scientific name, location. The latter are retrieved using standard database queries, whereas common names are processed through navigating in an ontology especially constructed for the system. Images themselves can be query parameters. In this case, the input image is processed using special purpose descriptors, under CBIR mechanisms.

Sinimbu supports two kinds of user profiles: biodiversity researchers, and non-experts; the query interface and results vary according to the profile. This increases the kinds of users (and uses) of the system.

3.2 Data Structures

The data used by Sinimbu is organized according to distinct structures, as shown in Figure 1. These structures are basically of three types: tables (using the PostgreSQL database system), an image repository (files of images and their descriptors), and a taxonomic ontology. Tests were restricted to museum curated data.

Database tables used by Sinimbu are the following:

- **Taxonomy:** Taxonomic nomenclature of the animals whose occurrence records appear in the database, as well as the year and author of the scientist originally responsible for naming that animal. Several fields may be missing, due to incomplete identification. Its key, *id_taxa* plays a major role in linking all data used by Sinimbu.

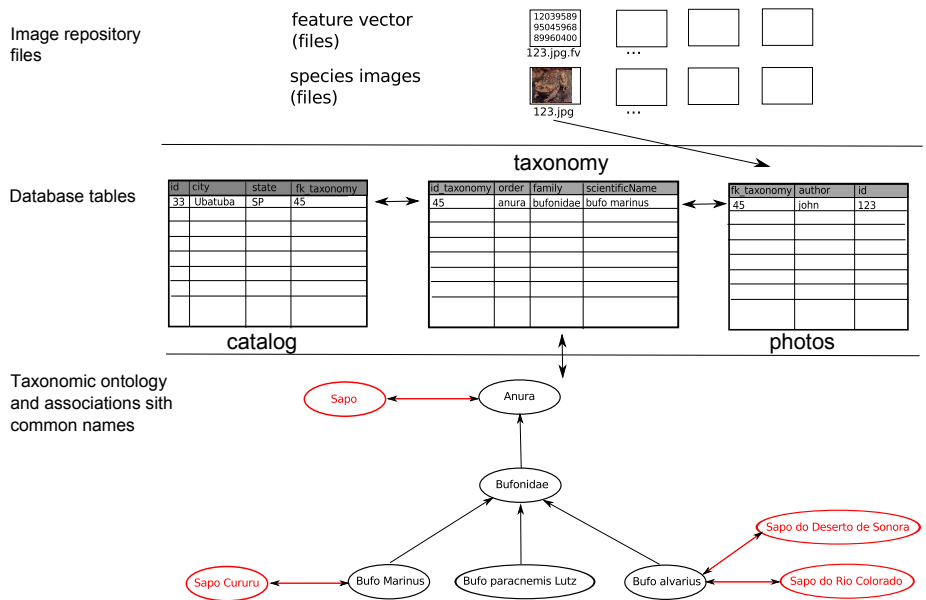


Fig. 1. Data structures in Sinimbu – some database tables and attributes are omitted

- **Catalog:** Entries of the museum catalog, containing occurrence records, with information of where, when, how, and who collected the specimen. These records are linked to the *taxonomy* table, uniquely identifying the corresponding animal.
- **Photos:** Information on images (photos of animals), also linked to the *taxonomy* table. Contains metadata such as the author of the photo, file name and whether it is public or not (non-public photos are used by content-based retrieval queries, but are not displayed to the general public, only to researchers with appropriate privileges).
- **Responsible:** Data on researchers responsible for the field trip in which observations were made. It is linked to the *catalog* table.
- **Location:** Textual information about some geographic region, such as country, county or state, being linked to the *catalog* table.

The identifier (primary key) of the records of table *taxonomy* is called *id_taxa*. It is the unique database identifier of some level of taxonomic description for a given species (i.e., the seven basic levels recognized internationally in the Linnaean taxonomic hierarchy for nomenclature – kingdom, phylum/division, class, order, family, genus, species). The values of the *id_taxa* attribute are artificially created, and are unique in the entire database. It is the basis for linking all information about all data associated with a given taxonomic classification – images, occurrence records, etc. For instance, Figure 1 shows there is a unique identifier (45) for the frog “*Bufo marinus*”; there are 6 such frogs in the University’s museum (and thus 6 occurrence records), and 2 photos. All records and photos are linked to *id_taxa*=45. In the *taxonomy* table, record with key 45 contains attribute values “Chordata (Phylum), Amphibia (Class), Anura (Order), Bufonidae (Family), *Bufo marinus* (the scientific name, Genus + species)”.

Sinimbu’s structures allow navigating from an image to its descriptors, and vice-versa, and from an image to the corresponding species, and to the associated occurrence records.

3.3 The Taxonomic Ontology

A taxonomic ontology [5] is a hierarchy of terms, under generalization/specialization relationships. Common names, in Sinimbu, are stored in a taxonomic ontology, associated with the Linnaean scientific taxonomic classification.. A given common name can be associated with distinct taxonomic levels, and a taxonomic term at any level can be linked to multiple common names.

Figure 1 (at the bottom) gives an example of this association: the *Anura* order corresponds to the *sapo* (frog) common name, while species *Bufo alvarius* is associated with *Sapo do Deserto de Sonora* and *Sapo do Rio Colorado*. From a common name, queries can retrieve species’ taxonomic classifications (and thus *id_taxa*), and from these find additional information (photos, occurrence data, etc). Also in the example, if a query asks for “Sapo”, then all descendants of “Anura” will be selected, because of ontological inheritance.

3.4 Architecture

Figure 2 presents a high level view of Sinimbu’s architecture, and its interaction with some of BioCORE’s services: Storage services (handle access to repositories), Supporting services (basic operations).

Besides the modules for Multimodal Search, Sinimbu includes the Taxonomy extractor (to build and maintain the taxonomic ontology) and our GP framework [6], used in extracting image descriptors and CBIR processing.

A query is processed as follows: end-users provide input parameters via the interface (images and/or text) – arrow numbered (1) in the figure. This is forwarded to Sinimbu’s Multimodal Search - arrow (2), where it is first processed by the Integrated Search Manager (3). This module examines the request, and interacts with distinct Retrieval modules (4), each of which for a specific modality, forwarding query requests to BioCORE’s supporting services (5). Once the

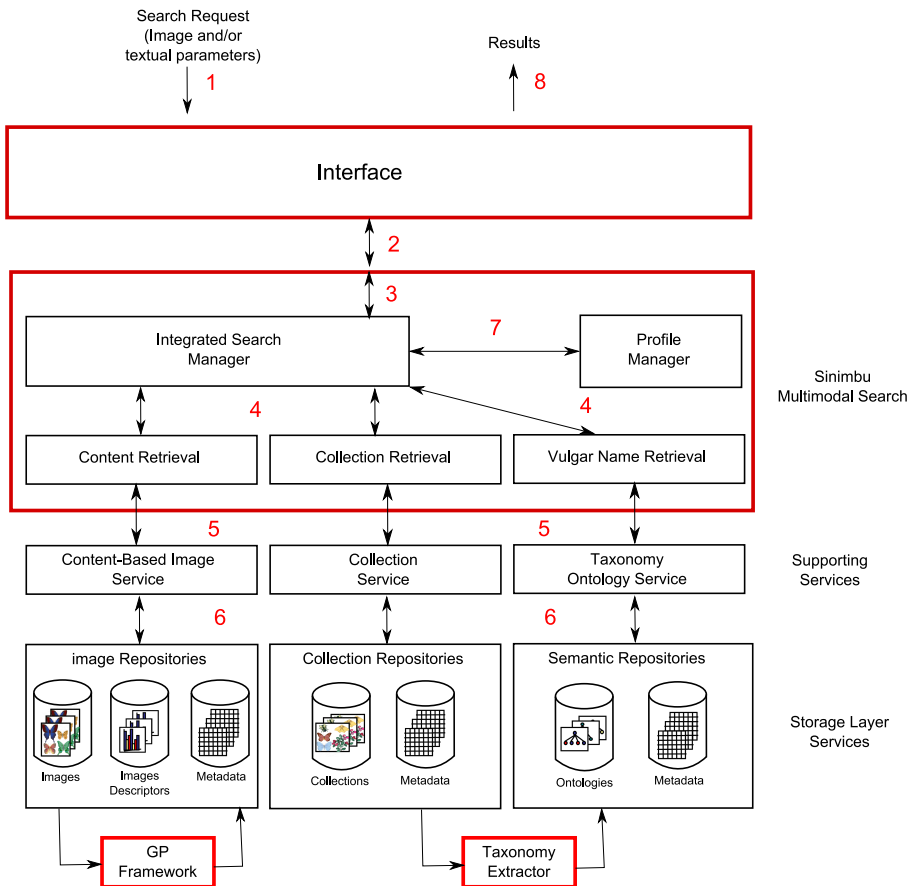


Fig. 2. Sinimbu - main blocks

results are returned, the Integrated Search Manager interacts with the user Profile Manager (7), in which the output visualization is built, forwarding this to presentation via the Interface (8). There are three kinds of data repositories accessed in such queries (6): Image, Collection and Semantic (ontologies).

Sinimbu’s Retrieval modules implement specific algorithms that respectively construct requests for CBIR, queries on common names and queries on occurrence records.

3.5 Module Invocation

Figure 3 shows the invocation of modules (and data flow) within Sinimbu. It shows users can enter images and four types of textual parameters (Taxon, name of person Responsible for a field trip, Collection Site and Common name). These textual parameters were indicated by our biology partners as being the most relevant for their present needs.

The first three parameters are forwarded to the Collection Retrieval Module, where they are processed by functions that construct and invoke SQL commands. SQL queries retrieve the *id_taxa* values of occurrence records whose attributes are substrings of the corresponding textual input parameters. The value of the Taxon parameter will be checked against all taxonomic levels of an occurrence record. For instance, a query with “Taxon = Bufo” will look for records in which the ”Bufo” substring appears as part of attributes Order, Family etc – and thus all species of family=“Bufonidae” will be selected.

Common names are processed by the Common Names Retrieval module. It implements queries on the ontology, and returns a list of Taxon strings. The Content Retrieval module invokes CBIR functions that return a list of identifiers of images similar to the input image, ranked by similarity. Taxons and image identifiers are then directed to the Collection Retrieval module, producing as result a list of *id_taxa* values that correspond to that taxon or that image.

At this point, there are several lists of *id_taxa* values, one for each input parameter. These lists are forwarded to the Integrated Search Module, which will combine these lists using weights defined by the user profile, generating a

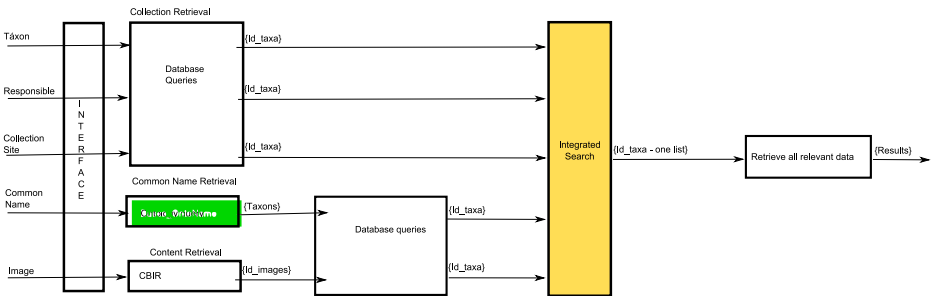


Fig. 3. Module execution flow

single list of *id_taxa* values, ranked by weight. This final list is then processed, returning all available information on the corresponding species, according to user profiles.

3.6 Content-Based Image Retrieval Module

CBIR processing in Sinimbu uses the GP Framework developed by us,

being based on genetic programming principles. Genetic programming (GP) is a machine learning technique which tries to solve problems based on biology evolutive principles. The basic structure in GP is the individual, which represents a possible solution for a given problem. The individuals are programs that during the evolutive process undergo successive recombinations and disturbances and are refined. At the end, better solutions for the identified problems are found. Genetic programming can be understood as a search in the space of all possible solutions for the individuals which best solve the problem.

The GP Framework is a CBIR infrastructure that combines an arbitrary number of descriptors $\langle f, d \rangle$ to perform CBIR in an image base, combining distances from these descriptors using functions that were previously found to be adequate to discriminate amongst them. To find the best individuals, the framework requires a set of categorized images for training. In our case, the GP Framework was used as follows. First, it preprocessed all images in the image repository using three color descriptors (JAC [20], BIC [16], ACC [13]) and two descriptors that encode texture (LAS [18] and QCCH [12]). Next, it constructed a global distance function D using genetic programming. The training set was a subset of the image repository. The GP individuals were functions that combined the distances among the images, for each descriptor – i.e., the new distance function D is a combination of the distances computed by the five descriptors used. This function is used to compare input (query parameter) images to the images in the repository. Figure 4 shows an example of GP individual as a function to combine descriptors from two images I_j and I_k . This individual corresponds to

the function $f(d_{1I_j I_k}, d_{2I_j I_k}, d_{3I_j I_k}) = \frac{d_{1I_j I_k} - d_{3I_j I_k}}{d_{2I_j I_k}} + \sqrt{d_{2I_j I_k} * d_{3I_j I_k}}$.

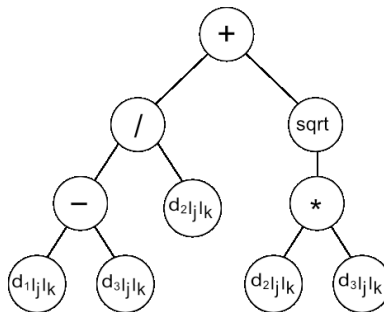


Fig. 4. Example of GP individual

When a new image is entered as a query parameter, it is processed against all descriptors, extracting its feature vectors under the different descriptor algorithms. Next, its distance to all other images is computed using function D . The result of this comparison is forwarded to the Content Retrieval module, which creates the list of image identifiers ranked according to the similarity with the input image.

3.7 Ontology Management Modules

The Common Name Retrieval module builds SPARQL queries to process common name requests on the ontology. The Taxonomy Extractor constructs the ontology from data stored in the (*taxonomy*) table (i.e., it is not an exhaustive list of species names, but just those of animals recorded in the database). This occurs every time the database is updated with new species names, upon user request. Common names are next linked to it, using OWL `EquivalentClass` relationships. Building the initial ontology with the common names was a very time-consuming task. Sinimbu common names are in Portuguese, and there is no authoritative source for such correspondences, so that most common names had to be inserted manually (less than 1% of the common names were available from the occurrence records).

4 Implementation

4.1 Data Sets and Technological Issues

The main data source for Sinimbu are records of the University's Zoology museum, one of the largest physical zoological collections in Brazil. It houses 17 scientific collections – both terrestrial and aquatic animals – with approximately 500 thousand animals (of which roughly 400 thousand invertebrates). Primary data sources to create the occurrence records include field notes, field tags, and notes taken during a field trip. Additional data sources include photos, annotations made by curators, and information on the environment. Data are still being catalogued into the database – at present, there are approximately 60 thousand curated records, plus 1200 curated animal photos, which were used in testing Sinimbu. Though this is not a large image base, its richness lies in its variety of animal species, and on the painstaking curation process each image undergoes to ensure retrieval reliability. The ontology covers 5 thousand species, being generated from the collection repository using the Taxonomy Extraction module. Over 200 common names were inserted, using some sites and documents on Brazilian species.

Occurrence data are stored in the PostgreSQL database system, with the PostGIS extension for geographic processing. This is the database management system chosen for BioCORE, thus allowing integration with the entire system. The ontology was defined in OWL (the standard), and common names were added using the Protégé ontology tool – one of the most widely used ontology

management tools. Images are stored in .jpg format, due to its compactness and ease of display; descriptors are stored in binary format, being generated by the GP Framework.

Sinimbu’s multimodal search modules were developed in JAVA, again for compatibility with BioCORE. The Content Retrieval module uses JNA (Java Native Access) to process feature vectors and distance functions (themselves implemented in C by the GP Framework). Access to the PostgreSQL database uses JDBC (Java Database Connectivity). The ontology is processed using the JENA ontology framework, which facilitates access to the corresponding structure.

4.2 User Session - Example

Suppose that a user wants to retrieve data on species that were collected at a place called “Jaboticatubas”, as shown in Figure 5.

There are 1379 records in the database satisfying this criterion. Figure 6 shows the first three results, corresponding to a hummingbird and two bats. Only one photo is displayed – the first record does not have any photos associated, and the third has photos, but they cannot be shown to non-authorized users. Images in the image repository can be private or public, and only the latter can be displayed as part of a non-expert query result. However, all images are used in CBIR processing.


Taxon	<input type="text"/>	Input Image 
Responsible	<input type="text"/>	
Collection Site	<input type="text" value="Jaboticatubas"/>	
Common Name	<input type="text"/>	
<input type="button" value="Search"/>		

Fig. 5. First query - Animals collected in a given location - “Site=Jaboticatubas”

Refining this search, now the user wants records associated with “Jaboticatubas” and common name “Sapo” (frog) - this query retrieves 1086 records, the first three being shown in Figure 7, now restricted to frogs only. Notice that now the first two records have public images associated.

Suppose that, finally, in this query sequence, the user also includes a query image of a frog – see final query on figure 8. The first three records appear in figure 9, showing that the query image is more similar to that of “Proceratus Cururu”. Notice that in this case the first two records of the second query (Figure 7) are inverted, and Proceratus Cururu appears in the first place, since it is more similar to the input image than the second record.

In this sequence of queries, we point out that the result is progressively refined, thereby filtering the number of records to be used in subsequent modeling




	<p>Common Names: ave, beija-flor</p> <p>Scientific Name: <i>Thalaurania furcata</i></p> <p>Collection Sites: Jaboticatubas</p> <p>More Collection Data</p>
	<p>Common Names: morcego</p> <p>Scientific Name: <i>Lonchophylla bokermanni</i></p> <p>Collection Sites: Jaboticatubas</p> <p>More Pictures More Collection Data</p>
	<p>Common Names: morcego</p> <p>Scientific Name: <i>Phyllostomus hastatus</i></p> <p>Collection Sites: Jaboticatubas</p> <p>More Collection Data</p>

Fig. 6. Partial result of the first query - “Site=Jaboticatubas”

and simulation computations. Both the second and the third queries return the same amount of records – 1086. However, the order is different (because of image similarity), and for most purposes only the topmost records need to be considered by the experts that are conducting this research. The use of images in preprocessing data, combined with textual parameters, provide results that are closer to what experts require in order to conduct their studies – images alone, or text alone are not as effective in filtering.

Once the experts determine the most relevant records from the final result, then they can proceed, if desired, to subsequent steps in checking models of habitat conditions, or interactions among species of interest.

5 Related Work

Most modern biodiversity information systems now provide Web interfaces, and vary greatly in range of functions supported, geographic regions covered, species groups and goals. Nevertheless, as said in the introduction, they concentrate in supporting access to occurrence data and correlating it to environmental variables. They vary from actual information systems (i.e., having a large set of analysis tools, and distinct kinds of results, such as graphs, tables, maps, charts) to portals from which scientists can download records of interest. GBIF [10] is perhaps the ultimate example of a portal, making millions of occurrence records available, mediating the access to thousands of provider sites.

Multimodality is being increasingly used to improve image retrieval systems – e.g., [4,12,15,17]. In such papers, authors show that a combination of textual and image parameters improves precision and recall of results, as opposed to




	<p>Common Names: sapo, rã, rã diurna Scientific Name: <i>Hylodes otavioi</i> Collection Sites: Jaboticatubas</p>
More Pictures	More Collection Data
<hr/>	
	<p>Common Names: sapo, sapo-cururu Scientific Name: <i>Proceratophrys cururu</i> Collection Sites: Jaboticatubas</p>
More Pictures	More Collection Data
<hr/>	
	<p>Common Names: sapo Scientific Name: <i>Scinax curucica</i> Collection Sites: Jaboticatubas</p>
	More Collection Data
<hr/>	

Fig. 7. Partial result - second query - “Site=Jaboticatubas and Common name=sapo”


<p>Taxon <input type="text"/></p> <p>Responsible <input type="text"/></p> <p>Collection Site <input type="text" value="Jaboticatubas"/></p>	<p>Searched Image</p> 
<p>Common Name <input type="text" value="Sapo"/></p>	
<p><input type="button" value="Search"/></p>	

Fig. 8. Third query - Providing input to Site, Common name and image parameters

strictly textual or strictly content-based queries. For instance, the work of At-nafu [4] presents a new data model for images in which retrieval is based on combining descriptors and metadata. Query parameters support combination of image content, and contextual and semantic information. A similar solution is presented by Addis [1], for images in art galleries. Here, users can either pose queries or navigate interactively among concepts. Multimodal queries can also be processed on videos – e.g., the work of Ammir [2], in which relevance feedback is adopted to improve the results, or on music – e.g. the work of Zhang [21].

Most multimodal systems, however, are not directed towards biology-related data. One of the main problems of such data, when images are involved, is the kind of image available (for instance, when a photo is taken in a natural environment, animals are often partially hidden, and moreover identifying characteristics are seldom available). Thus, most such systems concern images produced in closed environments or laboratories. For instance, C-DEM [11] mines genetic




	<p>Common Names: <code>sapo, sapo-cururu</code></p> <p>Scientific Name: <code>Proceratophrys cururu</code></p> <p>Collection Sites: <code>Jaboticatubas</code></p>
More Pictures	More Collection Data
	<p>Common Names: <code>sapo, rã, rã diurna</code></p> <p>Scientific Name: <code>Hylodes otavioi</code></p> <p>Collection Sites: <code>Jaboticatubas</code></p>
More Pictures	More Collection Data
	<p>Common Names: <code>sapo</code></p> <p>Scientific Name: <code>Scinax curticica</code></p> <p>Collection Sites: <code>Jaboticatubas</code></p>
	More Collection Data

Fig. 9. Partial result of 3rd query - Site, image and common name parameters

data from fruit flies, in what they name “image bioinformatics”. Query parameters combine data from genes (expressed as strings of characters), images of gene expressions and keywords that annotate the images. Users can request images that are similar to a given image, and/or related to the keywords provided, and/or to specific genes.

Arpah’s multimodal system [3] is also geared towards management of biological data, using images from flatworms. Queries combine taxonomic information on species, stored in an ontology, and image annotations. Over 900 images were annotated, discriminating among species’ morphological characteristics. Queries can either access the annotations themselves, or the ontologies, using SPARQL. Here, there is no image processing, but the multimodality refers to a combination of queries on ontologies and text.

Since queries in Sinimbu combine textual, ontological and image information, for biological data, it can be considered closest to C-DEM in modalities and nature. The parameters and goals are, however, very different (since the latter concentrates on genetic information). Moreover, C-DEM images are homogeneous, whereas Sinimbu’s repository is very heterogeneous, contemplating all kinds of animals (e.g., vertebrates and invertebrates) and photos taken in controlled (museum) and non-controlled (field trips) environments. Hence, no single descriptor is suitable – and thus we use a combination thereof.

6 Conclusions and Ongoing Work

There are many challenges in managing and querying data on species’ observations, ranging from the heterogeneity of the observations to the kinds of user that want to access these data. This hampers effective computational modeling

and simulation in biodiversity studies. Multimodal query systems increase the flexibility in handling these data, thereby allowing users to better specify their needs and interact with query results. This paper presented the Sinimbu multimodal query framework, in which query predicates combine text and image content, and are processed by a combination of database queries, ontology manipulation and CBIR. Though Sinimbu was validated only on zoological data, its implementation and architecture are general, so that there is no constraint in adding, e.g., botanical data. This would of course require extending the ontology and new tests on the GP Framework to identify a more adequate descriptor combination. Sinimbu has been validated with distinct kinds of user profiles, showing that it can help both experts and non-experts in querying occurrence records.

Visual (image) identification of animal species varies widely – e.g., some can be recognized by shape, others by color, and so on. Sinimbu tried to overcome this limitation by using multiple descriptors, and combining them using genetic programming. This is also a novelty in terms of systems that support queries on images of biological collections, which favor a single descriptor.

To the best of our knowledge, Sinimbu is the only framework that allows multimodal search on collection data, for biodiversity purposes, combining queries on images, text, and ontologies, and for distinct user profiles. Ongoing work includes, among others, enhancing the base of (Brazilian) common names, via Web mining of specific sites, which presents the challenge of homegeneizing such names and finding out the corresponding scientific names. Another direction is increasing customization possibilities based on user contexts.

Acknowledgements. The research described in this paper was partially funded by Brazilian agencies CNPq, FAPESP and CAPES, and by the INCT in Web Science.

References

1. Addis, M.J., Boniface, M.J., Goodall, S., Grimwood, P., Kim, S.H., Lewis, P., Martinez, K., Stevenson, A.: SCULPTEUR: Towards a New Paradigm for Multimedia Museum Information Handling. In: Fensel, D., Sycara, K., Mylopoulos, J. (eds.) ISWC 2003. LNCS, vol. 2870, pp. 582–596. Springer, Heidelberg (2003)
2. Amir, A., Berg, M., Permuter, H.: Mutual relevance feedback for multimodal query formulation in video retrieval. In: MIR 2005: Proc. of the 7th ACM SIGMM International Workshop on Multimedia Information Retrieval, pp. 17–24 (2005)
3. Arpah, A., Alfred, S., Lim, L.H.S., Sarinder, K.K.S.: Monogeneous image data mining using Taxonomy ontology. In: Int. Conf. on Networking and Information Technology (ICNIT), pp. 478–481 (2010)
4. Atnafu, S., Chbeir, R., Brunie, L.: Efficient content-based and metadata retrieval in image database. *Journal of Universal Computer Science* 8(6), 613–622 (2002)
5. Cullot, N., Parent, C., Spaccapietra, S., Vangenot, C.: Ontologies: A contribution to the DL/DB debate. In: Proc. of the 1st International Workshop on the Semantic Web and Databases, 29th VLDB Conf., pp. 109–129 (2003)

6. Torres, R.d.S., Falcão, A.X., Gonçalves, M.A., Papa, J.P., Zhang, B., Fan, W., Fox, E.A.: A genetic programming framework for content-based image retrieval. *Pattern Recognition* 42(2), 283–292 (2009)
7. Torres, R.d.S., Medeiros, C.B., Gonçalves, M.A., Fox, E.A.: A Digital Library Framework for Biodiversity Information Systems. *International Journal on Digital Libraries* 6(1), 3–17 (2006)
8. Daltio, J., Medeiros, C.B.: Aondê: An Ontology Web Service for Interoperability across Biodiversity Applications. *Information Systems* 33, 724–753 (2008)
9. Daltio, J., Medeiros, C.B., Gomes Jr, L.C., Lewinsohn, T.: A Framework to Process Complex Biodiversity Queries. In: *Proc. ACM Symposium on Applied Computing (ACM SAC)* (March 2008)
10. GBIF. Global Biodiversity Information Facility Portal (2011), <http://data.gbif.org/welcome.htm> (accessed June 2011)
11. Guo, F., Li, L., Faloutsos, C., Xing, E.P.: C-dem: a multi-modal query system for drosophila embryo databases. In: *Proc. VLDB Conference*, vol. 1(2), pp. 1508–1511 (2008)
12. Huang, C.-B., Liu, Q.: An Orientation Independent Texture Descriptor for Image Retrieval. In: *Int. Conf. on Communications, Circuits and Systems, ICCAS*, pp. 772–776 (2007)
13. Huang, J., Kumar, S.R., Mitra, M., Zhu, W.-J., Zabih, R.: Image Indexing Using Color Correlograms. In: *IEEE Conf. Computer Vision and Pattern Recognition*, p. 762 (1997)
14. ICMI. International Conference on Multimodal Interaction (2011), <http://www.acm.org/icmi/2011/>
15. Song, H., Li, X., Wang, P.: Multimodal image retrieval based on annotation keywords and visual content. In: *Proc. Int. Conf. on Control, Automation and Systems Engineering*, pp. 295–298 (2009)
16. Stehling, R.O., Nascimento, M.A., Falcão, A.X.: A compact and efficient image retrieval approach based on border/interior pixel classification. In: *Proc. 11th International Conf. on Information and Knowledge Management, CIKM 2002*, pp. 102–109 (2002)
17. Su, J.-H., Wang, B.-W., Hsu, T.-Y., Chou, C.-L., Tseng, V.S.: Multi-modal image retrieval by integrating web image annotation, concept matching and fuzzy ranking techniques. *International Journal of Fuzzy Systems* 12(2), 136–149 (2010)
18. Tao, B., Dickinson, B.W.: Texture recognition and image retrieval using gradient indexing. *Journal of Visual Communication and Image Representation* 11(3), 327–342 (2000)
19. Vilar, B., Malaverri, J., Medeiros, C.B.: A Tool based on Web Services to Query Biodiversity Information. In: *5th International Conference on Web Information Systems and Technologies - WEBIST*, pp. 305–310 (2009)
20. Williams, A., Yoon, P.: Content-based image retrieval using joint correlograms. *Multimedia Tools and Applications* 34, 239–248 (2007)
21. Zhang, B., Xiang, Q., Wang, Y., Shen, J.: CompositeMap: a novel music similarity measure for personalized multimodal music search. In: *Proc. of the 17th ACM International Conference on Multimedia, MM 2009*, pp. 973–974 (2009)

Comparison between Genetic Algorithms and Differential Evolution for Solving the History Matching Problem

Elisa P. dos Santos Amorim¹, Carolina R. Xavier^{2,3},
Ricardo Silva Campos⁴, and Rodrigo W. dos Santos⁴

¹ Dept. of Computer Science, University of Calgary

² Departamento de Ciência da Computação - UFSJ

³ COPPE - UFRJ

⁴ Programa de Pós Graduação em Modelagem Computacional - UFJF
epdamori@ucalgary.ca

Abstract. This work presents a performance comparison between Differential Evolution (DE) and Genetic Algorithms (GA), for the automatic history matching problem of reservoir simulations. The history matching process is an inverse problem that searches a set of parameters that minimizes the difference between the model performance and the historical performance of the field. This model validation process is essential and gives credibility to the predictions of the reservoir model. Four case studies were analyzed each of them differing on the number of parameters to be estimated: 2, 4, 9 and 16. Several tests are performed and the preliminary results are presented and discussed.

1 Introduction

Oil is one of the most important sources of energy in the world today. It is usually located inside porous rocks, called reservoirs, hundreds of meters bellow the surface. Its extraction is a very complex and costly process that involves a great amount of decisions that need to be as precise as possible in order to better explore the reservoir potential. Reservoir engineers are directly involved in this process of making decisions and they often rely on reservoir simulators to do so. Reservoir simulators are computational tools based on mathematical models that describe the fluid flow inside the reservoir rock. They are used to predict reservoir behavior under different oil exploration scenarios allowing engineers to test a variety of strategies before deciding which should be applied on the real field. The simulator models are highly dependent on parameters that describe the physical properties of reservoirs, such as permeability and porosity, and the reliability of predictions depends on good estimations for such properties. Unfortunately, it is not possible to perform a direct measurement of these properties for all reservoir extensions. Direct measurements are only provided on well locations which are usually hundreds of meters apart from each other.

An alternative for model validation is the estimation of the relevant properties by History Matching (HM) [1]. A log with information regarding production data, such as oil rate and bottomhole pressure measured on wells, is kept for reservoirs that have been in operation for some time. This log is often called *history* of the reservoir. History Matching process is an inverse problem that utilizes reservoir simulation to find a set of parameters that minimizes the difference between the simulated performance and the history data of the field. The problem is modeled as a minimization problem and there are different approaches for solving it.

Traditional Newton-like methods have been used before in [2]. Other work, based on singular value decomposition (SVD) was shown in [3]. In addition, free-derivative methods based on Genetic Algorithms were proposed in [4] and were compared to derivative methods in [5]. This work presents a performance comparison between Genetic Algorithms (GA) and Differential Evolution (DE) for solving the history matching inverse problem. Both algorithms belong to the class of Evolutionary Algorithms, which are population-based optimization techniques. More details about each method will be provided in Section 4.

This work is organized as follows: Section 2 introduces the direct problem formulation. Section 3 introduces the history matching theory. Section 4 presents the theory behind Evolutionary Algorithms and details concerning GA and DE. Section 5 presents the numerical experiments performed in this work. Section 6 presents results and Section 7 presents the conclusion of this work.

2 Reservoir Simulator: The Forward Problem

The problem treated in this paper is a two dimensional two-phase (water/oil) immiscible and compressible porous media flow in an environment with gravity. The system of partial differential equations which governs this flow is derived from the *law of mass conservation* and the *Darcy Law*. The law of mass conservation for both phases is written as

$$\phi \partial_t (\rho_\alpha s_\alpha) + \nabla \cdot (\rho_\alpha v_\alpha) = Q_\alpha, \quad (1)$$

where $\alpha = w$ denotes the water phase, $\alpha = o$ denotes the oil phase, ϕ is the porosity of the porous medium, and ρ_α , s_α , v_α and Q_α are, respectively, the density, saturation, volumetric velocity and flow rate in wells of the α -phase. The volumetric velocity (v_α) is given by the Darcy law and can be written as:

$$v_\alpha = \frac{K k_{r\alpha}(s_\alpha)}{\mu_\alpha} (\nabla p_\alpha - \rho_\alpha g \hat{D}), \quad (2)$$

where K is the effective permeability of the porous medium, $k_{r\alpha}$ is the relative permeability of α -phase, which is a function that depends on saturation, μ_α and p_α are, respectively, viscosity and pressure of the α -phase, g is the gravity acceleration and $\hat{D} = (0, 0, -1)$. We also have that

$$s_w + s_o = 1. \quad (3)$$

We introduce the phase mobility and transmissibility functions, respectively:

$$\lambda_\alpha(s) = \frac{k_{r\alpha}(s)}{\mu_\alpha}, \quad (4)$$

$$T_\alpha(s) = K\lambda_\alpha, \quad (5)$$

where $s = s_w$ from now on. The volumetric velocity can then be written as $v_\alpha = -T_\alpha \nabla p_\alpha$.

The capillary pressure is modeled by

$$p_w = p_o - cp(s_w). \quad (6)$$

Since the saturation and pressure of one phase is determined by the value of the same unknowns of the other phase, the problem will be solved with regard to water saturation (s_w) and oil pressure (p_o).

We assume that the density of the phases and the porosity of the reservoir rock are dependent on the oil pressure. Finally, we consider no flow boundary condition, $v_\alpha \cdot \nu = 0$, $x \in \partial\Omega$, where ν is the outer unit normal to the boundary $\partial\Omega$ of the domain Ω , and the initial condition is given by $s(x, 0) = s_0(x)$, $x \in \Omega$.

The final system of partial differential equations used in this work to model the fluid flow on porous media is given by

$$\begin{cases} \partial_t \phi \rho_\alpha s_\alpha + \nabla \cdot (\rho_\alpha v_\alpha) = q_\alpha \rho_\alpha, \\ v_\alpha = -T_\alpha(s_w)(\nabla p_\alpha - \rho_\alpha g \hat{D}), \\ s_o + s_w = 1, \\ p_w = p_o - p_c(s_w), \\ \phi = \phi(p_o), \\ \rho_l = \rho_l(p_o), \\ v_\alpha \cdot \nu = 0, x \in \partial\Omega, \\ s(x, 0) = s_0(x), x \in \Omega. \end{cases} \quad (7)$$

There are different numerical methods that can be used to solve system (7). The simulator used in this work implements a fully implicit method.

3 History Matching

History matching is a well known inverse problem in the oil industry [6]. In the forward problem, the physical properties of the reservoir are known and a simulator is used to calculate the production behavior of the reservoir. In the inverse problem (history matching), the goal is to estimate plausible reservoir physical properties, given the observed production data of a real reservoir. The forward and inverse problem schemes can be exemplified by Figure 1.

Since physical properties of the reservoir cannot be directly measured in all extensions of the reservoir, the history matching process is used to estimate such

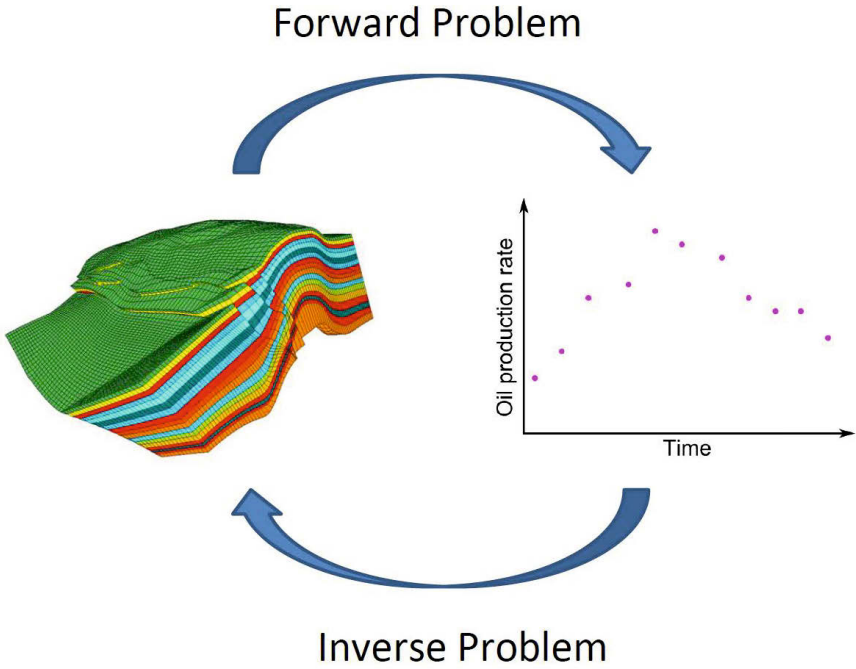


Fig. 1. History Matching: an inverse problem

properties. The estimated properties are used as the simulator’s parameters with the goal of predicting the reservoir behavior under different production scenarios.

In this work, the inverse problem proposed aims to estimate the absolute permeability field of a reservoir by history-matching its production data, which is given by the oil rate and bottom-hole pressure measure at well locations from time to time. We denote by K the vector of permeability to be determined, by $S(K)$ the vector of simulated data given the parameter K and by \bar{O} the vector of observed data. The problem consists on searching K that minimizes the least square formulation

$$f(K) = \|S(K) - O\|^2. \tag{8}$$

The problem to solve is then formulated as a minimization problem

$$\min_K f(K). \tag{9}$$

In the context of Evolutionary Algorithms, $f(K)$ is called *fitness function* on dealing with Evolutionary optimization algorithms. Its importance will be elucidated in the following sections. In this work we transform the fitness function in a relative error measurement, as follows

$$f(K) = \frac{\|S_o(K) - O_o\|^2}{\|O_o\|^2} + \frac{\|S_p(K) - O_p\|^2}{\|O_p\|^2}, \quad (10)$$

where subscripts o and p denote oil rate and bottom-hole pressure observations, respectively.

The following sections will introduce EAs and, more specifically, Genetic Algorithms and Differential Evolution, the methods used in this work to solve the minimization problem (9).

4 Evolutionary Algorithms

Evolutionary Algorithms (EA) are stochastic optimization methods inspired on Darwin's Evolution Theory and Natural Selection [7]. There are many different variants of EAs and the common underlying idea behind all these techniques is the same: given a population of individuals, the environmental pressure causes natural selection (survival of the fittest), which causes a rise in the fitness of the population. Given a quality function to be maximized, we can randomly create a set of candidate solutions, i.e., elements of the function's domain, and apply the quality function as an abstract fitness measure - the higher the better. Based on this fitness, some of the better candidates are chosen to seed the next generation by applying recombination and/or mutation to them. Recombination is an operator applied to two or more selected candidates (the so-called parents) and results one or more new candidates (the offspring). This process can be iterated until a candidate with sufficient quality (a solution) is found or a previously set computational limit is reached [8]. This process is exemplified by the pseudo-code [9].

Algorithm 1. EA pseudocode

```

Initialize population;
Evaluate individuals;
while stop criteria not met do
    Select individuals;
    Recombine individuals;
    Mutate individuals;
    Evaluate individuals;
end while

```

Selection, recombination and mutation are the three basic operators that steer EAs and the way they are implemented is what usually differ the variants of EAs techniques. The following sections will present a more detailed discussion about these operators on GA and DE.

4.1 Genetic Algorithms

Genetic algorithm was initially introduced by Holland as a means of studying adaptive behaviors [9]. However they have largely been considered as optimization methods since then. GAs follow the EA scheme presented previously. Traditionally, individuals are represented using a bit string, what requires a function to map each string to the parameter set to be optimized. However, since GA's invention, different approaches have been proposed to represent the individuals. The approach applied in this work is a floating point representation. It is an alternative representation in optimization problems with real-valued continuous variables, as is the case in this work. With this representation, there is no need for an explicit encoding mechanism. Each member of each population in the genetic algorithm is a floating-point vector. The genetic operators (mutation and crossover) in this case do not handle bit strings and are defined in a different manner.

Different ways of performing selection, mutation and recombination have also been proposed so far. The following sections will describe the operators used in this work.

Roulette Wheel Selection. In the roulette wheel selection approach an individual of the current population has a probability of being selected that is proportional to its fitness value. Thus, a more fitted individual is more likely to be selected, but a bad individual still has its chance, what is important to prevent the algorithm to quickly converge to local minima.

The probability of selecting a particular individual i in a maximization problem is given by

$$p_i = \frac{f_i}{\sum_{j=1}^{N_{pop}} f_j}, \quad (11)$$

where f_α is the fitness of individual α and N_{pop} is the size of the population. When dealing with minimization problems, which is the case of this work, instead of using f_j we use $\frac{1}{f_j}$.

This selection process can be compared as spinning a roulette wheel where its sectors are set equal to the probability of each individual. Figure 2 shows an example of this selection using 5 individuals.

In this work we used $\alpha = 0.36$.

Blend Crossover. The Blend-crossover (BLX- α) [10] generates two offspring from two individuals (parents). It randomly picks values that lie between two points that contain the two parents, but may extend equally on either side determined by a user specified parameter α , as shown on Figure 3.

Algorithm 2 presents a pseudo-code of the Blend-crossover.

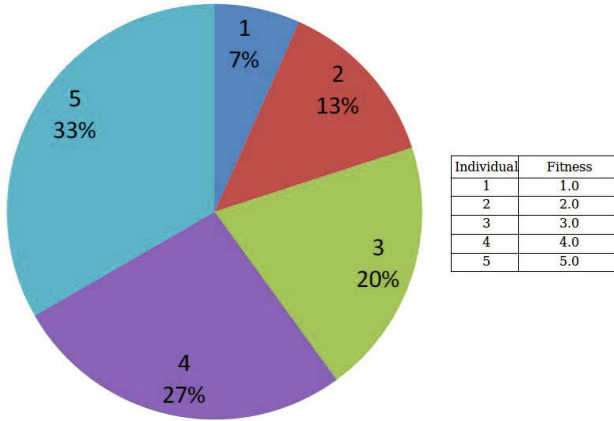


Fig. 2. Roulette wheel selection example

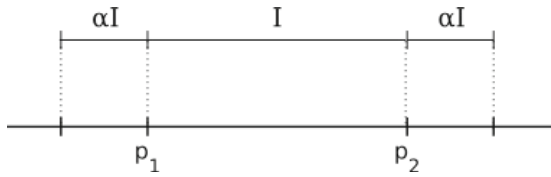


Fig. 3. Blend-crossover space. (p_1 and p_2 are the two parents)

Algorithm 2. Blend-crossover

Input: parents p_1 and p_2
 Output: offspring o^1 and o^2
for each parameter i **do**
 $d_i = \|p_i^1 - p_i^2\|$
 $X_i^1 = \min(p_i^1, p_i^2) - \alpha d_i$
 $X_i^2 = \max(p_i^1, p_i^2) + \alpha d_i$
 $o_i^1 = \text{rand}(X_i^1, X_i^2)$
 $o_i^2 = \text{rand}(X_i^1, X_i^2)$
end for

Mutation. The mutation used in this work consists on perturbing a parameter p_i of an individual in the following way

$$p_i = (1 + a) * p_i, \tag{12}$$

where $a = \text{rand}(-0.5, 0.5)$.

Elitism. When only offspring vectors are allowed to advance, there is no guarantee that the best-so-far solution will not be lost. Retaining the best-so-far solution is known as *elitism* and it plays an important role on the successful convergence of the algorithm. In this strategy, the best individual(s) of the previous generation is kept in the next generation if none of the offspring is better than it. In this work this strategy is applied and the number of best individuals kept is a parameter of the algorithm.

4.2 Differential Evolution

Differential Evolution (DE) was first introduced by Price and Storn [11] as a new EA technique. Since its invention it has been applied to numerous optimization problems and has presented very satisfactory results. Like nearly all EAs, DE is a population-based optimizer that begins with a randomly chosen initial population, whose parameters lie within preset parameter bounds. The operates through the same computational steps as employed by standard EAs presented previously. However, unlike traditional EAs, DE employs difference of the parameter vectors to explore the objective function landscape. This characteristic appears on the *mutation* operator.

The next sections will be devoted to explaining how mutation, recombination and selection are defined on DE.

Mutation: the Heart of DE. DE mutates and recombines the population to produce a population of N_p mutant vectors. In particular, *differential mutation* adds a scaled, randomly sampled, vector difference to a third vector. Equation (13) shows how to combine three different, randomly chosen vectors to create a mutant vector, v_i

$$v_i = x_{r0} + F \cdot (x_{r1} - x_{r2}). \quad (13)$$

The scale factor $F \in (0, 1^+)$, is a positive real number that controls the rate at which the population evolves. Where there is no upper limit on F , effective values are usually smaller than 1.0.

The base vector in $r0$ can be determined in a variety of ways, but in this work it was chosen randomly, with $r0 \neq i$. Except for being distinct from each other and from both i and $r0$, the difference vector indices $r1$ and $r2$ are also randomly selected [12].

Figure 4 illustrates the differential mutation in a 2D space.

Recombination. To complement the differential mutation, DE also employs *uniform crossover/recombination*, which builds trial vectors out of parameter values that have been copied from two different vectors. In particular, DE crosses each vector of the current population with a mutant vector as follows

$$u_i = \begin{cases} v_{i,j}, & \text{if } (\text{rand}_j(0, 1) \leq C_r) \\ x_{i,j}, & \text{otherwise,} \end{cases} \quad (14)$$

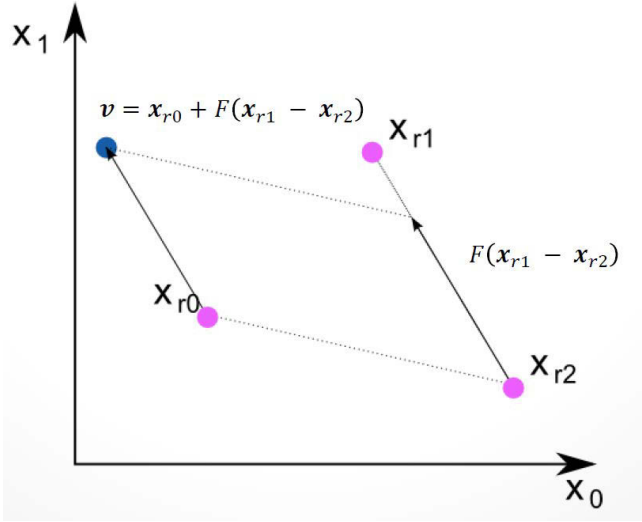


Fig. 4. Differential Mutation

that is, a new individual will be a mixture between parameters on the mutant vector and on the current population vector. The crossover probability $C_r \in [0, 1]$, is a user defined value that controls the fraction of parameter values that are copied from the mutant.

Selection. If the trial vector u_i has an equal or lower objective function value (for minimization problems) than that of its target vector x_i , it replaces the target vector in the next generation; otherwise, the target retains its place on the population for at least one more generation, as presented on Eq. (15).

$$x_{i,g+1} = \begin{cases} u_{i,g}, & \text{if } (f(u_{i,g}) \leq f(x_{i,g})) \\ x_{i,g}, & \text{otherwise.} \end{cases} \tag{15}$$

5 Numerical Experiments

The reservoir simulation we consider in this work is the classical five-spot configuration with 4 producer wells in the corners of the reservoir and one injection well in its center (see Figure 5). The reservoir is a square of sizes equal to 200m and 20m of depth. Each producer well produces a total of 100m³ per day. The reservoir’s history is given by the oil production rate and bottom-hole pressure measured on the producer wells and on all wells, respectively, on 300 days of simulation. The other parameters of the model are: porosity (0.2), relative permeability, given by the Corey curve, irreducible water saturation ($s_{iw} = 0.2$) and residual oil saturation ($s_{ro} = 0.2$). The spatial discretization used was $\Delta x = \Delta y = 7.7m$.

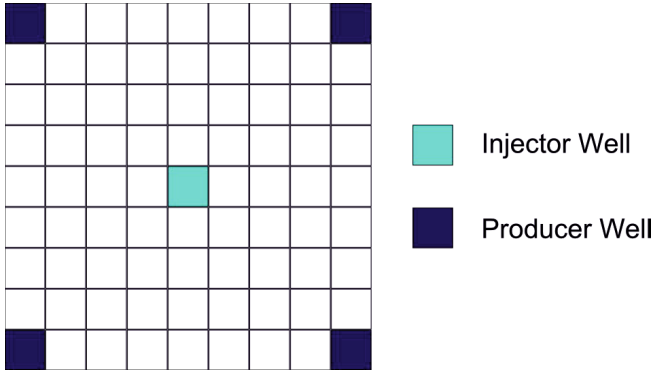


Fig. 5. 5-spot configuration

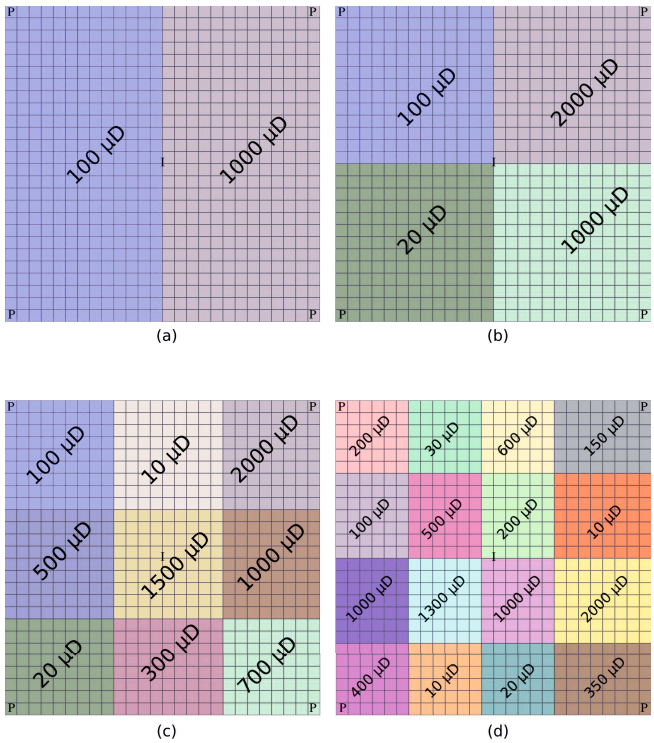


Fig. 6. Permeability field that generated 4 different histories. (a) 2 parameters, (b) 4 parameters, (c) 9 parameters and (d) 16 parameters.

The history data was produced synthetically using the simulator model described in Section 2. Four different synthetic histories were generated differing on the number of different permeability regions on the reservoir. The number of

these regions are 2, 4, 9 and 16 and the configuration of each model is shown on Figure 6.

For each case both GA and DE were applied. The algorithms have some parameters to be tuned. Parameters in common for both GA and DE are *population size* and *crossover rate* which were set to 30 and 0.90, respectively. Exclusive GA parameters are *mutation rate* and *elitism size*, set to 0.10 and 5 respectively. Parameter F of DE was set to 0.5. Initial populations were generated for each synthetic problem and the algorithms started from the same initial population. Stopping criteria are the maximum number of generations, 100, and the minimum fitness value, $1.e-6$, whichever comes first.

6 Results

This section presents the results of the experiments described on Section 5. Figure 7 shows the fitness evolution for 2, 4, 9 and 16 parameters optimization problems. Both algorithms were executed 4 times for each experiment, and the best fitness in each generation of every execution is displayed on the graphs. Table 1 presents the best found fitness for each example.

Table 1. Best fitness after 100 generations

Method \ # parameters	2	4	9	16
GA	9.05e-5	2.41e-2	3.43e-2	1.77e-1
DE	0.0	4.26e-7	1.37e-3	6.35e-2

We can observe that DE outperformed GA in every experiment presented in this work. In the problem of estimating 2 parameters, DE achieved a perfect matching (fitness = 0.0) before the 60th generation for every experiment, while the best run of GA got a fitness of $9.05e - 5$. The superiority of DE was also obvious in the problem with 4 parameters, where the best individual of DE was more than 5×10^4 better than the best solution found by GA. Although this advantage was not that prominent on the cases with 9 and 16 parameters, DE still achieved better results than GA.

Despite the unquestionable superiority of DE, it is interesting to notice by Figure 7 that GA was more efficient in the early iterations than DE, that is, GA converged faster to a better solution in the beginning of the optimization process. However, once close to the region of a good solution, GA was not successful in refining this possible solution. On the other hand, DE was more consistent and would continue to refine the solution even when it was very close to the optimum.

Tables 2, 3, 4 and 5 present the best parameter set found by GA and DE. TP means *target parameters*, that is, the parameters used to generate the history and, consequently, the optimum known set of parameters.

The relative error between the target parameter vector and the parameters found by the algorithms is presented in Table 6.

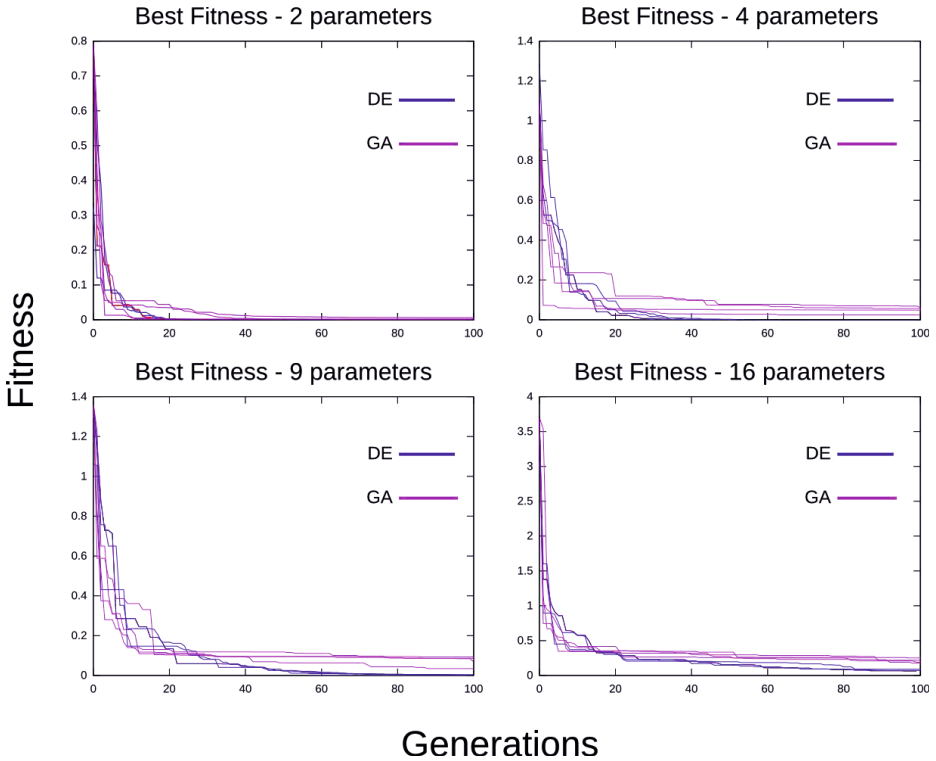


Fig. 7. Best fitness evolution throughout the generations. 4 runs of both GA and DE are shown for each case.

Table 2. 2 Parameters

TP	100	1000
GA	99.9922	999.7467
DE	99.9999	999.9997

Table 3. 4 Parameters

TP	100	20	1000	2000
GA	98.8882	20.0627	1289.6820	2368.3789
DE	100.0000	19.9999	1000.0007	2000.0050

Table 4. 9 Parameters

TP	100	500	20	10	1500	300	2000	1000	700
GA	100.2492	366.4448	20.0922	12.4617	1710.3032	455.0980	2980.9579	1213.4672	1203.6730
DE	99.93170	520.9520	19.9958	10.0148	1451.7166	298.6878	2044.6256	966.92989	713.73589

Table 5. 16 Parameters

TP	200	100	1000	400	30	500	1300	10
GA	143.1093	70.8814	1355.3798	391.0537	191.8145	997.6883	2492.9848	335.9915
DE	163.4741	37.4271	92.3983	382.8372	299.3884	202.9935	1374.7098	890.7038
TP	600	200	1000	20	150	10	2000	350
GA	2622.9554	174.7876	429.8657	381.0928	164.7305	5.5504	7.1481	1111.63595
DE	140.5125	349.5064	234.4274	1282.0209	165.7923	16.3574	8.3219	493.5829

Table 6. Relative Error between target and found parameters

# parameters \ Method	2	4	9	16
GA	2.5e-4	2.0e-1	4.0e-1	1.12e+0
DE	3.0e-7	2.3e-6	2.7e-2	9.6e-1

7 Conclusion

This work presented a comparison between Genetic Algorithms and Differential Evolution for solving the history matching problem, a well known reservoir engineering inverse problem. DE outperformed GA in every experiment presented, proving to be a very powerful optimization method and a good alternative for applying to history matching. It is interesting to note that GA performed better than DE on the initial generations, that is, the fitness value of the best individuals dropped much faster in the beginning of GA than DE. But GA was unsuccessful on refining the solution. On the other hand, DE could refine very well the solutions and achieved impressive fitness values. DE is a little bit simpler to implement than GA. It could be interesting to combine both methods, creating a hybrid optimization system, that would employ GA techniques in the beginning of the process and DE would follow on refining the solution.

Acknowledgments. This work was been partially funded by CNPq, Petrobras and Foundation CMG (Alberta Innovates).

References

1. Watson, A.T., Wade, J.G., Ewing, R.E.: Parameter and system identification for fluid flow in underground reservoirs. In: Proceedings of the Conference, Inverse Problems and Optimal Design in Industry (1994)
2. Brun, B., Gosselin, O., Barker, J.W.: Use of prior information in gradient-based history-matching. In: SPE Reservoir Simulation Symposium, pp. 13–23 (2001)
3. dos Santos Amorim, E.P., Goldfeld, P., Dickstein, F., dos Santos, R.W., Xavier, C.R.: Automatic History Matching in Petroleum Reservoirs Using the TSVD Method. In: Taniar, D., Gervasi, O., Murgante, B., Pardede, E., Apduhan, B.O. (eds.) ICCSA 2010. LNCS, vol. 6017, pp. 475–487. Springer, Heidelberg (2010)

4. Soleng, H.: Oil reservoir production forecasting with uncertainty estimation using genetic algorithms. *Evolutionary Computation* (1999)
5. dos Santos, E.P., Xavier, C.R., Goldfeld, P., Dickstein, F., Weber dos Santos, R.: Comparing Genetic Algorithms and Newton-Like Methods for the Solution of the History Matching Problem. In: Allen, G., Nabrzyski, J., Seidel, E., van Albada, G.D., Dongarra, J., Sloot, P.M.A. (eds.) *ICCS 2009, Part I. LNCS*, vol. 5544, pp. 377–386. Springer, Heidelberg (2009)
6. Oliver, D.S., Reynolds, A.C., Liu, N.: *Inverse Theory for Petroleum Reservoir Characterization and History Matching*, 1st edn. Cambridge University Press (2008)
7. Mitchell, M.: *An Introduction to Genetic Algorithms*. The MIT Press (1998)
8. Eiben, A.E., Smith, J.E.: *Introduction to Evolutionary Computing*. Natural Computing Series. Springer (2008)
9. Holland, J.: *Adaptation in natural and artificial systems: An introductory analysis with applications to biology, control, and artificial intelligence* (1992; First edition: 1975 The University of Michigan)
10. Eshelman, L.J., Schaffer, J.D.: Real-coded genetic algorithms and interval-schemata. *Foundation of Genetic Algorithms 2*, 187–202 (1993)
11. Storn, R., Price, K.: *Differential evolution - a simple and efficient adaptive scheme for global optimization over continuous spaces* (1995)
12. Kenneth Price, R.M.S., Lampinen, J.A.: *Differential Evolution: A Practical Approach to Global Optimization*. Natural Computing Series. Springer (2005)

An Adaptive Mesh Algorithm for the Numerical Solution of Electrical Models of the Heart

Rafael S. Oliveira^{1,2}, Bernardo M. Rocha^{3,4}, Denise Burgarelli⁵,
Wagner Meira Jr.², and Rodrigo W. dos Santos³

¹ Departamento de Ciência da Computação, Universidade Federal de São João de Rei

² Departamento de Ciência da Computação, Universidade Federal de Minas Gerais

³ Departamento de Ciência da Computação e Programa em Modelagem Computacional, Universidade Federal de Juiz de Fora

⁴ Laboratório Nacional de Computação Científica

⁵ Departamento de Matemática, Universidade Federal de Minas Gerais

Abstract. Computer models have become valuable tools for the study and comprehension of the complex phenomena of cardiac electrophysiology. However, the high complexity of the biophysical processes translates into complex mathematical and computational models. In this paper we evaluate a numerical algorithm based on mesh adaptivity and finite volume method aiming to accelerate these simulations. This is a very attractive approach since the spreading electrical wavefront corresponds only to a small fraction of the cardiac tissue. Usually, the numerical solution of the partial differential equations that model the phenomenon requires very fine spatial discretization to follow the wavefront, which is approximately 0.2mm . The use of uniform meshes leads to high computational cost as it requires a large number of mesh points. In this sense, the tests reported in this work show that simulations of two-dimensional models of cardiac tissue have been accelerated by more than 80 times using the adaptive mesh algorithm, with no significant loss in accuracy.

1 Introduction

Heart diseases are responsible for one third of all deaths worldwide [14]. The knowledge of cardiac electrophysiology is essential to understand many aspects of the cardiac physiological and pathophysiological behavior [17]. The electrophysiology is strongly coupled to the mechanical deformation that causes the heart to pump blood into the body.

Computer models [11,15] have become valuable tools for the study and comprehension of such complex phenomena, as they allow different information acquired from different physical scales and experiments to be combined to generate a better picture of the whole system functionality. Not surprisingly, the high complexity of the biophysical processes translates into complex mathematical and computational models. The modern cardiac models are described by non-linear systems of partial differential equations (PDE) coupled to a non-linear set of ordinary differential equations (ODE) resulting in a problem with millions of

variables and hundreds of parameters. The bidomain model [15] is considered to be the most complete description of the electrical activity in cardiac tissue. Under suitable assumptions the bidomain equations are reduced to a simpler model, called monodomain, which is less computationally demanding. Unfortunately, large scale simulations, such as those resulting from the discretization of an entire heart, remain a computational challenge. In spite of the difficulties and the complexity associated with the implementation and use of these models, the benefits and applications justify their use. Computer models have been used during the tests of new drugs, development of new medical devices and new techniques of non-invasive diagnosis for several cardiac diseases [9,18].

In the simulations of cardiac electrophysiology, the electric potential wave front that travels through the heart is very sharp. Due to this sharp spatial variation the numerical methods need fine spatial discretizations to follow the wavefront, which is approximately 0.2 mm [12], to ensure sufficiently accurate results. The execution of cardiac simulations on meshes with a large number of nodes is computationally expensive as it requires repeated solutions of linear systems with millions degrees of freedom. In addition, the memory requirements of simulations become increasingly large. The use of adaptive mesh methods provides a solution to these problems. By maintaining the extremely fine resolution only where it is needed (i.e., near the wavefront) the number of degrees of freedom is significantly reduced, resulting in faster computations, lower memory usage and reducing the need for disk space for the recording of the output files [20].

2 Monodomain Model

The wave of excitation propagates through the cardiac tissue because the cardiac cells are electrically coupled via special proteins called gap junctions. This phenomenon can be described mathematically by a reaction-diffusion equation called monodomain model, given by

$$\beta C_m \frac{\partial V(x, y, t)}{\partial t} + \beta I_{ion}(V(x, y, t), \boldsymbol{\eta}(x, y, t)) = \nabla \cdot (\boldsymbol{\sigma}(x, y) \nabla V(x, y, t)) + I_{stim}(x, y, t) \quad (1)$$

$$\frac{\partial \boldsymbol{\eta}(x, y, t)}{\partial t} = \boldsymbol{f}(V(x, y, t), \boldsymbol{\eta}(x, y, t)) \quad (2)$$

where V is the variable of interest and represents the transmembrane potential, i.e. the difference between intracellular to extracellular potential; $\boldsymbol{\eta}$ is a vector of state variables that also influence the generation and propagation of the electric wave, and usually includes the intracellular concentration of different ions (K^+ , Na^+ , Ca^{2+}) and the permeability of different membrane ion channels; β is the surface-volume ratio of heart cells; C_m is the membrane capacitance, I_{ion} the total ionic current, which is a function of V and a vector of state variables $\boldsymbol{\eta}$, I_{stim} is the current due to an external stimulus and $\boldsymbol{\sigma}$ is the monodomain

conductivity tensor. We assume that the boundary of the tissue is isolated, i.e., no-flux boundary conditions ($\mathbf{n} \cdot \sigma \nabla V = 0$ on $\partial\Omega$).

In this work the classical Luo–Rudy I (LRI) model [13] that describes the electrical activity of a general mammalian ventricular cell was considered to simulate the kinetics of I_{ion} in Eqs. (1) and (2). In this mammalian ventricular model, I_{ion} is defined as the following sum of currents:

$$I_{ion} = I_{Na} + I_{si} + I_K + I_{K1} + I_{Kp} + I_b, \tag{3}$$

where I_{Na} is the fast sodium current, I_{si} is the slow inward current, I_K is the time-dependent potassium current, I_{K1} is the time-independent potassium current, I_{Kp} is the plateau potassium current and I_b is time-independent background current. The LRI model is based on a system of 8 ODEs. The variables are V and another 7 auxiliary variables, $\boldsymbol{\eta}$, that describe ionic currents and intracellular calcium concentration. For a full specification of the model and its ionic currents see [13].

3 The Finite Volume Method

The finite volume method (FVM) is a mathematical method used to obtain a discrete version of partial differential equations. This method is suitable for numerical simulations of various types of conservation laws (elliptical, parabolic or hyperbolic) [7]. Like the finite element method (FEM), the FVM can be used in several types of geometry, using structured or unstructured meshes and generates robust numerical schemes. The development of the method is intrinsically linked to the concept of flow between regions or adjacent volumes, where the flux of a quantity such as mass or energy, is the amount of this quantity φ that crosses a border with area A . The amount of φ that crosses a control volume Ω_c per unit of time is calculated by integrating over these boundaries the difference between flows entering and leaving Ω_c , which is achieved by integrating the PDEs.

3.1 Monodomain Discretization Using FVM

This section presents a brief description of the FVM application to the spatial discretization of the monodomain equations. Detailed information about the FVM applied to the solution of monodomain can be found in [10,5].

The reaction and diffusion parts of the monodomain equations were split by employing the Godunov operator splitting [21]. Therefore, each time step involves the solution of two different problems: a nonlinear system of ODEs

$$\frac{\partial V}{\partial t} = \frac{1}{C_m} [-I_{ion}(V, \boldsymbol{\eta}) + I_{stim}] \tag{4}$$

$$\frac{\partial \boldsymbol{\eta}}{\partial t} = f(V, \boldsymbol{\eta}) \tag{5}$$

and a parabolic PDE

$$\beta \left(C_m \frac{\partial V}{\partial t} \right) = \nabla \cdot (\sigma \nabla V) \tag{6}$$

Depending on the numerical method used, the spatial discretization of the parabolic PDE results in a system of linear equations that must be solved at each time step.

The time derivative presented in (6), which operates on V is approximated by a first order implicit Euler scheme:

$$\frac{\partial V}{\partial t} = \frac{V^{n+1} - V^n}{\Delta t}, \tag{7}$$

where V^n represents the transmembrane potential at time t_n and Δt is the time step.

The diffusion term in (6) must be discretized in space. For this we will consider the following:

$$\mathbf{J} = -\sigma \nabla V \tag{8}$$

where J ($\mu A/cm^2$) expresses the density of intracellular current flow and

$$\nabla \cdot \mathbf{J} = -I_v. \tag{9}$$

In this equation, I_v ($\mu A/cm^3$) is a volumetric current and corresponds the left-hand side of (6), serving as the base for this finite volume solution.

For the space discretization we will consider a two-dimensional uniform mesh, consisting of regular quadrilaterals (called “volumes”). Located in the center of each volume is a node. The quantity of interest V is associated with each node of the mesh.

After defining the mesh geometry and dividing the domain in control volumes, the specific equations of the FVM can be presented. Equation (9) can be integrated spatially over an individual quadrilateral, leading to:

$$\int_{\Omega} \nabla \cdot \mathbf{J} dv = - \int_{\Omega} I_v dv. \tag{10}$$

Applying the divergence theorem yields,

$$\int_{\Omega} \nabla \cdot \mathbf{J} dv = \int_{\partial\Omega} \mathbf{J} \cdot \boldsymbol{\xi} ds, \tag{11}$$

where $\boldsymbol{\xi}$ is the unitary normal vector to the boundary $\partial\Omega$. Then, we have:

$$\int_{\partial\Omega} \mathbf{J} \cdot \boldsymbol{\xi} ds = - \int_{\Omega} I_v dv. \tag{12}$$

Finally, assuming that I_v represents an average value in each particular quadrilateral, and substituting (6) in (12), we have:

$$\beta \left(C_m \frac{\partial V}{\partial t} \right) \Big|_{(i,j)} = \frac{- \int_{\partial\Omega} J_{i,j} \cdot \boldsymbol{\xi} ds}{A_{i,j}}, \tag{13}$$

where $A_{i,j}$ is the area of control volume.

For this particular two-dimensional problem, consisting of a uniform grid of quadrilaterals with side h , the calculation of $J_{i,j}$ can be subdivided as a sum of flows on the faces:

$$\int_{\partial\Omega} J_{i,j} \cdot \xi ds = (J_{x_{i+1/2,j}} - J_{x_{i-1/2,j}} + J_{y_{i,j+1/2}} - J_{y_{i,j-1/2}})h \tag{14}$$

where $J_{x_{m,n}}$ and $J_{y_{m,n}}$ are calculated in faces $((m,n) = (i + 1/2, j), (i - 1/2, j), (i, j + 1/2), \text{ or } (i, j - 1/2))$ as follows:

$$J_{x_{m,n}} = -\sigma_x(m,n) \frac{\partial V}{\partial x} \Big|_{(m,n)} - \sigma_{xy}(m,n) \frac{\partial V}{\partial y} \Big|_{(m,n)} \tag{15}$$

$$J_{y_{m,n}} = -\sigma_{xy}(m,n) \frac{\partial V}{\partial x} \Big|_{(m,n)} - \sigma_y(m,n) \frac{\partial V}{\partial y} \Big|_{(m,n)} \tag{16}$$

For simplicity, we will consider a mesh with horizontally oriented fibers ($\sigma_{xy} = 0$). Therefore, the tensor $\sigma = \begin{pmatrix} \sigma_x & 0 \\ 0 & \sigma_y \end{pmatrix}$ must be evaluated at the faces of the volume. For this, we use the harmonic mean:

$$\sigma_{x_{i+1/2,j}} = \frac{2\sigma_{x_{i,j}}\sigma_{x_{i+1,j}}}{\sigma_{x_{i+1,j}} + \sigma_{x_{i,j}}} \tag{17}$$

A similar reasoning can be used to calculate $\sigma_{x_{i-1/2,j}}$, $\sigma_{y_{i,j+1/2}}$ and $\sigma_{y_{i,j-1/2}}$.

Uniform Non-adaptive Mesh. In this section we present the application of FVM using a uniform non-adaptive mesh. For this, we will approximate the partial derivatives of V at the interfaces using the following finite difference scheme, considering uniform space discretizations ($\Delta x = \Delta y = h$):

$$\frac{\partial V}{\partial x} \Big|_{(i+1/2,j)} = \frac{V_{i+1,j} - V_{i,j}}{h} \tag{18}$$

Equations for $\frac{\partial V}{\partial x} \Big|_{(i-1/2,j)}$, $\frac{\partial V}{\partial y} \Big|_{(i,j+1/2)}$ e $\frac{\partial V}{\partial y} \Big|_{(i,j-1/2)}$ can be obtained analogously.

Rearranging and substituting the discretizations of the equations (7) and (14) in (13) and decomposing the operators as described by equations (4), (5) and (6) yields

$$C_m \frac{V_{i,j}^* - V_{i,j}^n}{\Delta t} = - \frac{h \cdot (J_{x_{i+1/2,j}}^* - J_{x_{i-1/2,j}}^* + J_{y_{i,j+1/2}}^* - J_{y_{i,j-1/2}}^*)}{\beta h^2} \tag{19}$$

$$C_m \frac{V_{i,j}^{n+1} - V_{i,j}^*}{\Delta t} = -I_{ion}(V_{i,j}^*, \eta^n) \tag{20}$$

$$\frac{\partial \eta^{n+1}}{\partial t} = f(\eta^n, V^*, t) \tag{21}$$

where:

$$J_{x_{i+1/2,j}}^* = -\sigma_{x_{i+1/2,j}} \frac{V_{i+1,j}^* - V_{i,j}^*}{h} \tag{22}$$

Equation (22) represents the flux of cell (i, j) from the right edge of the quadrilateral to the neighbor cell, n is the current step, $*$ is an intermediate step and $n + 1$ is the next time step. Equations for $J_{x_{i-1/2,j}}$, $J_{y_{i,j+1/2}}$ and $J_{y_{i,j-1/2}}$ follow the same reasoning. Developing all the equations, we can now define the formula for each volume:

$$\begin{aligned} &(\sigma_{x_{i+1/2,j}} + \sigma_{x_{i-1/2,j}} + \sigma_{y_{i,j+1/2}} + \sigma_{y_{i,j-1/2}} + \alpha)V_{i,j}^* - \sigma_{y_{i,j-1/2}}V_{i,j-1}^* - \sigma_{x_{i+1/2,j}}V_{i+1,j}^* \\ &\quad - \sigma_{y_{i,j+1/2}}V_{i,j+1}^* - \sigma_{x_{i-1/2,j}}V_{i-1,j}^* \\ &= \alpha V_{i,j}^n \end{aligned} \tag{23}$$

where $\alpha = (\beta C_m h^2)/\Delta t$.

Adaptive Mesh. When the electrical wave is propagating through the heart, only a fraction of the excitable medium is occupied by wavefronts. In these regions, the solution or its derivatives change rapidly. Therefore, the numerical solution of the differential equations in these regions requires the use of an extremely fine computing mesh. Thus, the use of uniform meshes leads to a very high computational cost. Therefore, adaptive procedures that take into account the scale differences in the phenomena present reliable and efficient solutions [3].

Recently, the use of adaptive refinement to obtain meshes suitable for the representation of the cardiac electrophysiology equations has been investigated, see, for example [14,8,20,19].

In this section we show the FVM equations when we use a mesh with adaptive refinement called Autonomous Leaves Graph (ALG). ALG is a data structure that can be integrated to the linear system solver to properly represent different geometries, with adaptive refinement of complex boundaries. In this work, we decided to use the ALG because, unlike the methods used in [14,8,20] ALG is a generic data structure, which does not rely on any type of numerical method, on the geometry of the problem nor on the problem’s nature. For instance, in [4] the adaptive method was developed for finite differences and in [8] for finite elements. The geometry adopted by Southern *et al.* [19,20] relies on FEM and tetrahedral meshes. In Chery *et al.* [4] the authors use a method specific to hyperbolic PDEs. The ALG data structured is flexible enough to handle any of these tasks or particular implementations. Moreover, as described in [3], ALG proved to be very computational efficient, presenting lower computational cost than other techniques employed in this context, as quadtree and octree. ALG was also applied to the thermoacoustic problem, which involves solving a nonlinear system of Navier–Stokes equations [2]. It is noteworthy that the use of ALG method in simulations of the cardiac electrophysiology is one of the contributions of this work, since this approach was not found in the literature.

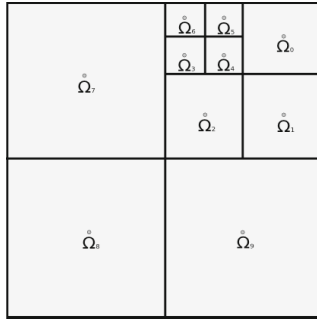


Fig. 1. Example of mesh refined using ALG adaptivity scheme

Figure 1 shows a domain consisting of a unitary square discretized using ALG. The enumeration of values $\Omega_0, \Omega_1, \Omega_2, \dots$ follows the modified Hilbert curve geometry. In this mesh, volumes Ω_7, Ω_8 and Ω_9 are in refinement level 1; Ω_0, Ω_1 and Ω_2 are in level 2 and $\Omega_3, \Omega_4, \Omega_5$ and Ω_6 are in level 3.

To exemplify the application of FVM with ALG we will use a tissue with horizontally oriented fibers. Therefore, we have the following finite difference scheme (considering $\Delta x_{i,j} = \Delta y_{i,j} = h_{i,j}$):

$$\frac{\partial V}{\partial x} \Big|_{(i+1/2,j)} = \sum_{k=1}^{m_1} \frac{V_{r,k} - V_{i,j}}{h_1}, \tag{24}$$

$$\frac{\partial V}{\partial x} \Big|_{(i-1/2,j)} = \sum_{k=1}^{m_2} \frac{V_{i,j} - V_{l,k}}{h_2}, \tag{25}$$

$$\frac{\partial V}{\partial y} \Big|_{(i,j+1/2)} = \sum_{k=1}^{m_3} \frac{V_{t,k} - V_{i,j}}{h_3}, \tag{26}$$

$$\frac{\partial V}{\partial y} \Big|_{(i,j-1/2)} = \sum_{k=1}^{m_4} \frac{V_{i,j} - V_{b,k}}{h_4}, \tag{27}$$

where m_1 is the number of neighbors at right of the cell centered at (i, j) , m_2 is the number of neighbors at left, m_3 is the number of neighbors above, m_4 is the number neighbors below; $V_{r,k}$ are neighbors at right, and $V_{l,k}$ are the neighbors at left, $V_{t,k}$ are the neighbors on top and $V_{b,k}$ are the neighbors on bottom. The discretizations are defined by:

$$\begin{aligned} h_1 &= h_{i,j} \text{ if } \mathcal{L}_{i,j} > \mathcal{L}_{r,k} \text{ and } h_1 = h_{r,k} \text{ otherwise,} \\ h_2 &= h_{i,j} \text{ if } \mathcal{L}_{i,j} > \mathcal{L}_{l,k} \text{ and } h_1 = h_{l,k} \text{ otherwise,} \\ h_3 &= h_{i,j} \text{ if } \mathcal{L}_{i,j} > \mathcal{L}_{t,k} \text{ and } h_1 = h_{t,k} \text{ otherwise,} \\ h_4 &= h_{i,j} \text{ if } \mathcal{L}_{i,j} > \mathcal{L}_{b,k} \text{ and } h_1 = h_{b,k} \text{ otherwise,} \end{aligned} \tag{28}$$

where \mathcal{L} is the refinement level of the cell. Rearranging and substituting the discretizations in (13) and decomposing the operators as described by equations (4), (5) and (6) yields:

$$C_m \frac{V_{i,j}^* - V_{i,j}^n}{\Delta t} = - \frac{(L_1 J_{x_{i+1/2,j}}^* - L_2 J_{x_{i-1/2,j}}^* + L_3 J_{y_{i,j+1/2}}^* - L_4 J_{y_{i,j-1/2}}^*)}{\beta A_{i,j}} \tag{29}$$

$$C_m \frac{V_{i,j}^{n+1} - V_{i,j}^*}{\Delta t} = -I_{ion}(V_{i,j}^*, \boldsymbol{\eta}^n) \tag{30}$$

$$\frac{\partial \boldsymbol{\eta}^{n+1}}{\partial t} = f(\boldsymbol{\eta}^n, V^*, t) \tag{31}$$

where:

$$L_1 J_{x_{i+1/2,j}} = -\sigma_{x_{i+1/2,j}} \sum_{k=1}^{m_1} \frac{V_{r,k} - V_{i,j}}{h_1} L_1 \tag{32}$$

$$L_2 J_{x_{i-1/2,j}} = -\sigma_{x_{i-1/2,j}} \sum_{k=1}^{m_2} \frac{V_{i,j} - V_{l,k}}{h_2} L_2 \tag{33}$$

$$L_3 J_{y_{i,j+1/2}} = -\sigma_{y_{i,j+1/2}} \sum_{k=1}^{m_3} \frac{V_{t,k} - V_{i,j}}{h_3} L_3 \tag{34}$$

$$L_4 J_{y_{i,j-1/2}} = -\sigma_{y_{i,j-1/2}} \sum_{k=1}^{m_4} \frac{V_{i,j} - V_{b,k}}{h_4} L_4. \tag{35}$$

For a regular grid we have $L_1 = h_1$, $L_2 = h_2$, $L_3 = h_3$ and $L_4 = h_4$. Therefore, we can simplify the above equations, obtaining:

$$J_{x_{i+1/2,j}} = - \sum_{k=1}^{m_1} \sigma_{x_{d',k}} (V_{d,k} - V_{i,j}) \tag{36}$$

$$J_{x_{i-1/2,j}} = - \sum_{k=1}^{m_2} \sigma_{x_{e',k}} (V_{i,j} - V_{e,k}) \tag{37}$$

$$J_{y_{i,j+1/2}} = - \sum_{k=1}^{m_3} \sigma_{y_{c',k}} (V_{c,k}^{n+1} - V_{i,j}) \tag{38}$$

$$J_{y_{i,j-1/2}} = - \sum_{k=1}^{m_4} \sigma_{y_{b',k}} (V_{i,j} - V_{b,k}) \tag{39}$$

where $\sigma_{x_{d',k}}$, $\sigma_{x_{e',k}}$, $\sigma_{y_{c',k}}$ and $\sigma_{y_{b',k}}$ are the conductivity values calculated using the harmonic mean as follows:

$$\sigma_{x_{r',k}} = \frac{2\sigma_{x_{i,j}}\sigma_{x_{r,k}}}{\sigma_{x_{r,k}} + \sigma_{x_{i,j}}} \tag{40}$$

$$\sigma_{x_{l',k}} = \frac{2\sigma_{x_{i,j}}\sigma_{x_{l,k}}}{\sigma_{x_{l,k}} + \sigma_{x_{i,j}}} \tag{41}$$

where $\sigma_{x_{r',k}}$ e $\sigma_{x_{l',k}}$ are the conductivities of the volumes k at right and left of the element (i, j) , respectively. $\sigma_{y_{t',k}}$ and $\sigma_{y_{b',k}}$ are calculated analogously.

Developing all the equations, we can now define the formula for each volume:

$$\alpha V_{i,j}^* - \sum_{k=1}^{m_1} \sigma_{x_{r',k}} (V_{r,k} - V_{i,j}) + \sum_{k=1}^{m_2} \sigma_{x_{l',k}} (V_{i,j} - V_{l,k}) - \sum_{k=1}^{m_3} \sigma_{y_{t',k}} (V_{t,k} - V_{i,j}) + \sum_{k=1}^{m_4} \sigma_{y_{b',k}} (V_{i,j} - V_{b,k}) = V_{i,j}^n \alpha \tag{42}$$

where $\alpha = (\beta C_m h_{i,j}^2) / \Delta t$.

4 Mesh Adaptivity and ALG

As discussed in Sec. 3.1, adaptive meshes are an alternative to accelerate simulations of cardiac electrophysiology. This section describes the ALG data structure as well as the refine and derefine operations.

4.1 Data Structure

As stated before, ALG stands for Autonomous Leaves Graph and its underlying data structure is composed by two types of nodes: *cell nodes*, which are the properly mesh cells, and the *transition nodes*, which are used to connect cells with different refinement levels. Considering a two-dimensional implementation, we have four pointers in each cell node: east, west, north and south; these pointers can connect the cell node either to another cell node or to a transition node. Transition nodes have only three pointers, to connect to cell nodes and/or transition nodes. Cell nodes have additional variables corresponding to the spatial coordinates of their centers and their physical states (usually the variable of interest). The nodes also carry information about their type (cell or transition node) and their level of refinement.

Figure 2 shows the resulting graph after the discretization of a unit square. The resulting graph has four cell nodes with links oriented along the four directions: north, along positive y direction; south, along negative y direction; east, along positive x direction; and west, along negative x direction. The remaining links that do not point to one of the four nodes in the square (i.e. the boundaries) are then directed to the four transition nodes, displayed as white circles.

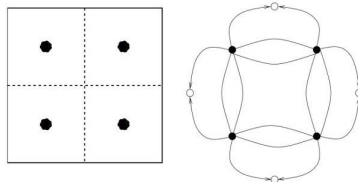


Fig. 2. Unit square and links for graph structure (adapted from [3])

4.2 Mesh Refinement

The refinement in ALG is implemented by replacing the basic structure of a cell node that will be refined by the structure developed for the unit square, as presented above. The node in the center of cell to be refined is replaced by the four nodes. The four outward links departing from the transition nodes are connected to the nodes to which the four original links were connected. Figure 3 show resulting graph after refining the northwest cell (Fig 2 unit square); the number placed next to each node corresponds to its level of refinement.

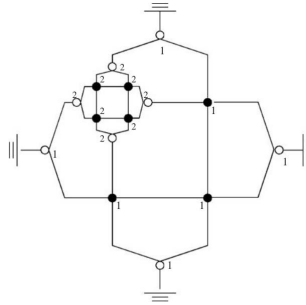


Fig. 3. Refining the northwest cell. (adapted from 3).

4.3 Mesh Derefinement

In order to preserve the basic building block structure of the graph, its required that a all four cells that are being derefined to be in the same bunch, allowing restoration of the previous configuration. This condition is needed to ensure that previous configurations of the mesh can always be recovered performing mutually-independent local changes. Figure 4 depicts the process of the bunch selection, collapse and the connection of the nodes in a refinement operation.

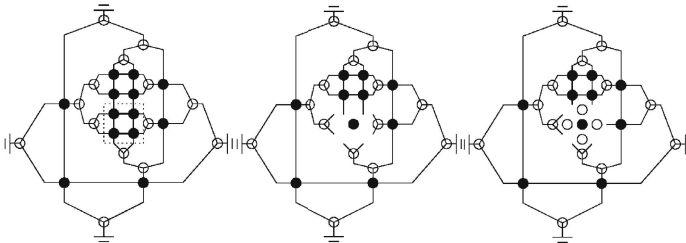


Fig. 4. Bunch selection, collapse and connecting nodes. (adapted from 3).

The necessary stages for derefining a bunch are as follows:

1. Transformation of the northeast node of the bunch in the resulting derefined node.

2. Filling the resulting node with the new data (for instance, its space coordinates, level and physical constants related to the problem).
3. Connection of the resulting node with its neighbors.
4. Connection of the neighboring nodes with the resulting node.
5. Release of the memory space of the eliminated nodes.

4.4 ALG and the Monodomain Problem

The following algorithm describes the steps used for the numerical resolution of monodomain model:

```

begin
  set cell model initial conditions;
  set monodomain initial conditions;
  assemble the monodomain matrix;
  while (t < t_final)
    update_cell_model_state_vector;
    solve_cell_model;
    conjugate_gradient
    refine_derefine
    reassemble the monodomain matrix if needed;
    t = t + dt
  end while
end

```

As can be seen in the above algorithm, we have to reassemble the monodomain matrix at each time step if a refinement or derefinement operation has been performed in that step. In this work, the criteria used for refinement and derefinement are based on the flux across the interface of neighboring cells. That is, if the absolute value of the flux is larger than a predefined refinement threshold (*ref_t*), the program chooses to refine this cell, whereas if the absolute value of the flux of all four cells of a bunch is less than an derefinement threshold (*dref_t*), the program chooses to derefine the bunch. For the monodomain application, the values for the refinement and derefinement thresholds were empirically found.

5 Methods

In this section, we discuss the experimental setup of the various cardiac simulations we performed.

5.1 Computational Simulations

To calculate the speedup achieved by using adaptive meshes, we first simulate the heart's electrical activity in four different configurations of two-dimensional tissue using fixed (non-adaptive) meshes. As we are mainly interested in the impact of spatial discretization on the execution times of the simulations, the configurations differ only in the space discretization value (referenced as *h*). We used the following values for *h*: 25 μm , 50 μm , 100 μm and 200 μm . For the adaptive meshes we used the following settings:

1. initial h 25 μm , with maximum h 100 μm and minimum h 25 μm ;
2. initial h 25 μm , with maximum h 200 μm and minimum h 25 μm ;
3. initial h 50 μm , with maximum h 100 μm and minimum h 50 μm ;
4. initial h 50 μm , with maximum h 200 μm and minimum h 50 μm .

The simulations were performed using computational meshes with $1.2\text{ cm} \times 1.2\text{ cm}$. The values used for β , C_m , σ_x and σ_y were 0.14 cm^{-1} ; $1.0\mu F/cm^2$; 0.0012 mS/cm and 0.0006226 mS/cm respectively. The time step of the numerical model was adjusted to $10\mu s$ in all experiments. The simulations were carried for 400 ms, resulting in a total of 40000 time steps after a single stimulus was introduced into the center of the tissue. For the solution of the linear system associated with the monodomain model we used the conjugate gradient method (CG) without preconditioner with a relative tolerance set to 1^{-16} and the maximum number of iterations set to 200.

5.2 Metrics and Computational Environment

The relative RMS errors between the solutions obtained by the algorithms that use adaptive meshes and the reference solution, were calculated using:

$$error = \frac{\sqrt{\sum_{i=1}^{nt} \sum_{j=1}^{nv} (V(i, j) - V_{ref}(i, j))^2}}{\sqrt{\sum_{i=1}^{nt} \sum_{j=1}^{nv} V_{ref}(i, j)^2}},$$

where nt is the number of time iterations, nv is the number of volumes, V_{ref} is the reference solution and V is the solution obtained by using the different configurations. The definition of speedup is the traditional, i.e., the ratio between the reference problem execution time and the execution time using different configurations. Errors and speedups of the different simulations were calculated using the most refined mesh (25 μm of spatial discretization) as the reference solution. To be able to calculate the errors between meshes with different discretizations we “refined” all the meshes to 25 μm . This refinement was made by iterating over the entire mesh and breaking volumes with more than 25 μm in smaller volumes of 25 μm . Each new created volume receives the value of V of the larger and original volume. The presented execution times reflect an average value of three executions. The codes were manually instrumented for performance evaluation. Comparative tests performed with and without instrumentation have indicated the instrumentation overhead to be irrelevant.

The data-structures and codes shown in section 4 were implemented using C++. All simulations were carried out on a Linux machine equipped with a quad-core Intel Core i7 860 2.80GHz and 8GB of memory.

6 Results

In this section we present the results with respect to execution time and speedup, as well as the numerical errors associated with the implementation using adaptive meshes and coarse meshes.

6.1 Coarse Meshes

The use of meshes with coarser spatial discretizations is an alternative that can reduce the simulation execution times. However, the use of this strategy can generate results with significant numerical errors, compared to the use of finer meshes.

Table 1. Errors and speedups using different coarse meshes compared to the reference simulation discretized with $h = 25\mu m$

Spatial discretization (h)	Speedup	Error
50 μm	4.86	1.36%
100 μm	23.5	5.71%
200 μm	140.79	15.28%

Table 1 shows the speedups and errors obtained for different space discretizations. We can notice that the use of larger values for h leads to a reduction in the execution times. By using $h = 50\mu m$ we obtained a 4.86-fold speedup. Despite the achievement of satisfactory speedups when we further increase h ($140.79\times$ with $h = 200\mu m$), the numerical errors significantly increase, reaching 15.3% ($h = 200\mu m$).

6.2 Adaptive Meshes

The use of adaptive meshes also aims to accelerate the simulations, but without allowing the error to grow proportionally to the speedup. Table 2 shows the execution times and errors obtained after using the ALG adaptive mesh in the cardiac electrophysiology simulation. Using an adaptive mesh with initial spatial discretization of $25\mu m$ and maximum of $200\mu m$, we obtained a $23.98\times$ speedup and an error below 1%. Using only coarser meshes we would have to accept an error greater than 5% to get a speedup greater than $20\times$, as shown in Table 1. With the meshes using initial spatial discretization of $50\mu m$ and maximum $200\mu m$ and $100\mu m$, we obtained speedups of $83.65\times$ and $15.72\times$ respectively. The errors obtained with these meshes were higher (2.24%, 1.83% respectively), but are still within acceptable limits depending on the accuracy requirement of the simulation.

Table 3 splits the total execution time in those related to the solution of the CG, to the assembly of the matrix (in the case of fixed mesh) and to the reassembly (adaptive mesh) of the matrices. We can see that the time to reassemble the

Table 2. Errors and speedups obtained using adaptive meshes

Spatial discretization (h)	Speedup	Error
Minimum 25 μm . Maximum 200 μm	23.98	0.74%
Minimum 25 μm . Maximum 100 μm	8.39	0.57%
Minimum 50 μm . Maximum 200 μm	83.65	2.24%
Minimum 50 μm . Maximum 100 μm	15.72	1.83%

matrices is at most 5% of the total time to solve all the linear systems. This shows that, using the adaptive scheme, the cost to rebuild the matrix at every refine or derefine operation is not insignificant. Nevertheless, the time spent solving the CG method is greatly reduced.

Table 3. Matrix assembly and GC execution times for three different simulations

Space discretization (h)	CG time (s)	Matrix assembly time (s)
25 μm	27307.4	0.29
Min. 25 μm . Max. 100 μm	2679.88	101.25
Min. 25 μm . Max. 200 μm	1197.68	48.25

Figure 5 shows the simulation results using ALG adaptive mesh. We can clearly see that the region delimited by the wavefront has a spatial discretization smaller than the rest of the tissue. The color code represents the distribution of transmembrane potential V at two different time instants.

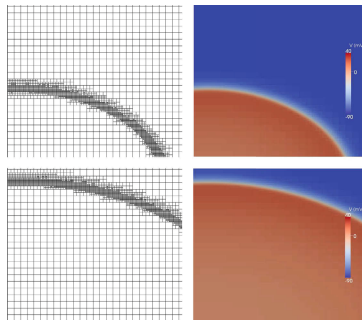


Fig. 5. Simulation using ALG adaptivity scheme. Zoom on the result of the simulated electric wave propagation (distribution of transmembrane potential V) in a ventricular tissue at 80 ms (top) and 130 ms (bottom).

In Fig. 6 we present a visual comparison between the action potential at the node (6400, 12800) in the fixed computational mesh (25 μm) and the adaptive mesh (Minimum 50 μm . Maximum 200 μm). It is clear that the error between

the reference solution and the solution with the adaptive mesh is extremely small, as shown in Table 2, and does not affect the behavior of the solution.

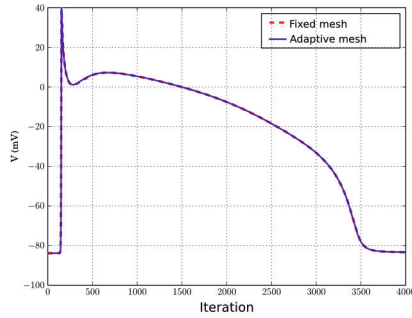


Fig. 6. Comparison of the transmembrane potential V over time between a node in the fixed mesh and the same node in the adaptive mesh

7 Conclusion

In this paper we developed and implemented an adaptive mesh approach in order to speed up cardiac electrophysiology simulations. The obtained results proved to be very promising, indicating that the use of ALG is able to reduce the execution time of a simulation by more than $80\times$, compared to the use of fixed meshes. In addition, the numerical accuracy was also kept under control (relative errors below 2.3%).

Although we have shown a significant improvement in the execution time of cardiac electrophysiology simulations, some techniques could be applied to further reduce the simulation execution times. For instance, given the inherently parallel computational power of graphical processing units (GPUs), we are planning to adapt the ALG method for this type of parallel environment. Some publications such as [6] and [16] achieved excellent results by using GPUs to solve the monodomain equations with non-adaptive meshes.

Acknowledgments. This work was partially funded by CNPq, Capes, Fapemig and InWeb.

References

1. Bendahmane, M., Bürger, R., Ruiz-Baier, R.: A multiresolution space-time adaptive scheme for the bidomain model in electrocardiology. *Numerical Methods for Partial Differential Equations* 26(6), 1377–1404 (2010)
2. Burgarelli, D., Kischinhevsky, M.: Efficient numerical simulation of a simplified thermoacoustic engine with new adaptive mesh refinement tools. *Computational Methods in Engineering* 99 (1999)

3. Burgarelli, D., Kischinhevsky, M., Biezuner, R.J.: A new adaptive mesh refinement strategy for numerically solving evolutionary pde's. *J. Comput. Appl. Math.* 196, 115–131 (2006)
4. Cherry, E.M., Greenside, H.S., Henriquez, C.S.: Efficient simulation of three-dimensional anisotropic cardiac tissue using an adaptive mesh refinement method. *Chaos: An Interdisciplinary Journal of Nonlinear Science* 13(3), 853–865 (2003)
5. Coudiere, Y., Pierre, C., Turpault, R.: A 2d/3d finite volume method used to solve the bidomain equations of electrocardiology. In: *Proceedings of Algorithmy*, pp. 1–10 (2009)
6. Sato, D., Xie, Y., Weiss, J.N., Qu, Z., Garfinkel, A., Sanderson, A.R.: Acceleration of cardiac tissue simulation with graphic processing units. *Med. Biol. Eng. Comput.* 47, 1011–1015 (2009)
7. Eymard, R., Gallouët, T., Herbin, R.: Finite volume methods. In: *Handbook of Numerical Analysis*, vol. 7, pp. 713–1018 (2000)
8. Franzone, P., Deuffhard, P., Erdmann, B., Lang, J., Pavarino, L.: Adaptivity in space and time for reaction-diffusion systems in electrocardiology. *SIAM Journal on Scientific Computing* 28(3), 942 (2007)
9. Gima, K., Rudy, Y.: Ionic current basis of electrocardiographic waveforms: A model study. *Circulation Research* 90, 889–896 (2002)
10. Harrild, D., Henriquez, C.: A finite volume model of cardiac propagation. *Annals of Biomedical Engineering* 25(2), 315–334 (1997)
11. Hodgkin, A., Huxley, A.: A quantitative description of membrane current and its application to conduction and excitation in nerve. *Journal of Physiology* 117, 500–544 (1952)
12. Hunter, P.J., Borg, T.K.: Integration from proteins to organs: the physiome project. *Nature Reviews Molecular Cell Biology* 4(3), 237–243 (2003)
13. Luo, C., Rudy, Y.: A model of the ventricular cardiac action potential. depolarization, repolarization, and their interaction. *Circ. Res.* 68(6), 1501–1526 (1991)
14. OMS: Organização Mundial da Saúde. *Publicação Eletrônica*. Último acesso em 17 de Agosto de 2011 (2010), <http://www.who.int/>
15. Plonsey, R.: Bioelectric sources arising in excitable fibers (ALZA lecture). *Ann. Biomed. Eng.* 16(6), 519–546 (1988)
16. Rocha, B.M., Campos, F.O., Amorim, R.M., Plank, G., dos Santos, R.W., Liebmann, M., Haase, G.: Accelerating cardiac excitation spread simulations using graphics processing units. *Concurrency and Computation: Practice and Experience* (2010)
17. Sachse, F.B.: *Computational cardiology: modeling of anatomy, electrophysiology, and mechanics*, vol. 2966. Springer (2004)
18. Weber dos Santos, R., Plank, G., Bauer, S., Vigmond, E.J.: Preconditioning Techniques for the Bidomain Equations. *Lecture Notes In Computational Science And Engineering* 40, 571–580 (2004)
19. Southern, J., Gorman, G., Piggott, M., Farrell, P.: Parallel anisotropic mesh adaptivity with dynamic load balancing for cardiac electrophysiology. *Journal of Computational Science* 3, 8–16 (2012)
20. Southern, J., Gorman, G., Piggott, M., Farrell, P., Bernabeu, M., Pitt-Francis, J.: Simulating cardiac electrophysiology using anisotropic mesh adaptivity. *Journal of Computational Science* 1(2), 82–88 (2010)
21. Sundnes, J.: *Computing the electrical activity in the heart*. Springer (2006)

Decision Model to Predict the Implant Success

Ana Cristina Braga¹, Paula Vaz², João C. Sampaio-Fernandes²,
António Felino², and Maria Purificação Tavares³

¹ Department of Production and Systems, University of Minho,
4710-057 Braga, Portugal
acb@dps.uminho.pt

² Dental Medicine Faculty, OPorto University,
4200-393 Porto, Portugal
{pvaz,jfernandes,afelino}@fmd.up.pt

³ CGC Genetics, Oporto,
4200-432 Porto, Portugal
mptavares@cgcgenetics.com

Abstract. In this work we propose to build a set of binary logistic models that could assess the probability of success or no success in oral rehabilitation process taking into account some genetic factors, individual habits clinical and non-clinical factors.

The study was conducted in a retrospective evaluation and consisted of 155 subjects undergoing oral rehabilitation in the Northern region of Portugal. We evaluated multiple factors in the construction of binary logistic regression models. We have chosen the model that gave statistically better discriminating power between success and failure, through the value of area under the ROC curve. The model that reveals better performance was Model 4, with $AUC = 0.789$ and a 95% confidence interval [0.715; 0.863].

Keywords: Logistic Regression, ROC curve, dental implant, no success.

1 Introduction

Implant-supported or implant-retained treatments provide predictable results with improved stability, retention, aesthetic and patient satisfaction [9]. However, there are specific groups of patients for which these results cannot be achieved simply and routinely.

A improved understanding on the process of establishment of different forms of no success of osseointegrated oral implants is essential to treat or to prevent this possible occurrence [9]. The criteria for failure and success of dental implants are well documented in specific literature (for example, in [2] and [6]). Most publications tend to focus mainly peri-implant disease (peri-mucositis and peri-implantitis) and their clinical signs or implant loss. However, there are negative aspects associated with biological complications which might be found in oral rehabilitation with dental implants, that should be also contemplate as no success, especially for clinical consequences that may entail [9].

The peri-implant disease in patients with oral rehabilitations with dental implants is characterized by an inflammatory host response due to the presence of certain bacteria that colonize the peri-implant sulcus. In an initial phase of peri-implant pathology can install peri-mucositis, a reversible inflammation of the soft tissues surrounding the dental implant.

Certain pathogenic bacteria, biomechanical overload, history of periodontitis, smoking habit, alcohol consumption and genetic susceptibility are some of the factors that have been discussed in the pathogenesis of peri-implantitis. The understanding of the osseointegrated implant failure as a multifactorial process and the clinical observation of repetitive unsuccessful dental implants in certain individuals raise interesting questions related to host susceptibility to failed dental implant [9]. Indeed, it is noted that implant losses tend to cluster in a specific group of individuals and it could indicate that specific host characteristics may disturb the osseointegration process and are influenced by genetic factors. As for genetic factors, the international research has focused on the role of some gene polymorphisms in the host tissue response.

In fact, interleukin-1beta (IL1B) and tumour necrosis factor alpha are the proinflammatory cytokines that more often have been implicated in host tissue response, especially in periodontal and peri-implantar tissue destruction. Therefore, for a few years, research was concerned with studying the role of IL1 gene polymorphisms in the periodontal disease or in the prevision of the implant success.

Modelling the relationship between explanatory and response variables is a fundamental activity encountered in statistics. Simple linear regression is often used to investigate the relationship between a single explanatory (predictor) variable and a single response variable. When there are several explanatory variables, multiple regression is used. However, often the response is not a numerical value. Instead, the response is simply a designation of one of two possible outcomes (a binary response) e.g. alive or dead, success or failure. Although responses may be accumulated to provide the number of successes and the number of failures, the binary nature of the response still remains.

Data involving the relationship between explanatory variables and binary responses abound in just about every discipline from engineering to, the natural sciences, to medicine, to education, etc.

The aim of this work was to evaluate which clinical and nonclinical factors that may contribute to the success or no success in placing implants in order to build a decision model based on the importance of each factor and thus evaluate the performance of the model through ROC curve.

2 Methodology

The study protocol, approved by the Ethical Committee of the Dental Medicine Faculty of OPorto University (Portugal) was outlined following the legal norms.

Two hundred unrelated caucasian individuals, with systemic health, who had at least one osseointegrated dental implant, were included in the present study.

To all subjects were carried out a clinical history about general and oral health, a clinical examination with implant assay, occlusion analysis and prosthetic evaluation.

The statistical methodology used for selection of influential factors, given the nature of involved variables was the binary logistic regression.

In any regression problem the key quantity is the mean of the response variable given the value of the independent variable. This quantity is commonly known as conditional mean and can be expressed by $E(Y|x)$, where Y denotes the response variable x and correspond to the value of the independent variable. Consider $\pi(x) = E(Y|x)$. The specific form of the logistic regression model for a binary response variable and a vector of p covariates x , is:

$$\pi(x) = \frac{\exp(\beta_0 + \beta_1x_1 + \beta_2x_2 + \dots + \beta_px_p)}{1 + \exp(\beta_0 + \beta_1x_1 + \beta_2x_2 + \dots + \beta_px_p)} \tag{1}$$

and gives the expected value of probability according the model. The transformation of $\pi(x)$ is usually called *logit* transformation. This transformation is defined in terms of $\pi(x)$, as

$$g(x) = \ln \left(\frac{\pi(x)}{1 - \pi(x)} \right) = \beta_0 + \beta_1x_1 + \beta_2x_2 + \dots + \beta_px_p \tag{2}$$

The importance of *logit* transformation is the fact of being a linear function of the parameters β . We could define the odds of $Y = 1$ versus $Y = 0$, for the covariate values $x = a$ versus $x = b$, as:

$$\Psi(a, b) = \frac{P(Y = 1|x = a)/P(Y = 0|x = a)}{P(Y = 1|x = b)/P(Y = 0|x = b)} \tag{3}$$

In a model with a single covariate, where the dependent variable is binary, the slope of the *logit* coefficient is identical to the logarithm *odds ratio*:

$$\hat{\beta}_1 = \ln \left[\hat{\Psi}(a, b) \right] \Rightarrow \hat{\Psi}(a, b) = \exp(\hat{\beta}_1)$$

For continuous covariates, the interpretation of the coefficient of the logistic regression model can be made taking into account an appropriate increment.

To evaluate the performance of the model will be carried out an analysis through ROC curves.

The origin of Receiver Operating Characteristic (ROC) analysis can be traced to the theory of statistical decision making, related to applications in signal detection and psychology [7,8] and, over the years, has become a powerful tool to measure diagnostic performance in medicine [3,5].

The ROC analysis can be done through a simple graphical method, the so-called ROC curve, and the performance of a given test or diagnostic system can be measured by simple indices of accuracy associated with this curve, such as

the area below it [11]. The index area under the ROC curve (AUC) is one of the most widely used indexes to summarize the quality of testing in this case the process associated with success in placing dental implants.

The area under the ROC curve AUC can be seen as a global measure of accuracy across all possible threshold values (c).

$$AUC = \int_0^1 ROC(t)dt = \int_{-\infty}^{+\infty} TPR(c)dFPR(c) \quad (4)$$

3 Results

This study was conducted in a target population consisting of 200 caucasian Portuguese patients rehabilitated with dental implants, aged between 21 and 78 years, with a good general state of health, where 45 individuals were eliminated for the inability to obtain all the information required.

The final sample was constituted by 155 subjects that were divided into 2 groups: 100 with successful dental implants and 55 with no success of dental implants.

The sample of 155 individuals consists of 57.42% females, with the remaining 42.58% of male. The distribution of individuals according to sex for each result of the dependent variable is the same, that is, for the two possible outcomes, success and no success, the sample has almost the same distribution according to sex. A independence test of chi-square ($\chi^2 = 0.020$, $df = 1$, $p > 0.05$) reveals that was no statistically significant association between sex and outcome of the implant.

3.1 Logistic Regression

For the construction of logistic regression models were used initially 57 variables of clinical interest, which appeared to be determining factors for the success or no success of oral rehabilitation.

Dental hygiene (categorized in poor, regular or good dental hygiene), pathology of the oral mucosa, type of surgery of dental implant placement (categorized in simple surgery of dental implant placement, surgery of dental implant placement with bone graft and/or biomaterials or both) presence of suppuration around dental implants, presence of fistula around dental implants, presence of peri-implantitis around dental implants, presence of peri-mucositis around dental implants, dental implants lost, dental implants lost before placement of the prosthesis, dental implants lost after placement of the prosthesis, amount of attached gingiva around dental implants (categorized in none, < 2 mm or ≥ 2 mm), gingival phenotype (categorized in thin, regular or thick gingival phenotype), are some of the clinical factors considered.

We also considered some variables associated with genetic characteristics like presence of cytosine in position -889 of IL1A gene (Allele1IL1A), presence of thymine in position -889 of IL1A gene (Allele2IL1A), presence of cytosine in

position +3953 of IL1B gene (Allele1IL1B), presence of thymine in position +3953 of IL1B gene (Allele2IL1B), positive result of genetic test for periodontitis (TGP® positive), positive result of genetic test for periodontitis (TGP® negative), presence of cytosine in position -889 of IL1A gene and cytosine in position +3953 of IL1B gene (TGP® negative1), presence of cytosine in position -889 of IL1A gene and thymine in position +3953 of IL1B gene (TGP® negative2), presence of thymine in position -889 of IL1A gene and cytosine in position +3953 of IL1B gene (TGP® negative3).

Table 1 presents the results obtained from the analysis of the evaluation of the influence of each variable (factor) in the outcome variable (success, no success) by univariate process. In the present work taking into account the *p* values obtained in the Wald statistic, were considered as candidates to integrate the model the variables marked with light grey in the table. In this table we list:

- estimates for the slope coefficients of the univariate logistic regression model containing only this variable, **B**;
- the estimated standard error for the coefficient of the slope, **SE(B)**;
- Wald statistic, **W** and respectively *p* value;
- estimates for odds ratio, $\hat{\psi} = \exp(\mathbf{B})$.

Table 1. Univariate logistic regression

Covariate	B	SE(B)	W	<i>p</i> value	exp(B)
Sex	-0.048	0.34	0.02	0.887	0.953
Dental hygiene			0.267	0.875	
Dental hygiene(1)	0.211	0.788	0.072	0.789	1.235
Dental hygiene(2)	0.028	0.761	0.001	0.97	1.029
Pathologyoral mucosa	-21.838	28420.722	-	-	-
Surgery			2.679	0.262	
Surgery(1)	0.766	0.476	2.595	0.107	2.152
Surgery(2)	0.492	0.573	0.739	0.39	1.636
PSupuration	-22.282	8770.825	-	-	-
PFistula	-21.916	16408.711	-	-	-
Pperimplatitis	-22.864	6698.828	-	-	-
Pperimucosistis	-22.374	8204.356	-	-	-
ImplantLost	-21.899	4346.863	-	-	-
BeforeProsthesis	-22.441	7882.490	-	-	-
AfterProsthesis	-22.197	9473.574	-	-	-
Gingiva	0.718	0.269	7.137	0.008	2.05
TypeGin			8.326	0.016	
TypeGin(1)	0.908	0.365	6.2	0.013	2.48
TypeGin(2)	1.506	0.699	4.638	0.031	4.507
Metal	-21.958	14210.361	-	-	-

Table 1. (Continued)

Covariate	B	SE(B)	W	<i>p</i> value	exp(B)
Angle			2.18	0.336	
Angle(1)	-0.672	0.657	1.047	0.306	0.511
Angle(2)	-1.365	1.238	1.217	0.27	0.255
PostCrossbite	-1.742	1.167	2.228	0.136	0.175
Bruxism	-0.25	0.395	0.402	0.526	0.778
DentalMobility	-1.368	0.481	8.075	0.004	0.255
DentalFrictionFacets	-0.938	0.396	5.601	0.018	0.392
OpenBite	-1.039	0.929	1.252	0.263	0.354
OcclusalInt	-0.284	0.611	0.216	0.642	0.753
Mastication	-0.69	0.82	0.709	0.4	0.501
ImplantOcclusion	-0.496	0.323	2.353	0.125	0.609
MaxillaryEd	-0.563	0.171	10.811	0.001	0.569
MandibularEd	-0.367	0.199	3.387	0.066	0.693
OdentMax			0.565	0.754	
OdentMax(1)	-0.693	1.19	0.339	0.56	0.5
OdentMax(2)	-0.073	0.884	0.007	0.935	0.93
OdentMand			4.032	0.258	
OdentMand(1)	-0.811	1.384	0.343	0.558	0.444
OdentMand(2)	0.288	1.607	0.032	0.858	1.333
OdentMand(3)	0.991	0.784	1.598	0.206	2.695
MaxImpFP			6.373	0.956	
MandImpFP			3.692	0.978	
NatMaxFP			6.76	0.034	
NatMaxFP(1)	0.118	0.935	0.016	0.9	1.125
NatMaxFP(2)	1.028	0.396	6.732	0.009	2.795
NatMandFP			1.713	0.425	
NatMandFP(1)	0.563	0.43	1.713	0.191	1.757
NatMandFP(2)	-21.7	40192.970	-	-	-
EdMaxPRP	-1.238	0.739	2.801	0.094	0.29
EdMaxTotal	-0.633	0.728	0.755	0.385	0.531
EdMandPRP	0.259	0.758	0.116	0.733	1.295
EdMandTotal	-10.91	20096.485	-	-	-
Medication	-0.661	0.34	3.784	0.052	0.516
Diabetes	-0.615	1.014	0.367	0.545	0.541
Tumor	0.513	1.167	0.193	0.66	1.67
Qhemotherapy	-21.819	40192.970	-	-	-
Radiotherapy	20.615	40192.970	-	-	-
Tobaccotoday	-0.006	0.239	0.001	0.982	0.995
Tobacco5years	-0.049	0.21	0.053	0.817	0.953
Tobaccoafter	-0.097	0.137	0.507	0.477	0.907

Table 1. (Continued)

Covariate	B	SE(B)	W	<i>p</i> value	exp(B)
Wine	-0.117	0.342	0.117	0.732	0.89
wineQuantity	-0.087	0.152	0.326	0.568	0.917
Beer	-0.154	0.443	0.121	0.728	0.857
BeerQuantity	0.139	0.138	1.011	0.315	1.149
Whitespirits	-0.13	0.484	0.072	0.788	0.878
WhitespiritsQuantity	-0.061	0.208	0.086	0.769	0.941
Allele1IL1A	0.938	0.344	7.41	0.006	2.554
Allele2IL1A	-0.862	0.343	6.324	0.012	0.422
Allele1IL1B	0.764	0.346	4.881	0.027	2.146
Allele2IL1B	-0.764	0.346	4.881	0.027	0.466
TGP® positive	-0.812	0.352	5.318	0.021	0.444
TGP® negative	0.958	0.351	7.436	0.006	2.607
TGP® negative1	0.924	0.346	7.114	0.008	2.518
TGP® negative2	0.811	1.131	0.514	0.473	2.25
TGP® negative3	-0.272	0.524	0.269	0.604	0.762

The values marked with dark grey in Table 1 indicate an instability due to the variable in question in the Wald statistic and the values indicated with light grey are statistically significant for a significance level of 0.05. Although the *p* value for the covariate Medication ($p = 0.052$) is greater than the alpha value used, we consider it as a candidate to incorporate the model.

After this univariate selection of candidate variables to incorporate in the model we proceeded with the construction of five models. In the construction of multiple logistic regression models to variable selection technique was used the forward stepwise technique, in order to select a set of variables that could contribute to the outcome and that this contribution is reveal statistically significant. The objective is to achieve a model that contains all variables that are important with regard to pre-established criteria of p_E and p_R values (p values of entry and removal of the variable in the model) chosen so that they become statistically and clinically significant. The values chosen for this analysis were: $p_R = 0.20$ and $p_E = 0.15$.

Categorical variables were coded according to the technique referred to Hosmer and Lemenshow [4]. Considering different combinations of input variables, based on the information in Table 1, we obtained five possible models for describing the probability of success of implants listed in Table 2.

For example, based on Model 4, an individual with no attached gingiva (Gingiva (1) = 0 and Gingiva (2) = 0), tooth mobility (DentalMobility = 1) with no dental friction facets (DentalFrictionFacets = 0), without fixed prosthesis on natural teeth maxillary (NatMaxFP(1) = 0, NatMaxFP(2) = 0), with the absence of Allele IL1A (AlleleIL1A = 0) has an estimated probability by the model equal to 0.173, which represents a no success outcome considering a cutoff value of 0.5.

Table 2. Logistic regression models

	B	SE(B)	W	p value	exp(B)
Model 1 Allele1IL1A	1.121	0.376	8.888	0.003	3.068
NatMaxFP			9.177	0.010	
NatMaxFP(1)	-0.059	0.976	0.004	0.951	0.942
NatMaxFP(2)	1.298	0.432	9.014	0.003	3.663
Medication	-0.890	0.376	5.616	0.018	0.411
Constant	0.073	0.318	0.053	0.818	1.076
Model 2 TGP® negativel	1.068	0.376	8.041	0.005	2.908
NatMaxFP			8.749	0.013	
NatMaxFP(1)	-0.095	0.980	0.010	0.922	0.909
NatMaxFP(2)	1.255	0.429	8.556	0.003	3.508
Medication	-0.875	0.374	5.475	0.019	0.417
Constant	0.150	0.307	0.239	0.625	1.162
Model 3 TGP® negativel	1.015	0.373	7.412	0.006	2.760
NatMaxFP			7.904	0.019	
NatMaxFP(1)	0.060	0.970	0.004	0.951	1.062
NatMaxFP(2)	1.182	0.423	7.809	0.005	3.261
Medication	-0.848	0.371	5.236	0.022	0.428
Constant	0.024	0.340	0.005	0.944	1.024
Model 4 Gingiva			6.459	0.040	
Gingiva(1)	1.101	0.436	6.378	0.012	3.007
Gingiva(2)	0.442	0.580	0.581	0.446	1.556
DentalMobility	-1.290	0.574	5.045	0.025	0.275
DentalFrictionFacets	-1.265	0.472	7.186	0.007	0.282
NatMaxFP			8.831	0.012	
NatMaxFP(1)	-0.648	1.000	0.419	0.517	0.523
NatMaxFP(2)	1.354	0.477	8.069	0.005	3.872
Allele1IL1A	0.867	0.401	4.691	0.030	2.381
Constant	-0.276	0.383	0.520	0.471	0.759
Model 5 Allele1IL1A	0.938	0.344	7.410	0.006	2.554
Constant	0.114	0.239	0.228	0.633	1.121

3.2 ROC Curves

The five models were evaluated by analysis of their estimated probabilities. Based on the observed values of result variable and these estimates probabilities, we used the index area under the ROC curve to evaluate the performance of each model. The results are in Table 3.

In terms of value of the index area under the ROC curve we see that model 4 is the one with better discriminating power. A value of $AUC = 0.789$ means that in 78.9% of the cases, the regression model considered hits in prediction. Figure 1 shows the graph of the empirical ROC curves generated for the five models. The positive diagonal corresponds to the chance line in which there is no discriminating power.

In Fig. 1 the five empirical ROC curves are plotted in unitary plan. We can visualize in this graph that the ROC curve with the greatest value of the

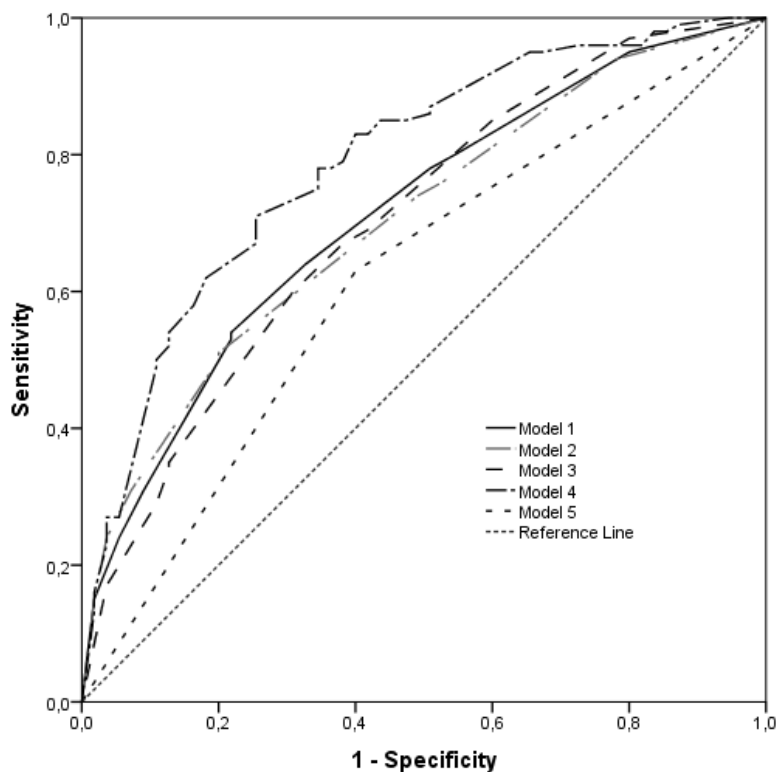
Table 3. Results of ROC analysis

Test Variable(s)	Area	Std. Error ^a	Asymptotic Sig. ^b	Asymptotic 95% CI	
				Lower Bound	Upper Bound
Model 1	0.712	0.042	< 0.001	0.629	0.795
Model 2	0.703	0.042	< 0.001	0.621	0.786
Model 3	0.702	0.044	< 0.001	0.616	0.787
Model 4	0.789	0.038	< 0.001	0.715	0.863
Model 5	0.615	0.047	0.018	0.522	0.708

^a Under the nonparametric assumption

^b Null hypothesis: true area = 0.5

index *AUC* corresponds to the model which presents a better performance, i.e., corresponds to the curve closest to the upper left corner in unitary ROC space.

**Fig. 1.** Empirical ROC curves for generated models

4 Conclusions

According to the results obtained it was found that, to measure the success and no success in the process of oral rehabilitation with implant placement, variables that can influence the process are the amount of attached gingiva around dental implants (Gingiva, categorized in none, < 2 mm or ≥ 2 mm), Dental Mobility, Dental Friction Facets, maxillary fixed prosthesis on natural teeth (NatMaxFP) and Allele 11L1A.

The different models took into account the values obtained in univariate analysis as well as the grouping of variables according to the nature of clinical and genetic factors. The performance assessment of different models estimated was based on the success and no success criteria defined in the literature ([2], [6] and [9]). It was found, through the index area under the ROC curve, that the Model 4 provide about 80% of the time properly. However, there would assessed, in cases where the observed value was not in agreement with that expected by the model, the factors which might have influenced the result.

Acknowledgments. This work is funded by FEDER Funds through the Operational Programme Competitiveness Factors - COMPETE and National Funds through FCT - Foundation for Science and Technology under the Project: FCOMP-01-FEDER-0124-022674.

References

1. Braga, A. C.: Curvas ROC: Aspectos funcionais e aplicações. Tese Doutorado. Universidade do Minho, (2001)
2. Gruica, B., Wang, H.Y., Lang, N.P. & Buser, D.: Impact of IL-1 genotype and smoking status on the prognosis of osseointegrated implants. *Clinical Oral Implants Research*, 15, 393-400 (2004)
3. Hanley JA, McNeil BJ.: The Meaning and Use of the Area under a Receiver Operating Characteristic ROC Curve. *Radiology*. 143, 29-36 (1985)
4. Hosmer, D., Lemeshow, S.: *Applied Logistic Regression*. John Wiley & Sons (1989)
5. Metz CE.: *Statistical Analysis of ROC Data in Evaluating Diagnostic Performance*. In: Herbert D, Myers R, editors. *Applications in the Health Sciences*. American Institute of Physics, 13, 365-84 (1986)
6. Misch, C.E., Perel, M.L., Wang, H.L., Sammartino, G., Galindo-Moreno, P., Trisi, P., Steigmann, M., Rebaudi, A., Palti, A., Pikos, M.A., Schwartz- Arad, D., Choukroun, J., Gutierrez-Perez, J.L., Marenzi, G. & Valavanis, D.K.: Implant success, survival, and failure: the International Congress of Oral Implantologists (ICOI) Pisa Consensus Conference. *Implant Dentistry* 17, 5-15 (2008).
7. Swets JA, Pickett RM.: *Evaluation of Diagnostic Systems Methods from Signal Detection Theory*. London: Academic Press (1982)
8. Swets JA.: *Signal Detection Theory and ROC Analysis in Psychology and Diagnostics*. Collected Papers. New Jersey, LEA (1996)
9. Vaz P., Gallas M.M., Braga A.C., Sampaio-Fernandes J.C., Felino A., Tavares P.: IL1 gene polymorphisms and unsuccessful dental implants. *Clinical Oral Implants Research* Nov 10. (2011) doi: 10.1111/j.1600-0501.2011.02322.x.

Multiscale Modeling of Heterogeneous Media Applying AEH to 3D Bodies

Bárbara de Melo Quintela, Daniel Mendes Caldas,
Michèle Cristina Resende Farage, and Marcelo Lobosco

Federal University of Juiz de Fora
{barbara,daniel.caldas}@ice.ufjf.br,
{michele.farage,marcelo.lobosco}@ufjf.edu.br
<http://www.ufjf.br/mmc/>

Abstract. The Asymptotic Expansion Homogenization (AEH) is a multiscale technique applied to estimate effective properties of heterogeneous media with periodic structure. The main advantages of AEH are the reduction of the problem size and the ability to employ an homogenized property that keeps information from the heterogeneous microstructure. The aim of this work is to develop a parallel program that applies both Finite Element Method (FEM) and AEH to estimate the elasticity properties of 3D bodies. A sequential version of the program, called HEA3D, was successfully implemented using FORTRAN. Also, a parallel version of the code was implemented using OpenMP and CUDA. The validation of the codes consisted of comparisons of the numerical results obtained, with numerical and experimental data available in the literature, showing good agreement. Significant speedups were obtained by the parallel version of the code.

1 Introduction

The Asymptotic Expansion Homogenization (AEH) is a multiscale technique applied to the estimation of effective properties of heterogeneous media with periodic microstructure. It has been successfully applied to heterogeneous materials such as composites with carbon nanotubes, concrete with different aggregates and even bones - to simulate bone regeneration [1-3].

In association with the Finite Element Method (FEM), the AEH requires the application of periodic boundary conditions, which must be taken into account during the generation of FE meshes. Such models represent periodic cells, which are representative volumes for heterogeneous media and, in some cases, present a geometric and physics complexity that demands refined meshes, leading to a significant computational cost.

A sequential version of the 2D program using C, and parallel versions using OpenMP and CUDA were implemented in a previous work [4]. The aim of this work is to develop a new parallel version of the program to estimate the elasticity properties of 3D bodies, using for this purpose both FEM and AEH. Again, OpenMP and CUDA were used in the parallelization of the code. Significant

speedups were obtained by the parallel version of the code, achieving speedups up to 5.3 times over its sequential version, a value very close to the maximum speedup that could be obtained according to the Amdahl's law.

The paper is organized as follows. Section 2 presents the Asymptotic Expansion Homogenization technique, while section 3 presents its sequential implementation. Section 4 discusses the parallelization approach. Sections 5 and 6 present numerical results and the speedups obtained, respectively, while Section 7 presents the conclusions of the work.

2 AEH Applied to Linear Elasticity

This section presents a brief description of the AEH technique applied to linear elasticity. The detailed description of the AEH formulation may be found in references [5, 6].

The Asymptotic *Expansion Homogenization* (AEH) is a multiscale technique relying on the assumption that a heterogeneous medium may be represented by a homogeneous periodic counterpart. The technique is based on the uncoupling of the different scales of a material, extrapolating the results from inferior or heterogeneous scales in order to obtain global or homogenized properties [6-9]. As applying the AEH, a very important aspect is the definition of the geometric and physical characteristics of the periodic cell, which is the smallest microstructural volume able to statistically represent the global constitutive behaviour of the medium. By knowing the heterogeneous properties of a cell, it is assumed that those properties are periodically repeated over the structure. Basically, in periodic structures that present two scales, the AEH consists of uncoupling those scales into a *microscale* and a *macroscale*.

In practical purposes, the main interest is getting to know the global behaviour of a heterogeneous body - such as a composite structure - by considering that the heterogeneities dimensions tend to zero [10]. The coefficients of the describing differential equations are the characteristics of the studied material, depending on ϵ , which is a scale parameter that relates the microscale to the macroscale. Concerning a composite with a ϵ -periodic distribution, those coefficients are not easy to evaluate. Consideration of the limit case of $\epsilon \rightarrow 0$ leads to a *homogenized* problem, with constant coefficients that may be calculated with the help of numeric techniques, such as the Finite Element Method [6, 10].

By considering a material whose microstructure is composed of multiple phases, periodically distributed over the body [6, 11], the periodic elastic material properties are defined by the following relation:

$$D_{ijkl}^\epsilon = D_{ijkl} \left(\frac{x}{\epsilon} \right), \quad (1)$$

where $()^\epsilon$ identifies quantities related to the *actual* non-homogeneous medium; the function D_{ijkl}^ϵ stands for the material's properties variations in the heterogeneous microstructure Y .

The linear elasticity problem is described by the equilibrium equation Eq. (2), boundary conditions Eq. (3) and Eq. (4), strain-displacement relation Eq. (5) and constitutive relation Eq. (6):

$$\frac{\partial \sigma_{ij}^\epsilon}{\partial x_j^\epsilon} + f_i = 0 \text{ in } \Omega; \tag{2}$$

$$u_i^\epsilon = 0 \text{ in } \partial_1 \Omega; \tag{3}$$

$$\sigma_i^\epsilon n_j = F_i \text{ in } \partial_2 \Omega; \tag{4}$$

$$\varepsilon_{ij}(u^\epsilon) = \frac{1}{2} \left(\frac{\partial u_i^\epsilon}{\partial x_j^\epsilon} + \frac{\partial u_j^\epsilon}{\partial x_i^\epsilon} \right); \tag{5}$$

$$\sigma_{ij}^\epsilon = D_{ijkl}^\epsilon \varepsilon_{kl}(u^\epsilon), \tag{6}$$

where σ_{ij}^ϵ is the ij term of the internal stresses tensor and f_1 is the body force in the dominium Ω ; u_i^ϵ is the displacement in direction i ; n_j is the vector normal to the boundary $\partial\Omega$ and F_1 is the external force applied on the boundary and ε_{ij} is the ij term of the strains tensor.

The displacements are approximated by an asymptotic series in ϵ , given by Eq. (7):

$$u_i^\epsilon(x^\epsilon) = u_i^{(0)}(x, y) + \epsilon u_i^{(1)}(x, y) + \epsilon^2 u_i^{(2)}(x, y) + \dots, \tag{7}$$

where $u_i^{(0)}$ is the macroscopic displacement and $u_i^{(1)}, u_i^{(2)}, \dots$ stand for the periodic displacements in more refined scales.

As the heterogeneous *actual* medium is represented by two coordinate systems (x and $y = x/\epsilon$), the derivatives originally in x^ϵ must be expanded in a chain rule given by:

$$\frac{\partial}{\partial x_i^\epsilon} = \frac{\partial}{\partial x_i} + \frac{1}{\epsilon} \frac{\partial}{\partial y_j}. \tag{8}$$

In order to obtain the uncoupled equations that describe the microscale and the macroscale problems, the displacement u_i is replaced by Eq. (7) in the set of equations Eq. (2) to Eq. (6). The basis of the approximation is the assumption of $\epsilon \rightarrow 0$, indicating that the number of periodic cells tends to infinity and the actual non-homogeneous structure is then approximated by a homogeneous one (Figure 2).

In order to validate such an approximation, the resulting coefficients of ϵ with negative exponent must be identically nulls. That leads to hierarchical equations that, along with appropriate boundary conditions and a sequence of steps, result in an auxiliary variational problem given by Equation 9.

$$\int_Y D_{ijkl} \frac{\partial \chi_k^{ij}}{\partial y_l} \frac{\partial v_i}{\partial y_j} dy = \int_Y v_j \frac{\partial D_{ijkl}}{\partial y_i} dY. \tag{9}$$

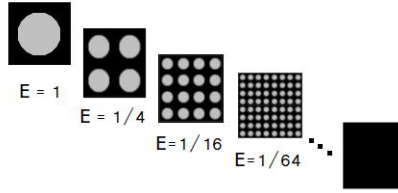


Fig. 1. Approximation of non-homogeneous periodic structure by an equivalent homogeneous one when $\epsilon \rightarrow 0$

After solving this problem, the homogenized elastic properties tensor is, finally, given by Eq. (10):

$$D_{ijkl}^h = \frac{1}{Y} \int_Y D_{ijkl}(y) \left[I_{ij}^{kl} - \frac{\partial \chi^{kl}}{\partial y_l} \right] dY, \tag{10}$$

where Y is the volume of the periodic body, χ is the variational Finite Element problem solution and D_{ijkl}^h is the solution of the microscale problem. Detailed information on this subject is found in reference [11].

2.1 FEM Applied to AEH

Elastic Corrector. The elastic corrector (χ) evaluation, by solving the system given by the Equation 9, is composed by n vectors, where n is the number of columns within the elastic matrix to be determined. These vectors are similar to displacement ones and gives the eigendeformations of the periodic cell. Applying FEM, the Equation 9 is rewritten as follow:

$$\sum_{i=0}^{nelm} \int_{Y_e} B^T D B dY \chi = \overbrace{\sum_{i=0}^{nelm} \int_{Y_e} B^T D dY}^{F^D}, \tag{11}$$

in which B is the differential operator, D is the elastic tensor, Y_e is the volume and $nelm$ is the total number of finite elements. F^D is then described as equivalent nodal charges and χ function is obtained from these approximations.

Periodic Boundary Conditions. The solution of the Equation (11), (χ_k^{ij}) , is obtained employing periodic boundary conditions of $u_k^{(1)}(x, y), k = 1, 2, 3$. Wang [12] explains these conditions through the following example: if the periodic cell were an hexahedron, as the one shown in Figure 2, the 6 faces could be described by Equation (12):

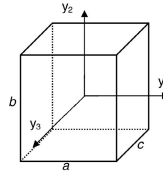


Fig. 2. Unit representative hexahedric cell. Adapted from [12].

$$(y_1, y_2, y_3)|_{face1}^{face3} = \left(\pm \frac{a}{2}, y_2, y_3 \right), \tag{12}$$

$$(y_1, y_2, y_3)|_{face2}^{face4} = \left(y_1, \pm \frac{b}{2}, y_3 \right),$$

$$(y_1, y_2, y_3)|_{face5}^{face6} = \left(y_1, y_2, \pm \frac{c}{2} \right),$$

where a , b and c are the edges lengths in directions y_1 , y_2 e y_3 , respectively. The periodic boundary conditions of $u_k^{(1)}$ require, thus, the following:

$$u_k^{(1)}|_{face1} = u_k^{(1)}|_{face3}, \tag{13}$$

$$u_k^{(1)}|_{face2} = u_k^{(1)}|_{face4},$$

$$u_k^{(1)}|_{face5} = u_k^{(1)}|_{face6}.$$

As the solution $\tilde{u}_k^{(1)}$ does not depend on y , Equation (13) could be rewritten as:

$$\chi_k^{ij}|_{face1} = \chi_k^{ij}|_{face3}, \tag{14}$$

$$\chi_k^{ij}|_{face2} = \chi_k^{ij}|_{face4},$$

$$\chi_k^{ij}|_{face5} = \chi_k^{ij}|_{face6},$$

adopting $\tilde{u}_k^{(1)} = 0$. Therefore, the characteristic function χ could be completely determined from Equations (11) and (14). To avoid rigid body motion, the displacements and rotations must be restrained [13].

Homogenized Elastic Matrix. After calculating χ component vectors, the homogenized elastic matrix (D^h) is determined applying Equation (10), rewritten in discrete form:

$$D^h = \sum_{k=1}^{nelm} \frac{Y^k}{Y} D^k (I - B^k \chi^k), \tag{15}$$

in which $nelm$ is the number of elements in unit cell; Y^k is the k element volume; Y is total cell volume; I is the identity matrix; B^k is the differential operator and χ^k is the nodal values of χ matrix associated to k element. If $\chi = 0$ the Equation (15) represents the arithmetic average of elastic properties of the finite elements belonging to the cell model. The AEH applied to Elasticity through FE method procedure could be summarized to [11]:

1. Identification of periodic cell which better represents the problem;
2. Discretization of the periodic cell with Finite Elements;
3. Solution of the system of equations described by (11), evaluating vectors that form χ ;
4. Evaluation of the average operation described by Equation (15), obtaining the homogenized tensor D^h .

3 Sequential Version

The sequential implementation of the HEA in its 3D version was implemented in FORTRAN. It is based on a program developed at COPPE/UFRJ [14] which was originally employed to analyse non-linear 3D mechanical problems using the *FEM* (Finite Element Method). This original program presents the following main features:

- i. Four node tetrahedral elements;
- ii. Pre-conditioned Conjugate Gradients (CG) Numerical Method to solve the system of linear equations with *EBE* (Element-by-Element) strategy to avoid assembly of global stiffness matrix [15];
- iii. Disjoint blocks of elements. The matrices elements are organized in such a way that there are several blocks, each one containing a number of element matrices which does not share common global nodes. This leads to a scenario where it is possible to explore parallel computation. In particular, it avoids race conditions when the final result is computed.

The main extensions made in this original code to evaluate homogenized elastic properties were: (a) inclusion of the periodic boundary conditions; (b) Assembly of the independent variables (right-hand side); and (c) Computation of homogenized matrix.

To solve the system equations, it is necessary to call the routine *pcgdiag* six times - for each of the six columns of the right-hand side. This routine solves each column sequentially employing the CG method. These calls are independent and could be run simultaneously exploring a multiprocessor configuration.

3.1 Matrix-Vector Multiplication

After its implementation, the code was instrumented in order to detect the most time-consuming routines. As expected, the hot spot of our sequential code is the resolution of the system of algebraic equations, once the analysis consists of a variational *FEM* problem with dg degrees of freedom. The instrumentation of the code revealed that CG method, used in the resolution of a system of algebraic equations, is responsible for about 85% of the total computation time. One of the routines that is used by the CG method is *smatv*, which computes the matrix-vector multiplication. A pseudo-code of this routine is shown below.

Sequential SMATV Routine

```

1. BEGIN
2.   ielm = 0
3.   FOR i = 1 TO nelblk
4.     nvec = block dimension
5.     FOR ke = ielm + 1 TO ielm + nvec
6.       find element nodes (no1,no2,no3,no4)
7.       find element equations
8.       FOR j = 1 TO 4
9.         IF (noj is periodic)
10.          exchange the equation with correspondent master node
11.        END IF
12.      END FOR
13.      multiply element matrix of index i by vector
14.      collects at correspondent global equation
15.    END FOR
16.    ielm = ielm + nvec
17.  END FOR
18. END

```

In this code, the variable *ielm* is used to control the index of the element inside the block; *nelblk* is the total amount of blocks and *nvec* is the size of the current block. The *SMATV* routine calculates the element's equations (lines 6 and 7) and proceeds with the matrix-vector multiplication (line 13). The four-noded tetrahedral elements have twelve equations to be solved - three degrees of freedom for each node. Finally, *SMATV* returns the result of the matrix-vector multiplication operation in a single global vector (line 14).

4 Parallel Versions

4.1 OpenMP

OpenMP (*Open Specifications for Multi Processing*) [16] offers a programming interface for shared memory parallel machines. The programmer uses compilation directives to identify the portions of the source code that should be executed in parallel. The programmer can also specify how the code should be executed.

It was adopted two different approaches to explore the OpenMP directives in HEA, which are the parallelization of:

- *PCGDIAG* routine calls to solve six columns simultaneously,
- Matrix-vector multiplication inside *SMATV* routine with element matrices organized in blocks without sharing nodes so that these blocks can be multiplied simultaneously without synchronization.

4.2 CUDA

A General Purpose Graphics Processing Units (GPGPUs) is a specialized hardware initially designed to accelerate the building of images intended for output

to a display. GPGPUs are now widely used in distinct hardware platforms, such as mobile phones, personal computers, and game consoles. Their highly parallel architecture made them a natural choice for algorithms where processing of large amounts of data can be done in parallel.

In order to take advantage of the wide availability of GPUs in personal computers and their highly parallel architecture, a parallel version of the *SMATV* code was implemented. CUDA was used for this purpose.

NVIDIA's CUDA (Compute Unified Device Architecture) [17] is a massively parallel high-performance computing platform on GPGPUs. CUDA includes development tools and libraries to hide the GPGPUs hardware from programmers.

In GPGPU, a parallel function is called kernel. A kernel is a function callable from the CPU and executed on the GPU simultaneously by many threads. Each thread is run by a stream processor. They are grouped into blocks of threads or just blocks. A set of blocks of threads form a grid. When the CPU calls the kernel, it must specify how many threads will be created at runtime. The syntax that specifies the number of threads that will be created to execute a kernel is formally known as the execution configuration, and is flexible to support CUDA's hierarchy of threads, blocks of threads, and grids of blocks.

Since all threads in a grid execute the same code, a unique set of identification numbers is used to distinguish threads and to define the appropriate portion of the data they must process. These threads are organized into a two-level hierarchy composed by blocks and grids and two unique coordinates, called `blockId` and `threadId`, are assigned to them by the CUDA runtime system. These two build-in variables can be accessed within the kernel functions and they return the appropriate values that identify a thread.

Some steps must be followed to use the GPU: first, the device must be initialized. Then, memory must be allocated in the GPU and data transferred to it. The kernel is then called. After the kernel have finished, results are transferred back to the CPU. Data transfer to/from the GPU memory is an expensive operation, so that it is important to minimize it in order to improve the performance of a parallel code.

Parallel Version of *Smatv* Using CUDA. A number of linear algebra packages are available for developers to enhance productivity during development of applications. A few examples in FORTRAN are CUBLAS and CULA, which are CUDA parallel versions of BLAS and LAPACK, respectively [18, 19]. Since the EBE strategy is adopted in the HEA code, it is not possible to adopt such packages keeping HEA original structure. For this reason, the parallel version of *smatv* was developed using CUDA. This routine was developed using the C programming language and linked to the HEA FORTRAN code.

The *SMATV* routine computes the matrix-vector multiplication of each element matrix, and this multiplication is made element by element, in disjoint blocks, what makes it ideal for parallelization. The disjoint characteristic of the element blocks makes the results of this matrix-vector multiplications to occupy distinguish positions in the result vector, therefore the threads that run concurrently in the GPU can compute its equations in parallel, without the concern of

writing in a memory position that is being used by another thread. Thus, the definition of critic sessions in the code is not necessary. Besides that, in some scenarios the routine is called more than 1000 times, changing only the data it is going to operate on, another desirable characteristic when working with parallel computing in GPGPUs.

To implement the parallel part of the code, the sequential *for* that was used to calculate the equations of each element in the block was substituted by a *kernel* call. Instead of a *for* with n iterations a *kernel* call is made by n threads. These threads are divided in blocks of threads, in a way that each block have 256 threads.

The sequential *for* is shown below:

```
1. for(ke = ielm+1; ke <= ielm+nvec; ke++){
```

In the parallel execution it was replaced by the following code:

```
1. int blocksize = 256
2. n_blocks = nvec/block_size + (nvec\%block_size == 0 ? 0:1);
3. smatv_cuda<<<n_blocks, block_size>>>(parameters);
```

The *kernel* function executes the same code that was executed by one iteration of the sequential inner *for*, but in parallel by many *threads*. the pseudo-code of the kernel function is as it follows:

```
1. find element nodes (no1,no2,no3,no4)
2. find element equations
3. FOR j = 1 TO 4
4.   IF (noj is periodic)
5.     exchange the equation with correspondent master node
6.   END IF
7. END FOR
8. multiply element matrix of index i by vector
9. collects at correspondent global equation
```

In order to avoid excess of memory transfers a function to allocate the variables in the GPU was created too. This function allocates and copies the values of the variables to the GPU outside the iterations of the method where the *SMATV* is called. Thus, only two memory copies are made between the CPU and the GPU at each call of the *SMATV* function. One before the *SMATV* routine, to copy the vector to the GPU memory, and one after, to get the result vector back to the CPU.

5 Numerical Experiments

Aiming to compare the performance of the sequential and parallel versions of the program, three distinct types of periodic cubic cells were considered to represent

composite materials. These cells are composed of two distinct phases: matrix and inclusion. Figure 3(a) shows a cubic cell representing a periodic part of a laminate material where the inclusion takes 20% of the microstructure. Figures 3(b) and 3(c) represent the same composite material reinforced with long fibres of circular transversal section occupying 47% of the cell.

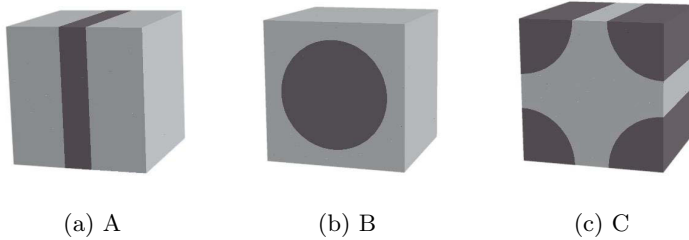


Fig. 3. Different periodic cells used to model distinct material microstructures: A - Laminate Material (20% inclusion); B and C - cylindric reinforcements (47% inclusion)

In order to validate our model, we assumed that the Poisson coefficient is null for Cell A (Fig. 3(a)). Employing the rule of mixtures - without considering the Poisson coefficient - the values of the Young moduli over directions 1, 2 and 3, as shown in Figure 4, can be obtained analytically [20]. The elasticity moduli

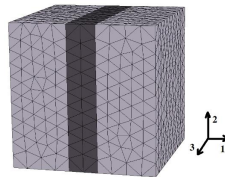


Fig. 4. Example of a linear tetrahedral finite element mesh over the geometry of a laminate microstructure

over direction 1 must be equal to E_{min} and directions 2 and 3 must present the same property, both equal to E_{max} (represented by Equations 16 and 17, respectively).

$$E_{max} = f_i \times E_i + (1 - f_i) \times E_m \tag{16}$$

$$E_{min} = \frac{(E_i \times E_m)}{(f_i \times E_m + (1 - f_i) \times E_i)} \tag{17}$$

in which E_{max} and E_{min} are, respectively, maximum and minimum composite elastic moduli, f_i is the volumetric fraction of the inclusion, E_i is the Young moduli of the inclusion and E_m is the Young moduli of the matrix.

Another validation experiment was performed comparing the results obtained with both cells B and C (Fig. 3(b) and Fig. 3(c)) to the values found in literature [13]. Two types of data were available for comparison purposes: characteristic displacements and the Frobenius norm of the homogenized tensor. The characteristic displacements or deformations are the result of the system solver procedure, which is an intermediate step of the homogenization, where each column gives a different eigenshape. The characteristic displacement obtained for Cell C (3(c)) compared to results found in literature [13] is shown in Figure 5. The HEA3D shear eigenshapes χ_{23} , χ_{13} and χ_{12} are presented in the right while the values from literature are presented in the left.

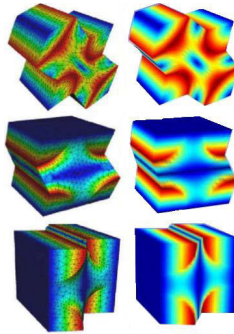


Fig. 5. Characteristic displacements. Values found in the literature [13] on the left side while values obtained from HEA3D using a linear tetrahedral mesh with 76131 degrees of freedom are presented on the right side.

The parameters employed within the analysis are given in Table 1.

Table 1. Mechanical properties of matrix and inclusion used for validation purposes

Property	value
Elasticity moduli of inclusion, E_i (GPa)	379.3
Poisson of inclusion, ν_i	0.1
Elasticity moduli of matrix, E_m (GPa)	68.3
Poisson of matrix, ν_m	0.3

The convergence of the method can be computed through the stabilization of the Frobenius norm (Equation 18) of the resulting homogenized matrix - D_h .

$$\|D_h\|_F = \sqrt{\sum_{i=1}^n \sum_{j=1}^n (d_h^{ij})^2} \quad , \tag{18}$$

where D_h is the homogenized matrix, n is the matrix order and d_h^{ij} is the ij^{th} term of the D_h matrix. The evolution of the norm, as the number of degrees of freedom increases, is shown in Figure 6.

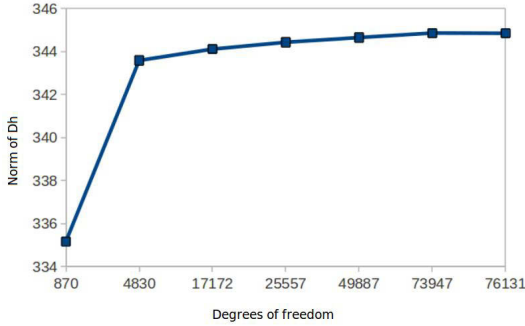


Fig. 6. Evolution of the Frobenius norm of the resulting homogenized matrix - Dh - as the number of the degrees of freedom of the system increases

6 Speedups

In this section, we present the speedups obtained with the parallel versions of our code. Both the sequential and parallel implementations have been tested on a dual Intel Xeon E5620 processors each with 4 cores, so 8 physical cores are available. Each core with 64 Kb cache L1 and 256Kb L2 and Hyper-threading (HT) which gives the support to 16 simultaneous threads per processor. This machine has a Tesla M2050 GPU, with 448 cores and 2.6 GB of global memory. The speedup factor was used to evaluate gains obtained by the parallel versions of the code over the sequential one. The acceleration can be calculated employing the following equation 6:

$$S(p) = \frac{t_s}{t_p}, \quad (19)$$

where t_s is sequential execution time and t_p is parallel execution time with p processors.

The execution times obtained by all versions of the code was measured 5 times and the standard deviation was lower than than 5%. Each execution of the code was measured using the Linux *time* application.

Three different types of domains were evaluated: cell A (Fig. 3(a)), cell B (Fig. 3(b)) and cell C (Fig. 3(c)) with five levels of refinement each.

6.1 OpenMP

Two distinct approaches were used in the parallelization of the code with OpenMP:

- The parallelization of the calls to *PCGDIAG* routine, in order to solve the six columns of the matrix simultaneously;
- The parallelization of the *SMATV* routine.

To simplify the comprehension of OpenMP results, the first approach is referenced as PD (*PCGDIAG*) and the second as ST (*SMATV*).

Table 2 presents the gains obtained for PD parallel version of the code. All experiments were performed using six processors - maximum number of threads required to evaluate simultaneously each column of the system. As an example, for input mesh A_1 the maximum speedup that could be obtained, according to the Amdahl's law [21], is 5.5. It is shown in the Table 2 that this approach, for this case, was 5.3 times faster than the sequential version, which is close to the maximum it could be reached.

Table 2. PD speedups obtained for A, B and C cell with distinct refinement. DFs = Degrees of Freedom.

Meshes	DFs	<i>Sps</i>	Meshes	DFs	<i>Sps</i>	Meshes	DFs	<i>Sps</i>
A_1	3231	5.3	B_1	10827	4.9	C_1	17172	4.6
A_2	4590	5.2	B_2	13884	5.1	C_2	25557	4.3
A_3	6264	5.1	B_3	30939	4.9	C_3	49887	4.0
A_4	10764	4.8	B_4	49845	4.3	C_4	73947	3.6
A_5	13668	5.2	B_5	57855	3.9	C_5	76131	3.5

It can be observed that instead of increasing, as the meshes become larger, the gains decreases. This could be explained by the fact that the input operations also increases with the input data and that this whole computation time is considered in the evaluation of the speedups.

For the ST approach, both the meshes and the number of threads were varied. The number of threads was limited to 16 because this is the maximum number of threads supported by the architecture. Table 3 present the speedups obtained with the input meshes representing cells A, B and C.

As one can observe, in general the speedup increases as number of cores increases. However, this is not observed for some cases when the number of cores increases from 8 to 16. It can be explained because the processor has in fact only 8 physical cores. The HT technology allows fast context switch between the threads but in all cases 16 threads are competing for using 8 physical cores. The context switch occurs mainly when there is an expensive failure, such as access to the L3 cache, main memory or I/O operations. Since some cell meshes are really small, they can fit entirely into L1 and L2 caches, so in these cases less expensive failures occurs leading to real competition between threads, which in turn decreases the gains.

Table 3. ST speedups for cells A, B and C with distinct refinements and number of threads

Mesheres	<i>Sps</i> 2	<i>Sps</i> 4	<i>Sps</i> 6	<i>Sps</i> 8	<i>Sps</i> 16
A_1	1.6	1.6	2.1	2.2	2.1
A_2	1.1	1.7	2.2	2.5	2.4
A_3	1.0	1.7	2.2	2.5	2.4
A_4	1.7	2.7	3.9	4.0	3.9
A_5	1.4	2.2	2.9	3.5	3.3
B_1	2.2	2.6	3.4	4.2	4.0
B_2	1.7	2.1	2.8	3.4	3.3
B_3	1.1	1.9	2.6	3.1	3.8
B_4	1.1	2.1	2.7	3.2	3.5
B_5	1.1	2.0	2.6	3.1	3.3
C_1	1.4	2.6	3.3	4.1	4.3
C_2	1.1	1.9	2.4	3.0	3.1
C_3	1.1	2.0	2.7	3.3	3.8
C_4	1.1	1.7	2.3	2.6	2.8
C_5	1.1	2.0	2.5	2.9	3.0

6.2 CUDA

To evaluate the performance gains of the CUDA implementation, the same cell configurations used in the OpenMP experiments were set. Table 4 presents the gains obtained for the CUDA parallel version of the code.

Table 4. CUDA speedups obtained for A, B and C cell with distinct refinements

Mesheres	<i>Sps</i>	Mesheres	<i>Sps</i>	Mesheres	<i>Sps</i>
A_1	0.2	B_1	1.0	C_1	1.6
A_2	0.2	B_2	1.0	C_2	1.7
A_3	0.3	B_3	–	C_3	2.3
A_4	1.2	B_4	2.1	C_4	3.8
A_5	1.1	B_5	2.4	C_5	2.1

The better speedup was obtained when using the C_4 mesh. The execution of the CUDA code for this mesh was 3.8 times faster than the sequential code. As the table shows, the code presents a slow down when small meshes are used (A_1, A_2 and A_3). This can be explained because the parallel overhead in copying the variables and making the calls to the GPU kernel are bigger than the gain obtained with the parallelization of the *for* loop in the GPU. In other words, the number of the iterations of the original loop in the sequential version is too small. As the size of the cell and its level of refinement increases, the amount of data that is processed concurrently at each time step gets higher and the time saved gets bigger, overcoming the parallel overhead. Therefore, the CUDA implementation starts to gain some advantage over the sequential one. It can also be noticed that

the speedup decreases when using the C_5 type of cell, when compared to C_4 cell. This can be due to the same reason that makes the speedup gain decrease as the meshes become larger in the OpenMP implementation: the input operations also increases with the use of a larger mesh, overcoming the time saved from the parallel processing.

7 Conclusion

This work presented a parallel implementation of the asymptotic expansion homogenization (AEH) technique using both CUDA and OpenMP. The experiments indicate that the parallelization was effective in improving the performance, providing gains up to 5.3, a value very close to the maximum speedup that could be obtained according to the Amdahl's law, 5.5. However, surprisingly this result was obtained using OpenMP. We believe that the CUDA version of the code could obtain a similar performance. In particular, CUDA's performance could be improved moving the solver code completely to the GPU would have a huge impact on computational time as it would avoid memory transfers at every iteration of the CG method. Also, the use of multiple GPUs to solve the six system equations could contribute to improve the performance of CUDA version of the code.

Acknowledgements. The authors would like to thank FAPEMIG, CNPq, CAPES and UFJF for supporting this study.

References

1. Kim, M., Park, Y.-B., Okoli, O.I., Zhang, C.: Processing, characterization, and modeling of carbon nanotube-reinforced multiscale composites. *Composites Science and Technology* 69(3-4), 335–342 (2009)
2. Lee, K., Park, J.: A numerical model for elastic modulus of concrete considering interfacial transition zone. *Cement and Concrete Research* 38(3), 396–402 (2008)
3. Sanz-Herrera, J., Garcia-Aznar, J., Doblare, M.: On scaffold designing for bone regeneration: A computational multiscale approach. *Acta Biomaterialia* 5(1), 219–229 (2009)
4. Quintela, B.M., Farage, M.C.R., Lobosco, M.: Evaluation of effective properties of heterogeneous media through a GPGPU based algorithm. In: XXXI CILAMCE, vol. XXIX, pp. 7085–7094 (2010)
5. Quintela, B.M.: Implementação Computacional Paralela da Homogeneização por Expansão Assintótica para Análise de Problemas Mecânicos em 3D: Master's Thesis. Federal University of Juiz de Fora, Juiz de Fora (2011) (in Portuguese)
6. Sanchez-Palencia, E.: Non-homogeneous media and vibration theory. *J. Ehlers Lecture Notes in Physics*. Springer (1980)
7. Murad, M.A., Guerreiro, J.N., Loula, A.F.D.: Micromechanical computational modeling of secondary consolidation and hereditary creep in soils. *Comput. Methods Appl. Mech. Engrg.* 190, 1985–2016 (2001)
8. Murad, M.A., Moyne, C.: Micromechanical computational modeling of expansive porous media. *C. R. Mechanique* 330, 865–870 (2002)

9. Romkes, A., Oden, J.T.: Adaptive modeling of wave propagation in heterogeneous elastic solid. *Comput. Methods Appl. Mech. Engrg.* 193, 539–559 (2004)
10. Cioranescu, D., Donato, P.: *An Introduction to Homogenization*, 1st edn. Oxford University Press (1999)
11. Chung, P.W., Tamma, K.K., Namburu, R.R.: Asymptotic expansion homogenization for heterogeneous media: computational issues and applications. *Composites: Part A* 32, 1291–1301 (2001)
12. Wang, W., Luo, D., Takao, Y., Kakimoto, K.: New solution method for homogenization analysis and its application to the prediction of macroscopic elastic constants of materials with periodic microstructures. *Computers & Structures* 84(15–16), 991–1001 (2006)
13. Oliveira, J., Da Cruz, J.P., Teixeira-Dias, F.: Asymptotic homogenisation in linear elasticity. Part II Finite element procedures and multiscale applications. *Computational Materials Science* 45, 1081–1096 (2009)
14. Coutinho, A.L.G.A., Martins, M.A.D., Alves, J.L.D., Landau, L., Moraes, A.: *A Edge-Based Finite Element Techniques for Nonlinear Solid Mechanics Problems*. *Int. J. Num. Meth. Eng.* 50, 2053–2058 (2000)
15. Liu, Y., Zhou, W., Qiang, Y.: A distributed memory parallel element-by-element scheme based on Jacobi-conditioned conjugate gradient for 3D finite element analysis. *J. Eng. Mech.* (1983)
16. Chapman, B., Jost, G., Van Der Pas, R.: *Using OpenMP: Portable Shared Memory Parallel Programming*. Scientific and Engineering Computation. The MIT Press (October 2007)
17. Nvidia: *Nvidia Cuda Programming Guide 2.0*: Nvidia (2008)
18. Nvidia: *Cuda: Cublas Library*: Nvidia (2008)
19. Cuda Tools: *Cuda Programmer's Guide*: Em Photonics, Inc. (2009)
20. Reddy, J.N., Miravete, A.: *Practical Analysis of Composite Laminates*. CRC Press (1995)
21. Farber, R.: *CUDA Application Design and Development*. Morgan Kaufmann (2012)

A Three-Dimensional Computational Model of the Innate Immune System

Pedro Augusto F. Rocha¹, Micael P. Xavier¹,
Alexandre B. Pigozzo¹, Barbara de M. Quintela¹, Gilson C. Macedo²,
Rodrigo Weber dos Santos¹, and Marcelo Lobosco¹

¹ Graduate Program in Computational Modelling, UFJF

² Graduate Program in Biological Science, UFJF

Abstract. The Human Immune System is a complex system responsible for protecting the organism against diseases. Although understanding how it works is essential to develop better treatments against diseases, its complexity makes this task extremely hard. In this work a three-dimensional mathematical and computational model of part of this system, the innate immune system, is presented. The high computational costs associated to simulations lead the development of a parallel version of the code, which has achieved a speedup of about 72 times over its sequential counterpart.

1 Introduction

Computational model is a popular tool to study the behavior of a complex system. This study is done through the simulation of distinct scenarios, which reflects the adjusts done in the parameters of the system under simulation. The results obtained from the computational experiments can then be used by experts to improve their understanding about the system. The system under study is often modelled using an explicit mathematical model, such as an ODE or PDE, although other implicit mathematical models, multi-agent systems or system dynamics, can also be used.

One particular complex system that has benefited from the computational modelling is the Human Immune System (HIS). The HIS is a complex network composed of specialized cells, tissues and organs that is responsible for protecting the organism against diseases caused by pathogenic agents. Although understanding how the HIS is essential to develop better drugs and treatments against diseases, its complexity and the intense interaction among several components, makes this task extremely hard. The use of computational models can help researchers to better understand how it works and their distinct components interacts, allowing them to test a large number of hypotheses in a short period of time.

This paper focus on the modelling of a part of the HIS, the innate immune system. The innate immune system is responsible for the first response against microorganisms or toxins that successfully enter into an organism. The main

contributions of this paper are the following. First we extend our previous works [1,2] and present a new three-dimensional model of the innate immune system. In particular, the current work focus on the simulation of the immune response to a potent immunostimulant in a microscopic 3D section of tissue, reproducing the initiation, maintenance and resolution of the innate immune response. Second, due to its huge computational cost, we present a parallel version of the 3D code using GPGPUs. A previous attempt to write a parallel version of the one-dimensional version of the code has used OpenMP and MPI [3]. The preliminary GPGPU results have shown that the parallelization process was very successful, yielding speedups up to sixty times.

This paper is organized as follows. In Section 2 the biological background is presented. Section 3 describes the mathematical model used in this work to model the innate immune system, while Section 4 presents its computational implementation and Section 5 presents its numerical results. Section 6 presents the parallelization of the code and the parallel results are presented and discussed in Section 7. The concluding remarks and future works are presented in Section 8.

2 Biological Background

The human body surfaces are protected by epitheliums, that constitutes a physical barrier between the internal and the external environment. However, it can eventually be crossed or settled by pathogens, causing infections. After crossing the epithelium, the pathogens find cells and molecules of the innate immune system that immediately develop an immune response. The strategy of the Human Immune System (HIS) is to keep some resident macrophages, called resting macrophages, into the tissue to look for any signal of invasion. When macrophages find such an invader they become active and ask the help of polymorphonuclear leukocytes (PMNs), such as the neutrophils. The cooperation between macrophages and PMNs is essential to mount an effective defense, because without the macrophages to recruit the PMNs to the location of invasion, the PMNs would circulate indefinitely in the blood vessels, impairing the control of huge infections. For example, protein granules produced by neutrophils contributes to increase the permeability of the walls of the blood vessels, called endothelium, allowing monocytes to enter into the tissues and mature into *resting* macrophages.

This initial response of the HIS starts an inflammatory process that has many benefits on the control of the infection. Besides recruiting cells and molecules of innate immunity from blood vessels to the location of the infected tissue, it increases the lymph flux containing microorganisms and cells that carry antigens to the neighbors lymphoid tissues, where these cells will present the antigens to the lymphocytes and will initiate the adaptive response. The adaptive response is part of the HIS that can adapt to protect the organism against almost any invader. Once the adaptive response is activated, the inflammation also recruits the effector cells of the adaptive immune system to the location of infection.

A component of the cellular wall of Gram-negative bacteria, such as LPS, can trigger an inflammatory response through the interaction with receptors on the surface of some cells. When receptors on the surface of macrophages bind to LPS, the macrophage starts to phagocytosis, degrading the bacteria internally and secreting proteins known as cytokines and chemokines, as well as other molecules.

The resolution of the inflammatory response also includes the production of anti-inflammatory mediators and the apoptosis (or programmed death) of effector cells of the HIS, such as the neutrophils. The anti-inflammatory cytokines are a set of immunoregulatory molecules that control the pro-inflammatory response. The cytokines act together with specific inhibitors and cytokines soluble receptors to regulate the immune response [4]. The main anti-inflammatory cytokines include the antagonist receptor of IL-1 (Interleukin 1), and the cytokines IL-4, IL-6, IL-10, IL-11 e IL-13 [4]. The IL-10 is a strong inhibitor of the production of many pro-inflammatory cytokines [5], among them the IL-8 and TNF- α (tumor necrosis factor α) by monocytes [6] and IL-8 by neutrophils [7,8].

The apoptotic cells keep the membrane integrity by a small period of time and so need to be quickly removed to prevent a secondary necrosis and, consequently, the release of cytotoxic molecules that causes inflammation and tissue damage [9]. As a consequence of the phagocytosis of apoptotic cells by macrophages or dendritic cells, these phagocytic cells produces anti-inflammatory cytokines. For example, macrophages secrete TGF- β (transforming growth factor β) that prevents the release of pro-inflammatory cytokines induced by LPS [10]. Also, the binding of the apoptotic cells to macrophage receptor CD36 (cluster of differentiation 36) inhibits the production of pro-inflammatory cytokines such as TNF- α , IL-1 β and IL-12 and also increases the secretion of TGF- β and IL-10 [11].

3 Mathematical Model

Biological systems span multiple scales from sub-cellular molecular interactions to individual complex organisms. The abstraction level of a model depends on the scale and granularity chosen and it has been a challenge to find a balance between scale, granularity and computational feasibility during the development of a model [12]. As models represent the reality, simplifications maintaining the main components are often used without losing reliability [13].

This paper models the response of the innate HIS to a potent immunostimulant in a three-dimensional (3D) section of a tissue. In particular, the mathematical model focus on the response to Lipopolysaccharides (LPS), a molecule that can be found in the membrane of bacteria. Previous works [12] has reproduced the initiation, maintenance and resolution of the innate immune response in a microscopic one-dimensional (1D) section of a tissue. The new 3D model proposed in this work aims to present more realistic results.

In this work, Partial Differential Equations (PDEs) have been employed to model the spatial and temporal behavior of the following components: LPS (A), macrophages, neutrophils (N), apoptotic neutrophils (ND), pro-inflammatory

cytokines (CH), anti-inflammatory cytokine (CA) and proteins granules (G). In this model, the macrophages are present in two states of readiness: *resting* (MR) and *hyperactivated* (MA). The proinflammatory cytokines, modelled by an unique equation in the model, are TNF- α and IL-8. The anti-inflammatory cytokine modelled is the IL-10. The IL-10 inhibits the activation and effector functions of T cells, monocytes and macrophages [14]. The different subsets of proteins granules [15] released by neutrophils during their extravasation from blood vessel to the tissues are represented by an unique equation.

The main differences related to the previous 1D model [12] are the following:

- a larger simulation space is used. An hexahedron is used instead of a line;
- the initial and boundary conditions were adapted for the 3D model;
- the diffusion and chemotaxis were applied in three directions, x , y and z .

3.1 LPS

The equations that models LPS are given by Eq. 1:

$$\begin{cases} maActivation = maActivationRate.MR.A/(1 + \theta_{CA}.CA) \\ \frac{\partial A}{\partial t} = -\mu_A A - maActivation - (\lambda_{N|A}N + \lambda_{MA|A}MA).A + D_A \Delta A \\ A(x, y, z, 0) = 100 \quad | \quad z \geq 0.9, \frac{\partial A(\dots, t)}{\partial n} |_{\partial \Omega} = 0 \end{cases} \quad (1)$$

The term $\mu_A A$ models the decay of LPS, where μ is the rate of decay. The term $maActivation$ models the activation of resting macrophages. This activation occurs when resting macrophages recognizes the LPS. After this recognition, the macrophages phagocyte the LPS. The term $\lambda_{N|A}.N$ models the phagocytosis of LPS by the neutrophils, where $\lambda_{N|A}$ is the rate of this phagocytosis. The term $\lambda_{MA|A}.MA$ models the phagocytosis of LPS by the active macrophages, where $\lambda_{MA|A}$ is the rate of this phagocytosis. The term $D_A \Delta A$ models the LPS diffusion, where D_A is the diffusion coefficient.

3.2 Macrophage

The equations related to resting macrophages (MR) are given by Eq. 2:

$$\begin{cases} Mrpermeability1 = (MrPmax - MrPmin).CH/(CH + keqch) + MrPmin \\ Mrpermeability2 = (MrPmax_g - MrPmin_g).G/(G + keq_g) + MrPmin_g \\ sourceMR = (Mrpermeability1 + Mrpermeability2) \\ \quad .(MrmaxTissue - (MR + MA)) \\ \frac{\partial MR}{\partial t} = -\mu_{MR}MR - maActivation + D_{MR} \Delta MR + sourceMR - \\ \quad - \nabla . (\chi_{MR} MR \nabla CH) \\ MR(x, y, z, 0) = 1, \frac{\partial MR(\dots, t)}{\partial n} |_{\partial \Omega} = 0 \end{cases} \quad (2)$$

The terms $Mrpermeability1$ and $Mrpermeability2$ model the increase in the endothelium permeability and its effects on the extravasation of monocytes induced by pro-inflammatory cytokines and proteins granules, respectively. The permeability of the endothelium of the blood vessels is modelled through a Hill equation [16].

The calculus of $Mrpermeability1$ involves the following parameters: a) $MrPmax$ is the maximum rate of increase in the endothelium permeability induced by the pro-inflammatory cytokine; b) $MrPmin$ is the minimum rate of increase in the endothelium permeability induced by the pro-inflammatory cytokine and c) $keqch$ is the concentration of pro-inflammatory cytokine that exerts 50% of the maximum effect in the increase in the permeability.

The calculus of $Mrpermeability2$ is similar to the calculus of $Mrpermeability1$, except for the parameters that are involved: $MrPmax-g$, $MrPmin-g$ and $keq-g$. The term $sourceMR$ represents the source term of macrophages, which is related to the number of monocytes that will enter into the tissue from the blood vessels. This number depends on the endothelium permeability ($Mrpermeability1 + Mrpermeability2$) and the capacity of the tissue to support the entrance of more monocytes ($MrmaxTissue$).

The term $\mu_{MR}MR$ models the resting macrophage apoptosis, where μ_{MR} is the apoptosis rate. The term $maActivation$, as explained before, models the activation of resting macrophages, representing the number of resting macrophages that are becoming active. The term $D_{MR}\Delta MR$ models the resting macrophage diffusion, where D_{MR} is the diffusion coefficient. The term $\nabla \cdot (\chi_{MR}MR\nabla CH)$ models the resting macrophage chemotaxis, where χ_{MR} is the chemotaxis rate.

After being activated, the macrophages are modelled by the following set of equations (Eq. 3):

$$\begin{cases} \frac{\partial MA}{\partial t} = -\mu_{MA}MA + maActivation + D_{MA}\Delta MA - \nabla \cdot (\chi_{MA}MA\nabla CH) \\ MA(x, y, z, 0) = 0, \frac{\partial MA(\dots, t)}{\partial n} |_{\partial\Omega} = 0 \end{cases} \tag{3}$$

The term $\mu_{MA}MA$ models the active macrophage apoptosis, where μ_{MA} is the rate of apoptosis. The term $D_{MA}\Delta MA$ models the active macrophage diffusion, where D_{MA} is the diffusion coefficient. The term $\nabla \cdot (\chi_{MA}MA\nabla CH)$ models the active macrophage chemotaxis, where χ_{MA} is the chemotaxis rate.

3.3 Neutrophil

The neutrophil equations (N) are given by Eq. 4:

$$\begin{cases} permeability = (Pmax - Pmin).CH / (CH + keqch) + Pmin \\ sourceN = permeability.(NmaxTissue - N) \\ \frac{\partial N}{\partial t} = -\mu_N N - \lambda_{A|N}A.N + D_N\Delta N + sourceN - \nabla \cdot (\chi_N N \nabla CH) \\ N(x, y, z, 0) = 0, \frac{\partial N(\dots, t)}{\partial n} |_{\partial\Omega} = 0 \end{cases} \tag{4}$$

The term $((Pmax - Pmin).CH)/(CH + Keqch) + Pmin$ models the increase in the endothelium permeability and its effects on neutrophils extravasation. In this term $Pmax$ represents the maximum rate of increase of endothelium permeability induced by pro-inflammatory cytokines, $Pmin$ represents the minimum rate of increase of endothelium permeability induced by pro-inflammatory cytokines and $keqch$ is the concentration of the pro-inflammatory cytokine that exerts 50% of the maximum effect in the increase of the permeability.

The term $\mu_N N$ models the neutrophil apoptosis, where μ_N is the rate of apoptosis. The term $\lambda_{A|N} A.N$ models the neutrophil apoptosis induced by the phagocytosis, where $\lambda_{A|N}$ represents the rate of this induced apoptosis. The term $D_N \Delta N$ models the neutrophil diffusion, where D_N is the diffusion coefficient. The term $sourceN$ represents the source term of neutrophil, i.e., the number of neutrophils that is entering into the tissue from the blood vessels. This number depends on the endothelium permeability (*permeability*) and on the capacity of the tissue to support the entrance of neutrophils ($NmaxTissue$). It can also represent concentration of neutrophils on blood. In this model we consider $NmaxTissue$ constant over time. The term $\nabla \cdot (\chi_N N \nabla CH)$ models the chemotaxis process of the neutrophils, where χ_N is the chemotaxis rate.

The equations of the apoptotic neutrophil (ND) are given by Eq. 5

$$\begin{cases} \frac{\partial ND}{\partial t} = \mu_N N + \lambda_{A|N} A.N - \lambda_{ND|MA} ND.MA + D_{ND} \Delta ND \\ ND(x, y, z, 0) = 0, \frac{\partial ND(\dots, t)}{\partial n} |_{\partial \Omega} = 0 \end{cases} \tag{5}$$

The terms $\mu_N N$ and $\lambda_{A|N} LPS.N$ were explained previously. The term $\lambda_{ND|MA} ND.MA$ models the phagocytosis of the apoptotic neutrophil carried out by active macrophages, where $\lambda_{ND|MA}$ is the rate of the phagocytosis. The term $D_{ND} \Delta ND$ models the apoptotic neutrophil diffusion, where D_{ND} is the diffusion coefficient.

3.4 Cytokines

The equations related to the model of the pro-inflammatory cytokine (CH) are given by Eq. 6

$$\begin{cases} \frac{\partial CH}{\partial t} = -\mu_{CH} CH + (\beta_{CH|N}.N + \beta_{CH|MA}.MA).A.(1 - CH/chInf)/ \\ \quad / (1 + \theta_{CA}.CA) + D_{CH} \Delta CH \\ CH(x, y, z, 0) = 0, \frac{\partial CH(\dots, t)}{\partial n} |_{\partial \Omega} = 0 \end{cases} \tag{6}$$

The term $\mu_{CH} CH$ models the pro-inflammatory cytokine decay, where μ_{CH} is the decay rate. The term $\beta_{CH|N}.N$ models the pro-inflammatory cytokine production by the neutrophils, where $\beta_{CH|N}$ is the rate of this production. The term $\beta_{CH|MA}.MA$ models the pro-inflammatory cytokine production by the active macrophages, where $\beta_{CH|MA}$ is the rate of this production. The saturation of this production is calculated by the equation $(1 - CH/chInf)$, where $chInf$ is an estimate of the maximum concentration of pro-inflammatory cytokine supported by the tissue. The production of pro-inflammatory cytokine decreases

when the anti-inflammatory cytokine acts on the producing cells. This influence of the anti-inflammatory cytokine is modelled by the term $1/(1 + \theta_{CA} \cdot CA)$. The term $D_{CH} \Delta CH$ models the pro-inflammatory cytokine diffusion, where D_{CH} is the diffusion coefficient.

The equations that models anti-inflammatory cytokines (CA) are given by Eq. 7

$$\begin{cases} \frac{\partial CA}{\partial t} = -\mu_{CA}CA + (\beta_{CA|MR} \cdot MR \cdot ND + \beta_{CA|MA} \cdot MA) \cdot (1 - CA/caInf) + \\ \quad + D_{CA} \Delta CA \\ CA(x, 0) = 0, \frac{\partial CA(\cdot, t)}{\partial n} |_{\partial \Omega} = 0 \end{cases} \tag{7}$$

The term $\mu_{CA}CA$ models the anti-inflammatory cytokine decay, where μ_{CA} is the decay rate. The term $\beta_{CA|MR} \cdot MR \cdot ND$ models the anti-inflammatory cytokine production by the resting macrophages in the presence of apoptotic neutrophils, where $\beta_{CA|MR}$ is the rate of the production. The term $\beta_{CA|MA} \cdot MA$ models the anti-inflammatory cytokine production by active macrophages, where $\beta_{CA|MA}$ is the rate of this production. The saturation of this production is calculated by equation $(1 - CA/caInf)$, where $caInf$ is the maximum concentration of anti-inflammatory cytokine into the tissue. The term $D_{CA} \Delta CA$ models the anti-inflammatory cytokine diffusion, where D_{CA} is the diffusion coefficient.

3.5 Protein Granules

Protein granules (G) are represented by the set of equations presented in Eq. 8

$$\begin{cases} \frac{\partial G}{\partial t} = -\mu_G G + \beta_{G|N} \cdot sourceN \cdot (1 - G/gInf) + D_G \Delta G \\ G(x, y, z, 0) = 0, \frac{\partial G(\dots, t)}{\partial n} |_{\partial \Omega} = 0 \end{cases} \tag{8}$$

The term $\mu_G G$ models the protein granules decay, where μ_G is the decay rate. The term $\beta_{G|N} \cdot sourceN$ models the production of the protein granules by the neutrophils that extravasate from the blood into inflamed tissue, where $\beta_{G|N}$ is the rate of this production. The saturation of the production of protein granules is calculated by equation $(1 - G/gInf)$, where $gInf$ is the maximum concentration of protein granules. The term $D_G \Delta G$ models the protein granules diffusion, where D_G is the diffusion coefficient.

4 Computational Model

The numerical method employed to implement the mathematical model was the Finite Difference Method [17], a method commonly used in the numeric discretization of PDEs. The Finite Difference Method is a method of resolution of differential equations that is based on the approximation of derivatives with finite difference.

Below we have an example of a finite difference operator used in the discretization of the Laplace operator that simulates the diffusion phenomenon in 3D:

$$D_O \left(\frac{\partial^2 O(x, y, z)}{\partial x^2} + \frac{\partial^2 O(x, y, z)}{\partial y^2} + \frac{\partial^2 O(x, y, z)}{\partial z^2} \right) \approx$$

$$D_O * ((o[x + 1, y, z] - 2 * o[x, y, z] + o[x - 1, y, z]) / \text{delta}X^2) \quad (9)$$

$$+ D_O * ((o[x, y + 1, z] - 2 * o[x, y, z] + o[x, y - 1, z]) / \text{delta}Y^2)$$

$$+ D_O * ((o[x, y, z + 1] - 2 * o[x, y, z] + o[x, y, z - 1]) / \text{delta}Z^2)$$

In Eq. 9 O represents the discretization of some types of cells, such as neutrophils, resting and activated macrophages; D_O is the diffusion coefficient of these populations of cells; x , y and z are positions in space; and $\text{delta}X$, $\text{delta}Y$ and $\text{delta}Z$ are the space discretization.

In three dimensions, the chemotaxis flux is as follows:

```

1 //flux at x-axis
2 if ((CH[0][x][y][z]-CH[0][x-1][y][z]) > 0) {
3   flux_left = -(CH[0][x][y][z]-CH[0][x-1][y][z]) * 0[0][x-1][y][z]/deltaX;
4 } else {
5   flux_left = -(CH[0][x][y][z]-CH[0][x-1][y][z]) * 0[0][x][y][z]/deltaX;
6 }
7 if (CH[0][x+1][y][z]-CH[0][x][y][z] > 0) {
8   flux_right = (CH[0][x+1][y][z]-CH[0][x][y][z]) * 0[0][x][y][z]/deltaX;
9 } else {
10  flux_right = (CH[0][x+1][y][z]-CH[0][x][y][z]) * 0[0][x+1][y][z]/deltaX;
11 }
12 fluxX = (flux_left + flux_right)/deltaX;
13
14 //flux at y-axis
15 if (CH[0][x][y][z]-CH[0][x][y-1][z] > 0) {
16   flux_left = -(CH[0][x][y][z]-CH[0][x][y-1][z]) * 0[0][x][y-1][z]/deltaY;
17 } else {
18   flux_left = -(CH[0][x][y][z]-CH[0][x][y-1][z]) * 0[0][x][y][z]/deltaY;
19 }
20 if (CH[0][x][y+1][z]-CH[0][x][y][z] > 0) {
21   flux_right = (CH[0][x][y+1][z]-CH[0][x][y][z]) * 0[0][x][y][z]/deltaY;
22 } else {
23   flux_right = (CH[0][x][y+1][z]-CH[0][x][y][z]) * 0[0][x][y+1][z]/deltaY;
24 }
25 fluxY = (flux_left + flux_right)/deltaY;
26
27 //flux at z-axis
28 if (CH[0][x][y][z]-CH[0][x][y][z-1] > 0) {
29   flux_left = -(CH[0][x][y][z]-CH[0][x][y][z-1]) * 0[0][x][y][z-1]/deltaZ;
30 } else {
31   flux_left = -(CH[0][x][y][z]-CH[0][x][y][z-1]) * 0[0][x][y][z]/deltaZ;
32 }
33 if (CH[0][x][y][z+1]-CH[0][x][y][z] > 0) {
34   flux_right = (CH[0][x][y][z+1]-CH[0][x][y][z]) * 0[0][x][y][z]/deltaZ;
35 } else {
36   flux_right = (CH[0][x][y][z+1]-CH[0][x][y][z]) * 0[0][x][y][z+1]/deltaZ;
37 }
38 fluxZ = (flux_left + flux_right)/deltaZ;

```

In this code fragment, ch represents the discretization of the pro-inflammatory cytokine; O represents the discretization of some types of cells; x , y and z are the positions in space; and $deltaX$, $deltaY$ and $deltaZ$ are the spatial discretization. The final result of the evaluation of the chemotaxis is:

$$-\nabla \cdot (\chi_O O \nabla CH) \approx -\chi_O * (fluxX + fluxY + fluxZ) \tag{10}$$

Where the speed of the movement is given by the term ∇CH and χ_O is the chemotaxis rate of the correspondent population of cells. This value is then used to choose between two schemes of finite differences: forward or backward.

Table 1. Initial Conditions. All values are estimated and represent the number of cells.

Parameter	Value and Position		
A_0	100,	$0 \leq x \leq 1$ & $0 \leq y \leq 1$ & $0.9 \leq z \leq 1$	
MR_0	1,	$0 \leq x \leq 1$ & $0 \leq y \leq 1$ & $0 \leq z \leq 1$	
MA_0	0,	$0 \leq x \leq 1$ & $0 \leq y \leq 1$ & $0 \leq z \leq 1$	
N_0	0,	$0 \leq x \leq 1$ & $0 \leq y \leq 1$ & $0 \leq z \leq 1$	
ND_0	0,	$0 \leq x \leq 1$ & $0 \leq y \leq 1$ & $0 \leq z \leq 1$	
CH_0	0,	$0 \leq x \leq 1$ & $0 \leq y \leq 1$ & $0 \leq z \leq 1$	
G_0	0,	$0 \leq x \leq 1$ & $0 \leq y \leq 1$ & $0 \leq z \leq 1$	
CA_0	0,	$0 \leq x \leq 1$ & $0 \leq y \leq 1$ & $0 \leq z \leq 1$	

Table 2. Time and Space Discretization

Parameter	Size	Discretization
Time	1day, symbolized by 10^6 iterations	$\delta T = 0.000001$
X-axis	1mm, symbolized by 11 points	$\delta X = 0.1$
Y-axis	1mm, symbolized by 11 points	$\delta Y = 0.1$
Z-axis	1mm, symbolized by 11 points	$\delta Z = 0.1$

Tables 1 and 2 present the initial conditions, the time discretization (δT) and the space discretization (δX , δY and δZ). All the parameters used in our simulations can be found at Table 3. Some values were estimated based on values found in the literature.

Table 3. The complete set of parameters used in the simulation

Parameter	Value	Unit	Reference
keq_{ch} and keq_g	1	cell	estimated
θ_{CA}	1	1/cell	estimated
$Pmax$	11.4	1/day	estimated based on [18]
$Pmin$	0.0001	1/day	estimated
$NmaxTissue$	8	cell	estimated
$MrPmax$ and $MrPmax_g$	0.1 and 0.5	1/day	estimated
$MrPmin$ and $MrPmin_g$	0.01 and 0	1/day	estimated
$MrmaxTissue$	6	cell	estimated
$maActivationRate$	0.1	1/cell.day	estimated
μ_A and μ_{MR}	0 and 0.033	1/day	[19]
$\lambda_{N A}$	0.55	1/cell.day	[19]
$\lambda_{MA A}$	0.8	1/cell.day	[19]
D_A	0.2	mm^2/day	estimated
D_{MR}	0.00432	mm^2/day	estimated
X_{MR}	0.0036	mm^2/day	estimated
μ_{MA}	0.07	1/day	[19]
D_{MA}	0.003	mm^2/day	estimated
X_{MA}	0.00432	mm^2/day	estimated
μ_N and μ_{CH}	3.43 and 7	1/day	estimated
$\lambda_{A N}$	0.55	1/cell.day	[19]
D_N	0.012096	mm^2/day	[20]
X_N	0.0144	mm^2/day	[21]
$\lambda_{ND MA}$	2.6	1/cell.day	[19]
D_{ND}	0.000000144	mm^2/day	[19]
$\beta_{CH N}$	1	1/cell.day	estimated
$\beta_{CH MA}$	0.8	1/cell.day	estimated
D_{CH}	0.009216	mm^2/day	[19]
μ_G and μ_{CA}	5 and 4	1/day	estimated
$\beta_{G N}$	0.6	1/day	estimated
D_G	0.009216	mm^2/day	estimated
$\beta_{CA MR}$	1.5	1/cell.day	estimated
$\beta_{CA MA}$	1.5	1/day	estimated
D_{CA}	0.009216	mm^2/day	estimated
$caInf$ and $chInf$	3.6	cell	estimated based on [6]
$gInf$	3.1	cell	estimated

5 Numerical Results

This section presents the numerical results of the simulation. The simulator was build using the C programming language. A numerical library, such as NAG [22], could be used to solve the PDEs. However, we decided to implement the numerical method to solve PDEs because a) we have the possibility to parallelize the code; b) most of the numerical libraries offer few functions that are suitable to our problem; and c) functions offered by such numerical libraries are hard to use because arguments supplied to functions must be in a specific format.

Due to the lack of space, the results obtained from the simulations for some types of cells are not presented. Figures 1, 2 and 3 depict the spatial and temporal distribution of antigens, resting macrophages and neutrophils, respectively, in a 1 mm^3 tissue.

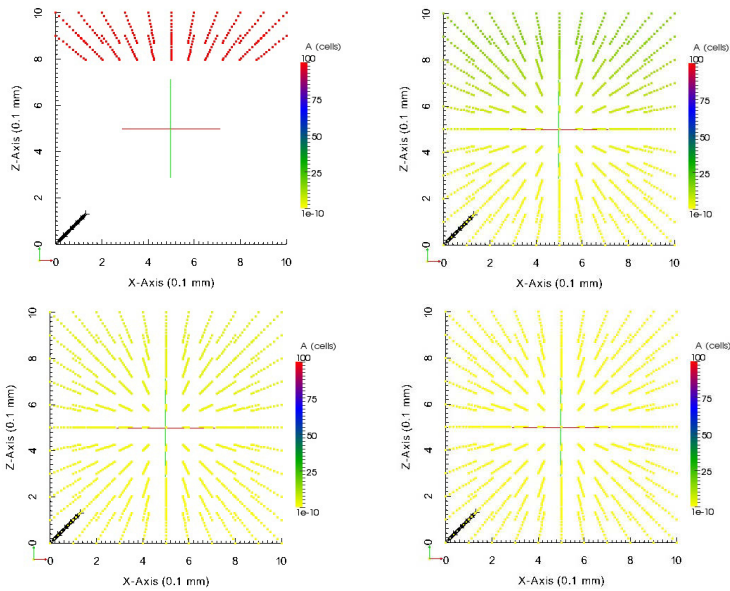


Fig. 1. Spatial and temporal distribution of antigens. Top left is the initial distribution, top right shows its distribution after 6 hours, bottom left after 12 hours and bottom right after 24 hours.

It can be observed that, at first, the number of resting macrophages decreases because they become active to attack LPS. Cytokines are produced and attract neutrophils to the place of infection. These neutrophils that are attracted also contributes to produce even more cytokines in the locations of the tissue where the LPS are more concentrated, resulting in a vigorous and rapid immune response. LPS are eliminated between 6 and 12 hours. After this, it can be observed that the number of resting macrophages start to increase again, while the number of neutrophils start to decrease.

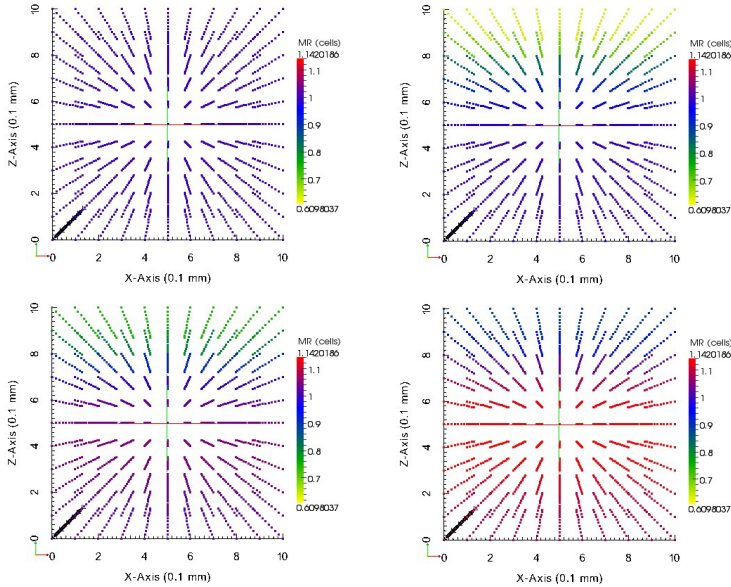


Fig. 2. Spatial and temporal distribution of resting macrophages. Top left is the initial distribution, top right shows its distribution after 6 hours, bottom left after 12 hours and bottom right after 24 hours.

6 Parallel Implementation

The long computational cost of the sequential implementation of the simulator leads the development of a parallel version the code using General-purpose Graphics Processing Units (GPGPUs). GPGPUs were chosen because of their ability to process many streams simultaneously. The present section describes the GPU-based version of the implemented code.

6.1 CUDA

NVIDIA's CUDA (Compute Unified Device Architecture)[\[23\]](#) is a massively parallel high-performance computing platform on GPGPUs. CUDA includes C software development tools and libraries to hide the GPGPU hardware from programmers.

In order to run an application, the programmer must create a parallel function called kernel. A kernel is a function callable from the CPU and executed on the GPU simultaneously by many threads. Each thread is run by a stream processor. They are grouped into blocks of threads or just blocks. The blocks can be one-, two- or three-dimensional. A set of blocks of threads form a grid, that can be one- or two-dimensional. When the CPU calls the kernel, it must specify how

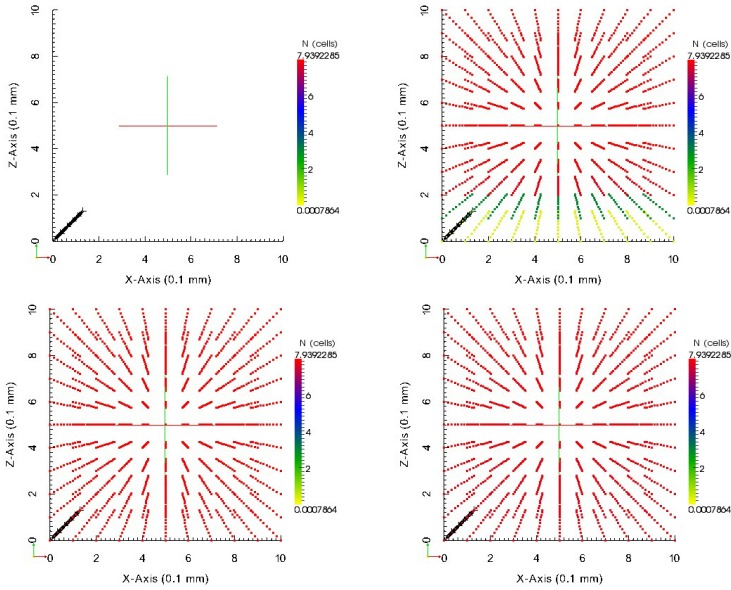


Fig. 3. Spatial and temporal distribution of neutrophils. Top left is the initial distribution, top right shows its distribution after 6 hours, bottom left after 12 hours and bottom right after 24 hours.

many threads will be created at runtime. The syntax that specifies the number of threads that will be created to execute a kernel is formally known as the execution configuration, and is flexible to support CUDA’s hierarchy of threads, blocks of threads, and grids of blocks. Since all threads in a grid execute the same code, a unique set of identification numbers is used to distinguish threads and to define the appropriate portion of the data they must process. These threads are organized into a two-level hierarchy composed by blocks and grids and two unique coordinates, called *blockId* and *threadId*, are assigned to them by the CUDA runtime system. These two built-in variables can be accessed within the kernel functions and they return the appropriate values that identify a thread.

Some steps must be followed to use the GPU: a) the device must be initialized; b) memory must be allocated in the GPU and data transferred to it; c) the kernel is called. After the kernel have finished, results are transferred back to the CPU.

6.2 Parallel Version

In the parallel version of the code, each thread is responsible for calculating the complete set of PDEs for each single point of the tissue’s space. Therefore, for each point (x, y, z) of the discretized space, there is a thread responsible for the computation of the PDEs. During the computation, the access to data produced

by neighbors threads is necessary. To avoid the use of synchronization, a buffer was implemented to allow that a thread, at time t , gets access to data produced by its neighbors at the time $t-1$. The use of a buffer is necessary because a programmer can not synchronize threads that execute in distinct blocks. Besides, the synchronization cost would be prohibitive. No race condition occurs because data being produced in time t are accessed just by the thread that is producing it. The buffer is implemented in such a way that there are two values associated for each point (x, y, z) of a given population of cells. One buffer entry is the data produced in time $t-1$, while the other one is data being produced in time t . These two buffer entries change their meaning at each time step, in order to avoid copy of data.

In order to store the values for each population of cells in each point of the space, an unidimensional vector was allocated in both CPU and GPU memories. Its length is equal to 8, which are the number of populations, times the number of positions in the tissue.

7 Experimental Evaluation

In this section, we present the speedups obtained with the parallel versions of our code. Both the sequential and parallel implementations have been tested on a dual Intel Xeon E5620 processors each with 4 cores, so 8 physical cores are available. Each core with 64 KB cache L1 and 256 KB L2 and Hyper-threading (HT) which gives the support to 16 simultaneous threads per processor. This machine has a Tesla M2050 GPU, with 448 cores and 2.6 GB of global memory. *gcc* 4.1.2 was used to compile the sequential version of the code, while *nvcc* release 3.2 was used to compile the parallel version. The execution times obtained by all versions of the code were measured 5 times and the standard deviation was lower than 0.13%. Each execution of the code was measured using the Linux *time* application.

The speedup factor was used to evaluate gains obtained by the parallel version of the code over the sequential one. The acceleration can be calculated employing the following Equation [\(11\)](#):

$$S(p) = \frac{t_s}{t_p} \quad (11)$$

where t_s is sequential execution time and t_p is parallel execution time with p processors.

In order to evaluate the performance gains obtained by the parallel version of the code, a tissue of volume equals to 64 mm^3 was used in the parallel experiments to simulate one day of infection (about one million of interactions). This tissue has a total of 64,000 points. The speedups are presented in Table [4](#).

Table 4. Speedup obtained by the CUDA parallel version of the code

Version	Runtime average (s)	Standard deviation	Speedup
Sequential	69,727.68	0.13 %	-
Parallel	970.84	0.06 %	71.82

8 Conclusion

This work presented a three-dimensional mathematical and computational model of the innate immune system. The simulation of one day of infection takes about 20 hours on a sequential machine. This long simulation time leads the development of a parallel version of the code. The CUDA version has achieved an speedup of about 72 times over its sequential counterpart. As future work, we plan to employ multiple GPU devices to increase the application speedup. The use of multiple GPU devices allows the allocation of more threads to compute the equations. The innate immune model will be extended to include more cells, such as Natural Killers and Dendritic Cells, and other substances, such as the proteins of the Complement System.

Acknowledgment. The authors would like to thank the Brazilian agencies CAPES, CNPq, FAPEMIG, FINEP and UFJF.

References

1. Pigozzo, A.B., Macedo, G.C., dos Santos, R.W., Lobosco, M.: Implementation of a Computational Model of the Innate Immune System. In: Liò, P., Nicosia, G., Stibor, T. (eds.) ICARIS 2011. LNCS, vol. 6825, pp. 95–107. Springer, Heidelberg (2011)
2. Pigozzo, A., Macedo, G., Weber, R., Lobosco, M.: On the computational modelling of the innate immune system. *BMC Bioinformatics* (2012) (Submitted, review in progress)
3. Pigozzo, A.B., Lobosco, M., dos Santos, R.W.: Parallel implementation of a computational model of the his using openmp and mpi. In: International Symposium on Computer Architecture and High Performance Computing Workshops, pp. 67–72. IEEE Computer Society (2010)
4. Opal, S.M., DePalo, V.A.: Anti-inflammatory cytokines. *Chest* 117(4), 1162–1172 (2000)
5. Fiorentino, D., Zlotnik, A., Mosmann, T., Howard, M., O’Garra, A.: Il-10 inhibits cytokine production by activated macrophages. *The Journal of Immunology* 147(11), 3815–3822 (1991)
6. de Waal Malefyt, R., Abrams, J., Bennett, B., Figdor, C., de Vries, J.: Interleukin 10(il-10) inhibits cytokine synthesis by human monocytes: an autoregulatory role of il-10 produced by monocytes. *J. Exp. Med.* 174(5), 1209–1220 (1991)

7. Cassatella, M.A., Meda, L., Bonora, S., Ceska, M., Constantin, G.: Interleukin 10 (il-10) inhibits the release of proinflammatory cytokines from human polymorphonuclear leukocytes. evidence for an autocrine role of tumor necrosis factor and il-1 beta in mediating the production of il-8 triggered by lipopolysaccharide. *The Journal of Experimental Medicine* 178(6), 2207–2211 (1993)
8. Marie, C., Pitton, C., Fitting, C., Cavaillon, J.M.: Regulation by anti-inflammatory cytokines (il-4, il-10, il-13, tgf) of interleukin-8 production by lps and/or tnf-activated human polymorphonuclear cells. *Mediators of Inflammation* 5, 334–340 (1996)
9. Kennedy, A., DeLeo, F.: Neutrophil apoptosis and the resolution of infection. *Immunologic Research* 43, 25–61 (2009), 10.1007/s12026-008-8049-6
10. Lucas, M., Stuart, L., Zhang, A., Hodivala-Dilke, K., Febbraio, M., Silverstein, R., Savill, J., Lacy-Hulbert, A.: Requirements for apoptotic cell contact in regulation of macrophage responses. *J. Immunol.* 177(6), 4047–4054 (2006)
11. Voll, R.E., Herrmann, M., Roth, E.A., Stach, C., Kalden, J.R., Girkontaite, I.: Immunosuppressive effects of apoptotic cells. *Nature* 390(6658), 350–351 (1997)
12. Fachada, N.: Agent-based simulation of the immune system. Master's thesis, Instituto Superior Tcnico de Lisboa (2008)
13. Cohen, I.R.: Modeling immune behavior for experimentalists. *Immunological Reviews* 216(1), 232–236 (2007)
14. Moore, K.W., de Waal Malefyt, R., Coffman, R.L., O'Garra, A.: Interleukin-10 and the interleukin-10 receptor. *Annual Review of Immunology* 19(1), 683–765 (2001)
15. Borregaard, N., Cowland, J.B.: Granules of the human neutrophilic polymorphonuclear leukocyte. *Blood* 10, 3503–3521 (1997)
16. Goutelle, S., Maurin, M., Rougier, F., Barbaut, X., Bourguignon, L., Ducher, M., Maire, P.: The hill equation: a review of its capabilities in pharmacological modelling. *Fundamental & Clinical Pharmacology* 22(6), 633–648 (2008)
17. LeVeque, R.J.: *Finite Difference Methods for Ordinary and Partial Differential Equations*. Society for Industrial and Applied Mathematics (2007)
18. Price, T., Ochs, H., Gershoni-Baruch, R., Harlan, J., Etzioni, A.: In vivo neutrophil and lymphocyte function studies in a patient with leukocyte adhesion deficiency type ii. *Blood* 84(5), 1635–1639 (1994)
19. Su, B., Zhou, W., Dorman, K.S., Jones, D.E.: Mathematical modelling of immune response in tissues. *Computational and Mathematical Methods in Medicine: An Interdisciplinary Journal of Mathematical, Theoretical and Clinical Aspects of Medicine* 10, 1748–6718 (2009)
20. Felder, S., Kam, Z.: Human neutrophil motility: Time-dependent three-dimensional shape and granule diffusion. *Cell Motility and the Cytoskeleton* 28(4), 285–302 (1994)
21. Chettibi, S., Lawrence, A., Young, J., Lawrence, P., Stevenson, R.: Dispersive locomotion of human neutrophils in response to a steroid-induced factor from monocytes. *J. Cell Sci.* 107(11), 3173–3181 (1994)
22. Pennington, S.V., Berzins, M.: New nag library software for first-order partial differential equations. *ACM Trans. Math. Softw.* 20(1), 63–99 (1994)
23. Kirk, D., Hwu, W.: *Massively Parallel Processors: A Hands-on Approach*. Morgan Kaufmann (2010)

System Dynamics Metamodels Supporting the Development of Computational Models of the Human Innate Immune System

Igor Knop¹, Alexandre Pigozzo¹,
Barbara Quintela¹, Gilson C. Macedo²,
Ciro Barbosa¹, Rodrigo Weber dos Santos¹, and Marcelo Lobosco¹

¹ FISIOCOMP, Universidade Federal de Juiz de Fora

² Immunology Lab, Universidade Federal de Juiz de Fora

Abstract. The human body is protected against pathogenic invasions by a complex system of cells, tissues and organs which form the Human Immune System (HIS). Understanding how the HIS works is therefore essential to obtain new insights into its nature and to deal effectively with diseases. Mathematical and computational modeling can be used for this purpose. Unfortunately, these complex mathematical models are very difficult to develop, understand and use by a more general and multidisciplinary team. This paper presents a System Dynamics Metamodeling tool, called JynaCore API, that supports the development of complex models using System Dynamics in a more abstract level. To demonstrate the power and usefulness of the proposed System Dynamics Metamodeling tool, in this work we present the development of a complex two-dimensional tissue model that simulates the dynamics of the immune response.

1 Introduction

The Human Immune System (HIS) is composed of two distinct parts, the innate immune system and the adaptive immune system [1]. The innate immune system is responsible for powerful nonspecific defenses that prevents or limits infections by most pathogenic microorganisms. This first line of defense against pathogenic microorganisms consists of physical barriers, such as the skin and mucous membranes, and the second line consists of cells, such as neutrophils, that recognize specific parts of pathogenic microorganisms, herein called antigens. Understanding how the HIS works is essential to obtain new insights into its nature and to deal effectively with diseases. However, the multiscale and multiphysics nature of the involved phenomena poses great challenges to the researchers of this field. Computational modeling can be used for perform experiments in silico, allowing researchers to speed up the discovery of new, cheaper and more effective drugs against diseases. In addition, computer models have become valuable tools for the study and comprehension of such complex phenomena, as they allow different information acquired from different physical scales and experiments

to be combined to generate a better picture of the whole system functionality. Not surprisingly, the high complexity of the phenomena translates into complex mathematical and computational models. Computational models of the HIS are very often developed using pure mathematical tools, such as nonlinear systems of partial differential equations, to describe the behavior of its components and their relationships. Unfortunately, these complex mathematical models are very difficult to develop, understand and use by a more general and multidisciplinary public. The complexity of the models has limited the number of research centers that develop and make efficient use of them.

In this paper we propose a solution for some of these challenges: JynaCore API, a System Dynamics Metamodeling tool that supports the development of complex models using System Dynamics in a more abstract level. Two levels of abstraction are used: domain modeling and instance modeling. First, instead of using pure mathematical equations, i.e. system of nonlinear ordinary equations, System Dynamics is used to describe the relations between the different variables of the model. System Dynamics uses stock, flux diagrams and simple equations to describe systems with complex dynamic behavior. A stock and flux diagram are a formal and quantitative way to express the main concepts of a system and their structural relations. Second, after a System Dynamics model is created, i.e. a domain model, one can instantiate it multiple times and connect the different instances with relations that are freely defined. To demonstrate the power and usefulness of our System Dynamics Metamodeling tool, in this work we present the development of a complex two-dimensional tissue model that simulates the dynamics of the immune response and that include important features such as diffusion and chemotaxis behavior of neutrophils.

2 System Dynamics

The System Dynamics use stock and flux diagrams and simple equations to describe systems with complex dynamic behavior. A stock and flux diagram are a formal and quantitative way to express the main concepts of a system and their structural relations. In System Dynamics, a stock and flux diagram is composed by four basic elements: stock; flux; auxiliaries and information. A stock express a quantity that can be accumulated in our system. In our model, for instance, we can express populations of neutrophils as stocks. A flux express how stock level varies in time. A stock level can only change due to a incoming flux (raising up an amount stored) or outgoing flux (lowering down an amount stored). An auxiliary is a way to isolate important data from the system. An auxiliary cannot directly change a stock level, but can be used to calculate a flux value. Information comes as visual representation in the model. When a flux or auxiliary uses a stock level in their equations, we trace a thin arrow from stock to flux or variable. With that visual aid we can see the feedback loops which increases the system understanding.

Fig. 1 presents an example of the basic stock-flux connection. The cloud symbol is an Infinite Stock that represents an accumulation that is out of our interest

in that specific model. Infinite stocks are considered capable of giving or receiving any value from fluxes. Hidden behind this intuitive and graphical description is a mathematical model based on an ODE.

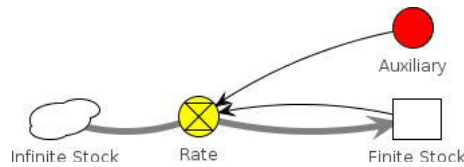


Fig. 1. System Dynamics basic elements

3 System Dynamics Metamodels

A model should answer a set of questions in a language which the user understands. System Dynamics is a formal language that can be used in multidisciplinary group as knowledge exchanging tool. All basic elements and relations of sub systems can be captured and associated together to system behaviour that emerges in an endogenous way. However the readability diminishes when more and more elements from sub systems are added. Marcio Barros proposed the System Dynamics Metamodeling [2], a new modeling language based on System Dynamics to limit the growing complexity, leverage readability and maintainability by dividing the model in two layers of interest.

The System Dynamics Metamodeling split model construction in two phases: domain modeling and instance modeling. A domain modeling describes behavior structures through classes. The Fig. 2 shows the relation between a domain model and an instance model. An instance model uses previously defined classes to create instance elements which can be associated and have properties changed to describe a specific system. An optional step in domain modeling consists of creating scenario models to encapsulate some structural model changes. Those scenarios can be used in various instance models to as an repeatable and encapsulated experiment.

3.1 Domain Model

A domain model try to capture properties, behavior and relation between a set of elements of a knowledge domain. It is an abstract description, therefore, it can not be realized in an simulation. To construct a domain model, the modeler should know the stock and flux diagrams from System Dynamics.

The main concept from domain models is the *class*. A class is a representation of a family of elements who owns a same behavior and properties. From a class we can describe instances, each one with its own states. To describe a class we use a stock and flux diagram as a complete and isolated system. We can define relations between classes that allow us to access external elements defined elsewhere.

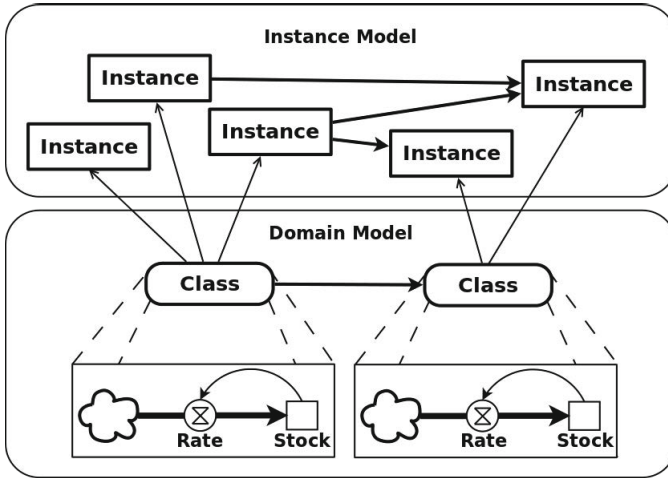


Fig. 2. System Dynamics Metamodeling. A domain model define behavior structures in classes and a instance model define individuals that implement those classes and their interrelations to model a specific system.

For instance, as a simple example, we can consider to create two classes: "Class A" and "Class B". Class A in Fig. 3(a) has a finite stock, a rate and an auxiliary. Class B in Fig. 3(b) has only an auxiliary and a property. The dashed auxiliaries are external elements accessed through relationships.

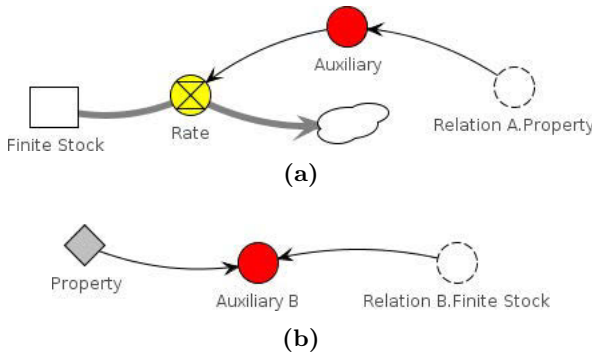


Fig. 3. System Dynamics Domain Model for two classes

3.2 Instance Model

Only after defining a domain model we can start modeling our system using domain classes. An instance model is a realization of the domain model on which we construct elements based on the available class structure.

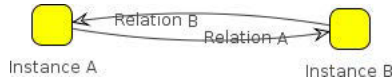


Fig. 4. System Dynamics basic elements

In using our domain model, we can consider to create simple instance model by instancing our domain classes and connecting them properly. Fig. 4 shows a simple example of an instance model.

4 HIS

Body surfaces are protected by epithelia, which constitutes a physical barrier between the internal and external environments. The body's epithelia form an effective block against the external environment, but eventually they can be crossed or settled by pathogens, causing infections. After crossing the epithelium, the pathogens encounter cells and molecules of the innate immune system that immediately develop a response. Reinforcing the innate immune response but taking days instead of hours to develop, the adaptive immune system is capable of eliminating the infection more efficiently than the innate immune system. The adaptive immune system is only present in vertebrates and depends primarily on the recognition executed by lymphocytes, that posses the ability to distinguish a pathogen and direct to it a stronger immune response.

The initial response of the body to an acute biological stress, such as a bacterial infection, is an acute inflammatory response [3]. The strategy of the HIS is to keep some resident cells on guard in the tissues to look for any signal of infection. When they find such a signal, the resident cells of the innate system start to produce substances such that the cytokine that recruit cells and molecules of innate immunity from blood vessels to the location of the infected tissue.

The LPS endotoxin is a potent immunostimulant that can induce an acute inflammatory response comparable to that of a bacterial infection. After the lyse of the bacteria by the action of cells of the HIS, the LPS can be released in the host, intensifying the inflammatory response and activating some cells of the innate system. The LPS can trigger an inflammatory response through the interaction with receptors on the surface of some cells. The commitment of this receptor activates these cells to phagocytose, degrading the bacteria internally and secreting proteins known as cytokines and chemokines, as well as other molecules.

The inflammation of an infectious tissue has many benefits in the control of the infection. Besides recruiting cells and molecules of innate immunity from blood vessels to the location of the infected tissue, it increases the lymph flux containing microorganisms and cells that carry LPS to the neighbors lymphoid tissues, where these cells will present the LPS to the lymphocytes and will initiate the adaptive response. Once the adaptive response is activated, the inflammation also recruits the effector cells of the adaptive immune system to the location of infection.

5 Methods

5.1 Mathematical Model

The model proposed in this work is a system of Partial Differential Equations (PDEs) based on the originally proposed by [4]. In this model, a set of equations describe the dynamics of the immune response to LPS in a microscopic section of tissue. In particular, the interactions among LPS, neutrophil and cytokine are modeled.

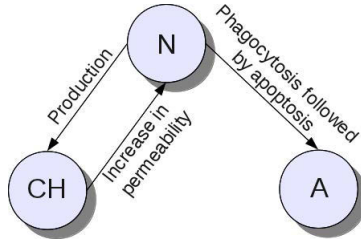


Fig. 5. Relations between the model components

Figure 5 presents schematically the relationship between neutrophils, pro-inflammatory cytokines and LPS. The LPS diffuse and cause a response in the neutrophils, that recognize these LPS and phagocyte them. The process of phagocytosis induces, in a rapid way, the apoptosis of neutrophils.

The pro-inflammatory cytokine is produced by neutrophils after the membrane receptors of these neutrophils recognize the LPS. The pro-inflammatory cytokine induces an increase in the endothelial permeability allowing more neutrophils to leave the blood vessels and enter the infected tissue. Besides, the pro-inflammatory cytokine is chemoattractant of neutrophils, guiding their movement. As a result the neutrophils move in the direction of the gradient of the pro-inflammatory cytokine.

The main characteristics of the mathematical model are:

- Neutrophils interact with pro-inflammatory cytokines and LPS;
- The interaction between neutrophils and LPS increases the production of cytokines;
- Cytokines induce an increase in the endothelial permeability and allows more neutrophils to come to the infected tissue;
- In the tissue, neutrophils move in the direction of the gradient of the pro-inflammatory cytokines (chemotaxis);
- Pro-inflammatory cytokines attracts the neutrophils to the location where the LPS concentration is higher.

Our set of equations is given below, where A , N and CH represent the population of LPS, neutrophils and pro-inflammatory cytokines, respectively.

The LPS equation is shown in Equation 1.

$$\begin{cases} \frac{\partial A}{\partial t} = -\mu_A A - \lambda_{N|A} A.N + D_A \Delta A \\ A(x, 0) = A_0 \quad | \quad 0 \leq x < 1, \frac{\partial A(\cdot, t)}{\partial n} |_{\partial \Omega} = 0 \end{cases} \quad (1)$$

The term $\mu_A A$ models the decay of the LPS, where μ_A is its decay rate. The term $\lambda_{N|A} A.N$ models the phagocytosis of LPS by neutrophils, where $\lambda_{N|A}$ is the phagocytosis rate. The term $D_A \Delta A$ models the diffusion of the LPS, where D_A is the diffusion coefficient. the amount of substance diffusing across a unit area through a unit concentration gradient in unit time.

The neutrophil equation is shown in Equation 2.

$$\begin{cases} permeability = ((Pmax - Pmin).CH / (CH + Keqch) + Pmin) \\ sourceN = permeability.(NmaxTissue - N) \\ \frac{\partial N}{\partial t} = -\mu_N N - \lambda_{A|N} A.N + D_N \Delta N + sourceN - \nabla \cdot (\chi_N N \nabla CH) \\ N(x, 0) = N_0, \frac{\partial N(\cdot, t)}{\partial n} |_{\partial \Omega} = 0 \end{cases} \quad (2)$$

The term $((Pmax - Pmin).CH / (CH + Keqch) + Pmin)$ uses a Hill equation 5 to model how permeability of the endothelium of the blood vessels depends on the local concentration of cytokines. Hill equations are also used, for example, to model drug dose-response relationships 6. The idea is to model the increase in the permeability of the endothelium according to the concentration of the pro-inflammatory cytokines into the endothelium. In the Hill equation, $Pmax$ represents the maximum rate of increase of endothelium permeability induced by pro-inflammatory cytokines, $Pmin$ represents the minimum rate of increase of endothelium permeability induced by pro-inflammatory cytokines and $keqch$ is the concentration of the pro-inflammatory cytokine that exerts 50% of the maximum effect in the increase of the permeability.

The term $\mu_N N$ models the neutrophil apoptosis, where μ_N is the rate of apoptosis. The term $\lambda_{A|N} A.N$ models the neutrophil apoptosis induced by the phagocytosis, where $\lambda_{A|N}$ represent the rate of this induced apoptosis. The term $D_N \Delta N$ models the neutrophil diffusion, where D_N is the coefficient of diffusion. The term $sourceN$ represents the source term of neutrophil, that is, the number of neutrophils that is entering the tissue from the blood vessels. This number depends on the endothelium permeability (*permeability*) and the capacity of the tissue to support the entrance of neutrophils ($NmaxTissue$), that can also represent the blood concentration of Neutrophils. In this model we consider it, $NmaxTissue$, constant over time. The term $\nabla \cdot (\chi_N N \nabla CH)$ models the chemotaxis process of the neutrophils, where χ_N is the chemotaxis rate.

Finally, the cytokine equation is shown in Equation 3.

$$\begin{cases} \frac{\partial CH}{\partial t} = -\mu_{CH} CH + \beta_{CH|N}.N.A + D_{CH} \Delta CH \\ CH(x, 0) = 0, \frac{\partial CH(\cdot, t)}{\partial n} |_{\partial \Omega} = 0 \end{cases} \quad (3)$$

The term $\mu_{CH} CH$ models the pro-inflammatory cytokine decay, where μ_{CH} is the decay rate. The term $\beta_{CH|N}.N.A$ models the production of the pro-inflammatory

cytokine by the neutrophils, where $\beta_{CH|N}$ is the rate of this production. The term $D_{CH}\Delta CH$ models the diffusion of the pro-inflammatory cytokines, where D_{CH} is the diffusion coefficient.

Table 1 presents the initial conditions and the values of the parameters used in the simulations.

Table 1. Initial conditions and parameters

Parameter	Value	Unit	Reference
N_0	$2, 0 < x < 5$	cell	estimated
CH_0	$0, 0 < x < 5$	cell	estimated
A_0	$50, 0 < x < 1$	cell	estimated
$Pmax$	10	1/day	estimated based on [7]
$Pmin$	1	1/day	estimated based on [7]
$NmaxTissue$	5	cell	estimated
$keqch$	1	cell	estimated
μ_A	0.005	1/day	[8]
$\lambda_{N A}$	0.55	1/cell.day	[8]
D_A	2000	$\mu m^2/day$	estimated
μ_N	3.43	1/day	[8]
$\lambda_{A N}$	0.55	1/cell.day	[8]
X_N	14400	$\mu m^2/day$	[9]
D_N	12096	$\mu m^2/day$	[10]
μ_{CH}	7	1/day	estimated
$\beta_{CH N}$	0.4	1/cell.day	[8]
D_{CH}	9216	$\mu m^2/day$	[8]

5.2 Jynacore API

Any computational modeling research group accumulates a growing number of new software tools and models. Those applications varies from new efficient simulators, proof of concept models and tools. In that highly experimental environment there is a need for flexible software tools that can fit in many use cases not previously foreseen.

There is a high number of commercial software tools to simulate stock and flux models that can be used to create and improve the understanding of a system. However, after model validation its hard to integrate them in new experimental applications due to the lack of an API or restrictive software licenses fees. The Jynacore API is as a open source software licensed in Lesser General Public License (LGPL) that do not provide a full modeling environment but encapsulate all simulation process including model description, use of multiple numerical methods and simulation data filtering. It was designed to allow the creation of new experimental computational modeling software with minimal restrictions. The API's source code comes with a complete Java implementation and two numeric methods to simulate stock and flux models of System Dynamics.

There are two ways to build a new model in the current Java implementation of Jynacore API: a) a simple XML, human readable file with stock and flux diagram elements describing the structure and Content MathML for the equations; b) direct API manipulation via Java classes. In both methods the model is kept in memory for future manipulation and simulations, which allows the user to modify the model during run time. The Jynacore API and its default implementation also allows the use of System Dynamics Metamodeling which split the modeling process in a two domain level: a domain model level, where the stock and flux constructors are used to describe a set of classes; and an instance model level, where a specific system is modeled using the classes previously defined in domain model.

5.3 Jynacore SIM

The JynaSIM is a desktop simulation environment built-in upon the Jynacore API and Java. JynaSIM can simulate stock and flux models and instance models in the case of System Dynamics Metamodeling.

The basic usage of JynaSIM is simple: after the XML file that describes a model is loaded, the user set up the simulation parameters and the numeric method to be used. Then, different scenarios can be simulated. JynaSIM also allows to filter the resulting data and to plot the model behavior on a chart. In addition, JynaSIM automatically extracts the model structured as described in the XML file and draws the diagrams and connections that graphically describe the model, using the System Dynamics language, i.e. stocks, flux, auxiliary variables and information arrows and connections. Figure 6 presents a snapshot of the JynaSIM desktop simulation environment.

6 Results

Our innate HIS model was built using the System Dynamics metamodeling tool.

6.1 Modeling the Antigen, Neutrophil and Cytokine Relations

The dimensionless model presented in Section 5.1 for the dynamics of neutrophils, antigens and cytokines was implemented using the System Dynamics stock and flux diagrams, as shown in Fig. 7.

The Fig. 8 shows the dynamics of our model of innate human system with the cytokine production during antigen phagocytosis from neutrophils. We can see the increase of neutrophils due to tissue increased permeability caused by the cytokine. It also shows the decrease of antigens until their complete elimination due to the immune response given by the neutrophils. With the elimination of the antigen the number of neutrophils goes to zero.

In the next sections we will include the spatial features of the model, i.e. diffusion and chemotaxis operators.

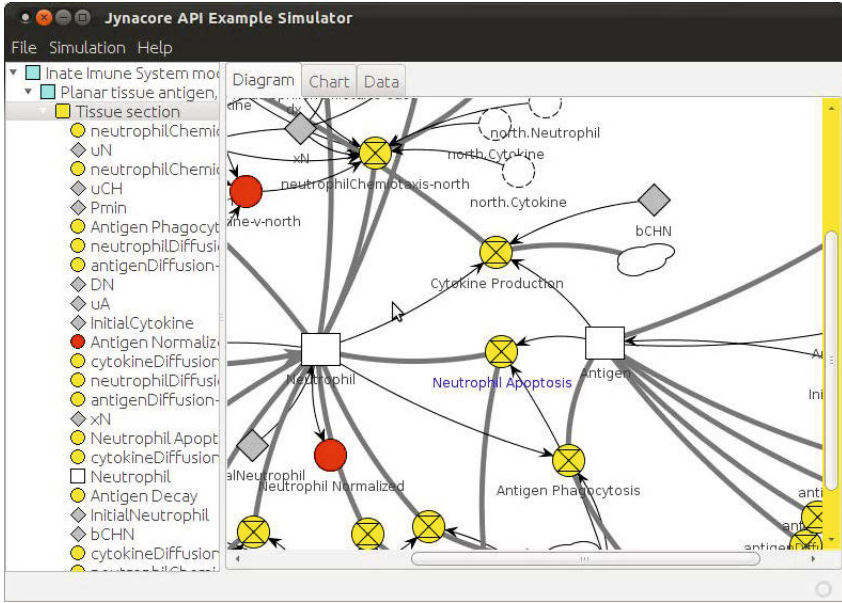


Fig. 6. JynaSIM desktop simulation environment

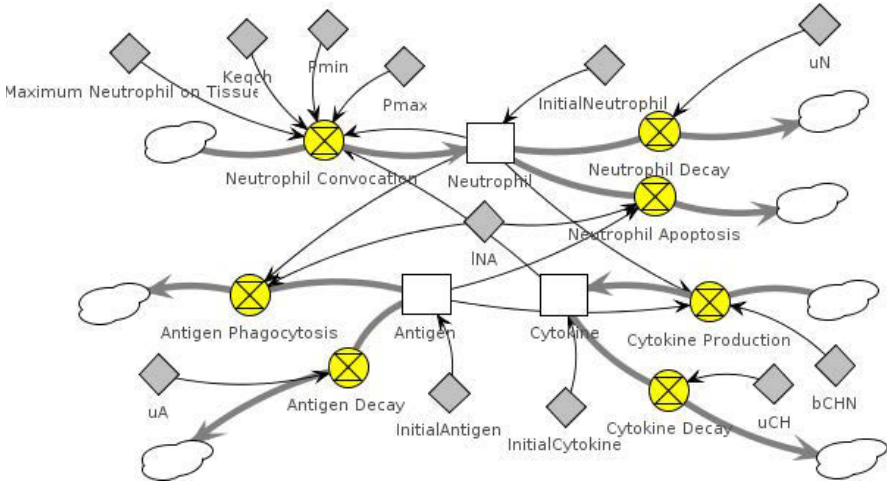


Fig. 7. The System Dynamics model of antigen, neutrophil and cytokine

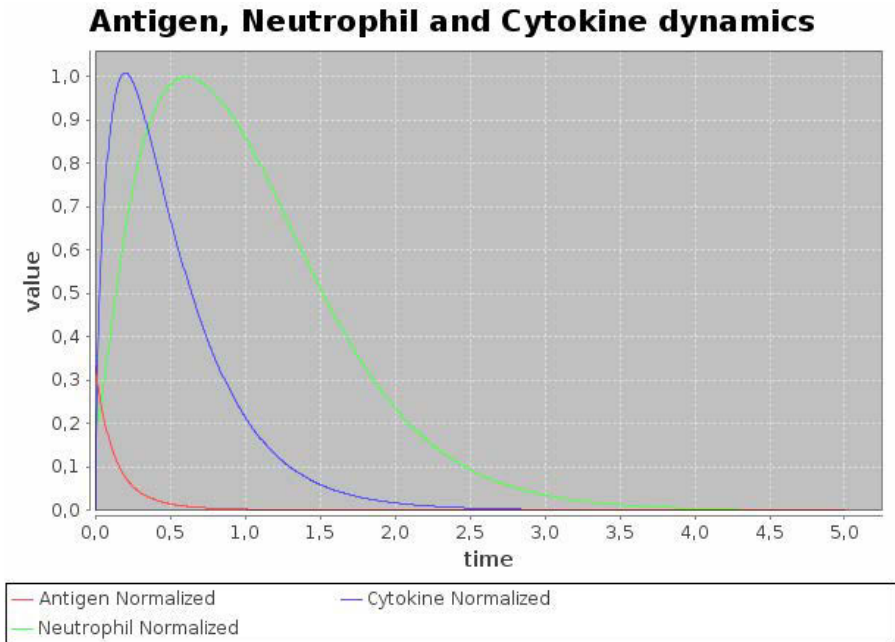


Fig. 8. The dynamics of antigen, neutrophil and cytokine in time

6.2 Modeling Diffusion in 1D

In our immune system model, we create a class "Cell" which describes the behavior of a microscopic section of tissue. In order to model an one-dimensional tissue, we use relationships between Cell instances in an discretized space by using "west" and "east" connections between neighboring Cells. For instance, Figure 9 presents how 1D diffusion of antigens is implemented using the System Dynamics Metamodeling tool. Each class "Cell" has two infinite stocks, *east.Antigen* and *west.Antigen* that will be used to calculate the incoming (or outgoing) population flux through the boundaries of this tissue volume. The values of the diffusion fluxes depend on the values *Antigen* of the neighbors. To express that, we use slashed line auxiliaries that are automatically associated during a relationship.

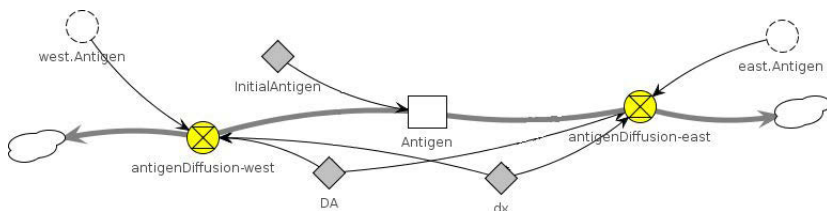


Fig. 9. Diffusion of antigens in Cell volume. We use a stock to model the amount of antigens in this Cell volume and two fluxes to describe the 1D diffusion to neighboring cells.

The initial antigen population is defined by the property *InitialAntigen* which is used as initial value in *Antigen* stock. The diffusion fluxes in Eq 4c and Eq 4d use the properties *dx*, tissue volume discretization, and D_A , diffusion coefficient of antigens, to calculate the amount of antigen population that leaves or enters the tissue volume. Both fluxes are based on the values of *Antigen* of the neighbors.

$$InitialAntigen = 5.0 \tag{4a}$$

$$Antigen(0) = InitialAntigen \tag{4b}$$

$$antigenDiffusion_{west} = D_A(Antigen - west.Antigen)/dx^2 \tag{4c}$$

$$antigenDiffusion_{east} = D_A(Antigen - east.Antigen)/dx^2 \tag{4d}$$

This method is also used to model neutrophil and cytokine diffusion. This is an intuitive and easy way to explain to newcomers in computational modeling the diffusion process of substances.

The Fig 10 shows a instance model with five Cells disposed in a linear form.

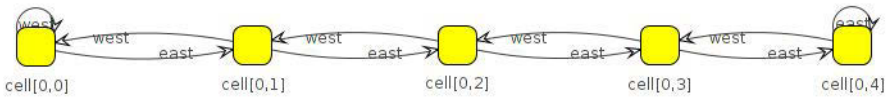


Fig. 10. Instance model with five sections of tissue

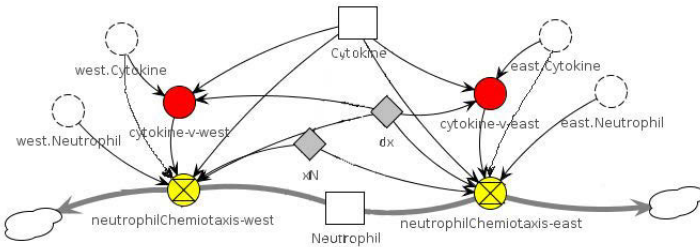


Fig. 11. Domain model of neutrophil chemotaxis for 1D tissue model

Each one of the class instances can have its own states and properties but the behavior is defined by their internal structure described in the domain class model. If the domain class changes, all instance models based on it have their behaviors changed.

6.3 Modeling the Neutrophil Chemotaxis in 1D

Similar to the implementation of the diffusion operator, the chemotaxis mathematical operator that models the transport of neutrophils in the direction of

the gradient of cytokines can also be implemented using our System Dynamics Metamodeling tool. Each class "Cell" has four infinite stocks, *east.Neutrophil*, *west.Neutrophil*, *east.Cytokine*, *west.Cytokine* that will be used to calculate the incoming (or outgoing) population flux through the boundaries of this tissue volume. For the chemotaxis, the values of the fluxes depend on the values of the *Neutrophil* and *Cytokine* of the neighbors. To express that, we use slashed line auxiliaries that are automatically associated during a relationship, see Figure 11.

To calculate the fluxes we also make use of the upwind formulation for finite volume schemes:

$$InitialNeutrophil = 1.0 \tag{5a}$$

$$cytokine_{v-west} = \frac{(west.cytokine - cytokine)}{dx} \tag{5b}$$

$$cytokine_{v-east} = \frac{(east.cytokine - cytokine)}{dx} \tag{5c}$$

$$Neutrophil(0) = InitialNeutrophil \tag{5d}$$

$$neutrophilChemiotaxis_{west} = \begin{cases} \text{if}(cytokine_{v-west} > 0.0) \\ X_N \cdot \frac{Neutrophil}{dx} \cdot \frac{(west.Cytokine - Cytokine)}{dx} \\ \text{else} \\ X_N \cdot \frac{west.Neutrophil}{dx} \cdot \frac{(Cytokine - west.Cytokine)}{dx} \end{cases} \tag{6a}$$

$$neutrophilChemiotaxis_{east} = \begin{cases} \text{if}(cytokine_{v-east} > 0.0) \\ X_N \cdot \frac{Neutrophil}{dx} \cdot \frac{(east.Cytokine - Cytokine)}{dx} \\ \text{else} \\ X_N \cdot \frac{east.Neutrophil}{dx} \cdot \frac{(Cytokine - east.Cytokine)}{dx} \end{cases} \tag{6b}$$

6.4 Two-Dimensional Tissue of HIS

We extended the linear model structure to include two other neighbors to every Cell class, or tissue volume: north and south. This allowed us to model and simulate the HIS response on a two-dimensional tissue. In Fig. 12 we used the four relationships in the same way as we did in the linear model.

As in the linear model, we can use the same domain class to create a model with any number of sections. Fig. 10 shows a model with twenty five sections of tissue distributed in an 5x5 array.

Fig. 13 presents neutrophil, cytokine and antigen kinetics on tissue for three different time instants of the simulation. Antigens population decreases due to phagocytosis by neutrophils. The neutrophils release cytokine on the tissue which increases endothelium permeability.

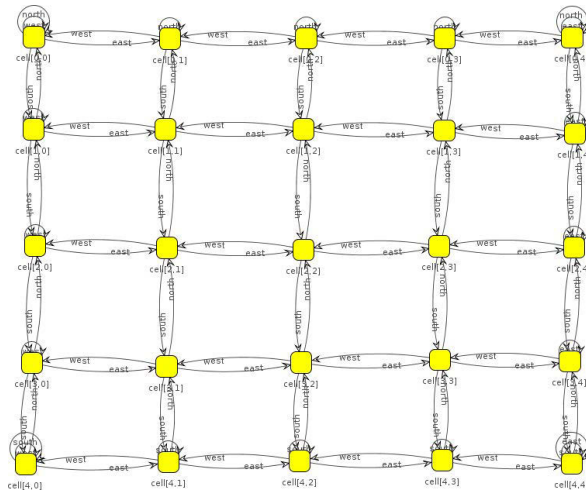


Fig. 12. Instance model with twenty five instances as a two-dimensional tissue

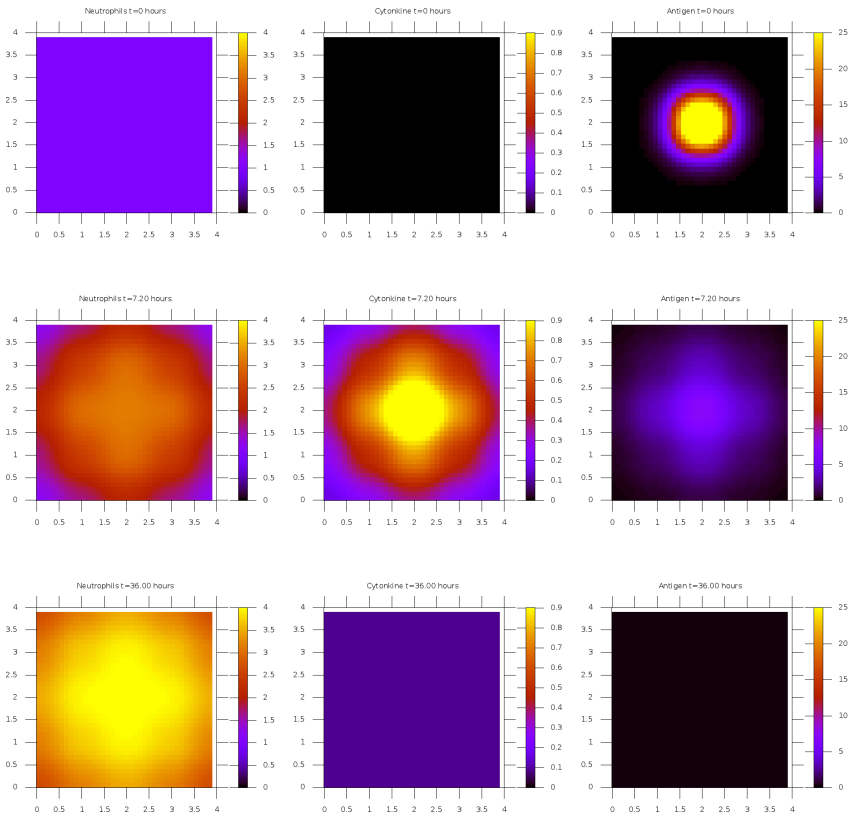


Fig. 13. Neutrophil, cytokine and antigen kinetics on tissue

7 Conclusions

In this work we presented a System Dynamics Metamodeling tool, called JynaCore API, that supports the development of complex models using System Dynamics in a more abstract level. Two levels of abstraction are used: domain modeling and instance modeling. First, instead of using pure mathematical equations, i.e. system of nonlinear ordinary equations, System Dynamics is used to describe the relations between the different variables of the model. Second, the System Dynamics models created can be instantiated multiple times and the relation between each instance can be freely defined. In this way, we could easily develop a two-dimensional tissue model that simulated the dynamics of the immune response and that included important features such as diffusion and chemotaxis behavior of neutrophils. We conclude that this new framework, based on the JynaCore API, can be used for building new models and new *in silico* experiments to support the development of computational Human Immune Systems.

Acknowledgment. The authors would like to thank the Brazilian agencies CAPES, CNPq, FAPEMIG, FINEP and UFJF.

References

1. Paul, W.E.: *Fundamental immunology*, 6th edn. Lippincott Williams & Wilkins, Philadelphia (2008)
2. De Oliveira Barros, M., Werner, C.M.L., Travassos, G.H.: A system dynamics meta-model for software process modeling. *Software Process: Improvement and Practice* 7(3-4), 161–172 (2002)
3. Murphy, K.M., Travers, P., Walport, M.: *Imunobiologia*, 7th edn. Garland Science (2010)
4. Pigozzo, A.B., Macedo, G.C., dos Santos, R.W., Lobosco, M.: Implementation of a Computational Model of the Innate Immune System. In: Liò, P., Nicosia, G., Stibor, T. (eds.) *ICARIS 2011*. LNCS, vol. 6825, pp. 95–107. Springer, Heidelberg (2011)
5. Goutelle, S., Maurin, M., Rougier, F., Barbaut, X., Bourguignon, L., Ducher, M., Maire, P.: The hill equation: a review of its capabilities in pharmacological modelling. *Fundamental & Clinical Pharmacology* 22(6), 633–648 (2008)
6. Wagner, J.G.: Kinetics of pharmacologic response i. proposed relationships between response and drug concentration in the intact animal and man. *Journal of Theoretical Biology* 20(2), 173–201 (1968)
7. Price, T., Ochs, H., Gershoni-Baruch, R., Harlan, J., Etzioni, A.: In vivo neutrophil and lymphocyte function studies in a patient with leukocyte adhesion deficiency type ii. *Blood* 84(5), 1635–1639 (1994)
8. Su, B., Zhou, W., Dorman, K.S., Jones, D.E.: Mathematical modelling of immune response in tissues. *Computational and Mathematical Methods in Medicine: An Interdisciplinary Journal of Mathematical, Theoretical and Clinical Aspects of Medicine* 10, 1748–6718 (2009)

9. Felder, S., Kam, Z.: Human neutrophil motility: Time-dependent three-dimensional shape and granule diffusion. *Cell Motility and the Cytoskeleton* 28(4), 285–302 (1994)
10. Chettibi, S., Lawrence, A., Young, J., Lawrence, P., Stevenson, R.: Dispersive locomotion of human neutrophils in response to a steroid-induced factor from monocytes. *J. Cell Sci.* 107(11), 3173–3181 (1994)

Exact and Asymptotic Computations of Elementary Spin Networks: Classification of the Quantum–Classical Boundaries

Ana Carla P. Bitencourt¹, Annalisa Marzuoli², Mirco Ragni³,
Roger W. Anderson⁴, and Vincenzo Aquilanti⁵

¹ Centro de Ciências Exatas e Tecnológicas

Universidade Federal do Recôncavo da Bahia, Cruz das Almas, Bahia, BR

² Dipartimento di Matematica ‘F Casorati’

Università degli Studi di Pavia and INFN, sezione di Pavia, 27100 Pavia, IT

³ Departamento de Física

Universidade Estadual de Feira de Santana, Feira de Santana, Bahia, BR

⁴ Department of Chemistry

University of California, Santa Cruz, California, USA

⁵ Dipartimento di Chimica

Università degli Studi di Perugia, 06123 Perugia, IT

vincenzoaquilanti@yahoo.it

Abstract. Increasing interest is being dedicated in the last few years to the issues of exact computations and asymptotics of spin networks. The large-entries regimes (semiclassical limits) occur in many areas of physics and chemistry, and in particular in discretization algorithms of applied quantum mechanics. Here we extend recent work on the basic building block of spin networks, namely the Wigner $6j$ symbol or Racah coefficient, enlightening the insight gained by exploiting its self-dual properties and studying it as a function of two (discrete) variables. This arises from its original definition as an (orthogonal) angular momentum recoupling matrix element. Progress also derives from recognizing its role in the foundation of the modern theory of classical orthogonal polynomials, as extended to include discrete variables. Features of the imaging of various regimes of these orthonormal matrices are made explicit by computational advances –based on traditional and new recurrence relations– which allow an interpretation of the observed behaviors in terms of an underlying Hamiltonian formulation as well. This paper provides a contribution to the understanding of the transition between two extreme modes of the $6j$, corresponding to the nearly classical and the fully quantum regimes, by studying the boundary lines (caustics) in the plane of the two matrix labels. This analysis marks the evolution of the turning points of relevance for the semiclassical regimes and puts on stage an unexpected key role of the Regge symmetries of the $6j$.

Keywords: Racah coefficients, $3nj$ symbols, Regge symmetries, Caustic, Ridges, Screen.

1 Introduction

This is an account of progress on understanding elementary spin networks in view of their ubiquitous occurrence in applications far beyond the theory of angular momentum in quantum mechanics where they were introduced by Wigner, Racah and others. They have been (and are) precious tools for computational nuclear, atomic, molecular and chemical physics: best known examples are vector coupling and recoupling coefficients and $3nj$ symbols [1, 2, 3, 4, 5, 6, 7, 8, 9, 10, 11, 12, 13, 14, 15].

The diagrammatic tools for “spin networks” were developed by the Yutsis school and by others [16, 17], and were given this collective name in connection with applications to discretized models for quantum gravity after Penrose [18], Ponzano and Regge [19], and many others (see *e.g.* [20, 21]).

The basic building blocks of (all) spin networks are the Wigner $6j$ symbols or Racah coefficients, which we study here by exploiting their self dual properties and consequently looking at them as functions of two variables. This approach is most natural in view of their origin as matrix elements describing recoupling between alternative angular momentum binary coupling schemes, or between alternative hyperspherical harmonics, or between alternative atomic and molecular orbitals, *etc.*, and utilizes progress in understanding their role in the foundation of the modern theory of classical orthogonal polynomials, as extended to include discrete variables [22]. Features of the imaging of the orthonormal matrices is made possible by computational advances, that permit to elaborate accurate illustrations and comparisons, using exact computations based on traditional and new recurrence relations, which allow in turn an interpretation of the observed behaviors in terms of an underlying Hamiltonian formulation. An unexpected key role of the (mysterious) Regge symmetries [23] of the $6j$ is briefly discussed. Suitable use of the results for discretization algorithms of applied quantum mechanics is stressed, with particular attention to problems arising in atomic and molecular physics.

For background information and notation, we will refer to our previous papers [7, 9, 11], regarding the one dimensional view, and also to [24, 25], where ample attention is devoted to the two dimensional perspective and where the related $4j$ model is elaborated in great detail.

2 Background Information

Semiclassical and asymptotic views are introduced to describe the dependence on parameters. They originated from the early association due to Racah and Wigner to geometrical features, respectively a dihedral angle and the volume of an associated tetrahedron (see Fig. 4 in [11]), which is the starting point of the seminal paper by Ponzano and Regge [19]. Their results provided an impressive insight into the functional dependence of angular momentum functions showing a quantum mechanical picture in terms of formulas which describe classical and non-classical discrete wavelike regimes, as well as the transition between them.

The symmetries with respect to exchanges among the matrix entries of the $6j$ (transpositions), easily understood also from the associated tetrahedron picture, are well characterized. Similarly, we find that the mirror symmetries can be exploited when the symbols are employed in applications beyond angular momentum theory, implying meaning of the entries as quantities that can have a sign.

From the detailed study of combinatorial properties (requiring only triangular relationships associated to angular momentum coupling, and the closure quadrilateral property associated to coupling of four angular momenta), it emerged very recently [24] how to uniquely assign labels to the elements of the grids for the matrix for which the orthonormalized Racah–Wigner coefficients are the elements. Features of zero volume and ridges are among properties that can be monitored on such square "screen": we sketch relationships and concept of Regge twins, "canonical" form and simplification of the following due to a suitable chosen ordering. From a computational viewpoint, explicit formulas are available as sums over a single variable. However, resorting to recursion formulas appears most convenient for exact calculations. Also, we will exploit them for semi-classical analysis, both to understand the high j -limit and, in reverse, to interpret the symbols as discrete wave-functions obeying Schrödinger type of difference (rather than differential) equations. We have derived and computationally implemented a two-variable recurrence that permits construction of the whole orthonormal matrix. The derivation follows our paper in [10] and is of interest also for other $3nj$ symbols in general. Separation of the two-variable recurrence relation leads to the basic three-term recurrence as depending on a single variable. It can be shown that it can be re-derived also from the Biedenharn–Elliot relationship in a form that shows the connection to a Schrödinger type of equation in the Hamiltonian formulation (for alternative Lagrangian formulations, see [25]). The following analysis of the caustics (and of the ridge curves, see below) is intended to characterize the modes of the spin network, as well as the guiding principles of the asymptotic analysis.

3 The Screen: Mirror, Piero and Regge Symmetries

Following e.g. the Schulten and Gordon approach [26,27], in [11] it is shown that the $6j$ symbol becomes the eigenfunction of the Schrödinger-like equation in the variable q , a continuous generalization of j_{12} :

$$\left[\frac{d}{dq^2} + p^2(q) \right] \Psi(q) = 0, \tag{1}$$

where $\Psi(q)$ is related to

$$\left\{ \begin{matrix} j_1 & j_2 & j_{12} \\ j_3 & j & j_{23} \end{matrix} \right\} \tag{2}$$

and p^2 is related with the square of the volume V of the associated tetrahedron (Fig 4 in [11]), whose edges are considered continuous and given by $J_1 = j_1 + 1/2$,

$J_2 = j_2 + 1/2$, $J_{12} = j_{12} + 1/2$, $J_3 = j_3 + 1/2$, $J = j + 1/2$, and $J_{23} = j_{23} + 1/2$. The Cayley–Menger determinant permits to calculate the square of the volume of a generic tetrahedron in terms of (squares of) its edge lengths according to

$$V^2 = \frac{1}{288} \begin{vmatrix} 0 & J_3^2 & J^2 & J_{23}^2 & 1 \\ J_3^2 & 0 & J_{12}^2 & J_2^2 & 1 \\ J^2 & J_{12}^2 & 0 & J_1^2 & 1 \\ J_{23}^2 & J_2^2 & J_1^2 & 0 & 1 \\ 1 & 1 & 1 & 1 & 0 \end{vmatrix}. \tag{3}$$

The condition for the tetrahedron with fixed edge lengths to exist as a polyhedron in Euclidean 3-space amounts to require $V^2 > 0$, while the $V^2 = 0$ and $V^2 < 0$ cases were associated by Ponzano and Regge to “flat” and nonclassical tetrahedral configurations respectively. Equivalent to (3) is the Gramian determinant, used in [24] and [25], which embodies a clearer relationship with a vectorial picture.

Major insight is provided by plotting both $6j$ s and geometrical functions (volumes, products of face areas, etc.) of the associated tetrahedra in a 2-dimensional $j_{12} - j_{23}$ plane (the square “screen” of allowed ranges of j_{12} and j_{23} to be used in all the pictures below). Actually both (3) and the Gramian are equivalent to the famous formula known to Euler but first found five centuries ago by the Renaissance mathematician, architect and painter Piero della Francesca. The formulas of course embody all the well known “classical” symmetries of geometrical tetrahedra, which show up in the $6j$ symbol as well on applying concerted interchanges of its entries. Non-obvious symmetries of particular relevance in what follows are listed below.

- (i) *The mirror symmetry.* The appearance of squares of tetrahedron edges entails that the invariance with respect to the exchange $J \leftrightarrow -J$ implies formally $j \leftrightarrow -j - 1$ with respect to the entries of the $6j$ symbol. Although this is physically irrelevant when the j s are pseudo-vectors, such as physical spins or orbital angular momenta, it can be of interest for other (e.g. discrete algorithms) applications. Regarding the screen, it can be seen that actually by continuation of the abscissa $x = J_{12}$ and ordinate $y = J_{23}$ to negative values, one can have replicas that can be glued by cutting out regions shaded in [9]. This allows mapping of the screen to the S^2 phase space found in [25].
- (ii) *Piero line.* In general, an exchange of opposite edges of a tetrahedron (or of the two entries in a column in the $6j$ symbol) corresponds to different tetrahedra and different symbols. In Piero formula, there is a term due to this difference that vanishes when any pair of opposite edges are equal. In general, a line can be drawn on the screen when ranges of j_{12} and j_{23} overlap and in the screen one may encounter what we call a Piero line: when two entries in a column are equal, this line is a diagonal corresponding to the exchange $x \leftrightarrow y$. Then, images on the screen will be symmetric with respect to such a line, as shown below with explicit examples.

(iii) *Regge symmetries.* The manifestation of these intriguing symmetries in the present context is of paramount interest: it might be elucidated through connection with the projective geometry of the elementary quantum of space, which is being reconsidered from the viewpoint of association to the polygonal inequalities (triangular and quadrilateral in the $6j$ case), which have to be enforced in any spin networks. We find it insightful to exhibit the basic Regge symmetry [23] in the following form

$$\left\{ \begin{matrix} j_1 & j_2 & j_{12} \\ j_3 & j & j_{23} \end{matrix} \right\} = \left\{ \begin{matrix} (j_1 + j_2 - j_3 + j)/2 & (j_1 + j_2 + j_3 - j)/2 & j_{12} \\ (-j_1 + j_2 + j_3 + j)/2 & (j_1 - j_2 + j_3 + j)/2 & j_{23} \end{matrix} \right\} = \left\{ \begin{matrix} j_1 + \rho & j_2 - \rho & j_{12} \\ j_3 + \rho & j - \rho & j_{23} \end{matrix} \right\}, \tag{4}$$

where $\rho = (-j_1 + j_2 - j_3 - j)/2 = [(j_2 + j) - (j_1 + j_3)]/2$. Often the Regge symmetry is written in terms of the semi-perimeter $s = (j_1 + j_2 + j_3 + j)/2$. Obviously, $s = \rho + j_1 + j_3 = -\rho + j_2 + j$.

The key observation is made in [25] that the range of both J_{12} and J_{23} , namely the “size” of the screen, is given by $2\min\{J_1, J_2, J_3, J, J_1 + \rho, J_2 + \rho, J_3 + \rho, J + \rho\}$. Therefore, for definiteness and no loss of generality, we are allowed in most cases to conveniently choose for the discussion whichever of the two $6j$ symbols twinned by (4) contains such a minimum value.

4 Features of the Tetrahedron Volume Functions: Caustics and Ridges

Looking at the volume V as a function of $x = J_{12}$ and $y = J_{23}$, and after some algebraic manipulations, we get the expressions for the x_{Vmax} and y_{Vmax} that correspond to the maximum of the volume for a fixed value of y or x (respectively), namely

$$x_{Vmax}^2 = \frac{A(J, J_2) + J_t^2 y^2 - y^4}{2 y^2}, \tag{5}$$

$$y_{Vmax}^2 = \frac{A(J_2, J) + J_t^2 x^2 - x^4}{2 x^2}, \tag{6}$$

where

$$A(a, b) = (J_1 + a)(J_1 - a)(J_3 + b)(J_3 - b), \tag{7}$$

$$J_t^2 = J_1^2 + J_2^2 + J_3^2 + J^2.$$

We call “ridge” curves the plots of Eqs. (5) and (6) on the x, y -screen. Each one marks configurations of the associated tetrahedron when two specific pairs of triangular faces are orthogonal. The corresponding values of the volume ($V_{max,x}$ and $V_{max,y}$) are

$$V_{max,x} = \frac{2 F(J_1, J, y)F(J_2, J_3, y)}{3 y}, \tag{8}$$

$$V_{max,y} = \frac{2 F(J_1, J_2, x)F(J, J_3, x)}{3 x}, \tag{9}$$

where

$$F(a, b, c) = \frac{\sqrt{(a + b + c)(a + b - c)(a - b + c)(-a + b + c)}}{4}, \tag{10}$$

is the area of the triangle with sides a , b and c .

Curves corresponding to $V = 0$ (the caustic curves) obey the equations

$$\begin{aligned} x_z^2 &= x_{V_{max}}^2 \pm \frac{12 V_{max,x}}{y}, \\ y_z^2 &= y_{V_{max}}^2 \pm \frac{12 V_{max,y}}{x}, \end{aligned} \tag{11}$$

Figure 1(a) shows these curves for the $\begin{Bmatrix} 45 & 30 & j_{12} \\ 55 & 60 & j_{23} \end{Bmatrix}$ case. The inside region enclosed by the ovaloid is that of finite volume tetrahedra, the ovaloids themselves correspond to configurations of flattened tetrahedra, specifically convex planar quadrilaterals at the upper right corner,concave planar quadrilaterals at both the upper left and and the lower right corners, and crossed planar quadrilaterals at the lower left corner.

For particular values of j_1 , j_2 , j_3 and j linear configurations are allowed as well. These interesting degenerate cases are illustrated in the other panels of Fig. 1. In Fig. 1(b) the case of $j_1 + j = j_2 + j_3$ is considered. The other interesting cases are obtained for $j_1 + j_2 = j_3 + j$ (Fig. 1(c)) and for $j_1 + j_3 = j_2 + j$ (Fig. 1(d)).

Note that, due to the symmetry properties of the $6j$ symbols, the cases $j_1 + j = j_2 + j_3$ and $j_1 + j_2 = j_3 + j$ are intrinsically equivalent. Figure 1(d) shows the effect of degeneracy with respect to the far from obvious Regge symmetry, which manifests as specularity with respect to the Piero line, in this case the diagonal from the origin in the square screen.

5 Symmetric and Limiting Cases

When some or all the j 's are equal, interesting features appear in the screen. Similarly when some are larger than others.

5.1 Symmetric Cases

For $j_1 = j_2$ plots of Eqs.(5,11) like those of Fig. 2 are obtained (equivalent to the $j_3 = j$ one, in virtue of standard symmetries).

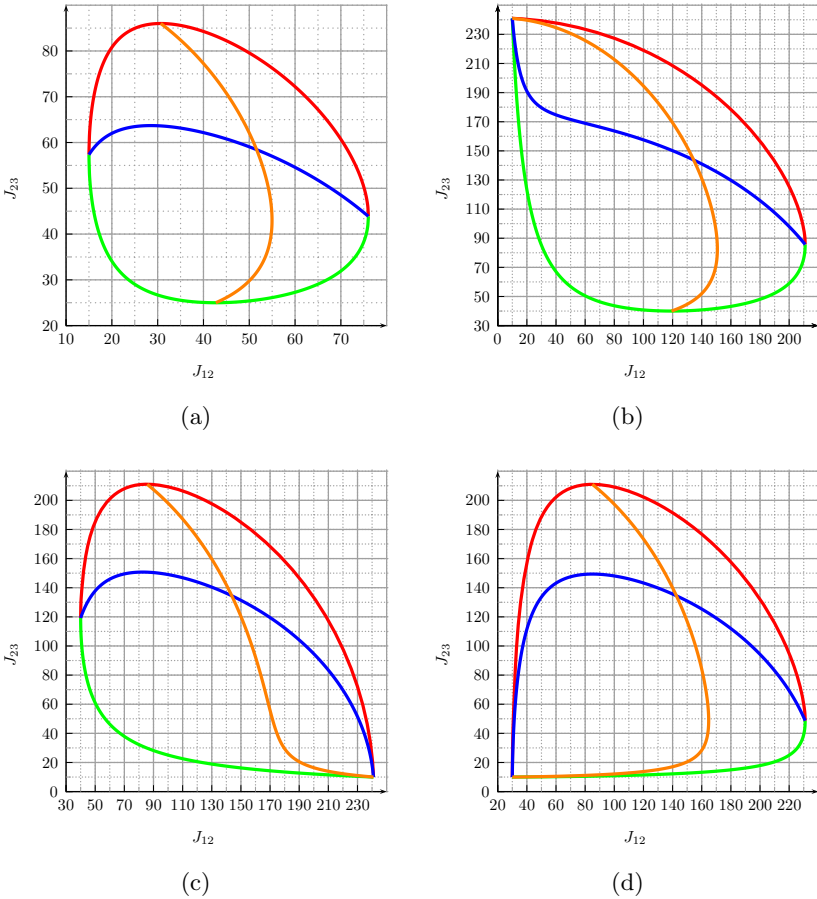


Fig. 1. Plots of the caustics and ridges given by Eqs. (5.11) for four sets of $6j$ -symbols. Panel 1(a), $j_1 = 45, j_2 = 30, j_3 = 55$ and $j = 60$. $15 \leq J_{12} \leq 76$ and $25 \leq J_{23} \leq 86$. Panel 1(b), $j_1 = 140, j_2 = 130, j_3 = 110$ and $j = 100$. $10 \leq J_{12} \leq 211$ and $40 \leq J_{23} \leq 241$. Panel 1(c), $j_1 = 140, j_2 = 100, j_3 = 110$ and $j = 130$. $40 \leq J_{12} \leq 241$ and $10 \leq J_{23} \leq 211$. Panel 1(d), $j_1 = 140, j_2 = 110, j_3 = 100$ and $j = 130$. $30 \leq J_{12} \leq 231$ and $10 \leq J_{23} \leq 211$.

For $j_1 = j_3$ plots of Eqs. (5.11) like that of Fig. 3 are obtained. By symmetry this case is equivalent to the $j_2 = j$ one.

Imposing both $j_1 + j = j_2 + j_3$ and $j_1 + j_2 = j_3 + j$ we have that $j_1 = j_3$ and $j_2 = j$. See Figs. 4(a) e 4(b).

Imposing both $j_1 + j = j_2 + j_3$ and $j_1 + j_3 = j_2 + j$ we have that $j_1 = j_2$ and $j_3 = j$. In these conditions, plots of Eqs. (5.11) like those of Fig. 5 are obtained.

This case is formally equivalent to the one where $j_1 = j$ and $j_3 = j_2$ which is obtained imposing $j_1 + j_2 = j_3 + j$ and $j_1 + j_3 = j_2 + j$.

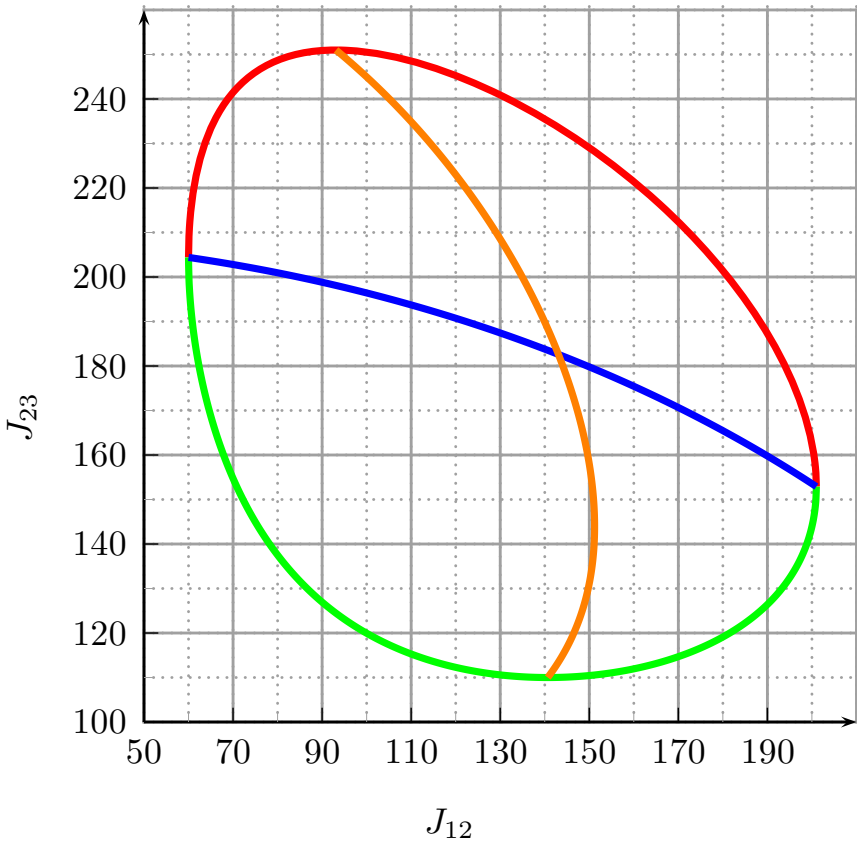


Fig. 2. Plots of the caustics and ridges (Eqs. 5.11) for the $6j$ -symbols with $j_1 = 100$, $j_2 = 100$, $j_3 = 150$ and $j = 210$. $60 \leq J_{12} \leq 201$ and $110 \leq J_{23} \leq 251$.

5.2 Limiting Cases

Interestingly, the Fig. 5 permits us to discuss the caustics of the $3j$ symbols as limiting case of the corresponding $6j$ where three entries are larger than the other ones, namely:

$$\begin{pmatrix} j_1 & j_2 & j_3 \\ m_1 & m_2 & m_3 \end{pmatrix} = \lim_{R \rightarrow \infty} \left\{ \begin{matrix} j_1 & j_2 & j_3 \\ l_1 + R & l_2 + R & l_3 + R \end{matrix} \right\}, \tag{12}$$

where

$$\begin{aligned} m_1 &= l_3 - l_2, \\ m_2 &= l_1 - l_3. \end{aligned} \tag{13}$$

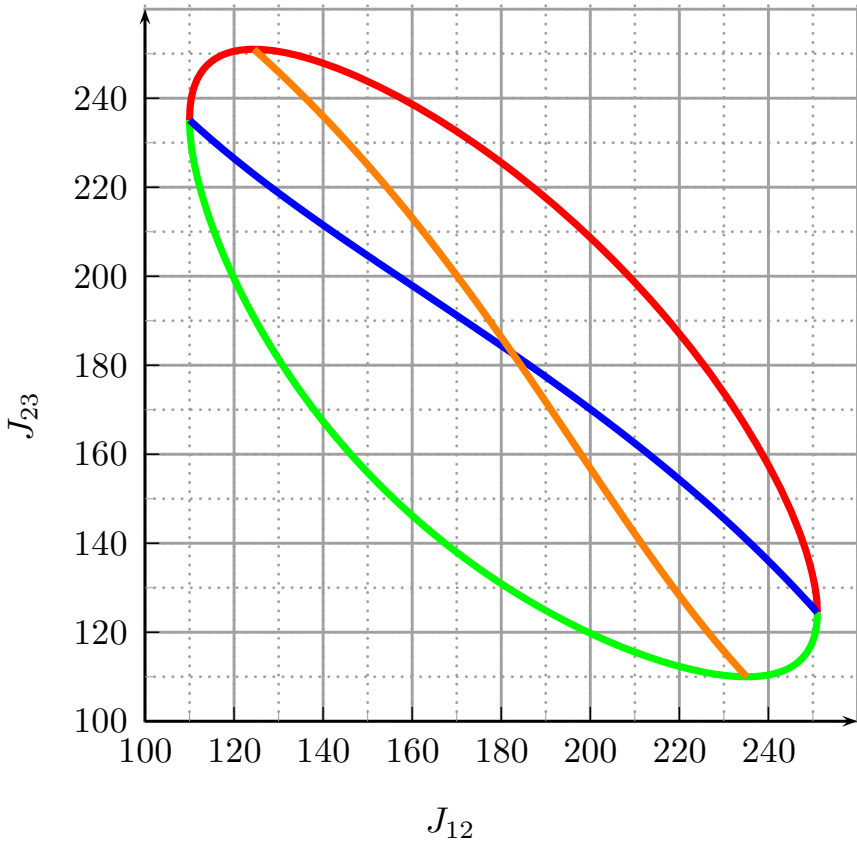


Fig. 3. Plots of the caustics and ridges (Eqs. 5.11) for the $6j$ -symbols with $j_1 = 100$, $j_2 = 150$, $j_3 = 100$ and $j = 210$. $110 \leq J_{12} \leq 251$ and $110 \leq J_{23} \leq 251$.

If we define

$$\begin{aligned}
 m_1 &:= F + D, \\
 m_2 &:= F - D, \\
 \bar{R} &:= R + l_3 - D,
 \end{aligned}
 \tag{14}$$

we have

$$\begin{pmatrix} j_1 & j_2 & j_3 \\ m_1 & m_2 & m_3 \end{pmatrix} = \lim_{\bar{R} \rightarrow \infty} \left\{ \begin{matrix} j_1 & j_2 & j_3 \\ \bar{R} + F & \bar{R} - F & \bar{R} + D \end{matrix} \right\}.
 \tag{15}$$

For $\bar{R} \rightarrow \infty$ it is $\bar{R} \pm F \simeq \bar{R}$.

The caustic of the $3j$ symbol is defined as

$$\begin{vmatrix} 0 & J_1^2 - m_1^2 & J_2^2 - m_2^2 & 1 \\ J_1^2 - m_1^2 & 0 & J_3^2 - m_3^2 & 1 \\ J_2^2 - m_2^2 & J_3^2 - m_3^2 & 0 & 1 \\ 1 & 1 & 1 & 0 \end{vmatrix} = 0,
 \tag{16}$$

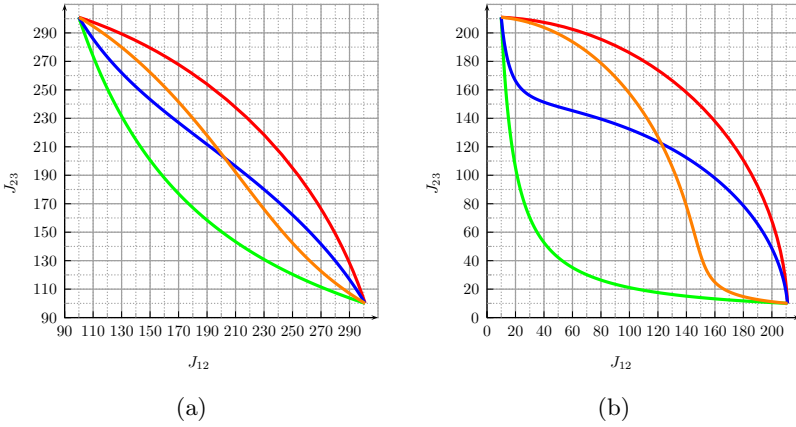


Fig. 4. Plots of the caustics and ridges (Eqs. 5.11) for two sets of $6j$ symbols. Panel (a), $j_1 = 200, j_2 = 100, j_3 = 200$ and $j = 100$. $100 \leq J_{12} \leq 301$ and $100 \leq J_{23} \leq 301$. Panel (b), $j_1 = 110, j_2 = 100, j_3 = 110$ and $j = 100$. $10 \leq J_{12} \leq 211$ and $10 \leq J_{23} \leq 211$.

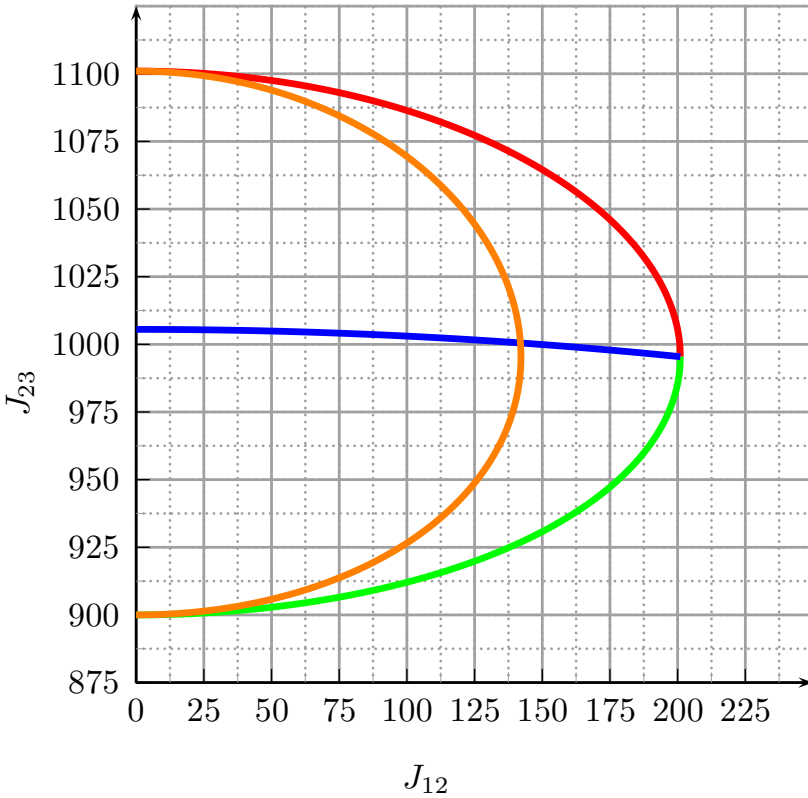


Fig. 5. Plots of the caustics and ridges (Eqs. 5.11) for the $6j$ symbols with $j_1 = 1000, j_2 = 1000, j_3 = 100$ and $j = 100$. $0 \leq J_{12} \leq 201$ and $900 \leq J_{23} \leq 1001$. According to the text, this figure also exemplifies features of ridges and caustics for a $3j$ symbol.

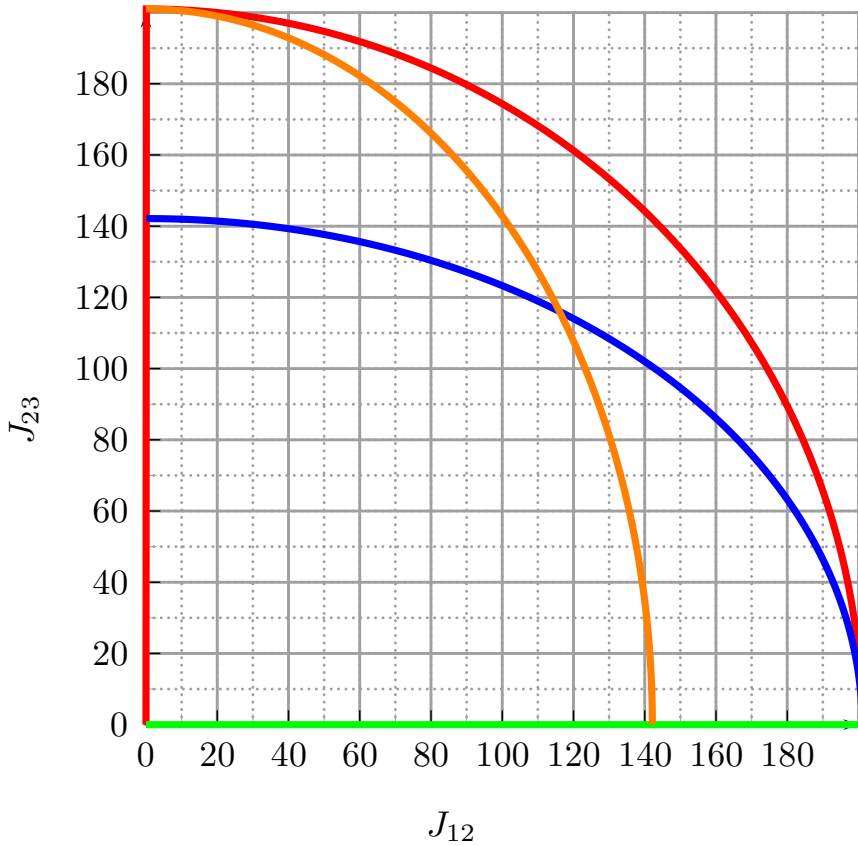


Fig. 6. Plots of the caustics and ridges (Eqs. 5.11) for the full symmetric $6j$ -symbols with $j_1 = 100, j_2 = 100, j_3 = 100$ and $j = 100$. $0 \leq J_{12}, J_{23} \leq 201$. This figure clearly points out the interest of extending the screen by mirror symmetries.

and

$$\begin{vmatrix} 0 & J_1^2 - m_1^2 & J_2^2 - m_2^2 & 1 \\ J_1^2 - m_1^2 & 0 & J_3^2 - m_3^2 & 1 \\ J_2^2 - m_2^2 & J_3^2 - m_3^2 & 0 & 1 \\ 1 & 1 & 1 & 0 \end{vmatrix} = \lim_{R \rightarrow \infty} \frac{\begin{vmatrix} 0 & (L_1 + R)^2 & (L_2 + R)^2 & (L_3 + R)^2 & 1 \\ (L_1 + R)^2 & 0 & J_3^2 & J_2^2 & 1 \\ (L_2 + R)^2 & J_3^2 & 0 & J_1^2 & 1 \\ (L_3 + R)^2 & J_2^2 & J_1^2 & 0 & 1 \\ 1 & 1 & 1 & 1 & 0 \end{vmatrix}}{2R^2}, \tag{17}$$

The case of caustics on the screen for four large entries, leading to reduced Wigner d matrices, is studied in [24].

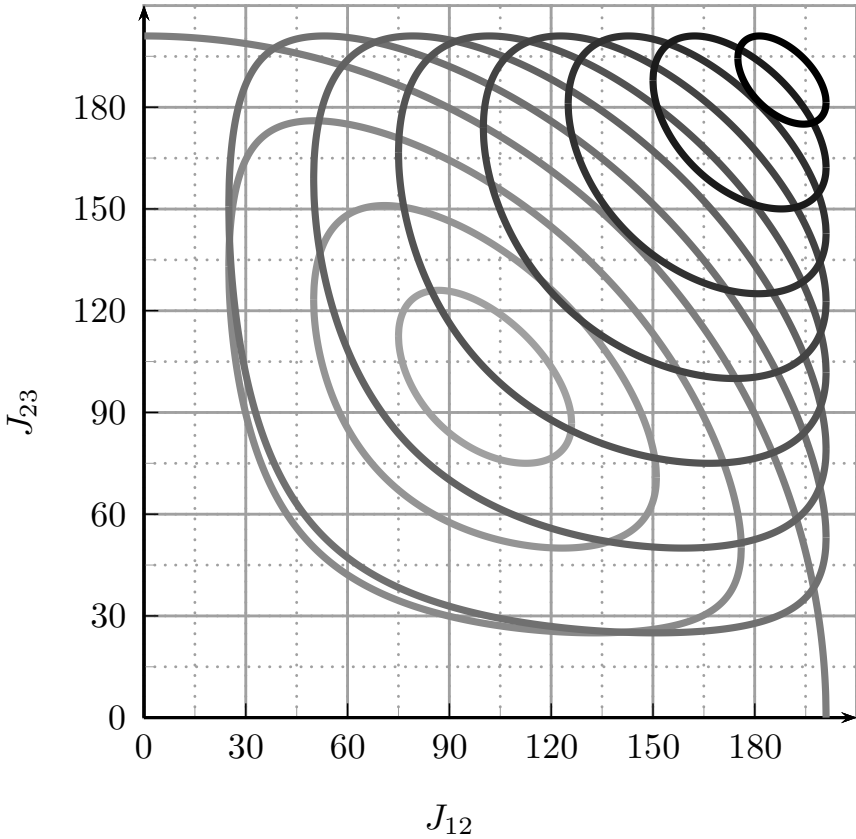


Fig. 7. Plots of the caustics and ridges (Eqs. 5.11) for $j_1 = j_2 = j_3 = 100$ while j varies from 25 (light line) to 275 (dark line) with step of 25 units

For $j_1 = j_2 = j_3 = j$ plots of Eqs. (5.11) like those of Fig. 6 are obtained. This case is obtained when $j_1 + j = j_2 + j_3$, $j_1 + j_2 = j_3 + j$ and $j_1 + j_3 = j_2 + j$.

Fig. 7 shows the caustics of a full-symmetric $6j$ when the symmetry is broken by varying j .

6 Remarks and Conclusion

Explicit computational formulas are available either as sums over a single variable and series. However recourse to recursion formulas appears most convenient for both exact calculations and -as we will emphasize elsewhere- also for semi-classical analysis, in order to understand high j limits and in reverse to interpret them as discrete wavefunctions obeying Schrödinger type of difference (rather than differential) equations. In further work, we derive and computationally

implement the two variable recurrence that permits construction of the whole orthonormal matrix. The derivation follows our paper in [10] and is of interest also for other $3nj$ symbols in general.

The extensive images of the exactly calculated $6j$'s on the square screens illustrate how the caustic curves studied in this paper separate the classical and nonclassical regions, where they show wavelike and evanescent behaviour respectively. Limiting cases, and in particular those referring to $3j$ and Wigner's d matrix elements can be analogously depicted and discussed. Interesting also are the ridge lines, which separate the images in the screen tending to qualitatively different flattening of the quadrilateral, namely convex in the upper right region, concave in the upper left and lower right ones, and crossed in the lower left region.

Interestingly, the Regge symmetries not only restrict the range of the discrete manifold, but also allow an assignment of the involved modes.

As a continuation of our recent work, this paper has demonstrated that interesting insight into properties of the basic building blocks of spin networks, the Wigner $6j$ symbols or Racah coefficients, is gained by exploiting their self dual properties and studying them as a function of two variables, an approach most natural in view of their origin as matrix elements. Features of their imaging of the orthonormal matrices are fostered by computational advances, which is being developed on traditional and new recurrence relations, which also allow interpretation of the underlying Hamiltonian mechanics: the borderline of the two limiting modes –quasi-classical and deeply quantum- has been the object of this paper. The characteristic features of this boundary line, described by the caustic curves which follow the turning points of the classical motion, have been elucidated. A key role was also revealed of the surprising Regge symmetries.

Further work based on these tools involves detailed studies of some of the important aspects considered too briefly or not at all in this paper, such as the classical, mirror and Regge symmetries, the limiting cases to the simpler $3j$ coefficients and rotation matrix elements, the extensions to higher $3nj$ symbols and to the so called q deformations.

Semiclassical and asymptotic analysis provide limiting relationships converging into the Askey scheme. Relationships also arose then with orthogonal polynomials, and indicate avenues to views to generalizations (continuous extensions, relationships with harmonics of rotation groups, and finally q -extensions, ...). All these extensions may need some modifications when detailed properties are discussed, but in general studying $6j$ symbols continues to deserve further work.

Use is finally pointed out for discretization algorithms of applied quantum mechanics, particular attention being devoted to problems encountered in atomic and molecular physics.

Acknowledgments. MR and ACPB acknowledge the CNPq agency for the financial support. MR is also grateful for the financial support by the FAPESB agency.

References

- [1] Aquilanti, V., Cavalli, S., Grossi, G.: Hund's cases for rotating diatomic molecules and for atomic collisions: angular momentum coupling schemes and orbital alignment. *Z. Phys. D.* 36, 215–219 (1996)
- [2] Aquilanti, V., Capecchi, G.: Harmonic analysis and discrete polynomials. From semiclassical angular momentum theory to the hyperquantization algorithm. *Theor. Chem. Accounts* 104, 183–188 (2000)
- [3] Aquilanti, V., Cavalli, S., Coletti, C.: Angular and hyperangular momentum recoupling, harmonic superposition and Racah polynomials. a recursive algorithm. *Chem Phys. Letters* 344, 587–600 (2001)
- [4] Aquilanti, V., Coletti, C.: $3nj$ -symbols and harmonic superposition coefficients: an icosahedral abacus. *Chem. Phys. Letters* 344, 601–611 (2001)
- [5] De Fazio, D., Cavalli, S., Aquilanti, V.: Orthogonal polynomials of a discrete variable as expansion basis sets in quantum mechanics. The hyperquantization algorithm. *Int. J. Quantum Chem.* 93, 91–111 (2003)
- [6] Aquilanti, V., Haggard, H., Littlejohn, R., Yu, L.: Semiclassical analysis of Wigner $3j$ -symbol. *J. Phys. A* 40, 5637–5674 (2007)
- [7] Aquilanti, V., Bitencourt, A.C.P., Ferreira, C.d.S., Marzuoli, A., Ragni, M.: Quantum and semiclassical spin networks: from atomic and molecular physics to quantum computing and gravity. *Physica Scripta* 78(058103), 7 pages (2008)
- [8] Anderson, R.W., Aquilanti, V., Ferreira, C.d.S.: Exact computation and large angular momentum asymptotics of $3nj$ symbols: semiclassical disentangling of spin-networks. *J. Chem. Phys.* 129(161101), 5 pages (2008)
- [9] Aquilanti, V., Bitencourt, A.C.P., Ferreira, C.d.S., Marzuoli, A., Ragni, M.: Combinatorics of angular momentum recoupling theory: spin networks, their asymptotics and applications. *Theor. Chem. Accounts* 123, 237–247 (2009)
- [10] Anderson, R.W., Aquilanti, V., Marzuoli, A.: $3nj$ morphogenesis and semiclassical disentangling. *J. Phys. Chem. A* 113, 15106–15117 (2009)
- [11] Ragni, M., Bitencourt, A.C.P., Ferreira, C.d.S., Aquilanti, V., Anderson, R.W., Littlejohn, R.: Exact computation and asymptotic approximation of $6j$ symbols. illustration of their semiclassical limits. *Int. J. Quantum Chem.* 110, 731–742 (2010)
- [12] Aquilanti, V., Haggard, H., Hedeman, A., Jeevanjee, N., Littlejohn, R., Yu, L.: Semiclassical mechanics of the Wigner $6j$ -symbol. *J. Phys. A* 45(065209) (2012)
- [13] Aquilanti, V., Cavalli, S., De Fazio, D.: Angular and hyperangular momentum coupling coefficients as hahn polynomials. *J. Phys. Chem.* 99, 15694–15698 (1995)
- [14] Aquilanti, V., Cavalli, S., De Fazio, D.: Hyperquantization algorithm I. Theory for triatomic systems. *J. Phys. Chem.* 109, 3792–3805 (1998)
- [15] Aquilanti, V., Cavalli, S., De Fazio, D., Volpi, A.: The A+BC reaction by the hyperquantization algorithm: the symmetric hyperspherical parametrization for $j > 0$. *J. Phys. Chem.* 39, 103–121 (2001)
- [16] Yutsis, A., Levinson, I., Vanagas, V.: *The Mathematical Apparatus of the Theory of Angular Momentum*. Program for Sci. Transl. Ltd., Jerusalem (1962)
- [17] Varshalovich, D., Moskalev, A., Khersonskii, V.: *Quantum Theory of Angular Momentum*. World Scientific, Singapore (1988)
- [18] Penrose, R.: Angular momentum: an approach to combinatorial space-time. In: Bastin, T. (ed.) *Quantum Theory and Beyond*. Cambridge Univ. Press (1971)
- [19] Ponzano, G., Regge, T.: Semiclassical limit of racah coefficients. In: *Spectroscopic and Group Theoretical Methods in Physics* (1968)

- [20] Rovelli, C.: Quantum Gravity. Cambridge University Press (2004)
- [21] Carfora, M., Marzuoli, A., Rasetti, M.: Quantum Tetrahedra. *J. Phys. Chem. A* 113, 15376–15383 (2009)
- [22] Koekoek, R., Lesky, P., Swarttouw, R.: Hypergeometric orthogonal polynomials and their q -analogues. Springer (2010)
- [23] Regge, T.: Symmetry properties of Racah's coefficients. *Nuovo Cimento* 11, 116–117 (1959)
- [24] Littlejohn, R., Yu, L.: Uniform semiclassical approximation for the Wigner $6j$ symbol in terms of rotation matrices. *J. Phys. Chem. A* 113, 14904–14922 (2009)
- [25] Aquilanti, V., Haggard, H.M., Hedeman, A., Jeevangee, N., Littlejohn, R., Yu, L.: Semiclassical mechanics of the Wigner $6j$ -symbol. *J. Phys. A* 45(065209) (2012)
- [26] Schulten, K., Gordon, R.: Exact recursive evaluation of $3j$ - and $6j$ -coefficients for quantum mechanical coupling of angular momenta. *J. Math. Phys.* 16, 1961–1970 (1975)
- [27] Schulten, K., Gordon, R.: Semiclassical approximations to $3j$ - and $6j$ -coefficients for quantum-mechanical coupling of angular momenta. *J. Math. Phys.* 16, 1971–1988 (1975)

Performance of DFT and MP2 Approaches for Geometry of Rhenium Allenylidenes Complexes and the Thermodynamics of Phosphines Addition

Cecilia Coletti and Nazzareno Re

Dipartimento di Scienze del Farmaco, Università degli Studi G. d'Annunzio, Via Dei Vestini,
31, I-66100 Chieti, Italy
{ccoletti,nre}@unich.it

Abstract. The performance of density functional theory (DFT) and Møller-Plesset perturbation second order theory (MP2) for prediction of the geometry of an important class of rhenium complexes and the thermodynamics of their reaction with nucleophiles has been assessed. In particular, we addressed the rhenium(I) allenylidene [(triphos)(CO)₂Re(=C=C=CPh₂)]⁺ species [triphos = MeC(CH₂PPh₂)₃] and its reaction toward tertiary phosphines. Several exchange-correlation functionals were tested and the results indicate that the usually employed GGA and hybrid functionals, such as BP86, BLYP, B3LYP and PBE while correctly predicting the geometry of these species, qualitatively and quantitatively fail to reproduce the thermodynamics for the addition of the phosphine nucleophiles, especially the first three ones, with errors up to 30 kcal mol⁻¹. Reasonable results, qualitatively in agreement with experimental evidence, can be obtained only through the use of a correlated wavefunction approach such as MP2 or of the more recently developed functionals M06 and M06-L.

Keywords: Rhenium allenylidenes, nucleophilic attack, phosphines, DFT, M06, MP2, exchange-correlation functionals.

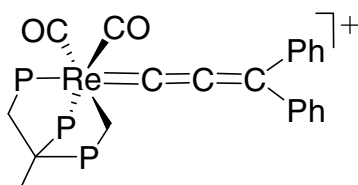
1 Introduction

The organometallic chemistry of group VIII transition metals is very important in catalytic applications and has attracted much interest from both a synthetic and a theoretical point of view.[1-2] Indeed, quantum chemistry modelling of these organometallic catalytic systems could greatly support the understanding of the detailed mechanisms of the corresponding catalytic processes thus allowing a rational design of new and improved catalysts.[2] Unfortunately quantitative energetic information on transition metal compounds and their reactions, such as reaction and activation enthalpies and free energies, is still elusive and require highly correlated wavefunction methods which are, however, computationally too heavy for the large size of many organometallic catalytic systems.[3] Although DFT methods have been more and more employed in the last two decades to study organometallic systems, [4] some

studies have recently pointed out several problems or even their failure especially for highly conjugated π -systems and for systems of large size, where mid-range correlation effects and dispersion interactions become important.[5] Along these lines, in the last years, a few studies have investigated the performance of newly developed DFT methods when applied to catalytic systems, mainly based on ruthenium.[6-7] In particular the newly developed DFT methods, such as M05, M05-2X, M06, M06-2X, M06-L, have been found to be able to reproduce with sufficient accuracy the behaviour of most of the considered systems.[7]

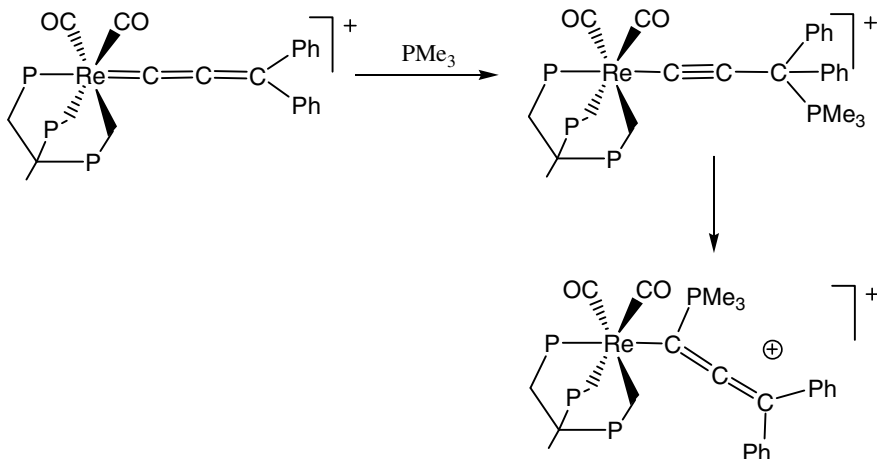
We have become interested on a recently developed class of allenylidene complexes, of the formula $[(\text{triphos})(\text{CO})_2\text{Re}(\text{=C=C=CRR}')^+]$, see Chart 1, based on the rhenium(I) synthon $[\text{Re}(\text{triphos})(\text{CO})_2]^+$ (triphos = MeC(CH₂PPh₂)₃).[8-9]

Chart 1. Allenylidene complexes of the $[(\text{triphos})(\text{CO})_2\text{Re}]^+$ synthon.



Transition metal allenylidenes, $[\text{L}_n\text{M}=\text{C}=\text{C}=\text{CRR}']^+$, [10] have received much attention in the last years for their applications to organic synthesis,[11] homogeneous catalysis, [12] and the design of new materials.[13] Indeed, the $\text{M}=\text{C}=\text{C}=\text{C}$ moiety, with its unsaturated carbon chain and its alternating array of electrophilic/nucleophilic carbon sites, makes allenylidene complexes unique organometallic reagents for use in both fundamental and applied chemistry, especially in processes whereby the formation of a C-C or C-heteroatom bond is sought. [11-12] The large majority of known allenylidene complexes contains d^6 transition metal ions, particularly ruthenium(II) and, to a lesser extent, iron(II) and osmium(II).[10] Experimental evidences[10] and theoretical calculations[14] have shown that for these complexes the α - and γ -carbon atoms of the allenylidene chain are electrophilic centers, while the β -carbon atom is nucleophilic.

The rhenium(I) allenylidenes have shown a diverse chemistry rivaling with that of the much more common isoelectronic d^6 -ruthenium allenylidenes,[15-16] and are particularly interesting as they have allowed a clear rationalization of the regioselectivity of the addition of tertiary phosphines to metal allenylidenes. Indeed, an investigation of the reaction of $[(\text{triphos})(\text{CO})_2\text{Re}(\text{=C=C=CPh}_2)]\text{OTf}$ (where OTf^- is the triflate ion), with tertiary phosphines PMe_3 , [15] has shown an initial attack at the C_γ -allenylidene carbon to give γ -phosphonioalkynyl species $[(\text{triphos})(\text{CO})_2\text{Re}\{\text{C}\equiv\text{CCPh}_2(\text{PMe}_3)\}]\text{OTf}$, which thermally and irreversibly isomerizes to the thermodynamically stable α -phosphonioallenyl species $[(\text{triphos})(\text{CO})_2\text{Re}\{\text{C}(\text{PMe}_3)=\text{C}=\text{CPh}_2\}]\text{OTf}$, see Scheme 1. Therefore, for these rhenium(I) allenylidenes it is experimentally verified that the phosphine nucleophiles first attack the allenylidene- C_γ carbon atom to give kinetic γ -phosphonioalkynyl products that thermally transform into thermodynamic α -phosphonioallenyl derivatives.

Scheme 1. Reactivity of [(triphos)(CO)₂Re{C=C=C(Ph)R}]OTf allenylidenes with PMe₃.

A recent theoretical study on this system has pointed out the failure of some of the most common DFT methods, in particular B3LYP, and shown that a correlated wavefunction method such as MP2 is required to give thermodynamic results consistent with the experimental observations.[8] Prompted by these preliminary results and by recent studies showing that newly developed DFT exchange-correlation functionals, such as those of the M06 family, specifically parametrized for organometallic chemistry and non-covalent interactions, perform better than older functional, such as BP86 or B3LYP, [17] we reinvestigated more thoroughly the rhenium allenylidene system, employing also the recently developed functionals and trying to point out the reasons of the previously noticed failures.

2 Computational and Methodological Details

All calculations were carried out using density functional theory and LMP2 as implemented in the Jaguar 7.5 suite[18] of ab initio quantum chemistry programs. Geometries were optimized with Jaguar, using different exchange correlation functionals, i.e. BP86,[19] BLYP,[20] PBE,[21] B3LYP,[22] M06[23] and M06-L.[23] The 6-31G** basis set was employed for the main groups atoms,[24] and the Los Alamos LACVP** basis, [25] including relativistic effective core potentials, for rhenium (BS1). The energies were reevaluated by additional single point calculations at each optimized geometry using the triple-zeta basis set 6-311++G**, [26] while rhenium was described by a modified version of LACVP**, designated as LACV3P++**, where the exponents were decontracted and a diffuse function added (BS2).

Along with DFT methods, the Møller-Plesset second order approach was employed,[27] both in the canonical MP2 form (limited to the smallest model only, model 1, see below) and the local version, LMP2,[28] which offers a lower

computational cost and a reduced basis set superposition error (BSSE). Indeed, previous calculations showed that LMP2 with triple- ζ plus polarization basis sets accurately reproduce the MP2 results for several kinds of systems.[29]

We optimized at the LMP2 level of theory the smallest model only, because the size of the allenylidene complex and attacking phosphine molecules and the large basis sets required to achieve a sufficient accuracy (with up to 104 atoms and 1520 basis functions), would prevent a full systematic optimization of all considered minima. These test calculations have shown that a further optimization at LMP2/BS1 level does not significantly affect either the geometries of the allenylidene complex and the products of the attack of the PMe_3 nucleophile to its C_α and C_γ atoms, or the corresponding reaction energies, see below. For the largest models we therefore performed single point LMP2/BS2 calculations on the PBE/BS1 geometries.

For the same reason PBE/BS1 geometry was also used to evaluate binding energies at the heavier canonical MP2 level of theory (MP2/BS2) for the smallest model.

The extent of the BSSE was also evaluated for model 1 by calculating counterpoise corrections according to Boys-Bernardi computational scheme.[30]

Vibrational frequency calculations based on analytical second derivatives at the PBE/BS1 level of theory were performed to confirm proper convergence to local minima for equilibrium geometries.

We make use of the restricted spin formalism throughout the whole study, since all molecules and fragments discussed in this work are closed shell species.

Bond dissociation energies between the nucleophiles and the allenylidene complexes have been calculated as energy difference between the energies of the addition products and those of the optimized reagents.

3 Results and Discussion

3.1 Allenylidene Complex

Benchmarking of Model Molecules and Geometry. Due to the large size of the considered rhenium(I) allenylidenes $[(\text{triphos})(\text{CO})_2\text{Re}(\text{C}=\text{C}=\text{CPh}_2)]^+$ complex, comprising eight phenyl groups, six from the ancillary tridentate tripodal ligand and two sitting on the C_γ carbon of the allenylidene moiety, and in an attempt to evaluate the possibility of reducing the large computational load required to perform high level calculations on the real complex, we tested three different models of increasing size which progressively approach the real complex cation and assessed the DFT and LMP2 methods on each of them. Notably, we considered a model where all the eight phenyl groups were replaced by hydrogen atoms (model 1), a model explicitly including only the two phenyl groups on the terminal carbon atom of the allenylidene chain (model 2) and finally a model where we included four phenyl rings, namely the two on the allenylidene unit and the two on the triphos ligand pointing toward the allenylidene moiety and thus responsible for possible steric clashes with the substituents on the phosphine nucleophiles attacking the allenylidene unit (model 3), see Figure 1. The theoretical study of these models is also useful to point out the effect of the phenyl substituents on the allenylidene moiety

and of the phenyl groups on the triphos ligand on the electronic structure and reactivity of the considered Re(I) allenylidene complex.

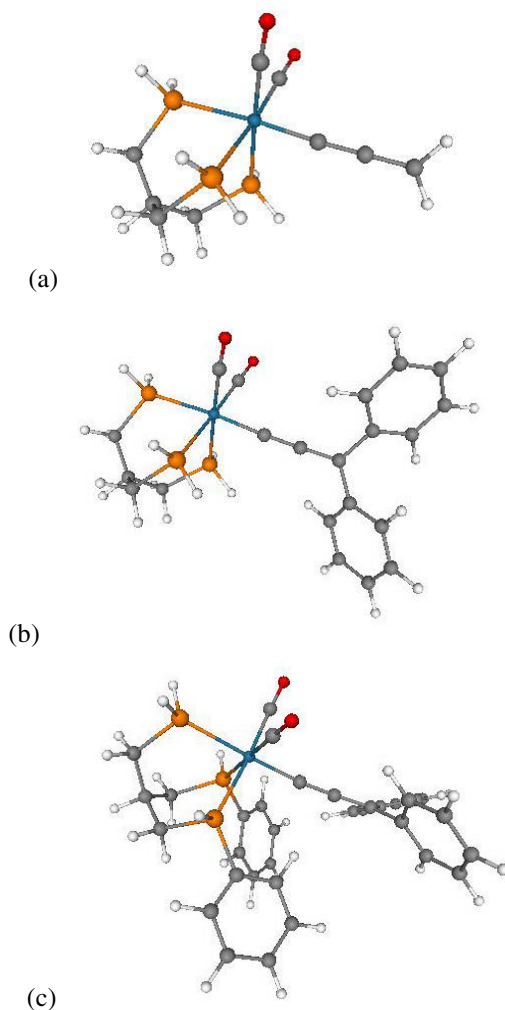


Fig. 1. Optimized geometries, at PBE/BS1 level, of the three considered models for the rhenium(I) $[(\text{triphos})(\text{CO})_2\text{Re}(\text{C}=\text{C}=\text{CPh}_2)]^+$ allenylidene complex cation including: (a) none, (b) two and (c) four out of the eight phenyl groups (see text). Carbon atoms are depicted in grey, oxygen in red, phosphorous in yellow, rhenium in blue.

For each of these models, some of the most common functionals employed in calculations on organometallics systems were benchmarked against the X-ray geometry and the experimentally observed pattern of thermodynamic stability.[15] In particular, we considered the popular BP86, BLYP, PBE and B3LYP functionals, that have been

shown in the last two decades to give fairly good results in the evaluation of the geometry of transition metal and organometallic complexes and the energetics of their reactions,[4] and the newly developed functionals M06 and M06-L which have been recently shown to best perform with transition metal systems.[7,17]

Table 1. Main geometrical parameters calculated at the BP86/BS1, BLYP/BS1, B3LYP/BS1, PBE/BS1, M06/BS1 and M06-L/BS1 levels for the three considered models and their comparison with the experimental X-ray data for the real complex. For the smallest model 1, geometry optimization has been carried out also at the LMP2/BS1 level.

System	Bond distances (Å)			Bond angles (°)			
	Re-C1	C1-C2	C2-C3	C1-Re-P1	C1-Re-P2	P-Re-P	C-Re-C
Model 1							
BP86	1.966	1.282	1.338	91.6	91.0	83.3	87.8
BLYP	1.977	1.281	1.338	91.8	91.1	83.4	87.9
B3LYP	1.968	1.273	1.328	91.8	91.0	83.4	88.1
PBE	1.966	1.282	1.336	91.4	91.0	83.2	87.8
M06	1.957	1.275	1.323	91.6	89.4	83.5	87.7
M06-L	1.967	1.276	1.327	92.9	91.3	80.5	88.0
LMP2	1.955	1.279	1.336	91.4	88.9	83.0	85.6
Model 2							
BP86	2.011	1.267	1.380	91.9	90.3	83.6	89.1
BLYP	2.025	1.265	1.381	91.7	90.9	83.5	89.2
B3LYP	2.018	1.255	1.370	91.9	90.4	83.7	89.3
PBE	2.006	1.266	1.377	91.8	90.0	83.4	89.2
M06	2.012	1.256	1.369	91.2	90.9	84.5	93.9
M06-L	2.012	1.256	1.370	90.5	89.8	82.5	89.4
Model 3							
BP86	2.007	1.270	1.377	99.5	92.8	87.3	94.2
BLYP	2.018	1.268	1.378	98.9	93.3	88.1	93.9
B3LYP	2.012	1.258	1.367	99.2	92.9	87.9	93.8
PBE	2.000	1.268	1.374	98.7	92.0	87.4	94.1
M06	2.000	1.260	1.365	95.8	89.6	87.3	94.4
M06-L	1.999	1.261	1.367	91.9	91.9	85.4	94.0
X-ray^a	1.996(4)	1.237(6)	1.359(6)	96.0(1)	94.6(1)	84.0(2)	91.4(2)

^aData from reference 15.

Geometry optimizations were performed on all the above models with the six considered functionals and the BS1 basis set, see the PBE/BS1 geometries in Figure 1, and the main geometrical parameters are reported in Table 1 together with the X-ray data. Table 1 shows that the geometrical parameters calculated for each of the three different

models vary slightly with the employed functional, with bond lengths within 0.01 Å and bond angles within 8°. Geometry optimization were also carried out at the LMP2/BS1 level, but – due to the large computational load – limited only to the smallest model 1: the calculated geometrical parameters do not significantly differ from those obtained at DFT levels. It is also worth noting that for the smallest model 1 the new M06 and M06-L functionals give results closer to those obtained at LMP2 level, and for the more realistic model 3 the same two functionals give results closer to the experimental values.

More importantly, the comparison of the calculated and the X-ray geometries indicates that the inclusion of the two phenyl groups on the C_γ is necessary to reproduce with sufficient accuracy the geometry of the Re=C=C=C core, because of conjugation effects, while the inclusion of two further phenyl groups on the triphos ligand allows to reproduce also the main bonding angles between the ligands around the metal center. The comparison of the calculated geometrical parameters with the X-ray data is therefore meaningful only for the largest model and shows a good agreement with the experimental data at essentially all considered levels of theory.

Bond Energies. We have then calculated the bond dissociation energy between the [(triphos)(CO)₂Re]⁺ fragment and the C=C=CPh₂ ligand and the results obtained for the considered DFT functionals and at the LMP2 level of theory for the largest model 3 are reported in Table 2.

The bond dissociation energy of the allenylidene unit calculated at the LMP2/BS2//PBE/BS1 level is 89.6 kcal mol⁻¹, and similar values are obtained at the M06/BS2//M06/BS1 (90.4 kcal mol⁻¹), M06-L/BS2//M06-L/BS1 (86.9 kcal mol⁻¹) and PBE/BS2//PBE/BS1 (88.0 kcal mol⁻¹) levels. Significantly lower values are obtained employing the traditional BP86 (83.7 kcal mol⁻¹), BLYP (76.7 kcal mol⁻¹), and B3LYP (78.8 kcal mol⁻¹) functionals.

We therefore notice that the new M06 and M06-L functionals give bond energy values very close to that calculated at LMP2 level, while the traditional DFT functionals give significantly lower values, by 6-11 kcal mol⁻¹, with the only exception of PBE.

Table 2. Calculated bond dissociation energies (kcal mol⁻¹) for the allenylidene complex [Cp(CO)₂Ru(C=C=CPh₂)]⁺ using different functionals and the LMP2 method. Only the largest model 3 has been considered.

Method	D _c
BP86/BS2//BP86/BS1	83.7
BLYP/BS2//BLYP/BS1	76.7
B3LYP/BS2//B3LYP/BS1	78.8
PBE/BS2//PBE/BS1	88.0
M06/BS2//M06/BS1	90.4
M06-L/BS2//M06-L/BS1	86.9
LMP2/BS2//PBE/BS1	89.6

3.2 Reaction with Phosphines

We then considered the products of the nucleophilic attack of trimethylphosphine, PMe_3 , to the Re(I) allenylidene complex. Geometry optimizations were performed for all three models with all considered functionals on both possible products, the α -phosphonioallenyl and the γ -phosphonioalkynyl complexes, using the BS1 basis set. Geometry optimizations were also performed at the LMP2/BS1 level but, due to the high computational load, only on the smallest model 1. The geometrical parameters calculated for model 3 are reported in Figure 2 and Table 3 and show an important difference between the classical DFT functionals BP86, BLYP, B3LYP and PBE and the newly developed M06 and M06-L: the latter ones lead to a slightly but significantly shorter $\text{C}_\alpha\text{-P}$ and $\text{C}_\gamma\text{-P}$ bond lengths. This difference can be ascribed to the main feature of the two new functionals specifically developed to reproduce the attractive

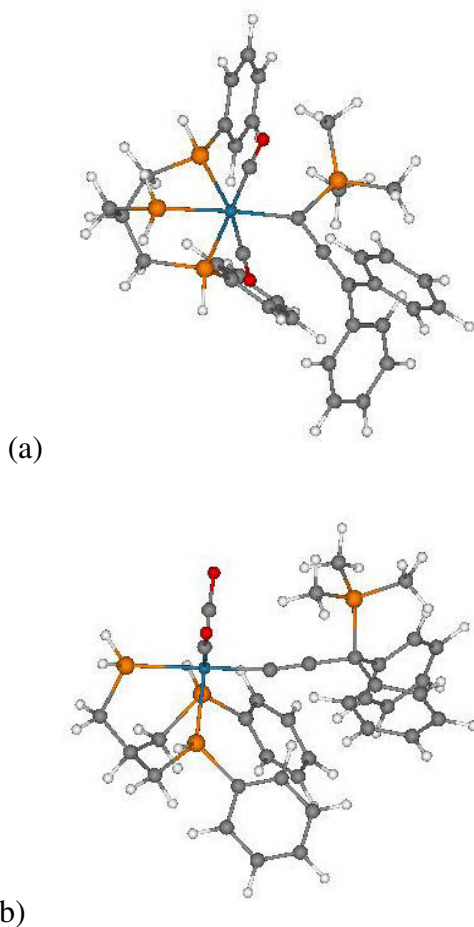


Fig. 2. Optimized geometries, at PBE/BS1 level, of (a) the α -phosphonioallenyl and (b) the γ -phosphonioalkynyl products, for model 3 (four phenyls) and PMe_3

dispersion interactions completely neglected by the traditional DFT functionals: therefore the BP86, BLYP, B3LYP and PBE functionals incorrectly overestimate the steric repulsion between the three methyl groups on the P atom and the two neighbouring phenyl groups on C_α and C_γ and lead to longer C_α -P and C_γ -P bond lengths while the M06 and M06-L functionals account for the attractive dispersion interactions among these groups leading to shorter C_α -P and C_γ -P bond lengths. This explanation is supported by the differences in the bond angles, see Table 3, showing that the phenyls approach more closely the methyl groups in the M06 and M06-L geometries.

For both products, the corresponding binding energies with respect to separated phosphine and metal allenylidene were calculated (using the energies re-evaluated with the BS2 basis set). For the smallest model 1, we also included the BSSE corrections calculated with the CP approach.[30] The results are reported in Table 4 for model 1 and Table 5 for models 2 and 3. First of all we see that in simplest model 1, with two hydrogen atoms on C_γ , the α -phosphonioallenyl and the γ -phosphonioalkynyl products are very close in energy, at almost all levels of theory, in disagreement with the experimental evidence showing a clear thermodynamic preference for the α -phosphonioallenyl derivative. The correct experimental trend is instead reproduced by both the larger models 2 and 3 showing, respectively, a preference of ca. 15-20 and 6-14 kcal mol⁻¹ for the α -phosphonioallenyl species. These results indicate that the inclusion in the model of at least the two phenyl substituents on the C_γ atom is necessary to determine the higher thermodynamical stability of the α -adduct, while the inclusion of two further phenyl groups on the triphos ligand appreciably reduces the energy difference between the two tautomers, likely due to steric congestion of the C_α position, and probably representing a more realistic picture of the energetics separating the pair of tautomers. Together with the benchmark on the geometrical parameters, see above, this result clearly indicates that only the largest model 3 can give a realistic representation of the experimental allenylidene.

Table 3. Geometrical parameters calculated at the BP86/BS1, BLYP/BS1, B3LYP/BS1, PBE/BS1, M06/BS1, M06-L/BS1 level for α -adduct and γ -adducts. Only the largest model 3 has been considered.

System	α -adduct			γ -adduct		
	P-C $_\alpha$	Re-P-CPh $_1$	Re-P-CPh $_2$	P-C $_\gamma$	P-C $_\gamma$ -CPh $_3$	P-C $_\gamma$ -CPh $_4$
BP86	1.821	126.1	133.6	1.940	105.3	107.5
BLYP	1.832	126.3	135.2	1.974	105.9	107.2
B3LYP	1.812	125.9	133.9	1.923	106.5	107.9
PBE	1.813	125.4	133.1	1.927	106.4	107.7
M06	1.789	123.6	126.0	1.888	107.1	108.6
M06-L	1.792	123.7	129.2	1.899	105.2	108.9

Although not directly comparable with the experimental data, the results for model 1 in Table 4 allow an interesting analysis of the effect of (i) performing a geometry optimization at the LMP2 level; (2) using the local LMP2 rather than the canonical MP2 level; and (iii) including the CP correction. We see that geometry optimization at LMP2 level has almost no effects on the phosphine binding energy, by less than 1 kcal mol⁻¹, in agreement with the little effects on the geometrical parameters (see above). The BSSE correction has only small effects on the binding energies calculated with all DFT functionals and the LMP2 approach, within 1-2 kcal mol⁻¹, while a large effect, of ca. 10-15 kcal mol⁻¹, has been observed with the canonical MP2 approach. Interestingly, the BSSE corrected MP2 bonding energies are very close to BSSE uncorrected LMP2 bonding energies showing that the use of the “local” LMP2 version gives a double advantage on the canonical MP2 form: a reduced computational load and the inclusion of most BSSE effects, as previously noticed for simpler systems.[29]

Tables 4 and 5 also show that the binding energies of PMe₃ to the C_α and C_γ atoms, calculated with the BP86, BLYP and B3LYP level, are much lower than those calculated at LMP2 or MP2 (limitately to model 1) while the values calculated with the M06 and M06-L functionals are much closer, with the PBE results in the middle. In particular, for the more realistic model 3, the binding energies of PMe₃ to C_α (leading to the thermodynamically most stable adduct) calculated with the BP86, BLYP and B3LYP functionals are ca. 25-30 kcal mol⁻¹ lower than those calculated at LMP2 level while that calculated with the PBE functional is ca. 15 kcal mol⁻¹ lower and those

Table 4. Binding energies (kcal mol⁻¹) of PMe₃ to the C_α and C_γ atoms of the rhenium(I) allenylidene calculated at the various levels of theory for the smallest model 1. Counterpoise corrections to BSSE were added in the last two columns.

Nucleophile	BE _{α-adduct}	BE _{γ-adduct}	BE ^{CP} _{α-adduct}	BE ^{CP} _{γ-adduct}
Model 1				
BP86	-36.3	-33.9	-34.0	-32.6
BLYP	-26.6	-25.2	-25.0	-24.1
B3LYP	-33.8	-32.9	-32.2	-31.8
PBE	-41.2	-37.7	-39.4	-36.4
M06	-46.9	-42.3	-44.6	-40.6
M06-L	-47.3	-40.3	-45.1	-38.1
LMP2 ^a	-45.6	-43.4	-44.0	-42.5
LMP2 ^b	-45.7	-43.7	-43.9	-41.3
MP2 ^c	-56.8	-51.5	-43.3	-42.3

^a At LMP2/BS2//PBE/BS1 level.

^b At LMP2/BS2//LMP2/BS1 level.

^c At MP2/BS2//PBE/BS1 level.

calculated with the M06 and M06-L functionals only 2-3 kcal mol⁻¹ lower. A similar trend is observed for the the binding energies of PMe₃ to C_γ, although the M06 and M06-L values are no longer so close to the LMP2 ones. The underestimation of the binding energies by the traditional DFT functionals BP86, BLYP, B3LYP and PBE is probably due to the neglect of the attractive dispersion interaction between the neighbouring phenyls and methyl groups, as supported by the longer C_α-P and C_γ-P bond lengths, see discussion above.

Interestingly, when we look at the absolute values of the binding energies for model 3, we see that the B3LYP functional lead to a barely stable (by 1.1 kcal mol⁻¹) and the BP86 and BLYP even to an unstable (by 0.6 and 7.7 kcal mol⁻¹) γ -adduct, while the PBE and even more the M06 and M06-L functionals and the LMP2 method lead to a clearly thermodynamically stable γ -adduct, respectively by 7.8, 20.4, and 16.5 and 33.3 kcal mol⁻¹, consistently with the experimental evidence showing that the γ -phosphonioalkynyl complex formed by the reaction of the considered rhenium allenylidene and PMe₃ is stable at room temperature for several days before it isomerizes to the thermodynamically more stable α -phosphonioallenyl species.¹⁵ These results suggest

Table 5. Binding energies (kcal mol⁻¹) of PMe₃ to the C_α and C_γ atoms of the rhenium(I) allenylidene calculated at various levels of theory for the two largest considered models 2 and 3

Nucleophile	BE _{α-adduct}	BE _{γ-adduct}	ΔBE _(α,γ)
Model 2			
BP86	-18.0	-2.4	-15.6
BLYP	-10.6	+4.8	-15.4
B3LYP	-19.1	-3.5	-15.6
PBE	-26.6	-10.4	-16.2
M06	-39.1	-22.4	-16.7
M06-L	-35.5	-15.8	-19.7
LMP2 ^a	-42.5	-32.7	-19.8
Model 3			
BP86	-9.0	+0.6	-9.6
BLYP	-2.6	+7.7	-10.3
B3LYP	-6.6	-1.1	-5.5
PBE	-19.3	-7.8	-11.5
M06	-31.7	-20.4	-11.3
M06-L	-30.8	-16.5	-14.3
LMP2 ^a	-34.2	-33.3	-0.9

^a At LMP2/BS2//PBE/BS1 level.

that only the LMP2 approach and the M06 and M06-L functionals lead to a realistic picture of the thermodynamics associated to the addition of a tertiary phosphine to the multiply unsaturated carbon chain of the rhenium allenylidene, a result supported by recent benchmark studies showing that the M06 and M06-L functionals outperform the traditional GGA and hybrid functionals such as BP86, BLYP and B3LYP.[5,7,17]

The large discrepancy between the classical DFT and LMP2 approaches is quite surprising and a definitive assessment of the two approaches would require a deeper methodological study with more accurate wavefunction methods such as CCSD(T) or CASSCF followed by multireference MP2 calculations and/or the comparison with experimental thermodynamic data. Unfortunately, the large size of these systems prevents more accurate post-SCF calculations nor any quantitative thermodynamic data are available. However, useful qualitative clues to the assessment of the DFT and LMP2 results come from careful considerations on the experimental results of the nucleophilic addition reaction of trimethylphosphine to [(triphos)(CO)₂Re(=C=C=CPh₂)]OTf.[15] In particular, in situ IR and NMR studies have allowed to characterize the γ -phosphonioalkynyl product and to observe that it is a stable species at room temperature for at least several days that only slowly converts into the more stable α -phosphonioallenyl isomer. This room temperature stability of the γ -phosphonioalkynyl product implies a free activation energy of at least 20-25 kcal mol⁻¹ for its dissociation to [(triphos)(CO)₂Re(=C=C=CPh₂)]⁺ and PMe₃. If we consider that (i) large and favorable zero-point and entropic contributions to this activation energy are expected (a value of ca. 5-10 kcal mol⁻¹), and (ii) the transition state must be less than 10-15 kcal mol⁻¹ above the dissociation products since the addition of phosphines has been observed to occur immediately at -78 °C (a value of ca. 10 kcal mol⁻¹ has been estimated in ref. 8), we are led to the conclusion that the reaction energy for the formation of the γ -adduct has to be higher than 20-25 kcal mol⁻¹. From Table 5 we see that only the results of the LMP2 (33.2 kcal mol⁻¹), M06 (20.1 kcal mol⁻¹) and to a lesser extent M06-L (16.5 kcal mol⁻¹) are consistent with this experimental constraint, the BP86, BLYP, B3LYP and PBE functionals leading to unreasonably low values.

On the basis of the above benchmark, we may conclude that only LMP2 and M06 and M06-L calculations, used in combination with the largest model 3, give a reasonable agreement with the available experimental data for the addition of the considered nucleophile. On the other hand, the BP86, BLYP, B3LYP and the PBE functionals, although able to reproduce the geometry and bonding features of this rhenium allenylidene complex, are less accurate in predicting the geometry of the phosphine adducts and, above all, grossly fail to predict the energetics of the addition of nucleophiles to metal allenylidenes, especially at the C _{γ} atom.

4 Conclusions

The performance of density functional theory (DFT) and Møller-Plesset perturbation second order theory (MP2) for prediction of the geometry of an important class of Rhenium complexes and the thermodynamics of their reaction with nucleophiles was assessed.

Several exchange-correlation functionals were tested and the results indicate that the usually employed GGA and hybrid functionals, such as BP86, BLYP, B3LYP and PBE, while correctly predicting the geometry of these species, qualitatively and quantitatively fail to reproduce the thermodynamics for the addition of the phosphine nucleophiles, especially the first three ones, with errors up to 30 kcal mol⁻¹. Reasonable results, qualitatively in agreement with experimental evidence, can be obtained only through the use of a correlated wavefunction approach, such as MP2 or of the more recently developed functionals M06 and M06-L. The latter two functionals also give a presumably better estimate of the geometries of the phosphine adducts to the considered allenylidene complex, in particular of the resulting C-P bond lengths.

Both geometry and binding energy errors by the traditional DFT functionals BP86, BLYP, B3LYP and PBE can be ascribed to the neglect of the attractive dispersion interaction between the neighbouring phenyls and methyl groups.

References

1. Steinborn, D.: *Fundamentals of organometallic catalysis*. Wiley-VCH, Weinheim (2012)
2. Hartwig, J.: *Organotransition metal chemistry: from bonding to Catalysis*. University Science Books, Sausalito (2010); Sautet, P., Delbecq, F.: *Chem. Rev.* 110, 178 (2010)
3. Jiang, W., De Yonker, N.J., Determan, J.J., Wilson, A.K.: *J. Phys. Chem. A* 116, 870 (2012)
4. Quintal, M.M., Karton, A., Iron, M.A., Daniel Boese, A., Martin, J.M.L.: *J. Phys. Chem. A* 110, 709 (2006); Harvey, J.N.: *Annu. Rep. Prog. Chem., Sec. C: Phys. Chem.* 102, 203 (2006)
5. Wodrich, M.D., Corminboeuf, C., von Ragué Schleyer, P.Y., Truhlar, D.: *Org. Lett.* 8, 3631 (2006); Zhao, Y., Truhlar, D.G.: *J. Phys. Chem. A* 110, 10478–10486 (2006); Grimme, S., Steinmetz, M., Korth, M.: *J. Chem. Theory Comput.* 3, 4245 (2007)
6. Fomine, S., Tlenkoplatchev, M.A.: *Organometallics* 26, 4491 (2007); Sieffert, N., Büehl, M.: *Inorg. Chem.* 48, 4622 (2009)
7. Sliwa, P., Handzlik, J.: *Chem. Phys. Lett.* 493, 273 (2010); Zhao, Y., Dutta, B.F.E., Curchod, B., Campomanes, P., Solari, E., Scopelliti, R., Rothlisberger, U., Severin, K.: *Chem. Eur. J.* 16, 8400 (2010); Kulkarni, A.D., Truhlar, D.G.: *J. Chem. Theory Comput.* 7, 2325 (2011)
8. Coletti, C., Gonsalvi, L., Guerriero, A., Marvelli, L., Peruzzini, M., Reginato, G., Re, N.: *Organometallics* 29, 5982 (2010)
9. Coletti, C., Gonsalvi, L., Guerriero, A., Marvelli, L., Peruzzini, M., Reginato, G., Re, N.: *Organometallics* 31, 57 (2012)
10. Bruce, M.I.: *Chem. Rev.* 98, 2797 (1998); Rigaut, S., Touchard, D., Dixneuf, P.H.: *Coord. Chem. Rev.* 248, 1585–1601 (2004); Cadierno, V., Gimeno, J.: *Chem. Rev.* 109, 3512 (2009)
11. Touchard, D., Dixneuf, P.H.: *Coord. Chem. Rev.* 409, 178–180 (1998); Bruneau, C., Dixneuf, P.H.: *Acc. Chem. Res.* 32, 311 (1999); Buil, M.I., Esteruelas, M.A., López, A.M., Oñate, E.: *Organometallics* 22, 162 (2003); Bruneau, C., Dixneuf, P.H. (eds.) *Metal Vinylidenes and Allenylidenes in Catalysis: From Reactivity to Applications in Synthesis*. Wiley-VCH, Weinheim (2008)
12. Abdallaoui, I.A., Sémeril, D., Dixneuf, P.H.: *J. Mol. Catal. A: Chem.*, 182–183, 577 (2002); Akiyama, R., Kobayashi, S.: *Angew. Chem., Int. Ed.* 41, 2602 (2002); Bruneau, C., Dixneuf, P.H.: *Angew. Chem., Int. Ed.* 45, 2176–2203 (2006)

13. Bunz, U.H.F.: *Angew. Chem., Int. Ed. Engl.* 35, 969 (1996); Roth, G., Fischer, H., Meyer-Friedrichsen, T., Heck, J., Houbrechts, S., Persoons, A.: *Organometallics* 17, 1511–1516 (1998); Dembiski, R., Bartik, T., Bartik, B., Jaeger, M., Gladysz, J.A.: *J. Am. Chem. Soc.* 122, 810 (2000)
14. Marrone, A., Re, N.: *Organometallics* 21, 3562 (2002); Marrone, A., Coletti, C., Re, N.: *Organometallics* 23, 4952 (2004); Auger, N., Touchard, D., Rigaut, S., Halet, J.-F., Sallard, J.-Y.: *Organometallics* 22, 1638 (2003); Coletti, C., Marrone, A., Re, N.: *Acc. Chem. Res.* 45, 139 (2012)
15. Mantovani, N., Marvelli, L., Rossi, R., Bianchini, C., de los Rios, I., Romerosa, A., Peruzzini, M.: *J. Chem. Soc., Dalton Trans.*, 2353 (2001)
16. Peruzzini, M., Barbaro, P., Bertolasi, V., Bianchini, C., de los Rios, I., Mantovani, N., Marvelli, L., Rossi, R.: *J. Chem. Soc., Dalton Trans.*, 4121 (2003); Mantovani, N., Bergamini, P., Marchi, A., Marvelli, L., Rossi, R., Bertolasi, V., Ferretti, V., de los Rios, I., Peruzzini, M.: *Organometallics* 25, 416 (2006)
17. Zhao, Y., Truhlar, D.: *Theor. Chem. Acc.* 120, 215 (2008); Truhlar, D.G.: *Acc. Chem. Res.* 41, 157 (2008)
18. Jaguar 7.5. Schrödinger, LLC, New York, NY (2007)
19. Becke, A.D.: *Phys. Rev. A* 38, 3098 (1988); Perdew, J.P.: *Phys. Rev. B* 33, 8822 (1986)
20. Lee, C., Yang, W., Parr, R.G.: *Phys. Rev. B* 37, 785 (1988)
21. Perdew, J.P., Burke, K., Enzerhof, M.: *Phys. Rev. Lett.* 67, 3865 (1996)
22. Becke, A.D.: *J. Chem. Phys.* 98, 5648 (1993); Lee, C.T., Yang, W.T., Parr, R.G.: *Phys. Rev. B* 37, 785 (1988)
23. Zhao, Y., Truhlar, D.G.: *J. Chem. Phys.* 125, 194101 (2006)
24. Hehre, W.J., Ditchfield, R., Pople, J.A.: *J. Chem. Phys.* 56, 22567–2261 (1972)
25. Hay, P.J., Wadt, W.R.: *J. Chem. Phys.* 82, 270, 284, 299 (1985)
26. Krishnan, R., Binkley, J.S., Seeger, R., Pople, J.A.: *J. Chem. Phys.* 72, 650 (1980)
27. Møller, C., Plesset, M.S.: *Phys. Rev.* 40, 618 (1934)
28. Saebo, S., Tong, W., Pulay, P.: *J. Chem. Phys.* 98, 2170 (1993)
29. Kaminski, G.A., Maple, J.R., Murphy, R.B., Braden, D.A., Friesner, R.A.: *J. Chem. Theory Comput.* 1, 248 (2005)
30. Boys, S.F., Bernardi, R.: *Mol. Phys.* 19, 553 (1970)

Author Index

- Abdullah, Noryusliza IV-364
Abdullah, Nurul Azma IV-353
Abid, Hassan III-368
Adewumi, Adewole IV-248
Afonso, Vitor Monte IV-274, IV-302
Agarwal, Suneeta IV-147
Aguiar, Rui L. III-682
Aguilar, José Alfonso IV-116
Ahmadian, Kushan I-188
Aларcon, Vladimir J. II-578, II-589
Albuquerque, Caroline Oliveira III-576
Alfaro, Pablo IV-530
Ali, Salman III-352
Alizadeh, Hosein III-647
Almeida, Regina III-17
Alonso, Pedro I-29
Alves, Daniel S.F. I-101
Amandi, Analía A. III-698, III-730
Amaral, Paula III-159
Amjad, Jaweria III-368
Ammar, Reda A. I-161
Amorim, Elisa P. dos Santos I-635
An, Deukhyeon III-272
Anderson, Roger W. I-723
Angeloni, Marcus A. I-240
Antonino, Pablo Oliveira III-576
Aquilanti, Vincenzo I-723
Arefin, Ahmed Shamsul I-71
Armentano, Marcelo G. III-730
Arnaout, Arghad IV-392
Aromando, Angelo III-481
Asche, Hartmut II-347, II-386, II-414, II-439
Aydin, Ali Orhan IV-186
Ayres, Rodrigo Moura Juvenil III-667
Azad, Md. Abul Kalam III-72
Azzato, Antonello II-686
- Bae, Sunwook III-238
Balena, Pasquale I-583, II-116
Balucani, Nadia I-331
Barbosa, Ciro I-707
Barbosa, Fernando Pires IV-404
Barbosa, Helio J.C. I-125
- Baresi, Umberto II-331
Barreto, Marcos I-29
Baruque, Alexandre Or Cansian IV-302
Bastianini, Riccardo I-358
Batista, Augusto Herrmann III-631
Batista, Vitor A. IV-51
Battino, Silvia II-624
Beaver, Justin IV-646
Bencardino, Massimiliano II-548
Berdún, Luis III-698
Berenguel, José L. III-119
Bernardino, Heder S. I-125
Berretta, Regina I-71
Biehl, Matthias IV-40
Bimonte, Sandro II-373
Bisceglie, Roberto II-331
Bitencourt, Ana Carla P. I-723
Blecic, Ivan II-481, II-492
Boavida, Fernando II-234
Bollini, Letizia II-508
Boratto, Murilo I-29
Borg, Erik II-347, III-457
Borruso, Giuseppe II-624, II-670
Boulil, Kamal II-373
Braga, Ana Cristina I-665
Brumana, Raffaella II-397
Bugs, Geisa I-477
Burgarelli, Denise I-649
Bustos, Víctor III-607
- Caiaffa, Emanuela II-532
Calazan, Rogério M. I-148
Caldas, Daniel Mendes I-675
Callejo, Miguel-Ángel Manso I-462
Camarda, Domenico II-425
Campobasso, Francesco II-71
Campos, Ricardo Silva I-635
Candori, Pietro I-316, I-432
Cannatella, Daniele II-54
Cano, Marcos Daniel III-743
Cansian, Adriano Mauro IV-286
Carbonara, Sebastiano II-128
Cardoso, João M.P. IV-217
Carmo, Rafael IV-444

- Carneiro, Joubert C. Lima e Tiago G.S. II-302
- Carpené, Michele I-345
- Carvalho, Luis Paulo da Silva II-181
- Carvalho, Maria Sameiro III-30, III-187
- Casado, Leocadio G. III-119, III-159
- Casado, Leocadio Gonzalez I-57
- Casas, Giuseppe B. Las II-466, II-640, II-686
- Casavecchia, Piergiorgio I-331
- Castro, Patrícia F. IV-379
- Cavalcante, Gabriel D. IV-314
- Cecchi, Marco I-345
- Cecchini, Arnaldo II-481, II-492
- Ceppi, Claudia II-517
- Cermignani, Matteo I-267
- Cerreta, Maria II-54, II-168, II-653
- Chanet, Jean-Pierre II-373
- Charão, Andrea Schwertner IV-404
- Cho, Yongyun IV-613, IV-622
- Cho, Young-Hwa IV-543
- Choe, Junseong III-324
- Choi, Hong Jun IV-602
- Choi, Jae-Young IV-543
- Choi, Jongsun IV-613
- Choi, Joonsoo I-214
- Choo, Hyunseung III-259, III-283, III-324
- Chung, Tai-Myoung III-376
- Ci, Song III-297
- Cicerone, Serafino I-267
- Ciloglugil, Birol III-550
- Cioquetta, Daniel Souza IV-16
- Clarke, W.A. IV-157
- Coelho, Leandro I-29
- Coletti, Cecilia I-738
- Conrado, Merley da Silva III-618
- Corea, Federico-Vladimir Gutiérrez I-462
- Coscia, José Luis Ordiales IV-29
- Costa, M. Fernanda P. III-57, III-103
- Costantini, Alessandro I-345, I-401, I-417
- Crasso, Marco IV-29, IV-234, IV-484
- Crawford, Broderick III-607
- Crocchianti, Stefano I-417
- Cuca, Branka II-397
- Cui, Xiaohui IV-646
- Cunha, Jácome IV-202
- da Luz Rodrigues, Francisco Carlos III-657
- Danese, Maria III-512
- Dantas, Sócrates de Oliveira I-228
- da Silva, Paulo Caetano II-181
- Daskalakis, Vangelis I-304
- de Almeida, Ricardo Aparecido Perez IV-470, IV-560
- de Avila, Ana Maria H. III-743
- de By, Rolf A. II-286
- de Carvalho, Andre Carlos P.L.F. III-562
- de Carvalho Jr., Osmar Abílio III-657
- Decker, Hendrik IV-170
- de Costa, Evandro Barros III-714
- de Deus, Raquel Faria II-565
- de Felice, Annunziata II-1
- de Geus, Paulo Lício IV-274, IV-302, IV-314
- Delgado del Hoyo, Francisco Javier I-529
- Dell'Orco, Mauro II-44
- de Macedo Mourelle, Luiza I-101, I-113, I-136, I-148
- de Magalhães, Jonathas José III-714
- De Mare, Gianluigi II-27
- Dembogurski, Renan I-228
- de Mendonça, Rafael Mathias I-136
- de Miranda, Péricles B.C. III-562
- de Oliveira, Isabela Liane IV-286
- de Oliveira, Wellington Moreira I-561
- de Paiva Oliveira, Alcione I-561
- Deris, Mustafa Mat I-87, IV-340
- De Santis, Fortunato III-481
- Désidéri, Jean-Antoine IV-418
- de Souza, Cleyton Caetano III-714
- de Souza, Éder Martins III-657
- de Souza, Renato Cesar Ferreira I-502
- de Souza Filho, José Luiz Ribeiro I-228, II-712
- De Toro, Pasquale II-168
- Dias, Joana M. III-1
- Dias, Luis III-133
- do Nascimento, Gleison S. IV-67
- Donato, Carlo II-624
- do Prado, Hércules Antonio III-631, III-657
- dos Anjos, Eudisley Gomes IV-132
- dos Santos, Jefersson Alex I-620

- dos Santos, Rafael Duarte Coelho IV-274, IV-302
- dos Santos, Rodrigo Weber I-635, I-649, I-691, I-707
- dos Santos Soares, Michel IV-1, IV-16
- e Alvelos, Filipe Pereira III-30
- El-Attar, Mohamed IV-258
- Elish, Mahmoud O. IV-258
- El-Zawawy, Mohamed A. III-592, IV-83
- Engemaier, Rita II-414
- Eom, Young Ik III-227, III-238, III-272
- Epicoco, Italo I-44
- Esmael, Bilal IV-392
- Ezzatti, Pablo IV-530
- Falcinelli, Stefano I-316, I-331, I-387, I-432
- Falcone, Roberto II-508
- Fanizzi, Annarita II-71
- Farage, Michèle Cristina Resende I-675
- Farantos, C. Stavros I-304
- Farias, Matheus IV-444
- Fechine, Joseana Macêdo III-714
- Fedel, Gabriel de S. I-620
- Felino, António I-665
- Fernandes, Edite M.G.P. III-57, III-72, III-103
- Fernandes, Florbela P. III-103
- Fernandes, João P. IV-202, IV-217
- Ferneda, Edilson III-631, III-657
- Ferreira, Ana C.M. III-147
- Ferreira, Brigida C. III-1
- Ferreira, Manuel III-174
- Ferroni, Michele I-358
- Fichtelmann, Bernd II-347, III-457
- Fidêncio, Érika II-302
- Figueiredo, José III-133
- Filho, Dario Simões Fernandes IV-274, IV-302
- Filho, Jugurta Lisboa I-561
- Fiorese, Adriano II-234
- Fonseca, Leonardo G. I-125
- Formosa, Saviour II-609
- Formosa Pace, Janice II-609
- Fort, Marta I-253
- França, Felipe M.G. I-101
- Freitas, Douglas O. IV-470
- Fruhwrith, Rudolf K. IV-392
- García, I. III-119
- García, Immaculada I-57
- Garrigós, Irene IV-116
- Gasior, Wade IV-646
- Gavrilova, Marina I-188
- Gentili, Eleonora III-539
- Geraldes, Carla A.S. III-187
- Gervasi, Osvaldo IV-457
- Ghandehari, Mehran II-194
- Ghazali, Rozaida I-87
- Ghiselli, Antonia I-345
- Ghizoni, Maria Luísa Amarante IV-588
- Girard, Luigi Fusco II-157
- Gomes, Ruan Delgado IV-132
- Gomes, Tiago Costa III-30
- Gonschorek, Julia II-208, II-220
- Gonzaga de Oliveira, Sanderson Lincohn I-172, I-198, I-610
- Görlich, Markus I-15
- Greco, Ilaria II-548
- Grégio, André Ricardo Abed IV-274, IV-286, IV-302
- Guardia, Hélio C. IV-560
- Gupta, Pankaj III-87
- Hahn, Kwang-Soo I-214
- Haijema, Rene III-45
- Han, Jikwang III-217
- Han, JungHyun III-272
- Han, Yanni III-297
- Handaga, Bana IV-340
- Hasan, Osman III-419
- Hashim, Rathiah II-728
- Hendrix, Eligius M.T. I-57, III-45, III-119, III-159
- Heo, Jaewee I-214
- Hong, Junguye III-324
- Huang, Lucheng I-447
- Ibrahim, Rosziati IV-353, IV-364
- Igounet, Pablo IV-530
- Ikhu-Omoregbe, Nicholas IV-248
- Im, Illkyun IV-543
- Imtiaz, Sahar III-339
- Inceoglu, Mustafa Murat III-550
- Iochepe, Cirano IV-67
- Ipbuker, Cengizhan III-471
- Ivánová, Ivana II-286
- Izkara, Jose Luis I-529

- Jeon, Jae Wook III-311
 Jeon, Woongryul III-391
 Jeong, Jongpil IV-543
 Jeong, Soonmook III-311
 Jino, Mario IV-274, IV-302
 Jorge, Eduardo IV-444
 Jung, Sung-Min III-376
- Kalsing, André C. IV-67
 Kang, Min-Jae III-217
 Karimipour, Farid II-194
 Kasprzak, Andrzej IV-514, IV-576
 Kaya, Sinasi III-471
 Khalid, Noor Elaiza Abdul II-728
 Khan, Salman H. III-339
 Khan, Yasser A. IV-258
 Khanh Ha, Nguyen Phan III-324
 Kim, Cheol Hong IV-602
 Kim, Hakhyun III-391
 Kim, Iksu IV-622
 Kim, Jeehong III-227, III-238, III-272
 Kim, Junho I-214
 Kim, Young-Hyuk III-248
 Kischinhevsky, Mauricio I-610
 Kluge, Mario II-386
 Knop, Igor I-707
 Komati, Karin S. II-739
 Kopeliovich, Sergey I-280
 Kosowski, Michał IV-514
 Koszalka, Leszek IV-576
 Koyuncu, Murat IV-234
 Kwak, Ho-Young III-217
 Kwon, Keyho III-311
 Kwon, Ki-Ryong IV-434
 Kwon, Seong-Geun IV-434
- Ladeira, Pitter Reis II-548
 Laganà, Antonio I-292, I-345, I-358,
 I-371, I-387, I-401, I-417
 Lago, Noelia Faginas I-387
 Laguna Gutiérrez, Víctor Antonio
 III-618
 Lanorte, Antonio III-481, III-512
 Lanza, Viviana II-686
 Lasaponara, Rosa III-481, III-497,
 III-512
 Le, Duc Tai III-259
 Lederer, Daniel II-263
 Le Duc, Thang III-259
 Lee, Dong-Young III-368, III-376
- Lee, Eung-Joo IV-434
 Lee, Hsien-Hsin IV-602
 Lee, Jae-Gwang III-248
 Lee, Jae-Kwang III-248
 Lee, Jae-Pil III-248
 Lee, Jongchan IV-613
 Lee, Junghoon III-217
 Lee, Kwangwoo III-391
 Lee, Sang Joon III-217
 Lee, Suk-Hwan IV-434
 Lee, Yunho III-391
 Leonel, Gildo de Almeida II-712
 Leonori, Francesca I-331
 Li, Yang III-297
 Lim, Il-Kwon III-248
 Lima, Priscila M.V. I-101
 Lin, Tao III-297
 Liu, Yi IV-100
 Lobarinhas, Pedro III-202
 Lobosco, Marcelo I-675, I-691, I-707
 Loconte, Pierangela II-517
 Lomba, Ricardo III-202
 Lombardi, Andrea I-387
 Lopes, Maria do Carmo III-1
 Lopes, Paulo IV-217
 Lou, Yan I-447
 Lubisco, Giorgia II-517
 Luiz, Alfredo José Barreto III-657
- Ma, Zhiyi IV-100
 Macedo, Gilson C. I-691, I-707
 Maffioletti, Sergio I-401
 Maleki, Behzad III-647
 Mancini, Francesco II-517
 Mangialardi, Giovanna II-116
 Manuali, Carlo I-345
 Marcondes, Cesar A.C. IV-470
 Marghany, Maged III-435, III-447
 Marimbaldo, Francisco-Javier Moreno
 I-462
 Marinho, Euler Horta IV-632
 Martins, Luís B. III-147
 Martins, Pedro IV-217
 Martucci, Isabella II-1
 Marucci, Alessandro II-532
 Marwala, T. IV-157
 Marwedel, Peter I-15
 Marzuoli, Annalisa I-723
 Mashkoor, Atif III-419
 Masini, Nicola III-497

- Mateos, Cristian IV-29, IV-234, IV-484
 Mazhar, Aliya III-368
 Mazón, Jose-Norberto IV-116
 McAnally, William H. II-578, II-589
 Medeiros, Claudia Bauzer I-620
 Mehlawat, Mukesh Kumar III-87
 Meira Jr., Wagner I-649
 Mele, Roberta II-653
 Melo, Tarick II-302
 Messine, F. III-119
 Miao, Hong I-447
 Milani, Alfredo III-528, III-539
 Min, Changwoo III-227, III-238
 Min, Jae-Won III-376
 Misra, A.K. IV-157
 Misra, Sanjay IV-29, IV-147, IV-234,
 IV-248
 Miziolek, Marek IV-514
 Mocavero, Silvia I-44
 Mohamad, Kamaruddin Malik IV-353
 Mohamed Elsayed, Samir A. I-161
 Monfroy, Eric III-607
 Monteserin, Ariel III-698
 Montrone, Silvestro II-102
 Moreira, Adriano II-450
 Moreira, Álvaro IV-67
 Moscato, Pablo I-71
 Moschetto, Danilo A. IV-470
 Müller, Heinrich I-15
 Mundim, Kleber Carlos I-432
 Mundim, Maria Suelly Pedrosa I-316
 Mundim, Maria Suely Pedrosa I-432
 Munir, Ali III-352, III-368
 Murgante, Beniamino II-640, II-670,
 III-512
 Murri, Riccardo I-401
 Musaoglu, Nebiye III-471

 Nabwey, Hossam A. II-316, II-358
 Nakagawa, Elisa Yumi III-576
 Nalli, Danilo I-292
 Nawi, Nazri Mohd I-87
 Nedjah, Nadia I-101, I-113, I-136, I-148
 Nema, Jigyasu III-528
 Neri, Igor IV-457
 Nesticò, Antonio II-27
 Neves, Brayan II-302
 Nguyên, Toàn IV-418
 Niu, Wenjia III-297
 Niyogi, Rajdeep III-528

 Nolè, Gabriele III-512
 Nunes, Manuel L. III-147

 O'Kelly, Morton E. II-249
 Oliveira, José A. III-133
 Oliveira, Rafael S. I-649
 Oreni, Daniela II-397
 Ottomanelli, Michele II-44

 Pacifici, Leonardo I-292, I-371
 Pádua, Clarindo Isaías P.S. IV-51
 Pádua, Wilson IV-51
 Pallottelli, Simonetta I-358
 Panaro, Simona II-54
 Pandey, Kusum Lata IV-147
 Paolillo, Pier Luigi II-331
 Park, Changyong III-283
 Park, Gyung-Leen III-217
 Park, Junbeom III-283
 Park, Sangjoon IV-613
 Park, Young Jin IV-602
 Parvin, Hamid III-647
 Parvin, Sajad III-647
 Pathak, Surendra II-589
 Pauls-Worm, Karin G.J. III-45
 Peixoto, Daniela C.C. IV-51
 Peixoto, João II-450
 Pepe, Monica II-397
 Perchinunno, Paola II-88, II-102
 Pereira, Gilberto Corso I-491
 Pereira, Guilherme A.B. III-133, III-187
 Pereira, Óscar Mortágua III-682
 Pereira, Tiago F. I-240
 Pessanha, Fábio Gonçalves I-113
 Pigozzo, Alexandre B. I-691, I-707
 Pimentel, Dulce II-565
 Pingali, Keshav I-1
 Pinheiro, Marcello Sandi III-631
 Pirani, Fernando I-316, I-387, I-432
 Piscitelli, Claudia II-517
 Poggioni, Valentina III-539
 Pol, Maciej IV-576
 Pollino, Maurizio II-532
 Poma, Lourdes P.P. IV-470
 Pontrandolfi, Piergiuseppe II-686
 Poplin, Alenka I-491
 Pozniak-Koszalka, Iwona IV-576
 Pradel, Marilys II-373
 Prasad, Rajesh IV-147
 Prieto, Iñaki I-529

- Proma, Wojciech IV-576
 Prudêncio, Ricardo B.C. III-562
- Qadir, Junaid III-352
 Qaisar, Saad Bin III-339, III-352,
 III-407
 Quintela, Bárbara de Melo I-675, I-691,
 I-707
- Ragni, Mirco I-723
 Raja, Haroon III-368, III-407
 Rajasekaran, Sanguthevar I-161
 Rak, Jacek IV-498
 Ramiro, Carla I-29
 Rampini, Anna II-397
 Rasekh, Abolfazl II-275
 Re, Nazzareno I-738
 Renhe, Marcelo Caniato II-712
 Resende, Rodolfo Ferreira IV-632
 Rezende, José Francisco V. II-302
 Rezende, Solange Oliveira III-618
 Ribeiro, Hugo IV-202
 Ribeiro, Marcela Xavier III-667, III-743
 Riveros, Carlos I-71
 Rocha, Ana Maria A.C. III-57, III-72,
 III-147
 Rocha, Bernardo M. I-649
 Rocha, Humberto III-1
 Rocha, Jorge Gustavo I-571
 Rocha, Maria Célia Furtado I-491
 Rocha, Pedro Augusto F. I-691
 Rodrigues, António M. II-565
 Romani, Luciana A.S. III-743
 Rosi, Marzio I-316, I-331
 Rossi, Elda I-345
 Rossi, Roberto III-45
 Rotondo, Francesco I-545
 Ruiz, Linnyer Beatrys IV-588
- Sad, Dhiego Oliveira I-228
 Salles, Evandro O.T. II-739
 Salles, Ronaldo M. IV-326
 Salvatierra, Gonzalo IV-484
 Sampaio-Fernandes, João C. I-665
 Samsudin, Nurnabilah II-728
 Sanches, Silvio Ricardo Rodrigues
 II-699
 Sanjuan-Estrada, Juan Francisco I-57
 Santos, Aduino IV-588
 Santos, Maribel Yasmina III-682
 Santos, Marilde Terezinha Prado
 III-667, III-743
 Santos, Teresa II-565
 Sarafian, Haiduke I-599
 Saraiva, João IV-202, IV-217
 Sarcinelli-Filho, Mario II-739
 Schirone, Dario Antonio II-1, II-17,
 II-88
 Sciberras, Elaine II-609
 Scorza, Francesco II-640
 Selicato, Francesco I-545, II-517
 Selicato, Marco II-144
 Sellarès, J. Antoni I-253
 Sertel, Elif III-471
 Shaaban, Shaaban M. II-316, II-358
 Shah, Habib I-87
 Shukla, Mukul IV-157
 Shukla, Ruchi IV-157
 Silva, António I-571
 Silva, João Tácio C. II-302
 Silva, José Eduardo C. I-240
 Silva, Rodrigo I-228
 Silva, Rodrigo M.P. IV-326
 Silva, Roger Correia I-228
 Silva, Valdinei Freire da II-699
 Silva Jr., Luneque I-113
 Silvestre, Eduardo Augusto IV-1
 Simões, Flávio O. I-240
 Simões, Paulo II-234
 Singh, Gaurav II-286
 Skouteris, Dimitris I-331
 Soares, Carlos III-562
 Song, Hokwon III-227, III-238
 Song, Taehoun III-311
 Soravia, Marco II-599
 Soto, Ricardo III-607
 Souza, Cleber P. IV-314
 Stanganelli, Marialuce II-599
 Stankute, Silvija II-439
- Tajani, Francesco II-27
 Tasso, Sergio I-358, IV-457
 Tavares, Maria Purificação I-665
 Teixeira, Ana Paula III-17
 Teixeira, José Carlos III-174, III-202
 Teixeira, Senhorinha F.C.F. III-147,
 III-202
 Tentella, Giorgio I-417
 Thom, Lucinéia IV-67

- Thonhauser, Gerhard IV-392
 Tilio, Lucia II-466, II-686
 Timm, Constantin I-15
 Tori, Romero II-699
 Torkan, Germano II-17
 Torre, Carmelo Maria I-583, II-116,
 II-144, II-157
 Traina, Agma J.M. III-743
 Treadwell, Jim IV-646
 Tricaud, Sebastien IV-314
 Trofa, Giovanni La II-144
 Trunfio, Giuseppe A. II-481, II-492
 Tsoukiàs, Alexis II-466
 Tyrallová, Lucia II-208, II-220

 Usera, Gabriel IV-530

 Vafaeinezhad, Ali Reza II-275
 Vargas-Hernández, José G. I-518
 Varotsis, Constantinos I-304
 Vaz, Paula I-665
 Vecchiocattivi, Franco I-316, I-432
 Vella, Flavio IV-457
 Verdicchio, Marco I-371
 Verma, Shilpi III-87
 Versaci, Francesco I-1
 Vieira, Marcelo Bernardes I-228, II-712

 Vieira, Wesley IV-444
 Vyatkina, Kira I-280

 Walkowiak, Krzysztof IV-498, IV-514
 Wang, Hao III-283
 Wang, Kangkang I-447
 Weichert, Frank I-15
 Won, Dongho III-391
 Wu, Feifei I-447

 Xavier, Carolina R. I-635
 Xavier, Micael P. I-691
 Xexéo, Geraldo B. IV-379
 Xu, Yanmei I-447
 Xu, Yuemei III-297

 Yanalak, Mustafa III-471

 Zaldívar, Anibal IV-116
 Zenha-Rela, Mário IV-132
 Zhang, Tian IV-100
 Zhang, Xiaokun IV-100
 Zhang, Yan IV-100
 Zhao, Xuying IV-100
 Zito, Romina I-583
 Zunino, Alejandro IV-29, IV-234,
 IV-484